

METALS HANDBOOK



VOL. 9
FRACTOGRAPHY AND ATLAS OF FRACTOGRAPHY

8th EDITION

IUPUI
UNIVERSITY LIBRARIES
COLUMBUS CENTER
COLUMBUS, IN 47201

METALS HANDBOOK, eighth edition

- Vol. 1. Properties and Selection of Metals (1961)
 - Vol. 2. Heat Treating, Cleaning and Finishing (1964)
 - Vol. 3. Machining (1967)
 - Vol. 4. Forming (1969)
 - Vol. 5. Forging and Casting (1970)
 - Vol. 6. Welding and Brazing (1971)
 - Vol. 7. Atlas of Microstructures of Industrial Alloys (1972)
 - Vol. 8. Metallography, Structures and Phase Diagrams (1973)
 - Vol. 9. Fractography and Atlas of Fractographs (1974)
 - Vol. 10. Failure Analysis and Prevention (in preparation)
 - Vol. 11. Nondestructive Inspection (in preparation)
 - Vol. 12. Mechanical Testing (planned)
-

PRINCIPAL SUBJECTS

Fractography

Introduction and historical background	1
Preparation and preservation of fracture specimens	9
Photography of fractured parts and fracture surfaces	11
Special techniques in fractography by light microscopy	24
Fractographic features revealed by light microscopy	27
Interpretation of light-microscope fractographs	36
The scanning electron microscope and its application to fractography	49
The transmission electron microscope and its application to fractography	54
Comparison of scanning and transmission electron microscopes for fractography	63
Interpretation of scanning-electron-microscope fractographs	64
Interpretation of transmission-electron-microscope fractographs	79
Discontinuities leading to fracture that are revealed by fractography	93
Use of fractography for purposes other than failure analysis	103
Use of fractography for failure analysis	106

Atlas of Fractographs

Light-microscope fractographs at low magnification	129
Light-microscope fractographs at high magnification	139
Scanning-electron-microscope (SEM) fractographs	161
Comparison of SEM and TEM stereofractographs	281
Transmission-electron-microscope (TEM) fractographs from replicas	297
Failure-analysis fractographs	377

METALS HANDBOOK

8th Edition

VOL. 9

Fractography and Atlas of Fractographs

*prepared under the direction of the
ASM HANDBOOK COMMITTEE*

John A. Fellows
Chairman of all Volume 9 committees and
Principal Technical Editor of Volume 9

Howard E. Boyer, Editor
William J. Carnes, Managing Editor—Copy and Production

Senior Editors:
Hugh Baker, Edward A. Durand,
Philip D. Harvey and Paul M. Unterweiser
Associate Editor: Helen Lawton Waldorf

Assistant Editors:
Helen V. Bukovics and Craig W. Kirkpatrick

Margaret W. Chevalier, Manager—Production Art
Jack W. Kothera, Assistant Manager—Production Art

Illustrators:
Charlene M. Christopher, Sandra L. Craig,
Richard J. Czentorycki and William C. Seamon



AMERICAN SOCIETY FOR METALS

Metals Park, Ohio 44073

TA
459
.A5
1961
V. 9

IUPUI
UNIVERSITY LIBRARIES
COLUMBUS CENTER
COLUMBUS, IN 47201

Copyright © 1974

BY THE
AMERICAN SOCIETY FOR METALS

All rights reserved

No part of this book may be reproduced, stored in a retrieval system, or transmitted, in any form or by any means, electronic, mechanical, photocopying, recording, or otherwise, without the prior written permission of the publisher.

First printing, August 1974

Nothing contained in the Metals Handbook is to be construed as a grant of any right of manufacture, sale, or use in connection with any method, process, apparatus, product, or composition, whether or not covered by letters patent or registered trade mark, nor as a defense against liability for the infringement of letters patent or registered trade mark.

Library of Congress Catalog Card Number: 27-12046

PRINTED IN THE UNITED STATES OF AMERICA

MEMBERS OF ASM HANDBOOK COMMITTEE (1973-1974)

GEORGE J. SHUBAT
CHAIRMAN (1972-)
Diamond Chain Co.
(Member, 1966-)

MICHAEL B. BEVER
VICE CHAIRMAN (1972-)
Massachusetts Institute of Technology
(Member, 1965-)

HOWARD E. BOYER
SECRETARY (1973-)
Editor - Metals Handbook
American Society for Metals

DONALD R. BETNER (1974-) <i>General Motors Corp.</i>	HERMAN D. GREENBERG (1972-) <i>Westinghouse Electric Corp.</i>	LYNN G. ROWELLS (1972-) <i>Sears, Roebuck & Co.</i>
HAROLD BOGART (1972-) <i>Ford Motor Co.</i>	J. A. HILDEBRANDT (1974-) <i>Clark Equipment Co.</i>	ROBERT C. RUHL (1971-) <i>Chase Brass & Copper Co.</i>
PRICE B. BURGESS (1973-) <i>Hayes-Albion Corp.</i>	F. L. JAMIESON (1974-) <i>Steel Co. of Canada</i>	EDWARD I. SALKOVITZ (1973-) <i>Office of Naval Research</i>
HENRY E. COLLINS (1973-) <i>TRW, Inc.</i>	JAMES F. KRIEG (1971-1974) <i>McDonnell Douglas Corp.</i>	O. G. SAUNDERS (1971-1974) <i>Hobart Manufacturing Co.</i>
E. PHILIP DAHLBERG (1974-) <i>Universal Oil Products Co.</i>	HENRY P. LANGSTON (1973-) <i>Hamilton Standard</i>	GERALD M. SLAUGHTER (1974-) <i>Union Carbide Corp.</i>
H. C. DILL (1971-1974) <i>Hughes Tool Co.</i>	GUNVANT N. MANIAR (1974-) <i>Carpenter Technology Corp.</i>	CHARLES O. SMITH (1973-) <i>University of Detroit</i>
W. G. FASSNACHT (1972-) <i>Bendix Corp.</i>	EDWARD W. O'BRIEN (1971-1974) <i>Oklahoma Steel Castings Co.</i>	RAYMOND WARD (1972-) <i>General Electric Co.</i>
GLENN A. FRITZLEN (1973-) <i>Cabot Corp.</i>		DANIEL S. ZAMBORSKY (1971-1974) <i>Warner & Swasey Co.</i>

PREVIOUS CHAIRMEN OF ASM HANDBOOK COMMITTEE

R. S. ARCHER* (1940-1942) (Member, 1937-1942)	J. F. HARPER* (1923-1926) (Member, 1923-1926)	W. J. MERTEN* (1927-1930) (Member, 1923-1933)
L. B. CASE* (1931-1933) (Member, 1928-1933)	C. H. HERTY, JR.* (1934-1936) (Member, 1930-1936)	N. E. PROMISEL (1955-1961) (Member, 1954-1963)
E. O. DIXON* (1952-1954) (Member, 1947-1955)	J. B. JOHNSON (1948-1951) (Member, 1944-1951)	W. A. STADTLER (1968-1972) (Member, 1962-1972)
R. L. DOWDELL* (1938-1939) (Member, 1935-1939)	R. W. E. LEITER* (1962-1963) (Member, 1955-1958, 1960-1964)	D. J. WRIGHT (1964-1965) (Member, 1959-1967)
J. P. GILL* (1937) (Member, 1934-1937)	G. V. LUERSEN* (1943-1947) (Member, 1942-1947)	J. EDWARD DONNELLAN (Secretary, 1924-1945)
J. D. GRAHAM (1965-1968) (Member, 1961-1970)		TAYLOR LYMAN* (Secretary, 1945-1973)

*Deceased

OFFICERS AND TRUSTEES OF THE AMERICAN SOCIETY FOR METALS

JOSEPH F. LIBSCH, PRESIDENT AND TRUSTEE
Lehigh University

ALBERT R. FAIRCHILD, SECRETARY AND TRUSTEE
Albert R. Fairchild & Associates

DEAN K. HANINK, VICE PRESIDENT AND TRUSTEE
General Motors Corp.

ROBERT H. SHOEMAKER, TREASURER
Kolene Corp.

TRUSTEES

WILLIAM D. MANLY (Past President)
Cabot Corp.

DAVID KRASHES
Massachusetts Materials Research, Inc.

NICHOLAS P. MILANO
Wallace-Murray Corp.

SOL L. GERTSMAN
*Department of Energy,
Mines and Resources (Ottawa)*

ABRAHAM HURLICH
General Dynamics Corp.

ROBERT F. HOCHMAN
*Georgia Institute of
Technology*

GEORGE H. SCHUBERT
Schubert Heat Treating, Inc.

RICHARD H. VAN PELT
Caterpillar Tractor Co.

MANAGING DIRECTOR: ALLAN RAY PUTNAM

Contributors to This Volume

Numbers refer to the pages where contributors are credited in the volume. Many members and friends of ASM not listed here have supplied information or reviewed proofs for this volume.

Franklin Alex, 106
M. A. Arkoosh, 128
David B. Ballard, 127, 128
R. D. Barer, 127
Cedric D. Beachem, 49, 127, 128
Roy E. Beal, 127, 128
Steven J. Berman, 127
M. Dilip Bhandarkar, 127, 128
A. S. Brar, 127
Edward V. Bravenec, 127
W. E. Brower, Jr., 128
H. C. Burghard, Jr., 106
J. J. Carden, 128
Frank L. Carr, 1, 127, 128
Robert A. Clark, 127
T. M. Clarke, 1
Thomas J. Connare, 127
J. F. Cotton, 127
T. W. Crooker, 128
T. R. Croucher, 128
E. Philip Dahlberg, 49, 128
T. M. Devine, 128
Eugene DiCesare, 127
Dwight R. Diercks, 127
D. J. Duquette, 127, 128
A. J. Edwards, 128
Nicholas Fiore, 127, 128
M. C. Flemings, 127, 128
Stephen Floreen, 127, 128
John H. Frome, Jr., 127
R. P. Gamble, 127, 128
William E. Gardner, 49, 127
M. Gell, 127, 128
W. W. Gerberich, 127
Ronald Gibala, 127
William A. Goering, 127
R. J. Goode, 128
R. A. Grange, 127, 128
Mary Ellen Gulden, 127
Henry T. Hadley, 127
E. G. Hamburg, 127
H. W. Hayden, 128
P. L. Hemmings, 127

Morse Hill, 1
William L. Holshouser, 106, 127, 128
W. A. Horwood, 127, 128
Michael Hovan, 127
James Lee Hubbard, 127
Abraham Hurlich, 127
O. T. Inal, 128
Frank L. Jamieson, 127
Walter L. Jensen, 49
Om Johari, 49, 127, 128
R. H. Jones, 127, 128
R. W. Judy, Jr., 128
Yoshiaki Kanai, 127
W. A. Keegan, 127
V. Kerlins, 128
Joseph A. Kies, 106
J. Kilpatrick, 98, 99
G. J. W. Kor, 127, 128
Victor A. Kortesoja, 127
K. G. Kreider, 127, 128
R. F. LaCroix, 127
E. A. Lange, 128
W. T. Lankford, Jr., 127, 128
Frank R. Larson, 106, 128
E. A. Lauchner, 127, 128
D. Lee, 127, 128
D. F. Lentz, 127
W. Barry Lisagor, 127
Ronald J. Livak, 127
M. L. Marx, 128
Steven Matthews, 127
R. D. Mayner, 128
James L. McCall, 1
Frank A. McClintock, 106
A. J. McEvily, 106
J. Corey McMillan, 1
Dale Meyn, 49, 127, 128
R. E. Morey, 128
L. E. Murr, 49, 127, 128
John B. Naslanic, 1, 127
Howard G. Nelson, 127, 128
Norman A. Nielsen, 106
F. E. Organ, 127, 128
E. R. Parker, 127, 128

Elio Passaglia, 127
George E. Pellissier, 49
Regis M. Pelloux, 49, 127, 128
Austin Phillips, 127, 128
André Pineau, 127, 128
K. M. Prewo, 127, 128
G. Rai, 127
G. A. Ratz, 127
R. A. Rawe, 128
A. Rukwied, 128
Emil Rusnak, 1
Stephen L. Scheier, 127
J. A. Scott, 128
Robert E. Shaffer, 127
S. N. Singh, 128
R. Patrick Skow, 127
Robert D. Sloan, 127, 128
J. S. Stein, 128
W. H. Steinman, 127
R. E. Stoltz, 127, 128
Leonard Sudenfield, 127
E. G. Takacs, 127
R. L. Terchek, 128
A. S. Tetelman, 128
Gareth Thomas, 127
J. K. Tien, 127, 128
T. Tom, 127, 128
E. T. Turkdogan, 127, 128
Paul J. Valdez, 127
J. Van Den Avyle, 127
L. F. Van Swam, 127
Joseph M. Walsh, 127
William R. Warke, 1
J. L. Welker, 127
Robert W. White, 127
Bennett V. Whiteson, 49, 127, 128
William Wiebe, 106
D. P. Williams, 128
James C. Williams, 49
W. E. Wood, 127, 128
Donald J. Wulpi, 106, 127, 128
V. F. Zackay, 127, 128
Carl A. Zapffe, 1, 127

FOREWORD

THIS NINTH VOLUME of the 8th Edition of METALS HANDBOOK, "Fractography and Atlas of Fractographs", represents a systematic and comprehensive treatment of a relatively new body of knowledge whose utility and importance have gained wide recognition.

The scope of this volume is both innovative and far-reaching. The coverage afforded fractography encompasses all significant elements of this science. Such coverage is achieved in a collection of definitive articles on all major aspects of fractographic technique and interpretation. In addition, a 351-page atlas, containing 1816 fractographs and related representations of fractures, is made available for use by the reader as a supplement to the articles or as a guide when examining fracture surfaces in which he has a direct and immediate interest.

That it was decided to include a volume on fractography in the 8th Edition is a tribute to the technical judgment and foresight of the Handbook Committee, whose members are responsible for the over-all planning of each volume in the Handbook series. That so ambitious a plan has been carried to successful completion is a tribute to the talents and hard work of the author committees, other contributors and reviewers, and the editorial staff — who, collectively, have produced a worthy forerunner of the projected companion volume on failure analysis. To all these men and women, we express our sincere gratitude. To the METALS HANDBOOK program, we renew our pledge of continuing support.

JOSEPH F. LIBSCH
President, ASM

ALLAN RAY PUTNAM
Managing Director, ASM

P R E F A C E

THIS IS THE NINTH in a series of volumes that will supersede the single-volume 7th edition of METALS HANDBOOK and greatly enlarge its scope.

The present volume completes a trilogy, inaugurated with the publication of Volume 7, whose principal subjects are the structure of metals and, in a practical vein, the significance of structure to the user of metals. Volume 7 offered a systematic introduction to these subjects via the medium of micrographs — 2821 in all — that comprised a unified atlas of microstructures of the whole range of major industrial alloys. Volume 8 followed, providing comprehensive coverage in the subject areas of metallographic techniques, the physical metallurgy of metal structures, and phase diagrams. Needed to complete the trilogy was a volume devoted exclusively to a new body of knowledge derived from examination and interpretation of features observed on the fracture surfaces of metals. With the publication of the present volume, that need has now been satisfied in a manner that emphasizes maximum usefulness to the reader.

That “Fractography and Atlas of Fractographs” is, as its title implies, essentially two books in one, is established in the following summary of its two sections — each of which complements the other.

Fractography. This 124-page section comprises 14 articles that, in addition to the text, present 107 line drawings or graphs, and 454 photographic illustrations of fracture surfaces and pertinent microstructural features. These articles were prepared by three committees of experts in fractography and related disciplines, serving under the chairmanship of John A. Fellows, who brought to this assignment the benefit of his many years of experience in industrial metallurgy and research, augmented by his special skills in planning and organization.

The first six articles contribute primarily to an understanding of the techniques in fractography by light microscopy and to the interpretation of light-microscope fractographs. However, other relevant aspects of light-microscope fractography are explored in these articles, including its history, the preparation and preservation of fracture specimens, and the application of photography. Of particular value both to seasoned practitioners and to beginners in fractographic techniques are the article on

special techniques by light microscopy, which describes the uses of replicas, fracture profiles and shadow casting, and the articles on fractographic features and the interpretation of light-microscope fractographs, which provide detailed and authoritative treatment of fundamental subjects.

It is generally conceded that the resurgence of engineering and scientific interest in fractography and the proliferation of practicing fractographers can largely be credited to the remarkable capabilities of the modern electron microscope. The impact of the electron microscope on the evolution of fractography and metallography in recent years may be compared to that of the light microscope on the emerging biological sciences of the 17th century — with one notable difference. Without benefit of photography, the capabilities of the early light microscope in exploring the microworld could not be shared visually with a mass audience. The electron microscope is not similarly circumscribed, nor is its utility limited to the laboratories that have access to one, although the number of such laboratories is increasing.

An article on the scanning electron microscope (SEM) and its application to fractography is the first of a series of five articles relating to the design and operation of electron microscopes, the application of the microscopes to fractography, the advantages and limitations of the two major types of electron microscopes, and the interpretation of electron-microscope fractographs. Early in the first of these articles, it is explained that the SEM is used at magnifications ranging from about 5 to 30,000 diameters, that its depth of field is about 300 times that of the light microscope, and that specimens can be tilted as much as 45° from the horizontal and still be in focus. When it is considered that the topography of most fracture surfaces is highly irregular, the capabilities of such an instrument in fractography are readily appreciated.

The transmission electron microscope (TEM), whose principle of operation is different from that of the SEM, shares essentially similar capabilities, except for certain inherent restrictions that are imposed on the specimens it can accommodate. These must be small enough to fit within a specimen-holder chamber, thin enough to be reasonably transparent to electrons, and varied enough in thickness

or density, or both, to provide adequate image contrast. As a consequence, the application of the TEM to the examination of fracture surfaces almost invariably requires the preparation of plastic, carbon, or conversion-oxide-film replicas of the surfaces. The technique of replica preparation, including the application of shadowing, is accorded extended treatment in the article "The Transmission Electron Microscope and Its Application to Fractography". The five-article series on electron-microscope fractography continues with a separate article comparing scanning and transmission electron microscopes for use in fractography, followed by articles that describe and illustrate the interpretation of fractographs produced with the aid of these instruments.

Following the articles on electron-microscope fractography is an article that illustrates and discusses the fractographic significance of features such as laps, seams, cracks, inclusions, porosity and other discontinuities that can lead to fracture. The interpretation of fractures involving such discontinuities often requires the use of the entire range of fractographic techniques.

Fractography is now widely employed in fundamental studies of fracture, as a tool in production-line evaluation of service-related properties, and as a diagnostic tool in failure analyses involving fractures. These and other uses of fractography are the subjects of the two articles that conclude the Fractography section of this volume. The use of fractography in failure analysis is often of most immediate and practical interest, and is the subject of the second of these two articles. This 19-page article provides an over-all view of all factors contributing to failure by fracture, including crack origin and crack-propagation path, loading, part configuration, dimensional requirements and service environment, and it relates each factor to fracture characteristics and analysis by fractography.

Atlas of Fractographs. The 351-page Atlas section is made up of six separate sections and contains 1816 illustrations, of which 1578 are light-microscope, SEM or TEM fractographs and the remainder

photographs, macrographs and micrographs that serve primarily to augment the information in the fractographs. The Atlas is by far the largest collection of fractographs ever assembled in a single volume; it is also the first to present a selection of stereofractographs for stereoscopic viewing by the larger technical community of nonspecialists. To facilitate stereoscopic viewing, a viewer is provided in the pocket on the inside back cover of this volume.

The Atlas is a product of careful and systematic planning. To help the user take full advantage of its contents, an instructive introduction to the Atlas (see page 125) was prepared to acquaint the user with the numbering system applied to illustrations, with the organization of the whole into six separate sections, with the arrangement of fractographs within each section, and with the listings of alloys (and, where applicable, components) on the title pages of each of the six sections. The introduction to the Atlas also presents two tables in which the distribution of the 1816 illustrations with respect to type of illustration and cause of fracture for various categories of alloys is accounted for.

The over-all plan and contents of the Atlas were designed with the needs and limitations of the general user in mind. His needs are expressed in the stated objective for preparing this Atlas: "... to provide the reader with a compilation of fractographs that are useful in trying to understand the causes, surface features, and mechanisms of fracture of industrial alloys." His limitations, it is assumed, arise from a limited knowledge of fractographs, their preparation, and their interpretation (this should be remedied by exposure to the Fractography section), and from lack of access to the more sophisticated equipment used by practicing fractographers — notably, the electron microscope. The user can be assured that the utility of this Atlas does not depend either on prior knowledge of fractography or on access to equipment more sophisticated than reasonably good eyesight and the stereo viewer provided with this volume.

HOWARD E. BOYER
Editor – Metals Handbook

Contents of Metals Handbook Volume 9

FRACTOGRAPHY

Introduction and Historical Background 1 to 9

Prehistoric experience with fracture	1
Fractography in the 16th to 18th centuries	2
Fractography in the 19th century	3
Fractography from 1900 to 1939	4
Microfractography rediscovered	6
Techniques for microfractography ..	6
Applications of microfractography ..	7
Correlation of fractographs with microstructure	7

Preparation and Preservation of Fracture Specimens 9 to 10

Care of metal fractures	9
Mechanical damage	9
Chemical (corrosion) damage	9
Coatings	9
Cleaning of metal fractures	9
Sectioning of a fracture	10
Opening secondary cracks	10
Effect of nondestructive inspection..	10

Photography of Fractured Parts and Fracture Surfaces 11 to 24

Visual examination	11
Setups for photography of fractured parts	11
Cameras	11
View cameras	11
Press-type cameras	12
35-mm single-lens reflex (SLR) cameras	12
Single-lens and twin-lens reflex cameras using roll film	12
Microscope systems	12
Lenses	13
Focusing	13
Lights	13
Lighting techniques	14
Lighting of etched sections	17
Lighting of highly reflective parts	17

Lighting of deeply etched specimens to show grain flow ...	17
Photography with ultraviolet illumination	17
Film	18
Exposures	18
Exposure meters	18
Light reflected from the subject ..	18
Light falling on the subject	19
Light level at the film plane	19
Exposure scales and computations ..	19
Test exposures	21
Film developing and printing	21
Printing procedures	22
Rapid printing processes	23
Stereo views	23
Auxiliary equipment	23

Special Techniques in Fractography by Light Microscopy..... 24 to 26

Replicas	24
Sectioning and study of fracture profiles	24
Shadow casting	25
Fracture-surface analysis	26
Etch pitting of fracture surfaces	26
Deep-field microscopes	26

Fractographic Features Revealed by Light Microscopy..... 27 to 35

Tensile-fracture surface marks in unnotched specimens	27
Cylindrical specimens	27
The fibrous zone	27
The radial zone	27
The shear-lip zone	28
Rectangular-section specimens	28
Chevron patterns	28
Woody fractures	29
Fatigue marks	29
Beach marks	29
Striations	30
Ratchet marks	30
Grain and cleavage facets	31
Secondary cracks	32

Discontinuities	32
Laps, seams and pits	32
Shrinkage and gas cavities	33
Hot tears	33
Weld imperfections	33
Inclusions; segregation	33
Dimples	33
Stress-corrosion cracking	35

Interpretation of Light- Microscope Fractographs..... 36 to 48

States of stress	36
Crack origins	38
Gross aspects of fractures	38
Clues to crack origins on fracture surfaces	38
Location of origins in impact-overload fractures	40
Location of origins in fatigue fractures	41
Location of origins in fractures caused by environment	42
Fractographic mapping to identify fracture origins	42
Fracture progress	42
Fracture changes during crack propagation	44
Changes caused by local differences in structure	44
Changes caused by changes in stress-intensity factor	44
Changes caused by altered environments	45
Changes caused by different stress states	47
Indeterminate fractures	48
Test fractures vs service fractures ...	48

The Scanning Electron Microscope and Its Application to Fractography..... 49 to 53

Principal features of scanning electron microscopes	49
Operation of scanning electron microscopes	50

The Scanning Electron Microscope and Its Application to Fractography (continued)

Modes of operation	50
Cathode-ray tubes	50
Vacuum system	50
Specimen stage; magnification	51
Specimen preparation	51
Stereography	51
Unique features	51
Attachments, accessories and auxiliary equipment	51
Spectrometers	51
Microprobe analyzers	52
Special stages	52
Transmission attachment	52
Cathodoluminescence	52
Solid-pair detector attachment	52
Production and viewing of SEM fractographs	53

The Transmission Electron Microscope and Its Application to Fractography..... 54 to 63

Transmission electron microscope ..	54
Microscope design; lens system ...	54
Specimens for transmission electron microscopy	54
Image quality	54
Intensity and contrast	55
Replicas of fracture surfaces	56
Cleaning of fracture surfaces for replication	56
Single-stage replicas	56
Thin single-stage plastic replicas ..	56
Thick single-stage plastic replicas ..	57
Single-stage, direct carbon replicas ..	58
Conversion-oxide-film replicas	58
Two-stage replicas	59
Shadowing of replicas	59
Coating of replicas	60
SEM vs TEM fractographs of different types of replicas	60
Location and orientation of replicas ..	60
Grids for indexing	60
Shadowing for indexing	61
Artifacts in replicas	61
Stereo viewing	63

Comparison of Scanning and Transmission Electron Microscopes for Fractography..... 63 to 64

Magnification	63
Resolution	63
Fidelity	63
Area of specimen covered	64

Interpretation of Scanning-Electron-Microscope Fractographs..... 64 to 78

Transgranular cleavage features	64
Tongues and microtwins	65
Cleavage-crack origins	65
Quasicleavage features	65
Dimples formed by microvoid coalescence	66
Tearing	68
Fatigue striations	68
Stage I of fatigue-fracture progress	68
Stage II of fatigue-fracture progress	69
Intergranular fracture	70
Features indicative of mixed mechanisms of fracture	71
Cleavage plus microvoid coalescence	71
Cleavage plus tearing	72
Cleavage plus fatigue-striation formation	72
Cleavage plus intergranular fracture	72
Microvoid coalescence plus tearing	73
Microvoid coalescence plus fatigue-striation formation	73
Microvoid coalescence plus intergranular fracture	74
Tearing plus fatigue-striation formation	74
Tearing plus intergranular fracture	74
Fatigue-striation formation plus intergranular fracture	75
Features of fractures resulting from chemical and thermal environments	75
High-temperature fractures	75
Stress-corrosion cracking and hydrogen embrittlement	76
Corrosion on fracture surfaces	78

Interpretation of Transmission-Electron-Microscope Fractographs..... 79 to 92

Transgranular fractures	79
Microvoid coalescence	79
Tearing	81
Cleavage	82
Quasicleavage	84
Fatigue	85
Intergranular fractures	89
Features of fractures resulting from chemical environments	90

Stress-corrosion cracking and hydrogen embrittlement	90
Corrosion fatigue	91
Embrittlement by liquid and solid metals	92
Corrosion products on fracture surfaces	92

Discontinuities Leading to Fracture That Are Revealed by Fractography..... 93 to 103

Laps, seams and cold shuts	93
Cracks	93
Inclusions	94
Stringers	98
Porosity	99
Segregation	100
Grain-boundary discontinuities	100
Unfavorable grain flow	103

Use of Fractography for Purposes Other Than Failure Analysis..... 103 to 105

Fracture-path studies	103
Deformation before and during fracture	104
Fracture-surface characteristics	104

Use of Fractography for Failure Analysis.. 106 to 124

Basic considerations in failure analysis	106
Loading	106
Material	106
Shape	106
Environment	106
Aspects of failure that can be resolved by fractography	106
Crack origin and crack-propagation path	106
Type of loading	107
Material of the part	109
Shape and surface of the part	109
Chemical and thermal environment	110
Change in fracture mechanism with size, shape and cross section of a part	112
Fractures by intergranular separation	112
Fractures resulting from corrosion ..	114
Service fractures	117
Growth rates of fatigue cracks	118

ATLAS OF FRACTOGRAPHS

Introduction..... 125 to 128

Objective	125
Organization and presentation	125
Distribution of content	126
Acknowledgments	126

Light-Microscope

Fractographs at Low Magnification..... 129 to 138

Carbon steel drive shaft of a marine tug	130
Carbon steel chassis frame bar; 1075 steel railroad rails	131
Low-carbon steel and low-alloy steel splined shafts	132
4340 steel piston rod and helicopter bolt	132
Steel armor plate (0.30% C, 3.65% Ni, 1.45% Cr)	133
Tool steels A4N and W1	133
Tool steels W2, L6 and S1	134
Tool steels T1 and M3, class 1	135
Stainless steels types 410, 431, 440C, 303(Se), 302B and 309	136
Stainless steel type 302	137
Aluminum alloy 355 cast turbo-supercharger impeller	137-138
Aluminum alloy 2024-T4	138
Brass ingot	138

Light-Microscope

Fractographs at High Magnification..... 139 to 160

Armco iron	140-142
Ship-plate steels	143
Carbon steel weld deposits	144
Stainless steels:	
Types 405 and 430	145-146
0.096% C, 22.14% Cr ferritic	146
Type 446	147-148
Ferrochromium alloys	148-149
Iron-silicon alloys	149-151
Aluminum alloy 7076-T6	152
Antimony	153
Bismuth	154
Antimony-bismuth alloys	155
Bismuth-zinc alloys	155
Vacuum-arc-cast molybdenum	156-157
Vacuum-arc-cast tungsten	158-159
Sintered tungsten powder compacts	159
Zinc	160

Scanning-Electron-Microscope (SEM)

Fractographs..... 161 to 280

Pure iron; iron with special additives; low-carbon irons;	
Armco iron	162-169
0.04 to 0.08% C steels	170-171

1015, 1020, 1021, 1022, 1025 and ASTM A36 steels	171-175
1042, 1050, 1060, 1080 and 1090 steels	176-183
1095 and 1115 steels	183
4070 steel	184
4130 steel	184-186
4140 steel	187
4340 steel	188-192
HY-180 steel	192
High-strength steel	193
300M steel	194-195
5155 steel	196
50100 and 52100 steels	197
Nitrided 7140 steel	198
8740 steel	199-201
Fe-3.9Ni and Fe-0.3Ni alloys	202
0.20C-1.0Mn-3.05Ni-1.65Cr-0.5Mo and 3.5Ni-1.5Cr-0.5Mo-0.1V steels	203
Fe-12Ni-0.5Ti alloy	204-205
18% Ni, grade 300, maraging steel	206-209
H11 tool steel	210-213
Fe-6.4Cr-3.2Ta alloy	214
Fe-6.2Ta alloy	214
0.18C-3.85Mo and 0.41C-4.2Mo steels	215
0.3C-0.6Mn-5.0Mo steel	216
0.4C-0.6Mn-5.0Mo and 0.42C-2.1Mo-5.2Co steels	217
0.43C-3.85Mo-9.0Co steel	218
13-8 PH stainless steel	219-221
17-7 PH stainless steel	222-223
Type 301 stainless steel	223
Type 304 stainless steel; 0.20C-2.0Mn-1.0Si-13.5Cr-8.8Ni-3.0Mo stainless steel	224
15.8Cr-12.5Ni and type 316L stainless steel	225
Alloys A-286 and Hastelloy X	225
Refractaloy 26 alloy	226
Alloy 718	227-229
U-700 alloy	230
Waspaloy alloy	231
MAR-M 200 alloy	231-232
IN-100 alloy	232-233
Alloy 713C	234
Duranickel alloy	235
Nickel 201	236
Aluminum casting alloys:	
333	237
356-T6	238-243
Wrought aluminum alloys 1100, 2014-T6, 2024-T4 and -T3	244-249
Wrought aluminum alloys 7075-T6 and -T651, and 7475-T6	249-261
67Al-33Cu eutectic alloy	262-263
Boron-fiber, Al-matrix and Ti-matrix (BORSIC) composites	264
Graphite-fiber, magnesium-matrix composite	265
99.999% copper	266-267
OFHC copper; free-machining copper (with Te)	268

Cu-2.5Be alloy; 64Cu-27Ni-9Fe alloy ..	269
Iridium wire and sheet	270
Lead-tin solders	270-272
Alloy HM21A (97Mg-2Th-1Mn)	272
TZM alloy (Mo-0.5Ti-0.08Zr)	272
Titanium alloy Ti-5Al-2.5Sn	273
Titanium alloy Ti-6Al-4V	273-279
Tungsten-fiber, silver-matrix composite	279
Zircaloy-2; Zircaloy-4	280

Comparison of SEM and TEM

Stereofractographs... 281 to 296

Plain carbon steel: impact fracture	282-283
0.65% C, 1.05% Mn steel: impact fracture	284
Class 612 (T2) high speed tool steel: impact fracture	285
4340 steel: tension-overload fracture; high-cycle fatigue fracture	286-287
Aluminum alloy 7075-T6: tension-overload fractures; low-cycle fatigue fracture; stress-corrosion fracture	288-293
Titanium alloy Ti-8Al-1Mo-1V: tension-overload fracture; high-cycle fatigue fracture; stress-corrosion fracture	294-296

Transmission-Electron-Microscope (TEM) Fractographs

From Replicas..... 297 to 376

Armco iron	298-299
Wrought iron	300
4130 steel	301
4140 steel	301
AMS 6434 steel	302-303
4315 steel	304
4340 steel	304-315
8740 steel	316-317
D-6ac steel	318
300M steel	318
1080 steel	318
Nitralloy G steel	319
9310 steel	319
Ductile iron	320
18% Ni maraging steel	320-321
Type 501 stainless steel	322-323
H11 tool steel	323-325
Type 410 stainless steel	326
Type 431 stainless steel	327
Type 633 (AM-350) stainless steel	328
13-8 PH stainless steel	328-330
17-4 PH stainless steel	330-331
Type 301 stainless steel	331
Type 302 stainless steel	331-333
Alloy 713LC	334

Table of Contents

Transmission-Electron-Microscope (TEM) Fractographs From Replicas (continued)

Alloy 713C	334-335
IN-100 nickel-base alloy	336
Alloy 718	336-339
Waspaloy	339-342
René 41 nickel-base alloy	343
L-605 cobalt-base alloy	343-345
U-700 nickel-base alloy	346-347
Alnico alloy	348
Aluminum casting alloys:	
319 (sand cast)	349
380 (die cast)	350-351
Wrought aluminum alloys:	
2018	352
2024-T3, -T851	352-353
7075-T6	354-361
7079-T6, -T651	362-363
Copper-2% Be alloy	364-365
Magnesium alloy AZ81A-T4	366
TZM molybdenum alloy	367
90% Ta-10% W alloy	367
Unalloyed titanium	368
Titanium alloys:	
Ti-5Al-2.5Sn; Ti-5Al-3Sn-2Mo-2V	369
Ti-6Al-4V	370-373
Ti-7Al-2Cb-1Ta	373
Ti-8Mn	374
Ti-13V-11Cr-4Al	374
Tungsten	375-376

Failure-Analysis

Fractographs.....	377 to 475
Armco iron; wrought iron	378
Galvanized steel	379
Low-carbon steel	379-380

1020 steel; cast 0.20% C steel	381-382
1030 steel	382
ASTM A515, grade 70, steel	383-385
1033 steel	386
1035 steel	387
1038 steel	388, 392
1039 steel	391
1040 steel	388-389
1041, 1041H, 10B41 (1541, 1541H, 15B41) steels	389-391, 393-394
T-2 nickel steel	393
Medium-carbon steel	394-395
11L40 steel; 1144 steel	396
1045 steel	397-403
1046 steel	402-404
1050 steel	405
1053 steel	406
1055 steel	407
1060 steel	407-409
10B62 (15B62) steel	408
1070 steel	409-411
High-carbon steel	410
1095 steel	411
4118 steel	412
4130 steel	413
4140 steel	414-417
4150 steel	415
0.26C-0.70Mn-0.8Ni-1.00Cr steel	418
D6B steel	419
AMS 6434 (4335 mod) steel	428
4340 steel	420-425, 427-433
High-strength low-alloy steel	426, 437
300M steel	434
4350 steel	434-435
4817 steel; 4820H steel	436
50B20 steel; 5046 steel	437
50B60 steel; 5132 steel	438
5135H steel	439
5145 steel	440
5160 steel	440-441
6150 steel	442
8617 steel	443
8620 steel	443-447
8640 steel	446-448
8645 steel	449
8650 steel	448
Ductile iron	450-451
Gray iron	451
Silcrome-1 steel	452
Type 410 stainless steel	452-453
Cast austenitic steel	454
13-8 PH stainless steel	454
15-5 PH stainless steel	454
Types 302, 304, 330 stainless steel	455
Aluminum casting alloy 218	456-457
Wrought aluminum alloys:	
2014-T6	458-461
2020-T651; 2024; 2024-T3, -T851	462
2025-T6	462-464
6061-T6; 7075-T6	465
7079-T6	465-467
7079-T651; 7106-T63; 7178-T6	467
Columbium; columbium alloy B-66 ..	468
99.999% Cu (Pd-coated); tough pitch copper; low-silicon bronze	468
Phosphor bronze C	468-469
80Cu-20Zn brass + 0.5% Sn	469
91-7-2 aluminum-silicon bronze	470
85-5-5-5 leaded red brass	470
60Cu-37.8Zn manganese bronze	471
48Cu-35Ni-11Sn-6Pb alloy	471
Titanium alloys:	
Ti-2Al-2Zr-2V-1Mo; Ti-2.5Al-16V	471
Ti-3Al	473
Ti-6Al-4V	472-474
Ti-7Al-2Cb-1Ta; Ti-7Al-1Mo-1V	474
Ti-7Al-3V; Ti-8Al-1Mo-1V	475
Tungsten	475

Some abbreviations and symbols used in this volume 476

INDEX..... 477 to 499

FRACTOGRAPHY

CONTENTS

Introduction and Historical Background	1
Preparation and Preservation of Fracture Specimens	9
Photography of Fractured Parts and Fracture Surfaces	11
Special Techniques in Fractography by Light Microscopy	24
Fractographic Features Revealed by Light Microscopy	27
Interpretation of Light-Microscope Fractographs	36
The Scanning Electron Microscope and Its Application to Fractography	49
The Transmission Electron Microscope and Its Application to Fractography	54
Comparison of Scanning and Transmission Electron Microscopes for Fractography	63
Interpretation of Scanning-Electron-Microscope Fractographs	64
Interpretation of Transmission-Electron-Microscope Fractographs	79
Discontinuities Leading to Fracture That Are Revealed by Fractography	93
Use of Fractography for Purposes Other Than Failure Analysis	103
Use of Fractography for Failure Analysis	106

Introduction and Historical Background

*By the ASM Committee on Fractography by Light Microscopy**

THE TERM "fractography" was coined in 1944 to describe the science of studying fracture surfaces, although fractures and fracture surfaces had been examined and studied for centuries as part of the art of metallurgy. The two chief metallurgical benefits of fractography are: (a) it is an important tool in failure analysis, and (b) it provides new information regarding the micromechanisms of fracture and the internal structural features of the solid state.

Study of the characteristics of fracture surfaces by light-microscope fractography is widely practiced, particularly when a low magnification of the fracture surface is adequate. This study can be accomplished with relatively simple equipment by people with moderate training. The first six articles in this volume describe and illustrate procedures employed in low-magnification fractography and include recommendations on procedures employed in studies of fracture surfaces at high magnifications.

The low-magnification, or macroscopic, field is arbitrarily assumed to be from less than actual size to not more than 50 diameters. The high-magnification, or microscopic, field extends from 50 diameters to an upper limit that depends



Arrows A point to two rib bones of an extinct bison, between which (at B) is lodged a fluted projectile now known as the Folsom point (Ref 1). Outline of weapon is retouched in photograph for clarity.

Fig. 1. The original Folsom find

on the numerical aperture of the objective lens, the wave length of the light used, and, to some extent, the contrast present in the metallic surface being examined. Fractographs at magnifications above that at which good resolution is obtained are useless, because they reveal no further detail—they merely enlarge the features.

Prehistoric Experience With Fracture

Controlled fracture is one of the earliest attainments of man. Production of lithic implements—stones given special shapes by controlled fracture—by Stone Age man was far in advance of the invention of the wheel. A classic example of this art is illustrated in Fig. 1, which shows a beautifully flaked Folsom point (identified by the skillful fluting running down the center) just as it was found, lying between two rib bones of an extinct bison that was excavated in New Mexico in 1927 (Ref 1).

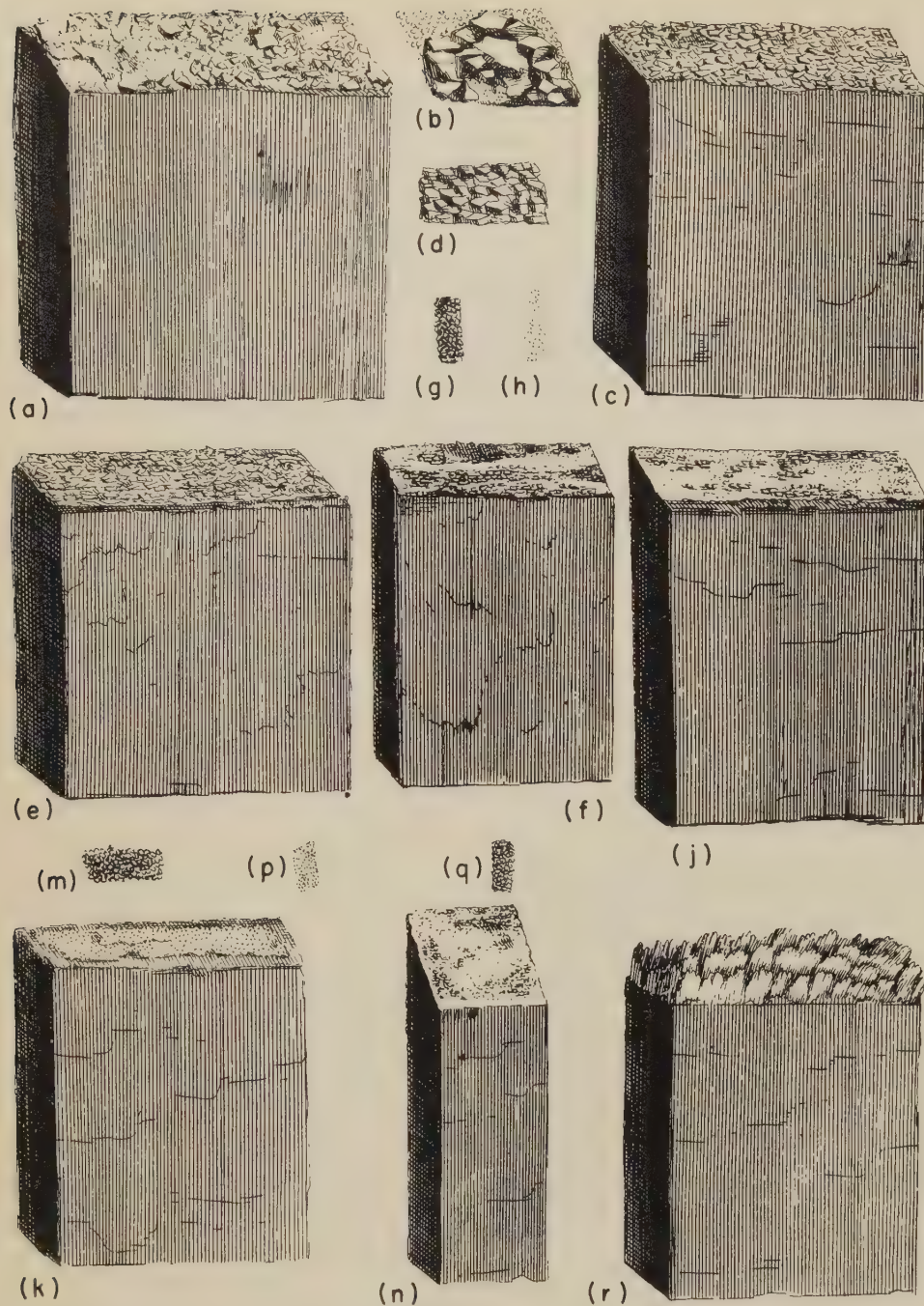
In preparing such weapons and implements, the ancient craftsmen had to know how to select the types of rock most favorable for fracture, how to detach the working cores from bedrock by building fires to produce thermal spalling, and how to shape the stone tools by pressure flaking. Their knowledge of fracture made it possible for them to produce implements that had remarkably keen and well-shaped cutting edges.

Other early examples of highly skillful fracturing and cutting of stone to precise dimensions include the Great Pyramid of

*JOHN A. FELLOWS, *Chairman*, Consultant to American Society for Metals; FRANK L. CARR, *Materials Engineer*, Army Materials and Mechanics Research Center; T. M. CLARKE, *Research Metallurgist*, Engineering Research, International Harvester Co.

MORSE HILL, *Consultant*; JAMES L. MCCALL, *Manager*, Materials Characterization Section, Battelle—Columbus Laboratories; J. COREY McMILLAN, *Chief*, Chemical Technology Unit, Boeing Commercial Airplane

Co.; JOHN B. NASLANIC, *Principal Test Engineer*, Materials Laboratory Dept., Ford Motor Co.; EMIL RUSNAK, *Research Metallurgist*, Materials Research and Engineering, International Harvester Co.; WILLIAM R. WARKE, *Associate Professor*, Department of Metallurgical and Materials Engineering, Illinois Institute of Technology; CARL A. ZAPFFE, *Consultant*; EDWARD A. DURAND, *Secretary*, Senior Editor, Metals Handbook, American Society for Metals.



(a) Type I fracture; large mirrorlike facets. (b) Same as (a), but as viewed with a hand lens. (c) Type II fracture; smaller facets and more regular distribution. (d) Same as (c), but as viewed with a hand lens. (e) Another type II fracture, but improved in regularity of distribution and reduced facet size compared with (c). (f) Type III fracture; advantageous occurrence of interposed areas of fibrous metal between facets. (g) Detail of facets in (f). (h) Detail of fibrous

metal in (f). (i) Type IV fracture; fibrous with very few reflecting facets.

(k) Type V fracture; framelike area surrounding an entirely fibrous center. (m) Same as (k), but as viewed with a hand lens; a type VI fracture would look like this, except for finer grain size. (n) Type VI fracture; an unusual type, with tiny facets in a fibrous background. (p) Detail of fibrous area in (n). (q) Detail of small facets in (n). (r) Type VII fracture; woody appearance.

Fig. 2. Sketches from R. A. F. de Réaumur (Ref 7) depicting seven categories of fracture appearance in iron and steel

Cheops, numerous obelisks, and the Temple of Amen at Al Karnak, all in Egypt; Stonehenge in England; a number of monoliths in Europe; and precision-fitted stone roads, aqueducts and fortresses in Peru. Although all of these applications involved knowledge of fracture as a means whereby an object could be shaped, they did not require interpretation of the fracture surfaces.

Fractography in the 16th to 18th Centuries

The way in which fracture appearance could be used to gage metal quality was a carefully guarded secret throughout the Middle Ages. One of the earliest disclosures was by Vannoccio Biringuccio in "De La Pirotechnia" (Ref 2),

published in 1540. He described the use of fracture appearance as a means of quality assurance for both ferrous and nonferrous alloys. Shortly thereafter, in 1556, Georgius Agricola published the famous "De Re Metallica" (Ref 3), from which the following quotation (in translation) describing a procedure for rating ferrous forgings is taken:

"Afterward the master, aided by his assistant, takes out a mass with the tongs and places it on the anvil, where it is pounded by the hammer which is alternately raised and dropped by means of the waterwheel; then, without delay, while it is still hot, he throws it into water and tempers it. When it is tempered, he places it again on the anvil, and breaks it with a blow from the same hammer. Then at once examining the fragments, he decides whether the iron in some part or other, or as a whole, appears to be dense and changed into steel."

Another early authority was Lazarus Ercker of Prague, who discussed fracture tests in a 1574 publication (Ref 4). The quality of copper, for example, was determined by examining the fracture surface of an ingot that had been notched and then broken by a transverse blow. Brass was similarly tested. A gray fracture surface was found to be associated with subsequent cracking during working; this gray surface was the result of the use of a special variety of calamine, which caused lead contamination of the ingot. Brittle fractures of silver were traced to lead and tin contamination.

In a 1627 report, Louis Savot (Ref 5) followed procedures recommended by Biringuccio for quality control in the manufacture of large bells. He recorded observations of grain size in fractured control samples as a guide for composition adjustments to resist impact loadings. At about the same time, Mathurin Jousse (Ref 6) described a method of selecting high-quality grades of iron and steel, based on the appearance of fracture samples.

Although the microscope was invented shortly after 1600, it was not until 1722 that its use for the study of metal fractures was first reported — by R. A. F. de Réaumur (Ref 7), who published a book containing engravings illustrating both macroscopic and microscopic reproductions of fracture surfaces of iron and steel. (At that time, it was necessary for the microscopist to sketch what he saw and then transfer the sketch to metal, wood or stone by engraving.) Although de Réaumur's sketches of fracture surfaces were unlike a modern fractograph, his study of the surfaces was conducted essentially as it would be today. One result of his work was the formulation of seven categories of fracture appearance in iron and steel. These are described below and shown in Fig. 2.

Type I Fracture. Large, irregularly arranged, mirrorlike facets, indicating inferior metal (Fig. 2a and b).

Type II Fracture. More regular distribution and smaller facets, indicating a slightly improved metal (Fig. 2c, d and e).

Type III Fracture. Interposed areas of fibrous metal between facets (Fig. 2f, g and h).

Type IV Fracture. Fibrous metal, with very few reflecting facets (Fig. 2i).

Type V Fracture. Framelike area surrounding an entirely fibrous center (Fig. 2k and m).

Type VI Fracture. An unusual type, with a few small facets in a fibrous background (Fig. 2n, p and q).

Type VII Fracture. Characterized by a woody appearance (Fig. 2r).

A second plate from de Réaumur's book (Fig. 3) concerns the use of fracture surfaces in appraising the completeness of conversion of iron to steel by the then current process of cementation (carburation). In his meticulous reproduction of detail he included phenomena still bothersome to metallurgists today, such as blistering, burning (overheating), brittle fracture, woody fracture, and others. Descriptions of the fractures characteristic of the various stages of conversion are given with Fig. 3. In summary, they are:

Woody fractures, characteristic of iron (Fig. 3a, b and c)

Fractures characteristic of partly converted metal (Fig. 3d, f and j)

Fractures characteristic of steel (Fig. 3e and g).

Figure 3(h) shows a fracture that is typical of an iron that will convert easily to steel, and Fig. 3(j) shows a fracture that is typical of an iron that will not convert to steel.

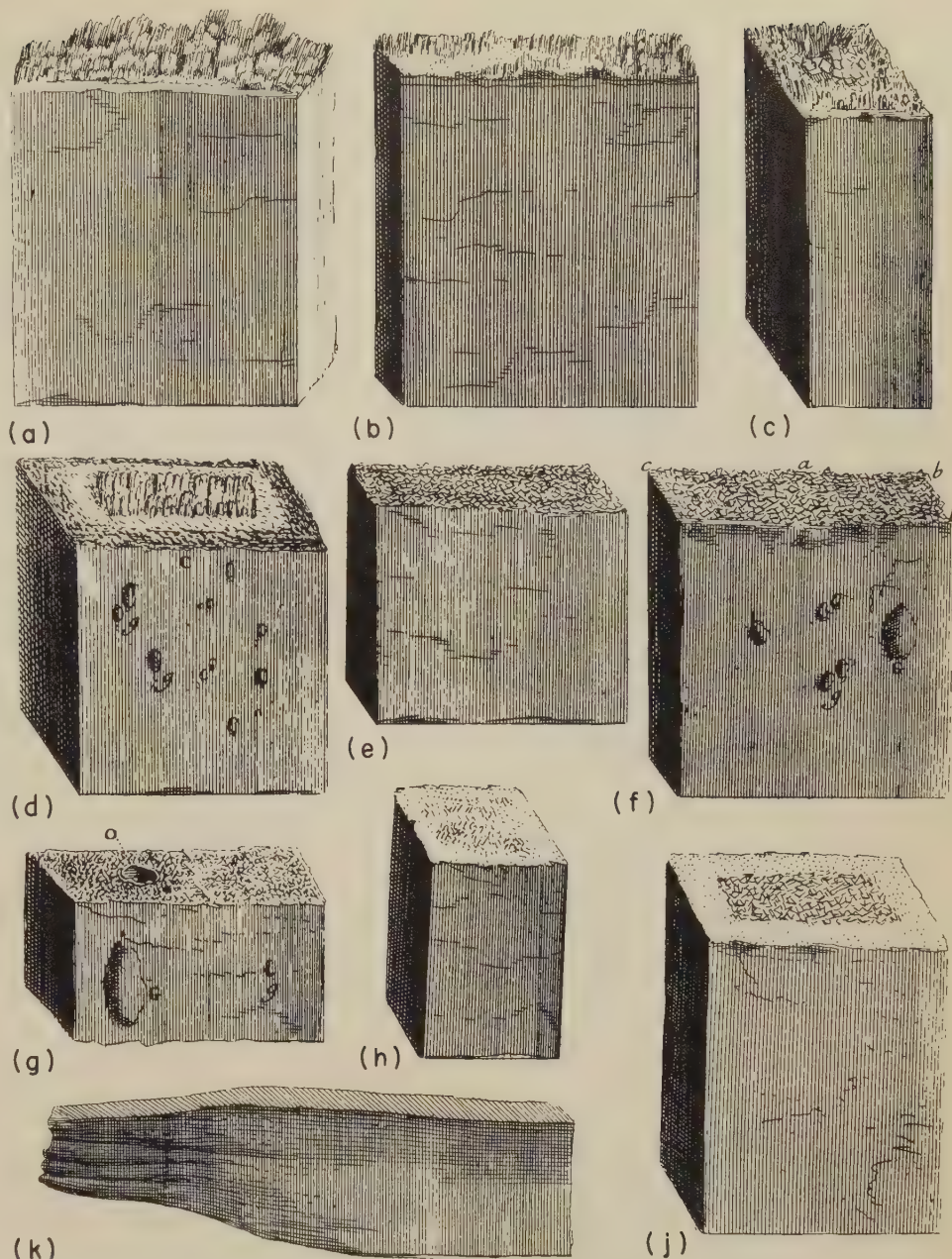
A third plate from de Réaumur (Fig. 4) displays his fracture studies at high magnifications and his fracture test. The "minute platelets" in Fig. 4(f) may have been pearlite, or cementite in some form, recorded a full century and a half before the founding of metallography.

Somewhat later (1750), Gellert in Germany described the fracture characteristics of metals and semimetals (Ref 8), mentioning the use of a fracture test for distinguishing between steel, wrought iron and cast iron. The test was also employed in appraising the effects of carburization and of heat treatment. Further, Gellert discussed causes of embrittlement of metals as disclosed by inspection of fracture surfaces.

Fractography in the 19th Century

With the development of metallography as a metallurgical tool, interest in the further development of fractography waned. The use of visual inspection of fractures as a means of quality control continued, but few investigators were interested in exploring fracture characteristics under the microscope and most metallurgical publications ignored fractures. David Mushet, for example, in 1840, refused to accept fractures as being metallurgically meaningful (Ref 9).

There were, however, areas of special interest where this view was not shared. In 1856, R. Mallet (Ref 10) associated fracture details in cannon barrels with the mode of solidification, referring to "planes of weakness" resulting from sharp angles in the contours of the barrels. This may have been the first example of failure analysis and the first recognition of the deleterious effects of stress concentrations in design. At the same time, the U. S. Army Ordnance Corps (Ref 11) employed fractography in conjunction



(a) Woody fracture, but without the distinctly clustered appearance of the fracture in Fig. 2(r). (b) Woody fracture combined with minutely granular areas. (c) Fracture exhibiting a combination of brittle facets, woody texture, and minutely granular areas. These fractures are typical of iron.

(d) Fracture in iron bar partly converted to steel, the outer minutely granular zone giving way to an inner framework of brittle facets, which surround, in turn, the woody center. (e) Fracture in steel produced from iron by cementation, showing a mass of small facets throughout the fracture, those in the center being somewhat larger. (f) Fracture in

iron bar converted to steel only from a-a to b-b and remaining as iron from a-a to c-c because of overheating in the furnace. (g) Fracture in steel; the lusterless, rough facets resulted from holding the specimen in the furnace for too long a time.

(h) Fracture in a type of iron that always produces very small facets when converted to steel. (j) A type II fracture in iron (see Fig. 2), indicating that the iron will fail to convert to steel in the center and will also produce an inferior fracture frame.

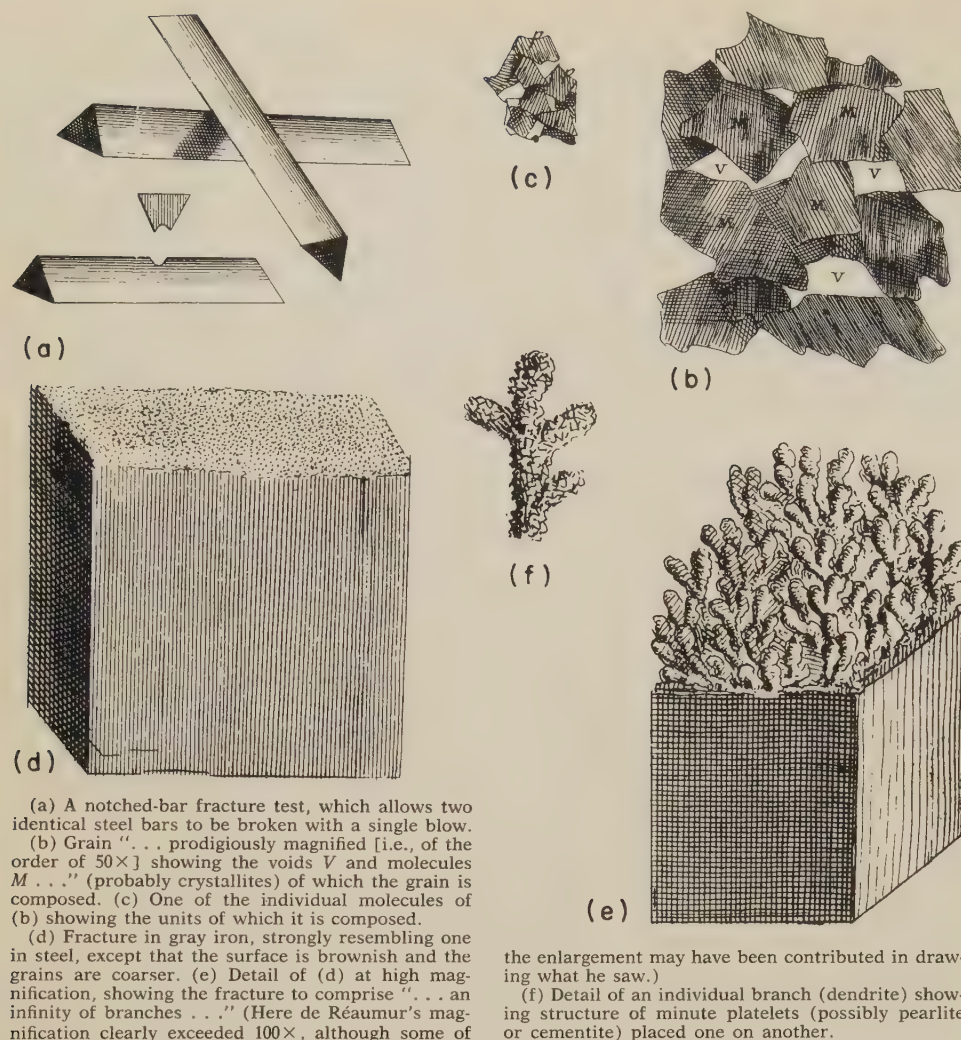
(k) Fracture in forged steel showing folding at left end, which could later cause cracking during heat treatment.

Fig. 3. Sketches from R. A. F. de Réaumur (Ref 7) defining fracture aspects that give evidence of the degree of conversion of iron to steel by the cementation process. In sketches (d), (f) and (g), small blisters are indicated by the letter g, large blisters are indicated by the letter G, and porosity is indicated by the letter O.

with mechanical testing for the study and evaluation of cannon barrels that had ruptured.

Interest continued in the recognition of categories of fracture characteristics. Tunner (Ref 12) published such a list in 1858, citing such conditions as hot shortness, cold shortness, overheating, and various types of tears. In 1862, D. Kirkaldy

(Ref 13) correlated the change in fracture appearance from fibrous to crystalline with specimen configuration, heat treatment, and strain rate. He reported that crystalline fractures were at 90° to the tensile axis whereas fibrous fractures were irregular and at angles other than 90°. Percy (Ref 14), a prolific author on metallurgical subjects, described by 1875



(a) A notched-bar fracture test, which allows two identical steel bars to be broken with a single blow.
 (b) Grain "... prodigiously magnified [i.e., of the order of $50\times$] showing the voids *V* and molecules *M*..." (probably crystallites) of which the grain is composed. (c) One of the individual molecules of (b) showing the units of which it is composed.
 (d) Fracture in gray iron, strongly resembling one in steel, except that the surface is brownish and the grains are coarser. (e) Detail of (d) at high magnification, showing the fracture to comprise "... an infinity of branches ..." (Here de Réaumur's magnification clearly exceeded $100\times$, although some of

the enlargement may have been contributed in drawing what he saw.)

(f) Detail of an individual branch (dendrite) showing structure of minute platelets (possibly pearlite or cementite) placed one on another.

Fig. 4. Sketches from R. A. F. de Réaumur (Ref 7) showing notched-bar fracture test, enlarged views of grains, and details of a fracture in cast iron



At top is a sketch of a fracture surface meeting a section at right angles. At bottom is a photomicrograph of a section parallel to the fracture surface, at $100\times$ (reduced here to $50\times$). Section surfaces were polish-etched with MgO in H_2SO_4 .

Fig. 5. Views of spiegeleisen by A. Martens (Ref 16, Fig. 11 and 12 of Plate 25)

six general types of fracture patterns. They were as follows:

- 1 **Crystalline**, with facets as in zinc, antimony, bismuth and spiegeleisen
- 2 **Granular**, with smaller facets, as in gray forged pig iron
- 3 **Fibrous**, a general criterion of quality
- 4 **Silky**, a finer variety of fibrous, such as in copper
- 5 **Columnar**, typical of high-temperature fracture
- 6 **Vitreous**, or glasslike.

Adolf Martens (for whom martensite is named) undertook studies of metal structure by examining newly fractured surfaces and polished and etched sections, both under the microscope. He published his first findings in Germany in 1878 (Ref 15, 16). His illustrations were hand engravings reproducing meticulous pencil drawings in some figures and photomicrographs in others. An example of each is shown in Fig. 5; both are of spiegeleisen, a high-carbon, high-manganese white cast iron. In the sketch at top in Fig. 5, Martens combined fractography and metallography by showing the intersection of a fracture surface with a polished and etched section cut at right angles, relating the structures of both; the photomicrograph at bottom in Fig. 5 shows a metallographic reproduction of a polished

and etched section of spiegeleisen at $100\times$ diameters (reduced to $50\times$ in Fig. 5).

A second plate, from a later article (1887) by Martens (Ref 17) is shown, in part, in Fig. 6. This is composed of fractographs produced by photography and then printed by a photogravure process. The fractures in Fig. 6 show features that Martens termed "Bruchlinien" (fracture lines)—which today would be called radial marks. The description of this fracture form by Martens antedates the reports by other investigators who usually are given credit for first treatment of this fracture feature.

In the field of macrofractography, Martens observed the fracture surfaces obtained in tension, torsion, bending and fatigue. In describing the topography of these surfaces, he differentiated between coarse radial shear elements and fine radial marks. He recognized that sharper radial marks occurred in fine-grained material and that all radial marks diverge from the fracture origin (that is, they point backward to the origin).

According to Sir W. C. Roberts-Austen (Ref 18), the influence of heat treatment on the appearance of steel fractures was first investigated systematically by D. K. Chernoff. Later (in 1885), Johann Augustus Brinell (the father of the Brinell hardness test) published (Ref 19) a summary of his investigation of this influence (see Table 1). The latter work was characterized by H. M. Howe as representing "the most important fracture studies ever made" (Ref 20).

Classic cup-and-cone tensile fracture was described by B. Kirsh (Ref 21) prior to 1889. He postulated a concept of crack propagation in tensile specimens that is retained today. He theorized that the crack origin was at the tensile axis in the necked region, that the origin grew concentrically in a transverse direction to produce the "bottom of the cup", and that the sides of the cone were formed by a maximum shear stress at final separation.

With regard to microfractography, however, because of an overriding interest in metallography, many noted metallurgical authorities classed it as leading "to nothing either correct or useful". Because of this attitude, microfractography became a forgotten art until well into the 20th century, with nothing being taught or acknowledged in the universities regarding earlier techniques and findings.

Fractography From 1900 to 1939

Macrofractography continued as a well-established expedient, if not a primary means of control and evaluation of metal quality, with steelmakers in general using the "nick-and-break" test. The categories of macrofracture features that had been developed in the period between de Réaumur and Brinell remained essentially unchanged when summarized by Tiemann (Ref 22) in 1919, as paraphrased in the list that follows:

- 1 **Granular or intergranular**. Also called coarse-grained, rough, bright crystalline, bright, granular crystalline. In exaggerated forms, it might be called brilliant, splendid, sanny fier, in special forms,

Table 1. Brinell's Studies of the Fracture of Steel of 0.52% Carbon Content (Condensed Statement)(a)

Designation letter of fracture	Brinell's descriptions			No. of cases	Microstructure, observed or inferred		Treatment	Brinell designations	
	Description of fracture		Carbon condition, hardening (H) or cement (C)		Pearlite	Ferrite		Designation number of experiments	Designation of fracture
	Structure	Color							
A	Coarse hackly. Facets shining.	Bluish	C	16	Sorbitic	Coarse network	Slow cooling after exposure to 1300 C without again heating to Ac3	11 to 14, 17 to 19, 31, 53-4, 57-8, 62, 75-6, 81	A
B	Medium hackly. Facets shining.	Bluish	C	5	Sorbitic	Medium-sized network	Slow cooling after exposure to about 1080 C	16, 30, 52, 56, 64	B
C	Fine hackly. Facets shining.	Bluish	C	5	Sorbitic or fine granular	Sorbitic or fine granular	Sorbitic pearlite of fracture carbon heated to between 500 C and about Ac1- 5 C and cooled slowly.	1, 2, 3	C
							Martensite heated to about Ac1- 5 C and cooled rapidly or slowly	43, 50	
				2	Sorbitic	Sorbitic	Martensite heated to about Ac3 and air cooled	29, 51	
				4	Sorbitic	Sorbitic	Coarsened network reheated to Ac3 and air cooled	15, 55, 63, 80	
D	Coarse granular crystalline. Facets silver shining (Metcalf, very lustrous).	White (Metcalf, yellowish)	H(b)	7	Long thin martensite needles from coarse austenite	Absent, its iron forming part of the martensite.	Quenched from about 1300 C without reheating beyond 300 C	6, 23, 24, 32, 39, 46, 61	D
				1			Quenched from about 1080 C after air cooling from about 1300 C	7	
				4			Quenched from about 760 or 850 C after air cooling from about 1300 C, or from molten	8, 72, 73, 78	
E	Fine granular crystalline. Facets silver shining (Metcalf, fiery).	H	6	Similar needles from intermediate-sized austenite	Absent, its iron forming part of the martensite.	Quenched from about 1080 C, without immediately preceding exposure to a higher temperature	5, 22, 38, 45, 60, 66	E
F	Bright porcelainic, no decided crystallization visible to the naked eye.	H	5	Fine martensite from fine austenite	Absent, its iron forming part of the martensite.	Heated to about Ac3, quenched, and not again heated beyond 300 C	4, 37, 40, 44, 47	F
				4			Heated from below Ar1 to about Ac3 and quenched	21, 59, 65, 82	
				1			Quenched from the molten	79	
H	Porcelainic; dull; fibrous. Wholly without crystallization.	Dark or ash gray	C(c)	4	Granular; from reheating martensite to 690 C	Banded	Martensite reheated to about 690 C, and cooled either rapidly or slowly	26, 34, 42, 49	H
				The pearlite and ferrite may be in alternate bands					
G	Leafy crystalline. Facets shining.	Bluish	H or C	2	Granular, banded, from reheating martensite to about 750 C	Banded	Martensite reheated to about 750 C (Ac3-10 C), and cooled rapidly or slowly	27, 35	G
I	Coarse crystalline. Facets shine like dull beaten silver.	H	1	Martensite		Quenched from about 750 C (Ac3-10 C), after starting the recalescence, by cooling to Ar1, 710 C	67	I

(a) This table, which is from Table 29 on pages 534-535 in Ref 20 (used with permission of McGraw-Hill Book Co.), summarizes reports by Brinell of his investigations into the influence of heat treatment on the appearance of fracture surfaces of 0.52% C steel (Ref 19).

(b) In two experiments, 24 and 32, the steel, hardened by quenching from "strong whiteness", and therefore with the carbon all hardening, was reheated to about 255 C. This, of course, converted a small part of the carbon into cementite, which would be in such fine emulsion that it

could not be recognized. This slight reheating of the martensite does not change the microstructure visibly, and the present experiments show that it does not change the fracture.

(c) In these four experiments the steel, hardened by quenching from "strong whiteness" or a "gentle yellow", was reheated to 690 C. This should certainly convert all its carbon into cementite. Brinell's test by nitric acid spotting indicated that the carbon was partly in the hardening state and partly as cementite. But here this test must mislead.

scorched, as for crucible steel held too long in the pot, and *staring*, if pieces of fuel have fallen in.

2 **Crystalline, transcrystalline or intercrystalline.** Sometimes *fine-grained*, *smooth*, *even*, *dull*, *gray-granular*, and *amorphous* (*porcelainic* or *aphanitic* is preferred).

3 **Silky.** Threadlike drawing out of fragments of the crystal in the act of rupture.

4 **Hackly or hooked.** Referring to a sharp, jagged and irregular fracture; called *needle fracture* if very sharp pointed.

5 **Fibrous.** Also *slaty*, *splintery*, *laminated*, *barked*.

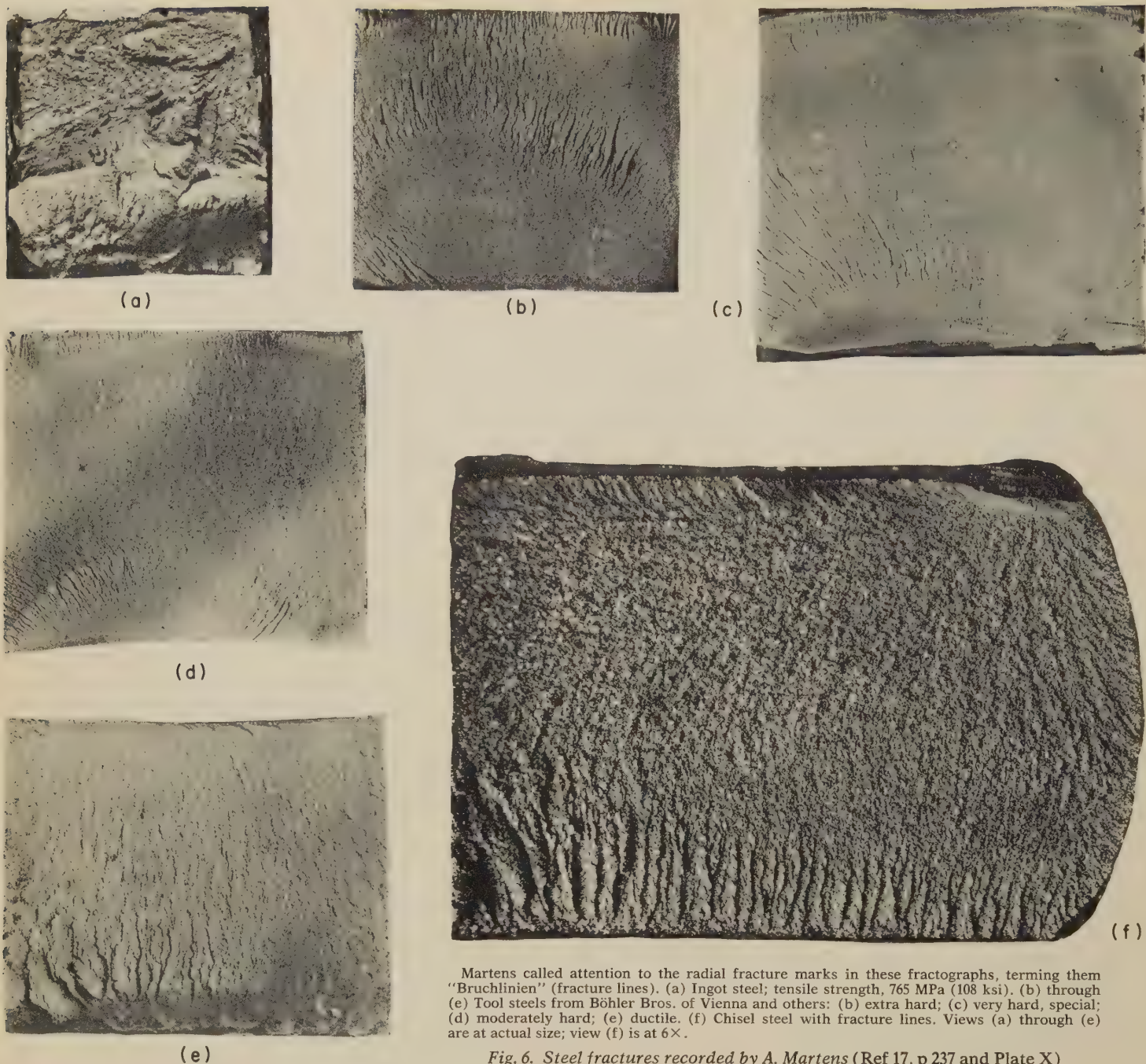
6 **Columnar.** Referring to a special coarse

type of fracture that is sometimes found on the periphery of castings.

Continued dependence on such features led to development in Sweden of the Jernkontoret special fracture tests (Ref 23, 24), beginning about 1930, and of the hardenability standard known as the P-F test (Ref 25, 26), which grew out of fracture studies of B. F. Shepherd (Ref 27, 28), shortly thereafter. Both the Jernkontoret special fracture test and the P-F test had the purpose of rating the prior austenite grain size in hardened tool and

die steels. Bain and Vilella (Ref 29) constructed charts that related the two tests to each other. Fracture tests were also standardized for use in rating the properties of cast nonferrous alloys. None of these techniques involved the use of a microscope.

The authors that have been cited are by no means inclusive of all who carried out early studies of fracture surfaces. They represent a somewhat arbitrary selection of those deemed to have made particularly significant contributions.



Martens called attention to the radial fracture marks in these fractographs, terming them "Bruchlinien" (fracture lines). (a) Ingot steel; tensile strength, 765 MPa (108 ksi). (b) through (e) Tool steels from Böhler Bros. of Vienna and others: (b) extra hard; (c) very hard, special; (d) moderately hard; (e) ductile. (f) Chisel steel with fracture lines. Views (a) through (e) are at actual size; view (f) is at $6\times$.

Fig. 6. Steel fractures recorded by A. Martens (Ref 17, p 237 and Plate X)

Microfractography Rediscovered

The rediscovery of microfractography in 1939 came about by reason of investigations by Carl A. Zapffe regarding the possible role of dissolved hydrogen in generating flake-type fissures in hardened steel. His curiosity had been aroused by the fact that steel, which ordinarily exhibits a fracture surface that is dull gray in appearance, should suddenly exhibit a bright and reflective fracture surface after being acted on by hydrogen. His impulse to examine the bright surfaces under the microscope had been suppressed because he was aware that the objective lens would be damaged if it made contact with the sharp prominences of the fracture. However, the conviction that the bright reflections from "fisheyes" in hydrogen-embrittled steel must derive

from the presence of flat mirrorlike facets encouraged Zapffe to risk possible damage to the microscope. He was rewarded when a cautious approach of the objective to a particularly interesting fisheye yielded a flash in the ocular lens, signaling that the lateral scan of the fracture had positioned a reflecting facet, still out of focus, in the optical axis of the instrument. All lateral motion of the specimen was halted, the objective was carefully lowered, and a sharp focus was achieved without damage to the lens surface. What Zapffe saw was an image of a crystallographic pattern of fissures and blocklike reliefs (caused by the cubic symmetry of the iron crystal), and blocklike pits that strongly suggested that minute bits of metal had been "exploded" away by the pressure of entrapped gas. It was evident that with suitable care in bringing the

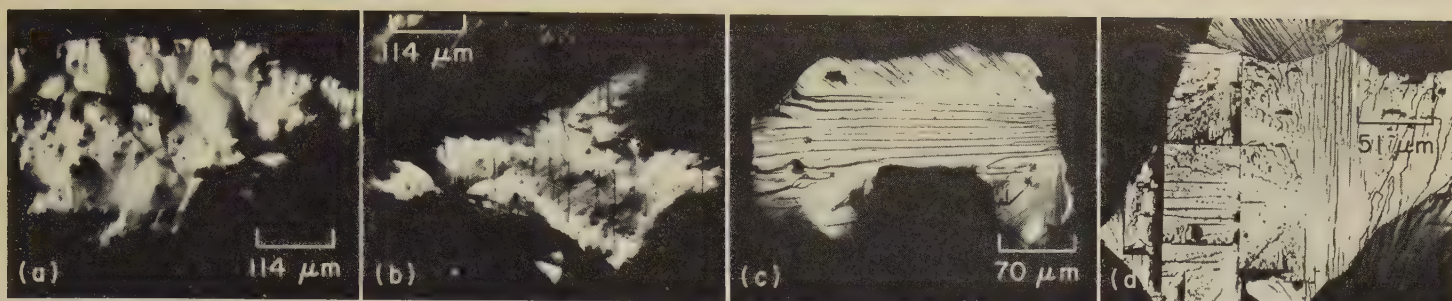
specimen toward the lens, photography of fracture facets at high magnification was entirely possible, and a new approach to microfractography had been opened.

The first fractographs appeared in print in a paper devoted to hydrogen embrittlement (Ref 30). Four examples of these are reproduced in Fig. 7.

Later work on stainless steels gave a new opportunity to explore the characteristics of brittle-fracture surfaces; this research, expanded to include other metals as a basis for generalizing the technique, was published in 1945 (Ref 31).

Techniques for Microfractography

Techniques employed by Zapffe in his early work with light-microscope fractography were similar in many respects to those used today.



Light fractographs

(a) Specimen heat treated 392 hr in moist hydrogen, 4 hr in dry hydrogen, and 24 hr in *vacuo*, all at 1000 to 1050 C (1832 to 1922 F), and finally cooled in *vacuo*. Charpy impact fractured at room temperature. Fracture is intergranular.

(b) Specimen with same thermal history as for (a), but also charged cathodically with hydrogen for 2 hr at 7.5 amp per square decimeter in 5% H_2SO_4 . The fracture is intergranular. The vertical lines were interpreted by Barrett and Derge (Ref 30, discussion) to be Neumann bands.

(c) Specimen heat treated 24 hr in moist hydrogen and 22 hr in dry nitrogen, both at 1000 C (1832 F), and cooled in nitrogen. Subsequently charged elec-

trolytically with hydrogen for 2 hr at 7.5 amp per square decimeter in 5% H_2SO_4 ; then the polarity was reversed for several minutes. The fracture is intergranular, with Neumann bands. The reversed-polarity treatment did not restore ductility.

(d) Specimen annealed 2 hr at 1000 C (1832 F) and furnace cooled. It was embrittled by pickling for 30 min in 10% H_2SO_4 at 90 C (194 F). Fractured by impact at room temperature immediately after pickling. The cleavage structure shows many crystallographic features; straight lines were interpreted as Neumann bands.

Fig. 7. Surfaces of fractures in hydrogen-embrittled ingot iron (Ref 30)

For laboratory tests, the first consideration was the production of a surface with relatively flat facets. Obtaining such facets was facilitated if the specimen was in a brittle condition when it was broken to induce cleavage along some crystallographic direction. For specimens with body-centered cubic and close-packed hexagonal crystal structures, four embrittling factors were utilized, singly or in combination, provided the purpose of the research did not forbid. These were: (a) low-temperature impact; (b) high-velocity impact; (c) multiaxial restraint; and (d) hydrogen embrittlement.

Positioning the specimen for observation in the microscope was done by either

of two procedures: (a) putting it on a metallographic stage that would permit horizontal motion in searching for a "blink" from a favorably oriented facet located by chance (this was often the only choice in examining large specimens), or (b) selecting a facet with favorable characteristics and adjusting the specimen orientation to gain the necessary reflection. The first stage used in Zapffe's studies was the double-ring apparatus shown in Fig. 8. It had tripod screws to allow moderate adjustments in positioning the specimen. Another device he employed was a concentric-dome design, shown in Fig. 9. The specimen was held by clamps or by seating in plasticine.

When points or prongs of a fracture interfered with the approach of the lens toward the site on the fracture to be studied, a small electric hand grinder (shown in Fig. 8), equipped with drills, wheels and polishing felts, was used to cut away the undesired projections.

Applications of Microfractography

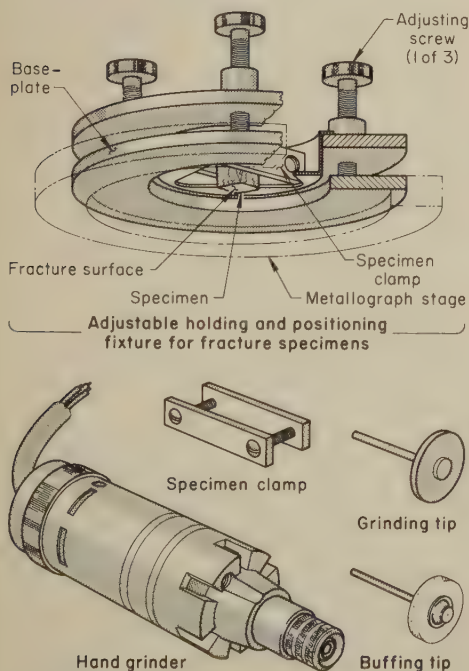
Failure analysis is the most important application of fractography. This is discussed in detail in the article beginning on page 106 in this volume.

Microfractography can also be a valuable source of information concerning the nature of a metal. For example, with microfractography transition temperature can be defined and brittleness as a result of increasing rate of load application can be detected (Ref 32); the structures associated with the property sometimes labeled "toughness" are discernible in fractographic patterns (Ref 33); changes in alloy content in binary alloys are revealed by changes in fracture patterns (Ref 34); and segregation has been studied in molybdenum (Ref 35, 36) and tungsten (Ref 37) systems, as well as the peculiar condition in ferritic stainless steels known as 475 C (887 F) embrittlement (Ref 38). Other aspects revealed include fatigue marks (Ref 39), evidence of hydrogen embrittlement (Ref 40), displays of defects in crystal growth (Ref 41), and proof of high-temperature dissociation reactions within inclusions (Ref 42).

Correlation of Fractographs With Microstructure

The features of a fracture surface may bear a resemblance to the microstructure, but more likely they do not. With fracture due to hydrogen embrittlement, the fractographs may show sharply defined, undeformed grains that conform exactly to the shapes that are visible in a polished and etched section. Such fractographs actually provide a better three-dimensional view of the grain structure, because the crack changes course to follow each grain boundary it encounters, in contrast to the single-plane section of a micrograph. In ductile fracture, the rough, dimpled surface shown on a fractograph bears no resemblance to the surfaces visible in a micrograph of a polished and etched section. The grains in ductile fracture have undergone major deformation, whereas embrittled material ruptures with little or no deformation.

Fracture by cleavage will often result in fracture surfaces that closely resemble



Baseplate fits into the circular opening in the stage of a metallograph. The superposed specimen holder is supported by three screws countersunk into the baseplate. The clamp is for positioning the specimen in the specimen holder. The electric hand grinder is used with the grinding and buffing tips for removing irregularities that could interfere with focusing.

Fig. 8. Apparatus for holding and surface preparation of fracture specimens for fractography (Ref 31)

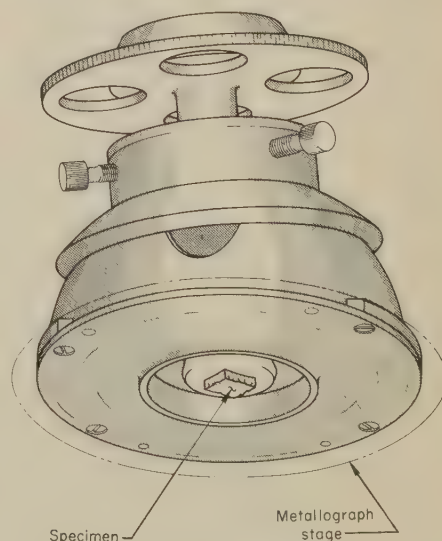
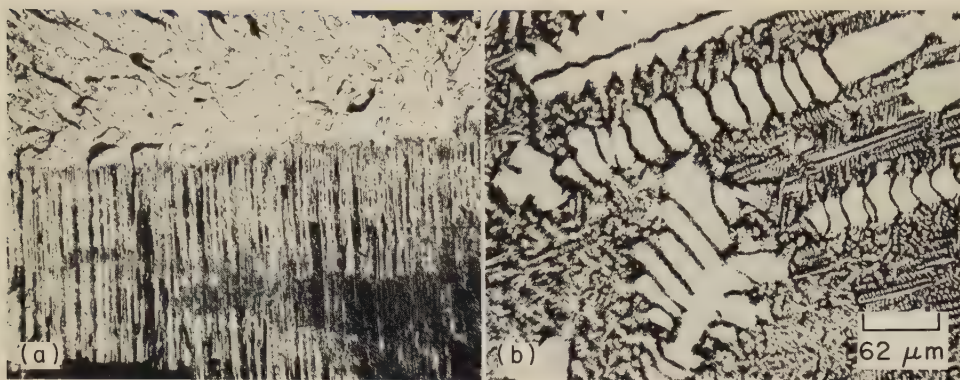


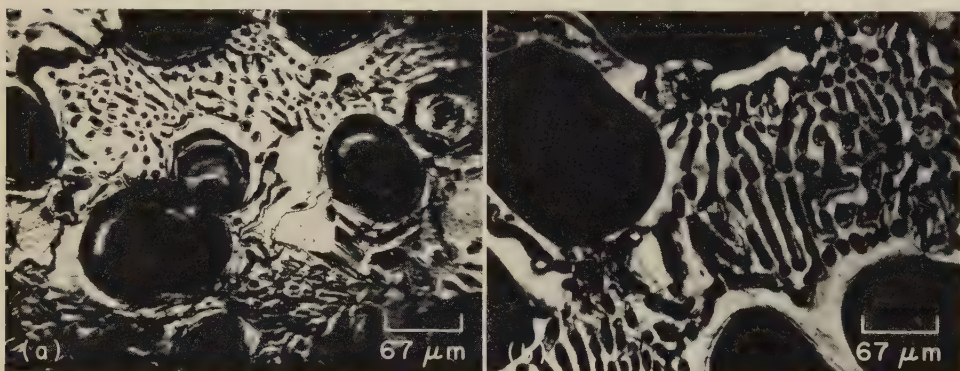
Fig. 9. A concentric-dome stage mount for fracture specimens. It permits horizontal motion by the metallograph stage and adjustment of specimen tilt to bring the selected facet into reflecting orientation.



(a) Light-microscope fractograph at 25X. The upper part shows a basal-plane fracture bearing semblances of river patterns that relate to the dendritic segregation present in the specimen. The lower portion shows secondary cleavage in an adjacent grain.

(b) Micrograph ($\text{FeCl}_3 + \text{HCl}$ etchant), at 162.5X. Dendritic segregation is present that is so marked as to resemble a two-phase system, even though this alloy is theoretically single phase at equilibrium.

Fig. 10. Comparison of a light-microscope fractograph (a) with a micrograph (b) of the microstructure of the same alloy (46Bi-54Sb with about 0.08% As), showing no visual resemblance. Specimen was water quenched in a heat-resistant-glass tube directly from the molten state and fractured by impact at room temperature.



(a) Light-microscope fractograph at 150X. Cleavage along the (0001) direction through the alpha-beta eutectic areas was deflected by the alpha (or alpha-prime) islands, following the alpha-eutectic interface. The alpha-island locations show as cavities with reflections from their interiors.

(b) Micrograph ($\text{CrO}_3 + \text{Na}_2\text{SO}_4$ etchant), at 150X. Similar to the fractograph (a), because the alpha islands etched dark.

Fig. 11. Comparison of a light-microscope fractograph (a) with a micrograph (b) of the microstructure of the same alloy (Zn-10.7Al), showing close visual resemblance. Specimen was cast from alloy melted in a fused-alumina boat under a reducing flame, cooled to room temperature, then annealed 45 hr at 370 C (698 F) in dried helium, quenched in ice water, and dried immediately. Fracture was by impact at room temperature.

the microstructure. This may be caused by the splitting of individual grains that are favorably oriented to permit cracking along a crystallographic plane with little deformation of the structure. The grain contours thus visible in a fractograph will be quite similar to those revealed in a micrograph.

In Fig. 10, the fractograph (a) does not directly resemble the micrograph (b). However, it does show the effect of the type of structure present on the crack-growth pattern. The material shown in Fig. 10 is 46Bi-54Sb alloy, which was water quenched in a heat-resistant-glass tube directly from the molten state and was fractured by impact at room temperature. The fracture followed a basal plane. The apparent river patterns were actually the result of the segregated dendritic structure in this alloy.

A nearly exact correspondence between a fracture surface and a microstructure (fractograph and micrograph) is shown in Fig. 11. The alloy depicted is cast Zn-10.7Al, annealed at 370 C (698 F) for

45 hr in carefully dried helium, quenched in ice water, dried, and fractured by impact at room temperature. The crack traverse in Fig. 11(a) cleaved the alpha-beta eutectic areas, but avoided the massive alpha (or alpha-prime) islands, following instead the alpha-eutectic interface, leaving large cavities that are out of focus but show some reflectance from the interiors. In the micrograph, Fig. 11(b), the eutectic has a very similar appearance; and because the alpha (or alpha-prime) islands are dark etching, they resemble the islands shown in the fractograph (Fig. 11a).

References

1. F. H. H. Roberts, The Early Americans, *Sci Am*, Vol 184 (No. 2), 1951, p 15-19
2. Vannoccio Biringuccio, "De La Pirotechnia", Venice, 1540; see translation by C. S. Smith and M. T. Gnudi, "The 'Pirotechnia' of Vannoccio Biringuccio", AIME, New York, 1942, 476 pages
3. Georgius Agricola, "De Re Metallica", 1st Edition, H. Froben, Basel, 1556, 624 pages; see translation by H. C. Hoover and L. H. Hoover, "Georgius Agricola's De Re Metallica", Dover, New York, 1950, 638 pages
4. Lazarus Ercker, "Beschreibung allerfürnemisten mineralischen Erztz und Berckwercksarten", 1st Edition, G. Schwartz, Prague, 1574; see translation of 2nd Edition by A. G. Sisco and C. S. Smith, "Lazarus Ercker's Treatise on Ores and Assaying", University of Chicago Press, 1951, 560 pages; see also E. V. Armstrong and H. S. Lukens, Lazarus Ercker and His "Proberbuch"; Sir John Pettus and His "Fleta Minor", *J Chem Educ*, Vol 16, 1939, p 553-562
5. Louis Savot, "Discours sur les médailles antiques", Paris, 1627; see Cyril Stanley Smith, "A History of Metallurgy", University of Chicago Press, 1960, p 99
6. Mathurin Jousse, "Fidelle ouverture de l'art de serrurier", La Fleche, Paris, 1627; see translation by C. S. Smith and A. G. Sisco, *Technol Culture*, Vol 2 (No. 2), 1961, p 131-145
7. R. A. F. de Réaumur, "L'Art de Convertir le Fer Forgé en Acier, et L'Art d'Adoucir le Fer Fondu" ("The Art of Converting Wrought Iron to Steel and the Art of Softening Cast Iron"), Michel Brunet, Paris, 1722, 568 pages; see translation by A. G. Sisco, "Réaumur's Memoirs on Steel and Iron", University of Chicago Press, 1956, 395 pages
8. C. E. Gellert, "Anfangsgründe der Metallurgischen Chemie" ("Elements of Metallurgical Chemistry"), J. Wendler, Leipzig, 1750, 338 pages; see translation by J. Seiferth, "Metallurgic Chemistry", T. Bechet, London, 1776, 416 pages
9. John Weale, "Papers on Iron and Steel, Practical and Experimental", London, 1840, 952 pages
10. R. Mallet, "Physical Conditions Involved in the Construction of Artillery", London, 1856
11. Officers of Ordnance Dept., U. S. Army, "Reports on the Strength and Other Properties of Metals for Cannon", H. Baird, Philadelphia, 1856
12. P. Tunner, "Das Eisenhüttenwesen im Schweden", Engelhardt, Freiberg, 1858, 86 pages
13. D. Kirkaldy, "Results of an Experimental Inquiry into the Tensile Strength and Other Properties of Various Kinds of Wrought Iron and Steel", Glasgow, 1862
14. J. Percy, "Metallurgy", 4 volumes, John Murray, London, 1861-1880
15. A. Martens, Über die Mikroskopische Untersuchung des Eisens, *Z Deut Ing*, Vol 22, 1878, p 11-18
16. A. Martens, Zur Mikrostruktur des Spiegeleisens, *Z Deut Ing*, Vol 22, 1878, p 205-274, 481-488
17. A. Martens, Ueber das Kleingefüge des Schmiedbaren Eisens, *Stahl Eisen*, Vol 7, 1887, p 235-242
18. Sir W. C. Roberts-Austen, "An Introduction to the Study of Metallurgy", 6th Edition, J. B. Lippincott Co., Philadelphia, 1910, p 13, 16
19. J. A. Brinell, Über die Texturveränderungen des Stahls bei Erhitzung und bei Abkühlung, *Stahl Eisen*, Vol 11, 1885, p 611-620
20. H. M. Howe, "The Metallurgy of Steel and Cast Iron", McGraw-Hill Book Co., New York, 1916, p 527, and Table 29 on p 534-535. (Translation and condensation, with slight amendments, of original diagram from reference 19, p 611)
21. B. Kirsh, Beiträge zum studium des Fliessens, *Mitt Hlg*, 1887, p 67; 1888, p 37; 1889, p 9; see also Gus C. Hennings, "Adolf Martens, Handbook of Testing Materials", Part I, Wiley, New York, 1899, p 103, 105
22. H. P. Tiemann, "Iron and Steel", 2nd Edition, McGraw-Hill, New York, 1919, 514 pages (see p 178)
23. R. Arpi, Report on Investigations Concerning the Fracture Test and the Swedish Standard Scale, (in Swedish), *Jernkontorets Ann*, Vol 86, 1931, p 75-95 (abstract in *Stahl Eisen*, Vol 51, 1931, p 1483-1484)
24. R. Arpi, The Fracture Test as Used for Tool Steel in Sweden, *Metallurgia*, Vol 11, 1935, p 123
25. B. F. Shepherd, The P-F Characteristics of Steel, *Trans Am Soc Metals*, Vol 22, 1934, p 979-1016
26. G. K. Manning, Shepherd Grain Size Fracture Standards, *Metal Progress*, Vol 42, Aug 1942, p 227
27. B. F. Shepherd, Carburization of Steel, *Trans ASST*, Vol 4, Aug 1923, p 171-196
28. B. F. Shepherd, A Few Notes on the Shimer Hardening Process, *Trans ASST*, Vol 5, May 1924, p 485-490
29. E. C. Bain and J. R. Vilella, Austenite Grain Size in Steel, "Metals Handbook", 7th Edition, American Society for Metals, Cleveland, 1948, p 405
30. C. A. Zapffe and G. A. Moore, a Micrographic Study of the Cleavage of Hydrogenized Ferrite, *Trans AIME*, Vol 154, 1943, p 335-359
31. C. A. Zapffe and Mason Clogg, Jr., Fractography—A New Tool for Metallurgical Research, *Trans Am Soc Metals*, Vol 34, 1945, p 71-107
32. C. A. Zapffe and C. O. Worden, Temperature and Stress Rate Affect Fractology of Ferritic Stain-

less, *Iron Age*, Vol 167 (No. 26), 1951, p 65-69

33. C. A. Zapffe, C. O. Worden and F. K. Landgraf, Cleavage Patterns Disclose "Toughness" of Metals, *Science*, Vol 108 (No. 2808), 1948, p 440-441

34. C. A. Zapffe, Etude Fractographique des Alliages Fer-Chrome, *Rev Met (Paris)*, Vol 44 (No. 3 and 4), 1947, p 91-96; see also C. A. Zapffe and F. K. Landgraf, Tearline Patterns in Ferrochromium, *J Appl Phys*, Vol 21 (No. 11), 1950, p 1197-1198

35. C. A. Zapffe, F. K. Landgraf and C. O. Worden, Transgranular Cleavage Facets in Cast Molybdenum,

Metal Progress, Vol 54 (No. 3), 1948, p 328-331

36. C. A. Zapffe, F. K. Landgraf and C. O. Worden, Fractographic Study of Cast Molybdenum, *Trans AIME*, Vol 180, 1949, p 616-636

37. C. A. Zapffe and F. K. Landgraf, Fractographic Examination of Tungsten, *Trans Am Soc Metals*, Vol 41, 1949, p 396-418

38. C. A. Zapffe, Fractographic Pattern for 475 C Embrittlement in Stainless Steel, *Trans AIME*, Vol 191, 1951, p 247-248

39. C. A. Zapffe and C. O. Worden, Fractographic

Registrations of Fatigue, *Trans Am Soc Metals*, Vol 43, 1951, p 958-969

40. C. A. Zapffe and G. A. Moore, A Micrographic Study of the Cleavage of Hydrogenized Ferrite, *Trans AIME*, Vol 154, 1943, p 335-359

41. C. A. Zapffe, F. K. Landgraf and C. O. Worden, History of Crystal Growth Revealed by Fractography, *Science*, Vol 107 (No. 2778), 1948, p 320-321

42. C. A. Zapffe, Dissociation Reactions Within Inclusions, *J Iron Steel Inst (London)*, Vol 154 (No. 2), 1946, p 155-161

Preparation and Preservation of Fracture Specimens

By the ASM Committee on Fractography by Light Microscopy*

CORRECT INTERPRETATION of a fracture depends on the degree to which it is free from foreign matter that might obscure its characteristics and thereby lead to erroneous conclusions. Usually, a fracture under investigation is exposed to many different examination procedures. Because some of these may affect subsequent examinations, and even may change the appearance of the fracture, a complete record of procedures used prior to and during study should be kept.

This article presents procedures for safeguarding fracture surfaces in storage against further contamination, for cleaning fracture surfaces, for sectioning of fractured parts to remove specimens, and for opening secondary cracks.

Care of Metal Fractures

When a fracture occurs and there is even a slight chance that it will be subjected to laboratory examination, several important steps must be followed if maximum information is to be obtained. Most of the procedures described here are independent of the particular examination techniques that will be employed.

The handling procedures that must be followed are based on recognition that the fracture surface contains much valuable information and that anything done to obliterate this information may obstruct an interpretation of the fracture. The damage that can occur to a fracture may be considered to be of two types—mechanical and chemical.

Mechanical damage may arise from several sources, including simply permitting the fracture to strike other objects. This can occur during the fracture event (for example, when aircraft landing gears scrape the runway), or in removing a fractured piece from its surroundings or transporting it from one place to another. Recognition of the consequences of damage, and use of good judgment, are the best ways to prevent

this type of damage. The fracture can usually be protected during shipment by taping cloth or cotton on the surface, but this may remove some loosely adhering material, which often contains the primary clue to the interpretation of the cause of the fracture. Touching the fracture with the fingers or rubbing it should definitely be avoided. Also, there appears to be an almost uncontrollable human desire to see if the two halves of a fracture fit together. This usually accomplishes nothing and almost always causes damage to the fracture surface, and therefore should be avoided.

Chemical (corrosion) damage to a fracture can be prevented in a number of ways, and each laboratory has its preferred method. Because the identification of foreign material present on a fracture surface may be important in the over-all interpretation of the cause of fracture, many laboratories prefer not to use corrosion-preventive coatings on the fractures. When possible, it is best to dry the fracture, preferably by use of a jet of dry compressed air (which will also blow extraneous foreign material from the surface), and then to place it in a desiccator or pack it with a desiccant.

Coatings. If analysis of foreign material on the fracture surface will not be required (for example, in the analysis of laboratory-produced fractures), a satisfactory method to preserve the fracture and prevent it from corroding is to apply a coating. When in the field, the fracture can be coated with a good grade of fresh axle grease. An alternative is to enclose the fractured piece in a plastic bag, together with silica gel. Coatings can be sprayed on the fracture or the fracture can be dipped in them. Clear plastic coatings through which a fracture can be seen are widely used. The plastics often used can be removed with trichloroethylene. At least one laboratory prefers clear acrylic lacquers for coating because they can be removed easily and completely with ketones. A solvent-cutback petroleum-base compound for rust prevention

(specified in MIL-C-16173) works well and can be removed without difficulty.

The only requirements for a coating are (a) that it will not chemically attack the fracture and (b) that it can be completely (and easily) removed. In general, cellulose nitrate lacquers and polyurethane paints, which have been used by some laboratories, are not satisfactory, because they are difficult to remove.

Another method of protecting fractures is to apply a replicating plastic onto the fracture surface. Cellulose acetate is most frequently used. It can be softened and removed using methyl acetate, acetone or a mixture of dimethyl ketone and toluene. One limitation of the replicating plastics is that they seldom can be completely removed. This becomes apparent when the fractures are examined by scanning electron microscopy.

Pressure-sensitive tapes with the adhesive in direct contact with the fracture should not be used. Many of the adhesives are difficult to remove, and they are likely to adsorb water, causing the fracture surface to corrode.

Cleaning of Metal Fractures

Usually, cleaning of the fracture is required, particularly when electron-microscope examinations are to be made. Cleaning is for the purpose of removing protective coatings, corrosion products, and loose deposits such as dust, which may obscure part of the fracture or make interpretation difficult. Prior to cleaning, however, consideration should be given to the possibility that the deposits on the fracture surface can yield important information regarding the cause or progress of the fracture.

Numerous cleaning procedures have been developed, each suited for a particular metal or the preference of a particular laboratory. The cleaning techniques commonly employed include:

1 **A dry air blast**, which will remove many loosely adhering materials. A soft artist's brush will assist in the removal, but ex-

*See page 1 for committee list.

treme care must be exercised to see that no damage is done to the fracture surface.

- 2 **Treating with inorganic solvents**, either by immersion or by a jet from a pump, to remove oil, grease, or plastic coatings. The removal can be assisted by using ultrasonic agitation (see item 4 in this list), heating the solvent, or using vapor degreasing methods. In general, brushing of the fracture should be avoided. Cleaning with clean spectrographic-grade solvents and collecting the spent solvent will permit later analysis of the surface materials.
- 3 **Treating with mild acid or alkaline solutions** (depending on the metal), which will attack deposits but to which the base metal is essentially inert. This treatment should be done only as a last resort because it will probably destroy the fine details on the fracture, making subsequent electron microscopy useless. Acetic acid, phosphoric acid, and sodium hydroxide, heated if required, have been used for cleaning iron-base alloys. Several commercial solutions can also be used satisfactorily, but care should be exercised to avoid removal of inclusions from the metal matrix. Ultrasonic agitation (see item 4, below) may be beneficial to assist in cleaning. Fairly heavy layers of rust and scale often can be removed by ammonium citrate and ammonium oxalate solutions. Another recommended procedure for iron-base alloys is an immersion dip for 1 to 15 min in a solution of 6N hydrochloric acid containing 2 grams per liter of hexamethylenetetramine. Sulfamic acid has also been used. Cleaning with nitric acid is best for titanium alloys. Cleaning of the fracture surfaces of aluminum alloys should be done only with organic solvents.
- 4 **Ultrasonic cleaning** with the water-base detergents sold for this purpose. This method has been quite effective and does not damage the fracture. Ultrasonic agitation with organic solvents or with mild acid or alkaline solutions can be used to assist in the removal of stubborn coatings, dirt or deposits. Oxidation and corrosion products have been rather successfully removed from steel fractures using simultaneous ultrasonic and cathodic cleaning in sodium carbonate or sodium hydroxide solutions.
- 5 **Applying and stripping of plastic replicas**, usually repeated from two to five times (see the article on The Transmission Electron Microscope and Its Application to Fractography, beginning on page 54). Loose debris will be entrapped in the soft plastic and will be removed when the plastic is stripped. Care must always be exercised to see that plastic is not left on the fracture surface.

Chemical reactions, such as oxidation, involve the base metal. Part of the fracture is destroyed by oxidation, and removal of the oxide layer will not return the fracture to its original detail. Any fracture that is mechanically or chemically damaged prior to examination cannot be restored to its original condition by any amount of cleaning.

Those directly concerned with the care and cleaning of fractures may wish to consult other recommendations of procedure. Suggestions for cleaning fractures in various metals and for cleaning with replicas are given on pages 59 to 61 in Chapter 4 of "The Elements of Fractography," by D. A. Ryder, AGARD-AG-155-71, Nov 1971 (Document No. AD-734619, Na-

tional Information Service, U. S. Dept. of Commerce, 5285 Port Royal Rd., Springfield, VA 22151).

Sectioning of a Fracture

It is frequently necessary to remove the portion containing a fracture from the total part, because the total part is to be repaired or to reduce the size of the specimen to be examined to a size that is convenient to handle. Many of the examination tools—for example, the scanning electron microscope and the electron microprobe analyzer—have specimen chambers that place limitations on the size of specimen they can accept.

It is important that records, either drawings or photographs, be kept to show the locations of the cuts made during sectioning.

All cutting should be done in such a way that fracture faces and areas adjacent to them are not damaged or altered in any way; this includes keeping the fracture surface dry, whenever this is possible. For large parts, the common method of specimen removal is flame cutting. The cutting must be done at a sufficient distance from the fracture so that the microstructure of the metal underlying the fracture surface is not altered by the heat of the flame and so that none of the molten metal from flame cutting is deposited on the fracture surface.

Saw cutting and cutoff-wheel cutting can be used for a wide range of part sizes. Dry cutting is preferable, because coolants may corrode the fracture or may wash away foreign matter from the fracture. A coolant may be required, however, if a dry cut cannot be made at a sufficient distance from the fracture to avoid heat damage to the fracture region.

Some of the coating procedures mentioned previously may be found to be useful during cutting and sectioning. For example, the fracture could be protected during flame cutting by taping a cloth over it, and be protected during sawing by spraying or otherwise coating it with a lacquer or a rust-preventive compound.

Opening Secondary Cracks

When the primary fracture has been damaged or corroded to a degree that prevents it from providing much information, it is desirable to open any secondary cracks to expose their fracture surfaces for examination and study. These cracks may provide more information than the primary fracture. If rather tightly closed, they may have been protected from corrosive conditions, and if they have existed for less time than the primary fracture, they may have corroded less. Also, primary cracks that have not propagated to total fracture may have to be opened.

In opening cracks of these types for examination, care must be exercised to prevent damage, primarily mechanical, to the fracture surface. This can usually be accomplished if opening is done in such a way that the two faces of the fracture are moved in opposite directions, normal to the fracture plane. Usually, a

saw cut can be made from the back of the fractured part to a point near the tip of the crack, using extreme care to avoid actually reaching the crack tip. This saw cut will reduce the amount of solid metal that must be broken. The final breaking of the specimen can be done in several ways: (a) by clamping the two sides of the fractured part in a tensile-testing machine, if the shape permits, and pulling; (b) by placing the specimen in a vise and bending one half away from the other by striking it with a hammer in a manner that will avoid damage to the crack surfaces; or (c) by gripping the halves of the fracture in pliers or vise grips and bending or pulling them apart.

It is desirable to be able to distinguish between a fracture surface produced during opening of a primary or secondary crack and the surface produced by primary or secondary cracking. This can be accomplished by making sure that a different fracture mechanism is active in making the new break, such as by performing the opening operation at a very low temperature. During low-temperature fracture, care should be taken to avoid condensation of water, because this could cause corrosion of the fracture surface.

It is recommended that both crack separations and crack lengths be measured prior to opening. Often the amount of strain that occurred in a specimen can be determined from a measurement of the separation between the adjacent halves of a fracture. This should be done before preparation for opening a secondary crack has begun. The lengths of cracks may also be important for analyses of fatigue fractures or for fracture-mechanics considerations.

Effect of Nondestructive Inspection

Many of the so-called nondestructive inspection methods are not entirely non-destructive. The liquid penetrants used for crack detection may corrode fractures in some metals, and they certainly will deposit foreign compounds on the fracture surfaces—both of which could lead to misinterpretation of the nature of the fracture. Frequently, the surface of a part containing, or suspected of containing, a crack is cleaned for more critical examination, and often rather strong acids that can find their way into a tight crack are used. Many detections of chlorine on a fracture surface of steel, for example, which were presumed to prove that the fracture mechanism was stress-corrosion cracking, have later been found to have been derived from the hydrochloric acid used to clean the part.

Even magnetic-particle inspection, which is often used to locate cracks in ferrous parts, may affect later examination. For example, arcing that may occur across tight cracks can affect fracture surfaces. Magnetized parts that are to be examined by scanning electron microscopy will require demagnetizing if scanning is to be done at magnifications above about 500 diameters.

Photography of Fractured Parts and Fracture Surfaces

*By the ASM Committee on Fractography by Light Microscopy**

PHOTOGRAPHY plays an important role in fractographic reporting. Photographic treatment often starts with a picture of the total fractured part. This is followed by photographing the fracture surface and associated details, and documentation of the successive steps in the fractographic examination.

The space in a fractographic laboratory allotted to photography should be determined by the type of work being contemplated. In general, the area should have a reasonably high ceiling, should be free of excessive vibrations and, most important, should be capable of being darkened. (Total darkness is not required, but when exposures are being made the area should be dark enough to avoid extraneous light or reflections.)

Visual Examination

The first step, before undertaking to photograph a fracture surface, should be a detailed and thorough examination of the specimen in the as-received condition to determine which features are most important, which aspects are extraneous (such as dirt or postfracture mechanical damage), and whether special treatment of the surface will be required. This scrutiny should begin with unassisted visual examination, continue with inspection with a hand-held magnifier (and with a penlight if helpful), and perhaps include study with a low-power stereomicroscope. Observations made in these surveys should be recorded for future review and determination of the probable causes of fracture. A list should be made of the features deserving photography, with the magnification that will probably be required.

The next step should be general photography of the entire fractured part and of the broken pieces, to record their size and condition and to show how the fracture is related to the components of the part. This should be followed by the careful examination of the fracture by studying its image on the ground-glass back of the camera or through the view finder. The examination should begin with the use of direct lighting and proceed using various angles of oblique lighting and dark-field illumination, to assess how the fracture characteristics can best be delineated and emphasized. It should also assist in determining which areas of the fracture are of prime interest and which magnifications will be possible (for a

given picture size) to bring out the fine details. Once this evaluation has been completed, it is appropriate to proceed with photography of the fracture, recording what each photograph shows and how it relates to the other photographs.

Setups for Photography of Fractured Parts

For parts and units that are too large to bring into the laboratory, photography at the site of fracture is required. White paper, or large cards or cloths, can be used to separate the object being photographed from a confusing background, or the angle at which the picture is taken can be selected to eliminate the confusing background. Suggestions about lighting for outdoor photography are given in the section on Lighting Techniques, beginning on page 14 in this article.

If possible, it is preferable to bring the parts or assemblies into the laboratory for photographing. For larger parts, background paper, which is available in white

or colors and in rolls of various widths, can be used to provide a neutral background. To maintain a uniform background, the bottom portion of the roll should be cut off as it becomes dirty.

It is convenient to place small parts on a table, or on a box about 3 ft square by 2 ft high (see Fig. 1). A 36-in.-wide roll of white paper can be used to provide a background. Modeling clay, blocks of wood, laboratory jacks, or blocks of foam plastic can be used to support the part. The support should be concealed, either by keeping it entirely under the part or by covering exposed areas with paper.

Use of middle-tone or black background papers will modify the apparent tonal relationships. Also, a black background will give clear areas on the negative, which can be marked with india ink for identification of the specimen. The identification will appear in white on the photographic prints. However, if the photograph is to be reproduced by offset lithography, large solid-black areas may not reproduce well.

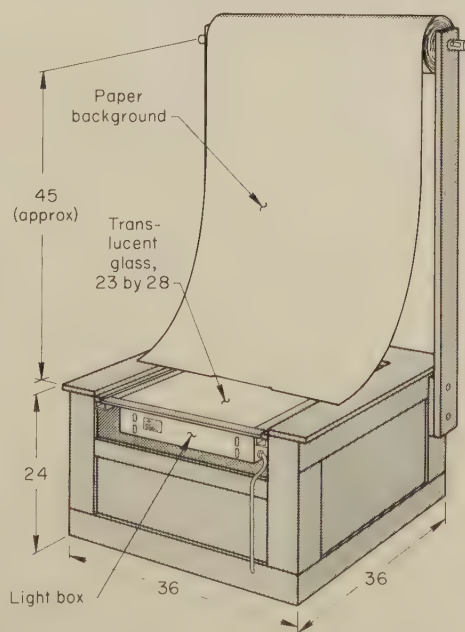
A workable setup for photographing specimens and small parts is with a view camera mounted vertically on an enlarger (or equivalent) stand. The longest-focal-length lens that will conveniently give the desired magnification to fill the image area should be chosen. Simple basic setups that should be satisfactory for photographing specimens and most small parts are shown in Fig. 2.

If a scale or ruler is to be used in the picture (and this is strongly recommended), it should be placed in the plane of maximum interest. Otherwise, the difference in perspective could cause a misleading reading.

Cameras

The camera selected for photographing fractured parts and fracture surfaces should be the one that will do the best job for the major part of the work of the laboratory. There is no one ideal camera.

View Cameras. Where most of the photography in the laboratory will consist of over-all pictures of broken parts and details of fracture surfaces at a moderate degree of magnification, a view camera offers the needed flexibility. A view camera is a definitive type and is available from most dealers. It is used on a stand and has more adjustments than other types of cameras. The 4-by-5-in. view cameras are increasing in popularity, but 8-by-10-in. view cameras are still far from obsolete. If photographic requirements



Box is mounted on casters. Construction is mainly of 3/4-in. plywood. Dowel at top holds 36-in.-wide roll of background paper. Set-in light box is fitted with a 23-by-28-in. translucent-glass upper surface that can be covered for protection when not needed. Box is useful for over-all photography with paper background, for shadowless illumination of parts on the light box, and for photocopying of transparencies, such as x-ray pictures.

Fig. 1. Box for photography of small parts

*See page 1 for committee list.

are specialized, the camera system can usually be adjusted to meet the requirements with the addition of appropriate components.

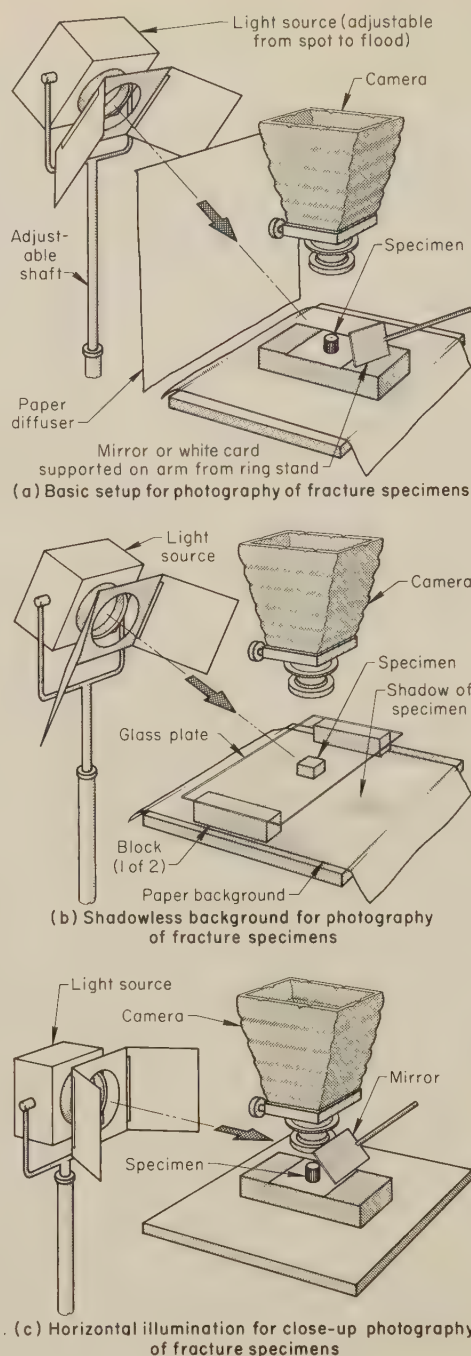
Advantages of view cameras are:

- 1 Cameras are available that have long bellows (they should be at least 50 cm long) to obtain the needed magnification. (Long bellows can also be provided for other cameras.)
- 2 The ground-glass back facilitates framing of views and focusing.
- 3 Various types and focal lengths of lenses can be used.
- 4 They include provision for movement of lens and film plane to control perspective and plane of sharp focus. The front should have rising, tilting and cross movements and the capability of pivoting the lens on its vertical axis. The back should have a four-way swing; a deep hood or reflex housing is also desirable.
- 5 A single picture can be taken. There is no need to finish or cut a roll of film.
- 6 The large film size permits adequate contact prints to be made, with good image definition.
- 7 The large variety of film sizes and types available offers considerable choice:
 - (a) There is a large selection of different types of cut film and plates for almost any situation (high-speed, high-contrast, fine-grain, infrared, color-positive, color-negative, and copy film).
 - (b) With proper adapters or holders, 4-by-5-in. or 5-by-7-in. film can be used in 8-by-10-in. cameras.
 - (c) Roll-film adapters are available to permit use of color or black-and-white roll film with from 8 to 20 exposures per roll.
 - (d) Film-pack adapters in a 4-by-5-in. size permit 16 exposures per film pack, and single films can be removed and processed separately if necessary.
 - (e) By adding a special Polaroid back, five different types of Polaroid film can be used, giving the view camera the advantages of the self-processing feature.

The main disadvantages of view cameras are that they are slower to use than other cameras and require a sturdy tripod or camera stand. To take advantage of the versatility of view cameras, the operator should consult a good book on view-camera techniques (see Selected References, at the end of this article).

Press-Type Cameras. The 4-by-5-in. press-type camera retains many of the advantages of the view camera, and incorporates an optical range finder for focusing and a view finder, so that it can be used as a hand camera. It has less bellows extension than the view camera, although actual-size close-up photographs are usually possible without use of auxiliary equipment. There is only limited adjustability of the lens and back, but this is enough to be useful. The other advantages of view cameras apply to press-type cameras, including the self-processing features obtained by using Polaroid film.

The press-type camera has wide applicability. It is easier to use than a view camera for oblique photography of parts and for photography of test setups. It can be used on a camera stand with short-focal-length lenses to make macrographs,



- (a) General arrangement of camera, light source with diffuser, and specimen. Size and angle of the beam of light should be adjusted to give the best display of texture. A reflecting mirror or white card can be used to fill in shadows.
- (b) Placing the specimen on a raised glass plate will throw the shadow beyond the view range of the camera and provide a shadowless background.
- (c) If the magnification desired requires the close approach of the camera to the specimen, which would throw a shadow on the fracture surface, a horizontal light beam reflected by a small mirror positioned near the camera lens will provide the proper angle of illumination.

Fig. 2. Basic setups and lighting employed in photographing of fracture specimens and small parts

and it can be teamed with a compound microscope for micrographs. If only one camera is to be purchased, a press-type camera should be considered.

35-mm single-lens reflex (SLR) cameras offer the size and flexibility that are of

particular advantage for field work, and they are especially well-suited for color photography. The 35-mm SLR also provides the "get what you see" feature of a view camera, unlike 35-mm view-finder cameras, with which the parallax encountered at close range limits the utility for low-magnification work.

Numerous accessories, lenses, and built-in exposure systems are available for 35-mm SLR cameras. Close-up photographs can be obtained by the use of the following accessories:

- 1 **Supplementary Close-up Lenses.** These are inexpensive +1, +2 and +3-diopter lenses. They do not require exposure compensation. Magnifications of 1× or greater cannot be obtained.
- 2 **Macrographic Lenses.** These are special lenses that can be focused close enough to obtain 1× magnification. Usually, exposure compensation is automatic.
- 3 **Extension Tubes.** These extend the lens as necessary to obtain the desired magnification, but because they are rigid, they limit the range over which the camera can be focused. Exposure compensation is required as tube length is increased.
- 4 **Bellows.** Using the proper lens (short-mount type), the bellows will permit focusing from infinity to about 3× or 5× magnification. Exposure compensation is required for the bellows extension.

The small size of the film for the 35-mm camera may be a disadvantage for black-and-white photography, because enlargement will be required. Also, the 20 or 36-exposure rolls may be considered a disadvantage where only one or two exposures are required. Because of the small size of the viewing screen, true assessment of lighting effects is more difficult, and the lack of tilt-and-swing functions of lens and film plane is a limitation in focusing.

Single-lens and twin-lens reflex cameras using roll film are lighter than 4-by-5-in. view or press cameras, and have the advantage of portability and convenience. The film sizes, No. 120 or No. 220 (giving 8, 10, 12, 16 or 24 exposures per roll), are adequate for high-quality enlargements. Accessories similar to those available for 35-mm cameras permit close-up photography, but there are still some limitations.

Microscope Systems. Low-magnification stereo and monocular microscopes with attached cameras are suitable for the photography of fracture surfaces. In general, these types of microscopes will cover a much smaller field than is obtainable with the single photographic objective lens. Some systems permit the eyepiece on the microscope to be removed to increase the size of the field.

Whereas camera systems have practical magnification limits of 15 to 20 diameters, much higher magnifications can be obtained with a microscope, the magnification being limited primarily by the diminishing depth of field at higher powers.

The usual microscope illuminator systems may or may not be satisfactory for fractography. The specimen size may also be limited to that which can be handled on the stage of the microscope.

An interesting variation of the stereo-microscope is the operation (surgical) microscope. This instrument uses long-focal-length objectives to provide long working distances at high magnifications. The working distance is approximately equal to the focal length of the objective lens, which may be from 100 to 400 mm. The long working distance permits different types of lighting to be used for the photography of fracture surfaces. It is also adaptable to the taking of stereo photomacrographs.

Lenses

Magnified images are obtained by using short-focal-length lenses on cameras and extending the bellows. The magnification can be determined by the formula:

$$M = \frac{B - f}{f} \quad (\text{Eq 1})$$

where M is the magnification, B is the bellows length (distance from film plane to lens), and f is the focal length of the lens. One difficulty with this formula is deciding exactly what point on the lens should be used to measure the bellows length, B . As a consequence, the following alternative expression proposed by R. B. Hooker is also used:

$$M = \frac{1}{2} \left[-2 + \frac{d}{f} \pm \sqrt{\left(\frac{d}{f}\right)^2 - 4} \right] \quad (\text{Eq 2})$$

where d is the object-to-image distance and f is the lens focal length (Close-up Photography Slide Rule, *Phot Appl Mag*, Vol 8, No. 1, Jan 1973, p 26).

The focal lengths of photographic lenses recommended in ASTM E2 for maximum resolution at various magnifications are as follows:

Linear magnification	Focal length
1 to 3×	152 mm (6 in.)
3 to 10×	72 mm
10 to 20×	40 mm
20 to 30×	32 mm

Other focal lengths, such as 158, 63, 42 and 16 mm, are also used.

For the 72, 40 and 32-mm lenses, it is desirable to use a lens cone to attach the lens to the lens board. This adds 100 mm or so to the bellows length, giving increased magnification. With short-focal-length lenses, the camera is very close to the specimen, which makes it difficult to light the specimen at the proper angle for fractography. The use of a lens cone helps in this respect. In general, the longest-focal-length lens that will conveniently give the desired magnification should be used. This will permit the greatest working distance between the lens and the specimen. For images having equal magnification, the depth of field will be essentially the same regardless of the focal length of the lens used. However, because of the difference in the distance of the camera from the object being photographed, there may be some difference in relative perspectives.

Lenses designed specifically for macrography will give the best image definition. Other high-quality lenses, such as motion-picture-camera lenses and those for 35-

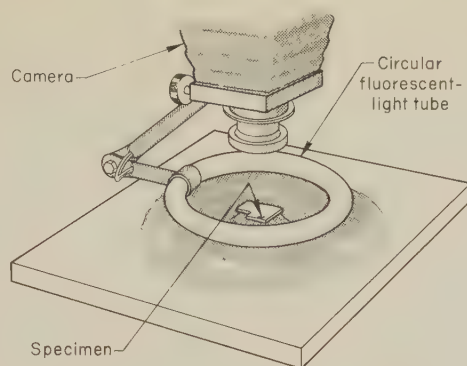
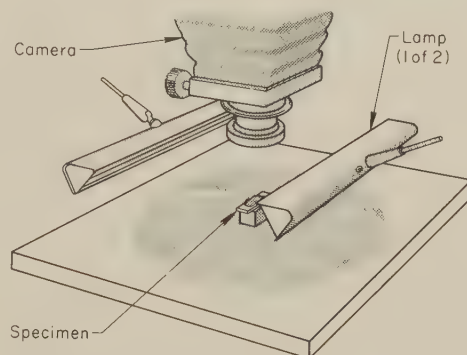
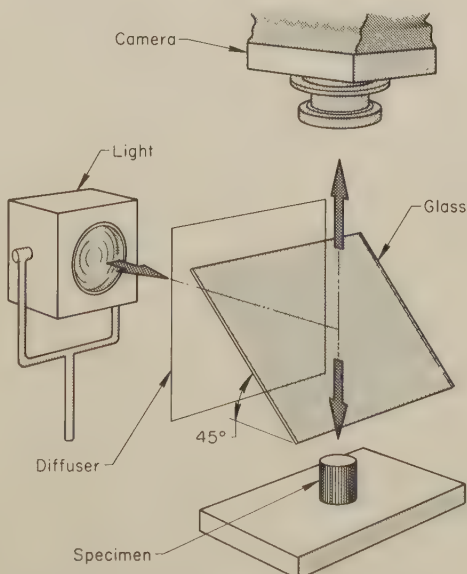


Fig. 3. Ring illumination by a circular fluorescent-light tube, which provides a soft, low-contrast, even illumination for 360° and generates a minimum of heat



With this setup, oblique lighting comes from two directions. It may be desirable to make one fluorescent lamp the principal source and to lighten the shadows it casts by positioning the other lamp farther from the specimen or by using a lower-intensity fluorescent tube.

Fig. 4. Parallel lighting



The glass plate below the lens is set at a 45° angle. It reflects the light beam to the specimen surface. A portion of this light is reflected from the specimen back through the glass plate to the camera lens. This results in two losses of light: a portion of the incident beam passes through the plate, and a portion of the reflected light is returned toward the source. About one quarter of the light (or even less, depending on the reflectance of the glass) reaches the lens. The vertical illumination used in metallographs is essentially the same as this.

Fig. 5. Vertical illumination

mm cameras, can be used, but it may be necessary to reverse the lens for optimum optical correction. Wide-angle lenses and very fast lenses may not be satisfactory because of their optical design.

Focusing

A magnifier should be used when focusing the image on the ground glass of the camera. For some photomacrography, and for photomicrography, a small clear spot at the center of the ground glass may help in focusing dim images. This can be obtained by cementing a microscope slide cover to the ground glass, using Canada balsam.

In general, the camera should be focused a third of the distance into the fracture surface. However, for photomacrography, it is frequently better to focus half the distance between the highest and lowest planes of interest.

The camera should be focused by first extending the bellows to achieve the desired magnification and then moving the entire camera up or down to obtain a sharp focus. Moving the lens for focusing changes image and specimen distances simultaneously, altering the magnification. In some laboratories, a stage is used that will permit raising or lowering the specimen so that the camera does not have to be moved. This can be either a laboratory jack or a converted microscope stage. The lens aperture should be stopped down as necessary for increasing the depth of field, but excessive stopping down will result in loss of resolution, due to diffraction.

The swing-and-tilt adjustments of the view camera make it possible to alter the plane of sharp focus so that it coincides with the area being photographed, thus giving sharp images over a wider range of distance than is possible by stopping down the lens only.

Lights

An important consideration in photography of fractured parts and fracture surfaces is lighting. It should be plentiful and flexible. Lights should be easily adjustable and be capable of maintaining a set position without shifting.

Overhead fluorescent lights can provide satisfactory lighting for the over-all photography of parts in black and white. If color photography is to be performed, filtration is necessary for proper color rendition. With cool-white fluorescent lights, a CC30M magenta filter should be satisfactory if used with daylight color film and exposure increased by two thirds of a stop. If much color work is considered, fluorescent tubes for correct color rendering may be obtained.

Photoflood or halogen-cycle lights on proper light stands can also be used for general photography. Photoflood lights should be 3200-K color temperature for type-B color film and 3400-K color temperature for type-A color film. Widely different light sources should not be mixed when color photography is being done, unless a particular out-of-balance color effect is specifically desired.

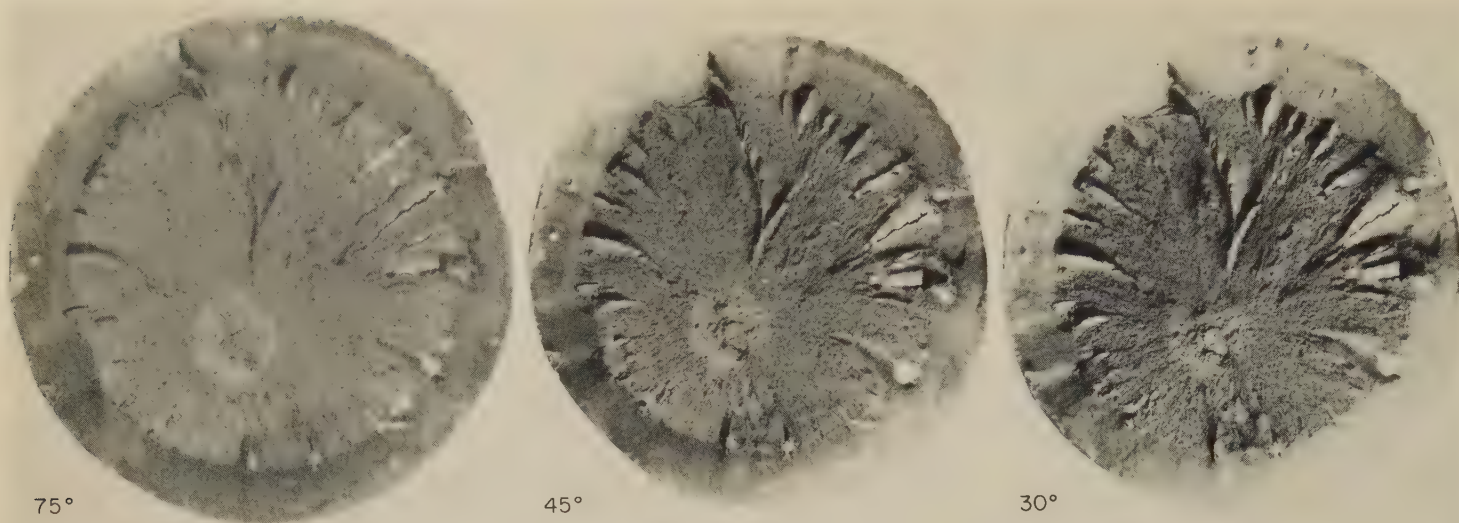
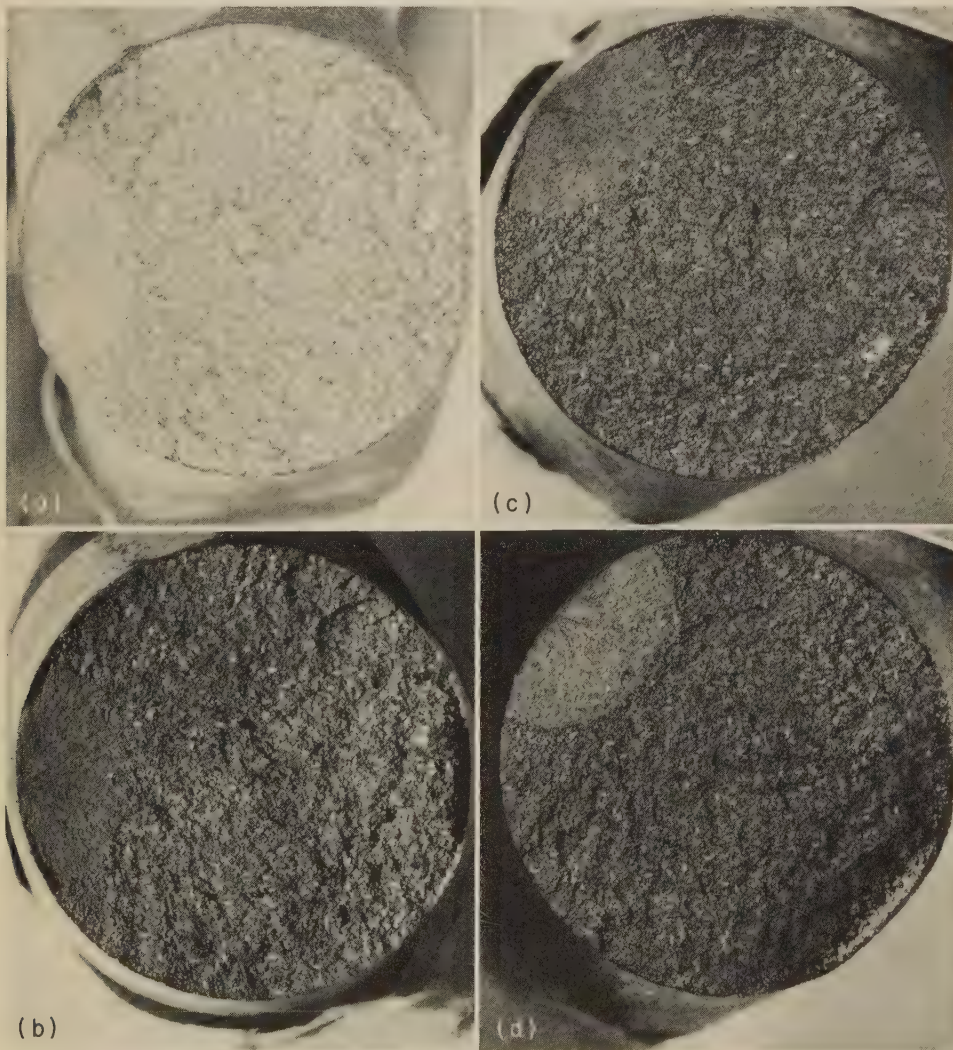


Fig. 6. Light fractographs (at 7 \times) showing effect of angle of incident light in delineating texture of a fracture surface of an unnotched laboratory tensile-test specimen of 4340 steel. The microstructure was tempered martensite. As the angle of illumination approaches 90°, the surface becomes featureless. The precise optimum angle of obliquity depends on the nature of the fracture markings.



Light fractographs

(a) Photographed with fluorescent-tube ring illumination; note low contrast and lack of detail.
 (b) Photographed with oblique light from a point-source lamp. General fracture area is contrastier than in (a), but fatigue zone is not well defined.

(c) Photographed with illumination from a mirror at camera lens. Quality is about the same as in (b).
 (d) Photographed with vertical illumination. For this particular fracture surface, vertical illumination gave the best contrast and detail of all features.

All at 2 \times

Fig. 7. Effect of illumination technique on appearance of a fracture surface of a laboratory fatigue-test specimen of 1039 steel, quenched and tempered to a hardness of Rockwell C 42

Several spotlights, capable of being focused from a narrow spot to a broad beam, are a necessity for good fractographic work. Two or three spotlights should be adequate to handle most work. These can be either 500-watt "keg" lights or 200-watt minispots. The 200-watt lights throw less heat. The lights should be equipped with "snoots" and barn doors for controlling the amount and direction of illumination.

A circular fluorescent-light tube that is large enough to surround the specimen or part provides good oblique illumination, but the height above the specimen surface is critical in obtaining the best angle of lighting (see Fig. 3 and 10). Lamps with long fluorescent tubes should be used for parallel lighting (see Fig. 4).

Electronic-flash lights and flashbulbs should be used mainly as fill light or when a specific color balance of light is required. Electronic-flash lights have built-in pilot lights to assist in setting up the desired light conditions. When used, the flash should be held away from the camera and one or more extension or slave lights should be added.

Lighting Techniques

Light levels are usually higher for outdoor photography than for indoor photography. Harsh shadows in outdoor photography can be avoided by taking the picture in open shade, or on a cloudy-bright day, or early in the morning, or late in the afternoon. Flash on the camera can also be used to fill in the harsh shadows caused by sunlight. However, unless unavoidable (as in some field work), flash should not be used as a primary light source (especially flash on the camera), because it usually results in harsh, unpredictable lighting, with great contrast.

For indoor photography, the usual technique for illumination of a part is to place one light to one side of and above the camera to light the part at a 45° angle, and a second light to the other side, at

about camera level, as a fill light. At times, a third light is placed slightly behind the part for backlighting.

Exposure-meter readings should be taken from the part, not from the white-paper background. Because most parts are dark, the white paper will usually be overexposed, which will minimize the shadows. With a standardized lighting setup, exposures will be consistent and there should be little difficulty in obtaining good negatives.

Basic lighting for photographing fracture surfaces and small parts is shown in Fig. 2. Three other illumination setups are shown in Fig. 3, 4 and 5.

Shadowless lighting of a surface can be obtained with a white background by supporting the specimen on a piece of glass above the background paper, or with a black background. For basic lighting, one spotlight is suggested. A piece of tracing paper placed between the light and the specimen will diffuse the light. The light is then raised or lowered, and the beam adjusted from flood to spot, to obtain the exact quality of lighting desired. Fracture texture is illuminated best when the light is placed at a relatively low angle. A spotlight beam without a diffuser, or a bare bulb with a small filament, will give high-contrast lighting. The advantages of this technique for revealing texture are illustrated in Fig. 6 for three different illumination angles. The angle of the incident light is much more important than its intensity.

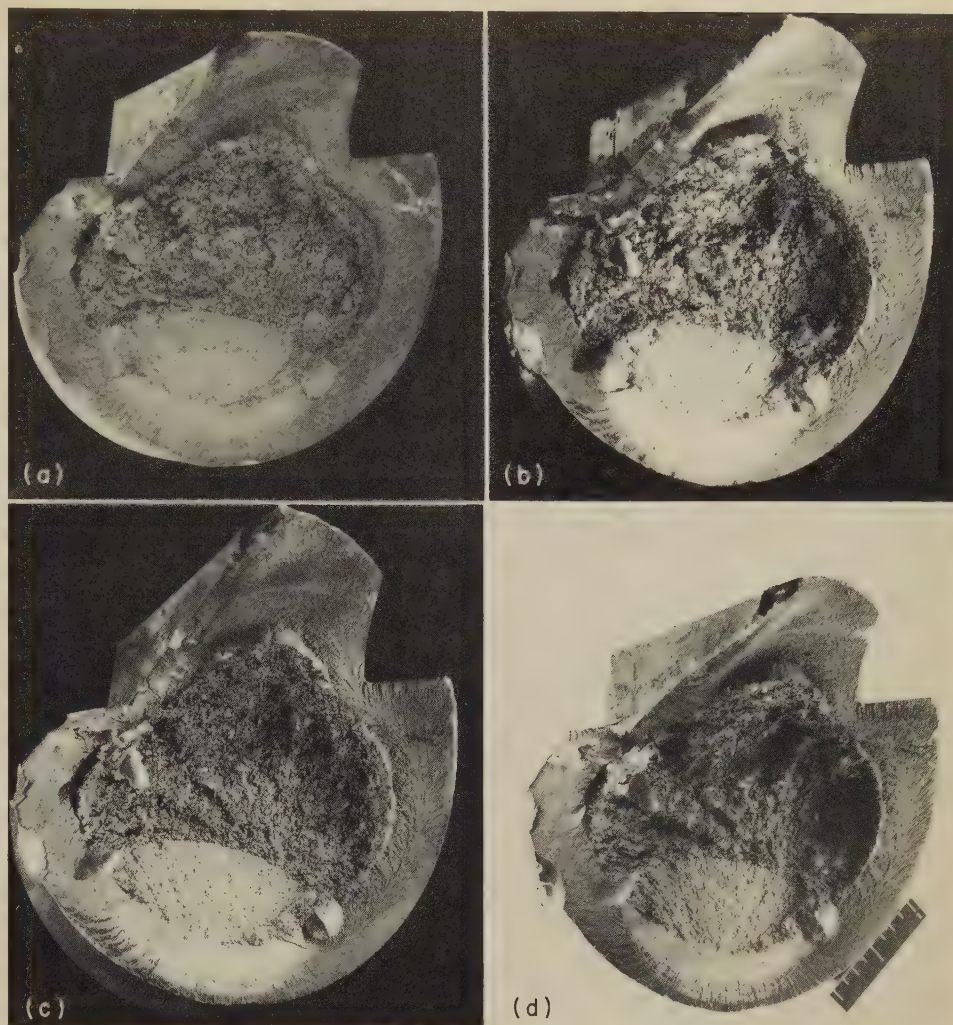
Figure 7 gives further examples of the effect of different methods of illumination on the appearance of a fracture surface. For this particular surface, ring illumination (Fig. 7a) is poorest and vertical illumination (Fig. 7d) provides the best over-all detail, mainly because of the better reflection from the fatigue zone.

Vertical illumination is achieved by placing a glass plate below the lens at a 45° angle to reflect the incident light to the specimen and then back through the glass plate to the lens (see Fig. 5). The effect is to convert light from a side source to illumination in the direction of the lens. This technique is especially useful for photographing the bottoms of cavities. Room lights should be dimmed, to avoid extraneous reflections.

Another comparison of illumination techniques is provided in Fig. 8, which shows the difference in fracture-surface appearance produced by (a) a circular flashtube around the lens, (b) oblique photoflood illumination, (c) parallel oblique fluorescent illumination, and (d) 360°-ring oblique fluorescent illumination.

A further illustration of the effects of different lighting is shown in Fig. 9. In Fig. 9(a), for which vertical illumination was used, the fatigue zone below the carburized case is clearly shown. In Fig. 9(b), for which oblique spotlighting with cross polarization was used, the fatigue zone is not shown at all, but a large silicate inclusion at the fatigue-crack origin is highlighted.

Figure 10 shows the importance of the position of the light source. For both photographs, the fracture was illumi-

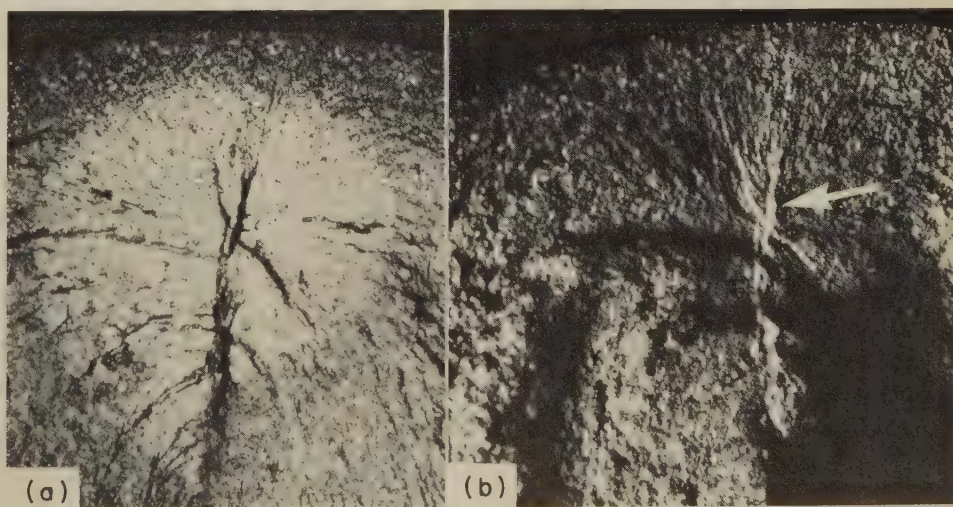


Light fractographs

All at 1/2x

(a) Illumination provided by a circular flashtube around the lens, resulting in a flat appearance. (b) Oblique illumination provided by photoflood lamp, highlighting the fatigue zone strongly. (c) Parallel oblique illumination provided by fluorescent tubes, resulting in less highlighting. (d) Ring lighting: 360° oblique illumination by circular fluorescent tubes, which gives good detail, except in the central shadows.

Fig. 8. Effect of illumination technique on appearance of a surface of a fatigue fracture in surface-hardened 15B28 steel. The fatigue crack originated at the interface between the hardened zone and the core.



Light fractographs

Both at 1 1/2x

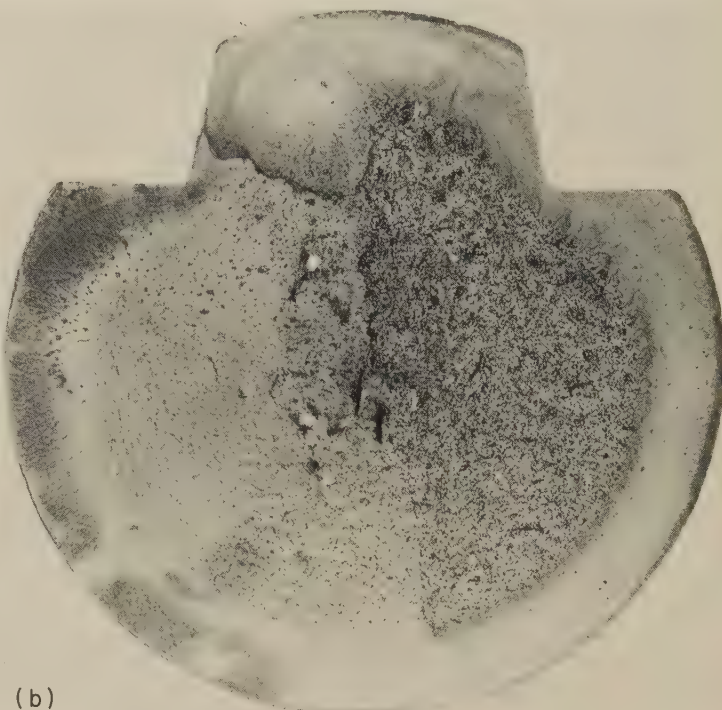
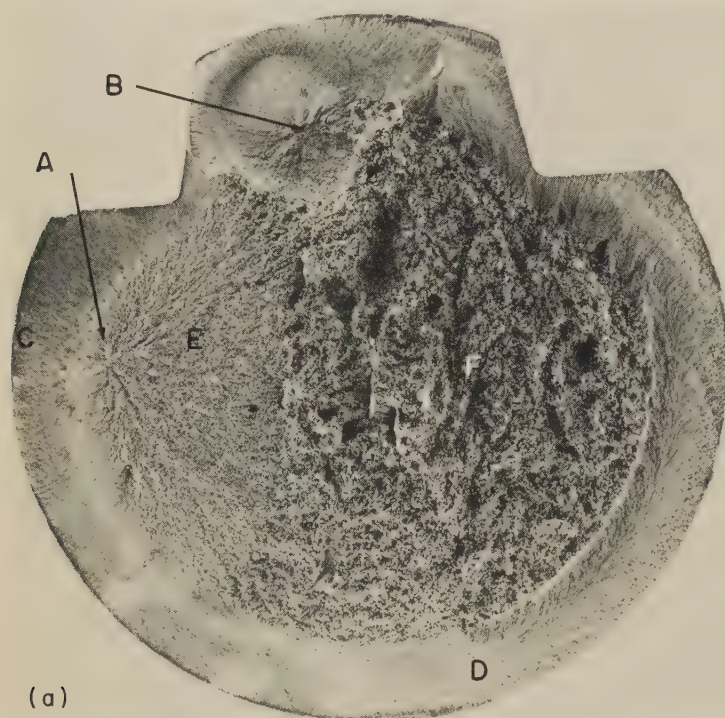
(a) Floodlight plus glass plate, to give vertical illumination. Fatigue zone is well defined. (b) Oblique spotlight with cross polarization. Fatigue zone is not shown, but a large silicate inclusion (at arrow) is highlighted at the crack origin.

Fig. 9. Effect of illumination technique on appearance of a fracture surface of a laboratory fatigue-test specimen of carburized-and-hardened 8620 steel

nated by a circular fluorescent-light tube. For Fig. 10(a), the incident light had the proper obliquity to bring out all details of the fracture surface. For Fig. 10(b), the light was moved up 1 in. and the degree of obliquity was thereby changed, with consequent loss of detail.

Fracture surfaces usually have numerous planes that will reflect small light sources as a series of catchlights. The catchlights appear in the image as blur circles and have a tendency to degrade the quality of the image. Stopping down the lens increases the size of the blur

circles because of diffraction from the iris diaphragm. However, the use of a controlled amount of diffusion minimizes the catchlight problem and decreases contrast in lighting, making it possible to obtain detail in some of the shadow areas. If a spotlight and tracing paper are used,



Light fractographs

These fractographs are of the surface of a fatigue fracture in a 1541 steel axle that was induction hardened to Rockwell C 50 and tested in rotating bending. The better-detailed fractograph at left shows that two fatigue cracks (one at A and the other at B) originated at the interface between the hardened zone and

the soft core. The crack that began at A progressed around the hardened zone, by fatigue in area C and by fast fracture in area D, before meeting the crack that began at B. The fatigue crack from A also penetrated the soft core, at area E. Final, fast fracture occurred in the soft core, at area F.

Both at 1.15×

Fig. 10. Change in fracture detail that resulted from a shift in the position of the light source. Illumination was by a circular fluorescent-light tube. The details in the surface are well revealed in (a) but are missing in (b), for which the light was moved up 1 in.



Light fractographs

Fig. 11. Surface of a fracture in an exhaust-valve stem of 21-4N (SAE EV 8) steel photographed with a 40-mm lens and with the specimen resting on (a) white paper and (b) black paper. In (a), lens flare from the white background obscured some of the detail. A clear picture resulted when the specimen was placed on black paper (b), which eliminated the lens flare.

Both at 10×

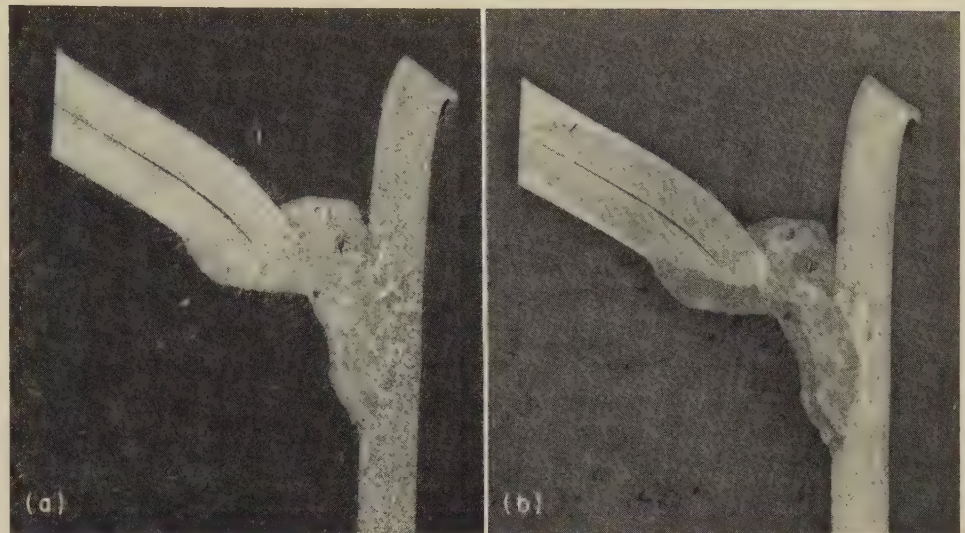
the desired degree of diffusion can be obtained by adjusting the distance between the tracing paper and the part being photographed (the nearer the part, the greater the contrast) and by adjusting the light from spot to flood. Similar lighting can be obtained using other sources, such as small fluorescent lights, but these generally do not have the degree of control obtainable with spotlights.

When photographing fracture surfaces, the specimen should be rotated under the lens and the effects of the lighting should be observed on the ground glass of the camera, in order to bring out the most detail in the areas of interest. In general, the light should be across the fracture grain, not parallel to it. Dark shadows on the side of the specimen away from the light, or behind shear lips, can be filled in with light reflected from a mirror or a white card, as in Fig. 2(a). It is preferable to use reflected light, as from a white card, to fill in shadows rather than a second light, which will only cast more shadows. The light from the card is softer and is easily controlled by adjusting the distance of the card from the specimen. Too strong a fill light may overpower the texture lighting. In lighting specimens, keep in mind that the angle of incidence equals the angle of reflection.

Lights should not shine on lens surfaces; this can lead to ghost images and lens flare. Where possible, use a lens hood, or keep the light off the lens with a black-paper baffle. With coated lenses and antihalation films, the use of white backgrounds in over-all shots generally causes no difficulty. On the other hand, when a lens with a very short focal length is used, in order to obtain magnification, it must be brought close to the specimen during photography, and lens flare can become a problem if the specimen is placed on white paper, as shown in Fig. 11(a). Usually this can be corrected by using black paper under the specimen, as for Fig. 11(b). If the desired magnification can be achieved, use of a telephoto lens can avoid the problem of proximity of the camera to the specimen. At magnifications of 15 to 20 diameters, there may be difficulty in getting the light to the fracture surface at the correct angle to delineate the details effectively.

Lighting of Etched Sections. Etched sections are best photographed using vertical illumination. Attempts to illuminate carburized or hardened cases obliquely usually result in tone reversal, with dark areas appearing white and white areas appearing dark. Steel weld specimens etched in ammonium persulfate solution can sometimes be photographed using an oblique spotlight, but usually more information is provided by vertical lighting. The macrographs in Fig. 12 compare oblique and vertical lighting for bringing out the structure of a weld. Figure 13 is a photograph of a properly illuminated weld.

Lighting of Highly Reflective Parts. Because of the high reflectivity of such parts as bearings, plated surfaces, and highly polished or ground objects, they require special techniques of lighting to reveal the details of fracture surfaces. It is



Macrographs (etchant: ammonium persulfate) Both at 4×
(a) Oblique lighting reveals the grain structure of the steel base metal but no detail of the weld beads.
(b) Vertical lighting shows the weld beads and the rim of the steel, but the grain structure is less distinct.

Fig. 12. Effect of oblique and vertical lighting on structures revealed in a macroetched section through a multiple-pass weld in 1008 steel strip



Macrograph (ammonium persulfate) 4×
Fig. 13. A properly illuminated section through a weld. Vertical lighting was used to reveal flow lines in the base metal, the heat-affected zone, and the successive weld beads. Base metal was 1018 steel; component, an axle housing.

recommended that they be entirely encircled by a cone or cylinder of tracing paper to diffuse incident light (Fig. 14). This "tent" is translucent and can be illuminated by several lights from the sides. Use of sprays and powders to reduce reflections is undesirable, because they cover up details.

Lighting of Deeply Etched Specimens To Show Grain Flow. Deeply etched specimens are photographed using a vertical setup and a single spotlight at a low angle

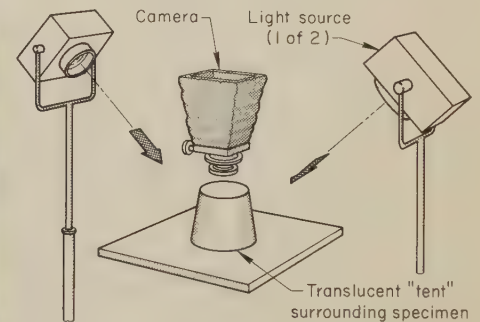


Fig. 14. "Tent" lighting used for photographing highly reflective parts

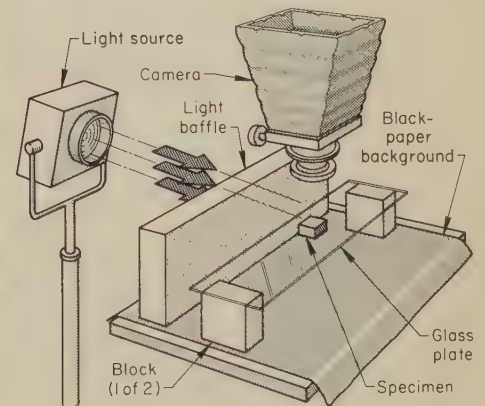
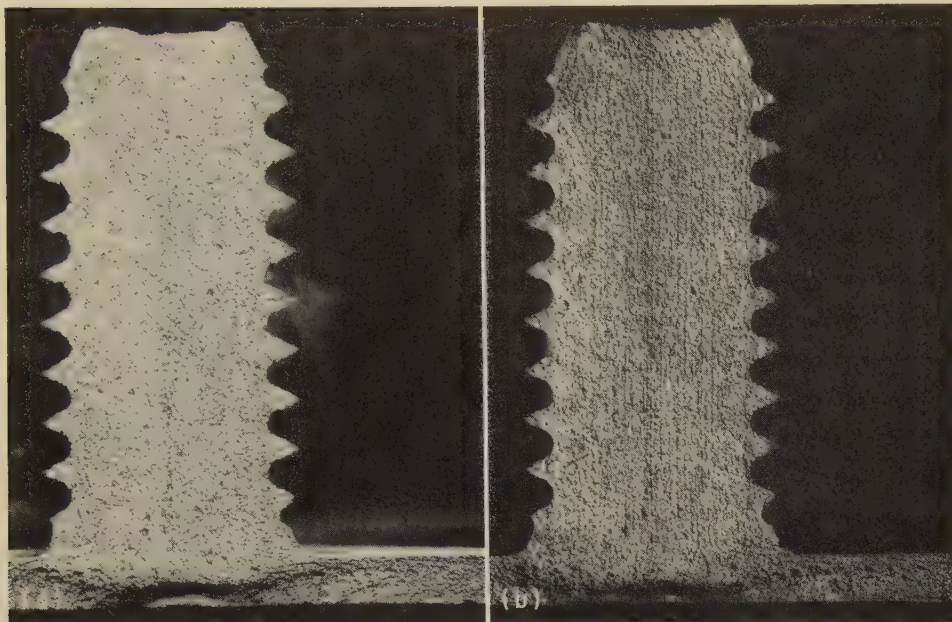


Fig. 15. Lighting for deeply etched specimens to show grain flow and inclusions

(Fig. 15). The specimen can be supported on a glass plate over a piece of black paper, to give a black background. The light should be shielded in such a manner that it does not illuminate the background paper. The direction of incident light must be across the grain flow to show the texture properly (see Fig. 16). Greater contrast is obtained if all room lights are off.

Photography With Ultraviolet Illumination. For black-and-white photography of



Macrographs (etchant: ammonium persulfate)
 (a) With illumination from the top, parallel with the grain flow, little detail is shown. (b) With illumination from the side, across the grain flow, flow lines are revealed.
 Both at $3\frac{1}{2} \times$

Fig. 16. Effect of direction of lighting in revealing grain flow in a deeply etched section through a 1010 steel stud that was attached to another part by resistance welding. Direction of grain flow was vertical.

fluorescent nondestructive-testing indications, an ultraviolet illumination source is required, with a yellow (K2) filter placed over the lens to prevent the ultraviolet light from directly affecting the film. The camera is focused on the area to be photographed, using white light. Then all room lights are turned off and the exposure is made using only the ultraviolet source. Long exposures are generally required. Typically, an exposure of 2 min at $f/11$ may be required on ASA (ANSI) 400 film. This can be decreased to 15 to 20 sec by using ASA (ANSI) 3000 Polaroid film. The Polaroid photograph can be copied if a film negative is required. If only one light is used (as is customary), it should be moved during the exposure to obtain equal illumination. The motion is usually both circular and back-and-forth over distances of 6 to 12 in.; the effect is reproducible because the long exposure time makes the motion noncritical. Background papers treated with brighteners that fluoresce under ultraviolet light should be avoided.

Nondestructive-testing indications can be photographed in color, if a UV or skylight filter is used over the camera lens.

Film

The black-and-white film used for over-all photography and photomacrography should be a moderately fast, fine-grain film with a long scale of gradation and good exposure latitude. Selection of a particular film is not as important as deciding on one film and using it consistently to become completely familiar with its response and characteristics. An advantage of using an ASA (ANSI) 400-speed cut film such as Tri-X is that type 52 ASA (ANSI) 400 Polaroid film can be used to

check exposures and lighting and no readjustments are needed in final photography on cut film. Other self-processing films available for 4-by-5-in. cameras are: Polaroid type 51 high-contrast film (ASA or ANSI 125 with floods, 200 with flash), type 55 P-N (positive-negative) ASA (ANSI) 50 film, type 57 ASA (ANSI) 3000 film, and type 58 ASA (ANSI) 75 color film.

When both monochromatic and color film are used, there is an advantage in selecting types that provide equivalent film speeds, thereby avoiding the need to change exposure when changing film type. In one procedure, Plus-X black-and-white ASA (ANSI) 125 film, Ektachrome X ASA (ANSI) 64 color film for transparencies, and Kodacolor X ASA (ANSI) 80 film for color negatives can be used interchangeably at a film speed of ASA (ANSI) 64. Another procedure uses Polaroid type 58 ASA (ANSI) 75 color film to check exposure and lighting. Then, without changing the exposure and lighting, the following can be used interchangeably: Ektapan black-and-white ASA (ANSI) 100 film, Ektachrome X ASA (ANSI) 64 color film for transparencies, and either Kodacolor X ASA (ANSI) 80 film with floodlights or Kodak CPS ASA (ANSI) 100 film with electronic flash for color negatives.

Because of their small size, 35-mm film negatives usually require enlargement, and so the emulsion grain size is a matter of importance. A black-and-white Kodak film for photomicrography (No. S0410) has an extremely fine grain, moderate film speed, and controllable contrast. A similar film in color (No. S0456) gives high definition and very high resolution, and has an extremely fine grain; its film speed of ASA (ANSI) 16 is a disadvantage, but there are many applications in fractography where it gives excellent results.

Selection of a color film will depend on the following considerations:

- 1 **End product desired** — transparencies or prints. Since good-quality prints can be made from transparencies as well as from color negatives, it may be advantageous to standardize on use of transparency film.
- 2 **Type of lighting to be used** — tungsten lamps or daylight
- 3 **Length of Exposure.** Different films (and color-correction filters) may be required for short exposures than for long exposures because of reciprocity-loss effects on color balance and exposure time.
- 4 **Color Balance Desired.** Different brands of color film will have different color characteristics.

If color balance is critical, the film should all be of the same lot number; it can be stored in a refrigerator until used. Tests should be conducted under standardized conditions, and color balance should be corrected as necessary with CC-type filters. Color film should be processed as soon as possible after exposure, to minimize color shift.

To identify exposures used, the film holders can be marked by filing small notches in the inside edge of the bottom strip. These will print out when the film is exposed. Another method is to photograph a series of numbers on high-contrast process or litho film, and then cut out and cement a number to one corner of the bottom strip of each film holder. The holders are then marked on the outside with the same number.

Exposures

Correct exposure has been obtained when: (a) after development, the detail and contrast can be reproduced by printing the negative on medium-contrast print paper; (b) over-all density of the negative is such that excessively long printing exposures are not needed; (c) shadows contain detail; and (d) highlights have gradation. If one type of film is used consistently, with a standardized processing procedure, confidence will increase with experience, and determination of exposure will not present a serious problem.

The methods used to determine proper exposure include the use of exposure meters, exposure scales and computations, and test exposures.

Exposure meters are of three types: those that measure light reflected from the subject, those that measure light falling on the subject, and those that detect light reaching the film.

Light Reflected From the Subject. Reflected-light meters have cadmium-sulfide or iron-selenium cells that change electrical resistance, or generate an electric current, when exposed to light. Because these meters are calibrated to give the correct exposure when the subject has 18% reflectance, the reflectivity of the subject must be taken into consideration. For example, if a white card having 90% reflectivity is photographed by the indicated reading, the negative will be underexposed and print out as 18% gray. However, for over-all photography with average subjects, this usually causes no problem and reflected-light meters are entirely practical. Problems may occur in photomacrography, mainly in obtaining a representative reading,

Table 1. Exposure Guide for Close-up Photography Using Film - Flash Guide Number 56 (See Text for Explanation, and Examples of Use)

0		¼ size		½ size		¾ size		1×		1½×		2×		2½×		3×	
		1½		2		3		4		5		6		7½		10	
AF ¹ FD		EF FD		EF FD		EF FD		EF FD		EF FD		EF FD		EF FD		EF FD	
32	21	40	14	48	10	56	7	64	5	72	4	80	4	88	4	96	3
22	31	28	20	33	14	39	10	44	8	50	6	55	6	61	5	66	5
16	42	20	27	24	19	28	14	32	11	36	8	40	8	44	7	48	6
11	61	14	39	17	27	19	20	22	15	25	12	28	11	30	10	33	9
8	..	10	54	12	38	14	27	16	21	18	17	20	15	22	14	24	13
5.6	..	7	..	9	53	10	39	11	30	13	24	14	22	16	19	17	18
4	..	5	..	6	..	7	54	8	42	9	33	10	30	11	27	12	25
2.8	..	4	..	4	..	5	..	6	60	7	46	7	43	8	39	8	38
2	..	3	..	3	..	4	..	4	..	5	..	5	60	6	55	6	50
GN × 12		Corrected guide number: GN × 12 ÷ (M + 1)															
672		540		450		380		336		300		300		300		300	

AF = actual *f*-stop; EF = effective *f*-stop; FD = flash distance in inches; GN = guide number; *M* = magnification

because of the small area to be photographed. Spot meters are available that will read light intensity from small areas.

Light Falling on the Subject. Incident-light meters are similar to reflected-light meters; in fact, most meters now made will take either type of reading. For an incident-light reading, the meter is held near the subject and the light is allowed to fall on a hemisphere or cone over the cell. The effect is the equivalent of taking a reflected-light reading from an 18%-reflectance gray card.

Light Level at the Film Plane. These meters are usually very sensitive cadmium-sulfide or photomultiplier devices that will measure the quantity of light that reaches the film, and therefore there is no necessity for making corrections for aperture setting or bellows extension. They can be built into the system or they can be a separate probe. Some photomicrographic units have built-in light-integrating systems that automatically close the shutter as soon as the proper amount of light has reached the film. The probe-type meter is most useful for determining proper exposure of bright areas of interest against dark backgrounds, and vice versa. Extraneous light must be avoided to prevent incorrect readings.

Exposure Scales and Computations. When electronic-flash units or flashbulbs are used, exposure is determined by use of a guide number, which is based on the film speed and the amount of light on the subject, and represents the *f*-stop multiplied by the distance in feet from the flash to the specimen to be photographed. For example, a guide number of 56 means *f*/2.8 at 20 ft, *f*/5.6 at 10 ft, or *f*/11 at 5 ft. Lenses are available that can be set for a given guide number and that will automatically change the *f*-stop as the lens is focused. Also, electronic-flash units are available that sense the amount of light reflected from the subject and quench the flash after the proper exposure.

The above two systems are not of much use in photomicrography. When flash is used for photomicrography with an extended bellows, two corrections must be made. First, as the bellows is extended, the effective lens aperture is no longer the *f*-stop that is engraved on the lens, but rather:

$$\text{Effective } f\text{-stop} = \frac{\text{Image distance}}{\text{Actual } f\text{-stop} \times \text{Focal length of lens}} \quad (\text{Eq 3})$$

or:

$$\text{Effective } f\text{-stop} = \frac{\text{Actual } f\text{-stop} \times (\text{Magnification} + 1)}{\quad} \quad (\text{Eq 4})$$

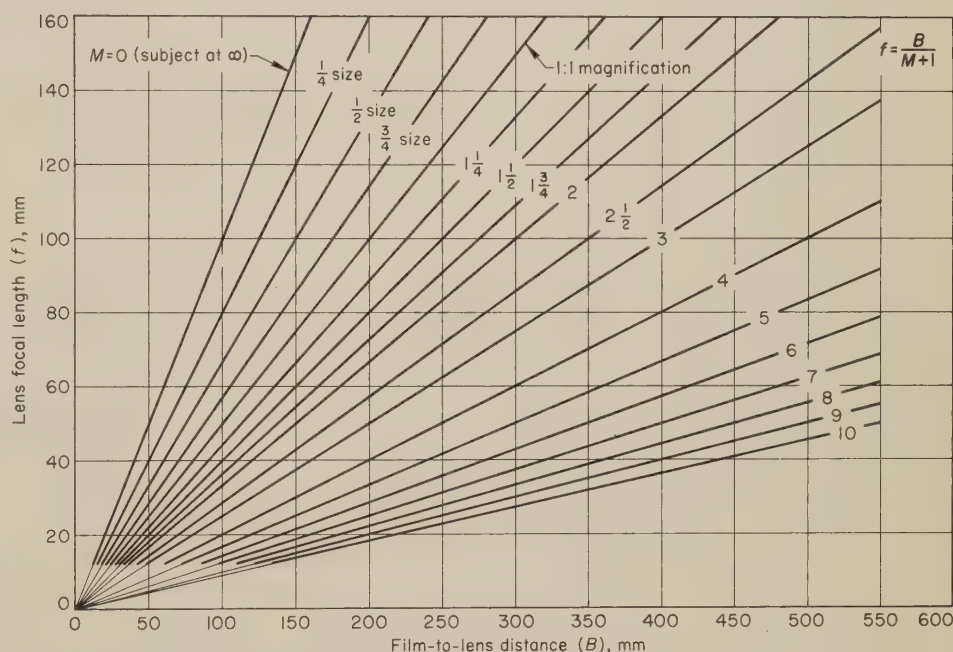


Fig. 17. Graph that permits determination of various magnification levels from film-to-lens distance and lens focal length

Second, because of the inefficiency of typical reflectors, which are not focused at close distances, an empirical correction must be applied to the guide number by dividing it by the quantity magnification-plus-one until it is the equivalent of a bare bulb, which is about half the given guide number and occurs at a magnification of approximately one diameter. For close-up photography, it is convenient to multiply the guide number by 12 and measure the flash-to-subject distance in inches rather than in feet.

To eliminate repeated computations, exposure charts can be prepared to give the correct exposure for any film-flash guide number for use at any magnification. One such chart is shown as Table 1, which was prepared for guide number 56, and which covers magnifications from 0 (that is, for a subject at "infinity") to three diameters. Below each value for the magnification in Table 1 is listed the relevant effective *f*-stop number and the correct distance for the flash from the subject. The formulas on which Table 1 is based (or by which other tables can be

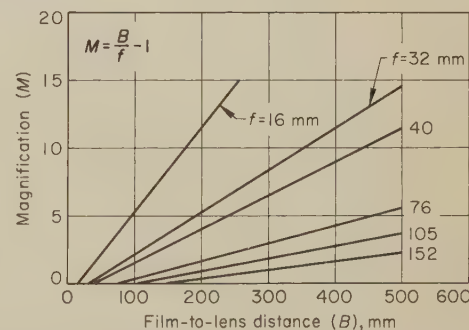


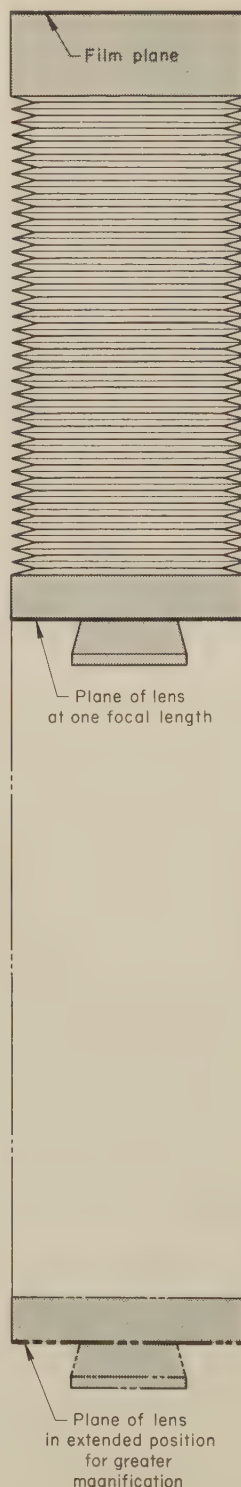
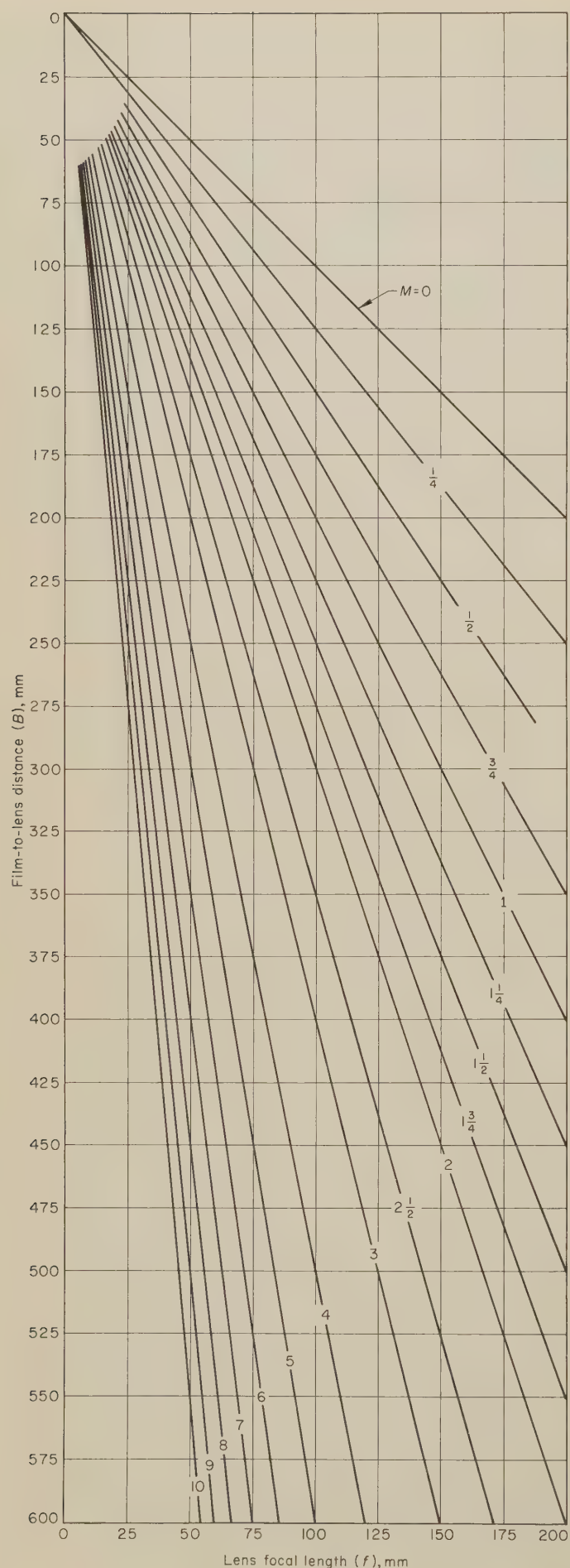
Fig. 18. Graph that permits determination of magnification from film-to-lens distance for a selected number of lens focal lengths

computed for other film-flash guide numbers and magnifications) are given in the list that follows:

1 Magnification. This is calculated by the formula:

$$M = \frac{B - f}{f} \quad (\text{Eq 5})$$

where *B* is the distance from the film to the lens and *f* is the focal length of the



lens. A convenient procedure, however, is to make use of a graph such as Fig. 17, which shows the combinations of focal lengths and film-to-lens distances for various magnifications, or Fig. 18, which shows the magnifications possible at any film-to-lens distance for each focal length. If either of these graphs is replotted with the film-to-lens abscissa in actual millimeters and is then mounted on a card and placed parallel with the camera track with the origin at the film plane, the magnification can be read directly from the lens position, taking into account the lens being used. This procedure is illustrated in Fig. 19. (The graphs in Fig. 17 to 19 cannot be used if magnification is calculated by use of equation 2, page 13; other graphs are required.)

- 2 **Exposure Increase Required.** Because the extension of the camera bellows to obtain a close-up photograph has the effect of increasing the effective f -stop to a value above the number shown on the lens, it is necessary to compensate for this loss of light by increasing the exposure by a factor determined according to the following formula:

$$\text{Exposure increase} = (M + 1)^2 \quad (\text{Eq 6})$$

- 3 **Effective f -Stop (EF).** As stated at the beginning of this section, this is given by:

$$\text{EF} = \text{Actual } f\text{-stop} \times (M + 1) \quad (\text{Eq 7})$$

- 4 **Corrected Guide Number.** For film-to-lens distances up to about two focal lengths, the empirical correction of a guide number for the film and flash unit in use is:

$$\text{Corrected GN} = \frac{\text{GN}}{M + 1} \quad (\text{Eq 8})$$

In Table 1, the value as usually expressed has been multiplied by 12 to convert the distance involved to inches. For a magnification of more than $1\times$, the flash-reflector combination becomes equivalent to a bare bulb, and a constant corrected GN of approximately $\text{GN}/2$ may be used for all higher magnifications.

- 5 **Flash Distance (FD) From Subject.** This is given by the relation:

$$\text{FD} = \frac{\text{Corrected GN}}{\text{EF}} \quad (\text{Eq 9})$$

Where the corrected GN is in inches, FD will be in inches.

The use of Table 1 is illustrated by the following example: Assume that an excellent picture has been obtained with the subject at "infinity" (that is, the lens was one focal length from the film), using an f -stop of 22 and an exposure of 1 sec, and that a picture at $1\frac{3}{4}\times$ is desired. Scanning the column under $1\frac{3}{4}\times$, with the camera adjusted for this magnification, an effective f -stop of 22 is provided by an actual f -stop of 8. The picture should therefore be taken with the aperture at

The graph is placed so that the origin is at the same height as the film plane and the abscissa extends downward. With the lens in place and the bellows extended to give the desired size of image on the ground glass, the position of the lens is read on the graph, and the intersection with the focal-length value for the lens is found. This point will be on or close to one of the diagonals indicating magnification. Its value (or an interpolated one) can then be found in Table 1 and the correct exposure determined.

If there is doubt concerning the exact point on the lens casing from which to measure the film-to-lens distance, the following steps should be taken. Focus the camera on a subject at an effective "infinite" distance. The image on the ground glass will then be at a distance of one focal length from the lens. For a magnification of 1, this distance should be doubled. That is, the bellows extension is determined by the relation:

$$B = f(M + 1)$$

and the lens position for any specific magnification can be identified as some multiple of that original "infinity" focus distance from the film plane.

Fig. 19. Chart illustrating procedure for use of the graph shown in Fig. 17 with a camera for determining magnification

$f/8$ at $7\frac{1}{2}$ sec ($1 \times 7\frac{1}{2}$). Or, if a flash is used, it should be moved up to 14 in. from the subject.

As another example of the use of Table 1, assume a successful picture has been obtained at $1\times$ with a 2-sec exposure and an f -stop (actual) of 8, and that a picture is desired at $3\times$. Following the $f/8$ line to $1\times$, the effective f -stop is found to be 16 and the 2-sec exposure to be 4 times that required at $M = 0$ ("infinity"). Under $3\times$, the effective f -stop of 16 is opposite an actual value of $f/4$, and the required exposure is 16 times that required at $M = 0$. Therefore, for the $3\times$ picture, the aperture should be $f/4$ and the exposure should be 8 sec ($2 \times 16/4$).

Test Exposures. Exposures obtained with metering systems are subject to inaccuracies caused by differences in the brightness of the subject and the background, the color response of the meter as compared to that of the film, corrections for bellows extension, shutter inaccuracies, and reciprocity failure (the non-proportional response of emulsions to light during very short and very long exposures). A method for bypassing these variations is to make a test exposure. In fact, sometimes, as for ultraviolet or infrared photography, the exposure must be determined mainly by experience and test exposures. Self-processing (Polaroid) film is very helpful for this purpose.

Assuming that a relatively long exposure is to be used, a step wedge should be produced by starting the exposure and then inserting the dark slide about $\frac{3}{4}$ in. at intervals of 1, 2, 4, 8, 16 and 32 sec. The film should then be processed and the most nearly correct exposure noted. If exposures are short, the step-wedge method may not be practical, and it is suggested that the exposure be estimated from the image brightness, based on previous experience. After an exposure is made using that setting, the results can be compared with a previously prepared set of prints illustrating correct exposure, plus the results of one, two and three f -stops over and under that exposure (see Fig. 20). Corrections in exposure should be made and a second trial picture taken. If the film used in the test does not have the same ASA (ANSI) rating as the film to be used for the final picture, the exposure must be changed to take into account the difference in film speeds. Or, rather than change aperture or shutter settings, a neutral-density filter can be used. For example, if an ND4 filter with ASA (ANSI) 400 Polaroid film is used to make the test, it can be removed for exposures on ASA (ANSI) 100 cut film.

Using black-and-white film, typical corrections for reciprocity failure are:

Meter reading	Multiply reading by
1 to 2 sec	1.4
2 to 6	2.0
6 to 16	2.8
16 to 35	4.0
35 to 70	5.6

Film Developing and Printing

The procedures for film developing and printing described in this section are effective, but others are also used. Sup-

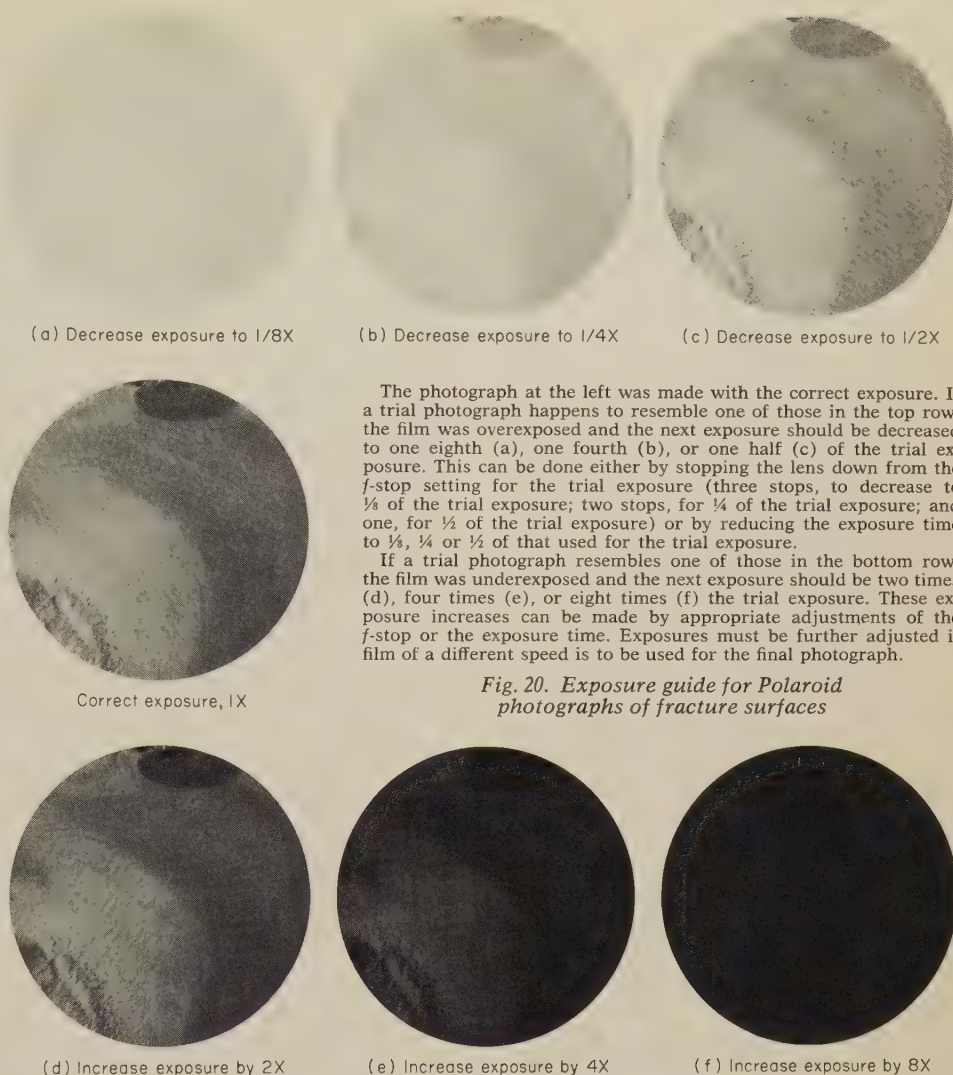


Fig. 20. Exposure guide for Polaroid photographs of fracture surfaces

pliers of photographic materials and equipment can provide information on alternative procedures.

Most black-and-white film can be developed in several types of developers, and the use of different formulas and a different degree of development can be of value if done judiciously. Truly consistent results, however, depend on the use of a standardized process based on the manufacturer's recommendations for developer, time, temperature and agitation.

Single sheets of exposed film can be processed in a tray, but the use of tanks and film hangers is usually more convenient. With a $3\frac{1}{2}$ -gal tank system and multiple film hangers that hold four 4-by-5-in. negatives each, 24 or more negatives can be developed at one time. Roll film is best developed on reels in tanks.

Improvements in emulsions have made it feasible to use moderately higher temperatures than were previously possible, with correspondingly shorter processing times. Processing temperature should be in the range between 18 and 24 C (65 and 75 F). A temperature of 24 C (75 F) is usually easier to maintain than one of 20 C (68 F). All solutions should be at approximately the same temperature. Development times should be long enough (4 or 5 min) so that minor variations do

not reduce uniformity. Developers are depleted by usage, and increased development time or the addition of replenishers may be required to maintain consistent results.

A water rinse after development and before fixing is usually adequate. Use of acetic acid stop baths can cause difficulties if the developer contains carbonates. Improved film emulsions do not require chrome-alum-hardener stop baths, except in unusual situations. A rapid fixing agent will completely fix the film in 2 to 4 min. As a general rule, the film should be fixed for twice the time required to clear the film. After fixing, the film must be washed for the recommended time. The use of hypo-clearing agents will substantially reduce the required washing time by converting thio-sulfates to compounds with greater solubility. Finally, the film is dipped into a very dilute solution of wetting agent in distilled water, drained or sponged off, and hung up to dry.

The dry negatives should be marked with india ink for identification, and stored in individual negative-protector envelopes. Roll film should be cut into strips of four to six frames and stored flat, not rolled. Never cut roll film, especially 35-mm film, into individual frames.

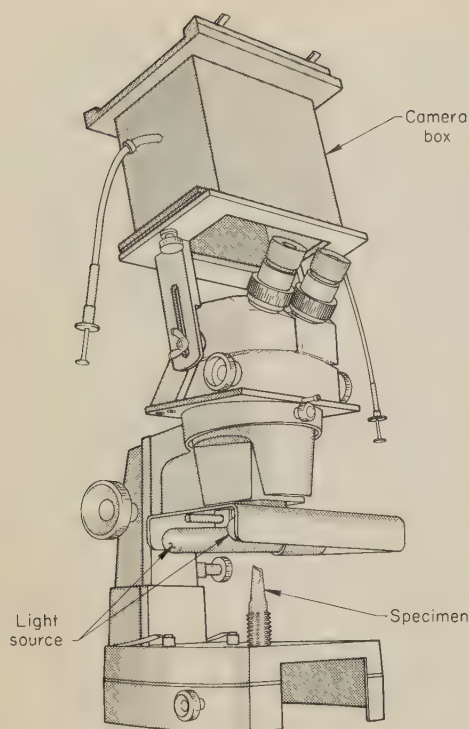
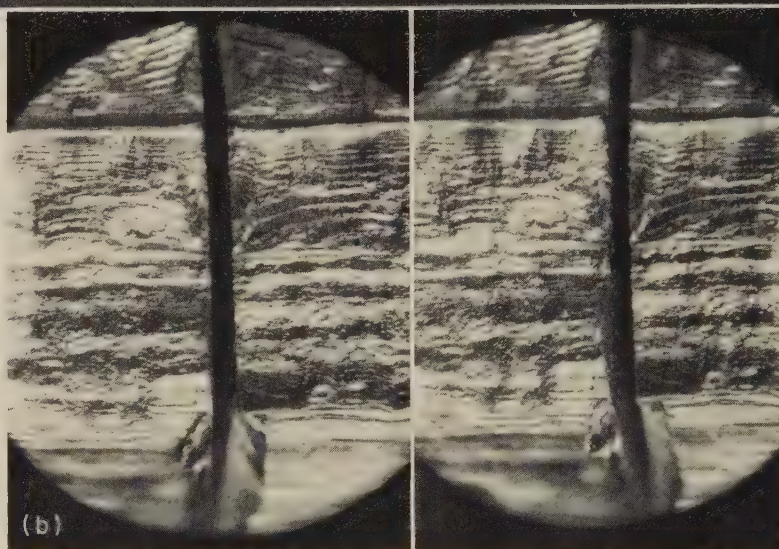
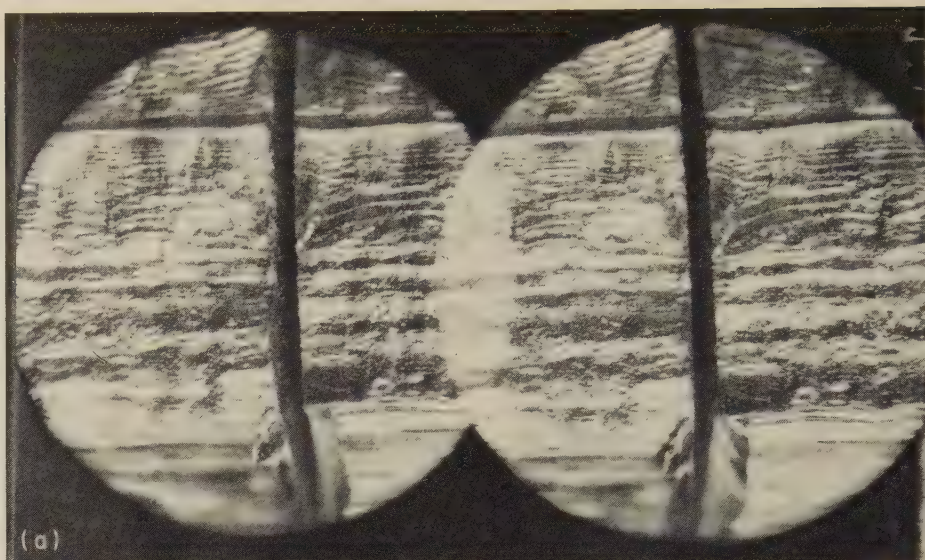


Fig. 21. Optical stereomicroscope with camera box partly removed for direct viewing. The light source is two 40-watt incandescent tubes above the specimen.

Printing Procedures. Photographic negatives are reproduced as positives on paper by contact printing and by projection printing. Considerable control can be exercised in the photographic printing process. The image quality present in the negative can be enhanced or degraded, depending on what is done in this step.

Print papers are supplied as contact or enlarging papers, in single or double weight, with warm brown-black, neutral, or cold blue-black image tones, in surfaces ranging from glossy to matte, and in grades of contrast from normal to very high or very low. The papers most often used for metallurgical subjects are single-weight and glossy, with blue-black image tones. The choice of contrast grade is determined by the negative. Correctly exposed and processed negatives can usually be printed on "normal"-grade papers. Thin negatives may require "harder", or greater-contrast, papers for satisfactory prints; heavy, overdeveloped negatives may require "softer", or lower-contrast, grades. At times, a normal negative will be printed on a higher or lower-contrast grade of paper to enhance the image. Multigrade papers are available in which the contrast is controlled by use of different color filters on the enlarger, thus making it possible to stock only one grade of paper. A special safelight filter is required with multigrade papers, to prevent fogging.

The printing exposure should be such that the proper tonal range is achieved with full development in the recommended developer at the proper temperature. Typical development times are 45 sec to 2 min for contact papers and 1 to 3 min for enlarging papers. Prints appear somewhat darker under the darkroom



Light fractographs (stereo pairs)

Both at 10×

Fig. 22. Stereo views of a low-cycle fatigue fracture in aluminum alloy 1100. (a) As photographed. (b) Interchanged for normal stereo viewing. Note that the heights and depths in (b) are the reverse of those in (a).

safelight, which results in a tendency to "pull" prints from the developer before they are fully developed. This practice yields prints with muddy gray tones, instead of good black tones.

After development, the print is drained for a few seconds, transferred to a 1.5% acetic acid stop bath for a minute or so, and then placed in the fixing bath. After the print has been in the fixing bath for at least 30 sec, it can be inspected by white light, and adjustments in printing exposure or grade of print paper can be made as required.

The use of a two-bath fixing system will ensure adequate fixing of the prints. After the print has been in the first fixing bath for 5 min, it is placed in the second bath for an additional 5 min. When 80 to 100 8-by-10-in. prints, or the equivalent, per gallon of fixing agent have been processed, the first bath is discarded and replaced with the second bath, and a new second bath is prepared.

Following fixing, the prints must be thoroughly washed for 30 min to 1 hr, depending on the efficiency of the print

washer and the weight of the paper. This is necessary to remove the thiosulfate compounds that can cause the image to fade in time. Hypo-clearing agent, used as directed, can substantially reduce washing time. The use of warm water to reduce washing time is not recommended, as this causes swelling of the emulsion and may result in difficulties in the glossing process.

The glossy finish on prints is obtained by rolling or squeegeeing the paper face down on ferrotype plates; plates of chromium-plated brass probably are the most satisfactory for the purpose. If many prints are to be produced, use of a motorized drum-type glossy drier and glossing solutions is desirable.

Rapid Printing Processes. When it is necessary to have prints available in the shortest possible time, use of the "stabilization process" or use of resin-coated papers is recommended. For the stabilization process, a special paper that contains developing agents in the emulsion is used. After printing exposure, the paper is fed into a mechanical processing machine,

which passes it through an activator solution to develop the image and then through a stabilizing solution so that it is no longer sensitive to light. A damp print is obtained in less than a minute. The image is not permanent and the paper

and TEM stereofractographs, beginning on page 281, and are not reviewed here.

Stereo images by light microscopy have been used only to a limited extent, because of the restricted depth of field. They provide a useful means of studying

two shutters. The dual-lens system provides the necessary difference in viewing angle, and no tilting of the specimen between exposures is needed. The stereo images are formed on a single piece of film (see Fig. 22a). The print from this can be viewed with 15° prism eyepieces to cross the images, or, for normal stereo viewing, the individual images can be cut apart and placed side by side in an interchanged position with a 55-mm interocular spacing as in Fig. 22(b).

With the stereomicroscope shown in Fig. 21, it is possible to observe the voids that are a part of ductile dimpled fracture, and, in brittle fractures, cleavage facets and some of the river marks can be discerned. It is most useful for preliminary examination of fracture surfaces, leaving final documentation of fine details for electron microscopy.

Another example of a light-microscope stereo pair is shown in Fig. 23. The subject is a fracture surface in a low-carbon steel casting that cracked along prior austenite grain boundaries during a straightening operation. The bold relief contours of the columnar fracture are evident when viewed in stereo.

If a tool such as a parallax bar is used, quantitative measurements of topographic depths and elevations can be obtained. This technique is used frequently in medicine but has found only limited use to date in fractography.

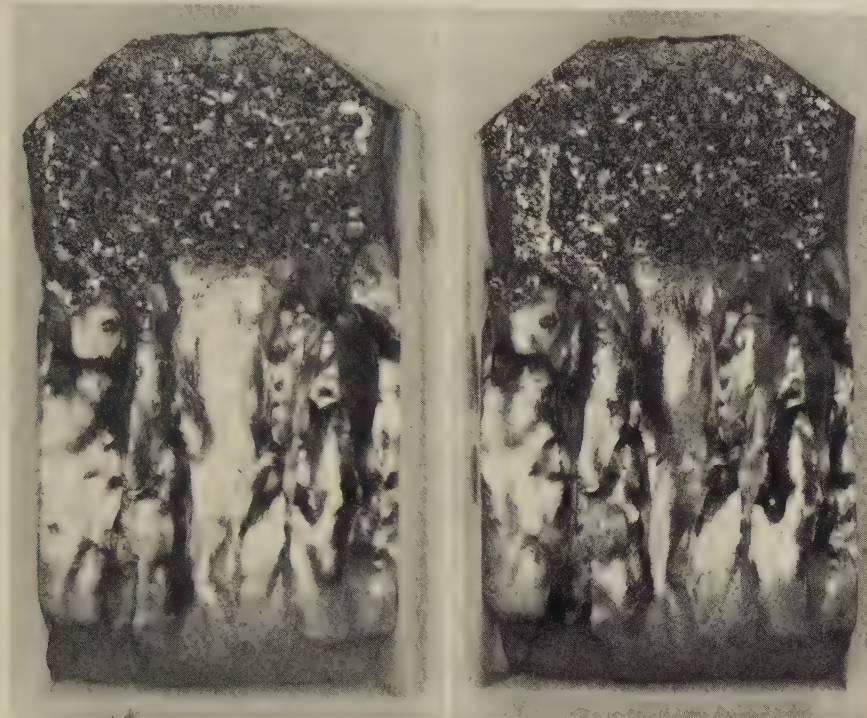
Auxiliary Equipment

For general photography, a sturdy tripod is essential. The tripod should have a head that will permit the camera to be rotated, tilted upward or downward, and pivoted a full 90° sideways. An elevating center pole is also helpful. The use of a tripod will permit exposures of 1 sec or longer when necessary with smaller f -stops, thus allowing an increase in the depth of field; it will improve composition by putting the camera in a fixed, predetermined position; and it will avoid the blurring that would occur with camera movement. A good tripod should make the use of flash unnecessary, except as a fill light. The use of a cable release is helpful in avoiding any camera motion during exposure.

For photomacrography, small-parts photography and copying, a camera stand similar to the stands used for vertical enlargers is useful. There should be provision for moving the entire camera up and down smoothly, independent of focusing adjustments. When long bellows extensions are required, horizontal camera stands may permit easier focusing.

The items listed below should be available for use in photography of fracture specimens:

- 1 **Blocks of wood** of various sizes for propping specimens in various positions.
- 2 **Laboratory jacks** for propping or supporting specimens.
- 3 **Blocks of rigid foam plastic** for propping specimens. The blocks can be cut to the desired shape and size.
- 4 **Moldable material**, such as modeling clay, silicone putty, or jeweler's wax, for supporting small parts. A leveling device



Light fractograph (stereo pair)

3×

The smooth columnar contours in the lower portions of the photographs were the result of cracking along prior austenite grain boundaries during straightening. The upper portions of the photographs also show intergranular fracture, but along ferrite grain junctions, produced by impact in the laboratory to expose the original crack surface.

Fig. 23. Stereo view of a fracture surface of cast experimental low-carbon steel

may stain in a few months, unless fixing and washing are done as in the conventional method.

Papers with a resin-coated base are available. These papers do not absorb the processing chemicals, and permanent prints can be obtained with 1 min of development, 2 min of fixing, and 4 min of washing. The prints are dried to a glossy finish by blotting. No special equipment is required.

Stereo Views

Stereo-pair photographs of fracture surfaces provide a means of viewing the fracture contours in simulated three dimensions. The basic technique for preparing such photographs entails taking two pictures of a subject area, the second from an angle slightly different from the first. The photographs are then examined under a visual condition in which, for example, the viewer's left eye focuses on the first picture and his right eye focuses on the second. The effect is to convince the brain that the eyes are indeed seeing a three-dimensional scene. If the angular displacement between the two pictures is appropriate (an included angle of 12° or 14° is desirable), the illusion is very vivid. The techniques for stereoscopic viewing are discussed in the introduction to the section of the Atlas that compares SEM

fractures at magnifications generally not greater than 200×. Three stereo-pair fractographs were published by Zapffe in 1943 in his initial paper on fractography (see Ref 30 on page 8). These were at relatively low power (10×), but show the contours in three dimensions.

Stereo-pair photographs can be taken using a single-lens camera, if it is provided with a mount that will pivot about a horizontal axis through the subject. After the subject is properly aligned beneath the camera with the mount vertical, the camera is swung to an angle of 6° to 7° from vertical and an exposure is made. The second exposure is made with the camera at the same angle as for the first exposure, but swung to the other side of the vertical, or zero, position.

An optical stereomicroscope for taking stereo-pair photographs is shown in Fig. 21. This is an effective tool for magnifications in the range of 20× to 200×. A diffuse light source is important at the high end of this range to minimize light scattering from specular reflections. Two incandescent tube lights, like those used for showcase illumination (40 watts each), provide a satisfactory intensity for the higher magnifications. For magnifications up to 50×, two 5-watt tubular fluorescent lamps are adequate.

The camera in Fig. 21 has a film plane about 3 cm above the eyepieces and has

can be used to press the specimen into the material to produce a parallel face. Where possible, the material should be placed under the specimen, or it should be covered, so it will not be visible in the photograph.

- 5 **Laboratory ring stands** with clamps for holding parts or reflectors.
- 6 **Mirrors**, of several sizes, to be used as reflectors to fill in shadow areas, to view the lens settings when the camera is in an awkward position, and to show both sides of the specimen in one picture, as when documenting strain-gage locations.
- 7 **White cards**, of several sizes, to be used as reflectors.
- 8 **Draftsman's tracing paper or film** for diffusion of light.
- 9 **Masking tape** for temporary support of

paper backgrounds and diffusers, and for holding offsize filters on the camera.

- 10 **Glass sheets**, 1-by-3-in. microscope slides, 2-by-2-in. or 3¼-by-4-in. cover glasses, and 4-by-5-in. or 5-by-7-in. (or larger) glass plates, for use as vertical illuminators or for supporting parts when shadowless backgrounds are desired. Clear acrylic plastic sheets can also be used for supporting parts.
- 11 **Magnets** for supporting or securing parts.
- 12 **Scales or rulers**, of various sizes, to place in pictures to show degree of magnification or reduction.

Selected References

H. Martin, Technical Photography, in "Technical Report", Vol VI (New Series), British Engine Boiler & Electrical Insurance Co., Manchester, UK, 1965,

p 91-116 (also available from Royal-Globe Insurance Co., 280 South Harrison St., East Orange, NJ, 07019) Leslie Stroebe, "View Camera Technique", Focal Press, Ltd., London, 1967

Roger P. Loveland, "Photomicrography — A Comprehensive Treatise", Vol 1 and 2, Wiley-Interscience, New York, 1970

Woodlief Thomas, Jr. (Editor), "SPSE Handbook of Photographic Science and Engineering", Society of Photographic Scientists and Engineers, Wiley-Interscience, New York, 1973

Eastman Kodak Co., Rochester, NY, Kodak Technical Publications with titles, numbers, and years of publication as follows:

Close-Up Photography (N-12A, 1969)

Copying (M-1, 1971)

Electron Microscopy and Photography (P-236, 1973)

Kodak Master Darkroom Dataguide (R-20, 1970)

Photography Through the Microscope (P-2, 1970)

Photomicrography (N-12B, 1969)

Photomicrography of Metals (P-39A, 1971)

Special Techniques in Fractography by Light Microscopy

*By the ASM Committee on Fractography by Light Microscopy**

THE SPECIAL TECHNIQUES discussed in this article are: the use of replicas in light-microscope fractography; sectioning and the study of fracture-surface profiles; shadow casting; microanalysis of fracture surfaces; etch pitting; and the use of deep-focus microscopes.

Replicas

Many of the replication methods described in the article "The Transmission Electron Microscope and Its Application to Fractography" (see page 54) are occasionally used in light-microscope fractography. Typical applications are in the study of fractured parts that are too large to bring into a laboratory and that cannot be adequately examined in the field, parts that for legal reasons may not be sectioned, and fracture surfaces with topographies that would prevent effective illumination for direct photography. A replica provides a permanent record of the fracture surface of a broken part, which can then be sectioned for destructive examination without loss of the original evidence of the cause and nature of the fracture.

The replication methods used in light microscopy are similar to those used in electron microscopy. However, light-microscope replicas are thicker, more easily handled, and less subject to deformation or collapse after removal from the fracture surface than TEM or SEM replicas. The usual procedure is to apply a thin layer of a fairly viscous solution of cellulose acetate in acetone on the fracture surface. A piece of thick cellulose acetate tape (0.010 to 0.015 in. thick) is pressed into the coating by hand for about 60 sec, and this tape is used to pull the replica away from the surface.

The original negative replica either can be viewed and photographed as stripped from the fracture surface or can be mounted and then shadowed by vapor

deposition to enhance contrast. Either carbon or a reflecting, noncorrodible metal (such as gold) can be used for shadowing. One method of mounting is to fasten the replica to a thin microscope slide using tape with adhesive on both sides or some other suitable adhesive. If a positive replica is desired, it can be formed by coating the shadowed face of the cellulose acetate replica with a thick layer of epoxy cement and then dissolving the original replica in acetone.

Epoxy resins and some liquid-rubber materials have also been used for replication of fracture surfaces. Coating replicas made from these materials with a metal such as gold increases surface reflectivity and facilitates examination by light microscopy.

A quick and simple method of recording the details of a fracture without photographic equipment is as follows: Apply a paste made of oil and graphite or molybdenum disulfide to the fracture surface with a brush. Press a strip of transparent tape on the coated surface (adhesive side down) and rub gently to make as complete contact with the surface as possible. Peel off the tape (which picks up the graphite or molybdenum disulfide) and mount on a piece of white paper. The graphite or molybdenum disulfide pattern constitutes a fractograph, which is ready for visual examination (see Fig. 1). The tape replica can be photographed if desired.

Figure 2 compares three fractographs of a cellulose acetate replica of a fatigue-fracture surface. The same area of the

replica was photographed with oblique illumination from a point-source lamp and by transmitted light. The replica then was shadowed with carbon by vapor deposition and photographed using oblique illumination from a point-source lamp. These three fractographs generally reveal the same topographic features (the same inclusion is visible at the center of each view), but the one made by using transmitted light (Fig. 2b) lacks depth.

Sectioning and Study of Fracture Profiles

Although recent advances in interpretation of fracture surfaces have furnished more accurate information regarding fracture mechanisms than can be obtained by sectioning a fracture and examining it by metallographic techniques, the latter method provides some types of useful information. It is helpful in determining the relationship between the fracture and the microstructure of the broken part and can be used to determine whether the crack followed an intergranular or a transgranular path. Furthermore, if the origin of the fracture is to be studied, it can be characterized more fully by the sectioning method. However, sectioning through a fracture origin is difficult and requires extreme care.

It is usually advantageous to plate the fracture surface of a specimen with a metal such as nickel prior to mounting and sectioning, so that the fracture edge

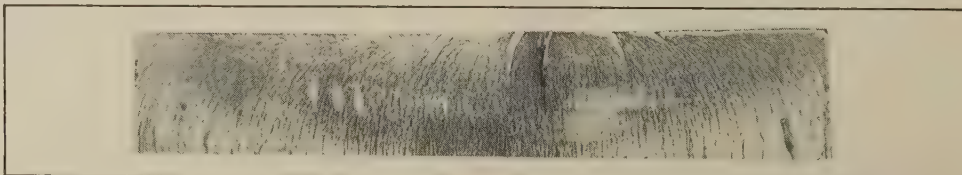
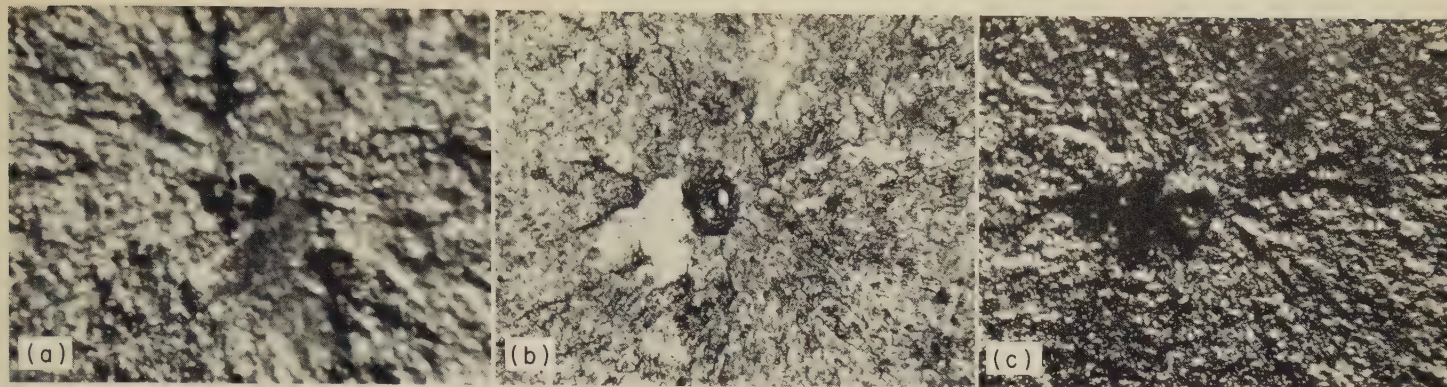


Fig. 1. Transparent-tape replica of a fracture surface. See text for a description of the technique used for preparation of replicas of this type.

*See page 1 for committee list.



Light fractographs
 (a) Replica photographed with oblique illumination from a point-source lamp. (c) Replica shadowed with a vapor-deposited coating and photographed using oblique illumination from a point-source lamp.
 (b) Same area of replica as (a), photographed with transmitted light.

Fig. 2. Comparison of three fractographs of a cellulose acetate replica of a fatigue fracture in an induction-hardened shaft of 15B28 steel. Fracture was initiated by the large inclusion shown in the center of the views, during rotating bending.

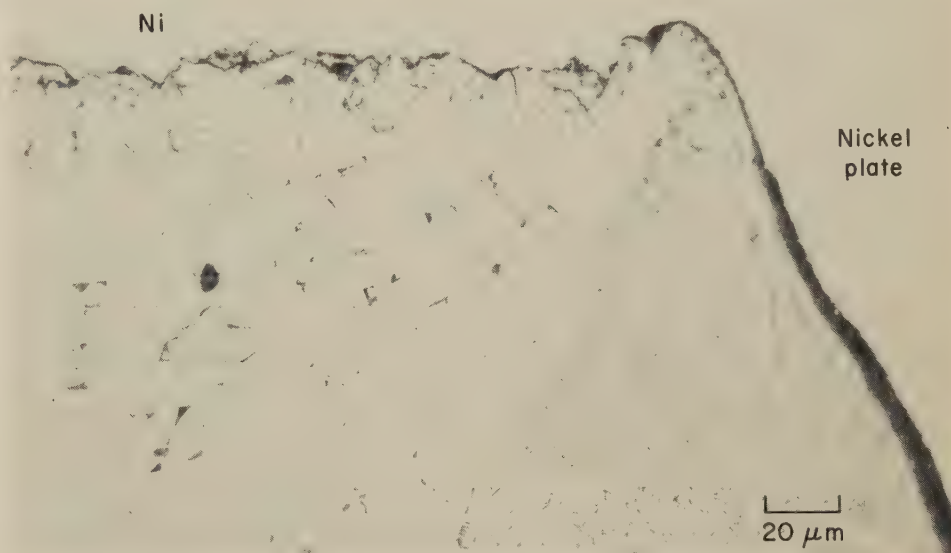
is supported and can be included in the examination. An example of the use of this technique is provided in Fig. 3, which shows a section through a welded low-carbon steel pipe. The section is bordered at the top by the surface of a stress-corrosion crack and at the right by the outside surface of the pipe (both shown in profile). Both of these surfaces were nickel plated to prevent rounding of the edges during polishing. This section shows the intergranular nature of the crack and the location of the crack relative to the end of a weld deposit (at right), which suggests that the heat of welding caused the stress; the source of the corrosion is not known.

The surface of a fracture in 8620 steel is shown in profile in Fig. 4. The appearance of some of the fracture contours suggests that they may have resulted from the presence of inclusions such as those visible near the fracture surface.

Another fracture profile is shown in Fig. 5. Cubic cleavage was produced in an impact bend test at -70°C (-94°F) in a specimen of essentially pure iron. The primary cleavage, which occurred on $\{100\}$ planes, was accompanied by secondary, diagonal cleavage on $\{112\}$ planes, causing abrupt deviations in direction of crack propagation.

Sometimes it is desirable to reassemble the two portions of a fractured part (the fracture surfaces should not actually touch) and mount and section them together. This has been found to be particularly advantageous for specimens containing welds in which the location of the crack origin—in the weld, in the heat-affected zone, or in the base metal—is to be investigated. Examination of only one side of the crack may not provide this information. One method of producing matched sections through a fracture is to align the portions of the broken part as perfectly as possible, coat them with epoxy resin and cement them together, then section the reassembled part through the fracture, mount in epoxy, and polish. This method usually gives better alignment than sectioning each portion separately.

Fracture-surface matching is also used to measure deformation. After the two segments of a fractured part are aligned,



Micrograph (etchant: picral)

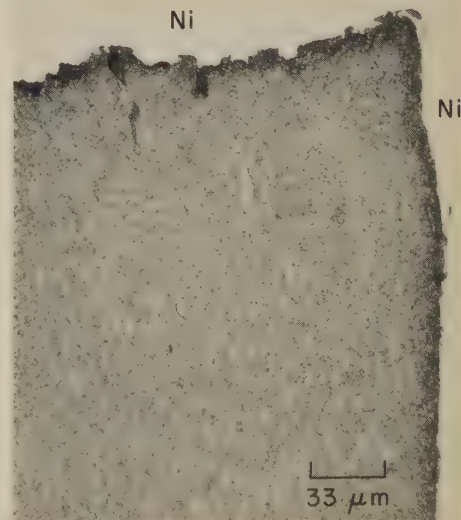
Fig. 3. Profile of a stress-corrosion crack in welded low-carbon steel pipe. Fracture surface is at top; weld is at right; external surface of the pipe is at far right. Protective nickel plate shows along the entire length of both edges.

mounted and sectioned for observation of the fracture in profile, measurement of the separation between the two fracture surfaces at various points will reflect the amount of deformation that occurred during fracture. This measurement may also assist in determining the direction of crack propagation and, therefore, the location of the crack origin (see the section on Crack Origins on page 38 in the article "Interpretation of Light-Microscope Fractographs").

Shadow Casting

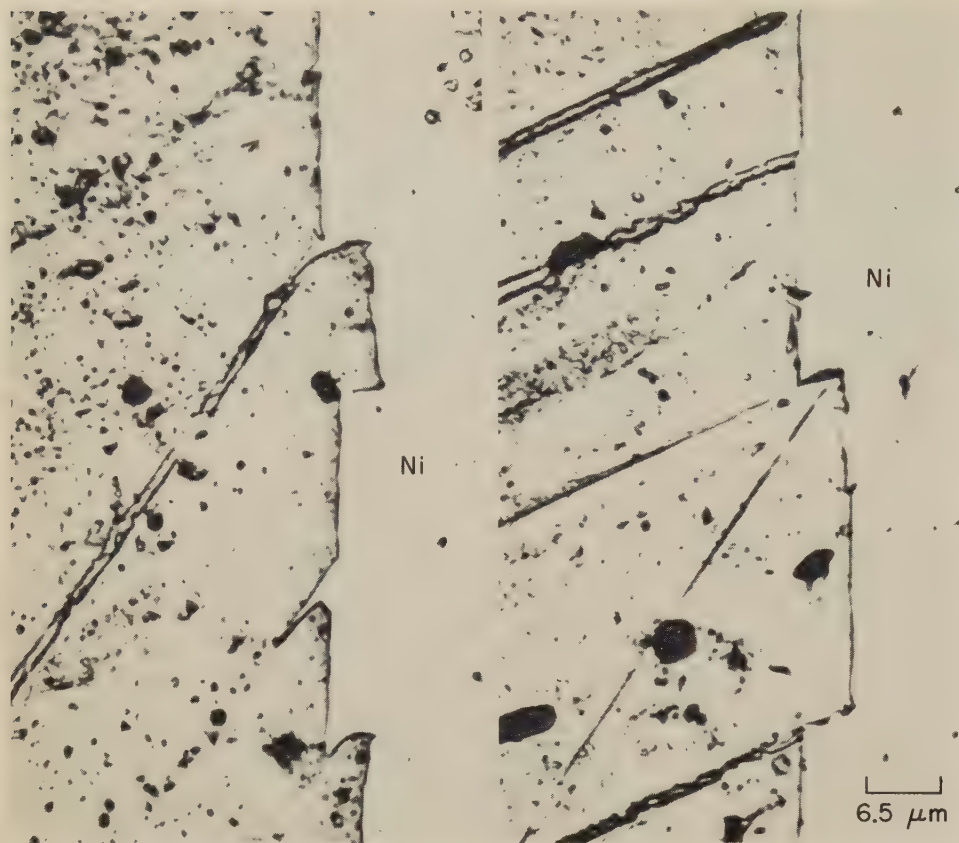
Shadow casting is used in light-microscope fractography for three purposes: (a) to increase reflectivity of fracture surfaces, (b) to increase contrast of fracture-surface features, and (c) to permit quantitative measurements of the heights of features.

Some fracture surfaces, especially those with tarnished facets, are difficult to examine at high magnification by light microscopy because of poor reflectivity. Reflectivity can be increased by vapor



Micrograph (etchant: picral)

Fig. 4. Profile (at top) of a fracture in 8620 steel. A protective nickel plate has preserved the fracture outline.



Micrograph (etchant: 10% nital)

A protective nickel plate has preserved the fracture outlines. Fracture was produced by an impact bend test at -70°C (-94°F), and is mainly on $\{100\}$ planes, with deviations on $\{112\}$ planes. (E. P. Klier, A Study of Cleavage Surfaces in Ferrite, *Trans Am Soc Metals*, Vol 43, 1951, p 935-957, Fig. 31)

Fig. 5. Two portions of the surface (shown in profile) of a cleavage fracture in a specimen of essentially pure iron

depositing a thin layer of a heavy metal on the surface to be examined. A non-corrodible, easily vapor-deposited, highly reflective metal, such as gold, is used. The fracture specimen is usually rotated during deposition so that essentially all surfaces are adequately coated.

If deposition is done at an angle to the surface, perhaps with the specimen being rotated during deposition, the contrast of the features can be increased. The material being deposited is built up on facets perpendicular to the direction of deposition faster than on features oriented at angles more nearly parallel to it. Features that cannot be brought out otherwise are often clearly revealed by shadow casting.

Shadow casting can be used to measure quantitatively the heights of features of fractures. If a heavy metal is deposited at a known angle to the surface of the fracture, the length of the shadow made by a feature can be used to determine mathematically the height of that feature. By knowing the deposition angle and measuring the length of the shadow, step heights as small as 50 Å can be calculated. One application of this technique in fractography has been the measurement of heights of cleavage steps.

Fracture-Surface Analysis

Concurrent with the many developments in the analysis and interpretation of fractures by examination of fracture-

surface topographies have been the development and use of certain analytical techniques for providing information regarding the chemical composition of fracture-surface constituents.

Dispersive and nondispersive x-ray spectrometers have been used for this purpose. They are employed as accessories to scanning electron microscopes and permit simultaneous viewing and chemical analysis of a surface. If it is desirable to detect the elements in extremely thin surface layers, the Auger (pronounced "oh-zhay") electron spectrometer and the ion-scattering spectrometer are useful. For chemical analysis of surface areas as small as 1 micron in diameter, the electron-microprobe analyzer is widely used. The area examined with the ion-microprobe analyzer is slightly larger (a few microns in diameter) than that examined with the electron-microprobe analyzer. The ion-microprobe analyzer has the advantage of being able to detect nearly all elements (including those of low atomic weights) in concentrations as low as 100 ppm. These instruments are described in greater detail in the section on Attachments, Accessories and Auxiliary Equipment, on page 51 in the article "The Scanning Electron Microscope and Its Application to Fractography".

The instruments discussed above are used for direct analysis of fracture surfaces; other techniques can be used for

analyzing material that has been removed from the surface of a fracture. For example, if material is removed in a replica (perhaps chemically extracted), it can be analyzed structurally by x-ray diffraction or electron diffraction. Also, depending on the quantity of material extracted, many of the routine chemical-analysis techniques may be applicable.

Analysis of fracture strain has been done using a transmission electron microscope. Films less than 1000 Å thick have been successfully prepared from the surfaces of certain special fractures involving either cleavage or, in some copper-base alloys, stress-corrosion cracking. An extremely flat fracture surface is needed for successful thinning. The procedure has been to coat the fracture surface with a protective lacquer and to thin it by electrolytic or chemical techniques until an electron-transmitting thickness is obtained. Examination of a specimen prepared in this manner can provide information regarding the dislocation density in the metal at the fracture surface.

Etch Pitting of Fracture Surfaces

Etch-pitting studies have been made for at least two purposes: to determine the crystallographic orientation of the fracture plane and to obtain a measure of the fracture strain through measurements of dislocation density. For additional information on applications of etch pitting and techniques employed, the reader is referred to pages 8, 112 and 113 in Volume 8 of this Handbook.

Deep-Field Microscopes

In an attempt to overcome the limitations imposed by the small depth of field of light microscopes, a microscope was developed a few years ago that allows high-magnification light photography of extremely rough fracture surfaces. This instrument, called a deep-field photographic microscope,* uses a very thin beam of light to illuminate the specimen. The light beam is at a constant distance from the objective of the microscope and is at the focal plane. While the photograph is being taken, the specimen is driven at a constant rate up through the beam of light. Because only the illuminated portions of the specimen are recorded on the photographic film, and because all the illuminated portions are in focus, the entire photograph is in focus. The deep-field photographic microscope was developed at about the same time as the scanning electron microscope but has found only limited use because most of its functions can be performed by the scanning electron microscope. Nevertheless, the deep-field photographic microscope is a valuable tool in certain fractographic studies, such as the remote examination of fractures in radioactive metals in "hot cells".

*Deep-Field Photographic Microscope, Model No. 66-8-DFM, is available from Electronics & Alloys, Inc., 145 S. Dean St., Englewood, NJ 07631.

Fractographic Features Revealed by Light Microscopy

By the ASM Committee on Fractography by Light Microscopy*

THE STUDY of fracture surfaces has generated a system of nomenclature for fracture features that result from various conditions of fracture, such as size and shape of the part or specimen, mechanical properties of the metal, temperature at fracture, environment, and condition of stress. Early attempts by de Réaumur, Martens, Brinell and Tiemann to evolve suitable descriptive terms are discussed in the article beginning on page 1 in this volume. The present article explains the terms currently in use to describe important fracture features, tells how these features are formed and how they may be recognized, and presents fractographs illustrating the various features.

Tensile-Fracture Surface Marks in Unnotched Specimens

The macroscopic appearance of a fracture surface has often been used to appraise the degree of ductility and of toughness present in a metal. According to the concepts of fracture mechanics, toughness is the critical mechanical property associated with fracture. The fracture surface contains vestigial marks that indicate the amounts of high-energy (ductile, or tough) and low-energy (brittle) crack extension that produced the fracture. Anything that influences toughness, such as the material, size and shape of the part, or the temperature, environment and method of loading, indirectly changes the fracture appearance. Therefore, the fracture features of a particular alloy are not constant from fracture to fracture, but instead conform to a systematically changing pattern dictated by changes in relative toughness for specific conditions of heat treatment and/or configuration.

Tensile-fracture surface marks have been classified into three zones by configuration (Ref 1, 2)—namely, (a) the fibrous zone, (b) the radial zone, and (c) the shear-lip zone. The three zones are illustrated schematically in Fig. 1.

Fractures consisting solely of one zone occur only under conditions of extreme ductility or brittleness. Most fracture surfaces contain two or all three zones in one of the following transitional sequences:

- 1 Fibrous plus shear-lip zones (see Fig. 2)
- 2 Fibrous plus radial plus shear-lip zones (see Fig. 3)
- 3 Radial plus shear-lip zones (see Fig. 4).

Cylindrical Specimens

The discussion that follows concerning the fracture-surface features illustrated in Fig. 2 to 4 (fibrous zone, radial zone,

and shear-lip zone) is based on fractures that are produced in unnotched, cylindrical tensile-test specimens.

The **fibrous zone** is a region of slow crack growth. It is located in the center of the fracture and surrounds the fracture origin, which is usually situated at or near the tensile axis. This zone consists of either a randomly fibrous area (Fig. 3a) or a series of fine circumferential ridges (Fig. 2 and Fig. 3b). The ridges lie normal to the direction of crack propagation, from the origin toward the periphery of the specimen. Randomly fibrous areas are typical of commercially pure iron and plain carbon steel. Circumferen-

tial ridges are most frequently observed on fractures of low-alloy steels, titanium alloys, and commercially pure metals. These marks are indicative of stable, subcritical crack extension requiring relatively high energy. A comprehensive fractographic study (Ref 3) of 4340 steel determined that, for various strengths and testing temperatures, crack propagation in a fibrous zone occurred by fracture resulting from microvoid coalescence. (This can be seen only at very high magnifications as by electron microscopy. See the section on Microvoid Coalescence and Fig. 1 on page 79 in the article on Interpretation of Transmission-Electron-Microscope Fractographs.)

The origin of fracture is centrally located in the fibrous zone, and it can usually be traced to a discontinuity—often, an inclusion or a cluster of inclusions. Occasionally, these may be seen at low magnification (such as 5×) at the apex of a conical mound (Ref 4).

The **Radial Zone**. With a change from slow crack growth to rapid or unstable crack propagation, radial marks that coincide with the general direction of crack extension develop. These diverging marks emanate either from the periphery of the fibrous zone (Fig. 3a and b) or, in the absence of a fibrous zone (that is, immediate unstable crack propagation), from the fracture origin itself (Fig. 4). The radial marks converge (point backward) toward the origin. Radial marks may be fine or coarse, depending on the microstructure and testing temperature. In high-strength steels with tempered-martensite structures, the radial marks on the fracture surfaces are fine. In contrast, the fractures of medium-strength steels with martensitic structures have coarse radial marks when broken at or near room temperature. With decreasing test temperature, however, there is an abrupt change to fine radial marks on fracture surfaces of the same steels.

Coarse radial marks on steels (observed within a relatively small temperature range) are shear elements sometimes called "radial shear". Longitudinal splits can be observed along the ridges or peaks of these radial-shear elements. The delamination may be caused by the high normal tensile stress resulting from the separation of the radial surfaces along the plane of maximum shear.

Fine radial marks are not indicative of a shear mechanism of fracture. On the basis of findings of a task group of ASTM Committee E-24, it can be stated that fine radial marks on fracture surfaces of 4340 steel are primarily indicative of quasi-cleavage fracture or intergranular fracture, or both (Ref 3).

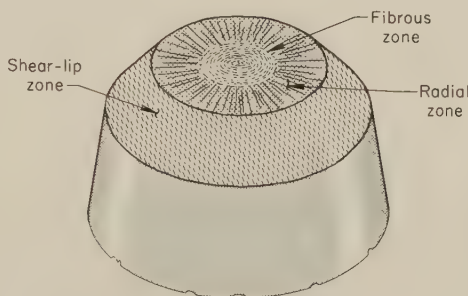
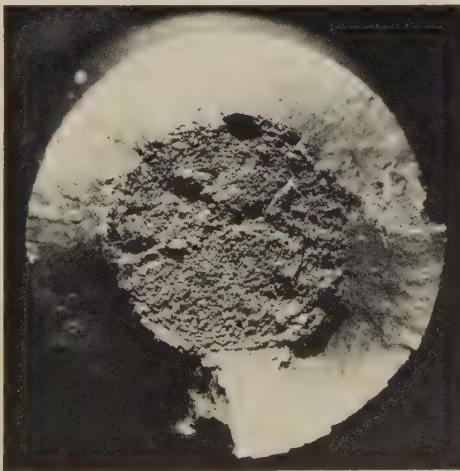


Fig. 1. Schematic representation of zones within a typical tensile fracture of an unnotched, cylindrical specimen. The surfaces of the fibrous and radial zones are usually normal to the tensile axis, as shown. The shear-lip surface is always at about 45° to the tensile axis.



Light fractograph About 11×
Fracture in a tensile-test specimen of 4340 steel that was tested at 120 C (248 F). The structure of the steel was tempered martensite; hardness was Rockwell C 46. Fracture started at the center of the fibrous zone, which exhibits circumferential ridges. The outer ring is the shear-lip zone.

Fig. 2. Tensile fracture containing a fibrous zone and a shear-lip zone (Ref 2)

*See page 1 for committee list.



Light fractograph

About 13×

(a) The steel had a pearlitic structure, a hardness of Rockwell C 15, and a yield strength of 483 MPa (70 ksi). The inner zone is randomly fibrous; the zone surrounding this inner zone (inside the outer shear lip) has radial marks. (Ref 2)

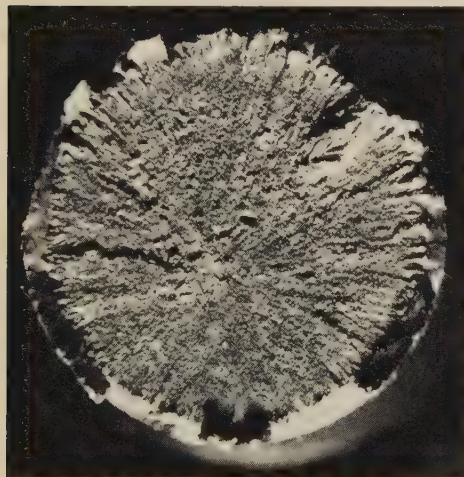


Light fractograph

About 13×

(b) The steel had a structure of tempered martensite and a hardness of Rockwell C 28. The inner, fibrous zone is circumferentially ridged; the intermediate zone has coarse radial marks; the outer ring is the shear-lip zone.

Fig. 3. Surfaces of fractures in two tensile-test specimens of 4340 steel with two different structures. Both surfaces contain fibrous, radial and shear-lip zones.



Light fractograph

12×

Fracture in an unnotched tensile specimen of 4340 steel that was tested at -196°C (-321°F). The structure of the steel was tempered martensite; the hardness was Rockwell C 35. This fracture has no fibrous zone. The radial marks occupy the entire area inside the narrow shear-lip zone.

Fig. 4. Surface of a tensile fracture containing a radial zone and a shear-lip zone (U. S. Army photograph)



Light fractograph

14×

Fracture in a 4340 steel tensile-test specimen tested at room temperature. Structure of the steel was tempered martensite; hardness, Rockwell C 28. The fracture resembles that in Fig. 3(b), but its origin (at the small inclusion) is to left of center, producing the curved radial shear marks.

Fig. 5. Surface of a tensile fracture showing curved radial shear marks (U. S. Army photograph)

Usually, radial marks on tensile specimens are straight. If the fibrous zone is very small or is absent, and if the origin of fracture is at a significant distance from the tensile axis, the radial marks deviate from linearity and curve toward either the free surface or the shear lip (as in Fig. 5).

Because fracture-surface marks are associated with both deformation and crack propagation, their appearance is indirectly dependent on the ductility of the metal. Environmental conditions that affect ductility, such as temperature, also affect the volume of metal that deforms. As the volume decreases, the radial marks show less relief. For extremely brittle metal, the amount of deformation ap-

proaches zero and the crack path follows planes of weakness in directions associated with the structure of each individual grain. Under these circumstances, crack propagation is by cleavage or by intergranular fracture, or by both of these mechanisms. If the metal has a sufficiently coarse grain size, the individual features can be identified macroscopically. If the metal has a fine grain size, the characteristics necessary for identification of features can be observed only at high magnifications. The macroscopic appearance of a radial zone that constitutes the entire fracture surface is nondescript. This type of fracture appearance indicates extreme brittleness and, depending on microstructure, carbon con-

tent, and grain size, may occur at very low temperatures for some low-alloy steels, at somewhat higher temperatures for plain carbon steels, and at room temperature for some heat-resisting alloys.

The Shear-Lip Zone. The other zone produced by fracture is the shear-lip zone. This consists of a smooth, annular area adjacent to the free surface of the specimen. In general, the size of the shear lip is a function of the stress state and the properties of the metal. There are four types of occurrence of shear-lip zones, three of which are transitional, namely:

- 1 Completely shear lip
- 2 Fibrous to shear lip
- 3 Fibrous to radial to shear lip
- 4 Radial to shear lip.

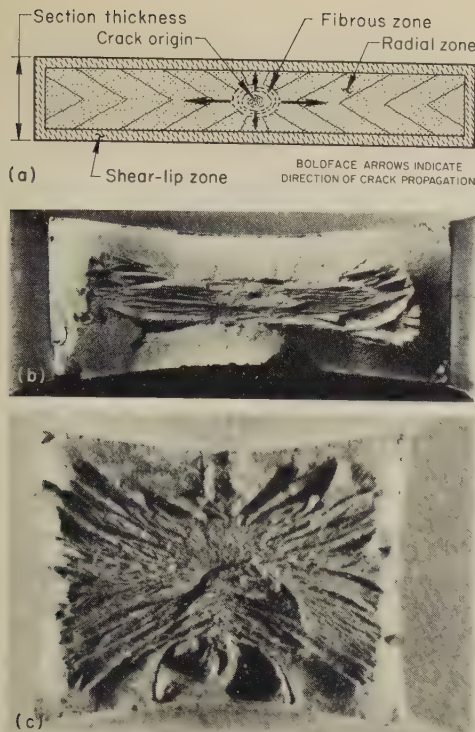
In general, each of the types can be produced by changing the diameter (that is, the stress state) of the specimen. The shear lip usually will not vary in width but will change in the percentage of the fracture surface that it occupies. One exception, for 4340 steel, has been reported (Ref 2, Fig. 10). Here, the shear lip did increase in width with increase in specimen diameter.

Environmental effects that decrease ductility diminish the size of the shear lip for any of the three transitional types listed above. The absence of a shear lip in an unnotched specimen can occur only as a limiting case of radial-to-shear-lip fracture, and then only when the metal is in an extremely brittle condition.

Rectangular-Section Specimens

The size and shape of a test specimen or part have a strong influence on fracture-surface marks. Because of the influence of specimen shape on the stress state, the relationship of the fracture zones in specimens with square and rectangular cross sections is quite different from that discussed in the previous section for specimens with round cross sections. The fibrous zone in an unnotched, rectangular specimen, for example, may be elliptical in shape, with the major axis parallel to the long sides of the rectangle. This type of fracture is shown diagrammatically in Fig. 6, with two examples of actual fracture surfaces. The major difference in fracture appearance due to specimen shape is in the radial zone. This can be radically different in fractures of thinner sections; the radial zone is suppressed in favor of a larger shear-lip zone (see Fig. 7). In very thin sections, in which plane-stress conditions apply, there is no radial zone. Changes in test temperature affect the fracture appearance in a somewhat similar manner (see the section on Changes Caused by Altered Environments on page 47 in the article on Interpretation of Light-Microscope Fractographs).

Chevron Patterns. The radial zone of rectangular specimens that have a width appreciably greater than the thickness exhibits chevron, or herringbone, patterns, as shown in Fig. 8. (See also Figs. 13, 14 and 38 in the article on Interpretation of Light-Microscope Fractographs, and fractograph 4273 on page 298 in the Atlas of Fractographs.) Chevron patterns are frequently associated with unstable,



(a) Schematic representation of tensile-fracture features in a specimen with a rectangular cross section. (b) Light fractograph of a rectangular steel specimen with fracture features conforming to those of the diagram. (c) Light fractograph of a rectangular steel specimen with a fracture similar to that of (b) but having a much narrower shear-lip zone.

Fig. 6. Fracture-surface marks in rectangular tension specimens (Ref 2)

relatively rapid crack propagation, and their appearance is the result of (a) the general direction of crack propagation, and (b) the inherent tendency of a propagating crack to take the direction giving the shortest path to a free surface. When these two directions coincide, as in a cylindrical specimen, straight, radial lines result, as in Fig. 4. When part of the free surface is appreciably closer to the crack front than the remainder of the free surface, this condition influences the direction of crack propagation (see Fig. 5), and the radial marks deviate from linearity and extend toward the free surface. With rectangular specimens having a sufficient ratio of width to thickness, the shorter distance to the free surfaces in the thickness direction is sufficient to modify the direction of propagation of each ligament of the crack front.

Apparently, there is a critical width-to-thickness ratio necessary to produce chevron patterns. But many rectangular specimens, such as fracture-toughness bend specimens, are almost square, and their fractures show no chevrons; instead, radial marks emanate either from the precracked fatigue zone, as in Fig. 9, or from a fibrous zone that was initiated from the fatigue crack, as in Fig. 10. In both Fig. 9 and Fig. 10, the marks point backward, toward the crack origin. This characteristic of radial marks and chevron patterns is useful in analyzing crack-propagation paths in fast fractures.

Woody Fractures. Fracture surfaces also display the influence of microstruc-

ture, as well as specimen size and shape. This is especially true in metals that have anisotropic properties as the result of processing—for example, slag stringers in wrought iron. Such anisotropy includes patterns due to porosity, inclusions, second phases, or alloy segregation, which are arranged in stringers, bands, or flow lines by the primary rolling or forging of the metal.

Figure 11 shows the effect of stringers caused by "mechanical fibering" on the fracture surfaces of Charpy impact specimens of a binary iron alloy with notches oriented in three directions relative to the stringers. These fractures are called woody or laminated fractures because of their extreme roughness.

A woody fracture, as the final phase of torsional-fatigue fracture, in a carburized and hardened shaft of aircraft-quality 9310 steel is shown in Fig. 12. The fracture origin was internal, at a large alumina inclusion in the core of the shaft. Torsional loading gave rise to crack propagation in the longitudinal direction of maximum shear stress (although cracking along the transverse direction of maximum shear stress is more common). The shearing action produced cracks on many parallel longitudinal planes, resulting in a region of woody features. The direction of crack propagation changed

when the crack reached the hardened case, conforming to 45° directions of maximum tensile stress.

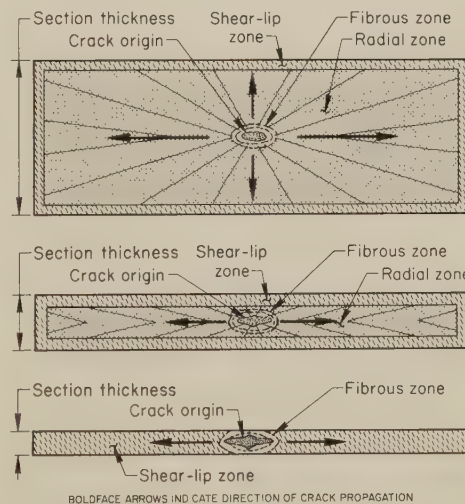
Fatigue Marks

The formation of cracks under conditions of repeated stress has been called fatigue cracking for a much longer period of time than this type of cracking has been understood. An example of the original lack of understanding of fatigue fractures is the early characterization of the fast-fracture portion as "crystallized metal". Fatigue zones in fatigue fractures exhibit several types of surface marks, such as beach marks, striations and ratchet marks.

Beach Marks. The term "beach mark" describes the macroscopic features present on the fracture surfaces in Fig. 13, 14 and 15. (Beach marks are also shown on numerous pages of the Atlas of Fractographs. See particularly pages 389 to 391, 395, 405, 407, 427, 446 and 447.) Terms other than beach marks have been used to describe this feature, such as clamshell, conchoidal and arrest marks. These fracture marks are most often associated with fatigue-crack propagation, but they are not restricted to fatigue (see Fig. 14), nor is the absence of beach marks evidence that fracture was not by fatigue.

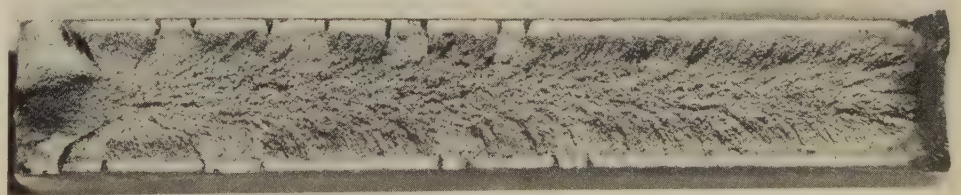
Beach marks are often found on fractures occurring in service and in fatigue testing of components, but are less common on fractures of laboratory test specimens, primarily because of the short times and uniform loading used for most laboratory tests.

The individual marks represent successive positions of the crack front where arrests of the crack occur as it propagates through the metal. They are always associated with stable crack propagation. Beach marks can be produced in several ways, including: (a) variation in cyclic loads, (b) differences in oxidation or corrosion of the fracture surface, and (c) slight plastic flow in the region of high stress concentration at the crack tip. The spacing and occurrence of beach marks can be used as a qualitative assessment of crack-propagation rate and cyclic history for those fractures clearly identified as fatigue fractures. A fine, uniform spacing of beach marks suggests relatively slow crack growth under minor deviations of a uniform cyclic-load condition. In addition, beach marks across the major portion of the fracture are indications of low cyclic loads, or possibly load "shedding", if an alternate crack path exists.



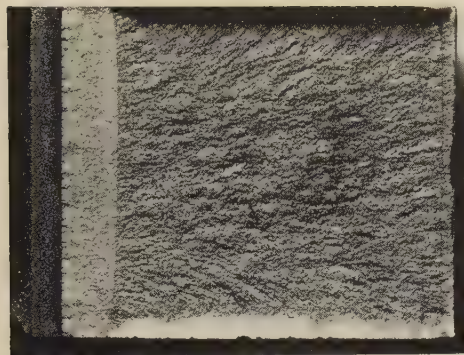
Schematic representation of the change in the size of the radial zone in the fracture surface of rectangular specimens of progressively decreased section thickness. The thinnest of the three examples has a small fibrous zone surrounding the origin and a shear-lip zone, but no radial zone.

Fig. 7. Fracture-surface marks in rectangular tension specimens as affected by section thickness (Ref 2)



The crack origin is at the left end of the specimen, and is adjoined by a small fibrous zone. The remainder of the fracture surface exhibits the special radial marks known as chevron, or herringbone, patterns. Note that the V's of the chevrons point back toward the crack origin. (U. S. Army photograph)

Fig. 8. Light fractograph of the surface of a high-velocity fracture in a specimen of steel plate, showing chevron patterns

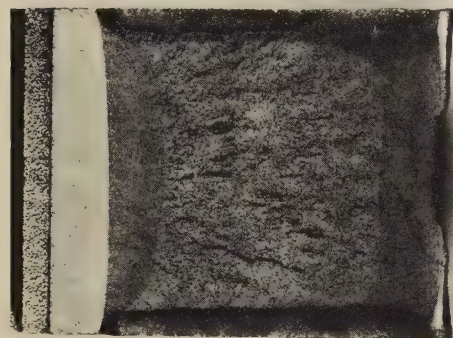


Light fractograph

3 1/3 X

The steel had a structure of tempered martensite and a hardness of Rockwell C 52.5. The machined notch prepared as a crack starter is at the extreme left. At the right of the notch is a zone of penetration by electrical discharge machining (EDM) to provide a sharper notch root. The fatigue crack is immediately to the right of the EDM notch. Test temperature was -73°C (-100°F). (U. S. Army photo)

Fig. 9. Fracture surface of a fracture-toughness bend specimen of 3%Ni-Cr-Mo steel, showing radial marks emanating from a precracked fatigue zone



Light fractograph

3 1/3 X

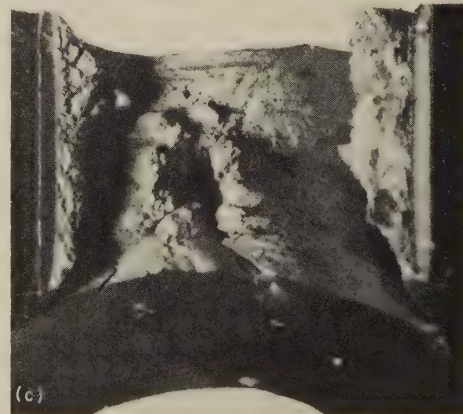
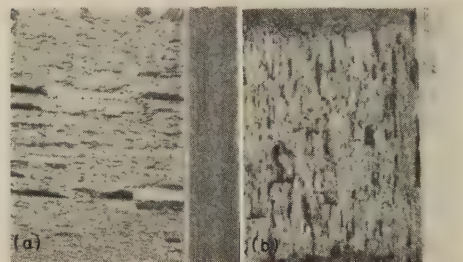
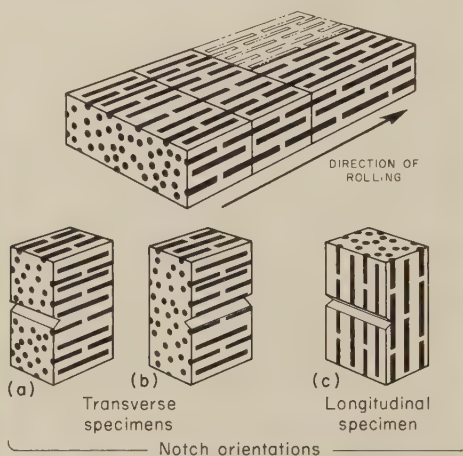
The steel had a structure of tempered martensite and a hardness of Rockwell C 42. From the left edge, in sequence, are the machined notch, the notch root machined by electrical discharge, the fatigue-pre-crack zone, the fibrous zone, the radial zone, and the shear-lip zone, which extends along three sides of the fracture. Test temperature was -73°C (-100°F). (U. S. Army photo)

Fig. 10. Fracture surface of a fracture-toughness bend specimen of 3%Ni-Cr-Mo steel, showing radial marks emanating from the fibrous zone

Striations. The term "striation" usually is restricted to a specific fracture feature that results from the propagation of fatigue cracks. Fatigue striations may be macroscopic, but they are most often microscopic and may often be found within the fine structure of individual beach marks. Examples of fatigue striations are shown in Fig. 16 and 17. (For other examples, see light-microscope fractographs 3524, 3525 and 3527 on page 152 in this volume.)

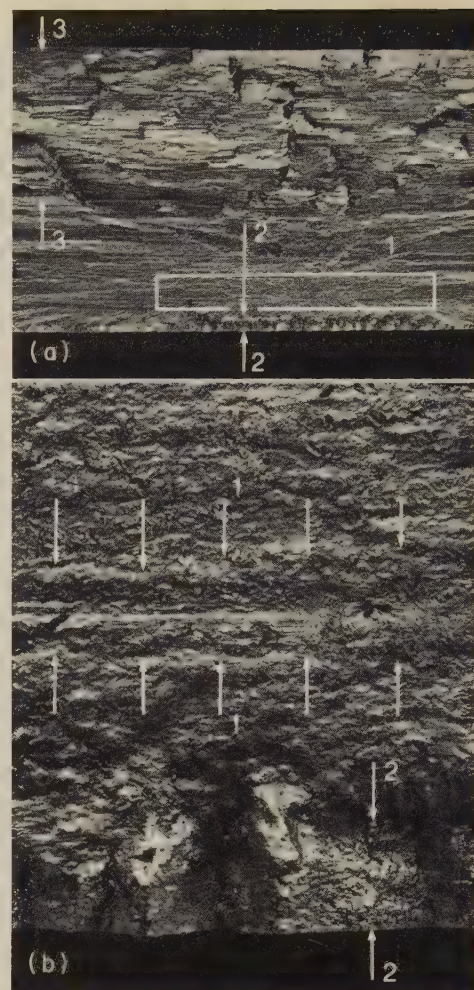
The presence of striations is definite evidence of fatigue crack propagation, but the absence of striations is not positive evidence to the contrary. It has been demonstrated that each striation is the result of a single cyclic-load excursion, and striation counting can be used to estimate the crack-propagation portion of fatigue life. However, under complex loading conditions, a striation may not be produced for every cyclic-load excursion.

Fatigue striations have been observed in many materials, including most metals and many nonmetals, and can take several forms. They can be clearly or poorly delineated and can take on several shapes. They are straight or curved, a variation usually attributed in metals to differences in stacking-fault energies. Other distinctive forms are brittle and ductile striations. Examples of both of these types can be seen in adjacent areas in high-strength aluminum alloys, as shown in Fig. 17 for aluminum alloy 7178-T6. For these alloys, some environmental factors, such as high humidity, promote the formation of brittle fatigue striations. By fatigue testing in desiccated air, it is possible to preclude completely the formation of brittle striations in alloys that show both types of fatigue striations when tested in laboratory air.



The isometric drawings above show transverse and longitudinal Charpy impact specimens taken from mechanically fibered material. The laminate characteristics of the fracture surfaces (light fractographs, at about $3\frac{1}{2}\times$) are directly related to the notch orientation in each example. (Ref 2)

Fig. 11. Woody fracture surfaces of notched specimens of a binary iron alloy



Light fractographs Actual size (a); $10\times$ (b)

The fatigue crack originated at a large alumina inclusion — within rectangle 1 in fractograph (a) and between arrows 1 in (b). Crack followed the approximate direction of the longitudinal plane of maximum shear stress, propagating in all directions from the inclusion to a final length of 1 ft. Beach marks are not evident because the mating surfaces rubbed. At the hardened case (between arrows 2), the crack changed direction to follow the 45° planes of maximum tensile stress. In the shaft interior, the crack propagated on many parallel and slightly offset shear planes, forming a woody fracture surface, as between arrows 3. The upper edge of fractograph (a) is a cut that was made after fracture.

Fig. 12. (a) Segment of a woody fracture resulting from torsional fatigue in a carburized and hardened shaft of aircraft-quality 9310 steel; profile of one surface of the shaft is at bottom. (b) Region at the shaft surface at the bottom of fractograph (a), at higher magnification.

Ratchet marks are macroscopic features that may be seen on fatigue fractures in shafts and flat leaf springs, and they may also occur in ductile fractures in over-torqued fasteners. In fatigue fractures, ratchet marks are the result of multiple fatigue-crack origins, each producing a separate fatigue-crack zone (see fractograph 4840 on page 389 and fractograph 4891 on page 405 in this volume). In shafts, the separately initiated cracks normally are propagated on planes slightly inclined to the plane of the shaft diameter. As two approaching cracks meet, a small step is formed. The small steps around the periphery of a shaft are the ratchet marks.

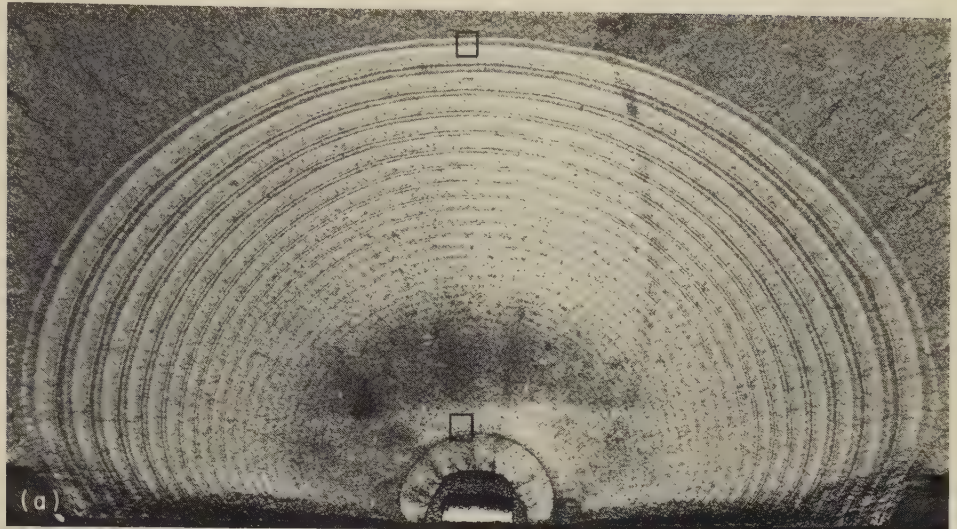


Light fractograph

Actual size

The light-colored, reflective bands are zones of slow crack propagation. At high magnifications, thousands of fatigue striations can be resolved within each band. The dull, fibrous bands are zones of crack propagation by microvoid coalescence.

Fig. 13. Beach marks on a fatigue fracture in an aluminum alloy 7075-T73 forging



Light fractographs

(a) Plate subjected to a series of varied loading cycles in the laboratory, which produced the series of beach marks. The crack origin, at the bottom center, was at a starter notch formed by electrical discharge machining.

About 5× (a); 60× (b); 60× (c)

(b) Area in lower square in (a), just above the beach mark registering the first change in loading. (c) Area in upper square in (a), just ahead of the zone of final, fast fracture. Both (b) and (c) contain faintly resolved, fine beach marks.

Fig. 15. Three views of a fatigue fracture in D-6ac steel plate, showing beach marks (Ref 5)

Although ratchet marks are most apparent on the periphery of fractures in shafts, the stepped appearance is characteristic whenever fatigue cracks emanate from several origins and subsequently meet to form one principal crack front (see Fig. 18).

The occurrence of ratchet marks requires virtually simultaneous initiation of several fatigue cracks, a situation that is favored by high stress and to a lesser extent by the presence of high stress-concentration factors, such as corrosion pits or grinding burns.

Grain and Cleavage Facets

Actual facets of separated grains are seldom seen in a light-microscope fractograph at any magnification. Under most circumstances, the random orientation of the grains and the roughness of the fracture make it difficult to find a large enough grain surface that is normal to the light axis of the microscope. In fractographs of intergranular fractures of very coarse-grained material, at a low

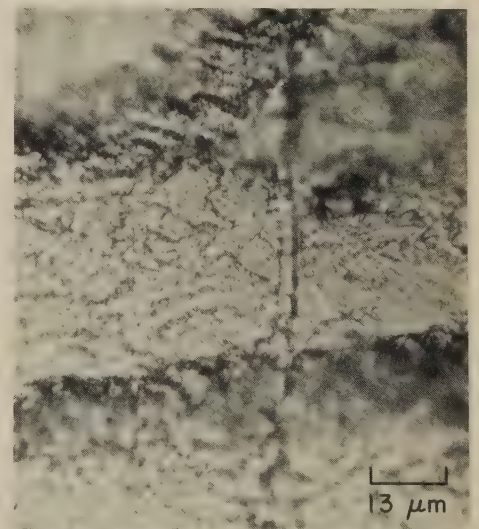


Light fractograph

4×

Tensile strength of the steel was 1780 to 1903 MPa (260 to 280 ksi). The beach marks are the result of differences in the rate of penetration of corrosion on the surface. They are in no way related to fatigue marks.

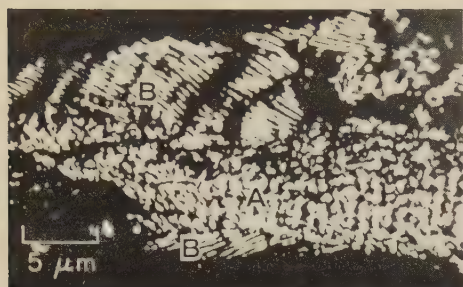
Fig. 14. Beach marks on a 4340 steel part that were caused by stress-corrosion cracking



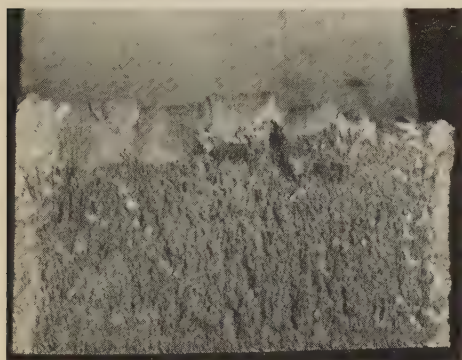
Light fractograph

750×

Fig. 16. Fatigue striations in aluminum alloy 7075-T651 plate. Note the fine, closely spaced, vertical striations at the left of the vertical step.



Light fractograph 2000×
Fig. 17. Brittle (A) and ductile (B) striations in high-strength aluminum alloy 7178-T6. The brittle striations always lead and the ductile striations trail off, like the wake of a ship.

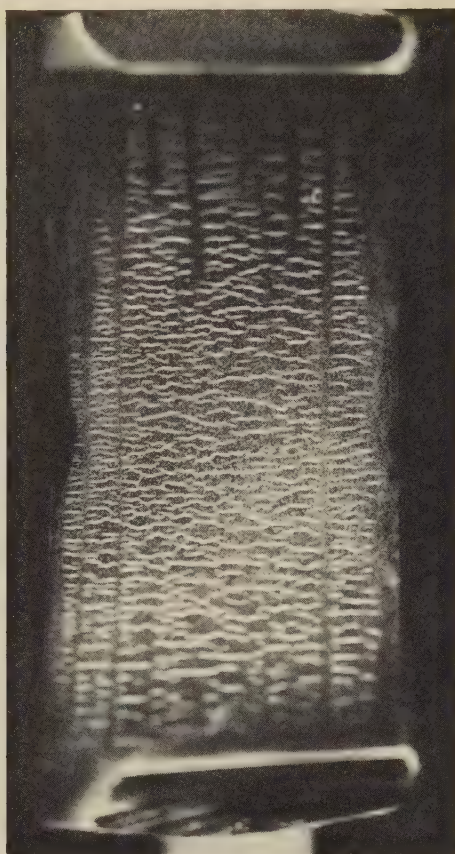


Light fractograph 7½×
Fig. 18. Ratchet marks in aluminum alloy 7075-T6 plate. The stepped appearance of these marks is characteristic whenever fatigue cracks emanate from several sites and later join to form one primary crack front.

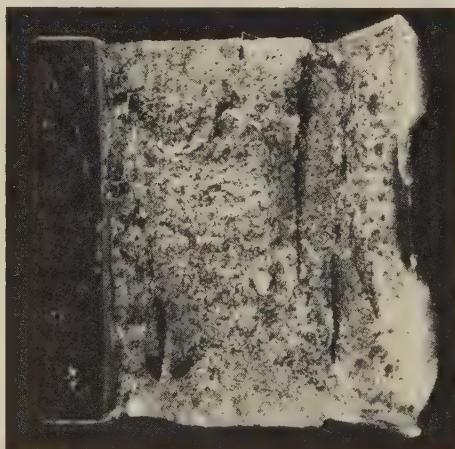


Macrograph (as polished; not etched) 3×
The crack was caused by dripping a 3¼% NaCl solution into the notch of a cantilever-bending tear-test specimen during testing. The microstructure of the steel was martensitic.

Fig. 19. Section through a stress-corrosion crack in high-strength 0.45% C, 9% Ni, 4% Co steel showing crack branching



Photograph Actual size
Fig. 20. Photograph taken under ultraviolet light of dye-penetrant indications showing extensive secondary cracking in a forging of high-strength 4340 (mod) steel with tensile strength of 1760 to 2070 MPa (270 to 300 ksi)



Light fractograph 5×
Fig. 21. Transverse secondary cracking in a Charpy impact specimen of ASTM A514, type F, structural steel at 760-MPa (110-ksi) tensile strength. Impact energy absorbed was 75 ft-lb at 27 C (80 F).

enough magnification to offer a good depth of field, grain facets are occasionally observed. An example is shown in fractographs 3460 and 3461 on page 137 in the Atlas of Fractographs, which display a "rock candy" fracture of type 302 stainless steel. An ingot of this stainless steel, which contained high silicon, was inadvertently overheated before re-

rolling, resulting in excessive grain growth and intergranular fracture. The individual grain facets are clearly evident.

With cleavage, the facets are likely to be relatively large and flat, and therefore they can be photographed quite successfully, as was demonstrated by the work of Zapffe cited in the article beginning on page 1. Examples of cleavage are shown in the section of the Atlas of Fractographs on Light-Microscope Fractographs at High Magnification; of particular interest are fractographs 3477 and 3478 (page 142) of Armco iron, fractographs 3481 to 3484 (page 143) of ship-plate steels, and fractograph 3532 (page 154) of commercially pure bismuth.

Secondary Cracks

Three types of secondary cracking can occur in association with the primary fracture. First are those cracks that are directly related to the primary fracture and that are the result of the same fracture mechanism. This type of secondary cracking is typified by crack branching (Fig. 19).

Another type of secondary cracking is also the result of the same fracture mechanism, but the cracks initiate and propagate from separate nuclei, and at no time do the separate cracks intersect or interact (Fig. 20). This type of cracking is often important in fracture analysis because it is not uncommon for the primary fracture surface to be damaged or corroded to the point that the mechanism of fracture cannot be determined, and examination of the secondary cracks may allow a determination.

A third type of secondary cracking is associated with the primary fracture, but the cracks are transverse to the general plane of primary fracture (Fig. 21). These cracks occur when the metal is unable to accommodate the transverse strains induced by the plastic deformation of the primary fracture. Fractures of this type are invariably associated with planes of weakness or brittleness induced by inclusion stringers or the grain boundaries of highly worked structures.

Discontinuities

Fractures originate from a broad variety of discontinuities within the metal structure, such as laps and seams from primary metal forming, shrinkage and gas cavities in cast structures, hot tears, inclusions, segregation of impurities, and imperfections in welds. Many of these features are familiar and do not need illustration. A few examples are discussed in the following paragraphs.

Laps, Seams and Pits. Surface discontinuities such as laps and seams are particularly conducive to fracture if present in high-hardness metals. They usually result in fatigue cracking if the part is subjected to repetitive loading, as in coiled springs. Examples of fractures from such discontinuities are presented by the following fractographs, which appear on pages 408 and 409 in the section on Failure-Analysis Fractographs in the Atlas of Fractographs: fractographs 4907 and

4910 for 1060 steel springs; 4904 for a 10B62 steel spring at 460 Bhn; and 4912 and 4913 for a 1070 steel spring at Rockwell C 54, which displays two seams, one visible on the surface and the other exposed by the fracture.

Pits are also found to be nucleation sites of fatigue fractures, especially in service involving heavy bending loads. Fractograph 5077 (page 448) shows the fracture in a sprocket-drive pinion of 8650 steel. Severe end loading of the teeth on this pinion produced several surface pits, one of which generated sufficient stress concentration to initiate a fatigue crack and ultimate fracture.

Shrinkage and Gas Cavities. The shrinkage of metal during solidification creates internal cavities unless sufficient additional metal is fed to the casting from risers or hot tops. Such cavities often escape detection and give rise to fracture in service. Shrinkage cavities display exposed dendritic surfaces because solidification was halted locally due to the lack of additional metal. In ingots that are hot worked to a structural shape, the internal cavities are normally eliminated by the metal flow induced by rolling, forging or extruding. However, if the total reduction of cross section is small, the dendritic areas may persist "unhealed" and result in fracture in service. An example of casting shrinkage is shown at location C in Fig. 19 on page 40 in the article on Interpretation of Light-Microscope Fractographs, and also in fractograph 3423 (page 131) in the Atlas of Fractographs in this volume.

Cavities also can be formed by pockets of gas. Gas may result during solidification from the evolution of hydrogen that was absorbed during melting or pouring, from entrapment of air during pouring, from moisture in the mold, and from reaction of the metal with contaminants.

Cavities formed by gas are often more rounded than those formed by shrinkage; also, they can be "healed" by hot work if their surfaces are not oxidized.

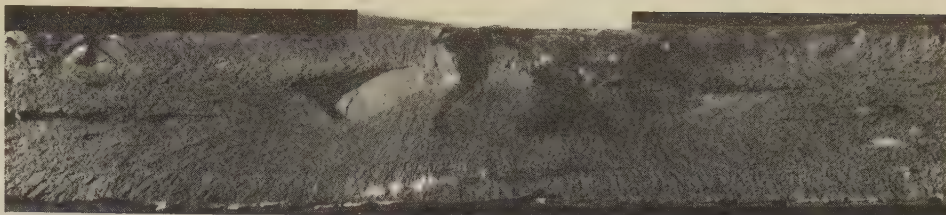


Light fractograph

4½×

The hot tear occurred as a result of contraction during cooling in the mold. The large cleavage facets at the top of the fractograph are the origin of the tear. Note the coarse river patterns on these cleavage facets.

Fig. 22. Surface of a fracture in a 0.30% C steel casting that contained a hot tear



Light fractograph

1½×

The motor case fractured during hydrostatic testing. A crack was found beneath a gas tungsten-arc repair weld that had been made on the inner surface of the case (surface at top in this fractograph) in the heat-affected zone of a longitudinal submerged-arc

assembly weld. The crack was about 1.4 in. long, parallel to and 0.47 in. beneath the outer surface of the motor case (surface at bottom here). Radial marks are visible that confirm that fracture proceeded to the left and to the right. (Ref 6)

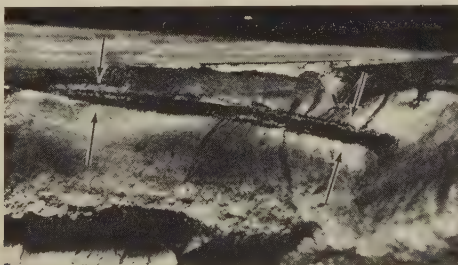
Fig. 23. Crack origin in the weld-related catastrophic fracture of a 260-in.-diam solid-propellant rocket motor case made of 18% Ni, grade 250, maraging steel



Light fractograph

35×

Fig. 24. Large nonmetallic inclusion just below the surface in 1053 steel induction hardened to Rockwell C 60. The inclusion initiated bending-fatigue fracture.



Light fractograph

3¾×

Fig. 25. A massive subsurface nonmetallic inclusion (between arrows) that initiated a bending-fatigue fracture in a carburized gear tooth of 4118 steel

Examples of fractures resulting from internal cavities are presented in photograph 4809 and fractograph 4810 (page 382) for a cast 0.30% C steel spindle that had a dendritic shrinkage cavity.

Hot Tears. A fracture in a large carbon steel casting initiated by a hot tear that occurred during cooling in the mold is shown in Fig. 22. The tear area is along the top of Fig. 22. It contains large facets believed to be the result of cleavage of the grains of large size that existed after solidification of the melt. The facet orientations reflect the local grain orientations.

Weld Imperfections. Improper welding techniques are a common cause of imper-

fections that can lead to fracture. Special precautions are necessary to avoid brittle fractures from welding in steels containing more than 0.25% C. Figure 23 shows a catastrophic fracture in a solid-propellant rocket motor case that was initiated at a weld imperfection.

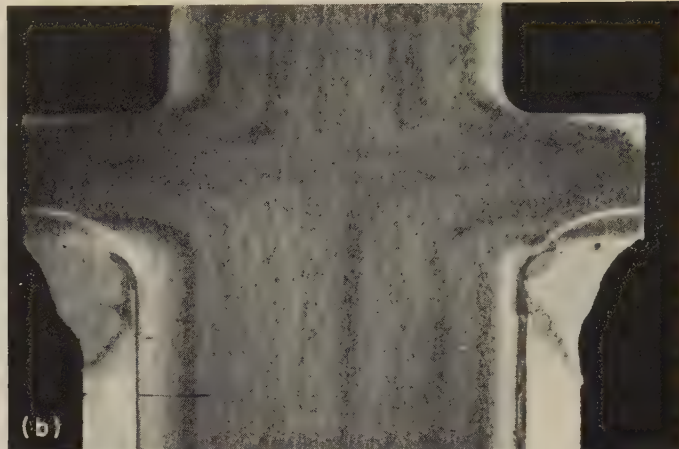
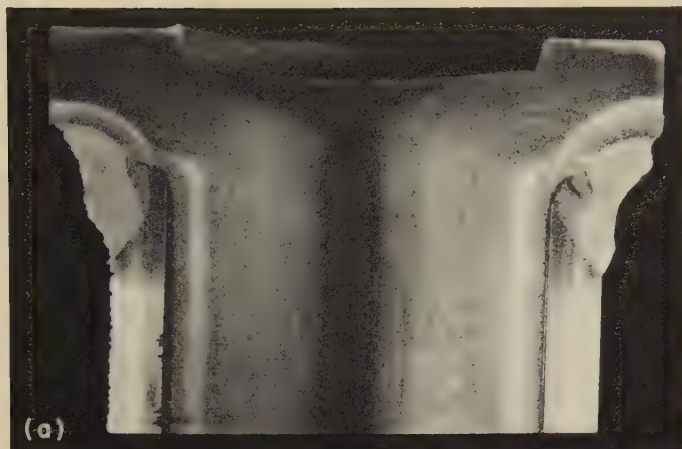
Several examples of fractures originating at weld imperfections are shown in the Atlas of Fractographs in this volume: illustrations numbered 4818 to 4827 (pages 384 and 385) show a fracture initiated by a crack that formed at the toe of a flange weld in a pressure vessel; 4828 to 4831 (page 386) show a fracture that originated in a cracked weld deposit on the edge of a steel angle used in a roof truss; 4864 to 4867 (pages 394 and 395) show a fatigue fracture that grew from a crack at the toe of a weld joining a reinforcing plate to an I-beam of a dragline-excavator A-frame; and 4880 (page 401) shows a fatigue crack that originated in a weld deposit that served as a stop in the keyway of a 1045 steel shaft that had been quenched and tempered to a hardness of Rockwell C 40.

Inclusions. The role of nonmetallic inclusions in initiating tensile fracture is mentioned in the discussion under "Woody Fractures" on page 29. Inclusions also serve as crack-origin sites in other types of fracture. They initiate fracture whenever their shape and location in the cross section gives rise to a serious stress concentration. Two examples of fatigue cracks originating at inclusions are shown in Fig. 24 and 25.

Segregation. Figure 26 shows two track-bar studs formed from bar stock that had been upset to form a flange for welding. The stud in Fig. 26(a) displays pronounced centerline segregation, which provided a plane of weakness within the flange after upsetting. This resulted in fracture of this stud at a torque of 70 ft-lb. The stud in Fig. 26(b), with no segregation, did not fracture at 170 ft-lb of torque on the nut; this stud shows the complete flowline pattern produced in upsetting.

Dimples

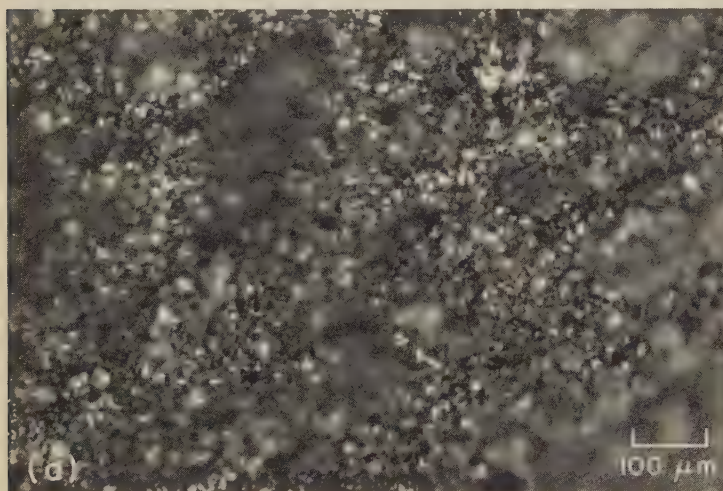
An aspect of ductile fracture that is seen clearly only at high magnification is dimples. They are caused by microvoid coalescence. This mechanism, and its appearance in fracture surfaces, is treated in detail in the articles on electron microscopy in this volume.



Macrographs (etchant: ammonium persulfate solution)

Both at 3×

Fig. 26. (a) Fracture in a track-bar stud initiated by centerline segregation, which was present in the bar stock. When the bar was upset to form a flange for welding, it was weakened in the flanged area, and the stud fractured at 70 ft-lb of torque on the nut. (b) A track-bar stud without centerline segregation, which did not fracture at 170 ft-lb of torque.



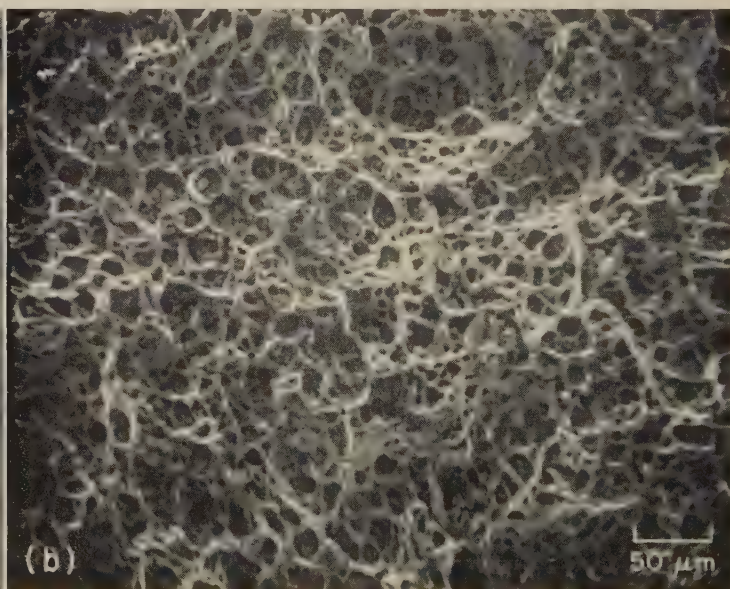
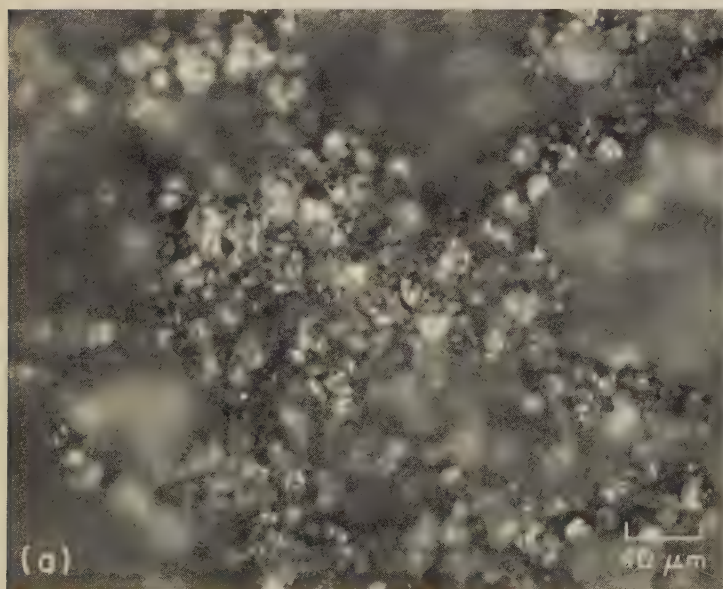
Light fractograph

100×

SEM fractograph

100×

Fig. 27. Dimpled fracture from uniaxial tension in 1020 steel. (a) Light-microscope fractograph showing very small and quite large dimples. The bottoms of the large dimples are out of focus. (b) Scanning-electron-microscope (SEM) fractograph of a surface of the same fracture as in (a), showing sharp detail of both the small and the large dimples. Note that the large dimples have small dimples within them. See also Fig. 28 and 29, for light and SEM fractographs of this surface at higher magnifications.



Light fractograph

250×

SEM fractograph

200×

Fig. 28. Same steel and same features revealed as in Fig. 27, but at a higher magnification. In the light-microscope fractograph (a), the shallow depth of field is apparent. More detail is revealed in the scanning-electron-microscope fractograph (b).

Because dimples are very small and a high magnification is required for observing them, they offer difficulties for light-microscope fractography. This is illustrated by Fig. 27 to 29. More of the light-microscope fractograph is out of focus as the magnification is increased. With each light-microscope fractograph in Fig. 27 to 29 is a scanning-electron-microscope (SEM) fractograph (see the articles on pages 49 to 78) that provides a clearer picture of the dimpled surface.

Stress-Corrosion Cracking

When the combined effects of chemical environment and stress are sufficiently unfavorable, corrosion may penetrate a

part, following paths that are susceptible to attack by reason of local segregation, such as grain boundaries. If the part fractures, the surfaces exposed will normally be coated with a layer of corrosion products, and secondary stress-corrosion cracking may be extensive. An example of such a fracture in D-6ac steel is shown in Fig. 30. A layer of corrosion products is visible in profile on the fracture surface, and intergranular corrosion is evident in the secondary cracks.

References

1. F. R. Larson and F. L. Carr, How Failures Occur . . . Topography of Fracture Surfaces, *Metal Progress*, Vol 85, Feb 1964, p 74-78
2. J. Nunes, F. L. Carr and F. R. Larson, Macrofractographic Techniques, in "Techniques of Metals

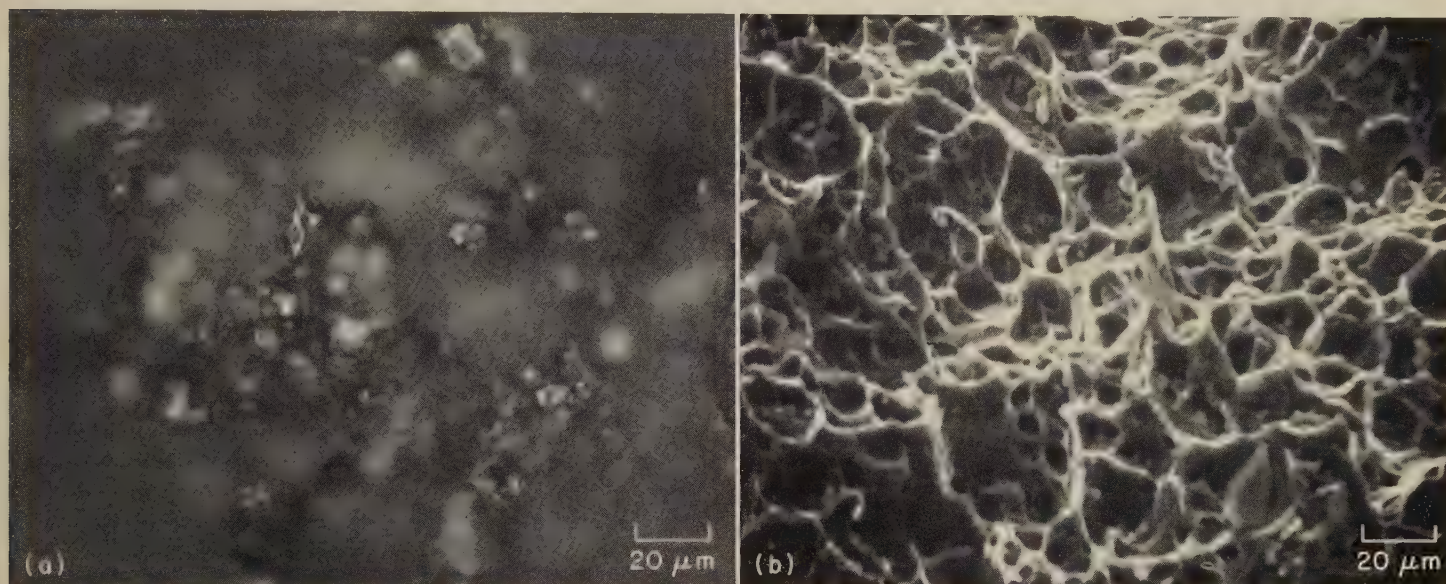
Research", Vol 2, Part 1, Wiley, New York, 1968, p 379-444

3. F. L. Carr, C. Biehler, A. Connolly, R. Dragen, J. Faller, O. Johari, R. Morais, M. T. Parker and R. H. Sailors, Correlation of Microfractography and Macrofractography of AISI 4340 Steel — A Report of ASTM E-24.2 Task Group, in "Applications of Electron Microfractography to Materials Research", STP 493, American Society for Testing and Materials, Philadelphia, 1971, p 36-54

4. J. A. Kies, A. M. Sullivan and G. R. Irwin, Interpretation of Fracture Markings, *J Appl Phys*, Vol 21, July 1950, p 716-720

5. C. E. Feddersen, "Fatigue Crack Propagation in D6AC Steel Plate for Several Flight Load Profiles in Dry Air and JP-4 Fuel Environments", AFML-TR-72-20, Battelle Memorial Institute, Columbus, Ohio, Jan 1972, 82 pages

6. J. E. Srawley and J. B. Esgar, "Investigation of Hydrotest Failure of Thiokol Chemical Corporation 260-Inch-Diameter SL-1 Motor Case", NASA TM X-1194, National Aeronautics and Space Administration, Washington, D. C., Jan 1966, 105 pages



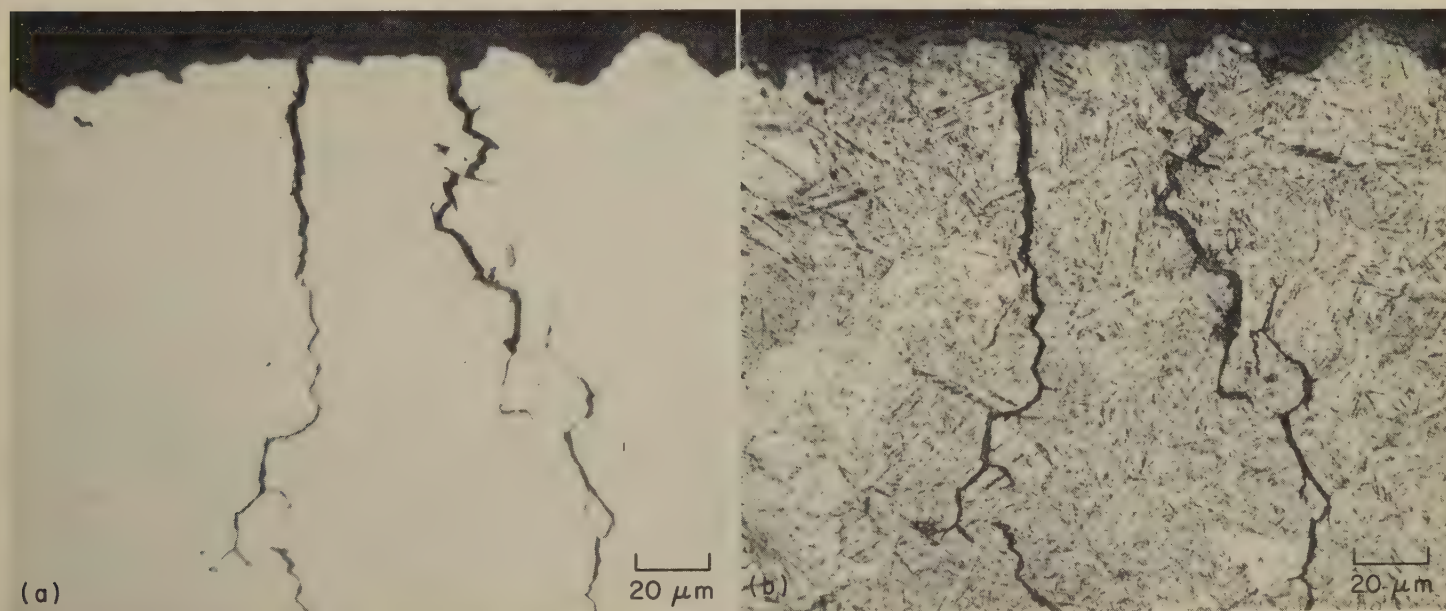
Light fractograph

500×

SEM fractograph

500×

Fig. 29. Same steel and same features revealed as in Fig. 27 and 28, but at a still higher magnification. (a) Relatively little can be seen of the surface. Specimens with cleavage facets are more amenable to such high-magnification photography. (b) All heights and depths are shown, and small inclusions are delineated within small dimples.



Micrograph (as polished; not etched)

500×

Micrograph (etchant: picral)

500×

Fig. 30. Profile of a stress-corrosion fracture in D-6ac steel that was initiated by exposure to chlorides. Note the layer of corrosion products on the fracture surface (at top in these micrographs) and the deep secondary cracks that were formed by stress-corrosion penetration along grain boundaries. The microstructure of the steel is tempered martensite.

Interpretation of Light-Microscope Fractographs

By the ASM Committee on Fractography by Light Microscopy*

THE USEFULNESS of a fractograph depends directly on the knowledge that can be gained from a study of it. The fractograph should tell something about the conditions of stress, the effect of temperature and chemical environment, and the origin of the fracture and how the crack progressed to final rupture. Interpretations that are possible from an examination of light-microscope fractographs are discussed in this article.

States of Stress

Information regarding the stresses that caused a fracture can be learned from a casual examination of the fractured part.

In many types of fracture, the general plane of fracture is perpendicular to the maximum principal tensile stress. These types, called group I fractures in the following discussion, include cleavage and other brittle fractures, ductile fractures (also called microvoid coalescence and dimpled rupture) under plane-strain conditions (in thick sections), fatigue fractures (at least in the intermediate stages), and stress-corrosion cracks.

Other types of fracture propagate along planes of maximum shear stress. These types, called group II fractures here, include ductile fractures under plane stress (that is, in thin sections or near free surfaces), shear fractures, the very early stages of fatigue fractures in pure or relatively impurity-free metals, the intermediate stages in some torsional-fatigue fractures (see Fig. 12 on page 30 in the article on Features Revealed by Light Microscopy), and the later stages of fatigue-crack propagation in some sheet materials.

To illustrate these stress types, it is appropriate to review the stress directions in some simple shapes and loading conditions. Figure 1 schematically depicts the orientation of the normal and shear-stress systems at any surface or internal point in pure tension, torsion and compression. In addition, the single-overload-fracture behaviors of both ductile and brittle materials are illustrated in the sketches with each type of load. Figure 1(a) depicts a cylindrical bar under pure tension. The tensile stress component, σ_1 , is longitudinal, and the compressive stress component, σ_3 , is transverse. The shear stresses, τ , are both at 45° to the specimen axis. In a ductile material, the shear stress causes considerable deformation (elongation and necking) prior to fracture. Cracking in tension originates near the center of the specimen and propagates toward the surface, ending with a conical shear lip (group II fracture), usually at approxi-

mately 45° to the axis. In a brittle material, a single-overload fracture (group I) is roughly perpendicular to the tensile-stress direction, but with little permanent deformation. The elastic-stress distribution in pure tension, in the absence of a stress concentration, is uniform across

the section. Thus, fracture can originate at any location within the highly stressed volume.

With torsional loading as shown in Fig. 1(b), the tensile and compressive stresses are at 45° to the specimen axis, and mutually perpendicular. The shear

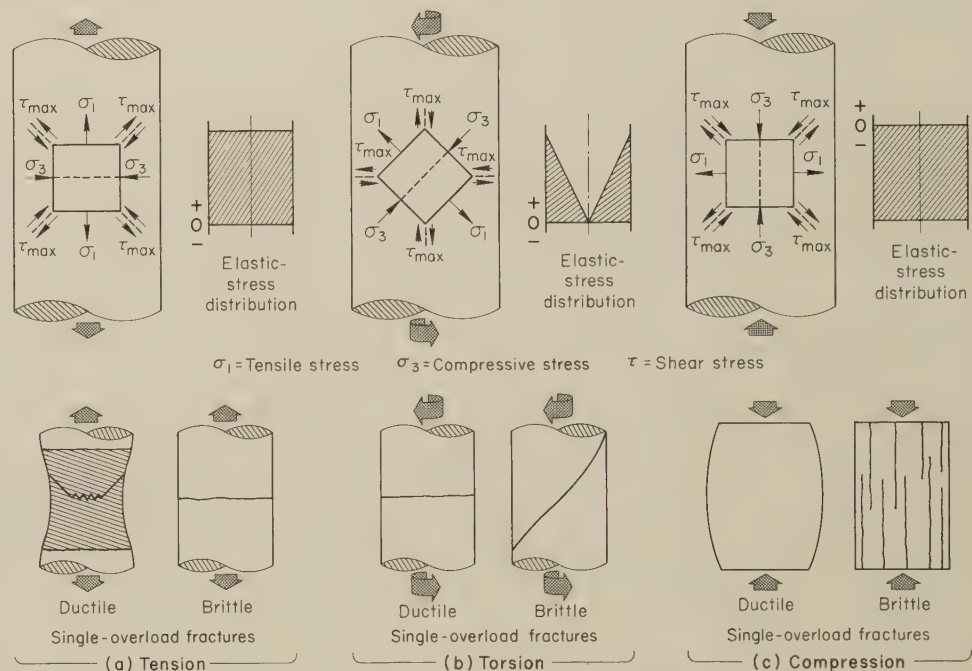
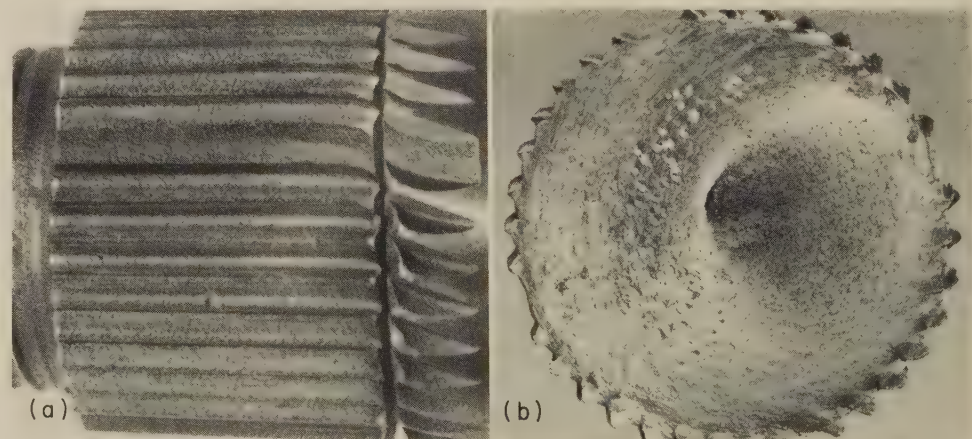


Fig. 1. Normal and shear-stress orientations under simple tension, torsion and compression of a cylinder. See text for discussion.



Photograph

(a) Photograph of the shaft showing the deformation of the splines in the region of fracture, which would not occur if the fracture were caused by fatigue. The shaft, 1½ in. in diameter, was made of 6118 steel and had a hardness of Rockwell C 23. Being made of a ductile metal, it was twisted in pure torsion with a single overload, yielding the fracture on the transverse shear plane shown in (b).

About 2×

Light fractograph

(b) Fracture surface of the shaft, showing the rotary deformation characteristic of a single-torsion-overload fracture in a ductile metal. If there is a combined bending component, the region of final, fast fracture will be offset from the center of the section. This type of fracture should not be confused with one resulting from rotating-bending fatigue, which does not have the gross distortion seen here.

About 2×

Fig. 2. Splined shaft of 6118 steel that fractured from a single torsional overload

*See page 1 for committee list.

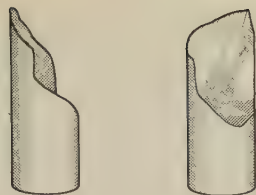
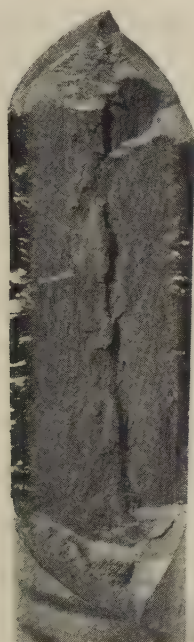


Fig. 3. Torsional brittle fracture of chalk. Fracture follows the 45° direction of maximum tensile stress.



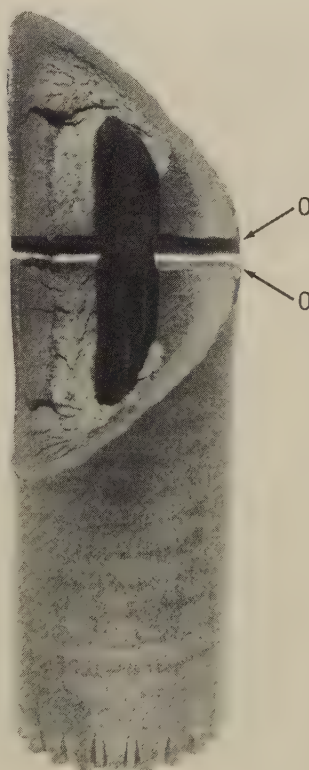
Light fractograph About 0.95×
Fig. 4. A torsional-fatigue fracture in a 1-in.-diam induction-hardened 1037 steel shaft that finally fractured in longitudinal shear. No clear point of origin is visible because the surfaces rubbed as the crack propagated.

stresses are in the longitudinal and transverse directions. In a ductile material, the shear stresses again cause considerable deformation prior to fracture, although the deformation often is not obvious because the shape of the part is not changed except for flow on the surface (see Fig. 2a). Torsional single-overload fractures (group II) of a ductile material usually occur on the transverse shear plane, straight across the cylinder, and exhibit a telltale swirled appearance (Fig. 2b). The final-fracture area will be at the center of the bar; slight bending will cause it to be off-center. A brittle material in pure torsion will fracture in a plane perpendicular to the tensile stress component, σ_1 , which is 45° to the specimen axis (group I fracture). A spiral-type fracture is one characteristic of this type of loading and material, and can be demonstrated by twisting a piece of chalk to fracture (see Fig. 3). The elastic-stress distribution in pure torsion is maximum at the surface and zero at the center. Thus, fracture normally originates at the highest-stressed region (the surface) in pure torsion. Longitudinal torsional fractures are sometimes observed (for example, Fig. 4), because longitudinal planes have the same magnitude of shear stress as trans-

verse planes and longitudinal planes usually have lower toughness, due to the shape and distribution of inclusions. Additional examples of torsional-stress fractures are presented in Fig. 5 and 6.

When a cylinder is loaded in axial compression (Fig. 1c), the compressive stress component, σ_3 , is axial, and the tensile stress component, σ_1 , is transverse. The shear stresses, τ , are at 45° to the specimen axis, as they are during axial tension loading. In a ductile material, the shear stresses again cause considerable deformation but do not usually result in fracture. The specimen simply gets shorter and bulges under the combined influence of the shear stresses and the frictional restraint imposed by the compressive load on the end faces. A brittle material in pure compression—that is, without buckling—will fracture perpendicularly to the maximum tensile stress component. Because the tensile stress is transverse, the brittle-fracture direction is longitudinal, or parallel to the axis of the specimen. The elastic-stress distribution in pure compression, in the absence of a stress concentration, is again uniform across the section. If any fracture occurs, it is likely to be in the longitudinal direction as the diameter of the specimen expands and stretches the circumference.

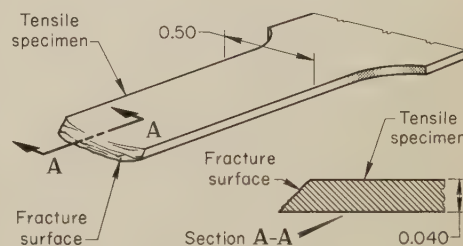
When a member is stressed in bending, the convex surface is stressed in tension and will have a stress distribution similar to that shown in Fig. 1(a). Conversely, the concave surface is stressed



Light fractograph About 0.8×
Fig. 5. Torsional-fatigue fracture in a 1½-in.-diam induction-hardened hollow steel shaft (drilled). Fatigue crack initiated at a cross hole (at O's) and propagated in shear in the 45° tensile plane.



Light fractograph About 2×
Fig. 6. A final fracture by mixed tension and shear in a 1-in.-diam induction-hardened smooth 1037 steel shaft that broke as the result of torsional fatigue. Smooth areas (A) at shaft surface are initial fatigue-crack zones.



Fracture was along the direction of maximum shear stress. The fracture lacks evidence of the direction of crack propagation because chevron marks are absent.

Fig. 7. A full-slant shear fracture in a thin sheet steel specimen broken in tension

in compression; it will have a stress distribution similar to that shown in Fig. 1(c). Approximately midway between the two surfaces will be the neutral axis, where all stresses will be zero.

A shear fracture in a thin section (0.50 in. wide by 0.040 in. thick) is shown in Fig. 7. The fracture occurred in tension. Most of the fracture surface is at 45° to the specimen thickness—that is, in the plane of maximum shear stress. This type of fracture is often called a slant fracture and sometimes a plane-stress fracture.

Fracture appearance is modified to a greater or lesser degree when the shape of the part or the stress state is more complex. For example, steps, grooves and holes will modify the stress state and change the principal normal and shear stress directions in their immediate vicinity. A fatigue crack growing from the fillet at a step in a shaft under rotating bending will have a dished surface, as shown in fractograph 4833 on page 387. The presence and degree of dishing are indicators of the involvement and severity of the stress concentration at the fillet.

As another example, suppose a shaft is designed on the basis that it will be sub-

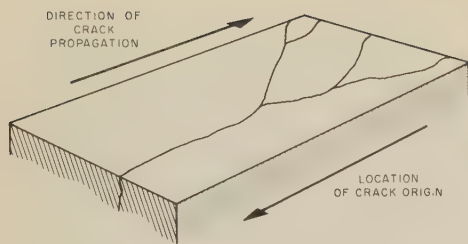


Fig. 8. Schematic representation of the information conveyed by crack branching with regard to the location of the crack origin

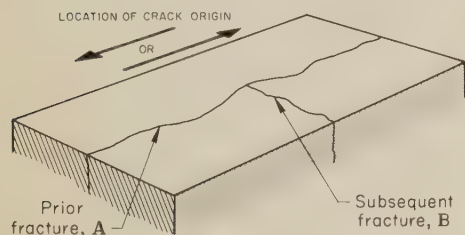


Fig. 9. Schematic representation of the T-junction method of determining which fracture surface to search to locate the crack origin. Because B does not cross A but meets it at about 90°, B occurred later and cannot contain the crack origin.

jected to only a bending load. And suppose that, after testing the shaft to fracture, it is noted that the cracks that formed do not run at 90° to the stresses caused by bending but are consistently at a somewhat smaller angle. This suggests that loads in addition to the design load have been imposed on the shaft and that they may be partly responsible for the fracture. Investigation of the direction of cracking could lead to an understanding of the secondary stresses, and ultimately to an improved design. It should be noted that the secondary stresses could be of applied, assembly or residual nature.

Crack Origins

An interest in the exact location of the point of origin of a fracture derives from the importance of determining what initiated the fracture. The initial examination of a fracture is concerned with the recognition of all features that may point to the crack origin.

Gross Aspects of Fractures. Some indications of crack-propagation direction can be seen by examination of the gross aspects of a broken part. They relate to the order in which events occurred, sometimes called "fracture sequencing". The fragments of a fractured structure can be reassembled in approximate juxtaposition, without allowing the fracture surfaces to touch, and then the telltale indications should be sought.

First, a fast-running crack in sheet or plate will frequently branch as it propagates but will almost never join another crack to continue as a single crack. Second, if a running crack joins a preexisting fracture, it will usually meet it at approximately a 90° angle, not at a shallow angle. Third, it is almost impossible for an intersecting crack to cross and propagate beyond a preexisting fracture. These con-

siderations lead to the following useful guidelines concerning crack origins:

- 1 The direction to the crack origin is always opposite to that of crack branching, as shown in Fig. 8.
- 2 If a crack meets another at about 90°, it occurred later and the origin should not be sought in it but in the earlier crack. This is known as the T-junction method of crack-origin location (see Fig. 9).

The initial section to fracture (containing the crack origin) transfers its original load to adjoining sections, in all probability overstressing them. If these sections do not contain imperfections, succeeding fractures (assuming a normally ductile material) will be preceded by a certain amount of gross plastic deformation. Therefore, in any array of several fragments of a structure, that portion most likely to contain the fracture origin will be the one that exhibits the least flow, necking, bending or other manifestation of plastic deformation. If a crack has followed a line of bolt holes or rivet holes, the hole that is located nearest the origin will be undeformed and circular and the other holes will be deformed and elongated.

A related phenomenon is associated with catastrophic crack propagation of the ductile type. If crack initiation has been by a local macroscopic brittle mechanism (fatigue cracking, stress-corrosion cracking, or hydrogen embrittlement) and the subsequent propagation has been by a ductile, or partly ductile, mechanism, a strain mismatch will be found on carefully aligning the fragments next to each other (without allowing the fracture surfaces to touch). The closest match will be found between the fragments that were the last to fracture, and the greatest mismatch (largest gap) will be found at the origin.

Clues to Crack Origins on Fracture Surfaces. The exact identification of the site of fracture origin is usually established from a study of the fracture-surface features and a knowledge of the metal, heat treatment, and type of loading. With one notable exception (full-slant shear fracture), every type of fast-running or catastrophic fracture will produce surface marks that will be indicative of crack-growth direction. Radial marks, for example, will lie perpendicular to the crack front and thus radiate from and point to the origin. These marks, which are shown in Fig. 3 and 4 on page 28 in the article on Fractographic Features Revealed by Light Microscopy, result when the crack propagates in segments on slightly different levels that are joined by cleavage steps or microshear lips.

A form of radial mark that is especially helpful in locating a crack origin is the chevron pattern produced in many materials by high-velocity fracture (see Fig. 8 on page 29 in the article on Fractographic Features Revealed by Light Microscopy). It is seen most clearly in low-carbon steel plate. The apexes of the V-shape chevron patterns point in a direction opposite to that of crack propagation. Thus, the apexes point toward, and

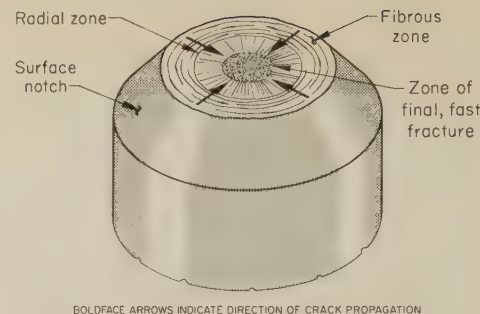


Fig. 10. Schematic representation of the fracture zones of a notched tensile specimen of circular cross section

Unlike the fractures shown for smooth (un-notched) tensile-test specimens in Fig. 2 to 4 on pages 27 and 28, this fracture contains no shear-lip zone. Initial fracture occurs completely around the specimen, in the root of the notch.

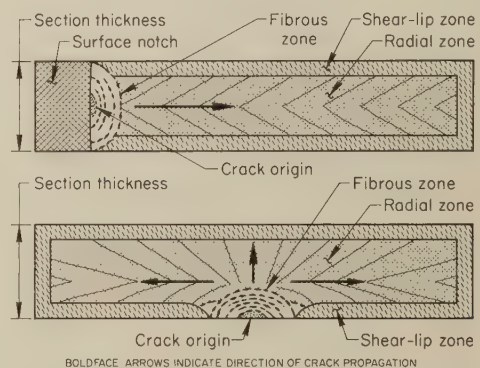


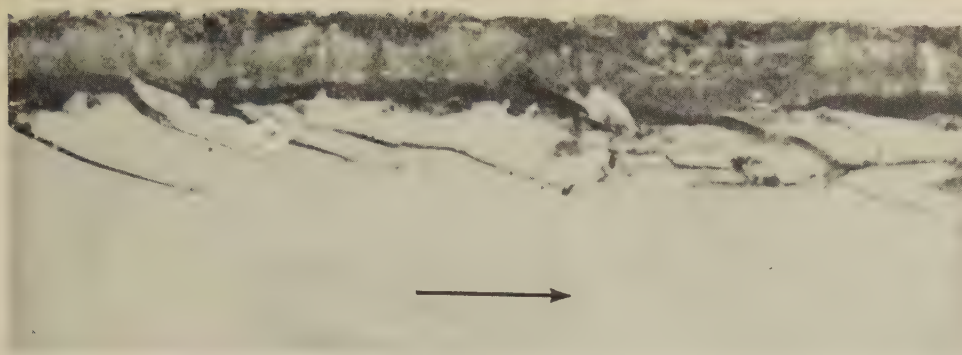
Fig. 11. Schematic representation of the fracture features that are exhibited in notched tensile specimens of rectangular cross section (Ref 4)

A fibrous zone is generated from the notch and extends for a short distance. A radial zone then supplants the fibrous zone, and a shear-lip zone is formed wherever the radial zone approaches the edge of the specimen.

can be followed directly to find, the fracture origin. Chevron patterns have been important aids in locating crack origins in fractures in ships, pipelines, railroad tank cars, pressure vessels, and rocket-motor cases. References 1 and 2 contain information concerning the mechanism of formation of chevron and related fracture patterns. Plate V in Ref 3 is a good photograph of discontinuous fracture.

Reverse chevron patterns (Fig. 10 in Ref 1) may be produced under special conditions: (a) when the nucleations are caused to occur under surface scratches, where stress is concentrated; and (b) when nearly plane-strain conditions are introduced at the roots of the scratches so that locally the K_{Ic} is reduced nearly to K_{Ic} . The latter condition produces a main crack front that is concave in the forward direction. (The normal front is convex in the forward direction.) Instead of tear lines, a crack front of this type provides shear-lip marks that are beach marks, which can easily be misunderstood by the uninitiated.

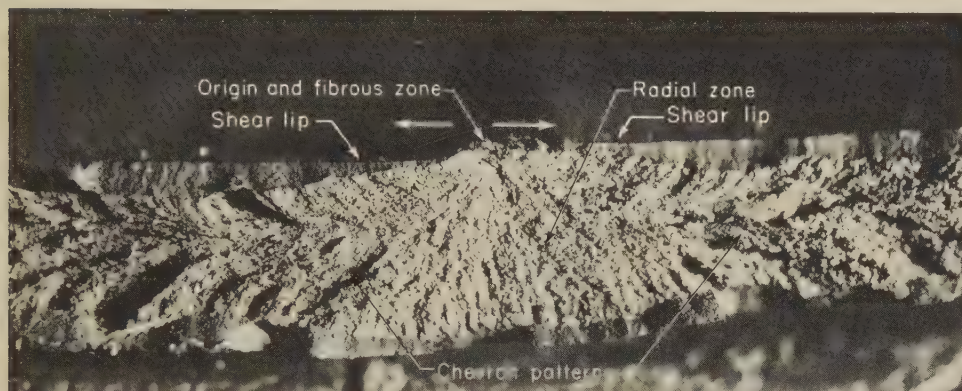
Fibrous marks, tear ridges and beach marks can also be utilized as indicators of the location of a crack origin, just as the concentric rings on the surface of a pond indicate where a stone entered the water. Where the curvature of such marks



Light fractograph

5×

Fig. 12. Use of plastic tape (light gray, at bottom) to indicate the direction of crack propagation (arrow) by tears produced in the tape during fracture. Tape was applied to a motor case of 4130 steel that was proof tested by hydraulic loading. An oblique view of the fracture surface of the motor case is seen at top.

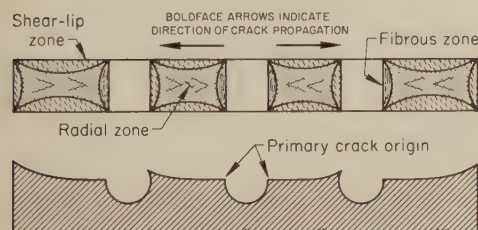


Light fractograph

6×

The shear lip increases in width with increasing distance from the origin. The radial marks below the origin and the chevron patterns to the left and right also indicate the directions of fracture.

Fig. 13. Fracture in a welded pressure vessel of 4340 steel displaying a flat origin at the top with a shear lip beginning on either side of it (Ref 4)

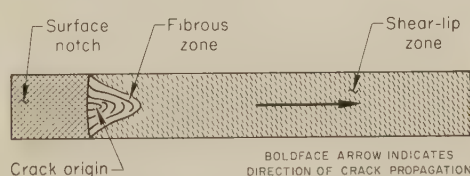


A flat area is associated with the crack origins and with each site of crack reinitiation. The interruption of the crack by a hole has created a final shear lip within the hole.

Fig. 14. A schematic representation of fracture marks associated with crack propagation that was interrupted by drilled holes (Ref 4)

is slight, the origin is generally on the concave side of the crack-front curve.

Surface notches alter the position of the crack origin, the direction of crack growth, and the sequence of fracture-zone features. Figure 10 shows schematically that, unlike the fractures in smooth (un-notched) cylindrical tensile-test specimens shown in Fig. 2 to 4 in the article on Fractographic Features Revealed by Light Microscopy (see pages 27 and 28), the fracture in a notched, cylindrical tensile-test specimen will not begin at the center of the section, but will begin at the root of the notch, with final fracture at the center of the specimen, and there will



The triangular area of the fibrous zone points in the direction of crack propagation. This transition may not take place in low-strength, ductile metals, which may show a flat fracture with lateral contraction increasing with distance from the fracture origin.

Fig. 15. A schematic representation of a full-shear-lip fracture evolving from a fibrous crack origin at a surface notch (Ref 4)

be no shear-lip zone. A different situation exists in fractures of rectangular specimens (see Fig. 11): A fibrous zone will be generated from the notch, but since the notch will not normally extend completely around the perimeter as in Fig. 10, the fibrous zone will be succeeded within a short distance by a radial zone, which in turn will be replaced by a shear-lip zone at the edges of the specimen.

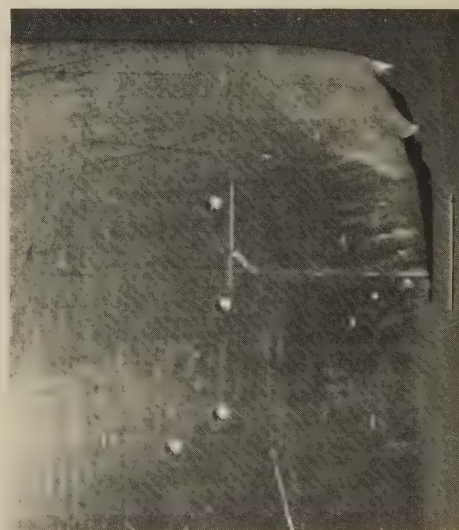
In proof testing, the direction of crack propagation can be recorded by applying plastic tape around the component to be tested in areas where fracture is anticipated. The tears produced in the tape during fracture will reveal the direction of crack propagation, as shown in Fig. 12.

In general, the region of a crack origin will be flat and will lack any free-surface shear-lip zone. The shear-lip zone appears only at some distance from the origin and becomes larger as the distance increases (see Fig. 13).

If crack propagation is interrupted by a drilled hole (Fig. 14) or similar feature, the pattern of shear lips and regions of crack reinitiation can often provide clues as to the directions of crack growth.

On occasion, the flat surface at a crack origin will change to a full shear lip. At the transition, there will be a triangular area of the fracture surface that will point in the direction of crack propagation, as illustrated in Fig. 15. In ductile, thin sheet metal, fracture is frequently by 100% shear (a full-slant fracture), creating none of the usual marks that point to the crack origin. The only helpful indications are nonfracture edge marks, like those in Fig. 16 and 17. Saw teeth, as in Fig. 16, usually point back toward the crack origin but are less reliable indicators than are the strain marks visible at the fracture edge in Fig. 17. Strain marks are either analogous to or identical with Lüders lines and emanate from the edges of the crack front at various positions during crack progression. They are reliable indicators of fracture direction in thin metal sheets and are particularly helpful in interpreting long, running fractures in ductile, or partly ductile, pipe and pressure vessels.

Usually, crack origins are found at free surfaces, and are traceable to the presence of stress concentrations, bending or torsional components of load, or the influence of an aggressive environment. Subsurface origins are the exception. They usually result from such factors as surface hardening (the softer, weaker



Macrograph

3×

The saw teeth at the upper right corner point back toward the crack origin. Saw teeth are sometimes useful indicators of crack origin, but are considered less reliable than the strain marks in the fractured specimen shown in Fig. 17 (at right). Arrow indicates direction of crack propagation.

Fig. 16. Fractured specimen of titanium alloy Ti-6Al-4V sheet, 0.085 in. thick, that gave an 85% ductile tear with a prominent shear lip. Fracture surface is shown in profile at right.

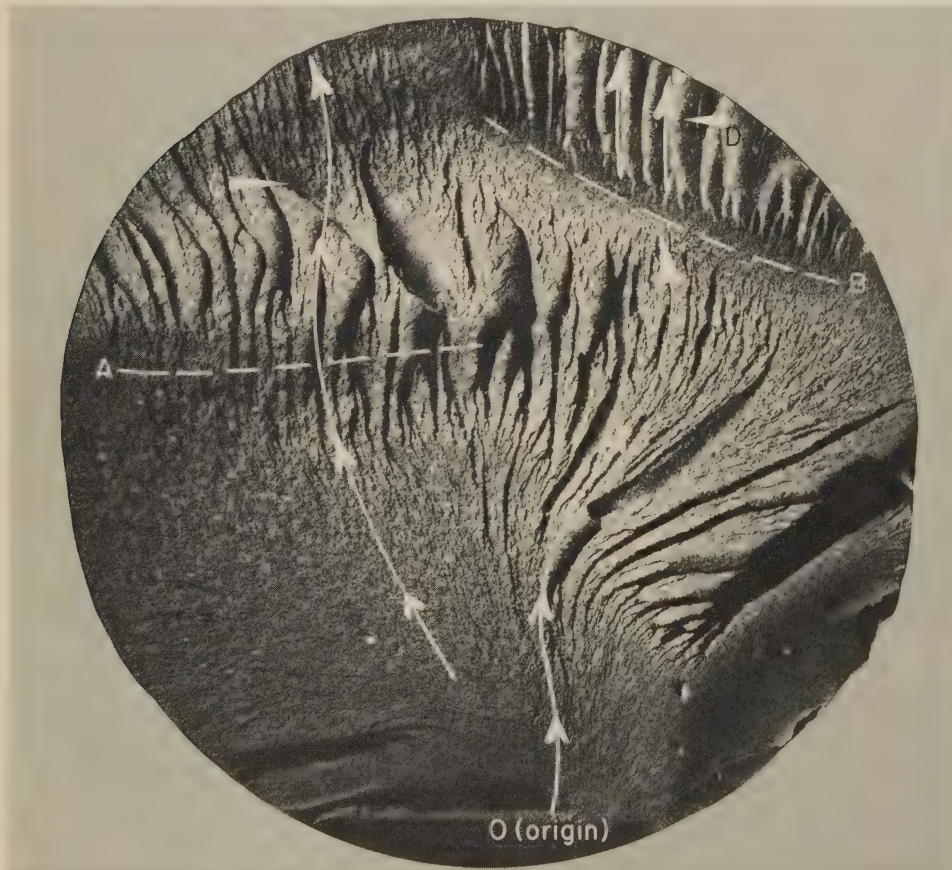


Macrograph

10½×

The shearing, at 45° to the longitudinal axis, was on a plane nearly normal to the thickness direction of the plate. The wavy strain marks at the right edge are believed to be analogous to or identical with Lüders lines. The marks formed at the edge of the crack front at various locations as it propagated. Arrow shows direction of crack propagation.

Fig. 17. Fractured specimen of titanium alloy Ti-6Al-4V sheet, 0.055 in. thick, that gave a 100% shear fracture. Fracture surface is shown in profile at right.



Light fractograph

3×

Fracture origin can be found in three ways: by tracing the radial marks in the lower portion of the fracture to their point of convergence (the arrows on the curved lines indicate the direction of crack propagation); by drawing normals to the crack-

material being below the surface) or the presence of large internal discontinuities, or from direct tensile overloading of a smooth (unnotched) part. A conclusion that the origin is subsurface should in general be suspect (except in fractures involving hydrogen embrittlement or a subsurface discontinuity), and the surface of the part should be scrutinized further.

Location of Origins in Impact-Overload Fractures. Figure 18 shows the fracture of a 12% Cr steel bar that was notched and then struck with a hammer. Two blows were necessary to complete the fracture. The fracture marks are radial. They may be traced downward to a common intersection. Also present are crack arrests, one at A and a second at B, where fracture progress came to a complete halt before the second blow was struck. The arrest marks are parallel to the crack front, and lines drawn normal to them should intersect at or near the origin. The contours of the final fracture marks, at C and D, also point to the general location of the beginning of fracture.

In Fig. 19, a fracture in a cast steel frame bar, chevron patterns (perhaps most distinct at A) point downward toward the bottom flange. Within the flange are less distinct chevron patterns (at B) suggesting that the crack origin



Light fractograph

0.4×

Chevron marks at A point to bottom flange and at B along that flange to origin (O) at its left tip. At C, at midpoint of bottom flange, is a pattern of dendrites; these are not radial marks.

Fig. 19. Locating the origin in a fracture in a cast steel frame bar of a tractor chassis

was at O rather than at the dendritic area C, as might be assumed at first glance.

Variations in overload fractures are seen in steels of different hardness. Surface-initiated fractures in high-hardness steels frequently have shallow shear lips that begin on either side of the crack origin. In lower-carbon steels, the chevrons may converge at a region just below a shear lip. The area of crack origin in high-hardness medium-carbon and high-carbon steels is usually finely faceted (excluding fatigue origins) and may be predominantly intergranular. At increasing distances from the origin, the fracture topography is less faceted, because of increasing amounts of dimpled rupture. Or there may be an abrupt transition to the dull, nonreflective aspect of dimples, as shown in Fig. 20. In other fractures, there may be a mixture of intergranular and dimpled fracture. This may be recognized as patches with contrasting reflectivity, at magnifications as low as five diameters.

In case-hardened parts, the fracture through the high-hardness zone at the surface can occur by a single overload, and crack arrest occurs in the softer core. A beach-mark region in the core is not conclusive evidence that fracture was initiated by a fatigue mechanism in the high-hardness zone.

A special aspect of radial marks is that their appearance depends in part on whether the crack-growth velocity at the surface is greater or less than that below the surface. If crack-growth velocity is at a maximum at the surface, they will have the fan-shaped appearance shown in Fig. 21. If the crack-growth velocity is greatest below the surface, the result is chevron patterns, as in Fig. 22. Both patterns appear to radiate from the fracture origin.

The appearance of radial marks also is influenced by the configuration of the part or specimen undergoing fracture. Chevron patterns occur most frequently in fast fracture of parts or specimens

arrest fronts labeled A and B; and by projecting the tangents to the final radial marks at C and D toward the bottom. The crack came to a full stop at B with the first hammer blow and resumed motion at the second hammer blow.

Fig. 18. Locating the origin in an impact fracture, produced by two hammer blows, in a notched bar of 12% Cr steel

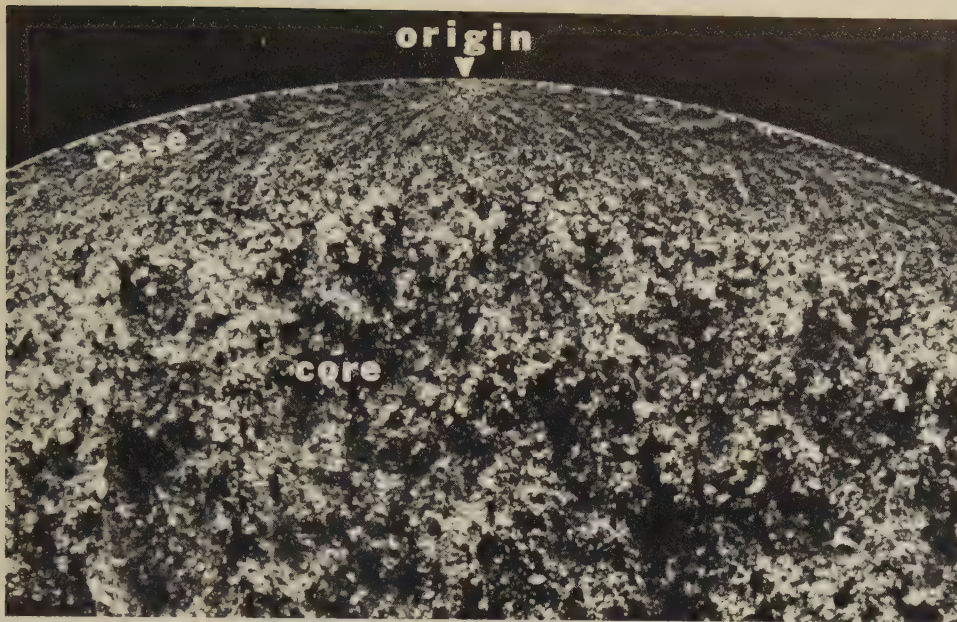


Fig. 20. Light fractograph showing a fracture surface of a carburized shaft of 8620 steel broken in bending by a dynamic single overload. The region of small facets is the crack origin. The chevron patterns in the case point toward the origin. Rupture in the core is known to be dimpled.

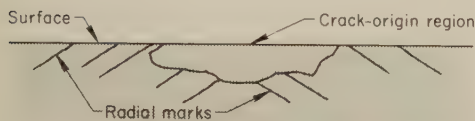


Fig. 21. Radial marks typical of crack propagation that is fastest at the surface (if propagation is uninfluenced by the configuration of the part or specimen)

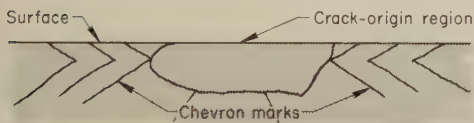


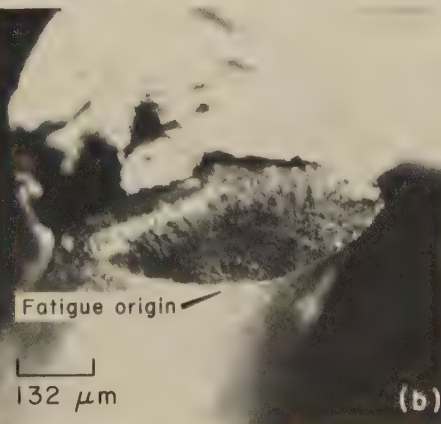
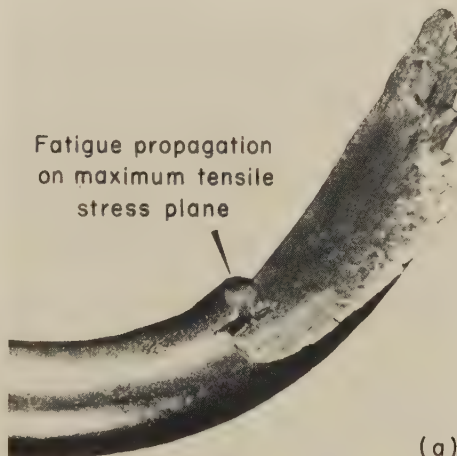
Fig. 22. Chevron patterns, typical of crack propagation that is fastest below the surface, and also observed in fractures of parts or specimens having a thickness much smaller than the length or width

having a thickness much smaller than the length or width. The cases of case-carburized, flame-hardened, and induction-hardened parts also fulfill this condition (see Fig. 20).

Location of Origins in Fatigue Fractures. Fatigue fractures, which generate the well-known beach marks, show different amounts of relief, depending on whether they are low-cycle or high-cycle in nature, the latter having considerably smoother surfaces at the origins. Finely detailed beach marks can be seen in the torsional-fatigue fracture of Fig. 23.

Case-hardened parts subjected to bending or torsion may experience initiation of fatigue near the case-core interface, because the strength gradient there is steep. Figure 10 in the article on Photography (see page 16) shows two crack origins at this location; the clearly developed chevron patterns in the case-hardened zone point toward both origins, in some areas to the origin labeled A and in others to origin B.

Fatigue propagation
on maximum tensile
stress plane



Light fractographs 22.5× (a); 76× (b)

The fatigue crack propagated in the plane of maximum tensile stress in a wire section that was loaded primarily in torsion. The higher-magnification view at bottom displays fine beach marks that are concentric with a tiny longitudinal step (not discernible in this view) that was the crack origin.

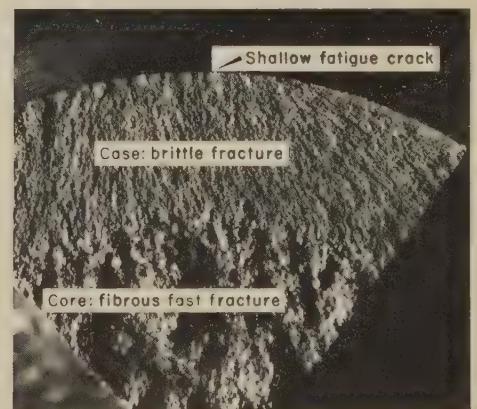
Fig. 23. Locating the origin of a torsional-fatigue fracture in a high-hardness steel music wire spring

The fatigue-crack regions in high-hardness steels are usually quite small relative to the cross-sectional area unless the nominal stresses are low. The fatigue-crack regions, which are transgranular, are usually surrounded by finely faceted, fast-fracture regions, which may be shown by electron microscopy to be intergranular. If the fracture occurs in less than about 4000 cycles, there may be little or no visual evidence to distinguish the fracture from a single-overload fracture. In hardened cases, a magnification of 50× may sometimes be necessary to distinguish clearly the fatigue-crack region from the surrounding fast-fracture region. The fatigue-crack region is less reflective (duller) and smoother than the intergranular region (see Fig. 24). A chevron pattern, such as that shown in Fig. 22, is commonly observed in fractures through hardened cases. If there

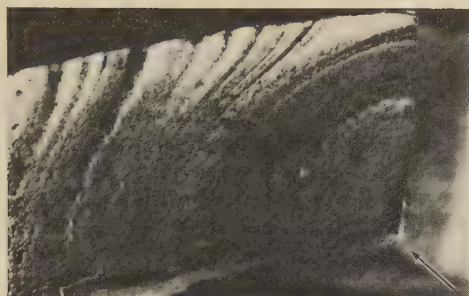


Light fractograph 40×
A very small fatigue-crack region (at arrow) is surrounded by a finely faceted region of final, fast fracture in the case. Fracture of the tooth took place after about 20,000 cycles. The fatigue-crack region had a slightly different orientation than the surrounding fast-fracture region; this condition, and the extreme care taken in getting proper lighting, resulted in the exceptionally good contrast between the two regions.

Fig. 24. Origin of fracture at fatigue-crack region at the surface of a carburized alloy steel gear tooth. Case hardness, Rockwell C 63; core hardness, Rockwell C 36.



Light fractograph 31/2×
Fig. 25. Fracture surface of an induction-hardened shaft of medium-carbon steel showing a shallow fatigue crack at the outer rim that propagated from many origins. Fracture was of the single-overload type through the remainder of the case and the core.



Light fractograph 5×
A line drawn perpendicular to the beach marks, within the region in which they have not yet reached the upper surface, will show that the lower right corner (arrow) is the site of the origin.

Fig. 26. Use of beach marks to locate origin of fatigue fracture in a 4340 steel socket

are multiple crack origins, as in Fig. 25, the fatigue-crack regions may have many jagged steps, due to the linking of adjacent smooth-textured fatigue cracks that have slightly different orientations. The fatigue-crack regions usually have radial-type marks that converge at the origins.

Beach marks (crack-arrest lines), which are generated both by fatigue conditions and by stress corrosion, are vestiges of temporary positions of the crack front. The direction of crack growth can be determined by erecting a perpendicular to beach marks in the center of a fracture and seeking the crack origin along this direction from the concave side of the beach marks. Figure 26 shows the use of beach marks to locate the origin of a fatigue fracture; Fig. 27 shows the use of crack-arrest lines to locate the origin of a stress-corrosion fracture.

Location of Origins in Fractures Caused by Environment. High-hardness steel parts can fracture under very low static stresses, externally applied or residual, if they are embrittled by hydrogen absorption or subjected to an environment capable of causing stress corrosion. Hydrogen-embrittlement fractures, frequently the result of electroplating, can be difficult to distinguish from stress-corrosion fractures, especially when the corrosive environment is a source of hydrogen. Both mechanisms usually result in faceted, intergranular fracture origins. If corrosion products are present, they will usually be more uniformly distributed in fractures resulting from hydrogen embrittlement and be more concentrated in the origin regions in fractures resulting from stress corrosion. Stress-corrosion cracks initiate at the surface of the part. Hydrogen-embrittlement cracks can initiate below the surface. Figure 28 shows a multiple-origin stress-corrosion fracture in a stud made of maraging steel. The fracture was produced in the laboratory under a static load with distilled water as the corrodent. The concentric rings of corrosion identify the crack origins. They indicate changes in rates of corrosion cracking and are not indicative of fatigue.

Fractographic Mapping To Identify Fracture Origins. If none of the methods described thus far reveals crack origins, microscopic examination at higher magnifications and fractographic mapping

are recommended. Fortunately, the fracturing of a metal produces the same patterns on all size scales. In fractographic mapping, certain sites are selected on a grid and examined under a microscope. The results can be plotted on a facsimile of the fracture surface, as in Fig. 29. The combined evidence of the observations makes it possible to deduce the location of the crack origin.

Under some circumstances, even fractographic mapping may not be effective. Gray iron, for example, produces fracture surfaces that are very difficult to analyze, because rupture is accompanied by very little strain, producing only exceedingly tiny facets. Interpretation, in turn, may be obscured by the interfering influence of a pearlitic structure. A recourse, to be undertaken only after completion of all other studies of the surface, is to refit the matching pieces of the fracture and search for slight misalignment arising from a strain differential between the beginning and ending of the fracture. This procedure will, of course, damage the fracture surfaces and should be used only after other studies are completed.

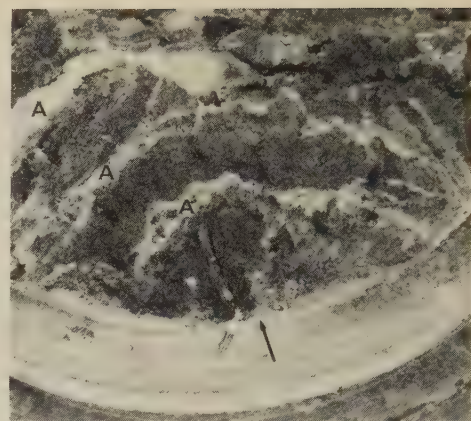
An alternative is to search the fracture surface with a low-power stereomicroscope for evidence of undercutting, which can occur during the joining of micro-crack fronts that have been advancing on different levels. If the fracture is moving upward from one stratum to another, the last tiny segment between these levels to part will be bent slightly upward. The plotting of such evidence can be utilized to create another type of fractographic map for identification of the crack origin.

Another alternative is to examine the external surface of the fractured part for secondary cracks. This procedure assumes that several cracks may have been formed in a single area, with one of them becoming the primary fracture.

Fracture Progress

Many types of fractures, including most service fractures, occur by a sequence involving crack initiation, subcritical crack propagation (due to ductile crack extension, fatigue, corrosion fatigue, stress-corrosion cracking, or hydrogen embrittlement), and fast fracture, when the remaining cross section can no longer support the applied load. The fracture processes leave telltale marks on the fracture surfaces, which enable a trained investigator to locate the initiation sites, to discern the propagation direction and crack-front shape, and to distinguish the fast-fracture zone. This information can lead to an understanding of the stress levels and conditions leading to fracture.

Two efforts to systematize and categorize such information are represented by the charts in Fig. 30, derived from Lipson (Ref 5) and Jacoby (Ref 6, 7) and in Fig. 31, also derived from Jacoby (Ref 6, 7). Although these two charts were developed primarily for fatigue fractures, they apply equally well to fracture under other conditions where stable, subcritical crack growth occurs. Figure 32, also from Jacoby (Ref 7), depicts crack-initiation sites in rectangular members under ten-

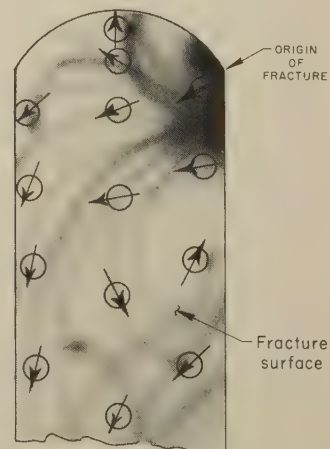


Light fractograph 4×
Fig. 27. Use of crack-arrest lines (A) to locate origin of a stress-corrosion fracture in a stressed manganese bronze bolt exposed to water. The arrest lines are roughly concentric about the origin (at arrow).



Light fractograph 2.8×
Steel hardness was Rockwell C 50. Fracture was produced under a static load with distilled water as the corrodent. Rings of corrosion product surround the three crack origins. The rings are beach marks, but not a result of fatigue.

Fig. 28. Multiple origins in a stress-corrosion fracture in a maraging steel stud



Arrows show the directions of crack propagation at various locations as indicated by the microscopic fracture marks observed. These combine to define fracture propagation paths and the location of the crack origin.

Fig. 29. Schematic representation of fractographic mapping of data obtained from examination under the microscope of a fracture that was featureless at low magnification

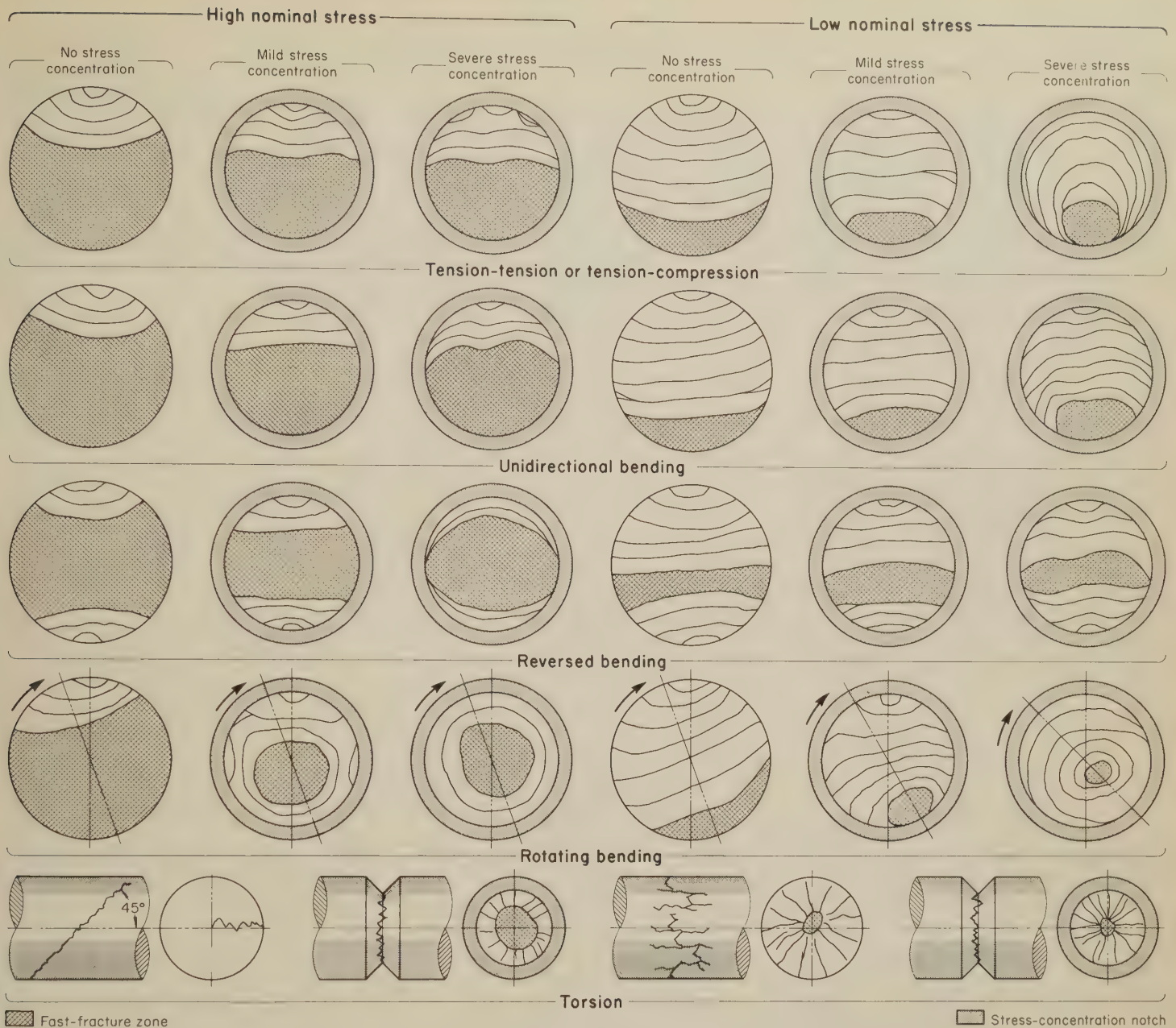


Fig. 30. Schematic representation of fatigue-fracture surface marks produced in smooth and notched components with circular cross section under various loading conditions (Ref 5-7)

sion and, with appropriate modifications described by Jacoby (not shown in Fig. 32), under bending.

The charts in Fig. 30, 31 and 32 are intended to be employed only as guidelines. Deviations from these charts will be found for various material conditions, test conditions, and service conditions.

Figures 30, 31 and 32 are based on the following principles:

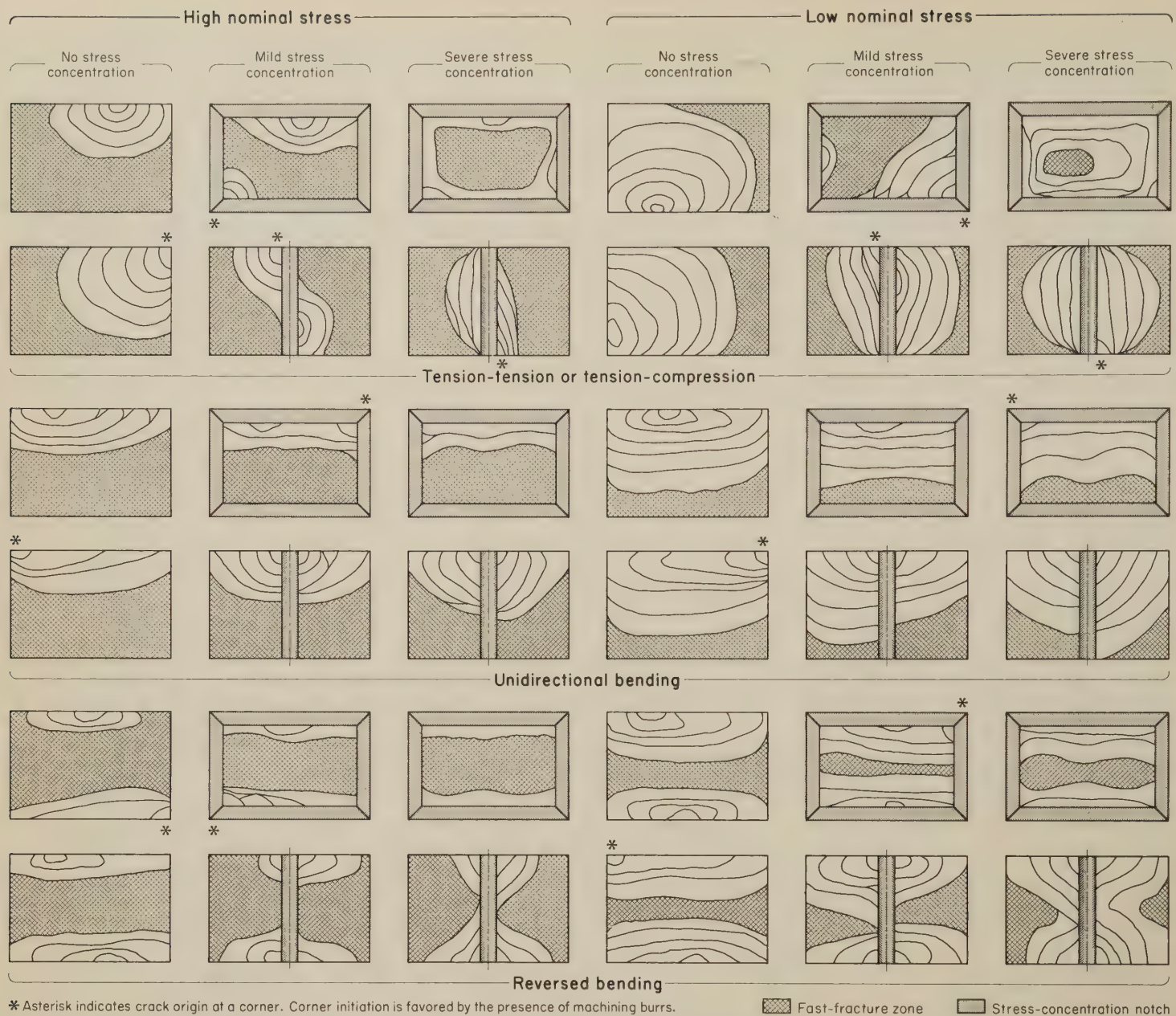
- 1 As the local stress in regions of potential crack initiation increases, the number of active crack nuclei or initiation sites increases. Therefore, at high overstress or in the presence of a severe stress concentration, multiple origins will be observed, in most instances with the cracks from these origins eventually uniting to form a single crack front. Before that union, the individual microcracks will be separated by small, vertical ledges, which have been termed ratchet marks. On the other hand, at just above the fatigue

limit, or minimum stress for fracture, a single origin will be achieved and the entire fracture will emanate from it.

- 2 In the absence of stress concentrations at the surface, cracks propagate more rapidly near the center of a section than at the surface. This occurs because constraint causes the stresses to be triaxial and more severe away from the surface. However, when there is a stress-concentrating notch at the surface (such as a thread with a sharp root), the stress in the zone of influence of this notch may be more severe than it is farther below the surface. Under conditions of severe notching, W-shaped crack fronts will sometimes be observed.
- 3 For a given material, the area of the region of catastrophic fracture (or final, fast fracture) relative to the area of the region of subcritical crack propagation will increase with increasing nominal stress. Under an overload that is slightly more than adequate to cause fracture, the region of final, fast fracture will be rela-

tively small; under a much higher applied stress, the region of final, fast fracture will be relatively large.

- 4 In fracture by rotating bending, the final-fracture region will often be rotated, or offset, toward the origin in a direction opposite to the direction of rotation. Also, all other conditions being the same, the final-fracture region will move toward the center of the section as the nominal stress increases (see Fig. 30).
- 5 Fracture initiation usually occurs at or near free surfaces. In bending or when stress concentrations are present, the free surface will be subjected to the greatest stress. Subsurface origins have been observed in tension-tension or tension-compression fatigue if there is a large inclusion or imperfection in the interior of the specimen or part, but this is unusual. Crack initiation at corners (as in Fig. 31) or at the ends of drilled holes (as in Fig. 32) may result from the presence of burrs remaining at these locations after machining.



* Asterisk indicates crack origin at a corner. Corner initiation is favored by the presence of machining burrs.

Fast-fracture zone Stress-concentration notch

Fig. 31. Schematic representation of fatigue-fracture surface marks produced in components with square and rectangular cross sections and in thick plates under various loading conditions (Ref 6, 7)

Use of these principles, and the charts based on them, involves only a few steps. First, the fracture is examined for the number of origin sites. Multiple origins, indicated by several ratchet marks, mean a high stress or several separate stress concentrations at the origin area. A single nucleation site means a lower applied stress and low stress concentration. Next, the shape and location of the propagating crack front or fronts are evaluated and interpreted in terms of the type of loading (such as tension, bending, reversed bending, torsion) and the stress concentration at the surface (that is, whether the crack front is leading or trailing). Finally, the location and size of the region of final fracture are taken as an indication of the nominal stress level. Figures 33, 34 and 35 give examples of the application of this procedure to the interpretation of fatigue fractures in a steel bolt and in two steel shafts.

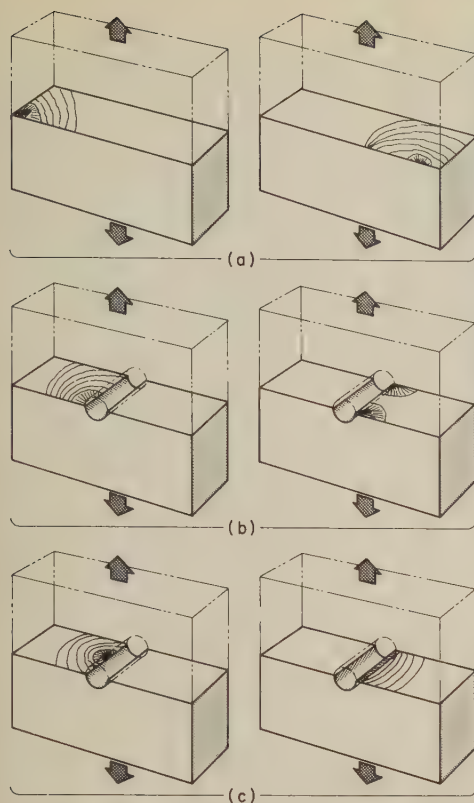
Fracture Changes During Crack Propagation

Several influences may affect the growth of a crack, causing it to progress thereafter by a mechanism of fracture different from that in effect when cracking started. These influences include: (a) local differences in microstructure; (b) changes in stress-intensity factor, K ; (c) changes in chemical or thermal environment; (d) differences in stress state.

Changes Caused by Local Differences in Structure. Microstructure exerts a pronounced influence on local fracture appearance. The presence of two or more types of microstructure may result in different fracture mechanisms being involved, and a different fracture appearance. A simple example is a fracture in a chilled white iron part. Fracture is by cleavage through the chilled zone and is fibrous in the pearlitic zone.

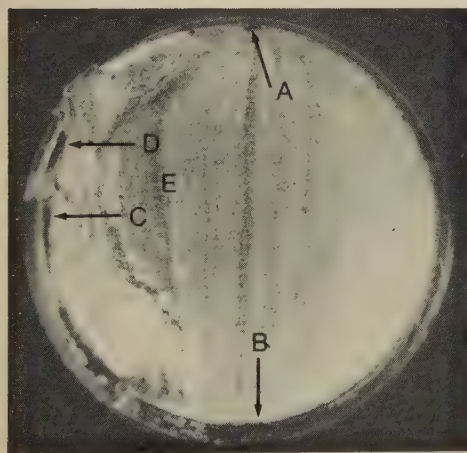
Another structure difference is that of case and core in carburized, flame-hardened, and induction-hardened parts. The difference in properties between such structures can cause a crack to proceed by quite different fracture mechanisms in adjacent regions. An example of this occurrence is the fracture of the induction-hardened 1541 steel shaft that is shown in Fig. 10 on page 16. In this shaft, fatigue originated at two locations at the interface between the case and the core because of the very sharp change in strength across that interface. The difference in fracture-surface features between the case and the core is marked. Furthermore, the fracture in the case is at high velocity, with distinct chevron marks, and that in the final-fracture zone in the core is coarsely fibrous.

Changes Caused by Changes in Stress-Intensity Factor. With stable crack propagation, the stress intensity (K) at the



(a) Crack initiation at one corner and at a face of an unnotched specimen. (b) Crack initiation at one corner and at two corners in a drilled hole in a specimen. (c) Crack initiation in the center of a drilled hole in a specimen and occurring simultaneously over the entire length of the hole.

Fig. 32. Crack initiation in unnotched and notched (drilled) specimens with rectangular cross sections (Ref 7)

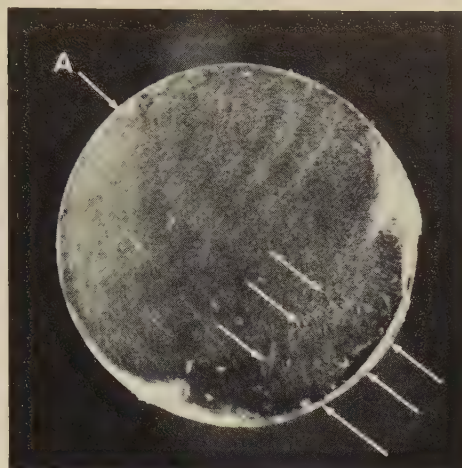


Light fractograph $2\frac{1}{2}\times$

Interpretation of the fracture surface indicates: (a) loading was mainly by unidirectional bending; (b) stress concentration was high (many closely spaced origins along thread root at right, between A and B, and leading crack edges); (c) small reversed bending load or backlash may have been present (secondary origins at C, D); and (d) nominal stress was low (small region of final, fast fracture at E).

Fig. 33. Fatigue fracture in a steel bolt

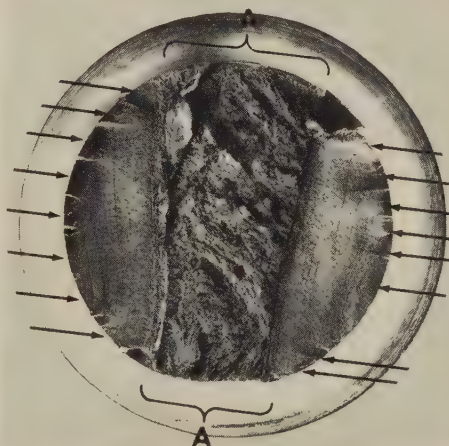
crack tip is constantly changing. A classic example of the effect of this change occurs under sinusoidal fatigue loading. The initial fracture mechanism (fatigue) is characterized by very slow growth rate. As the crack extends, the crack-tip stress intensity increases, as does the crack-



Light fractograph $3\times$

Interpretation of the fracture surface indicates: (a) the loading was rotating bending; (b) there was no marked stress concentration (single origin at A); and (c) the nominal stress was low (small region of final, fast fracture between sets of arrows).

Fig. 34. Fatigue fracture in a steel shaft



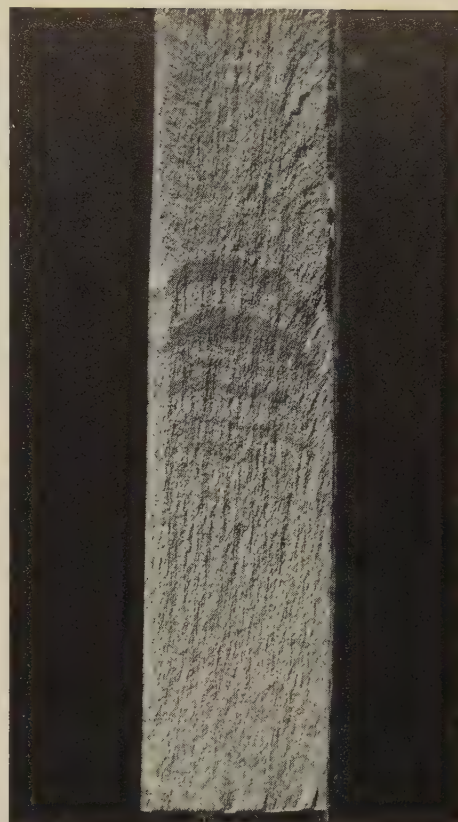
Light fractograph $0.9\times$

Interpretation of the fracture surface indicates: (a) loading was by reversed bending; (b) stress concentration was mild (several origins at arrows on both sides); and (c) nominal stress was moderate to high (fairly large region of final, fast fracture between brackets at A's).

Fig. 35. Fatigue fracture in a 1.94-in.-diam 1050 steel shaft (Ref 8)

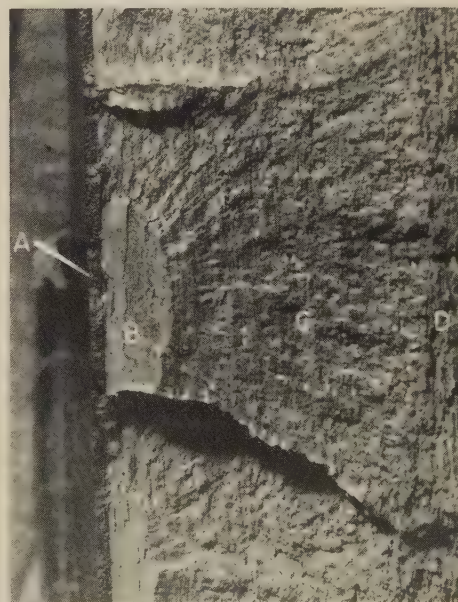
propagation rate. At higher K values, fatigue is no longer the dominant feature, and tearing of the material becomes increasingly prevalent. Fracture changes of this kind are shown in Fig. 36.

Changes Caused by Altered Environments. A fracture-mechanism change as a result of different chemical and stress environmental conditions is shown in Fig. 37. A corrodent generated small pits below a layer of chromium plate and provided the environment for the growth of stress-corrosion cracks, which originated at the pits. The stress may have been residual or applied. As the stress-corrosion cracks grew, the stress intensity at the crack tip increased for the applied cyclic loads. At some critical level of environment and cyclic-stress intensity, the fracture mechanism changed to one of pure fatigue. The fatigue cracks propagated until the critical crack-tip stress-intensity



Light fractograph $1.6\times$

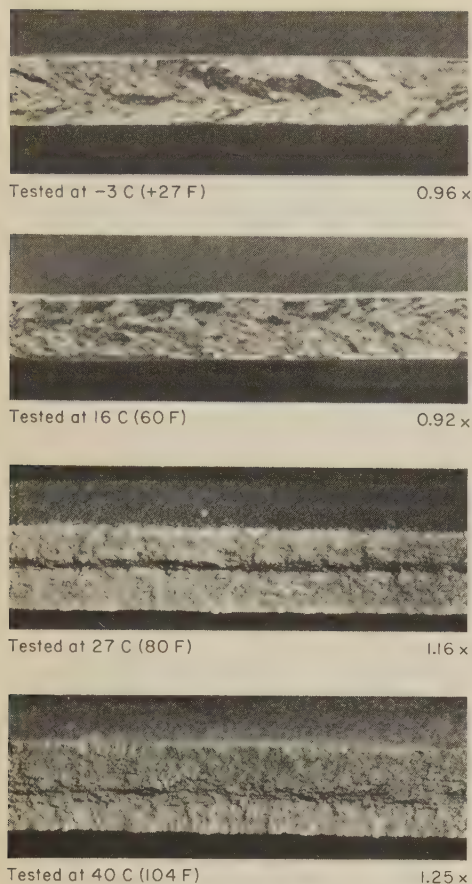
Fig. 36. Changes in mechanism of fatigue-fracture propagation in aluminum-clad aluminum alloy 7075-T6 plate. The fracture marks changed with changes in stress intensity as the crack moved toward the top.



Light fractograph $5.7\times$

Small corrosion pits formed beneath the layer of chromium plate, as at A, and generated stress-corrosion cracks B. Growth of these cracks altered the stress intensity at the crack tips, leading to propagation of fatigue cracks C. Final, fast fracture D occurred when the critical crack-tip stress-intensity value was reached.

Fig. 37. Changes in fracture mechanism and appearance that were caused by changes in chemical and stress environment for a chromium-plated aluminum alloy 7079-T6 forging



Light fractographs showing fracture surfaces of four sections cut from a single length of low-carbon steel pipe, which were burst by hydraulic pressure at the temperatures indicated. The steel had a yield strength of 414 MPa (60 ksi).

Fracture mechanism was changed by the test temperature, as attested by the chevron pattern with minute shear-lip zones at -3°C ($+27^{\circ}\text{F}$), by the chevron pattern with 15% shear-lip zone at 16°C (60°F), and by the 100% shear pattern at 27°C and 40°C (80 and 104°F).

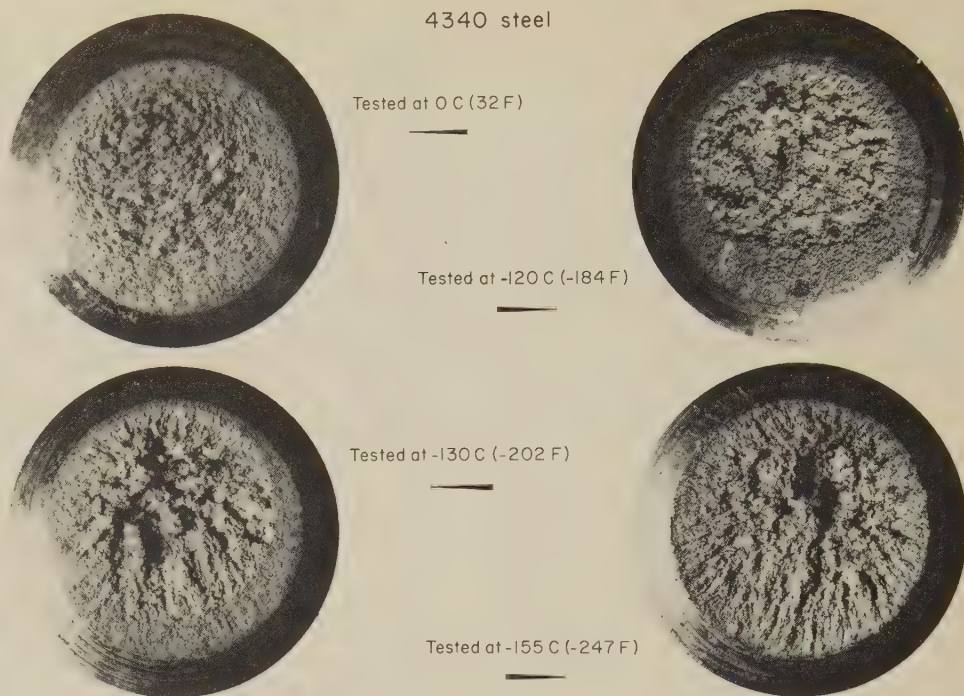
Velocity of crack propagation also displayed a transition. It was 1665 ft per second at -3°C ($+27^{\circ}\text{F}$), 1425 ft per second at 16°C (60°F), and about 440 ft per second at the higher temperatures.

Fig. 38. Transition of fracture appearance with changes in test temperature (Ref 9)

values were reached, and then unstable fracture occurred in an essentially ductile manner.

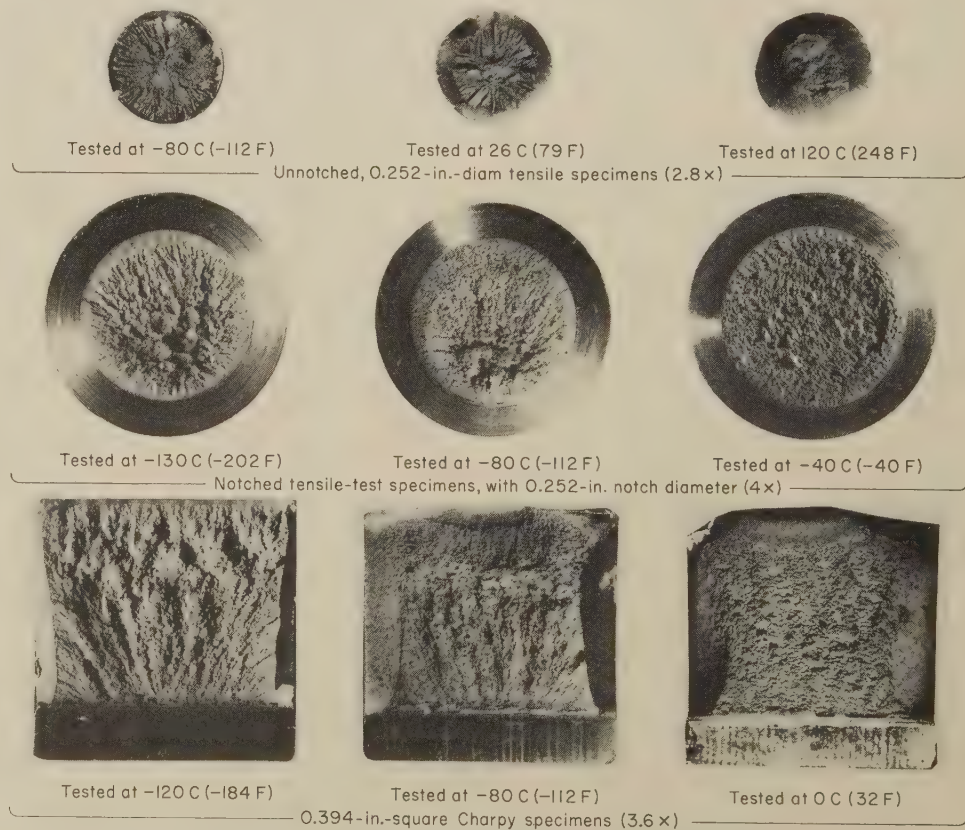
An example of the effect of temperature environment is provided in Fig. 38, which shows the surfaces of four fractures in carbon steel pipe (all from the same pipe length) obtained in tests at four different temperatures. The increase in test temperature caused an abrupt transition in fracture mechanism from a flat, high-velocity type with a chevron pattern at 16°C (60°F) and below, to full shear at 27°C (80°F) and higher.

Figure 39 presents another example of changes in fracture appearance caused by decreasing test temperatures, for sharply notched (root radius, 0.001 in.) tensile specimens. In this series, the circumferential fibrous ridges in the fracture at 0°C (32°F) were gradually replaced by a central zone (the last to fracture) of radial marks as the test temperature was lowered, until at -155°C (-247°F), the fracture was completely radial.



Specimens broke at the temperatures indicated. The radius at the root of the notch for each specimen was 0.001 in. Each of the fractures originated in the notch. The fracture at 0°C (32°F) is 100% fibrous with circumferential ridges. At -120°C (-184°F), the fibrous marks give way to an inner, circular zone of radial marks. At -130°C (-202°F), the radial zone is larger, and at -155°C (-247°F), a radial type of fracture has completely replaced the fibrous type.

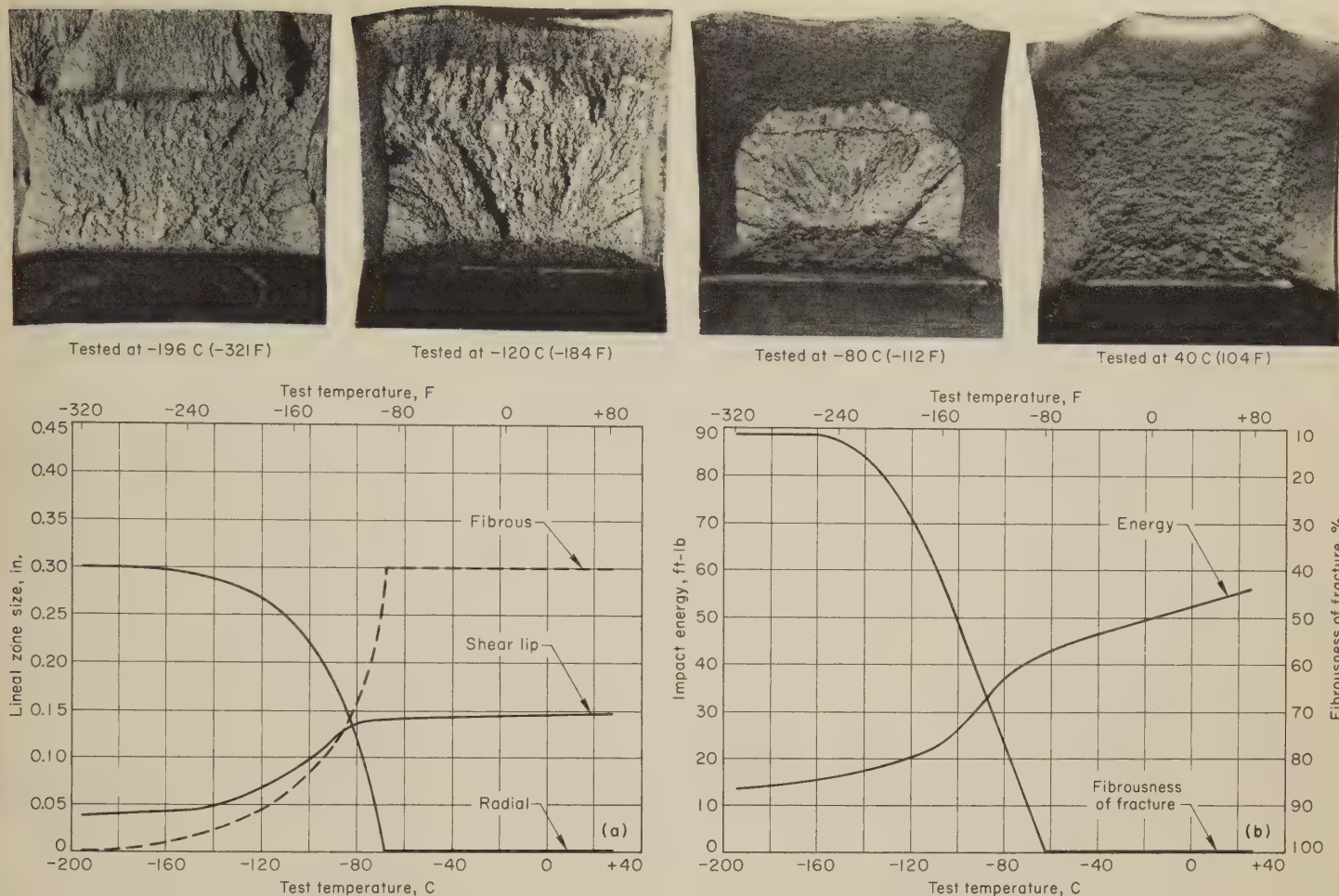
Fig. 39. Fracture appearance as affected by test temperature, for four notched tension-overload fractures in 4340 steel (light fractographs, all at about $9\frac{1}{4}\times$)



All specimens were cut from $\frac{1}{8}$ -in.-square 4340 steel bar stock, heat treated as follows: held 1 hr at 899°C (1650°F) and air cooled, held 1 hr at 843°C (1550°F) and oil quenched, then held 1 hr at 538°C (1000°F) and oil quenched. Specimens of all three

types show the same transition with increasing test temperature, from completely radial marks to mixed radial and fibrous marks to circumferential fibrous ridges. The only difference is in the temperature at which the transition is complete.

Fig. 40. Light fractographs showing effect of test temperature on fracture appearance, for three types of 4340 steel test specimens (Ref 10)



Light fractographs ($4.4\times$) at top show 0.394-in.-square Charpy impact specimens cut from $\frac{1}{16}$ -in.-square bar stock and heat treated as follows: held at 871 C (1600 F) and oil quenched, held $1\frac{1}{2}$ hr at 554 C (1030 F) and oil quenched, then held 3 hr at 299 C (570 F) and air cooled. Specimens were tested at 40 C (104 F), at -80 C (-112 F), at -120 C (-184 F), and at -196 C (-321 F).

Lineal measurements were made parallel to the notch for the shear-lip zones, perpendicular to the notch for the fibrous zone (from the fracture origin in

the notch to the initiation of radial marks), and perpendicular to the notch for the radial zone (from the termination of the fibrous zone to the shear lip). The measurements gave the three curves in graph (a).

The curve of percentage of fibrousness of fracture in graph (b) was constructed from visual estimates of the fibrous-plus-shear-lip zones. This curve, together with the impact-energy curve in graph (b), shows that the transition temperature for fracture appearance is essentially the same as for impact energy.

Fig. 41. Transition curves for fracture appearance and impact energy versus test temperature for 4340 steel (Ref 4)

This same behavior is reflected in Fig. 40 for three types of test specimens that were fractured at three selected temperatures. The change from the radial fractures obtained at the lowest temperature of each series to the circumferential fibrous ridges in the highest-temperature fracture in each series is clearly evident.

Figure 41 shows how such changes in fracture appearance may be utilized to obtain a transition curve of fracture features that relates to a corresponding transition curve for impact energy for the same material. The fractographs were obtained at temperatures of 40 C (104 F), -80 C (-112 F), -120 C (-184 F) and -196 C (-321 F). Measurements of the fibrous, radial, and shear-lip fracture zones provide essentially the same ductile-to-brittle transition temperature as do the Charpy impact-energy values.

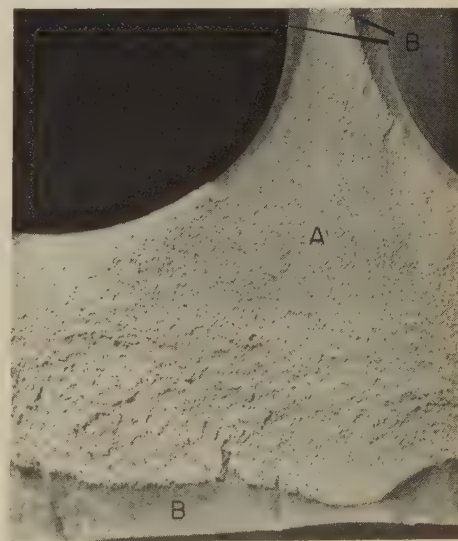
Fractographs 4961 to 4979, pages 422 to 425, show other examples of the effect of test temperature on fracture appearance.

Changes Caused by Different Stress States. Different fracture appearances result from differences in stress state. Often, a fracture has two distinct types of regions: (a) a flat region essentially nor-

mal to the primary stress direction, and (b) a region of inclined fracture (the shear-lip zone). The first region is the result of plane-strain fracture, the second of plane-stress fracture. These fracture regions are shown in Fig. 42.

Plane-strain fracture occurs in thick sections and in notched members. Plane-stress fracture occurs when the fracture intersects any unnotched free surface; its extent is governed by the plastic-deformation characteristics of the metal. Thin sheets of a ductile metal characteristically fracture completely in the plane-stress manner. This feature is related to the size of the plastic zone at the crack tip. Figure 43 is a schematic representation of the location of this plastic zone.

Another change in stress state that can affect fracture appearance is that provided by differences in stress concentration, such as caused by differences in the root radius of notched tensile specimens. Figure 44 shows this effect in two fractures in 4340 steel specimens obtained at -40 C (-40 F). The root radius shown in Fig. 44(a) was 0.1 in., and the fracture shows a central fibrous zone containing the origin, a radial zone surrounding this,



Light fractograph $1.1\times$
Flat region A is normal to the principal stress axis and was formed by plane-strain fracture. The shear lips, B, were the result of plane-stress fracture.

Fig. 42. Two distinctly different types of fracture regions in an aluminum alloy 7075-T6 forging

and an outer shear-lip zone. On the other hand, the notch in Fig. 44(b) had a root radius of 0.01 in., and the fracture shows an outer ring of fibrous circumferential ridges that began in the notch and a final central region of radial marks. There was no shear-lip zone.

Indeterminate Fractures

With a few metals, fractography provides little information for fracture analysis. For example, it is often difficult to determine the location of crack origins, the direction of crack propagation, and the mechanism of fracture in gray iron and magnesium alloys.

Test Fractures Versus Service Fractures

Caution should be used in depending on laboratory fractures to interpret service fractures. There is a strong inclination to simplify test conditions in the laboratory. Usually, a single static or cyclic load is applied and a relatively constant environment is maintained. As a result, beach marks are not formed. On the other hand, most components in service experience a wide variety of loads and a considerable day-to-day variation in environment. Often, these variations produce the features, such as beach marks, on the fracture surface that enable one to interpret the fracture. A lab-

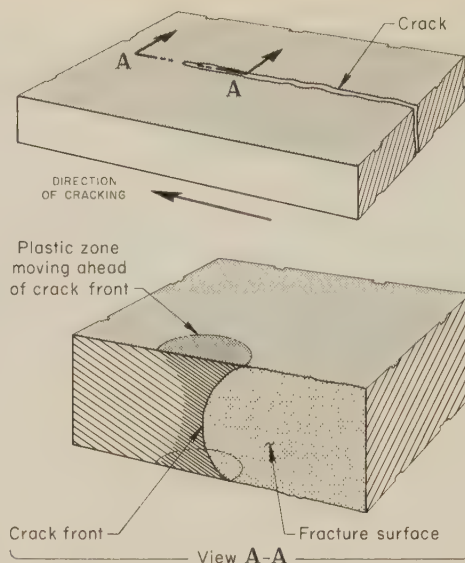


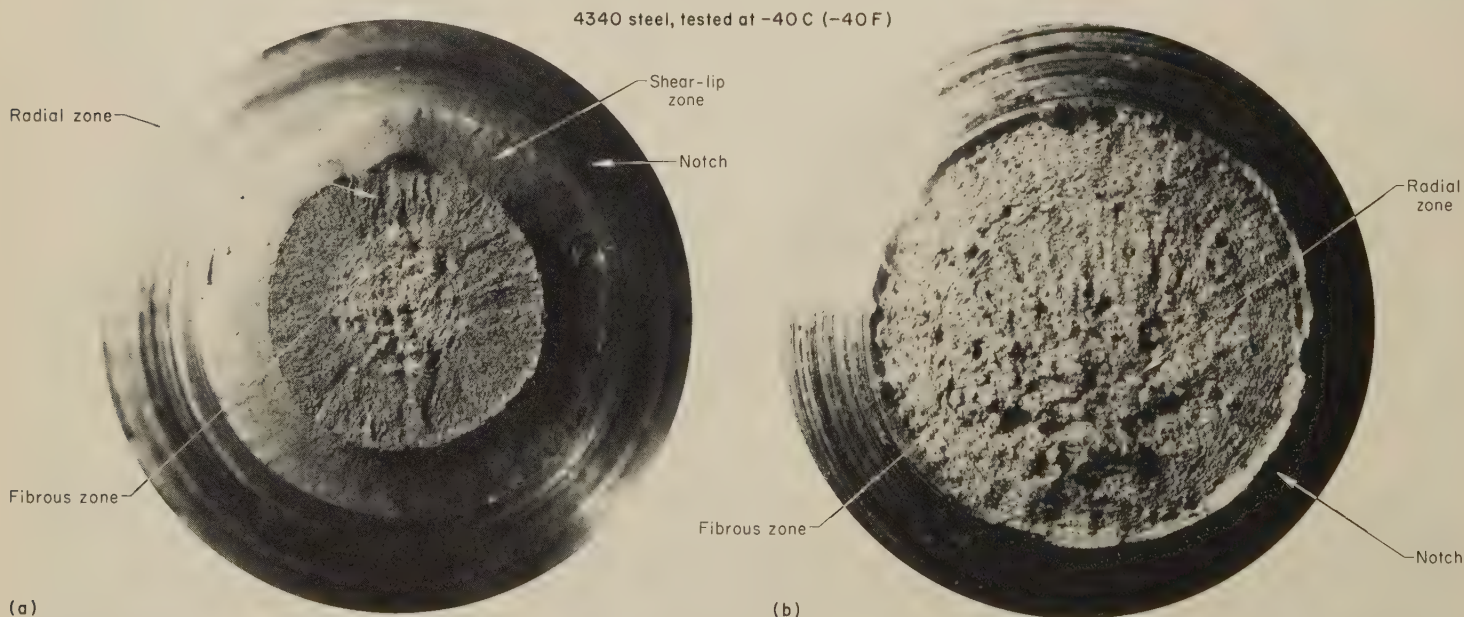
Fig. 43. Plastic zone at the crack tip of a thin sheet. Here, the fracture is usually completely in the plane-stress mode. (Derived from Ref 11)

oratory test that is intended to represent service conditions closely may actually produce a fracture with a surface that bears little resemblance to that of the service fracture. This result does not necessarily invalidate the test if it is properly designed as to loading procedures and levels, but it may result in the incor-

rect conclusion that the service fracture was from a different cause because the fracture surfaces do not look alike.

References

1. J. A. Kies, A. M. Sullivan and G. R. Irwin, Interpretation of Fracture Markings, *J Appl Phys*, Vol 21, No. 7, 1950, p 716-720
2. G. M. Boyd, The Propagation of Fracture in Mild Steel Plates, *Engineering*, Vol 175, Jan 16, 1953, p 65-69; Jan 23, 1953, p 100-102
3. C. F. Tipper, "The Brittle Fracture Story", Cambridge University Press, Cambridge, England, 1960
4. J. Nunes, F. L. Carr and F. R. Larson, Macrofractographic Techniques, in "Techniques of Metals Research", Vol 2, Part 1, R. F. Bunshah, Ed., Interscience-Wiley, New York, 1968, p 379-444
5. Charles Lipson, Why Machine Parts Fail, Part 5. Bending and Tensile Fractures, *Machine Design*, Vol 22, Sept 1950, p 147-150
6. G. Jacoby, Fractographic Methods in Fatigue Research, *Exptl Mech*, Vol 5, Mar 1965, p 65-82
7. G. Jacoby, "Application of Microfractography to the Study of Crack Propagation Under Fatigue Stresses", NATO-AGARD Rept 541, 1966, 187 pages
8. D. J. Wulpi, "How Components Fail", American Society for Metals, Metals Park, Ohio, 1966, 56 pages (see p 40)
9. A. R. Duffy, G. M. McClure, R. J. Eiber and W. A. Maxey, Fracture Design Practices for Pressure Piping, in "Symposium on Line Pipe Research", Catalog No. L 30000, American Gas Assn., Arlington, Va., 1966
10. F. L. Carr and F. R. Larson, Fracture Surface Topography and Toughness of AISI 4340 Steel, *ASTM J Mater*, Vol 4(4), 1969, p 865-867
11. H. W. Liu, discussion on Critical Appraisal of Fracture Mechanics, in "Symposium on Fracture Toughness Testing and Its Research Applications", STP 381, American Society for Testing and Materials, Philadelphia, 1965, p 23-29; also, "Qualitative Discussion on the Effects of Strain Within Plastic Enclave of Fracture Criterion", GALCIT, SM 63-32, Graduate Aeronautical Laboratories, California Institute of Technology, 1963



Light fractographs

Fractographs show notched 4340 steel specimens, with two different notch-root radii, tested in tension overload at -40°C (-40°F). Room-temperature tensile strength was 1151 MPa (167 ksi).

(a) Notch-root radius of 0.1 in. produced a normal tensile fracture having a central fibrous zone, a surrounding radial zone, and an outer shear-lip zone of

final, fast fracture. The notched tensile strength of this specimen was 1544 MPa (224 ksi). (b) Notch-root radius of 0.01 in. altered the stress state, caused the fracture to initiate in the notch, and produced an initial ring of fibrous circumferential ridges and a central radial zone. The notched tensile strength of this specimen was 1758 MPa (255 ksi).

Fig. 44. Change in fracture appearance effected by change of notch-root radius

The Scanning Electron Microscope and Its Application to Fractography

By the ASM Committee on Fractography by Electron Microscopy*

THE SCANNING electron microscope (SEM), although a relatively new instrument in the metallurgical laboratory, was derived from early work in the fields of electromagnetics, vacuum-tube electronics, and vacuum-pumping technology. Developmental steps include Stintzing's patent application of 1927 (Ref 1) and the work of Knoll (Ref 2), who in 1932 described an instrument that used cold cathode discharge as an electron source and that had two magnifying lenses but no condenser lens. Von Ardenne (Ref 3) built a microscope in 1938 that was used to make electron micrographs in the transmission mode. In 1942, a more practical scanning electron microscope (Ref 4) demonstrated a resolution of 500 Å. This instrument was hindered by (and finally abandoned because of) the lack of noise-free amplification of the video signal. In the 1950's, developmental work progressed rapidly and concurrently at Cambridge, England, under Oatley (Ref 5) and at Lyon, France, under Bernard and Davoine (Ref 6). By 1957, image quality was greatly improved at Cambridge by the introduction of the photomultiplier tube.

In the period from 1955 to 1959, the Cambridge instruments attained resolutions in the range of 200 to 600 Å, and at least one of these instruments was used in routine research (Ref 7, 8). In the early 1960's, Stewart developed the first successful commercial scanning electron microscope (Ref 9, 10). Important developmental work took place in the USSR under Spivak and Saparin (Ref 11) and in Japan under Kimoto (Ref 12) and Kimura (Ref 13). By 1965, commercial instruments were available with guaranteed resolutions of 250 Å. More recent improvements have been made by Crewe (Ref 14) at the University of Chicago. His instrument, which is not commercially available, has a resolution of 10 Å and uses a field-emission electron source. This instrument operates in the transmission mode, which limits its use to thin foils or replicas. Its value for replicas, however, is reduced by the lower resolution inherent in replicas as compared to the high resolution of the microscope.

Principal Features of Scanning Electron Microscopes

A scanning electron microscope (SEM) is a combination of electron-optical, vacuum, and electronic-control devices for impinging a beam of electrons on a pinpointed spot on the surface of a target specimen and collecting and displaying the signals given off from that target. The SEM was developed initially to obtain information about surface topography and was thought of as complementing the capabilities of the light microscope and the transmission electron microscope. However, the development of an assortment of related capabilities has converted the SEM into a tool that can be used for total material characterization.

The SEM is capable of magnifications from about 5 to 240,000 diameters, but its useful upper limit in fractography is perhaps 30,000 diameters. It has a

resolution limit of approximately 100 Å. The depth of field is about 300 times that of the light microscope. This corresponds to a useful depth of field of over 1000 microns at 100 diameters and of about 10 microns at 10,000 diameters. Specimens can be tilted as much as 45° in either direction and still be in focus. The working distance from the objective aperture to the specimen is typically 10 to 25 mm.

A typical arrangement of the components of a scanning electron microscope for use in fractography is shown in Fig. 1. An electron gun at the top of a column emits electrons from a heated filament and accelerates them in a constant stream down the column. The specimen being examined is near the lower end of the column. As the electrons speed toward the specimen, they pass through two or more electromagnetic lenses that focus the stream of electrons into the shape of a small beam so that the impact spot on the specimen is of minimum size.

The resolution of the SEM is determined mainly by the size of the spot (the smaller the spot, the higher the resolution), and the size of the spot is determined by the electron optics of the column, the size of the filament tip emitting the electrons, the electron-beam current, and the accelerating voltage in the column. For example, for every hundredfold increase in beam current, there is a tenfold increase in beam diameter, which will cause a corresponding increase in the spot diameter. Ovality of the spot impairs resolution and can be corrected by the "stigmator" control.

When the accelerating voltage is low (in the range of 2.5 to 10 kv), chromatic aberration of the incident beam is high, which results in extremely poor resolution unless contamination of the column can be avoided through a "self-cleaning" capability of the instrument. When the accelerating voltage is high (in the range of 30 to 50 kv), the size of the spot is increased by two factors: (a) the higher energy of the beam electrons causes them to penetrate into the specimen, which enlarges the zone of internal scattering that generates the backscattered electrons; and (b) a transverse

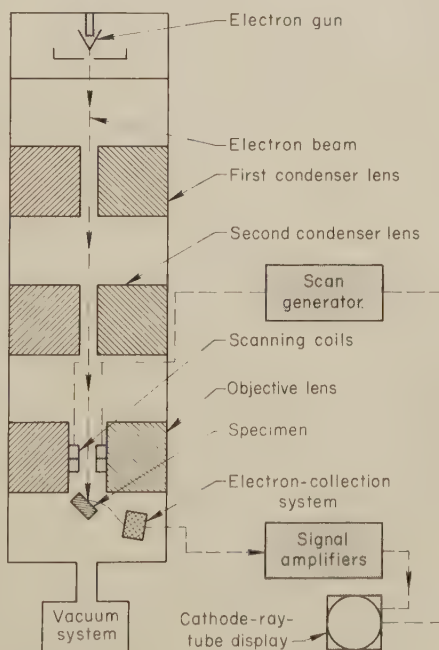


Fig. 1. Essential components of a scanning electron microscope (Ref 15)

*JOHN A. FELLOWS, *Chairman*, Consultant to American Society for Metals; CEDRIC D. BEACHEM, *Research Metallurgist*, Metallurgy Div., Naval Research Laboratory; E. PHILIP DAHLBERG, *Associate Research Coordinator*, Materials Science Laboratory, Universal Oil Products Co.; WILLIAM E. GARDNER, *Laboratory Director*, Technology of Materials.

WALTER L. JENSEN, *Research Group Engineer*, Metallurgy and Failure Analysis, Lockheed-Georgia Co.; OM JOHARI, *Manager*, Metal Physics Research, IIT Research Institute; DALE MEYN, *Physical Metallurgy Branch*, Metallurgy Div., Naval Research Laboratory; L. E. MURR, *Professor and*

Head, Department of Metallurgical and Materials Engineering, New Mexico Institute of Mining and Technology; GEORGE E. PELLISSIER, *Manager*, Mechanical and Materials Systems Dept., RRC International, Inc.

REGIS M. PELLOUX, *Associate Professor*, Department of Metallurgy and Materials Science, Massachusetts Institute of Technology; BENNETT V. WHITESON, *Project Materials and Process Engineer*, McDonnell Douglas Astronautics Co.-East; JAMES C. WILLIAMS, *Technology Staff*, North American Rockwell Aerospace Group, North American Rockwell International; EDWARD A. DURAND, *Secretary*, Senior Editor, Metals Handbook.

effect is contributed by the higher energy of the low-angle backscattered electrons that interact with protuberances of the rough fracture surface and generate secondary backscattered electrons that also constitute an enlargement of spot size. For optimum operation of the instrument, therefore, use of an accelerating voltage of 20 to 25 kv is desirable.

When the fracture surface is impacted by the focused stream of primary electrons, it emits several useful signals, such as backscattered electrons, secondary electrons, cathodoluminescence, x-rays, and transmitted electrons; a fraction of the incident beam of electrons is absorbed. The useful signals generated by the interactions of the incident beam with the specimen are illustrated in Fig. 2. From a fractographic standpoint, most interest is in the emitted secondary and reflected backscattered electrons.

The electrons emitted from the specimen move to a suitable detector or collector and subsequently generate a current, which is amplified and used to control the brightness of a spot on a cathode-ray tube. This spot represents the intensity of the signal emitted from the one spot on the specimen that is momentarily impacted by the incident electron beam. The display image is created by coupling a raster-scan generator to the scanning coils in the electron optical column and to the deflection plates of the cathode-ray tube for readout display. The fracture surface is scanned by the incident beam in a raster pattern, and the cathode-ray tube displays the same pattern on a larger scale. The brightness (contrast) of the spot-to-spot buildup of the display image is modulated by the signal strength of the electrons collected from the fracture surface at each instant. The signal can be electronically enhanced to improve the brightness and contrast of the image. The visual-display cathode-ray tube makes use of a long-persistence phosphor for retention of the image while it is being built up line by line.

Operation of Scanning Electron Microscopes

The two modes of scanning electron microscopy suitable for fractography, a few suggestions on the operation of scanning electron microscopes, and the method of determining magnification are discussed below.

Modes of Operation. Figure 2 shows the useful signals generated by the various interactions of the incident electron beam with the specimen, and the devices used to detect or collect the signals. Although both secondary and backscattered electrons are used for fractography, the secondary electrons are almost always the preferred signal because they offer better resolution, produce an abundant signal, and permit viewing of areas of the specimen that are not in a direct line of sight with the collector. There are occasions, however, where it is necessary to sacrifice resolution in order to improve image contrast, especially with smooth specimens and at low magnifications.

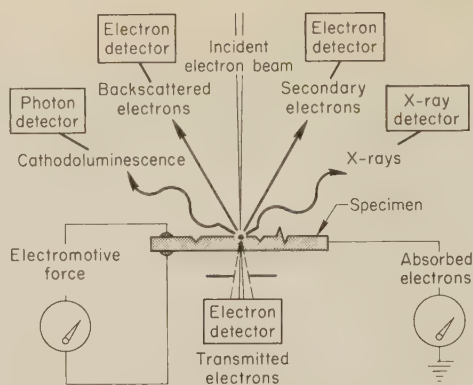


Fig. 2. Useful signals generated by an electron beam (Ref 16)

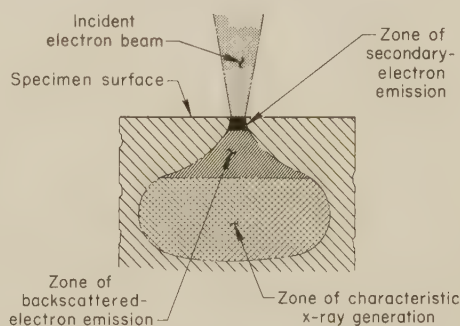


Fig. 3. Pattern of zones in a specimen that are sources of signals generated by an incident electron beam

This is accomplished by using the backscattered-electron mode of operation. Backscattered electrons possess high energy, travel at high velocity, and travel from the specimen to the detector in straight-line paths that produce shadow effects and, consequently, high image contrast. The backscattered-electron mode of operation is particularly useful for stereography.

A considerable loss of resolution is inherent in the backscattered-electron mode of operation. Backscattered electrons are electrons with high energy (equivalent to that provided by the accelerating voltage, which is usually in the range of 20 to 25 kv). The electrons escape from as deep as 300 Å in the specimen. Because of scatter within the specimen, the resultant source is much larger in diameter than the incident-beam diameter (see Fig. 3). On the other hand, the secondary electrons that are generated possess energies of about 20 ev, and not more than 50 ev, which is no more than is required for the electrons to escape from the top 100-Å layer of the specimen. A zone within 100 Å of the surface, then, constitutes the source of secondary electrons that can be captured by the electron collectors; the secondary electrons generated farther within the specimen do not have enough energy to escape. The difference in the volume of the source for the two types of electrons accounts for the difference in resolution obtainable.

The relative quantity of secondary electrons versus backscattered electrons captured by the electron collector is controlled by the use of a bias voltage ap-

plied to the collector. A typical secondary-electron collector is shown in Fig. 4. It consists of a Faraday cage (defined as a grounded metallic screen completely surrounding a space to protect that space from external electrostatic influences) with a large-mesh collector-screen front grid to which a bias potential of between +250 and -30 volts is applied. A positive voltage attracts the low-energy (low-velocity) secondary electrons but does not deflect the high-energy (high-velocity) backscattered electrons, which continue to move in straight lines from their points of emergence from the specimen surface. By adjusting the bias voltage upward, a greater proportion of secondary electrons is captured. If the bias voltage is made negative, the secondary electrons are repelled and the electrons captured will be essentially of the backscattered type. A minimum collection of backscattered electrons can be achieved by tilting the collector to an angle at which the straight-line path of such electrons will miss the aperture of the electrostatic lens inside.

In place of the usual provision for a grid bias voltage, sometimes the phosphor on the scintillator is coated with a thin-film conductor to which the bias is applied.

The electrons that pass through the collector-screen front grid are accelerated by the electrostatic lens to make impact on a disk of scintillating material with sufficient energy to produce light. The light pipe (or light guide) attached to the scintillator permits light-signal transmission without electrical noise to a photomultiplier, which produces the electric signal used to modulate the brightness of the cathode-ray tube. Although the secondary-electron collector may also be used for collecting backscattered electrons by removing or reversing the bias potential of the grid, it is frequently more effective to provide separate collectors so that each collector can be most favorably positioned.

Cathode-Ray Tubes. The final image is usually shown on one of two cathode-ray tubes, one for visual examination and the other for photographic reproduction. The first permits a rapid visual survey of the fracture and a choice of magnification for a specific area or feature, employing brief sweep time, few lines per picture, and a long-persistence phosphor. The recording cathode-ray tube can then be operated with a short-persistence phosphor, a large number of lines per picture, and a single sweep, to avoid blurring in the recorded image. This dual arrangement facilitates the effective use of the instrument.

Vacuum System. The electron optical column must be operated at a pressure below 10^{-4} torr for routine, trouble-free functioning of a scanning electron microscope. Higher pressures allow greater opportunity for oil vapor to flow back from the diffusion pump into the column, which results in decreased resolution and signal amplitude due to formation of a carbon polymer deposit on the specimen surface (oil molecules adsorbed on the surface break down under the impact of the electron beam). This problem can be minimized by using a "cold finger" close

to the specimen to condense the contaminants; this is discussed on page 56 in the section on Intensity and Contrast in the article "The Transmission Electron Microscope and Its Application to Fractography". (Contamination can also occur by handling the specimen, the stage, or other internal components of the column with bare hands.) A further reduction in operating pressure will improve SEM image quality; however, lower operating pressures increase delays, because each time a specimen is changed, the column must be pumped down to the lower pressure.

Specimen Stage. Ideally, the specimen stage is omnidirectional, which permits lateral, vertical, rotational and tilting movement of the specimen relative to the electron beam. This movement permits examination of all surfaces of the specimen except the one on which it rests—that is, five of the six sides of a cube. For maximum flexibility of movement, the specimen may be up to 25 mm in diameter and 25 mm thick. Usually, it is attached to a stage mounting stub with electrically conductive cement or a metal spring, to prevent buildup of a charge.

Magnification. Because the image is formed one small spot at a time in a regular geometric pattern, magnification is determined by the ratio of the size of the raster scan on the cathode-ray tube to that on the specimen; and because the size of the display cathode-ray tube is fixed, the magnification is selected by varying the size of the area of the specimen scanned by the electron beam. For example, if the display area of the cathode-ray tube is a square 100 mm on a side, and the area of the specimen scanned is a square 0.1 mm on a side, the magnification is 1000 diameters. High magnifications are easily obtainable, but magnifications below about 5 diameters are limited by the difficulty of maintaining linearity of the scan over the large deflection angles required to cover a relatively large area.

The ease with which the magnification can be changed rapidly is of special benefit; it permits the fractographer to observe and become oriented to fracture features at a low, familiar magnification before making a study of the same spot at a high magnification. Magnification corrections must be made if the working distance is changed and, depending on the instrument, may be required if the accelerating voltage is altered. Foreshortening occurs when the specimen is tilted.

Specimen Preparation

The main requirement of a specimen for examination by scanning electron microscopy is that it be of a size small enough to fit into the SEM chamber. This frequently requires sectioning of the fractured part. Alternatively, a thick single-stage or two-stage replica of the fracture can be prepared as described on pages 57 and 59 in the article on The Transmission Electron Microscope and Its Application to Fractography.

It is necessary that the specimen or replica for SEM viewing be electrically

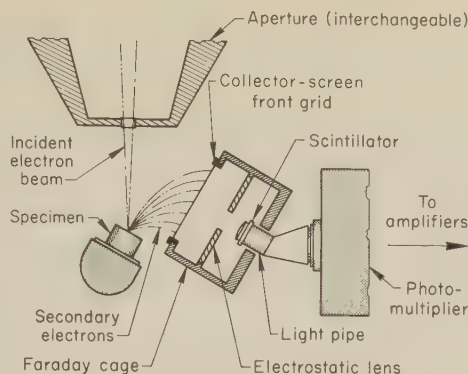


Fig. 4. A typical secondary-electron collector (Ref 17)

conductive to prevent electrical charging effects, which could distort the image. This is not a problem in fractographic study of a metal surface unless a layer of corrosion products is present. Often, it is advisable to clean metal surfaces that are not fresh fractures and to remove extraneous material and anything that would outgas in the vacuum. (See the article on Preparation and Preservation of Fracture Specimens, on pages 9 and 10.)

Residual magnetism is a difficulty with iron and nickel alloys, especially if the part has been subjected to a magnetic flux, as in magnetic-particle inspection. Defocusing of the beam and resultant loss of resolution will occur if the part or the specimen cut from the part is not demagnetized.

If a plastic replica is to be examined, a continuous electrically conductive coating of a noncorrodible metal (palladium, platinum or carbon-platinum) about 100 Å thick should be applied by vacuum deposition to the surface to be viewed. (Deposition by sputtering also is adequate, and is easier.) Alternative conductive coatings, which can be applied to phosphate coatings on steel and to oxide coatings, are the "antistatic" solutions (fatty acids in isopropyl alcohol). An electrically conductive coating also may be advisable on a metal surface having a nonconductive layer of corrosion products present after cleaning. Usually, a clean metal specimen requires only mounting and electrical grounding with a specimen holder.

Stereography

Because of its great depth of field, a scanning electron microscope produces a realistic, three-dimensional image and makes qualitative interpretation of fracture topography relatively easy. If it is desirable to increase the three-dimensional effect, stereo pairs of photographs may be taken of the same area on the specimen (this is discussed on page 23 in the article on Photography of Fractured Parts and Fracture Surfaces, in this volume) and the stereo pairs may be viewed simultaneously as a stereograph. Stereography can also be used to obtain height and depth measurements of fracture topography, which may be useful for determinations of volume or surface area (Ref 18). The analytical techniques employed for this purpose are similar to those used in aerial photography.

Two methods have been devised to produce stereoscopic effects for direct viewing. One method makes use of paired detectors that have different angular relationships with respect to the fracture surface. The two images received by the detectors can then be viewed individually and simultaneously.

The other method involves the use of special deflection coils that cause the beams striking the fracture surface to alternate between two angles. A multiplex system is used to separate the images as the electron beam rapidly "wobbles" while it scans the specimen.

Although stereoscopy permits quantitative calculations and aids in recognition of image artifacts caused by charging of the specimen, most fractographic purposes can be satisfied with a single photograph taken with the incident electron beam at an angle to the specimen surface. Tilting accentuates the shadow effect to take full advantage of the large available depth of field.

Unique Features

The scanning electron microscope permits direct examination of the fracture surface without need for preparation of thin films or surface replicas. It allows an initial assessment of the surface at relatively low magnification from an image that resembles the macroscopic appearance. This aids the interpretation of fracture features. The SEM also has the advantage of great depth of field.

A fundamental uniqueness of the scanning electron microscope lies in the method of image formation. Unlike the transmission electron microscope, there is no magnification or image formation in the column of the scanning electron microscope, the one function of the magnetic lenses being the production of an electron beam with as small a diameter as possible at the point of contact with the specimen. The information signal from the SEM is, therefore, a scalar quantity, actually a count of the photons or electrons leaving the spot on the specimen that is being impacted by the electron beam. This one-dimensional signal is easily processed electronically and permits a complete separation between the electron beam striking the specimen and the information signal.

Attachments, Accessories and Auxiliary Equipment

Anyone considering the purchase of a scanning electron microscope for fractographic analysis should be aware of the numerous attachments available for enhancing its utility. With proper detecting and analyzing equipment, the SEM can be used to perform analytical functions that otherwise would require several separate instruments.

Spectrometers. Probably the most useful accessories to date are the various spectrometer attachments that can be added to give microanalytical capabilities. These fall into two main categories: dispersive and nondispersive. Dispersive

spectrometers utilize wave-length dispersive x-ray optics. A diffracting spectrometer with an analyzing crystal or pseudo-crystal is ordinarily used. This type of spectrometer, with the necessary interchangeable apertures and suitable detectors, constitutes an instrument very similar to a conventional electron-beam x-ray microprobe analyzer. The degree of sophistication is limited largely by the laboratory budget.

Nondispersive (now generally known as energy-dispersive) spectrometers are widely used with the SEM. Applicability is found in fractographic studies in the identification of precipitates and corrosion products. These spectrometers are essentially doped, single-crystal silicon detectors that are responsive to the energy levels of the various x-ray wave lengths. The detector is coupled to a multichannel analyzer for identification of the energy levels. For most detectors, all elements having atomic numbers down to that of sodium (atomic No. 11) can be analyzed in concentrations as low as approximately 0.1%, and all elements can be analyzed simultaneously. With the best instruments, lower concentrations (1 ppm for some elements) and elements with atomic numbers down to that of oxygen (atomic No. 8), can be detected. The signals obtained can be processed and integrated easily. With more advanced systems or the availability of a computer, it is possible to obtain quantitative, as well as qualitative, analysis. The inability to detect elements with a low atomic number and the requirement of cooling the detector with liquid nitrogen are minor disadvantages of the energy-dispersive systems.

The Auger electron spectrometer has been used recently to analyze fracture surfaces. Of primary interest has been the detection of embrittling elements, such as antimony, arsenic and bismuth, on exposed grain-boundary facets of fractures. The size of the area examined varies greatly with test conditions; it is larger than for the electron microprobe analyzer and may range between 1 and 50 microns in diameter. The Auger electron spectrometer is sensitive to only the first few surface layers. At present, it can provide only semiquantitative information, but this is adequate for most studies.

Auger electrons, emitted under electron bombardment at moderate voltage, may be detected as peaks in the energy spectra of the secondary electrons generated. Such peaks signify the presence in the impacted surface of chemical elements that are associated with the observed peak energies. Elements with atomic numbers down to that of lithium (No. 3) can be detected. For most of the elements below calcium (atomic No. 20), the sensitivity is very high. Sulfur, for example, can be detected at a concentration as low as 0.1 ppm on a nickel surface. The main difficulties with the Auger spectrometer are the need for an ultrahigh vacuum (greater than 10^{-8} torr) and the spurious results that may arise from haphazard surface contamination. The capabilities of the Auger electron spectrometer are discussed further in Ref 19.

The ion-scattering spectrometer has been used to a limited extent for fracture-surface analysis. This instrument analyzes the elements in only the atomic layers closest to the surface and thus is particularly sensitive for studies of embrittling elements (arsenic, antimony and bismuth) in grain-boundary films on intergranular fracture surfaces. The region examined (a fixed spot, not a scan) can have a diameter as small as a few microns or as large as several millimeters. The instrument will detect all elements with atomic numbers above that of the ionizing gas employed (argon is frequently used). For further information on the ion-scattering spectrometer, see Ref 20.

Microprobe Analyzers. The electron microprobe analyzer has been widely used for determining the chemical composition of constituents on the surface of a specimen. This instrument is capable of chemically analyzing areas on a surface that are as small as 1 micron in diameter. Although the rather rough surfaces of fractures generally limit the quantitative accuracy of the information that can be obtained from an electron microprobe analyzer, in many instances qualitative or semiquantitative information may be all that is required. The lower limit of concentration that the analyzer can detect is approximately 0.1%. Examples of the use of an electron microprobe analyzer include: (a) identification of nonmetallic inclusions that may be present at the origin of a crack; (b) analysis of the inclusions initiating microvoids in ductile dimpled fractures; and (c) analysis of corrosion or oxidation films. For more information on electron microprobe analyzers, see Ref 21.

The ion microprobe analyzer is a relatively new analytic tool. Like the electron microprobe analyzer, it can provide information on the elements present in rather small, selected spots (a few microns in diameter) on a fracture surface. It has the advantage of being able to detect all elements, including those of low atomic number and those in concentrations as low as about 100 ppm. For more information on this instrument, see Ref 22.

Special Stages. Of particular interest to the field of fracture micromechanics is the availability and use of tensile stages, hot stages, and cold stages. The larger scanning electron microscopes have adequate space for these accessories. The tensile stage used in conjunction with the visual cathode-ray tube enables the observation and recording of a tensile fracture as it happens, provided the motion to be observed is slow. Rapid motion can be clearly observed only with a TV scan-rate image, which is achieved on many instruments only with a special attachment. Hot stages that operate at temperatures as high as about 1000 C (1832 F) and cold stages that operate at temperatures as low as liquid-nitrogen temperature (-196 C, or -321 F) are available commercially. Combinations of hot or cold stages with tensile-testing capabilities are always special modifications.

Transmission Attachment. A commercially available accessory for most scanning electron microscopes is the trans-

mission accessory. This usually consists of a modified specimen stage to permit transmission of the electrons through it and an electron-collection system mounted below the specimen. This attachment can be used only for replicas or for thin specimens, but the thickness limitation is not so severe as for traditional transmission-electron-microscopy methods. Thin specimens up to 0.5 micron thick can be examined. As with reflected scanning-electron-microscope images, contrast and brightness can be enhanced electronically. Through the proper selection of aperture, both dark-field and bright-field images can be obtained. In some systems, selection of the dark-field or bright-field image is made by the addition of a deflection coil and an aperture between the specimen and the electron collector. Experimental scanning transmission electron microscopes have been developed that have resolutions better than 20 Å.

Cathodoluminescence. The addition of a suitable photon detector will permit imaging of cathodoluminescence. Some compounds (many of which contain oxygen) emit light when bombarded by an electron beam. The signal can be used to modulate the electron beam in the cathode-ray-tube displays to obtain an image. By use of proper filters, differentiation can be made among infrared, visible and ultraviolet wave lengths. Oxides and inclusions on fracture surfaces have been detected by this means.

Solid-Pair Detector Attachment. A solid-pair detector attachment is an accessory that makes it possible to record separately, in a single scan, the qualitative pattern of changes in distribution of chemical elements present in a fracture surface, and the topography of the surface contours in the same fracture region. This is possible because a backscattered-electron signal is affected by the type of chemical element present in the fracture surface at the point where the signal is generated. The effect is proportional to the atomic number of the element present—the number of backscattered electrons emitted is high when the element hit by the primary electron beam has a high atomic number. Because of this characteristic, the contrast achieved on the cathode-ray tube is a function of the chemical-element variations across the region scanned, as well as a function of the surface contours.

To achieve separate registry of these effects, two detectors are mounted in the scanning electron microscope in symmetrically opposed positions above the specimen (see Fig. 5a). The backscattered-electron signals, received simultaneously by these two detectors from the points on the fracture surface being scanned by the incident electron beam, are equivalent in terms of response to the atomic numbers of the chemical elements present, but are complementary in terms of the surface contours. This second effect occurs because the two detectors "see" the surface from different angles and one side of a hill will direct a high-intensity signal to detector A and a low-intensity signal to detector B. Conversely, when the incident

beam reaches the other side of the hill, the signal to detector A will be low in intensity and that to detector B will be high (see Fig. 5b).

The signal received by each detector is transmitted to a separate operational amplifier and then fed to a computer handling both circuits, usually an analog computer. These inputs are added for viewing on one indicator and are subtracted for viewing on another indicator. Addition of the signals magnifies the effect of the atomic numbers of elements present but cancels out the effect of topography, as suggested in $A+B$ in Fig. 5(b). Subtraction of the signals fed to the other indicator cancels out the effect of atomic number but magnifies the effect of topography, as shown in $A-B$ in Fig. 5(b). The best results are obtained when (a) the atomic-number differences in the composition are great, (b) segregation of elements exists, and (c) the fracture surface is quite rough.

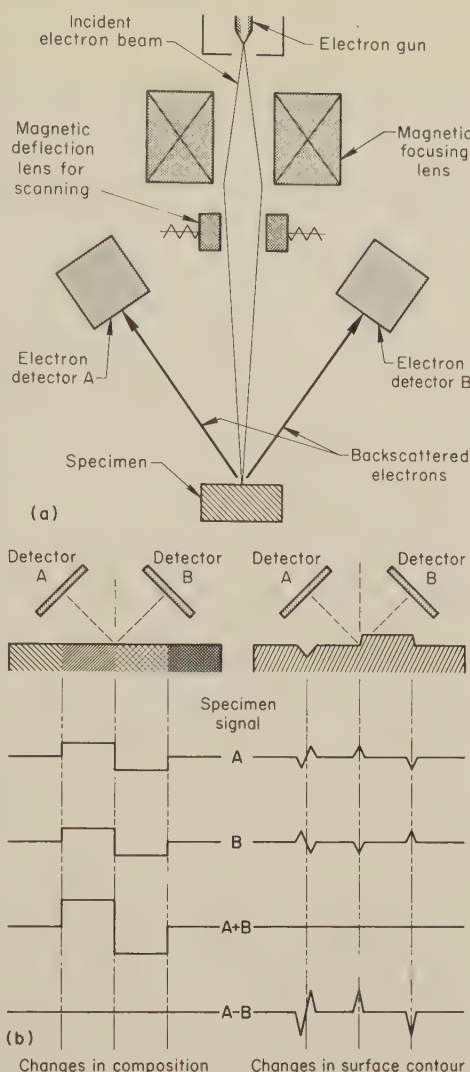
Production and Viewing of SEM Fractographs

Following the initial visual inspection (by the unaided eye, or with a hand lens or a low-power stereomicroscope) that is the first step in studying of any fracture, preliminary viewing of the fracture surface with a scanning electron microscope may then be undertaken using the range of lower magnifications available (that is, from 5 to perhaps 50 diameters). In this perusal with the SEM one should appraise the probable mechanism of fracture and identify regions of the fracture surface for later reproduction as fractographs at appropriate magnifications.

For each fractograph, the crack depth, the over-all direction of crack propagation, and the over-all shape of the crack front should be determined; then, if the stress-intensity factor is known from a fracture-mechanics test, the size of the plastic zone that existed at the crack tip can be estimated. In all fractographs, whether they are of a cleavage fracture or of a ductile fracture, the size of the features observed should be related to the dimension of the plastic zone to which they were associated during fracture.

Measurement of shear-lip widths (which are related to K_{max}) and identification of over-all crack-front shapes can be done by making a detailed montage of low-magnification SEM fractographs.

To simplify identification in the fractograph of crack-propagation direction, it is usually convenient to orient a specimen so that propagation is from the lower part to the upper part of the photograph and to view the fracture at an angle of 30° to



The detectors are symmetrically placed as shown in (a) for the determination of topographic features and chemical elements in the specimen surface. The backscattered-electron signals are added and subtracted, as shown schematically in (b), for individual viewing of the changes in composition and changes in surface contour.

Fig. 5. Detector arrangement and signal representation for a solid-pair detector

45°. It is more important to maintain the over-all direction of crack propagation along the short dimension of the photograph than to maintain a constant tilt angle. Very often, to get better contrast of a given region on a rough fracture surface, the tilt angle may have to be as much as 60°. Finally, it is important that an SEM fractograph be viewed right side up; if the effect of shadowing is inverted, features can be quite misleading and the fracture may thereby be completely misunderstood. The greatest change in ap-

pearance is for dimples. When an SEM fractograph is inverted, dimples look like projections rather than depressions.

References

1. H. Stintzing, "Method and Device for Automatically Assessing, Measuring and Counting Particles of Any Type, Shape and Size", German Patent No. 485,155; date of application, 13 May 1927; granted, Oct 1929
2. M. Knoll and E. Ruska, *Z Physik*, Vol 78, 1932, p 318-339
3. M. Von Ardenne, The Scanning Electron Microscope—Theoretical Fundamentals, *Z Physik*, Vol 109, 1938, p 553-572; *Z Tech Physik*, Vol 19, 1938, p 407
4. V. K. Zworykin, J. Hillier and R. L. Snyder, A Scanning Electron Microscope, *ASTM Bull*, Aug 1942, p 15-23
5. C. W. Oatley, The Scanning Electron Microscope, *New Scientist (England)*, 12 June 1958, p 153-155
6. R. Bernard and F. Davoine, The Scanning Electron Microscope, *Ann Univ Lyon*, Third Series, Sciences, Section B, Vol 10, 1957, p 78-86
7. K. C. A. Smith and C. W. Oatley, The Scanning Electron Microscope and Its Fields of Application, *Brit J Appl Phys*, Vol 6, Nov 1955, p 391
8. K. C. A. Smith, Scanning Electron Microscopy in Pulp and Paper Research, *Pulp Paper Mag Can*, *Tech Sect*, Vol 60, Dec 1959, p 3-9
9. A. D. G. Stewart, Investigation of the Topography of Ion Bombarded Surfaces with a Scanning Electron Microscope, in "Electron Microscopy", Vol 1, Sydney S. Breeze, Jr. (Ed.), Academic Press, New York and London, 1962, p D-12
10. "Scanning Electron Microscope", The Cambridge Instrument Co., 1965
11. G. V. Spivak, G. V. Saparin and N. A. Pereverzev, Potential Distribution in a p-n Junction as Observed by Electron-Optical Scanning, *Bull Acad Sci USSR, Phys Ser (USA)*, Vol 26, 1962, p 1362-1365 (translated from *Izv Akad Nauk SSSR, Ser Fiz*, Vol 26, 1962, p 1339-1342)
12. S. Kimoto, H. Hashimoto and M. Sato, On a Scanning Electron Microscope, in "Electron Microscopy 1966", Vol 1, Ryozi Uyeda (Ed.), Maruzen Co., Ltd., Tokyo, 1966, p 197-198
13. H. Kimura, H. Higuchi, H. Tamura and M. Maki, New Scanning Electron Microscope and Its Application, in "Electron Microscopy 1966", Vol 1, Ryozi Uyeda (Ed.), Maruzen Co., Ltd., Tokyo, 1966, p 195-196
14. A. V. Crewe, High Resolution Scanning Electron Microscopy, in "Scanning Electron Microscopy/1969", IIT Research Institute, Chicago, 1969, p 11
15. Victor A. Phillips, "Modern Metallographic Techniques and Their Applications", Wiley-Interscience, New York, 1971, p 425
16. S. Kimoto and H. Hashimoto, On the Contrast and Resolution of the Scanning Electron Microscope, in "Scanning Electron Microscopy/1968", IIT Research Institute, Chicago, 1968, p 65
17. E. W. White, H. A. McKinstry and G. G. Johnson, Jr., Computer Processing of SEM Images, in "Scanning Electron Microscopy/1968", IIT Research Institute, Chicago, 1968, p 95-103
18. G. S. Lane, Dimensional Measurements, in "The Use of the Scanning Electron Microscope", Pergamon Press, New York, 1972, Ch 11, p 219
19. W. C. Johnson, D. F. Stein and A. Joshi, Auger Electron Spectroscopy—A Review, *Can J Spectry*, Vol 17, No. 2, May 1972, p 88-92
20. R. S. Carbonara, Ion Scattering Spectroscopy for Microstructural Analysis, in "Microstructural Analysis Tools and Techniques", J. L. McCall and W. M. Mueller (Editors), Plenum Press, New York, 1973, p 315-329
21. D. R. Beaman and J. A. Isasi, "Electron Beam Microanalysis", ASTM STP 506, American Society for Testing and Materials, Philadelphia, 1972, 80 pages
22. H. Liebl, Ion Microprobe Analyzers, *Anal Chem*, Vol 46, No. 1, 1974, p 22A-30A

The Transmission Electron Microscope and Its Application to Fractography

*By the ASM Committee on Fractography by Electron Microscopy**

THE APPLICATION of transmission electron microscopes (TEM) to the study of fracture surfaces and related phenomena made it possible to obtain magnifications and depths of field much greater than those obtainable with light microscopes. This article considers the transmission electron microscope and its operation, and the replication of fracture surfaces. The advantages and limitations of the TEM for fractography, and the interpretation of TEM fractographs are discussed in subsequent articles.

The Transmission Electron Microscope

The beginnings of the transmission electron microscope can be traced to developments in electron optics during the early 1930's (see Ref 1-3). The original prototype electron microscope was constructed by Ruska in about 1934; it had a resolving power exceeding that of ordinary light microscopes and employed a magnetic lens. The first practical electron microscope was described by von Borries and Ruska (Ref 4) in 1939, and a similar microscope was described by Prebus and Hillier (Ref 5) in the same year. The microscope designed by von Borries and Ruska was the prototype of the Siemens microscope, and the one designed by Prebus and Hillier, after modification to include stable power supplies designed by Vance (Ref 6), became the prototype of the RCA microscope. Within five years, commercial instruments were being produced by several manufacturers. By 1950, electron microscopes with routinely attainable resolving powers of 20 to 10 Å were generally available.

The first application of the electron microscope to fractography was cited in a discussion prepared by Barrett and Derge and appended to a 1943 paper (Ref 7). A photograph of a polystyrene-silica replica of a cleavage surface of 4.96% Si ferrite was shown at a magnification of 8000 diameters.

Microscope Design. The components of the transmission electron microscope are represented schematically in Fig. 1 and are compared there with counterparts in the light microscope. The TEM has some features that are similar to those of the scanning electron microscope (SEM), but the principle of operation is different. The SEM concentrates the electrons to as dense and small a beam as possible; magnification of the image is performed by the relative raster scans of the specimen

and the cathode-ray tube. The TEM, on the other hand, obtains magnification with the magnetic lenses below the specimen in the evacuated column; then, the transmitted signal impinges directly on either a fluorescent screen or a photographic emulsion.

Basically, the TEM consists of an electron source (gun) that ejects a stream of electrons from a heated filament into a chamber evacuated to a pressure of 10^{-4} torr or less. The filament is held at a high accelerating potential relative to a grounded anode beneath it. The stream of electrons passes through a central hole in the anode and then through a condenser consisting of one or two magnetic lenses, which focus the beam on the specimen. The electrons that are not absorbed or reflected pass through three magnetic lenses, forming in succession three images, each magnified in turn to yield the intended over-all magnification, which may be as low as 210 diameters to as high as 300,000 diameters. In fractography, however, the useful upper limit is perhaps 30,000 diameters.

The accelerating voltage is most commonly in the range of 20 to 120 kv, although microscopes of some designs are available that use 200 to 1000 kv. In fractographic studies of replicas, the potential that is preferred is about 40 kv, and it rarely exceeds 50 kv.

Lens System. The magnetic lenses of the TEM consist of magnetic coils with iron pole pieces. The magnification possibility of a single lens depends on the magnitude of the current passing through the coil. The lens aperture is much smaller than that of the glass lenses used in light microscopes. A typical aperture diameter for a magnetic lens of 2500-micron (0.1-in.) focal length might be 50 microns, giving a half-aperture angle of about 0.01 radian, in contrast with a half-aperture angle of about 1.05 radians (60°) for a good glass objective lens.

The low efficiency of this small half-aperture angle is offset to some degree by the larger depth of field of the magnetic lens (about 2 microns) and its great depth of focus, which for practical purposes is limited only by the vertical dimensions of the TEM chamber.

The condenser lens, or lenses, make it possible to focus on the specimen a reduced image of the electron source, which can be adjusted to a spot as small as 2 microns in diameter. This provides good illumination of an adequate area (at 5000 \times , the final image of the spot would be 1 cm across) and decreases the contamination of the specimen surface caused by breakdown of adsorbed mole-

cules of diffusion-pump oil to carbon polymer as a result of electron bombardment (see the subsequent discussion under "Intensity and Contrast", beginning on the next page in this article).

The objective lens (below the specimen) maintains the magnification at a fixed value, determined in part by the focal length of the lens and by the position of the specimen; the final (projector) lens usually provides a series of magnification steps, and the intermediate lens provides an adjustment of magnification to the desired intermediate level (by altering the current).

Specimens for transmission electron microscopy must have the following characteristics: (a) they must be reasonably transparent to electrons; (b) they must have sufficient local variations of thickness or density, or both, to provide adequate contrast in the image; and (c) they must be small enough to fit within the specimen-holder chamber of the TEM. Transparency to electrons is provided by plastic or carbon replicas of the fracture surface. Usually, fractures are too rough to permit electrolytic thinning. Replica preparation is described in the sections that begin on page 56.

The replica is usually positioned by a stage that permits motion in two directions, perpendicular to each other and to the electron beam. A tilting stage is also desirable for fractographic work. It allows angles of tilt up to at least 10° from the horizontal, either about two perpendicular axes or perhaps about one axis but with full rotation. Tilting enables the preparation of stereo-pair photographs, and it allows alterations in contrast by, in effect, changing the local thickness of the replica in the path of the transmitted electron beam.

The image of the replica is first examined visually on the fluorescent screen, and the region with the best examples of surface features of interest is selected. Then, the best magnification and the best contrast for this region are determined. The fluorescent screen is lifted out of the way and the image is recorded on a photographic plate or film previously introduced through an airlock.

Image Quality. The quality of the image is affected by magnification, image intensity, image contrast, the resolution obtainable, and the degree of purity maintained on the specimen surface during the observation. The choice of magnification depends on the size and characteristics of the surface features to be examined. If resolution of very small details is desired, high magnification is essential. Magnifications can be easily calibrated

*See page 49 for committee list.

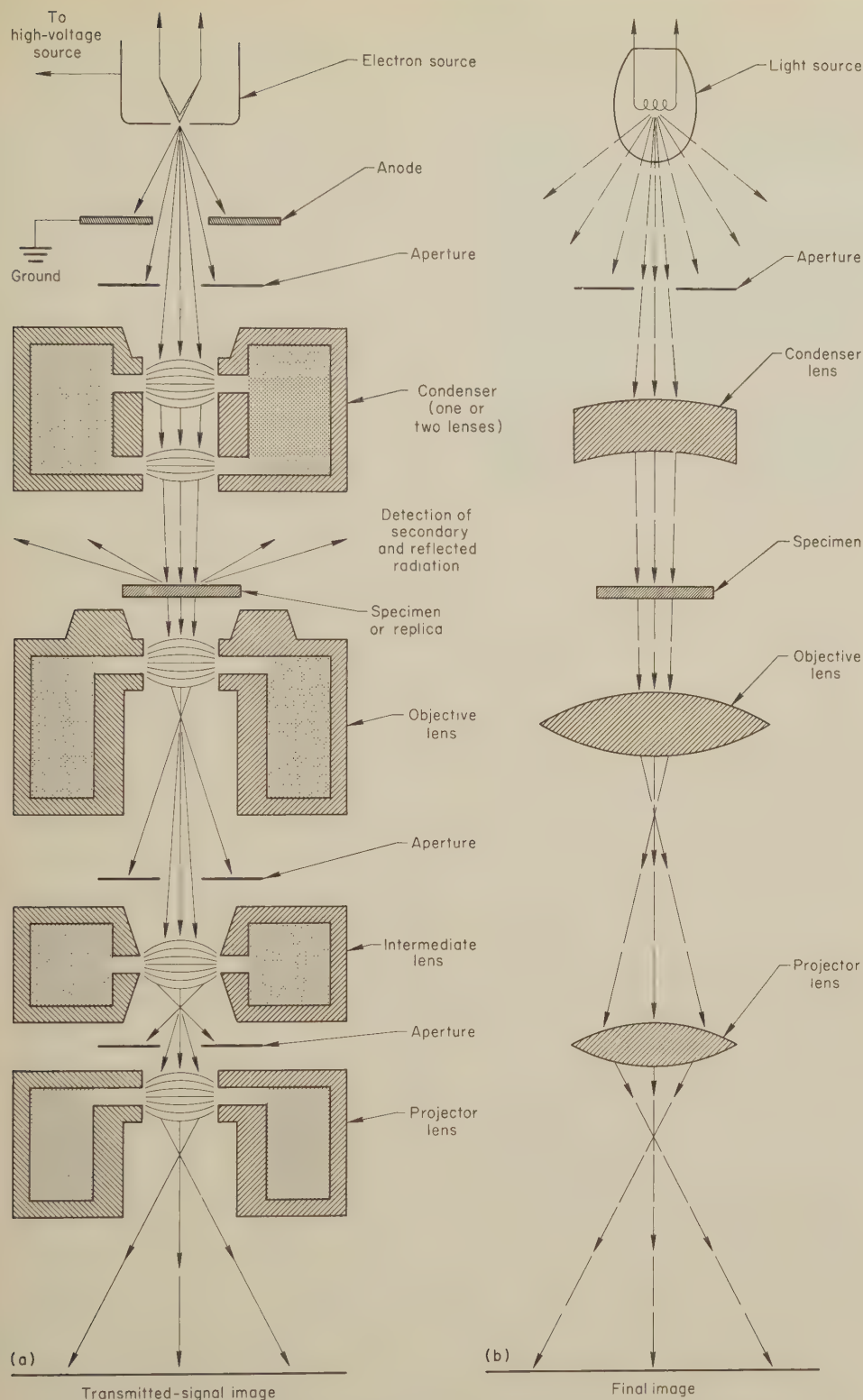


Fig. 1. Schematic representation comparing basic components of (a) a transmission electron microscope (TEM) and (b) a light microscope

using replicas with standard grids. These are available from companies dealing in electron-microscope supplies. The replica grids are made to a known number of grid lines per unit length (75 to 200), and therefore it is possible to determine the linear image magnification of a test photograph. If the amperage of the electrical current through the coils of the intermediate (or other reference) lens is

recorded for the photograph, a graph such as that of Fig. 2 can be prepared, relating magnification measured from the replica grid to current setting for the lens over an acceptable range. The curve that results will, of course, be applicable only to the specific instrument on which the calibration was made and only for the specific accelerating voltage that was used during calibration.

Intensity and Contrast. The intensity of the image increases in direct proportion to the accelerating potential, varies inversely with the atomic number of the elements in a thin-foil specimen, and is inversely affected by specimen or replica thickness. The intensity is also altered by tilting the specimen or replica, which introduces an effective change in thickness in the direction of electron-beam travel.

The image contrast can usually be improved by using a smaller objective-lens aperture. Theoretically, this impairs resolution. However, reduction of aperture diameter to as little as 40% of the usual diameter introduces no significant loss in resolution for magnifications up to 20,000 \times . In other respects, contrast improves with greater differences in the effective thickness of the replica (thickness parallel to the beam direction). Lower accelerating voltage also results in improved contrast. For example, a voltage of 100 kv gives a flat picture, but reducing the voltage to 40 kv results in good contrast. Shadowing the replica by vapor deposition of chromium, platinum, palladium or gold-palladium, as described on pages 59 and 60 in this article, will further enhance the contrast.

Resolution of lines or points that are extremely close together can be attained by the use of high magnification. The separations are then made large enough

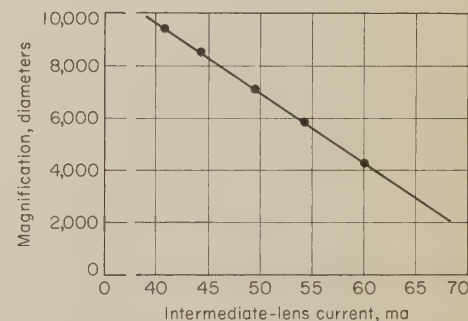


Fig. 2. Typical magnification-calibration curve for a transmission electron microscope. Magnification is measured from a replica grid and is plotted against the current settings of the intermediate lens.

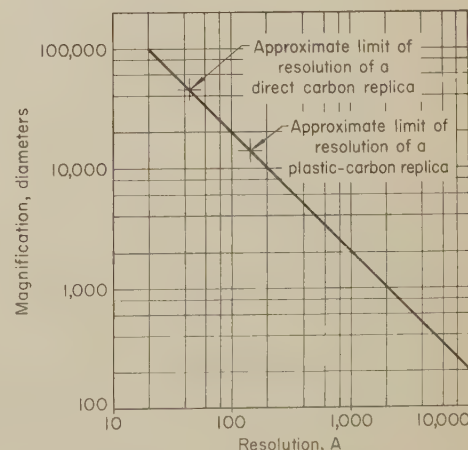
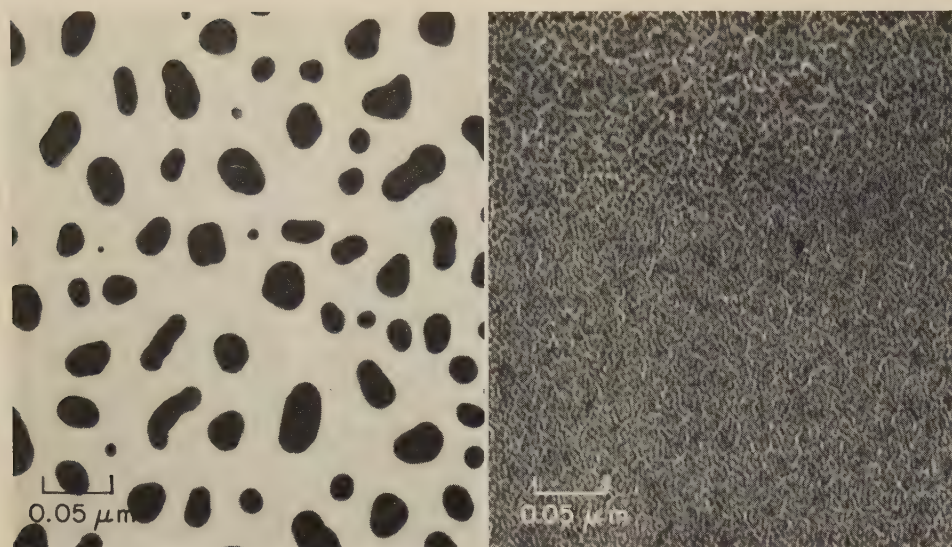


Fig. 3. Relation between resolution and the magnification required for the eye to perceive this resolution



TEM micrograph (carbon replica) 180,000× TEM micrograph (carbon replica) 190,000×
 Fig. 4. Comparison of aggregate size in vapor-deposited coatings of gold (micrograph at left) and palladium (micrograph at right). Mean thickness of coatings was 30 Å.

so that the eye can distinguish the two separate features that exist.

Figure 3 shows the relationship between resolution (the ability to distinguish between two finitely separated features) and the magnification necessary for the eye, which has a resolution of about 0.2 mm (2×10^6 Å), to utilize this resolution. Resolution is proportional to the electron wave length; detection of the smallest possible separation is achieved at very short wave lengths. Because the electron wave length is inversely proportional to the accelerating voltage, the resolution should be best at maximum operating voltage. Resolution also depends on the objective-lens aperture; larger openings permit better resolution.

A further consideration in obtaining optimum resolution is the metal used for shadowing the replica. The vapor-deposited metal should have the smallest possible size of atomic aggregates. Figure 4 shows the advantage in this respect of palladium vapor deposits over gold vapor deposits at magnifications much higher than those useful for fractography.

The sharpness, or clarity, of the image also depends to a large extent on the degree of purity maintained on the specimen surface while under electron bombardment. Molecules of hydrocarbons, emitted by vacuum greases and diffusion-pump oils, are present in most electron microscopes. These molecules are adsorbed on the specimen surface and are broken down by the electron beam, to produce a carbon polymer deposit. The layer of deposit obscures detail and causes loss of contrast and resolution. This problem is minimized by use of as low a beam intensity as possible to decrease the amount of heating and the size of the area subject to contamination, and by the use of a "cold finger" filled with liquid nitrogen and positioned close to the specimen. The cold surface of the finger condenses the contaminants, reducing their buildup on the specimen by up to 95%. If the chamber is opened very often, there can be a problem of frost forming on the finger.

A final consideration is the interplay between resolution and depth of field. The depth of field is related to the ratio between the limit of resolution desired and the half-aperture angle at the specimen. An increase in aperture ideally offers improved resolution, but the use of a large aperture when magnification is very high minimizes the depth of field. In theory, then, quality is improved by the use of lower accelerating voltages and smaller apertures, to give good contrast, a large depth of field, and good resolution.

Replicas of Fracture Surfaces

Direct examination of a fracture surface can be made with a scanning electron microscope (SEM), but replicas offer the unique capability of transposing topographic information from the actual fracture surface to a high-fidelity facsimile that can be conveniently handled and transported, and readily examined in the TEM, SEM or light microscope. Use of a replica is of great importance when the fracture surface to be studied is located on a large structure, vessel or machine that cannot be moved to the laboratory. Other advantages (as well as limitations) of replicas will be considered in the course of this discussion.

Replicas used for fractography are broadly classified as single-stage and two-stage replicas. Because the TEM image of a replica is basically a shadowgraph, it will look the same using a single-stage replica taken from the fracture surface or a two-stage replica with the second stage taken from a thick plastic "negative" first-stage replica, except for such details as carbon folds and other artifacts of two-stage plastic-carbon replication. The broad, systematic difference between single-stage and two-stage transmission replicas is in the way they are shadowed, which gives rise to some differences in how the shadows must be interpreted. These differences are discussed on pages 59 and 60 in this article, under "Shadowing of Replicas".

Cleaning of Fracture Surfaces for Replication

The important first step in all replication methods is cleaning of the fracture surface to remove contaminants. Initial cleaning of fracture surfaces is discussed in detail in the article that begins on page 9 in this volume, and in Ref 8 of the present article.

The final stage of cleaning usually consists of successively applying and mechanically stripping several plastic films prior to formation of the replica to be used for examination. The films applied for cleaning should be relatively thick (at least 0.125 mm). They should be allowed to dry thoroughly before removal. Otherwise, small regions of the film that adhere tightly to the fracture surface may tear out when the film is stripped off, leaving bits of film on the surface that are difficult to detect and subsequently remove and that effectively represent artifacts that can be picked up in the final replica.

Single-Stage Replicas

There are three methods of producing single-stage replicas: (a) a film of plastic can be applied or formed on the fracture surface, (b) a film of carbon can be formed directly on the fracture surface by vacuum vapor deposition, and (c) a conversion oxide film can be formed on the fracture surface by chemical or chemical-plus-thermal treatment of the surface.

Single-stage replicas may be examined directly or after they have been shadowed (shadowing of replicas is discussed on pages 59 and 60). Because the replicas are examined in transmission, it is difficult to visualize the actual topographical shapes; shadowing the replica usually eliminates this difficulty.

A replica can be directly examined in a transmission electron microscope if it is sufficiently thin (of the order of 1500 Å in thickness). For examination by reflection in a scanning electron microscope (with either the secondary-electron-emission or the backscattered-electron mode of operation) or in a light microscope, it is made thicker.

Thin Single-Stage Plastic Replicas. The formation of a single-stage replica is depicted schematically in Fig. 5. The contrast obtained with single-stage replicas in a transmission electron microscope derives solely from the greater effective thickness (the greater distance the electrons travel perpendicularly through the film) of the replica in regions corresponding to the sides of hills and valleys in the fracture surface, resulting in relatively more absorption or scattering of the electrons and darkening in the electron image. Usually, an inadequate degree of contrast is afforded by the use of plastic only, and so a shadowing technique involving the vacuum vapor deposition of a heavy metal is employed to enhance contrast (see pages 59 and 60).

Because thin single-stage plastic replicas are fragile and are difficult to remove from a rough fracture surface, their

use is generally limited to polished-and-etched specimens. On the few occasions when they are used on fracture surfaces, they usually cannot be stripped without chemical assistance, and they are likely to collapse or break open at local regions corresponding to sharp hills and valleys on the fracture surface. In fractography, thin single-stage plastic replicas are useful only for investigation of relatively smooth fracture surfaces, when the highest fidelity and greatest resolution are needed to reveal fractographic details.

The actual mechanics of preparation of thin (1000 to 1500 Å, or 0.0001 to 0.00015 mm) single-stage plastic replicas for fractographic purposes is the same as for metallographic examination with a transmission electron microscope. The plastic, in a suitable solvent, is applied in the form of a dilute solution, ranging in concentration from one to a few per cent, depending on the film thickness desired. The plastic-solvent combinations most widely used are: (a) cellulose acetate (acetyl cellulose) with acetone; (b) cellulose nitrate with amyl, ethyl or methyl acetate; (c) polyvinyl formal with ethylene dichloride; and (d) polystyrene with benzene.

Because moisture collects in droplets, causing the formation of holes and artifacts in the replica, it is to be avoided in the plastic solution and in condensate form on the fracture surface.

The plastic-solvent solution is flowed onto the clean fracture surface. Thickness of the film is controlled by tilting the specimen to drain off some of the solution. The film should be allowed to dry thoroughly before any attempt is made to strip it from the fracture surface. Heating of the film is not recommended, because this may cause the formation of a solvent-vapor bubble, followed by rupture of the film when the bubble bursts.

The replica can be removed from the fracture surface by either of two methods. The simpler method consists of mechanical stripping by teasing an edge of the replica away from the surface in the presence of water; the capillary action of the water may be sufficient to free a portion of it. The more effective method consists of dissolving a very small amount of the underlying metal in the fracture surface by chemical etching or electropolishing. However, care must be taken to avoid formation of gas bubbles, which can deform and fragment the replica. This technique alters or destroys the fine fractographic features in the area replicated, preventing a meaningful second replication.

After it is stripped, the replica is washed in distilled water. It is then floated face-down on the surface of distilled water, and replica grids are brought in contact with its top surface. The replica is cut around the grids, and then, with grids attached, it is placed face-up on a glass slide and allowed to dry. After this, the replica is shadowed.

Thick single-stage plastic replicas are used extensively in fractography, both for the first stage in the two-stage replication technique (see page 59 in this article)

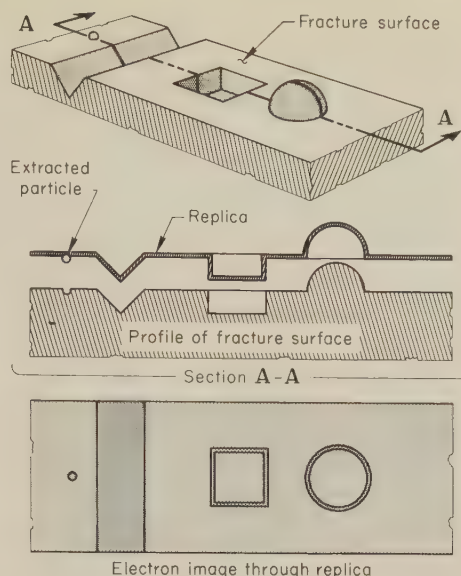


Fig. 5. Schematic views illustrating the single-stage replication technique

and for SEM and light-microscope examinations (particularly for field investigations of fractures occurring in service). Thick replicas can be more readily stripped, even from relatively rough fracture surfaces, they are more durable and do not easily tear or collapse, and they provide sufficient resolution for viewing of fine fractographic features.

Thick single-stage plastic replicas usually range in thickness from about 0.025 to 0.305 mm (250 times thicker than the thin single-stage plastic replicas). This thickness corresponds to the thickness range of the commercially available plastic tape and sheet used for replication. The thinner replicas (0.025 mm) in this category are preferred, because they dry more quickly, but use of thicker replicas may be dictated by the roughness of the fracture surface. In a seldom-used technique, an initially thin replicating film is built up and reinforced by additional plastic layers until the composite is strong enough to maintain its integrity during mechanical stripping. Because thick replicas are intended for reflection viewing, or for the first stage in two-stage replication, there is no upper limitation on thickness such as that imposed on replicas for direct examination in a transmission electron microscope.

To prepare a thick replica, a strip is cut from the plastic tape or sheet, and one side is softened by applying a few drops of solvent. The plastic-solvent combinations most commonly used are cellulose acetate with acetone, and cellulose nitrate with amyl acetate. Excess solvent is drained from the plastic strip a few seconds after the solvent has been applied. The softened face of the strip is placed on the fracture surface by contacting one edge and then slowly and progressively draping the remainder down on the surface, allowing for the escape of air and vapor. (As an additional means of removing air and vapor bubbles, the fracture surface can be wetted with the solvent immediately before the plastic strip is placed onto the surface.) The plastic strip

is pressed down firmly for 10 to 15 sec with a finger or a resilient pad

For a properly softened and drained plastic strip, the hardening time varies from 10 to 60 min, depending on the thickness. The degree of softening, the amount of solvent draining, and the time of pressure application and subsequent drying are all critical. Optimum combinations are best determined by experiment and observation. If the plastic strip is insufficiently softened, the plastic will not conform accurately and completely to the contour of the fracture surface; this will result in low fidelity and the generation of artifacts. If the plastic strip is too soft, entrapped solvent vapor will cause bubble artifacts, and the strip will tear when pressure is applied. The surface of the plastic strip should be semifluid on the softened side and firm on the back.

Application of additional layers of plastic strip will facilitate removal of a replica from a rough surface. The application procedure is essentially the same as for the initial replica layer, but the amount of softening of the contact surface of the second layer, which is necessary for good adhesion, is less.

The stripped replica is shadowed and then coated with an electrically conductive film for SEM viewing, or it is shadowed before proceeding to second-stage replication.

An alternative method of preparing thick plastic replicas consists of brushing or flowing a concentrated (40 to 60%) solution of cellulose acetate in acetone, or of cellulose nitrate in amyl, ethyl or methyl acetate, onto the fracture surface. This method does not produce a high-fidelity replica, and so is used mainly for replicating rough fracture surfaces that are to be examined for gross fracture features only. The replicating solution has the consistency of molasses. After it has been applied to the fracture surface, it is allowed to dry and harden to a tacky consistency, and a strip of the same type of plastic is pressed into it. Some fractographers prefer to apply a dry plastic strip immediately on the solution, using firm thumb or finger pressure for about 3 to 5 min while the solvent of the solution partly dissolves the strip and the replica partly dries. Long drying times (about 30 min or more) are required before stripping. Application of a stream of warm air may facilitate drying, but entrapment of vapor bubbles is a problem. The replica is mechanically stripped and then shadowed.

Another method consists of pressing a wafer of polystyrene onto the fracture surface, while simultaneously heating the wafer and the specimen. This thermal molding method, in addition to having the obvious advantage of being a "dry" method, is capable of replicating rough surfaces and of providing good resolution. Its unfavorable feature is the multiple-step, time-consuming procedure required. Commercially available pellets of polystyrene are melted down between glass platens (such as microscope slides), in an oven at 165°C (329°F), to form flat wafers upon cooling. A wafer is pressed onto the fracture surface by means of a

platen and weight or clamp, and the assembly is placed in an oven at 165 C (329 F). The assembly is heated to temperature, and held for about 5 min. Then it is cooled to room temperature and the replica is mechanically stripped. The replica may be shadowed, or be shadowed and coated with a conductive film, depending on how it is to be viewed.

Single-Stage, Direct Carbon Replicas. The direct carbon replication method is usually superior to the plastic replication method for obtaining thin replicas for TEM examination. Furthermore, carbon replicas are stronger and more stable under electron-beam bombardment in the TEM. They are durable, and have high fidelity and resolution. They are free of many of the artifacts that can be present in plastic replicas. Carbon replicas are used for the investigation of the most delicate fracture features by transmission electron microscopy.

Single-stage carbon replicas are prepared directly from the fracture surface. Deposition of the carbon film on the surface is carried out in a laboratory vacuum evaporator operating at a pressure of 10^{-4} torr or less. The carbon source consists of two spectrographic carbon rods, heated by electrical contact resistance. The rods are held horizontal in spring-loaded holders to maintain contact. Their contact tips are specially shaped—one rod is sharpened to a point and the other is machined to a small (about 1-mm), uniform diameter. The specimen is placed face-up on a small, rotating stage (driven by an externally controlled variable-speed motor), which is below and vertically in line with the carbon source (contacting tips of the rod electrodes). The spacing between source and specimen should be no less than about 10 cm, to avoid heating of the specimen by radiation.

The area outside the region to be replicated is usually masked with adhesive tape or stop-off lacquer before carbon deposition; this will facilitate stripping of the replica. Frequently, the fracture surface is preshadowed with carbon or a heavy metal before deposition of the uniform carbon film. The preshadowing is also conducted in the vacuum evaporator.

The thickness of the carbon film can be controlled by completely evaporating a premeasured length of the 1-mm-diam electrode; a length of 1 cm is usually optimum. Alternatively, a strip of dead-white paper or card stock can be placed near the specimen and the darkening caused by carbon deposition can be visually calibrated and plotted against deposition time or total amount of carbon evaporated (or both), or against the degree of transparency of a sequence of carbon deposits of increasing thickness. The specimen should be rotated slowly during carbon deposition to provide a uniformly thin and continuous film that will resist breakup during stripping.

Stripping of carbon replicas usually requires dissolution of some underlying metal from the fracture surface, either by chemical or electrochemical etching. The solutions and conditions used are the same as those used for preparation of

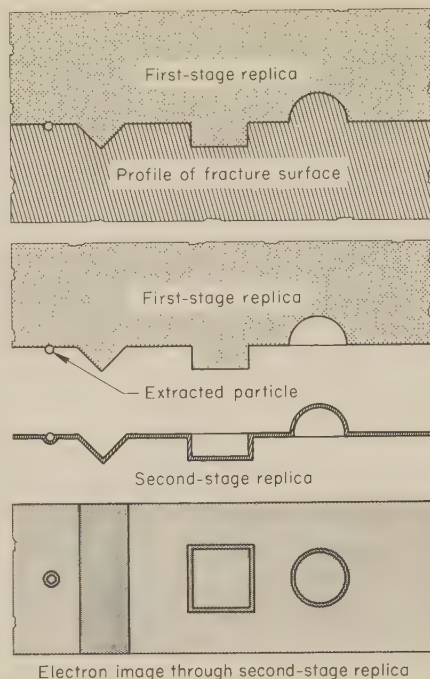


Fig. 6. Schematic views illustrating the two-stage replication technique

metallographic specimens of the same metals, particularly for making extraction replicas for TEM investigations (see pages 102-103 in Volume 8 of this Handbook for details).

To facilitate the release of the carbon film, the replica is scribed into a pattern of small squares, about the same size as the piece of grid to be used, before etching or electropolishing. The time to effect release of a replica may vary from minutes to hours, depending on the etching rate of the metal and the topography of the fracture surface. After the replica is released, it floats on the surface of the etchant; it is lifted off and rinsed in a series of alcohol or distilled-water baths. Dilute acids (a 5 to 10% solution of hydrochloric acid in alcohol, for example) may be used to dissolve reaction products and metallic debris, provided the acid does not attack the metal used for shadowing. Carbon films have a strong tendency to curl when stripped. Curling is minimized by shadowing with platinum, and sometimes curled replicas can be salvaged by alternate immersion in distilled water and alcohol. After application of the grid, the grid and replica are dried by carefully touching an edge of a piece of filter paper to the junction of the tweezer points that hold the grid and replica and the grid itself. Drying is done at room temperature.

Conversion-Oxide-Film Replicas. The fracture surfaces of some metals and alloys, notably aluminum and aluminum alloys, nickel and nickel alloys, titanium, high-alloy refractory metals, and austenitic stainless steels, can be oxidized to provide a thin, microscopically "structureless" oxide film of controlled thickness. This film is strong, dimensionally stable, and rigid enough to resist deformation and flattening during stripping and subsequent handling. The main requirement is that the oxide film be essentially "struc-

tureless". Films that are microcrystalline, porous or granular do not provide adequate fidelity in replicating the fine features of the fracture surface. Local variations in fracture-surface composition, including the presence of segregate phases, solid-state precipitates, and non-metallic inclusions, cause local differences in replica thickness and topography. These effects may not be relevant to the processes involved in crack propagation and fracture, and thus may interfere with fractographic interpretation. On the other hand, they may yield additional useful information. In general, those metals and alloys that have useful corrosion passivity and that form uniform, thin, continuous oxide films can be replicated by this method. Except for the austenitic stainless steels, the method is not applicable to ferrous alloys.

Oxidation of the clean fracture surface is achieved either electrolytically in an aqueous solution at room temperature, or by immersion in a molten salt bath at elevated temperature. Aluminum and its alloys can be suitably oxidized in a 3% tartaric acid electrolyte, adjusted to a pH of 5.5 with ammonium hydroxide, using the specimen as the anode and high-purity aluminum as the cathode, at a potential of 20 volts, for 5 to 10 min. Austenitic stainless steels, nickel, and nickel alloys can be thermally oxidized by heat tinting in a molten salt bath composed of 50 wt % each of sodium nitrate and potassium nitrate at 425 C (797 F). The time of immersion is determined by intermittently withdrawing the specimen and visually inspecting it; when the oxide film has grown to a thickness that produces a light-yellow interference color, it constitutes a suitable replica, and the specimen is removed from the bath.

Conversion-oxide-film replicas are more difficult to strip from the fracture surface than are single-stage carbon replicas. The oxide films on aluminum and its alloys can be removed electrolytically in a solution of 20% perchloric acid in alcohol, using the specimen as the anode and high-purity aluminum as the cathode; a potential of about 12 volts is applied until the oxide film is released.

Some solutions of perchloric acid and organic materials can be ignited or exploded, but solutions of perchloric acid in alcohol are believed to be safe to mix and use provided the following precautions are strictly observed. The alcohol-perchloric acid solution should be made up in small quantities, with the acid being added to the alcohol, and stored in glass-stoppered bottles that are filled by the solution. Evaporated alcohol should be promptly replaced, keeping the bottles filled. While the solution is being used, it must not be allowed to become heavily contaminated with dissolved metal, and spent or exhausted solution should be promptly discarded. No departure should be allowed from the prescribed formula, the method of mixing, or the strength of the acid used. The solution should always be protected from heat or fire.

Undermining of the oxide film by dissolution of some of the underlying metal in the fracture surface is also required

for austenitic stainless steels, nickel, and nickel alloys. The more aggressive action of a solution of bromine in methyl alcohol is needed. *Use of the bromine solution is hazardous in several respects. In contact with the skin, bromine will cause severe, third-degree burns, even with immediate first aid. Bromine vapor is dangerous to inhale. If the bromine solution becomes overheated during mixing or use, it may erupt violently.* For these reasons, the entire operation should be carried out in a well-ventilated hood, the solution should be cooled in an ice bath during mixing, and bromine concentration should not exceed 10%.

Before dissolving the underlying metal, the oxide film should be cut into small squares, the size of the piece of grid to be used, to facilitate the lifting of the film and thus to shorten the time of treatment. Solution concentrations of 2 to 3 ml of bromine per 100 ml of methyl alcohol are adequate for nickel and nickel alloys; higher concentrations (7 to 10 ml of bromine per 100 ml of methyl alcohol) are required for austenitic stainless steels.

After the film squares are released, they are collected on 200-mesh corrosion-resistant wire screen and are washed by several immersions in fresh methyl alcohol. The cleaned replicas are picked up on TEM replica grids, with the side of the replicas that was next to the fracture surface facing up. The replicas are then dried. Because they provide adequate image contrast in the TEM, oxide replicas usually are not shadowed.

Two-Stage Replicas

Two-stage replication can yield either thin second-stage replicas for transmission viewing in a transmission electron microscope or thick second-stage replicas for viewing by reflection in a scanning electron microscope or a light microscope.

There are two methods commonly used for preparing a final replica from a first-stage plastic replica. With the first method, a carbon replica is formed by vacuum vapor deposition of carbon on a first-stage plastic replica. With the second method, a plastic replica is formed by applying to a first-stage plastic replica a softened strip (or a solution) of a second, chemically different plastic that is not soluble in the solvent or solvents used to prepare the first plastic replica, and whose solvent, in turn, will not affect the first plastic replica. Because of the superior characteristics of carbon replicas in TEM examinations, and because the equipment for producing them is usually available, carbon replicas have supplanted plastic replicas for the second stage of replication; only in very special applications is a plastic second stage used. Figure 6 shows schematically the formation of a two-stage replica.

The procedure for preparing two-stage plastic-carbon replicas is a combination of thick, single-stage plastic replication and single-stage carbon replication of that plastic replica, with an intervening shadowing step. The two-stage method is applicable to analysis of service fractures, where portability and integrity of the

replica are of paramount importance. It is more susceptible than the single-stage carbon replication method to the generation of artifacts.

After a thick first-stage plastic replica has been prepared, in accordance with the procedure outlined on page 57, the replica is stretched out flat and face-up on a clean glass microscope slide. The replica is taped down at the edges to keep it flat. The slide bearing the replica is placed in a vacuum evaporator, operating at a pressure of less than 10^{-4} torr, for shadowing and for formation of a carbon second-stage replica. The carbon for the second step is deposited at about 45° to the replica surface. Replicas of rough fracture surfaces can be rotated continuously during deposition, on a small, motor-driven platform, to ensure uniform carbon deposition, especially on steeply tilted facets of hills and valleys and in sharp declivities at an angle to the surface, and to preclude confusing double shadows.

The thickness of the carbon film deposited is important. For high resolution, a thinner carbon film (yellowish interference color) is preferable, but when integrity of the film is a problem, such as in the replication of very rough surfaces, a thicker film (grayish interference color) is needed to provide resistance to film breakup during subsequent dissolution of the first-stage plastic replica. The thickness is controlled by the amount of carbon evaporated, which can be judged by the length of carbon rod consumed or by the degree of darkening of a piece of white paper located alongside the replica.

The separation of the carbon replica from the first-stage plastic replica is best done by dissolution of the plastic in successive baths of fresh acetone. The replica "sandwich" is first examined under a bench microscope to select regions of interest, which are removed as small squares by gentle slicing with a razor blade. The size should be about $\frac{1}{2}$ mm larger than the grid, which usually is 2.3 or 3.0 mm square, to provide ultimate support. (The overlap will fold over the edges of the grid by surface tension and hold the replica in place.)

Up to ten squares, carbon-side up, are placed in a 50-cc petri dish and carefully covered with about 5 mm of acetone. Gentle heat from a lamp to stimulate circulation and evaporation will assist in freeing the carbon replica, which should float to the top in about 5 min. A gentle jet of acetone slowly expelled from a medicine dropper will aid in freeing replicas that are not too fragile. Each replica when free is sucked up by the partly filled dropper and transferred to the next dish of acetone. The carbon replica actually curls up during entry and uncurls during ejection, but if either entry or ejection is performed forcefully, the replica will be torn. The dropper is then cleaned with fresh acetone and after 2 to 3 min, the squares are transferred to the last dish of acetone, where they remain for 5 to 15 min of final cleaning. The following technique of "fishing" to position the replica on the grid can easily be learned with a little practice:

"Fishing" Technique for Positioning Replicas on Grids. Grip an edge of a grid with tweezers and bend the edge slightly upward so that when the grid is immersed in the last dish of acetone, the grid plane is still horizontal. If the acetone is not too shallow, the replicas will be moving slowly about. Position the grid beneath a replica and raise the grid to the surface; the replica will be held to the grid by surface tension and mechanical friction. If positioned properly, the edges of the replica will overhang the edges of the grid (except at the side next to the tweezers; the carbon should not touch the tweezers, because it will adhere). If positioned incorrectly, lower the grid a bit to free the replica and relocate it; do this quickly, because motion of the acetone at the surface is rapid.

Raise the grid from the acetone and begin drying by carefully contacting the junction between the tweezers and the grid with absorbent paper. Maintain pressure on the tweezers; otherwise, the grid may be drawn up between the tweezer points by surface tension and the replica destroyed. Hold the grid until the replica is dry; then place it, replica-side up, in a clean, dry receptacle.

Shadowing of Replicas

Most untreated replicas do not provide enough contrast to permit full realization of maximum fidelity and resolution of the features of fracture surfaces. This deficiency may result in failure to detect or recognize small, but important, features, such as fine fatigue striations, even though their dimensions are well within the resolution limits of the replication method and the viewing instrument. Also, in two-dimensional viewing of replicas, questions frequently arise concerning the degree of vertical relief—that is, whether certain fracture features are higher or lower than others, and by how much. For these reasons, most replicas are shadowed (or "shadow cast") by directional vapor deposition in vacuum of a heavy metal at an oblique angle to the replica surface. Contrast is enhanced by the buildup of more electron-opaque material (compared to the replicating material) at the leading edges or frontal slopes of hills and at the trailing edges or upward slopes of valleys in the replica ("snowdrift" effect). The length of the shadows provides an estimate of the relative height or depth of such features, and more accurate measurement is possible by suitable calibration of shadow length. The shadowing processes for single-stage plastic replicas and for two-stage plastic-carbon replicas are shown in Fig. 7, together with one method for shadow-length calibration. Although shadowing can give useful indications of vertical dimensions, the most reliable method for obtaining depth and height perception and measurement is by stereography.

When viewing a fractograph of a shadowed replica, it should be remembered that the dark portions in the print represent regions where the shadowing layer is thick, and shadows on the print represent regions where less shadowing metal was deposited. Because shadowing metal will not deposit in thick layers at the bottoms of depressions, it can be deduced that features that appear as light regions were depressions in the surface.

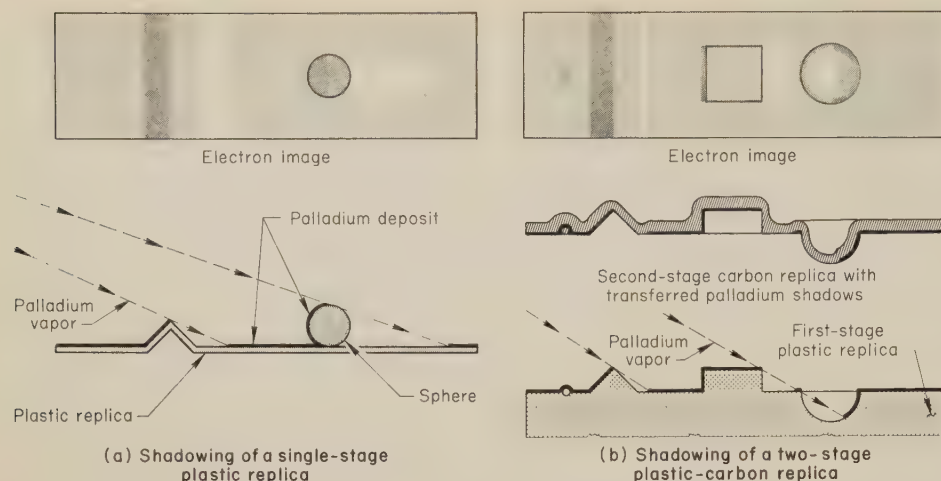


Fig. 7. Shadowing processes for single-stage plastic replicas (a) and two-stage plastic-carbon replicas (b). A sphere of known size can be placed on a replica, as in (a), to calibrate shadow length.

If the shadowing metal is deposited directly on the fracture surface, as in single-stage direct carbon replicas, a light region observed in the replica was a depression on the fracture surface. On the other hand, if the shadowing metal is deposited on a thick first-stage plastic replica, a light region inside a feature on a second-stage carbon replica shows that it was a hill on the actual fracture surface. For this reason, sound interpretation of a fractograph depends on knowing the replication procedure used.

The shadowing of replicas and of fracture surfaces is carried out in a laboratory vacuum evaporator fitted with holders for tilting and rotating the replica or specimen and with fixtures for supporting the evaporation sources, which are connected to electrical vacuum lead-throughs for resistance heating. Special spring-loaded devices are used for continuously feeding opposed carbon rods (electrodes) into contact. Spiral tungsten filaments, in the form of baskets, are used for resistance heating and evaporation of the metals used for shadowing (except for platinum, which alloys readily with tungsten). Evaporation is carried out at a pressure of less than 10^{-4} torr, to prevent oxidation of the vaporized metal and to avoid deposition of a granular shadow.

The vaporized metal atoms travel in essentially straight lines from the evaporation source, impinge at an oblique angle on the tilted replica, and condense. Generally, an angle of 45° is used, but a more oblique angle (15° to 30°) produces longer shadows and more clearly delineates small elevations and depressions (fine fatigue striations, for example). To use shallow deposition angles satisfactorily, the replica should be generally flat; otherwise, some areas will be masked. If the nature and orientation of the surface features of interest are known, or can be surmised, before shadowing, the direction of shadowing that will produce the most definitive shadows can be selected. For example, to accentuate fatigue striations most effectively, shadowing metal should be deposited in a direction oriented 90° to the striations, which

will make the shadowing direction parallel to the direction of crack propagation. If the crack-propagation direction on the microscopic scale differs from that on the macroscopic scale, it may be necessary to make and shadow more than one replica.

Depending on their tilt and orientation, some facets on fracture surfaces will receive a thicker deposit than others. For example, on the side of a protuberance facing the evaporation source, the deposit will be thicker than on the side away from the source (the opposite is true for depressions). This difference in deposit thickness will result in a difference in the degree of electron absorption or scattering in a transmission electron microscope, which enhances the image contrast of the feature. The degree of scattering increases with the atomic number of the shadowing element; for this reason, heavy metals (those with high atomic numbers—namely, chromium, platinum, palladium, germanium and gold-palladium alloys) are commonly used. They minimize the thickness of shadow needed to provide adequate image contrast. Thick deposits are generally undesirable because they may obscure fine topographic details, and the shadows may be difficult to interpret.

The thickness of the shadow deposits is a function of the amount of shadowing material vaporized, which can be controlled by completely evaporating a pre-measured amount. Alternatively, if an excess of shadowing material is placed in the evaporator, a piece of white paper (or card) having an upright tab can be placed near the replica, with the tab facing the evaporation source, so that the relative darkening of the paper in front of the tab, as compared to the shadow behind it, can be visually monitored and evaporation stopped at a suitable stage.

Coating of Replicas

Replicas that are to be viewed in an electron microscope must possess sufficient electrical conductivity, at least in their surfaces, to "bleed off" the electrical charge caused by impingement of the electron beam. Otherwise, the charge

builds up locally and intermittently, and interacts with the beam, causing image instability and distortion.

The carbon replicas used for examinations in transmission electron microscopes are sufficiently conductive to avoid this problem, particularly when supported on fine-mesh metal screens (replica-support grids) that, in turn, are in good contact with the metallic specimen holder and thus are grounded to the instrument. Thin plastic replicas have some tendency to charge, but only over short distances of less than a replica-grid opening; although troublesome, replica and image instabilities are not serious.

To circumvent the problem of surface electrical charging of thick plastic replicas during examination in a scanning electron microscope, a very thin (about 100 Å), but continuous, metallic film of good electrical conductivity is applied to the replica surface, using vacuum vapor deposition. The metal (often palladium) is deposited on the replica surface at right angles to the surface, while the replica is rotated to ensure a uniformly thin coating. The edge of this coating is grounded to the specimen holder of the microscope by means of a flexible, metal-coated tape or by painting on a bridging strip of metal-containing paste.

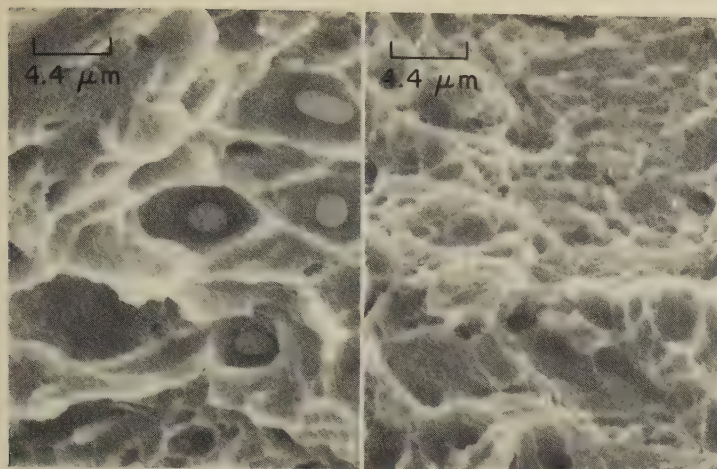
SEM vs TEM Fractographs of Different Types of Replicas

Figure 8 compares the appearance of fracture-surface features (particularly dimples) as seen in an SEM direct fractograph and in SEM and TEM fractographs of different types of replicas of the same fracture surface. The fracture surface shown is one obtained in an impact test of a Charpy V-notch specimen of vanadium-modified 4335 steel.

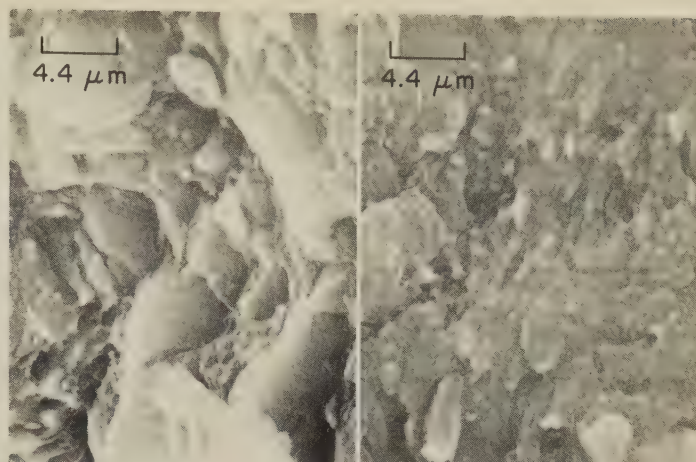
Location and Orientation of Replicas

For most electron-microscope fractographic investigations, especially those conducted in conjunction with service fractures, it is important to be able to relate the location and orientation of fractographic features observed in replicas to gross features (such as general topography, surface texture, fracture origins, beach marks, and inclusions) of the fracture itself. Indexing of replicas, particularly two-stage replicas, to ensure unequivocal referencing, is often difficult.

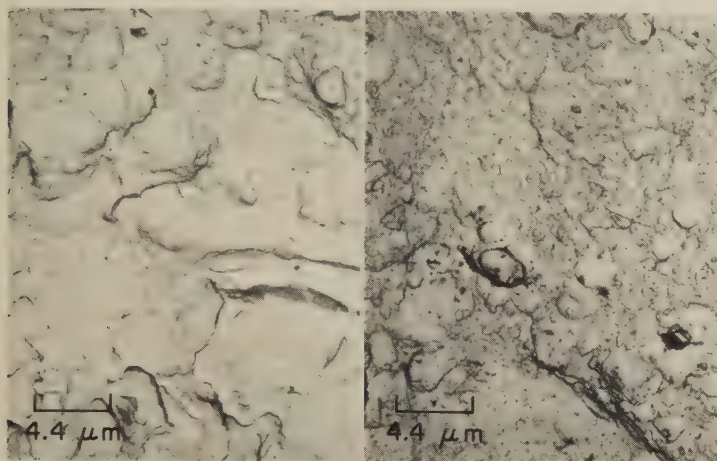
Grids for Indexing. Special TEM replica grids (finder or locator grids) are available that have prominent and unambiguous features for indicating the rotational orientation of the grid, as it is viewed. The grids also contain indexed grid openings that locate the field of view with respect to the perimeter of the grid and its rotational indicator. When the grids are affixed to the replica, assuming that the orientation and location of the replica up to this stage are known, fractographic features observed can be related to the fracture surface of the specimen. The grids are placed on the replica under a



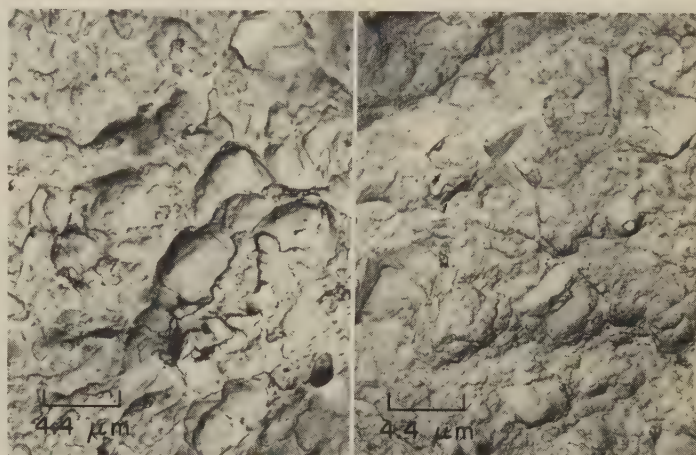
SEM fractographs taken directly from the fracture surface; 2250 \times



SEM fractographs of a thick, single-stage, gold-coated plastic replica; 2250 \times



TEM fractographs of a two-stage, unshadowed, plastic-carbon replica; 2250 \times



TEM fractographs of a two-stage, chromium-shadowed (at 50°), plastic-carbon replica; 2250 \times

Fig. 8. Comparison of the appearance of dimples in a fracture surface as seen in an SEM direct fractograph and in SEM and TEM fractographs of different types of replicas. The fractographs are of a Charpy V-notch impact specimen of vanadium-modified 4335 steel. Each pair of fractographs shows two areas near the root of the notch that exhibit dimples of different sizes.

stereoscopic light microscope, at a magnification of ten diameters or more.

To maintain orientation-location indexing of the replica from the time it is stripped from the original fracture surface until the replica grids are applied requires a system of marking and coding of the replica, usually by cutting the replica to a special shape or by notching, and careful attention to transfer of such markings at each stage of replication.

Shadowing for Indexing. The shadowing of replicas, although intended primarily to enhance image contrast of small fractographic features, also helps in interpreting these features. Specifically, the characteristics of the shadows (their relative location, length and intensity) can be used to identify a feature as an elevation or a depression, and to estimate relative heights and depths of features. For this purpose, it is essential to know the direction and angle at which shadowing was applied. This can be done at the time of shadowing, by recording the shadowing direction with respect to the already-marked orientation of the replica, and its relation to the original fracture. Many fractographers shadow in the direction of crack propagation.

Artifacts in Replicas

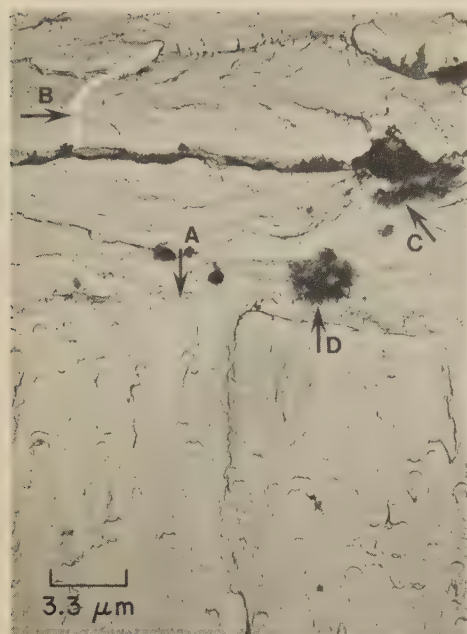
The disadvantage most often encountered with any replication process is the presence of features on the replica that do not accurately reflect the details of the fracture surface, such as the artifacts shown in Fig. 9.

Poor technique in the formation of the first-stage plastic replica is a principal cause of artifacts in two-stage replicas. If the fracture surface is not cleaned properly, foreign material is likely to appear in the replica, as shown at arrow C in Fig. 9. If the plastic solution for the first-stage replica is not flowed into all recesses of the fracture surface, air or solvent vapor may become trapped, and will appear in the replica as smooth rounded areas. Many fractographers circumvent this problem by applying solvent to the fracture surface immediately before forcing a piece of presoftened plastic strip onto it. During the 10-to-15-sec interval before the plastic begins to set, the dry top of the piece of plastic is pressed, using tweezers, to chase visible bubbles away from the area to be replicated.

The most frequently encountered artifact is the small-bubble artifact—that is,

a bubble embedded in the plastic (see Fig. 10). Small-bubble artifacts result from release of solvent vapors at the fracture surface. They occur at irregularities on the fracture surface, and resemble bubbles that arise from scratches on the bottom of a beaker when water is being boiled. They are caused by the high vapor pressure of excess solvent as it attempts to diffuse out of the plastic. They can be avoided by using plastic strip that is thick enough to allow the dry back (or top) side to act as an absorbent sink for the solvent. Ideally, the plastic strip is softened on one side only, and softened no more than is necessary to make it conform to the fracture surface.

Another artifact is encountered in the deposition of carbon for single-stage, direct carbon replicas. Frequently, features 20 to 50 Å in major dimension are to be resolved. If too much carbon is deposited, the fine features are distorted by enlargement or are totally hidden. If fine features are to be retained, the replica must be made as thin as possible. Although most fractographers prefer replicas that are strong enough to remain intact over an entire 75-mesh grid, others, in the interest of fine detail, prefer a

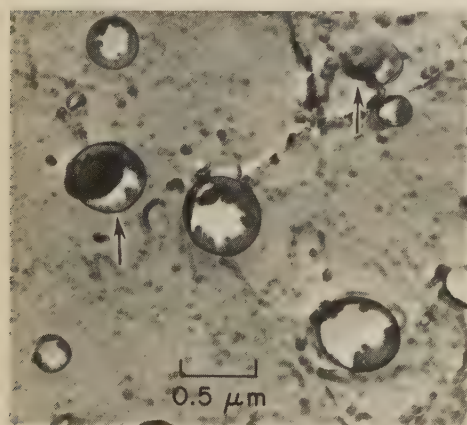


TEM fractograph (p-c replica)

3000×

The appearance of the bottom half of the fractograph (below arrow A) is the result of tears in the first-stage plastic replica, and is not at all representative of the fracture surface. A crack in the carbon second-stage replica is indicated by arrow B, a particle from the improperly cleaned fracture surface is indicated by arrow C, and residual plastic from incomplete dissolution of the first stage is indicated by arrow D.

Fig. 9. Four types of artifacts found on two-stage, plastic-carbon replicas



TEM fractograph (p-c replica)

20,000×

The thin film of plastic between the bubble and the replicated surface is seen to be partly removed from the plastic replica at the bubbles indicated by arrows. It evidently adhered to the fracture surface at the other bubbles.

Fig. 10. Bubble artifacts caused by an excess of solvent (acetone) in the cellulose acetate used to make a plastic replica

replica that is so thin that it will not remain intact over more than half the grid openings of a 200-mesh grid.

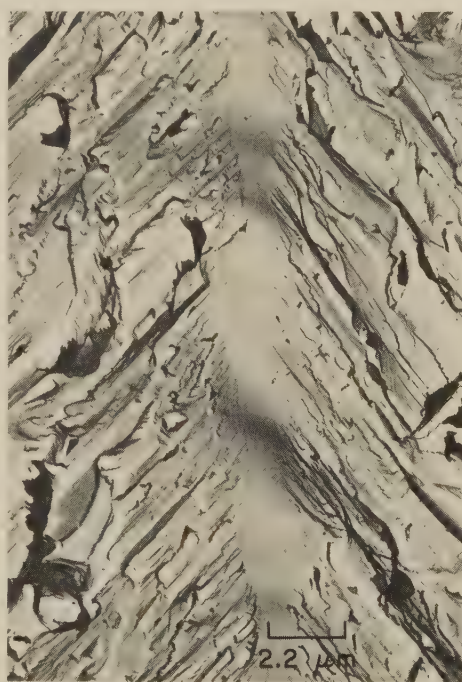
Artifacts that arise during removal of the replica from the fracture surface are of three types. In single-stage, direct carbon replicas, holes occur if the carbon adheres to the fracture surface. In plastic single-stage or first-stage replicas, some of the plastic is usually trapped in deep crevices and remains there when the remainder of the replica is removed. This results in a characteristic torn-plastic



TEM fractograph (p-c replica)

3000×

Fig. 11. Scraping artifacts (as at arrows), which resemble linear striations, on the sides of dimples



TEM fractograph (p-c replica)

4500×

Fig. 12. Distortion artifact at the {100} cleavage plane (narrow central strip) in tungsten. This plane was originally flat but became distorted as the replica dried, giving the undulating appearance.

feature, such as is shown in the lower half of Fig. 9. Another common artifact develops when the plastic scrapes against the fracture surface as it is pulled off. This gives rise to linear marks such as those indicated by arrows in Fig. 11. These linear marks usually occur at several neighboring features. When viewed in stereo, they are seen to be on the sides of hills on the replica (all on one side or the other, depending on the direction of stripping and scraping). This type of replica



TEM fractograph (p-c replica)

22,500×

Fig. 13. Palladium-shadowed replica of a fracture in nickel showing reticulated shadowing metal on dimples. Reticulation was caused by the melting of the shadowing metal in the microscope and the formation of globules.

artifact is particularly troublesome because it bears a close resemblance to valid linear striations.

With the single-stage direct carbon technique, artifacts can result from use of a washing or freeing chemical that attacks the extracted particles on the shadowing metal.

With the two-stage plastic-carbon technique, artifacts, in the form of cracks, can develop at the bottoms of troughs or the tops of ridges when the replica is cut into grid-size pieces. The problem can be avoided by cutting the plastic replica into grid-size pieces *before* the carbon is deposited. In general, replicas should be cut by gently slicing them, using several light cuts, rather than by pushing the cutting blade straight through.

A further problem encountered in making replicas by the two-stage, plastic-carbon technique arises from the fact that the plastic expands as it soaks up solvent during the dissolution process. Expansion exerts tensile forces on the thin carbon film that are usually sufficient to stretch it and possibly to produce a crack (see arrow B in Fig. 9). This can be avoided by using a relatively thin layer of plastic, thereby limiting the tensile forces, or by using the so-called wax technique. The wax technique involves forming a frame of paraffin wax around the replica, which prevents the plastic from swelling laterally in the solvent.

The most severe damage often occurs during drying of the final carbon replica, when surface tensions are very high. The folding and tearing that occur during drying are major limitations of the replication technique. They can be avoided by freeze-drying the replica, although this

is a complicated procedure. The smoother the surface, the less damage occurs in drying. Replicas of flat fatigue-fracture surfaces and of the intergranular surfaces of fine-grained metals are barely affected, whereas replicas of irregular cleavage-fracture surfaces and surfaces including large ridges and valleys undergo severe distortion. Sometimes, slight distortions are noted. In the fracture in tungsten shown in Fig. 12, the {100} cleavage plane, which was originally flat, has an undulating appearance.

Artifacts that arise after a replica is inserted in the microscope include contamination, reticulation, and melting of materials contained in the replica. Contamination resulting from the action of the electron beam is unavoidable and increases with exposure time (see the section on Intensity and Contrast, page 55 in this article). Reticulation occurs when the shadowing metal gets hot enough to

melt and form globules, such as those shown in Fig. 13. Reticulation can be avoided by using a less finely focused electron beam, or by using platinum as the shadowing metal. Use of a less finely focused beam also avoids melting of other materials contained in the replica.

Stereo Viewing

For stereo viewing, two photographs are taken. The first is taken with the replica tilted 5° or 6° from the horizontal in one direction, such as the left, and the second is taken with the replica tilted the same angle to the right, producing an included angle of 10° or 12° between the two positions. When the fractographs are printed and placed under a stereo viewer, features are readily apparent in three dimensions. By interchanging the two prints under the viewer, relief is reversed — hills become depressions, and vice

versa. For additional discussion of stereo-fractography, the reader is referred to pages 22, 23, 51, 281 and 282 in this volume.

References

1. C. J. Davisson and C. J. Calbick, *Electron Lenses*, *Phys Rev*, Vol 38, 1931, p 585
2. E. Brüche and H. Johannson, *Elektronenoptik und Elektronenmikroskop*, *Naturwissenschaften*, Vol 20, 1932, p 353-358
3. M. Knoll and E. Ruska, *Beitrag zur geometrischen Elektronenoptik (I)*, *Ann Physik*, Vol 12, 1932, p 607-661
4. B. von Borries and E. Ruska, *Aufbau und Leistung des Siemens-Übermikroskopes*, *Z Wiss Mikrosk*, Vol 56, 1939, p 317-333
5. A. Prebus and J. Hillier, *The Construction of a Magnetic Electron Microscope of High Resolving Power*, *Can J Research*, Vol A17, 1939, p 49-63
6. A. W. Vance, *Stable Power Supplies for Electron Microscopes*, *RCA Rev*, Vol 5, 1941, p 293-300
7. C. A. Zapffe and G. A. Moore, *A Micrographic Study of the Cleavage of Hydrogenized Ferrite*, *Trans AIME*, Vol 154, 1943, p 335-359
8. D. A. Ryder, "The Elements of Fractography", AGARD-AG-155-71, Nov 1971, p 59-61 in Chapter 4 (Document No. AD-734619, National Information Service, U. S. Dept. of Commerce)

Comparison of Scanning and Transmission Electron Microscopes for Fractography

By the ASM Committee on Fractography by Electron Microscopy*

BOTH the scanning electron microscope (SEM) and the transmission electron microscope (TEM) have specific advantages and disadvantages. Neither offers the full range of capabilities of the other. Each has important functions in fractography, and each will continue to complement the other in general use.

Magnification

For the examination of flat surfaces, the upper limit of magnification for scanning electron microscopes is about 240,000 \times and the upper limit of magnification for transmission electron microscopes is about 300,000 \times . For fractographic purposes, however, the useful maximum magnification for both instruments is the same — about 30,000 \times .

At the low end of the range, magnifications as low as 5 \times can be achieved with the SEM (particularly if specimen height is low), whereas the lower limit for the TEM is about 210 \times . Because all studies of a fracture surface begin with visual examination, often supplemented by scrutiny with a low-power stereoscopic microscope, viewing of important surface features at high magnification is arrived at more simply with the SEM than with the TEM. The field can be rapidly examined at 10 \times to 20 \times to locate the areas previously identified in the visual survey as meriting further study, then enlargement on the viewing screen can be increased in steps, to the magnification

deemed appropriate. In contrast, the initial magnification in the transmission electron microscope of about 210 \times minimum means that the sites previously selected for further study are more difficult to locate and to recognize.

Resolution

The resolution capabilities of the scanning electron microscope lie in the range of 70 to 100 Å. The transmission electron microscope can resolve much finer details, of the order of 25 to 50 Å, in fracture replicas. Low-relief contours are difficult, or impossible, to resolve with the SEM on unshadowed fracture surfaces or replicas. Even when the resolution of the SEM is theoretically adequate, with good-quality replicas the TEM provides better resolution of the finer details of fracture surfaces, such as minute fatigue striations, tear ridges on separated-grain surfaces of hydrogen-embrittled metals, and fine river patterns, and better and more uniform contrast of fine details of low vertical relief, such as those present in areas of serpentine glide, ripples or stretching.

Fidelity

The scanning electron microscope presents a faithful rendition of the fracture surface by direct examination of the specimen. One disadvantage is that foreshortening of features will be induced if the specimen is tilted. This can lend an oval appearance to dimples that actually are equiaxed. The fidelity of the transmis-

sion-electron-microscope fractograph rests on how faithfully the replica reproduces the fracture topography (thinning of fracture specimens for electron transmission usually is not feasible). Good replication techniques can minimize the occurrence of artifacts, but replicas are extremely delicate films and are easily torn on fracture surfaces that change abruptly in elevation and slope and have sharp projections and deep crevices. Although small surface details are faithfully reproduced, large contours of the surface may sag or collapse because of lack of replica strength or they may be flattened by the drying process used in replica preparation.

An SEM view or photograph will give a three-dimensional effect, which a TEM view or photograph will not give as well. But a TEM stereograph conveys a sense of shape that essentially duplicates that offered by an SEM stereograph of the identical location and orientation. The section of the *Atlas of Fractographs on Comparison of SEM and TEM Stereofractographs*, which begins on page 281, illustrates this similarity and demonstrates that complete fidelity of reproduction of the contours of a TEM replica is not realized unless it is viewed as a stereo pair. (See also pages 22, 23 and 51.)

The replica technique makes it possible to reproduce selected areas of a specimen without sectioning. A replica can be used in the SEM if desired, but, for direct viewing of the fracture surface, any large part must be cut up to make available a specimen small enough to be placed in-

*See page 49 for committee list.

side the instrument. Where preservation of the fractured part intact is important because of involvement in litigation, replication of surfaces is a major advantage.

Area of Specimen Covered

With a tilting and rotating stage in the scanning electron microscope, all sur-

faces of the specimen (up to about 1 in. across), except its base, can be scanned in most models. This capability permits full examination of fracture edges. The great depth of field of the SEM permits registry of both the fracture contours at the crack origin and the adjacent free surface, which may exhibit evidence of secondary cracks. The replicas used in the

transmission electron microscope usually cover an area not more than 3 mm square; thus, the preparation of many overlapping replicas is required to survey a surface area equivalent to that available in the SEM. Also, for full coverage of a single area, at least two replicas are needed so that the area masked by the supporting grid can also be examined.

Interpretation of Scanning-Electron-Microscope Fractographs

*By the ASM Committee on Fractography by Electron Microscopy**

AT LOW MAGNIFICATIONS, the features in scanning-electron-microscope (SEM) fractographs strongly resemble the aspects of the fracture apparent to the naked eye; but at high magnifications, more detail is visible and needs to be categorized and described if the fractograph is to be related to the micro-mechanisms of fracture that were active.

It is important to realize that microscopic features of fractures ordinarily differ widely within a small area, and at the high magnifications normally used with scanning electron microscopes, many views are required in order to characterize the nature of a fracture. This is illustrated in many of the exhibits in the Atlas of Fractographs in this volume, in which three or four views of the same fracture show the features of different local fracture mechanisms.

In this article, the common microscopic features of fracture surfaces revealed by scanning electron microscopes are discussed and illustrated, and the effects of chemical and thermal environments on fracture characteristics are described.

The principal categories of fracture features that are reviewed in this article are itemized in the list that follows:

- 1 Cleavage features (tongues, microtwins, and location of cleavage-crack origins)
- 2 Quasicleavage features
- 3 Dimples from microvoid coalescence
- 4 Tear ridges
- 5 Fatigue striations
- 6 Separated-grain facets
- 7 Mixed fracture features, including binary combinations of cleavage features, dimples, tears, fatigue striations, and intergranular-fracture features
- 8 Features of fractures resulting from chemical and thermal environments.

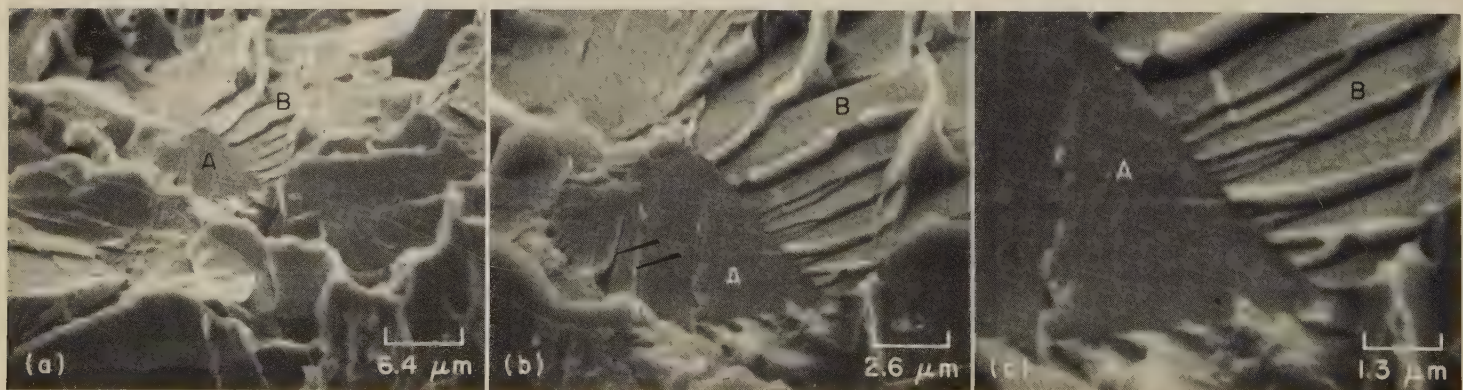
The special aspects of microvoid coalescence that have received such separate labels as serpentine glide, ripples and stretching, as well as the fracture characteristics involving slip in the general sense, are dealt with in the article on Interpretation of TEM Fractographs (see page 79), and are not treated here. Many of these features, being low in contrast and of extremely fine detail, are nearly invisible in SEM fractographs.

Transgranular Cleavage Features

In cleavage fracture, the fracture path follows a transgranular plane that is usually a well-defined crystallographic plane. This plane of fracture is one of the {100} planes in most body-centered-cubic metals. Cleavage fracture is produced,

usually at low temperature, under a condition of high triaxial stress — that is, at the root of a notch — or at a high deformation rate, as, for example, by impact loading. Cleavage fractures are typically found in body-centered-cubic metals such as iron, molybdenum, tantalum and chromium and in hexagonal, close-packed metals such as zinc, titanium and magnesium. Cleavage also occurs in face-centered-cubic metals under certain conditions: in aluminum alloys by cracking from contact with mercury, in brass by stress-corrosion cracking, and in many alloys by corrosion fatigue.

Figure 1 provides three views, at increasing magnification, of an area in an impact fracture exhibiting features that are typical of cleavage. It is apparent that the fracture plane changes orientation from grain to grain. As a result, the average grain size can be measured on the fractograph and related to grain-size measurements on a metallographic section. The change of orientation from grain to grain leads to a branching of the crack along different planes and to a very chaotic over-all appearance of the fracture surface. At higher magnification, however, many features typical of cleavage can be identified. In Fig. 1(b), the evidence of change in orientation between



SEM fractographs

The specimen was tilted in the scanning electron microscope at an angle of 40° to the electron beam. The cleavage planes followed by the crack show various alignments, as influenced by the orientations of the individual grains. Grain A, at the center in fractograph (a), shows two sets of tongues (see arrowheads in fractograph b) as the result of local cleavage along the {112} planes of

microtwins created by plastic deformation at the tip of the main crack on {100} planes. Grain B and many other facets show the cleavage steps of river patterns. The junctions of the steps point in the direction of crack propagation from grain A through grain B, at an angle of about 22° to the horizontal plane. The details of these forks are clear in fractograph (c). See also Fig. 2 and 3.

Fig. 1. Cleavage fracture in a notched impact specimen of hot rolled 1040 steel broken at -196 C (-321 F), shown at three magnifications

grain A and grain B is particularly clear because of the river patterns that begin in grain B at the interface. The river patterns, which represent steps between different local cleavage facets of the same general cleavage plane, are well defined. They run from left to right. River-pattern steps are usually the result of cleavage along second-order cleavage planes and, to minimize the energy of fracture, they join like river tributaries in the direction of crack propagation. Thus, by following a river pattern, it is possible to determine the direction of crack propagation. The height of river-pattern steps is further related to the angle between the tensile-stress axis and the orientation of the cleavage plane within a particular grain. A grain that has no, or few, river patterns may have been oriented at a right angle to the main tensile axis, causing the fracture to propagate very easily on a single plane. River patterns are modified by the presence of inclusions and precipitates.

Tongues and Microtwins. A second feature of cleavage fracture, found very often in iron and low-carbon steel, is referred to as a "tongue". Tongues appear on cleavage facets as very fine slivers of metal (see arrowheads on grain A in Fig. 1; for further detail, see grain A in Fig. 2). These minute slivers of metal are usually aligned along well-defined crystallographic directions. It has been shown that such features result from cleavage across microtwins formed by plastic deformation at the tip of the main propagating crack. The plane of the microtwins is a $\{112\}$ plane making an angle of 35° with the $\{100\}$ cleavage plane of the main fracture path. Thus, by tilting and rotating the specimen, it is possible to measure this angle and also to align the specimen so that the cleavage facet is at a right angle to the incident electron beam. The intersection between the main cleavage plane and the tongue is along a $[110]$ direction. By measuring the angle between the different $[110]$ traces, the exact angle between the cleavage plane and the electron-beam axis can be determined.

Cleavage-Crack Origins. Some of the main features to be looked for in a cleavage fracture include: (a) the origin of the main crack, (b) the origins of secondary cracks, and (c) the local directions of crack propagation. In Fig. 2(a) and (b), a well-defined origin is evident at C, at a carbide particle at a grain boundary. From the particle, which is small (about 1 micron in diameter), the crack propagated through the surrounding grains by cleavage. The propagation in the grain at B is typical of the type of cleavage where the crack propagates along different levels and behaves as if the grain were made up of layers. There is also a wide-open secondary crack, at D, in the upper part of Fig. 2(a), indicating the presence of cracking normal to the main fracture plane.

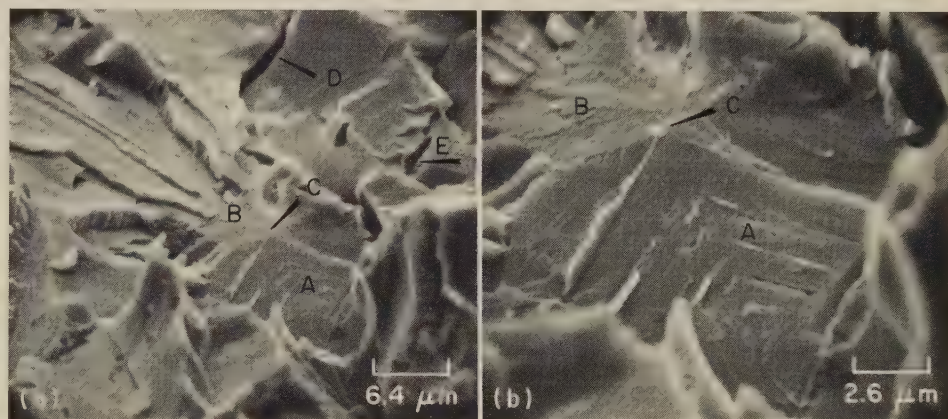
In grain A in Fig. 2, below the origin, are well-defined, feathered tongues, which were formed by fracture along microtwins. Tongues are sometimes associated with secondary microcracks. The tongues intersect the main cleavage plane along $\langle 110 \rangle$ directions. The fact that the two

$\langle 110 \rangle$ directions are not at exact right angles to each other indicates that the cleavage facet was oriented at an angle other than 90° to the beam axis.

In Fig. 3(a) and (b) is another example of crack initiation at, and propagation from, a fractured carbide particle (A), at a junction of four grains. The fracture features in adjacent grains differ, being either tongues or well-defined river patterns. The river-pattern lines shown in grain B, emanating from the origin, are attributed to the presence of screw dislocations threading through the cleavage plane. Screw dislocations result in an increase in the height of river-pattern steps as a crack propagates. The density of river patterns has been related to the density of dislocations and to the degree of cold work present in the grain before cleavage occurs. The river patterns in Fig. 3 are difficult to see and to identify; in order to increase the contrast of faint river patterns, it is recommended that the fracture surface be shadowed with an extremely thin film of gold to enhance the edges of the river-pattern steps.

Quasicleavage Features

In steels that have been quenched to form martensite and then tempered to precipitate a fine network of carbide particles, the size and orientation of the available cleavage planes within a grain of prior austenite may be poorly defined. True cleavage planes have been replaced by smaller, ill-defined cleavage facets, which usually are initiated at carbide particles or large inclusions. The small cleavage facets have been referred to as quasicleavage planes because, although they look like cleavage planes with river patterns radiating from the initiation sites, until recently they have not been clearly identified as crystallographic planes. Inoue *et al* (Ref 1) and Beachem (Ref 2) have concluded that the quasicleavage facets in quenched-and-tempered steels do conform to $\{100\}$ planes. Inoue *et al*, using electron-diffraction examinations of martensite packets, found that the lath surfaces were predominantly $\{100\}$ oriented and argued that natural cleavage perpendicular to the lath sur-

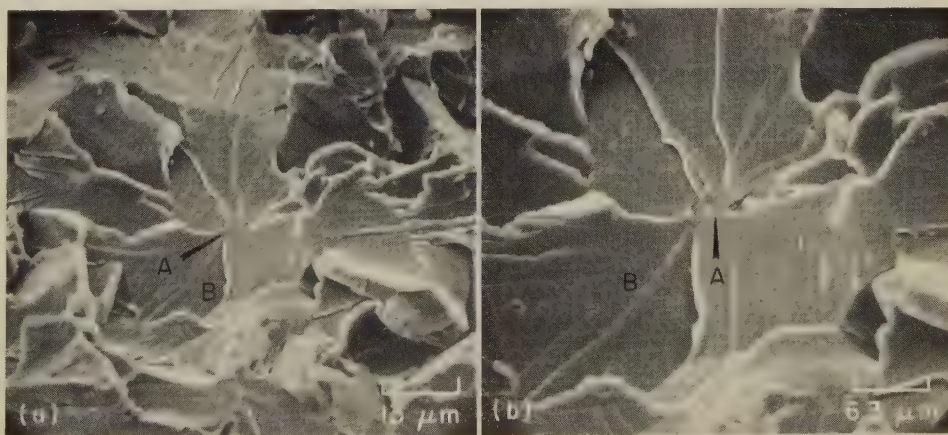


SEM fractographs

Grain A shows two well-defined sets of feathered tongues that are approximately orthogonal. A small carbide particle, C, at the boundary of grains A

and B initiated the local cleavage crack through the surrounding grains. Secondary cracks are at D and E. Note succession of cleavage steps in grain B.

Fig. 2. Tongues in a second area of cleavage of the 1040 steel specimen of Fig. 1, at the same 40° tilt. The same area is shown in both fractographs, but at different magnifications.



SEM fractographs

Cleavage spread in several directions from fractured carbide particle, A, at junction of four grains. Cleavage features differ from grain to grain, with river patterns visible in some and tongues in others.

River-pattern lines in grain B are attributed to interaction of local screw dislocations with cleavage plane. Height of steps increases in direction of crack propagation, to the left and downward.

Fig. 3. A site of cleavage-crack nucleation in the fracture surface of the 1040 steel specimen of Fig. 1 and 2, at the same 40° tilt to the electron beam. The same area is shown in both fractographs, but at different magnifications.

face must also be $\{100\}$ oriented. Bechem observed that Fe_3C platelets grew on $\{110\}$ planes in $\langle 111 \rangle$ directions at angles of 45° and 90° to each other. Such angles satisfy the relationships for $\{110\}\langle 111 \rangle$ habit-plane intersections with $\{100\}$ ferrite planes.

Quasicleavage facets on a fracture surface of a quenched-and-tempered 4340 steel specimen broken by impact at -196°C (-321°F) are shown in Fig. 4. The poorly defined cleavage facets are connected by tear ridges and shallow dimples.

Quasicleavage, or cleavage in complex microstructures, is more difficult to identify than the cleavage found in low-carbon steel made up of ferrite and pearlite. When identification is uncertain, it is essential to relate the fracture features to the microstructure, including the prior austenite grain size, the martensite plate size, and the distribution, size, spacing, and volume fraction of fine carbide particles precipitated during tempering.

Quasicleavage should not be confused with the decohesion along certain crystal-

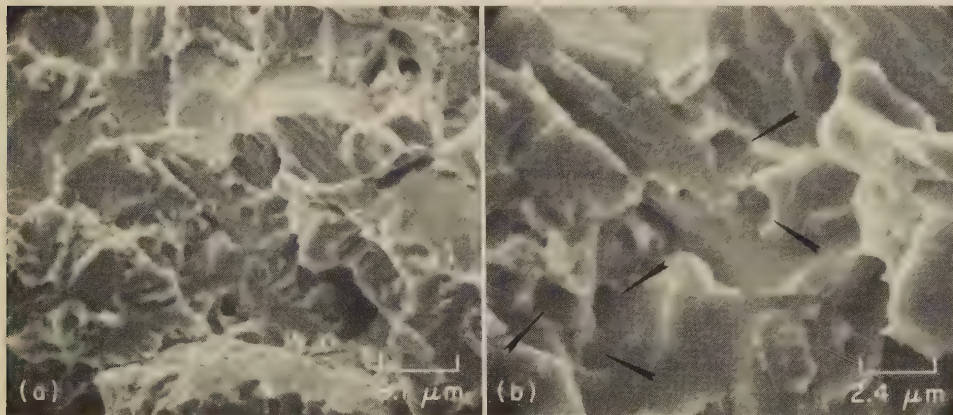
lographic planes that can occur by shear, by sliding off (plastic shear), or by separation along weak, still poorly defined interfaces. This type of decohesion has been referred to as glide-plane decohesion.

Dimples Formed by Microvoid Coalescence

If the temperature of fracture is raised from very low (for example, liquid-nitrogen temperature) to higher levels, the fracture mechanism changes from brittle or cleavage fracture to ductile fracture by microvoid initiation, growth and coalescence. At low magnification, the fracture surface may exhibit both fibrous and cleavage regions. Fibrous regions are usually observed (a) near the free surface in a shear-lip zone, or (b) at the origin of fracture at the center of a smooth (unnotched) tensile specimen. Cleavage regions are typically observed in the surfaces of flat, plane-strain fractures and in regions of high crack veloc-

ity. However, at high magnification, the fibrous-fracture region, and also the cleavage region, may show successive fracture mechanisms—that is, the fracture features may include both cleavage facets and dimples. (A dimple is half of a microvoid through which fracture has occurred.) Both dimples and cleavage facets are visible in the Charpy impact fracture shown in Fig. 5. An over-all view of the region of transition between ductile and cleavage fracture is shown in Fig. 5(a). The upper portion of the fracture surface in this view is a result of cleavage, and the lower portion is a result of fracture by microvoid coalescence. The cleavage facets in Fig. 5(a) and (b) are at a considerable distance from the notch, which is below the region shown in the fractograph. In the intermediate-magnification view of the region of microvoid coalescence (Fig. 5c), facet A cannot be positively identified as a cleavage-fracture feature; it could be the result of a fracture along a grain boundary, or even possibly a microvoid surface that has stretched. Around this facet is a region of ductile fracture, which originated at the interface between the matrix and a carbide particle (in the deep dimple).

Identification of ductile fractures with a scanning electron microscope is simple, because dimples are easily distinguished from cleavage, fatigue, and intergranular-fracture features. Microvoids are initiated at interfaces between the matrix and particles such as carbides, precipitates and inclusions, and also at imperfections such as microporosity and microcracks. They grow under the triaxial stress conditions ahead of the crack tip and expand until they coalesce to leave behind on the fracture surface the familiar hemispheroidal cavities that are known as dimples. The shape and depth of dimples, or microvoids, can be related to the size of, and spacing between, initiating particles, to the condition of applied stress (tension, shear or torsion), and to the fracture toughness of the specimen. Figure 6(a) shows a ductile-fracture sur-

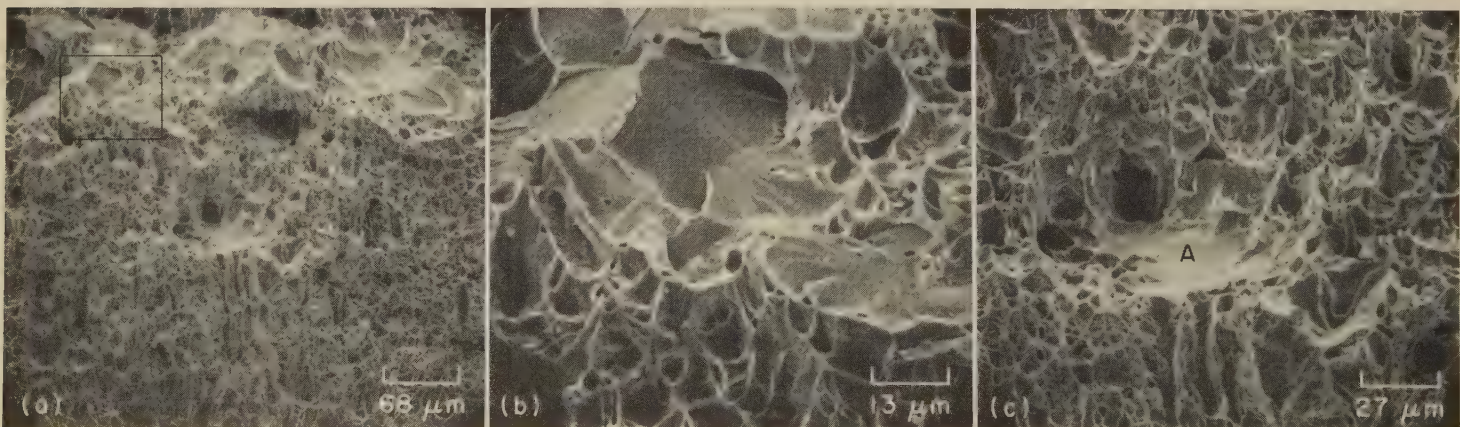


SEM fractographs

The small cleavage facets in martensite platelets contain river patterns and are separated by tear ridges. Shallow dimples, marked by arrowheads, are also visible. Direction of crack propagation is from

bottom to top in each fractograph. The specimen was heat treated at 843°C (1550°F) for 1 hr, oil quenched, and tempered at 427°C (800°F) for 1 hr. Fracture was by Charpy impact at -196°C (-321°F).

Fig. 4. Quasicleavage in the surface of an impact fracture in a specimen of 4340 steel. The same area is shown in both fractographs, but at different magnifications.



SEM fractographs

The machined notch of the specimen was below the region shown in (a). The over-all direction of crack propagation was upward. Although equiaxed dimples predominate, certain grain orientations near the top of (a) were unfavorable for ductile fracture by microvoid coalescence and local cleavage occurred, as shown in detail in (b), which is a higher-magnification view of the

outlined area in (a). Fractograph (c), a higher-magnification view of the region at the center of (a), shows a deep dimple, which initiated the local ductile fracture immediately surrounding it. The smooth surface at A shows no river patterns and should not be identified as a cleavage facet; it could be a grain-boundary surface, or perhaps a region of stretching. See also Fig. 6, 7 and 8.

Fig. 5. Dimples and cleavage facets exhibited in three aspects of a Charpy impact fracture at room temperature in a specimen of hot rolled 1040 steel, tilted in the scanning electron microscope at an angle of 30° to the electron beam

face, typical for 1040 steel, with initiation sites differing from dimple to dimple. In the center of the view, dimples were initiated at spherical precipitates or inclusions marked A, probably manganese sulfide, aluminum oxide or complex silicate particles. Above these, at B, initiation of a large dimple took place as a result of the fracture of a small pearlite colony, which is clearly shown in Fig. 6(b). [A pearlite colony, which consists of alternate lamellae of cementite (Fe_3C) and ferrite platelets, will break promptly and easily when acted on by the large plastic strain present at the tip of a crack.] The three dimples in Fig. 6(b) have essentially the same shape; few features are seen on the interior walls. Near the dimples, there are some wavy, fine slip lines (such as at C in Fig. 6b), indicating growth of the dimples by slip on many systems.

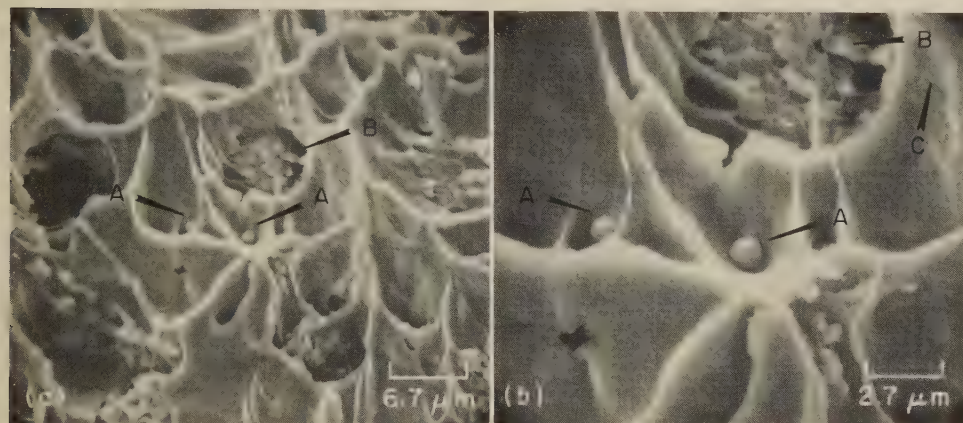
Until recently (see discussion, and Fig. 6, on page 105), dimples have been classi-

cally divided into three groups: equiaxed dimples, shear dimples, and tear dimples. Schematic diagrams illustrating how these are conventionally formed are shown in Fig. 1 on page 79. Examples of equiaxed dimples are shown in Fig. 5 and 6 here. Equiaxed dimples do not always appear exactly equiaxed in SEM fractographs, because tilt angles of 30° to 45° are often used to provide good contrast, and therefore the dimples may appear slightly distorted. However, the shear-lip zone of a Charpy impact, tensile-test, or fracture-toughness specimen will display a well-defined network of oval dimples elongated in the same direction — the direction of shear. In Fig. 7, which shows a portion of the shear-lip zone of the fracture surface of a Charpy impact specimen, the direction of shear is 45° to the direction of crack propagation. All of the dimples are parallel to the direction of shear. The long dimensions of shear dimples in one fracture surface all point in

the same direction; those of shear dimples in the mating fracture surface all point in the opposite direction. These two directions correspond with the opposite shear directions across the fracture plane. With shear dimples, it is quite difficult to identify the site of microvoid initiation, because the carbide particle or inclusion responsible may be hidden below the surface, which may have been rubbed or flattened out by shear displacement during fracture.

Tear dimples are formed by nonaxial stress conditions, such as those that exist in notched plane-strain fracture-toughness specimens and in drop-weight tear-test specimens. Nonaxial stress conditions are found also in the test where a wedge is forced into a notch (see Ref 13 in the list on page 92). The elongated microvoids that become tear dimples are formed in a narrow band just ahead of a well-developed crack front, such as the tip of a fatigue crack. Figure 8 shows the nature of crack propagation from the root of the notch in a Charpy impact specimen. The lower third of the fractograph shows the machined surface at the root of the notch. The fracture originated at this highly distorted surface during the Charpy test. One major crack formed from many crack nuclei, and the propagation of this crack took place by microvoid initiation, growth and coalescence. Coalescence of the microvoids resulted from tearing or opening of the crack under the applied load. This action formed the elongated dimples known as tear dimples, which have the appearance of parabolas pointing in the direction of crack initiation. On the mating surfaces of this fracture, the parabolas of the dimples are the same — on both sides, they point in the same direction, toward the site of crack initiation. Tear dimples are rare, which indicates that tensile tearing is not a predominant mechanism of fracture.

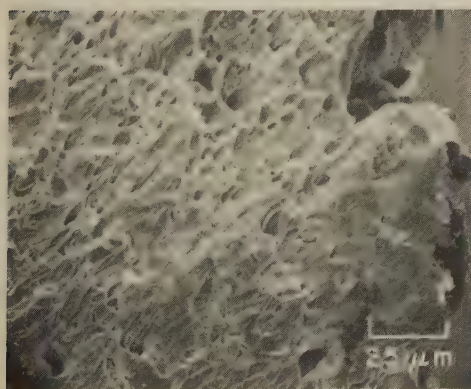
In ductile fractures, the sizes and shapes of dimples are seldom uniform. In engineering materials with an appreciable variation in size and distribution



SEM fractographs

The dimples at the center of these views were initiated at an interface between the matrix and globular inclusions (marked A), which probably are sulfide, aluminum oxide or complex silicate particles.

Fig. 6. Two different types of dimple-initiation sites, as exhibited in views at two magnifications of another area of the Charpy impact fracture shown in Fig. 5, at the same 30° angle of tilt to the electron beam

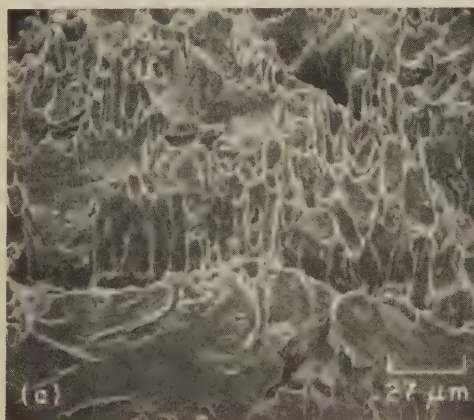


SEM fractograph

400×

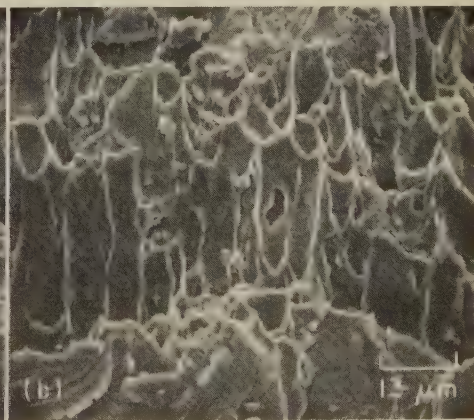
The free edge of the shear-lip zone is the vertical margin at the right. The dimples are elongated, and their rounded ends point in the same direction. The mating surface of this shear-lip zone would show similar elongated, parallel dimples, but their rounded ends would point in a direction opposite to that shown here.

Fig. 7. Shear dimples in the shear-lip zone of the Charpy impact fracture in 1040 steel shown in Fig. 5



SEM fractographs

Tear dimples resemble slim parabolas and point toward the site of crack initiation at the notch root, which is shown in the lower third of these fractographs. Unlike shear dimples, the tear dimples on the mating surface of this fracture would point in the same direction — toward the notch.



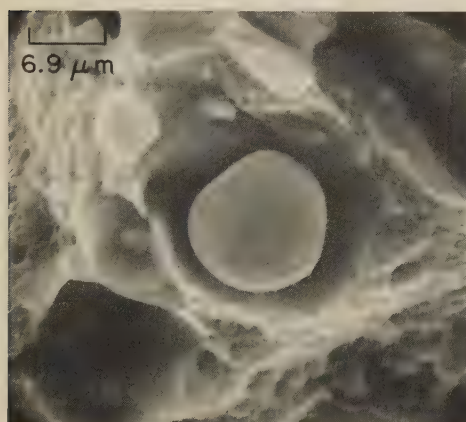
375× (a); 750× (b)

Occasionally, when the over-all shape of the fracture surface is unknown, a comparison of the mating fracture surfaces to observe the relative directions of dimple orientation may be the only method of determining whether the dimples present were formed by shear or by tearing.

Fig. 8. Tear dimples in a fracture region at the root of the notch of the Charpy impact specimen of 1040 steel in Fig. 5, shown in two views at different magnifications

of precipitate particles, dimples may exhibit a wide range of dimensions. This is shown in Fig. 9, in which a fracture surface in aluminum alloy 7075-T6 displays large dimples that are associated with large iron-rich inclusions (1 to 10 microns in diameter). In contrast, there is also a network of very small dimples, about a tenth to a fiftieth the size of the large dimples, resulting from microvoid initiation around the fine precipitates that strengthen this aluminum alloy.

Another example of a wide range in dimple sizes is provided in Fig. 10, which shows the fracture surface of a fracture-toughness specimen of aluminum alloy 2024-T5. The moderately large dimples, which contain broken inclusions, are outlined by tear ridges, and they contrast sharply with the extremely fine dimples present on some of the steep slopes of the even larger dimples.

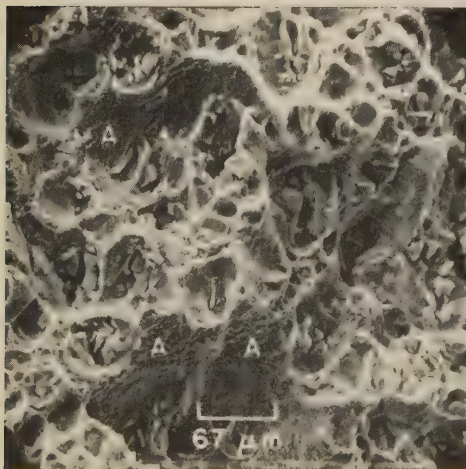


SEM fractograph

1440×

At center is a very large iron-rich inclusion, which rests within the large dimple it nucleated. In the surrounding surface areas are many extremely small dimples. The yield strength of this specimen was 517 MPa (75 ksi), and the hardness was Rockwell B 95.

Fig. 9. A fracture in aluminum alloy 7075-T6 showing a marked variation in size of dimples



SEM fractograph

150×

The moderately large dimples shown here contain inclusions, most of which have fractured. On the walls of the even larger dimples are many extremely fine dimples, as at locations marked A. The direction of crack propagation was from bottom to top.

Fig. 10. Fracture surface of an aluminum alloy 2024-T5 fracture-toughness specimen, showing a wide range in size of dimples

Tearing

Tearing designates a mechanism of local fracture that is often found at a discontinuity in the crack advance by another fracture mechanism. It occurs when small regions or ligaments fracture by plastic flow or necking. Tearing is frequently observed when small unbroken areas remain behind the main crack front. The occurrence of tearing is accompanied by the formation of tear ridges, which are typically sharp and thus produce bright contrast in the SEM image. Tearing may also produce flat-topped, featureless areas having some of the characteristics of local glide-plane decohesion.

Fatigue Striations

The study of surface characteristics of fatigue fractures with the SEM provides certain advantages, as well as certain disadvantages, when compared with the TEM replica technique. The advantages offered by the use of the SEM include:

- 1 Easier identification and evaluation of the origin of the fatigue fracture, whether near a free surface, at an edge, or at the bottom of a notch or a groove
- 2 Better differentiation between stages I and II of fatigue-fracture progress (see below for definition and discussion) by viewing the over-all fracture at low magnification not obtainable with a TEM
- 3 More reliable measurements of crack depths and crack-growth rates, which are used in fracture-mechanics evaluation of loads or for estimation of total number of cycles to failure
- 4 Simpler quantitative analysis of fracture surfaces to determine which portions of fracture surfaces resulted from microvoid coalescence, from intergranular separation, and from cleavage fracture.

The main disadvantage of scanning electron microscopy for the investigation of fatigue fractures is that fatigue striations are not as sharply defined as with transmission electron microscopy. This lack of resolution occurs because a striation represents only a small surface displacement, which often fades out in the electron image. By shadowing the fracture surface with a gold-palladium film 100 Å thick, it is possible to enhance striation contrast markedly. Striation spacings as small as 250 Å have been measured in aluminum alloys with the SEM. With scanning electron microscopes that have resolutions better than 100 Å, spacings as small as 100 Å can be resolved.

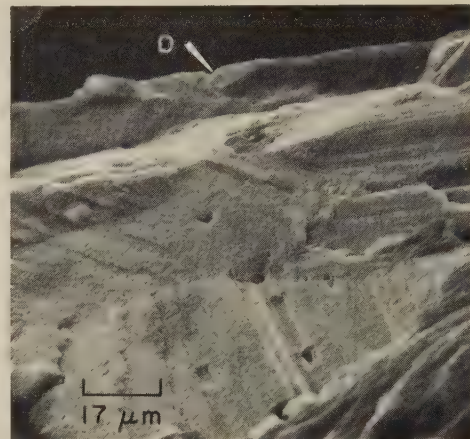
It is desirable to reveal as much as possible of the surface details within all secondary cracks associated with fatigue-crack branching. This can best be achieved with the specimen oriented with the crack-propagation direction pointing toward the secondary-electron collector to gain maximum penetration of the primary electron beam into the depth of the secondary cracks.

The SEM fractographs in Fig. 11 to 21 show some of the characteristic features of fatigue-fracture surfaces. For further treatment of the subject, see the review by Plumbridge and Ryder (Ref 3).

Stage I of fatigue-fracture progress is characterized by the initiation of cracks

and their propagation by slip-plane fracture, extending inward from the surface at approximately 45° to the stress axis. This stage is illustrated at a magnification of 600 diameters in Fig. 11 and 12.

The crack origin can best be found by first viewing the fracture surface at low magnifications from 25 to 100 diameters. In each grain the fracture surface is along a well-defined crystallographic plane (see Fig. 11), which should not be confused with a cleavage plane although it has the same brittle appearance. A stage I fracture never extends over more than a few grains (about 2 to 5) around the origin. There are usually no fatigue striations

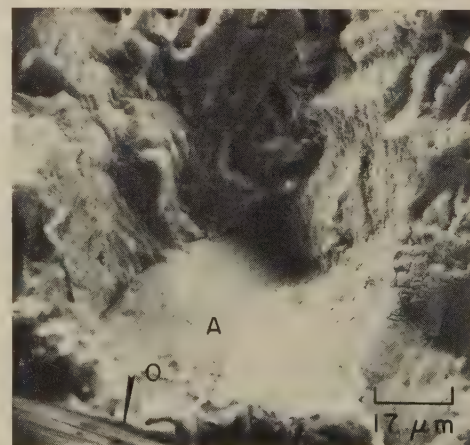


SEM fractograph

600×

The fracture origin is at O, near the top of the fractograph, in a free surface of the specimen. The change of orientation of the fracture plane from grain to grain is well demonstrated. Within a given grain, the fracture is along a {111}-type plane. The ridge patterns within each grain are parallel to the direction of crack propagation. Each ridge is probably in a <110> direction, which is the intersection of two {111} slip planes. The presence of inclusions does not affect the fracture path. Stage I of fatigue-fracture progress extended over 3 or 4 grains; stage II began at bottom right.

Fig. 11. Stage I of fatigue-fracture progress in a smooth (unnotched) specimen of aluminum alloy 2024-T3



SEM fractograph

600×

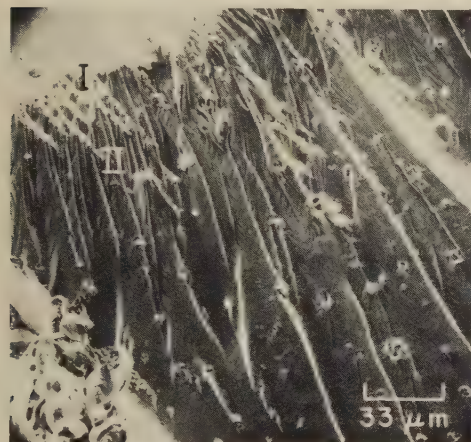
The origin of the fracture was at O. The stage I crack propagated through grain A. On the right and left of grain A, extensive rubbing of the fracture surfaces led to a featureless, rumpled surface. Stage II fracture proceeded from the edges of grain A.

Fig. 12. Stage I of a fatigue fracture in a smooth (unnotched) specimen of aluminum alloy 7075-T6 tested in reversed bending

associated with a stage I fracture surface. If by chance striations are present, they can best be observed by means of TEM replicas.

The presence of a stage I crack indicates a low cyclic stress amplitude, and the lower the stress amplitude, the longer the stage I crack. Evaluation of a reference low-stress, long-life fatigue specimen is the best way to identify clearly the characteristic features of a stage I crack in a given material.

Stage II of Fatigue-Fracture Progress. The transition from stage I to stage II of fatigue-fracture progress is characterized by the change of orientation of the main fracture plane in each grain from one or two shear planes to many parallel



SEM fractograph

300×

The transition from stage I (upper left) to stage II is well defined. The presence of (Fe,Si)-rich inclusions did not affect the fracture path markedly. The inclusions, which were fractured, range from 5 to 25 microns in diameter. The stage II area shows a large number of approximately parallel fatigue patches containing very fine fatigue striations that are not resolved at this magnification.

Fig. 13. Transition from stage I to stage II of a fatigue fracture in a coarse-grained specimen of aluminum alloy 2024-T3

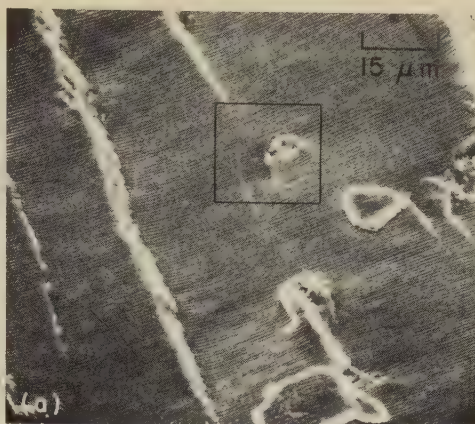


SEM fractograph

180×

The fracture surface is made up of facets, each facet corresponding to a specific grain, thus allowing the grain size to be measured. The orientations and levels of facets change from grain to grain. The presence of large inclusions results in local ductile fracture by microvoid growth. The crack-propagation direction is from bottom to top in this view.

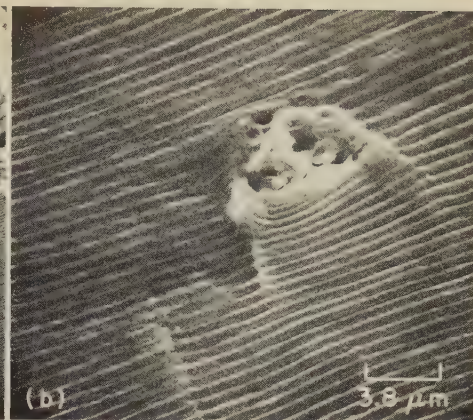
Fig. 14. Stage II of a fatigue fracture in a fine-grained specimen of aluminum alloy 2024-T3 tested in dry air



SEM fractographs

(a) The uniformity of the crack-propagation process is well illustrated. There was little or no interaction of the fracture process with the inclusion within the rectangle. The long ridges are believed to be high-angle steps at subgrain boundaries.

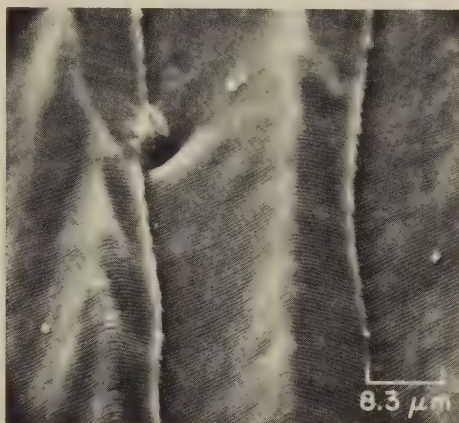
(b) Higher-magnification view of the region outlined by the rectangle in fractograph (a), showing



650× (a); 2600× (b)

the continuity of the fracture path through and around the inclusion. Fracture "wake lines" are visible and indicate that the direction of crack propagation was toward the lower right corner of the fractograph. These wake lines originate at the inclusion and run normal to the crack front in the direction of crack propagation.

Fig. 15. Ductile fatigue striations in aluminum alloy 2024-T3

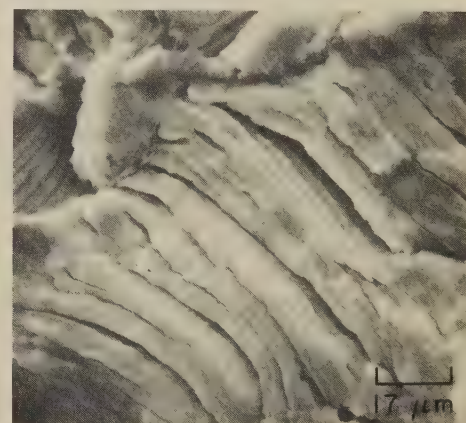


SEM fractograph

1200×

Crack propagation was from bottom to top in this view. In each fatigue patch, the bend in the crack front, as indicated by the bend in the ductile fatigue striations, is associated with the difference in orientation of a [110]-type direction in two different (100) planes.

Fig. 16. Dependence of orientation of the fatigue crack front on crystallographic structure in aluminum alloy 2024-T3



SEM fractograph

600×

At high growth rates (10^{-4} in. per cycle or more), a large plastic zone exists in front of the crack, which may cause extensive secondary cracking. Each secondary crack propagates as a fatigue crack, creating a network of secondary fatigue striations. The local crack direction, which is toward the upper right, may differ markedly from the over-all direction of crack propagation because of the chaotic nature of the fracture surface.

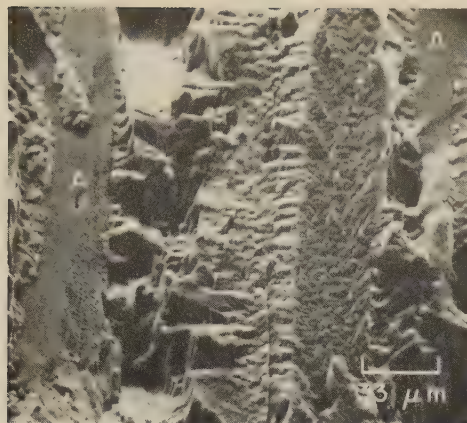
Fig. 17. Ductile striations in a fatigue fracture in aluminum alloy 2024-T3 that occurred at a high growth rate caused by a high range of stress intensity (ΔK) at the crack tip

plateaus separated by longitudinal ridges. The plateaus are usually normal to the direction of maximum tensile stress. Figure 13 shows a transition from stage I to stage II in a coarse-grained specimen of aluminum alloy 2024-T3. Orientations and levels of facets change from grain to grain, as shown in Fig. 14, which is an over-all view of stage II of fatigue-fracture progress in a fine-grained specimen of aluminum alloy 2024-T3.

Figures 15, 16 and 17 present details of "ductile" fatigue striations in stage II of fracture progress in aluminum alloy 2024-T3. At high rates of crack growth (Fig. 17), the striations become wavy, with a rough front, and many secondary cracks are observed. In aluminum alloys tested in a corrosive environment (water or seawater), the striations form on crystallographic fracture planes and are called "brittle" striations (Fig. 18). Within each grain the fracture path associated with

corrosion fatigue looks like a cleavage plane. Because of the difference in orientation from grain to grain, part of the crack front will propagate in a ductile manner, creating alternate patches of ductile and brittle striations. At high rates of crack growth, transgranular corrosion fracture is accompanied by extensive dimple formation around large inclusions (Fig. 19).

In steels, fatigue striations that are formed at ordinary crack-growth rates are not always as well-defined as they are in aluminum alloys. Figures 20 and 21 show typical fatigue-fracture surfaces in type 304 stainless steel and in 18% Ni, grade 250, maraging steel. The striations that are formed at very low crack-growth rates (less than 5×10^{-6} in. per cycle)

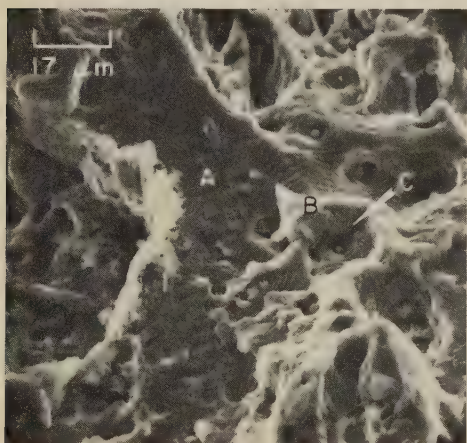


SEM fractograph

300×

The presence of seawater at the crack tip changed the topography of the fatigue striations from ductile to brittle. Brittle striations indicate corrosion fracture in most aluminum alloys. The roughness of the fracture surface is the result of the crystallographic mode of fracture. Two patches of ductile striations are visible at A. Direction of crack propagation was from bottom to top in this view.

Fig. 18. Brittle striations in a corrosion-fatigue fracture in aluminum alloy 7075-T6



SEM fractograph

600×

Fracture shows brittle striations, such as at A, and tearing, such as at B, around dimples initiated by inclusions, such as at C. There are patches of ductile fatigue striations adjacent to the dimples. The chaotic nature of the fracture path is related to the large size of the plastic zone ahead of the crack tip.

Fig. 19. Corrosion-fatigue fracture in aluminum alloy 7075-T6 that occurred at a high growth rate caused by a high range of stress intensity (ΔK) at the crack tip

are difficult to resolve and often cannot be distinguished from the network of slip lines and slip bands associated with plastic deformation at and near the fracture surface. Under these circumstances, measurement of striation spacing is difficult, if not impossible.

Intergranular Fracture

Intergranular fracture is simply described as grain-boundary separation. It can occur by catastrophic brittle separation, or by separation plus microvoid coalescence on the interfaces of grains. Such fractures are regarded as the result of a severe reduction in grain-boundary energy by a Gibbsian (thermodynamic) adsorption mechanism. In its simplest form, segregation of metallic or gas-metal

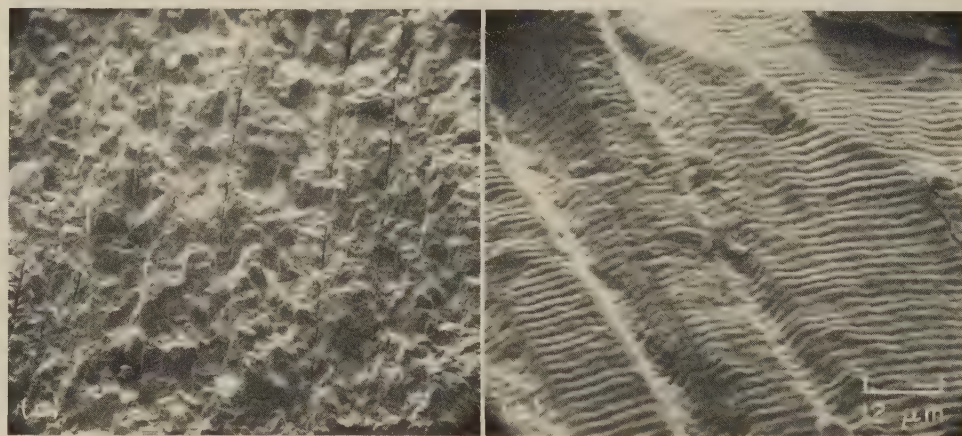
impurities can alter the grain-boundary free energy. Furthermore, grain-boundary energy can vary over a temperature range, leading to brittle-ductile fracture transitions and thermally induced brittle or ductile fractures. Variations in segregation at grain boundaries can also lead to mixed mechanisms of fracture, characterized by the appearance of dimpled areas in an intergranular fracture. Intergranular brittle fracture is usually the result of segregation of a thermally activated impurity, which allows the grains to separate along smooth interfacial planes. Typical examples of fractures involving grain-boundary segregation are shown for tungsten, iridium and a tungsten-rhenium alloy in Fig. 22. In the fracture in iridium (Fig. 22b), phosphorus segregation was detected at the exposed grain surfaces by Auger electron spectroscopy. Bulk atomic-absorption spectroscopic analysis showed 5 ppm of potassium in the pure tungsten (Fig. 22a), and 50 ppm of potassium in the tungsten-rhenium alloy (Fig. 22c). The presence of potassium at the surface of the fracture in the tungsten-rhenium alloy was confirmed by Auger electron spectroscopy. Concentrations of potassium at the grain boundaries are thought to have given rise

to the microvoids or "bubbles" that are visible on the fracture surface (Fig. 22c).

With hydrogen embrittlement, intergranular fracture can occur as shown in Fig. 23. Fracture can occur early under sustained loading if the metal was previously embrittled, or it can result from progressive embrittlement in salt air under service loadings. Depending on the environment, the fracture surface may display greater or lesser amounts of corrosion products.

Intergranular fracture also results from stress-corrosion cracking, as shown in Fig. 24. Corrosion products are frequently observed on the separated-grain facets of stress-corrosion cracks (Fig. 24d). Often the intergranular mechanism will be active in only a portion of the fracture if penetration by stress corrosion is only partial. Beyond the corrosion penetration, there will be evidence of ductile fracture by microvoid coalescence, as shown in Fig. 24(b).

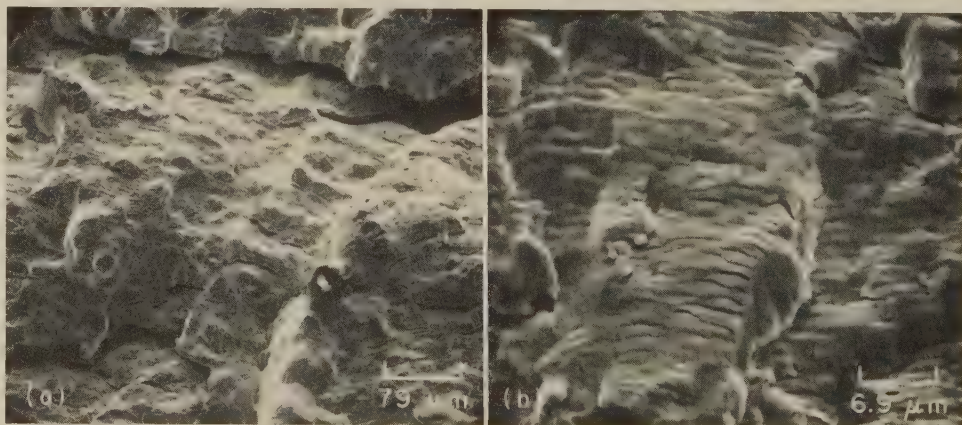
Intergranular fracture is identified by the presence of separated-grain facets and should be considered the major mechanism of fracture if such facets constitute a statistically significant portion of the fracture surface. Furthermore, when fracture proceeds along grain



SEM fractographs

39× (a); 810× (b)

Fig. 20. Fatigue fracture in type 304 stainless steel tested at room temperature. The vertical secondary cracks in (a) are grain-boundary separations. The well-defined striations in (b) resulted from the planar slip characteristic of stainless steels.



SEM fractograph

125× (a); 1440× (b)

Extensive secondary cracking can be seen in the lower-magnification fractograph (a), and is clearly evident in the one at higher magnification (b). Secondary cracks formed at the roots of many fatigue striations. The range of stress intensity (ΔK) at the crack tip was 76.9 MPa·m^{1/2} (70 ksi·in.^{1/2}).

Fig. 21. Fatigue fracture in 18% Ni, grade 250, maraging steel tested at room temperature



SEM fractographs

(a) Sintered tungsten rod drawn to 0.060-in. diam, recrystallized at 10^{-6} torr and 2600 C (4712 F) for 100 hr, fractured in tension. (b) Iridium sheet annealed for 50 hr in purified helium at 1700 C (3092 F), broken by bending.

(c) Tungsten - 3 wt % rhenium alloy that was prepared in the same manner as the sintered tungsten rod in fractograph (a). Microvoids ("bubbles") at grain boundaries resulted from segregation of potassium (an impurity).

Fig. 22. Intergranular brittle fractures in tungsten, iridium, and a tungsten - 3 wt % rhenium alloy

boundaries, river patterns are completely absent, and it is usually easy to identify triple points at which three (or more) grain boundaries meet.

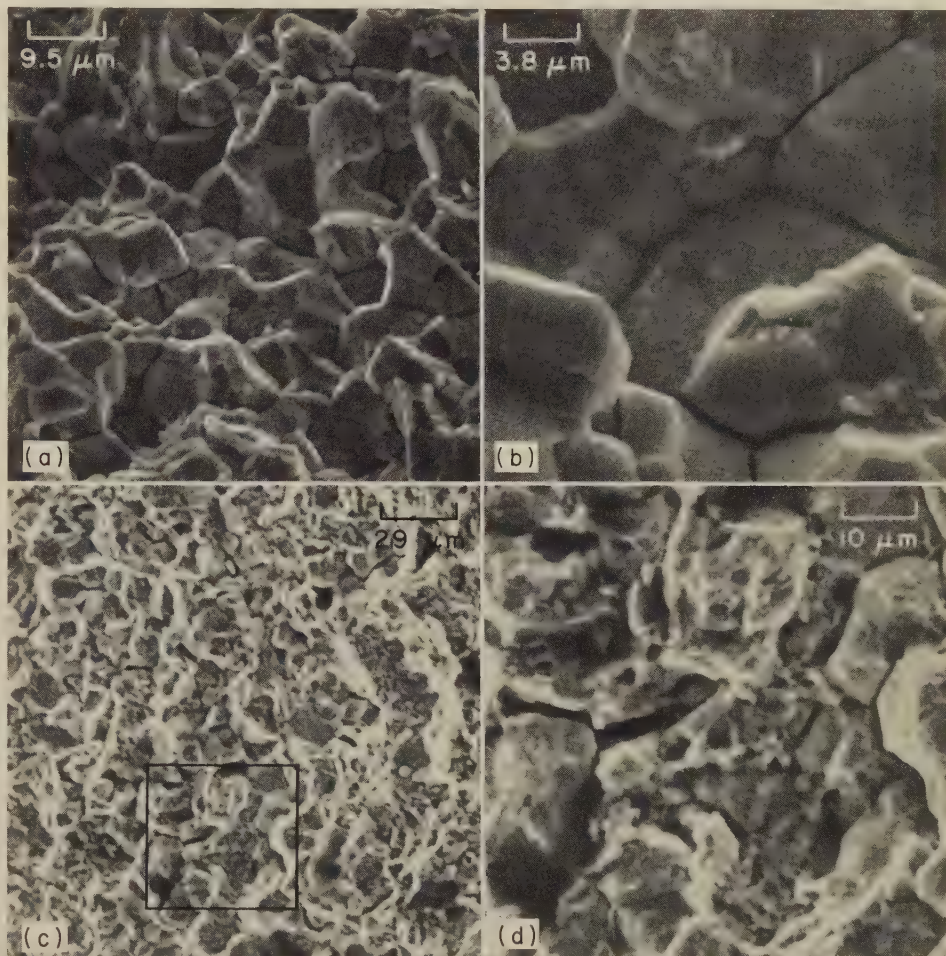
Features Indicative of Mixed Mechanisms of Fracture

A fracture that occurs by operation of two or more intermingled mechanisms of fracture is generally labeled a "mixed-mode" fracture. This is not to be confused with the successive operation of different fracture mechanisms, which can be analyzed sequentially and therefore require no special discussion. The occurrence of fracture by mixed mechanisms often indicates (a) that the usual factors that determine the operative mechanism, such as state of stress, loading history, microstructure and environment, favor both mechanisms; and (b) that the local fracture mechanism is determined by a combination of deviations in these factors and the influence of secondary variables, such as local grain orientation.

The reasons for mixed mechanisms of fracture are as diverse as the fractures in which they have been observed. However, it is useful to identify the individual fracture mechanisms that contribute to such mixtures and to establish the circumstances that can lead to their individual occurrence. These circumstances establish limits. The occurrence of mixed mechanisms of fracture usually indicates that interacting influences have caused the fracture to depart from either limiting mechanism. The following examples will be discussed on this basis; however, it should be remembered that the specific circumstances that result in the observed fracture may well be peculiar to the specific situation described.

The fracture mechanisms that will be treated in combinations are (a) transgranular cleavage, (b) microvoid coalescence, (c) tearing, (d) fatigue-striation formation, and (e) intergranular fracture. These mechanisms are individually described in the preceding sections, and no additional discussion is needed here. The fracture mechanisms will be taken in pairs that are representative of most of the possible mixed-fracture situations.

Cleavage plus microvoid coalescence is a mixture of fracture mechanisms that can occur in alpha and alpha-beta titanium alloys by stress-corrosion crack-



SEM fractographs

(a) and (b). Low and high-magnification fractographs of a 4340 steel test specimen that fractured at 75% of its yield strength due to hydrogen embrittlement following exposure to a 2% NaCl solution. (c) and (d). Two fractographs of the fracture in a

1050× (a); 2600× (b); 350× (c); 1000× (d) cadmium-plated helicopter rotor of 4340 steel (with vanadium added) after exposure to a marine environment. The outlined region in (c) is shown at a higher magnification in (d). Corrosion products are visible on the separated-grain facets.

Fig. 23. Two examples of intergranular fracture resulting from hydrogen embrittlement

ing and in low-alloy steels at temperatures within the ductile-brittle-transition temperature range. With the titanium alloys, the cleavage plane lies near the basal plane of the hexagonal alpha phase. Thus, in single-phase alpha titanium alloys, the grains that are oriented with their *c*-axes parallel to the stress axis have a high normal stress component on the cleavage plane and will fracture by cleavage. Grains with different orientations will have lower resolved normal

stresses and can undergo plastic deformation and exhibit a ductile mechanism of fracture—often dimple formation by microvoid coalescence. In alpha-beta titanium alloys, the regions of beta phase, or beta transformation product, are usually not susceptible to cleavage fracture in a stress-corrosion test; these regions will fracture in a ductile manner, whereas the primary alpha phase will fracture by cleavage. Mixed fracture mechanisms can result from quite dif-

ferent causes, and caution must be exercised in inferring the cause of fracture from the fracture features alone. An example of a mixture of cleavage facets and dimples is shown in Fig. 25.

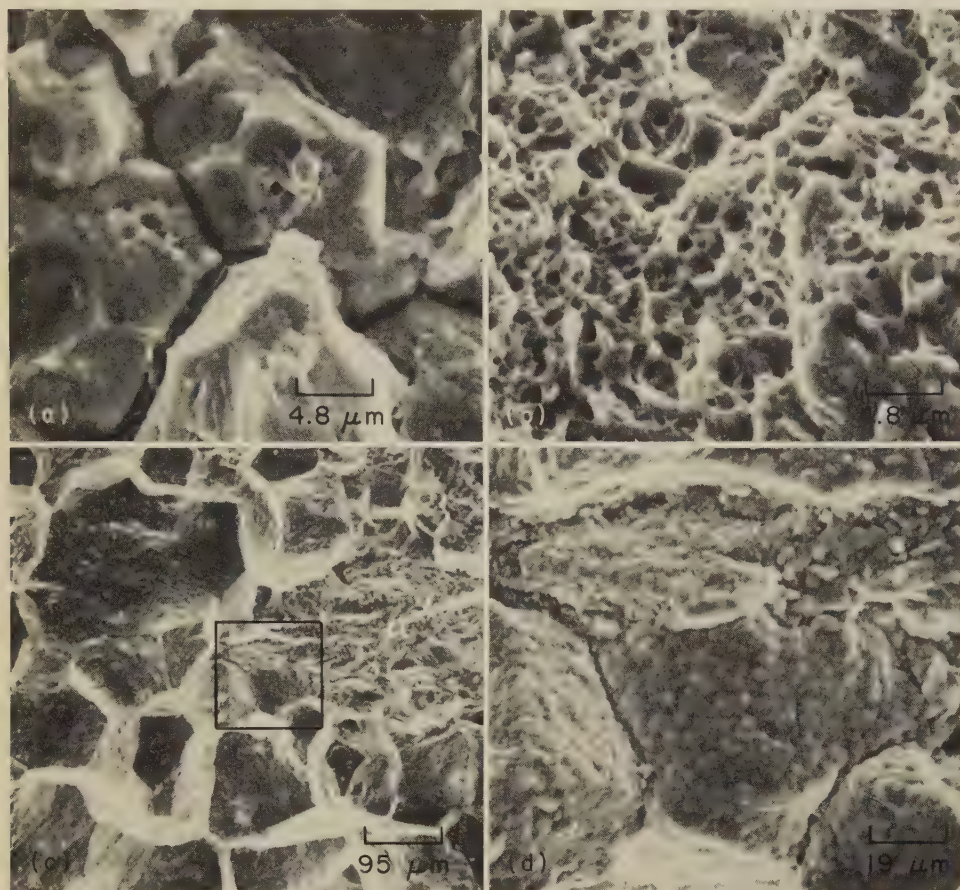
Cleavage plus tearing occurs in anisotropic single-phase metals that have high ductility and moderate strength, and in

two-phase systems in which the phases have different mechanical properties or crystal-lattice symmetry. Tearing can occur in place of the microvoid coalescence described in the preceding paragraph if the ductility is sufficiently high and the flow stress sufficiently low that the material can fracture by slip. The variations

in metal properties that promote tearing instead of dimple formation are complex and insufficiently understood to permit detailed analysis. In the present context, it is sufficient to say that tearing is indicative of extensive ductility. An example of a fracture resulting from cleavage plus tearing is shown in Fig. 26.

Cleavage plus fatigue-striation formation is observed in high-strength, low-ductility metals and in metals of lower crystallographic symmetry (see the fracture in alpha titanium in Fig. 27). Those grains that are favorably oriented with respect to the cyclic stress axis fracture by sudden cleavage, and those oriented to relax the load by cyclic plastic relaxation fracture incrementally by fatigue.

Cleavage Plus Intergranular Fracture. Both cleavage fracture and intergranular fracture are characteristically low-energy mechanisms, and the simultaneous opera-

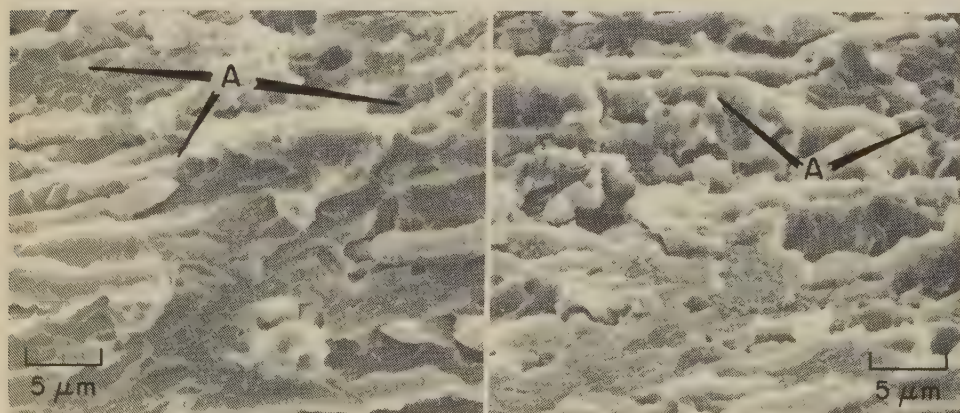


SEM fractographs

(a) and (b). Fracture in a 300M steel aircraft landing gear that resulted from stress-corrosion cracking. The stress-corrosion-cracking portion of the fracture is intergranular, as shown in (a). Beyond the corrosion penetration, the fracture induced by the cracking is transgranular dimpled rupture, as shown in (b).

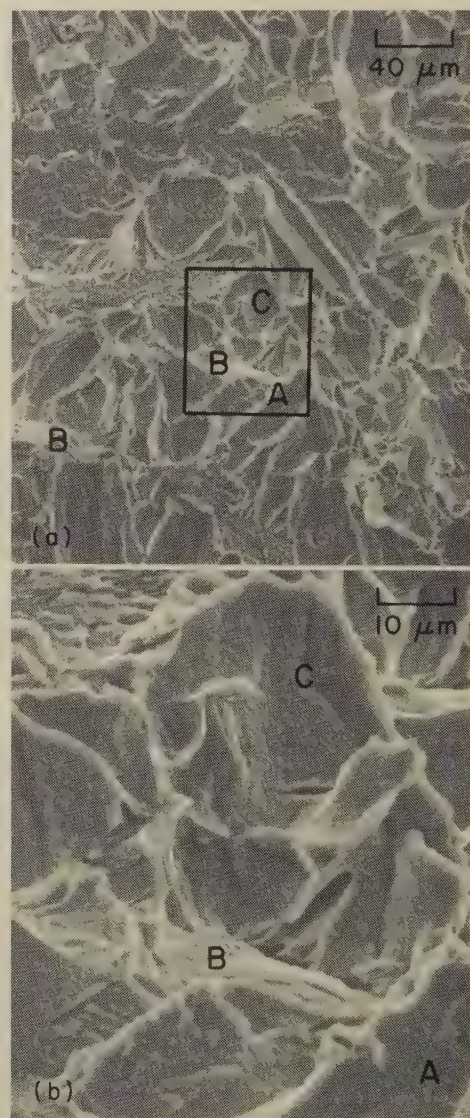
(c) and (d). Fracture in a U-700 turbine blade. Fracture is presumed to have been the result of combustion-gas attack, which induced stress-corrosion cracking. The region outlined by the rectangle in (c) is shown at a higher magnification in (d), which makes the corrosion products on the separated-grain facets more easily seen.

Fig. 24. Intergranular stress-corrosion fractures, and a region of transgranular fracture induced by stress-corrosion cracking



SEM fractographs

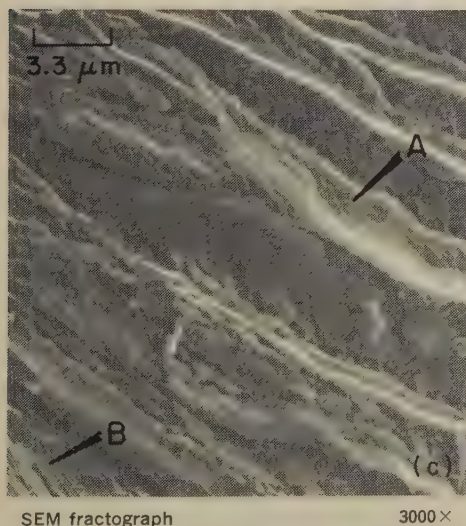
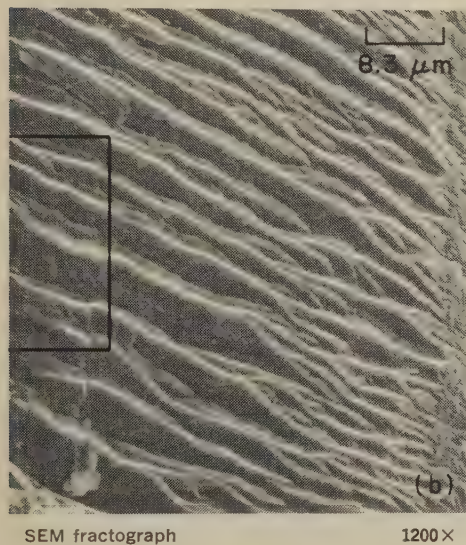
Fig. 25. Intermingled cleavage facets and dimples in two views of a stress-corrosion fracture in a step-cooled two-phase Ti-6Al-2Sn-4Zr-6Mo alloy exposed to a 3½% NaCl aqueous solution. Cleavage facets formed in the alpha phase, and poorly developed dimples, such as at the sites marked A, formed in the beta phase.



SEM fractographs

The region outlined in fractograph (a) is shown at higher magnification in fractograph (b). Cleavage facets are visible, such as at A, separated by areas of tearing, such as at B. A number of large, smooth facets, such as at C, are believed to have been caused by plastic shear. The area of tearing, B, in fractograph (b) could be mistaken for fatigue striations.

Fig. 26. A fracture formed mainly by cleavage and tearing in unalloyed titanium



Essentially all of the features in (a) are cleavage facets with highly developed river patterns of cleavage steps. In (c), very fine fatigue striations can be detected between cleavage steps, as at A and B. The outlined regions in (a) and (b) are shown at higher magnifications in (b) and (c), respectively.

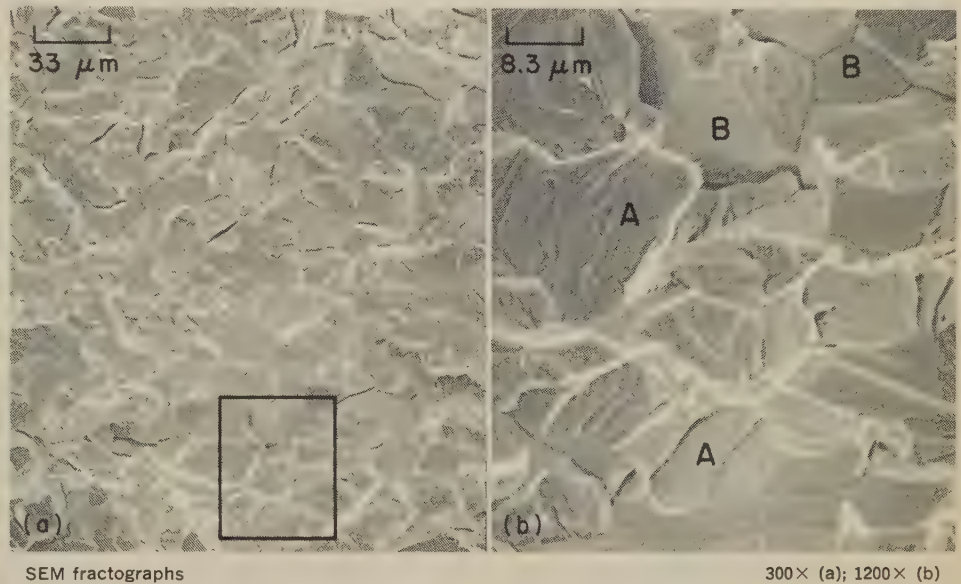
Fig. 27. Fracture surface of an alpha titanium alloy showing regions of cleavage facets interspersed with minute regions of fatigue striations that are visible only at high magnification

tion of both can occur when the resolved stresses for grain-boundary separation and for transgranular cleavage are approximately equal. Also, if the preferred grain-boundary fracture path is not continuous and if the cleavage stress is relatively low, the regions that do not fracture intergranularly can fracture by cleavage. An example of this type of fracture is shown in Fig. 28.

Microvoid coalescence plus tearing is often observed in high-strength, high-toughness structural materials such as titanium and steel. Occurrence of fracture by microvoid coalescence at numerous sites ahead of the main crack front and the subsequent linking of these regions by tearing is the most common

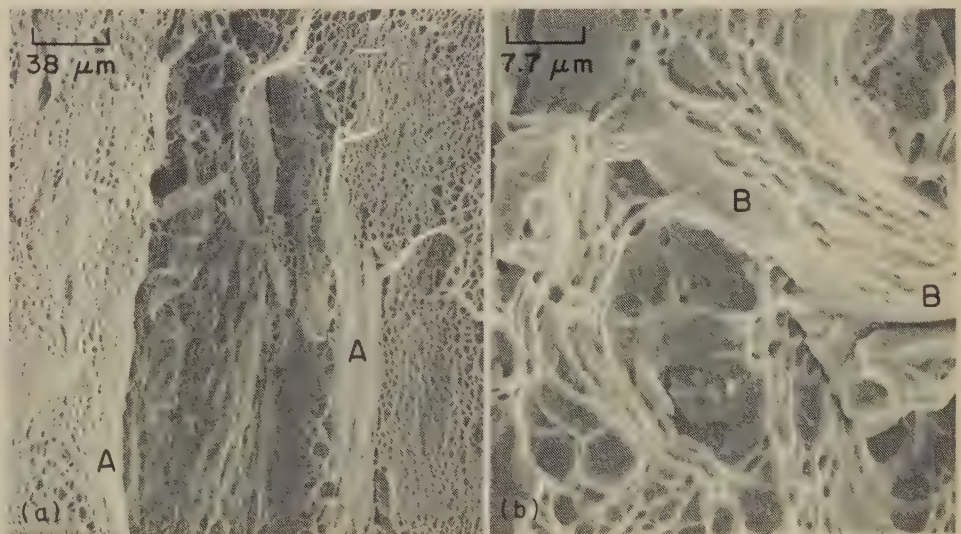
form of this mixture of fracture mechanisms. This type of fracture occurs frequently in two-phase metals such as titanium alloys, where one phase is susceptible to fracture by tearing. An example of a combination of these fracture mechanisms is shown in Fig. 29.

Microvoid Coalescence Plus Fatigue-Striation Formation. The principal factor that promotes dimple formation by microvoid coalescence is the propensity of the material to nucleate microvoids compared to its susceptibility to some other type of fracture. Also, external factors such as stress state and strain rate can influence the mechanism by which fracture occurs. Metals that contain hard particles show a strong tendency toward



This fracture surface is largely made up of cleavage facets, as at the sites marked A in fractograph (b), but intermingled with the cleavage facets are intergranular fracture surfaces, as at the sites marked B. The outlined region in fractograph (a) is shown at higher magnification in fractograph (b).

Fig. 28. Combined cleavage and intergranular fracture in alloy Cb-752 (Cb-10W-2.5 Zr) containing 750 wt ppm of oxygen



This fracture surface contains a mixture of dimples (much in the majority) and regions of tearing. Fractograph (a) shows extensive regions of dimples adjacent to two tear ridges, marked A. Fractograph (b), at a higher magnification, shows details of regions of tearing, marked B, adjacent to dimpled regions.

Fig. 29. Fracture surface resulting from microvoid coalescence plus tearing of a tensile-test specimen of Ti-8Mo-8V-2Fe-3Al that had been quenched from 900 C (1652 F) and aged 144 hr at 350 C (662 F)

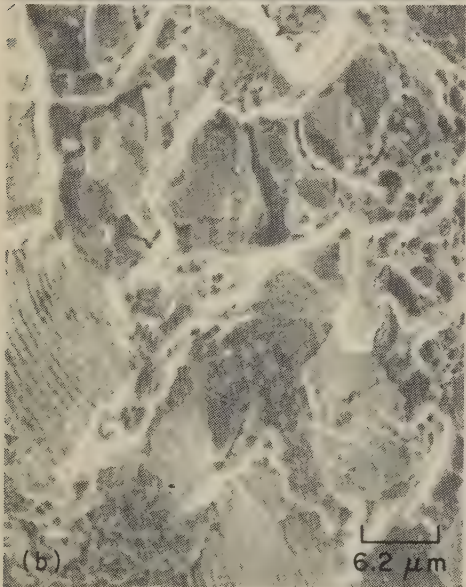
microvoid formation under overloading conditions and are also likely to show mixed dimples and striations under fatigue loading conditions, especially at cyclic stress-intensity levels approaching that for rapid fracture. An example of this type of fracture in aluminum alloy 2024-T851 is shown in Fig. 30.

Microvoid coalescence plus intergranular fracture is less commonly observed than tearing plus intergranular fracture. In metals that have a preferred but incompletely developed intergranular fracture path, the remaining material can fracture by microvoid coalescence. When this fracture mixture is observed, intergranular fracture typically accounts for a lower percentage of the fracture area than it does in tearing plus intergranular fracture. An example of this type of fracture is shown in Fig. 31.

Tearing plus fatigue-striation formation is a common type of fracture. It occurs at cyclic stress-intensity levels that approach the K_{Ic} of the metal. That is, intermixed regions of ductile tearing and striations are often seen in fatigue specimens with crack depths approaching that which corresponds to catastrophic fracture. The local variations in fracture type are probably related to local variations in grain orientation. For example, one grain may fracture by fatigue whereas an adjacent grain may be so oriented that it sustains heavy shear-band formation and fractures by tearing. The next grain may fracture by fatigue, leading to the mixed mechanisms shown in Fig. 32 and 33.

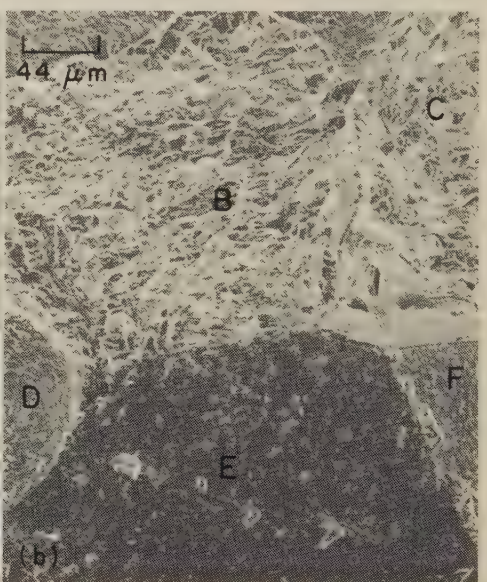
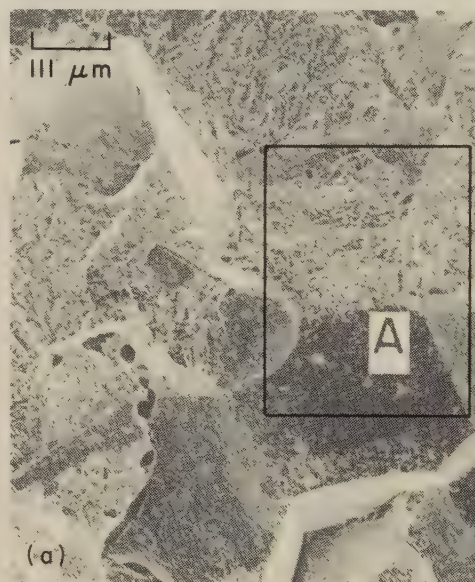
Tearing plus intergranular fracture is a relatively common mixture of fracture mechanisms, especially in materials such as carburized steels, which typically ex-

hibit intergranular fracture in the fully hardened case. In these materials, particular combinations of such factors as strain rate and temperature can promote the fracture of some grains by tearing. An example of such a mixed-mechanism fracture is shown in Fig. 34. Other metals in which mixed intergranular fracture and tearing have been observed are hydrogen-embrittled Monel (see Fig. 35) and temper-embrittled steel. In these metals, the occurrence of this mixture of fracture mechanisms indicates a degree of embrittlement lower than that which would lead to completely intergranular fracture. This lower degree of embrittlement might result from a less severe environment (low hydrogen pressure) in hydrogen-embrittled Monel, and from incomplete grain-boundary segregation in temper-embrittled steel.



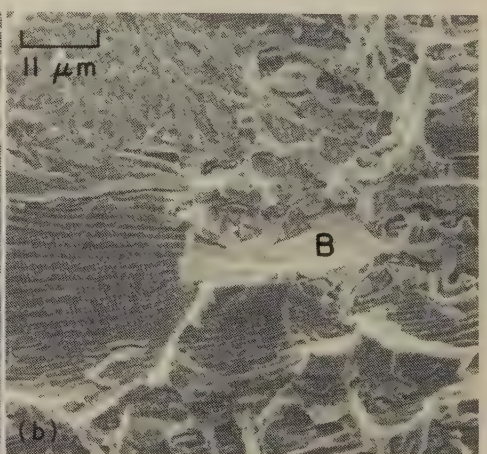
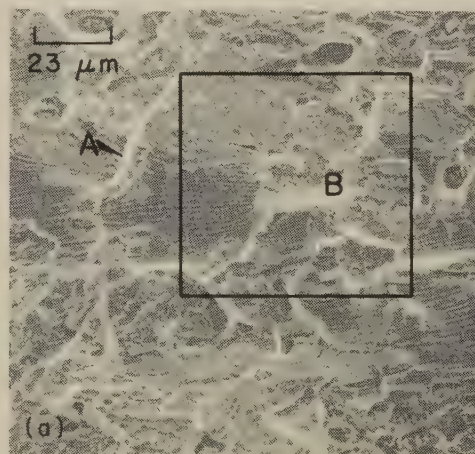
SEM fractographs Both at 1600×
Orientation of fatigue striations differs from patch to patch, particularly in fractograph (a). Dimples in fractograph (b) are associated with inclusions.

Fig. 30. Intermingled dimples and fatigue striations in low-cycle fatigue-test fractures in aluminum alloy 2024-T851 at a high range of stress intensity (ΔK) at crack tip



SEM fractographs 90× (a); 225× (b)
Fractograph (b) is a higher-magnification view of the outlined region at A in fractograph (a). It displays regions of dimples formed by microvoid coalescence, such as those at B and C, interspersed with regions of intergranular fracture surfaces, such as those at D, E and F.

Fig. 31. Mixture of dimples and intergranular fracture surfaces in a fracture in a 3340 steel specimen that had undergone incomplete reversible temper embrittlement



SEM fractographs 440× (a); 880× (b)
In fractograph (a), tear ridges can be seen between fatigue-striation patches, as at arrow A. Fractograph (b) is a view at higher magnification of the region outlined by the rectangle in (a). Also present are broader areas of tearing, such as at B, that have some resemblance to glide-plane decohesion or stretching.

Fig. 32. Fracture surface showing mixed tearing and fatigue-striation formation in a fatigue-test specimen of aluminum alloy 7075-T6

Fatigue-striation formation plus intergranular fracture is the cyclic-loading analog of intergranular fracture plus either tearing or microvoid coalescence. It typically occurs in metals that have incompletely developed preferred fracture paths at the grain boundaries. In such metals, intergranular fracture occurs in the regions that have a preferred grain-boundary fracture path. The remaining regions cannot readily fracture intergranularly; they fracture in fatigue and exhibit the usual striations associated with transgranular fatigue cracking. This type of fracture occurs much less frequently than the other mixed mechanisms. However, Fig. 44 and 45 show both fatigue striations and separated-grain facets in Monel 400.

Features of Fractures Resulting From Chemical and Thermal Environments

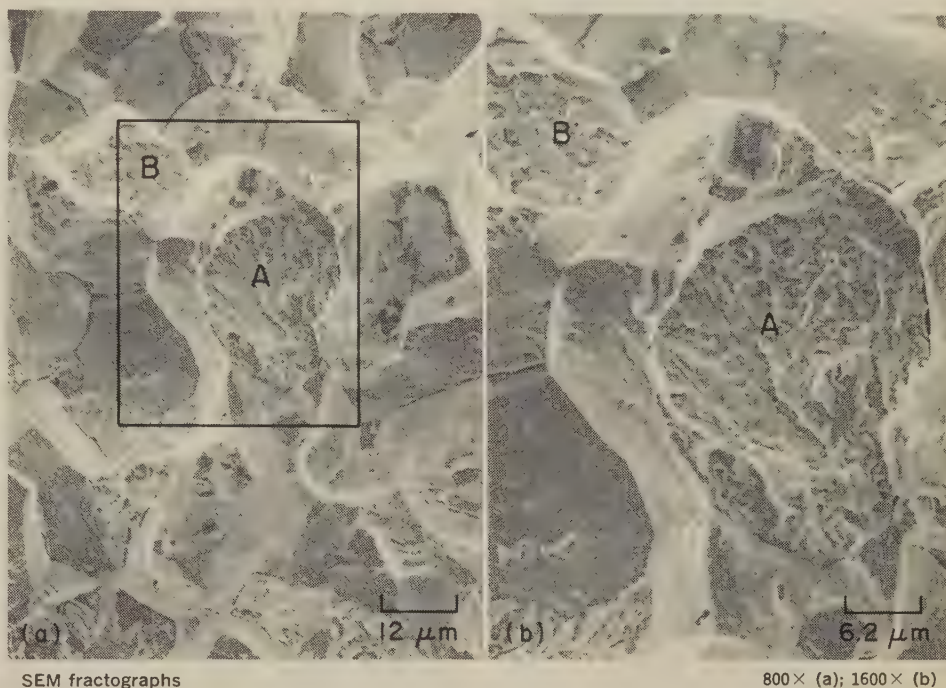
For a specific metal or alloy, certain fracture mechanisms, such as cleavage, microvoid coalescence, fatigue, and intergranular separation, are often associated with particular environmental and stress states. The accumulation of experience with such fractures arising from known states of environment and stress makes it possible to ascertain, with the aid of fractography, the causes of fractures occurring under unknown service conditions. Some instances in which environment caused a specific fracture response that can be characterized through electron-microscope fractography are indicated in this section; other instances are indicated in the counterpart section that begins on page 90 in this volume.

For example, alpha and alpha-beta titanium alloys fracture by microvoid coalescence when overloaded, regardless of temperature. In low-carbon steel, simi-

lar features are observed only if the temperature at fracture is above the nil-ductility transition temperature of the steel. Below this temperature, the steel fractures by transgranular cleavage. Other fracture mechanisms in titanium alloys (corrosion fatigue, stress-corrosion cracking, hot-salt cracking, or liquid-metal embrittlement) can result in fracture surfaces that exhibit fatigue striations, transgranular cleavage, or intergranular fracture. When these mechanisms are

operative, the association of dimple formation with overstress is not maintained and an analysis of the fracture surface is not straightforward.

High-Temperature Fractures. Overload fractures as the result of stress rupture or high-temperature creep are often initiated by nucleation of microvoids at grain-boundary quadruple points as a result of grain-boundary sliding or local melting. Subsequent vacancy diffusion and slip can enlarge the voids into fissures, which

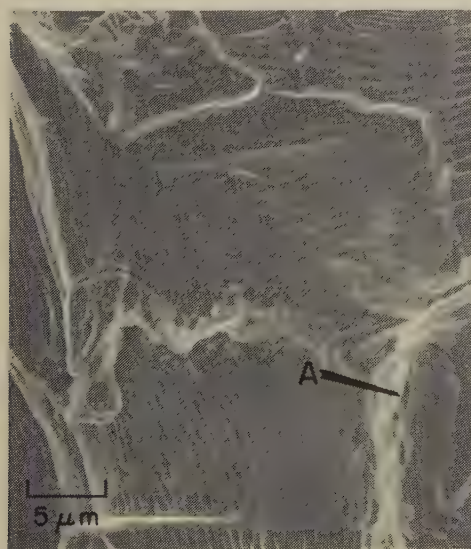


SEM fractographs

800× (a); 1600× (b)

The combination of strain rate and temperature was conducive to the fracture of some grains by tearing, as at A and B, in a fracture that otherwise was very definitely intergranular. Fractograph (b) is a higher-magnification view of the outlined region in fractograph (a). The transgranular facets at A and B show light-toned lines that are presumed to be tear ridges.

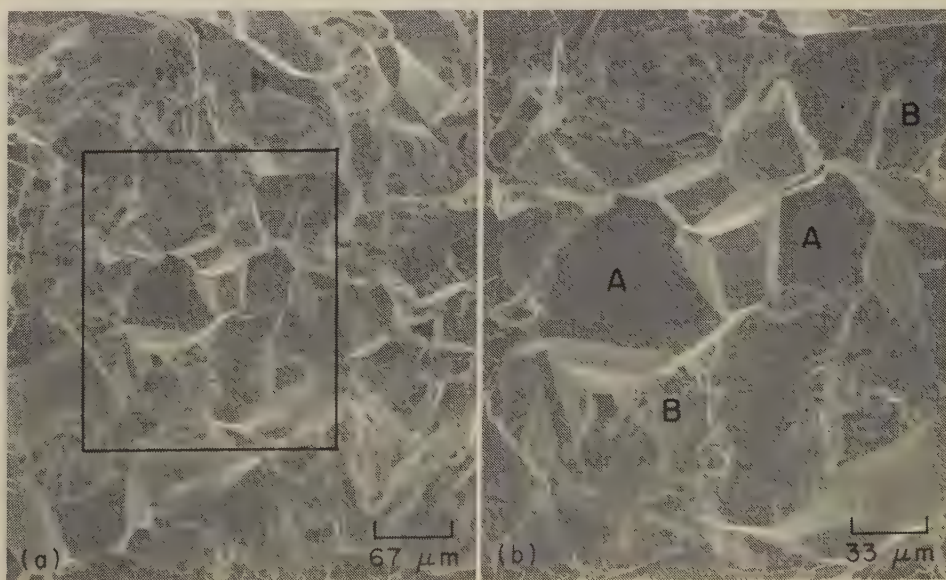
Fig. 34. Fracture surface through the fully hardened case of a carburized low-alloy steel, showing a mixture of tearing and intergranular separation



SEM fractograph

2000×

Fig. 33. Fracture surface of a fatigue-test specimen of unalloyed titanium, showing patches of fatigue striations separated by narrow tear ridges, as at A. The pronounced variations in striation orientation indicate local changes in the direction of fatigue-crack propagation.



SEM fractographs

150× (a); 300× (b)

Fractograph (b) is a higher-magnification view of the outlined region in fractograph (a). Separated-grain facets are clearly evident, as at A, and adjacent grains display transgranular-fracture facets bordered by tear ridges, as at B.

Fig. 35. Fracture surface of a Monel specimen, showing a mixture of tearing and intergranular fracture. Specimen was fractured in a gaseous hydrogen environment.

propagate along the grain boundaries, resulting in intergranular cracking. As an example of a high-temperature fracture of this type, Fig. 36 shows a fracture surface of an aluminum alloy 1100 tube that fractured at a temperature at or near its melting point. Separation occurred along the grain boundaries. The grains are elongated and their edges are rounded.

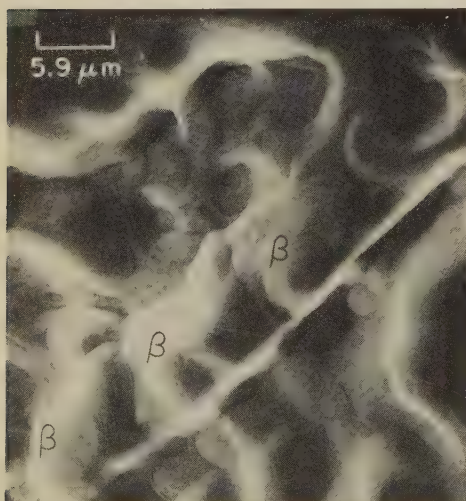


SEM fractograph

640×

Grains are elongated and have rounded edges. They lack the usual flat grain facets seen in room-temperature intergranular fractures. The grain surfaces show evidence of oxidation, which must have occurred at the elevated temperature during and after final fracture.

Fig. 36. Fracture surface produced by stress rupture in an aluminum alloy 1100 tube stressed at 3.45 MPa (500 psi) at a temperature at or near the melting point of the alloy



SEM fractograph

1700×

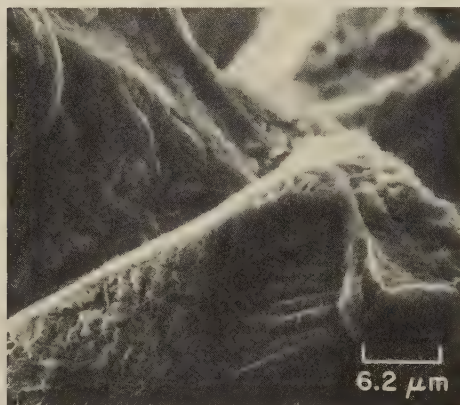
The fracture surface contains many voids and hills having a geometric pattern of facets with steps. The letters β mark three hills.

Fig. 37. Separated-grain surface near the edge of a fracture in a specimen of OFHC copper creep tested at 540 C (1004 F) and a stress of 10.3 MPa (1.5 ksi) (Ref 4)

They do not show the flat, smooth facets that would be expected with low-temperature intergranular fracture. Oxidation of the grain surfaces during and after final fracture is evident from the fine surface texture.

When stress and temperature are such that fracture occurs only after an extended period, the separated-grain surfaces can exhibit complex patterns of voids and hills having superimposed facets with steps. Figure 37 shows such a separated-grain surface near the edge of a fracture in a specimen of OFHC copper broken in creep testing at 540 C (1004 F) and a stress of 10.3 MPa (1.5 ksi).

Exposure of certain alloys to high temperatures can result in embrittlement and subsequent intergranular fracture as



SEM fractograph

1620×

Fig. 38. Intergranular fracture in copper alloy CDA No. 715 (copper nickel, 30%) that became embrittled by grain-boundary oxidation during extended exposure to high-temperature steam in a heat exchanger. Crack penetration (which was cyclic, as intergranular layers of oxide formed, broke and re-formed) produced fine striations that could be mistaken for fatigue striations.



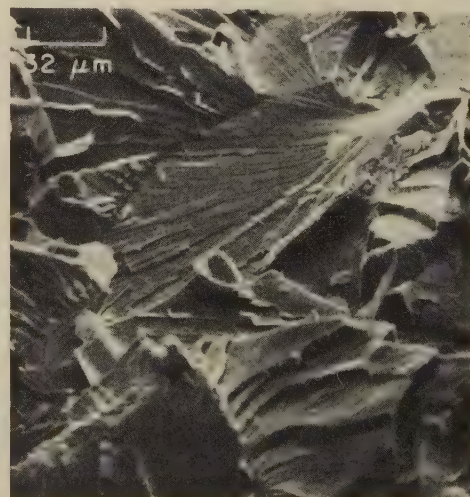
SEM fractograph

1800×

Fig. 39. Intergranular stress-corrosion fracture in vanadium-modified 4340 steel that occurred after exposure to a salt-water environment. Secondary intergranular cracks nearly surround some of the grains. The fracture is almost 100% intergranular except for local regions (see arrowheads), where some evidence of ductile fracture exists.

a consequence of internal oxidation along grain boundaries. Figure 38 shows the grain facets developed in copper alloy CDA No. 715 (copper nickel, 30%) that fractured after extended exposure to high-temperature steam in a heat-exchanger application. The grain boundaries had been altered by the formation of nickel and copper oxides, and fracture had propagated through the brittle oxide layer. Separation can occur discontinuously as the oxide is formed, broken and re-formed. The resulting fracture will show the cyclic nature of crack propagation, evidenced as a series of microstriations similar to those formed in fatigue. A continuous fracture propagated through a previously oxide-embrittled microstructure may show intergranular facets that are modified only by the oxide layers and deformation lines associated with the plasticity generated during fast fracture.

Stress-Corrosion Cracking and Hydrogen Embrittlement. Fractures in quenched-and-tempered high-strength steels by stress-corrosion cracking and hydrogen embrittlement are intergranular when the stress intensity at the tip of the propagating crack is low. The fracture path is along prior austenite grain boundaries, and the fine detail revealed on the grain facets can be related either to plasticity effects associated with the fracturing process or to corrosion effects associated with certain aqueous environments, when these are present. The intergranular fracture that developed in a vanadium-modified 4340 steel that had been exposed to a salt-water environment is shown in Fig. 39. The highly crystalline surface shows very little transgranular cracking, and no indication of the existing martensitic structure is evident. The grain facets show evidence of some ductility during fracture, but it is confined to the extremely narrow regions of the grain boundaries. Secondary cracking normal



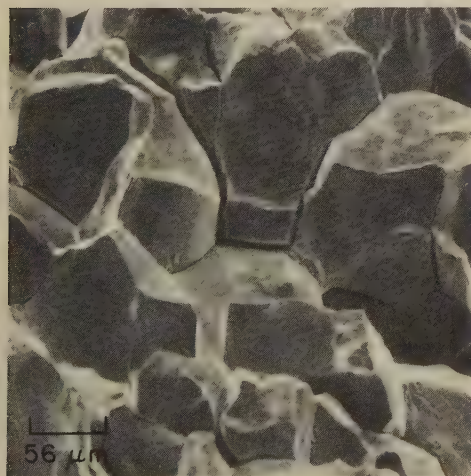
SEM fractograph

315×

Fig. 40. Transgranular stress-corrosion fracture in a pressure vessel of type 316 stainless steel that broke after extended exposure to a chloride-containing environment at elevated temperatures and pressures. Individual grains are outlined by changes in direction of local cleavage. River patterns in facets are separated by tear ridges.

to the main fracture plane is indicated by the cracks extending around some of the grains. In this steel, overload fractures at low temperatures and quench cracking also are characterized by fracture at prior austenite grain boundaries. Quench cracks may or may not be connected with an external surface. If the cracks reach or are generated from an external surface, their surfaces will become oxidized in a subsequent tempering treatment. The resulting oxide film is usually dark and tightly adherent. It is readily recognizable and is quite unlike ambient-temperature corrosion products. The thinness of the oxide coating, however, prevents its being resolved in the scanning electron microscope. Where the quench cracks are entirely internal, there will be no identifying film and no inherent characteristic that will differentiate them from cracks caused by residual internal stress aggravated by service stresses.

The fracture path resulting from stress-corrosion cracking can be either intergranular or transgranular. The same alloy system will often show both types of fracture, depending on the state of cold work, heat treatment, or other variable. One such alloy system is the austenitic stainless steels. Exposure of these alloys to aqueous environments containing chloride ions often results in stress-corrosion cracks that propagate in a highly branched system of transgranular cleavage cracks. Figure 40 shows the fracture topography resulting from a service fracture of a pressure vessel made of type 316 austenitic stainless steel. The vessel cracked after extended use in chloride-containing atmospheres at elevated temperatures and pressures. The fracture is completely transgranular. Individual grains are delineated by changes in crack elevation and propagation direction. The flat cleavage facets exhibit river patterns and tear ridges, which developed as the various cracks joined.

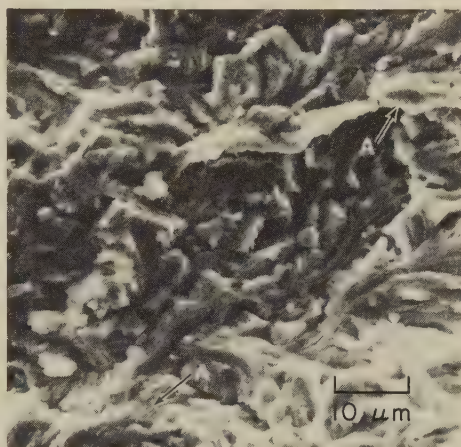


SEM fractograph 180×

Fig. 41. Intergranular corrosion fracture near a circumferential weld in a thick-wall tube made of type 304 stainless steel. The heat-affected zone of the weld was sensitized by the temperature of welding, and consequently it was susceptible to intergranular attack. Note the smooth grain facets and the secondary cracks at the grain boundaries.

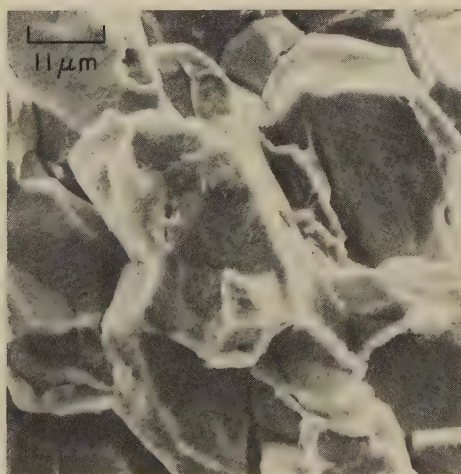
Figure 41 shows an intergranular fracture that developed near a circumferential weld in a thick-wall tube of type 304 stainless steel. Such fractures develop with or without applied stress and are considered a result of intergranular corrosion. Steels in the sensitized condition (where exposure to elevated temperatures can cause carbide precipitation at the grain boundaries and subsequent chromium depletion nearby) are particularly susceptible to intergranular cracking and fracture. For the tube in Fig. 41, high welding temperature caused the heat-affected zone to become sensitized. The grain facets are smooth and show only limited slip deformation. Secondary cracking has occurred around some grains. There is no visible evidence of carbide precipitation.

Stress-corrosion cracking in copper alloys results, for the most part, from a



SEM fractograph 1000×

Fig. 42. Transgranular stress-corrosion fracture in condenser tubing of copper alloy CDA No. 687 (aluminum brass, arsenical). Fracture originated on the inside surface of the tube and propagated radially. The two subgrain regions indicated by A's display striations of various orientations.



SEM fractograph 900×

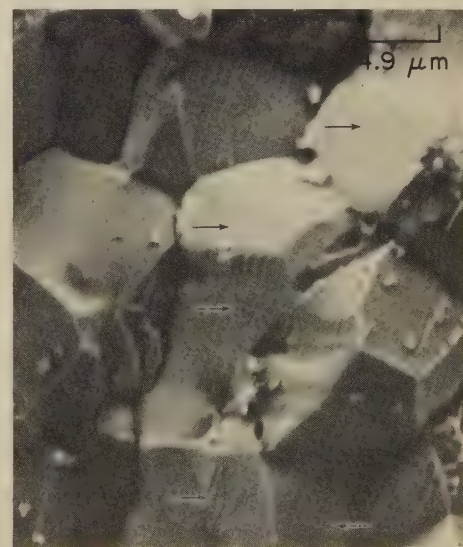
Fig. 43. Intergranular fracture in tubing made of nickel-copper alloy Monel 400, after exposure to high-temperature high-pressure steam. Secondary cracks are also intergranular. There is no grain-boundary deformation. The grainy appearance of grain facets suggests corrosion.

sustained tensile stress and the action of ammonia in the presence of moisture and oxygen. Figure 42 shows a very irregular transgranular fracture surface generated in condenser tubing of annealed copper alloy CDA No. 687 (aluminum brass, arsenical). The fracture was initiated at the inside surface of the tube and propagated radially. Although the over-all fracture plane in the central portion of the fractograph is flat, the fracture surface is composed of a large number of small regions that are inclined at random angles and contain short, fine striations. These regions are of subgrain size and probably



SEM fractograph 1350×

Fig. 44. Mixed intergranular-transgranular fracture in a specimen of Monel 400 that resulted from room-temperature, fully reversed-bending fatigue. Specimen was tested in air. Many of the regions of transgranular fracture show fatigue striations (see arrows) produced by the plastic flow that took place at the crack tip as it cyclically opened and closed.



SEM fractograph 2050×

Fig. 45. Reversed-bending fatigue fracture in a specimen of Monel 400, showing fatigue striations on separated-grain facets (see arrows). The way in which the striations formed is not understood. If it is assumed that they were produced during the closing of the crack surfaces in the compression half of the bending cycle, they might be likened to tire tracks.



SEM fractograph

1100×

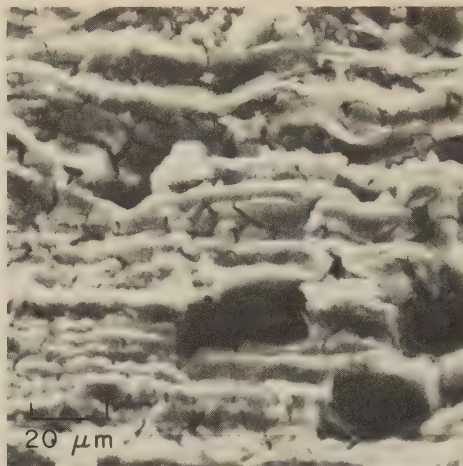
Crack propagation was by transgranular cleavage through the alpha and beta phases. Fissures normal to the cleavage plane formed at alpha-beta interfaces to produce the layered structure.

Fig. 46. Stress-corrosion cracking in titanium alloy Ti-7Al-2Cb-1Ta due to exposure to a solution of 3½% NaCl in water

result from crack interaction with precipitate dispersions in the microstructure.

Nickel-copper alloy Monel 400, which is highly resistant to stress-corrosion cracking in both the annealed and the cold worked states, has been observed to fracture, on rare occasions, in an intergranular fashion when exposed to high-temperature high-pressure steam. A fracture that occurred in Monel 400 steam-line tubing is shown in Fig. 43. The grains show no evidence of grain-boundary deformation, but their grainy surfaces suggest mild corrosion. The fracture is entirely intergranular.

Accelerated laboratory generation of fractures of the type shown in Fig. 43 in specimens of Monel 400 always requires high stress levels and an environment of ammonium hydroxide or hydrazine. The possibility that corrosion fatigue is responsible for this service fracture must, therefore, be considered. Monel 400 has been shown to exhibit decidedly intergranular fractures when fatigue tested at maximum strains near the yield point. Figures 44 and 45 show fracture surfaces from laboratory fatigue tests of Monel 400 generated in fully reversed bending. In Fig. 44, the fracture mechanism is



SEM fractograph

500×

Fig. 47. Corrosion products on a stress-corrosion fracture in cold worked type 201 stainless steel. The ridges present here correspond to bands in the microstructure. The layer of corrosion products makes it impossible to determine the mechanism of fracture.



SEM fractograph

1800×

Fig. 48. Corrosion pitting on grain-boundary facets of intergranular stress-corrosion cracks in copper alloy CDA No. 360 (free-cutting, leaded brass). Corrosive attack was assumed to have resulted from galvanic action between the brass matrix and the lead precipitate (see text).

mixed intergranular-transgranular, with some of the transgranular portions of the fracture exhibiting fatigue striations associated with the plastic flow occurring with the cyclic opening and closing of the crack tip. In Fig. 45, where the fracture is totally intergranular, evidence of the cyclic nature of the cracking can be seen in the fatigue striations on the separated-grain facets. The mechanism by which striations are formed on separated-grain

facets is not understood, but it may be associated with the closing together of the crack surfaces during the compression portion of the bending cycle. In both Fig. 44 and 45, the fracture surfaces have a different appearance than the corroded surface of the service fracture in Fig. 43.

The fracture surface generated in titanium alloy Ti-7Al-2Cb-1Ta exposed to a solution of 3½% NaCl in water is shown in Fig. 46. In the area shown, the cracking mechanism was transgranular cleavage. The cleavage crack propagated across a mixed alpha-beta microstructure. The layered surface resulted because some splitting occurred normal to the cleavage plane at the alpha-beta interfaces. An identical fracture topography results in this alloy when the environmental medium is liquid mercury, the only difference being in the orientation of the principal fracture plane relative to the hexagonal unit cell of the alpha titanium. Cracking resulting from mercury attack is parallel to the basal plane; that resulting from salt-water attack is inclined to the basal plane at a small angle.

Corrosion on Fracture Surfaces. Fractography of service fractures is hampered when the materials that fracture are exposed to corrosive environments before analysis of the fracture surface can be carried out, and the fine detail of the fracturing process is obliterated. Figure 47 shows a fracture surface in cold worked type 201 stainless steel that fractured in an environment that severely corroded the steel. The parallel ridges in the fractograph correspond to the banded condition of the microstructure. The "mudcake" corrosion products covering the surface, together with the corrosion pits, prevent positive identification of the operative fracture mechanism.

Figure 48 shows the corrosion pitting of intergranular facets that occurred in leaded copper alloy CDA No. 360 (free-cutting brass) fractured by stress-corrosion cracking. Using an energy-dispersive x-ray detector, the flocculent material within the corrosion pits was determined to be lead. Corrosion was assumed to have resulted from the galvanic action between the brass matrix and the lead precipitate exposed to the corrodent by the stress-corrosion crack.

References

1. T. Inoue, S. Matsuda, Y. Okamura and K. Aoki, The Fracture of a Low Carbon Tempered Martensite, *Trans Japan Inst Metals*, Vol 11, Jan 1970, p 36-43
2. C. D. Beachem, Orientation of Cleavage Facets in Tempered Martensite (Quasi-Cleavage) by Single Surface Trace Analysis, *Met Trans*, Vol 4, Aug 1973, p 1999-2000
3. W. J. Plumbridge and D. A. Ryder, The Metallography of Fatigue, *Met Rev*, Vol 14(136), Aug 1969, p 119-142
4. A. Rukwied and D. B. Ballard, Scanning Electron Microscope Fractography of Continuously Cast High Purity Copper after High Temperature Creep, *Met Trans*, Vol 3, Nov 1972, p 2999-3008; see Fig. 11d, p 3007

Interpretation of Transmission-Electron-Microscope Fractographs

By the ASM Committee on Fractography by Electron Microscopy*

THE FRACTURE features revealed by transmission electron microscopes can vary widely from spot to spot within a small area, and many views of a fracture may be necessary to characterize its nature fully. The Atlas of Fractographs in this volume presents many exhibits in which three or four views of the same small area show different features.

*See page 49 for committee list.

Fractures are classified by fracture path, fracture mechanism, and fracture features. There are two fracture paths: transgranular (or transcrystalline) and intergranular (or intercrystalline).

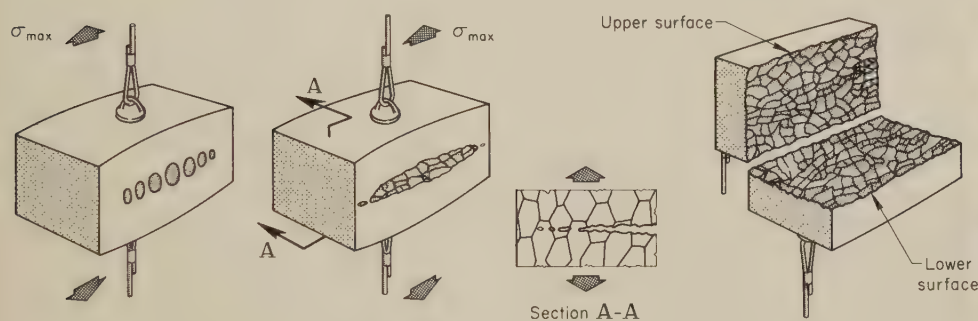
Transgranular Fractures

The fracture mechanisms (and related microscopic features) of transgranular fracture are: microvoid coalescence (dim-

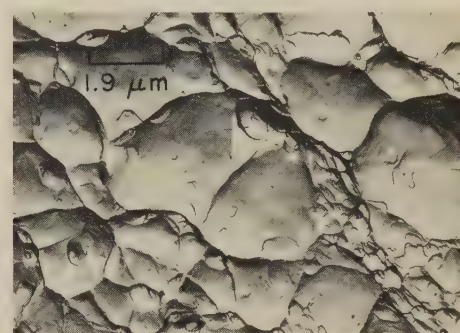
ples), tearing (tear ridges), cleavage (river patterns, feather marks), and fatigue (striations).

Microvoid coalescence produces a dimpled appearance on the fracture surface. The dimple feature is found most often when a metal has been subjected to a single load to fracture or in areas where a tearing type of fracture has occurred.

Microvoids usually initiate during plastic flow at inclusions, undissolved second-

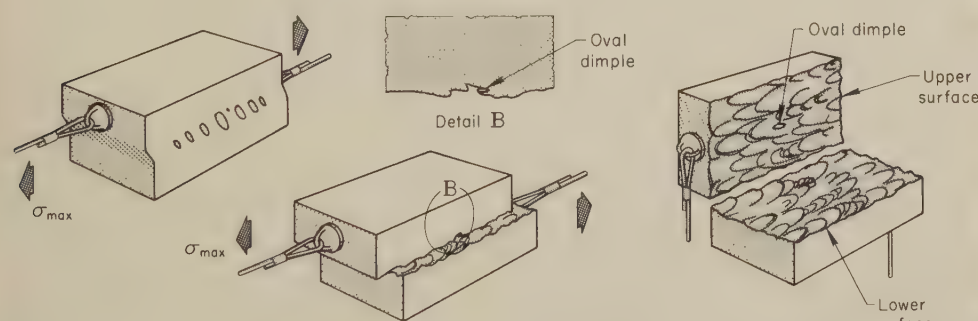


(a) Equiaxed dimple (tension)

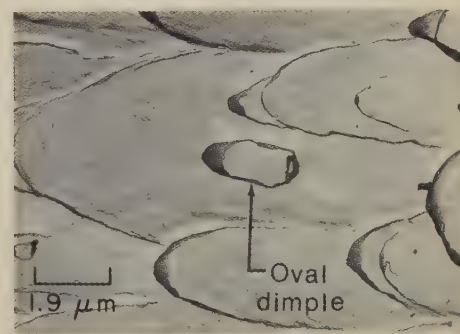


TEM fractograph (p-c replica)

5300X

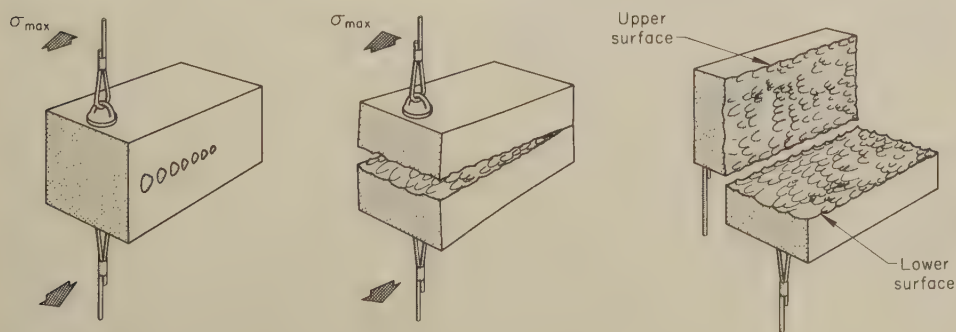


(b) Elongated dimple (shear)

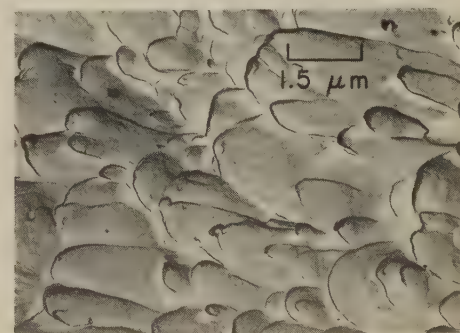


TEM fractograph (p-c replica)

5400X



(c) Elongated dimple (tensile tearing)



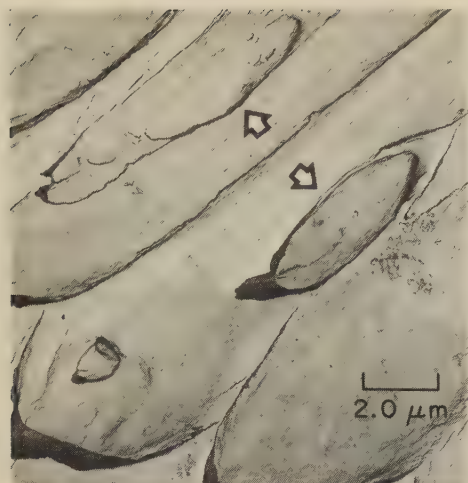
TEM fractograph (p-c replica)

6500X

Fractographs show shapes of dimples formed. (a) In tension, equiaxed dimples are formed on both fracture surfaces. (b) In shear, elongated dimples

point in opposite directions on matching fracture surfaces. (c) In tensile tearing, elongated dimples point toward fracture origin on matching fracture surfaces.

Fig. 1. Influence of direction of maximum stress (σ_{max}) on the shape of dimples formed by microvoid coalescence



TEM fractograph (p-c replica) 4900×
Fig. 2. Oval dimples (at arrows) that formed in flatter, more highly stretched portions of elongated dimples on a fracture surface of titanium alloy Ti-6Al-4V

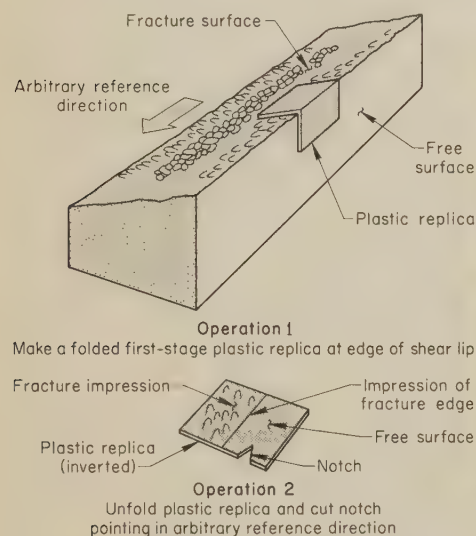
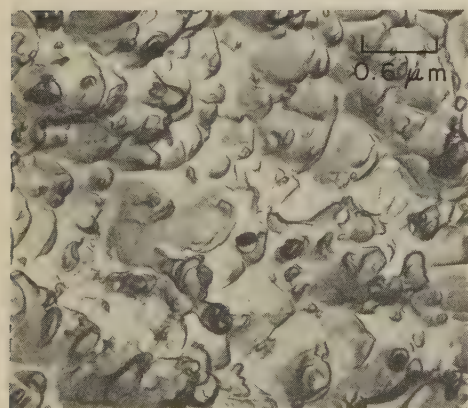


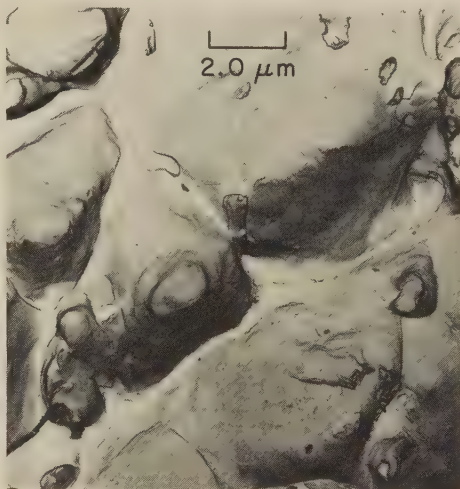
Fig. 3. Schematic representation of a replication technique that permits positive identification of the direction of shear fracture from the orientation of "open" elongated dimples on the acute-angle edge of a shear lip



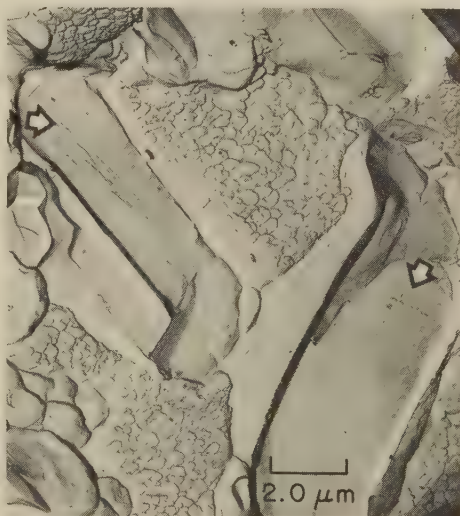
TEM fractograph (p-c replica) 18,200×
Fig. 4. Small dimples that formed at nucleation sites provided by dispersed particles of ThO₂ on a fracture surface of TDNi (thoriated nickel). The particles are at the apexes of the dimples.



TEM fractograph (p-c replica) 4900×
Fig. 5. Large, elongated dimples on a fracture surface of titanium alloy Ti-6Al-4V. There were relatively few nucleation sites for microvoids.



TEM fractograph (p-c replica) 4900×
Fig. 6. Deep, conical dimples on a fracture surface of ductile 1018 steel



TEM fractograph (p-c replica) 4900×
Fig. 7. Fracture of large second-phase particles (at arrows) in the matrix of cast aluminum alloy 356-T6. Matrix dimple size was not affected by the mechanism that caused fracture of the particles.

phase particles (such as carbides), grain boundaries, cleavage planes, or at any site where a discontinuity concentrates the plastic flow. Separation at the site of microvoid initiation can occur across a second-phase particle or at a particle-matrix interface. As the plastic strain increases, the existing microvoids grow, new microvoids are initiated, and eventually the enlarged microvoids grow into close enough proximity so that the thin ridges, or membranes, separating them rupture and fracture occurs. The resultant fracture surfaces have numerous cuplike depressions, or "dimples" (Ref 1).

The shape of a dimple is influenced by the relative stress directions operating to make the microvoid grow, as shown in Fig. 1. When the fracture is caused by simple tension, dimples usually have an equiaxed appearance, as shown in Fig. 1(a). When a shearing motion takes place, as in a shear-lip or torsion fracture, the dimples have an elongated, parabolic shape, and the dimples on opposing fracture surfaces point in opposite directions (Fig. 1b). A fracture that takes place by tensile tearing also produces elongated dimples, but the dimples on opposing fracture surfaces point in the same direction (toward the fracture origin), as shown in Fig. 1(c). Occasionally, oval dimples form in the flatter, more highly stretched portions of elongated dimples, as the result of the breaking open of small subsurface microvoids that intersect the surface of existing microvoids (see Ref 2, Fig. 1b and Fig. 2).

The direction of fracture propagation on a fracture surface created by a through-the-thickness crack in sheet or plate usually can be determined from the orientation of shear dimples. For a rapidly propagating fracture, "open" elongated dimples along the acute-angle edge of a shear lip (see Fig. 3) point in a direction opposite to the direction of fracture propagation—they point back to the fracture origin. These open dimples occur only along the acute-angle edge of the shear lip. Dimples that occur along an obtuse-angle edge of the shear lip and at the center of the fracture surface exhibit a more random orientation and cannot be used for determination of fracture-propagation direction. The acute-angle edge of the shear lip should be replicated by the conventional two-stage, plastic-carbon technique in such a way as to overlap the edge of the fracture (see Fig. 3), choosing an area with the flattest available profile edge (edge undulations introduce anomalies in dimple orientation). To orient the replica with respect to the fracture surface, the replica should be cut in a manner that will identify the arbitrary reference direction. The orientation of the open dimples on the edge of the fracture can then be observed in a transmission electron microscope and the fracture direction determined in terms of the arbitrary reference directions. Although the open dimples along the acute-angle edge of the shear lip accurately indicate the local direction of fracture propagation, a running fracture can exhibit occasional local reversals from the principal propagation direction. Therefore, it is essential

that a sufficient number of individual, unbiased determinations of fracture-propagation direction be made in order to characterize the propagation direction accurately. When properly applied, this technique is a reliable (and often the only) means of determining the shear-fracture direction.

Dimple size (diameter and depth) appears to depend on the number of microvoid-initiation sites available and the relative plasticity of the matrix. For example, the fracture surface of thoriated nickel, which contains a large number of dispersed particles of thorium oxide (and therefore a large number of initiation sites for microvoids), has more and smaller dimples than the fracture surface of unalloyed nickel would have (see Fig. 4 for a fractograph of a fracture surface of TDNi). The fracture surface of a titanium alloy with relatively few microvoid-initiation sites exhibits fewer and larger dimples (Fig. 5). Some very ductile materials have deep conical dimples (Fig. 6). Large second-phase particles that fracture by cleavage have little effect on matrix dimple size (Fig. 7), but small particles that act as microvoid-initiation sites strongly influence dimple shape (Fig. 8).

The increase in free surface that results from microvoid nucleation can be quite great. Because the growth of a free surface takes place by plastic deformation (hundreds of thousands per cent elongation), strain marks are occasionally evident on large dimples. These marks include serpentine glide, ripples and stretching. Serpentine glide is postulated to be caused by the appearance of new free surfaces resulting from glide on a series of near-parallel planes that are favorably oriented (Fig. 9 and 10). As straining continues, the distinct glide planes are smoothed out and ripples are formed, as shown in Fig. 11. Further straining virtually obliterates the surface marks (see Fig. 12); the mechanism that causes this relatively featureless appearance is called stretching. Some investigators have referred to these smooth features as having been formed by glide-plane decohesion or by ductile cleavage (Ref 3, 4).

In titanium alloys, the anisotropic deformation characteristic of the alpha phase when interacting with the beta phase leads to fracture-surface patterns like those shown in Fig. 13. The fracture surface indicates an extremely elongated, acicular microstructure. The long troughs are analogous to the dimples that form in alloys that have more-or-less equiaxed, isotropically deforming grains.

Some investigators (Ref 1, 5, 6) have related the size of the stretched zones that appear in fractures of fatigue-pre-cracked fracture-toughness specimens to the critical plane-strain stress-intensity factor, K_{Ic} . The stretched zone occurs at the root of the fatigue precrack, and it is postulated that the extent of the stretched zone is a function of the amount of localized plastic flow at the crack tip before the onset of rapid crack propagation (see Fig. 14 and 15).

Tearing designates a local type of fracture that is often found at a discontinuity



TEM fractograph (p-c replica) 6500×
Fig. 8. Small, second-phase particles (at arrows) that acted as microvoid-initiation sites and strongly influenced the shape of dimples on a fracture surface of 17-4 PH stainless steel

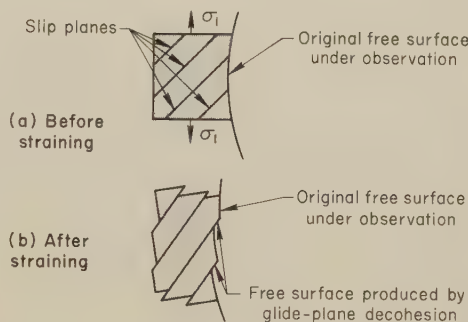
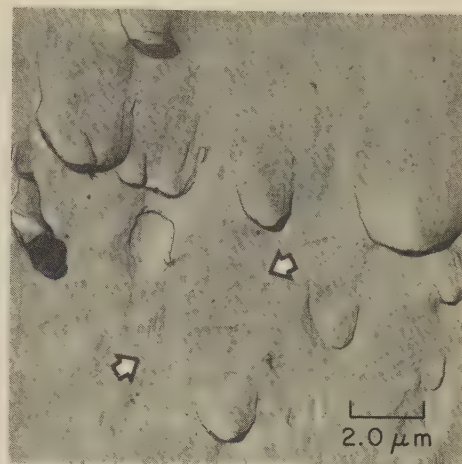


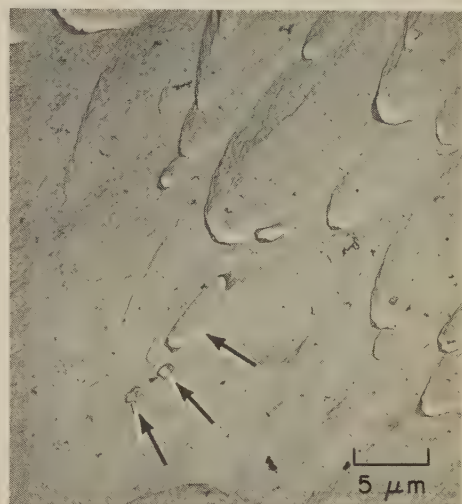
Fig. 9. Simple model for fracture by glide by a slip process (σ_1 = tensile stress caused by straining). Glide by twinning may also produce new free surfaces.



TEM fractograph (p-c replica) 2000×
Fig. 10. Serpentine glide on a fracture surface of Armco iron. Distinct slip steps, produced by glide-plane decohesion, may be seen between the arrows. Replica was palladium shadowed.



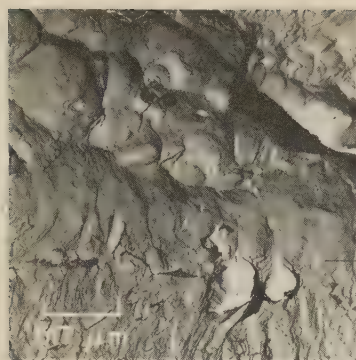
TEM fractograph (p-c replica) 4900×
Fig. 11. Ripples (between arrows) on a dimpled fracture surface of type 302 stainless steel



TEM fractograph (direct carbon replica) 2000×
Fig. 12. Stretched regions, shear dimples, and three oval tear dimples (at arrows) on a fracture surface of type 304 stainless steel. Replica was palladium shadowed.

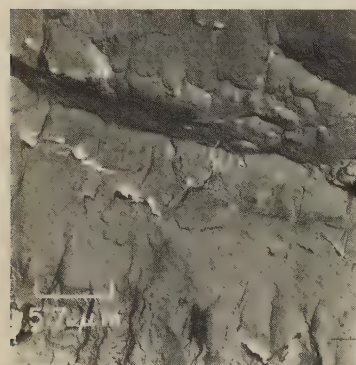


TEM fractograph (p-c replica) 3000×
Fig. 13. Troughs formed in a fracture surface of beta-annealed titanium alloy Ti-8Al-2Cu-1Ta by nucleation, growth and coalescence of linear microvoids during fast fracture



Rapid fracture
↓
Stretched zone
↓
Fatigue

TEM fractograph (p-c replica) 1750×
Fig. 14. Stretched zone in a fracture surface of a fracture-toughness specimen of 0.600-in.-thick plate of 18% Ni, grade 200, maraging steel tested at -196°C (-321°F).
 $K_{Ic} = 69.1 \text{ MPa}\cdot\text{m}^{1/2}$ ($62.9 \text{ ksi}\cdot\text{in.}^{1/2}$).



Rapid fracture
↓
Stretched zone
↓
Fatigue

TEM fractograph (p-c replica) 1750×
Fig. 15. Stretched zone in a fracture surface of a fracture-toughness specimen of 0.300-in.-thick plate of 18% Ni, grade 200, maraging steel tested at -196°C (-321°F).
 $K_{Ic} = 139.5 \text{ MPa}\cdot\text{m}^{1/2}$ ($127 \text{ ksi}\cdot\text{in.}^{1/2}$).



TEM fractograph (p-c replica) 6000×
Fig. 16. Cleavage fracture in a low-carbon steel with a tensile strength of about 415 MPa (60 ksi); an unusual fracture for a ductile metal of this sort. See Fig. 17 for microstructure of the steel.

in the crack advance by another fracture mechanism. It occurs when small regions or ligaments fracture by plastic flow or necking, and is accompanied by the formation of tear ridges.

Tearing is often observed as "flaps" in plastic-carbon replicas, because the relatively sharp relief of tear features causes the plastic replica to tear. The tears in the plastic replica then become carbon



Micrograph (etchant: nital) 400×
Fig. 17. Microstructure of the low-carbon steel for which a cleavage fracture is shown in Fig. 16. Grain-boundary network of free ferrite (at arrows) is believed to be responsible for the cleavage fracture.

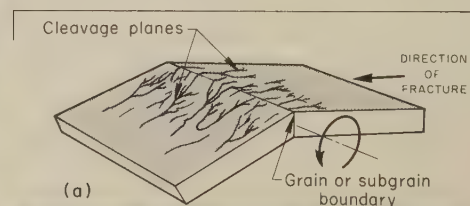


TEM fractograph (p-c replica) 4900×
Fig. 18. River patterns on a fracture surface of an Alnico alloy specimen. The white arrows point to a cleavage step; the black arrow shows the direction of crack propagation.

"flaps" on the second-stage replicas. Although the "flaps" are themselves artifacts, their presence is an indication that a sharp change in fracture topography is present.

Cleavage fracture is defined as separation that occurs on well-defined crystallographic planes in metals that exhibit little or no ability for cross slip. Therefore, the cleavage fracture mechanism usually is limited to metals with body-centered-cubic (bcc) or hexagonal, close-packed (hcp) crystal structures. Under certain conditions, however, separation along well-defined crystallographic planes has been observed in metals with face-centered-cubic (fcc) crystal structures: in aluminum alloys by cracking from contact with mercury, in brass by stress-corrosion cracking, and in many alloys by corrosion fatigue. Cleavage cracks appear to originate at locations where crystallographic slip is inhibited, such as at grain boundaries, at intersections between twins and slip planes, at inclusions, and at second-phase particles.

Cleavage describes a fracture mechanism; it may not be indicative of the relative ductility of a material. For example, the fracture surface of beryllium consists primarily of cleavage facets even when the metal has undergone 20% elongation before fracture. Cleavage can also occur in a low-carbon steel with a tensile strength of about 415 MPa (60 ksi), even though it may be quite ductile and should display fracture by micro-



TEM fractograph (p-c replica) 4900×
(a) Fracture model showing fracture direction, cleavage planes and low-angle grain or subgrain boundary. (b) Low-angle tilt boundary in a fracture surface of columbium alloy B-66 (5% Mo, 5% V, 1% Zr). Black arrows show fracture direction; white arrow shows a tilt boundary.

Fig. 19. Effect of low-angle tilt boundary on cleavage-crack propagation

void coalescence. An example of cleavage in low-carbon steel is shown in Fig. 16. A study of the microstructure of this steel (Fig. 17) revealed segregation of ferrite at the prior austenite grain boundaries. This ferrite network is believed to be responsible for the cleavage fracture.

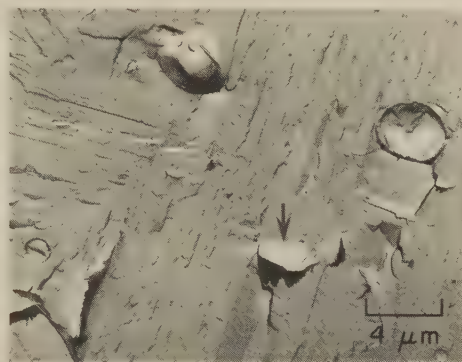
Ideally, cleavage fractures would be expected to have flat, featureless surfaces, because of the dependence of the fracture path on crystallography. However, engineering metals are polycrystalline; their individual grains may be randomly oriented with respect to one another and contain imperfections. These conditions produce fracture-surface marks, or decorations, that are distinct and easy to identify with a transmission electron microscope.

One of the principal features of cleavage fracture is a surface mark called river patterns (see Fig. 18). This feature is usually observed within a grain, and is a step between cleavage-crack segments on parallel cleavage planes in the grain. As the cleavage-crack segments run through a grain, they grow in width and approach each other. The resultant steps observed between cleavage planes are fractures of the thin ligaments joining the cleavage-crack segments. These steps converge in the direction of local crack propagation. When the running cleavage crack has to

change direction as it crosses a misoriented adjacent grain or subgrain, fracture decorations change. For example, if the adjacent grains or subgrains are only slightly misoriented (as in a low-angle tilt boundary), the cleavage steps are continuous across the boundary (see Fig. 19).



TEM fractograph (p-c replica) 5500X
Fig. 21. Cleavage feather marks (at A) on a fracture surface of unalloyed tungsten. The decorations at B resemble very fine river patterns, rather than feathers. Arrow shows fracture direction.



TEM fractograph (p-c replica) 2500X
Fig. 22. Cleavage tongues, such as at arrow, which formed along twin-matrix interfaces in Armco iron fractured at dry-ice temperature



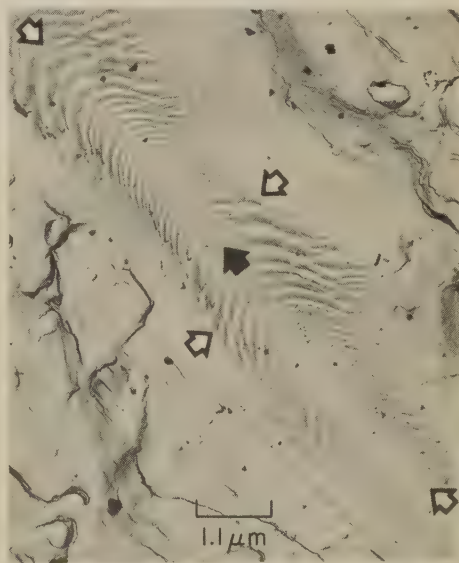
TEM fractograph (p-c replica) 2000X
Cleavage occurred along the central strip on a {100} plane in a <100> direction. On either side, the herringbone marks resulted from fracture on {100} planes in <110> directions and along {112}<110> twin interfaces.

Fig. 23. Herringbone pattern on a fracture surface of an Fe-Cr-Al alloy

If an adjacent grain or subgrain is axially misoriented relative to the local fracture direction, the boundary of that grain is a twist boundary. New cleavage steps will form when the propagating crack crosses the twist boundary (Fig. 20).

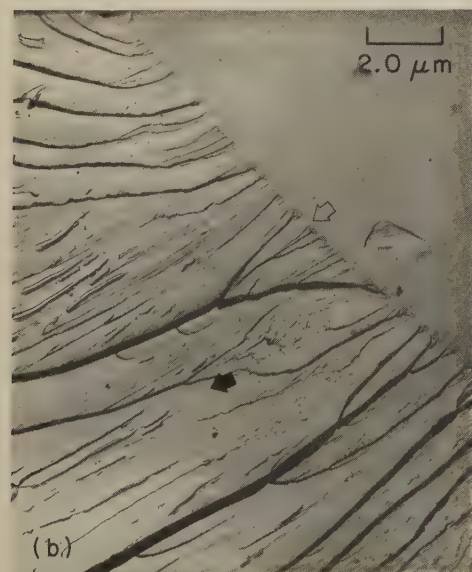
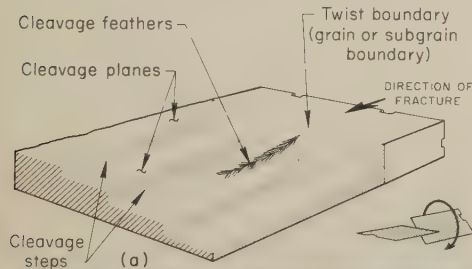
Another distinct cleavage-fracture feature is called "feather marks" (Fig. 20, 21). Feather marks have an appearance similar to chevron patterns in that they usually point back in the direction of local crack origin. It should be noted that the ability to distinguish fracture direction on cleavage surfaces of specific grains may not help in determining the macroscopic fracture direction. Cleavage fracture may take place by very local separation ahead of the moving crack front. Local crack-growth direction is highly dependent on crystallographic orientation. It may be totally unrelated to the macroscopic crack-growth direction, but it still may be used to find the fracture origin. (See the section on Fractographic Mapping To Identify Fracture Origins on page 44 in the article on Interpretation of Light-Microscope Fractographs.)

Cleavage tongues (Fig. 22) have been observed on some materials. This feature is ascribed to the local deviation of a cleavage-plane crack as it intersects a boundary between a deformation twin and the matrix. The twin-surface projection (tongue) corresponds to a matching depression in the mating fracture surface (Ref 7). Another feature of cleavage fracture is herringbone pattern, which is shown in Fig. 23. This fracture feature has been observed principally in body-centered-cubic materials and is related to cleavage of the {100} plane fracturing in the <100> direction at the center of the herringbone. The herringbones on either side are related to {100} planes fracturing in the <110> direction and along {112}<110> twin interfaces. Both cleavage tongues



TEM fractograph (p-c replica) 9000X
Black arrow indicates the direction of fracture propagation. Note that the Wallner lines cross each other, a circumstance that differentiates Wallner lines from fatigue striations.

Fig. 24. Wallner lines (between white arrows) on a fracture surface of an aluminum alloy A356-T6 casting



TEM fractograph (p-c replica) 4900X
(a) Fracture models showing a twist boundary and the new cleavage steps that develop as the propagating crack crosses a twist boundary. (b) Cleavage steps initiating at a twist boundary (open arrow) on a fracture surface of columbium alloy B-66 (5% Mo, 5% V, 1% Zr). Solid black arrow indicates fracture direction. Feather marks exist between steps.

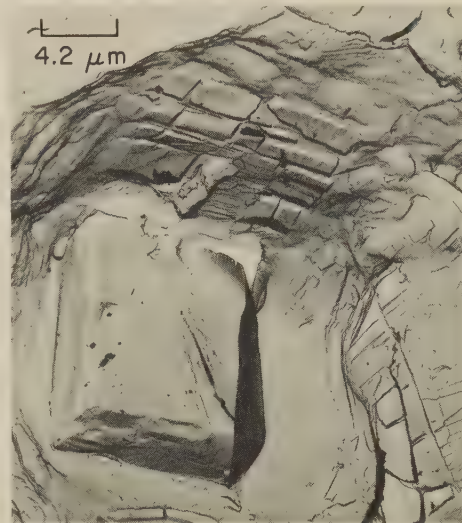
Fig. 20. Effect of twist boundary on cleavage decoration

and herringbone patterns are related to the interaction of cleavage fracture with deformation twins.

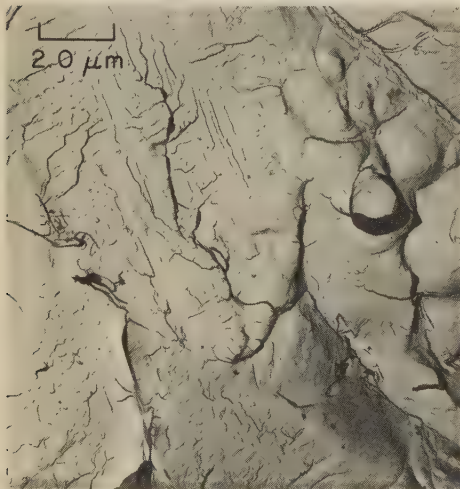
Many engineering metals contain brittle, intermetallic second-phase particles. Occasionally, marks known as Wallner lines appear on these brittle phases (Fig. 24). This feature is assumed to result from the interaction of a propagating crack front and elastic stress waves in the material. Wallner lines appear as parallel cleavage steps, creating a rippled pattern. They can be observed to cross each other and are distinguishable from fatigue striations, which never cross each other.

Quasicleavage. Fractures resulting from microvoid coalescence and from cleavage are relatively easy to identify, and the mechanisms of separation are reasonably well understood. However, many high-strength engineering metals fracture by quasicleavage, which is a mixed mechanism involving both microvoid coalescence and cleavage. These fractures are not to be confused with those in which cleavage appears in brittle second phases with the characteristic

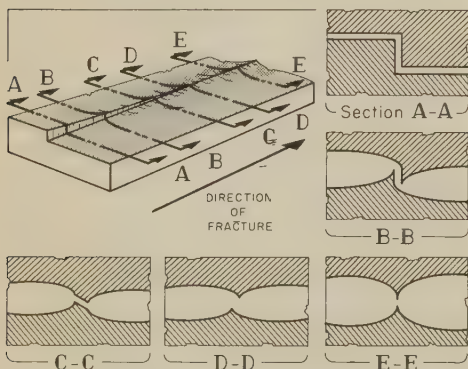
dimples of microvoid coalescence appearing in the more ductile matrix. In quasicleavage, there is no apparent boundary between a cleavage facet and a dimpled area bordering the cleavage facet (Fig. 25). A schematic representation of quasicleavage is given in Fig. 26.



TEM fractograph (p-c replica) 2400×
Fig. 27. Cleavage in a large second-phase particle on a fracture surface of A-286 steel

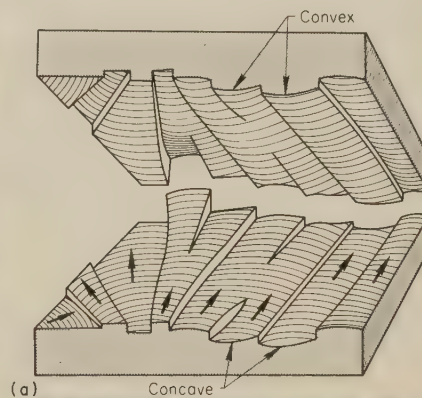


TEM fractograph (p-c replica) 4900×
Fig. 25. Effect of quasicleavage—mixed cleavage and microvoid coalescence—on the fracture-surface appearance of 17-4 PH stainless steel



At the top left is the lower surface of a fracture, showing a step at the lower left and a ridge at the upper right. At right and at bottom are sections through the fractured member, showing profiles of both the upper and the lower fracture surfaces.

Fig. 26. Fracture model showing a cleavage step blending in with a tear ridge in a quasicleavage fracture surface



TEM fractograph (p-c replica) 2000×
(a) Fracture model of fatigue striations, showing striation plateaus and tear ridges. Arrows indicate the directions of crack propagation.
(b) Fatigue striations on a fracture surface of a 5-in.-thick plate of aluminum alloy 2024-T851. Arrow indicates the direction of crack propagation.

Fig. 28. Fracture model and fractograph of fatigue striations

The mechanism of quasicleavage is not well understood, although it can be identified by its fracture features. However, the occurrence of quasicleavage is common, and its appearance is usually distinguished by the following:

- 1 Fracture by quasicleavage appears to be initiated within facet boundaries. This is in contrast to fracture by cleavage, which is usually initiated from one edge of the region being cleaved (Fig. 27).
- 2 Cleavage steps in quasicleavage appear to blend directly into tear ridges of the adjacent dimpled areas.

In quenched-and-tempered steels, small, ill-defined cleavage facets, which are usually initiated at precipitated carbide



TEM fractograph (p-c replica) 4000×
Fig. 29. Stage I of fatigue-fracture progress in aluminum alloy 2024-T4. Fracture surface resembles cleavage; it does not have fatigue striations. Arrow indicates direction of crack propagation.

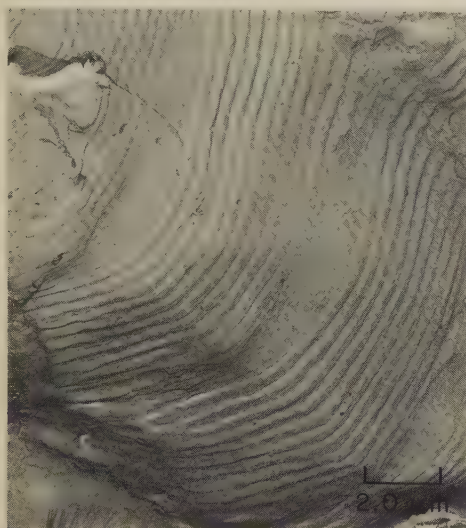


TEM fractograph (p-c replica) 4900×
The striations are closely spaced and propagate on flat plateaus joined by shear steps (at white arrows). Black arrow indicates direction of crack propagation.

Fig. 30. High-cycle fatigue striations in a fracture surface of aluminum alloy 6061-T6



SEM fractograph 2400×
Fig. 31. Striation plateaus and shear steps (at arrows) in a fatigue fracture in aluminum alloy 2219-T87

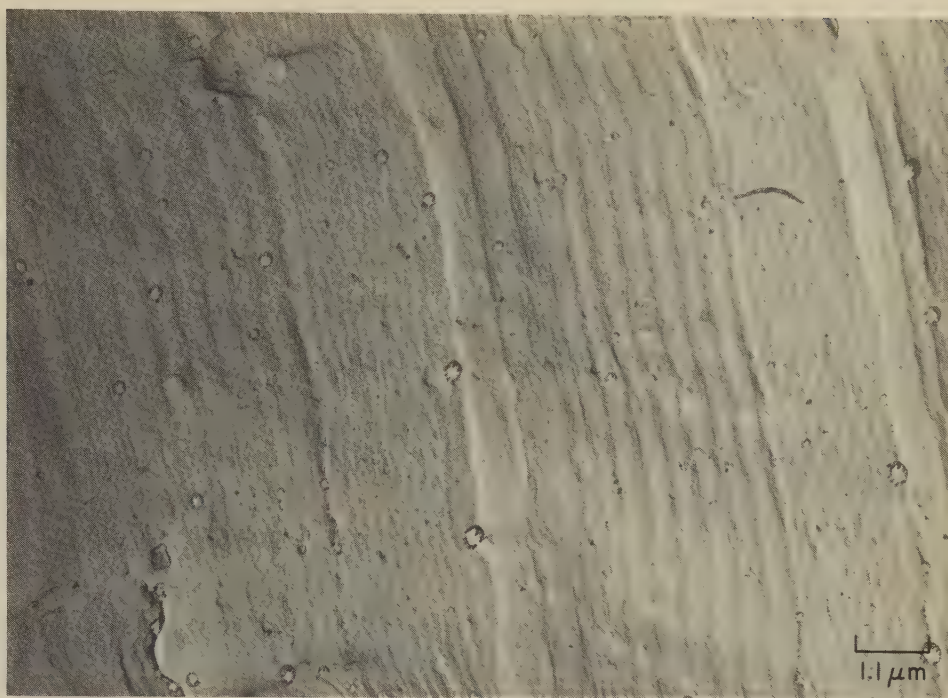


TEM fractograph (p-c replica) 4900×
Fig. 32. Effect of spectrum loading on fatigue-striation spacing in a laboratory test fracture in aluminum alloy 7075-T6

particles, are connected by tear ridges and shallow dimples. Until the work of Inoue *et al* and Beachem (Ref 1 and 2, page 78), these facets were not considered true cleavage planes (hence the term "quasicleavage"). It is now evident, however, that they do represent a form of cleavage on {100} planes.

When tested under embrittling conditions, such as those imposed by corrosive mediums or triaxial stress states, quasicleavage can occur in metals that normally are not known to have active cleavage planes (for example, austenitic stainless steels, and nickel and aluminum alloys). One explanation is that the facets that exhibit quasicleavage features fractured ahead of the moving crack front; then, as the stress increased, the cleavage facet extended by tearing into the matrix around it by microvoid coalescence.

Fatigue. Fractures caused by damage from cyclic stress (fatigue) are common in metals. Damage from fatigue has been studied extensively, and many theories have been presented that describe the irreversible metallurgical damage and



TEM fractograph (p-c replica) 8800×
Fig. 33. Surface of a fracture in aluminum alloy 7075-T6 showing the result of spectrum loading that was applied in ten-cycle blocks as follows: ten cycles at ± 77.6 MPa (± 11.25 ksi), and ten cycles at ± 17.2 MPa (± 2.5 ksi)

crack initiation and growth. Fortunately, the part of the fatigue process that entails crack growth leaves clear fractographic evidence, commonly known as fatigue striations (Fig. 28). It has been shown by several investigators that each fatigue striation is the result of a single stress cycle. The corollary of this statement is not necessarily true—a stress cycle does not always produce a striation. Fatigue striations differ in appearance (or may not occur), depending on environmental effects, the relative ductility of the metal, the stress level propagating the crack, and the stress state.

The initial portion of fatigue-fracture progress, which has been termed stage I cracking, is generally attributed to slip-plane fracture from repetitive reversing of the operative slip system in the metal. There are usually no fatigue striations associated with stage I cracking. In fact, the fracture has the appearance of cleavage, with little or no evidence of plastic behavior (see Fig. 29). The area of stage I of fatigue cracking is usually very small (frequently two to five grains deep); in some instances (depending on the material, environment, and stress level), it may not be discernible. Stage II of fatigue-fracture progress begins with the formation of characteristic striations, described in the following paragraphs.

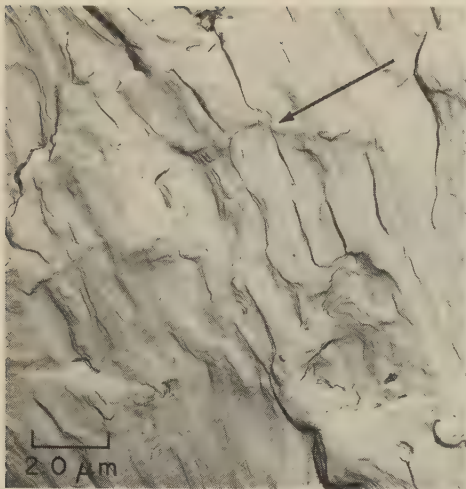
High-cycle fatigue fractures* generally have closely spaced and well-defined fa-

tigue striations. These striations usually propagate on many flat plateaus or facets that are joined by shear steps (Fig. 30). Often, the junction of the striation-marked facets is very narrow and appears in the form of a line on a fractograph. Figure 31, an SEM fractograph, shows the relationship of the areas of striation to the shear steps quite clearly. Zones within stage II fatigue areas that do not show striations may appear to be rubbed, fairly flat, and featureless.

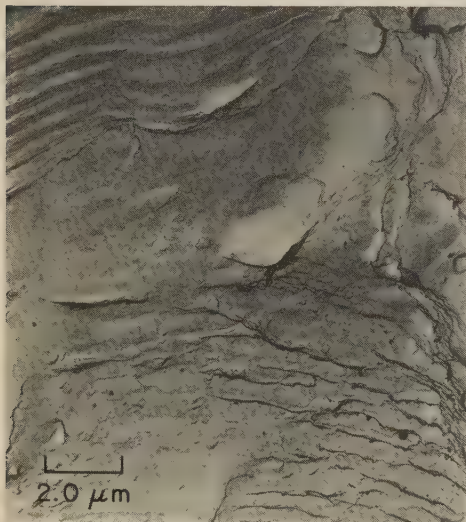
Under actual operating conditions, a propagating fatigue fracture is usually subjected to repeated loads of different magnitude. These "spectrum" loads (repeated sequences of different loads) are reflected in the fracture appearance by a variation in the fatigue-striation spacing in the plane and direction in which the crack is propagating, as seen in the laboratory test fracture in Fig. 32. Because the stress level influences striation spacing, many investigators have proposed quantitative relationships between striation spacing and cyclic-stress levels. By judicious use of striation-spacing measurements, it is possible to provide an estimate of the stress levels the fractured part may have been subjected to (Ref 8).

Often, spectrum fatigue loading can result in crack arrest. For example, if cyclic stress at high amplitude is followed by cyclic stress at low amplitude, there may be no evidence of striation formation for several cycles. In Fig. 33, it can be seen that a change from ten cycles of an alternating stress at ± 77.6 MPa (± 11.25 ksi) to ten cycles at ± 17.2 MPa (± 2.5 ksi) resulted in no striation formation for a brief initial period. Consequently, it is not always possible to count fatigue striations to determine the total number of cycles to which a part may have been sub-

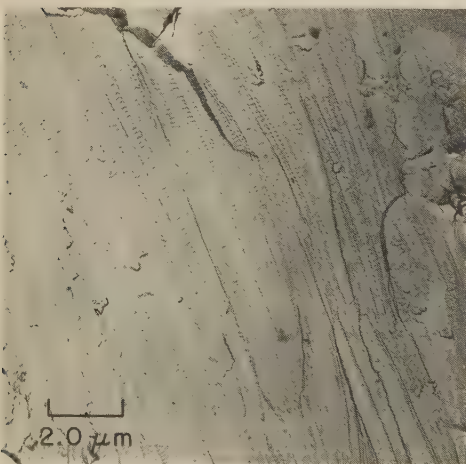
*The dividing line between high-cycle and low-cycle fatigue fractures is often considered to lie at about 100,000 cycles. Actually, however, this distinction is more likely to be determined by whether the dominant component of the strain imposed during cyclic stressing is elastic (high-cycle) or plastic (low-cycle), which in turn depends on the properties of the metal as well as on the stress level. In extreme conditions, the dividing line between high-cycle and low-cycle may even be below 100 cycles.



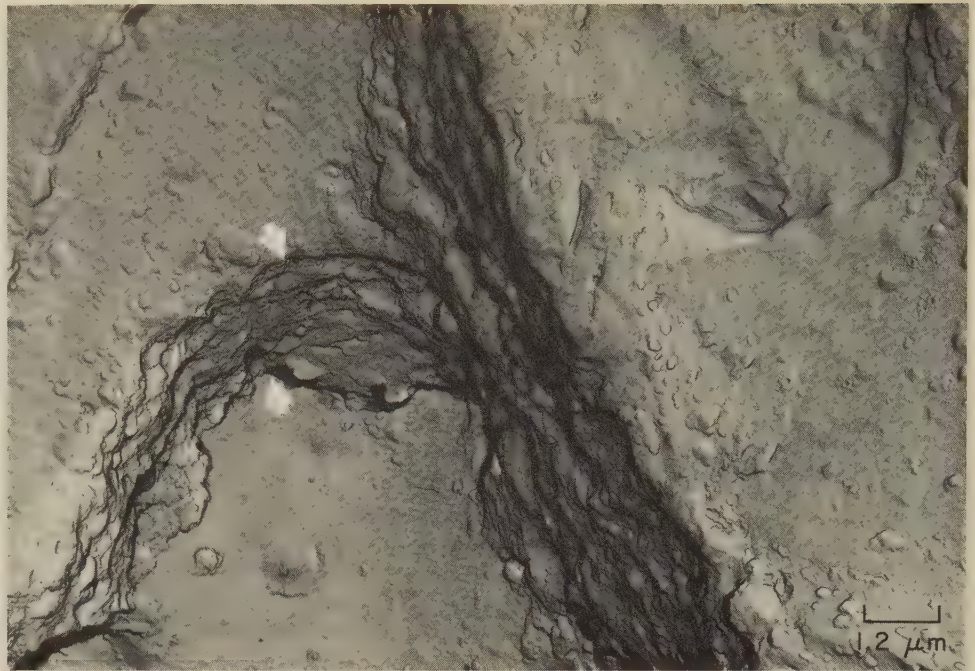
TEM fractograph (p-c replica) 4900×
Fig. 34. Fracture surface of titanium alloy Ti-6Al4V showing low-cycle fatigue striations (2350 cycles to fracture). Arrow indicates fracture direction.



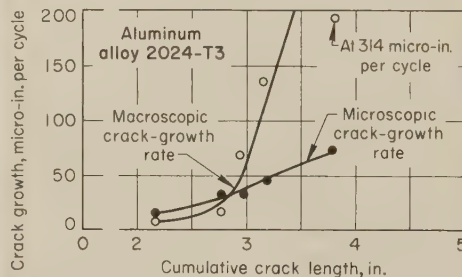
TEM fractograph (p-c replica) 4900×
Fig. 35. Fracture surface of aluminum alloy 7075-T6 showing well-formed low-cycle (700 cycles to fracture) fatigue striations at top left. Striations at bottom left are faint, perhaps have been rubbed. Those at right seem flattened to narrow grooves.



TEM fractograph (p-c replica) 4900×
Fig. 36. "Tire tracks" on a fatigue-fracture surface of aluminum alloy 6061-T6



TEM fractograph (p-c replica) 8200×
Fig. 37. Surface of a fatigue fracture in aluminum alloy 2014-T6 showing dimples that formed between plateaus containing fatigue striations. The tensile tear (between arrows) connects two levels of crack propagation.



Data were obtained on specimens of aluminum alloy 2024-T3, 0.050 in. thick, fatigue tested at a frequency of 1000 cycles per minute. Microscopic rate was determined by striation spacing. Macroscopic rate was estimated from observed crack growth in successive groups of stress pulses.

Fig. 38. Relation between microscopic and macroscopic crack-growth rates and cumulative crack length in fatigue fracture

jected before fracture. However, the use of striation counting for just this purpose is described in the article on The Use of Fractography for Failure Analysis, which begins on page 106 in this volume.

Striations in low-cycle fatigue fractures* appear to be rather broad, widely spaced, and often discontinuous (Fig. 34 and 35). In many metals and alloys, especially in ultra-high-strength and low-strength materials, the striations may not be formed. In some metals, low-cycle fatigue fractures occur by a mechanism resembling microvoid coalescence (Ref 9) and show no evidence of striations.

A fracture feature associated with high-stress, low-cycle fatigue is known as "tire tracks" (Fig. 36). Tire tracks are most frequently observed on relatively steep slopes of the fracture surface. They are evidence of mechanical damage on the fracture surfaces caused by the repeated

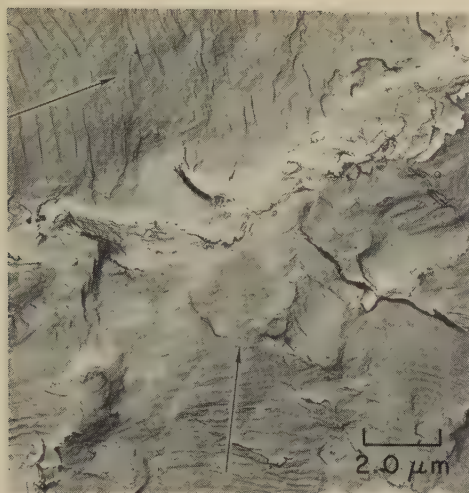


TEM fractograph (p-c replica) 4900×
Fig. 39. Striations on two joining, independent fatigue-crack fronts on a fracture surface of aluminum alloy 6061-T6. The two arrows indicate direction of local crack propagation.

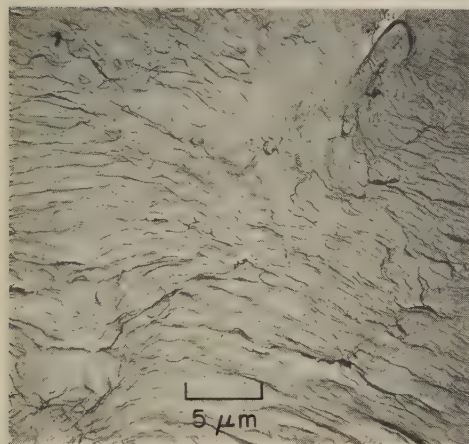
impacting and relative motion of the two mating surfaces. Sometimes, tire tracks are caused by loose particles caught between the mating fracture surfaces. Tire tracks are not fatigue striations, but they are reliable indicators of fatigue fracture.

As a fatigue crack grows to near-critical size, bands of dimples can be seen between plateaus containing fatigue striations (Fig. 37). The appearance of both dimples and striations on the same fracture surface explains why the spacing of fatigue striations does not correlate well with macroscopic crack-growth rates (Ref 10 and Fig. 38), especially at higher crack-growth rates. The macroscopic crack-growth rate is the sum of the nor-

*See footnote on page 85.

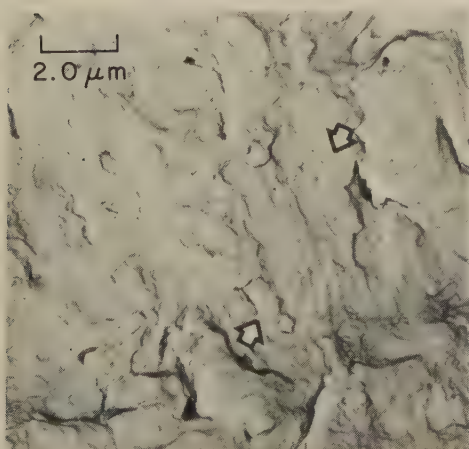


TEM fractograph (p-c replica) 4900×
Fig. 40. Extreme differences in local crack-propagation directions on a fatigue-fracture surface of titanium alloy Ti-6Al-4V, as indicated by the striations (and the arrows)

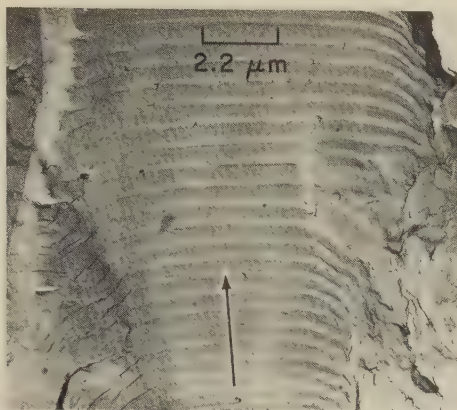


TEM fractograph (p-c replica) 2000×
The poorly formed and very irregular fatigue striations here are typical of those on fracture surfaces of very soft metals. These are often difficult to interpret because of their deformed shapes.

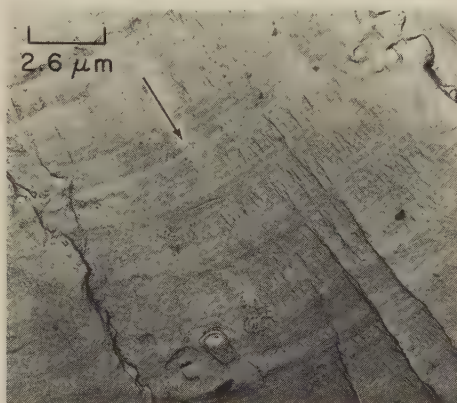
Fig. 41. Fatigue striations in a fracture surface of soft aluminum alloy 1100



TEM fractograph (p-c replica) 4900×
Fig. 42. Poorly formed striations (between arrows) on a fatigue-fracture surface of D-6ac steel with a tensile strength of 1795 to 1930 MPa (260 to 280 ksi)



TEM fractograph (p-c replica) 4550×
Fig. 43. "Ductile" fatigue striations on a fracture surface of aluminum alloy 7079-T651. Arrow indicates fracture direction.



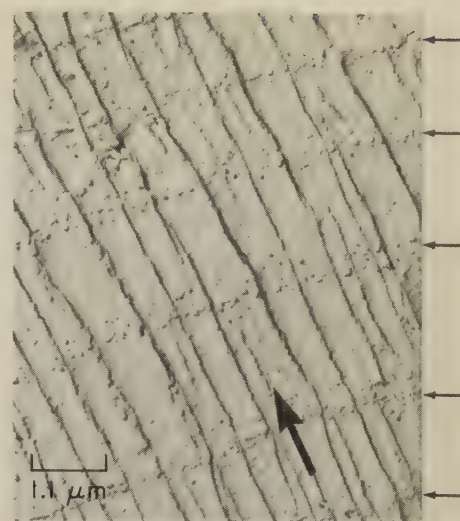
TEM fractograph (p-c replica) 3900×
Fig. 44. "Brittle" fatigue striations on a fracture surface of aluminum alloy 7075-T6 exposed to a corrosive environment. Arrow indicates fracture direction.

mal fatigue process causing striations and the dimple-fracture component caused by tensile tearing.

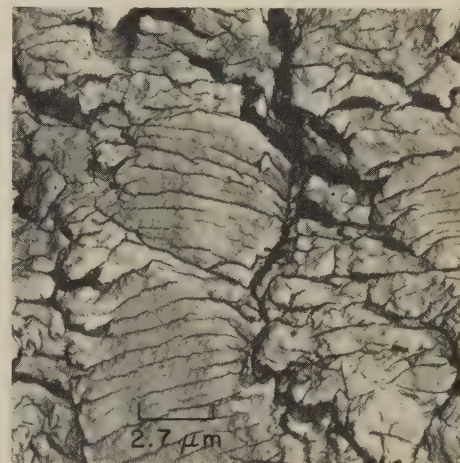
Fatigue striations usually bow outward in the direction of local crack propagation. However, this feature cannot be depended on to denote the direction of macroscopic crack growth, because the fatigue striations on a single fracture surface can indicate crack growth in several different directions (Fig. 39 and 40).

Fatigue striations are best seen on fracture surfaces of alloys of moderate hardness. In general, the very soft metals, such as pure aluminum, yield fatigue fractures characterized by irregular, poorly formed striations (Fig. 41). Very hard metals, such as low-alloy steel at a tensile strength of 1795 to 1930 MPa (260 to 280 ksi), produce poorly formed striations, which are difficult to interpret (Fig. 42).

Occasionally, distinction is made between "ductile" and "brittle" striations observed on the surfaces of fatigue fractures in aluminum alloys. Ductile striations (Fig. 43) are more commonly observed than brittle striations (Fig. 44). In Fig. 45, note that the brittle striations appear to combine the features of cleavage (steps) and fatigue (striations that appear very flat). Generally, brittle striations can be attributed to the effect of an environmental factor acting at the crack



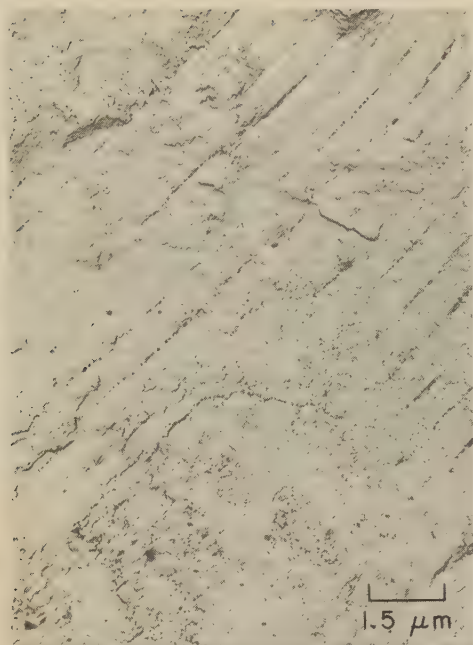
TEM fractograph (p-c replica) 8700×
Fig. 45. "Brittle" fatigue striations (at horizontal arrows) on an apparently cleaved fracture surface of a magnesium alloy AZ91-T6 casting. Arrow on fractograph shows direction of crack growth.



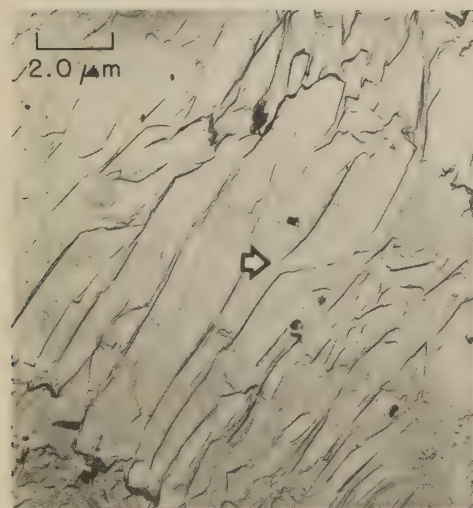
TEM fractograph (p-c replica) 3750×
Fig. 46. Secondary cracking at fatigue striations on a fracture surface of titanium alloy Ti-6Al-4V exposed to a hydrogen atmosphere at room temperature

front. For example, the fatigue fracture shown in Fig. 44 is the result of crack propagation in aluminum alloy 7075-T6 in a corrosive environment. Similarly, secondary cracking at the fatigue striations is observed in some alloys (Fig. 46). Brittle striations are usually observed where crack-propagation rates are slow enough to allow the environmental interaction to occur ahead of the moving crack. At higher crack-growth rates, the speed of crack propagation appears to be faster than the diffusion rate of the embrittling species, and ductile striations are produced (Ref 11). A further complication introduced with a corrosive environment is the deposition or growth of corrosion products on fracture surfaces, which will mask fatigue striations (Fig. 47).

Some fracture features resemble fatigue striations, but are related to other damage or fracture mechanisms. Tire tracks have already been discussed (see page 86 and Fig. 36). Ripples, which are



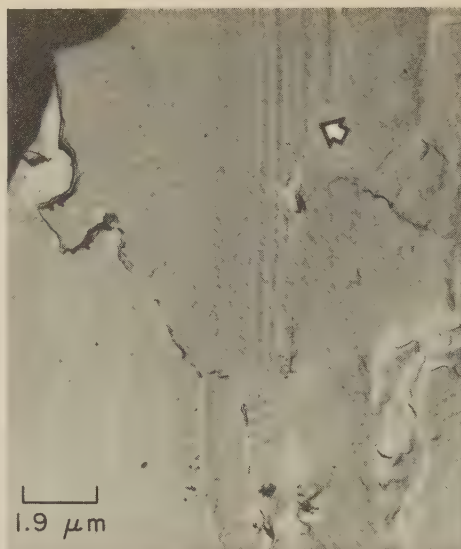
TEM fractograph (p-c replica) 6500×
Fig. 47. Masking effect of corrosion products on fatigue striations on a fracture surface of aluminum alloy 7075-T6



TEM fractograph (p-c replica) 4900×
Fig. 48. Tension-overload fracture in an aluminum alloy 7075-T6 spot-weld nugget. The lamellar structure, which is forked (arrow), could be confused with fatigue striations.

discussed on page 81 and shown in Fig. 11, can have an appearance similar to that of striations. However, ripples (or deformation steps) can cross over each other; fatigue striations cannot. Also, ripples appear to be smoother than most fatigue striations.

With alloys that have a regularly spaced lamellar structure of intermetallic phases, fracture surfaces sometimes have features that resemble fatigue striations. The fracture shown in Fig. 48 was produced in tensile testing of an aluminum alloy 7075-T6 spot-weld nugget. The fracture shows a lamellar structure of eutectic particles that might be confused with fatigue striations. Unlike fatigue striations, however, the eutectic particles



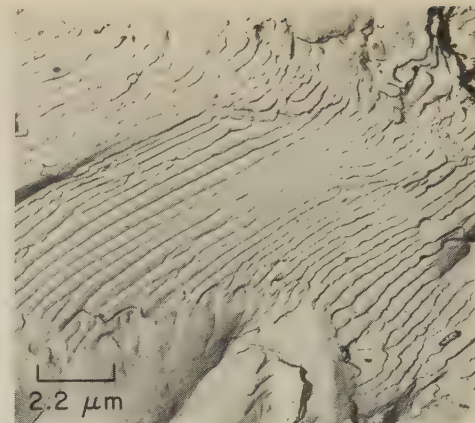
TEM fractograph (p-c replica) 5400×
Fig. 49. Rub marks (at arrow) on the surface of a fatigue fracture in aluminum alloy 7075-T6



TEM fractograph (p-c replica) 5600×
Fig. 50. Rub marks on an overload-fracture surface of AMS 6265 (9310) steel. The light lines are cracks in the replica.

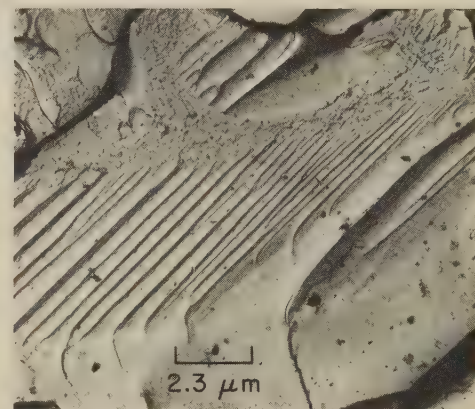
usually have considerable width and they may fork, which fatigue striations have never been observed to do. Wallner lines, which are discussed on page 84 and are illustrated in Fig. 24 on page 83, also have a striated appearance, but the fact that Wallner lines cross each other rules out fatigue.

Rub marks, which may consist of sets of parallel lines (Fig. 49), are commonly observed on fatigue fractures, especially when the cyclic stress has a compressive component. Like tire tracks, rub marks are not fatigue striations but indicate mechanical damage. Because they have been seen in fractures resulting from a single load application (Fig. 50), they are not reliable indicators of fatigue.



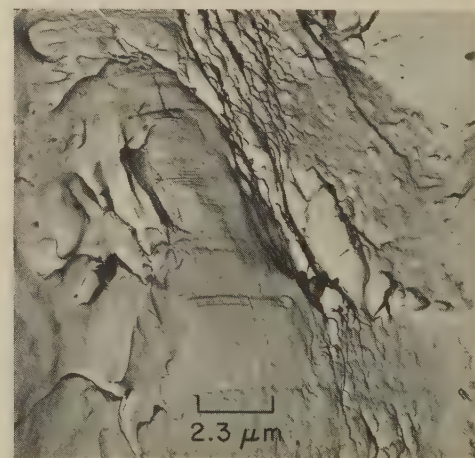
TEM fractograph (p-c replica) 4560×
No fatigue striations were observed anywhere on the fracture surface. Penetration of platelets into the surrounding matrix shows that they are pearlite platelets, not fatigue striations.

Fig. 51. Lamellar pearlite platelets on a fatigue-fracture surface of gray iron



TEM fractograph (p-c replica) 4400×
The steps, which formed at acicular alpha platelets, resulted from the differences in amount of flow of the alpha and beta phases that occurred during forging. Note that the steps penetrate into the surrounding matrix, which shows that they are not fatigue striations.

Fig. 52. Lamellar array of steps on a fracture surface of a titanium alloy Ti-6Al-4V forging



TEM fractograph (p-c replica) 4400×
Fig. 53. Scratch-mark artifacts on a plastic replica, produced by contact with promontories of the fracture surface during stripping. These marks, reproduced on the second-stage (carbon) replica, bear a resemblance to fatigue striations.

Other examples of fracture features that resemble fatigue striations are shown in Fig. 51, 52 and 53; these are:

- 1 The lamellar structure created by a pearlite colony in gray iron (Fig. 51)
- 2 The lamellar array of steps on a fracture surface of forged titanium alloy Ti-6Al-4V that resulted from the differences in the amount of flow of the alpha and beta phases that occurred during forging (Fig. 52)
- 3 Scratch-mark artifacts on a plastic replica that were produced by contact with promontories of the fracture surface during stripping (Fig. 53).

None of these types of striations should be confused with fatigue striations.

Intergranular Fractures

Intergranular fracture occurs by grain-boundary separation. Most intergranular fractures have appearances that make them easily distinguishable from other types of fractures. However, intergranular fractures that appear similar may have resulted from different causes. Among the causes of intergranular fracture are the presence of grain-boundary phases that are weak or brittle, and environmental or mechanical factors such as stress corrosion, hydrogen damage, heat damage, and triaxial stress states.

In some instances, intergranular fracture will show evidence of microvoid coalescence within a very small layer of metal at the grain interfaces. High-strength aluminum alloys frequently fracture by grain-boundary separation with microvoid coalescence (Fig. 54). It has been postulated that the fracture proceeds along alloy-depleted zones in the grain boundaries, which are soft in comparison with the matrix. This is a brittle fracture in the macroscopic sense and plastic in the microscopic sense. Many intergranular fractures, such as those caused by hydrogen embrittlement, stress corrosion, brittle grain-boundary phases,

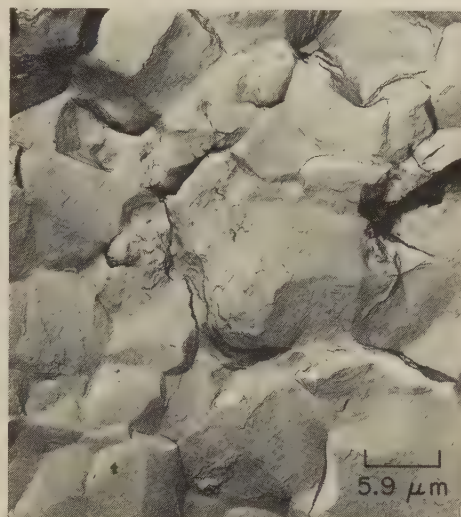
quench cracking, and grinding cracks, show little or no evidence of microvoid coalescence; they have a "rock candy" appearance (Fig. 55).

In interdendritic fracture of welds and castings (Fig. 56), features have a more rounded appearance, but the fractures are classified as intergranular. Fractures that occur along flattened grains (typical of parting planes in forgings) are virtually featureless (Fig. 57), because of the low angles between adjacent grains. If the shadowing angle used during replication is lessened, features will be brought into greater relief when examining these fractures.

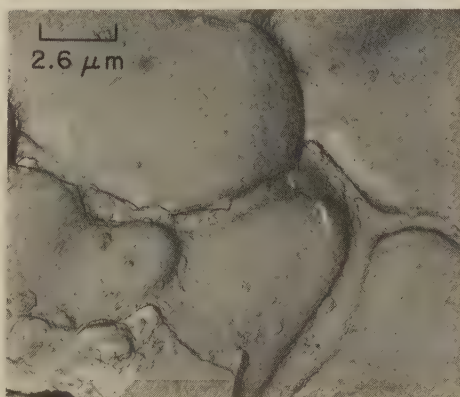
Geometric patterns are commonly observed in the fracture surfaces of welds and castings. These patterns are found in areas of voids and porosity, and are typical of the solidification and growth of a free surface from a melt (Fig. 58 and 59). Fractures through some material imperfections, such as hydrogen flakes in steel (see fractographs 4344 and 4345, on page 312) and unhealed porosity in aluminum



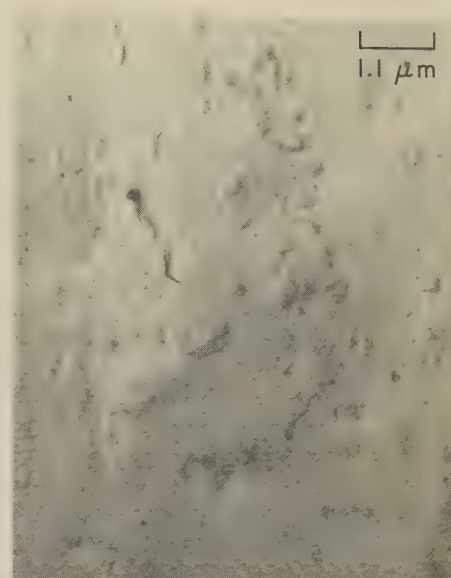
TEM fractograph (p-c replica) 6500×
Fig. 54. Grain-boundary fracture in aluminum alloy 7075-T6 showing very shallow dimples, which resulted from microvoid coalescence, on the grain surfaces



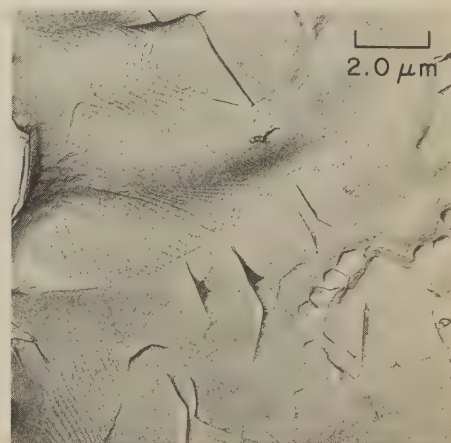
TEM fractograph (p-c replica) 1700×
Fig. 55. Intergranular fracture in 4340 steel with a tensile strength of 1795 to 1930 MPa (260 to 280 ksi), showing equiaxed grains that have separated without microvoid coalescence; a "rock candy" fracture surface



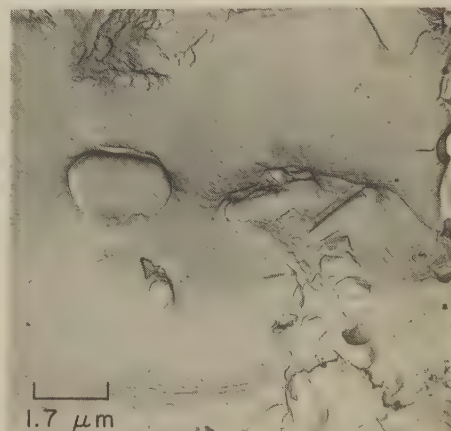
TEM fractograph (p-c replica) 3900×
Fig. 56. Intergranular fracture along a cored (segregated) grain-boundary network in a weld of aluminum alloy 2014-T6. No evidence of microvoid coalescence.



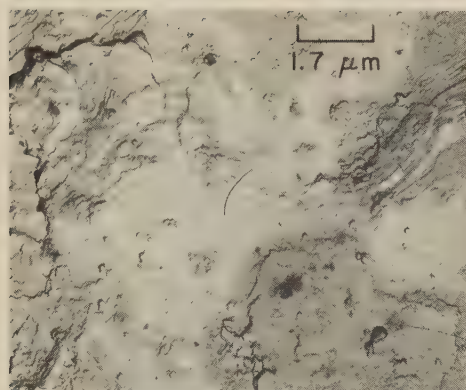
TEM fractograph (p-c replica) 8700×
Fig. 57. Intergranular fracture surface of an aluminum alloy 7079-T6 forging. Fracture followed the parting plane of the forging. It is essentially featureless because of the low angles between the elongated, flattened grains.



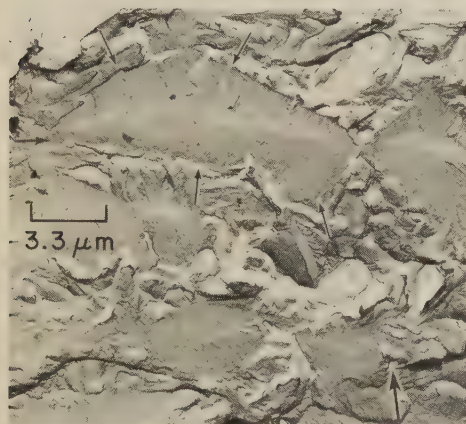
TEM fractograph (p-c replica) 4900×
Fig. 58. Geometric patterns exposed by a fracture through a porous weld in aluminum alloy 2014



TEM fractograph (p-c replica) 5900×
Fig. 59. Geometric patterns exposed by a fracture through a cavity in an aluminum alloy 356-T6 casting



TEM fractograph (p-c replica) 5900×
Fig. 60. Geometric patterns exposed by a fracture through unhealed porosity in an aluminum alloy 2014-T6 forging



TEM fractograph (p-c replica) 3000×
Fracture surface shows cleavage facets and dimples. The small arrows enclose an isolated cleavage facet. The large arrow indicates the direction of macroscopic crack propagation.

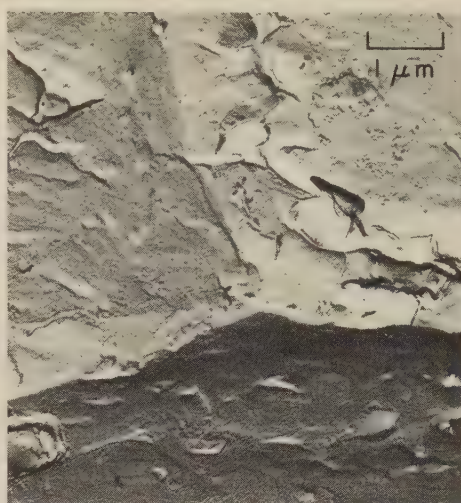
Fig. 61. Fracture surface of titanium alloy Ti-6Al-4V broken by stress-corrosion cracking in methanol (Ref 12)

forgings (Fig. 60), have the same appearance. The latter are not true intergranular fractures, but are significant because they represent fracture through a loosely bonded, or an unbonded, interface.

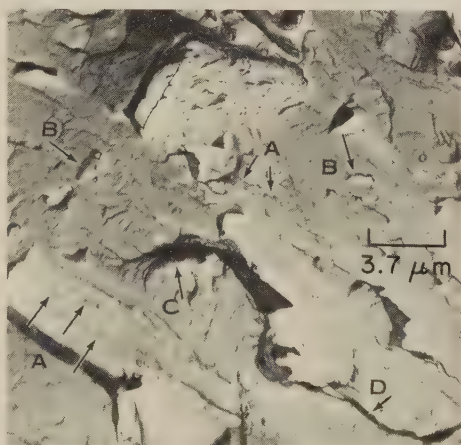
Features of Fractures Resulting From Chemical Environments

This section, together with a counterpart section on page 75, discusses the role of the electron microscope in revealing some of the characteristic fracture features that result from specific combinations of chemical environments and stress. The section on page 75 discusses also the influence of thermal environment (that is, high temperature) on fracture features. The environmental factors considered in the present section are stress-corrosion cracking and hydrogen embrittlement, corrosion fatigue, embrittlement by liquid and solid metals, and the presence of corrosion products on fracture surfaces.

Stress-Corrosion Cracking and Hydrogen Embrittlement. In stress-corrosion cracking and hydrogen embrittlement, the initiation and growth of cracks, or the extension of existing cracks, result from



TEM fractograph (p-c replica) 10,000×
Fig. 62. Intergranular fracture surface of 4340 steel. Fracture was caused by stress-corrosion cracking in 3 1/2% NaCl solution.



TEM fractograph (p-c replica) 2680×
Fracture was caused by stress-corrosion cracking in a 3 1/2% NaCl solution. Stress intensity at the tip of the crack in this region of fracture was low. See also Fig. 64, on the opposite page.

Fig. 63. Transgranular-cleavage fracture in a specimen of 4315 steel, showing tear ridges (A), tongues (B), shallow dimples (C), and secondary cracks (D) (Ref 13)

the combined action of a corrodent and applied or residual stresses. Structures designed to withstand high levels of stress without catastrophic fracture can be severely jeopardized in service when, as a result of stress corrosion, subcritical cracks grow to critical size at low stress levels. In certain alloys, the corrosive environment that causes cracking also affects the resulting topography of the fracture surface. For example, fractures in high-strength aluminum alloys are distinctly intergranular when fracture occurs by stress-corrosion cracking, and the continuous grain-boundary path in the short transverse direction of wrought products makes this direction least resistant to stress-corrosion cracking.

Titanium alloys have been observed to crack by a stress-corrosion-cracking mechanism in a wide variety of environments. Crack extension occurs by transgranular cleavage accompanied by some microvoid growth and coalescence. The

ratio of the areas that fractured by cleavage to those that fractured by microvoid coalescence is directly related to the level of stress intensity at the tip of the propagating crack. Figure 61 shows the fracture surface that developed when titanium alloy Ti-6Al-4V was stressed in methanol at room temperature. The alloy had been solution annealed, quenched and aged at 538 C (1000 F) to develop a yield strength of 1070 MPa (155 ksi). The fracture surface (see Fig. 61) consists of large, flat cleavage facets interconnected by areas of dimples. The cleavage facets show tear ridges and river patterns corresponding to the joining together of cracks propagating at different levels along the main fracture plane. The small arrows in Fig. 61 enclose an isolated cleavage facet; the large arrow indicates the direction of macroscopic crack propagation.

In quenched and tempered high-strength low-alloy steels that have a yield strength of 1035 to 1725 MPa (150 to 250 ksi), fracture by hydrogen embrittlement and by stress-corrosion cracking is typically intergranular when the applied stress-intensity level is low. Fracture initiated by diffusion of hydrogen into the steel, such as may occur during electroplating, can be distinguished from fracture initiated by corrosive attack in aqueous mediums because the crack-initiation sites associated with hydrogen embrittlement are mainly subsurface whereas those associated with stress-corrosion cracking are at the surface. However, fractures associated with stress-corrosion cracking are distinguished by pronounced secondary cracks or deep crevices, and the fractures show a greater amount of corrosion products at the origin and in the slow-growth region than in the rapid-fracture (dimpled) region. A belief that fine tear ridges (hairline indications) were more common on separated-grain facets caused by hydrogen embrittlement than on those caused by stress-corrosion cracking is now held invalid; both mechanisms form tear ridges equally often.

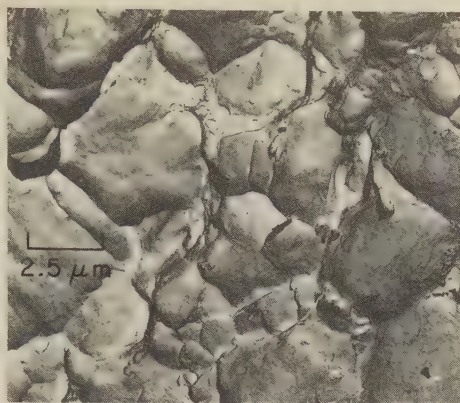
In both hydrogen embrittlement and stress-corrosion cracking of high-strength steels, fractures occur along prior austenite grain boundaries. There is no evidence on the fracture surfaces of the martensitic microstructure of the steels. At high magnification, evidence of a limited amount of ductility can be observed in the form of ridges or dimples on the separated-grain facets. Transgranular cleavage may succeed intergranular separation as the crack lengthens, because of increasing stress intensity.

In Fig. 62, linear marks are visible on the surface of a fracture produced by stressing in a sodium chloride solution a specimen of 4340 steel that had been quenched and tempered to a yield strength of 1380 MPa (200 ksi). Because all of the marks appear as ridges extending above the grain facets when viewed using stereo techniques, they are believed to be associated with the final tearing apart of small uncracked ligaments on the grain surfaces. Evidence of ductility is limited to a very narrow layer on either side of the grain boundary at which separation occurred.

Intergranular separation in high-strength low-alloy steels may be caused not only by stress-corrosion cracking and by hydrogen embrittlement, but also by grinding cracking, heat-treat cracking, quench cracking, temper embrittlement, blue brittleness, liquid-metal embrittlement, solid-metal embrittlement, and overload fracture at low temperature. Also, intergranular separation is not the only type of fracture mechanism associated with stress-corrosion cracking or hydrogen embrittlement in these steels. Both transgranular cleavage and microvoid coalescence have been identified with subcritical, slow crack growth in stress-corrosion environments. A pre-cracked specimen of hardened and tempered 4315 steel stressed in a 3½% NaCl solution exhibited either cleavage or microvoid coalescence, depending on the stress-intensity level at the tip of the growing crack. Figure 63 shows a fracture surface of this steel that resulted from cracking at a low stress-intensity level. The appearance is typical of transgranular cleavage. The flat facets show tear ridges, tongues, shallow dimples, and secondary cracks. In the initial portion of this test, the stress-intensity level was high and the same specimen cracked by the growth and coalescence of microvoids, and the fracture appearance (Fig. 64) that resulted is more typical of fracture by mechanical overload than of fracture by stress-corrosion cracking. The dimple surfaces show stretched regions that are similar to those produced by mechanical overload, and no special features identifying the subcritical nature of the cracking are evident.

An example of intergranular separation in high-strength steels from environmental embrittlement is shown in Fig. 65. A maraging steel with a yield strength of 1725 MPa (250 ksi) was stressed while being electrolytically charged with hydrogen in a bath of 3½% NaCl and water. The single grain-boundary facet shown is covered with a large number of intergranular precipitates. In several areas, tear ridges can be observed; these are associated with cracking around the precipitate particles. The tear ridges were formed when the cracks that were initiated as the result of hydrogen charging grew together.

Corrosion Fatigue. In some metals and alloys, the propagation of fatigue cracks is strongly influenced by environment. The influence is demonstrated in changes in the rate of crack propagation and in changes in the appearance of the fracture surface. As an example, for a specimen of aluminum alloy 2024-T3, the crack-propagation rate in fatigue testing at relatively low amplitude in air was found to be three times the rate for testing in vacuum. The change in fracture appearance was equally dramatic, as shown in Fig. 66. The most striking difference in appearance is the lack of regular fatigue striations in the region that cracked while being tested in vacuum (region A in Fig. 66). This region appears essentially flat and featureless, and there is no correlation between fracture appearance and the cyclic nature of the imposed loading.



TEM fractograph (p-c replica) 3960×
Fracture was caused by stress-corrosion cracking in a 3½% NaCl solution. Stress intensity at the tip of the crack in this region of fracture was high—95% of the plane-strain fracture toughness (K_{Ic}) of the material.

Fig. 64. Dimples resulting from microvoid coalescence on the fracture surface of the specimen of 4315 steel in Fig. 63 (Ref 13)

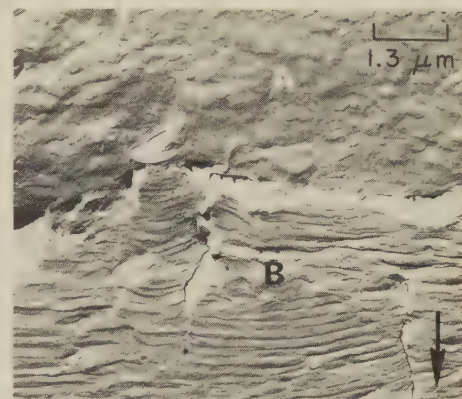


TEM fractograph (p-c replica) 10,000×
Fig. 65. Fracture around precipitates in a grain-boundary surface in maraging steel with a yield strength of 1725 MPa (250 ksi). Note the tear ridges (as at arrows). Fracture was by hydrogen embrittlement during stressing. (Ref 14)

In contrast, the regular fatigue striations produced by fracture while testing in air (region B in Fig. 66) correlate with the crack advance of each loading cycle. The striations resulted from the plastic deformation that occurred at the crack tip as the crack was opened during the tensile portion of the load cycle.

Figure 67 shows the fracture surface of a specimen of aluminum alloy 2024-T3 that was fatigue tested in air and in vacuum at a much lower stress amplitude than the specimen of Fig. 66. At this low stress amplitude, the plasticity producing fatigue striations in the portion tested in air (region A in Fig. 67) is less and the striations are very flat, leaving an impression of transgranular cleavage when viewed at this magnification. This region exhibits linear features that resemble tear ridges and fine river patterns.

Depending on the stress level and cyclic frequency in fatigue testing or in service, certain environments can cause the replacement, or partial replacement, of the fatigue striations generated by mechanical deformation at the crack tip with a fracture that resembles the stress-corrosion cracking that is characteristic of the specific alloy and environment. Figures 68



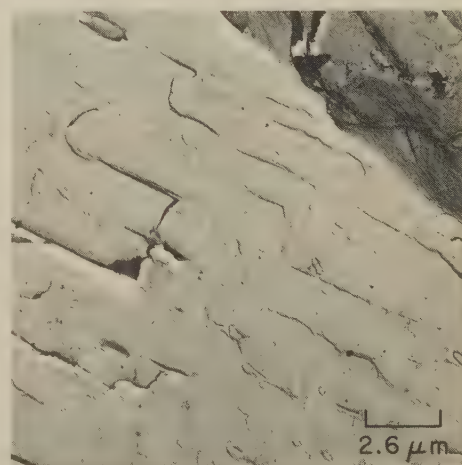
TEM fractograph (p-c replica) 7500×
Stress amplitude was low, but higher than for the fracture shown in Fig. 67. Arrow, at lower right, indicates direction of crack propagation.

Fig. 66. Fatigue fracture in aluminum alloy 2024-T3 tested first in vacuum (region A) and then in air (region B) (Ref 15)

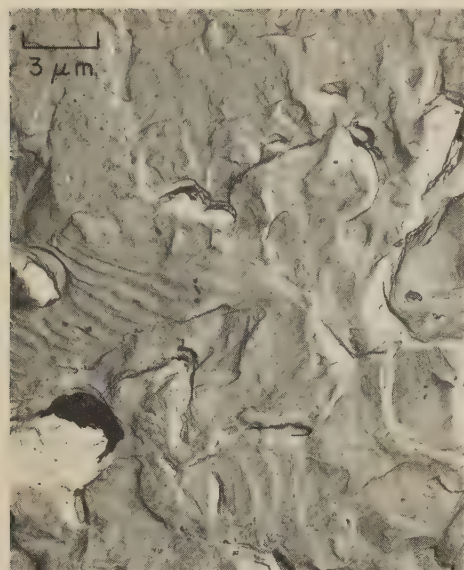


TEM fractograph (p-c replica) 3000×
Stress amplitude was much lower than for the fracture shown in Fig. 66. Flat fatigue striations would be visible in region A by stereoscopic examination or at a higher magnification. Arrow, at bottom, indicates direction of crack propagation.

Fig. 67. Fatigue fracture in aluminum alloy 2024-T3 tested first in air (region A) and then in vacuum (region B) (Ref 15)



TEM fractograph (p-c replica) 3900×
Fig. 68. Transgranular cleavage facets on a corrosion-fatigue fracture surface of titanium alloy Ti-8Al-1Mo-IV tested at a frequency of ½ cycle per second in a 3½% NaCl solution at crack-growth rates ranging from 20 to 200 micro-in. per cycle. Compare Fig. 69. (Ref 16)



TEM fractograph (p-c replica) 3300×
Fig. 69. Coarse fatigue striations and rugged cleavage facets on a corrosion-fatigue fracture surface of titanium alloy Ti-8Al-1Mo-1V tested at a frequency of 1/2 cycle per second in a 3 1/2% NaCl solution at crack-growth rates of over 200 micro-in. per cycle. Compare Fig. 68. (Ref 16)



TEM fractograph (p-c replica) 3600×
Fig. 70. Mixture of separated-grain facets and transgranular cleavage facets on the surface of a fracture in titanium alloy Ti-6Al-4V that was exposed to solid cadmium at 149 C (300 F) (Ref 17)

and 69 show fracture surfaces obtained from specimens of titanium alloy Ti-8Al-1Mo-1V tested in a 3 1/2% NaCl solution at amplitudes producing crack-growth rates ranging from 20 to 200 micro-in. per cycle for Fig. 68 and in excess of 200 micro-in. per cycle for Fig. 69. The appearance of the fracture surface in Fig. 68 is typical of stress-corrosion cracking in this alloy; transgranular cleavage predominates. The fine detail on the cleavage facets is related to the two-phase microstructure of the alloy. At high amplitudes (Fig. 69), the fracture surface consists of coarse fatigue striations and rugged cleavage facets.



TEM fractograph (p-c replica) 2700×
Mud-crack pattern resulted from replication of corrosion products that adhered to the surface and obscured it. Black patches, such as at arrows, are corrosion debris that were lifted off the fracture with the first-stage replica.

Fig. 71. Mud-crack pattern on the surface of an intergranular fracture in aluminum alloy 7079-T651 caused by stress-corrosion cracking in a 3 1/2% NaCl solution (Ref 18)

Because monotonic stress-corrosion cracking depends on both stress and the generation of a critical environment at the crack tip, its capability of significantly contributing to cracking under corrosion-fatigue conditions depends on the level of the stress intensity and the length of time this level is maintained during the fatigue cycle. For cyclic stressing below the minimum required for stress-corrosion cracking under monotonic loading, the difference between fatigue-crack propagation in a vacuum and in a corrosive environment can be attributed to the interaction of the environment and the fresh metal surface that is continually exposed to it by the cyclic stressing.

Embrittlement by Liquid and Solid Metals. Liquid-metal environments have been known to cause cracking of some alloys. A metal in the solid state can have a similar effect. The resulting fracture path can be either transgranular or intergranular, depending on the alloy, its microstructure, and the nature of the environment. Figure 70 shows a fracture surface of a specimen of solution treated and aged titanium alloy Ti-6Al-4V that cracked after exposure to solid cadmium at 149 C (300 F). The fracture occurred by a mixture of intergranular cracking and transgranular cleavage.

Corrosion Products on Fracture Surfaces. The fine details of fracture surfaces are often obscured by the products of corrosion that occurred subsequent to cracking, making analysis of the fracture surface difficult. If the corrosion products

are not tightly bound to the fracture surface, they can be incorporated in and removed by the replica. If corrosion products are not removed with the replica, their exposed surfaces will be replicated, producing artifacts that will interfere with fracture-surface analysis. Figure 71 shows corrosion products that formed on the fracture surface of aluminum alloy 7079-T651 after stress-corrosion cracking in a 3 1/2% NaCl solution. The black angular patches are corrosion debris lifted off the fracture with the first-stage plastic replica. The mud cracks and flat facets represent areas where the corrosion products remained on the surface of the separated-grain facets and were replicated.

References

1. W. A. Spitzig, G. E. Pellissier, C. D. Beachem, A. J. Brothers, M. Hill and W. R. Warke, A Fractographic Analysis of the Relationships Between Fracture Toughness and Surface Topography in Ultra-high-Strength Steels, in "Electron Fractography", ASTM STP 436, American Society for Testing and Materials, Philadelphia, 1968, p 17-31
2. C. D. Beachem and D. A. Meyn, Fracture by Microscopic Plastic Deformation Processes, in "Electron Fractography", ASTM STP 436, American Society for Testing and Materials, Philadelphia, 1968, p 59-88
3. C. Crussard, J. Plateau, R. Tamhankar, G. Henry and D. Lajeunesse, A Comparison of Ductile and Fatigue Fractures, in "Fracture", B. L. Averbach, D. K. Felbeck, G. T. Hahn and D. A. Thomas (Editors), Wiley, New York, 1959, p 524-561
4. H. C. Rogers, The Tensile Fracture of Ductile Metals, *Trans AIME*, Vol 218, June 1960, p 498
5. D. Killpatrick, D. L. Corn and G. R. Stoelckinger, Cryogenic Fracture Toughness of 18 Nickel, 200 Grade Maraging Steel Plate and Welds, Report MDC G2922, McDonnell Douglas Astronautics Co., Huntington Beach, Calif., Apr 1972
6. A. J. Brothers, M. T. Parker, W. A. Spitzig, W. Wiebe and U. E. Wolff, Correlation of Fracture Toughness, K_{Ic} , With Fractographically Derived Plastic Stretched Zone Width, in "Applications of Electron Microfractography to Materials Research", ASTM STP 493, American Society for Testing and Materials, Philadelphia, 1971, p 3-19
7. C. D. Beachem, The Formation of Cleavage Tongues in Iron, Report of NRL Progress, Naval Research Laboratory, Feb 1966, p 519
8. A. Phillips, V. Kerlins and B. V. Whiteson, "Electron Fractography Handbook, Supplement II", AFML-TR-64-416, Air Force Materials Laboratory, Wright-Patterson Air Force Base, Ohio, 1965, p 6-59 to 6-108, Subsection C
9. R. R. Hilsen, C. S. Yen and B. V. Whiteson, Low-Cycle Fatigue of Ti-6Al-4V at -423 F, in "Symposium on Fatigue Tests of Aircraft Structures: Low-Cycle, Full-Scale, and Helicopters", ASTM STP 338, American Society for Testing and Materials, Philadelphia, 1963, p 62-75
10. B. V. Whiteson, A. Phillips, V. Kerlins and R. A. Rowe, Special Fractographic Techniques for Failure Analysis, in "Electron Fractography", ASTM STP 436, American Society for Testing and Materials, Philadelphia, 1968, p 151-178
11. G. F. Pittinato, Hydrogen Enhanced Fatigue Crack Growth in Ti-6Al-4V ELI Weldments, *Met Trans*, Vol 3, Jan 1972, p 235-243
12. D. A. Meyn, Effect of Crack Tip Stress Intensity on the Mechanism of Stress-Corrosion Cracking of Titanium-6Al-4V in Methanol, *Corrosion Sci*, Vol 7, No. 10, Oct 1967, p 721-723
13. C. D. Beachem, A New Model for Hydrogen-Assisted Cracking (Hydrogen "Embrittlement"), *Met Trans*, Vol 3, No. 2, Feb 1972, p 437-451
14. Plastic Deformation at Crack Tips During Hydrogen-Assisted Cracking of Maraging Steel, Report of NRL Progress, Mar 1971
15. D. A. Meyn, The Nature of Fatigue Crack Propagation in Air and Vacuum for 2024 Aluminum, *Trans Am Soc Metals*, Vol 61, No. 1, Mar 1968, p 52-61
16. D. A. Meyn, An Analysis of Frequency and Amplitude Effects on Corrosion Fatigue Crack Propagation in Ti-8Al-1Mo-1V, *Met Trans*, Vol 2, No. 3, Mar 1971, p 853-865
17. D. A. Meyn, Solid Cadmium Cracking of Titanium Alloys, *Corrosion*, Vol 29, No. 5, May 1973, p 192-196
18. D. A. Meyn, Fractographic Diagnosis of Stress-Corrosion Cracking in Al-Zn-Mg Alloys, *Corrosion*, Vol 26, No. 10, Oct 1970, p 427-429

Discontinuities Leading to Fracture That Are Revealed by Fractography

By the ASM Committee on Fractography by Electron Microscopy
and the ASM Committee on Use of Fractography for Failure Analysis†*

THE CAUSE of fracture of a stressed part is often the presence of an internal or a surface discontinuity. The manner in which these types of discontinuities cause fracture and affect the features of fracture surfaces is described and fractographically illustrated in this article.

Discontinuities such as laps, seams, cold shuts, previous cracks, porosity, inclusions, segregation, and unfavorable grain flow in forgings often serve as nuclei for fatigue fractures or stress-corrosion fractures because they increase both local stresses and reactions to detrimental environments. Large discontinuities may reduce the strength of a part to such an extent that it will fracture under a single application of load. However, a discontinuity should not be singled out as the sole cause of fracture without considering other possible causes or contributing factors. Thorough failure analysis may show that the fracture would have occurred even if the discontinuity had not been present.

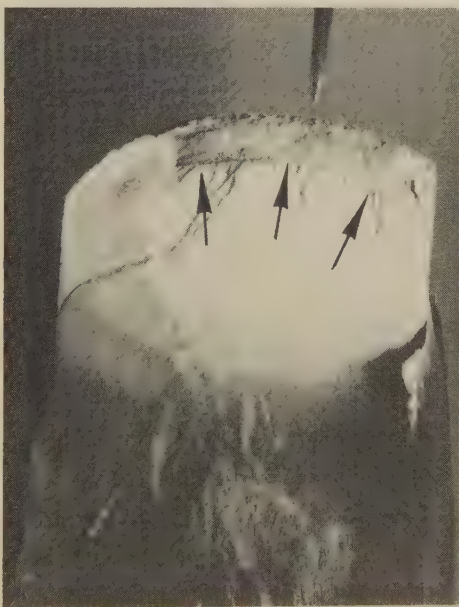
Fractures that originate at, or pass through, significant metallurgical discontinuities usually show a change in texture, surface contour, or coloration in the vicinity of the discontinuity. Often, examination of a suspect area at several different magnifications and under several different lighting conditions will help to determine whether a significant discontinuity is present and may provide information about its size and type. Varying the angle of incident light during examination with a low-power stereomicroscope may be especially helpful. Sometimes, segregation or unfavorable grain flow may contribute to fracture without showing evidence that can be detected by direct visual examination. Even when visual indications of a metallurgical discontinuity are present, corroborating evidence should be obtained from other sources, such as examination of metallographic sections through the suspect area or study of local variations in chemical composition by electron microprobe analysis or Auger spectroscopy.

Even though cracks usually originate at discontinuities, type of discontinuity does not necessarily determine fracture mechanism. For example, fracture from a gross discontinuity, such as a rolling lap, can occur by any of the common fracture mechanisms. In general, discontinuities act as fracture-initiation sites and

cause fracture initiation to occur earlier, or at lower loads, than it would in material free from discontinuities.

Laps, Seams and Cold Shuts

An observer who has some familiarity with the characteristics of various types of fractures in the material being examined can usually find indications of a discontinuity if one was present at the fracture origin. A flat area that, when viewed without magnification, appears black or dull gray and does not exhibit the normal characteristics of fracture indicates the presence of a lap, a seam or a cold shut. (Such an area may appear to have resulted from the peeling apart of two metal surfaces that were in intimate contact, but not strongly bonded together.) The surface of a seam that resulted in a fatigue fracture of a 1046 (mod) steel crankshaft is shown in Fig. 1. A lap, a seam or a cold shut is fairly easy to identify under a low-power stereomicroscope also, because the area of any of these discontinuities is distinctly different in texture and color from the remainder of the fracture surface.



Light fractograph 4.2×
The seam was in the area between the fracture edge indicated by the pointer and the line indicated by the arrows. Hardness of the steel was 255 Bhn.

Fig. 1. Fatigue fracture that propagated from a seam in the counterbalance cheek of a forged 1046 (mod) steel crankshaft

Figure 2 demonstrates the depth of field and general utility of the scanning electron microscope at low magnification for identifying discontinuities such as seams and laps. The fractographs in Fig. 2 show laps that had been rolled into the thread roots of a 300M steel stud during thread rolling. The laps served as origins of a stress-corrosion crack that partly severed the stud. Both surfaces of a lifted lap (Fig. 2c) were heavily oxidized (Fig. 2d and e), indicating that the lap was formed before the stud was heat treated (to produce a tensile strength of 1930 to 2070 MPa, or 280 to 300 ksi). The appearance of the stress-corrosion crack near the origin is shown in Fig. 3. (The fractographs in Fig. 3 illustrate the difference in appearance of intergranular fracture and corrosion products when viewed with a scanning electron microscope and with a transmission electron microscope.)

A lap in an aluminum alloy 7075-T6 forging is shown in Fig. 4. This lap was formed when a free surface was folded over during a forging operation. When the fold area was broken open, it appeared anomalous and tarnished, with some indication of oxidation products.

Cracks

The cause and size of a preexisting crack are of primary importance in fracture mechanics, as well as in failure analysis, because of their relationship to the critical crack length for unstable crack growth. Figure 5 shows a fracture in a highly stressed 4340 steel part. A narrow zone of corroded intergranular fracture at the surface of the part is adjoined by a zone of uncorroded intergranular fracture, which in turn is adjoined by a dimpled region. The part had been reworked to remove general corrosion products shortly before fracture. It was concluded that the rework failed to remove about 0.004 in. of a preexisting stress-corrosion crack, which continued to grow after the part was returned to service.

In Fig. 6, the light fractograph shows a preexisting cleavage crack that grew from several origins and served as the nucleus for an overload fracture in a 300M steel part that had been heat treated to a tensile strength of 1930 to 2070 MPa (280 to 300 ksi); the transmission-electron-microscope fractograph in Fig. 6 shows the presence of corrosion products on the fracture surface.

*See page 49 for committee list.

†See page 106 for committee list.

The heat-treat cracks that most commonly contribute to service fractures are the transformation-stress cracks and quenching cracks that occur in steel. When a heat-treat crack is broken open, the surface of the crack usually has an intercrystalline or intergranular texture. If a crack has been open to an external surface of the part (so that air or other gases could penetrate the crack), it usually has been blackened by oxidation during subsequent tempering treatments or otherwise discolored by exposure to processing or service environments. The appearance of such a crack is shown between the two arrows in Fig. 7.

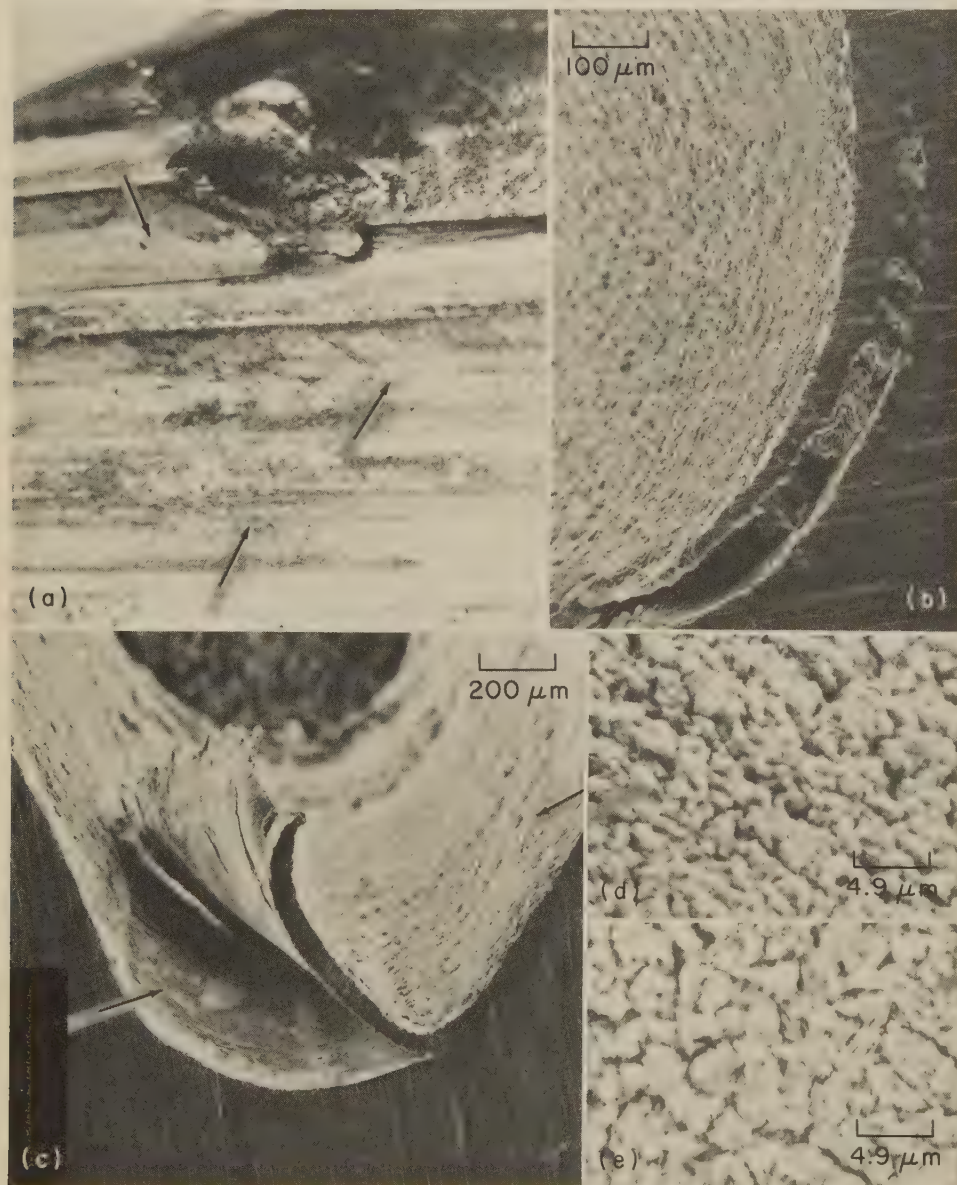
Heat treatment in the temperature range of 204 to 538 C (400 to 1000 F) may produce temper colors (various shades of straw, blue or brown) on the surface of a crack open to an external surface. The

appearance of temper colors is affected by the composition of the steel, the time (as well as the temperature) of exposure, the furnace atmosphere, and the environment subsequent to the heat treatment that produced the temper color.

Incomplete fusion or inadequate weld penetration can produce a material discontinuity similar to a crack. Subsequent loading can cause the discontinuity to grow, as in Fig. 8, which shows a fracture in a weld in commercially pure titanium that broke by fatigue from crack nuclei, on both surfaces, that resulted from incomplete fusion during welding.

Inclusions

Discontinuities in the form of inclusions, such as oxides, sulfides, and silicates, can initiate fatigue fractures in

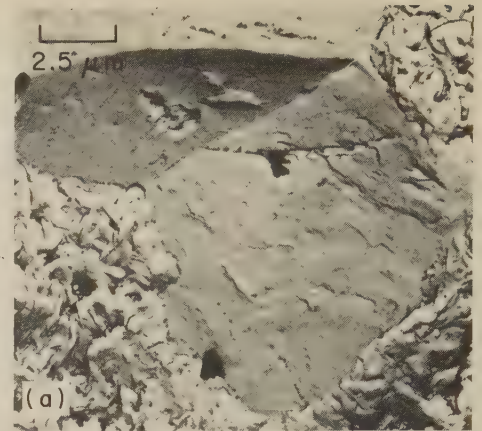


(a) Light fractograph, at 10X, showing laps (at arrows). (b) SEM fractograph, at 100X, giving detail of a lap. (c) SEM fractograph, at 50X, showing heavily oxidized surfaces of a lifted lap; the oxidation indicates that the lap was present before heat

treatment of the stud. Arrow at right points to area shown in fractograph (d), and arrow at left points to area shown in fractograph (e).

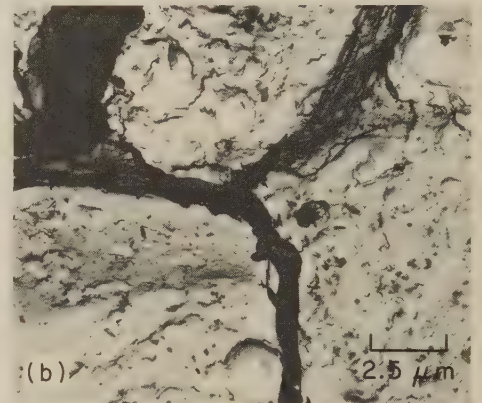
(d) and (e) SEM fractographs showing oxidized surfaces of the lifted lap in fractograph (c) at 2040X.

Fig. 2. Laps formed during thread rolling of a 300M steel stud. See Fig. 3 for views of the stress-corrosion crack initiated by the laps.



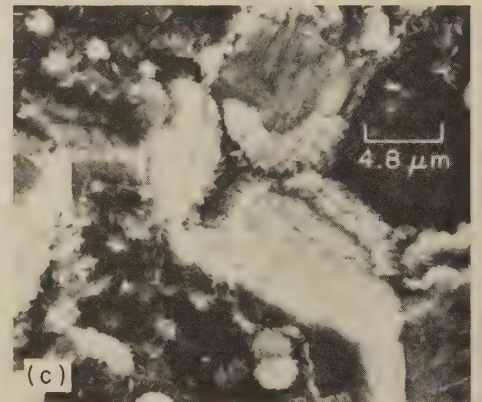
TEM fractograph (p-c replica)

4000X



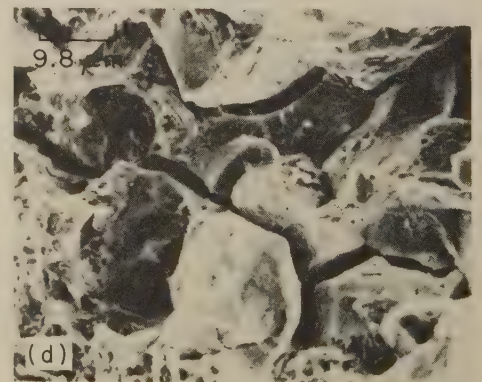
TEM fractograph (p-c replica)

4000X



SEM fractograph

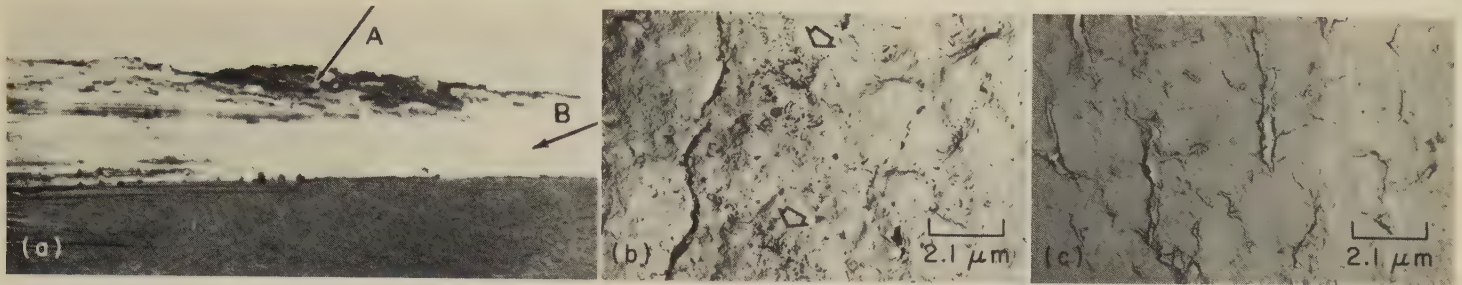
2065X



SEM fractograph

1020X

Fig. 3. TEM and SEM views of the stress-corrosion crack in the 300M steel stud for which Fig. 2 shows laps formed during thread rolling. Note intergranular nature of the fracture, corrosion products, and secondary grain-boundary cracks.



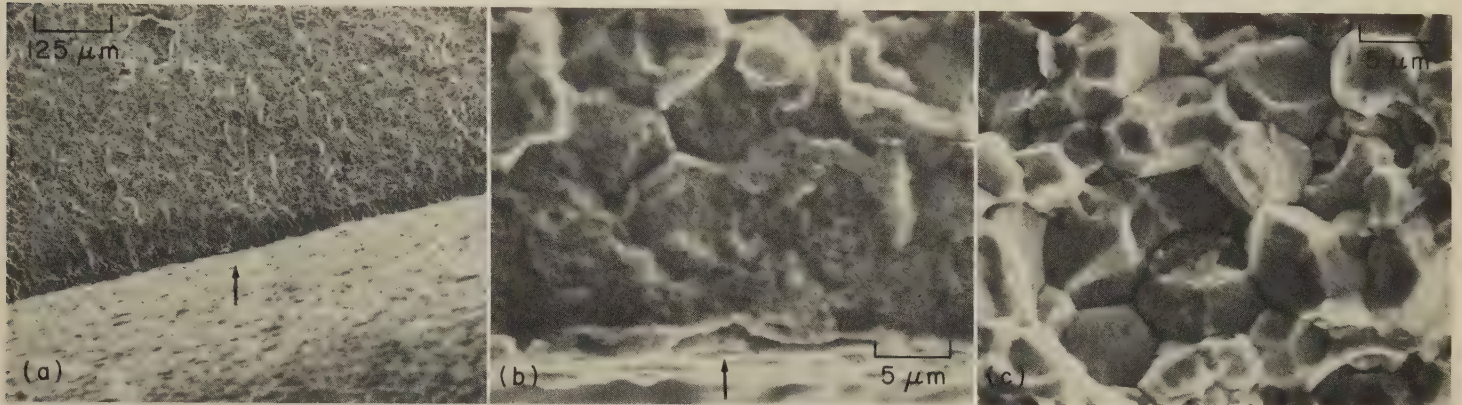
Light fractograph

2× TEM fractograph (p-c replica)

4875× TEM fractograph (p-c replica)

4875×

Fig. 4. Surface lap (fold) found in a test specimen from an aluminum alloy 7075-T6 forging. The area that had been folded over had a flat, anomalous appearance. There were some oxides on its surface, as at A in (a) and at the arrows in (b). The light region B in (a) is a saw cut made to facilitate breaking open the lap.



SEM fractograph

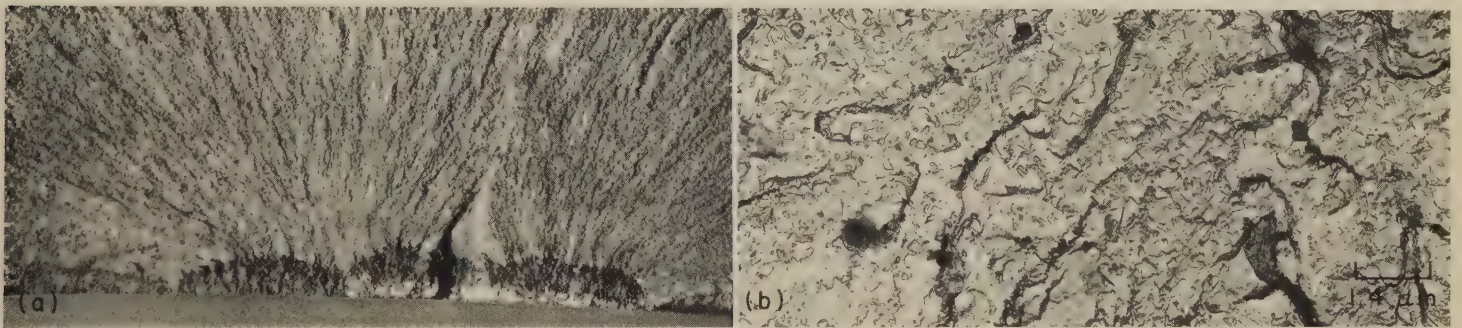
80× SEM fractograph

2000× SEM fractograph

2000×

(a) and (b) Remains of an old crack along the edge of the surface of the part (arrows); note dark zone in (a) and extensively corroded separated-grain facets in (b). (c) Clean intergranular portion of crack surface, formed at the time of final fracture.

Fig. 5. Fracture caused by a portion of an old intergranular stress-corrosion crack that was not removed in reworking. Part was made of 4340 steel, heat treated to a tensile strength of 1790 to 1930 MPa (260 to 280 ksi).

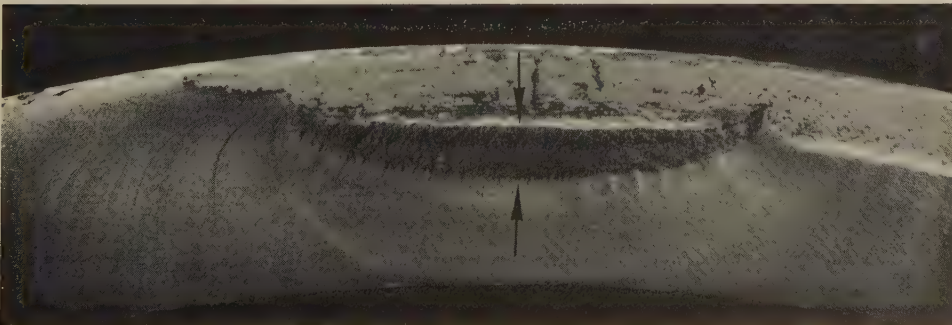


Light fractograph

About 5× TEM fractograph

7000×

Fig. 6. Preexisting cleavage crack (in light fractograph) that grew from several origins and served as the nucleus for an overload fracture in a 300M steel part that had been heat treated to a tensile strength of 1930 to 2070 MPa (280 to 300 ksi). TEM fractograph shows corrosion products on the fracture surface.

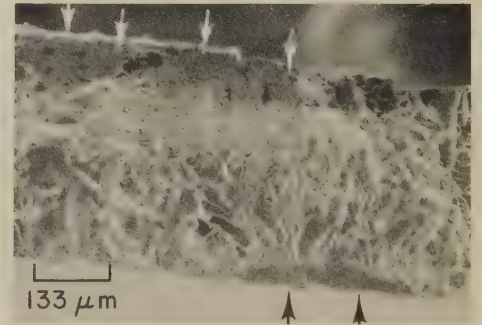


Light fractograph

4×

The quenching crack was in the dark, granular area between the two arrows. Metallographic examination showed that this portion of the fracture was intergranular and was covered with a black oxide scale. Oxidation occurred during heat treatment following the quenching operation.

Fig. 7. Fatigue fracture that propagated from a quenching crack in a 4350 steel forging that had a hardness of Rockwell C 35



SEM fractograph

75×

Fig. 8. Fracture in a weld in commercially pure titanium, showing incomplete fusion. Unfused regions, on both surfaces (arrows), served as nuclei of fatigue cracks that developed later under cyclic loading.



parts subjected to cyclic loading. In addition, such inclusions have been identified as initiation sites of ductile fractures in aluminum alloys and steels by several investigators (Ref 1-3). At relatively low strains, microvoids form at inclusions, either by fracture of the inclusion or by decohesion of the matrix-inclusion interface. Figure 9 shows a fracture surface of aluminum alloy 2124-T851 containing

TEM fractograph

1300×

Fig. 9 (at left). Fracture surface of aluminum alloy 2124-T851, showing large dimples (at A's) that initiated at large inclusions (arrow at C). Cracking was produced by relatively little strain. During final, fast fracture, many small dimples (such as at B) formed at fine particles.

large inclusions (one of which is shown in Fig. 9) that initially fractured to form microvoids. With additional straining, the microvoids grew to the size represented by the large dimples. During final fracture, many small dimples formed at fine particles.

The ductile-fracture mechanism for 4340 steel is similar to that for aluminum. The mechanism for 18% Ni maraging steel differs in that a relatively few large microvoids grow until they meet in final fracture and form dimples; there is no formation of small dimples. This difference is shown in Fig. 10.

Figure 11 shows typical fracture-surface characteristics produced by plane-strain fracture-toughness tests of two experimental heats of quenched-and-tem-



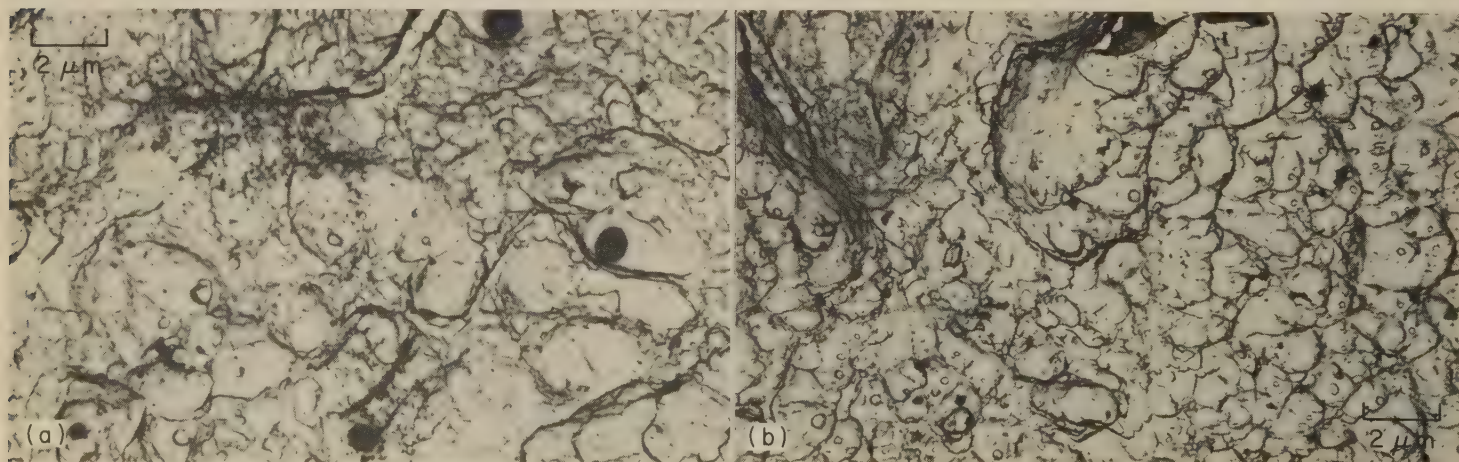
TEM fractographs (p-c replicas)

(a) Fractograph taken adjacent to the fatigue crack in a plane-strain fracture-toughness specimen of commercial-quality 4340 steel. At A is a large dimple; B indicates a region of small dimples. Note similarity of appearance of this fracture surface to that in area B of the fracture surface shown in Fig. 9.

4100× (a); 2400× (b)

(b) Fractograph taken adjacent to the fatigue crack in a plane-strain fracture-toughness specimen of high-quality 18% Ni maraging steel. At X is a cleaved particle of titanium carbonitride at the bottom of a large dimple. Note the absence of small dimples, such as are present in region B in (a).

Fig. 10. Comparison of dimple formation at inclusions in 4340 steel and in 18% Ni maraging steel



TEM fractographs

(a) Specimen from heat containing 0.049% sulfur. Large, shallow dimples were nucleated by relatively coarse sulfide particles. (b) Specimen from heat containing 0.008% sulfur. Many small dimples were nucleated by small carbide particles, but there were relatively few large dimples derived from sulfide particles.

Both at 5000×

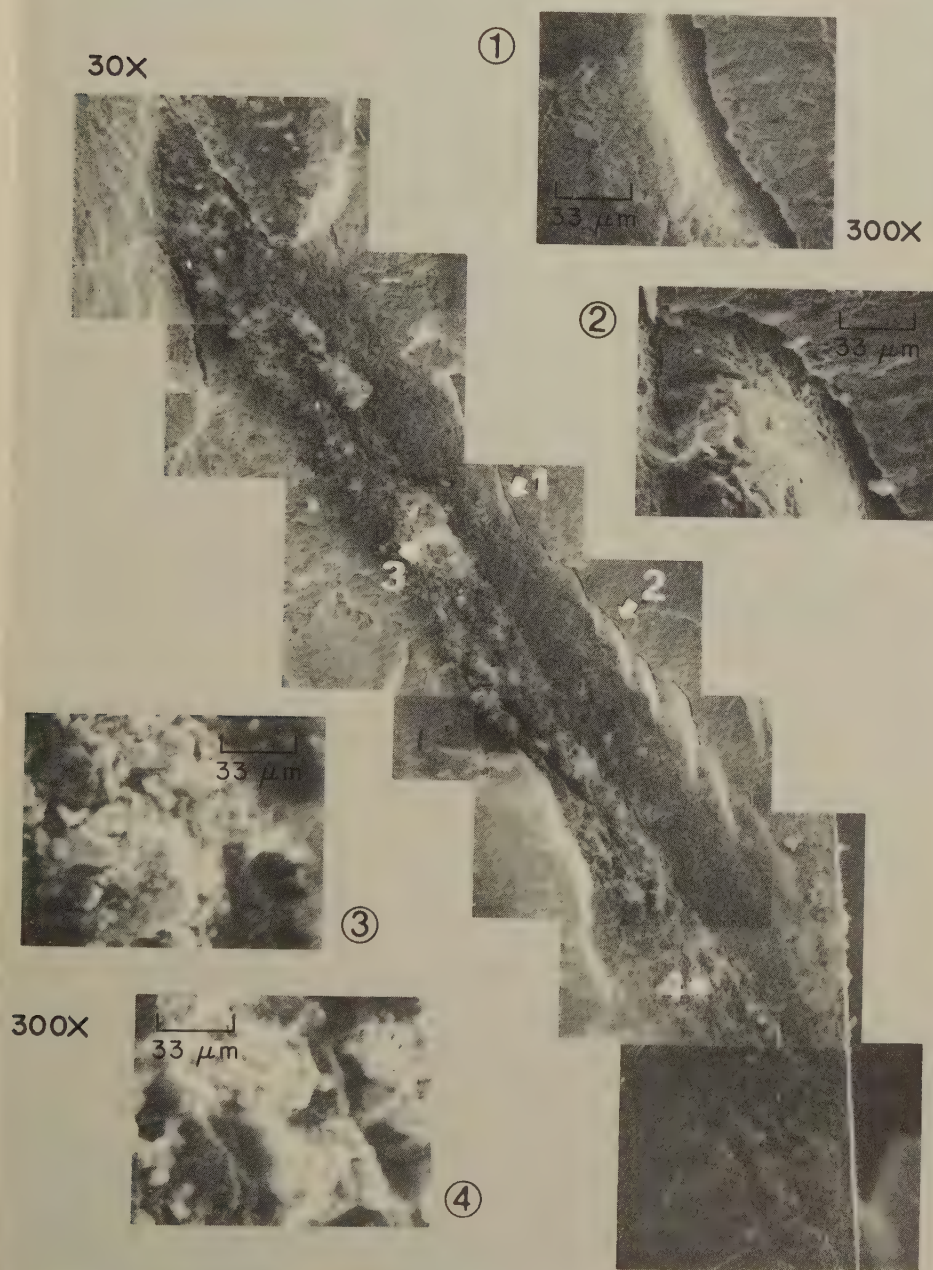
Fig. 11. Fracture surfaces of two plane-strain fracture-toughness specimens from experimental heats of martensitic 0.45% C nickel-chromium-molybdenum steel containing different amounts of sulfur. Both specimens were tempered at 427 C (800 F).

pered 0.45% C nickel-chromium-molybdenum steel with extremes of sulfur content. Because high-purity materials and carefully controlled melting procedures were used, both heats were remarkably free of nonmetallic inclusions, except for sulfide particles (Ref 1). The fracture surfaces of specimens from both heats of steel consisted predominantly of equiaxed dimples. The fracture surface of the 0.049% S steel (see Fig. 11a) consists of many large, shallow dimples that appear to have been nucleated during the fracture process by numerous, relatively coarse sulfide particles. In contrast, the fracture surface of the 0.008% S steel

(see Fig. 11b) shows relatively few large dimples (and associated sulfide particles) and many small dimples, which evidently were nucleated by small carbide particles.

The very large inclusion shown in the SEM fractographs in Fig. 12 was found in the fracture surface of a case-hardened 9310 steel forging that broke in service. X-ray analysis of the inclusion led to the deduction that it was a fragment of the firebrick lining of the pouring ladle.

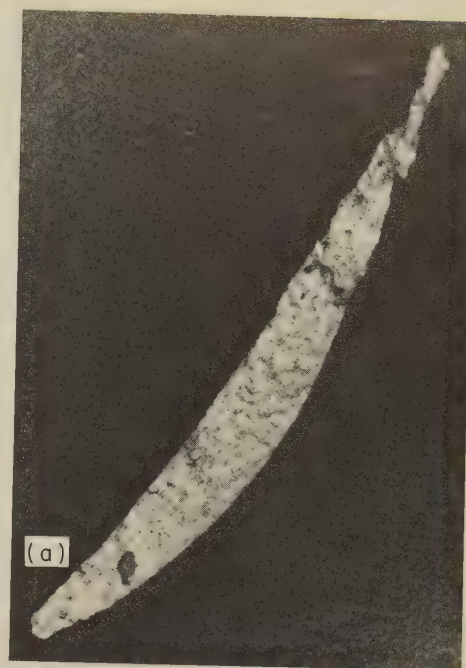
Figure 13 shows a large inclusion in a fracture surface of a cast aluminum alloy A357-T6 blade of a small, high-speed air turbine and two views of the fracture-surface features around this inclusion.



SEM fractographs

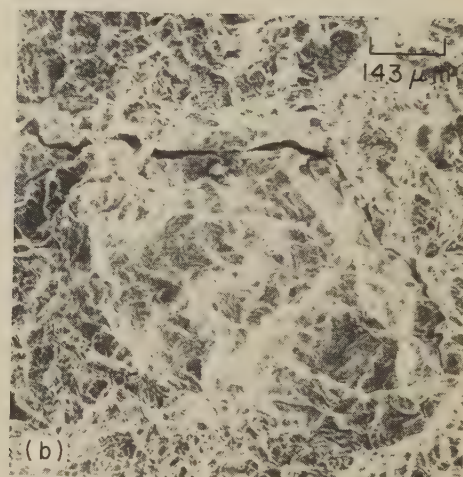
The diagonal view is a composite of several fractographs showing a very large inclusion, which was a fragment of the pouring-ladle firebrick lining. Fractographs 1, 2, 3 and 4 are higher-magnification views of areas indicated respectively by arrows 1, 2, 3 and 4 in the diagonal view.

Fig. 12. Inclusion in a surface of a service fracture in a case-hardened 9310 steel forging



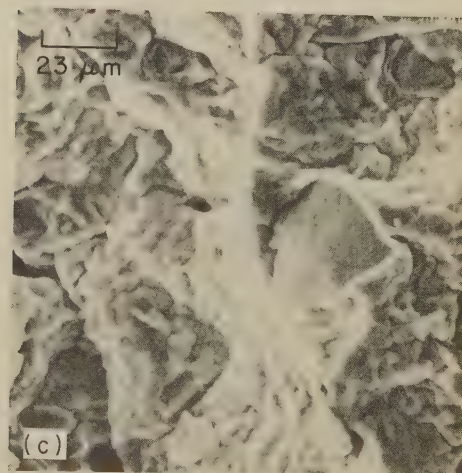
Light fractograph

About 0.4X



SEM fractograph

About 70X

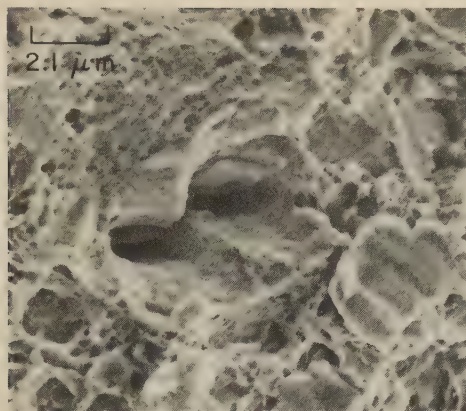


SEM fractograph

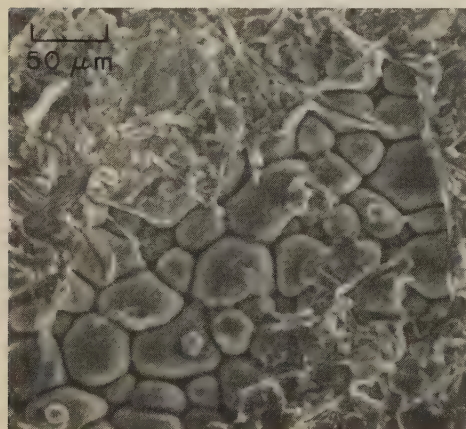
430X

(a) Over-all view of the fracture surface, showing a large inclusion (dark) near the tip of the blade. (b) and (c) Decohesion at the interfaces between the inclusion and the aluminum matrix.

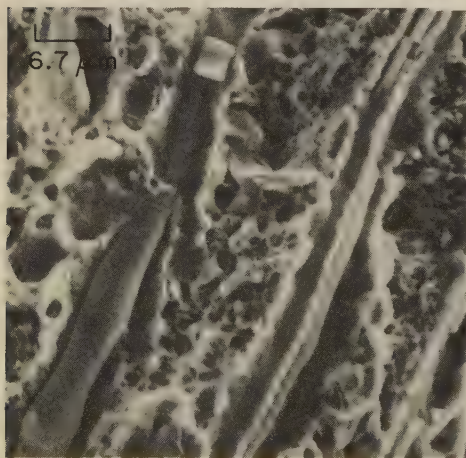
Fig. 13. Fracture surface of a cast aluminum alloy A357-T6 air-turbine blade



SEM fractograph 4700×
Fig. 14. Fracture surface of 4340 steel heat treated to a tensile strength of 1790 to 1930 MPa (260 to 280 ksi), showing deep dimples containing the inclusions that initiated them (J. Kilpatrick, Delta Air Lines)



SEM fractograph 200×
Fig. 15. Halide-flux inclusion (rounded granules) in the joint between an actuator and an attachment bracket of aluminum alloy 6061 that were joined by dip brazing using an Al-12Si brazing alloy



SEM fractograph 1500×
Stringers are visible as parallel features inclined about 30° to right of vertical. They were not identified as to composition, but may be accidentally entrapped slag that was elongated in the major direction of flow during forging.

Fig. 16. Stringers on the surface of a fracture that occurred during straightening of a 4340 steel forging that had been heat treated to a tensile strength of 1380 to 1520 MPa (200 to 220 ksi)

Figure 14 shows the fracture features associated with inclusions in 4340 steel with a tensile strength of 1790 to 1930 MPa (260 to 280 ksi).

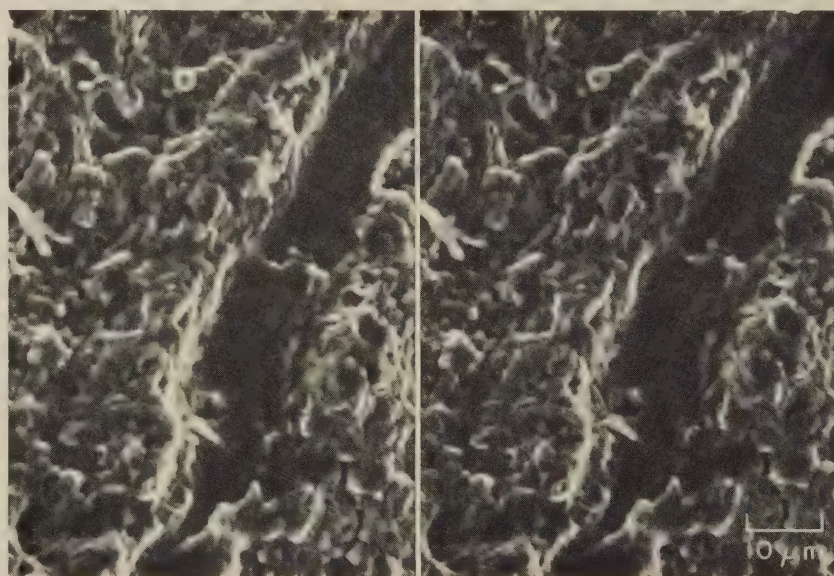
Entrapped flux in a brazed joint can effectively reduce the strength of the brazement and also can create a long-term corrosion problem. An aluminum alloy 6061 attachment bracket was dip brazed to an actuator of the same alloy in a flux consisting of a mixture of sodium, potassium and lithium halides that conformed to AMS 3415 and 3416, and the assembly was heat treated to the T6 temper after brazing. Here the flux inclusion, shown in Fig. 15, reduced the cross section of the joint, and an overload fracture occurred in the Al-12Si brazing alloy.

Stringers are elongated nonmetallic inclusions, or metallic or nonmetallic constituents, oriented in the direction of

working. Nonmetallic stringers usually form from deoxidation products or slag, but may also result from the intentional addition of elements such as sulfur to enhance machinability. Figure 16 shows unidentified stringers on the fracture surface of a 4340 steel forging. Overload cracking occurred during straightening after the forging had been heat treated to a tensile strength of 1380 to 1520 MPa (200 to 220 ksi).

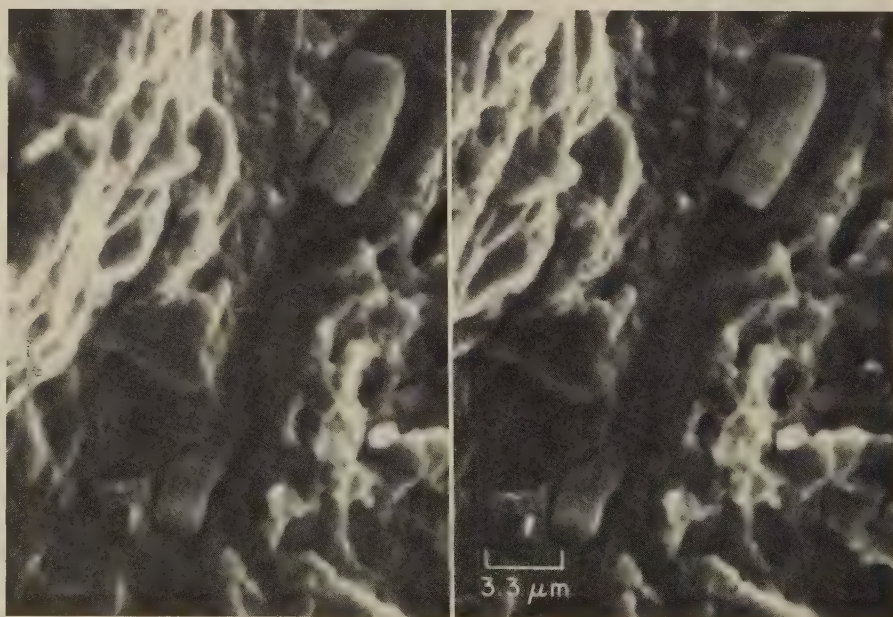
The stereo pairs of SEM fractographs in Fig. 17 show a stringer similar to those in Fig. 16, and two stringer troughs, in a fracture in 4340 steel heat treated to a tensile strength of 1310 to 1450 MPa (190 to 210 ksi).

Figure 18 presents a comparison of the appearance of stringers and troughs when examined with a scanning electron microscope and with a transmission electron



SEM fractograph (stereo pair)

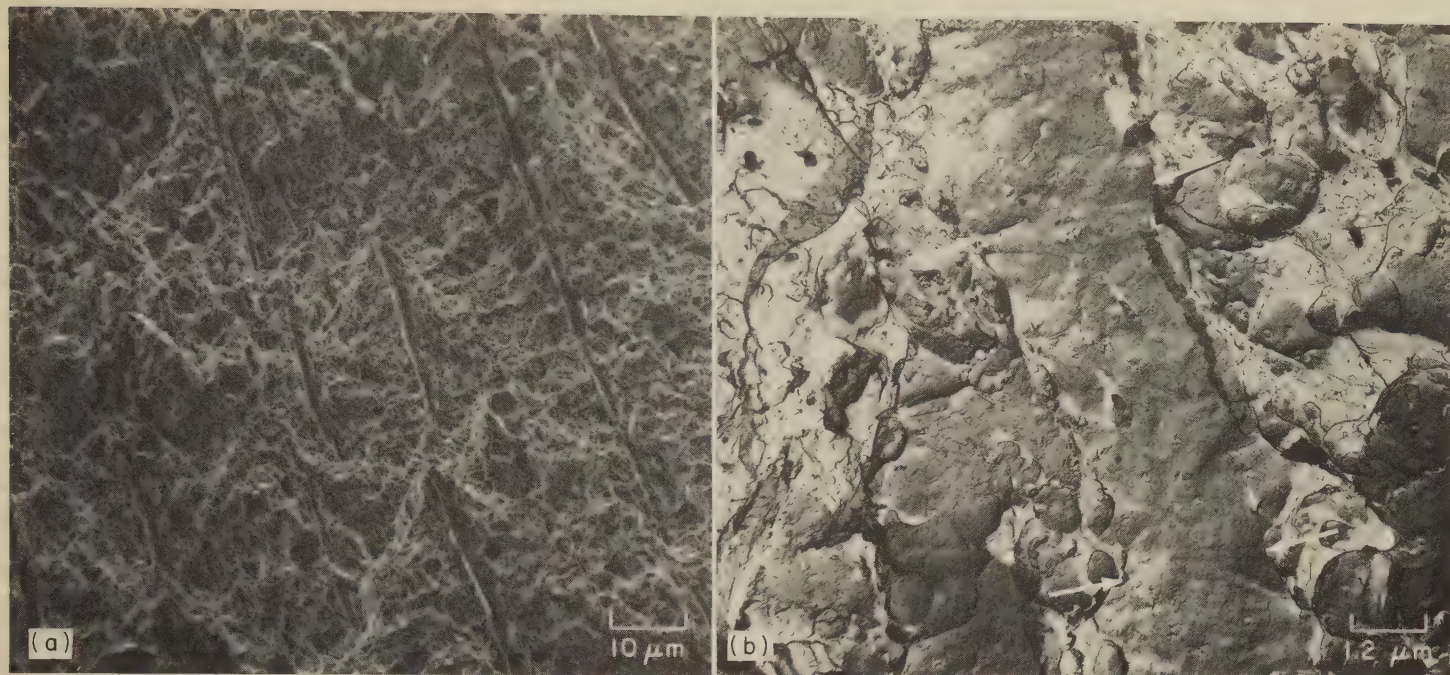
1000×



SEM fractograph (stereo pair)

3000×

Fig. 17. Stringer and two stringer troughs on the fracture surface of 4340 steel heat treated to a tensile strength of 1310 to 1450 MPa (190 to 210 ksi). Stereofractograph at top shows a trough that earlier contained a stringer. Stereofractograph at bottom shows a trough that still contains two portions of a stringer.



SEM fractograph

960×

TEM fractograph

8160×

Fig. 18. Stringer troughs in the surface of an overload fracture in 4340 steel heat treated to a tensile strength of 1790 to 1930 MPa (260 to 280 ksi). (a) SEM fractograph showing several troughs. (b) TEM fractograph showing dimples of various sizes on either side of a trough (between pairs of arrows). (J. Kilpatrick, Delta Air Lines)

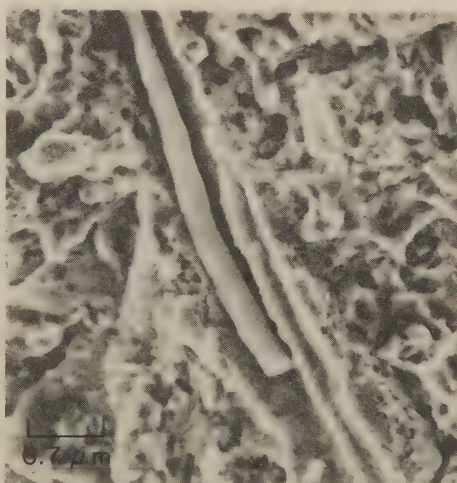
microscope. The fractographs show an overload-fracture surface of 4340 steel heat treated to a tensile strength of 1790 to 1930 MPa (260 to 280 ksi).

Figure 19 shows a sulfide stringer in a trough on a fracture surface of 6150 steel heat treated to a tensile strength of 1240 to 1380 MPa (180 to 200 ksi).

Porosity

Porosity is the name applied to a condition of fine holes or pores in a metal. It is most common in castings and welds, but residual porosity from the cast ingot sometimes still persists in forgings. In fractures that occur through regions of excessive porosity, numerous small depressions or voids (sometimes appearing as round-bottom pits) or areas with a dendritic appearance can be observed. At low magnification, fractures through regions of excessive porosity may appear "dirty" or "sooty" because of the large number of small voids, which look like black spots. A large shrinkage cavity in a fracture through a cast 0.20% C steel spindle shaft is shown in Fig. 20. A dendritic structure is visible in a portion of the cavity.

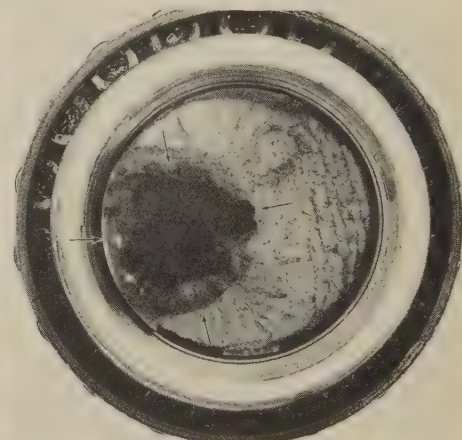
Molten aluminum alloys are likely to absorb hydrogen from moisture in the atmosphere or in products of combustion. Liberation of the hydrogen during solidification of the metal can cause gas porosity. A fracture in an aluminum alloy 220-T6 casting is shown in Fig. 21(a). A metallographic section cut from an area adjacent to the fracture is shown in Fig. 21(b). Figure 22 shows random porosity (with pores surrounded by dimples) in a fracture of a cast aluminum alloy A357 air-turbine blade. Fracture was caused by overload from an impact.



SEM fractograph

1500×

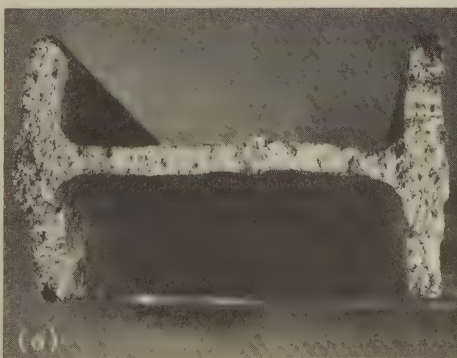
Fig. 19. Sulfide stringer in trough on fracture surface of 6150 steel heat treated to a tensile strength of 1240 to 1380 MPa (180 to 200 ksi)



Light fractograph

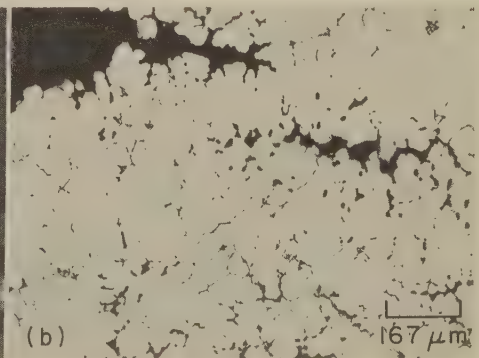
0.8×

Fig. 20. Fracture through a large shrinkage cavity (arrows) in a spindle shaft made of cast 0.20% C steel. A dendritic structure is present on the surface of the cavity (this is shown more clearly in fractographs 4809 and 4810 on page 382).



Light fractograph

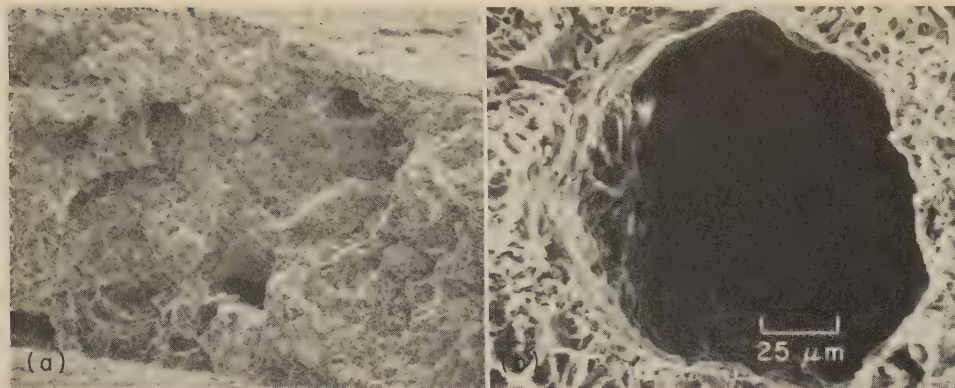
1.2×



Micrograph (Keller's reagent)

60×

Fig. 21. (a) Fracture through excessive porosity in an aluminum alloy 220-T6 casting. Large voids appear as black spots. (b) Appearance of microporosity in a metallographic section adjacent to the fracture.



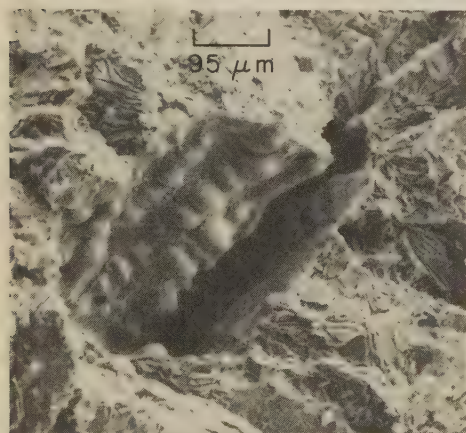
SEM fractographs

40× (a); 400× (b)

Fig. 22. Porosity in a fracture of a cast aluminum alloy A357 blade from a small air turbine. The blade fractured by overload from an impact to its outer edge.

Figure 23 shows a shrinkage void intersected by the fracture surface of a cast aluminum alloy A357-T6 gear housing. The dendrite nodules in the void indicate that the cavity was caused by unfavorable directional solidification during casting. The fracture was caused by overload.

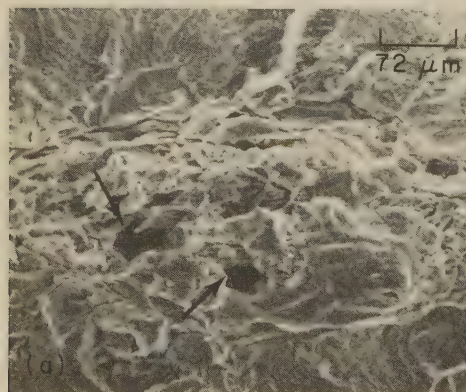
Figure 24 shows SEM fractographs of the surface of a fatigue fracture in a resistance spot weld that broke during bond testing of an aluminum alloy 7075-T6



SEM fractograph

105×

Fig. 23. Shrinkage void with dendrite nodules on a fracture surface of a cast aluminum alloy A357-T6 gear housing that broke by overload



SEM fractographs

140× (a); 700× (b)

Fig. 24. Fatigue-fracture surface of a resistance spot weld that broke during bond testing of an aluminum alloy 7075-T6 specimen. (a) Note voids (at arrows) caused by molten-metal shrinkage in the weld nugget. (b) Both fatigue striations and shrinkage voids are evident, which indicates that the fracture path favored the porous areas.

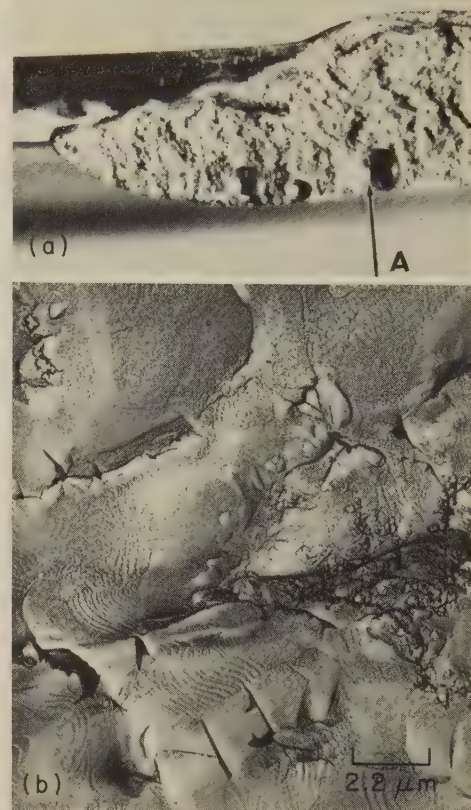
specimen. The voids in the weld nugget are apparent in both fractographs. The fatigue-fracture path appears to favor the voids.

The fracture shown in Fig. 25 revealed cavities that had formed from gas trapped during solidification of aluminum alloy 2014 weld metal. These spherical cavities had smooth surfaces with steplike geometric patterns (see Fig. 25b). Figure 26 shows similar features on the surface of a void in a gas tungsten-arc weld in maraging steel; the weld was made using modified 18Ni-9Co-5Mo steel filler wire.

Traces of porosity are sometimes found in forgings. Figure 27 shows a fracture in an aluminum alloy 2014 forging that contained porosity, which appears as small, shiny, flakelike regions. At high magnification, some areas of porosity show the same steplike geometric patterns as those shown in Fig. 25(b), and other areas show oxide scale. The presence of oxide scale probably accounts for the pores not "healing" during forging.

Segregation

The portion of a fracture in a region of segregation may appear either more brittle or more ductile than the portion in the surrounding regions. Differences in fracture texture may be slight and therefore difficult to evaluate. Fractographic evidence of segregation should always be



(a) A light fractograph, at 3×, showing a trapped-gas cavity at A. (b) A TEM fractograph, at 4550×, showing trapped-gas cavities that have smooth interior surfaces containing elaborate steplike geometric patterns.

Fig. 25. Two views of a fracture surface of aluminum alloy 2014 weld metal showing trapped-gas cavities

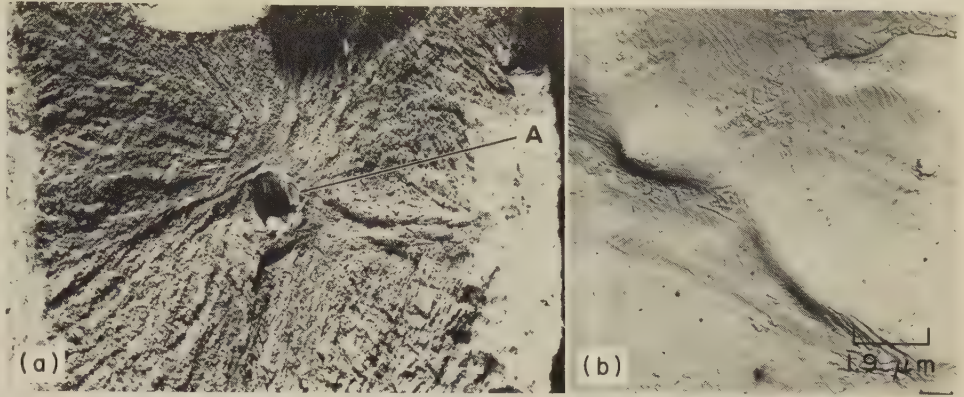
confirmed by comparing the microstructure and chemical composition of the material in the suspect region with those in other locations in the same part. A fracture through a region of segregation in an annealed titanium alloy Ti-6Al-4V forging is shown in Fig. 28(a). The appearance of the microstructure adjacent to the fracture is shown in Fig. 28(b) and (c).

Grain-Boundary Discontinuities

Grain-boundary discontinuities are material discontinuities such as embrittling phases and melted eutectic. For example, the 18% Ni maraging steels become severely embrittled if they are heated to temperatures of 1093 C (2000 F) or higher and cooled slowly through the range of 982 to 760 C (1800 to 1400 F) without sufficient simultaneous hot working. The embrittlement is of an intergranular nature, and fracture takes place predominantly along prior austenite grain boundaries. Fracture surfaces of fracture-toughness specimens of unembrittled, heat treated maraging steels consist almost entirely of equiaxed dimples, but fracture surfaces of specimens of embrittled maraging steel are intergranular, with quite smooth and only slightly curved contours. Figure 29(a) is a TEM fractograph of an extraction replica showing the segregate embrittling phase in a com-

mercial maraging steel that contained 0.027% C and 0.001% N. The segregate phase has been identified as titanium carbonitride, $Ti(C,N)$. It appears to be an almost continuous film. In Fig. 29(b), an embrittled experimental heat of maraging steel with a higher nitrogen content but lower carbon (0.004% C, 0.003% N) shows evidence of a smaller amount of the same embrittling phase.

When aluminum alloys are overheated, eutectic melting can occur at grain boundaries, as shown in Fig. 30 and 31. The fractographs in Fig. 30 show large, smooth, rounded grain-boundary constituents in surfaces of a fracture in aluminum alloy 2014-T6. The fracture through the matrix is featureless, except for an oxide film. The fracture resulted from overload at elevated temperature during a fire. Tension-overload fracture

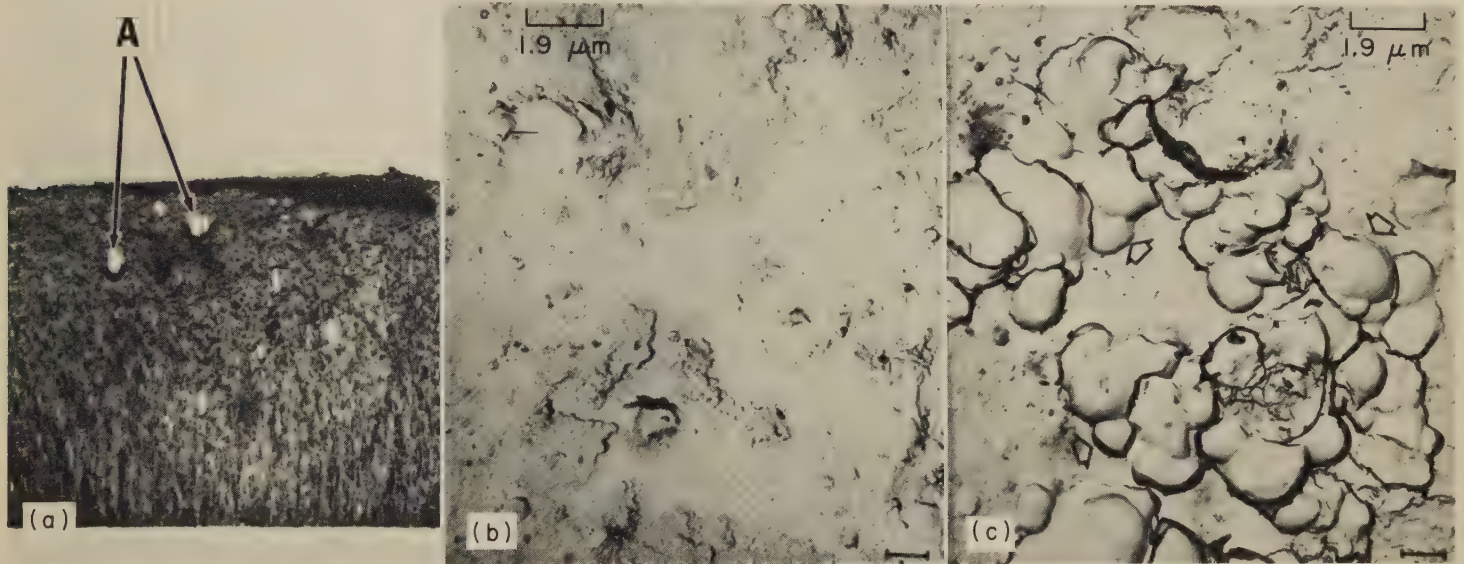


Light fractograph

4× TEM fractograph (p-c rep.)

5250×

Fig. 26. Fracture through porosity that was formed in a weld nugget during welding of 18Ni-7Co-5Mo maraging steel with modified 18Ni-9Co-5Mo steel filler wire. The surface of the void, A in (a), was fairly smooth and shiny to the edge but showed geometric patterns at high magnification (b).



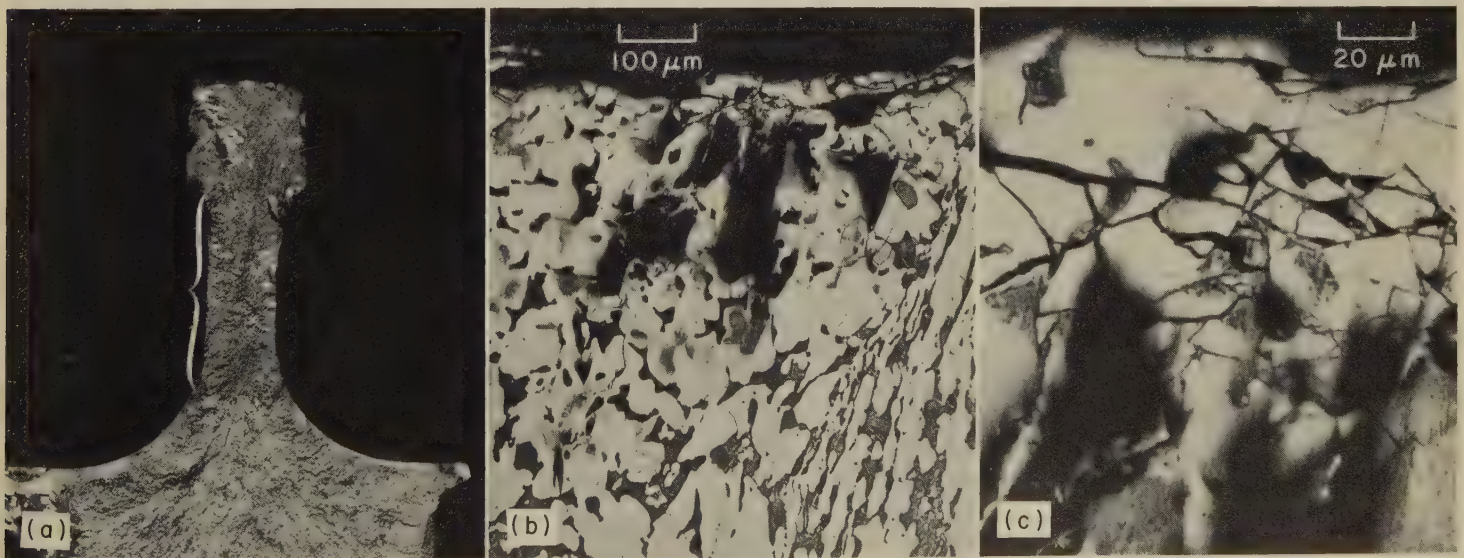
Light fractograph

2× TEM fractograph (direct carbon replica)

5200× TEM fractograph (direct carbon replica)

5200×

Fig. 27. Fracture through porosity in an aluminum alloy 2014 forging. At low magnification (a), the porosity appears as small, shiny, flake-like regions (arrows at A), but at high magnification some areas show typical geometric patterns (b) and oxide scale (arrows in c).



Light fractograph

1.8× Micrograph (Kroll's reagent)

100× Micrograph (Kroll's reagent)

500×

(a) Fracture in segregated area (bracketed) shows some evidence of porosity and appears much more brittle and granular than the remainder of the frac-

ture. (b) Metallographic section through the region of segregation and porosity. (c) Higher-magnification view of part of (b), showing extensive microcracking.

Fig. 28. Fracture through a region of segregation in an annealed titanium alloy Ti-6Al-4V (AMS 4928) forging



TEM fractograph (extraction replica) 5250×

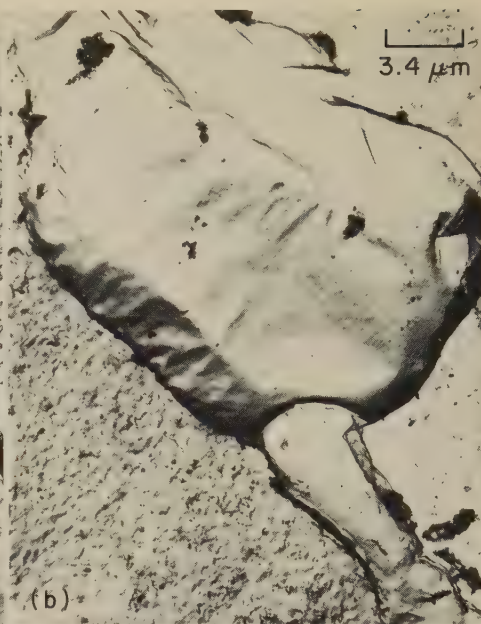


TEM fractograph (extraction replica) 5250×

(a) Maraging steel containing 0.027% C and 0.001% N. Slow cooling through the range of 982 to 760 C (1800 to 1400 F), without adequate accompanying hot work, precipitated a brittle film of titanium carbonitride at the grain boundaries. The dark particles present throughout this surface are fragments of titanium carbonitride that adhered to the replica.

(b) Maraging steel containing 0.004% C and 0.003% N. Like the steel shown in fractograph (a), this steel was also slowly cooled through the range of 982 to 760 C (1800 to 1400 F) without adequate accompanying hot work. Titanium carbonitride precipitated at the grain boundaries, but because of the lower carbon content of this steel compared with that of the steel in (a), a smaller amount precipitated.

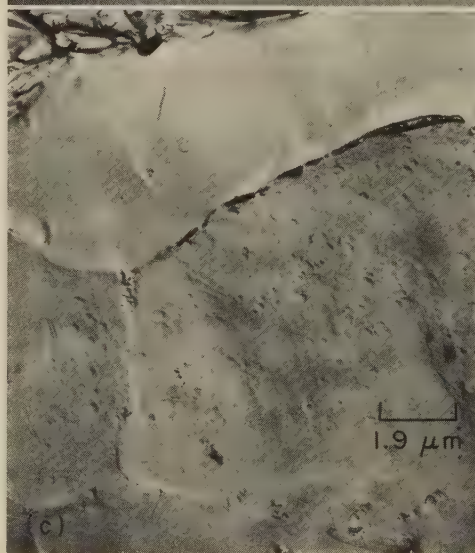
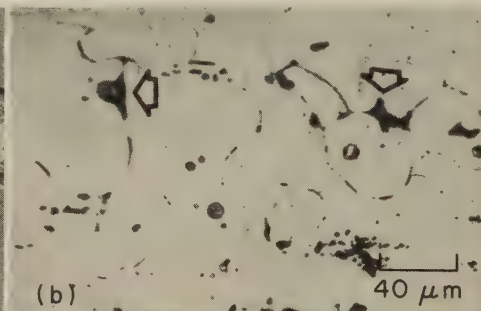
Fig. 29. Fracture surfaces of two fracture-toughness specimens of 18% Ni maraging steel containing different amounts of carbon and nitrogen, and showing different amounts of embrittling phase



TEM fractographs

Both at 2900×

Fig. 30. Surfaces of a fracture in aluminum alloy 2014-T6 that resulted from overload at a high temperature caused by a fire. The smooth, rounded features resulted from eutectic melting of the alloy at the grain boundaries. The fracture surface of the matrix is featureless, except for the presence of an oxide film.



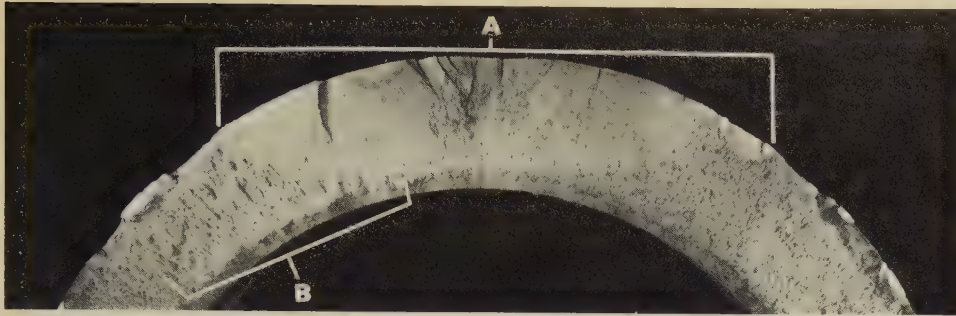
(a) Light-microscope fractograph, at 4×, showing the surface of the tension-overload fracture.

(b) Micrograph, at 250×, of an as-polished section taken near the fracture surface, showing evidence of intergranular eutectic melting (see arrows).

(c) and (d) TEM fractographs, both at 5200×, of plastic-carbon replicas, showing region A in frac-

tograph (a). The facets in fractograph (c) are believed to have resulted from separation at melted grain-boundary eutectic. Note the region of small dimples at top left. The features at lower left in (d) are artifacts that resulted from tearing of the first-stage replica. The separated-grain facets in fractograph (c) are smoother than those in (d).

Fig. 31. Tension-overload fracture of a specimen of extruded aluminum alloy 2014 after it had been deliberately overheated to cause intergranular eutectic melting. Solution heat treatment of the specimen was at 527 C (980 F) for 30 min, and was followed by water quenching and aging at 171 C (340 F) for 8 hr.



Light fractograph

Several fatigue-crack origins were found in the area indicated by bracket A. Numerous small discontinuous marks nearly perpendicular to the direction of crack propagation were determined by

metallographic examination to be related to forging flow lines and large, elongated sulfide inclusions. Woody appearance outside fatigue zone, in bracketed region B, also suggests unfavorable grain flow.

Fig. 32. Fatigue fracture through a region of unfavorable grain flow and large inclusions in an aircraft landing-gear axle forged from 4340 steel

of a specimen of extruded aluminum alloy 2014 produced the fracture surface shown in Fig. 31. The specimen had been overheated intentionally to produce eutectic melting. This fracture displays a few intergranular areas (which probably separated at melted grain-boundary eutectic) and small dimples.

Unfavorable Grain Flow

Grain flow in an unfavorable direction may be indicated by a woody fracture in some materials and by a flat, delaminated appearance in others. A region of woody fracture is marked by bracket B in Fig. 32, which shows a fatigue fracture in a forged

4340 steel aircraft landing-gear axle. The fatigue fracture occurred in a region where the resistance of the material to fatigue cracking was low because the fluctuating loads were applied nearly perpendicular to the direction of grain flow. In high-strength aluminum alloy extrusions and hot rolled products, tension loads are occasionally applied perpendicular to the flow direction, which may cause splitting along flow lines. This somewhat resembles the pulling apart of laminated material. Splitting may also appear as secondary cracks perpendicular to the primary fracture when these materials are broken by bending loads.

References

1. G. E. Pellissier, Effects of Microstructure on the Fracture Toughness of Ultrahigh-Strength Steels, *Eng Fract Mech*, Vol 1 (No. 1), 1968, p 55-75
2. J. R. Low, Jr., R. H. Van Stone and R. H. Merchant, "An Investigation of Plastic Fracture in Aluminum Alloys", NASA-CR-131100; TR-2, Carnegie-Mellon University, Pittsburgh, May 1972; available from National Technical Information Service (N73-19521)
3. T. B. Cox and J. R. Low, "Investigation of the Plastic Fracture of High Strength Steels", NASA-CR-131102; TR-4, Carnegie-Mellon University, Pittsburgh, Oct 1972; available from National Technical Information Service (N73-19523)

Use of Fractography for Purposes Other Than Failure Analysis

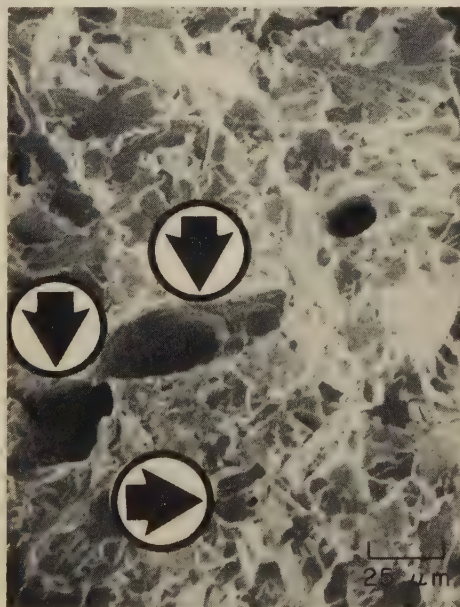
By the ASM Committee on Fractography by Electron Microscopy*

FRACTOGRAPHY is employed as a production-line evaluation tool and as a research tool in controlling and understanding the properties that metals exhibit in service, in addition to its use in failure analysis. This article discusses and illustrates applications of scanning and transmission electron fractography for purposes other than failure analysis. Some uses of light-microscope fractography for these purposes are mentioned on page 7 in this volume.

Fracture-Path Studies

Although the central interest of fractography is the nature of the topography of a fracture, an interpretation of the fracture features for an increased understanding of various aspects of the fracture process is also important. A study of a fracture surface can provide the following information relevant to the fracture process: (a) an estimation of the force involved in breaking the piece, (b) an assessment of the degree of deformation that occurred during separation, and (c) the reason for material weakness in the path of that particular fracture.

Fracture paths are investigated by two procedures. One is by examining the fracture surface at various magnifications available through the different fracto-



SEM fractograph

400X

The microvoids were partially grown in tension at room temperature. They were cleaved open at dry-ice temperature to reveal the size and shape of the cavities that had not yet coalesced. The microvoids at the vertical arrows have almost coalesced. The tensile axis was perpendicular to the cleaved surface. Compare with Fig. 2.

Fig. 1. Microvoids (at arrows) in a cleavage fracture in ASTM A302, grade B, pressure-vessel steel (Ref 2)

graphic techniques. This procedure provides the maximum area for study and is a fruitful approach if the contours of the fracture path are of primary interest. The second procedure is the study of cross sections that are normal to the path of a halted crack or of a completed fracture. Although the second procedure provides a more limited profile of the fracture path, its use is essential if the primary concern is the relationship of the fracture path to the underlying microstructure. Much may be learned by examining under the microscope the intersection of the fracture surface with a polished-and-etched section prepared at a right angle to the fracture surface (see Fig. 19, 20, 28, 29, 32 and 36 in Ref 1).

A method of appraisal sometimes used is to expose a partial fracture by cleavage of the remaining unfractured section at subzero temperature, thus avoiding cutting and any flow it might cause at the crack surface of interest. It will also avoid confusion as to which fracture area was initial and which final. For example, Fig. 1 and 2 (from Ref 2) show cleavage-fracture surfaces in an alloy steel specimen that had been precracked in fatigue, strained in tension almost to total fracture at room temperature, chilled to liquid-nitrogen temperature, and fractured by cleavage—first perpendicular to the previous tension, and then again at a right angle. Figure 1 shows the first

*See page 49 for committee list.

cleavage surface, which intersects deep microvoids. Figure 2 shows the second cleavage surface, which intersects the first cleavage surface near the top of the view and exposes the shape and depth of some of the original microvoids.

Figure 3 shows another structure revealed by fracture sectioning: the pores in sintered metals. Exposure of structures by fracturing is a preferred technique for such materials as gems, wood,

shellfish, frozen tissues of animals and plants, and clay. Fracturing is always preferable to cutting for the study of microstructures wherever less deformation will be produced by fracturing than by cutting and polishing.

Deformation Before and During Fracture

Plastic deformation is an inherent part of the fracture event, and therefore knowledge of the requirements of plasticity before and during fracture is helpful in appraising fractures. Standard ten-

Fracture-Surface Characteristics

Much can be inferred concerning the microstructure of a metal from fractographic examinations. The grain size of quenched-and-tempered steels, for example, can readily be estimated by examining the fracture surface, provided that the grains are large and that standard broken specimens are available for reference standards.

Fracture surfaces displaying patterns of parallel or concentric fibrous ridges usually are produced by microvoid formation and coalescence, as discussed on page 27 in the article on Features Re-



SEM fractograph 137X

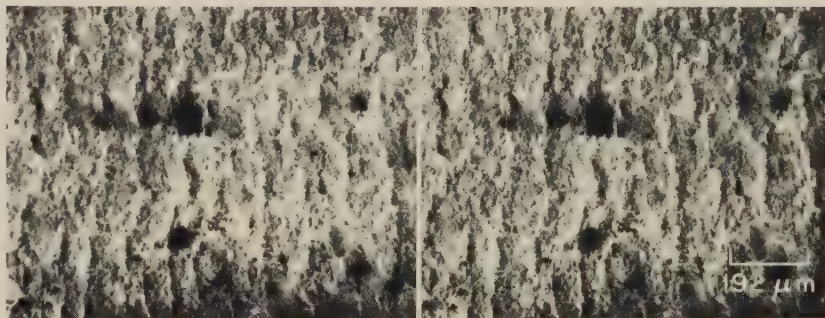
The tensile direction during microvoid growth was vertical. The surface of the first cleavage fracture is visible at the top of the view. The horizontal bars between the sets of vertical arrows give an indication of the depth of the microvoids.

Fig. 2. Microvoids in the same specimen (with the same treatment) as shown in Fig. 1, but with the cleavage fracture normal to that in Fig. 1 (Ref 2)



TEM fractograph (p-c replica) 1350X

Fig. 3. Pore sizes and shapes revealed by fracturing a specimen of sintered tungsten. The arrow points to a pore.



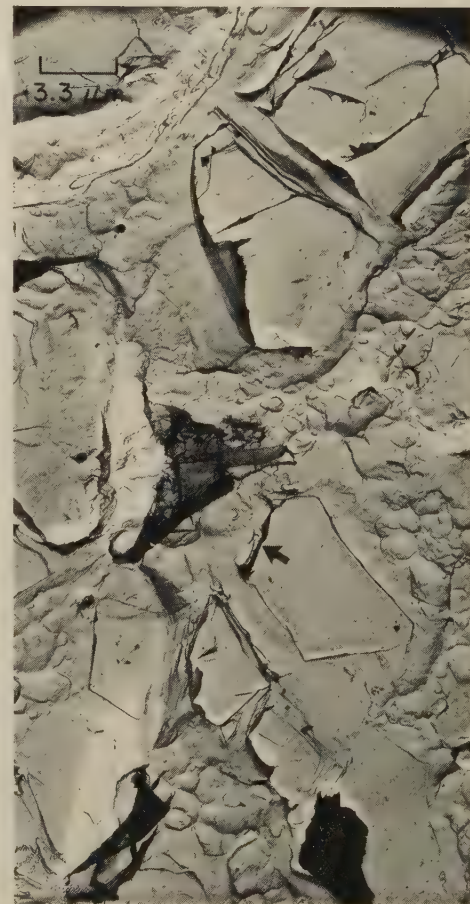
SEM fractograph (stereo pair)

52X

Fig. 4. Alternating ridges and valleys, appearing as vertical lines, formed in the fibrous fracture surface of a 10% Ni, 2% Cr, 1% Mo, 8% Co steel. Fracture propagated from left to right.

sion and bending tests that define or require certain degrees of plasticity before fracture are described in ASTM E8 (Tension Testing of Metallic Materials), E16 (Free Bend Test for Ductility of Welds), and E190 (Guided Bend Test for Ductility of Welds). Low-magnification analysis of deformation on the fracture surfaces themselves is discussed in ASTM A370 (Mechanical Testing of Steel Products), E338 (Sharp-Notch Tension Testing of High-Strength Sheet Materials), E399 (Plane-Strain Fracture Toughness of Metallic Materials), and E436 (Drop-Weight Tear Tests of Ferritic Steels). These compare the relative amounts of shear and cleavage in a fracture, affording a measure of the relationship of macroscopic fracture-surface appearance to toughness.

Studies of the amount of plastic deformation existing in fracture surfaces have been made with selected-area electron-channeling-pattern techniques. (The patterns are made possible by the fact that backscattered electrons emitted by a fracture surface in a scanning electron microscope will provide a spatial pattern that is blurred if the surface layers have been deformed but that is sharp if the surface is undeformed.) Using this technique, Stickler and Booker (Ref 3) have examined cross sections of cracks, and Newbury, Christ and Joy (Ref 4) have studied deformation on fracture surfaces. This technique and examination of thin-foil specimens are helpful in revealing the microscopic deformation associated with crack growth. Such a technique might also be useful in assessing the degree of deformation around microvoids, such as those shown in Fig. 1 and 2.



TEM fractograph (p-c replica) 3000X

Fig. 5. A low-energy fracture along the rolling plane in 18% Ni maraging steel. Fracture started at inclusions, such as at arrow, which had broken during rolling.

vealed by Light Microscopy. Fracture surfaces with these fibrous ridges are shown in Fig. 2 and 3(b) in that article (see pages 27 and 28) and in Fig. 4 here. The spacing of the fibrous ridges has been related to fracture toughness (Ref 5), and the mechanisms of their formation have been discussed (Ref 6).

It is often possible at higher magnifications to see the microconstituents that represent the weak component that may be responsible for fracture. This has been done for the effects of sulfide-inclusion spacings on fracture toughness (Ref 7, 8). Fracture originating at broken inclusions in a maraging steel is shown in Fig. 5.

One of the earliest projects in the development of fractography as a tool in failure analysis was to identify and categorize the fine features present on fracture surfaces of specimens broken under known conditions. The differences in dimple shapes, the marks on cleavage and intergranular facets, and the features produced by fatigue, by stress-corrosion cracking, by hydrogen embrittlement, and by creep were classified. This work is still continuing because the fracture mechanisms once considered to be distinctly delineated are now being found to have variations that need further exploration and classification. For example, quasi-cleavage in tempered martensitic steels is now known to follow the {100} plane in the ferrite matrix and frequently to possess deformation marks closely akin to dimples, and so quasi-cleavage has been taken partly out of its classification group to bridge the gap between cleavage and microvoid coalescence.

Another area in which earlier concepts have changed and study continues concerns microvoid coalescence. Investigators of fracture features used to say that there were three types of dimples (equiaxed, shear and tear dimples). However, precision matching of surface replicas has shown recently that there are at least eight varieties (Fig. 6) and that there may be as many as 14 ways of forming dimples, depending on the crack-tip stress states (Ref 9). This is an important advance in theory because detailed analysis of dimple shapes permits the reconstruction of local crack-tip strain conditions, thereby shedding some light on local crack-tip stress states.

Another concern of the fractographer is in regard to the chemical constituents and segregation that may be present on a fracture surface. Electron-beam microprobe analysis, x-ray spectroscopy, and Auger electron spectroscopy provide the means for making the necessary analyses to determine possible chemical causes of variations in microstructure. Inclusions in the fracture can be extracted by rep-

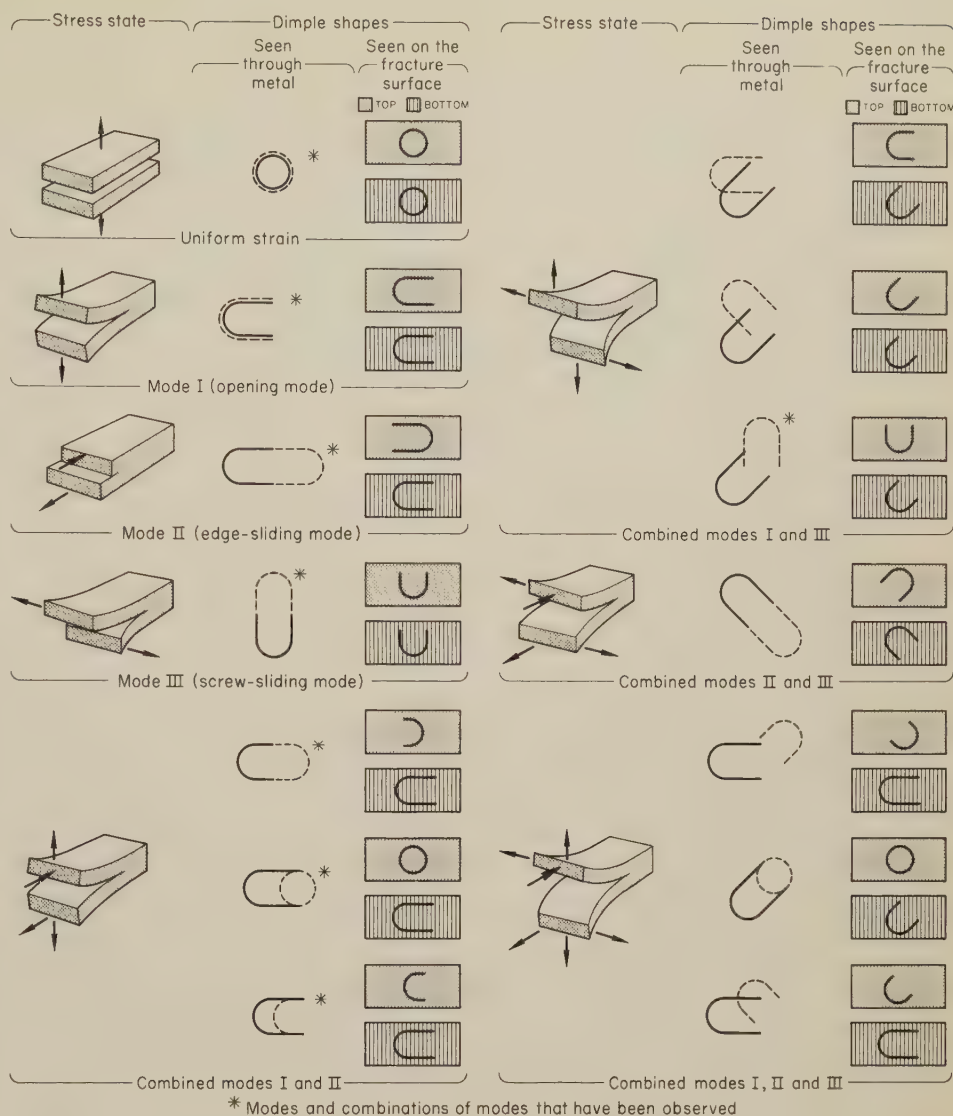


Fig. 6. Fourteen probable combinations of mating dimple shapes resulting from different stress states, which cause the crack tip to deform by various modes

licas for examination in a transmission electron microscope. The outcome of such investigations is a better understanding of the effect of microstructural variations on fracture properties.

References

1. G. E. Pellissier, Effects of Microstructure on the Fracture Toughness of Ultrahigh-Strength Steels, *Eng Fracture Mech*, Vol 1, 1968, p 55-75
2. C. D. Beachem, T. C. Lupton and B. F. Brown, A New Technique for Examining Microscopic Fracture Processes at Crack Tips, *Met Trans*, Vol 2, Jan 1971, p 141-143
3. R. Stickler and G. R. Booker, Application of Selected-Area Electron Channeling Patterns Obtained in the SEM to Deformation Studies, in "Electron Microscopy and Structure of Materials", G. Thomas, R. M. Fulrath and R. M. Fisher (Eds.), University of California Press, Berkeley and Los Angeles, 1972, p 301-312
4. D. E. Newbury, B. W. Christ and D. C. Joy, Relevance of Electron Channeling Patterns to Embrittlement Studies, *Met Trans*, Vol 5, 1974, to be published
5. George R. Yoder, Fractographic Lines in Maraging Steel—A Link to Fracture Toughness, *Met Trans*, Vol 3, 1972, p 1851-1859
6. C. D. Beachem and G. R. Yoder, Elastic-Plastic Fracture by Homogeneous Microvoid Coalescence Tearing Along Alternating Shear Planes, *Met Trans*, Vol 4, 1973, p 1145-1153
7. A. J. Birkle, R. P. Wei and G. E. Pellissier, Analysis of Plane-Strain Fracture in a Series of 0.45C-Ni-Cr-Mo Steels with Different Sulfur Contents, *Trans Am Soc Metals*, Vol 59, 1966, p 981-990
8. J. Nutting, Some Aspects of Structure Property Relationships in Materials, in "Electron Microscopy and Structure of Materials", G. Thomas, R. M. Fulrath and R. M. Fisher (Eds.), University of California Press, Berkeley and Los Angeles, 1972, p 617-636
9. C. D. Beachem, The Effects of Crack-Tip Plastic Flow Directions upon Microscopic Dimple Shapes, *Met Trans*, submitted for publication in 1974

Use of Fractography for Failure Analysis

*By the ASM Committee on Use of Fractography for Failure Analysis**

THE PURPOSE of failure analysis is to determine the cause or causes of failure of a part or component so that the proper remedial action can be taken to avoid similar failures in companion parts or components. Failure can occur in many ways, such as by wear or erosion of a surface, distortion of a shape, loss of hardness of a tool, or loss of elasticity of a spring, to name a few that do not involve actual breakage. However, the type of failure discussed in this article involves complete or partial fracture of a member of a structure.

This article considers how an examination of a fracture, employing fractographic techniques, can assist in identifying the cause of failure and suggest steps for ensuring that it does not happen again. Interpretation of the fractographic findings is discussed, and examples of their application are presented.

Basic Considerations in Failure Analysis

The basic cause of any fracture is stress (applied and residual combined) that exceeds the load-bearing capacity of the part. This stress may be produced by the interaction of many complex factors, all of which must be evaluated before the cause of fracture can be accurately determined. Some of the questions that should be raised concerning the nature, history, functions and properties of the fractured part, and the manner in which it interacts with other parts, are set forth in the list that follows:

Loading. Were the nature, rate and magnitude of the applied load correctly anticipated in the design of the part? Were repeated or cyclic loadings involved? What was the direction of the principal stress relative to the shape of the part? Were residual stresses present to an undesirable degree?

Material. Was the recommended alloy used? Were its mechanical properties at the level expected? Were surface or internal discontinuities present that could have contributed to failure? Did the microstructure conform to that prescribed?

Shape. Did the part comply with all pertinent dimensional requirements of the specification? Did the part have sufficient section thickness to prevent local overloading? Were fillets formed with sufficiently large radii? Were there adequate clearances between interacting parts? Were any of the contours

deformed during service? Was there evidence of mechanical surface damage?

Environment. Was the part exposed to a corrosive environment or to excessively high or low temperatures? Was the surface of the part suitably protected? Were the properties of the part altered by the exposure? Was there interaction (for example, galvanic) between the material of the part and that of adjacent components?

Aspects of Failure That Can Be Resolved by Fractography

Examination of a fracture begins with visual scrutiny, which establishes (a) whether there is gross evidence of mechanical abuse, (b) whether there are indications of excessive corrosion, (c) whether the part is deformed, (d) whether there are obvious secondary fractures, (e) whether the origin of the crack can be readily identified, and (f) whether the direction of crack propagation can be easily recognized. Often it is helpful to have an undamaged part of the same design as the fractured part available during this portion of the examination. The findings of this scrutiny will permit many deductions to be drawn concerning the service conditions existing at and prior to the time of fracture. These findings can then be extended by an examination of the fracture surface at low magnification with a stereomicroscope and then at high magnification by scanning electron microscopy, transmission electron microscopy (with the aid of replicas), metallography (occasionally), or some combination of these examination techniques. A survey at low magnification is important for identification of those areas that need further inspection at high magnification. The salient features are recorded in fractographs of appropriate magnification for report purposes, and for future reference should subsequent handling or sectioning destroy evidence needed for failure analysis.

Care must be taken in handling fractured parts to be studied and in preparation of fracture specimens. Evidence that may be useful in establishing the origin and mechanism of fracture can easily be altered or destroyed by carelessness in collecting fractured parts or in performing failure analysis. Methods for preserving, cleaning and sectioning of fracture

surfaces and fractured parts are described in the article that begins on page 9 in this volume.

The size of a specimen that can be viewed is often limited, especially in a scanning electron microscope, and it may be necessary to section a fractured part. This must be done carefully so that features on the fracture surface are not altered. In the following example, attempts to cut a thin specimen from a fractured part changed the nature of marks on the fracture surface.

Example 1. Alteration of Fracture-Surface Features by Improper Specimen-Preparation Procedure (Fig. 1)

Cracks that had formed in a cast pump impeller made of low-strength stainless steel casting alloy CN-7M (0.07% max C, 20% Cr, 29% Ni, 2% Mo, 3% Cu) were opened up for examination. A hacksaw cut was made close to the fracture surface to remove a thin specimen for examination by scanning electron microscopy. Because of plastic deformation and slip being imposed on the crack surface, a false (artifact) feature was produced (see the lower part of Fig. 1a). This artifact could be confused with either fatigue striations or corrosion crack-arrest marks.

The impeller had been used to pump strong sulfuric acid. Crack surfaces that were unaffected by the cutting showed pits (see Fig. 1b) that had been produced by corrosion cratering and that completely obliterated the striations that presumably had formed earlier. Round-bottom pits caused by corrosion cratering are not to be confused with dimples formed by microvoid coalescence.

Crack Origin and Crack-Propagation Path. Establishing the origin of a fracture is essential in failure analysis, and the location of the origin may have a large influence in determining which measures should be taken to prevent a repetition of the fracture. For example, if the crack origin is at the surface, surface strengthening (case hardening, shot peening) should be undertaken. If the origin is subsurface, higher over-all strength, greater cross section, or fewer internal discontinuities may be needed. The features that help identify the crack origin, such as concentric fibrous marks, radial marks, and beach marks, and the fracture-surface characteristics that show the direction of crack propagation (and conversely, the direction toward the origin), such as chevron marks, crack branching, and river patterns, have been treated in

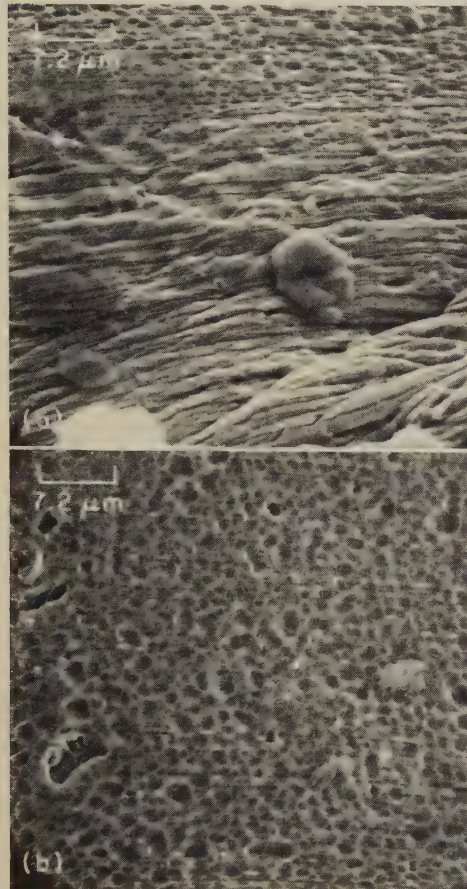
*JOHN A. FELLOWS, *Chairman*, Consultant to American Society for Metals; FRANKLIN ALEX, *Ogden Air Logistics Center/MAN*, Hill Air Force Base; H. C. BURGHARD, JR., *Senior Research Engineer*, Southwest Research Institute.

WILLIAM L. HOLSHOUSER, *retired* (formerly Chief, Laboratory Services Staff, Bureau of Aviation Safety, National Transportation Safety Board); JOSEPH A. KIES, *Consultant*; FRANK R. LARSON, *Metals Research Div.*, Army Materials and Mechanics Research Center, Department of the Army; FRANK A. MCCLINTOCK, *Professor*, Department of Mechanical Engineer-

ing, Massachusetts Institute of Technology; A. J. McEVILY, *Head*, Department of Metallurgy, University of Connecticut; NORMAN A. NIELSEN, *Research Fellow*, Experimental Station, E. I. du Pont de Nemours & Co., Inc.; WILLIAM WIEBE, *Senior Research Officer*, Structures and Materials Laboratory, National Aeronautical Establishment, National Research Council of Canada.

DONALD J. WULPI, *Head*, Engineering Metallurgy Laboratory, Motor Truck Div., International Harvester Co.; EDWARD A. DURAND, *Secretary*, Senior Editor, Metals Handbook, American Society for Metals.

detail in the article on Fractographic Features Revealed by Light Microscopy, beginning on page 27 in this volume. By a study of these features, crack progress can be traced back to the point of origin, and then it can be ascertained whether the crack was initiated by an inclusion, a porous region, a segregated phase, a corrosion pit, a machined notch, a forging lap, a nick, a mar, or another type of discontinuity, or was simply the result of overloading.



SEM fractographs Both at 1400×

(a) Artifact that was produced by hacksaw cutting a thin specimen from the cracked area is shown in the lower part of the fractograph.

(b) Surface features of the crack consist of corrosion-produced round-bottom pits.

Fig. 1. Artifact produced in preparing a specimen for examination by scanning electron microscopy. Specimen was cut from a cracked area of a cast CN-7M stainless steel pump impeller used for pumping sulfuric acid. (Example 1)

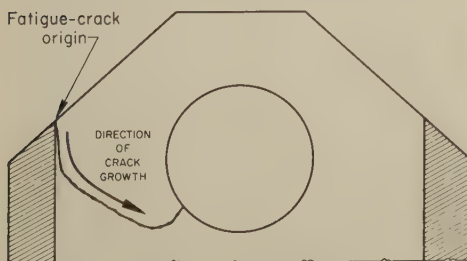


Fig. 2. Schematic diagram showing the location of the crack origin and the direction of the crack growth in the fatigue fracture of the 4340 steel rotor fitting of Fig. 3 (Example 2)

In the following example, fractography was used to identify the origin and mechanism of a fracture in a steel fitting.

Example 2. Fracture That Originated at a Stress-Concentration Site in a 4340 Steel Rotor Fitting (Fig. 2 and 3)

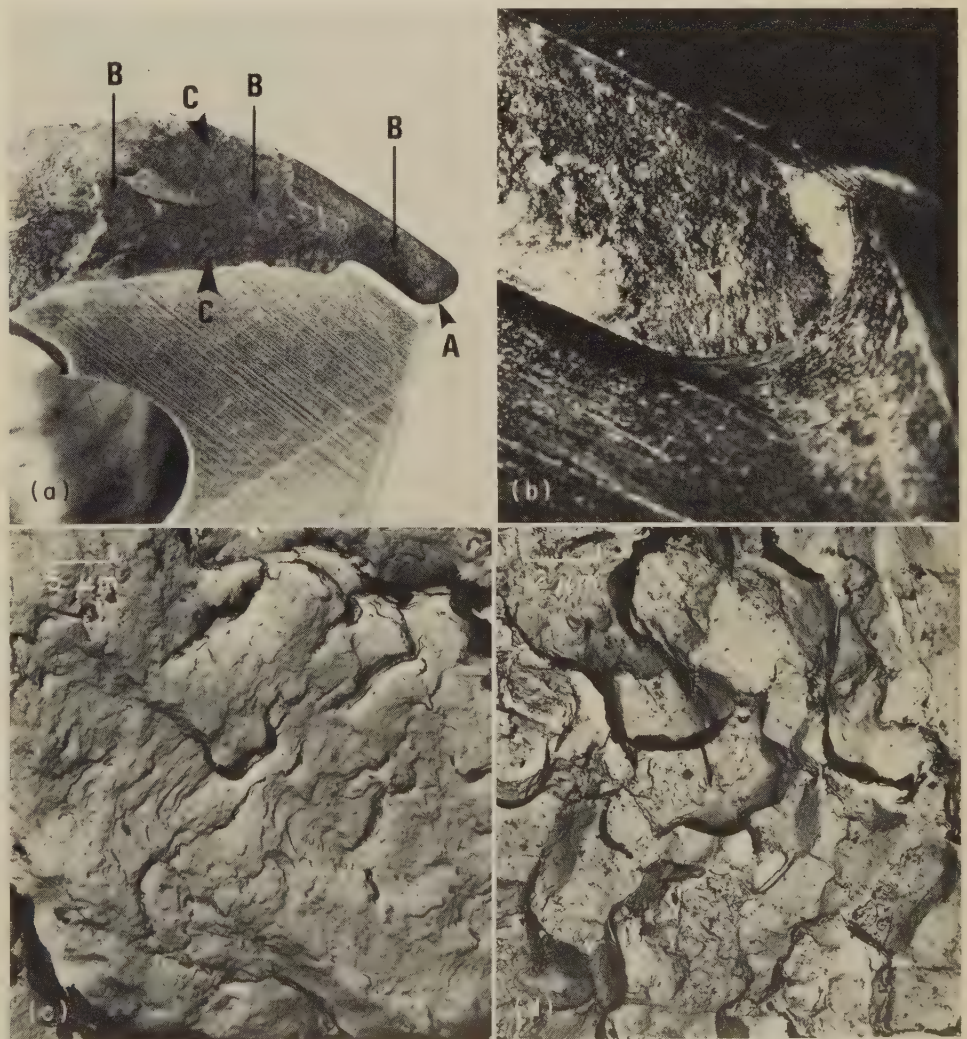
The crack that led to fracture of a cadmium-plated 4340 steel rotor fitting originated, as indicated in Fig. 2, at the corner of a rectangular longitudinal through-hole, where it intersects the top surface. The fracture profile also is shown in Fig. 2. Examination of the upper fracture surface as positioned in Fig. 2 revealed three clearly delineated fracture-surface areas; these are identified as areas A, B and C in Fig. 3(a). An enlarged view of area A and a portion of area B are shown in Fig. 3(b). The initial 0.7-mm portion of the crack (area A) was determined by fractography to have been formed by fatigue (Fig. 3c). Longitudinal tool marks in the hole (see Fig. 3a) extended into the fillet. Area B, which is representative of the major portion of the fracture surface, exhibited intergranular fracture (Fig. 3d). The shear-lip zone (area C) was so identified by the presence of elongated dimples.

Because the fitting had been cadmium plated and propagation of fracture had been intergranular, it was suspected that hydro-

gen embrittlement was responsible for the fracture. On the other hand, the large amount of corrosion products on intergranular areas of the fracture surface suggested stress-corrosion cracking as the operative fracture mechanism along grain boundaries. The possibility that corrosion fatigue was responsible for the fracture was eliminated when a thorough fractographic traverse of the intergranular area failed to reveal evidence of fatigue striations. However, the initiation of the crack by fatigue offers evidence suggesting that the fitting would have broken anyway, even if it had never been cadmium plated. From this point of view, hydrogen embrittlement could be regarded as a contributing cause, but not as a fundamental cause, of the fracture.

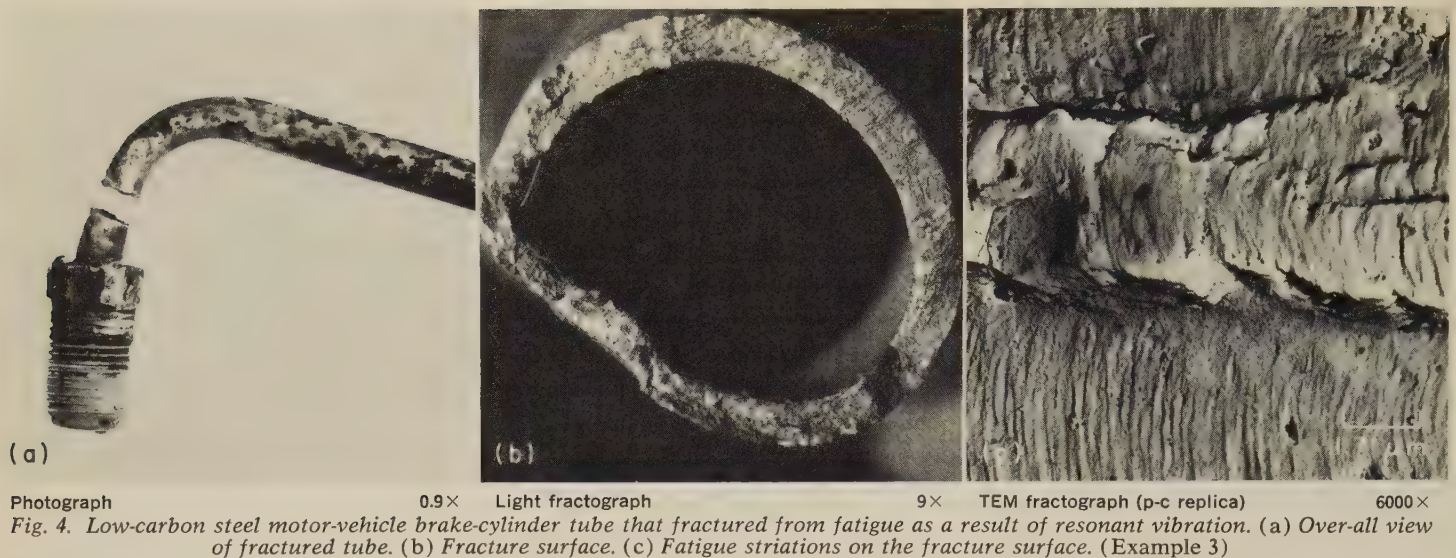
Remedial action resulting from the fractographic investigation included design modifications of the fitting directed toward the elimination of stress concentrations at the site of the fatigue-crack origin, and measures to prevent hydrogen embrittlement of the steel during cadmium plating.

Type of Loading. The design of a part anticipates a specific mode of loading in service. Whether or not loading was as expected is of prime concern in studying a fracture. Much can be learned regard-



(a) Light fractograph, at 1.6×, showing fatigue-fracture zone A, intergranular-fracture zones B and shear-lip zones C of the fracture. (b) Light fractograph, at 10×, showing area A at a higher magnification and the fatigue-fracture origin. (c) TEM fractograph (plastic-carbon replica), at 6800×, showing poorly defined fatigue striations in area A. (d) TEM fractograph (plastic-carbon replica), at 800×, showing intergranular fracture at area B.

Fig. 3. Fracture surface of a 4340 steel rotor fitting; see also Fig. 2 (Example 2)



ing the type and magnitude of applied stress from fractographic inspection. Obviously, if the type of stress that caused fracture is radically different from the type that was anticipated, a change of treatment in service or a new design may be required.

Resonant vibration that occurred in a motor vehicle while cruising at normal speed resulted in fatigue fracture of a brake-cylinder tube, as described in the following example.

Example 3. Fatigue Fracture of a Motor-Vehicle Brake-Cylinder Tube Caused by Resonant Vibration (Fig. 4)

Fractographic examination of a fractured low-carbon steel brake-cylinder tube (Fig. 4a and b) for a large motor vehicle indicated that the tube had fractured in fatigue (Fig. 4c), even though no macroscopic evidence of fatigue was visible on the fracture surface.

Investigation into the source of cyclic stresses showed that resonant vibration of the tube assembly in service occurred at a frequency of about 240 cycles per second, and that the maximum amplitude of vibration of the tube occurred at the normal cruising speed of the vehicle. Laboratory fatigue tests

at the same resonance reproduced the service fracture. Remedial action involved a method of clamping of the brake-cylinder tube that would prevent vibration.

The articles on interpretation of light-microscope, scanning-electron-microscope (SEM) and transmission-electron-microscope (TEM) fractographs — which begin on pages 36, 64 and 79, respectively — discuss and illustrate the features of tension, torsion and shear fractures. In ductile materials, these types of fractures are easily recognized; there is no mistaking the dimple shapes produced by tension, shear and tearing. In brittle materials, however, the evidence is less clear; it is difficult to determine, either in pure cleavage or in complete intergranular separation, that the fracture was produced by one particular type of stress rather than another.

Fatigue fractures (the most frequent type of fracture in machinery parts) result from progressive growth of one or more fatigue cracks generated by repetitive cyclic loading. The cracks may start at any one of several surface or subsur-

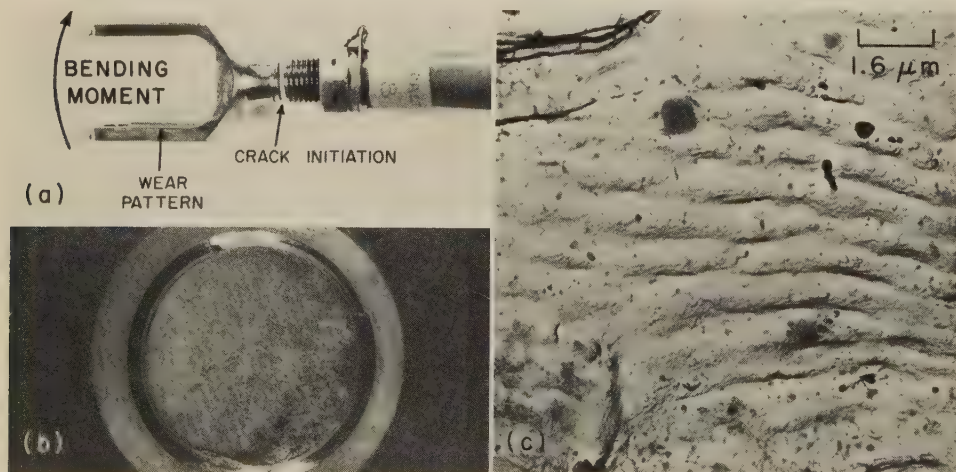
face discontinuities. Identification of the crack origin is important, as previously stated. Usually, the repetitive nature of the load cycles is reflected in a stepwise growth of the fatigue crack, producing the parallel microscopic marks known as fatigue striations. These can be recognized by following the guidelines described in the articles on interpretation of SEM and TEM fractographs (see pages 64 and 79), and their presence can be regarded as positive proof of a condition of cyclic loading, as discussed and illustrated in the following example.

Example 4. Fatigue Fracture of a Control-System Clevis for a Rotary-Wing Aircraft, Which Resulted From Improper Assembly (Fig. 5)

Electron-microscope fractographic examination of a clevis made of titanium alloy Ti-6Al-4V (Fig. 5a and 5b) that was retrieved from the wreckage of a rotary-wing aircraft indicated fracture by fatigue, as evidenced by the striations in Fig. 5(c).

Evidence of a wear pattern in the form of an arc on the inner surface of one of the fingers of the clevis (Fig. 5a) suggested that the shank had been subjected to bending-moment forces oriented favorably for crack initiation at the observed origin. Investigation indicated that the wear pattern and the cyclic bending loads had resulted from malfunction of a bearing in the linkage component attached to the clevis. This malfunction was attributed to faulty assembly procedures during installation of the bearing.

The absence of fatigue striations should not be interpreted as definite proof that the part did not undergo cyclic loading, because striations are sometimes masked or erased by corrosion and because some materials (high-strength steels, for example) do not readily form distinct striations. If the evidence shows that a fracture was by fatigue when none was anticipated, the service application was evidently in error and should be corrected. To accomplish this, either the peak stress should be reduced, or the material should be improved. In steels, for example, at best the fatigue limit is about half the yield strength, and may be much lower if the surface is decarburized or has small discontinuities.



(a) Photograph, at 0.4x, of fractured clevis, showing orientation of bending moment, wear-pattern location, and crack-initiation site in shank. (b) Light fractograph, at 2.8x, showing fracture surface of clevis. (c) TEM fractograph (p-c replica), at 6400x, showing fatigue striations on fracture surface.

Fig. 5. Fracture of a titanium alloy Ti-6Al-4V clevis from a control system for a rotary-wing aircraft (Example 5)

The orientation of the principal applied stress cannot always be explicitly deduced from an inspection of the fracture surface, but certain approximations can be made. If the dimples are equiaxed, the fracture probably resulted from simple tension and the stress axis probably was normal to the approximate plane of the fracture. If the dimples are elongated, the fracture was produced either by shear or by tearing. In a shear fracture, the principal stresses will be aligned as discussed in the articles on interpretation of SEM and TEM fractographs (see pages 64 and 79). If the fracture was by tearing, more information may be needed to determine whether fracture was by tension on a side-notched member or was by bending. If dimples are not present and the fracture was by transgranular cleavage, the river patterns will offer clues as to the local directions of crack propagation, but these local paths depend mainly on crystallographic orientation and not on the alignment of the stress axis. With transgranular cleavage and intergranular fracture, more can be learned about the over-all orientation of the stress by visual inspection of the part than by microscopic examination of features on the fracture surface.

The magnitude of applied stress can be qualitatively inferred from fractographic examination, but a quantitative estimate is not possible. One appraisal depends on noting whether or not the part has undergone marked distortion or obvious plastic flow. Appreciable deformation results only from a stress that is high relative to the yield strength of the material. Other clues are offered by the relative proportions of various fracture features. The article on Interpretation of Light-Microscope Fractographs (see page 36) points out that in fatigue fractures, a small fatigue zone with wide striation spacing coupled with a large region of final, fast fracture signifies high loading. A low fatigue stress can be inferred from a large fatigue zone, very closely spaced striations, and a small region of final, fast fracture. Other factors to be taken into account include whether or not the part was notched (contained stress concentrations) and whether it fractured by transgranular cleavage or by grain-boundary separation. The absence of gross deformation is not conclusive evidence that the applied stress was low.

Material of the Part. Many questions concerning the relation of the material of a part to fracture can be answered through fractography; others require additional techniques, such as mechanical testing, metallography, chemical analysis, electron microprobe analysis, x-ray diffraction analysis, imaging by cathodoluminescence, and Auger spectroscopy. When these investigations are performed by auxiliary equipment on either a scanning or a transmission electron microscope, they may be considered to be fractographic procedures.

Brittleness or ductility may be revealed by fractography. In general, a ductile alloy will fracture by microvoid coalescence and a brittle alloy will fracture by transgranular cleavage or by intergranu-

lar separation. This is oversimplification (most fractures display a mixture of features), but it is the basic premise.

Metallographic examination of sections normal to the fracture surface will disclose the nature of the microstructure and whether the heat treatment was satisfactory. If subsequent overheating occurred, a micrograph will reveal the effect it had. If the grain boundaries contain brittle films contributing to intergranular fracture, a micrograph may show them.

High-magnification fractographs will show whether or not a metal was "clean"—that is, whether there were few or many inclusions. Micrographs will also reveal inclusions, but fractographs will give more information regarding their shapes, because the fracture process usually separates most of the inclusion particle from its original pocket, affording a nearly three-dimensional view. Many examples of inclusions are included in the Atlas of Fractographs (see "Inclusions" in the Index to this volume).

If segregation of elements or alloy phases occurred in an alloy, fractography may sometimes detect the pattern of segregation as a departure from the normal arrangement of fracture features. The degree of success in identifying segregation will depend somewhat on how gross the pattern of segregation is. If the pattern is extremely fine, its discovery may require the use of metallography and electron microprobe analysis.

Study of the fracture surface will reveal whether discontinuities from processing led to the initiation of fracture. Forging laps and seams are readily recognized because the surfaces of these imperfections bear none of the characteristic features of fracture. Shrinkage porosity in castings displays dendrite contours within the shrinkage cavities that are unique in shape and are not to be confused with fracture. Cracks formed prior to or during heat treatment can usually be distinguished from the surface exposed during subsequent crack propagation because of oxide or corrosion-product layers on the surfaces of the so-called heat-treat cracks. The exact nature of the layers depends on whether the part was heated after a crack originated during heat treatment (or hot forming) and on whether the crack was penetrated by liquid or gaseous corrodents before crack propagation began in service. Regardless, a prior crack surface is easily recognized.

Welds are also potential sources of cracks; the cracks can occur either within or at the surface of the weld metal, or can form in the heat-affected zone of the base metal. If they were formed at ambient temperature, they are likely to resemble the final fracture in surface appearance. If they occurred before the part cooled from the welding temperature, oxide films should be visible on the surfaces of those cracks that were open to the external surface. Cracks that were entirely internal will have escaped oxidation. Fractographic examination will locate all open, oxidized cracks, but more positive identification of welding cracks is provided by metallographic examination of transverse sections through the

weld and the heat-affected zone to study the relationship between the cracks and the weld, as in the following example.

Example 5. Fracture Resulting From Improper Welding and Heat Treatment of a 4340 Steel Axle (Fig. 6 and 7)

Fracture started in a weld deposit (Fig. 6a) on a 4340 steel axle and propagated through the 6-by-6-in. cross section of the axle. Examination of TEM replicas from within the weld showed the fracture to be intergranular (Fig. 6b). The high hardness of the heat-affected zone (Fig. 7) indicated martensite formed by the mass quench of the heavy section, possibly generating small quench cracks that served as fracture initiators. The fracture through the axle was brittle, as confirmed by fractographic evidence of cleavage (Fig. 6c) in all areas outside the weld deposit. Ambient temperature at fracture was about 10°C (50°F).

Spectrographic analysis indicated that the composition of the steel was within specified limits. However, hardness measurements, Charpy impact tests, and metallographic examination confirmed the brittle condition of the steel, and indicated that it was not in the tempered condition specified, and the presence of the hard heat-affected zone adjacent to the weld (Fig. 7) proved that the specified postweld heat treatment had been omitted.

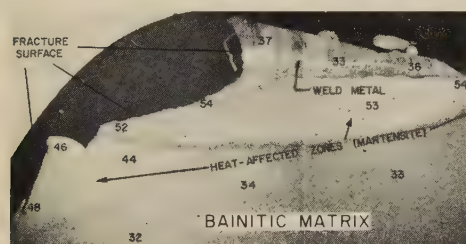
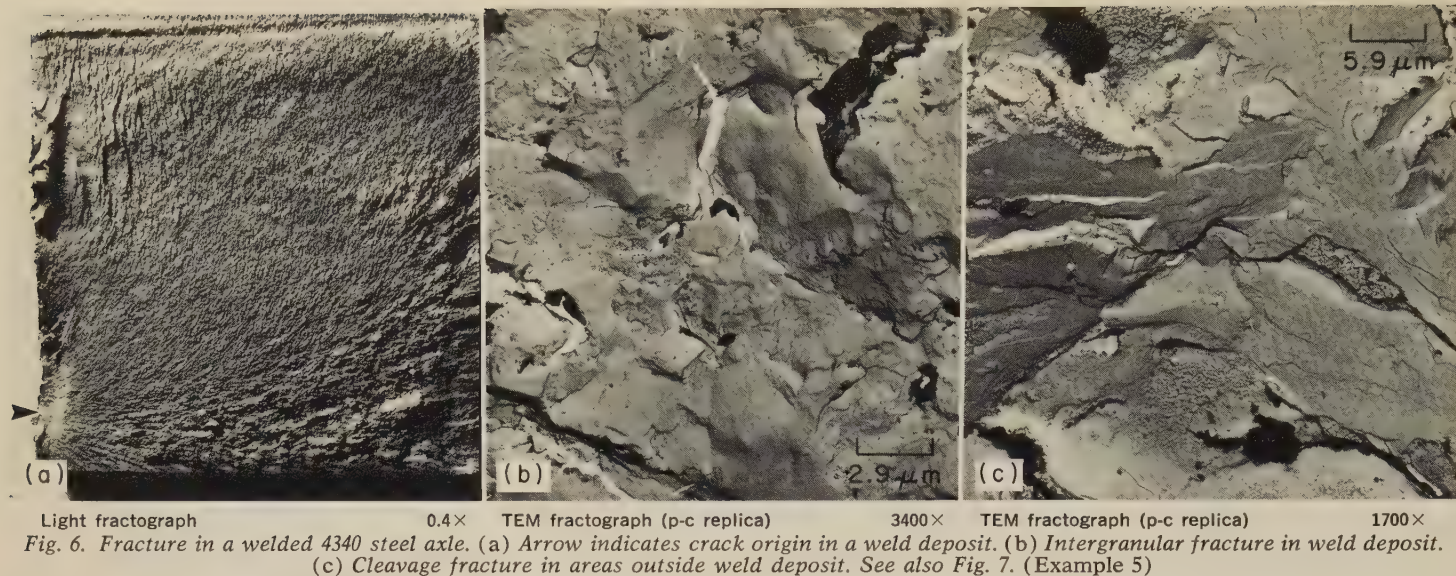
Shape and Surface of the Part. Overloading can produce noticeable distortion of a part. The initial visual scrutiny of a part, both with the unaided eye and with a low-power stereomicroscope, should include a critical examination for evidence of distortion. However, this will provide proof of overloading only if the part has high ductility and relatively low yield strength. With parts made of high-strength steels, proof that overloads were well above the design limit is more difficult to establish.

A careful scan of the exterior surface of the part in the area adjacent to the fracture is required to determine whether specific stress raisers are present of a type that could have initiated the fracture. A simple nick, gouge or deep scratch, frequently the result of careless handling before installation, can initiate fracture. If there are no sharp grooves, any marks present may be considered innocuous and unrelated to the fracture. On the other hand, if any marks possess sharp reentrant angles, they constitute sites of stress concentration, a frequent cause of crack initiation. In this situation, the obvious remedy is more careful handling procedures and better inspection.

Tool marks are another source of stress concentrations. A fillet that has too small a radius, even though the surface of the fillet may be an excellent example of high-grade machining, is a recognized initiation site for fatigue cracks. Sharp-bottomed tool marks can initiate fatigue fractures even though the general contour of the area has a generous radius. In the following example, a file or grinding mark on a fillet with an apparently adequate radius was thought to have nucleated fatigue cracks.

Example 6. Improper Surface Finish in a Fillet of an Aircraft Generator Gear-Box Casting (Fig. 8)

The macroscopic crack-arrest lines on the fracture surface of a cast magnesium alloy AZ91-T6 generator gear box (Fig. 8a) sug-



Macrograph (etchant: 2% nital) 12X
Fig. 7. Metallographic section of the 4340 steel axle of Fig. 6 in the region of crack origin, showing the weld metal, the heat-affected zone adjacent to the weld metal, and the Rockwell C hardness at various locations (Example 5)

gested that the fatigue crack had nucleated at point A, with subsequent simultaneous crack growth along segments B and C. Although fractographic examination suggested that cleavage was the primary mechanism of fracture, close scrutiny of many areas that were apparently cleaved revealed the presence of a large number of closely spaced fatigue striations (Fig. 8b).

A series of scored lines approximately parallel to the crack was observed on the

fillet adjacent to crack origin A and the counterbore of the bolthole (Fig. 8c). The lines appeared to be file or grinding marks. It was thought likely that the fatigue crack was nucleated in one of these small grooves. Low-stress, high-frequency vibration during operation of the gear box was considered to be the source of cyclic loading. Because of the low level of stressing, the indicated remedial action was to provide a finer surface finish in the more highly stressed regions of the casting.

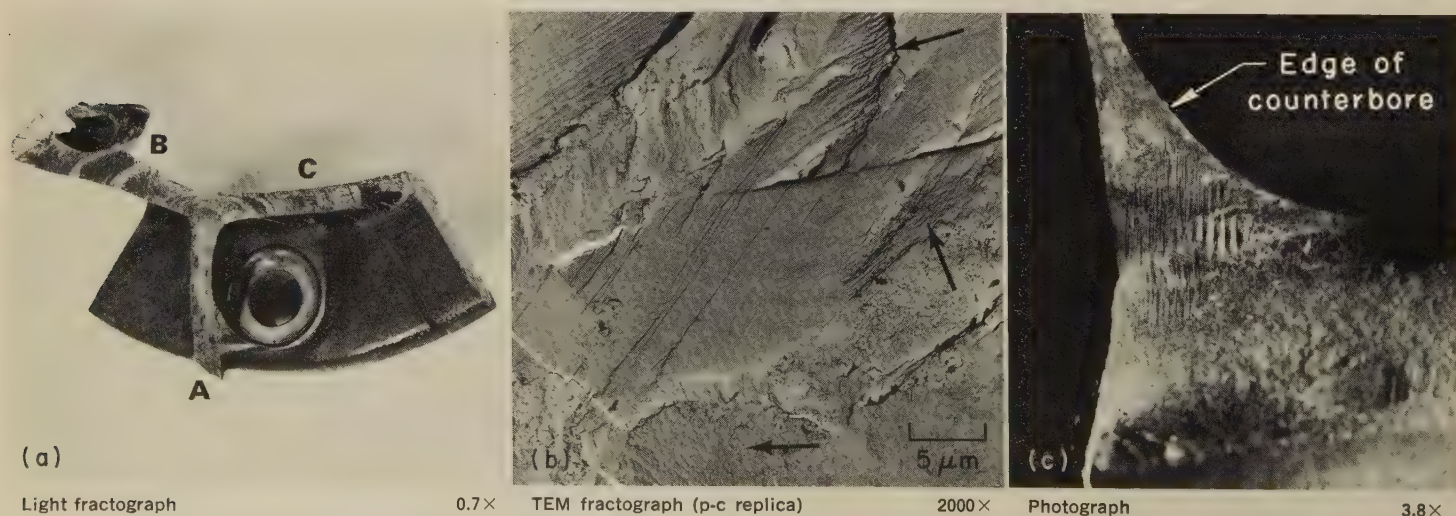
The scanning electron microscope is useful in examining fracture surfaces for tool marks because its great depth of field permits a sharp image of both the edge of the fracture surface and the abutting external contours of the part.

Scanning electron microscopes can be used to determine whether surface discontinuities such as forging laps, secondary cracks, and corrosion pits are present in the surface adjacent to the fracture. The examination may indicate (a) that a group of discontinuities of a specific variety was present in the surface; (b) that one or more of these may have been responsible for the fracture; and (c) that the remaining associated

discontinuities testify to the nature of crack initiation even though the discontinuity that initiated the fracture may no longer be distinguishable.

A further aspect of surface (and of microstructure) that should be explored is whether the surface layers of a part are different in composition, hardness and microstructure from the interior of the part. Differences could result from decarburization, from case hardening by carburization, flame hardening or induction hardening, or from cold work, such as shot peening or surface rolling. Fractography will reveal the presence of such differences by the changes in fracture features between the surface and the interior. Identification of the nature of each layer requires chemical and metallographic analysis.

Chemical and Thermal Environment. Fracture of a part in service is often intimately associated with the type of environment to which the part was exposed. Active chemical environments include water, salt air, salt water, acid solutions, alkaline solutions, molten metal and even solid metal. Thermal en-



vironments that affect metal properties and fracture include exposure to low (cryogenic, for example) temperatures and high temperatures.

If the fracture resulted from corrosion, the surface of the part and the surface of the fracture will probably contain corrosion products, and fractography will reveal their presence. Their composition can be determined by analysis (wet chemistry, electron microprobe, x-ray diffraction, x-ray spectroscopy, electron diffraction, or Auger spectroscopy). If stress-corrosion cracking has occurred, the fracture is often intergranular and the quantity of corrosion products coating it will be greatest near the crack origin and least at the region of final fracture. The absence of visible corrosion products does not necessarily rule out stress-corrosion cracking as the cause of fracture. Metallographic sectioning and examination can supply additional evidence concerning corrosion along grain boundaries and the depth of secondary grain-boundary cracks.

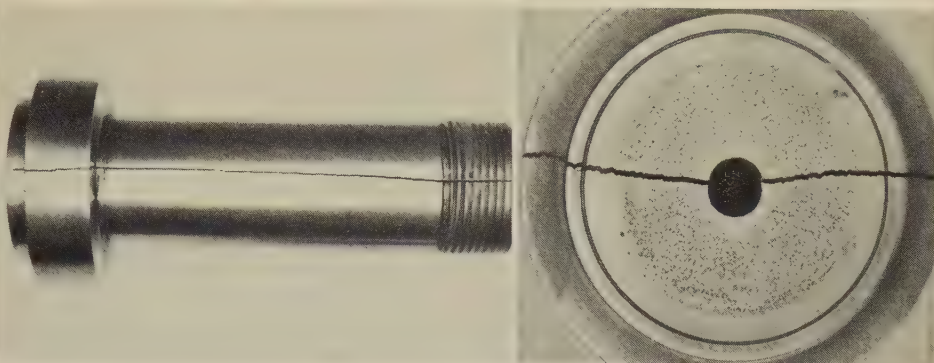
A part exposed to hydrogen may become embrittled. Like stress-corrosion cracking, hydrogen embrittlement will produce intergranular fracture, ideally with very clean separated-grain facets. (Often, hydrogen embrittlement can be so localized that it may not be detected.) In actual service, however, there is no clear distinction between fractures caused by stress-corrosion cracking and those caused by hydrogen embrittlement. In high-strength steels, for example, the two types of fracture are nearly impossible to tell apart. Hydrogen embrittlement in the type 431 stainless steel part described in the following example was distinguished from stress-corrosion cracking by careful fractographic examination.

Example 7. Hydrogen Embrittlement of a Type 431 Stainless Steel Mushroom-Head Closure (Fig. 9, 10 and 11)

The type 431 stainless steel mushroom-head closure shown in two views in Fig. 9 fractured in service at a hydrogen pressure of 3000 atm. Fracture occurred at room temperature after miscellaneous chemical service that included exposures to hydrogen at temperatures from ambient to 350 C (662 F).

The fracture surface displayed areas of both transgranular cleavage, as shown in the stereo pair of Fig. 10, and intergranular separation, as shown in the stereo pair of Fig. 11, which is characteristic of hydrogen embrittlement of high-strength steels. Debris from the final reaction to which the part was exposed has resulted in artifacts on the TEM replicas, but there appears to be no evidence of grain-boundary corrosion in Fig. 11. This is an important finding in that it differentiated this intergranular fracture, which was caused by hydrogen embrittlement, from similar ones produced by stress-corrosion cracking. Only by meticulous fractographic examination can clues be gained that make it possible to distinguish between these two fracture mechanisms.

If the part underwent abnormal heating or cooling, features on the fracture surface will indicate this. Usually, fracture at cryogenic temperatures is characterized by extremely brittle cleavage. The presence of flat cleavage planes with tongues on the fracture surface of a nor-



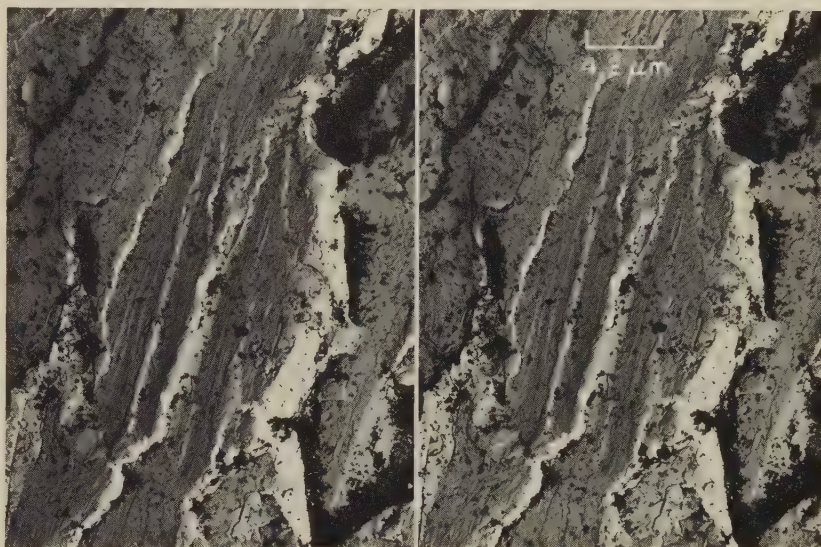
Photograph

1/2×

Photograph

1×

Fig. 9. Two views of a fracture from hydrogen embrittlement in a type 431 stainless steel mushroom-head closure. See also Fig. 10 and 11. (Example 7)

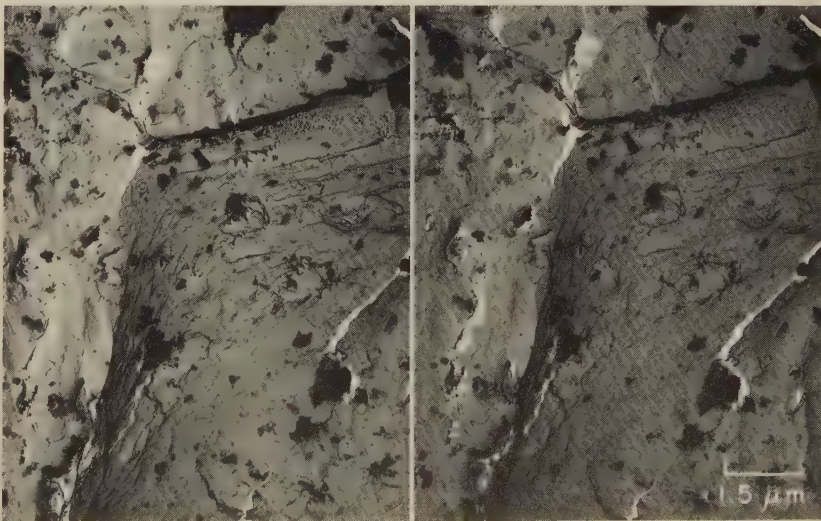


TEM stereo pair (p-c replica)

2400×

When viewed in 3-D, this stereo pair shows a massive ridge running from top to bottom at the left, with pronounced cleavage steps on its right-hand slope. The corrosion debris remaining from service and extracted by the replica may be seen projecting from the surface.

Fig. 10. Transgranular cleavage in an area of the surface of the hydrogen-embrittlement fracture of the type 431 stainless steel mushroom-head closure shown in Fig. 9. See also Fig. 11. (Example 7)



TEM stereo pair (p-c replica)

6600×

When viewed in 3-D, the somewhat rounded separated-grain surfaces show cavities akin to dimples in appearance but more probably sites of previous intergranular inclusions. The corrosion debris may be seen projecting from the fracture surface.

Fig. 11. Intergranular separation in an area of the surface of the hydrogen-embrittlement fracture of the type 431 stainless steel mushroom-head closure of Fig. 9 and 10 (Example 7)

mally ductile alloy should be interpreted as a fracture at very low temperature. However, cooling the part to liquid-nitrogen temperature and returning it to room temperature will not usually influence subsequent fracture unless residual austenite was present prior to the low-temperature treatment.

Heating a part to an abnormally high temperature produces certain changes that can be recognized by fractography, such as oxidation of the surfaces of the part and any fracture, warpage, softening of heat treated steels, and partial melting at locations of chemical segregation. Determination of the cause of fracture in these circumstances will require a comparison of the fractographic findings with the service conditions that were originally anticipated.

Fracture by high-inertia collision (as for vehicles) is a somewhat unusual influence of environment. The cause of such a fracture is usually obvious, but situations arise in which the major question is whether a specific crack or fracture formed during impact or was present before it happened. Fractographic exam-

ination can help to establish whether the fracture is fresh, whether it bears evidence of application of an abrupt over-stress, and whether its origin and path of crack growth relate to the over-all deformation produced by the collision.

Change in Fracture Mechanism With Size, Shape and Cross Section of a Part

The shape, size and cross section of a specimen or structural component can have a large effect on both the macroscopic and the microscopic appearance of the fracture surface, especially when pronounced stress raisers are present. Holes, corners, notches, machining marks and, most of all, preexisting cracks actively influence fracture appearance. Pronounced stress raisers are more likely to be contained in a large part than in a small part, because a large part has greater volume and surface area.

The dimensions of a part affect the mechanism of fracture. If the fracture mechanism in iron, quenched-and-tem-

pered steels, or other body-centered-cubic metals changes from microvoid coalescence to {100}-plane cleavage, the likelihood is that the change was a result of an increase in section thickness. Thicker parts experience more triaxiality and constraint in the zone immediately ahead of the crack tip and therefore are more likely to fracture by plane-strain crack propagation.

In a component made of material that does not fracture by cleavage or by intergranular separation, an increase in section thickness may be indicated by a change in fracture-surface features from shear dimples (for a thin sheet) to tear dimples (for a heavy plate). The macroscopic change would be from a full-slant fracture to one that is flat and perpendicular to the stress axis.

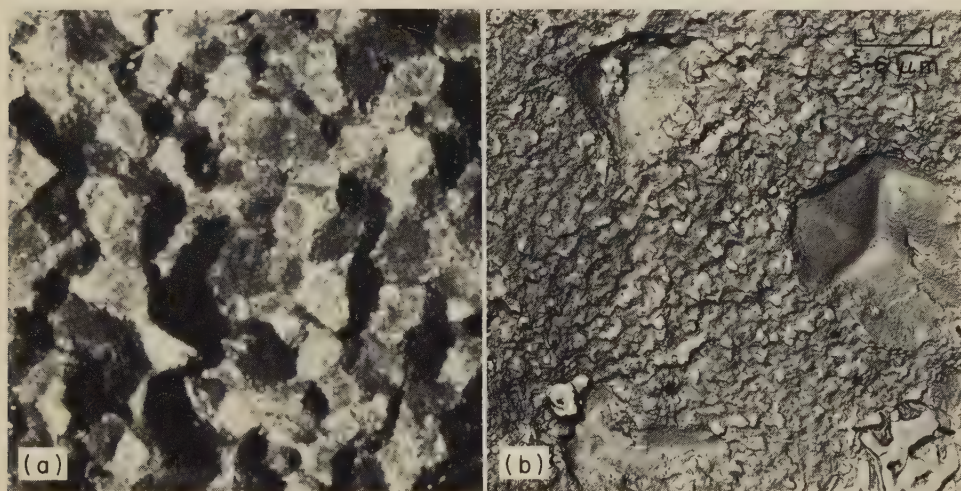
Another change in fracture mechanism with change in section thickness occurs in components exposed to corrosive environments. For a part exposed to salt water, a change from microvoid coalescence to intergranular separation or to cleavage could be associated with an increase in thickness, even if the stress-intensity factor is lower.

Evidence of fracturing along the grain boundaries of an otherwise ductile alloy may signify that the load was applied in a direction perpendicular to the rolling direction. This is particularly true for precipitation-hardening stainless steels and the 7xxx series of aluminum alloys, which often develop banded structures during rolling or forging. The largest boundaries of the grains are parallel to the rolling direction, and elemental and particle segregation can increase the probability that voids will be initiated along these grain boundaries. To prevent recurrence of this type of fracture, the part should be redesigned to reorient the direction of loading.

Fractures by Intergranular Separation

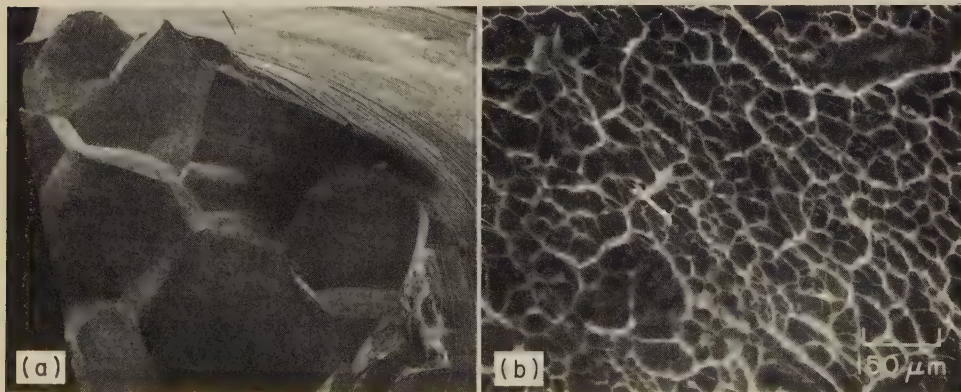
Intergranular fracture is generally associated with either of two conditions: (a) marked differences between the mechanical properties of the grain boundaries and those of the grains themselves, or (b) environmental conditions that favor crack propagation along grain boundaries. Alloy segregation or depletion at grain boundaries and the formation of precipitate particles or continuous films are examples of microstructural factors that contribute to intergranular fracture. In certain alloys, fractures resulting from stress-corrosion cracking or from hydrogen embrittlement are characteristically intergranular; the individual facets may be relatively featureless, exhibiting only fine tear ridges or hairline marks, or they may be characterized by varying degrees of corrosion pitting or corrosion products.

Elevated-temperature creep-to-rupture fractures are often completely intergranular, although their appearance may be altered by deformation of individual grains or by postfracture oxidation. Deformation of the matrix frequently re-



Light fractograph 22× TEM fractograph (p-c replica) 1800×
(a) Coarse separated-grain facets indicate that hot pressing produced a new macrostructure unrelated to original powder-particle size. (b) Fractograph at higher magnification shows oxidation and inclusions on a separated-grain facet.

Fig. 12. Intergranular fracture of a powder metallurgy compact made of nickel-base heat-resisting alloy 713LC and creep-to-rupture tested in air at 760 C (1400 F) and 585 MPa (85 ksi)



SEM fractographs 10× (a); 67× (b)

Fig. 13. (a) Tensile-test fracture surface of a specimen of alloy Al-4.2Cu, showing separated-grain facets. (b) Uniform dimples on a portion of one facet of the fracture surface shown in (a). This is characteristic of microvoid coalescence in the grain-boundary zone.

The microstructure of the specimen indicated alloy depletion at grain boundaries.

sults in noticeable curvature of individual facets and sometimes contributes to flattening of the over-all fracture surface.

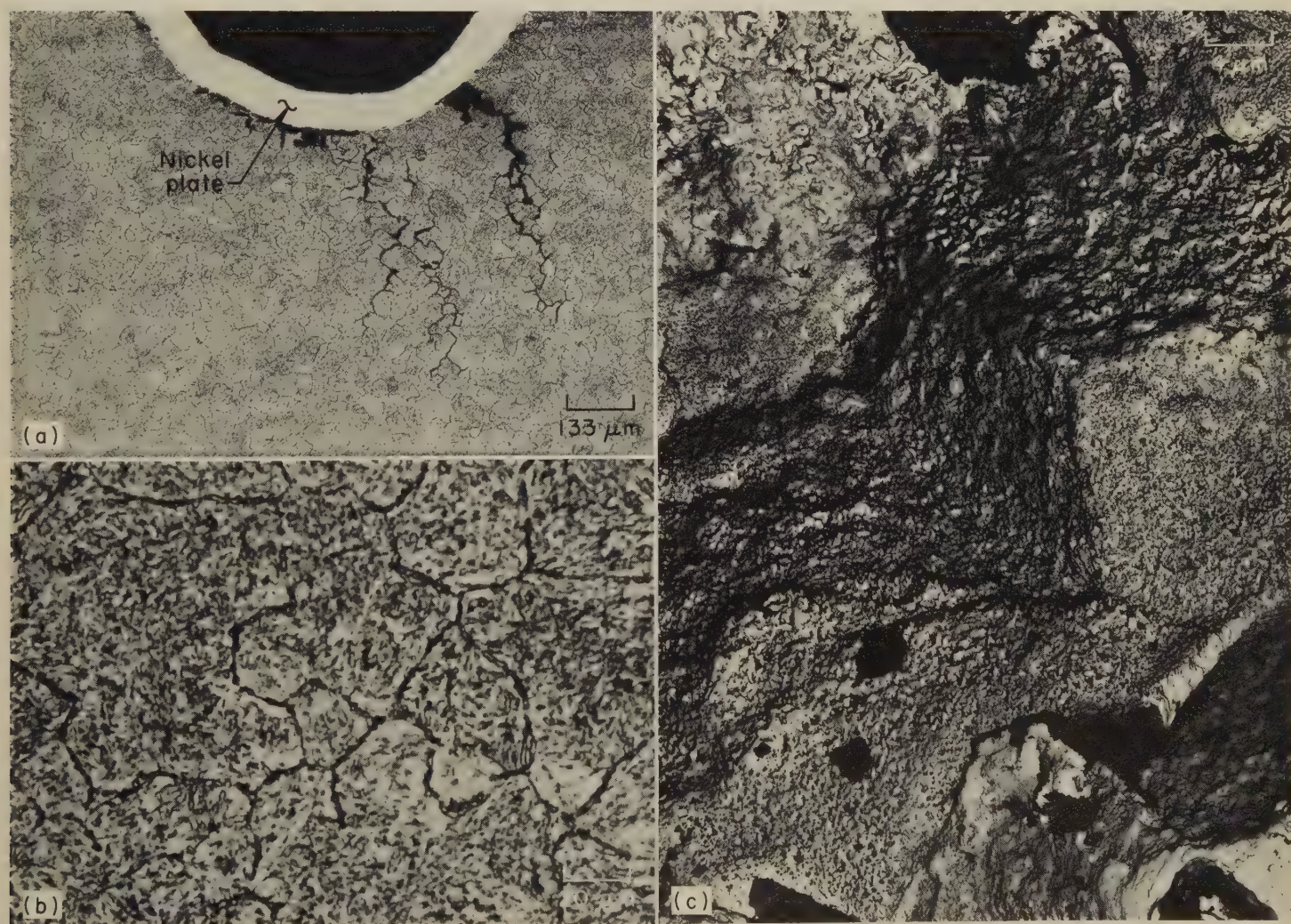
Whether or not a fracture is intergranular can often be determined by inspection at low magnification. (Higher magnifications are sometimes necessary for positive identification, particularly for fine-grained materials.) Fractography at assorted magnifications can usually yield clues of the underlying cause of grain-boundary separation. For parts prepared from hot isostatically pressed powder metallurgy compacts, for example, examination of creep-to-rupture surfaces can provide information on how thoroughly the particles of the powder were bonded together. Figure 12 shows a fracture surface of a powder metallurgy compact of nickel-base heat-resisting alloy 713LC that was creep tested to rupture at a temperature of 760 C (1400 F) and a stress of 585 MPa (85 ksi). The coarse separated-grain facets are clearly evident in Fig. 12(a), indicating that the hot pressing produced a new macrostructure unrelated to the original powder-particle sizes and orientations. A higher-magnification view of one of the separated-grain facets (Fig.

12b) shows that inclusions were located at grain boundaries. Other surface features are oxidation products, which formed before cooling from the test temperature. For more complete appraisal of factors contributing to fracture, metallographic examination of sections normal to the fracture surface would be essential to confirm more precisely the microstructure of the powder metallurgy compact and the grain-boundary constituents.

Fractographic examination provides information concerning local properties of an alloy at its grain boundaries. Where the yield strength of grain-boundary zones is lower than that of the matrix, fracture can develop by microvoid growth and coalescence within the grain-boundary zones. The fracture surfaces resulting from this process are characterized by numerous small dimples superimposed on separated-grain facets, as shown in Fig. 13(b). Figure 13 presents views, at two magnifications, of a tensile-test fracture in a coarse-grained, high-purity aluminum-copper alloy. Examination of this fracture surface at a magnification where the field of view is of the order of a single grain can lead to misinterpreta-

tion of the uniform dimples as evidence of transgranular fracture instead of intergranular fracture. Careful examination of a fracture surface over a wide range of magnifications is imperative for accurate interpretation of fine-scale topography.

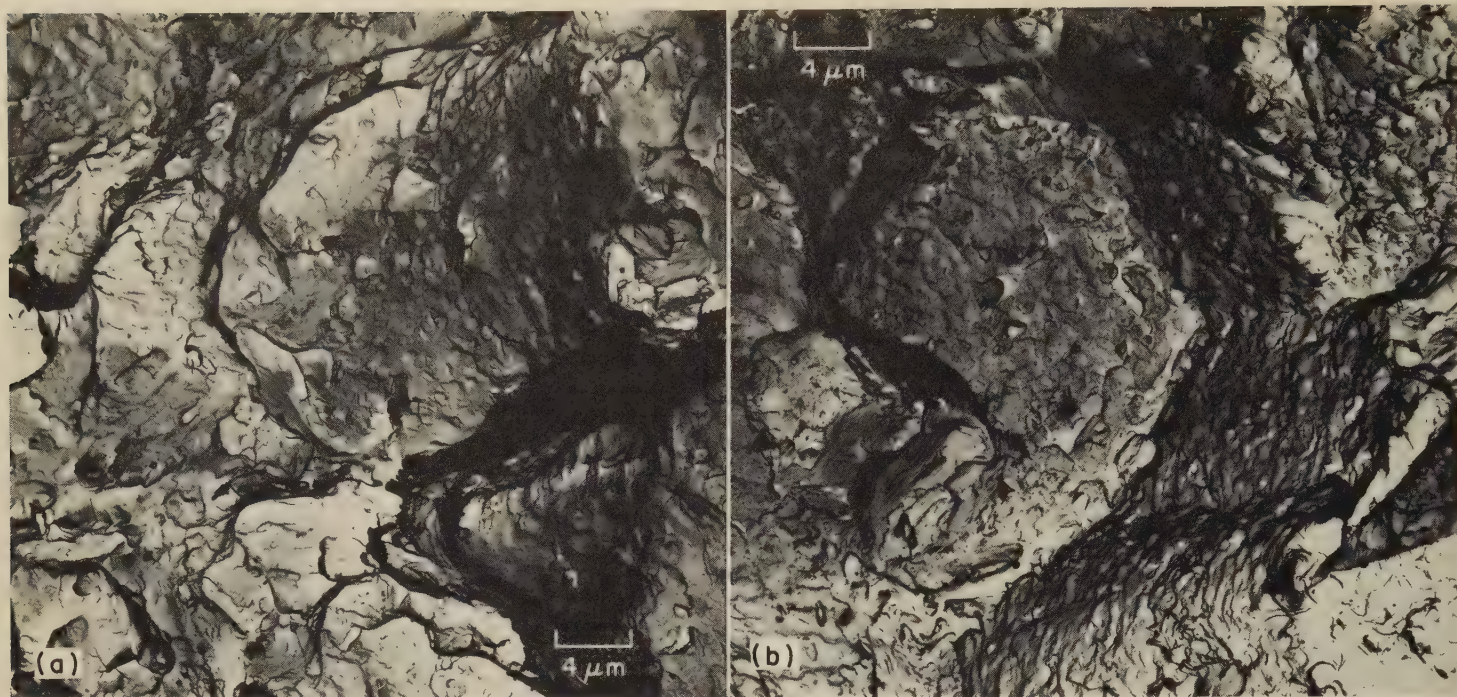
Figures 14 and 15 show an intergranular fracture in a 12% Cr stainless steel stud. Excessive grain-boundary carbide precipitation resulted in intergranular stress-corrosion cracking during exposure to a moist environment in service, as shown in Fig. 14(a) and (b). Subcritical crack growth by this mechanism eventually resulted in brittle fracture of the stud after the development of a relatively small crack at the thread root. Figure 14(c) shows the fine-scale topography in the fracture-initiation zone, where crack growth was subcritical. Consideration of the conditions under which final fracture occurred and of subsequent mechanical-property tests indicated an abnormally low fracture toughness for the 12% Cr stainless steel used in making the stud. Fractographic examination of the area of final, fast fracture, and of toughness-test specimens, showed mixed mechanisms of fracture—transgranular zones charac-



Micrographs (etchant: picral) 75× (a); 500× (b)
(a) and (b) Improper heat treatment resulted in excessive carbide precipitation at grain boundaries, and intergranular cracking occurred at roots of nickel-plated threads during service in a moist environment. Growth of stress-corro-

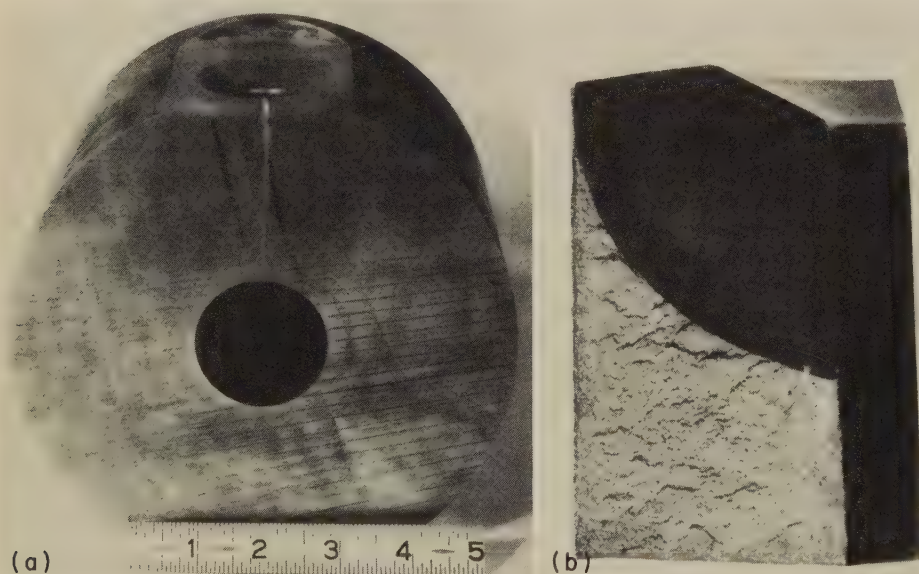
TEM fractograph (p-c replica) 2500×
sion cracks to a critical size resulted in brittle fracture of the stud.
(c) The fracture-initiation zone of the broken stud. Note the well-defined intergranular facets and evidence of corrosion on the fracture surface.

Fig. 14 Fracture resulting from stress-corrosion cracking in a 12% Cr stainless steel stud (see also Fig. 15)



TEM fractographs (p-c replicas)
 (a) Area of final, fast fracture of the broken stud. Note mixed quasicleavage facets and dimples, and separated-grain facets. (b) Localized zone of separated-grain facets in final-fracture area of the broken stud. Small dimples can be seen on some facets. Dimples at upper right may be in a local region of transgranular fracture.

Fig. 15. Fracture resulting from stress-corrosion cracking in a 12% Cr stainless steel stud (see Fig. 14)



Photograph 3X Light fractograph 23X
 (a) Section cut through valve block showing magnetic-particle indications outlining a crack beginning in the shoulder of the valve port, at top, and extending to the primary bore, at center.
 (b) Corrosion-fatigue crack in a valve block similar to that shown in photograph (a). The crack, which terminates in an arc, is very smooth and has been darkened by the presence of corrosion products. The light-toned fracture surface below and to the left of the crack surface was produced when the valve block was broken to expose the fatigue crack.

Fig. 16. Valve blocks of 4340 steel that cracked in service from corrosion fatigue. See also Fig. 18 and 19. (Example 8)

terized by dimples and quasicleavage facets, and a significant amount of intergranular separation (see Fig. 15). Classification of a fracture as intergranular on the basis of observations made in a limited area can thus be entirely erroneous.

Fractography can assist in determining the grade of stainless steel of a fractured part before results of chemical analysis are available. For example, fracture re-

sulting from stress-corrosion cracking in an annealed-and-quenched austenitic stainless steel in a magnesium chloride solution will be transgranular; fracture under similar conditions in a hardened martensitic stainless steel will be intergranular. However, care is essential in distinguishing between these two fracture mechanisms, because scanning and transmission electron microscope frac-

tographs of these fractures in both types of steel may exhibit an apparent "rock candy" surface. This is evidently because the transgranular fracture in the austenitic stainless steels follows either sub-grain boundaries or certain planes of weakness in a manner by which an angular pattern is formed as the crack crosses from one grain to the next.

Fractures Resulting From Corrosion

Analysis of the cause of fracture in metal parts and components that have been exposed to corrosive environments is often difficult because of interactions of fracture mechanisms or because fractures generated by different mechanisms may have similar appearances. Stress-corrosion cracking, corrosion fatigue, and fatigue alone can be confused. Arrests in stress-corrosion cracks produce striations that are very similar to fatigue striations in appearance. Corrosion fatigue, a combination of fracture mechanisms, may make it difficult to determine which mechanism played the dominant role, because corrosion of the crack surface behind the advancing crack front may obscure the fatigue striations and suggest erroneously that fatigue was not involved. Examples 8, 9 and 10, which follow, describe the use of fractography to investigate fractures that have occurred under corrosive conditions.

Example 8. Corrosion-Fatigue Cracking of 4340 Steel Hypercompressor Valve Blocks and Packing Retainers (Fig. 16 to 19)

Typical corrosion-fatigue cracks in valve blocks of 4340 steel heat treated to a hardness range of Rockwell C 32 to 35 are shown in Fig. 16. The transverse Charpy impact strength of the steel was 10 ft-lb at room temperature, which was considered normal.

Figure 17(a) shows a packing retainer of the same material as the valve blocks (4340 steel); Fig. 17(b) shows a fatigue crack in a retainer that was purposely broken open for inspection. Note the smoothness of the crack surfaces (compare Fig. 16b and 17b), a result of the combination of fatigue and corrosion. The valve blocks and packing retainers were used in polyethylene-processing equipment.

The fracture surface of the valve block in Fig. 16(b) was examined at high magnification, establishing the presence of fatigue striations (Fig. 18a) at the crack tip and corrosion pits and associated secondary cracks (Fig. 18b and 18c) in the primary bore. One pit-crack system was the origin of the corrosion-fatigue crack that penetrated the valve block. Figure 18(d), which shows the fracture surface immediately below the primary bore surface, indicates that intergranular stress-corrosion cracking occurred early in the generation of the corrosion-fatigue crack. The fatigue striations that are faintly visible in Fig. 18(a), a light-microscope fractograph, are displayed more clearly in the TEM fractographs in Fig. 19.

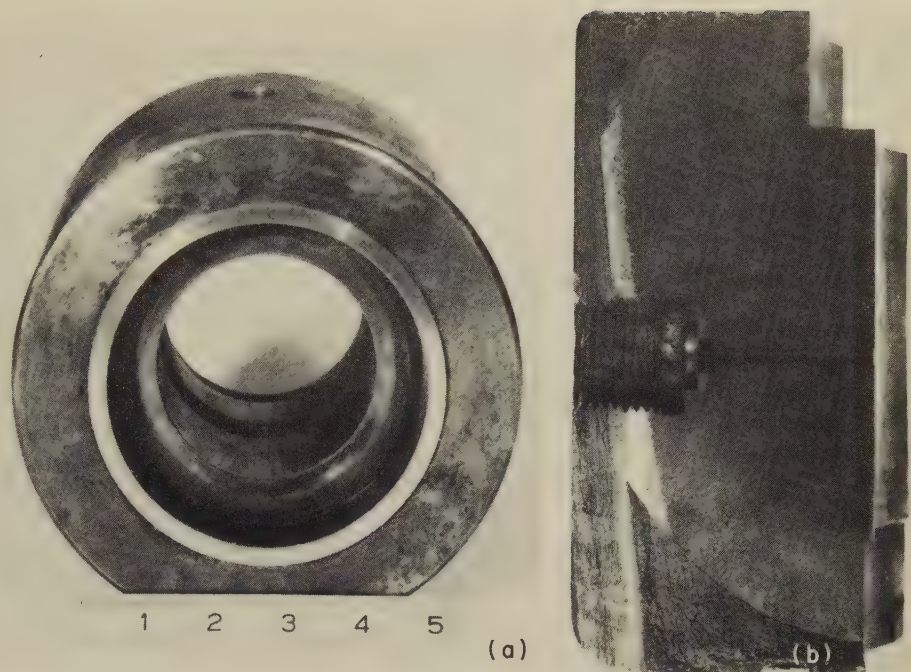
The evidence provided by fractography led to the conclusion that the corrosion-fatigue cracking was the result of high-stress pulsations in the presence of pitting attack from the glycerine lubricant that had been contaminated with water containing a chloride. The glycerine absorbed the water and also decomposed to form organic acids. Mineral oil, under conditions of maximum dryness, was recommended in place of the glycerine.

Some aspects of the appearance of fractures caused by stress-corrosion cracking in stainless steels frequently bear a considerable resemblance to fatigue striations; others are entirely dissimilar. These characteristics may be observed in stress-corrosion-crack surfaces of parts made from types 304 and 316 stainless steel. Conditions under which these characteristics occur are discussed in the following example.

Example 9. Characteristics of Fracture Features Caused by Stress-Corrosion Cracking in Types 304 and 316 Stainless Steel (Fig. 20 to 25)

Stress-corrosion cracking resulted from exposure of type 304 stainless steel tubing to a boiling solution of 42 wt % $MgCl_2$. The fracture surface in Fig. 20(a) shows features that indicate a mixture of fracture mechanisms, none of them fatigue. The fracture surface displays a large intergranular facet surrounded by small, irregular transgranular quasicleavage facets. The intergranular separation was probably a result of a fortuitous grain orientation in the path of the advancing transgranular stress-corrosion crack. Figure 20(b) displays closely spaced marks that might be mistaken for fatigue striations, or for crack arrests that occurred during stress-corrosion cracking. Close scrutiny, however, reveals the presence of many fine forks of a river pattern, created by cleavage steps. The crack propagated from upper right to lower left. See Fig. 21 for true fatigue striations.

The fracture in Fig. 21 resulted from cyclic fatigue-stress loading of type 304 stainless steel in air (under "dry" conditions). No evidence of corrosion is apparent on the striations. A slightly different appearance is presented in Fig. 22, which shows a fracture surface of a specimen of type 304 stainless steel that was broken in concentrated $MgCl_2$ at 60 C (140 F) under cyclic loading. The fracture has been superficially roughened by corrosion and the fatigue striations are still clearly visible. It is evident, therefore, that fatigue was the major mechanism of fracture and that corrosion had only a modest effect.



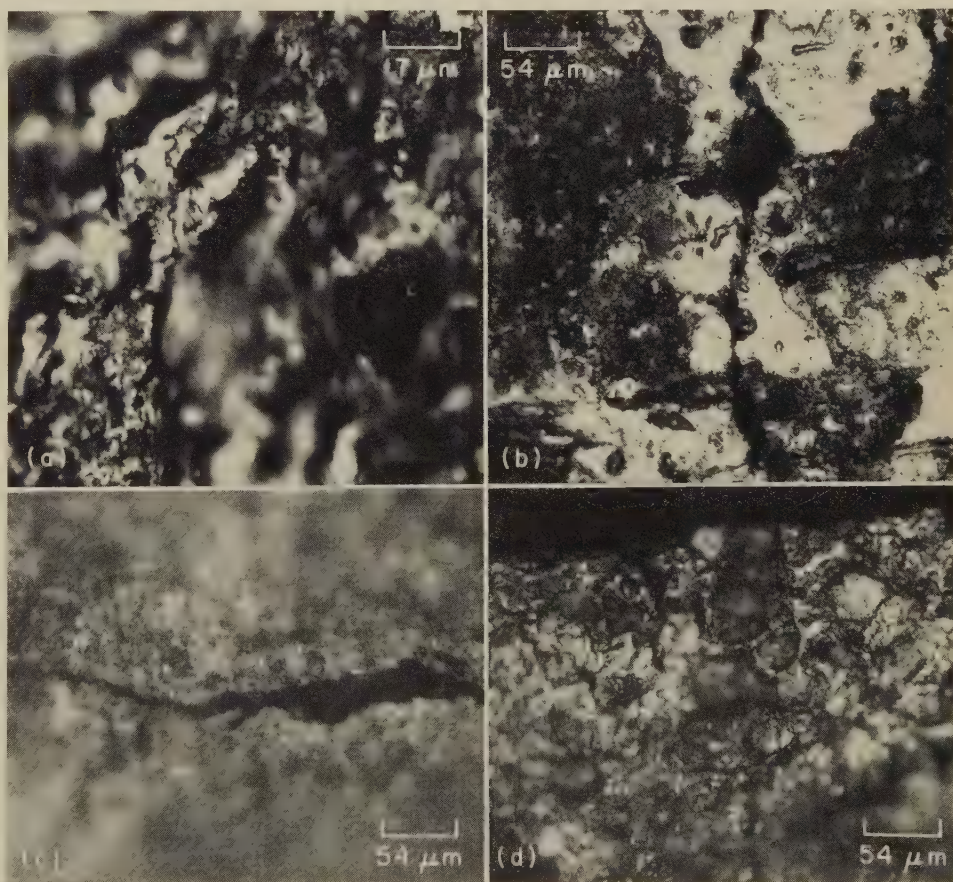
Photograph

(a) Over-all view of a packing retainer. (b) Packing retainer broken open for inspection, showing a corrosion-fatigue crack that penetrated nearly through

$\frac{3}{8}\times$ Light fractograph

the full section. Cut at extreme left was made to permit opening of the fatigue zone, which is extremely smooth and shows effects of corrosion.

Fig. 17. Packing retainer of 4340 steel that cracked by corrosion fatigue (Example 8)



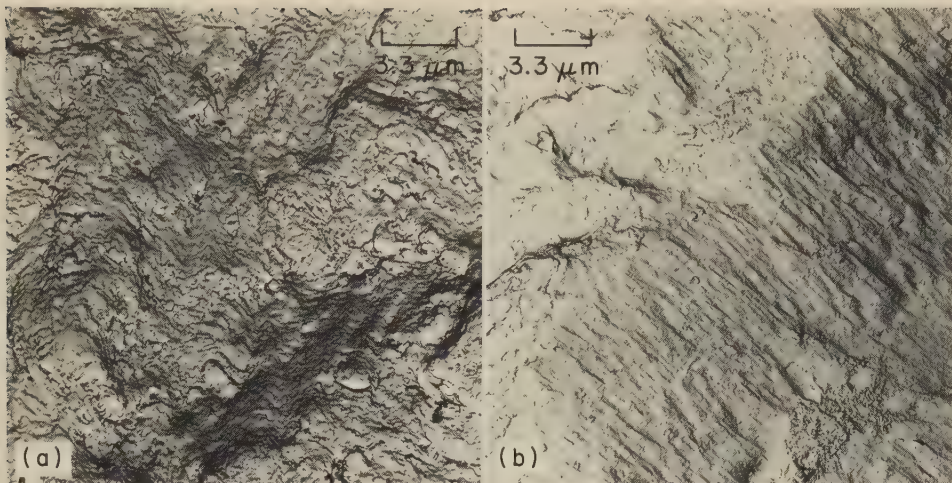
Light fractographs

(a) Fatigue striations at the crack tip that did not corrode. (b) Bore surface, showing corrosion pits and secondary cracks. (c) Elongated pit and crack at the rounded surface connecting the bore and the valve port. A pit-crack system like this initiated the

575 \times (a); 185 \times (b, c and d)

corrosion-fatigue crack that penetrated the valve block. (d) Surface of the crack at a point near the primary bore; separated-grain facets suggest that stress-corrosion cracking occurred early in the generation of the corrosion-fatigue crack.

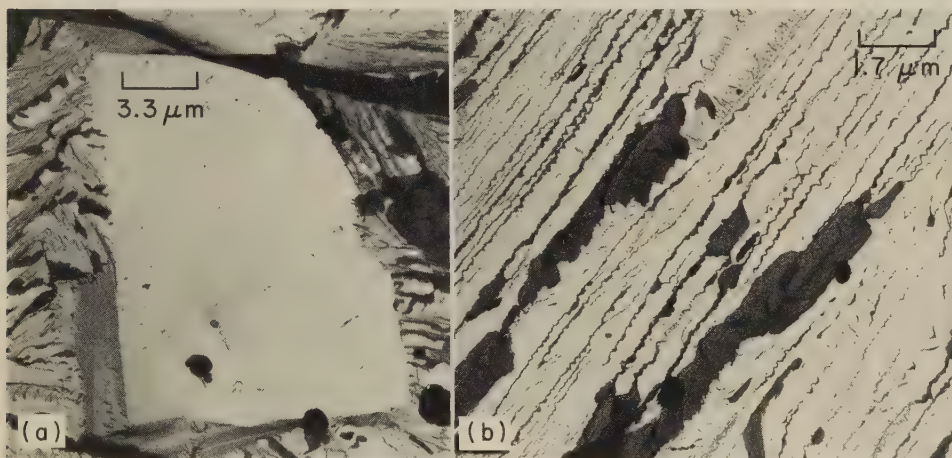
Fig. 18. Areas of the corrosion-fatigue crack in the 4340 steel valve block in Fig. 16(b). See also Fig. 19. (Example 8)



TEM fractographs (p-c replicas)

Both at 3000×

Fig. 19. Fracture surface at the tip of the corrosion-fatigue crack in the 4340 steel valve block in Fig. 16(b), as shown by TEM fractographs. The fatigue striations, which are only faintly visible in Fig. 18(a), a light fractograph, are clearly displayed here. There is also indication of a small amount of corrosion. (Example 8)



TEM fractograph (p-c replica)

3000×

TEM fractograph (oxide replica)

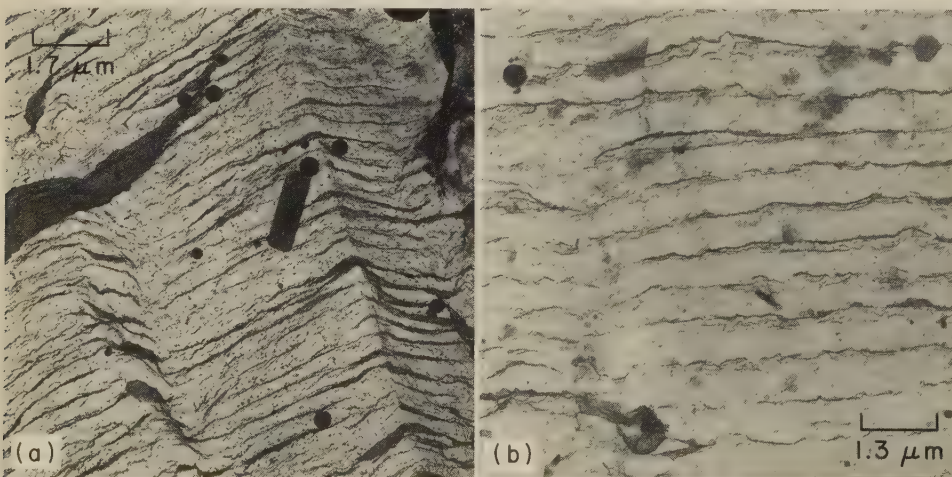
6000×

(a) The large central facet is a separated-grain surface. Around it are irregular quasicleavage facets of transgranular fracture.

(b) Example of fine marks that might be mistaken for either stress-corrosion striations or fatigue

striations, but whose branched nature indicates that they are river patterns formed by cleavage steps. The dark patches are films of corrosion products extracted with the oxide replica. Compare with the fatigue striations shown in Fig. 21.

Fig. 20. Fracture surface of type 304 stainless steel tubing that cracked after exposure to a boiling solution of 42 wt % $MgCl_2$ (Example 9)



TEM fractograph (oxide replica)

5750×

TEM fractograph (p-c replica)

7800×

(a) Striations have different orientations on either side of a tilt boundary (at right). Cyclic loading was in air; corrosion was not involved. (b) Striations show no evidence of corrosion (see Fig. 22).

Fig. 21. Oxide and plastic-carbon replicas of a fatigue-fracture surface of type 304 stainless steel, showing regular fatigue striations (Example 9)

Another fracture resulting from combined stress-corrosion cracking and fatigue is presented in Fig. 23. The component was a pressure-gage Bourdon tube fabricated of either type 304 or type 316 stainless steel. Fracture was caused by water leaking into the diphenyl oxide-diphenyl mixture (Dowtherm) carried by the tube. In Fig. 23(a), gross secondary cracks that lend a woody appearance can be seen at lower left; at upper right is a system of cleavage steps that display the forks and branches of a river pattern. The facets are crossed by very fine marks that resemble (but that probably are not) true fatigue striations. Other examples of these fracture features are shown in Fig. 23(b) and (c). Figure 23(d) displays a unique network of stress-corrosion cracks that have not yet been described in the literature on fractography of stainless steels but that nevertheless have been seen many times by at least one laboratory.

A fracture in a specimen of type 316 stainless steel is shown in two views in Fig. 24. These may be compared with Fig. 20(a) and (b) because the transgranular stress-corrosion crack that caused the fracture in Fig. 24 was also induced by exposure to a boiling solution of 42 wt % $MgCl_2$. The view in Fig. 24(a) is of cleavage facets with feather marks, which were largely characteristic of the entire fracture. However, Fig. 24(b) displays an area of "rock candy" intergranular fracture that could have been overlooked in a superficial examination. There is a possibility that corrosion-generated hydrogen may have caused local hydrogen embrittlement and the very clean intergranular separation. There is no evidence of corrosion on the grain facets.

When there is no corroding agent present, fatigue fractures in type 316 stainless steel display none of the features cited above but instead show the expected fatigue striations (like those in the type 304 stainless steel

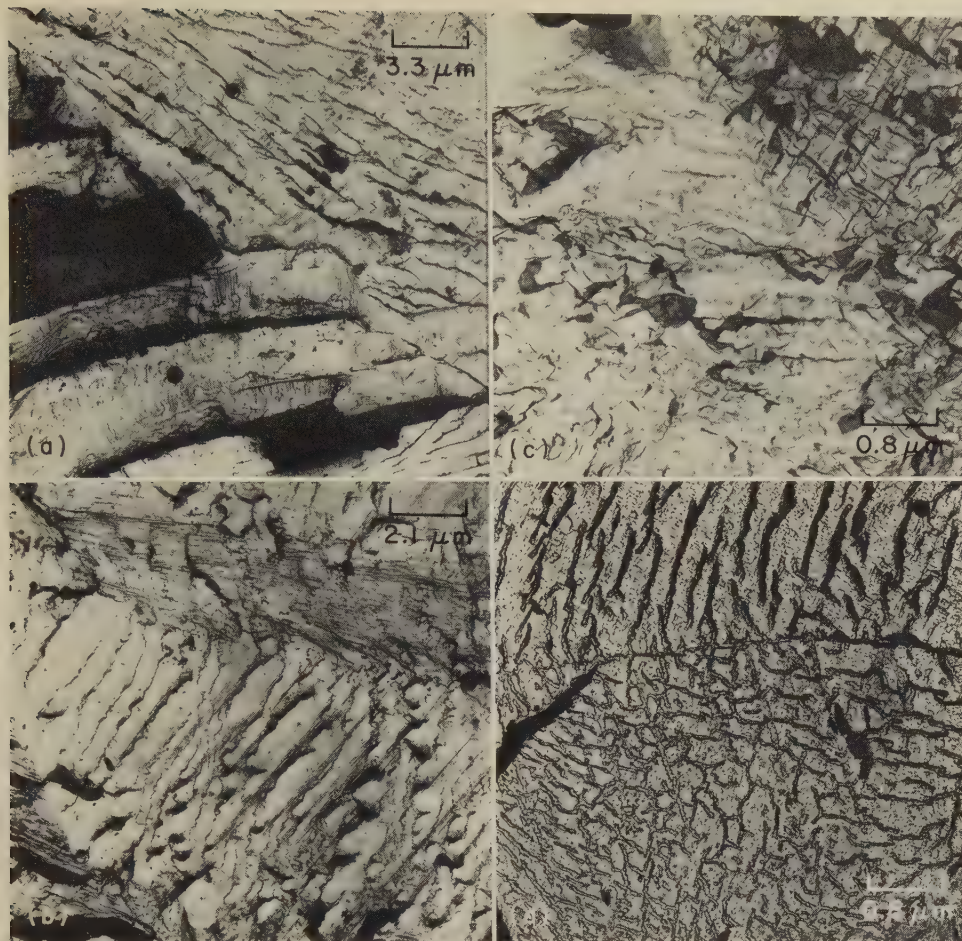


TEM fractograph (p-c replica)

30,000×

The fracture has been superficially roughened by corrosion, and the fatigue striations are clearly visible. There is also a suggestion of secondary fissures in some of the striations. Compare with Fig. 21.

Fig. 22. Corrosion-fatigue fracture produced by application of cyclic stress to type 304 stainless steel exposed to a concentrated $MgCl_2$ solution at 60 C (140 F) (Example 9)



TEM fractographs (oxide replicas)

(a) At lower left is a region of gross secondary cracks, which give a woody appearance. Segments between the cracks show fine cross marks that are not fatigue striations. At upper right is a diagonal system of branched cleavage steps, also with fine marks that are not fatigue striations.

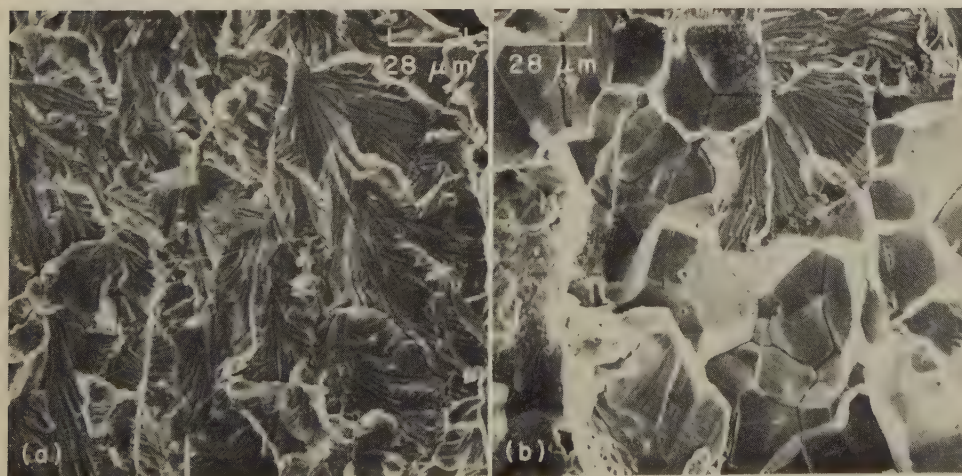
(b) In the central area, there are stress-corrosion-crack arrests. At lower left, there appears to be a partial view of fatigue striations with corroded

surfaces, which lend a woody appearance. At top is a region where the fracture has been rubbed.

(c) Stress-corrosion cracking showing a complicated interlocking of fissures. Central area may contain somewhat irregular fatigue striations.

(d) A "worm tracks" area, an unusual example of a cobweb network of stress-corrosion cracks on the fracture surface. A grain boundary appears to cross the field a third of the way down from the top.

Fig. 23. Fracture surface of a stainless steel pressure-gage Bourdon tube that cracked because of attack by diphenyl oxide-diphenyl mixture (Dowtherm) that had absorbed water from a leak (Example 9)



SEM fractographs

The fracture in general exhibited the fan-shaped or feather-shaped transgranular cleavage features shown in (a). In a hasty scrutiny, the presence of local areas of "rock candy" intergranular fracture,

such as those in (b), might be missed. This raises the question of whether corrosion-generated hydrogen caused local embrittlement. The separated-grain facets in (b) show no trace of corrosion.

Fig. 24. Surface of a fracture in type 316 stainless steel resulting from stress-corrosion cracking by exposure to a boiling solution of 42 wt % $MgCl_2$ (Example 9)

shown in Fig. 21). Figure 25 is a TEM fractograph that shows fatigue striations in a specimen of type 316 tested in air under a preload of 345 MPa (50 ksi) with a cyclic load of 345 MPa (50 ksi) and that broke after 226,000 cycles. This fractograph suggests that some rubbing of the fracture surface took place, but in other respects this is an example of a conventional fatigue fracture.

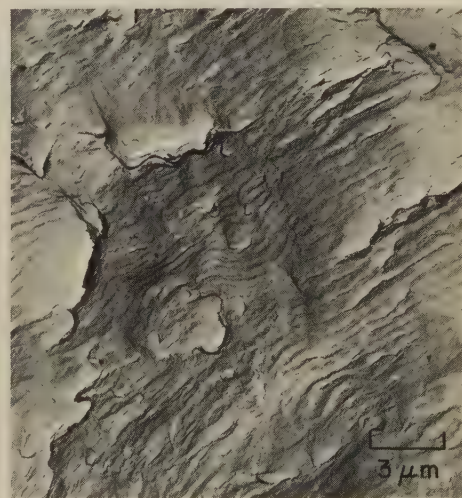
Another example of how fractography can assist in determining the cause of a fracture is presented below.

Example 10. Intergranular Fracture of Hastelloy C-276 by Gaseous HCl Attack (Fig. 26)

The fracture shown in Fig. 26 occurred in a pressurized reactor system made of Hastelloy C-276 as the result of exposure to a corrosive gas at elevated temperature. The gas atmosphere was hydrogen chloride containing 3.6% water and 13.0% $AlCl_3$. The operating temperature varied between 300 and 500 C (572 and 932 F). Although the reactor was operating above atmospheric pressure, the operative stresses involved in the intergranular fracture were external in origin. Fracture occurred after 2600 hr of service and was initiated during the last 240 hr of operation. Figure 26 shows that the fracture followed the grain boundaries, with no sign of dimpled rupture or transgranular cleavage. The corrosive attack on the separated-grain facets apparently took place after the crack had partly opened. Secondary grain-boundary cracks have nearly separated some individual grains from the remainder of the grains.

Service Fractures

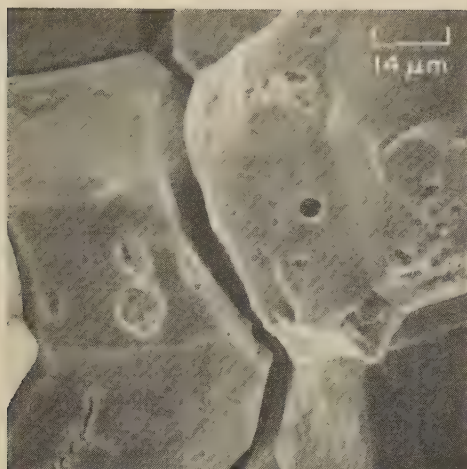
Service fractures include those attributable to results of (a) inadequate design, like improper fillet radii or too-small cross sections; (b) fabrication damage, like seams, laps and weld-crater cracks; (c) unfavorable environment, such as a corrosive atmosphere; and (d) inadequate maintenance, such as loose fittings. The next example describes a fracture that occurred when manufacturing procedures departed from design specifications.



TEM fractograph (p-c replica) 3300×

Fatigue patches separated by tear ridges are apparent. The appearance of the surface at left and at upper right suggests that rubbing occurred after the crack front passed.

Fig. 25. Fatigue striations in the surface of a fracture in type 316 stainless steel (Example 9)



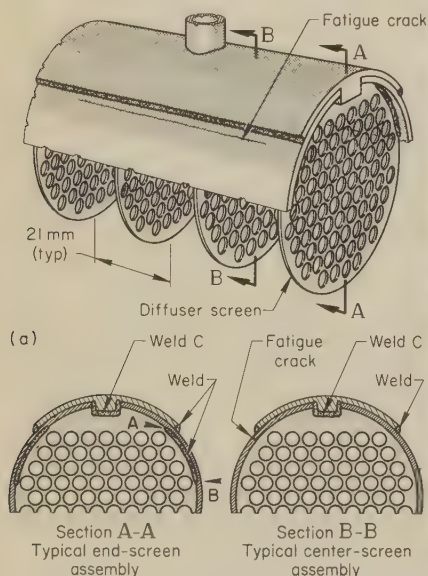
SEM fractograph 700×
The part was a component in a pressurized reactor system operating at 300 to 500 C (572 to 932 F) and was exposed to gaseous HCl containing 3.6% H₂O and 13.0% AlCl₃. Note the deep secondary cracks. The separated-grain facets display evidence of corrosive attack.

Fig. 26. Intergranular fracture in Hastelloy C-276 (Example 10)

Example 11. Fatigue Crack That Resulted From Improper Fabrication of a Radiator Assembly for an Aircraft Hydraulic System (Fig. 27)

A longitudinal crack was found in the shell of a section of an aluminum alloy 2024-T6 radiator assembly (Fig. 27a). The radiator contained diffuser screens spaced at intervals of 21 mm along the length of the shell. The two end screens were firmly attached to the shell wall over the length AB (see view A-A in Fig. 27a), thereby acting as wall stiffeners. The two center screens were attached only by weld C, as shown in view B-B in Fig. 27(a), leaving the wall unsupported.

Examination of the fracture surface revealed no obvious macroscopic features to indicate the mechanism of fracture. Electron-microscope fractographic examination revealed well-formed fatigue striations (Fig. 27b) whose orientations intimated that the



(a) Radiator assembly, showing change in wall thickness, location of crack, and position of diffuser screens. Views A-A and B-B show the locations of the welds that secured the screens to the shell wall. (b) TEM fractograph (plastic-carbon replica), at 7700×, showing fatigue striations on the crack surface.

Fig. 27. Fatigue crack in the shell of a section of an aircraft hydraulic radiator assembly made of aluminum alloy 2024-T6 (Example 11)

fracture had started at the inner surface of the cylinder wall, and had propagated through the wall, penetrating the outer surface. The change in wall thickness (see Fig. 27a) was a probable cause of stress concentration, and cyclic loading in the form of internal hydraulic-pressure pulses undoubtedly produced circumferential flexing of the shell. The length of wall left unsupported by the unattached screens corresponded to the length and location of the fatigue crack.

Failure analysis using fractography revealed the crack origin and fracture mechanisms of the cracking described in the following example. Changes in design did not eliminate the problem, but a laboratory test indicated that certain maintenance and inspection procedures could be used to follow the progress of crack growth and allow removal of the part before fracture occurred.

Example 12. Fatigue Cracks in an Aluminum Alloy 2014-T6 Forged Compressor Disk for an Aircraft Engine (Fig. 28 to 31)

Fatigue cracks originated on the rear side of tenons of an aircraft-engine compressor disk forged of aluminum alloy 2014-T6, as shown in Fig. 28. The crack origin was in an area that was in contact with the blade root. Corrosion pits and occasional fretting had been seen in this area. The fracture mechanism could not be determined on initial inspection, because the crack, when opened up, showed no beach marks (Fig. 29).

TEM fractographs (Fig. 30a and b) taken from the early and central portions of the crack surface in Fig. 29 displayed no fatigue striations but exhibited cleavage-type features, characterized by what resembled coarse river patterns. At the crack tip, however, rather widely spaced striations (Fig. 30c) were found; these occurred in groups (suggesting blocks of a loading spectrum) superimposed on the cleavage-type features.

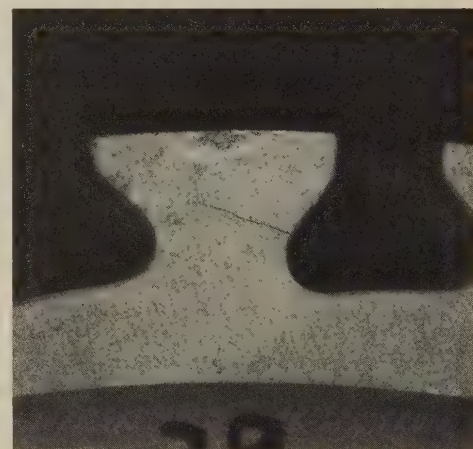
A laboratory fatigue-test fracture in the same material exhibited very fine, uniform, well-defined fatigue striations in areas where the crack-growth rate was 3.0 micro-in. per cycle or greater (Fig. 31a). In areas where the crack-growth rate was 1.2 micro-in. per cycle or less (Fig. 31b), cleavage-type features

were found that bore a close resemblance to those present in the service fracture.

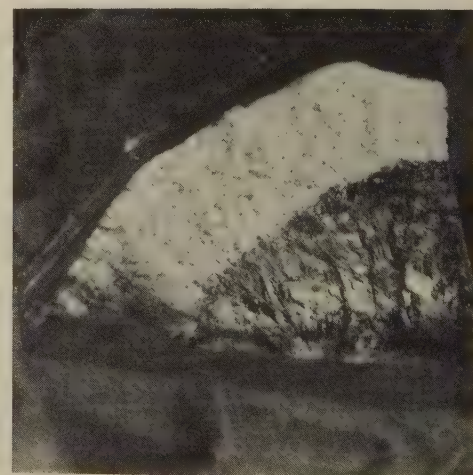
As a result of these observations, it was concluded that the crack in the compressor-disk tenon propagated in fatigue at a low rate of crack growth. The cause of origination of the crack was not definitely established, but was attributed to fretting corrosion. A change in the tenon cross section (fewer blades per disk) did not eliminate the problem. Coating of the surface was not feasible because press-fit assembly of the compressor blade would remove a coating. The relative vibratory motions of the blade and the disk would also damage a coating. It was finally decided to increase the frequency and effectiveness of ultrasonic inspection. Fortunately, it was observed that the fatigue cracks grew steadily at first and then at a very reduced rate as the crack induced a change in loading; this made it possible to detect the crack and to remove the disk before the occurrence of final fracture.

Growth Rates of Fatigue Cracks

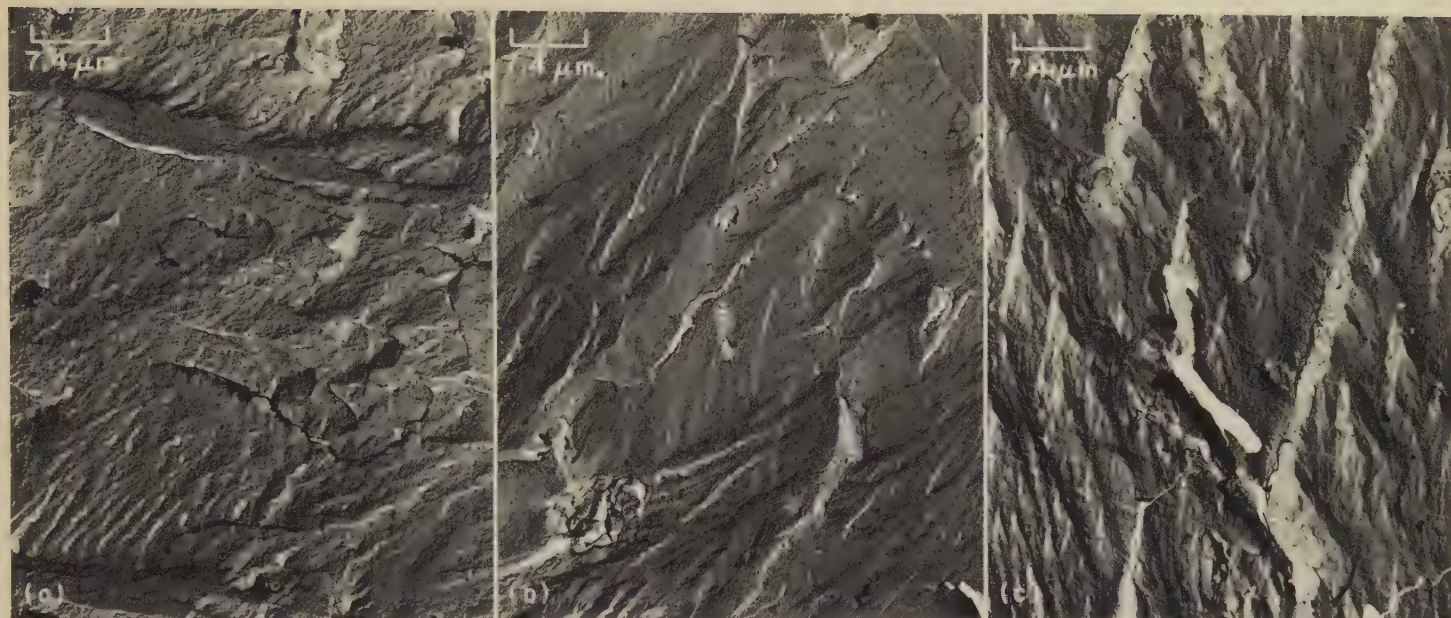
In service fractures involving fatigue, information concerning cyclic stress levels and rates of crack propagation in a



Photograph 3×
Fig. 28. Service-induced crack on rear side of tenon of aircraft-engine compressor disk forged of aluminum alloy 2014-T6. See also Fig. 29 to 31. (Example 12)



Light fractograph 7×
Fig. 29. Fracture surface of cracked compressor-disk tenon shown in Fig. 28. Light-colored area is fresh fracture formed in breaking the crack open. There is no evidence of fatigue. See also Fig. 30 and 31. (Example 12)

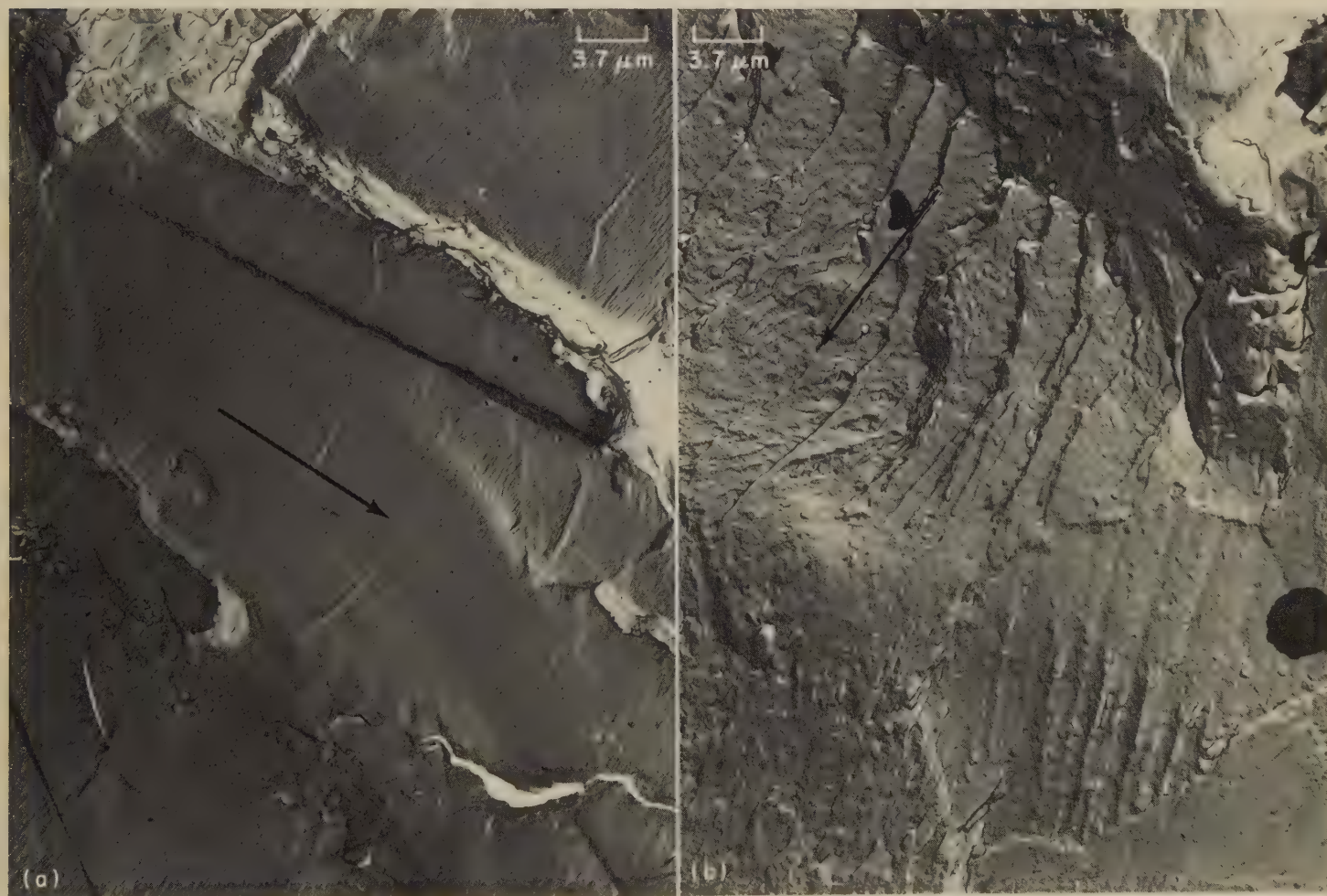


TEM fractographs (p-c replicas)

All at 1350X

The cleavage-type features (coarse river patterns) shown in (a) and (b) were typical of the central portion of the crack surface and the region near the origin. No striations indicative of fatigue were evident in those zones. Isolated areas of widely spaced striations superimposed on cleavage-type features as in (c) were observed near the crack tip.

Fig. 30. Surface of the crack in the compressor-disk tenon of Fig. 28 and 29. See also Fig. 31. (Example 12)



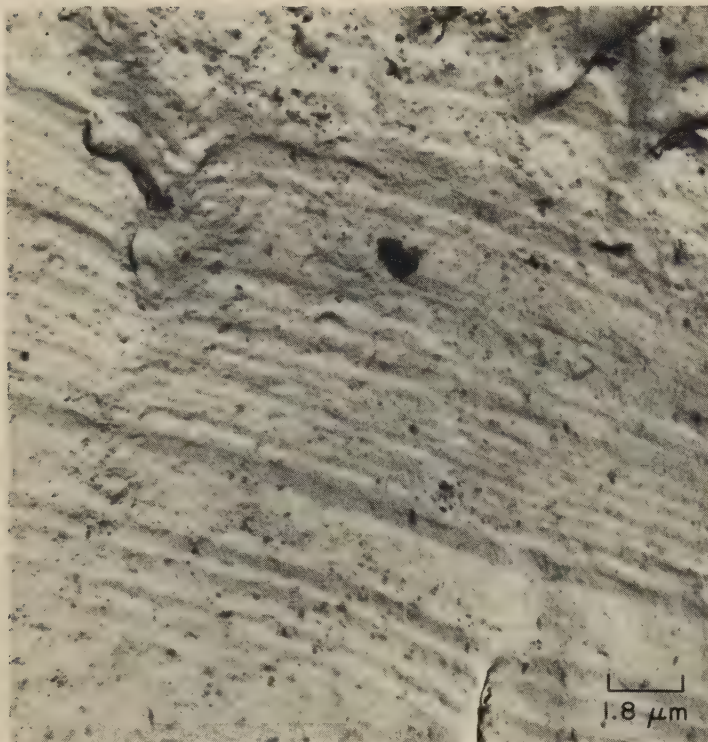
TEM fractographs (p-c replicas)

Both at 2730X

(a) Fine, uniform, well-defined fatigue striations in a fracture area where crack-growth rate was 3.4 micro-in. per cycle. This is typical of fracture areas where crack-growth rate was 3.0 micro-in. per cycle or greater.

(b) Coarse cleavage-type steps, resembling those in Fig. 30, in a fracture area where crack-growth rate was 1.2 micro-in. per cycle. This is typical of areas where crack-growth rate was 1.2 micro-in. per cycle or less (see Ref 1 and 2).

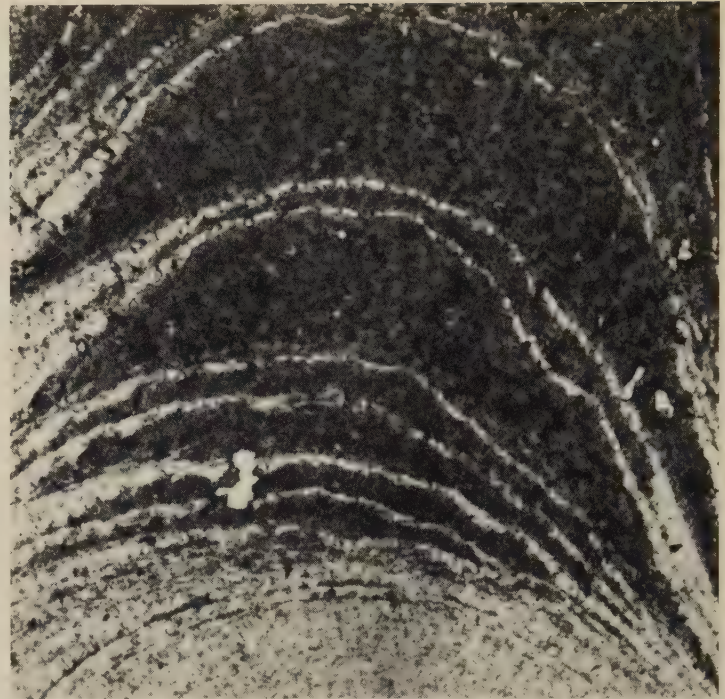
Fig. 31. Two areas, with different crack-growth rates, of a fracture surface of a laboratory fatigue-test specimen of aluminum alloy 2014-T6, the same material as that of the compressor-disk forging in Fig. 28 to 30. Arrows indicate direction of crack propagation. (Example 12)



TEM fractograph (plastic-carbon replica)

5600×

Fig. 32. Randomly spaced fatigue striations in a service fracture of an extruded aluminum alloy 2024-T3 aircraft-wing spar cap



Transmitted-light fractograph (through plastic replica)

7×

Fig. 33. Macroscopic crack-growth bands on the surface of a service fracture in a forged aluminum alloy 7075-T6 aircraft component. Higher magnification showed fatigue striations in narrow, bright bands, and ductile dimples in wider, dull bands.

component is of extreme importance to design and materials engineers. It is generally conceded that a striation on a fatigue-fracture surface results from the application of a single loading cycle, and it follows that, under ideal conditions, estimates of crack-growth rates can be made by striation-spacing measurements at successive locations of crack penetration.

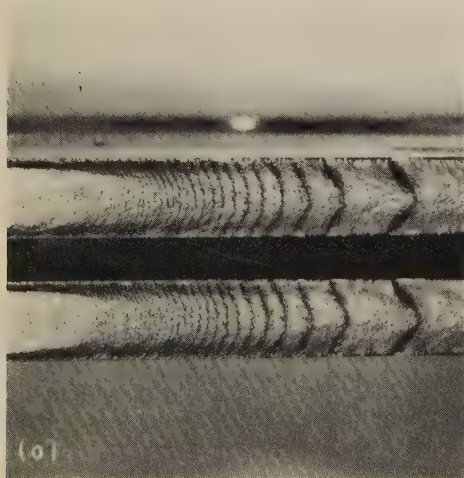
Correlations between macroscopic crack-growth rates obtained by visual monitoring and microscopic growth rates derived from striation counting and spacing measurements have been found by several investigators (Ref 3, 4). They have concluded that within certain in-

tervals good agreement existed between the fractographic approach and visually measured crack-growth rates, but, in general, wide variations may exist between the two. It has been suggested by Whiteson *et al* (Ref 4) that the difference between the measurements can be accounted for by the presence of areas of microvoid coalescence on a fatigue-fracture surface. Notwithstanding the observed variations, estimates of crack-growth rates in service fatigue fractures have been made on the basis of striation studies. This would appear to be reasonable whenever striation spacings are found to be fairly uniform in a field of

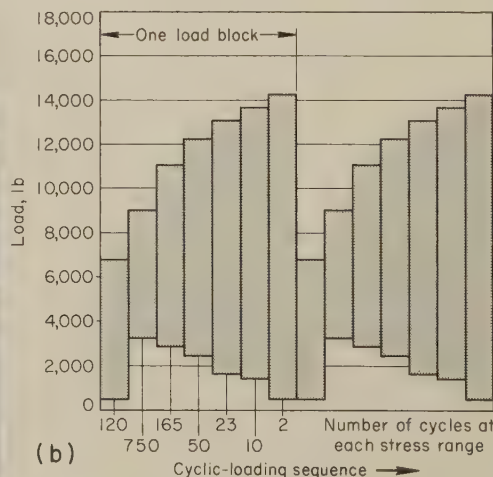
view, provided a careful traverse of the fracture surface is made to correlate striation spacings with crack depth. Such measurements, together with interpolation to allow for those areas of the replica obscured by the specimen grid, can yield information of engineering value, provided the limitations of accuracy of such estimates are taken into account.

Complications may arise in determinations of crack-growth rate from fatigue-striation measurements when cyclic service loads are not of uniform amplitude. Randomly spaced striations such as those in Fig. 32, which shows a service fracture in an aluminum alloy 2024-T3 spar cap for an aircraft wing, would not be of value in determining growth rates. The difficulty of such determinations is compounded by the fact that, in a random cyclic-load spectrum, the lower load amplitudes may not be of sufficient magnitude to produce resolvable striations, or, as has been observed by Whiteson *et al* (Ref 4), when abrupt changes from high-level to low-level alternating stresses occur, there may be a period of ten cycles or more during which the fatigue crack does not propagate. Whether constant or random cyclic-stress levels exist, it is frequently found that the fatigue striations are formed only in scattered areas on the fracture surface, and that they are poorly defined or partly obscured by corrosion or mutilation of the fracture surface. Under these circumstances, quantitative fractographic fatigue evaluations are extremely difficult or impossible to perform.

There are, however, instances in which relatively simple, yet reliable, determination of crack-growth rate by striation measurement will yield useful engineer-



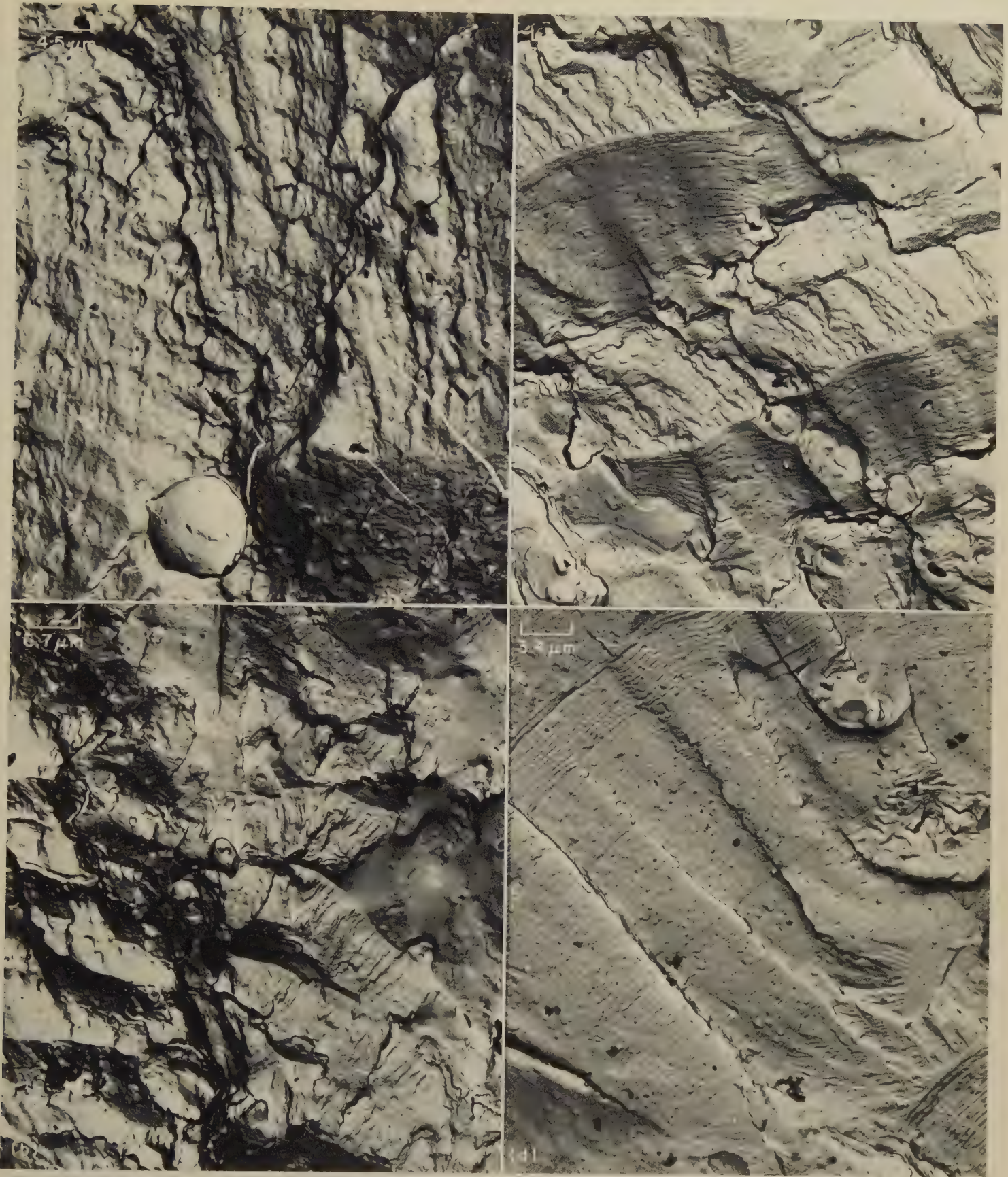
(a) Photograph, at 2X, showing typical fatigue crack-growth bands on the mating surfaces of a fracture in an aluminum alloy 2024-T3 main-spar web of an aircraft wing that was subjected to a repetitive



cyclic-loading spectrum. The aluminum alloy was fabricated as rolled sheet.

(b) Cyclic-loading spectrum that produced the fatigue-crack-growth bands shown in (a).

Fig. 34 Effect of cyclic-loading spectrum on macroscopic crack-growth-band spacing in aluminum alloy 2024-T3. See also Fig. 35 and 36. (Example 13)



TEM fractographs (p-c replicas)

(a) Crack-growth bands at a distance of 0.1 mm from crack origin. Striation-band spacing, 3.0 microns. Striations from individual load cycles not visible.
 (b) Crack-growth bands at 0.3 mm from crack origin. Striation-band spacing, 11.5 microns. Alternate changes in plane of crack propagation and small areas of finely spaced striations from individual load cycles are visible.

(c) Crack-growth bands at a distance of 0.6 mm from the crack origin. Striation-band spacing is 16.0 microns. Bands of striations are visible.
 (d) Crack-growth bands at a distance of 1.5 mm from the crack origin. Five load levels of the spectrum are clearly resolvable by striation spacings and cycle counts. Striation-band spacing is 32.0 microns.

Fig. 35. Fatigue-crack-growth bands at various distances from the crack origin in the aluminum alloy 2024-T3 spar web of Fig. 34, which was fatigue tested to fracture. See also Fig. 36. (Example 13)

ing information. Many fatigue-fracture surfaces exhibit macroscopic growth lines that have been referred to as clam-shell marks, beach marks, or crack-arrest lines. The formation of these lines has been attributed to either (a) sudden changes in cyclic stress levels, or (b) arrest of crack growth by a period of rest, with a subsequent accretion of corrosion products at the crack tip.

Another kind of macroscopic feature that has been observed, usually in the later stages of fatigue-crack growth in service fractures, consists of a pattern of alternate bright and dull bands. Figure 33 shows macroscopic crack-growth bands in a fracture of an aluminum alloy 7075-T6 aircraft component. Microscopic fatigue striations were observed in the narrow bright bands; the wider dull bands contained ductile dimples. These features indicate intermittent fatigue interspersed between episodes of limited fast fracture.

Macroscopic crack-growth bands may likewise be encountered on fracture sur-

faces of laboratory fatigue specimens that have been subjected to repetitive, sequential, programmed loading. Fractographic examination has indicated that there is a one-to-one correspondence between a load block (see Fig. 34b) of the cyclic-loading spectrum and the formation of a band on the fracture surface. Although it is not always clear precisely why the bands are visible, they have been shown, in the early stages of crack growth, to represent alternate changes in the plane and type of crack propagation. The next three examples describe instances where band counting and study were used to determine crack-growth rate, and where this information was employed in preventing further fractures.

Example 13. Determination of Crack-Growth Rate in an Aluminum Alloy 2024-T3 Main-Spar Web During a Fatigue Test (Fig. 34, 35 and 36)

The mating fracture surfaces of an aluminum alloy 2024-T3 main-spar web of an aircraft wing that fractured during a fatigue

test (Ref 5) are shown in Fig. 34(a). The repetitive-load spectrum, based on flight-load measurements, is illustrated graphically in Fig. 34(b).

At a crack penetration of 0.1 mm from the point of crack nucleation, the bands had a spacing of 3.0 microns and did not exhibit resolvable striations corresponding to the individual load cycles of the spectrum (Fig. 35a). At a crack penetration of 0.3 mm, the bands had a spacing of about 11.5 microns and exhibited repetitive changes in the plane of crack propagation as well as small groups of finely spaced striations representing individual load cycles (Fig. 35b). At a crack penetration of 0.6 mm, band spacing had increased to 16.0 microns and striations from individual load cycles were clearly resolvable (Fig. 35c) between the striation-free bands that had apparently formed during application of the lower loads of the spectrum. At a crack penetration of about 1.5 mm from the crack origin, band spacing was about 32.0 microns. Figure 35(d) shows well-defined striations that formed in response to the higher cyclic-load levels of the spectrum. The striations could be readily related to the stress conditions that generated them from their relative spacings and from striation counting. In the later stages of fatigue-crack growth, dimpled areas were observed between the macroscopically visible crack-growth bands.

The wing shape and the location of the internal fatigue cracks were such that the observation of crack growth was impossible during the course of the fatigue test. Because the main objective was to gain information concerning the moment of crack initiation and the rate of crack growth in the spar structure, a fractographic traverse of the fracture surface was undertaken to determine these in retrospect. A sketch of the fractured spar, indicating the various crack segments, is shown in Fig. 36(a), and a plot of crack length versus the number of applied load blocks for one of the segments, segment W, is given in Fig. 36(b).

Study of the crack-propagation rates revealed that the total time for crack growth from initiation at rivet hole 1 (Rh 1 in Fig. 36a) to segment U was approximately equivalent to 26,000 flying hours. The total endurance of the wing structure was about 48,000 flying hours. It was concluded that the exis-

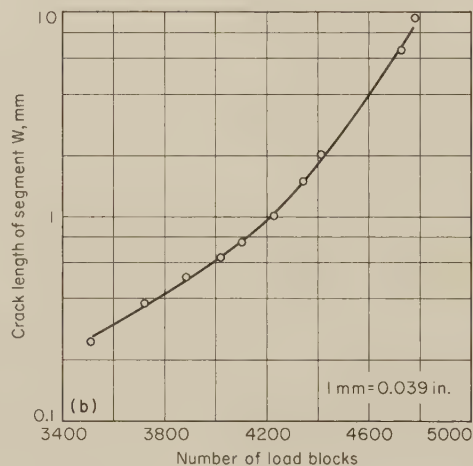
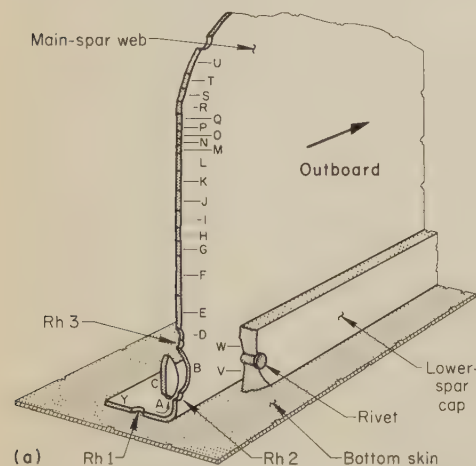
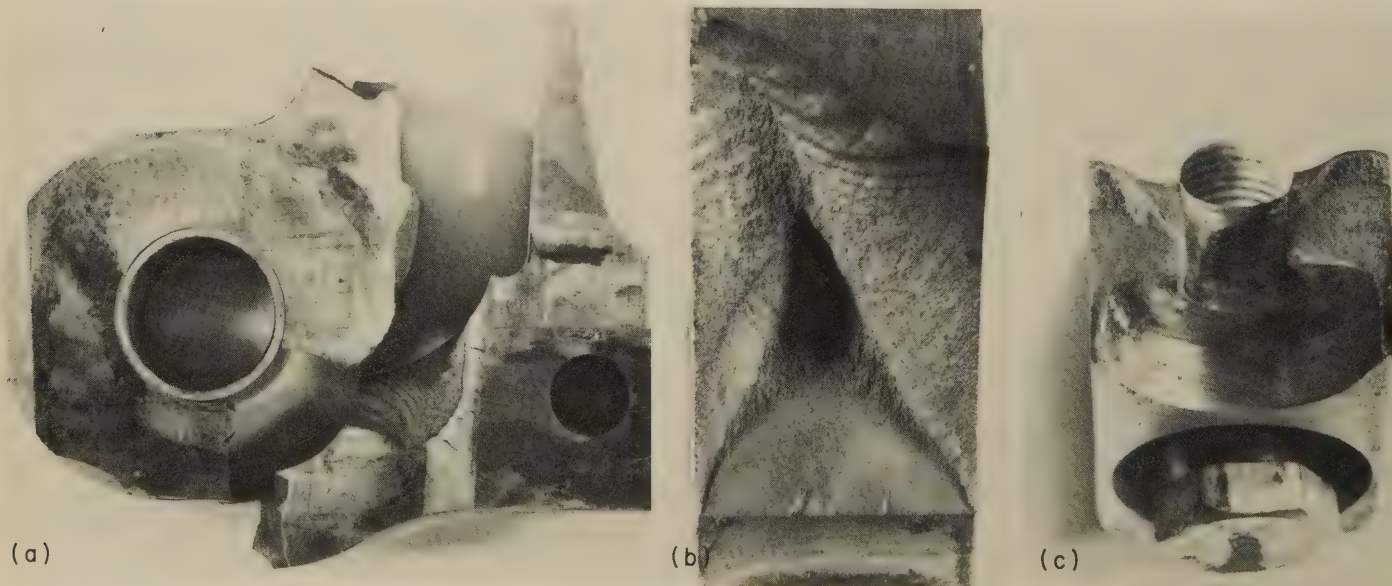


Fig. 36. Fracture of main spar (a) of aircraft wing (see Fig. 34) in programmed-loading fatigue test, showing the various crack segments. (b) Crack depth versus number of applied load blocks for segment W of the fracture surface. (Example 13)



Light fractographs

Fig. 37. Fracture surfaces of a 4340 steel finger from a main-wing transport joint that fractured in a full-scale programmed aircraft fatigue test (see also Fig. 38). (a) A fractured finger. (b) Surface of the major critical crack. (c) Surface of a less-critical crack in the vertical member. (Example 14)

1.5× (a); 1.6× (b); 1.7× (c)

tence of such a crack should be detectable shortly after 20,000 to 25,000 flying hours, long before it could reach any unstable rate of growth. The fracture of segments V and W conformed to the same time relationships. Figure 36(b) illustrates how determination of crack-growth rate based on fatigue-band counts, which indicate the number of applied load blocks, can be used to predict the number of flying hours that a spar can be used before a crack may become unstable, and to offer assurance that properly timed inspections will detect such cracks soon enough to avoid fractures in service.

Example 14. Determination of Crack-Growth Rate for 4340 Steel Fingers for an Aircraft-Wing Transport Joint (Fig. 37 and 38)

Measurements of crack-growth rate were made on two fingers (one of which is shown in Fig. 37a) from a main-wing transport joint that had fractured during a full-scale programmed aircraft fatigue test. The fingers were made of 4340 steel heat treated to a tensile strength of 1350 MPa (196 ksi) and a hardness of Rockwell C 41 (microstructure was tempered martensite). The crack-growth histories, as derived from band counts on

two of the fracture surfaces, shown in Fig. 37(b) and (c), are given graphically in Fig. 38(a) and (b), respectively.

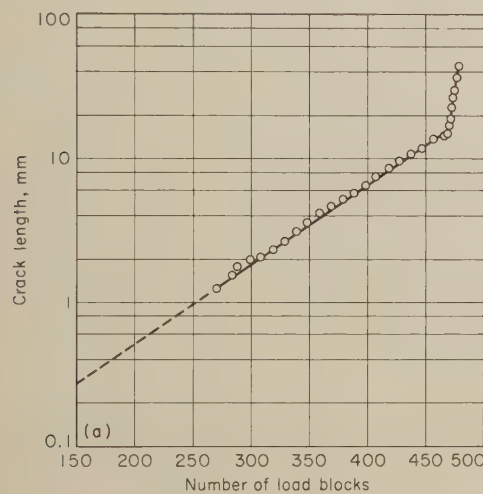
A total of 483 load blocks were applied during the test. The line count was started from the final-block band, working back to the crack origin. In this way, it was possible to identify each band by block number. Over the initial portions of the crack, where the finely spaced bands were too poorly defined to permit them to be counted, the curves relating the number of load blocks to crack length were extrapolated to provide the following information:

- 1 The critical cracks in both fingers, running from the bottom of the U between the two vertical members of the fingers to the large bolthole, appeared to have been initiated at approximately the same time. It was estimated that the crack in each finger was about 0.3 mm in depth when 150 load blocks had been applied, and that the crack-growth rates were similar during the first 10 mm of penetration depth.
- 2 The less-serious crack in each of the vertical members of the fingers (Fig. 37c) grew at a much greater initial rate—a

6.5-mm crack depth in the vertical members, compared to the penetration of 0.3 mm by the critical cracks after 150 load blocks.

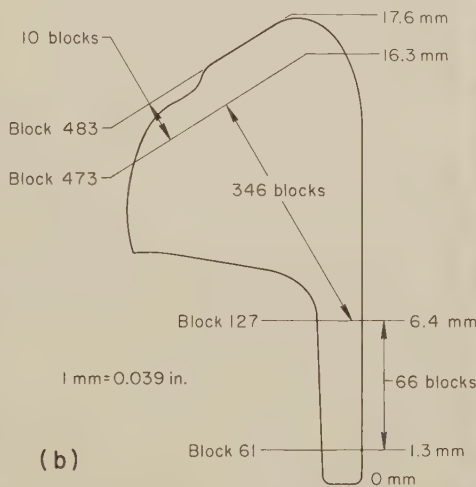
- 3 Final, fast fracture of the sections remaining at the ends of all four cracks occurred simultaneously. This was demonstrated by the presence of four extra-wide block bands on all four fracture surfaces, corresponding to blocks 440 to 443. (The four bands of the fracture shown in Fig. 38c were formed by loading-system perturbations during the course of these four load blocks.) In all four cracks, fast fracture occurred at a count of 40 bands after the fourth extra-wide band previously identified as band 443.

On the basis that a load block was equivalent to 50 flying hours, the derived quantitative fractographic information suggested that the onset of cracking in the critical region of the steel fingers would probably have occurred prior to the completion of 7500 hours of aircraft operation. Because the growth of the critical cracks could not be monitored without removal of the wings from the aircraft, the crack in the vertical member, which *could* be observed, served as an in-



(a) Crack length versus the number of applied load blocks for the major critical fatigue crack in the finger (the surface of this crack is shown in Fig. 37b).

(b) Sketch that relates fatigue-crack growth to the number of applied load blocks on the surface of a less-critical crack in the vertical member (surface



(b)

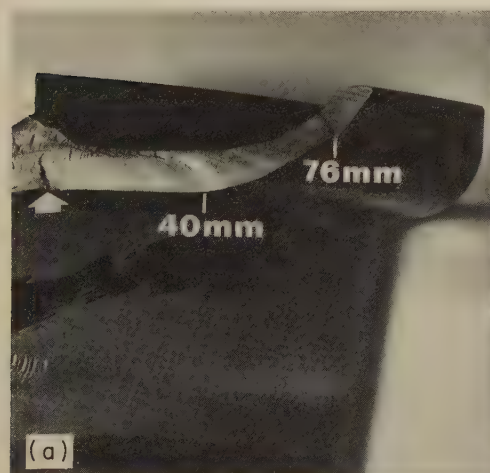


(c)

at upper right in Fig. 37c). The outline shows the shape of the fracture surface.

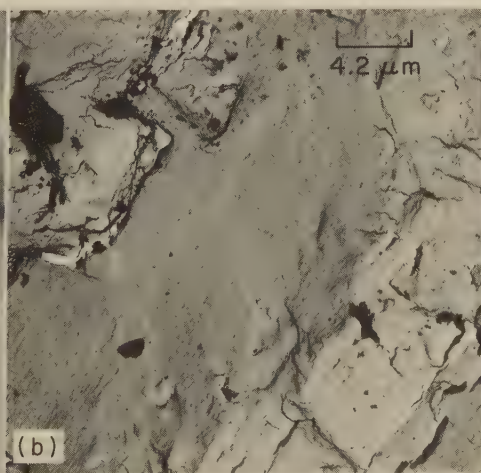
(c) Transmitted-light fractograph, at 14 \times , through a plastic replica of the fracture surface, showing four extra-wide bands (between arrows) corresponding to load blocks 440 to 443 on the fracture surface.

Fig. 38. Analysis of fatigue-crack-growth rate for the 4340 steel finger in Fig. 37 (Example 14)

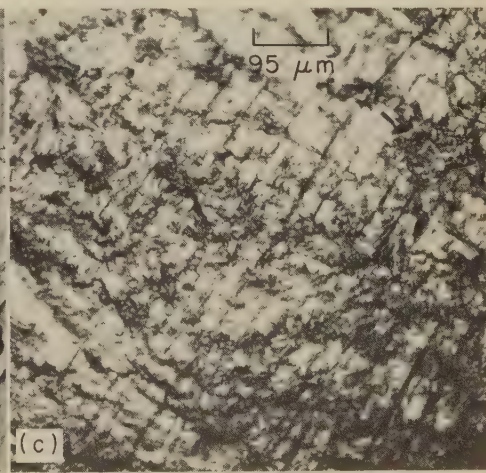


Light fractograph

(a) Fracture surface showing macroscopic bands of fatigue-crack growth. The location of the crack origin is indicated by the arrow. The growth of the fatigue crack was symmetrical in both directions from the origin; 76 mm therefore equals the half-crack length.



0.5 \times TEM fractograph (p-c replica)



2400 \times Transmitted-light fractograph

105 \times

(b) A TEM fractograph of fine fatigue striations in crack-growth bands.
(c) Microscopic fatigue-crack-growth bands corresponding to the bands shown in fractograph (a). This transmitted-light fractograph was made through a plastic replica of the fracture surface.

Fig. 39. Fatigue crack that formed in service in a forged aluminum alloy 2014-T6 aircraft wheel. See also Fig. 40. (Example 15)

indicator crack. The greater initial growth rate of the indicator crack facilitated the estimation of the time of crack initiation in the critical regions. Periodic monitoring of the length of the indicator cracks was of considerable value in the scheduling of ultrasonic crack-detection procedures in the critical regions of the steel fingers.

Example 15. Determination of Fatigue-Crack-Growth Rates for Aluminum Alloy 2014-T6 Aircraft Wheels (Fig. 39 and 40)

The lines observed on the fracture surfaces of fractured aircraft wheels made of aluminum alloy 2014-T6 have been correlated with crack growth during aircraft landing cycles (Ref 6). A landing cycle of a typical jet transport aircraft is probably best thought of as the total of roll miles and maneuvers of the aircraft on the ground, from time of engine start at a terminal ramp to engine shutdown at the succeeding ramp.

In interpreting service fractures, assumptions must be made concerning the significance of macroscopic crack-growth lines. Such assumptions appear to be justified in the study of the fractured aircraft wheels, where the fairly regular spacings of the majority of the marks within long crack segments strongly suggested repeated loading sequences appropriate to aircraft landing cycles.

Information on rate of fatigue-crack growth was gathered from the fracture surface of a wheel over a distance of 76 mm from the crack origin (Fig. 39a). The fracture-surface topography, illustrated in Fig. 39(b) (a TEM fractograph), shows bands containing areas of fine striations that, on the basis of a sampling of macroscopic band-spacing measurements, are believed to correspond to the macroscopic crack-growth lines shown in Fig. 39(c), a transmitted-light fractograph.

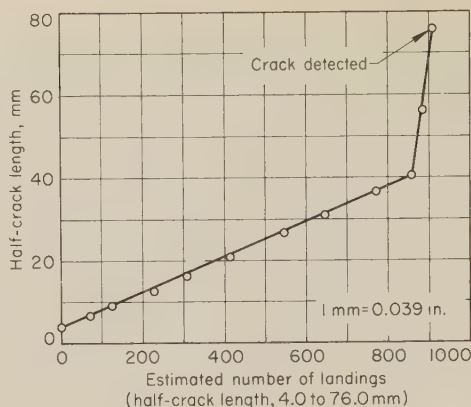


Fig. 40. Fatigue-crack length vs estimated number of landings (after crack initiation) for the fractured alloy 2014-T6 aircraft wheel in Fig. 39 (Example 15)

The graph in Fig. 40 accounts for 903 bands over the half-crack length from 4 to 76 mm. (The total number of landings, including those prior to crack initiation, was far greater than 903.) The crack exhibited an approximately constant growth rate of some 47 microns per band over the interval from 4 to 40 mm of crack length. Over the interval from 40 to 76 mm, the crack-growth rate exhibited an abrupt increase to about 650 microns per band. This latter interval corresponded to a clearly defined change in fracture-surface topography (Fig. 39a) with a definitely coarser texture than the initial 40 mm of crack growth.

The derivation of information in this manner, from several types of aircraft wheels, has facilitated the revision of nondestructive-inspection schedules, for the purpose of

preventing disintegration of the wheels in service. It was decided to schedule a complete nondestructive inspection of all aircraft wheels after completion of 125 to 150 landings, which corresponds to the schedule of wheel removals for change of tires. (The length of service at which such inspections were to begin varied with the type of aircraft.) The fractographic measurements of crack-growth rate predicted that any crack that originated in a wheel following one of these inspections would not reach a critical size until after the next inspection was scheduled to be made, and therefore that the crack would be detected and the wheel would be removed from service.

References

1. J. A. Feeney, J. C. McMillan and R. P. Wei, Environmental Fatigue Crack Propagation of Aluminum Alloys at Low Stress Intensity Levels, *Met Trans*, Vol 1, June 1970, p 1741
2. H. C. Burghard, Jr., Metallurgical Analysis of Cracking in Compressor Discs of the T53-L13 Gas Turbine, *Proc 8th Symp Nondestr Eval Aerosp Weapons Syst Nucl Appl*, Western Periodicals, Inc., North Hollywood, Calif., 1971, p 299-310
3. J. C. McMillan and R. W. Hertzberg, Application of Electron Fractography to Fatigue Studies, in "Electron Fractography", ASTM STP 436, American Society for Testing and Materials, Philadelphia, 1968, p 89-123
4. B. V. Whiteson, A. Phillips, V. Kerlins and R. A. Rowe, Special Fractographic Techniques for Failure Analysis, in "Electron Fractography", ASTM STP 436, American Society for Testing and Materials, Philadelphia, 1968, p 151-178
5. W. Wiebe, "Quantitative Fatigue Crack Propagation Analysis by Means of Electron Fractography", NRC NAE LR-450, National Research Council of Canada, National Aeronautical Establishment, Ottawa, Ont., Canada, Mar 1966, 33 pages
6. W. Wiebe, "A Fractographic Study of the Fatigue Failure of Aircraft Wheels", NRC NAE LR-541, National Research Council of Canada, National Aeronautical Establishment, Ottawa, Ont., Canada, Nov 1970, 26 pages

ATLAS OF FRACTOGRAPHS

Prepared by John A. Fellows

CONTENTS

Introduction	125
Light-Microscope Fractographs at Low Magnification	129
Light-Microscope Fractographs at High Magnification	139
Scanning-Electron-Microscope (SEM) Fractographs	161
Comparison of SEM and TEM Stereofractographs	281
Transmission-Electron-Microscope (TEM) Fractographs From Replicas	297
Failure-Analysis Fractographs	377

Introduction

By JOHN A. FELLOWS

AN EARLY PLAN for the make-up of Volume 7 of the Eighth Edition of METALS HANDBOOK was a threefold coverage to include an atlas of microstructures, a treatment of metallography and alloy phase diagrams, and an atlas of fractographs. However, as work proceeded and material became progressively available, it became evident that this format would be entirely too unwieldy, and ultimately it became desirable to issue each section as a separate volume. Part of the expansion of material originally intended for Volume 7 stemmed from the decision to introduce the Atlas of Fractographs with a group of committee-generated articles designed to: (a) describe and illustrate fractographic techniques; (b) identify and interpret the features of fracture surfaces revealed at high magnification, particularly by electron microscopy; and (c) enumerate benefits that fractography can provide in both failure analysis and basic research in fracture mechanisms.

Objective

The objective in preparing this Atlas has been to provide the reader with a compilation of fractographs that are useful in trying to understand the causes, surface features, and mechanisms of fracture of industrial alloys. It thus follows a close parallel to the Atlas of Microstructures (Volume 7) and is intimately related to both Volumes 7 and 8 in the numbering system chosen for the micrographs and fractographs of the three volumes. These run consecutively with numbers 1 to 2821 appearing in Volume 7, numbers 2822 to 3417 in Volume 8, and numbers 3418 to 5233 in Volume 9. This unbroken series was chosen to permit simple reference without possible confusion; each number occurs once and one

time only. This series, however, does not apply to the illustrations contained in the articles preceding the Atlas in this volume—those illustrations have been identified by a separate series of figure numbers within each article.

Organization and Presentation

As the Contents List above indicates, the Atlas contains six sections. The first two are historical in nature, consisting of examples of the original work in fractography of Carl A. Zapffe, prepared by light microscopy. The third section is devoted mainly to scanning-electron-microscope (SEM) fractographs, while the fifth section offers a counterpart of fractographs prepared from replicas with the transmission electron microscope (TEM). Section four presents a comparison of SEM and TEM techniques provided by stereo-pair fractographs of identical fields of view. When these stereofractographs are viewed in 3-D (attention is called to the suggestions for stereo viewing on pages 281 to 282, and to the stereo viewer in the envelope on the inside of the back cover), they make possible point-by-point comparisons of similar surface contours revealed by the two methods. The sixth and final section is made up largely of fractographs prepared by any of the three procedures (light microscopy, SEM and TEM) from fractures in service. A majority of these were processed as part of the analyses of the causes of these fractures.

The arrangement of the fractographs within each section is by alloy grade, following an order similar to that used in Volume 7, which in turn was patterned after the organization of Volume 1, "Properties and Selection of Metals". In general, this order conforms to the following: (a) iron; (b) carbon steels;

(c) low-alloy steels; (d) cast irons; (e) tool steels; (f) stainless steels and heat-resisting alloys; (g) refractory alloys; (h) nonferrous alloys. This is intended to promote ease of use of Volume 1 in connection with this Atlas in relating properties and applications of metals to fracture behavior and characteristics.

The initial page of each section carries a list of the alloys contained in the section and the pages on which their fractographs appear. This is supplemented by a running head in boldface type at the top of each page identifying the alloys represented in the fractographs on the page and (space permitting) citing the mechanism of fracture for each alloy. With each fractograph or group of related fractographs is a caption naming the alloy grade or chemical composition of the specimen, what is known of its history of fabrication and heat treatment and of its properties, and a brief review of the fracture-surface features displayed, the mechanism of fracture, and the cause where possible. In general, property and temperature values are quoted in metric units with the English equivalents noted in parentheses.

Wherever possible, the fractographs display the appearance of the fracture surface first at low magnification and then show the details visible at higher magnification by either light microscopy, SEM or TEM. When appropriate, photographs of the part, macrographs of important sections, and photomicrographs of the metallic structure have been included to make it easier to understand the fracture. The etchant used with each micrograph is noted below the picture. (Etchants are identified as to common name, ASTM number, and composition on pages 341 and 342 in Volume 7 of this Handbook; information on preparation,

handling and use of etchants is presented in Volume 8, on pages 34 to 36 and in the articles on Metallographic Techniques.)

Distribution of Content

The total numbers of each type of illustration devoted to each of an arbitrary series of alloy categories are enumerated in Table 1. Table 2 summarizes the number of fractures from various causes represented in the Atlas, both as broken parts and broken test specimens. These have not been differentiated in citing the causes of fracture. As might be antici-

pated, fatigue fractures represent the most common cause, amounting to approximately a third of the total.

Acknowledgments

On the opposite page is a citation in alphabetical order of the contributors to the Atlas who made this compilation possible and to whom the Society and staff owe especial thanks. Unlisted but equally deserving of mention are the even more numerous individuals who contributed anonymously through their participation in the preparation and interpretation of

fractographs, or who made such contributions possible by executive approval of the laboratory program that generated them. More explicit acknowledgments are also made on page 128 through the listing of references to journals and reports in which specific fractographs in the Atlas have previously been published. Special acknowledgment and sincere thanks are due Prof. Lynn J. Ebert of the Division of Metallurgy and Materials Science, Case Western Reserve University, who voluntarily and painstakingly reviewed and constructively criticized the captions for the 1816 illustrations in the Atlas.

Table 1. Distribution of Content of This Atlas as to Types of Illustrations for Various Alloy Categories

Alloy category	Types of atlas illustrations						Total illustrations
	Photo-graphs	Macro-graphs	Micro-graphs	Light fracto-graphs	SEM fracto-graphs	TEM fracto-graphs	
Irons	2	..	6	16	29	12	65
Low-carbon steels	5	5	10	16	25	7	68
Medium-carbon steels	16	9	4	60	12	..	101
High-carbon steels	9	..	2	23	19	1	54
Low-carbon alloy steels	3	1	..	3	13	6	26
Medium-carbon alloy steels	25	2	17	121	92	82	339
High-carbon alloy steels	2	..	3	7	11	2	25
Case-hardened steels	9	12	1	3	25
Tool steels	30	20	10	60
Precipitation-hardening and martensitic stainless steels	3	..	6	49	40	49	147
Austenitic stainless steels	1	..	2	13	14	15	45
Nickel-base alloys	1	1	1	28	50	68	149
Cobalt-base alloys	3	..	15	18
Miscellaneous iron-base alloys(a)	3	..	7	35	6	7	58
Aluminum alloys	33	5	21	64	127	93	343
Composites	13	..	13
Copper alloys	4	..	6	10	24	15	59
Titanium alloys	3	1	3	22	40	61	130
Miscellaneous nonferrous alloys(b)	2	..	5	38	36	10	91
Total	121	24	93	550	572	456	1816

(a) Miscellaneous iron-base alloys include: ferritic iron-chromium alloys, ferritic iron-silicon alloys, cast irons, and magnetic alloys. (b) Miscellaneous nonferrous alloys include: antimony alloys, bismuth alloys, columbium alloys, iridium, lead solders, magnesium alloys, molybdenum alloys, tantalum alloys, zinc alloys, and zirconium alloys.

Table 2. Causes of Fractures Illustrated in This Atlas for Various Alloy Categories

Alloy category	Sources of fracture		Causes of fractures illustrated in atlas						Total
	Parts	Test specimens	Fa-tigue	Im-pact	Tension over-load	Miscel-laneous(a)	Bend-ing	Stress-corrosion cracking	
Irons	2	41	2	28	5	2	6	..	43
Low-carbon steels	12	26	9	16	12	1	38
Medium-carbon steels	50	7	36	8	8	2	3	..	57
High-carbon steels	22	11	21	10	..	1	..	1	33
Low-carbon alloy steels	2	12	3	5	3	1	2	..	14
Medium-carbon alloy steels	66	90	47	19	43	22	15	10	156
High-carbon alloy steels	10	10	11	9	20
Case-hardened steels	23	..	19	2	..	1	1	..	23
Tool steels	5	30	16	6	8	3	..	2	35
PH and martensitic stainless steels	6	51	12	15	13	7	6	4	57
Austenitic stainless steels	7	15	10	..	4	5	3	..	22
Nickel-base alloys	2	47	19	2	11	13	4	..	49
Cobalt-base alloys	3	1	..	2	3
Miscellaneous iron-base alloys(b)	11	25	7	23	4	1	1	..	36
Aluminum alloys	39	64	39	9	21	14	5	15	103
Composites	8	7	1	8
Copper alloys	14	19	7	..	8	7	5	6	33
Titanium alloys	1	51	13	4	13	4	11	7	52
Miscellaneous nonferrous alloys(c)	1	61	4	37	15	2	4	..	62
Total	273	571	276	193	177	87	66	45	844

(a) Miscellaneous causes of fracture include: corrosion fatigue, shear overload, torsion overload, stress-rupture, sustained load, thermal shock, and hydrogen embrittlement. (b) Miscellaneous iron-base alloys include: ferritic iron-chromium alloys, ferritic iron-silicon

alloys, cast irons, and magnetic alloys. (c) Miscellaneous nonferrous alloys include: antimony alloys, bismuth alloys, columbium alloys, iridium, lead solders, magnesium alloys, molybdenum alloys, tantalum alloys, zinc alloys, and zirconium alloys.

Contributors of Illustrations in the Atlas of Fractographs

DAVID B. BALLARD, Metallurgist, Metallurgy Div., National Bureau of Standards; R. D. BARER, Section Head, Materials Engineering, Defence Research Establishment Pacific, Canada; CEDRIC D. BEACHEM, Research Metallurgist, Metallurgy Div., Naval Research Laboratory; ROY E. BEAL, Assistant Director, Metals Research Div., IIT Research Institute; STEVEN J. BERMAN, Graduate Student, Dept. of Metallurgy and Materials Science, Massachusetts Institute of Technology.

M. DILIP BHANDARKAR, Graduate Student, Lawrence Berkeley Laboratory, University of California; A. S. BRAR, Senior Scientist, Normandale Div., Control Data Corp.; EDWARD V. BRAVENEC, Senior Metallurgist, Armco Steel Corp.; FRANK L. CARR, Materials Engineer, Army Materials and Mechanics Research Center, Dept. of the Army; ROBERT A. CLARK, Graduate Student, Dept. of Materials Science and Engineering, University of California, Berkeley.

THOMAS J. CONNARE, Manager, Metallurgical Engineering, Standard Steel Div., Titanium Metals Corp. of America; J. F. COTTON (retired), formerly Research and Development Specialist, Lockheed-Georgia Co.; EUGENE DICESARE, Mechanical Engineer, Army Materials and Mechanics Research Center, Dept. of the Army; DWIGHT R. DIERCKS, Assistant Metallurgist, Materials Science Div., Argonne National Laboratory.

D. J. DUQUETTE, Professor, Materials Div., Rensselaer Polytechnic Institute; NICHOLAS FIORE, Professor, Metallurgical Engineering and Materials Science, University of Notre Dame; M. C. FLEMINGS, Professor, Dept. of Metallurgy and Materials Science, Massachusetts Institute of Technology.

STEPHEN FLOREEN, Research Fellow, Paul D. Merica Research Laboratory, International Nickel Co., Inc.; JOHN H. FROME, JR., Metallurgist, W. B. Coleman Co.; R. P. GAMBLE, Graduate Student, Dept. of Geology and Geophysics, Yale University; WILLIAM E. GARDNER, Laboratory Director, Technology of Materials (formerly Sloan Research Industries, Inc.); M. GELL, Research Supervisor, Materials Engineering and Research Laboratory, Pratt & Whitney Aircraft Div., United Aircraft Corp.

W. W. GERBERICH, Graduate Student, Lawrence Berkeley Laboratory, University of California; RONALD GIBALA, Associate Professor, Dept. of Metallurgy and Materials Science, Case Western Reserve University; WILLIAM A. GOERING, Supervisor, Materials and Fasteners Engineering Dept., Product Development Group, Ford Motor Co.; R. A. GRANGE, Staff Scientist, Research Laboratory, U. S. Steel Corp.; MARY ELLEN GULDEN, Senior Research Engineer, Solar Div., International Harvester Co.

HENRY T. HADLEY, Supervisor—Welding, Metallurgy and Materials Engineering, Pacific Car and Foundry Co.; E. G. HAMBURG, formerly Senior Research Engineer, Research Laboratory, U. S. Steel Corp.; P. L. HEMMINGS, Graduate Student, Lawrence Berkeley Laboratory, University of California; WILLIAM L. HOLSHOUSER (retired), formerly Chief, Laboratory Services Staff, Bureau of Aviation Safety, National Transportation Safety Board.

W. A. HORWOOD, Graduate Student, Lawrence Berkeley Laboratory, University of California; MICHAEL HOVAN, Graduate Student, Dept. of Metallurgy and Materials Science, Massachusetts Institute of Technology; JAMES LEE HUBBARD, Research Scientist, Engineering Experiment Station, Georgia Institute of Technology; ABRAHAM HURLICH, Manager of Materials Technology, Convair Aerospace Div., General Dynamics Corp.

FRANK L. JAMIESON, Supervising Metallurgist, Metallurgical Laboratory, Steel Company of Canada, Ltd.; OM JOHARI, Manager, Metal Physics, Metals Div., IIT Research Institute; R. H. JONES, Graduate Student, Lawrence Berkeley Laboratory, University of California; YOSHIKAKI KANAI, Senior Research Engineer, Technical Research Laboratory, Mitsubishi Steel Manufacturing Co., Ltd.; W. A. KEEGAN, Assistant Materials Project Engineer, Materials Engineering and Research Laboratory, Pratt & Whitney Aircraft Div., United Aircraft Corp.; G. J. W. KOR, Senior Scientist, Research Laboratory, U. S. Steel Corp.

VICTOR A. KORTESJOJA, Chief Metallurgist, Metal Stamping Div., Ford Motor Co.; K. G. KREIDER, formerly Materials Supervisor, United Aircraft Research Laboratories, United Aircraft Corp.; R. F. LACROIX, Assistant Materials Project Engineer, Materials Engineering and Research Laboratory, Pratt & Whitney Aircraft Div., United Aircraft Corp.; W. T. LANKFORD, JR., Manager, Steel Processing, Research Laboratory, U. S. Steel Corp.; E. A. LAUCHNER, Senior Metallurgist, Materials Engineering, Aircraft Div., Northrop Corp.

D. LEE, Metallurgist, Metallurgy and Ceramics Laboratory, Research and Development Center, General Electric Co.; D. F. LENTZ, Research Metallurgist, Armco Steel Corp.; W. BARRY LISAGOR, Materials Research Engineer, NASA Langley Research Center; RONALD J. LIVAK, Production Control Engineer, Precision Founders, Inc.

STEVEN MATTHEWS, Research Engineer, Stellite Div., Cabot Corp.; D. A. MEYN, Research Metallurgist, Naval Research Laboratory; L. E. MURR, Professor and Head, Dept. of Metallurgical and Materials Engineering, New Mexico Institute of Mining and Technology; JOHN B. NASLANIC, Principal Engineer, Materials Laboratory Dept., Ford Motor Co.; HOWARD G. NELSON, Research Scientist, Ames Research Center—NASA.

F. E. ORGAN, formerly Research Metallurgist, Pratt & Whitney Aircraft Div., United Aircraft Corp.; E. R. PARKER, Professor of Metallurgy, Lawrence Berkeley Laboratory, University of California; ELIO PASSAGLIA, Chief, Metallurgy Div., National Bureau of Standards; REGIS M. PELLOUX, Associate Professor, Dept. of Metallurgy and Materials Science, Massachusetts Institute of Technology.

AUSTIN PHILLIPS, Research Engineer, McDonnell Douglas Astronautics Co.; ANDRÉ PINEAU, Research Scientist, Centre des Matériaux, École des Mines de Paris; K. M. PREWO, Research Metallurgist, United Aircraft Research Laboratories, United Aircraft Corp.; G. RAI, Graduate Student, Dept. of Metallurgy and Materials Science, Massachusetts Institute of Technology; G. A. RATZ, Senior Research Engineer, Research Laboratory, U. S. Steel Corp.; STEPHEN L. SCHEIER, Metallurgical Consultant.

ROBERT E. SHAFFER, Associate Professor of Engineering, Mechanical Engineering Dept., State University of New York at Buffalo; R. PATRICK SKOW, Plant Metallurgist, B. F. Goodrich Engineered Systems Co.; ROBERT D. SLOAN (retired), formerly President, Sloan Research Industries, Inc.; W. H. STEINMAN, Technical Director, Niagara Wire Weaving Co., Ltd.; R. E. STOLTZ, Graduate Student, Dept. of Metallurgy and Materials Science, Massachusetts Institute of Technology; LEONARD SUDENFIELD, Engineering Assistant, Dept. of Metallurgy and Materials Science, Massachusetts Institute of Technology; E. G. TAKACS, Research Engineer, Advanced Materials Div., Armco Steel Corp.

GARETH THOMAS, Professor of Metallurgy, Dept. of Materials Science and Engineering, University of California, Berkeley; J. K. TIEN, Associate Professor, Henry Krumb School of Mines, Columbia University; T. TOM, Graduate Student, Lawrence Berkeley Laboratory, University of California; E. T. TURKDOGAN, Manager, Chemical Metallurgy, Research Laboratory, U. S. Steel Corp.; PAUL J. VALDEZ, Chief Metallurgist, Solar Div., International Harvester Co.; J. VAN DEN AVYLE, Graduate Student, Dept. of Metallurgy and Materials Science, Massachusetts Institute of Technology.

L. F. VAN SWAM, Graduate Student, Dept. of Metallurgy and Materials Science, Massachusetts Institute of Technology; JOSEPH M. WALSH, Assistant Materials Project Engineer, Materials Engineering and Research Laboratory, Pratt & Whitney Aircraft Div., United Aircraft Corp.; J. L. WELKER, Senior Product Engineer, Truck Engineering Center, International Harvester Co.; ROBERT W. WHITE, Senior Engineering Specialist, Vought Systems Div., LTV Aerospace Corp.

BENNETT V. WHITESON, Project Materials and Process Engineer, McDonnell Douglas Astronautics Co.; W. E. WOOD, Graduate Student, Lawrence Berkeley Laboratory, University of California; DONALD J. WULPI, Head, Engineering Metallurgy Laboratory, International Harvester Co.; V. F. ZACKAY, Professor of Metallurgy, Lawrence Berkeley Laboratory, University of California; CARL A. ZAPFFE, Consulting Metallurgist.

Reference Sources of Contributors to the Atlas of Fractographs

Many contributors who provided fractographs for this Atlas did so by making available prints of fractographs that had been included in earlier publications. These contributors are included as authors in the following list of references that cites the journals or papers in which the fractographs appeared. The identity of these pictures in this Atlas is given by the bracketed boldface numerals that appear at the end of each reference citation.

- M. A. Arkoosh and N. F. Fiore, Elevated Temperature Ductility Minimum in Hastelloy X, *Met Trans*, Vol 3, Aug 1972, p 2235-2240. [3902-3904]
- C. D. Beachem, Effect of Test Temperature Upon the Topography of Fracture Surfaces of AMS 6434 Sheet Steel Specimens, U. S. Naval Research Laboratory Memorandum Report 1293, Washington, D.C., Mar 1962. [4297-4299]
- C. D. Beachem, Characterizing Fractures by Electron Fractography, Part IV—The Slow Growth and Rapid Propagation of a Crack Through a Notched Type 410 Stainless Steel Wire Specimen, U. S. Naval Research Laboratory Memorandum Report 1297, Washington, D.C., Apr 1962. [4428-4432]
- C. D. Beachem, Fracture Analysis of a C-141 Landing Gear Cylinder, U. S. Naval Research Laboratory Memorandum Report 1524, Washington, D. C., Apr 1964. [4351-4355]
- C. D. Beachem and D. A. Meyn, Illustrated Glossary of Fractographic Terms; Section 2: Glide Plane Decohesion, Serpentine Glide, Ripples, Stretching, Microvoid Coalescence, U. S. Naval Research Laboratory Memorandum Report 1547, Washington, D. C., June 1964. [4318-4320]
- C. D. Beachem, Electron Microscope Fracture Examination to Characterize and Identify Modes of Fracture, U. S. Naval Research Laboratory Report 6293, Washington, D. C., Sept 28, 1965. [4396-4401, 4727, 4728, 4733-4736, 4774-4776]
- C. D. Beachem, Microscopic Fracture Processes, p 244-347 and p 320 in "Fracture: An Advanced Treatise", Vol I (edited by H. Liebowitz), Academic Press, Inc., New York and London, 1968. [4307, 4401, 4787-4789, 4990-4992, 5147, 5152, 5187, 5217, 5221]
- R. E. Beal, Soldered Joint Properties at Radiator Operating Temperatures, Copper Development Assn., Inc., Technical Report, New York, N. Y., Feb 1971. [4151-4157, 4161-4165]
- R. E. Beal, How Soldering Process Variables Affect Joint Strength, Copper Development Assn., Inc., Technical Report, New York, N. Y., Aug 1969. [4149, 4150, 4158-4160]
- W. E. Brower, Jr., and S. N. Singh, Microcracks Associated With Inclusions in As-Cast Iron and Their Role During Fracture, *Met Trans*, Vol 3, Nov 1972, p 3025-3031. [3564-3568]
- J. J. Carden, T. R. Croucher, E. A. Lauchner and R. L. Terchek, Employing the Scientific Approach to Metallurgical Failure Analysis (published as Making Failure Analysis Foolproof, in *Iron Age*, Vol 202, No. 25, Dec 19, 1968, p 58-60). [4673-4684]
- E. P. Dahlberg, An Electron Microscope Study of Crack Surfaces in a Tungsten Rocket Nozzle Insert, U. S. Naval Research Laboratory Memorandum Report 1217, Washington, D. C., Sept 1961. [4781-4784]
- D. J. Duquette and M. Gell, The Effects of Environment on the Elevated Temperature Fatigue Behavior of Nickel-Base Superalloy Single Crystals, *Met Trans*, Vol 3, July 1972, p 1899-1905. [3934-3938]
- A. J. Edwards, C. D. Beachem and E. P. Dahlberg, Fractography With the Electron Microscope, Part XIV, Wrought Iron, U. S. Naval Research Laboratory Memorandum Report 1454, Washington, D. C., Sept 1963. [4280-4287]
- S. Floreen, H. W. Hayden and T. M. Devine, Cleavage Initiation in Fe-Ni Alloys, *Met Trans*, Vol 2, May 1971, p 1403-1406. [3763-3768]
- R. A. Grange, The Rapid Heat Treatment of Steel, *Met Trans*, Vol 2, Jan 1971, p 65-78. [3736-3738]
- W. L. Holshouser, Metallurgical Report No. 65-9, Civil Aeronautics Board, Washington, D. C., Mar 15, 1965. [5019-5024]
- W. L. Holshouser, Metallurgical Report No. 66-1, Civil Aeronautics Board, Washington, D. C., Aug 3, 1965. [5206-5213]
- W. L. Holshouser, Metallurgical Report No. 66-10, Civil Aeronautics Board, Washington, D. C., Oct 26, 1965. [5129-5132]
- W. L. Holshouser, Metallurgical Report No. 66-16, Civil Aeronautics Board, Washington, D. C., Mar 11, 1966. [4934-4938]
- W. L. Holshouser, Metallurgical Report No. 67-21, National Transportation Safety Board, Washington, D. C., May 11, 1967. [5158-5163]
- W. L. Holshouser, Metallurgical Report No. 67-23, National Transportation Safety Board, Washington, D. C., June 9, 1967. [4926-4928]
- W. L. Holshouser, Metallurgist's Factual Report No. 68-20, National Transportation Safety Board, Washington, D. C., Dec 11, 1967. [5141-5146]
- W. L. Holshouser, Metallurgical Laboratory Report No. 70-17, National Transportation Safety Board, Washington, D. C., Feb 25, 1970. [5167-5169]
- W. L. Holshouser, Metallurgical Laboratory Report No. 70-27, National Transportation Safety Board, Washington, D. C., June 4, 1970. [5083-5087]
- W. L. Holshouser, Metallurgical Laboratory Report No. 71-13, National Transportation Safety Board, Washington, D. C., Jan 20, 1971. [5050-5055]
- W. L. Holshouser, Metallurgical Laboratory Report No. 71-31, National Transportation Safety Board, Washington, D. C., June 30, 1971. [5170-5177]
- W. A. Horwood, M.S. Thesis LBL-1121, University of California, Berkeley, Dec 1972. [3773-3784]
- O. Johari, Comparison of Transmission Electron Microscopy and Scanning Electron Microscopy of Fracture Surfaces, *J Metals*, June 1968, p 26-32. [3899, 3900, 4208, 4209]
- R. H. Jones, E. R. Parker and V. F. Zackay, Use of an Allotropic Phase Change to Enhance Ductility in Fe-Ta Alloys, p 829-848 in "Electron Microscopy and Structure of Materials", G. Thomas (Ed.), University of California Press, Berkeley, 1972. [3832, 3833]
- R. W. Judy, Jr., T. W. Crooker, R. E. Morey, E. A. Lange and R. J. Goode, Fractographic Analysis of Ti-7Al-2Cu-1Ta and Ti-6Al-4V Fractures Developed in "Wet" Fatigue, U. S. Naval Research Laboratory Report 6330, Washington, D. C., Jan 14, 1966. [4762-4769]
- G. J. W. Kor and E. T. Turkdogan, Sulfides and Oxides in Fe-Mn Alloys: Part III. Formation of Oxy-sulfides during Freezing of Steel, *Met Trans*, Vol 3, May 1972, p 1269-1278. [3574-3578]
- W. T. Lankford, Jr., Some Considerations of Strength and Ductility in the Continuous Casting Process, *Met Trans*, Vol 3, June 1972, p 1331-1357. [3590-3599]
- F. R. Larson and F. L. Carr, How Failures Occur—Topography of Fracture Surfaces, *Metal Progress*, Feb 1964, p 77. [4999-5002]
- D. Lee, The Role of Plastic Anisotropy in the Fatigue Behavior of Zircalloy, *Met Trans*, Vol 3, Jan 1972, p 315-332. [4210-4212]
- M. L. Marx, Metallurgical Laboratory Report No. 71-30, National Transportation Safety Board, Washington, D. C., June 21, 1971. [4929-4931]
- M. L. Marx, Metallurgical Laboratory Report No. 72-5, National Transportation Safety Board, Washington, D. C., Sept 27, 1971. [3947-3950]
- M. L. Marx, Metallurgical Laboratory Report No. 72-10, National Transportation Safety Board, Washington, D. C., Oct 28, 1971. [3976-3984]
- R. D. Mayner, Metallurgical Laboratory Report No. 71-28, National Transportation Safety Board, Washington, D. C., Apr 30, 1971. [5006-5009]
- R. D. Mayner, Metallurgical Laboratory Report No. 72-14, National Transportation Safety Board, Washington, D. C., Dec 28, 1971. [4981-4986]
- R. D. Mayner, Metallurgical Laboratory Report No. 72-15, National Transportation Safety Board, Washington, D. C., Dec 7, 1971. [5010, 5011]
- D. A. Meyn, Observations on Micro-Mechanisms of Fatigue Crack Propagation in 2024 Aluminum, U. S. Naval Research Laboratory Memorandum Report 1707, Washington, D. C., June 1966. [4610-4615]
- D. A. Meyn, C. D. Beachem and E. P. Dahlberg, Fracture Analysis of Two Steel Pieces for the Civil Aeronautics Board, U. S. Naval Research Laboratory Technical Memorandum 6320-51, Washington, D. C., Mar 27, 1967. [4402-4408]
- L. E. Murr and O. T. Inal, Characterizing Materials by Electron Transmission, Scanning Electron, and Field-Ion Microscopy, *Metals Eng Quart*, Aug 1972, p 30. [4146, 4147]
- H. G. Nelson, D. P. Williams and J. S. Stein, Environmental Hydrogen Embrittlement of an α - β Titanium Alloy: Effect of Microstructure, *Met Trans*, Vol 3, Feb 1972, p 469-475. [4173-4177, 4190-4207]
- H. G. Nelson, D. P. Williams and A. S. Tetelman, Embrittlement of a Ferrous Alloy in a Partially Dissociated Hydrogen Environment, *Met Trans*, Vol 2, Apr 1971, p 953-959. [3671-3673]
- F. E. Organ and M. Gell, The Effect of Frequency on the Elevated Temperature Fatigue of a Nickel-Base Superalloy, *Met Trans*, Vol 2, Apr 1971, p 943-952. [3923-3928]
- A. G. Pineau and R. M. Pelloux, Influence of Strain-Induced Martensitic Transformations on Fatigue Crack Growth Rates in Stainless Steels, *Met Trans*, Vol 5, May 1974, p 1103-1112. [3897]
- A. Phillips and V. Kerlins, Analyzing Fracture Characteristics by Electron Microscopy, *Metal Progress*, Vol 95, No. 5, p 81-84, 1969. [4327, 4328, 4347, 4348, 4608, 4609, 4620-4623]
- A. Phillips, V. Kerlins, R. A. Rawe and B. V. Whiteson, Electron Fractography Handbook, Specific Applications of Electron Fractography, Technical Report AFML-TR-64-416, Supplement II, Wright-Patterson Air Force Base, Ohio, Mar 1968. [4272-4274, 4362-4364, 4373-4378, 4509-4546, 4549-4580, 4693-4710, 5018]
- A. Phillips, V. Kerlins and B. V. Whiteson, Electron Fractography Handbook, Technical Report ML-TDR-64-416, Wright-Patterson Air Force Base, Ohio, Jan 31, 1965. [4275, 4276, 4315-4317, 4321-4326, 4341-4346, 4356-4361, 4389-4395, 4409-4411, 4424-4427, 4433-4442, 4455, 4460-4475, 4480-4492, 4547, 4548, 4581-4587, 4616-4619, 4626-4629, 4649-4652, 4657-4660, 4689-4692, 4711-4721, 4729-4732, 4737-4744, 4770-4773, 4777-4780, 5186]
- K. M. Prewo and K. G. Kreider, The Transverse Tensile Properties of Boron Fiber Reinforced Aluminum Matrix Composites, *Met Trans*, Vol 3, Aug 1972, p 2201-2211. [4110-4114]
- A. Rukwied and D. B. Ballard, Scanning Electron Microscope Fractography of Continuously Cast High Purity Copper After High Temperature Creep, *Met Trans*, Vol 3, Nov 1972, p 2999-3008. [4121-4132]
- J. A. Scott, How Electron Fractography Works in Practice, *Metal Progress*, Vol 95, No. 5, p 84-85, 1969. [4329, 4330, 4349, 4350, 4624, 4625]
- S. N. Singh and M. C. Flemings, Influence of Ingot Structure and Processing on Mechanical Properties and Fracture of a High Strength Wrought Aluminum Alloy, *Trans TMS*, Vol 245, Aug 1969, p 1811-1816. [4032-4034]
- R. D. Sloan, "Applications of Modern Research Techniques to Solving Material Problems: A Comparison of Scanning and Transmission Electron Microscopy as Applied to Failure Analysis in Metals", Sloan Research Industries, Inc., Santa Barbara, Calif., undated. [3706-3709, 3744-3751, 3804-3827, 3856-3874, 3911-3922, 4045-4056, 4365-4372, 4412-4423, 4443-4454, 4493-4508, 4633-4648, 4745-4760]
- R. E. Stoltz and R. M. Pelloux, Mechanisms of Corrosion Fatigue Crack Propagation in Al-Zn-Mg Alloys, *Met Trans*, Vol 3, 1972, p 2433. [4088, 4089]
- J. K. Tien and R. P. Gamble, The Room Temperature Fatigue Behavior of Nickel-Base Superalloy Crystals at Ultrasonic Frequency, *Met Trans*, Vol 2, July 1971, p 1933-1938. [3930-3933]
- T. Tom, Doctorate in Engineering Thesis LBL-1856, University of California, Berkeley, Sept 1973. [3843]
- D. P. Williams and H. G. Nelson, Embrittlement of 4130 Steel by Low-Pressure Gaseous Hydrogen, *Met Trans*, Vol 1, Jan 1970, p 63-68. [3666-3670]
- D. P. Williams and H. G. Nelson, Gaseous Hydrogen-Induced Cracking of Ti-5Al-2.5Sn, *Met Trans*, Vol 3, Aug 1972, p 2107-2113. [4170-4172]
- W. E. Wood, E. R. Parker and V. F. Zackay, Report LBL-1474, Lawrence Berkeley Laboratory, University of California, May 1973. [3661, 3664]
- D. J. Wulpi, "How Components Fail", American Society for Metals, Metals Park, Ohio, 1966. [4808, 4811, 4832, 4833, 4836-4841, 4846, 4879, 4881-4886, 4890-4892, 4920, 4923-4925, 4954, 5025-5027, 5029, 5032, 5056, 5057, 5059, 5073-5075, 5077]
- V. F. Zackay, E. R. Parker and D. Bhandarkar, The Structure and Properties of a Non-Carbon Containing BCC Iron Alloy at Room and Elevated Temperatures, to be published in "Rate Processes in Plastic Deformation", American Society for Metals, Metals Park, Ohio, 1974. [3828-3831]

Light-Microscope Fractographs at Low Magnification

Historic examples from Carl A. Zapffe

CONTENTS

Carbon steel drive shaft of a marine tug	130
Carbon steel chassis frame bar; 1075 steel railroad rails	131
Low-carbon steel and low-alloy steel splined shafts	132
4340 steel piston rod and helicopter bolt	132
Steel armor plate (0.30% C, 3.65% Ni, 1.45% Cr)	133
Tool steels A4N and W1	133
Tool steels W2, L6 and S1	134
Tool steels T1 and M3, class 1	135
Stainless steels types 410, 431, 440C, 303(Se), 302B and 309	136
Stainless steel type 302	137
Aluminum alloy 355 cast turbosupercharger impeller	137-138
Aluminum alloy 2024-T4	138
Brass ingot	138

THE FIRST article in this volume has outlined the pioneer role that Carl A. Zapffe played during the period of 1939 to 1955 in the development of modern fractography. Although his most significant contribution was the demonstration of the feasibility of photography of fracture-surface features at high magnification, much of his work was also related to the interpretation of service and quality-control fractures viewed and photographed at magnifications generally less than ten diameters. This first section of the Atlas of Fractographs therefore appropriately presents a selection of such fractographs from his collection. These illustrate the fracture features that he found significant in seeking to identify the cause and location of crack initiation, the directions of crack propagation, and the fracture mechanisms that could be deduced.

The fracture examples in this section fall mainly into three categories:

- 1 Service and/or hot working fractures
- 2 "Nick-and-break" fractures, mainly of tool steel, produced for the purpose of appraising rod and billet quality of internal structure.
- 3 Test fractures, in part in tension and in part in fatigue, illustrating the effect of test conditions or prior history on the surface configurations.

The types of loading include tension overload, transverse impact, notch bending, torsion, repetitive stress states in fatigue, and the complex stresses involved in ingot or billet rolling.

The causes of fracture in service include stress-corrosion cracking, hydrogen damage, fatigue arising from surface stress concentrations, and impact. The

fracture features that are displayed involve cleavage; fatigue beach marks; intergranular separation; fibrous, radial and shear-lip markings in tension fractures; crack-arrest markings in impact fractures involving more than one stress pulse; chevron markings in catastrophic rupture; and "fisheyes" and porosity due to hydrogen damage.

The sequence of these fractographs, as the Contents List above demonstrates, has been arranged according to alloys. The types of fracture mechanisms are therefore scattered in a random manner through the section. There would be some advantages in assembling all fractures of a given type in one group, but then the various examples of fracture of a specific alloy would be scattered. The present arrangement was chosen as being of most benefit to Handbook users who are alloy-oriented.

The fractographs here and in the second section of the Atlas were selected from two monumental manuscripts by Zapffe that remain unfinished at this date—one a treatise on fractography, and the other a related work on hydrogen embrittlement. Some aspects of these works are of sufficient interest to deserve brief mention here.

Zapffe's studies of metallic fractures verified what had been intuitively postulated—namely, that fracture-surface characteristics depend in a very sensitive fashion on the properties of the metal in question as well as on the type of loading or the environment. It was demonstrated very early, for example, that a ductile metal such as Armco ingot iron would become exceedingly brittle and fracture by cleavage with essentially no measur-

able plastic deformation if subjected to impact at the temperature of liquid nitrogen. It became apparent, therefore, that specific fracture markings were not inherent for a given alloy *per se*, but rather represented the manifestation of a particular fracture mechanism that was dictated by the combination of temperature, type of loading, and type of chemical environment. In other words, the fractures in very dissimilar metals possessing very different properties could, nevertheless, be made essentially counterparts if the needed adjustments in rate and type of loading, temperature, and environment were provided.

This led Zapffe to the discovery that the fracture features and the interpretations of fracture mechanisms that had been characterized for metals were equally pertinent for nonmetals. One example was found in the study of fractures in abrasive grinding wheels. Here it was found that configurations in grinding-wheel fractures were also typical of those in fractures in brittle metal, allowing the same conclusions to be drawn as to the location of the crack origin and the paths of crack propagation. This situation was also found to be true for fractures of glass, in which the sequence of fracture events could be interpreted in exactly the same manner as for certain counterparts in metals.

These similarities between fractures in nonmetals and metals have been cited merely to point out the general nature of fracture characteristics. Interesting though examples of nonmetallic fracture surfaces are, they have been omitted from this Atlas as being inappropriate in a handbook on metals.

Light Fractographs, Macrograph, Micrograph: Carbon Steel Drive Shaft of a Marine Tug, Fractured by Corrosion Fatigue in Seawater



Light fractograph

3418 Fracture surface of a carbon steel drive shaft of a 200-gross-ton marine tug. The shaft failed by corrosion fatigue after seawater displaced the lubricant between the shaft and the stern tube. Beach marks indicate that the fracture origin was at left (arrow). See also 3419 to 3422.

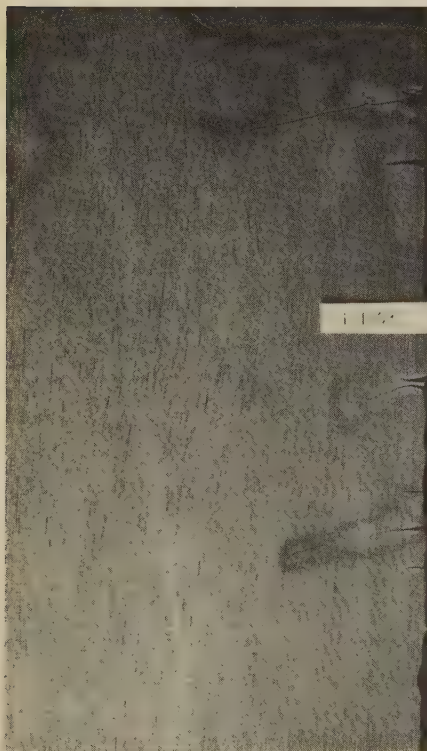
0.8×



Light fractograph

3419 Side view of the fractured drive shaft in 3418. Note the serrated profile (retouched for clarity) of this edge of the fracture surface and the diagonal cracks on the shaft surface. The cracks were caused by corrosion fatigue from the combination of reversed shaft torsion, perhaps some bending, and seawater attack.

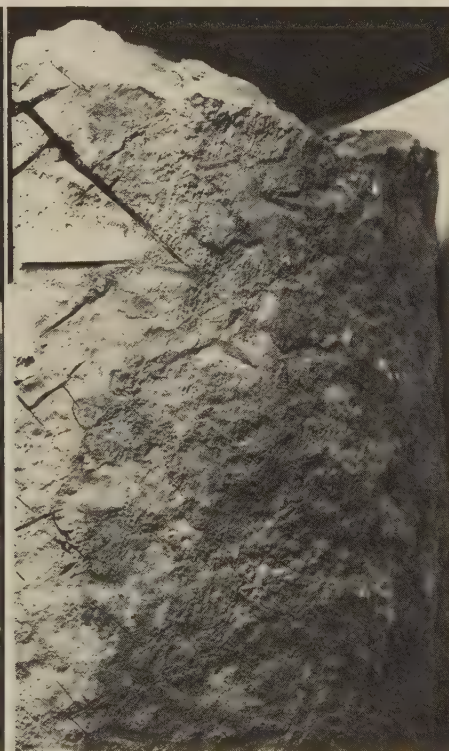
0.8×



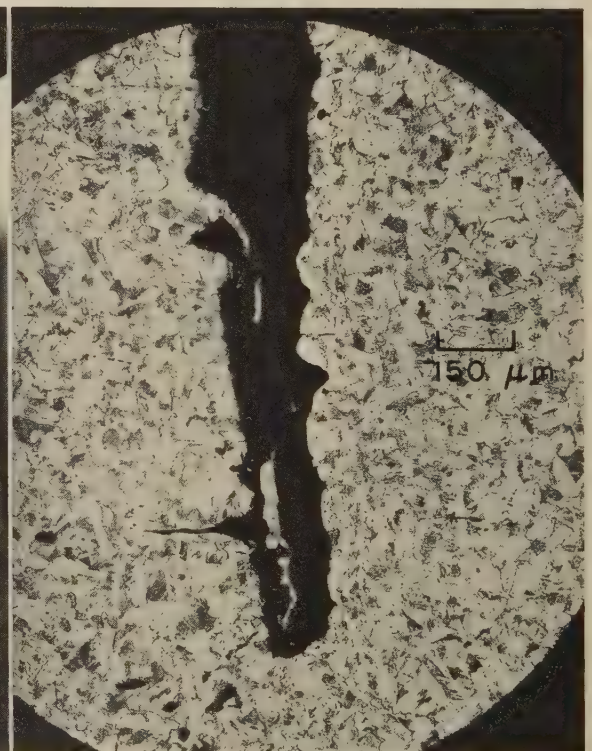
Macrograph (nital etch)

3420, 3421 Macrograph 3420 (at left) shows a macroetched section of the fractured shaft in 3418. Fractograph 3421 (at right) is a view at 90° to that in 3420 and shows the shaft surface, containing diagonal cracks (3420 shows depths of these cracks). Note in 3421 that the seawater produced not only corrosion-fatigue cracking but general surface corrosion as well.

0.6× Light fractograph



0.6×



Micrograph (picral etch)

3422 A section of the fractured shaft shown in 3418, revealing the bottom of one of the corrosion-fatigue cracks. Note that corrosion blunted the tip of the main crack but not the tip of the sharp secondary crack at left, which formed later.

67×

Light Fractographs: Impact Fracture in a Cast Carbon Steel Chassis Frame Bar;
Fatigue Cracks From Hydrogen-Induced Flakes in 1075 Steel Railroad Rails



Light fractograph

3423 Surface of a transverse fracture produced by impact in a cast carbon steel frame bar of a tractor chassis. A region of weakness is evident in the area of internal shrinkage porosity marked by the arrowhead at bottom. This area of porosity can be identified by the fine-scale dendrites above the arrowhead to left and right.

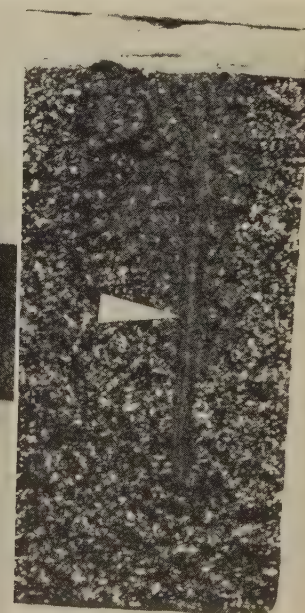
2.2×



Light fractograph

3424 Surface of a transverse fracture in an AREA 110-lb railroad rail made of 1075 steel. The fracture nucleus (small dark area near the top of the railhead) is a hydrogen-induced flake (or "fisheye"), which initiated a fatigue crack (large light zone surrounding the nucleus).

5/8×



Light fractographs

3425, 3426, 3427, 3428

Fractographs 3425 (left), 3426 (left center) and 3427 (right center) show surfaces of "transverse fissures" that occurred in the heads of AREA 131-lb railroad rails made of 1075 steel. All three fissures were caused by the presence of hydrogen-induced flakes (or "fisheyes"), which appear as dark gray areas within the bright zones. These bright zones are fatigue cracks that were initiated by the flakes. Beach marks are visible in the fatigue zones, particularly near the initiations of final, fast fracture. Fractograph 3428 (at far right) shows the surface of a longitudinal fracture in an AREA 131-lb rail of 1075 steel that had been hydrogen embrittled. The white arrowhead points to an unusually large nonmetallic stringer that acted as a site for hydrogen segregation.

Actual size

Light Fractographs: Low-Carbon and Low-Alloy Steel Splined Shafts (Torsional-Fatigue Fractures);
4340 Steel Piston Rod (Fatigue Fracture); 4340 Steel Helicopter Bolt (Notch-Bend Fracture)



Light fractograph

3429, 3430

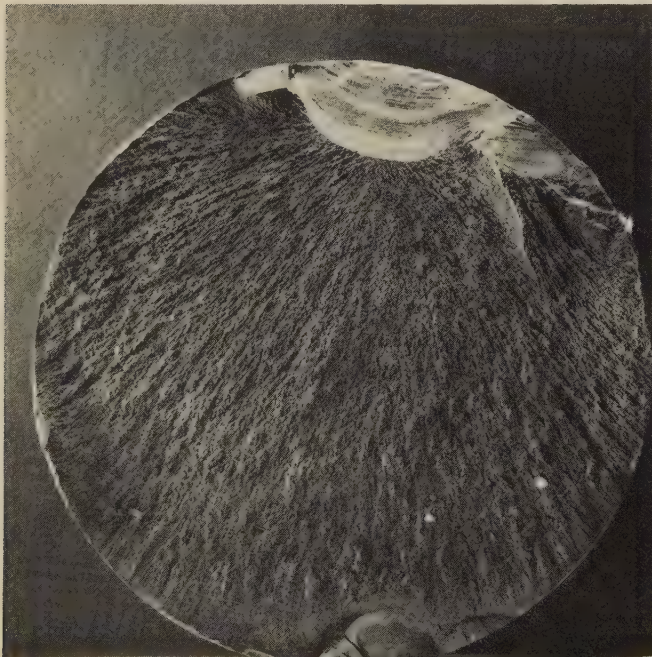
1.7×



Light fractograph

1.4×

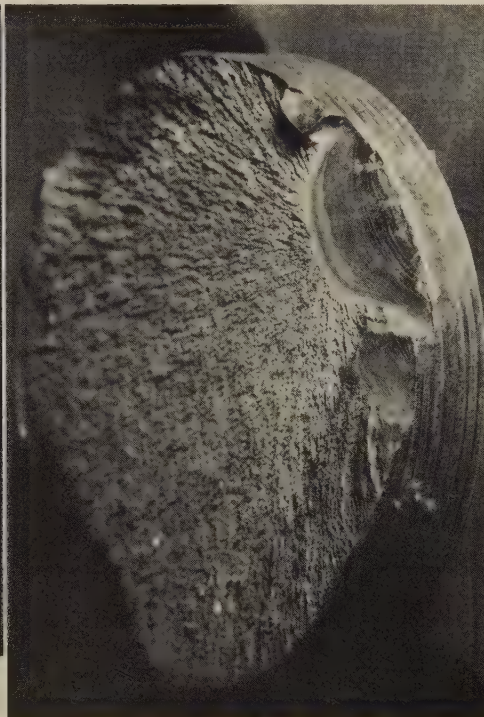
Multiple-origin fracture surfaces in two splined steel shafts. The fracture in 3429 (at left) is in a 2½-in.-diam shaft of low-carbon steel in the as-hot-worked condition that was tested in torsional fatigue. The fracture in 3430 (at right) is in a 1¼-in.-diam automotive shaft of low-alloy steel that failed by torsional fatigue in service. In both fractures, fatigue cracks originated at the sharp notches in the groove fillets at the base of the splines and propagated both circumferentially (connecting with one another in the process) and radially toward the center. Also in both fractures, the fractured parts were sufficiently locked together by the complex fracture path that rubbing obliterated nearly all details of the fatigue cracks.



Light fractograph

3431, 3432

About ½×



Light fractograph

2/3×

Two views of the surface of a fatigue fracture in a 5/8-in.-diam threaded piston rod of 4340 steel heat treated to 341 Bhn. The full-face view in 3431 (at left) shows plainly the beach marks in the region of the primary fatigue crack, at top. Secondary fatigue cracks are visible on either side of it as well as at the bottom. The oblique view in 3432 (at right) reveals that the fatigue cracks began at the roots of the threads, the origin of the primary crack being two threads to the right of the abutting secondary cracks. Although these reduced-size views do not permit detailed scrutiny, it seems evident that the thread roots were too sharp, causing stress concentrations locally. Beyond the fatigue-zone limits, failure was by radial fibrous fast fracture.

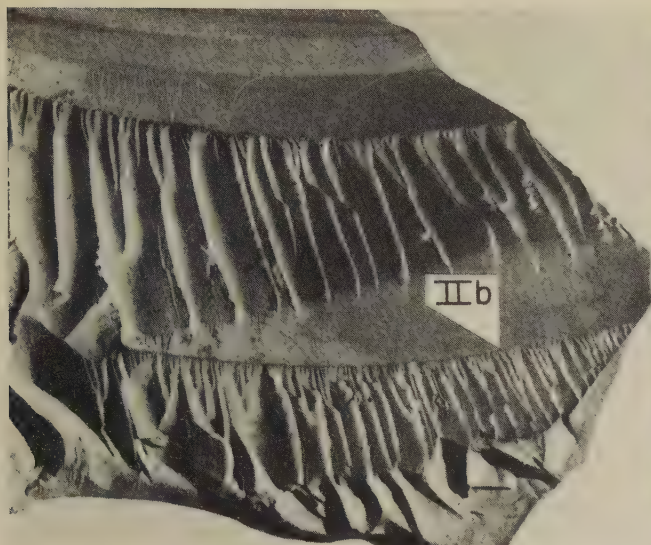


Light fractograph

2½×

3433 Matching fracture surfaces of a 4340 steel helicopter bolt that was broken by notch bending. Observe the fine markings, which are fibrous tear ridges. Note the very large shear lips.

Light Fractographs: 0.30C-3.65Ni-1.45Cr Steel Armor Plate (Impact Fracture); A4N Tool Steel (Tensile Fracture); Class 110 (W1) Tool Steel (Fatigue Fractures)



Light fractograph

0.8×

3434 Surface of an impact fracture in a 4-in.-thick section of class A steel armor plate (0.30% C, 3.65% Ni, 1.45% Cr). The fracture temporarily halted (at arrow-head marked "IIb") before completing the penetration; this interruption was probably due to a pulsation in stress.



Light fractograph 2¼×

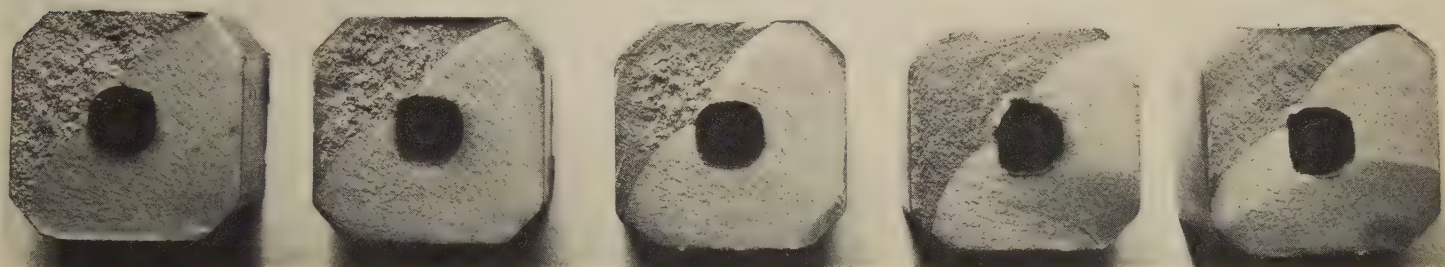
3435 Mating fracture surfaces of eccentrically loaded tensile specimen of A4N tool steel. Note fibrous zones of initial fracture (A).



Light fractograph

1.8×

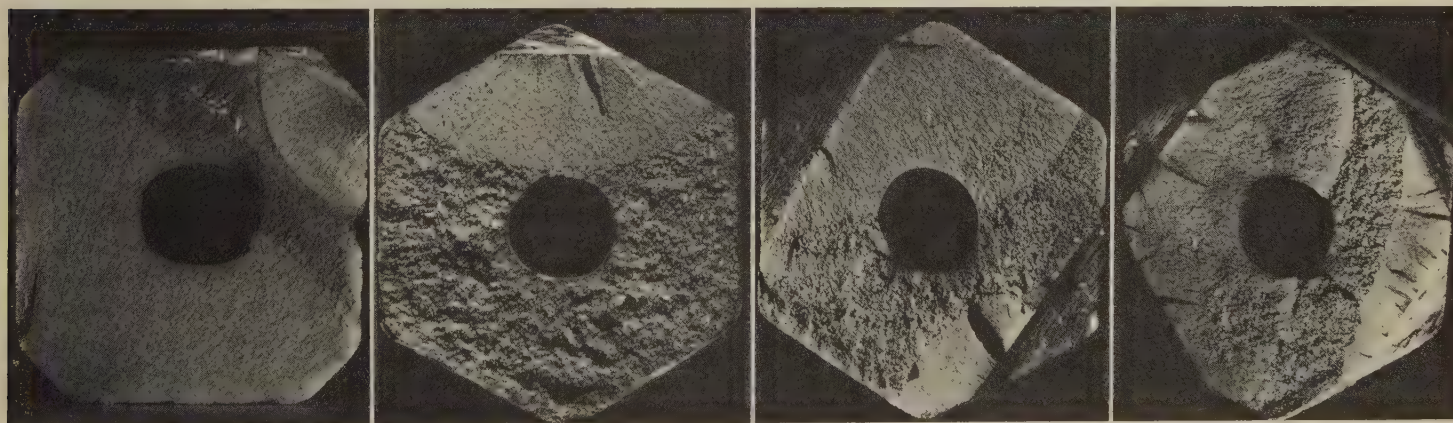
3436 A surface of a fatigue fracture that originated at the inside of a hollow drill of class 110 (W1) tool steel. Fracture initiation was attributed to distortion of the bore of the drill during the production of a hot upset joint.



Light fractographs

1½×

3437 Five fatigue-fracture surfaces that were produced in reversed bending in a pneumatic testing machine. The material is class 110 (W1) tool steel. The lighter areas of the fracture surfaces are the fatigue zones — all of which were initiated at the lower right corners. Note the lack of beach marks, which indicates that during each test the load amplitude and environment were uniform. The dark regions at the upper left corners are the regions of final, fast fracture.



Light fractographs

2×

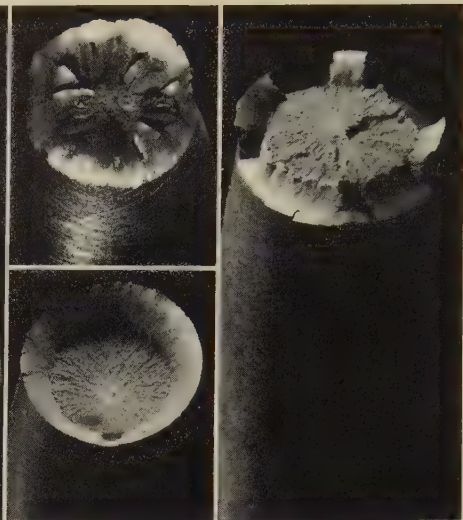
3438, 3439, 3440, 3441 Four fatigue-fracture surfaces that were produced in bending in the laboratory with the use of assorted notches to simulate service conditions; the material is class 110 (W1) tool steel. The specimen in 3438 (far left), which was tested without a notch and fractured after 432,000 cycles at 365 MPa (53 ksi), shows two crack origins at opposite corners where bending was maximum. The specimen in 3439 (second from left) had a single notch at top and broke after 20,500 cycles at 434 MPa (63 ksi); note the small shear lip around the region of fast fracture at bottom. The specimen in 3440 (third from left) was notched at two corners that were along an axis not in the plane of bending and broke after 50,000 cycles at 338 MPa (49 ksi); the two resulting fatigue cracks therefore had somewhat distorted shapes. The specimen in 3441 (far right) was notched at four sites — two in the bending plane and two in a plane at 60° from it — and broke after 10,260 cycles at 434 MPa (63 ksi). The four notches produced fatigue zones, which formed two major crack fronts that nearly penetrated the section.



Light fractograph

Actual size

3442 Surface of a catastrophic fracture in an open-header die of class 120 (W2) tool steel that was case carburized to 0.95% C at the surface, heat treated in the range of 815 to 845 C (1500 to 1553 F), and water quenched. This die was used for cold forming and upsetting square heads. Upsetting stresses opened a small fatigue crack in the hardened case in the top edge near the upper right corner; it is to this area that the markings of radial fibrous fracture in the core of the die may be traced. The region of fast fracture encompasses nearly the entire fracture surface. Note the fine-grained, sharply defined case that frames the fibrous core.



Light fractographs
3443,
3444, 3445

About 2½×

Fracture surfaces of three tensile-test specimens of tool steels: in 3443 (top left), high-nickel class 241 (L6), showing a central fibrous area, a region of radial shear, and a shear lip; in 3444 (bottom left) and 3445 (right), low-carbon class 244 (L6) broken at 23 and 427 C (73 and 800 F), respectively, both showing cup-and-cone fractures.



Light fractograph

3×

3446 Surface of an impact fracture in a shear blade of class 234 (L6) tool steel heat treated to a hardness of Rockwell C 55. The impact generated the two crack fronts whose junction may be seen at the secondary fissure that enters the field of view at lower right; the radial markings on either side clearly meet this fissure at divergent angles. A third and separate crack front (at top left) met these two crack fronts at the wide secondary crack beneath the projecting shards.

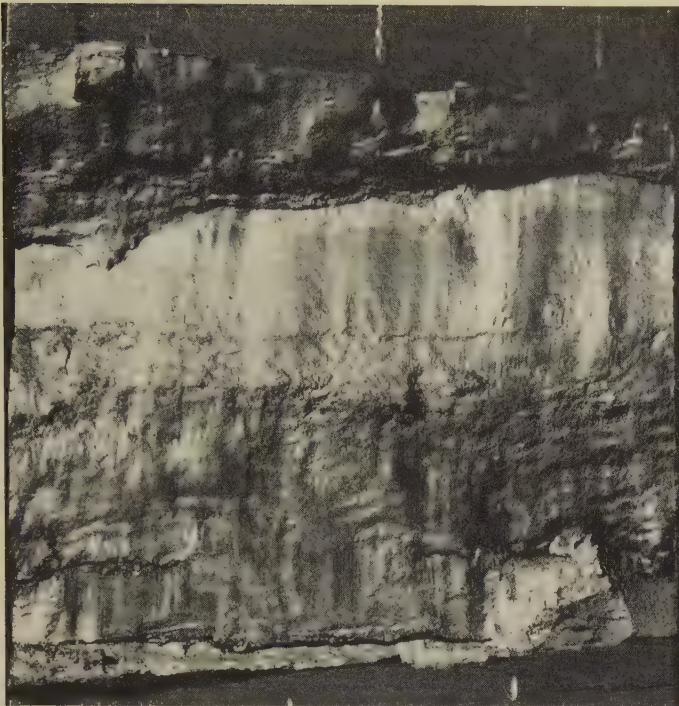


Light fractograph

2×

3447 Surface of a low-cycle fatigue fracture in the collar of a rivet-heading tool of class 320 (S1) tool steel heat treated to a hardness of Rockwell C 56 to 58. Following the development of the smooth fatigue zone at right, fracture occurred in a few hours of service, generating the unusual beach marks at center and left.

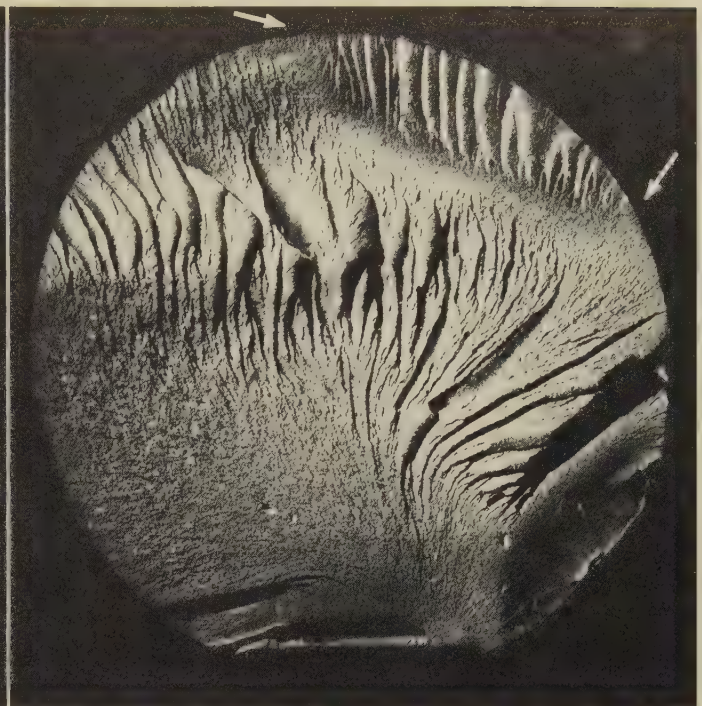
**Light Fractographs: Impact Fractures in Class 610 (T1)
and Class 651 (M3, Class 1) Tool Steels**



Light fractograph

2.3×

3448 A "hammer-burst" fracture at the center of a 5 1/4-in.-diam, 1 1/2-in.-thick forged disk of class 610 (T1) tool steel. This longitudinal fracture shows a surface of either a lap or a cold shut; the appearance of such a fracture is often called "platy" or "laminated".



Light fractograph

2.6×

3449 An impact fracture in a 1 1/4-in.-diam notched bar of annealed class 610 (T1) tool steel broken for inspection by two hammer blows. The crack from the first blow started at the notch at bottom and halted at the arrows, penetrating the area at top right only with the second blow. See 3450, 3451.



Light fractograph

1.9×

3450 An impact fracture in a 1 1/4-in.-diam notched bar of class 610 (T1) tool steel that was broken for inspection same as the bar in 3449. The crack resulting from the first hammer blow, which started at the notch at right, shows the network of intersecting fine markings called "Wallner lines". The crack that resulted from the second hammer blow is at left.

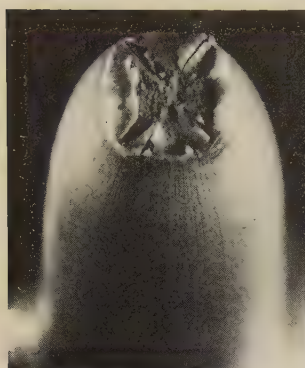


Light fractograph

1.7×

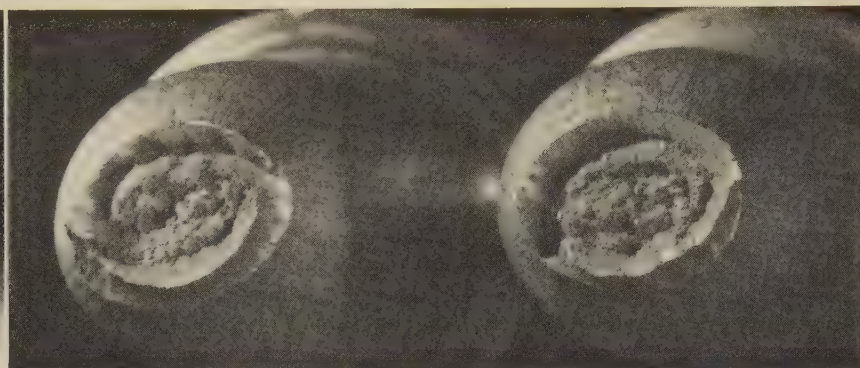
3451 An impact fracture in a notched bar of class 651 (M3, class 1) tool steel broken for inspection same as in 3449 and 3450. The crack from the first hammer blow originated in the notch at right (origin is readily located by tracing back to beginning of fan-shaped pattern of radial marks); this crack penetrated the area at left with the second hammer blow.

Light Fractographs: Stainless Steels 410 (Low-Carbon and Standard) and 431 Fractured by Tension; 431, by Impact; 440C, by Torsion; 303(Se), by Notch Bending; 302B and 309, During Rolling



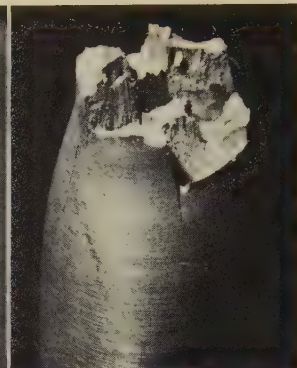
Light fractograph
3452, 3453

2.8×



Light fractograph

2½×



Light fractograph

2.4×

Tensile-test fractures in hot rolled type 410 stainless steel bar, showing contours that reflect high ductility and mechanical anisotropy, the latter of which resulted from rolling. At left (3452) is one fracture surface of a low-carbon specimen heated 6 hr at 745 C (1373 F) and air cooled before testing. At right (3453) are the mating fracture surfaces of a specimen tested in the as-hot-rolled condition. Both "square" (3452) and oval (3453) fracture surfaces are unusual in round bars.

3454 Surface of tensile fracture in hot rolled type 431 stainless steel that was tempered at 663 C (1225 F).



Light fractograph

2½×

3455 Mating surfaces of an impact fracture in a specimen taken from a flat bar of type 431 stainless steel oil quenched from 954 C (1750 F) and tempered to a hardness of 248 Bhn.



Light fractograph

2×

3456 Torsion fracture in type 440C stainless steel annealed at 871 C (1600 F), pickled in 15% H₂SO₄ plus an inhibitor, and cold drawn. Chevron pattern at edge indicates that the crack ran clockwise from its origin at top. Note pronounced radial marks.



Light fractograph

¼×

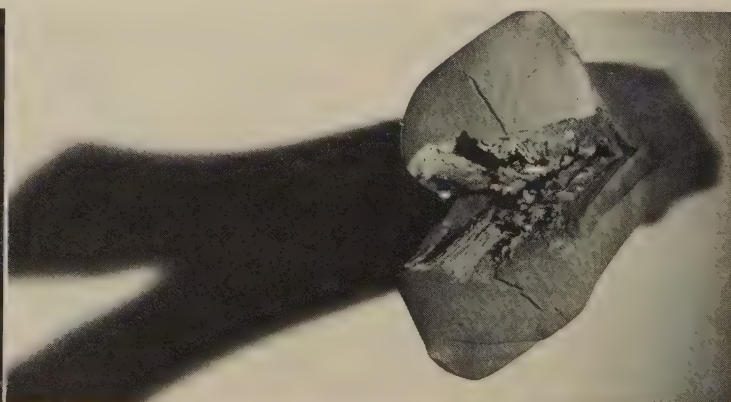
3457 Woody fracture surface of an ingot of 302B stainless steel (2-3% Si) that broke during an early blooming-mill pass because of casting-dendrite patterns. The ingot had a high silicon content and was overheated.



Light fractograph

½×

3458 Surface of a fracture produced by notching and bending a hot rolled ¾-in.-diam bar of type 303(Se) stainless steel. The woody nature of the fracture is due to centerline segregation of selenium, which altered the ductile behavior of the central zone. Such fractures are sometimes termed "fibrous".



Light fractograph

½×

3459 End of a billet of type 309 stainless steel, showing a woody, longitudinal fracture. The outer layers of the billet deformed properly during rolling, but excessive segregation at the center resulted in the formation of a brittle region, which led to this classic "alligator" fracture.

Light Fractographs, Photographs, Micrograph: "Rock Candy" Fracture in Type 302 Stainless Steel;
Fractured Cast Aluminum Alloy 355 Turbosupercharger Impeller



Light fractograph

$\frac{2}{3}\times$

3460 Surface of a "rock candy" fracture in a bloom of type 302 stainless steel. An abnormally high silicon content, and inadvertent overheating at 1357 C (2475 F) for $\frac{3}{4}$ hr after the first blooming-mill pass, caused excessive grain growth; second pass then resulted in intergranular fracture. See 3461.



Light fractograph (H_2SO_4 cleaning; HNO_3/HF brightening)

$1\frac{1}{2}\times$

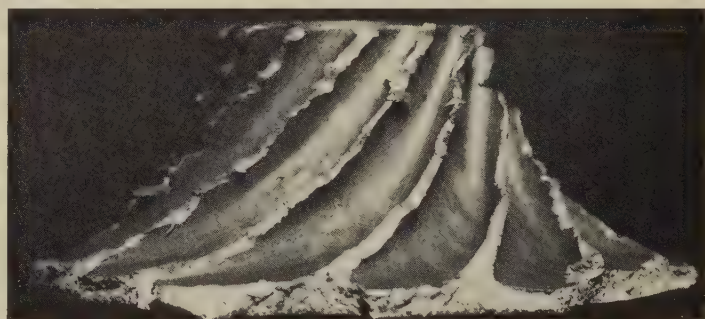
3461 Higher-magnification view of fracture surface in 3460 (above). This bloom fractured during rolling, splitting apart and wrapping itself around the roll. Note lack of deformation of grains. The fracture surface was cleaned with H_2SO_4 and was brightened with a solution containing HNO_3 and HF.



Photograph

About $0.6\times$

3462 Plan view of the collected fragments of a fractured turbosupercharger impeller that was cast of aluminum alloy 355 and that fractured due to internal stresses developed by gas porosity that evolved during freezing. See also 3463 to 3466.



Photograph

Actual size

3463 Elevation view of the hub of the impeller shown in 3462 (above), displaying the surfaces of the fractured vanes. Note the mechanical damage of the edges of the vanes; much fracture detail was destroyed by this damage after fracture.

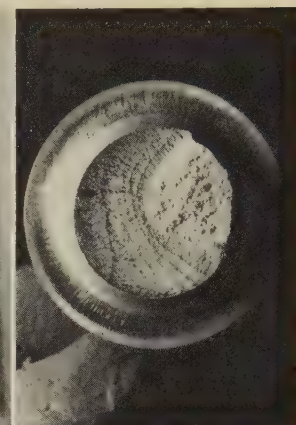
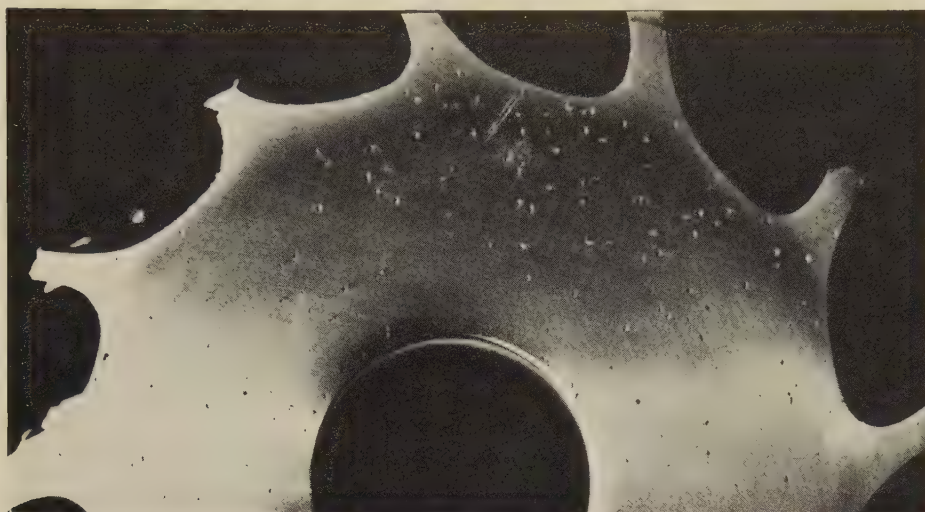


Micrograph (Keller's reagent)

$150\times$

3464 Microstructure of the cast aluminum alloy 355 impeller shown in 3462. The large void was formed by solidification shrinkage. See also 3465 and 3466 (next page).

Macrograph and Light Fractographs: Cast Aluminum Alloy 355 Impeller (Continued);
Fatigue Fracture in Aluminum Alloy 2024-T4; Brass Ingot Fractured in Rolling

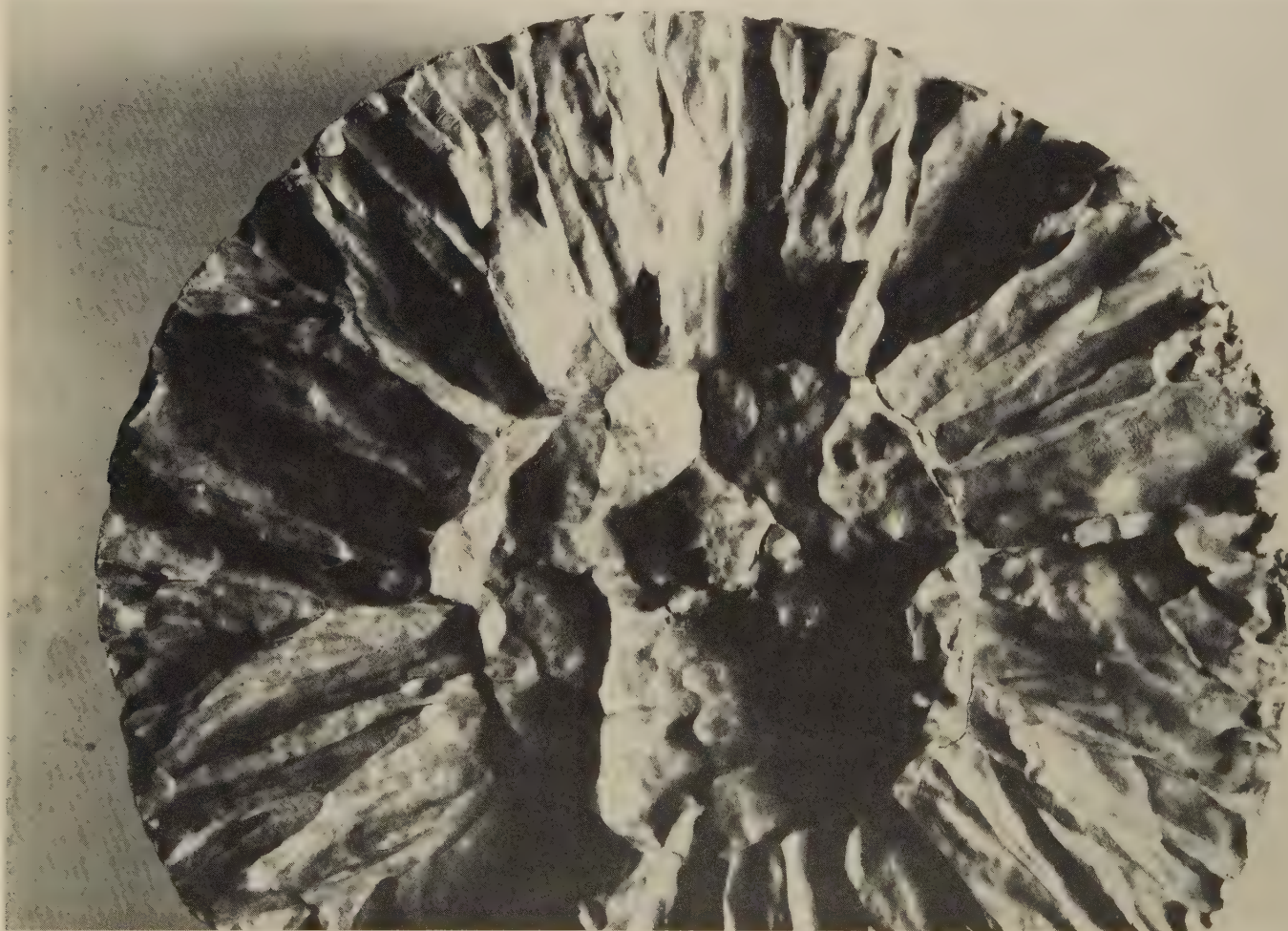


Macrograph (as polished; not etched)

3465, 3466 Continuation of the series begun in photograph 3462 on the preceding page, on a fractured impeller hub cast of aluminum alloy 355. Macrograph 3465 (at left) is of half a section through the hub, showing the coarse, and highly dispersed, gas porosity due to gas that had been in solution in the melt but precipitated as bubbles during freezing of the casting. Fractograph 3466 (at right) shows a fracture surface of one of the fragments of the hub shown in photograph 3463. The small reflecting spots are the shiny walls of bubbles intersected by the fracture; note that these spots are distributed quite uniformly.

2X Light fractograph 3X

Light fractograph 4X
3467 Fatigue-fracture surface of an aluminum alloy 2024-T4 specimen that was broken after 43 million cycles of stress to 138 MPa (20 ksi). Note the crack-growth halts that resulted from machine slowdowns.



Light fractograph

3468 Surface of a fracture in a 7 1/2-in.-diam brass ingot that broke because of casting-dendrite patterns. The combination of overheating prior to rolling, a segregation in structure in the central region, and the stresses applied by rolling reduction was sufficient to generate an interdendritic rupture. Note, however, that although the fracture mechanism is interdendritic, there is relatively little secondary cracking detectable. Note also that the interdendritic surfaces are remarkably smooth.

0.85X

Light-Microscope Fractographs at High Magnification

Historic examples from Carl A. Zapffe

CONTENTS

Armco iron	140-142	Aluminum alloy 7076-T6	152
Ship-plate steels	143	Antimony	153
Carbon steel weld deposits	144	Bismuth	154
Stainless steels:		Antimony-bismuth alloys	155
Types 405 and 430	145-146	Bismuth-zinc alloys	155
0.096% C, 22.14% Cr ferritic	146	Vacuum-arc-cast molybdenum	156-157
Type 446	147-148	Vacuum-arc-cast tungsten	158-159
Ferrochromium alloys	148-149	Sintered tungsten powder compacts	159
Iron-silicon alloys	149-151	Zinc	160

THE LIGHT-MICROSCOPE fractographs presented in this section were selected from the collection of Carl A. Zapffe, who was the first to demonstrate that such photographs could be taken of a rough fracture surface using a standard metallograph. One basic factor that was very much in his favor in this endeavor was that the "fisheyes" in hydrogen-embrittled steel that originally aroused his curiosity possessed facets of appreciable size that were quite flat. This situation also applied to the cleaved surfaces that he subsequently studied in alloys that were broken, in many instances, at liquid-nitrogen temperatures to secure similar flat and mirrorlike facets. Other alloys were sufficiently brittle to permit this type of cleavage at room temperature or even appreciably higher temperatures.

Essentially all of the fractures reproduced in this section were the result of laboratory impact tests—the type of loading most favorable to production of the desired cleavage. The only exceptions are the fatigue fractures in aluminum alloy 7076-T6 (page 152) reported by Zapffe and Worden in 1950 (in Ref 39, page 8). These photographs are notable in that they are believed to be the first ever taken of fatigue striations, although Zapffe did not appreciate the true nature of these features. This was a remarkable achievement, considering the limited depth of field of the metallograph.

Unlike the other sections of this Atlas, the fracture mechanisms illustrated in this section are limited to two: fatigue (for the aluminum alloy) and cleavage (for the remainder). The characteristics of the cleavage facets vary considerably, depending on the metal and the test temperature. Some are so close to theoretical separations along a single crystallographic plane that they strongly resemble

a polished surface. Others show many complex cleavage steps and river patterns for circumstances that provide a greater degree of toughness.

In a number of instances, photomicrographs of the internal structure near or adjacent to the fracture surface have been included where it is evident that the fracture features are related in some fashion to the microstructure. In many of the alloys tested, comparisons are provided showing the effect of previous heat treatments on the nature of the fracture surface. Effects of hydrogen embrittlement and of variations in impact velocity are illustrated in certain cases. The series of ship-plate fractures (page 143) shows diminishing toughness with decreasing manganese contents (1.09% Mn to 0.81% Mn to 0.37% Mn). The sequence on carbon steel weld deposits (page 144) shows embrittlement from hydrogen emitted from electrode coverings, and avoidance of the embrittlement by use of a low-hydrogen covering or thorough drying, or both.

The fractures of molybdenum and tungsten are interesting in that they display the influences of carbides and oxides on fracture behavior. Zapffe reported that molybdenum had been found to be forgeable provided carbides were present, even though the impact fractures usually followed the carbide-metal interfaces. Leaf-like molybdenum oxides, on the other hand, contributed to brittleness, as would be expected from their shape.

Zapffe's studies revealed that fractography could identify many of the crystallographic features of such metals as antimony, bismuth and zinc. The cleavage facets of these metals reveal the presence and orientation of twin bands, kink bands and slip bands produced by the fracture process. Measurements of angles of these features on intersecting cleavage surfaces such as those shown in fracto-

graphs 3534 and 3535 (page 154) make possible the positive identification of the crystal planes on which all aspects of the fractures were active. He did, in fact, use such information to construct three-dimensional crystal models showing the facets and band structures in their correct relationships.

The magnifications employed in the fractographs in this section range from 65 diameters to 3400 diameters—a quite remarkable upper level in view of the very restricted depth of field available. (The limit of resolution, however, may be no more than about 1500 diameters.) The clarity of detail is therefore very much a function of the degree to which the facet surface under study approached a plane mirror in flatness. The applicability of this technique has therefore its greatest advantage when utilized for specimens that exhibit nearly perfect cleavage. But for surfaces such as the dimples of a fibrous tensile fracture, very little of the surface contours can be brought into sharp focus if any appreciable magnification is desired.

Despite the limitations that the light microscope imposes on fractography, and the consequent restricted use of this technique that is evident since Zapffe publicized his findings, the light-microscope fractographs did provide an important accomplishment—namely, the awakening of general interest in what could be learned from the study of fracture surfaces. Therefore, although fractographic techniques employing scanning and transmission electron microscopes have replaced the procedures illustrated in this section of the Atlas, these light-microscope fractographs nonetheless are of historical importance as a successful pioneering effort that was the forerunner of the very sophisticated fractographic expertise that is now widely shared.

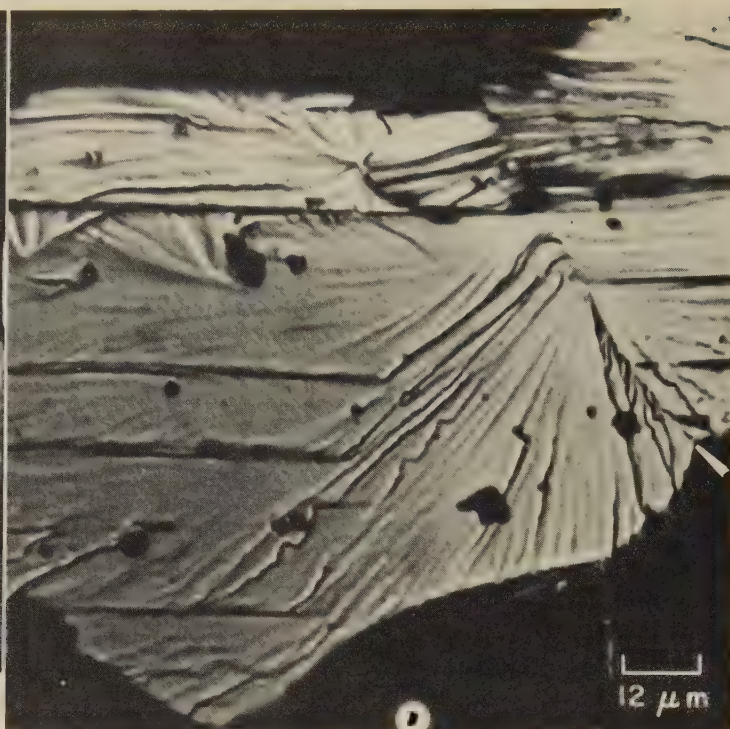
Light Fractographs: Armco Iron Fractured by Impact at -196°C (-321°F),
Showing Effect of Annealing at Various Temperatures



Light fractograph

800×

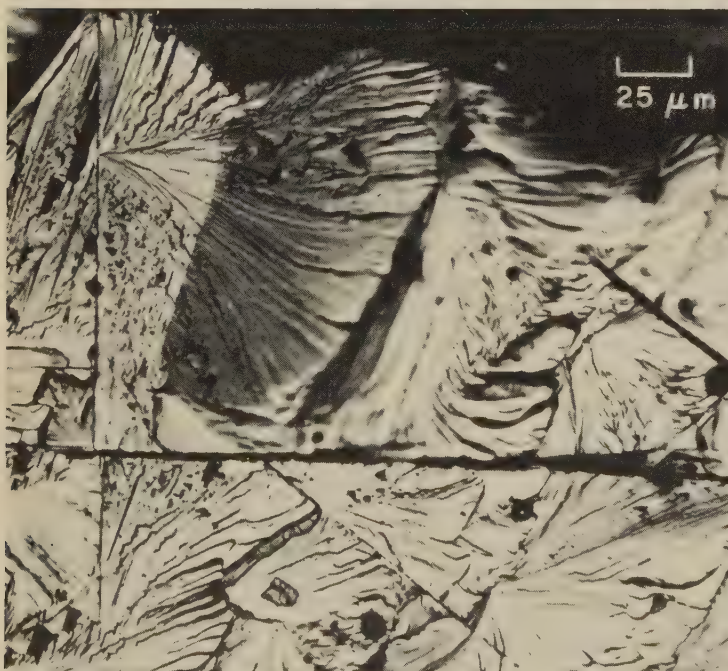
3469 Surface of an impact fracture in a notched $\frac{1}{4}$ -in.-square specimen of as-rolled Armco ingot iron (0.013% C, 0.019% Mn, 0.003% P, 0.018% S, 0.001% Si, 0.02% Ni) that was broken at -196°C (-321°F). The crack entered the area at bottom in this view, and progressed upward by quasicleavage. The two diagonal lines are mechanical twins. Fractographs 3470 to 3472 show the effect of annealing at various temperatures on the appearance of impact fractures in this same material; fractographs 3473 to 3480 (next two pages) show fractures of this material as affected by heat treatment, cold work, and hydrogen embrittlement.



Light fractograph

825×

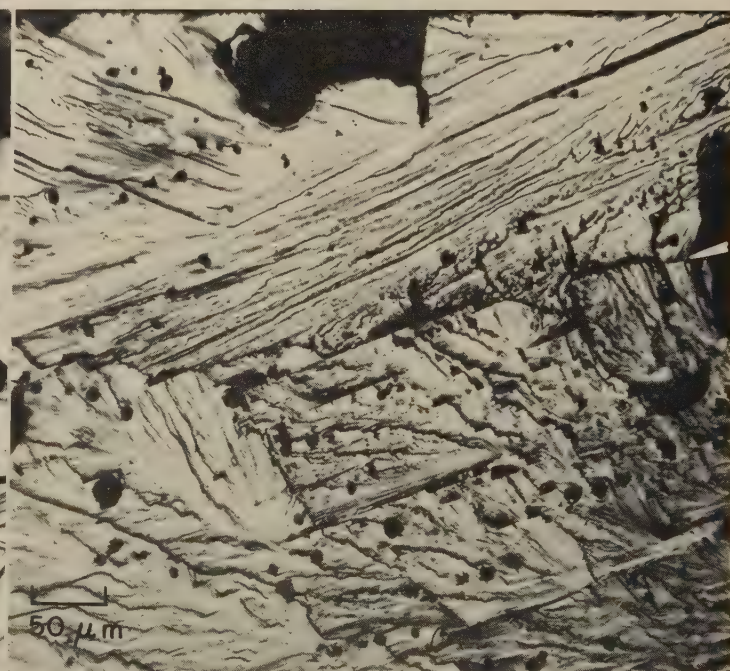
3470 Impact-fracture surface of a specimen of the same material as in fractograph 3469, but which was annealed at 1000°C (1832°F) for 2 hr and furnace cooled before impact at -196°C (-321°F). Fracture was by cleavage parallel to a crystallographic plane. The discontinuity at arrow (near right edge) is believed to lie at a grain boundary. The dark "holes" presumably were the sites of inclusions. See also fractographs 3471 and 3472.



Light fractograph

400×

3471 Impact-fracture surface of a specimen of the same material as in 3469 and 3470, but which was annealed at 1200°C (2192°F) for $1\frac{1}{2}$ hr and furnace cooled before impact at -196°C (-321°F). Crack propagation was mainly from left to right by cleavage, which produced many local river patterns. A prominent set of intersections of $\{112\}$ twins with the plane of the fracture facet is evident at several definite angles. See also 3472.

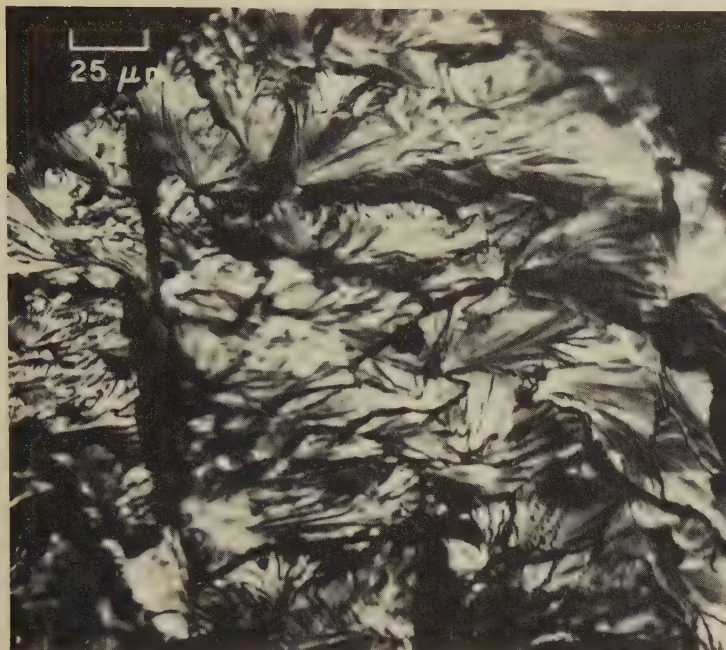


Light fractograph

200×

3472 Impact-fracture surface of a specimen of the same material as in 3469, 3470 and 3471, but which was annealed at 1350°C (2462°F) for $1\frac{1}{2}$ hr and furnace cooled before impact at -196°C (-321°F). Annealing at a higher temperature than that for 3471 resulted in a very coarse grain size. This facet shows two crack origins, at upper and lower right, with the two crack fronts joining at the dark fissure denoted by the arrow at right edge (above center).

Light Fractographs: Armco Iron Fractured by Impact at -196°C (-321°F) (Effect of Heat Treatment and Cold Work); and at Room Temperature (Effect of Cold Work and Hydrogen Embrittlement)



Light fractograph

400×

3473 Impact fracture in a specimen of the same Armco ingot iron as in fractograph 3469 (opposite page), but which was heated at 1200°C (2192°F) for $1\frac{1}{2}$ hr and water quenched before impact at -196°C (-321°F). This is a cleavage fracture, but the surface is quite distorted. See also fractograph 3474, at right.



Light fractograph

400×

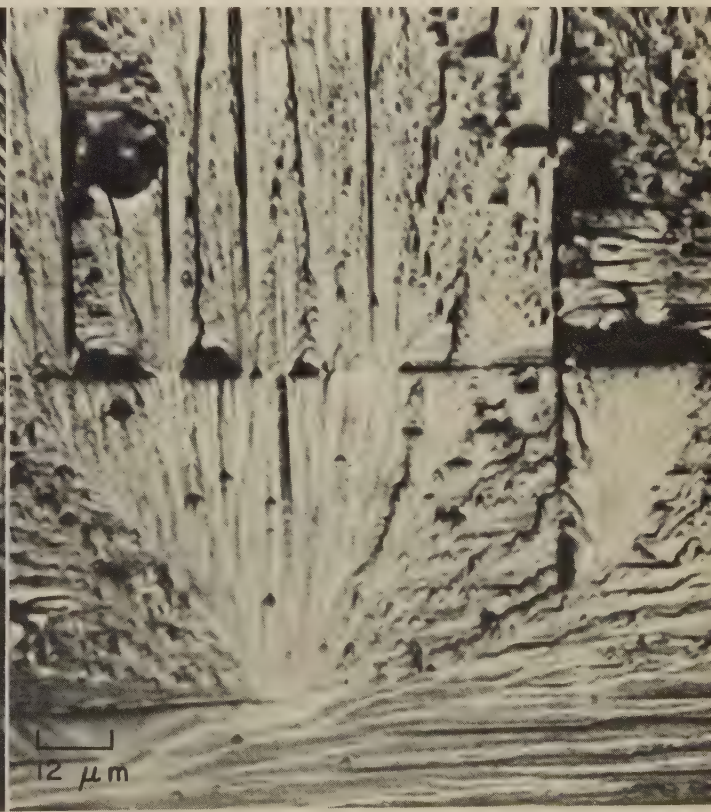
3474 Impact fracture in a specimen of the same material and heat treatment as in 3473, but which was then heated to 700°C (1292°F), held at temperature for 1 hr, and furnace cooled, before impact at -196°C (-321°F). Primary crack origin is at top here, slightly to right of center. There are many involved river patterns. Note the blocklike steps at upper left.



Light fractograph

800×

3475 Effect of cold work after heat treatment on impact fracture in same Armco iron as in 3469-3474. Prior to impact at -196°C (-321°F), specimen was heated 2 hr at 1000°C (1832°F), furnace cooled, then hammered at room temperature to 50% reduction in thickness. Coarse river patterns somewhat resemble those in 3469. The central secondary cleavage resulted from twinning.

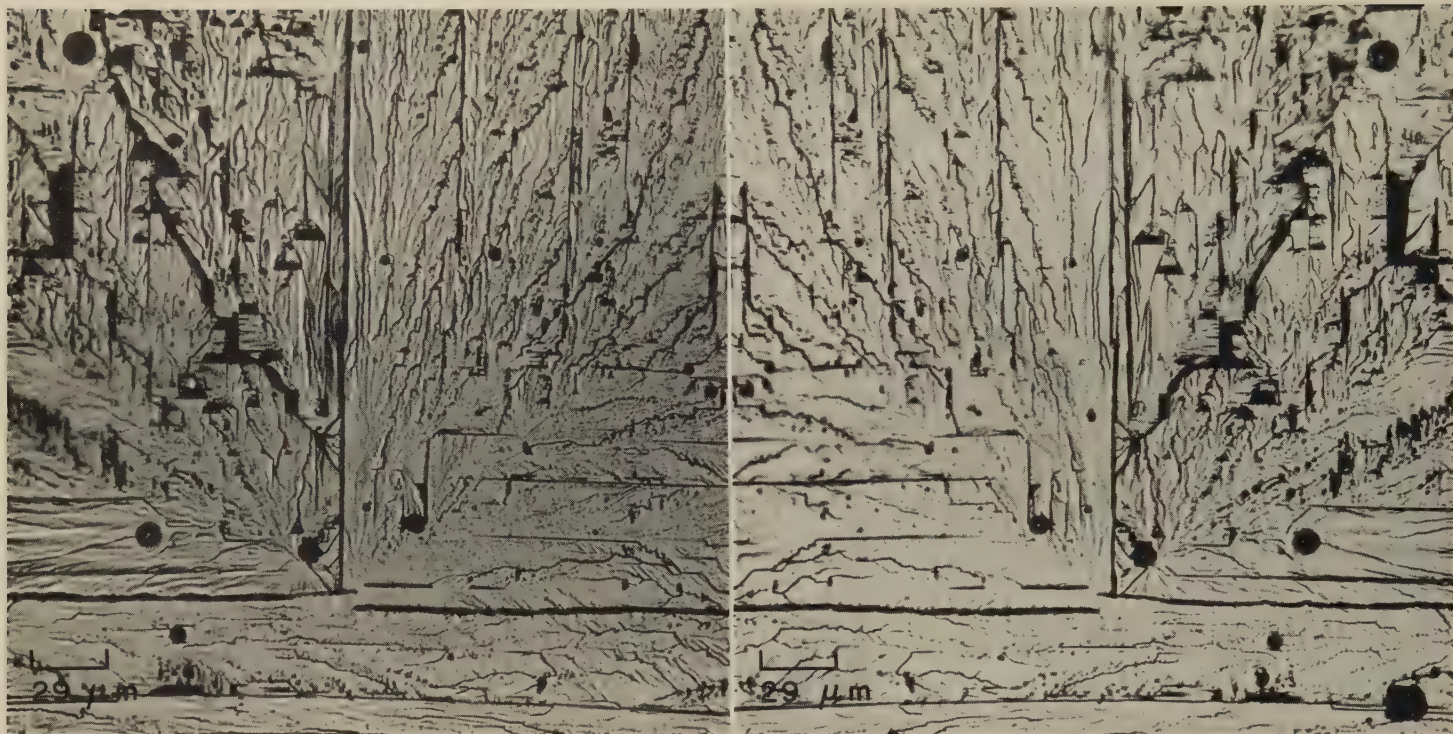


Light fractograph

800×

3476 Impact fracture in a specimen of the same material, and with the same thermal and mechanical treatment, as in 3475, but which was embrittled by cathodic charging of hydrogen and was fractured by a hammer blow at room temperature. The crack entered the area that appears at lower left in this view. Cubic symmetry indicates that this is a (001) facet.

Light Fractographs: Effect of Hydrogen Embrittlement and/or Cold Work on Room-Temperature Impact Fractures in Armco Ingot Iron



Light fractograph

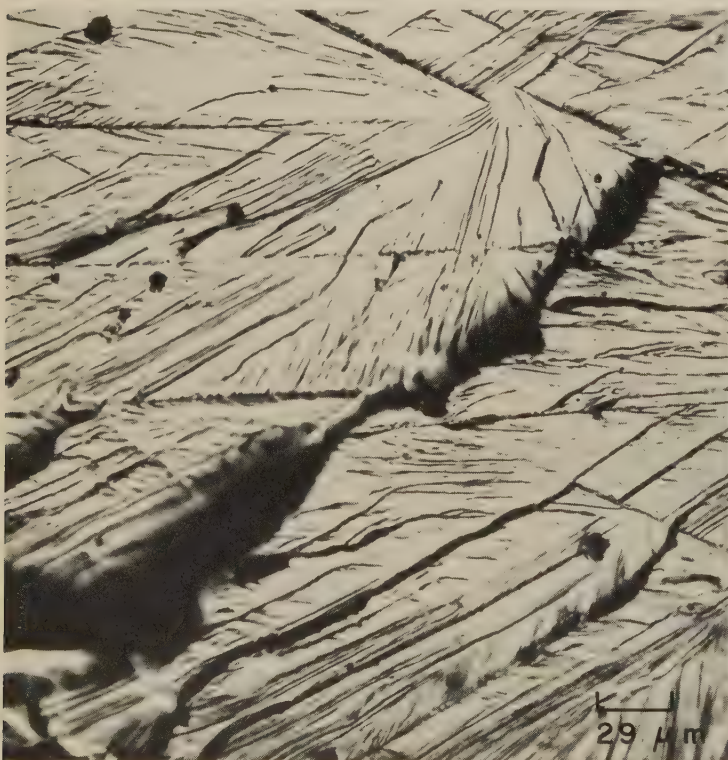
3477, 3478

Mating surfaces of a fracture in a ¼-in.-square specimen of Armco ingot iron cut from a hot rolled ¼-in.-thick plate, annealed at 1250 C (2282 F) for 2 hr, and furnace cooled. Hydrogen embrittlement was produced by cathodic treatment for 90 min in 10% H₂SO₄ at 90 C (194 F). The specimen was then notched and broken by impact at room temperature. These views show a portion of a single grain. The crack entered the area shown here at extreme left and right, near bottom. The cubic nature of the fracture pattern indicates that this is a (001) facet intersected by {112} twins. Gas holes (or inclusions) affect the fracture pattern locally.

350×

Light fractograph

350×

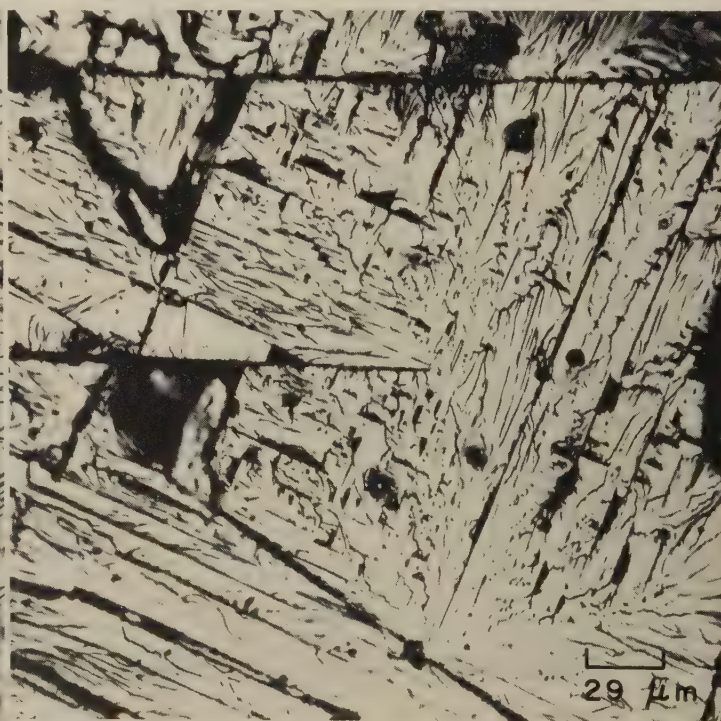


Light fractograph

3479

Fracture surface of a specimen of Armco ingot iron that was annealed at 1250 C (2282 F) for 2 hr and furnace cooled, then reduced 20% in thickness and broken by impact at room temperature. The primary cleavage fracture follows a (001) plane; the secondary traces are along {112} and {110} planes.

350×



Light fractograph

3480

Fracture surface of a specimen of Armco ingot iron that received the same thermal and mechanical treatment given the specimen in 3479 (left), and then was cathodically hydrogen embrittled for 30 min in 10% H₂SO₄ at 90 C (194 F) and broken by impact at room temperature. The crack entered the area shown here at bottom center and produced a (001) facet that is much flatter than that shown in fractograph 3479.

350×

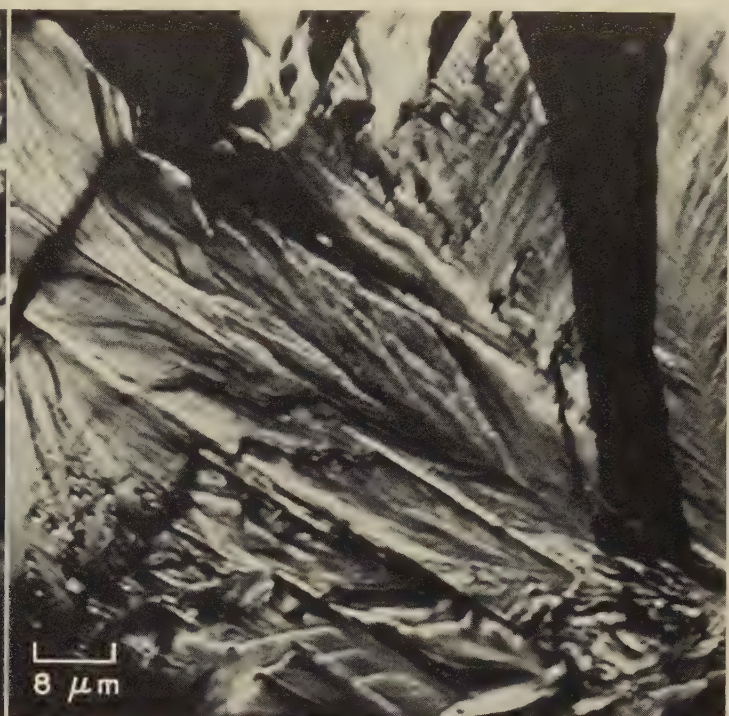
Light Fractographs: Ship-Plate Steels* Fractured by Impact at -196°C (-321°F), Showing Effect of Decreasing Manganese Content; and Fractured at 35°C (95°F)



Light fractograph

3481 Surface of a fracture in a specimen of ship-plate steel* (0.23% C, 1.09% Mn, 0.05% Si) that was water quenched from 868°C (1594°F), tempered 2 hr at 704°C (1300°F) and broken by impact at -196°C (-321°F). The coarse river patterns in this rough surface denote high "toughness". Compare with 3482 and 3483.

1250×



Light fractograph

3482 Surface of a fracture in a specimen of as-rolled ship-plate steel* (0.17% C, 0.81% Mn, 0.16% Si; fully killed) that was broken by impact at -196°C (-321°F). The crack entered at lower right here and generated a facet much flatter than that in 3481, but left very distinct fracture-progress markings.

1250×



Light fractograph

3483 Surface of a fracture in a specimen of as-rolled ship-plate steel* (0.22% C, 0.37% Mn, 0.009% Si; rimmed) that was broken by a hammer blow at -196°C (-321°F) after being stored for 4 months. This flat facet, which is typical of brittle fractures, shows intersections by {112} twins. See also fractograph 3484.

1500×



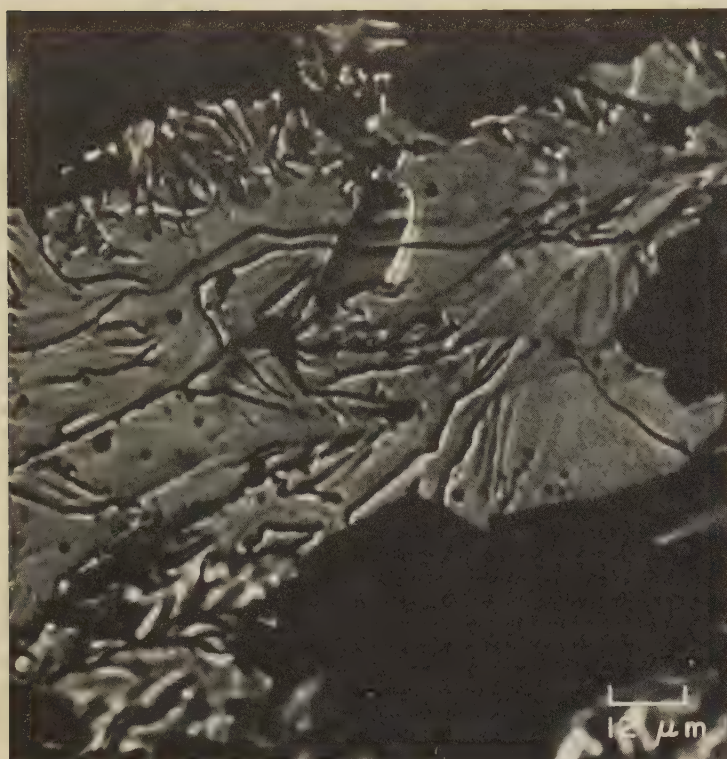
Light fractograph

3484 Surface of a fracture in a specimen of the same ship-plate steel* as in 3483 (left), and in the same condition, but broken by impact at 35°C (95°F), showing severe notch sensitivity. Note the diagonal spine.

850×

*The ship-plate steels shown on this page are described in an article by E. P. Klier, F. C. Wagner and M. Gensamer, The Correlation of Laboratory Tests With Full Scale Ship Plate Fracture Tests, *J Am Welding Soc*, Vol 27, 1948, p 71s-96s.

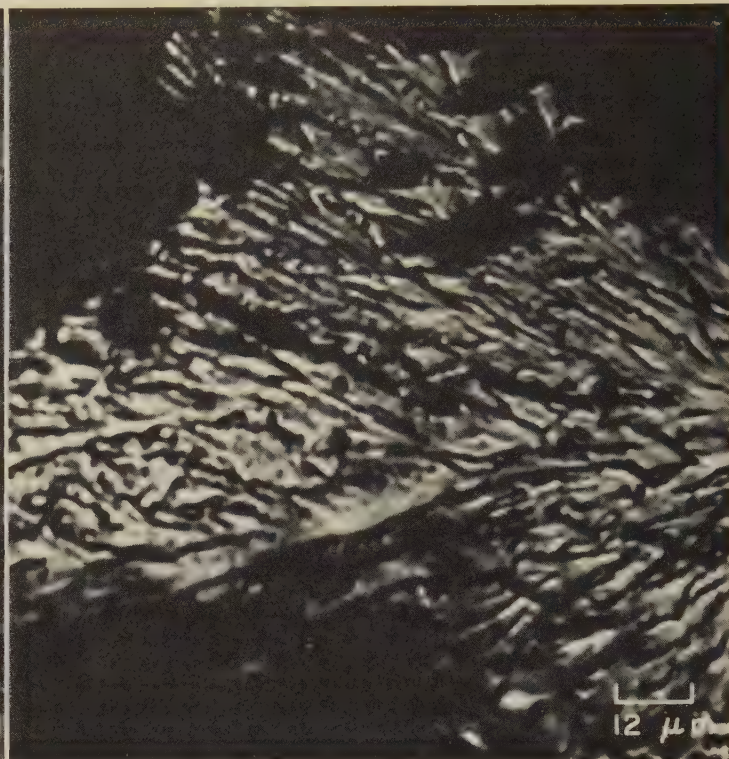
Light Fractographs: Carbon Steel Weld Deposits Fractured by Impact at -196°C (-321°F),
Showing Effect of Hydrogen Pickup From Electrode Coverings



Light fractograph

800×

3485 Fracture surface of a carbon steel weld deposit broken by impact at -196°C (-321°F). The deposit was in a 90° T-joint of $\frac{1}{4}$ -in.-thick plate fillet welded with a $\frac{5}{32}$ -in.-diam E6010 electrode in a single pass using direct current. This brittle cleavage facet resulted from hydrogen pickup during deposition from the cellulosic covering of the E6010 electrode. See 3486-3488.



Light fractograph

800×

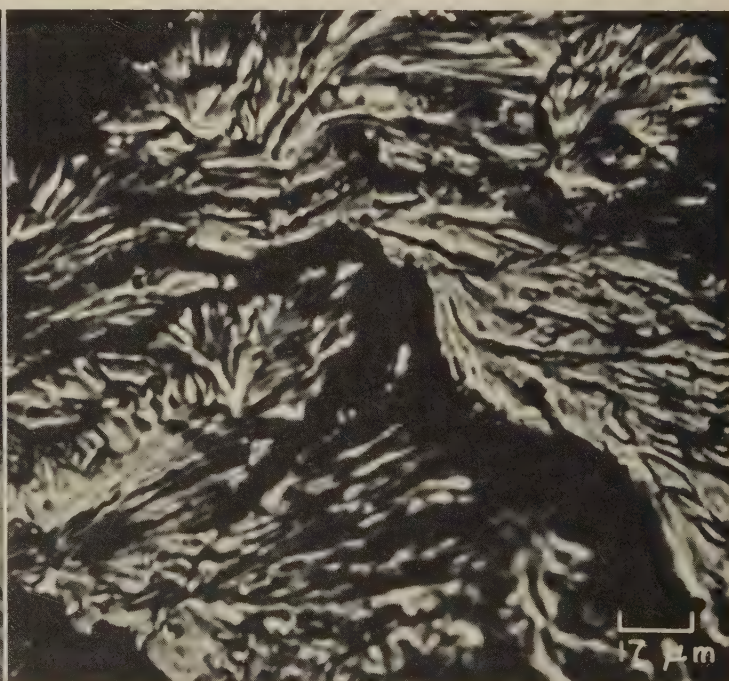
3486 Fracture surface of a carbon steel weld deposit produced, and impact tested, under the same conditions as for 3485 except for the use of fully dried low-hydrogen E6015 covered electrodes. The rough surface with coarse river patterns, which is characteristic of "toughness", is similar to that in 3481 (preceding page). See also fractographs 3487 and 3488, below.



Light fractograph

600×

3487 Fracture surface of a weld deposit made under the same conditions as for 3486 except the E6015 electrodes were inadequately dried, by being held 1 hr at 149°C (300°F) rather than the recommended 315°C (600°F), which failed to eliminate hydrogen from the covering. Result was a brittle fracture, as typified by this flat facet (which is like 3485). See 3488.



Light fractograph

600×

3488 Fracture surface of a deposit from the same fillet weld as the one that provided the specimen in 3487, but taken from the last portion of the bead. The resemblance of the facet to that in fractograph 3486 indicates that the heat given off by the arc had dried the electrode covering before the final portion of the weld bead was laid down, eliminating the earlier brittleness.

Light Fractographs and Micrograph: Fracture in Decarburized Zone of Type 405 Stainless Steel;
Type 430 Stainless Steel Fractured by Impact at Various Test Temperatures



Light fractograph 600×
3489 Fracture surface in a decarburized zone of type 405 stainless steel. Cleavage crack with cubic symmetry entered zone from lower right. See also 3490.



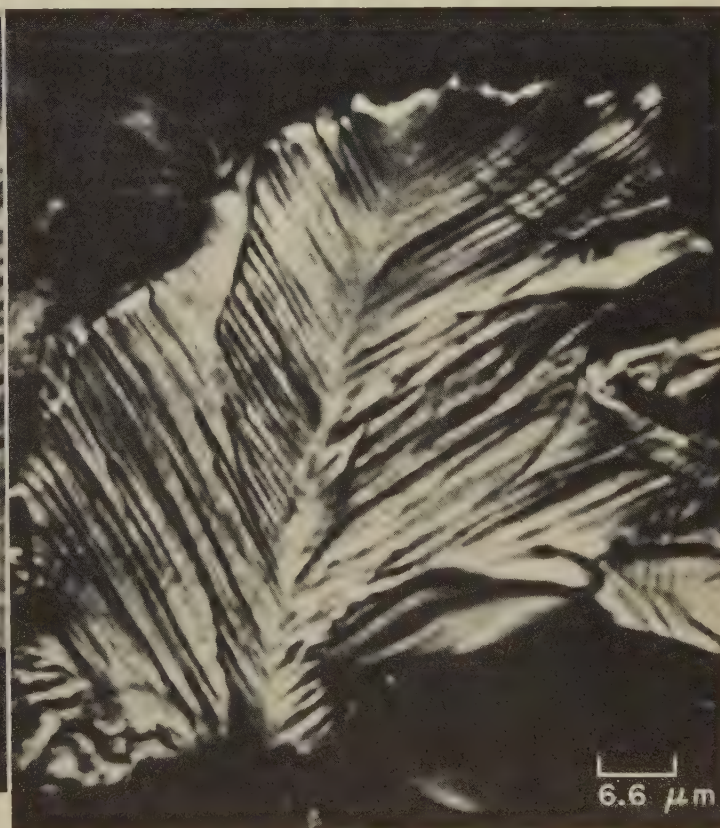
Micrograph (HCl and picric acid) 80×
3490 A polished and etched section through the specimen in 3489, displaying the large grains that resulted from a prolonged decarburizing treatment.



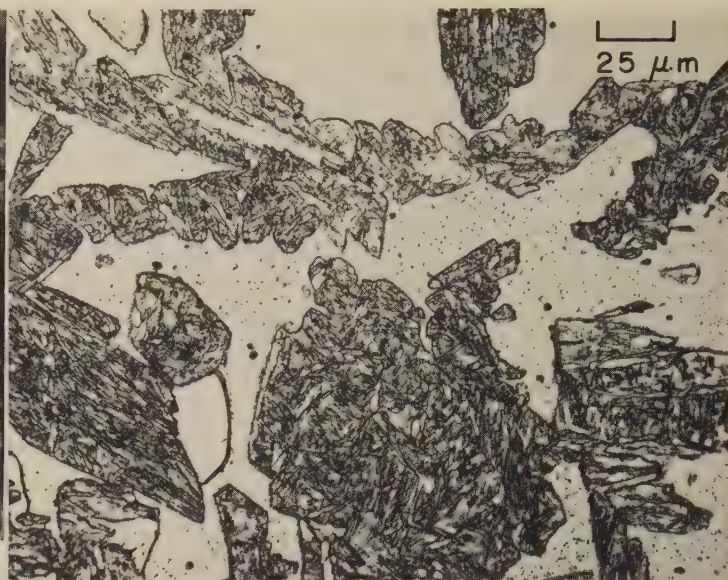
Light fractograph 1100×
3491 Impact-fracture surface of a notched specimen of type 430 stainless steel that was heated for 3 hr at 1050 C (1922 F) and furnace cooled, then broken at room temperature. A blocklike pattern of brittle cleavage on a (001) facet. This is typical of fractures in chromium ferrite, for temperatures as low as -196 C (-321 F).



Light fractograph 1525×
3492 Impact-fracture surface of a notched specimen of type 430 stainless steel that was heat treated the same as the specimen in fractograph 3491, but was broken at 100 C (212 F). The blocklike pattern of brittle cleavage visible in 3491 is not exhibited here, and this facet conforms less closely to the expected (001) plane; both indicate decreased brittleness.



Light fractograph 1525×
3493 Fracture surface of a specimen of type 430 stainless steel with the same heat treatment as specimens in 3491 and 3492, but broken by a hammer blow at 200 C (392 F). The spine separates orthogonal markings.



Light fractograph

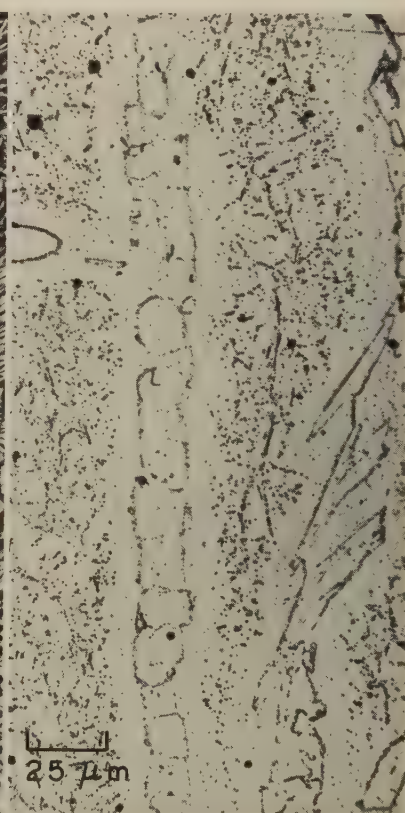
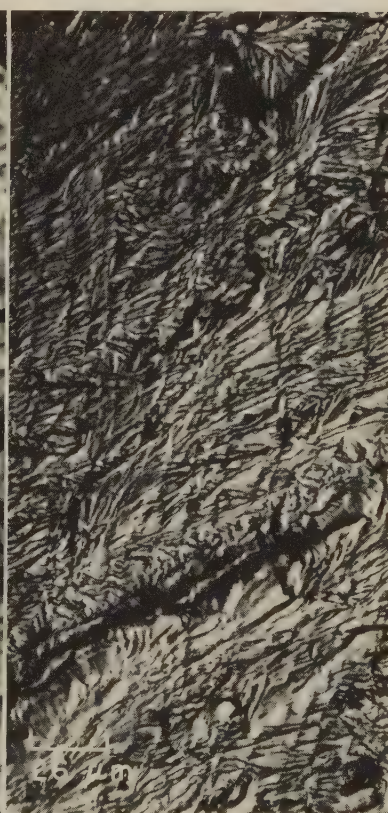
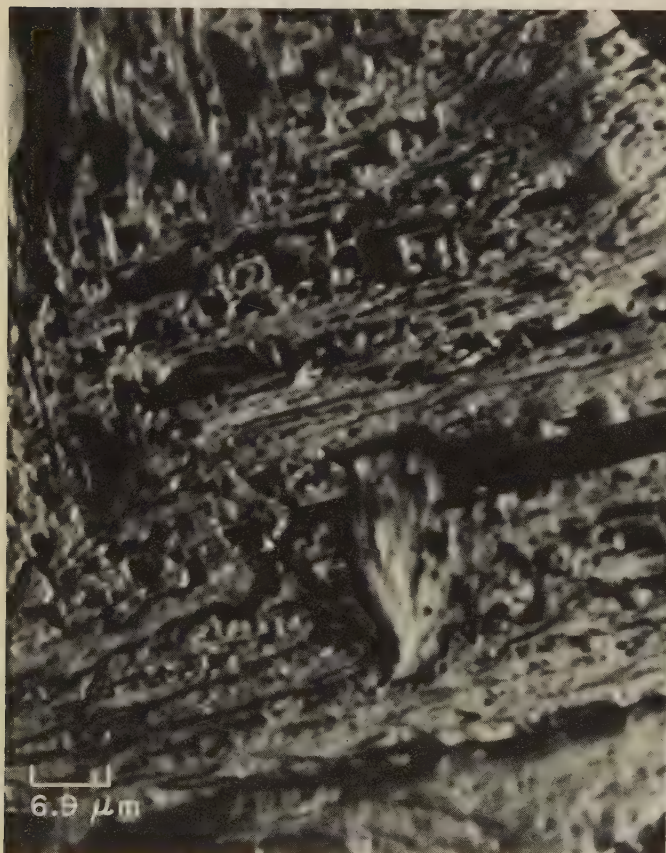
600×

3494 Surface of an impact fracture in type 430 stainless steel (0.103% C, 17.16% Cr) cast as a 5-lb laboratory heat, forged to a 1-in.-square bar, heat treated ¼ hr at 982 C (1800 F), oil quenched, then broken at room temperature. River patterns are visible on facets of ferrite grains. Dark areas are martensite regions that were circumvented by the crack. See also 3495.

Micrograph — hydrochloric and picric acids

400×

3495 Polished-and-etched section through the type 430 stainless steel specimen shown in fractograph 3494 (at left). In contrast to 3494, here the acicular structure of the martensite (dark-etching areas) is visible and ferrite (light-etching) is structureless.



Light fractograph

1450×

3496 Surface of an impact fracture in a specimen of type 430 stainless steel (0.061% C, 0.45% Mn, 0.37% Si, 16.9% Cr) annealed at 1052 C (1926 F) for 3 hr, furnace cooled, then broken at room temperature. Crack front entered this region at lower left. Shown is a portion of a (001) facet, presenting a blocklike pattern with cubic symmetry, similar to the pattern shown in fractograph 3491.

Light fractograph

390×

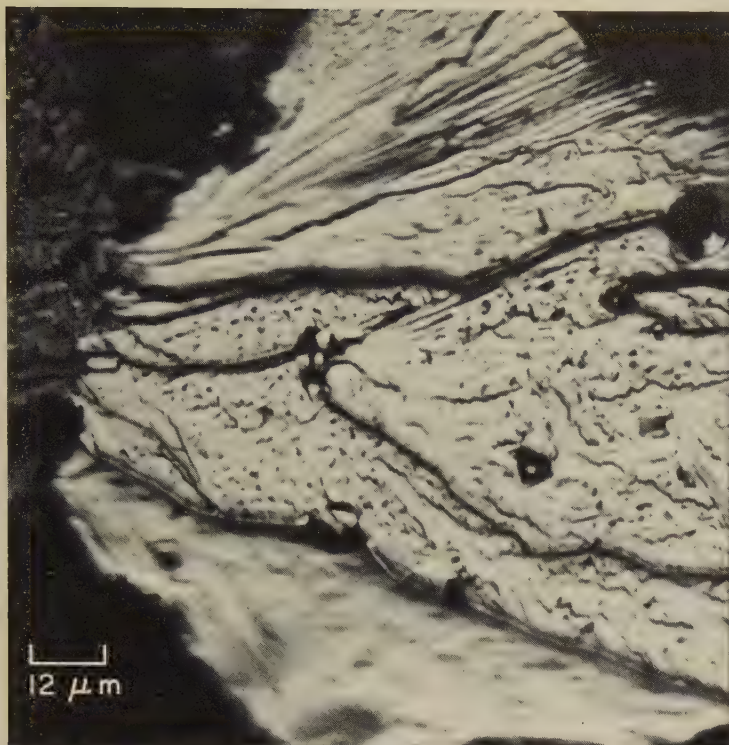
3497 Impact-fracture surface in 0.096C-22.14Cr ferritic stainless steel cast and forged as in 3494, annealed at 871 C (1600 F), oil quenched from 982 C (1800 F), broken at room temperature. Crack propagation was from left to right. This appears to be a cleavage fracture. See also 3498.

Micrograph — HCl, picric acid

400×

3498 A polished-and-etched section through the specimen in 3497. In contrast to 3495 (type 430 stainless), there is no martensite visible here, and the entire field consists of chromium-iron ferrite outlined by carbides precipitated during heat treatment. Relatively few inclusions are present.

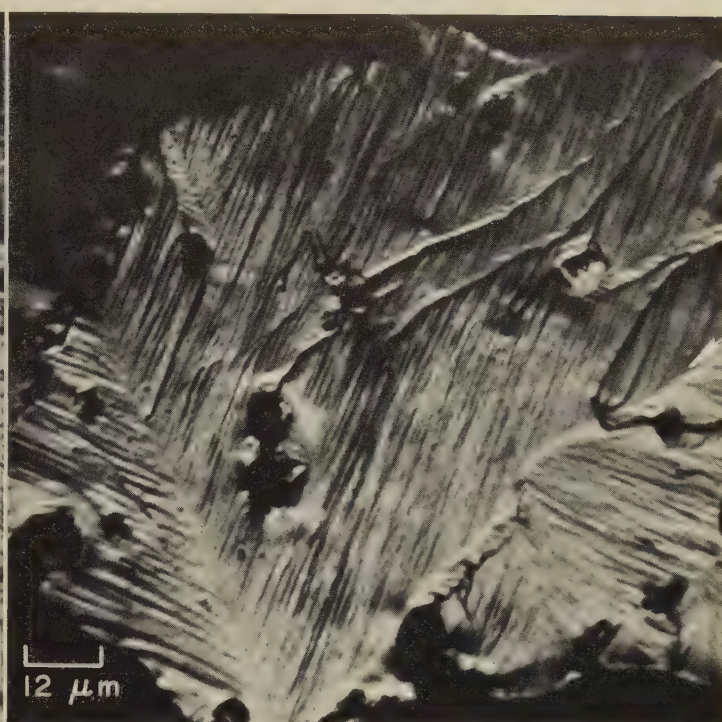
Light Fractographs: Impact Fractures in Type 446 Stainless Steel at Different Test Temperatures and Impact Velocities



Light fractograph

850×

3499 Surface of an impact fracture in a specimen of type 446 stainless steel (0.145% C, 25.99% Cr) that was heat treated at 1150 C (2102 F) for 2½ hr and furnace cooled, then broken by a hammer blow at 200 C (392 F). Although no blocklike pattern is visible here, this fracture facet is still flat enough to indicate brittleness. See also fractographs 3500 to 3502.



Light fractograph

850×

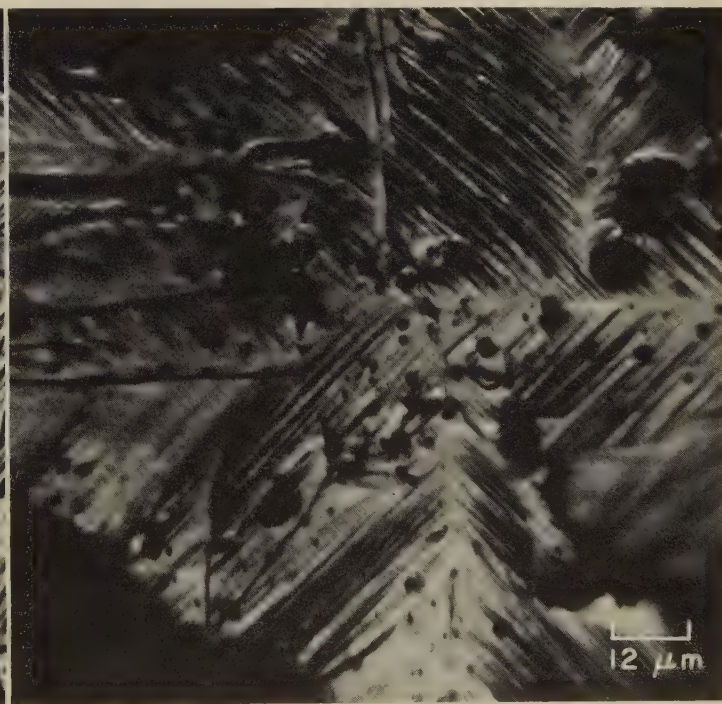
3500 Surface of an impact fracture in a specimen of the same stainless steel and heat treatment as in 3499, but broken by a hammer blow at 350 C (662 F). Note the similarity of this fracture to the ship-plate fracture at 35 C (95 F) in 3484, which shows the same spine structure with 45° and 90° symmetry. Arrowhead at center of right edge points to a diagonal boundary, which is believed to denote the meeting of two crack fronts.



Light fractograph

850×

3501 Fracture surface of a specimen of the same stainless steel and heat treatment as in 3499 and 3500, broken at 350 C (662 F) by the impact of a 0.22-caliber rifle bullet fired at a range of 24 in. The facet resulting from this combination of impact velocity and test temperature resembles one produced by a hammer blow at 35 C (95 F) in the same material.



Light fractograph

850×

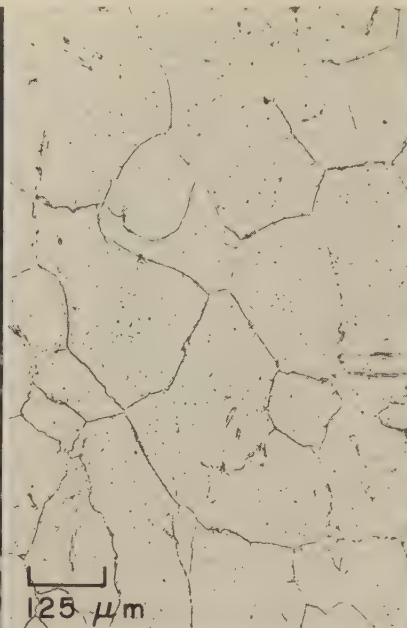
3502 Fracture surface of a specimen of the same stainless steel and heat treatment as in 3499, 3500 and 3501, broken at 475 C (887 F) by the impact of a 0.22-caliber rifle bullet. This facet, when compared with that in 3500, suggests that the higher testing temperature and the higher impact velocity had a net combined effect that yielded a fracture of similar brittleness.



Light fractograph

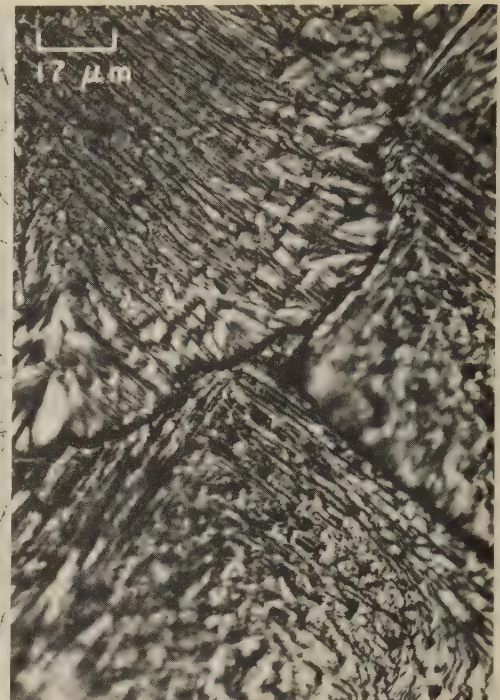
850×

3503 Surface of an impact fracture in a specimen of type 446 stainless steel (0.10% C, 26.10% Cr) that was forged, heat treated 40 hr at 871 C (1600 F), furnace cooled, annealed 2½ hr at 1150 C (2102 F), furnace cooled, then broken at room temperature. Crack front entered this grain at top left, producing fracture along a (001) facet. See 3504.



Micrograph (mixed acids in glycerol) 80×

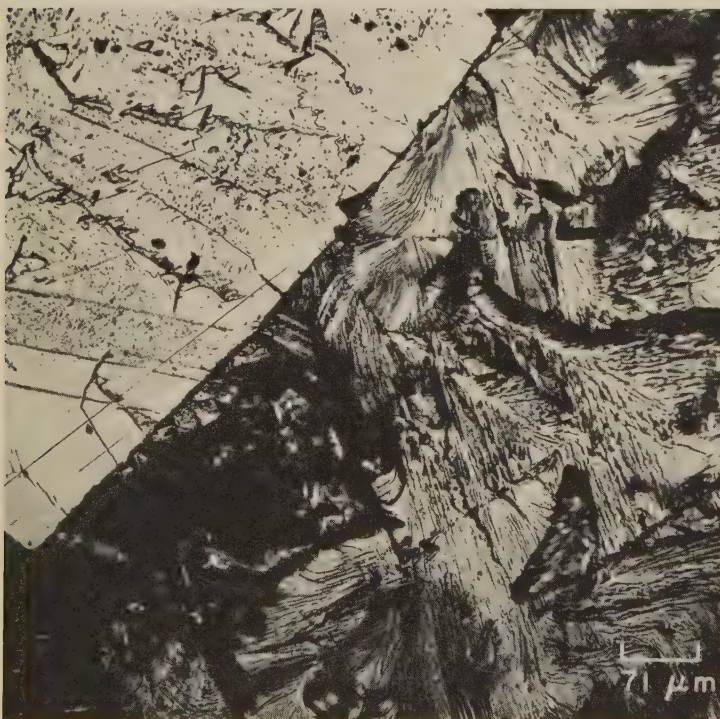
3504 A polished-and-etched section through the specimen of 446 stainless steel shown in fractograph 3503 (left), revealing coarse-grained chromium-iron ferrite containing carbide particles and inclusions. Grain growth occurred during the high-temperature anneal at 1150 C (2102 F) that was used to ensure a cleavage fracture.



Light fractograph

590×

3505 Surface of an impact fracture in a specimen of type 446 stainless steel (0.107% C, 28.67% Cr) that was prepared as a 5-lb laboratory casting, forged, extensively recrystallized at 871 C (1600 F) for 40 hr, air cooled, then broken by a hammer blow at room temperature.



Light fractograph

140×

3506 Surface of an impact fracture in low-carbon ferrochromium alloy (0.05% C, 70% Cr) broken at room temperature. The crack front entered this area from the left. The light region left of the sharp diagonal boundary is a cleavage facet on a (112) plane; the darker region to the right of the boundary is an area of less-perfect cleavage showing river patterns.



Light fractograph

140×

3507 Surface of an impact fracture in high-nitrogen ferrochromium alloy (0.75% N) broken at room temperature, showing elaborate fracture pattern. Two crack fronts entered this area, at upper left and at lower left, and met at the thin discontinuity at arrows, which may be a grain boundary. Note the closely matching, nearly opposite patterns.

Light Fractographs: Room-Temperature Impact Fractures in 0.17C-70Cr Commercial Ferrochromium Alloy and in As-Cast 0.034C-1.59Si and 0.038C-4.24Si Iron-Silicon Alloys



Light fractograph

325×

3508 Surface of an impact fracture in a specimen of commercial ferrochromium alloy (0.17% C, 70% Cr) that was broken at room temperature. This unusually smooth surface resembles the "glassy" fractures observed in very brittle materials and is believed to be a facet of a carbide particle. See 3509.



Light fractograph

275×

3509 A different area of the impact-fracture surface in 3508, showing mainly the river patterns expected in cleavage facets of grains of solid solution. Crack front entered this area from top left; crack propagation was only slightly affected by the transecting boundary (possibly a grain boundary) at arrows.



Light fractograph

390×

3510 Surface of an impact fracture in a specimen of an as-cast iron-silicon alloy (0.034% C, 1.59% Si) that was broken at room temperature. Crack front entered this area from the top as cleavage and changed to less-perfect cleavage with river patterns at boundary at midheight.



Light fractograph

370×

3511 Impact-fracture surface of a specimen of an as-cast iron-silicon alloy (0.038% C, 4.24% Si) prepared as a 5-lb laboratory casting and broken at room temperature. The fracture entered from top right. The interruptions in crack propagation suggest stress pulsations. See 3512.



Light fractograph

400×

3512 Impact fracture in a specimen of same as-cast Fe-Si alloy as in 3511, also broken at room temperature, showing a portion of a single grain containing cell-like units bounded by intersections of the fracture surface by {112} twins (each cell contains its own river patterns). See 3513.

Light Fractographs, Micrographs: Impact Fractures in Iron-Silicon Alloys 0.038C-4.24Si;
0.042C-4.96Si (Effect of Illumination); 0.038C-11.84Si (Effect of Microstructure)



Light fractograph 400×
3513 Surface of an impact fracture in a specimen of the same as-cast iron-silicon alloy (0.038% C, 4.24% Si) as in 3511, 3512 (preceding page), also broken at room temperature, showing cubic symmetry with {112} Neumann bands (twins).



Light fractograph 800×

3514, 3515

Two obliquely illuminated views of the same facet in the surface of an impact fracture in an iron-silicon alloy (0.042% C, 4.96% Si) cast as an ingot 12 by 12 by 36 in., cooled under hot slag. This facet exhibits mechanical twins (Neumann bands), the sloping surfaces of which are in shadow in 3514 (left), with illumination from below, and are highlighted in 3515 (right), with illumination from above, illustrating the differences in surface level that are caused by twinning. The river patterns on this facet are uninterrupted by the twins.



Light fractograph 800×



Light fractograph 1600×

3516, 3517, 3518

Fractograph 3516 (left) is of the surface of an impact fracture in an as-cast specimen of an iron-silicon alloy (0.038% C, 11.84% Si) cast as a 5-lb laboratory ingot and broken by a hammer blow at room temperature, showing a very elaborate surface pattern. The crack front entered this region from upper right, producing markings that are similar to the chevron markings visible in some low-magnification fractographs; markings like those here have also been likened to a "barley shell" etch pattern. The orientations of the diagonal fissures are believed to have been influenced by crystal structure. The microstructure of this specimen, which is shown in micrographs 3517 (center) and 3518 (right), consists of very large ferrite grains containing intricate networks of what may be surface microcracks.

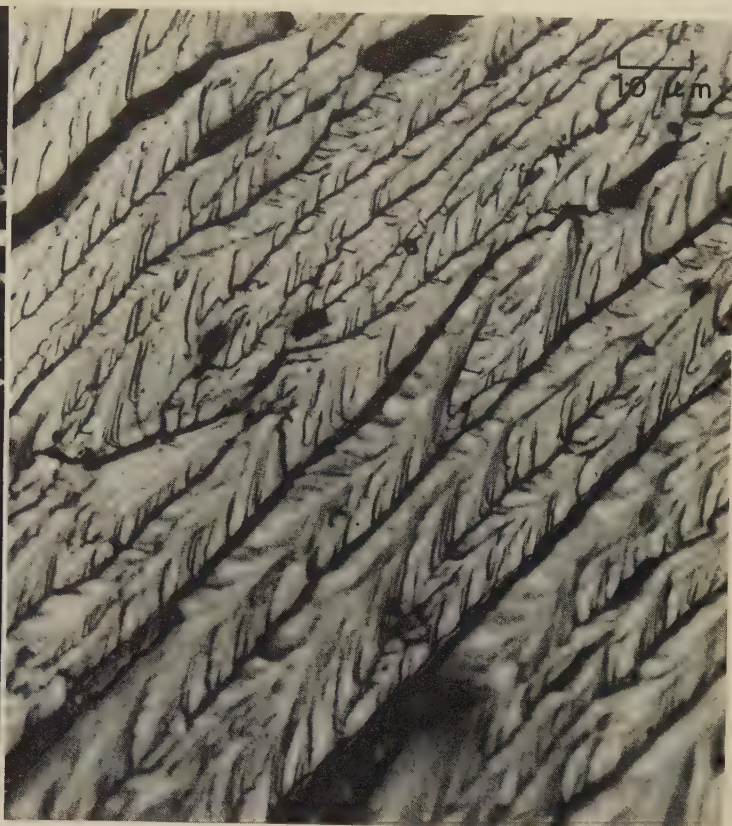


Micrograph (etchant: 20% HNO₃) 97×

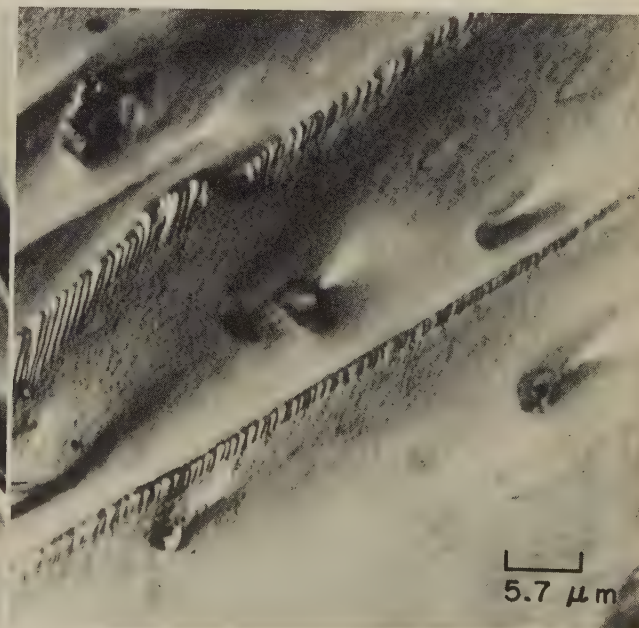
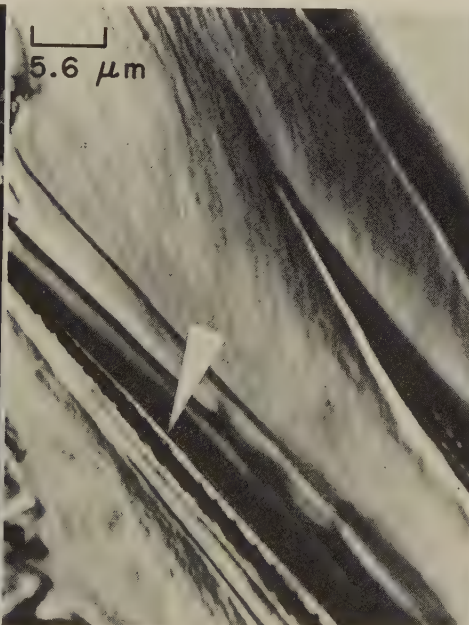
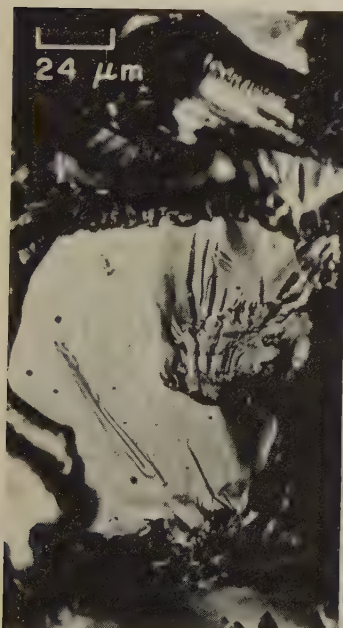


Micrograph (etchant: 20% HNO₃) 970×

Light Fractographs: Room-Temperature Impact Fractures in Iron-Silicon Alloys
0.038C-11.84Si (Effect of Microstructure, Continued) and 0.052C-18.10Si

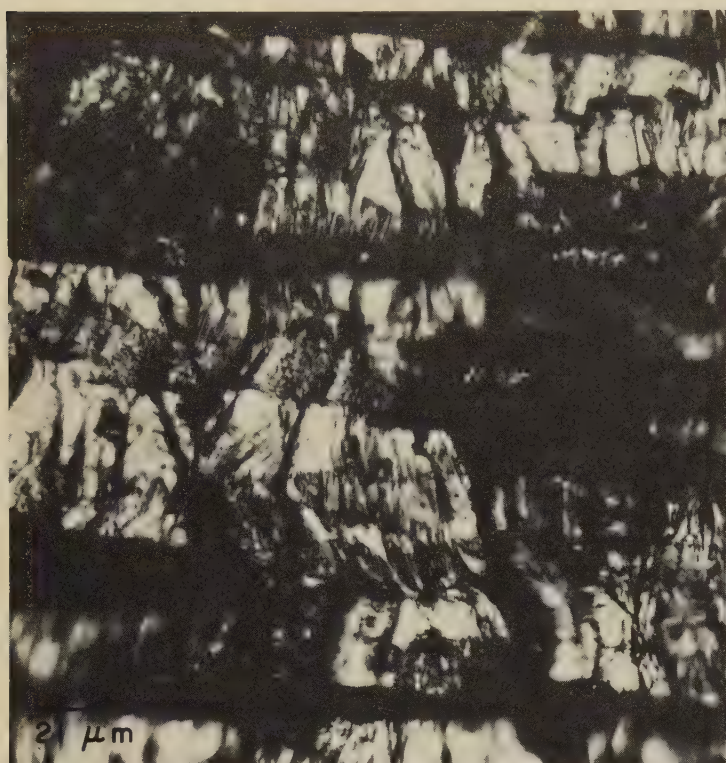


Light fractograph 220× Light fractograph 1090×
3519, 3520 Surfaces of impact fractures in two specimens of the iron-silicon alloy in 3516 (0.038% C, 11.84% Si), also broken at room temperature. Note the very pronounced spines (at arrowheads) in 3519 (left), which are believed to have resulted from the influence of a local multiphase microstructure. The ridge-and-groove fracture markings exhibited in 3520 (right), which are similar to those in 3519, suggest a lamellar microstructure.



Light fractograph 420× Light fractograph 1775× Light fractograph 1765×
3521, 3522, 3523 Surfaces of impact fractures in three specimens of an iron-silicon alloy (0.052% C, 18.10% Si) that were taken from a 5-lb laboratory ingot and broken at room temperature. Fractograph 3521 (left) shows a typical cleavage facet in the epsilon phase (FeSi). The fracture behavior is glasslike. Fractograph 3522 (center) exhibits features (such as the one at arrowhead) with an unusual needlelike form, embedded in ferrite dendrites. These features are believed to be solid-state precipitates, possibly the eta phase (Fe_5Si_3). Fractograph 3523 (right) shows unusual parallel ridges with edges containing lamellae of fairly uniform thickness. Very faint fracture-progress markings, particularly at inclusion sites, indicate that the crack front proceeded from lower left to upper right, parallel with the ridges.

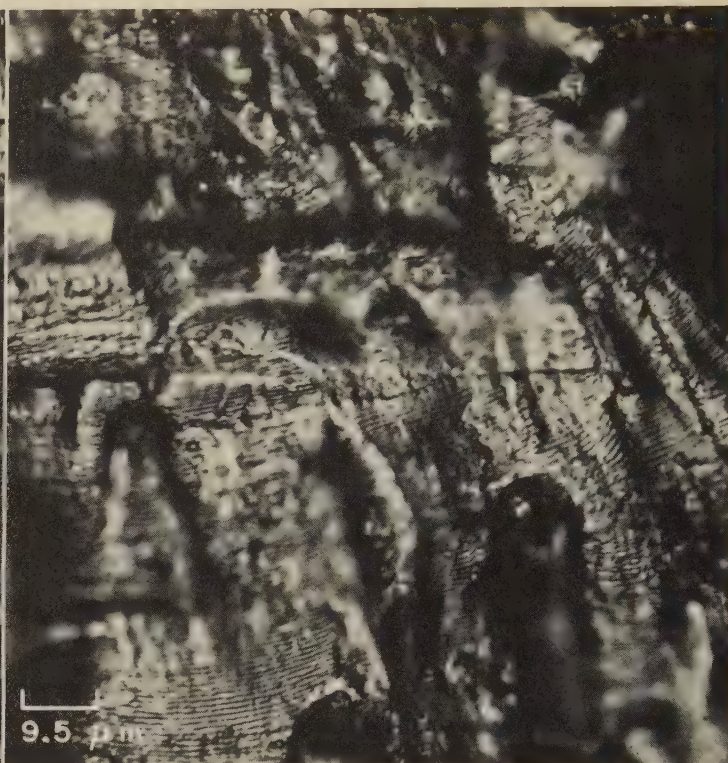
Light Fractographs: Aluminum Alloy 7076-T6 Fractured by High-Cycle Fatigue, by Notched Impact (Adjacent to Fatigue-Fracture Surface), and by Low-Cycle Fatigue



Light fractograph

3524, 3525

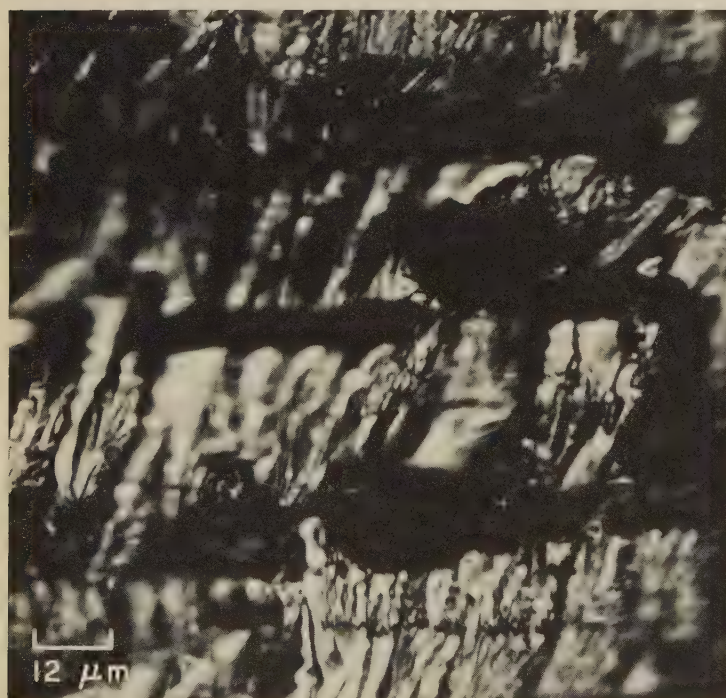
475×



Light fractograph

1050×

Two views, at different magnifications, of the surface of a high-cycle fatigue fracture in a specimen of aluminum alloy 7076-T6 cut from a 0.188-in.-thick sheet and tested in completely reversed bending, at a maximum stress of 172 MPa (25 ksi) and at room temperature, to failure at 336,000 cycles. Propagation of the fatigue fracture created strata (possibly the traces of grain boundaries) along planes normal to the bending direction. Fatigue striations can be seen faintly within the strata in 3524 (left) and are clearly visible in 3525 (right), each striation having resulted from one full cycle of bending-stress reversal. See also 3526 and 3527.



Light fractograph

3526

850×



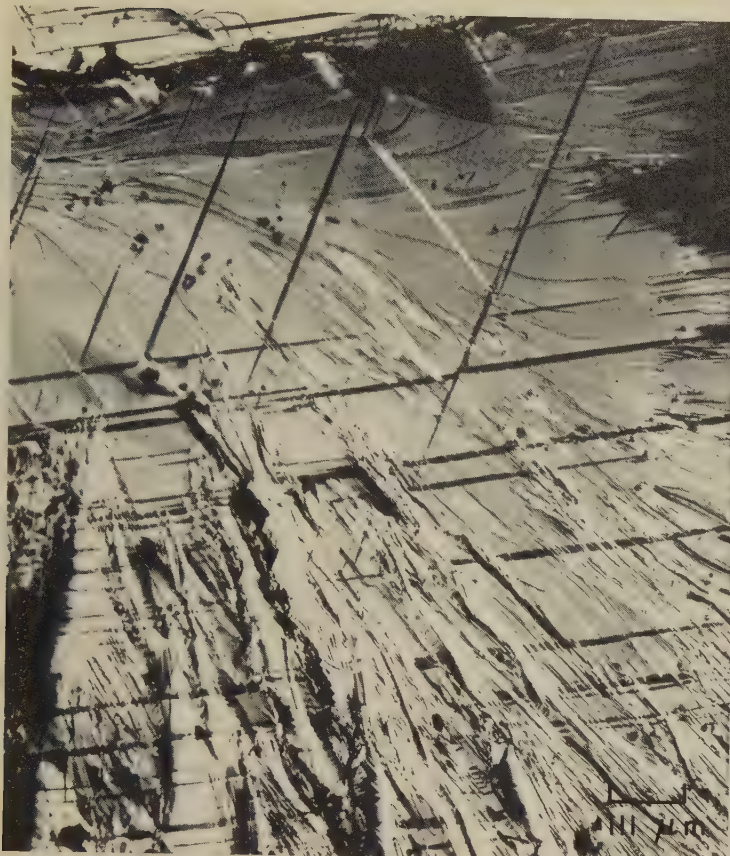
Light fractograph

475×

Fracture in the aluminum alloy 7076-T6 specimen in 3524 and 3525, obtained by notching 0.25 in. from the fatigue-fracture surface in those views and breaking by impact at room temperature. Strata like those in 3524, presumed to have been caused by the fatigue test, are present here, but were absent in a similar impact fracture (not shown) 0.60 in. from the fatigue fracture.

Surface of a low-cycle fatigue fracture in a specimen of the same aluminum alloy 7076-T6 sheet shown in 3524, 3525 and 3526. This specimen was tested in reversed bending at a maximum stress of 310 MPa (45 ksi) and failed at 18,000 cycles. The surface is considerably more distorted than that shown in 3524, but scattered fatigue striations are visible.

Light Fractographs: Cleavage Fractures Produced by Room-Temperature Impact in Specimens of Cast Polycrystalline Antimony (99.83% Sb), As-Cast and After Heat Treatment

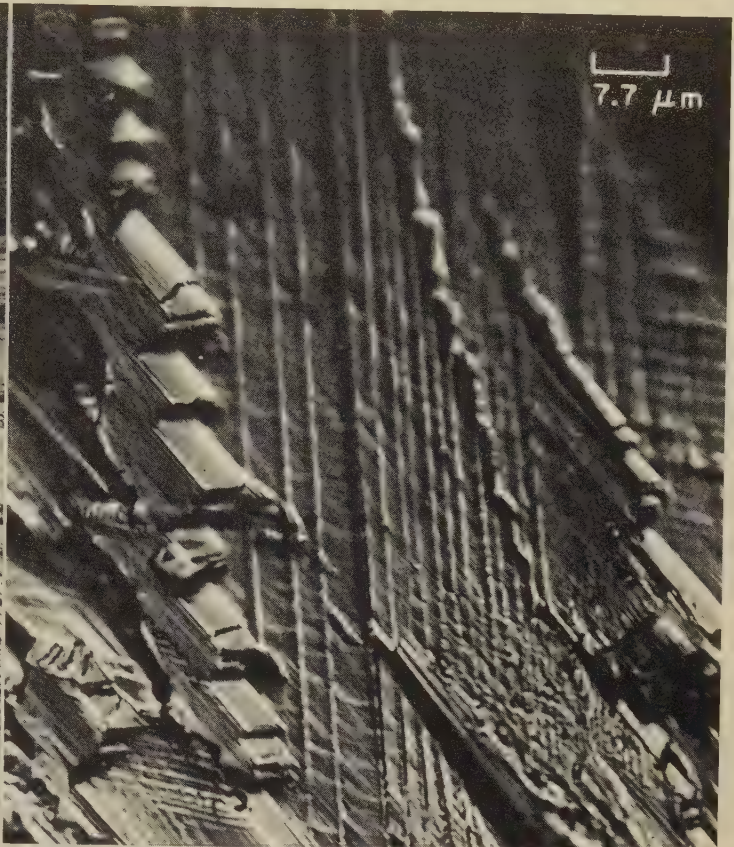


Light fractograph

3528, 3529

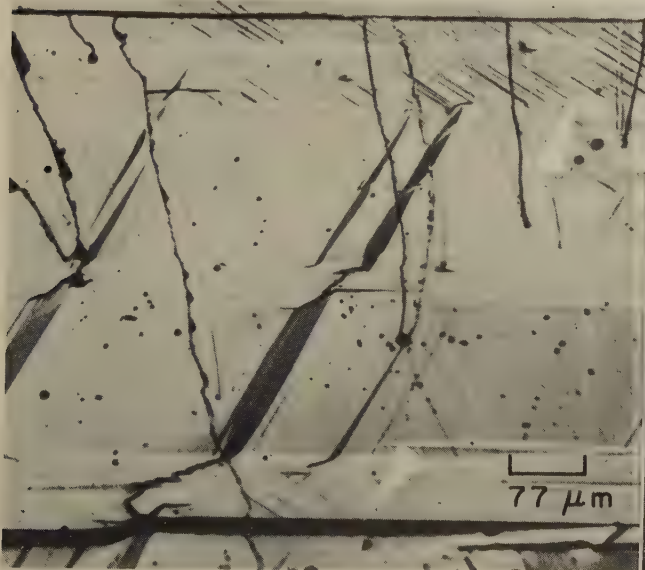
Two dissimilar regions of the surface of a cleavage fracture produced by impact at room temperature in as-cast polycrystalline antimony (99.83% Sb, 0.04% S, 0.035% As, 0.035% Pb, 0.015% Fe, 0.01% Cu). In the region shown in 3528 (left), the crack front entered at upper left as cleavage on the (0001) basal plane. The three sets of trigonally symmetrical bands with mutual angles of 60° are intersections of the fracture surface by a $\{10\bar{1}4\}$ system of twins. Fractograph 3529 (right) shows the surface of a secondary crack, which contains elaborate detail involving intersecting traces of both $\{10\bar{1}4\}$ and $\{10\bar{1}1\}$ planes (determined by measurement of relative angles). The vertical steps (at left and at right) in this complicated fracture path suggest a mosaic formed by defects.

90×



Light fractograph

1300×



Light fractograph

3530, 3531

Surfaces of basal-plane (0001) cleavage fractures produced by impact at room temperature in two specimens of the same polycrystalline antimony as in 3528 and 3529 (above). Fractograph 3530 (left) shows a fracture in as-cast material, which is characteristic of fractures produced in this material at temperatures within the range of -196°C (-321°F) to 631°C (1168°F). The heavy, dark bands (such as the one at the arrowhead at bottom) are first-order twins, and the fine lines (arrowhead at upper right) are second-order twins, or "twins within twins". The fracture shown in 3531 (right) was produced after the specimen had been heated in helium to 650°C (1202°F) and furnace cooled. As in 3530, the bands were caused by twinning, which occurred on $\{10\bar{1}4\}$ planes.

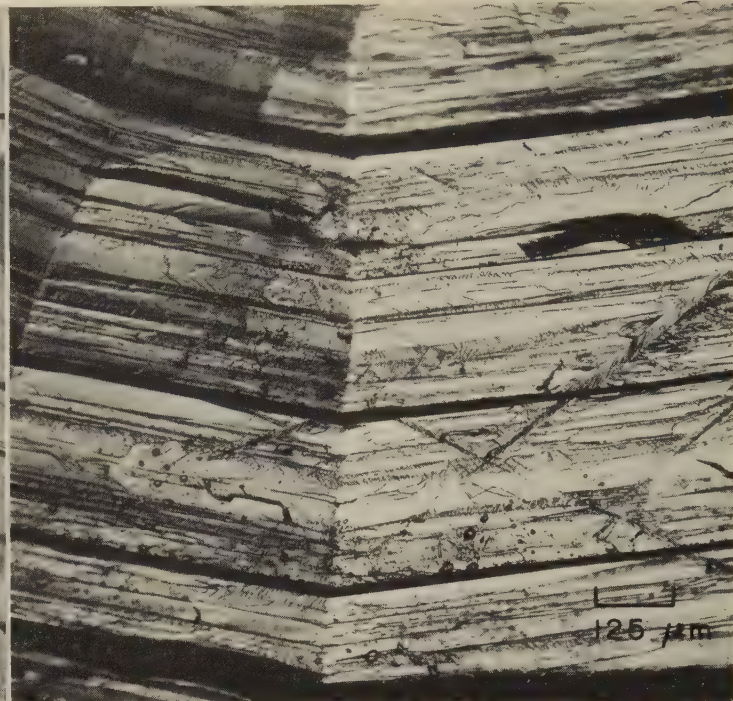
130×

Light fractograph



860×

Light Fractographs: Cast Specimens of CP-Grade Bismuth (99.8% Bi) Fractured by Impact at Room Temperature, Showing the Influence of Crystal Structure



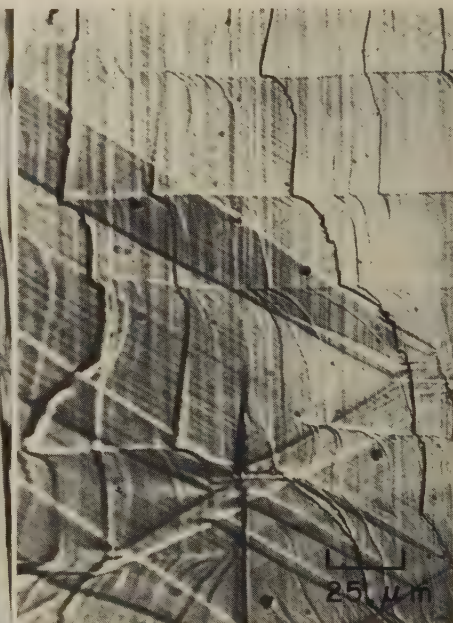
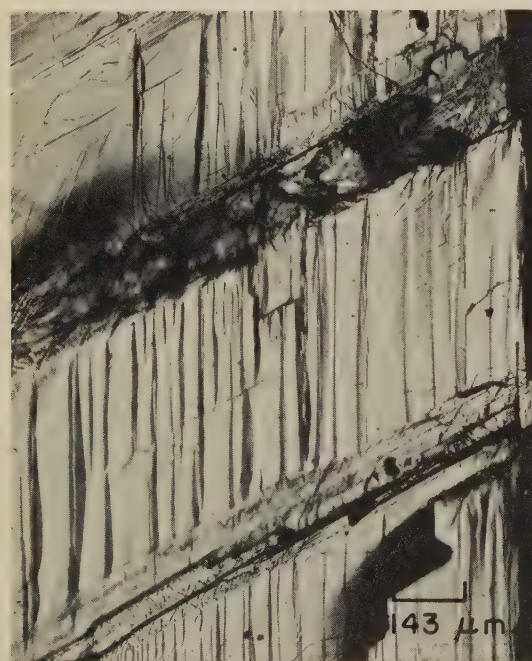
Light fractograph
3532, 3533

500×

Light fractograph

80×

Surfaces of room-temperature impact fractures in two specimens of as-cast CP-grade bismuth (99.8% Bi, 0.01% Ag, 0.005% Pb, 0.01% Fe, 0.005% Cu, 0.01% S). Fractograph 3532 (at left) shows a cleavage facet conforming approximately to a basal (0001) plane and showing cleavage steps crossing three parallel twin bands that are remarkably uniform in width. At right (fractograph 3533) is a transverse fracture surface in a specimen that was produced by melting the bismuth in a gas flame, drawing it up into a Pyrex tube, and cooling in contact with the melt. The sharp, roughly vertical discontinuities are radial dendrite boundaries resulting from crystal growth conforming to the curvature of the tube. Angle measurements suggest that this is an (00 $\bar{1}$ 1) facet crossed by {10 $\bar{1}$ 4} twins and {0001} basal planes.



Light fractograph

70×

Light fractograph

70×

3534, 3535

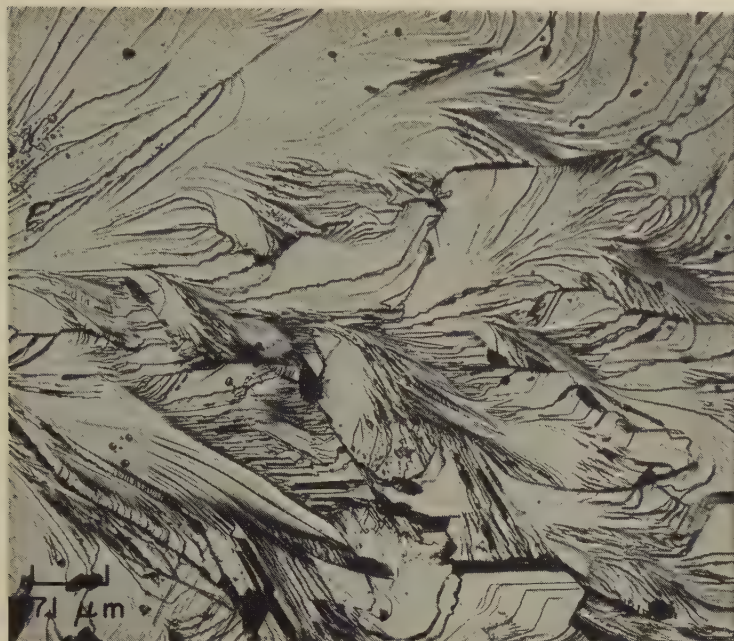
Matched fractographs of two intersecting cleavage facets produced by room-temperature impact fracture of a single grain of CP-grade bismuth prepared to illustrate the identification of crystallographic planes by comparison of common features. At left (fractograph 3534) is a typical facet of a basal (0001) plane, with broad diagonal bands that are intersected at right by the secondary cleavage facet that is shown in the fractograph at right (3535). Reference to the faces of a model of a bismuth crystal permits explicit identification of the broad bands as {10 $\bar{1}$ 4} twins, the vertical laminae as {0001} planes, and the secondary cleavage facet as a (10 $\bar{1}$ 1) plane.

Light fractograph

400×

3536 Room-temperature impact fracture in CP-grade bismuth, showing horizontal wavy lines (called "riffls") caused by kinking on the {11 $\bar{2}$ c} family of planes. Also visible are several shaded bands that are shown to be twins by intersections at bottom of view. Cleavage steps were formed after "riffls" and twins; then came the formation of the vertical striations.

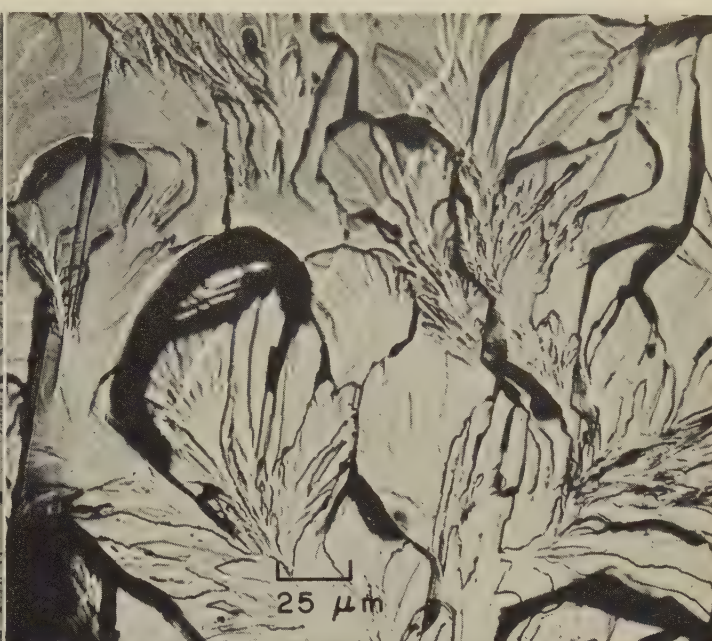
Light Fractographs: Cast Bismuth Alloys (90Bi-10Sb, 10Bi-90Sb, 97Bi-3Zn and 96Bi-4Zn)
Fractured by Impact, Showing Effects of Structure



Light fractograph

3537, 3538

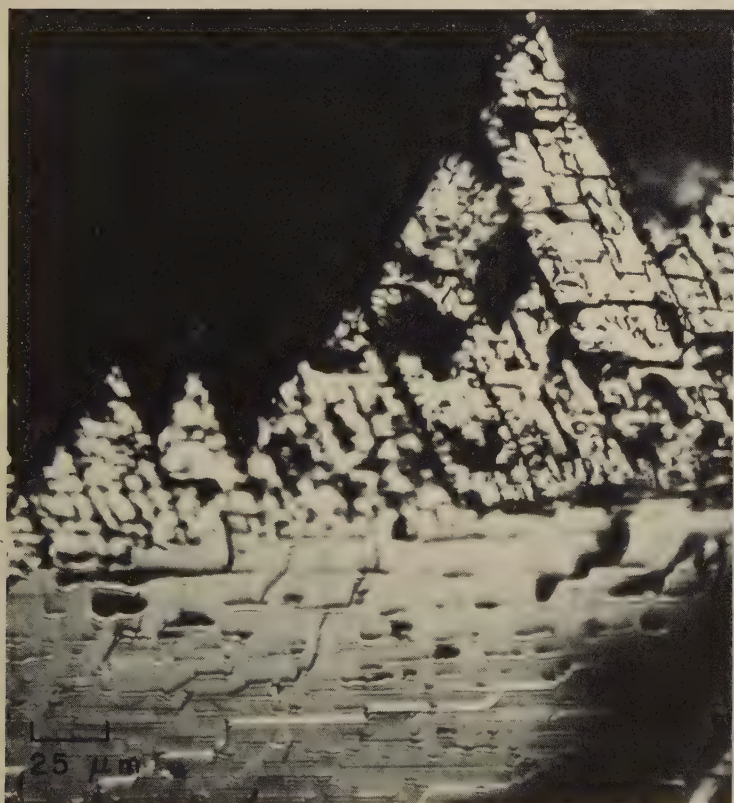
140×



Light fractograph

400×

Two similar fracture surfaces of as-cast specimens of antimony-bismuth alloys having markedly different compositions. Specimens were prepared by furnace cooling the molten alloy from 700 C (1292 F) and then were broken by impact at room temperature. Specimen at left (fractograph 3537) analyzed 89.79% Sb, 9.89% Bi, 0.22% As; it shows a basal-plane type of cleavage facet with departures from a true plane that resemble river patterns. Specimen at right (fractograph 3538) analyzed 89.51% Bi, 10.35% Sb, which is nearly an analogue of the composition of the specimen at left. Allowing for the difference in magnifications, the fracture surface in 3538 is remarkably like that in 3537, showing a complex system of cleavage steps that separate smooth, nearly perfect planar areas.



Light fractograph

3539, 3540

400×

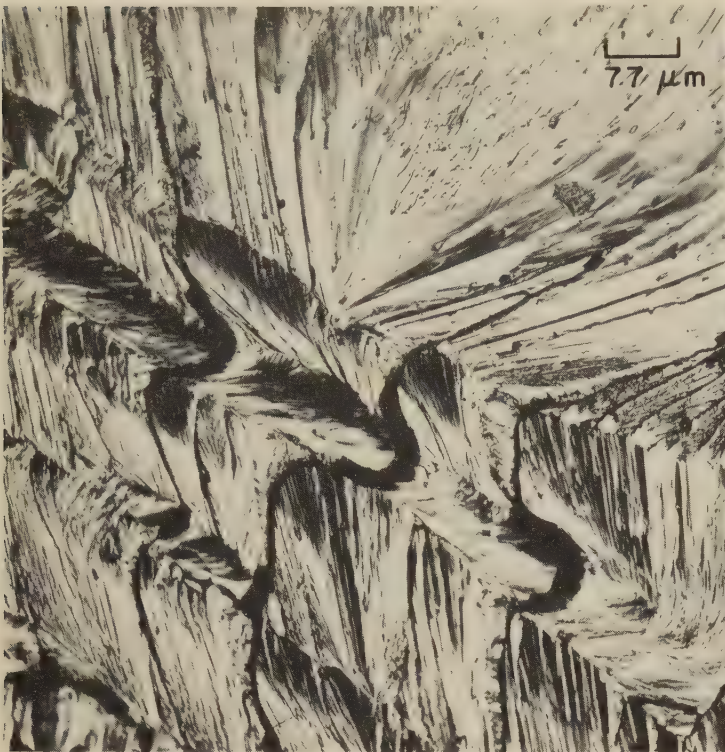


Light fractograph

200×

Two markedly different fracture surfaces of specimens of bismuth-zinc alloys with similar compositions. Both specimens were melted under helium, superheating in fused-quartz tubes to 500 C (932 F) before freezing, and were fractured by impact at -196 C (-321 F). Specimen at left (fractograph 3539), of 97% Bi-3% Zn, displays an area (above center) of unusual trigonal symmetry; in the area below center, excess zinc (eutectic composition is near 2.7% Zn) may have been enclosed in the eutectic. Specimen at right (fractograph 3540), of 96% Bi-4% Zn, consists of a complex array of zinc-rich dendrites in a eutectic matrix; note the 60°-related angles between the secondary planar fissures. Fractograph 3540 was made using special oblique illumination.

Light Fractographs: Vacuum-Arc-Cast Molybdenum Fractured by Impact at Room Temperature, Showing Effect of Oxygen Content and Cold Work



Light fractograph

130×

Light fractograph

1500×

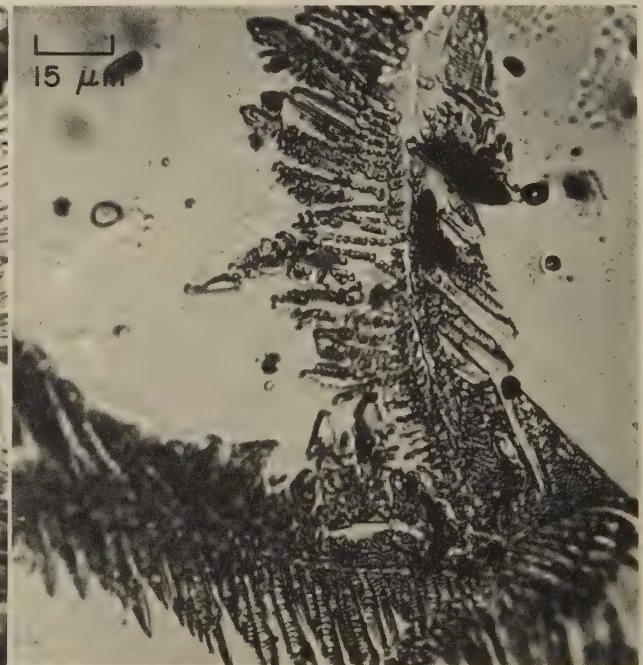
3541, 3542 Two views of an impact-fracture surface of an as-cast specimen of forgeable high-carbon molybdenum. Specimen was made by vacuum-arc melting pressed molybdenum powder, deoxidizing the melt by addition of 0.04% C, and then chill casting on a water-cooled copper starting plug. Fracture was by a single blow at room temperature. Fractograph at left (3541) shows a transgranular facet with a complex rupture path that may reflect the influence of chill casting. Fractograph at right (3542) is a highly magnified view of a facet that is believed to contain cleavage and twinning. Dark boundaries in 3542 may be cleavage steps; light ridges may be twins lying at angles of about 67° , which is consistent with mutual intersections of the $\{112\}$ family of planes.



Light fractograph

235×

3543 Surface of an impact fracture in a vacuum-arc-cast specimen of high-oxygen molybdenum that was cold worked after casting, by hammering, then broken at room temperature. Preheat of the melt was to 2600 C (4712 F). Region at upper left resembles the fracture details at lower left in fractograph 3541. The many separate crack fronts are in sharp contrast to the smooth secondary cleavage that slopes to lower right.

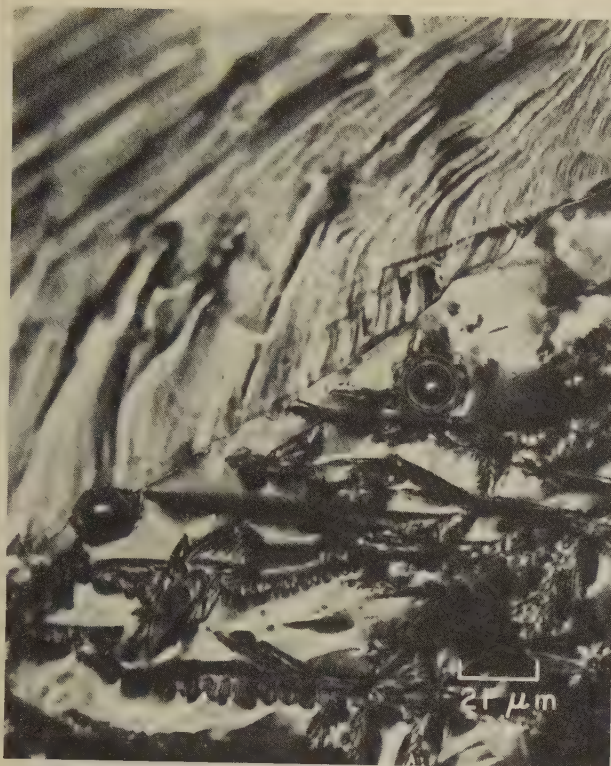


Light fractograph

660×

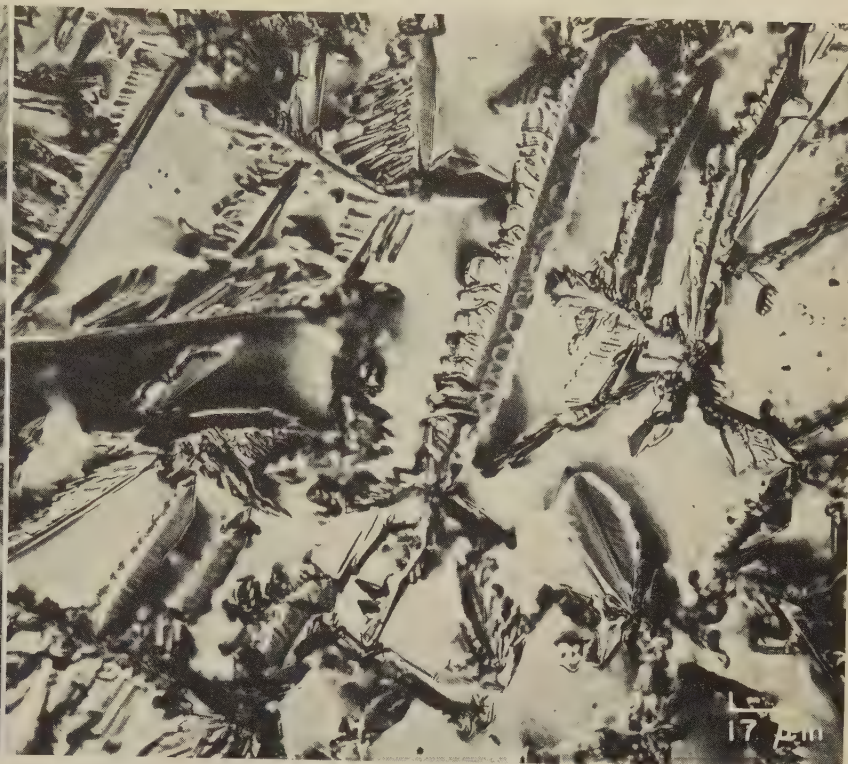
3544 Room-temperature impact fracture in vacuum-arc-cast molybdenum that contained high oxygen and was not forgeable. Cleavage has exposed an internal penetration of MoO_3 along both sides of what is believed to be a grain boundary. The MoO_3 inclusion appears as a beaded and fernlike growth, probably on an intergranular surface. See 3548, on the opposite page.

Light Fractographs: Vacuum-Arc-Cast Molybdenum Fractured by Impact at Room Temperature, Showing Effect of Carbide and Oxide Inclusions



Light fractograph (composite)

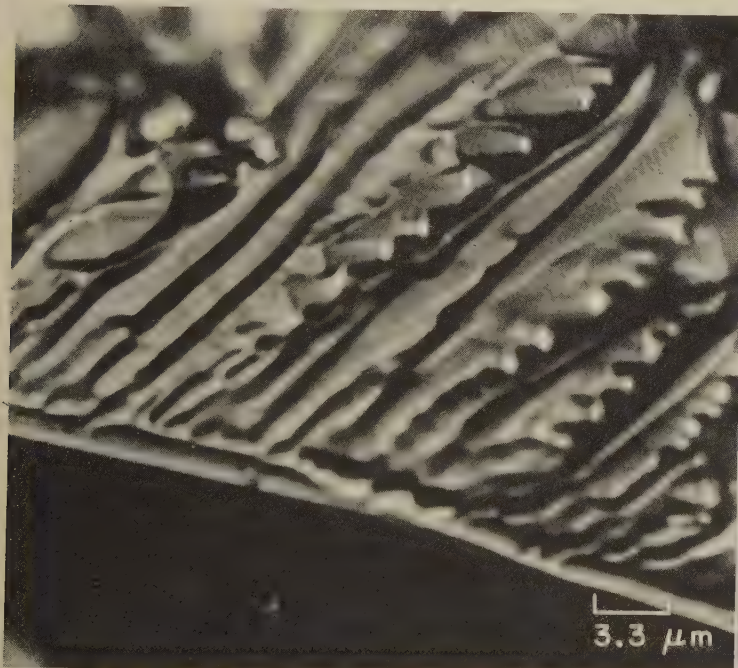
475×



Light fractograph

600×

3545, 3546 Two views of the surface of an impact fracture in a specimen of vacuum-arc-cast molybdenum that was broken at room temperature, displaying different fracture mechanisms. At left (3545) is a composite fractograph of an area in which the crack front entered from upper right as a transgranular separation but, on encountering the diagonal grain boundary, was abruptly deflected and changed to an intergranular separation. The deflection was so great that both facets could not be brought into simultaneous focus, and two exposures were necessary. The lower facet in 3545, and the view of the fracture surface in 3546, both display featherlike carbide inclusions against featureless separated-grain surfaces. (See 3547, below, for a high-magnification view of one of these carbide "feathers".) The spheroidal features in 3545 are gas cavities.



Light fractograph

3000×

3547 A high-magnification view of a molybdenum carbide "feather" precipitated at a grain boundary in an impact-fractured specimen of vacuum-arc-cast molybdenum. These grain-boundary carbides, which are visible in the lower part of composite fractograph 3545 and in fractograph 3546, do not represent any harmful effect on the forgeability of cast molybdenum.



Light fractograph

660×

3548 View of a different area in the fracture surface of the high-oxygen, vacuum-arc-cast molybdenum specimen in fractograph 3544 (facing page), showing a less common form of molybdenum oxide than the granular structure visible in 3544. This oxide inclusion has a structure similar to a palmetto leaf, and indicates an extremely advanced stage of oxidation.

Light Fractographs: Room-Temperature Impact Fractures in Vacuum-Arc-Cast Tungsten,
Showing Effects of Deoxidation With Carbon and With Aluminum



Light fractograph

3549, 3550

Two views of the surface of a room-temperature impact fracture in a specimen of vacuum-arc-cast tungsten that was deoxidized by addition of 0.04% C to the melt. Fractograph 3549 (left) shows a system of cleavage facets separated by pronounced cleavage steps. Many of these steps originated at small pits or inclusions. Fractograph 3550 (right) reveals a more regular region of the fracture surface, showing many markings that cross the direction of crack propagation. These markings may have resulted from brief pauses in crack growth or from changes in crack-growth direction caused by microstructural features. At bottom in 3550, tungsten carbide inclusions are visible at a grain boundary. These inclusions faintly resemble the molybdenum carbide inclusions in 3545, but there is no suggestion here of the wide distribution of carbides that is evident in 3545.

450×



Light fractograph

725×

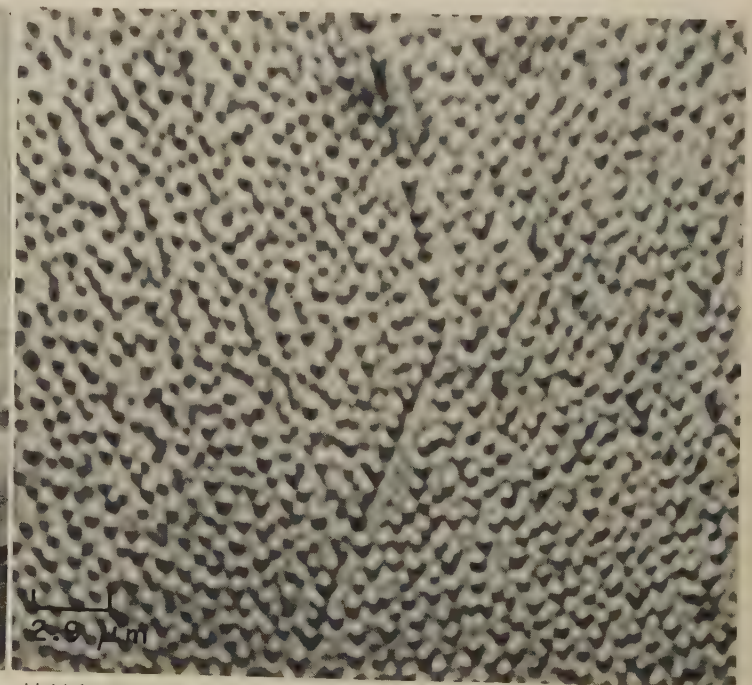


Light fractograph

3551, 3552

Two views of the surface of a room-temperature impact fracture in a specimen of vacuum-arc-cast tungsten that was deoxidized by adding 1.0% Al to the melt. The fracture was intergranular, as shown in 3551 (left). Many fine grain boundaries or subgrain boundaries are visible. Several gas cavities are present; the protuberances presumably are inclusions. The fine grain boundary. See also fractograph 3553 (on the opposite page).

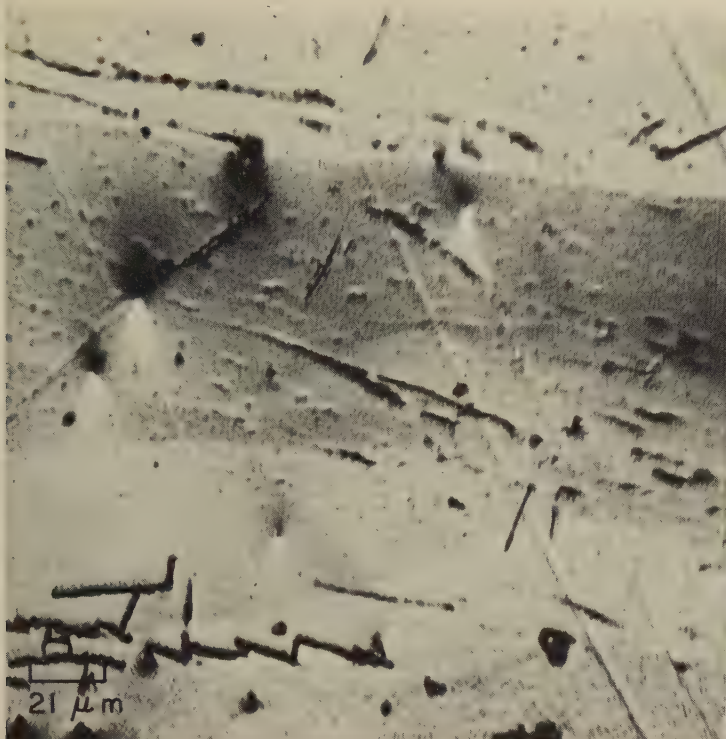
200×



Light fractograph

3400×

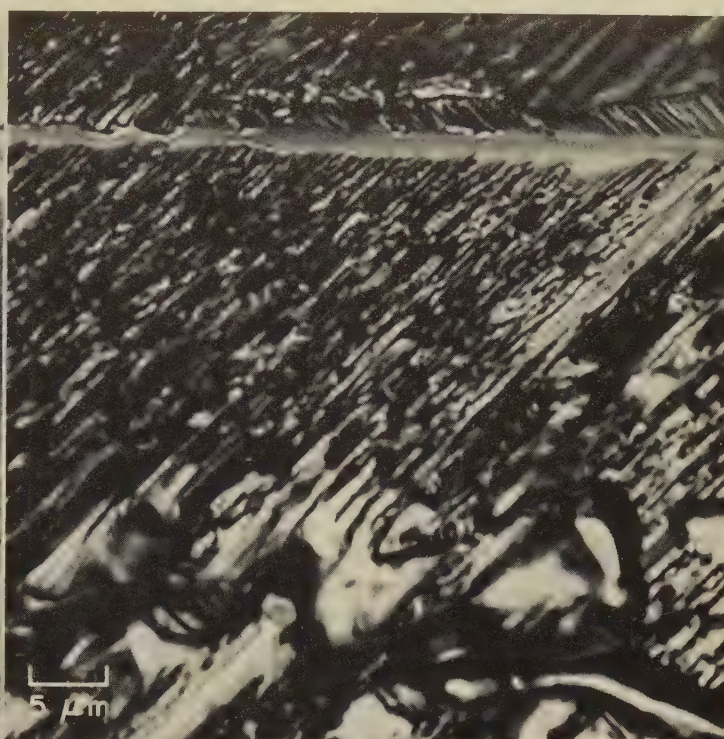
Light Fractographs: Effects of Deoxidation on Fractures in Vacuum-Arc-Cast Tungsten (Continued);
Impact Fractures in Rods Made by Hot Swaging 99.9+ % Tungsten Powder Compacts



Light fractograph

475×

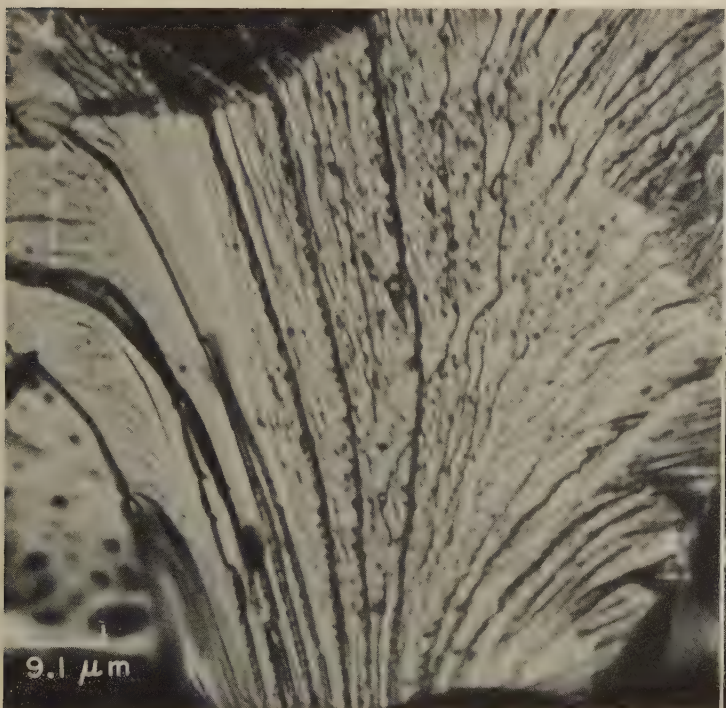
3553 Surface of a room-temperature impact fracture in a specimen of the same aluminum-deoxidized tungsten as in 3551 and 3552. Here, fracture was by transgranular cleavage. The diagonal lines are crystallographic markings that show that the differently shaded zones are regions of a single grain. The jagged lines are a precipitate, possibly Al_2O_3 .



Light fractograph

2000×

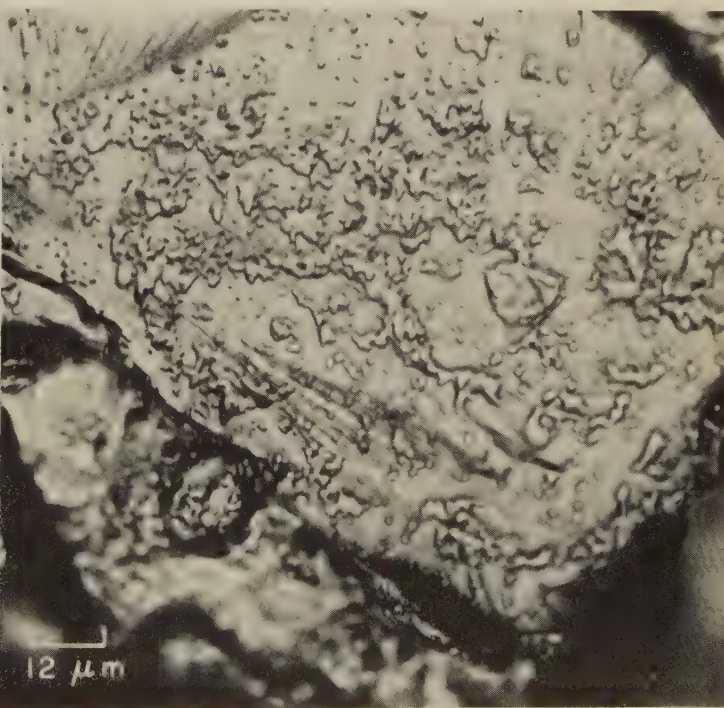
3554 Surface of a room-temperature impact fracture in a specimen of vacuum-arc-cast tungsten deoxidized by adding 0.04% C to the melt, showing crystallographic fracture patterns involving a spine (near top of fractograph). In spite of its appearance, the demarcation at bottom is not a grain boundary, because the fracture lines cross it unaltered.



Light fractograph

1100×

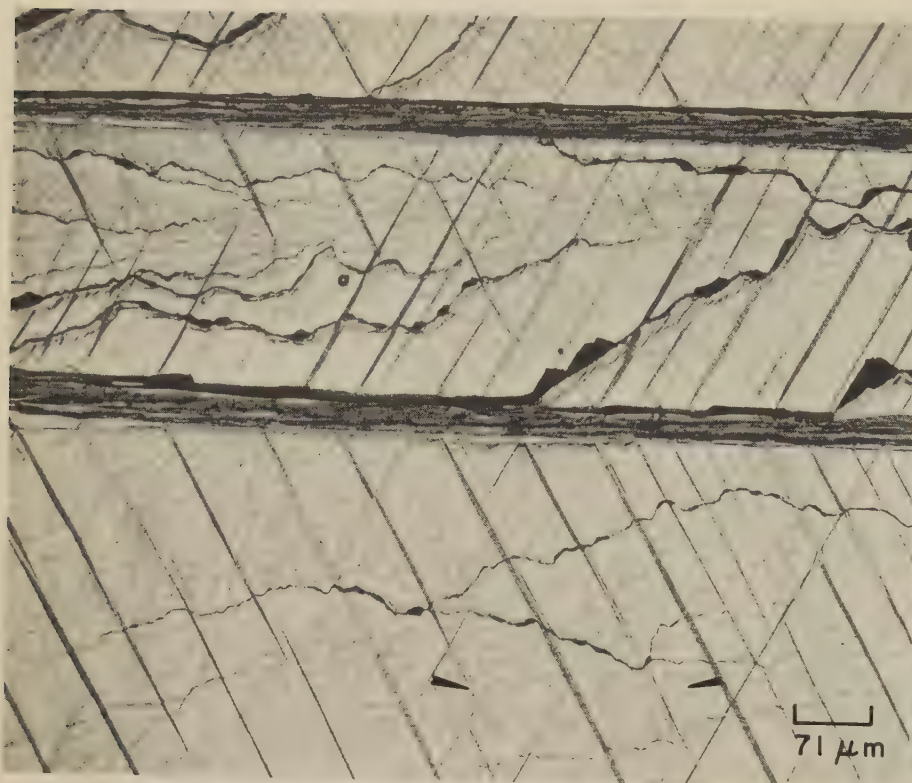
3555, 3556 Surfaces of room-temperature impact fractures in two tungsten rods prepared by hot swaging compacts of high-purity tungsten powder containing a small percentage of rare earths (99.9+ % W, <0.02% R_2O_3). In 3555 (left), the presence of pits and particles in the central region suggests incomplete densification; the fracture patterns at left and at right closely resemble those in cast metal. In 3556 (right), it is evident that incomplete bonding was achieved in swaging, leaving small islands of coalesced powder not joined to the major grain. These islands provided paths of weakness that determined the entire fracture path, producing in a sense an intergranular fracture.



Light fractograph

850×

Light Fractographs: CP-Grade and 99.999% Zinc Fractured by Impact at Room Temperature, Showing Influence of Crystal Structure



Light fractograph

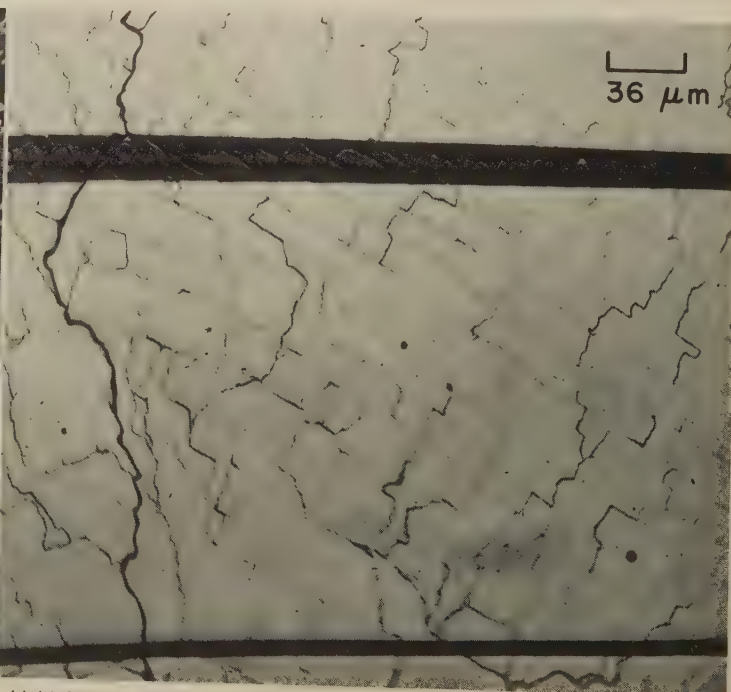
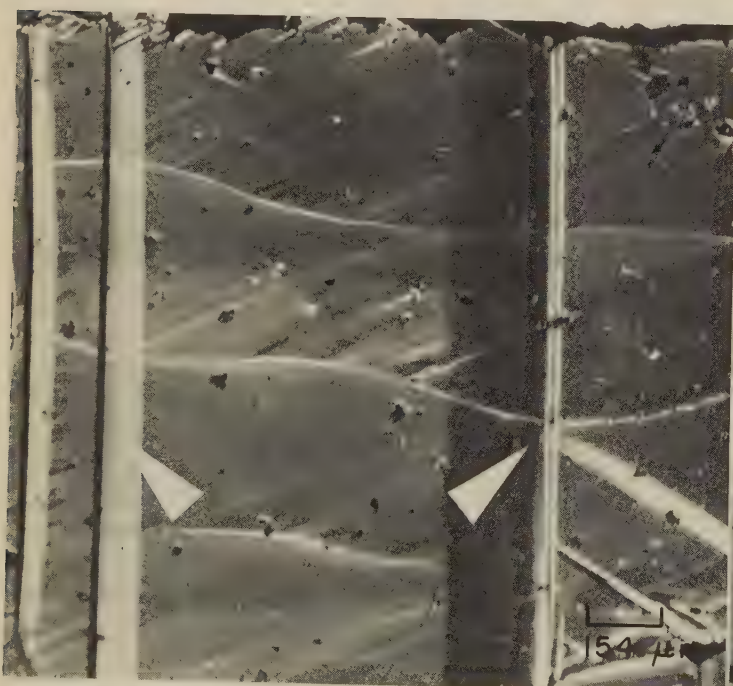
3557, 3558

Two views, each showing a basal plane (0001) cleavage facet in a single grain in impact-fracture surfaces of polycrystalline specimens of CP-grade zinc broken at room temperature. In fractograph 3557 (left), the heavy horizontal marks are $\{10\bar{1}c\}$ twin bands; the lighter, diagonal marks are either twin or kink bands; and the faint vertical lines (at arrows) may be tracings of $\{11\bar{2}c\}$ planes. Specimen in fractograph 3558 (right) was heavily deformed in compression before being fractured. This view shows heavy vertical and diagonal $\{10\bar{1}c\}$ twin bands plus accommodation kink bands, and (at arrow) light traces of $\{2\bar{1}\bar{1}c\}$ planes at 60° to horizontal.

140×

Light fractograph

125×



Light fractograph

3559, 3560

Impact-fracture surfaces of two specimens of 99.999% zinc that were broken at room temperature. At left (fractograph 3559) is the basal cleavage of a single crystal, photographed with an opaque-stop metallograph, showing a pair of twins (at arrowheads) with opposite slopes. The shading also indicates opposite slopes for the accommodation kink bands adjacent to the twins. Fractograph 3560 (at right) is of a cast polycrystalline specimen. The light, diagonal traces may be of a $\{11\bar{2}c\}$ form that is akin to the faint vertical markings at the arrows in fractograph 3557; note that these traces deflect the many fine secondary fissures but that the dark, horizontal bands are entirely unaffected.

65×

Light fractograph

275×

Scanning-Electron-Microscope (SEM) Fractographs

Prepared by John A. Fellows

CONTENTS

Pure iron; iron with special additives; low-carbon irons;	
Armco iron	162-169
0.04 to 0.08% C steels	170-171
1015, 1020, 1021, 1022, 1025 and	
ASTM A36 steels	171-175
1042, 1050, 1060, 1080 and	
1090 steels	176-183
1095 and 1115 steels	183
4070 steel	184
4130 steel	184-186
4140 steel	187
4340 steel	188-192
HY-180 steel	192
High-strength steel	193
300M steel	194-195
5155 steel	196
50100 and 52100 steels	197
Nitrided 7140 steel	198
8740 steel	199-201
Fe-3.9Ni and Fe-0.3Ni alloys	202
0.20C-1.0Mn-3.05Ni-1.65Cr-0.5Mo	
and 3.5Ni-1.5Cr-0.5Mo-0.1V steels	203
Fe-12Ni-0.5Ti alloy	204-205
18% Ni, grade 300, maraging	
steel	206-209

H11 tool steel	210-213
Fe-6.4Cr-3.2Ta alloy	214
Fe-6.2Ta alloy	214
0.18C-3.85Mo and 0.41C-4.2Mo steels	215
0.3C-0.6Mn-5.0Mo steel	216
0.4C-0.6Mn-5.0Mo and	
0.42C-2.1Mo-5.2Co steels	217
0.43C-3.85Mo-9.0Co steel	218
13-8 PH stainless steel	219-221
17-7 PH stainless steel	222-223
Type 301 stainless steel	223
Type 304 stainless steel; 0.20C-	
2.0Mn-1.0Si-13.5Cr-8.8Ni-	
3.0Mo stainless steel	224
15.8Cr-12.5Ni and type 316L	
stainless steels	225
Alloys A-286 and Hastelloy X	225
Refractaloy 26 alloy	226
Alloy 718	227-229
U-700 alloy	230
Waspaloy alloy	231
MAR-M 200 alloy	231-232
IN-100 alloy	232-233
Alloy 713C	234
Duranickel alloy	235
Nickel 201	236

Aluminum casting alloys:	
333	237
356-T6	238-243
Wrought aluminum alloys 1100,	
2014-T6, 2024-T4 and -T3	244-249
Wrought aluminum alloys 7075-T6	
and -T651, and 7475-T6	249-261
67Al-33Cu eutectic alloy	262-263
Boron-fiber, Al-matrix and Ti-	
matrix (BORSIC) composites	264
Graphite-fiber, magnesium-	
matrix composite	265
99.999% copper	266-267
OFHC copper; free-machining	
copper (with Te)	268
Cu-2.5Be alloy;	
64Cu-27Ni-9Fe alloy	269
Iridium wire and sheet	270
Lead-tin solders	270-272
Alloy HM21A (97Mg-2Th-1Mn)	272
TZM alloy (Mo-0.5Ti-0.08Zr)	272
Titanium alloy Ti-5Al-2.5Sn	273
Titanium alloy Ti-6Al-4V	273-279
Tungsten-fiber, silver-matrix	
composite	279
Zircaloy-2; Zircaloy-4	280

THE SEM fractographs in this section were provided by the contributors listed on pages 127 and 128. Some of the fractures shown have been reproduced only by high-magnification SEM fractographs; others are shown both in photographs and in low-magnification light fractographs as well as in SEM fractographs at high magnification; in certain instances, a sequence of SEM fractographs has been made available that reproduces the fracture at successive stages of magnification from very low to very high. Where appropriate, photomicrographs of internal structure details that contributed to the cause of the fracture have been included.

With but a few exceptions, the SEM fractographs are single views of the conventional type that normally are taken at an angle between 30° and 45° to the plane of the fracture surface in order to lend a three-dimensional aspect to the picture. In many instances, the fracture surfaces have been shadowed with a metal such as platinum, palladium or chromium to provide increased contrast. The nominal magnification is noted below the right edge of each print, and a magnification marker designating an equivalent length in microns is shown in all views except those at less than 50 diameters.

The exceptions to the general category of SEM fractographs are stereo pairs,

which are presented as fractographs 3563 (page 162), 3573 (page 165), and 4121 through 4132 (pages 266 and 267). These display remarkable three-dimensional features when viewed according to the recommendations given in the Introduction to the section on Comparison of SEM and TEM Stereofractographs (pages 281 and 282). A simple cardboard stereo viewer is provided in the pocket on the inside back cover of this volume, and the reader is urged to accustom himself to its use to gain the full advantage of seeing these stereographs in 3-D. Most readers, in fact, should be able to train their eyes with relatively little effort to see the stereo pairs in 3-D without a viewer, following the suggestions under "Stereoscopic Viewing" on pages 281 and 282.

The fracture mechanisms identified in the SEM fractographs in this section, and the various types of loading that produced these fractures, both represent the range of normal experience. The fracture mechanisms and loading types appear in a haphazard sequence throughout the section, however, because the arrangement has been by alloy type rather than by type of fracture, as is indicated in the Contents List above.

Tension-overload fractures are shown for a wide variety of specimens and conditions, including unnotched specimens,

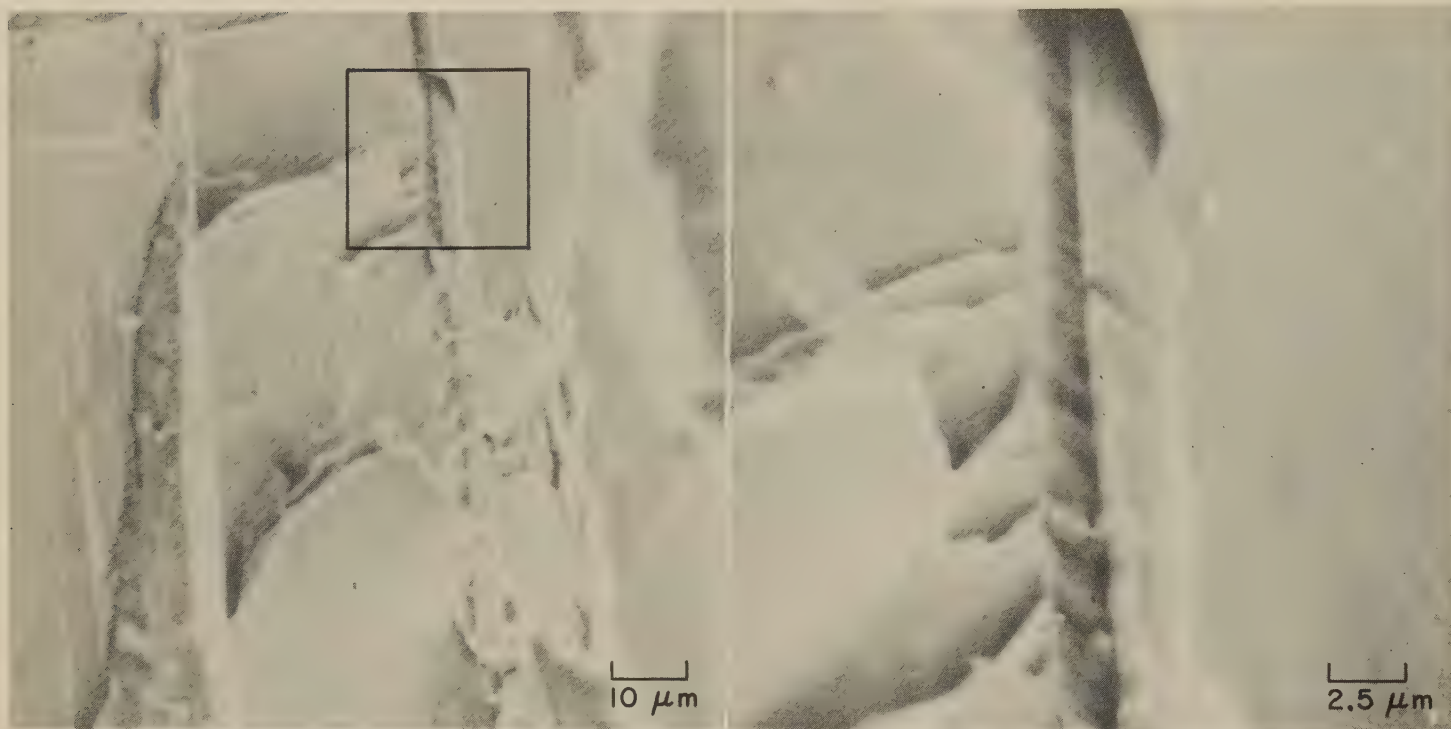
fracture-toughness specimens, specimens of different heat treatments, and tests conducted at assorted temperatures and under various atmospheres. Many service fractures are also included.

Fatigue loadings are second only to tensile loadings in frequency of representation in the fractographs here. They include high-cycle and low-cycle categories plus tension-tension and tension-compression types. Examples of fatigue in corrosive mediums and in embrittling atmospheres are also represented. Service fractures are represented as well as laboratory-test fractures.

Many impact fractures are reported; a significant number of these occurred at -196 C (-321 F), but others occurred at room temperature and above. Other types of loading represented are bending, reversed bending, rotary bending, torsion, and elevated-temperature loadings of creep and stress-rupture tests.

The fracture features that are displayed by the SEM fractographs include: cleavage and quasicleavage facets; equiaxed, shear and tear dimples; fatigue striations; intergranular facets; and examples of combinations of these types. Stress-corrosion cracking, hydrogen embrittlement, corrosion fatigue and internal porosity are also involved in the causes of fractures shown here.

SEM Fractographs: High-Purity Iron Fractured at -196°C (-321°F) by
Notched Bending, and by Charpy Impact (Stereo Pair)



SEM fractograph

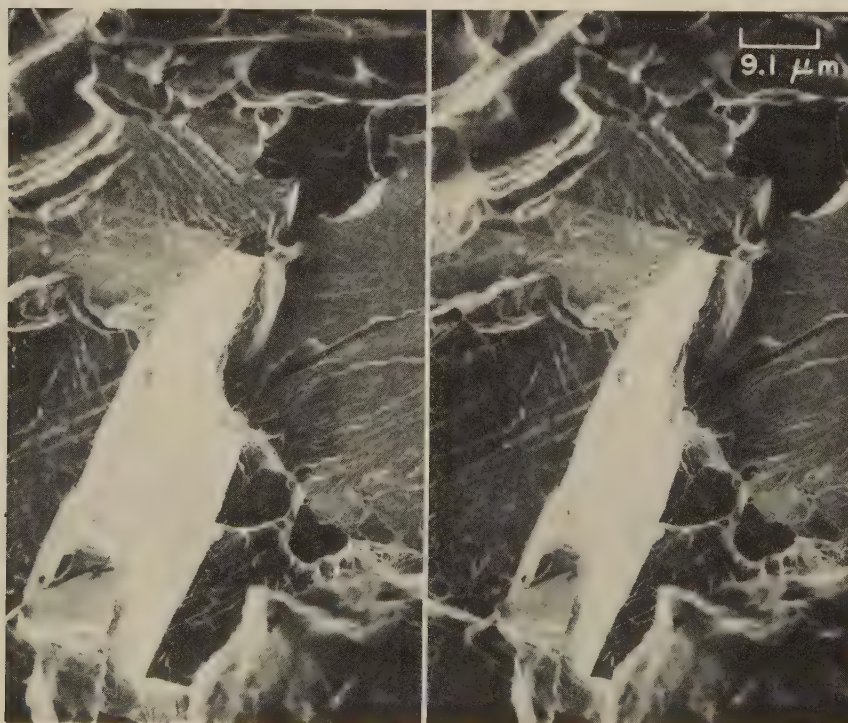
1000×

3561 Surface of a fracture that was obtained by bending a notched specimen of high-purity iron (containing less than 1 ppm of carbon) at -196°C (-321°F). The root of the notch was oriented parallel to the $\langle 110 \rangle$ crystal direction. Cleavage on several parallel planes is evident. Area in rectangle is shown in 3562.

SEM fractograph

4000×

3562 Higher-magnification view of the area within the rectangle in fractograph 3561 (at left). The vertical mark is a twin from which numerous cracks have nucleated. A straight groove at the center of the twin shows evidence of a shear-type fracture. Note the parallel cleavage steps within the twin.



SEM fractograph (stereo pair)

1100×

3563 Stereo pair of scanning electron microscope views of the fracture surface of a Charpy impact test bar of high-purity iron. The specimen was broken after being cooled to equilibrium in liquid nitrogen (-196°C ; -321°F). The use of a

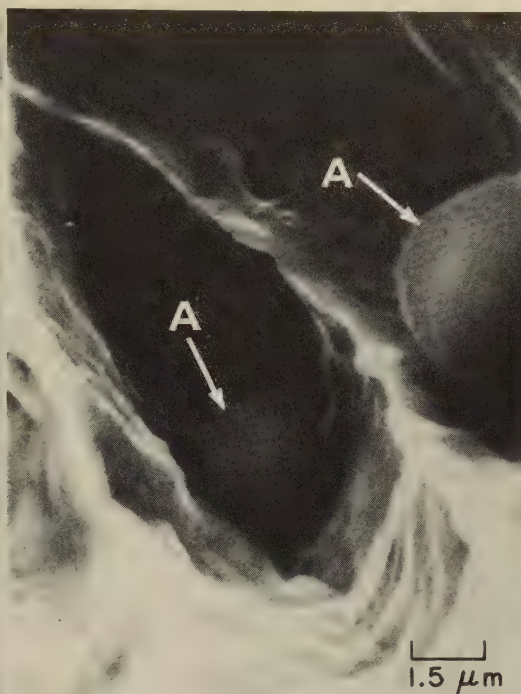
stereo viewer (or of any of the other stereographic techniques described on pages 281 and 282) is highly recommended, because it is only by these methods of appraisal that the angular relationships of the fracture facets can be appreciated.

With 3-D viewing, it will be observed that surprisingly flat cleavage has taken place on a variety of sharply divergent crystal planes. There are fine river patterns evident on nearly all of the facets. The cleavage steps that delineate the "river" systems are, however, very minute in height, providing only very small departures from a single crystallographic plane of crack growth. Characteristic of iron when fractured at low temperature is the formation of "tongues", one of which is located at the lower end of the very bright facet. Note that there even appears to be a river pattern on the left-hand portion of the "tongue". A second, smaller tongue projects from the facet shown obliquely at top left. The edges of some of the facets are exceedingly sharp. One example is the lower right-hand edge of the bright facet. Another that appears to be razor sharp is to the left of and just above the same very bright facet.

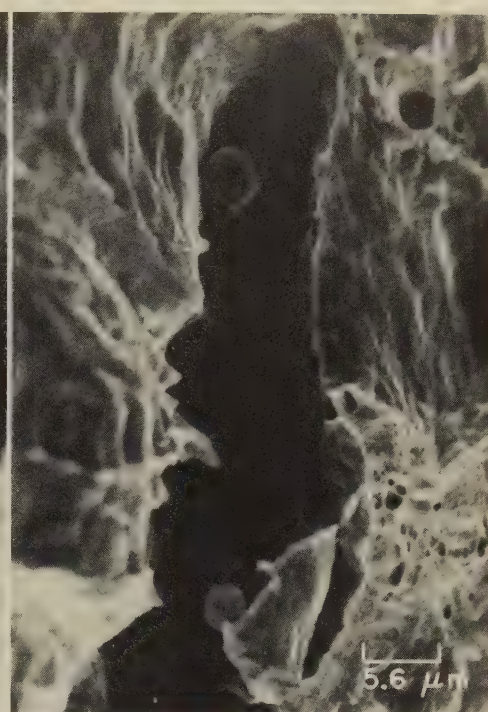
SEM Fractographs: High-Purity Iron, With and Without Additions of Silicon and of Fe_2O_3 , Fractured in Tensile Tests



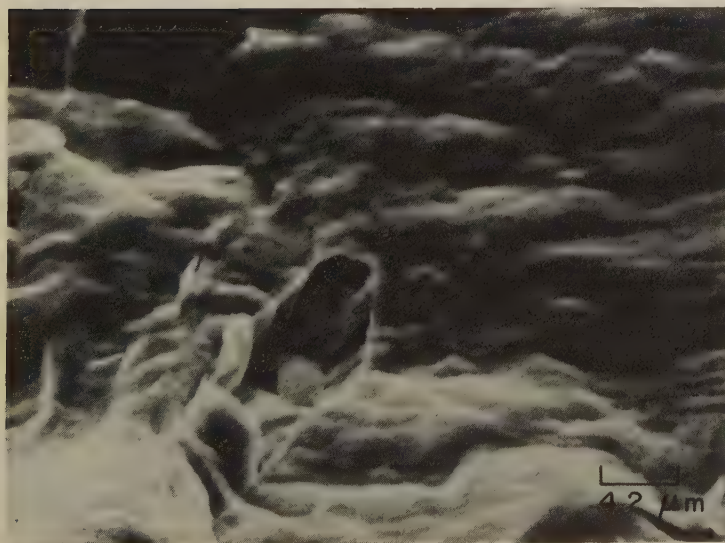
SEM fractograph 6500×
3564 Surface of a tensile-test fracture in a specimen of pure iron that was broken at room temperature. The reduction in area was nearly 100%, which produced a very limited fracture surface. Present are the dimples characteristic of tension overload, but no nonmetallic inclusions were found throughout the fracture.



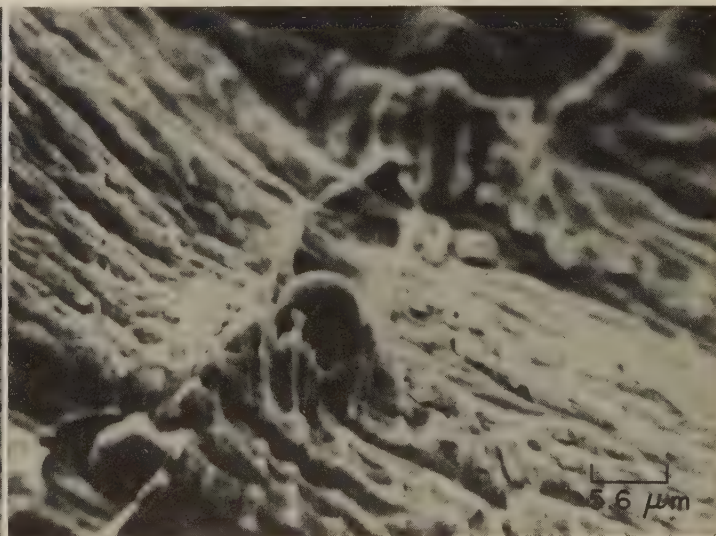
SEM fractograph 6500×
3565 Room-temperature tensile-test fracture in a specimen taken from an ingot prepared by adding 0.05% pure silicon to pure iron in a vacuum melt equilibrated at 1550 C (2822 F) in a silica crucible. Fracture surface shows dimples that contain spherical SiO_2 inclusions averaging 3.4 μm in diameter. Separation of inclusions from the matrix was indicated (arrows A). See 3567 and 3568.



SEM fractograph 1800×
3566 Surface of a room-temperature tensile-test fracture in a specimen taken from an ingot prepared by adding Fe_2O_3 to pure iron in a vacuum melt equilibrated at 1550 C (2822 F) in a silica crucible. The ingot contained 0.07% oxygen in the form of FeO. The fracture surface contains dimples that initiated at globular FeO inclusions averaging 5.2 μm in diameter.

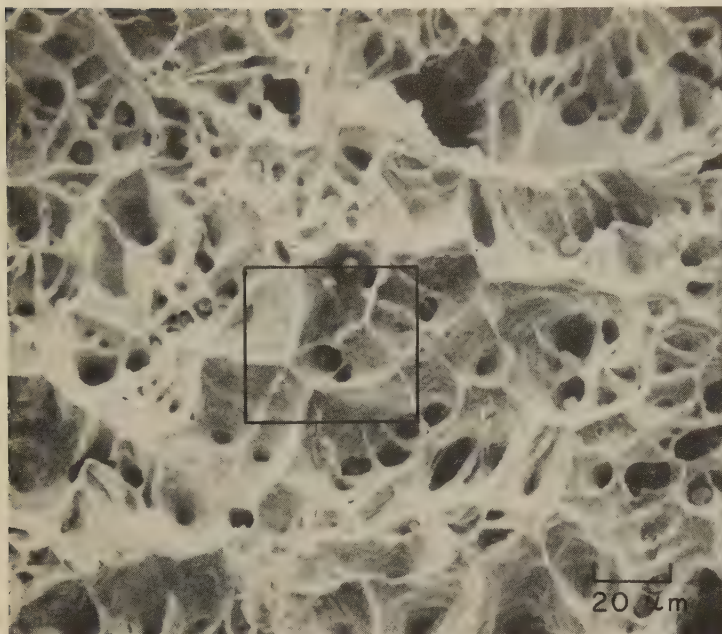


SEM fractograph 2400×
3567 View of the shear-lip region of the fracture surface shown in fractograph 3565. The surface here is greatly distorted, similar to the interior of the dimples visible in 3565. The globular inclusion is SiO_2 .

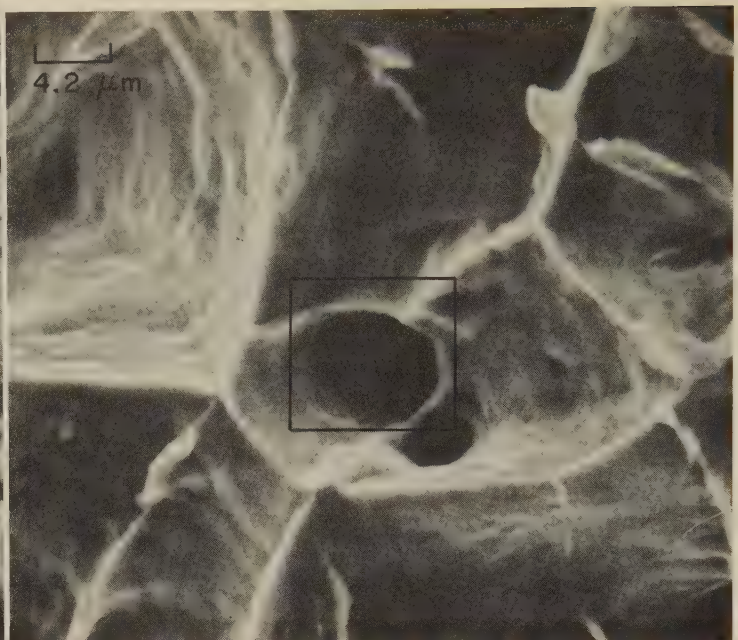


SEM fractograph 1800×
3568 Lower-magnification view of the shear-lip region shown in 3567. Coarse, globular FeO inclusions appear to lie in a trough in every instance; this is attributed to deformation by rigid-body rotation.

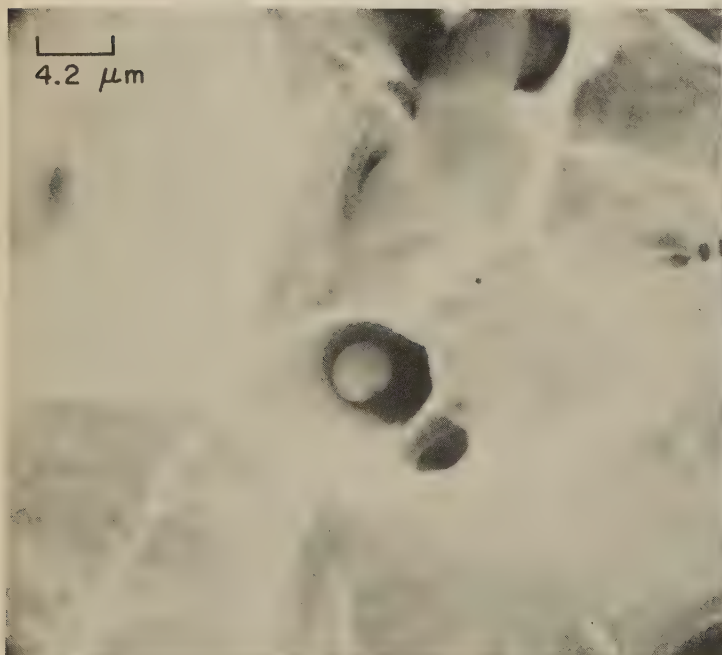
SEM Fractographs: Low-Carbon, High-Oxygen Iron Fractured in Tensile Tests at Room Temperature



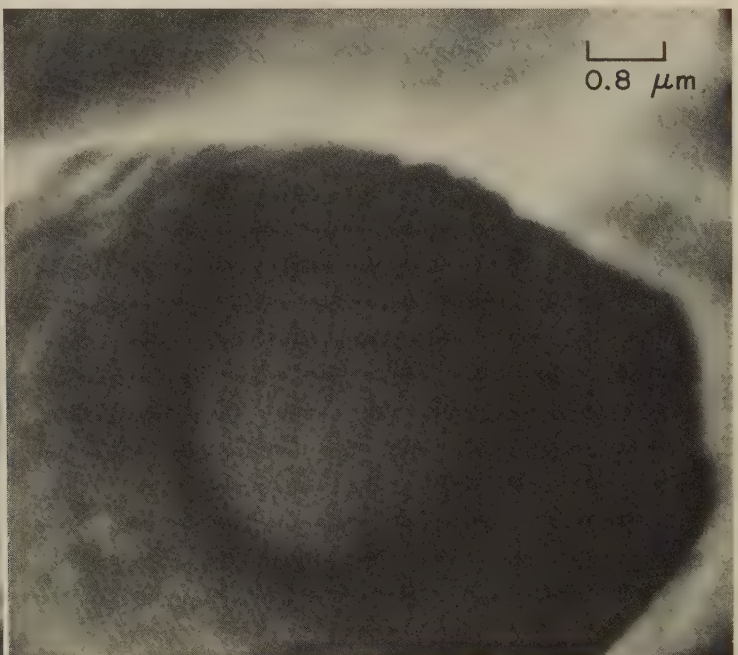
SEM fractograph 500×
3569 Surface of tensile-test fracture in specimen of low-carbon, high-oxygen iron that was broken at room temperature. Many of the equiaxed dimples contain spheroidal particles of FeO. The rectangle marks the area shown at higher magnification in fractographs 3570 (right) and 3571 (below).



SEM fractograph 2400×
3570 Enlargement of the area within the rectangle in 3569 (left), showing the surface contours of the dimple cavities of the very ductile fracture. Dimly visible in the central dimple is a globular particle of FeO; the particle is shown more clearly in 3571. The rectangle here indicates the area shown in 3572 (below).

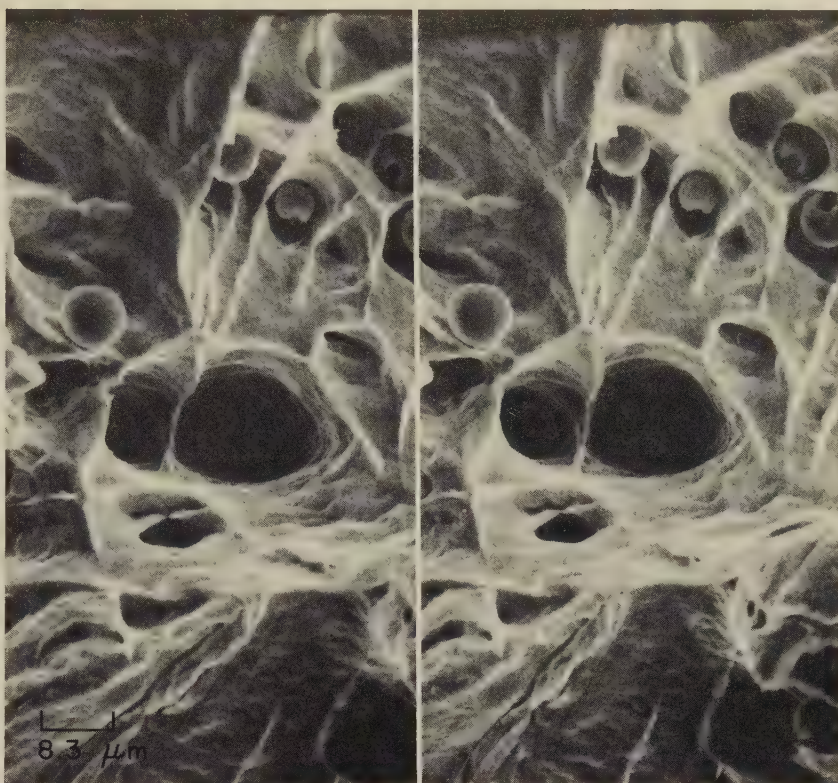


SEM fractograph 2400×
3571 Same fracture-surface area as that shown in fractograph 3570 (at right, above), but processed with a different exposure to bring out the shape and size of the globular particle of FeO in the central dimple. The small dark spot at the lower right on the FeO particle is a shrinkage area.



SEM fractograph 12,000×
3572 A further enlargement of the dimple shown in 3569 (center of outlined area) and in 3570. The particle of FeO is remarkably spherical. It seems evident that during the flow leading to fracture the matrix separated and drew away from the FeO particle without fracturing it.

3573 Stereo pair of scanning electron microscope fractographs of the surface of a tensile-test fracture obtained at room temperature. The alloy was a low-carbon iron to which an appreciable amount of Fe_2O_3 had been added to form an aggregate of FeO inclusions. The dimples that are characteristic of ductile rupture are evident here, and many of these dimples contain one or more globular oxide inclusions that are readily apparent. There appear to be two sizes of these oxide inclusions — some being about $6\text{ }\mu\text{m}$ in diameter and others about $3\text{ }\mu\text{m}$ in diameter. Unlike many inclusions displayed in other fractographs, which have relatively smooth, unbroken contours, several of the particles shown here possess sizable surface defects. Some of these defects may be exposed internal shrinkage cavities. The surfaces of the dimples show contours that vaguely resemble fatigue-striation marks. The differences in topographic contours of the dimples displayed in this stereo pair of fractographs can be appreciated only by viewing them stereographically. Whether this is achieved with the aid of the viewer supplied with this volume or a commercially available optical viewer, or with the use of a vertical piece of cardboard to separate the vision of the eyes (as discussed under "Stereoscopic Viewing" in the introduction to the section of this Atlas that follows, "Comparison of SEM and TEM Stereofractographs"), is not of any real importance. However, only by the use of some technique of this sort can the observer train his eyes to view the two prints independently and thereby gain a three-dimensional aspect. It then becomes apparent that the dimples are chimneylike cavities with nearly vertical walls in many instances and with bottoms at great depth that appear black and without detail. The FeO inclusions appear to cling to the cavity walls, many at a point partway to the bottom of the "chimney". Most of the separating walls between adjacent chimneys are extremely thin, which makes it surprising that these walls did not rupture at a point closer to the bottom of the chimney.



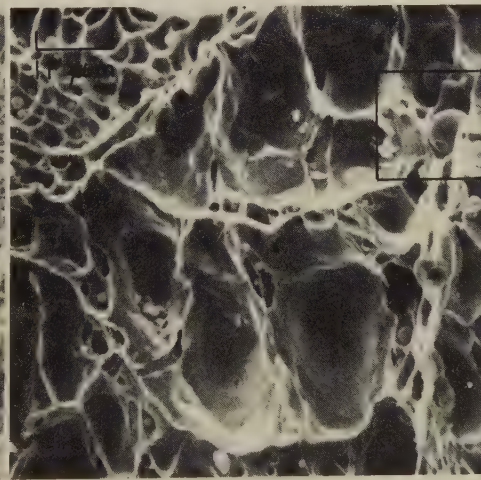
SEM fractograph (stereo pair)

1200×



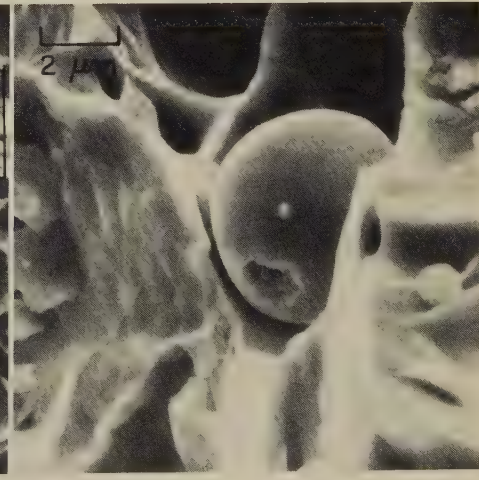
SEM fractograph

80×



SEM fractograph

950×



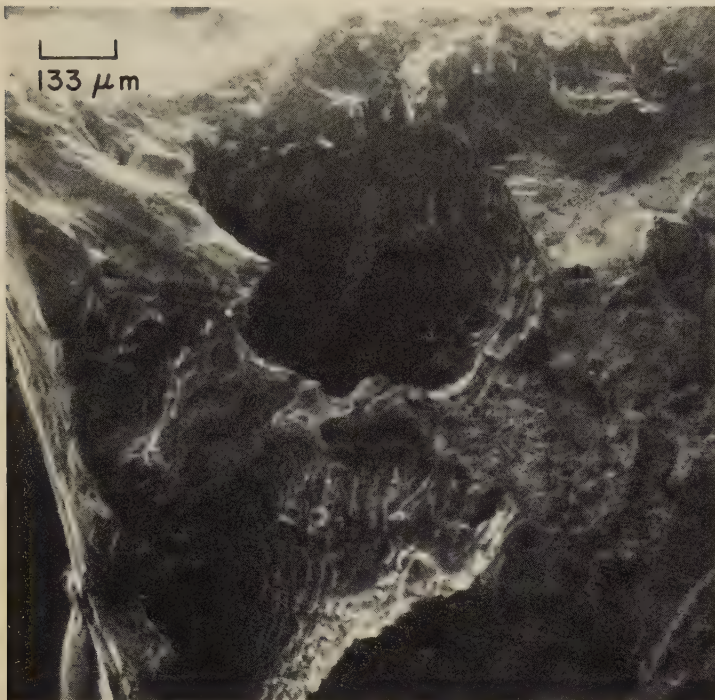
SEM fractograph

5000×

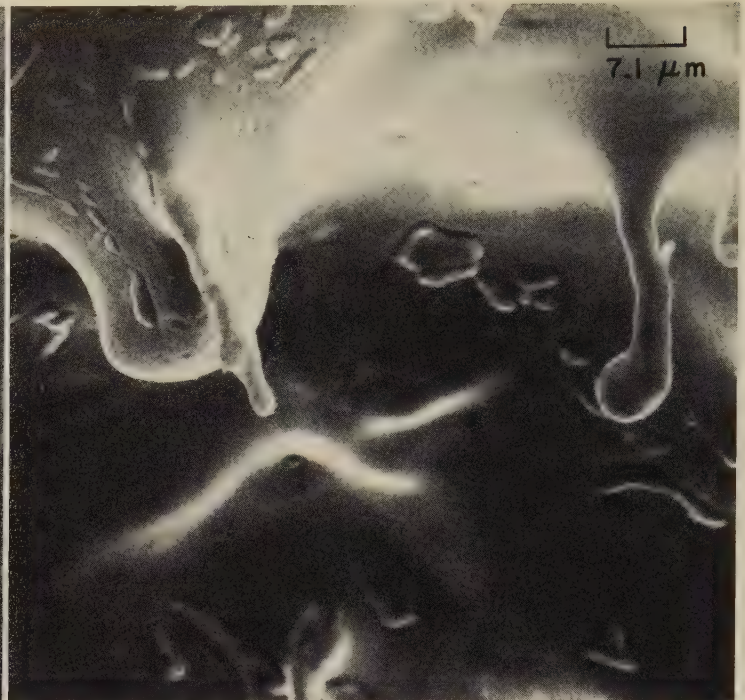
3574, 3575, 3576

Sequence of SEM fractographs, at increasing magnifications, which show a fracture in an iron alloy containing 0.14% S and 0.04% O. The fracture was obtained by bending at room temperature. Several spheroidal oxide inclusions and sulfide inclusions are visible, most of them having diameters in the range of 1 to $3\text{ }\mu\text{m}$. The rectangle in fractograph 3574 (left) indicates the area that is shown at higher magnification in fractograph 3575 (center), and the rectangle in 3575 indicates the area that is shown at still higher magnification in fractograph 3576 (right). The $6\text{-}\mu\text{m}$ -diam oxysulfide particle in fractograph 3576 shows a shrinkage cavity plus a white spot from an electron beam impingement in fluorescent x-ray analysis. It is quite evident that, during the process of microvoid coalescence, the iron matrix has become detached from the globular inclusions at the metal-to-oxide and metal-to-sulfide interfaces, leaving these inclusions unaffected by the applied stresses and severe deformation taking place around them.

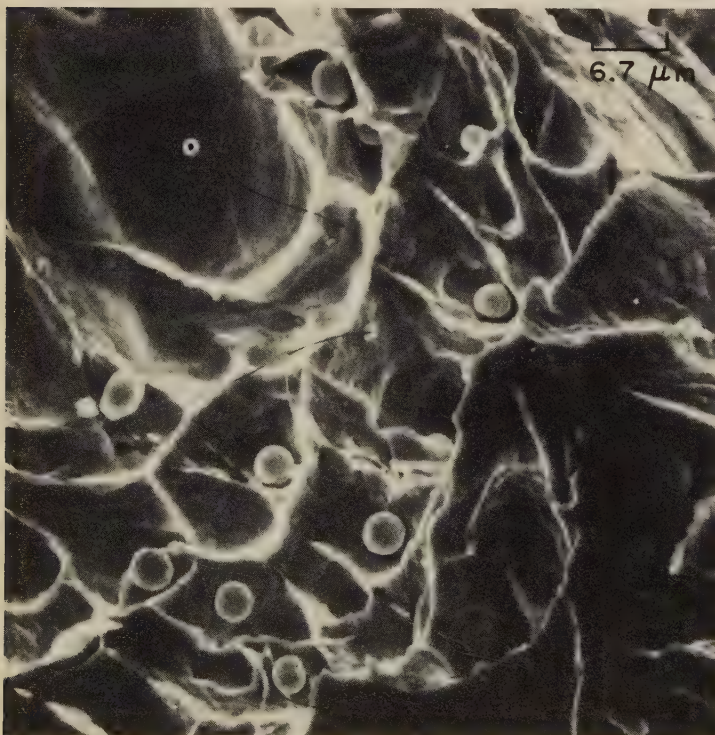
SEM Fractographs: Bending Fractures in Cast High-Sulfur, High-Oxygen Iron as Affected by a Manganese Addition



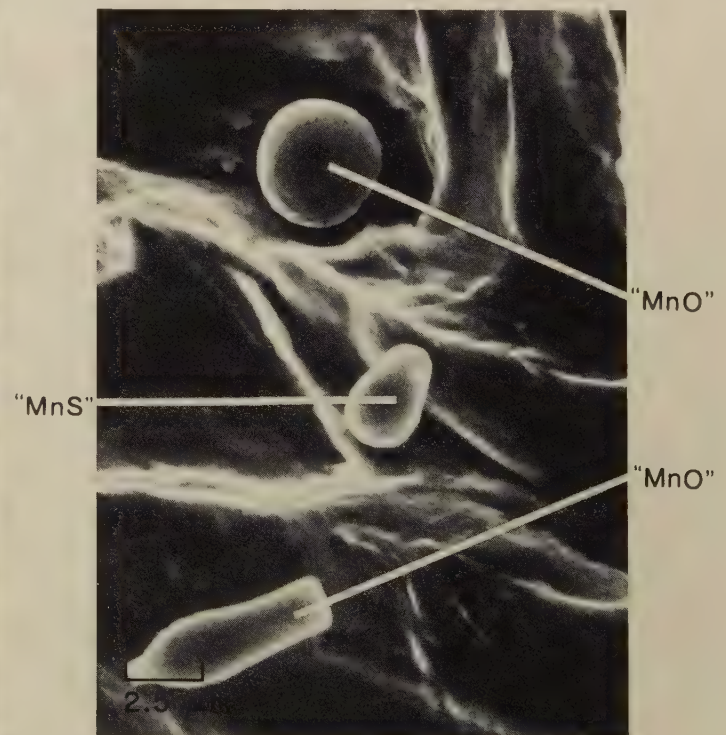
SEM fractograph 75×
3577 Fracture produced at room temperature by bending iron containing 0.02% C, 0.14% S and 0.04% O that had been cast in a 7 by 7 by 20 cm ingot mold. A carbon-FeO reaction caused blowholes such as that shown at top. Note the fine lamellar structure at bottom. See also 3578.



SEM fractograph 1400×
3578 Higher-magnification view of the blowhole shown at the top in fractograph 3577 (at left), showing the interior of the blowhole that resulted from the carbon-FeO reaction. The pendants are droplets of a liquid oxysulfide that spread over the surface of the blowhole during freezing of the ingot.

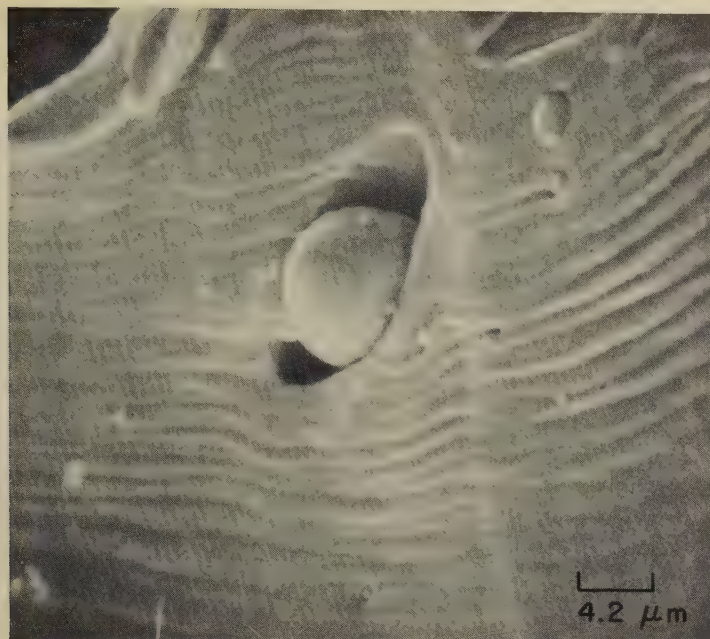


SEM fractograph 1500×
3579 Fracture by room-temperature bending in casting of similar composition to that of casting in 3577 (above) but containing 1.1% Mn. The numerous inclusions contained within the dimples are particles of manganese oxide and manganese sulfide that were trapped between growing dendrite branches.



SEM fractograph 4000×
3580 A higher-magnification view of the same fractured specimen shown in fractograph 3579 (left). X-ray fluorescent analysis of the inclusions indicates that some of them are Mn(Fe)O and that others are Mn(Fe)S, but the exact amount of contained iron was not determined.

SEM Fractographs: Room-Temperature Fractures in Low-Carbon, High-Oxygen Iron by Fatigue, and in Armco Iron by Charpy Impact



SEM fractograph

2400×

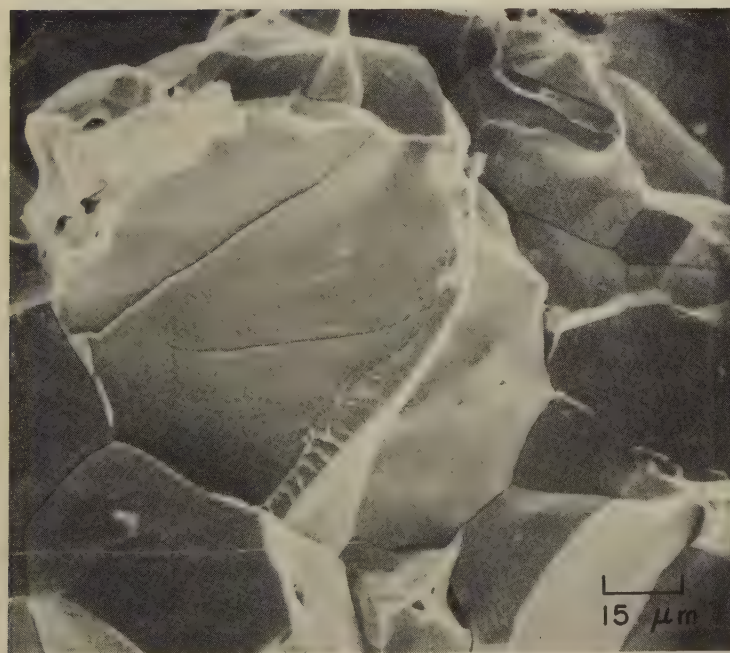
3581 Low-carbon iron containing a high percentage of oxygen, fractured in fatigue at room temperature. A large oxide inclusion has been nearly completely disengaged from its original pocket. Fatigue striations detour around, or extend into, the pocket. Crack propagation was from bottom to top.



SEM fractograph

55×

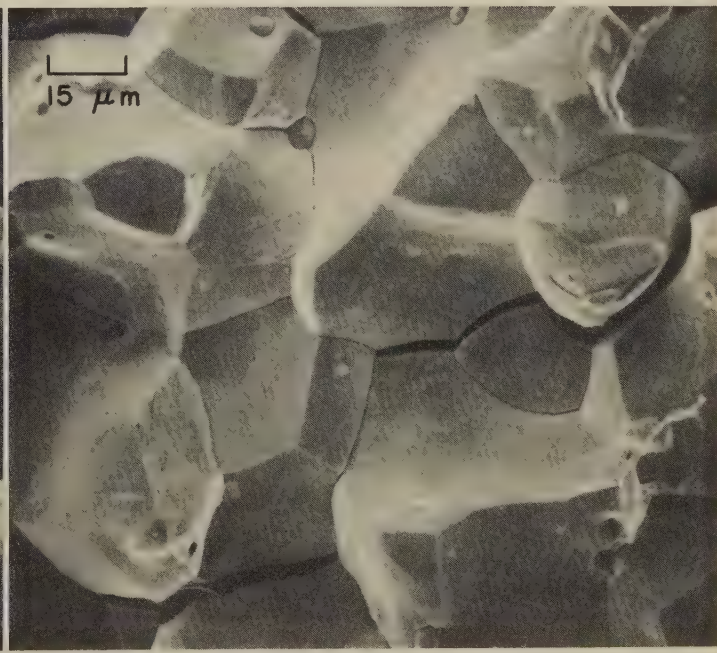
3582 Intergranular fracture that was generated in a specimen of oxygen-embrittled Armco iron by a Charpy impact test at room temperature. The grain facets appear sharp and clean. Note the secondary cracks, which follow grain boundaries. See also 3583 and 3584.



SEM fractograph

655×

3583 View of another region of the surface of the impact fracture in Armco iron in 3582, showing facets that resulted from a combination of intergranular rupture and transcrystalline cleavage. Note the array of small river patterns at the bottom edge of the large facet at center. See also fractograph 3584.

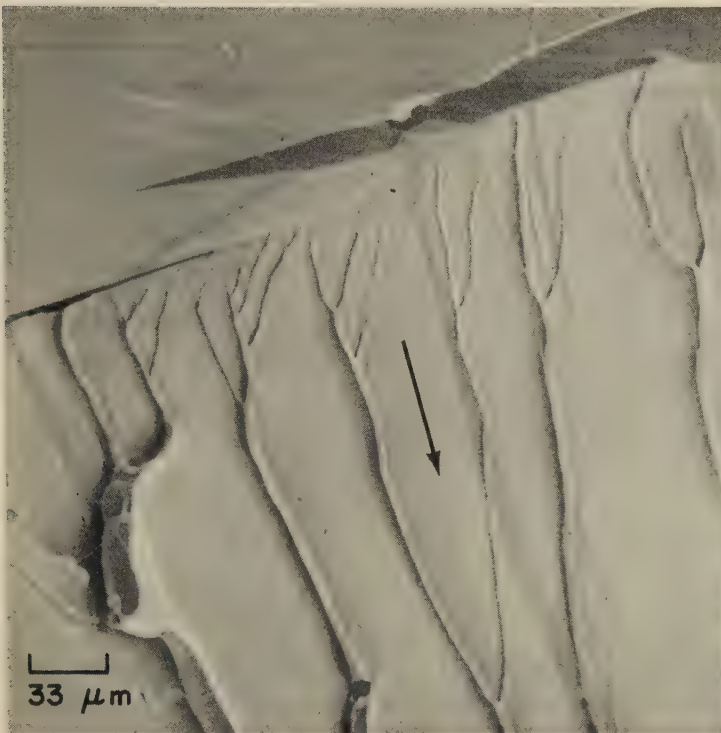


SEM fractograph

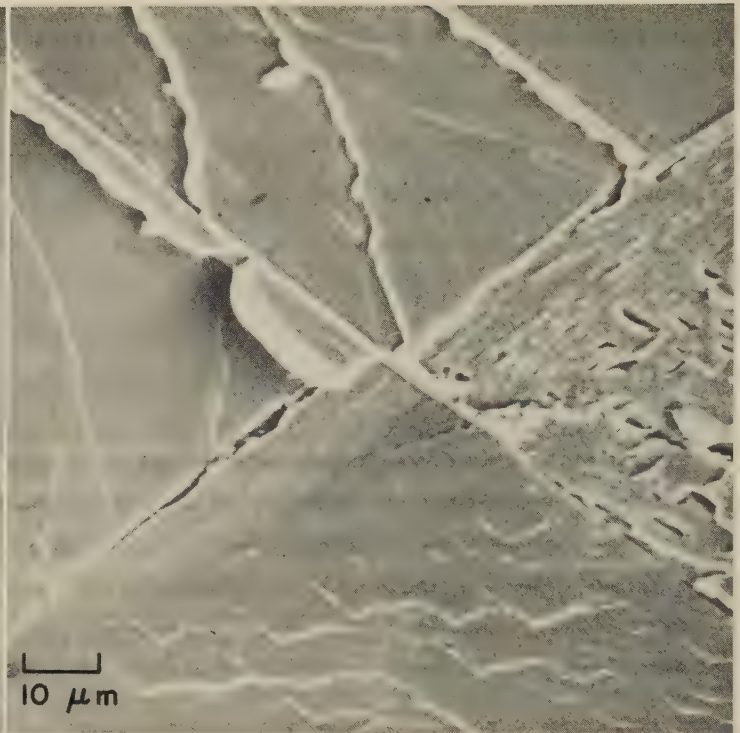
670×

3584 View of a third region of the surface of the impact fracture in Armco iron in 3582 and 3583. Note the almost perfect grain-boundary surfaces and the sharp edges and points at which the separated-grain facets meet. The secondary cracks are equally clean separations.

SEM Fractographs: Impact Fractures in a 0.01% C, 0.24% Mn, 0.02% Si Iron,
at -196°C (-321°F) and at 100°C (212°F)



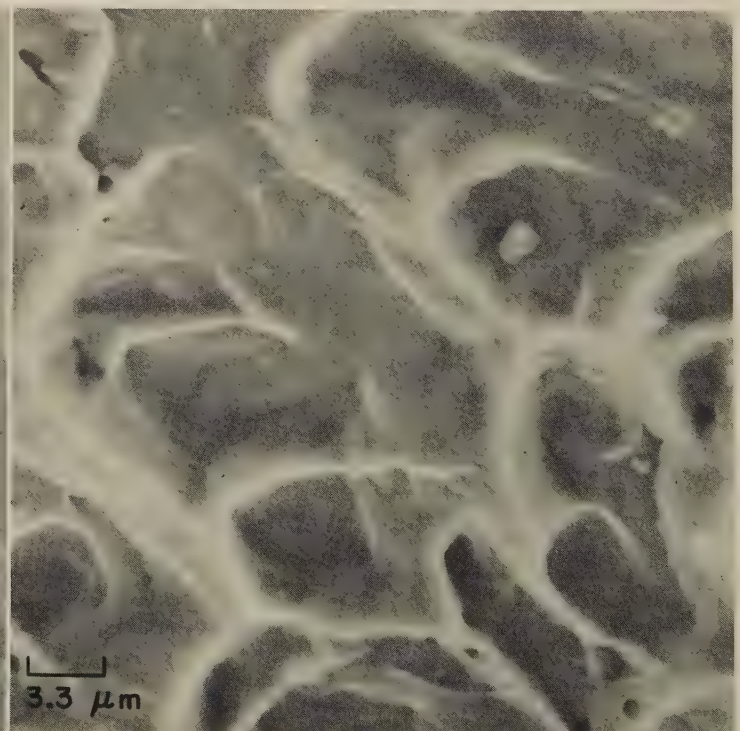
SEM fractograph 300×
3585 Fe, 0.01% C, 0.24% Mn and 0.02% Si, heat treated at 950°C (1742°F) $\frac{1}{2}$ hr, air cooled. The structure is ferrite. Hardness, 62 dph. The fracture was generated by impact at -196°C (-321°F). Cleavage steps beginning at the twin at top form a sharply defined river pattern. Crack propagation was in direction of arrow.



SEM fractograph 1000×
3586 Higher-magnification view of the specimen in 3585, showing the blocklike cleavage pattern that is characteristic of low-temperature impact of low-carbon iron. The well-defined tongue at the center of the fractograph is typical. Secondary cracks are visible as well.



SEM fractograph 300×
3587 Impact fracture generated at 100°C (212°F) in the same material as that shown in 3585 (above). Absorbed energy was 1.6 kgm/cm^2 . Most of the surface is composed of smooth grain-boundary facets, but there is a small area of somewhat elongated dimples near the center.



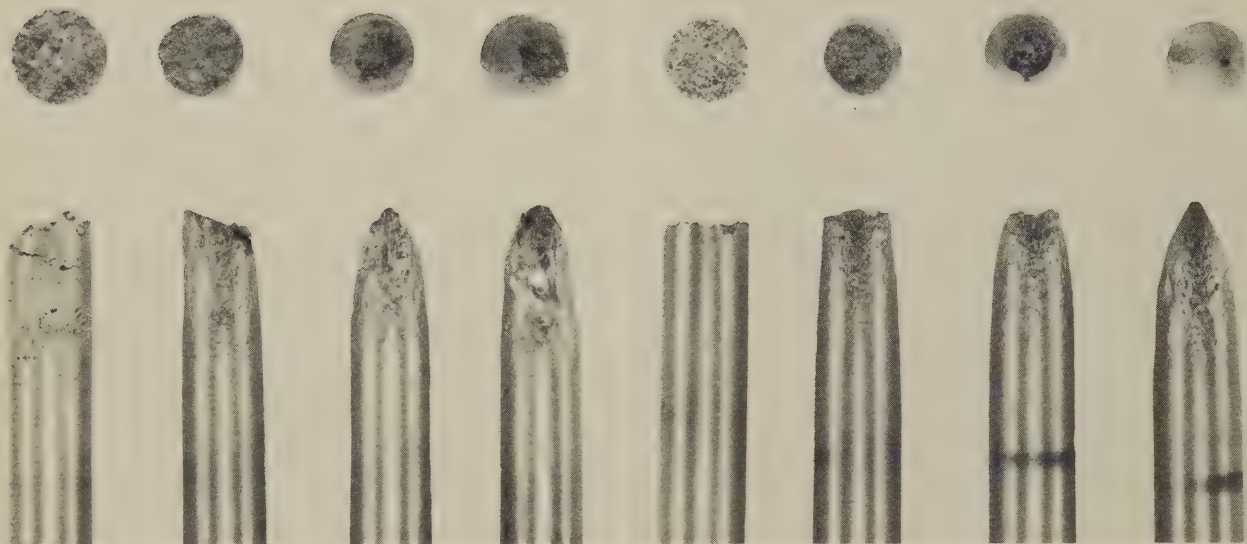
SEM fractograph 3000×
3588 Higher-magnification view of a dimpled area of the fracture shown in fractograph 3587 (at left). The rupture is completely transgranular at this location. Note the slight elongation of the dimples, which reflects the ductile tearing that occurred during impact testing.

SEM Fractographs: Notched Specimen of High-Purity Iron Containing 0.023% C
Fractured by Bending at -196°C (-321°F)



SEM fractographs (overlapping views) 4000×
3589 Two overlapping views of the surface of a brittle fracture in a specimen of high-purity iron containing 0.023% carbon. The specimen was aged at 400°C (752°F) for 1 hour. After being machined to final dimensions and notched parallel to the $\langle 110 \rangle$ direction of the crystal, the specimen was fractured by bending at -196°C (-321°F). Note that the cleavage surface intersects a twin boundary that extends across both prints. The fracture has departed from the general plane of propagation at several points in the twinned metal (upper portion of the prints); the small angle of departure indicates that the plane of the twin is nearly parallel to the general plane of the crack. Many of these departures bear some resemblance to the tongues that are characteristic of cleavage in iron at dry-ice temperature, but they appear to lack the typical projecting overhang that has been observed in so many studies. In addition to these features, a number of cleavage steps in various orientations are visible, some of these being quite irregular in contour and quite unlike the symmetrical blocklike patterns sometimes encountered in fracture surfaces of iron specimens fractured at this very low temperature.

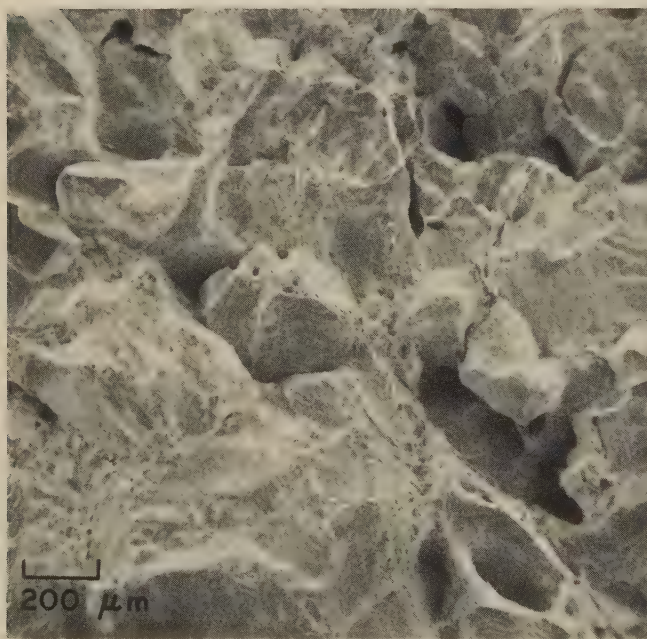
Macrographs, SEM Fractographs: High-Temperature Tensile-Test Fractures in 0.04 to 0.08% C Steels as Influenced by Mn:S Ratios



Macrographs

3/4 X

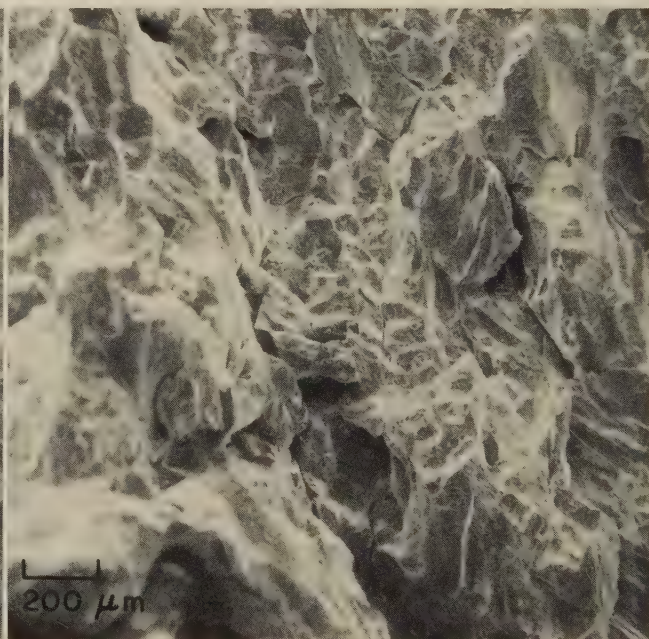
3590, 3591 Fractures obtained in tension in low-carbon steel specimens that were tested at elevated temperature. The specimens were taken from a series of 500-lb laboratory heats melted to yield a range of carbon contents (0.04 to 0.08%) and a range of Mn:S ratios (11:1 to 68:1). The ingots were rolled to 3/4-in. and 5/8-in. plate at 1177 C (2150 F). The specimens shown in 3590 (left) were machined, placed within a silica sleeve in a Gleeble test unit and remelted in the central region of the gage length. They were then solidified *in situ*, cooled to 1427 C (2600 F) at 14 C (25 F) per second, cooled to either 1093 C (2000 F) or 927 C (1700 F) at 5.5 C (10 F) per second, and then pulled to rupture. From left to right, the Mn:S ratios were 11, 22, 38 and 63 to 1, and the reductions in area were 6, 37, 63 and 83%. The specimens shown in 3591 (right) were "sensitized" in the Gleeble test unit by heating to 1427 C (2600 F), holding for 300 sec, and then cooling at 5.5 C (10 F) per second to 1093 C (2000 F), and were broken in tension at the latter temperature. From left to right, the Mn:S ratios were 14, 22, 36 and 62 to 1, and the reductions in area were 4, 47, 74 and 99%.



SEM fractograph

50 X

3592 Fracture in low-carbon steel containing 0.065% C, 0.52% Mn, 0.01% P, 0.022% S and 0.076% Si (Mn:S ratio, 23.6:1). The specimen was "sensitized", and broken in tension, as described above for 3591. Under these conditions, a low Mn:S ratio would result in a completely intergranular fracture. However, because of the intermediate ratio here (23.6:1), the grain-boundary facets show dimples in many areas, indicating ductility. Reduction in area was 33%, which agrees with the appearance of the fracture surface.

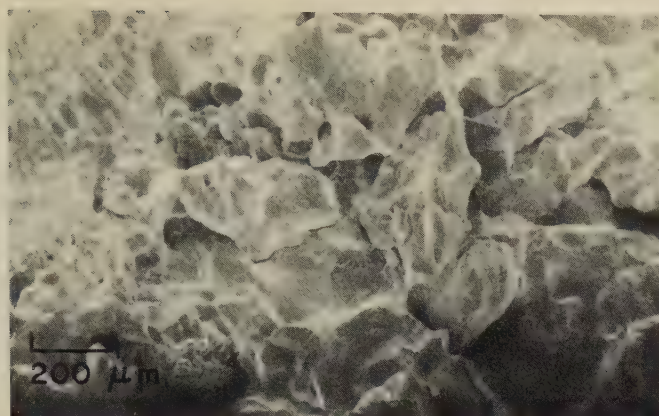


SEM fractograph

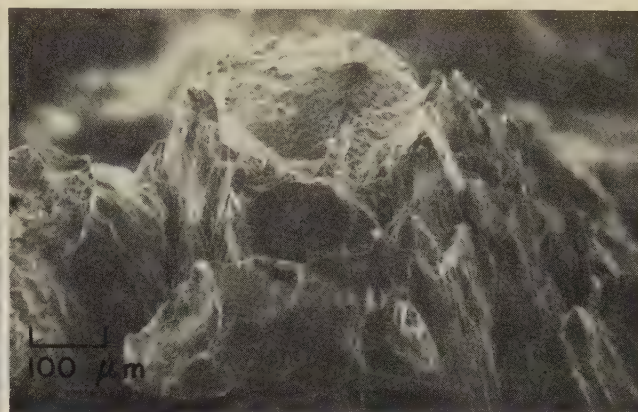
50 X

3593 Surface of fracture obtained in test bar of low-carbon steel containing 0.041% C, 0.62% Mn, 0.008% P, 0.028% S, 0.032% Si (Mn:S ratio, 22.1:1). The test bar was remelted in its central zone in a Gleeble test unit, solidifying *in situ* in its quartz sleeve. Following controlled cooling from the freezing point, the test bar was pulled in tension at 927 C (1700 F). Although the path of this fracture was largely intergranular, there is also transgranular cleavage, and some facets show very fine dimples.

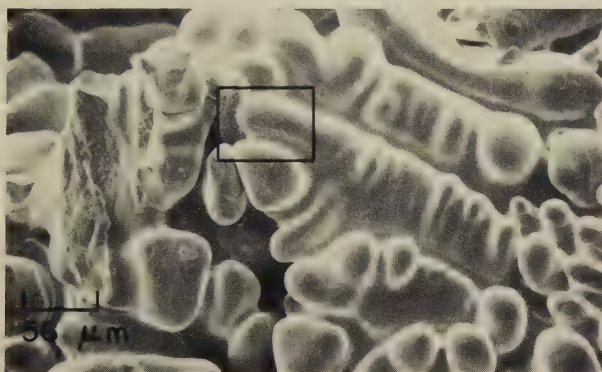
SEM Fractographs: Effect of Mn:S Ratios on High-Temperature Tensile Fractures in 0.04 to 0.08% C Steels (Continued); Similar Fractures in 1015 Steel



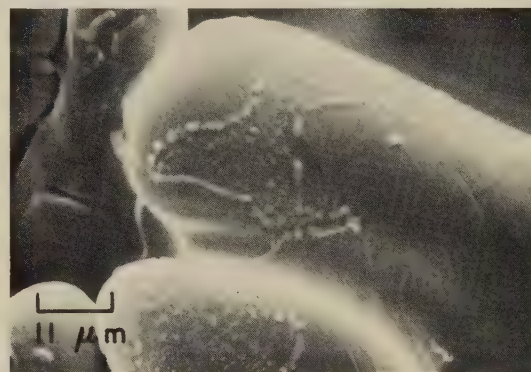
SEM fractograph 50×
3594 Fracture very similar to that shown in fractograph 3593. The Mn:S ratio of the steel was 11:1. Tensile rupture (after remelt) occurred at 1093 C (2000 F). The crack followed an intergranular path, but microscopic dimples were found when the fracture surface was examined at higher magnification.



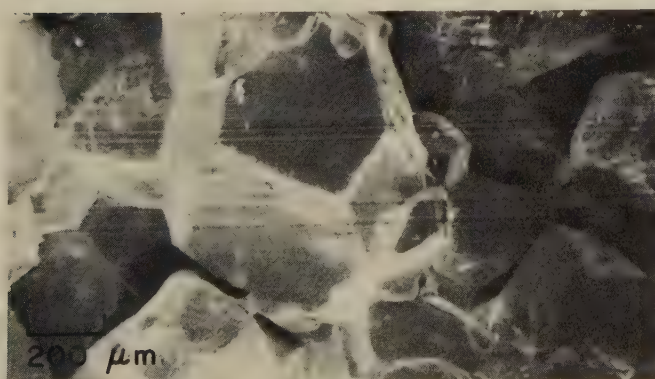
SEM fractograph 100×
3595 Tensile fracture (oblique view) obtained at 927 C (1700 F), after remelt *in situ*, in low-carbon steel (0.054% C, 0.41% Mn, 0.029% P, 0.017% S and 0.041% Si; Mn:S, 24:1). An x-ray spectrum taken at a grain boundary showed a high percentage of sulfur, but no phosphorus (possibly obscured by the sulfur).



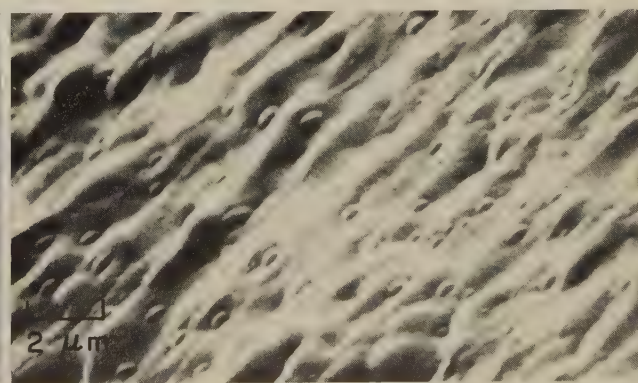
SEM fractograph 180×
3596, 3597 Two SEM views, at different magnifications, of the surface of a brittle fracture in a specimen of 1015 steel whose central zone was remelted in a Gleeble test unit, resolidified, cooled *in situ* to 1427 C (2600 F) and held for 20 sec at that temperature, and then fractured in tension. This specimen contained 0.024% P, but a specimen (from a companion melt) that contained 0.005% P ruptured in the same brittle fashion when remelted and tested in exactly the same manner. Fractograph 3596 (left) indicates that the fracture followed an interdendritic path through regions that had not yet solidified at 1427 C (2600 F). The rounded dendrite surfaces thus exposed are obvious, and the only evidence of a torn surface is in a small area at extreme left. Fractograph 3597 (right), which is a higher-magnification view of the area within the rectangle in 3596, shows patterns of what were confirmed by x-ray fluorescent analysis to have been, at the moment of fracture, liquid droplets of manganese oxysulfide on the dendrite surfaces. These patterns were the only evidence of segregation that was discovered within the fracture, the presence of phosphorus not being detected.



SEM fractograph 900×

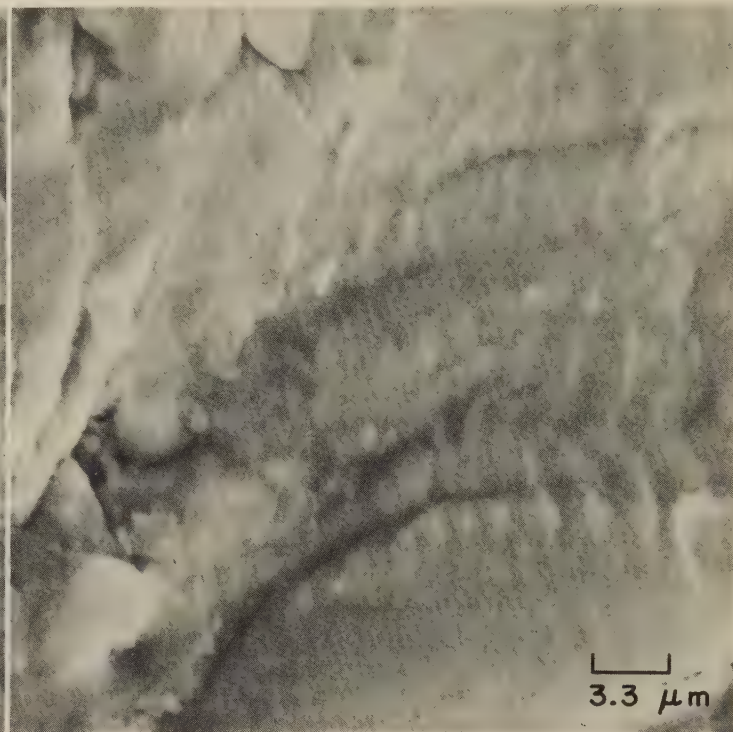
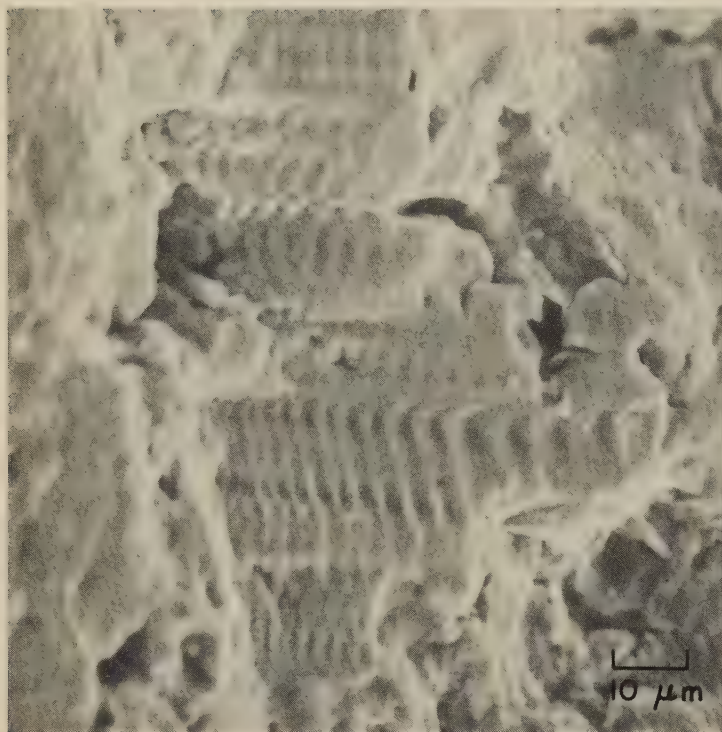


SEM fractograph 50×
3598 Intergranular fracture in a specimen of 1015 steel that was "sensitized" in a Gleeble at 1427 C (2600 F), cooled to 1093 C (2000 F) and broken in tension. The Mn:S ratio was 19:1 (0.45% Mn, 0.024% S). Note pronounced secondary cracking. See 3599.



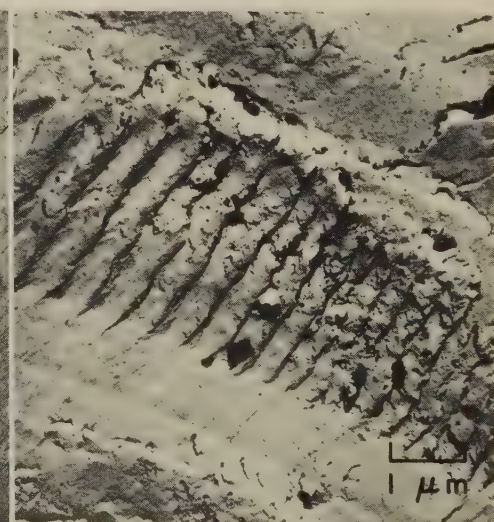
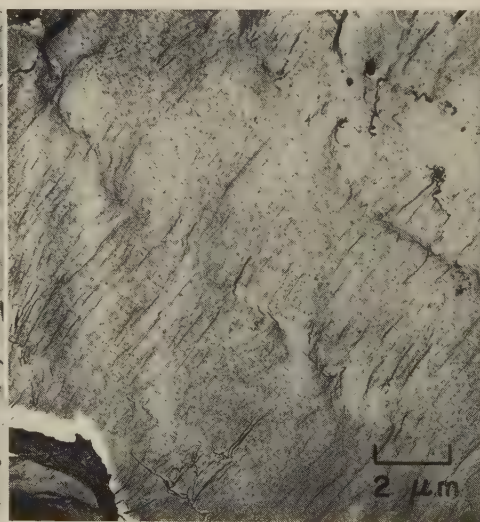
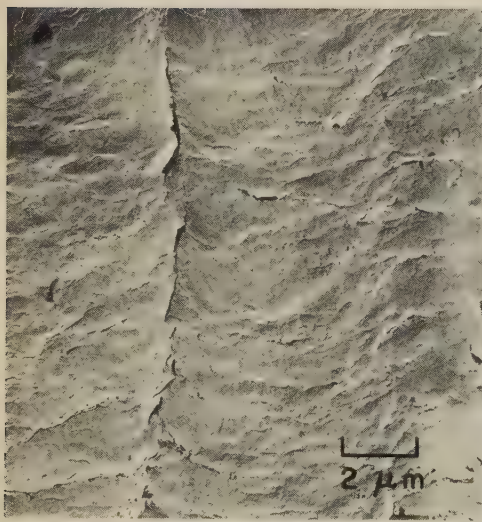
SEM fractograph 5000×
3599 Higher-magnification view of the fracture in 3598 (at left), showing an unusual rippled surface quite uncharacteristic of cleavage or microvoid coalescence. The larger "bumps" contain manganese and sulfur; the smaller ones were not identified.

SEM and TEM Fractographs: Comparison of Low-Cycle and High-Cycle Fatigue Fractures in 1020 Steel by Rotary Bending



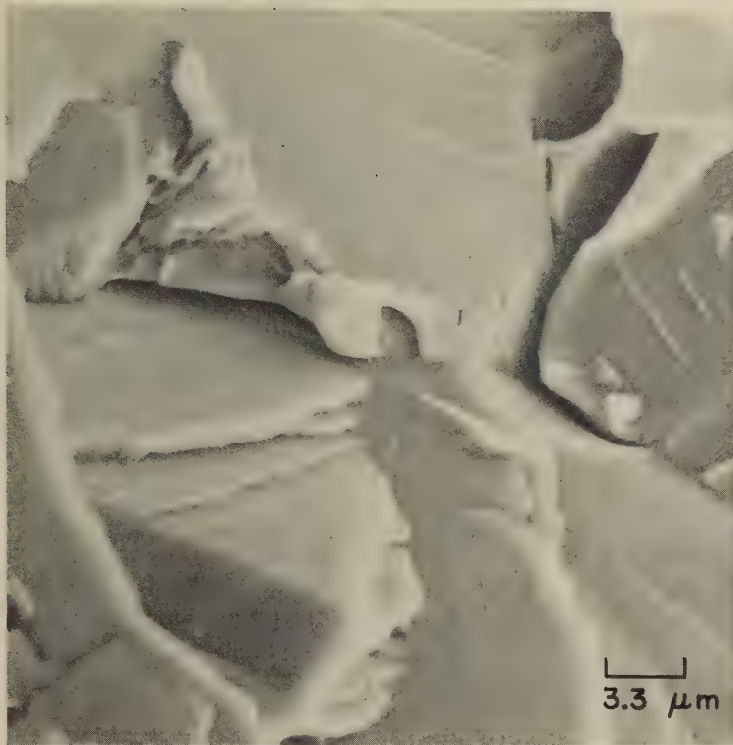
SEM fractograph 1000×
3600 Fracture produced in low-cycle rotary-bending fatigue at room temperature in a specimen of 1020 steel containing 0.20% C, 0.52% Mn and 0.22% Si and normalized at 900 C (1652 F) to a hardness of 146 dph. Applied stress was 480 MPa (69.6 ksi); fracture occurred at 3100 cycles. Surface is quite irregular; area at left is out of focus in the foreground, and upper right recedes into the background. Note abrupt angles in striations. See 3601.

SEM fractograph 3000×
3601 Fracture produced in high-cycle rotary-bending fatigue at room temperature in a specimen of the same material and hardness level as that in fractograph 3600. Applied stress was 252 MPa (36.6 ksi); fracture occurred at 1,505,200 cycles. Fatigue striations are much less sharply defined than in 3600, and the striation spacing is somewhat less, as would be expected at this lower stress level. Secondary cracking is apparent. See 3602 to 3604.



TEM fractograph (p-c replica) 5000× TEM fractograph (p-c replica) 5000× TEM fractograph (p-c replica) 10,000×
3602, 3603, 3604 Three transmission electron microscope views of the surface of the high-cycle fatigue fracture in 1020 steel shown in fractograph 3601 (above, right). Although they illustrate the same fracture as that in SEM fractograph 3601, fractographs 3602 (left) and 3603 (center) both show fatigue striations with considerably finer spacings. This demonstrates the excellent capability of the transmission electron microscope in resolving such low-relief, low-contrast features. In both 3602 and 3603, note the tear ridges between fatigue patches, a feature that is similar to that observed in fatigue fractures in aluminum alloys. Fractograph 3604 (right) illustrates "tire tracks", a fatigue-fracture characteristic that is more typical of aluminum alloys than of steel. The pattern of "tire tracks" extends diagonally from lower right to upper left; a rub mark lies below it.

SEM Fractographs: 1021 Steel Notched Specimens Fractured by Impact
at -196°C (-321°F) and at 100°C (212°F)



SEM fractograph

3000×

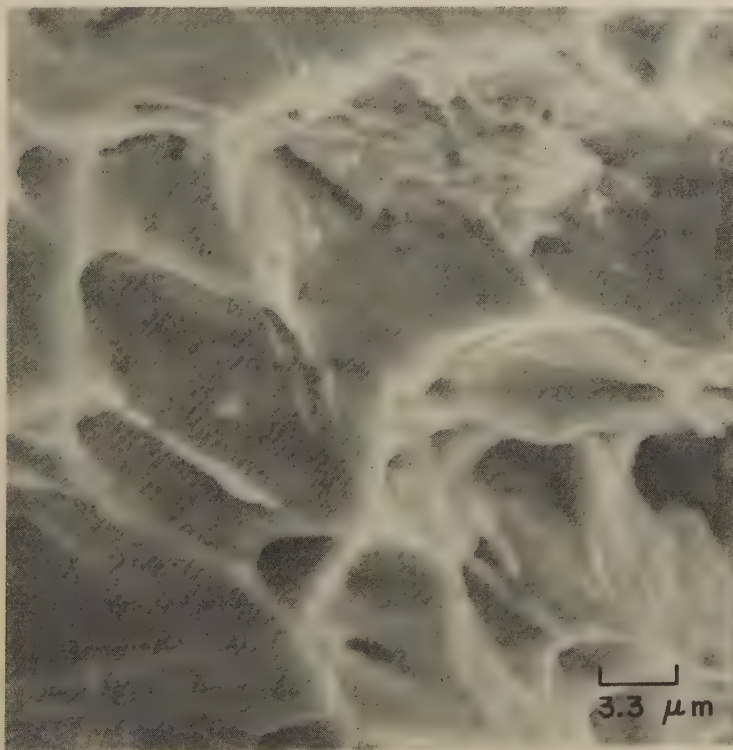
3605 Cleavage fracture in 1021 steel heat treated at 900°C (1652°F) for $\frac{1}{2}$ hr and air cooled. Ferrite-pearlite structure. Hardness, 120 dph. The specimen was notched, and was broken by impact at -196°C (-321°F). The cleavage occurred on various $\{100\}$ planes having different orientations. See fractographs 3606 to 3608.



SEM fractograph

3000×

3606 Another SEM view of the fracture in 3605 (left), showing similar flat cleavage facets along crystallographic planes, but also showing very pronounced steps that form a gross example of a river pattern beginning at either a twist or a tilt boundary. See also fractographs 3607 and 3608.



SEM fractograph

3000×

3607 Same steel (1021) and heat treatment as in fractographs 3605 and 3606, but a notched specimen broken by impact at 100°C (212°F). Ductile dimples are present in a wide variety of sizes, ranging from 1 to $10\text{ }\mu\text{m}$ in diameter. See also fractograph 3608.



SEM fractograph

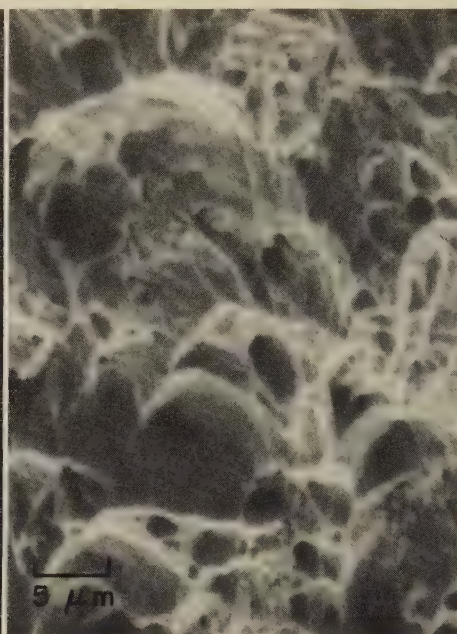
3000×

3608 Another view of the impact fracture shown in fractograph 3607 (at left). Again, dimples are seen in a wide range of sizes. Some dimples hold small intermetallic inclusions; others have smooth walls such as those of dimples produced by stretching.

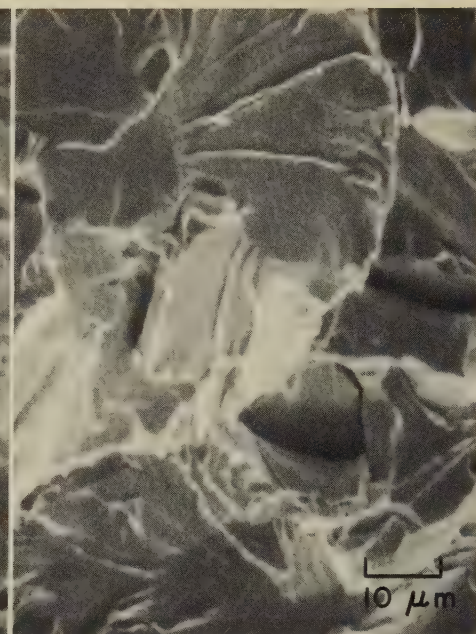
SEM Fractographs (With Light Fractograph, Macrograph and Micrographs):
Impact Fracture in a 1022 Steel Strut as Influenced by Forged Structure



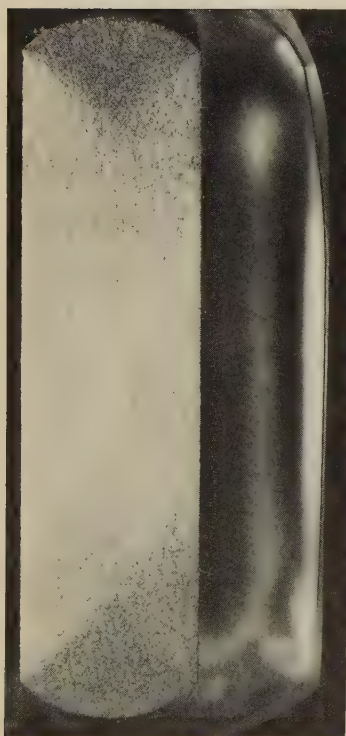
Light fractograph 6½×
3609 Impact fracture in Charpy specimen from 1022 steel strut cold formed from hot rolled round. Fracture propagated in a ductile manner from root of notch, converting to cleavage fracture near top. See 3610 to 3614.



SEM fractograph 2000×
3610 Scanning view of ductile crack-initiation area of fracture in 3609. This region of the forging was well worked, and shows dimpled rupture. See 3612 and 3613.



SEM fractograph 1000×
3611 Scanning view of the cleavage portion of the fracture shown in 3609. This region of the forging was lightly worked, as is shown in 3614 (below). See also 3612 and 3613.



Macrograph - nital 2½×
3612 Polished cross section from the cold formed strut shown in 3609 (above). Note the light working of the wedge-shaped end regions.

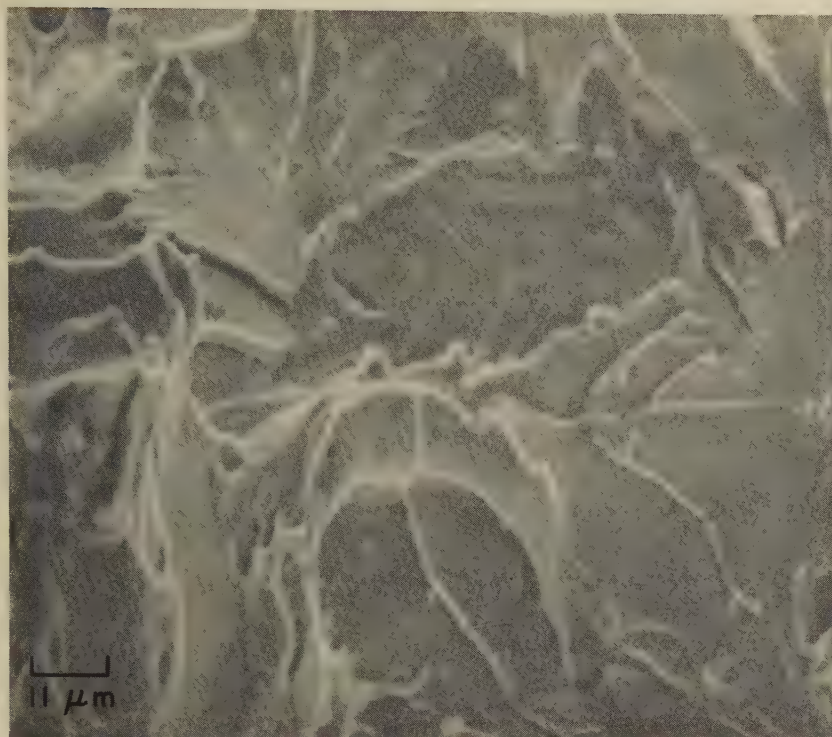


Micrograph - nital 100×
3613 Higher-magnification view of the central region of the section in 3612, showing the thoroughly worked structure that yielded the ductile fracture shown in fractograph 3610 (above). See also micrograph 3614 (at right).

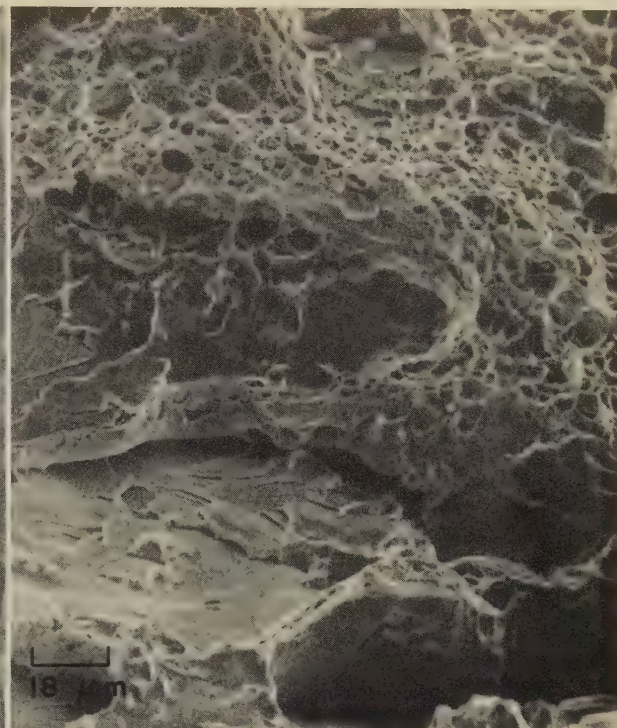


Micrograph - nital 100×
3614 Higher-magnification view of one of the wedge-shaped end regions of the section in 3612, showing the equiaxed grain structure (coarser than the structure in 3613) that yielded the cleavage fracture shown in 3611 (above).

SEM Fractographs, Micrograph: Impact Fractures in 1022 Steel at -9°C ($+16^{\circ}\text{F}$) and in 1025 Steel at Room Temperature; Tension-Overload Fracture in ASTM A36 Steel at Room Temperature



SEM fractograph 900×
3615 Charpy impact fracture in specimen taken from 1022 steel vehicle-arm forging. The part had been heat treated to a hardness of Rockwell B 70.5. Impact was at -9°C ($+16^{\circ}\text{F}$), which is below the transition temperature for this material. Fracture mechanism was brittle cleavage; there is no evidence of dimples.



SEM fractograph 565×
3616 Room-temperature Charpy impact fracture in a specimen of 1025 steel. Unlike that in 3615, this specimen shows two mechanisms of fracture—namely microvoid coalescence at the top and cleavage below. Note the pronounced steps.

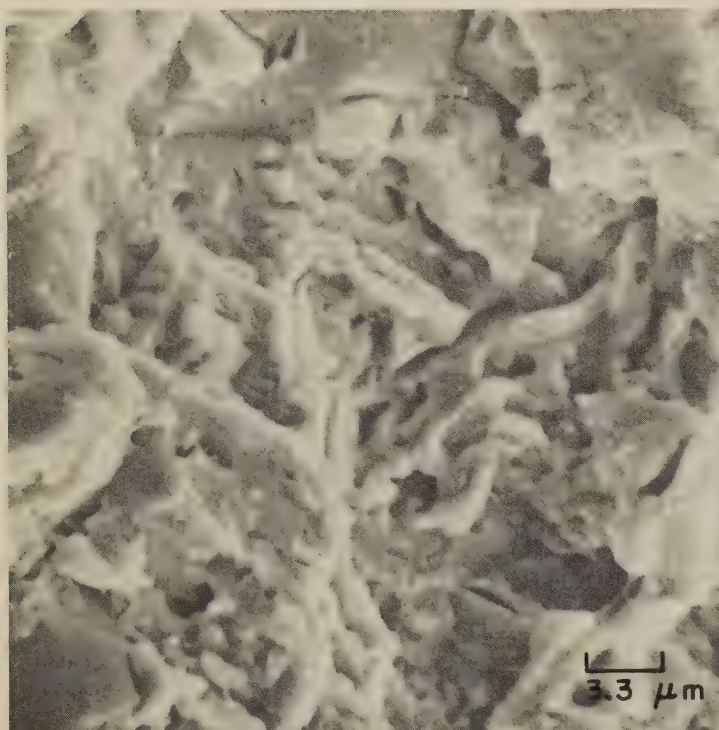


SEM fractograph 850×
3617 Tension-overload fracture in a specimen taken from a latch-arm forging of ASTM A36 steel. The forging had been normalized; the tension test was performed at room temperature. Most of the fracture-surface facets have been identified as cleavage, but there is some evidence of dimples—particularly at left center. Note the abrupt changes in river patterns. See also micrograph 3618 (at right).

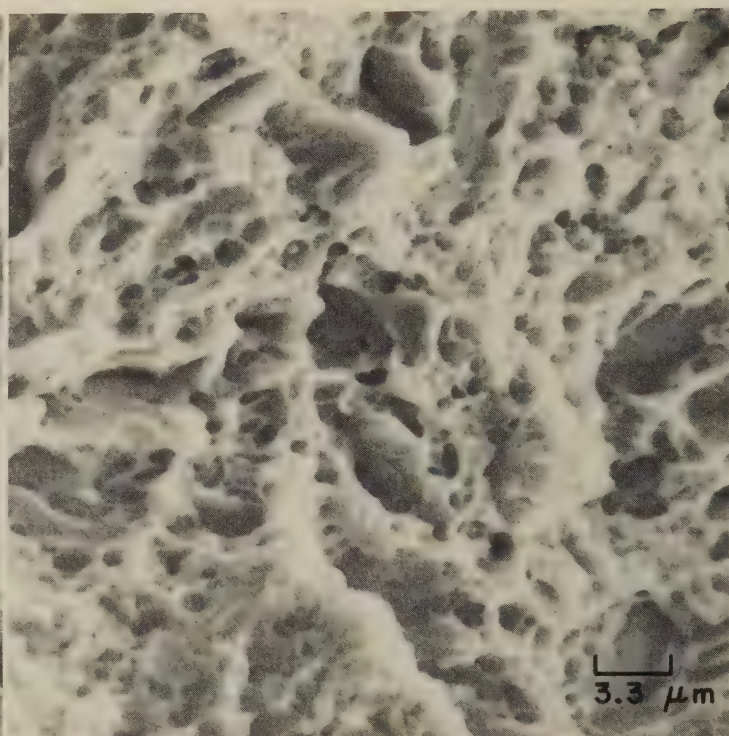


Micrograph—10% nital 150×
3618 Section of the ASTM A36 steel test specimen in 3617 (left), showing ferrite-pearlite microstructure. Tensile properties of the steel were below specifications.

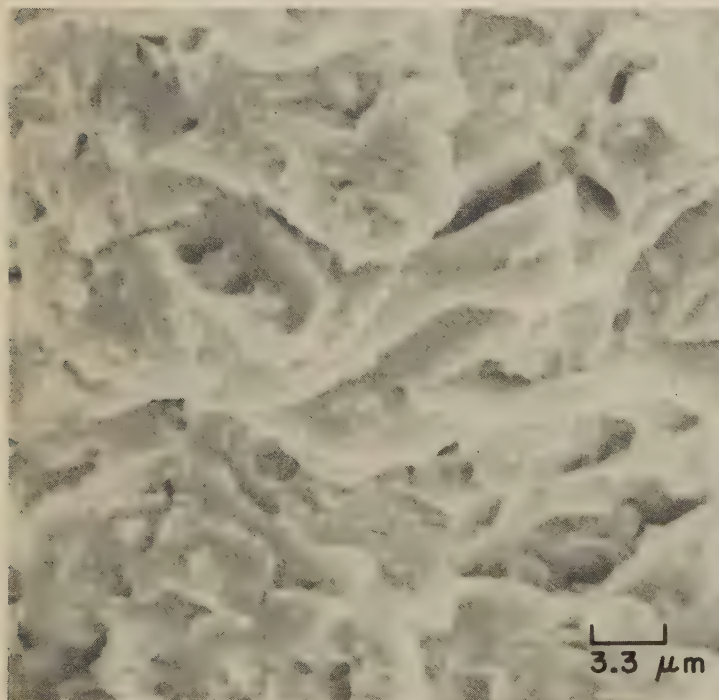
SEM Fractographs: Impact Fractures in 1042 Steel as Influenced by Heat Treatment and by Test Temperature



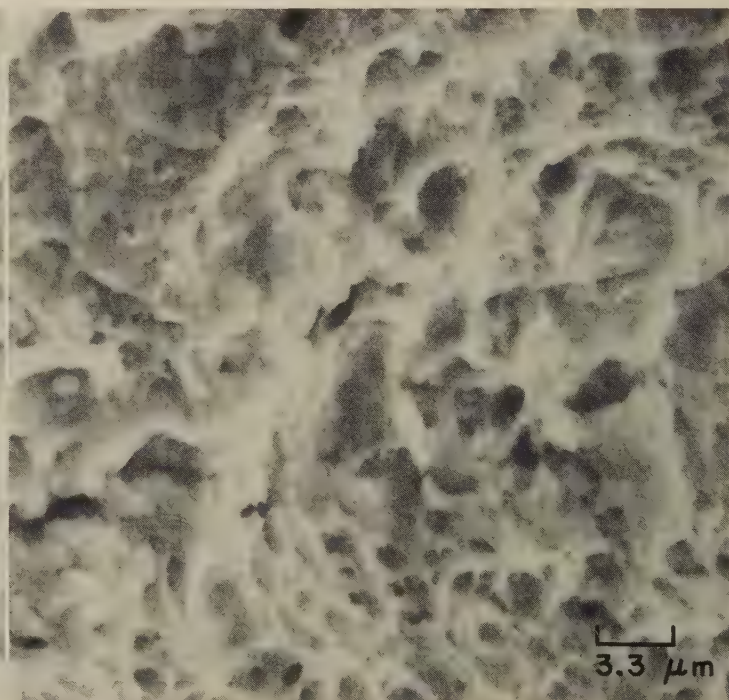
SEM fractograph 3000×
3619 Water quenched. Structure, slightly tempered martensite. Hardness, 660 dph. Fractured by impact at -196°C (-321°F) with an impact energy of 0.1 kgm/cm^2 . Complex cleavage steps about a few intergranular facets.



SEM fractograph 3000×
3620 Same as fractograph 3619 (at left), but this specimen was fractured by impact at 100°C (212°F) with an energy of 0.2 kgm/cm^2 . Note that this fracture has occurred almost completely by microvoid coalescence.



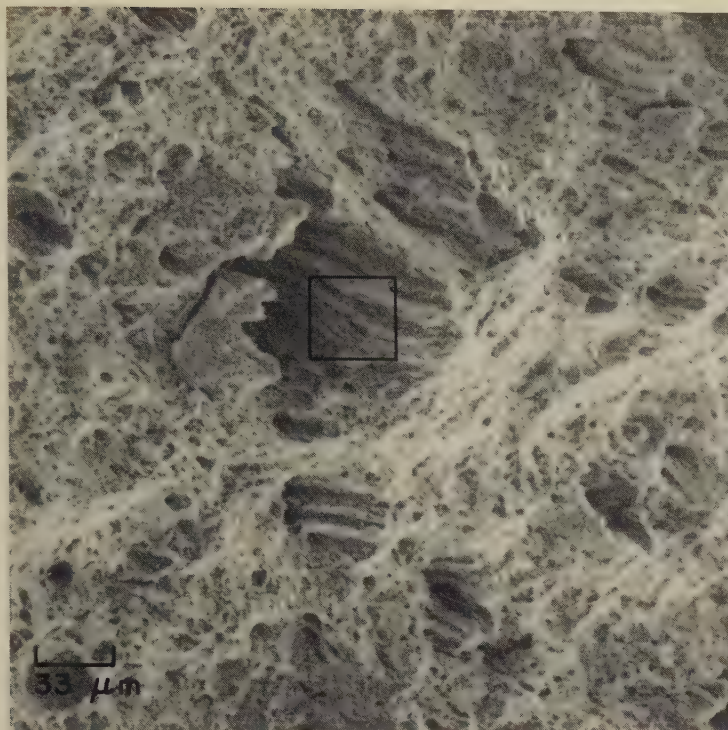
SEM fractograph 3000×
3621 Water quenched, and tempered for 1 hr at 500°C (932°F), giving a hardness of 335 dph. The specimen was then fractured by impact at -196°C (-321°F) with an energy of 1.4 kgm/cm^2 . Complex array of transgranular cleavage steps with several suggestions of small dimples.



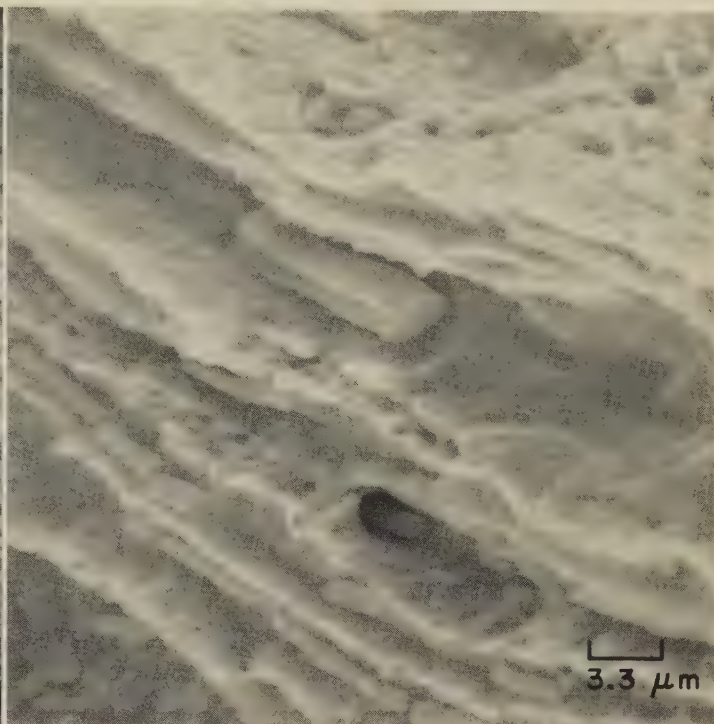
SEM fractograph 3000×
3622 Same as fractograph 3621 (at left), but fractured by impact at 100°C (212°F) with an impact energy of 8.8 kgm/cm^2 . This fracture surface shows much more flow than does the surface of the fracture shown in 3620 (above). Several of the dimples have been appreciably elongated.

The SEM fractographs above, and those on the facing page, show the surfaces of impact fractures obtained in specimens of 1042 steel (0.45% C, 0.62% Mn, 0.27% Si) that had been heat treated $\frac{1}{2}$ hr at 850°C (1562°F).

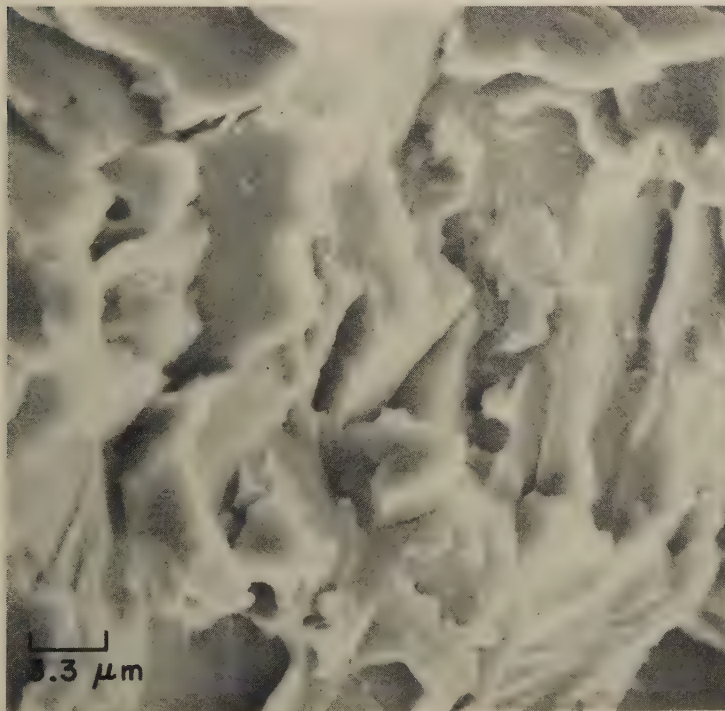
SEM Fractographs: Impact Fractures in 1042 Steel as Influenced by
Heat Treatment and by Test Temperature (Continued)



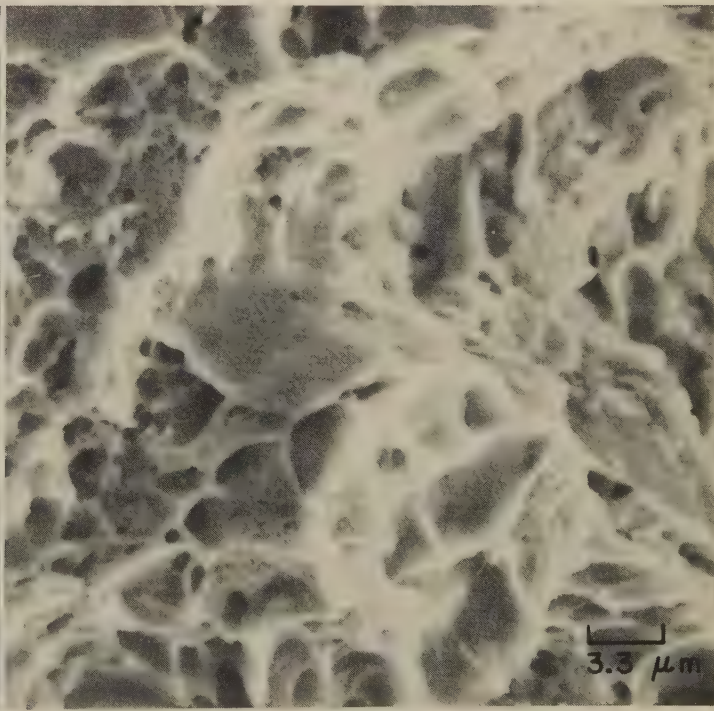
SEM fractograph 300×
3623 Same as 3622 (facing page), but at lower magnification. The dimpled rupture shows secondary cracks with stringer-type characteristics probably reflecting the orientation of the original rolling direction. See 3624 for enlargement of area in square.



SEM fractograph 3000×
3624 Higher-magnification view of the area within the square at center of fractograph 3623 (at left), showing more clearly the details of the inclusion stringers that were aligned by the rolling process. Local segregation of nonmetallic inclusions is indicated.



SEM fractograph 3000×
3625 After the ½-hr heat treatment at 850 C (1562 F), this specimen was air cooled. Hardness, 199 dph. The specimen was then broken by impact at -196 C (-321 F). The transgranular cleavage shows fine river patterns.



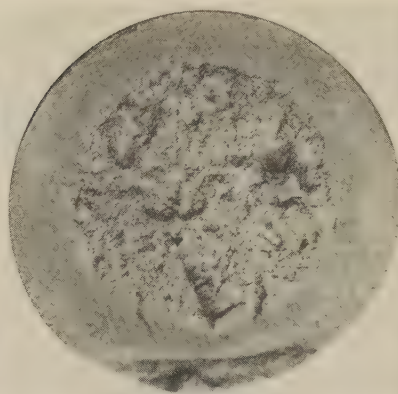
SEM fractograph 3000×
3626 Same as 3625 (left), but broken by impact at 100 C (212 F). As expected at this higher temperature, many of the dimples are highly elongated; several show a smoothness suggestive of the beginnings of stretching.

The SEM fractographs above, and those on the facing page, show the surfaces of impact fractures obtained in specimens of 1042 steel (0.45% C, 0.62% Mn, 0.27% Si) that had been heat treated ½ hr at 850 C (1562 F).

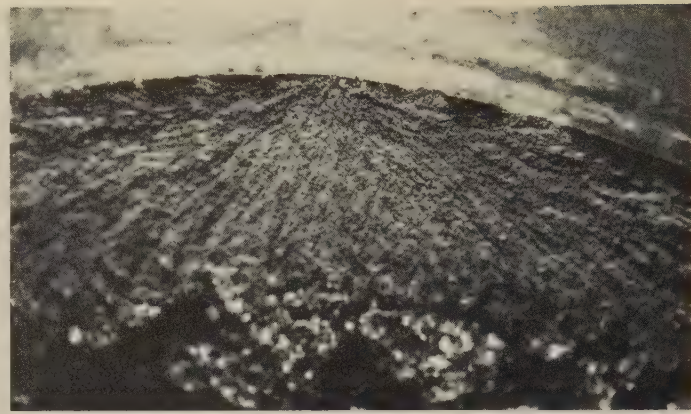
Light and SEM Fractographs: Service Impact Fracture of a 1050 Steel Automotive Rear Axle



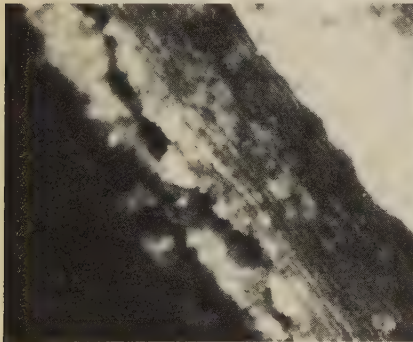
Light fractograph 1.5×
3627 Surface of an impact fracture in a 1050 steel automotive rear axle. The perimeter is fine grained; the core is fibrous. Note spill area. See 3628-3634.



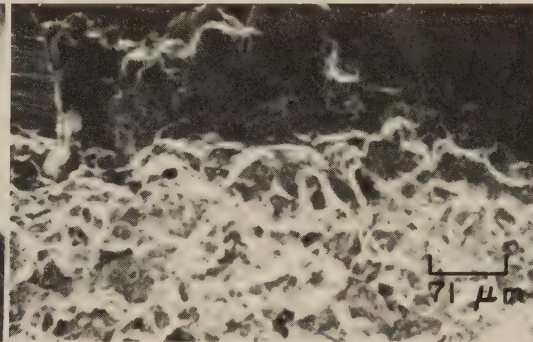
Light fractograph 1.5×
3628 End view of the fracture shown in 3627. Fine chevron marks are visible in the perimeter and point to the origin of the fracture (at top).



Light fractograph 4×
3629 Higher-magnification view of fracture origin in 3628, showing more clearly the chevron marks radiating from the crack nucleus at the edge at top center. Note poorly contoured fillet on axle surface immediately adjacent to fracture origin. See 3630 to 3632.



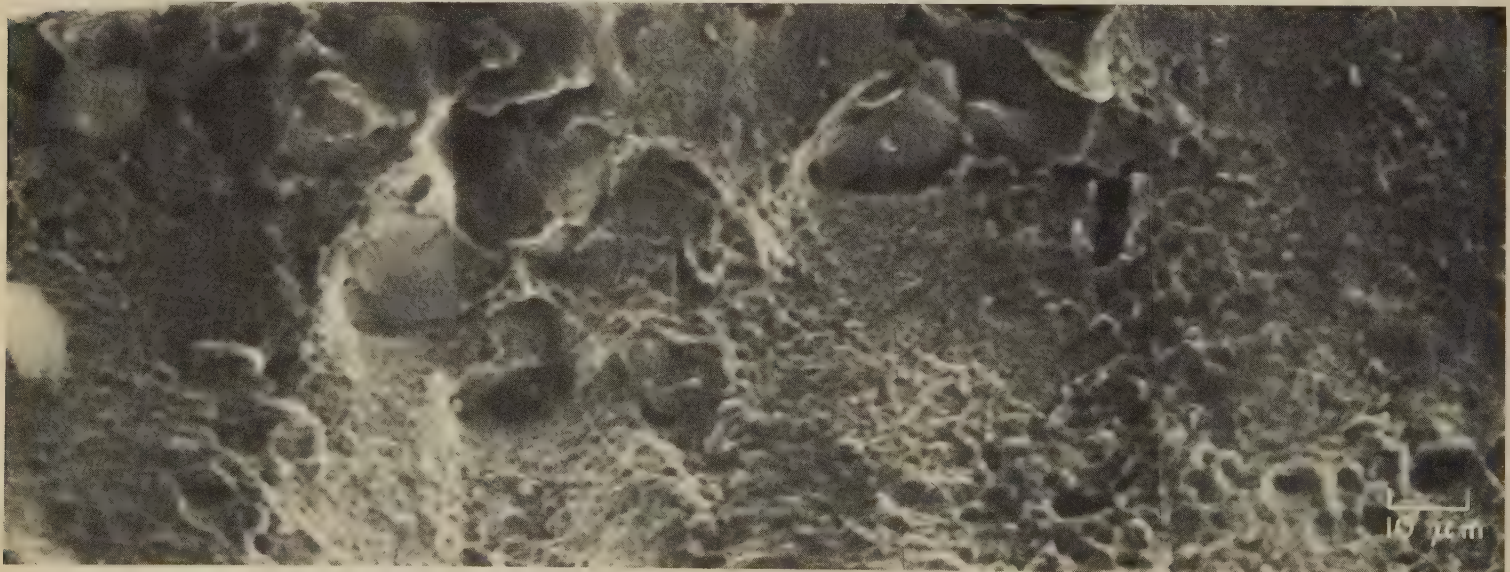
Light fractograph 30×
3630 A still more highly magnified view of the fillet and edge of the crack origin shown in 3629. Note the rough machining marks in the fillet.



SEM fractograph 140×
3631 Oblique view of the fracture-origin area in 3628 to 3630, showing the tool marks in the fillet above and the overload-tension dimples below. No evidence of harmful inclusions was found in subsequent sectioning.

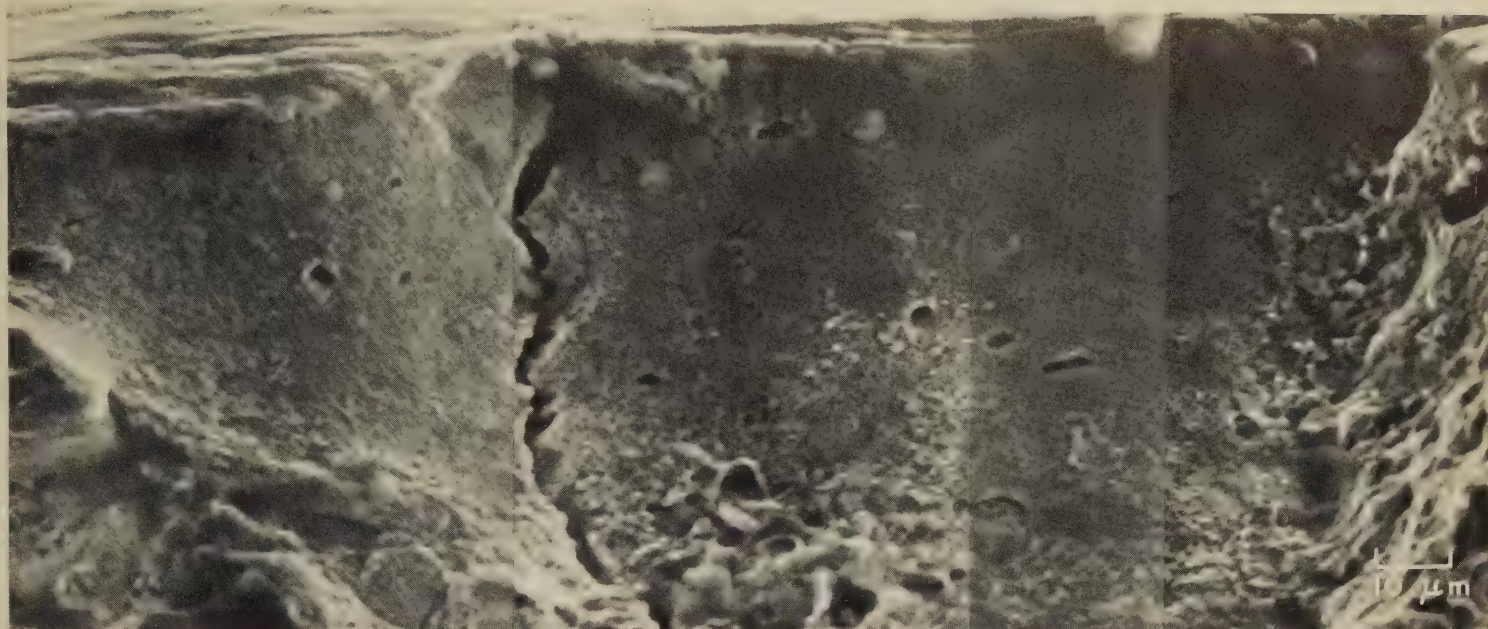


SEM fractograph 140×
3632 Same area as shown in fractograph 3631, but viewed from a different angle. The area of the crack origin (see 3633, 3634) lies in the fracture surface where it intersects the fillet surface (at top).



SEM fractograph (composite) 1000×
3633 Composite of four SEM views of the fracture-origin area shown in fractograph 3632, covering approximately one-half of the region visible in 3632 (left edge to center). It is evident that the first shallow penetrations of the crack were by stage I of fatigue-fracture progress and thus generated no fatigue striations. Penetration of the crack shortly transformed to advance by microvoid coalescence under impact. Note that the dimples visible here are exceedingly fine. The remainder of the fracture-origin area visible in fractograph 3632 (right edge to center) is shown as another composite in fractograph 3634 (top of facing page).

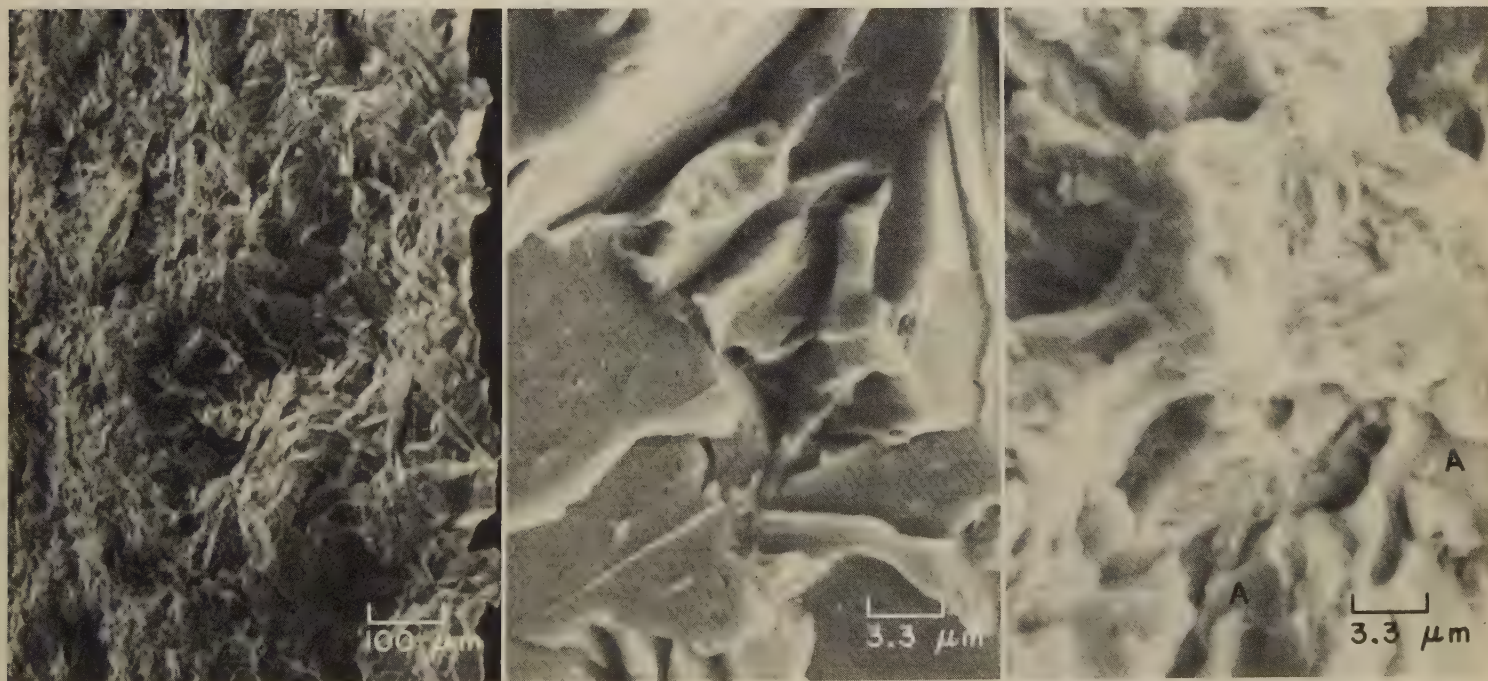
SEM Fractographs: Impact Fracture of a 1050 Steel Axle (Continued);
Impact Fracture of High-Silicon 1060 Steel at -196°C (-321°F)



SEM fractograph (composite)

1000×

3634 Composite of four SEM views of the fracture-origin area shown in fractograph 3632, encompassing approximately one-half of that area (right edge to center). This composite completes a scan that was begun in 3633 (bottom row on facing page). Note the secondary crack, which is normal to the fillet and to the fracture surface, and which never grew beyond approximately 0.08 mm in length. Barely visible to the right is a transition to a dimpled overload type of rupture. No traces of fatigue striations are visible in the fatigue area, which (as in fractograph 3633) is consistent with stage I of fatigue-fracture progress.



SEM fractograph

100×

3635 Surface of impact fracture obtained at -196°C (-321°F) in modified 1060 steel (1.7% Si) decarburized 2 hr at 1075°C (1967°F), cooled to 850°C (1562°F), and oil quenched. Depth of decarburization, 0.30 mm. See 3636, 3637.

SEM fractograph

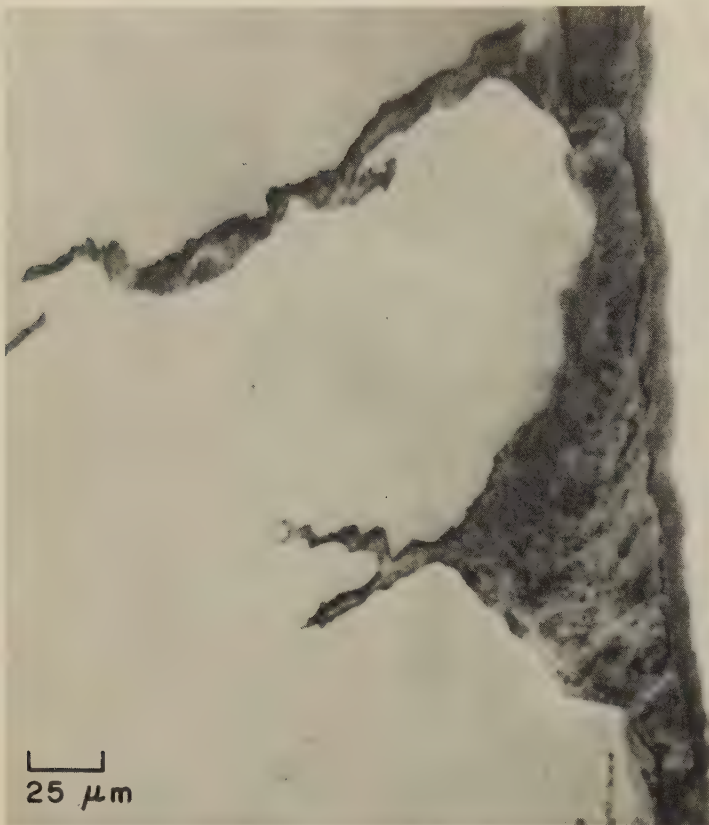
3000×

3636 Higher-magnification view of the decarburized zone (at right) in the specimen shown in fractograph 3635, showing that in this zone fracture was of the cleavage type. Note the feathery fine river patterns at top. See also 3637.

SEM fractograph

3000×

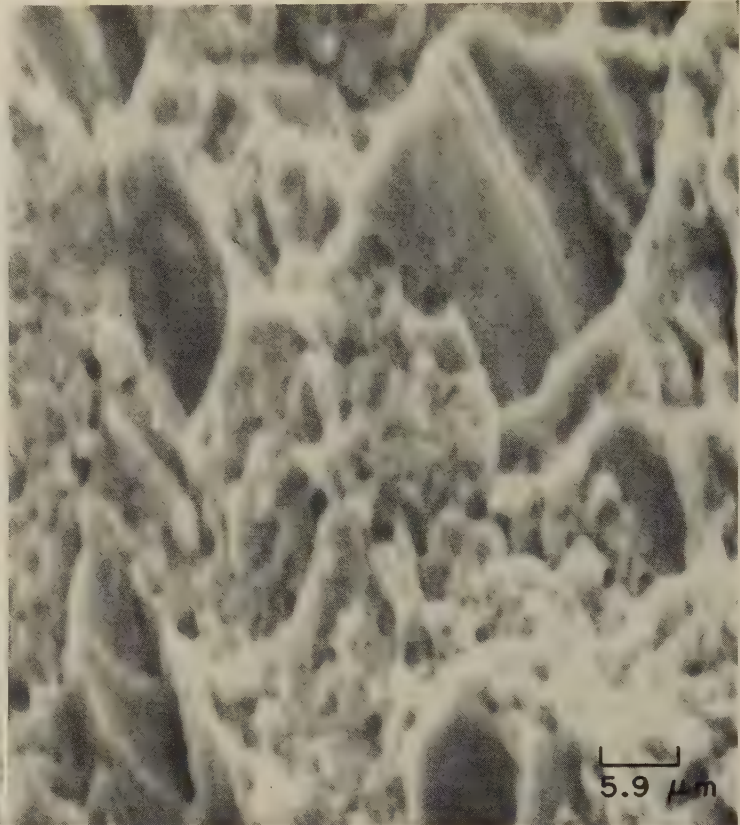
3637 Higher-magnification view of region below decarburized zone in 3635. In this region, the fracture appears to have progressed by more than one mechanism; small cleavage facets (marked A) and suggestions of small dimples both can be seen.



SEM micrograph - as polished

400×

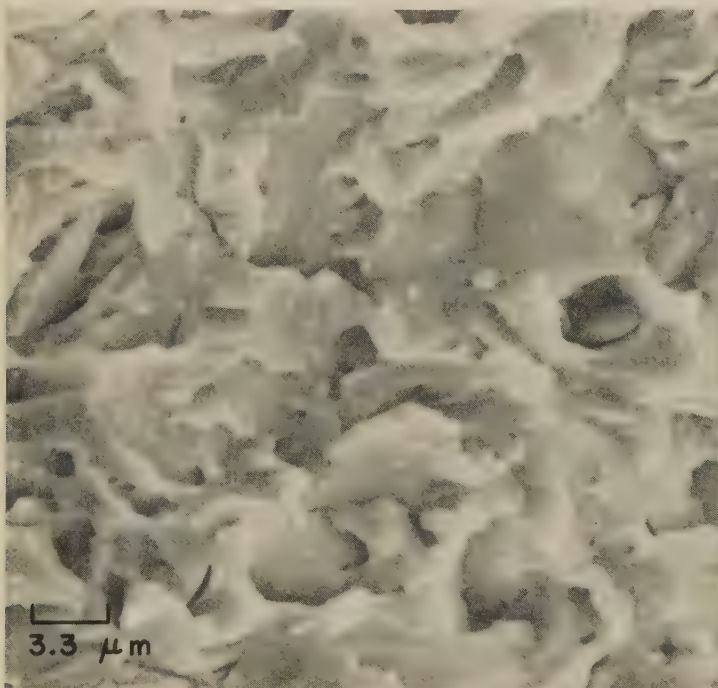
3638 Polished longitudinal section through a cold drawn wire (from a wire rope) of 1080 steel, showing corrosion pits, in the wire surface (right), from which stress-corrosion cracks have grown. Final rupture was by fast fracture (see 3639).



SEM fractograph

1700×

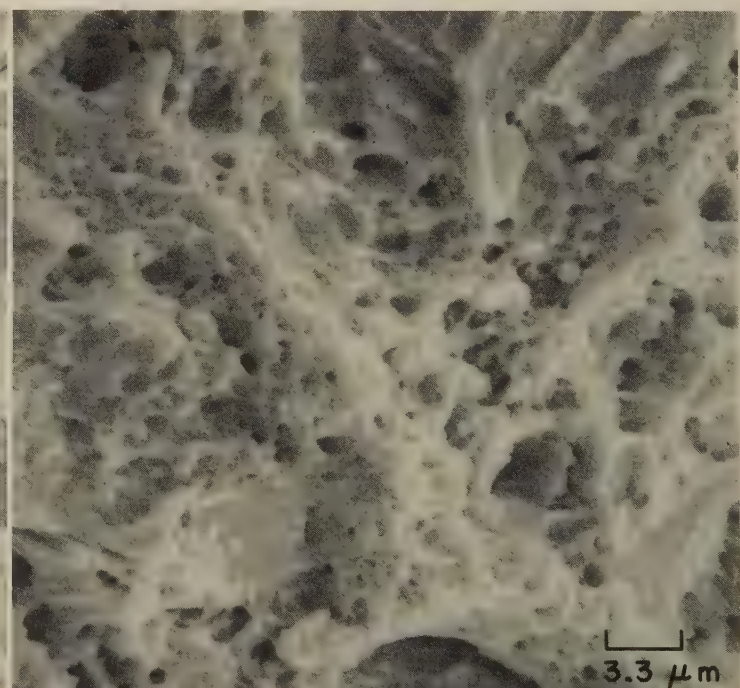
3639 Final fracture surface of the 1080 steel wire in 3638. The fracture began as stress-corrosion cracking (see 3638) and terminated in fast fracture. This view shows a region of fast fracture that consists generally of dimples.



SEM fractograph

3000×

3640 Specimen of 1090 steel austenitized at 850°C (1562°F) $\frac{1}{2}$ hr, salt quenched to 280°C (536°F), held 1 hr, water cooled. Hardness, 602 dph. Microstructure, bainite and fine pearlite. Broken by impact at -196°C (-321°F). Complicated system of cleavage facets and steps. See also fractograph 3641.

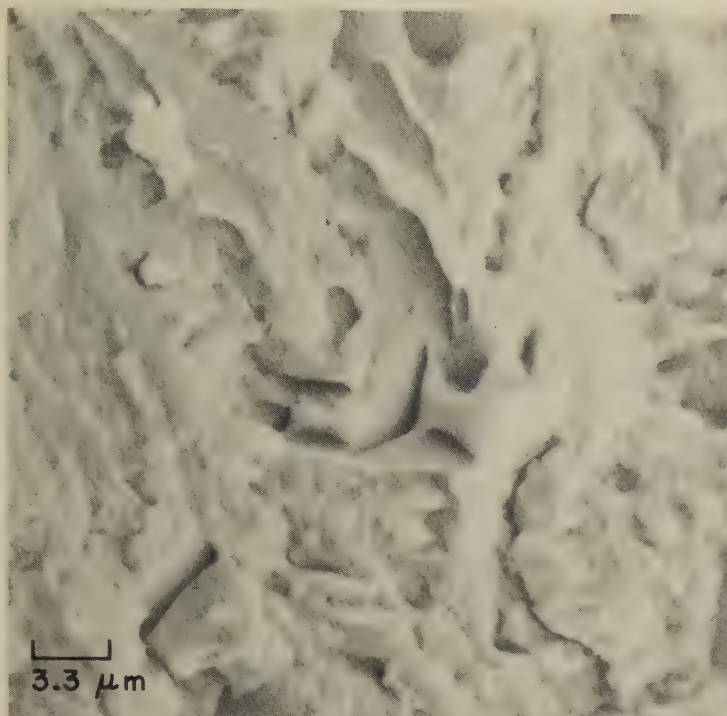


SEM fractograph

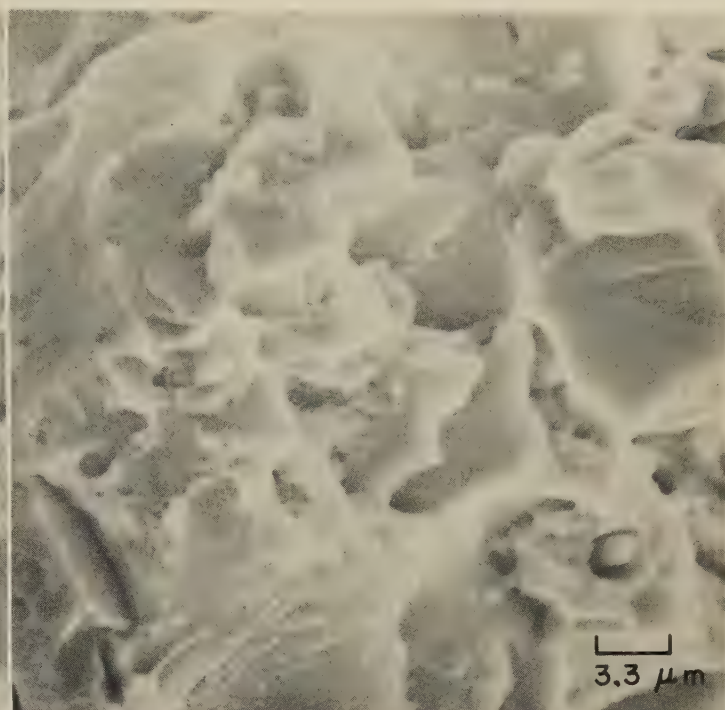
3000×

3641 Another specimen of 1090 steel, given the same heat treatment as described in 3640 (left), but broken by impact at 100°C (212°F). A large portion of the fracture surface is composed of small dimples. See fractographs 3642 to 3652, on the next three pages.

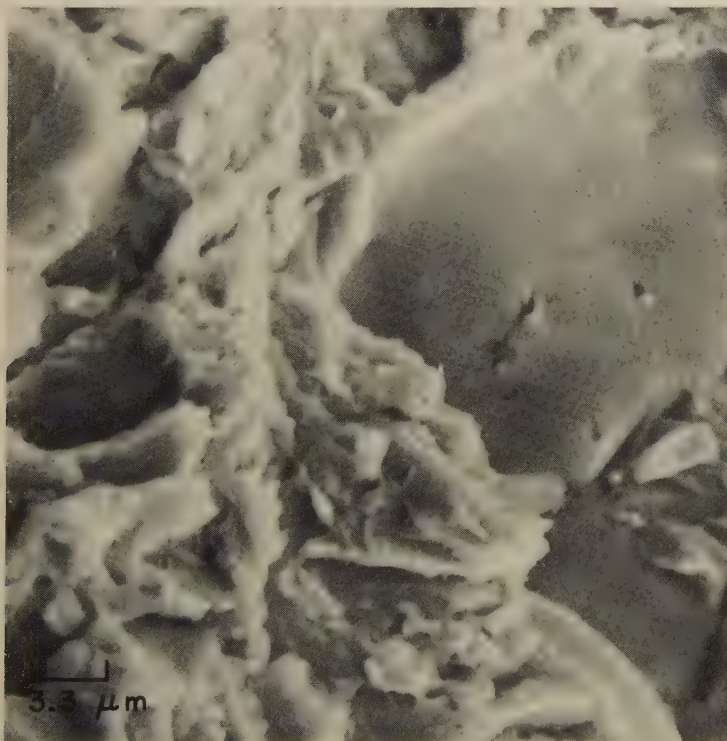
SEM Fractographs: Impact Fractures of 1090 Steel as Influenced by Heat Treatment and by Test Temperature



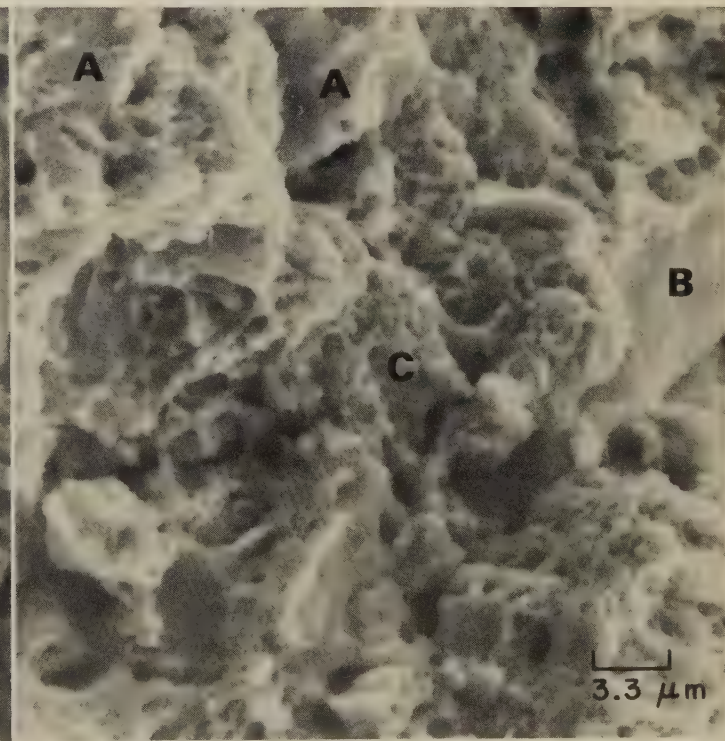
SEM fractograph 3000×
3642 Fracture in 1090 steel heat treated ½ hr at 850 C (1562 F), and air cooled. Hardness, 697 dph. Structure, martensite. This specimen was fractured by impact at -196 C (-321 F), producing a complex-cleavage fracture surface. Small secondary cracks are evident. See also 3643.



SEM fractograph 3000×
3643 Same steel and same heat treatment as in fractograph 3642 (left), but fractured by impact at 100 C (212 F). Cleavage facets are the dominant feature here, but a few small dimples can be seen also; one of them is located at lower right and contains an inclusion.

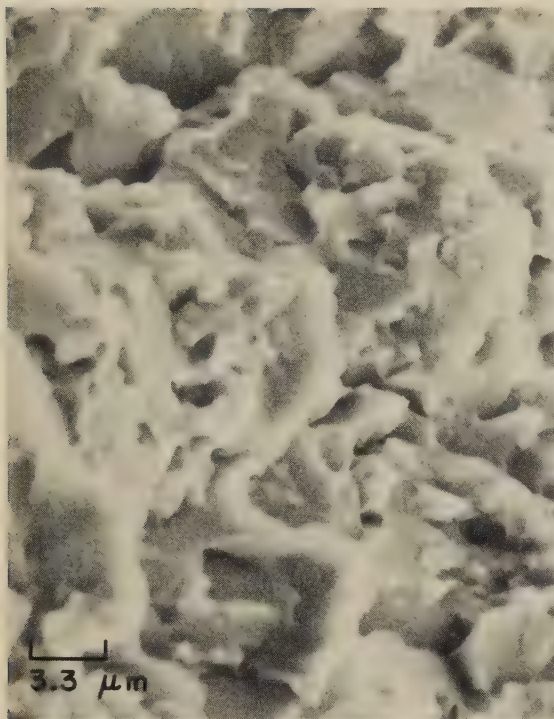


SEM fractograph 3000×
3644 Fracture in 1090 steel heat treated ½ hr at 850 C (1562 F), oil quenched, tempered 1 hr at 400 C (752 F). Hardness, 501 dph. Specimen was broken by impact at -196 C (-321 F). Intricate-cleavage areas interspersed with broad facets of intergranular fracture. See 3645.



SEM fractograph 3000×
3645 Same steel and same heat treatment as in 3644 (left), but broken by impact at 100 C (212 F). This fracture surface contains a few cleavage facets (A) and shows evidence of some grain-boundary rupture (B), but mostly it consists of a general array of very fine dimples (C).

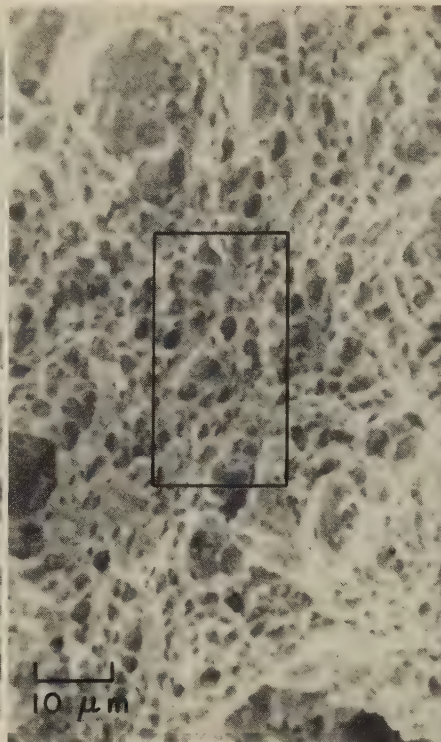
SEM Fractographs: Impact Fractures of 1090 Steel as Influenced by Heat Treatment and by Test Temperature (Continued)



SEM fractograph

3000×

3646 Fracture in 1090 steel heat treated ½ hr at 850 C (1562 F), oil quenched, tempered 20 hr at 715 C (1319 F), air cooled. Microstructure, spheroidized carbide. Hardness, 189 dph. Impact was at -196 C (-321 F). Impact energy, 0.3 kgm/cm². Uniform, petal-like cleavage steps. See also fractographs 3647 and 3648, at right.

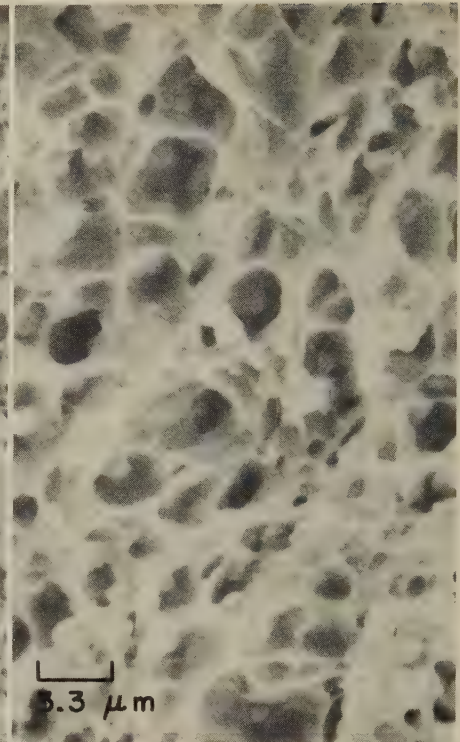


SEM fractograph

1000×

3647, 3648

Two SEM fractographs, at two different magnifications, showing a fracture in a specimen of the same steel as in 3646 (at left). This specimen received the same heat treatment as that described in 3646, but was fractured by impact at 100 C (212 F). Impact energy was 17.1 kgm/cm². A finely dimpled structure. The rectangle in fractograph 3647 (left) indicates the area shown at higher magnification in fractograph 3648 (right).



SEM fractograph

3000×

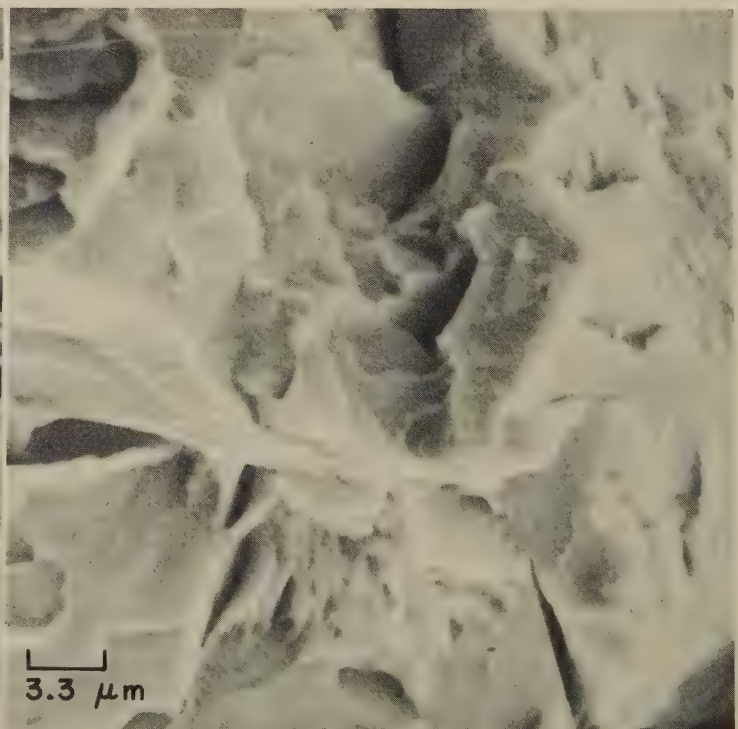


SEM fractograph

3000×

3649, 3650

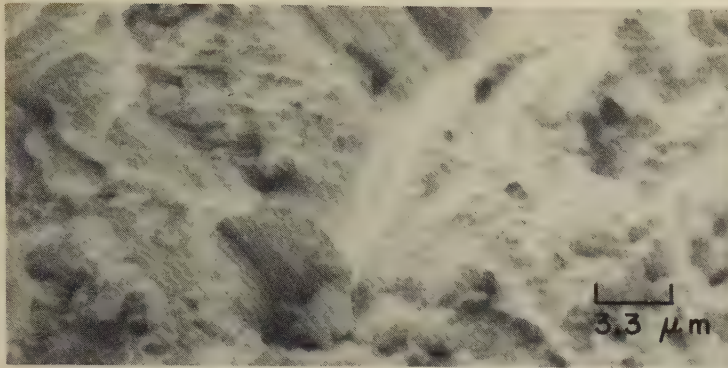
Two SEM fractographs showing different regions of a fracture in 1090 steel that was heat treated ½ hr at 850 C (1562 F) and air cooled (same as 3642). Microstructure is pearlite. Hardness, 300 dph. The specimen was fractured by impact at -196 C (-321 F). The fracture surface consists of cleavage facets. In fractograph 3649 (left), the orientation of the pearlite lamellae with the fracture surface allows the pronounced secondary cracking to be seen. In the area shown in fractograph 3650 (right), the presence of the lamellae has influenced crack propagation, producing cleavage steps. See also 3651 and 3652.



SEM fractograph

3000×

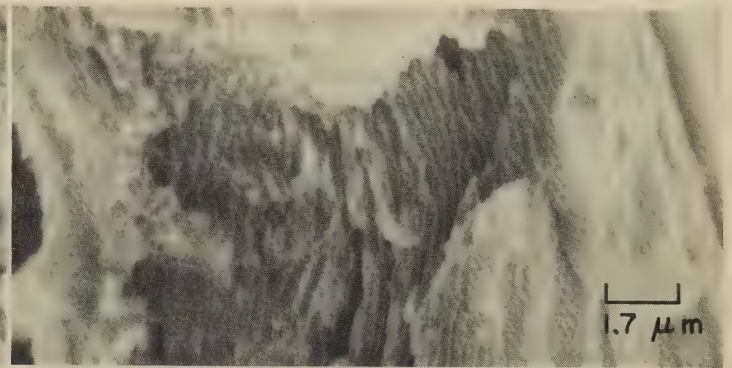
SEM and Light Fractographs: Impact Fractures of 1090 Steel (Continued); Fatigue Fractures of a 1095 Steel Clutch-Assembly Spring and an 1115 Steel Clutch Shaft



SEM fractograph

3000×

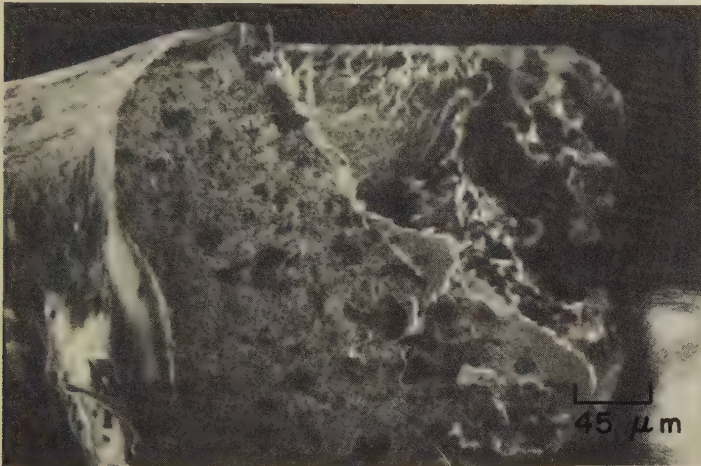
3651 Fracture surface in a specimen of the same steel, heat treatment and hardness as 3649 and 3650, but fractured by impact at 100 C (212 F). At this location, crack propagation was transverse to pearlite lamellae, which are plainly visible and could easily be mistaken for fatigue striations. See also 3652 (right).



SEM fractograph

6000×

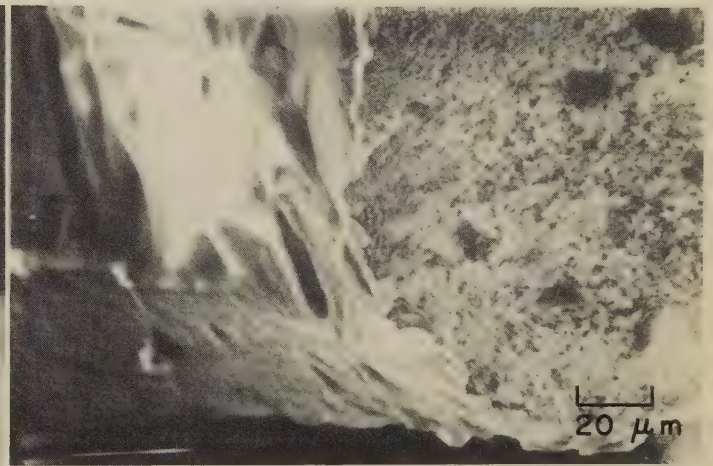
3652 Same as 3651 (at left), but showing a different region of the fracture surface at higher magnification. Note that in several local areas the pearlite lamellae have been separated by secondary cracks in a manner similar to, but less pronounced than, that shown in 3649.



SEM fractograph

220×

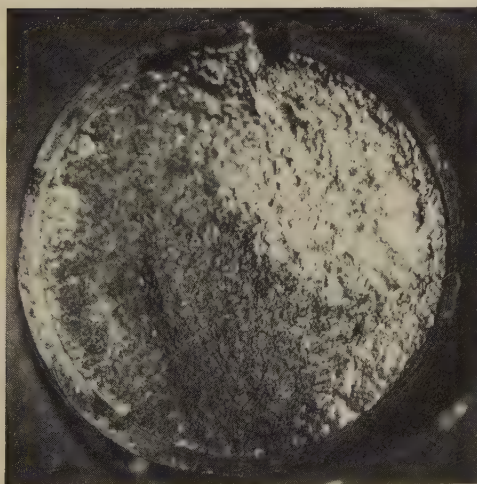
3653 1095 steel spring that fractured by fatigue in a card-tape-punch clutch assembly. The origin of the initial (fatigue) fracture is at lower left. The surface of the final abrupt fracture is at upper right. There appears to be evidence of smeared metal in the center of the fatigue-fracture surface.



SEM fractograph

1000×

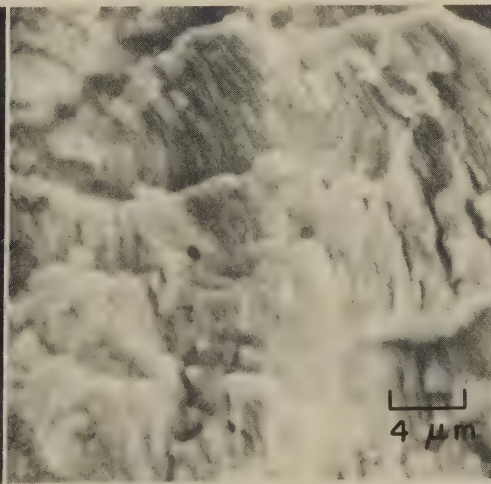
3654 Higher-magnification view of the fracture-origin area in 3653 (left). Just inside the fracture edge at bottom is a faint trace of features that bear a resemblance to fatigue striations. The adjacent outside surface of the spring appears to have undergone mechanical damage.



Light fractograph

6×

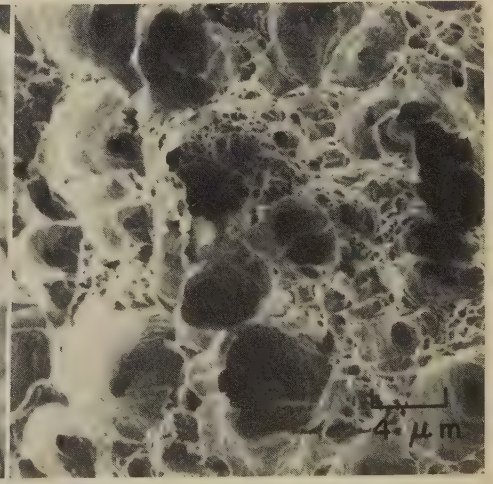
3655 Fracture surface of a broken clutch shaft of an air conditioner. Material is free-machining resulfurized 1115 steel. Note dark oxidized area. See also fractographs 3656 and 3657, at right.



SEM fractograph

2500×

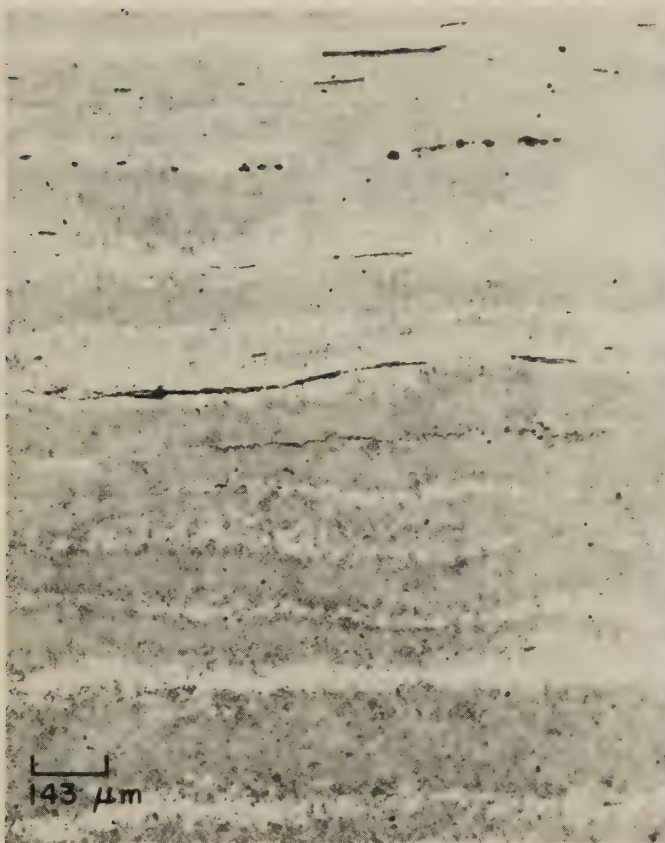
3656 SEM fractograph of region in oxidized area in 3655. Distinct striations indicate that initial cracking was by fatigue. Secondary fissures may be due to sulfide inclusions.



SEM fractograph

2500×

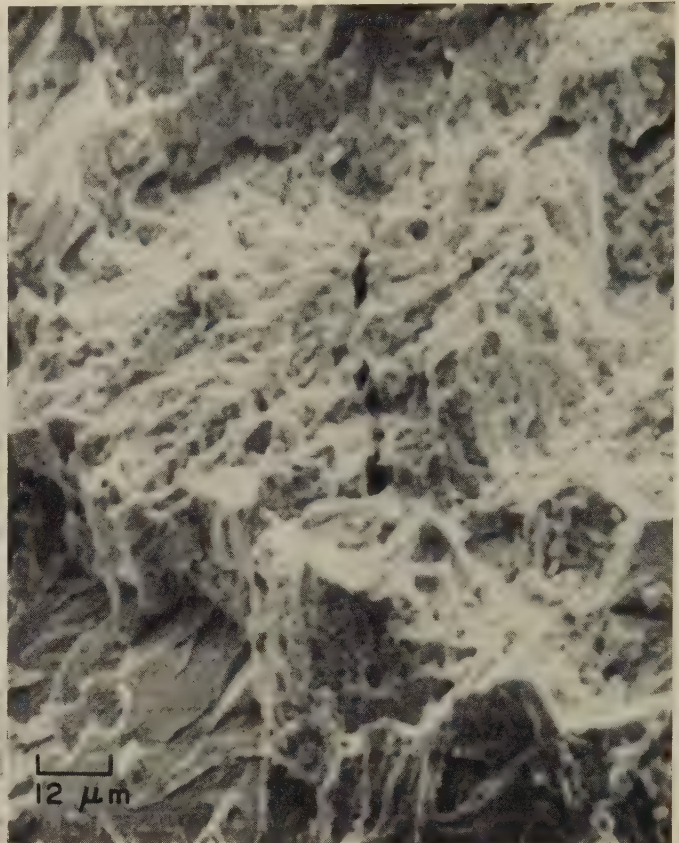
3657 SEM fractograph of a region in the bright area in 3655, showing variegated dimples, which indicate that final rupture was by ductile fast fracture. See also fractograph 3656, at left.



Micrograph - 3% nital

70×

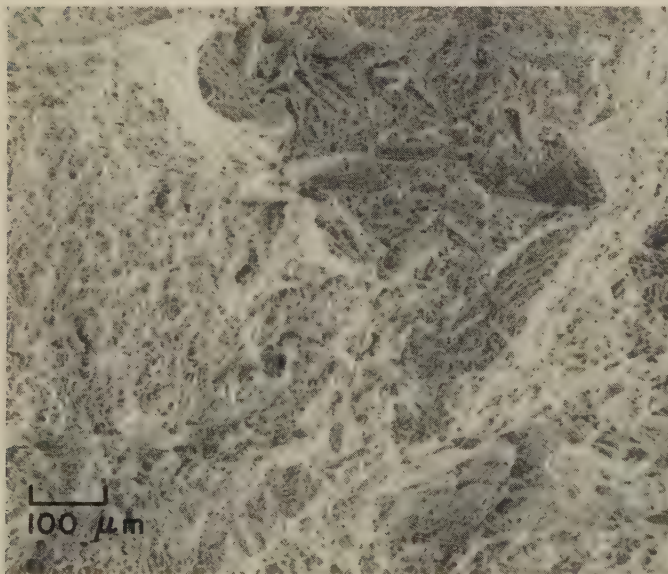
3658 Polished longitudinal section through a forged bar of 4070 steel that partially hardened in segregated regions during cooling from the normalizing temperature. Microstructure: dark bands consisting of pearlite and upper bainite; light bands consisting of martensite and retained austenite and containing black stringers of MnS. See 3659.



SEM fractograph

850×

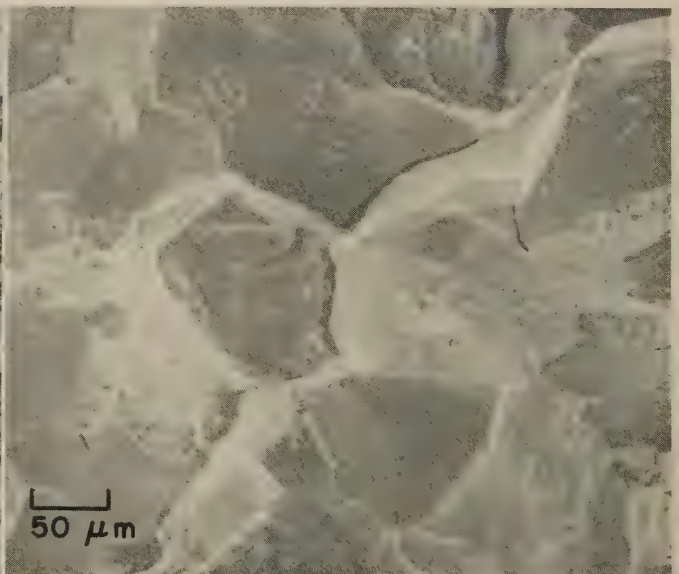
3659 Surface of a fracture in the bar shown sectioned in 3658. Fracture occurred both by cleavage and by microvoid coalescence. A longitudinal cleavage step extends diagonally across the area at lower left. This step and similar steps in the fracture surface could not be correlated with specific features of the banded microstructure in 3658.



SEM fractograph

100×

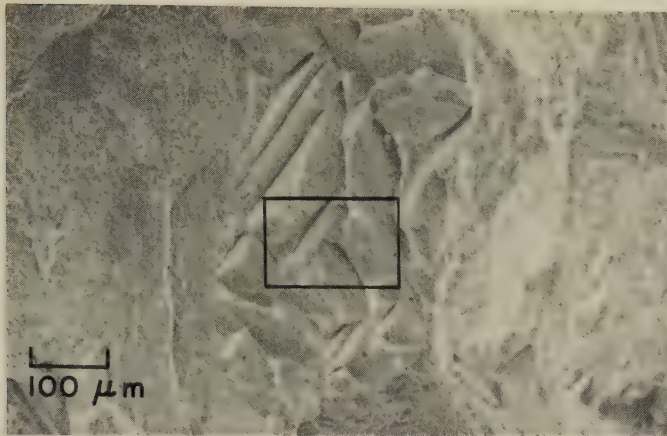
3660, 3661 Fracture surfaces of specimens of 4130 steel that were fractured in plane-strain fracture-toughness tests at room temperature. Both specimens were given experimental heat treatments aimed at increasing fracture toughness. The specimen shown in 3660 (left) was austenitized at 1204 C (2200 F) and quenched in iced brine; K_{Ic} was 100 ksi·in.^{1/2} (110 MPa·m^{1/2}). The surface shows relatively large dimples and a few quasicleavage facets. The specimen shown in 3661 (right) was given the same heat treatment as described for 3660, but was then tempered for 1 hr at 350 C (662 F); K_{Ic} was 68 ksi·in.^{1/2} (75 MPa·m^{1/2}). The surface shows facets of intergranular rupture and scattered areas of dimples. See 3662 to 3665 (facing page) for effects of other heat treatments on the fracture behavior of this steel.



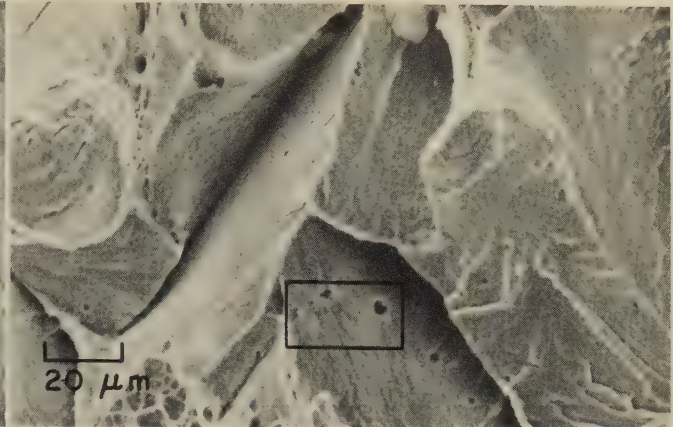
SEM fractograph

200×

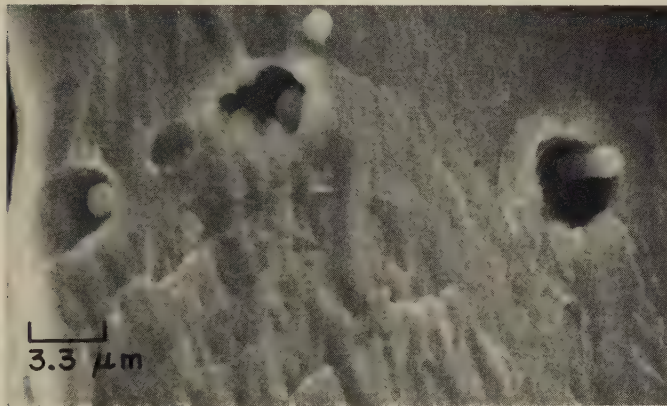
SEM Fractographs: Effect of Heat Treatment on Fracture-Toughness-Test Fractures in 4130 Steel (Continued); Fracture Produced in 4130 Steel in a Fracture-Toughness Test in Air



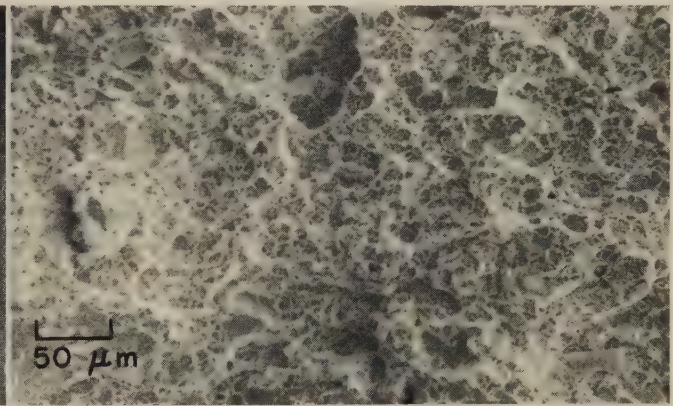
SEM fractograph 100×
3662 Fracture surface of a 4130 steel specimen given the same heat treatment as described for 3660, but oil quenched from the austenitizing temperature. The specimen was broken in a plane-strain fracture-toughness test at 22 C (72 F). Fracture shows pronounced angular cleavage in central region and finer cleavage details elsewhere. Rectangle marks area shown enlarged in 3663 (right).



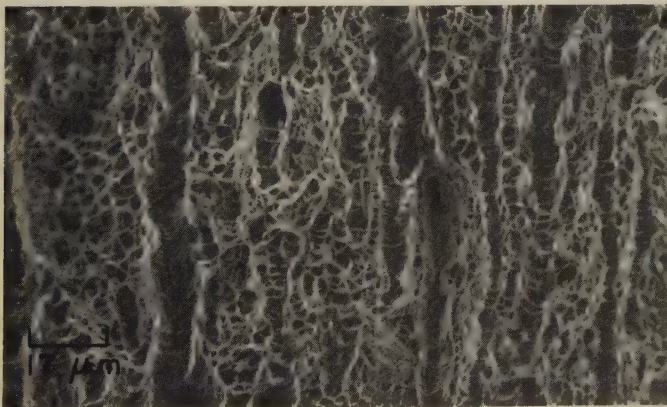
SEM fractograph 500×
3663 A higher-magnification view of the area within the rectangle at center in fractograph 3662 (at left), revealing more clearly the cleavage facets, which have radically different orientations. A few dimples can be seen at top left and at bottom left. The rectangle here indicates the area that is shown at an even greater magnification in fractograph 3664 (below, left).



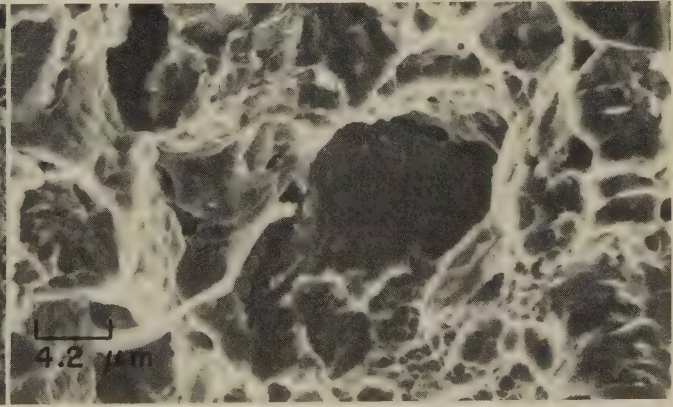
SEM fractograph 3000×
3664 A higher-magnification view of the area within the rectangle in fractograph 3663, showing a portion of one cleavage facet. Contained in the facet are several voids, each of which has opened around an inclusion. The marks on the facet do not suggest that these voids aided nucleation of the fracture.



SEM fractograph 200×
3665 Fracture surface of 4130 steel specimen austenitized at 871 C (1600 F) and oil quenched (standard heat treatment). Broken in a plane-strain fracture-toughness test at 22 C (72 F). K_{Ic} was 55 ksi·in.^{1/2} (60 MPa·m^{1/2}), appreciably less than the fracture toughness of the specimen in 3660; however, the fracture surfaces of these specimens are very similar.

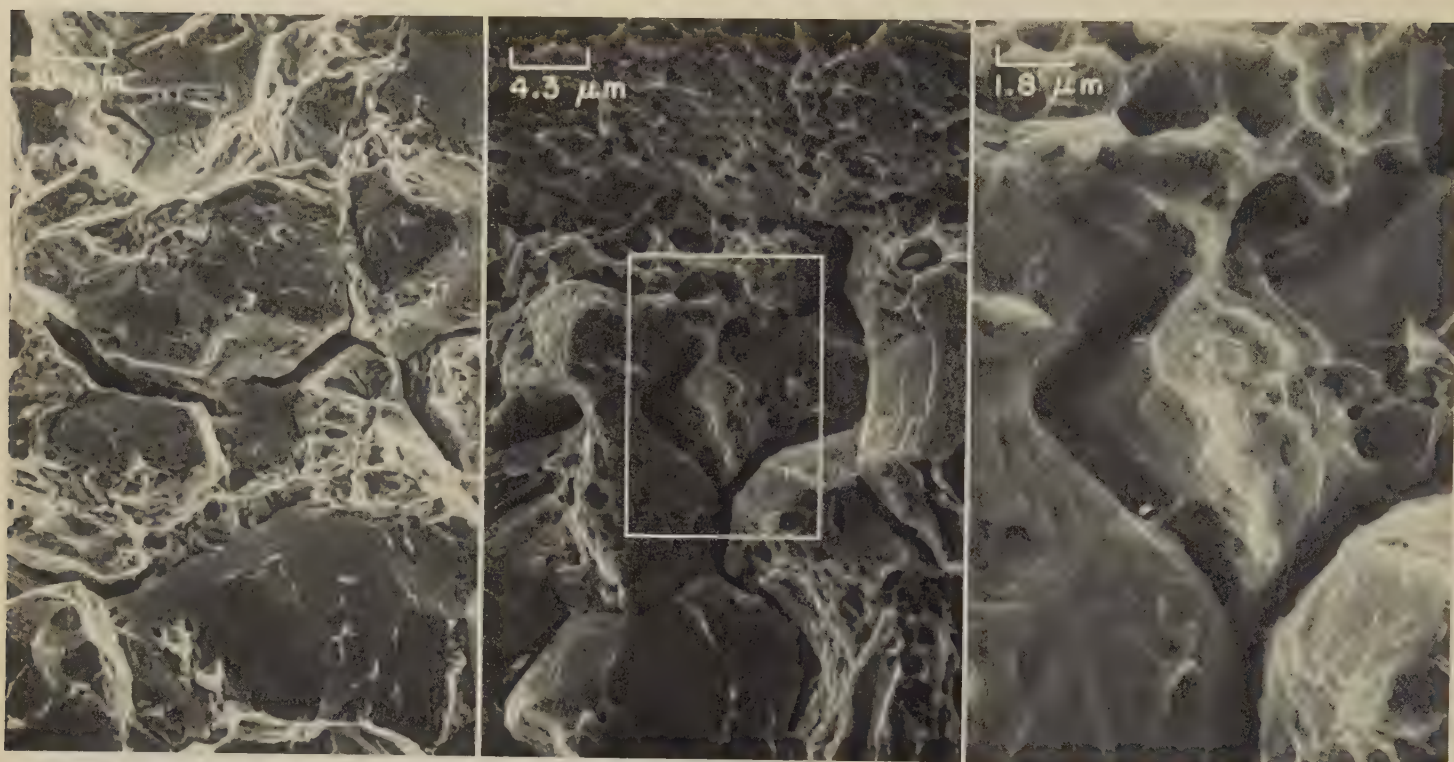


SEM fractograph 600×
3666, 3667 Two SEM views, at different magnifications, of the surface of a fracture in a specimen of 4130 steel that was austenitized at 843 C (1549 F), oil quenched, and tempered for 2 hr at 250 C (482 F). The fracture was produced in a toughness test in air; the rate of crack growth was in the range of rapid, unstable fracture. Dimples in an extremely wide variety of sizes, and channels formed by linear coalescence of voids, are evident. See also fractographs 3668 to 3673 for the fracture behavior of this material when tested in a hydrogen atmosphere.



SEM fractograph 2400×

SEM Fractographs: Effect of Test Temperature and Degree of Hydrogen Dissociation on Fractures Produced in 4130 Steel in Slow-Crack-Growth-Rate Tests in Hydrogen



SEM fractograph

1000×

SEM fractograph

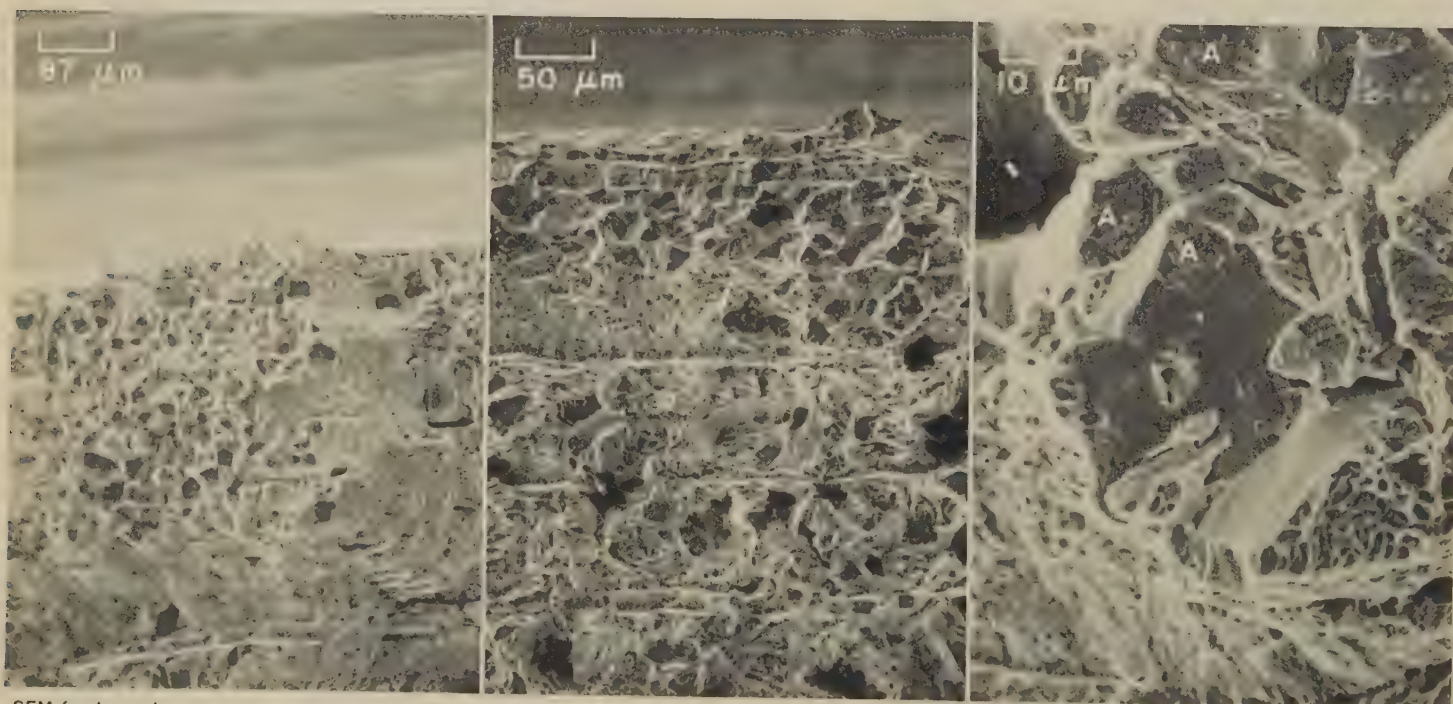
2350×

SEM fractograph

5600×

3668, 3669, 3670

Fracture surfaces of two specimens of 4130 steel that were given the same heat treatment as described in 3666 and 3667. The specimen shown in 3668 (left) was tested in one atmosphere of hydrogen at 24 C (75 F); the specimen shown in 3669 (center) and 3670 (right) was tested in one atmosphere of hydrogen at 80 C (176 F). Note that the area within the rectangle in 3669 is shown at higher magnification in 3670. In contrast to those in 3666 and 3667, these fracture surfaces show completely intergranular fractures with deep secondary cracks between the grains. The fracture in 3669 and 3670 also shows a considerable number of dimples that were formed by microvoid coalescence. See also 3671 to 3673 (below) for the fracture behavior of this material in an atmosphere of partially dissociated hydrogen.



SEM fractograph

115×

SEM fractograph

200×

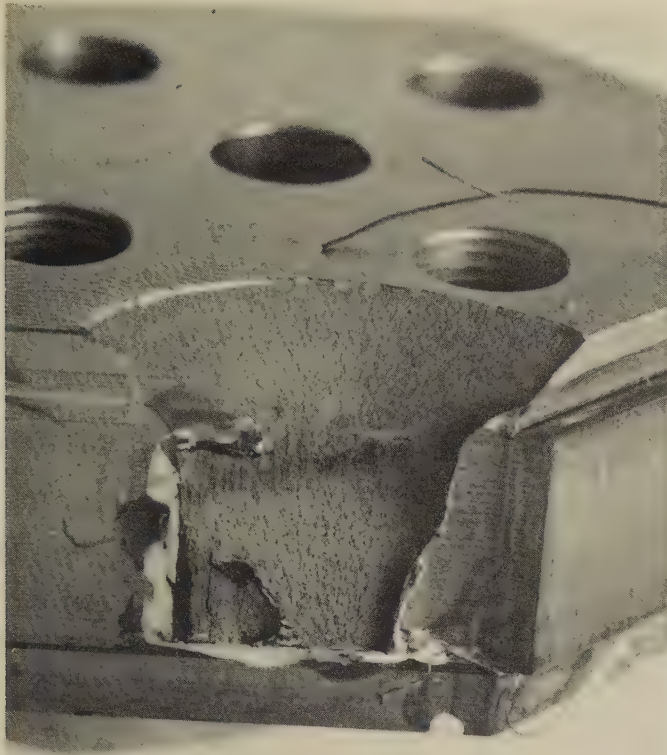
SEM fractograph

1000×

3671, 3672, 3673

Three SEM views, at different magnifications, of the surface of a fracture in a specimen of the same steel and heat treatment as in 3666 to 3670, tested for stable crack-growth rate in 0.1 atmosphere of partially dissociated hydrogen at 80 C (176 F). Similar to the fracture in 3669 and 3670, this fracture shows facets of intergranular rupture intermingled with fracture surface parallel with the notch could be indications of temporary arrests of crack penetration. The horizontal marks in the A) visible in 3673 (right) are fine tear ridges typical of hydrogen embrittlement.

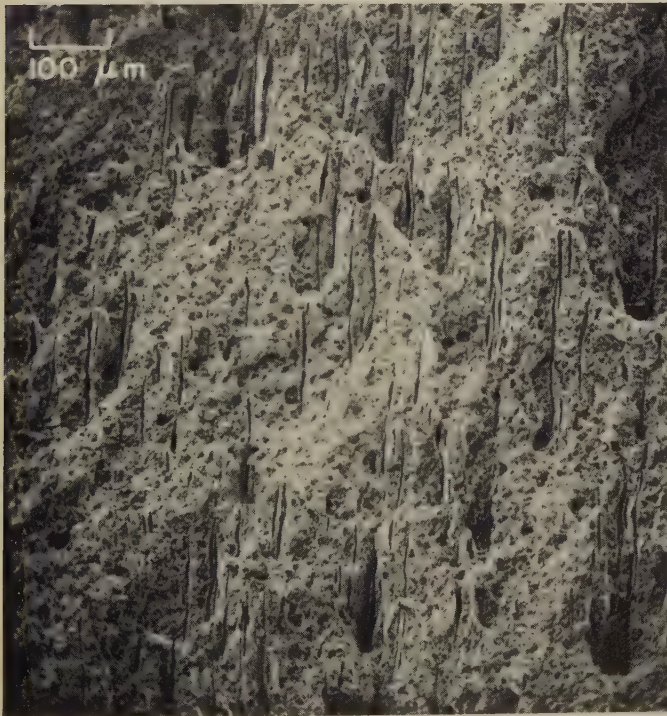
Light and SEM Fractographs: 4140 Steel Load Cell Fractured by Sudden Overload;
Fatigue Fracture in 4140 Steel Heat Treated to High Strength



Light fractograph Actual size
3674 Fracture surface of a broken 4140 steel load cell. The radial marks indicate that two crack origins formed at the bottom surface of the cell, apparently near the toe of a weld. Note the continuous shear lip around the top edge. See also fractographs 3675 and 3676.



Light fractograph Actual size
3675 Mating fracture surface to that shown in 3674 (left). There appears to be no evidence of fatigue marks; however, fatigue cracking may have taken place within a very small area at the crack origins. Fracture was evidently caused by a sudden overload. See fractograph 3676.

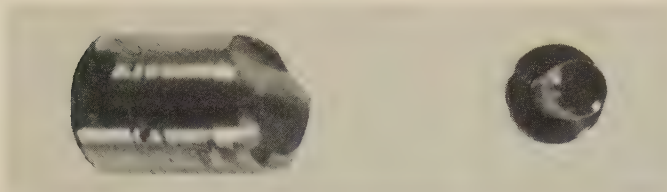


SEM fractograph 100×
3676 Magnified view of the fracture surface in 3674, taken at an area away from the edge, and showing the dimples that are typical of transgranular fast fracture. Vertical marks are sulfide stringers.



SEM fractograph 720×
3677 Fracture surface of a 4140 steel specimen that was heat treated to high strength and broken in fatigue. Deep secondary cracks are present. Features that appear to be fatigue striations (such as at arrows) may actually be fissures.

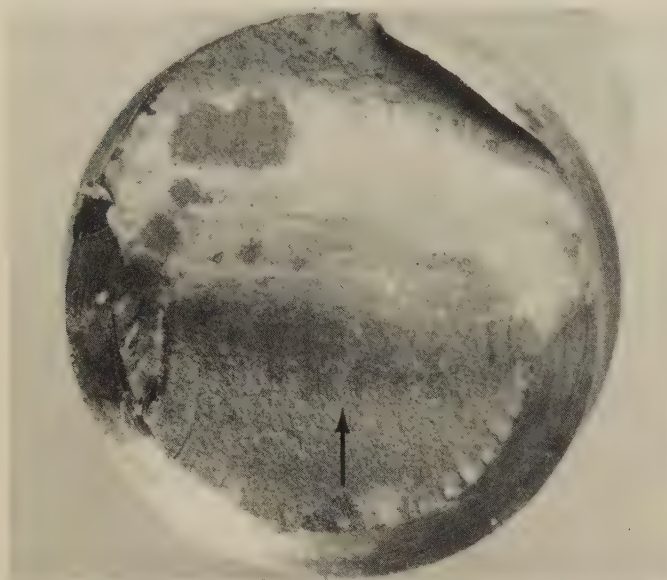
Photographs, Light Fractographs, SEM and TEM Fractographs: 4340 Steel Connecting-Rod Bolts
Fractured in a Fatigue Test



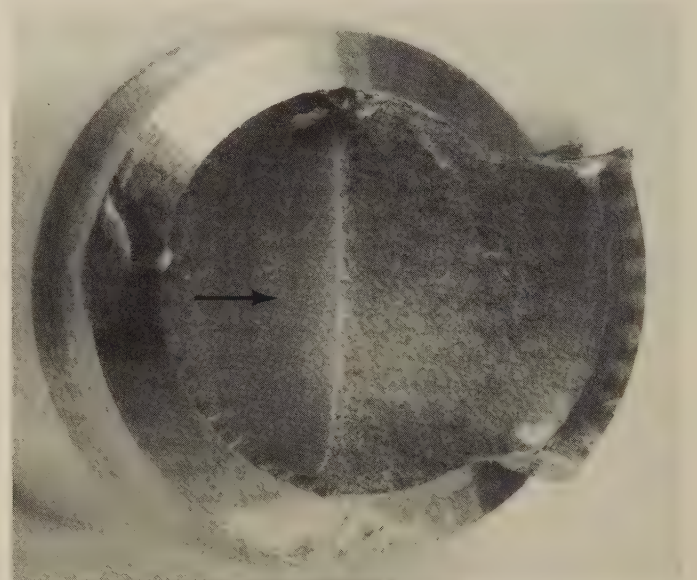
Photograph 1.75× Photograph 0.7×
3678, 3679 Views at different magnifications and at different orientations showing the mating halves of a fractured experimental connecting-rod bolt of 4340 steel that had been quenched and tempered to a hardness of Rockwell C 34 and that broke in a fatigue test. The crack origin is at the root of the thread that is visible at the bottom of the fracture surface at right in 3678 (left). See 3680-3685.



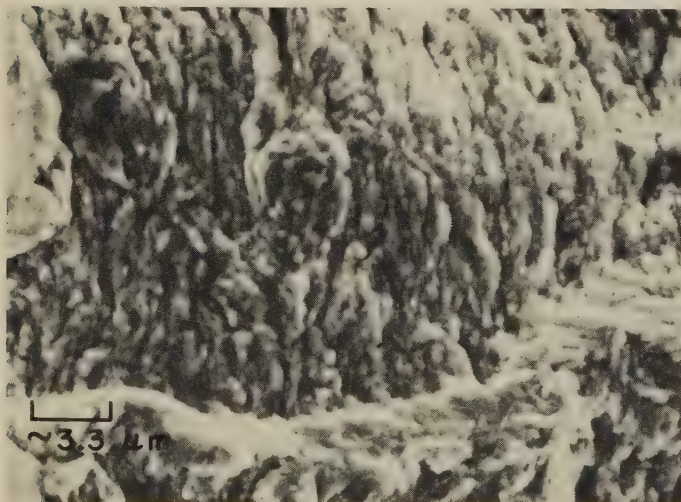
Photograph 1.75× Photograph 0.7×
3680, 3681 Views at different magnifications and at different orientations showing the mating halves of the second bolt from the experimental connecting rod described in 3678 and 3679, also of 4340 steel and quenched and tempered to a hardness of Rockwell C 34. Again, the crack origin is at the root of a thread, which is visible at the top of the fracture surface at right in 3680 (left). See also 3683 (below).



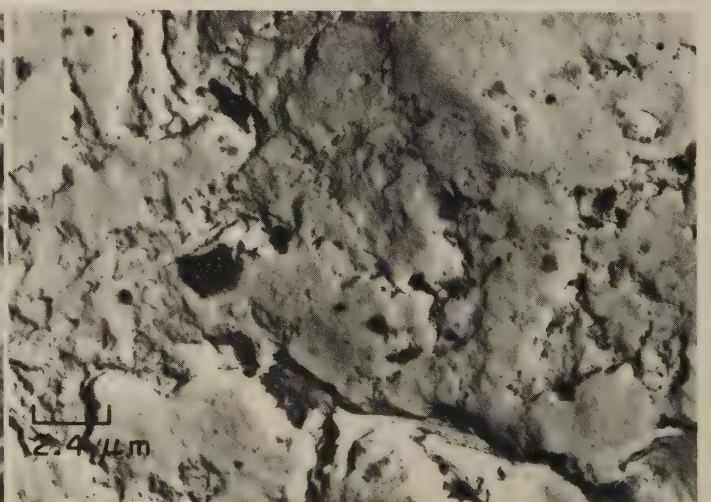
Light fractograph 7×
3682 End-on view, at higher magnification, of the fracture surface at right in 3678. A very smooth fatigue zone begins at several nuclei along the bottom and extends nearly through the entire section. Final, fast fracture produced the sharp shear lip at top. Arrow shows crack-growth direction.



Light fractograph 7×
3683 End-on view, rotated 90° and enlarged, of fracture surface at right in 3680. There appear to be several crack origins in the thread root at left. The fatigue zone is unusually smooth and terminates at about midsection. Shear lip spans two threads. Arrow shows crack-growth direction.



SEM fractograph About 3000×
3684 Higher-magnification view of the fracture surface shown in 3682, taken near the crack-initiation area. The dark features are believed to be striations. Some of them appear to have fissures associated with them. See also 3685.

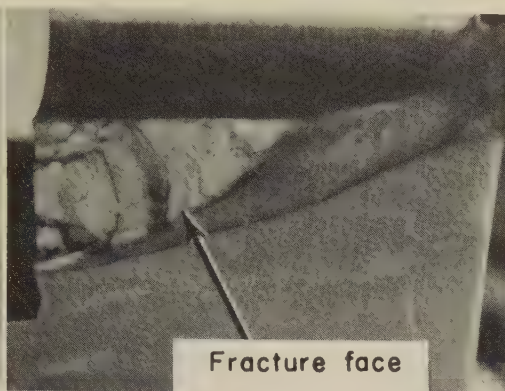


TEM fractograph 4100×
3685 Plastic-carbon replica of the fracture surface in 3682, but showing a different area than that in 3684 (left). Surface is essentially featureless, indicating a region of smeared metal that formed after the crack front had passed by.

Photograph, Light Fractographs, SEM Fractographs, Light Micrographs: 4340 Steel Actuator Arm
From an Aircraft Maneuvering-Flap Assembly, Fractured in a Fatigue Test

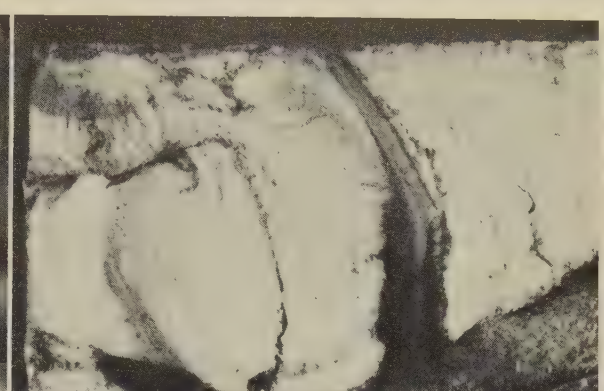


Photograph $\frac{1}{2}\times$
3686, 3687, 3688



Fracture face

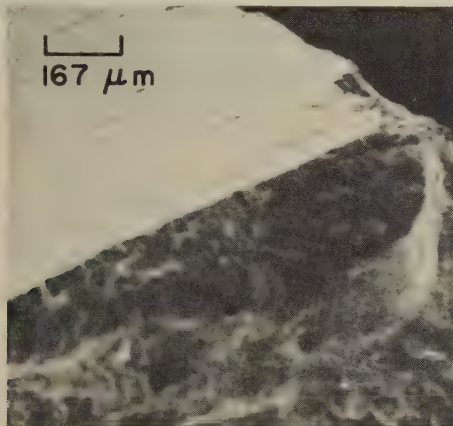
Light fractograph



$2\times$ Light fractograph

$6\times$

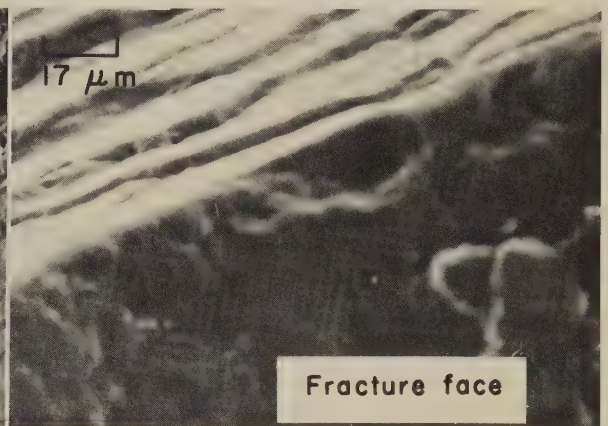
4340 steel actuator arm from an aircraft maneuvering-flap assembly, which had been subjected to a fatigue test. In 3686 (left), which is a photograph of a portion of the actuator arm, a small crack is visible in the right side of the bearing hole (at arrow). Fractograph 3687 (center) shows a section through the cracked actuator arm in 3686, which was cut and then broken along the crack to expose the fracture surface. The bearing hole (at top) had been chromium plated, and then the entire actuator arm had been cadmium plated all over. Fractograph 3688 (right) shows a higher-magnification view of the fracture surface in 3687, and reveals the presence of a precrack at the site of nucleation of the main (fatigue) fracture (upper left corner). Fatigue striations were found in the area of nucleation. The chromium layer is visible at top right. See also 3689 to 3693 (below).



SEM fractograph



$60\times$ SEM fractograph

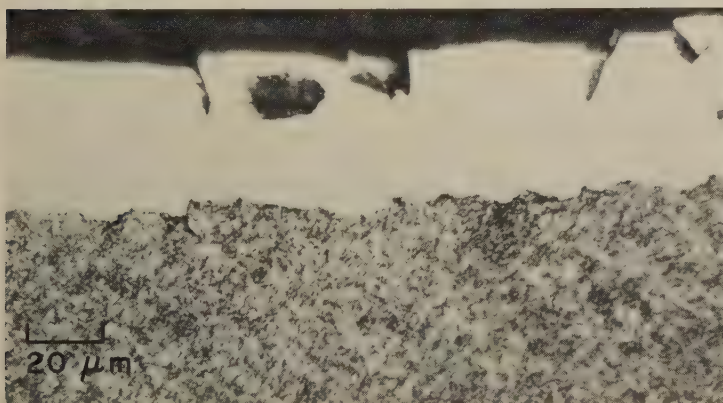


$170\times$ SEM fractograph

$600\times$

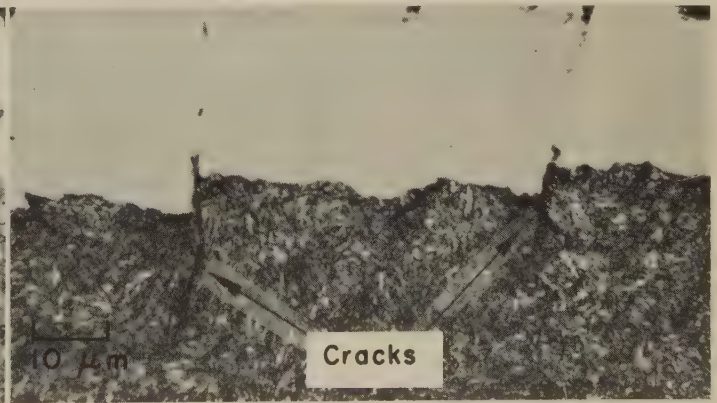
Fracture face

Three SEM fractographs that reveal the nature of the chromium plating in the bearing hole in the actuator arm shown in 3686 to 3688. Fractograph 3689 (left) is an oblique view showing the fracture surface (dark) and the plated surface of the bearing hole (light). Numerous parallel cracks in the chromium plating, parallel with the fracture surface, are clearly revealed. Fractograph 3690 (center), a view normal to the plated surface of the bearing hole, shows at higher magnification the network of cracks visible in 3689. The wear pattern on the plated surface is evident. Fractograph 3691 (right) shows, at still higher magnification, the edge of the fracture surface shown in 3689. Deformation of the hole has caused steps in the chromium plating. See 3692-3693.



Light micrograph (nital)

$500\times$



Light micrograph (nital)

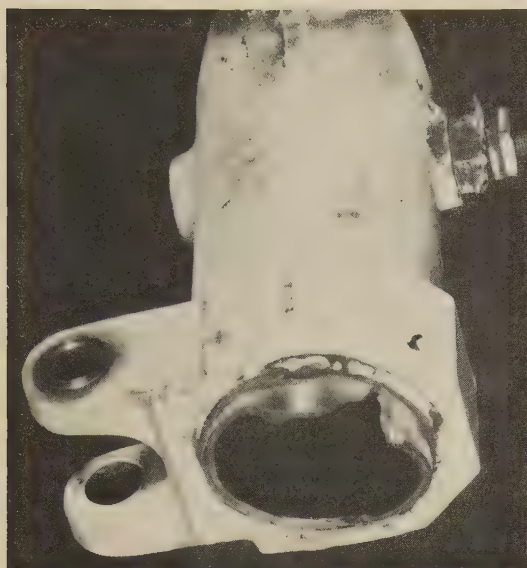
$1000\times$

Cracks

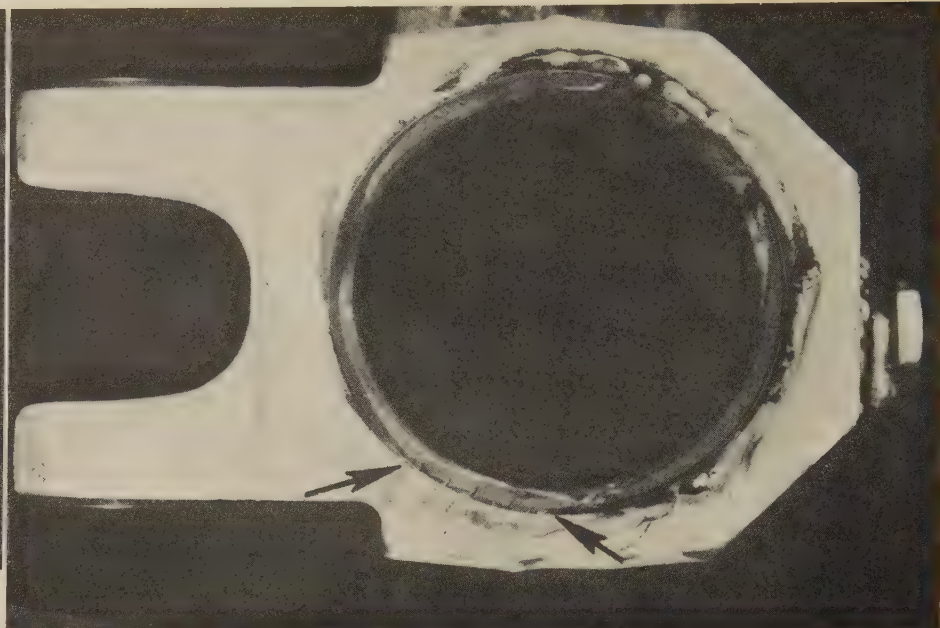
3692 Section through the 4340 steel actuator arm shown in 3686, normal to the axis of the cracked bearing hole. The white layer at top is the chromium plating on the bare surface of the hole; note the closely spaced cracks, and the steps formed by deformation of the hole, which tilted the plate segments created by the cracks. See also 3693 (right).

3693 Portion of micrograph 3692, shown at higher magnification to reveal more clearly that the cracks, which began in the chromium plating, penetrate the steel substrate as well. The hardness of the chromium layer is Rockwell C 62, and the hardness of the 4340 steel is Rockwell C 42; a heavy load was needed, therefore, to propagate the cracks into the steel substrate.

Photograph, Light Fractographs, SEM Fractographs: 4340 Steel Tube, in a Landing-Gear Piston Assembly, That Cracked During Heat Treatment and That Fractured in Fatigue



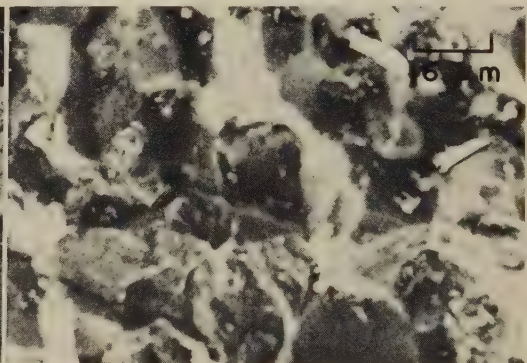
Photograph 3694 4340 steel tube (protruding from the socket of an aircraft landing-gear piston assembly) that cracked during heat treatment and that fractured in fatigue. The tube (2¼-in. OD, ½-in. wall) had been fitted ¾ in. into the socket and furnace brazed to it. Hardness of the tube, Rockwell C 47 to 48 (Rockwell C 43 to 46 was specified). See also 3695 to 3699.



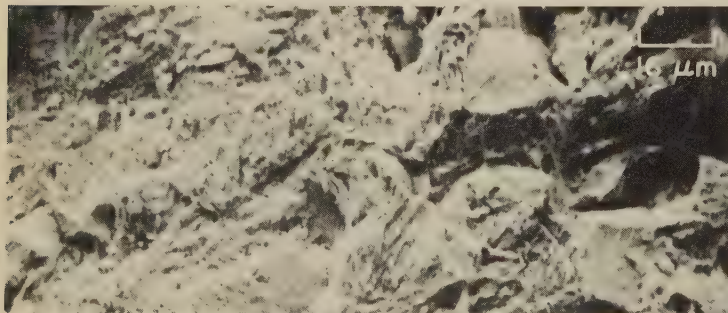
Light fractograph 3695 End-on view of the fractured tube shown in 3694 (at left), revealing a series of cracks at the outside surface at the point where the tube meets the socket. These cracks had merged to form a fracture (between the arrows at bottom) about ¾ in. long and approximately 0.05 in. deep at the point of initial penetration. See also fractograph 3696.



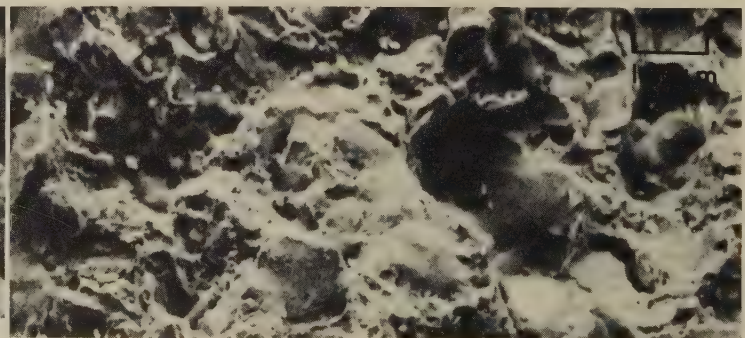
Light fractograph 3696 Higher-magnification view of the crack-origin region in 3695. At the outer (bottom) edge of the tube, the surface of the initial crack (a) is covered with a dark, high-temperature type of oxide evidently formed during heat treatment after brazing. Area (b) is a region of fatigue-crack growth. The remainder of the fracture surface (c) is the region of final, fast fracture. See 3697 to 3699.



SEM fractograph 3697 SEM fractograph of a portion of the oxidized region (a) of the fracture surface shown in 3696. The rupture is intergranular, and is attributed to cracking that occurred at high temperature.



SEM fractograph 3698 SEM fractograph taken near the edge of the region of fatigue-crack growth (b) in fractograph 3696, at the transition from intergranular (upper right) to transgranular fracture. Fatigue striations either are not visible at this stage of cracking or are hidden by debris.

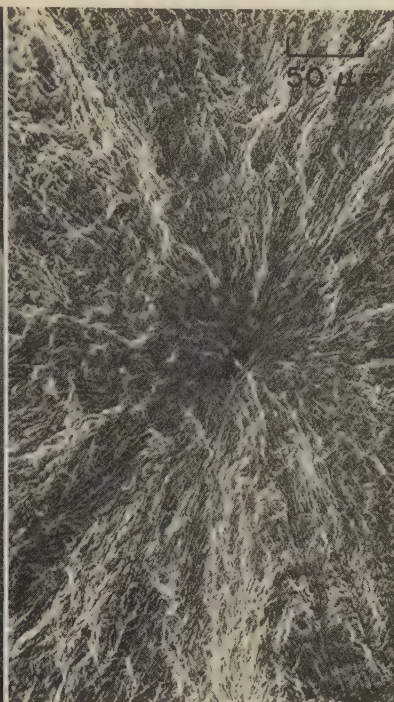


SEM fractograph 3699 SEM fractograph that was taken in the region of final, fast fracture (c) in fractograph 3696. The features here suggest a transgranular mechanism of rupture, in part by microvoid coalescence and in part by quasicleavage.

SEM Fractographs: Electroslag Remelt 4340 Steel Test Bar That Was Fractured in a Tension-Tension Fatigue Test



SEM fractograph 20×
3700 Surface of a fatigue fracture that occurred in tension-tension ($R = 0.1$) in a test bar of electroslag remelt 4340 steel heat treated to a hardness of Rockwell C 55. The origin of the fracture is an inclusion at the center of the "star" at right. See also fractographs 3701 to 3705, at right and below.



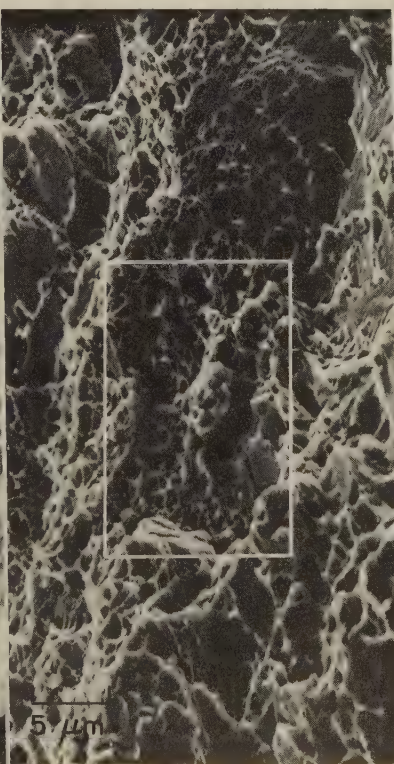
SEM fractograph 200×
3701 A higher-magnification view of the center of the "star" in 3700, showing the inclusion (dark, at center) that initiated the crack. Fine radial marks are evident. See fractograph 3702.



SEM fractograph 2000×
3702 Higher-magnification view of the inclusion (fracture origin) shown at center in 3701 (left). Little evidence of fatigue striations is found this close to the origin. See also fractograph 3703, at left below.



SEM fractograph 5000×
3703 View, at still higher magnification, of the inclusion in fractographs 3701 and 3702, showing that the inclusion was fractured by cleavage. The cleavage surface bears a bright metal sliver (at arrow).

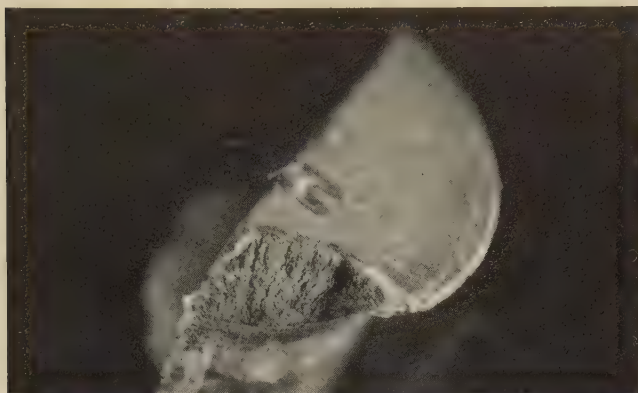


SEM fractograph 2000×
3704 Same fracture surface as in 3700, but a view from the region of fast fracture. Typical dimples, and local facets of quasi-cleavage. See also 3705.



SEM fractograph 5000×
3705 Higher-magnification view of the area within the rectangle in fractograph 3704 (left), showing more distinctly that the dimples are present in a wide variety of sizes.

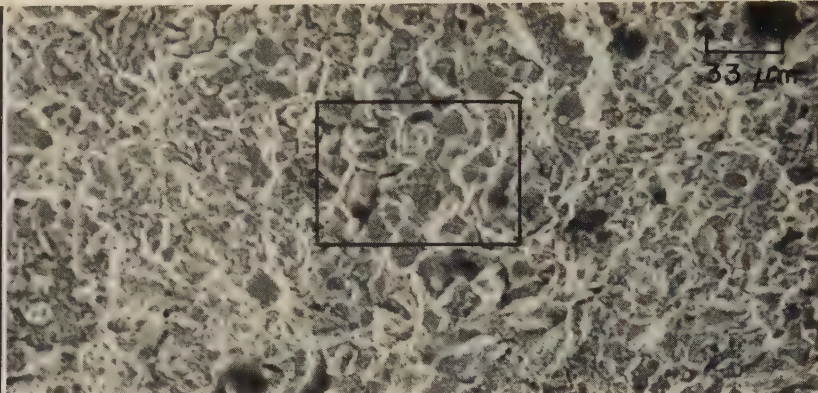
Light and SEM Fractographs: 4340 Steel Stud Head Fractured Because of Hydrogen Embrittlement;
HY-180 Steel Specimens Fractured by Overload in Air and by Sustained Load in Hydrogen



Light fractograph

6×

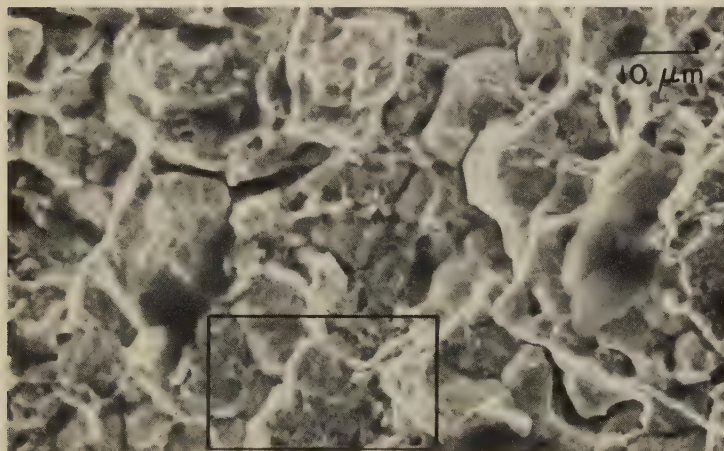
3706 Fractured head of a 4340 steel stud that had been hydrogen embrittled by electroplating without subsequent baking. The details of the fracture surface are shown, at successively higher magnifications, in 3707 (at right) and in 3708 and 3709 (below).



SEM fractograph

300×

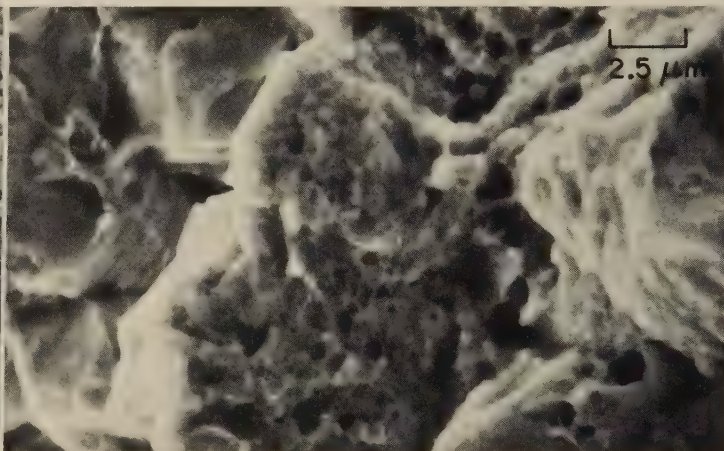
3707 Fracture surface of the broken stud head in 3706, showing the intergranular facets that are characteristic of hydrogen embrittlement. Voids (dark) suggest local dimpled rupture, but at this relatively low magnification a positive interpretation cannot be made. See 3708, a higher-magnification view of area in rectangle.



SEM fractograph

1000×

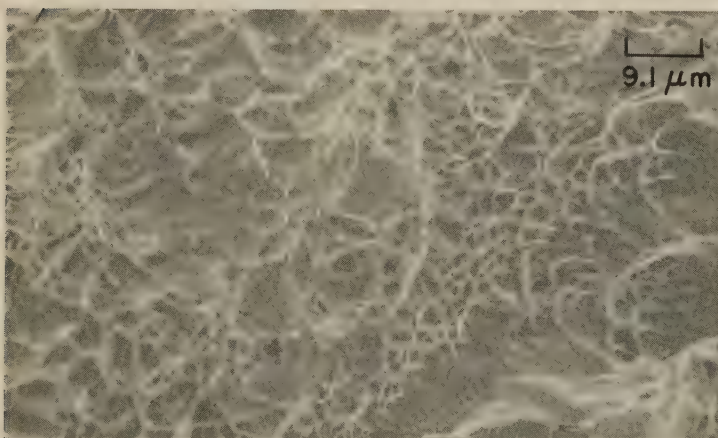
3708 Higher-magnification view of the area within the rectangle in fractograph 3707 (above, right). Both intergranular facets and secondary intergranular cracks are clearly visible. A few areas suggest microvoid coalescence. See also fractograph 3709 (right), which is a higher-magnification view of the area in the rectangle here.



SEM fractograph

4000×

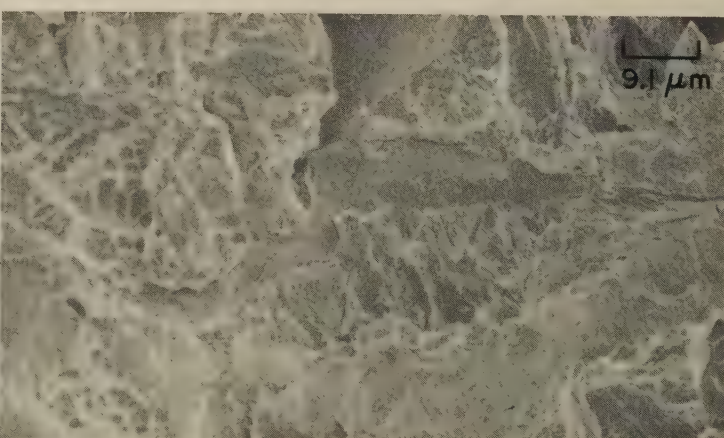
3709 Higher-magnification view of the area within the rectangle in 3708 (at left). Intergranular facets containing extremely small dimples are visible at center and at top. Secondary intergranular cracks are clearly evident at left. Elsewhere, the mechanism of fracture is a mixture of microvoid coalescence and intergranular rupture.



SEM fractograph

1100×

3710 Surface of a fracture in a specimen of HY-180 steel broken by mechanical tensile overload in air, showing dimples of rather uniform size with no indications of secondary cracking. Large level areas (such as those at left of and below center) suggest local stretching. See 3711.



SEM fractograph

1100×

3711 Surface of a fracture in a specimen of HY-180 steel that broke under sustained tensile load in one atmosphere of hydrogen. The crack apparently was propagated by mixed mechanisms — dimpled rupture at left, intergranular rupture at upper left and at right, and quasicleavage at center.

SEM Fractographs: High-Strength Steel Studs Fractured in Seawater by Overload and by Stress-Corrosion Cracking



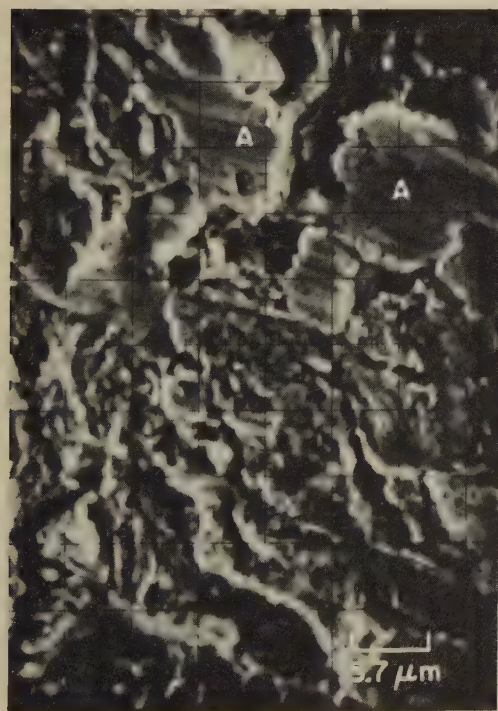
SEM fractograph 56×
3712 Surface of a fracture in an experimental high-strength steel stud that had been fired into a structure submerged in seawater, for anchorage during salvage. The fracture was initiated at a point beneath the surface of the stud. See also fractographs 3713 to 3717, at right and below.



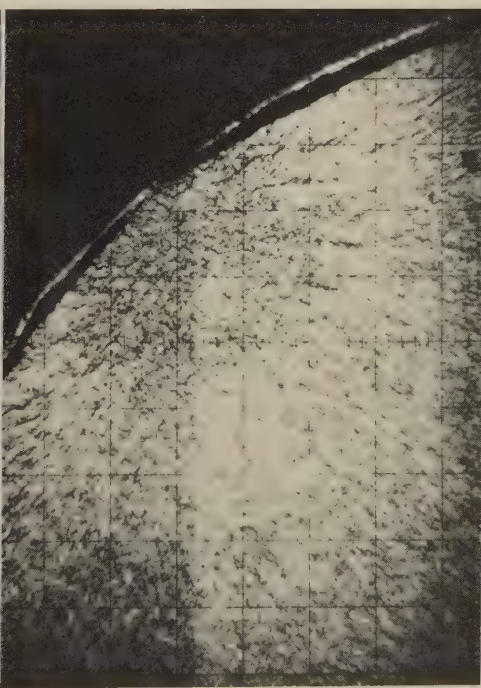
SEM fractograph 176×
3713 Same as 3712, but at higher magnification. The surface had been machined away inadvertently, but not deeply enough to obscure the fracture origin and the marks that radiate from it. See 3714 for higher-magnification view of area in rectangle, which contains the origin.



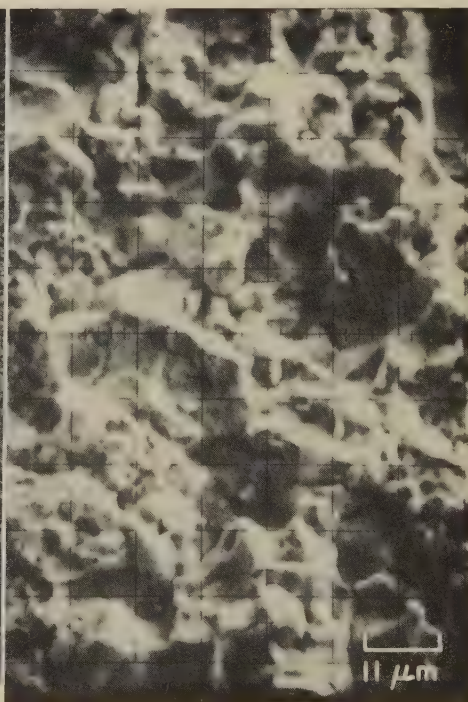
SEM fractograph 440×
3714 Higher-magnification view of the area in the rectangle in 3713. Fracture surface suggests mechanical overload failure, but is partly obscured by products of subsequent corrosion. See 3715 for a higher-magnification view of the fracture-origin area (in rectangle).



SEM fractograph 1760×
3715 Higher-magnification view of the area in the rectangle in 3714. This portion of the fracture surface shows quasi-cleavage facets mixed with dimples. The areas marked A are scraped asperities.



SEM fractograph 17×
3716 Fracture surface of a companion stud to the one shown in 3712. This stud fractured by stress-corrosion cracking, thereby increasing the load on the stud shown in 3712 and contributing to its overload fracture. See also 3717.

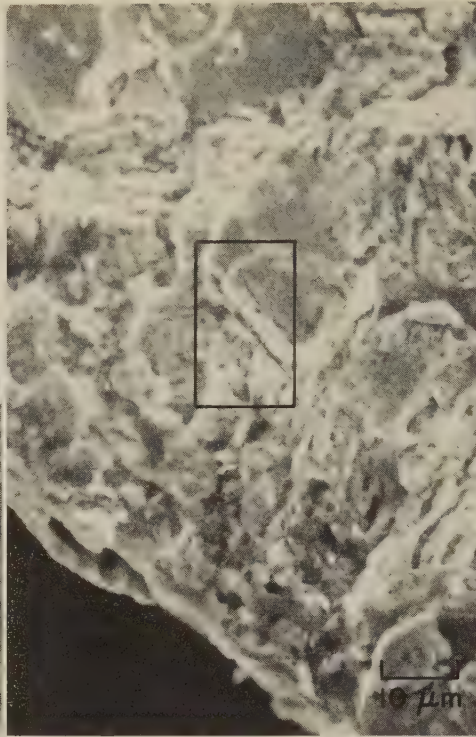


SEM fractograph 880×
3717 Higher-magnification view of the fracture surface in fractograph 3716 (at left), showing the intergranular characteristics that are typical of stress-corrosion cracking.

Light Fractograph, SEM Fractographs: Plated 300M Steel Landing-Gear Bolt-Torque Link
Fractured by Intergranular Stress-Corrosion Cracking



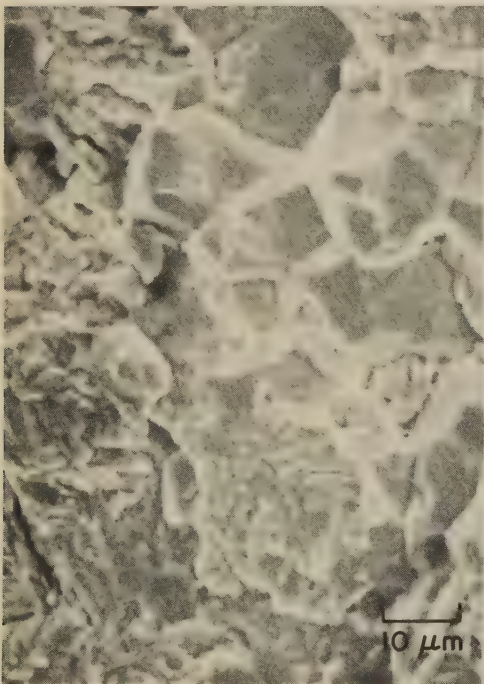
Light fractograph 23×
3718 Surface of intergranular stress-corrosion crack in a thread of a landing-gear bolt-torque link made of 300M steel. The crack was discovered in final inspection before service, and was exposed by sectioning and laboratory final fracture. See also 3719 to 3729.



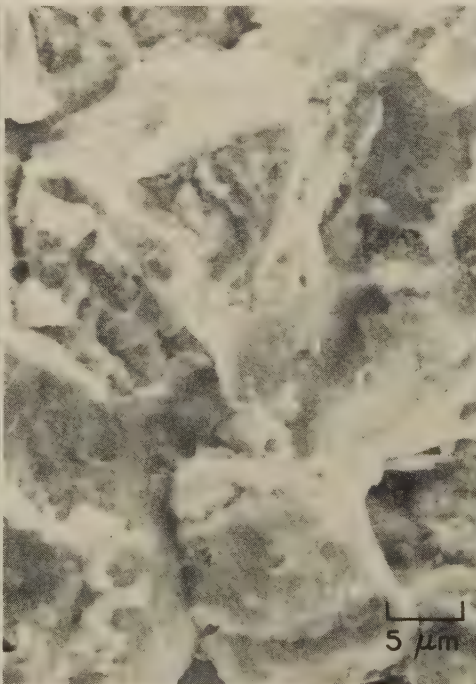
SEM fractograph 1000×
3719 SEM view of a region of the outer edge of the fracture surface in 3718, showing the intergranular nature of the stress-corrosion crack. The part had been plated and stripped. See also fractograph 3720, a higher-magnification view of the area in the rectangle.



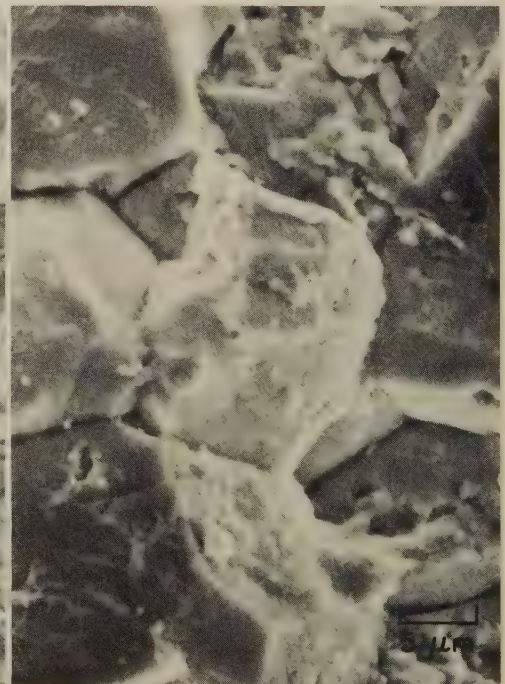
SEM fractograph 5000×
3720 Higher-magnification view of the area within the rectangle in fractograph 3719. The fracture surface appears to be obscured by corrosion products, which may be concealing evidence of dimples or of cleavage facets. See also fractographs 3721 to 3723, below.



SEM fractograph 1000×
3721 Interior region of fracture surface in 3718, a short distance from edge in 3719, showing smaller amount of corrosion products than in 3719. Intergranular facets are interspersed with a few transgranular facets.

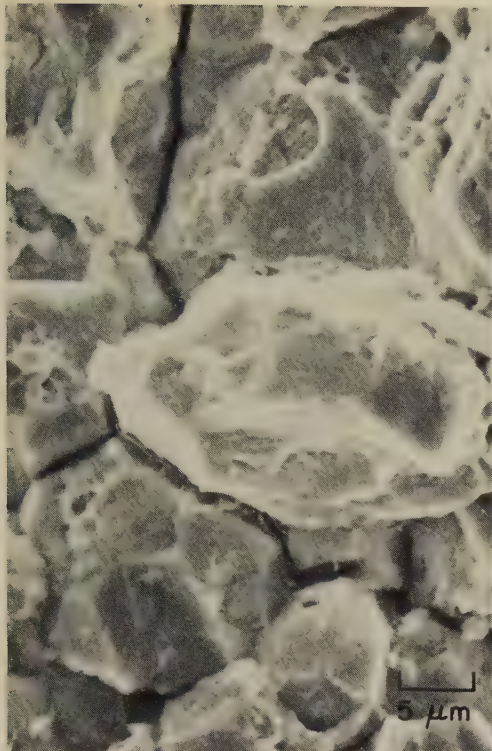


SEM fractograph 2000×
3722 Interior region about as far from edge in 3719 as 3721 is. A considerable amount of corrosion products is present, and the fracture seems to be completely intergranular with slight secondary cracks. See also 3723.

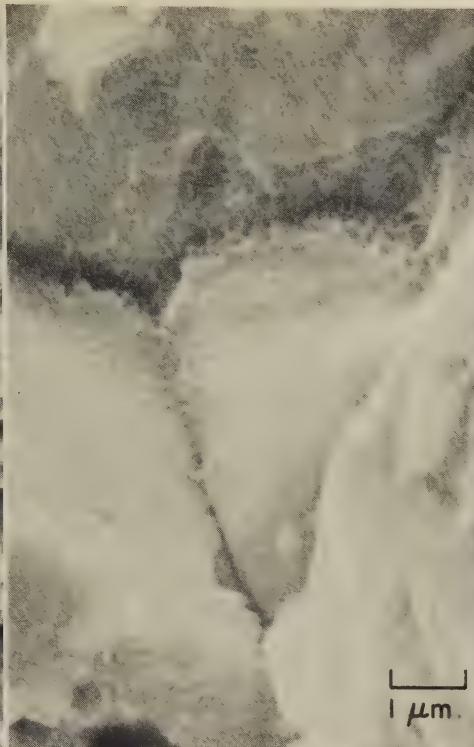


SEM fractograph 2000×
3723 A view of a region adjacent to that shown in fractograph 3722 (left), revealing distinct grain-boundary secondary cracks. Hairline indications are visible on several of the grain facets. A slight amount of debris is present as well.

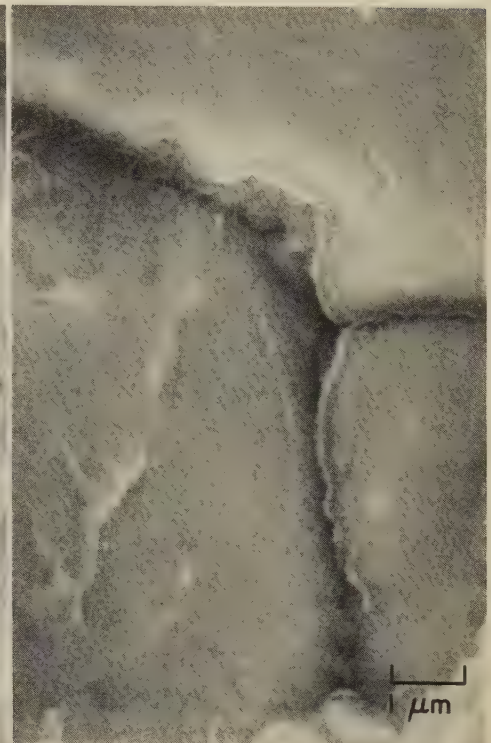
SEM Fractographs: Plated 300M Steel Landing-Gear Bolt-Torque Link Fractured by Intergranular Stress-Corrosion Cracking (Continued)



SEM fractograph 2000×
3724 Same fracture surface as in 3718 to 3723, showing a region farther from the outer edge than those in 3721 to 3723. Fracture path is completely intergranular, and pronounced grain-boundary secondary cracks are evident.



SEM fractograph 10,000×
3725 Same fracture surface as in 3718 to 3724, but a region farther from the outer edge than that in 3724 and shown at higher magnification. Intergranular path of fracture; fine dimples at grain boundaries and on several facets.



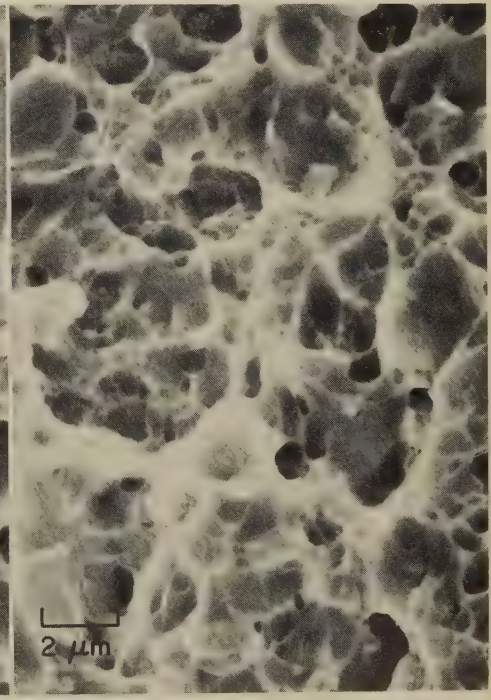
SEM fractograph 10,000×
3726 Another region of the fracture surface in 3718 to 3725, similar to that shown in 3725 (left), but still farther from the outer edge of the crack. This region shows grain-boundary secondary cracks that contain fine dimples.



SEM fractograph 1000×
3727 A region at edge of fast-fracture (bright) zone of fracture surface in 3718, showing junction of this zone (bottom) with one that underwent stress-corrosion cracking. See 3728, a higher-magnification view of the area within the rectangle.

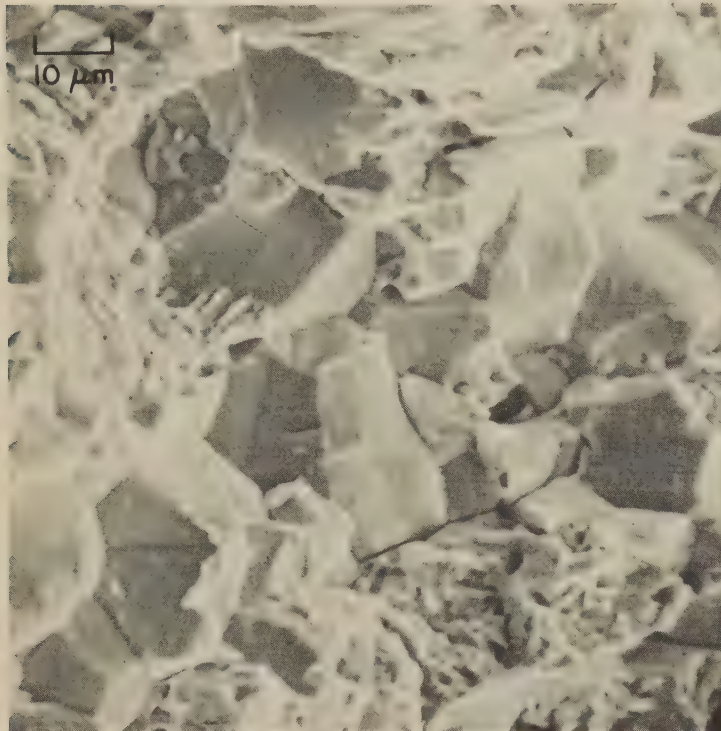


SEM fractograph 5000×
3728 Higher-magnification view of the area defined by the rectangle in fractograph 3727 (left), showing even more clearly than 3727 the abrupt termination of stress corrosion and the complete change to dimpled rupture (bottom).

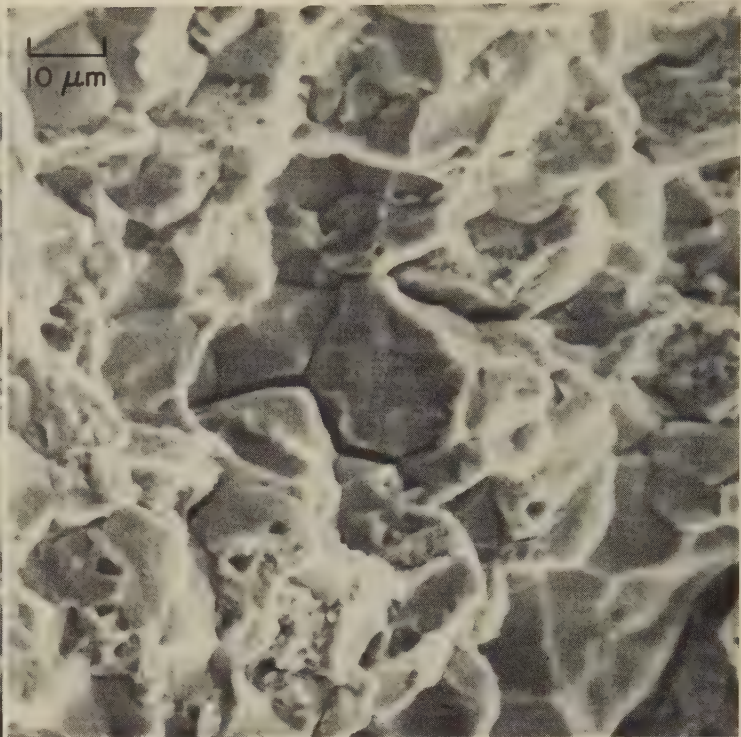


SEM fractograph 5000×
3729 Fracture surface of a thread adjacent to the one in 3718. This thread was cut, notched and broken in the same manner, but no prior crack was discovered and the dimpled rupture visible here covers the entire fracture surface.

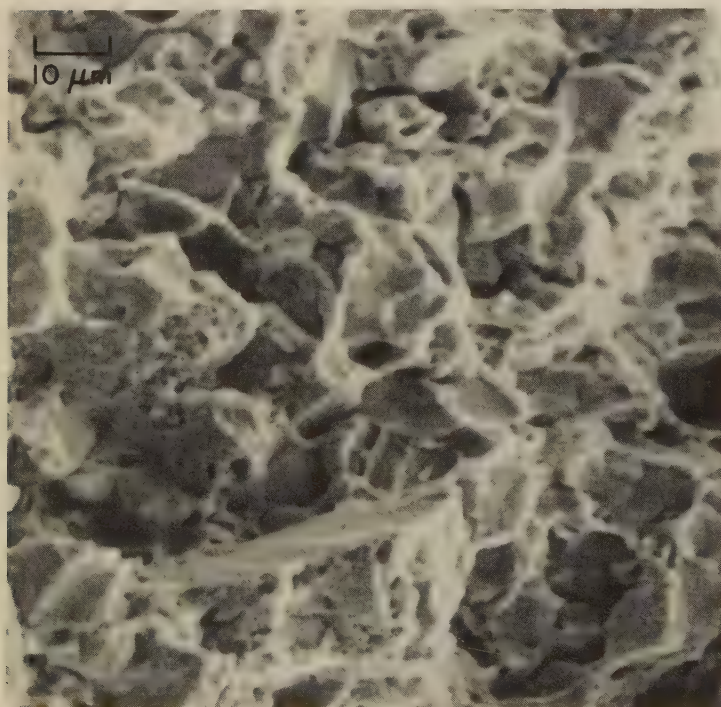
SEM Fractographs: 5155 Steel Specimens, Fractured by Impact at -196°C (-321°F), at Room Temperature and at 100°C (212°F), and Fractured by Reversed Torsion Fatigue



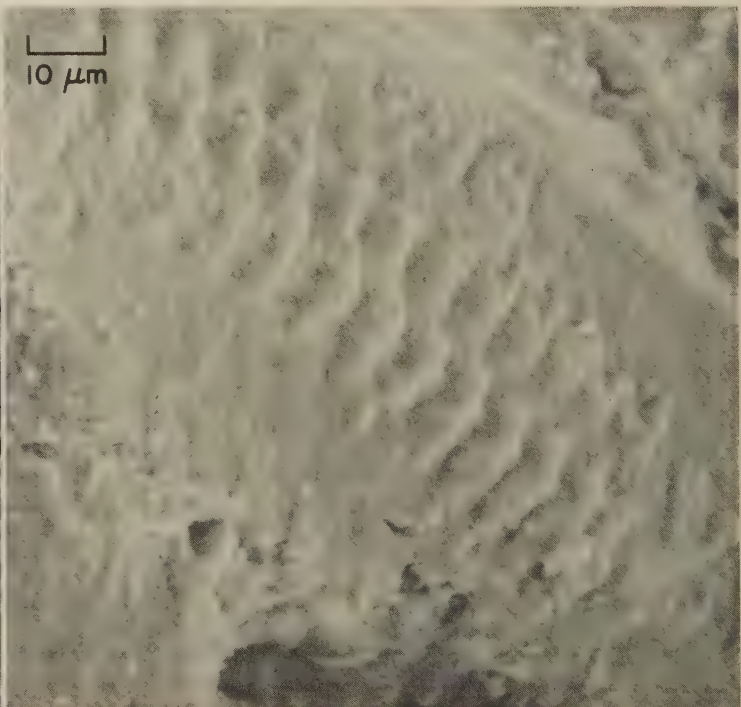
SEM fractograph 1000×
3730 Surface of a fracture in a specimen of 5155 steel that had been heat treated at 850°C (1562°F) for $\frac{1}{2}$ hr, oil quenched, and tempered at 350°C (662°F) for 1 hr. Hardness is 520 dph. The fracture was produced by impact at -196°C (-321°F). The fracture surface is rated as 95% brittle and 5% ductile. See also fractographs 3731 and 3732.



SEM fractograph 1000×
3731 Surface of a fracture in a specimen of 5155 steel that had been given exactly the same heat treatment as described for 3730 (at left), but that was broken by impact at room temperature. This higher fracture temperature produced a surface that is rated as 75% brittle and 25% ductile. Note the greater incidence of dimples. See also fractograph 3732.

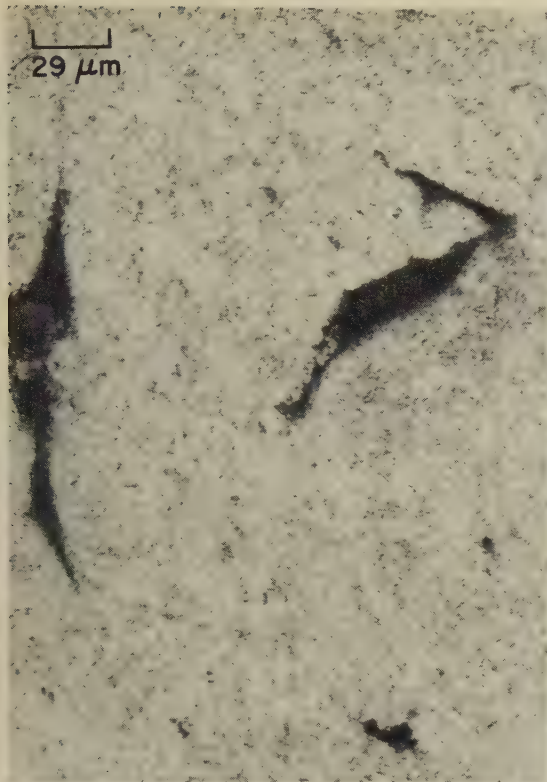


SEM fractograph 1000×
3732 Surface of a fracture in a specimen of 5155 steel that had been given exactly the same heat treatment as described for 3730 and 3731, but that was broken by impact at 100°C (212°F). The higher ductility of this fracture surface (rated 60% brittle, 40% ductile) compared with 3731 correlates with the greater number of fine dimples visible here.



SEM fractograph 1000×
3733 Surface of a fatigue fracture in a specimen of 5155 steel that was broken in reversed torsion under a maximum stress of 1177 MPa (171 ksi). The specimen had been heat treated at 850°C (1562°F) for $\frac{1}{4}$ hr, oil quenched, and tempered at 450°C (842°F) for 1 hr. The hardness of the specimen was 425 dph. Fracture occurred at 2600 cycles. Note the fatigue "tire tracks".

Micrograph, SEM Fractographs: Fractured 50100 Steel Forging; 52100 Steel Specimens
Given Various Heat Treatments and Fractured by Impact at -196°C (-321°F)



Micrograph - 3% nital

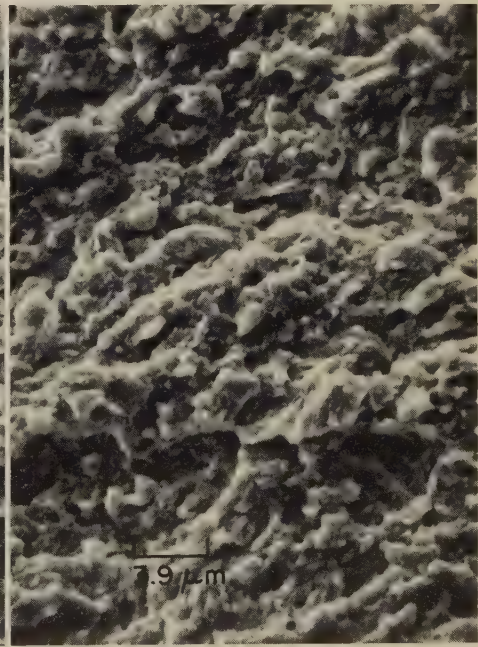
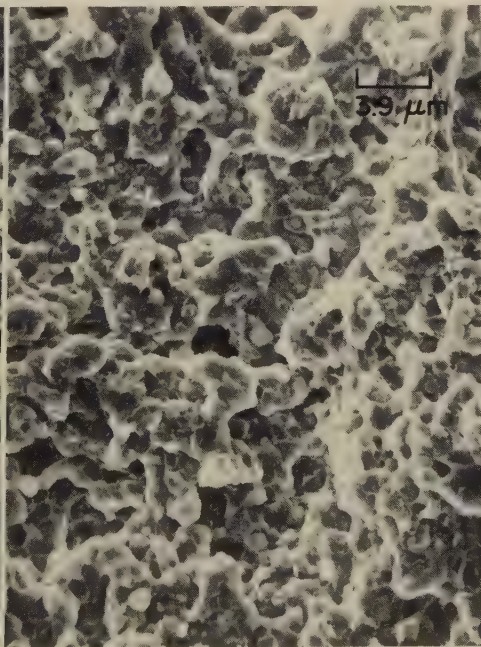
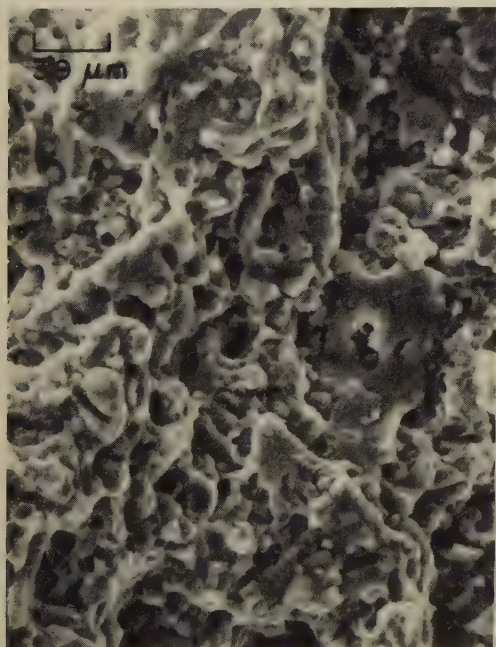
350×

3734 Martensitic structure of a 50100 steel forging that was austenitized and water quenched. Because of inadequate flow in forging, grains are large and casting voids remain, both of which led to the fracture shown in 3735.

SEM fractograph

150×

3735 Surface of a partly intergranular, partly transgranular quench crack in the 50100 steel forging shown in micrograph 3734 (at left). Both the large grain size and the presence of angular casting voids facilitated propagation of the intergranular portions of the fracture. At higher magnification, the transgranular portions of the fracture surface may exhibit dimples.



SEM fractograph

2250×

SEM fractograph

2250×

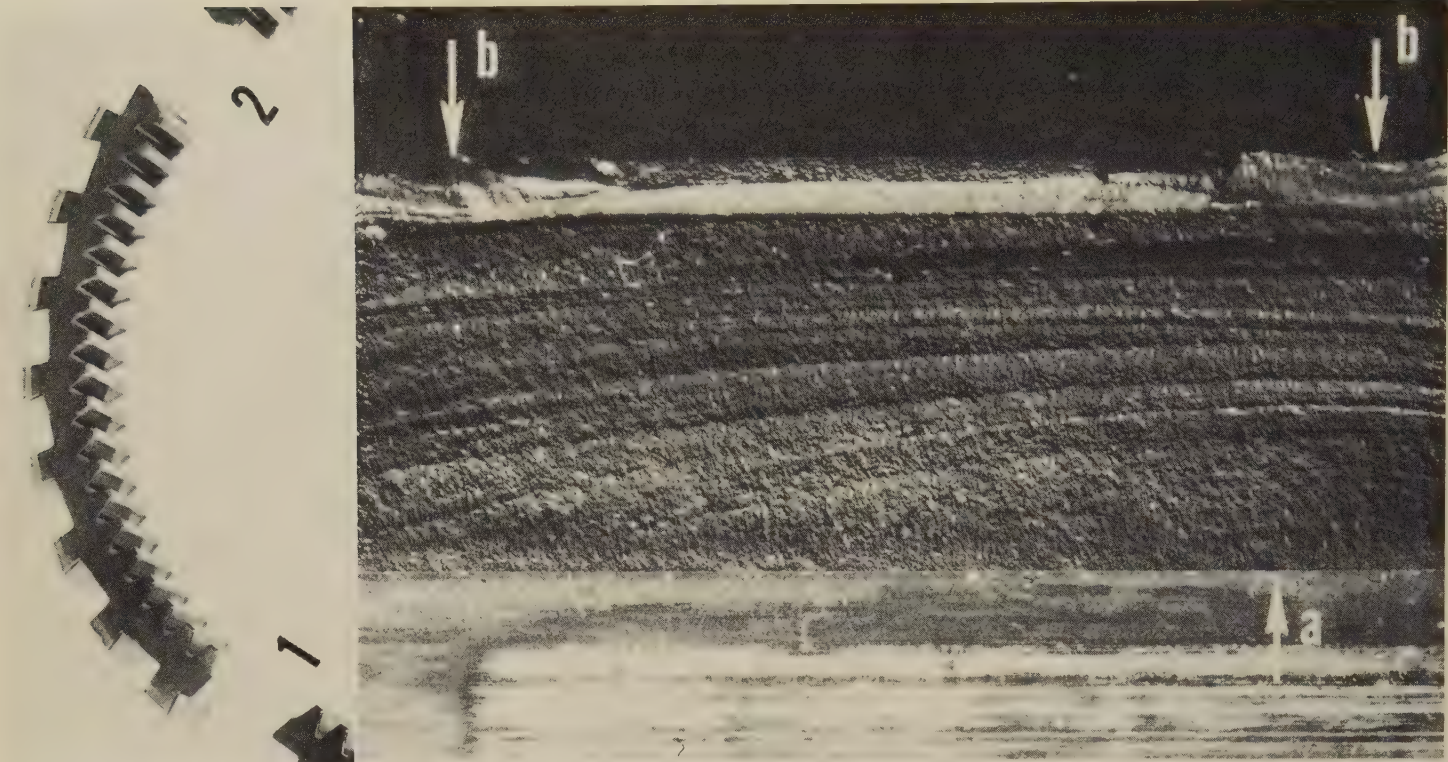
SEM fractograph

2250×

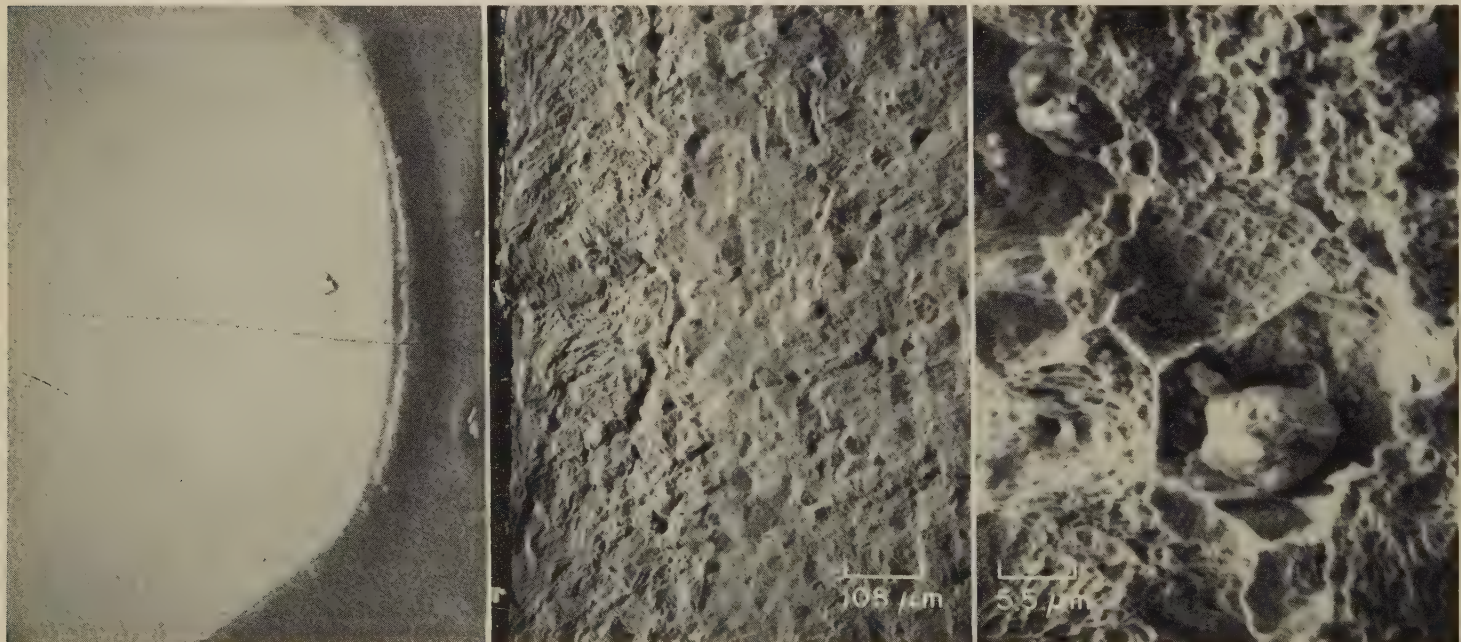
3736, 3737, 3738

Fracture surface of three specimens of 52100 steel that were notched and broken by impact at -196°C (-321°F), presented to show the effect of rapid heating in austenitizing. The specimen in 3736 (left) had been heat treated at 845°C (1553°F) for 20 min and oil quenched (a conventional heat treatment), then tempered at 177°C (351°F). The specimen in 3737 (center) had been given two austenitizing cycles of rapid heating to 863°C (1585°F), holding for 1 min and oil quenching, and then had been tempered at 177°C (351°F). The specimen in 3738 (right) had been heat treated at 1095°C (2003°F) for 10 min and quenched in warm oil, tempered for 3 hr at 370°C (698°F), rapidly heated to 845°C (1553°F), held for 1 min and oil quenched, then tempered at 177°C (351°F). The successive decrease in size of cleavage facets and dimples from 3736 to 3737 to 3738 indicates successively decreasing size of acicular needles of martensite as a result of the different heat treatments.

Photograph, Light Fractograph, SEM Macrograph, SEM Fractographs:
Nitrided 7140 Steel Transmission Gear Fractured by Fatigue



Photograph 0.6× Light fractograph 8×
3739, 3740 Fractured 7140 steel free-wheeling transmission gear that had been nitrided to a surface hardness of Rockwell 15N 91; core hardness was Rockwell C 36. The gear fractured by fatigue, breaking into three segments, one of which is shown in 3739 (left). All three fractures were similar. Fractograph 3740 (right) shows a surface of fracture No. 1. Arrow "a" points to the approximate location of the origin of the main fatigue crack, in the root of an inner tooth. This crack grew, making the clearly defined beach marks visible here, to meet two subordinate cracks (at arrows "b") that originated near a wear pattern between two outer teeth. In addition to the cracks that resulted in the fracture of the gear into three segments, similar cracks were observed in the roots of several inner teeth. One of these cracks is shown in macrograph 3741, and the surface of another is shown in fractograph 3742.



SEM macrograph 47×
3741 An oblique view of a fatigue crack in the root (light region at left) of an inner tooth of the gear segment in 3739. (The dark region at right is the side of the gear.) This crack is typical of several that were found in the roots of inner teeth. See also fractograph 3742.

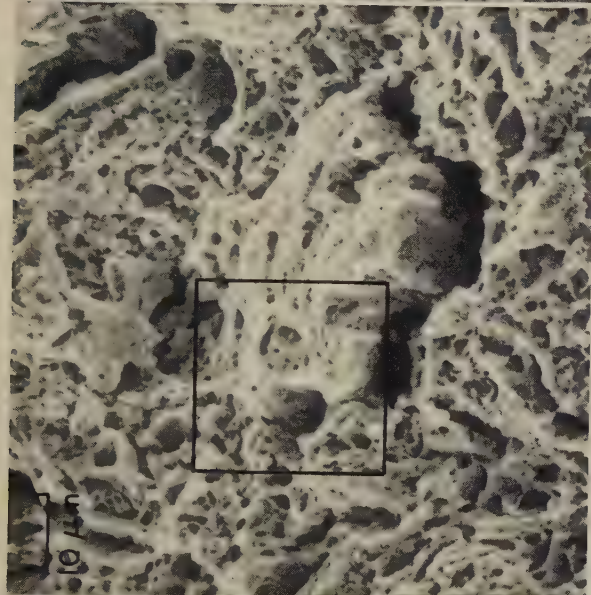
SEM fractograph 93×
3742 Surface of a fatigue crack similar to that shown in 3741. This surface was exposed by application of a single overload in the laboratory. The left third of this fractograph shows the nitrided case. See fractograph 3743 (at right) for a view of the overload portion of this fracture.

SEM fractograph 1825×
3743 Overload fracture produced to expose the fatigue crack in 3742, showing the dimples expected in this type of fracture. The large inclusions visible here were nowhere found to be associated with crack origins, which appeared to be related to tool marks.

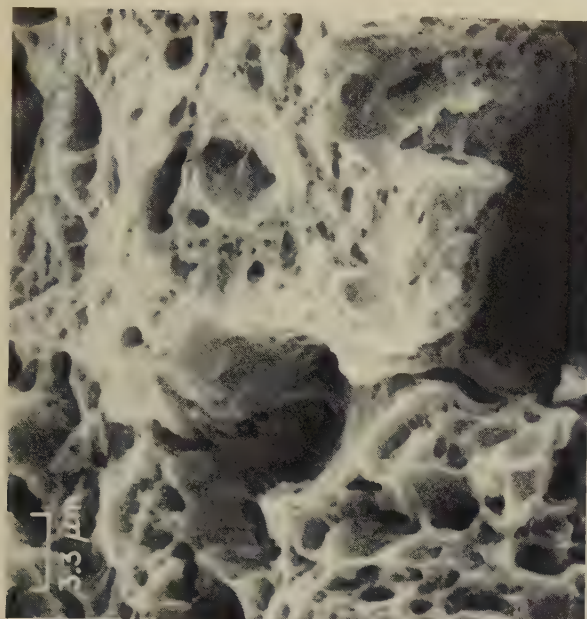
Light Fractographs, SEM Fractographs: Unnotched and Notched 8740 Steel Specimens That Were Fractured by Tensile Overload



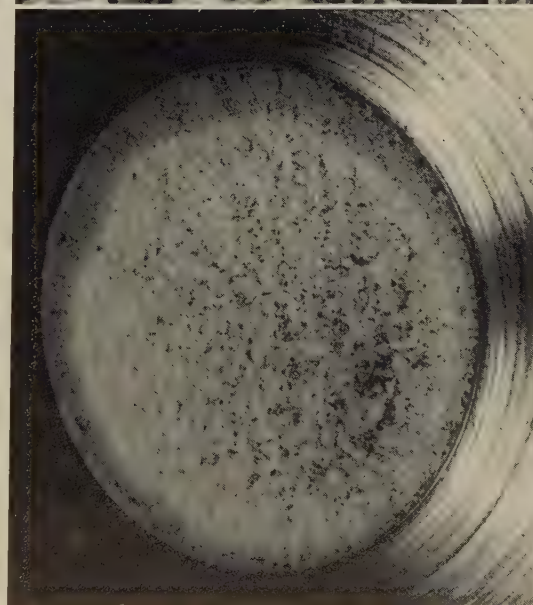
Light fractograph
3744 Tensile-overload fracture in an unnotched specimen of 8740 steel; tensile strength 1351 MPa (196 ksi). A cup-and-cone fracture with a fibrous zone containing radial features between the central fibrous region and the shear lip. See 3745-3746.



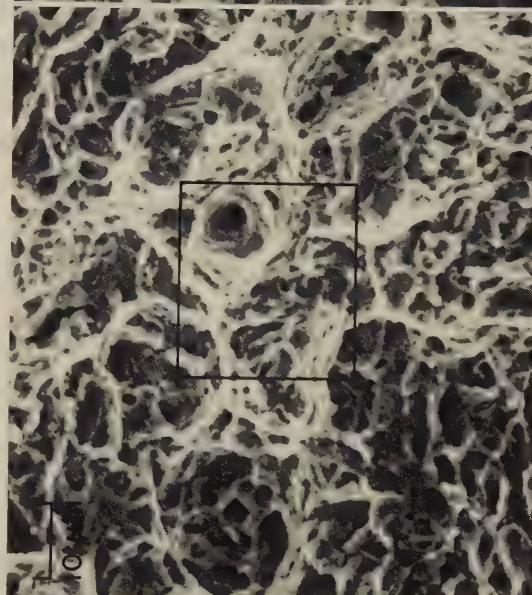
SEM fractograph 1000×
3745 Area adjacent to one of the radial features in 3744, showing dimples, which are typical of tensile-overload fracture. Note the scattered secondary cracks, which appear to be unusually deep. See 3746, a higher-magnification view of area in the rectangle.



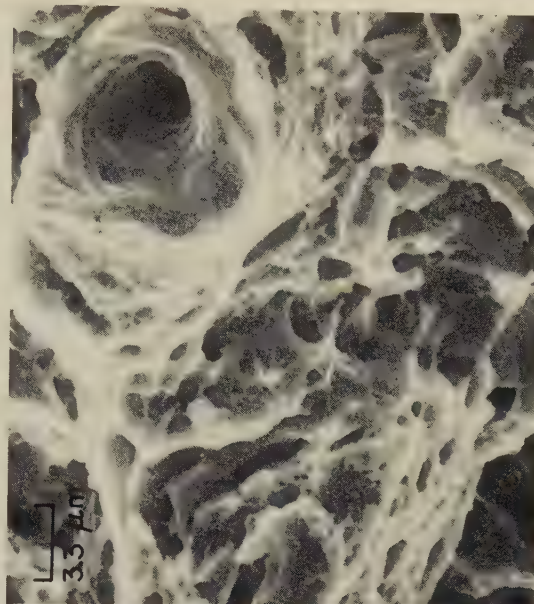
SEM fractograph 3000×
3746 Area outlined by the rectangle in fractograph 3745 (at left), shown at higher magnification. A wide range of sizes of the dimples is clearly visible. Unlike many other dimpled fractures, the one here appears to contain no evidence of inclusions.



Light fractograph 9×
3747 Surface of tensile-overload fracture in a notched specimen of 8740 steel heat treated to a tensile strength of 2044 MPa (296.5 ksi). Fracture originated around the periphery of the specimen at the root of the notch. Radial features are evident. See also 3748 to 3751 (at right, and on the next page).

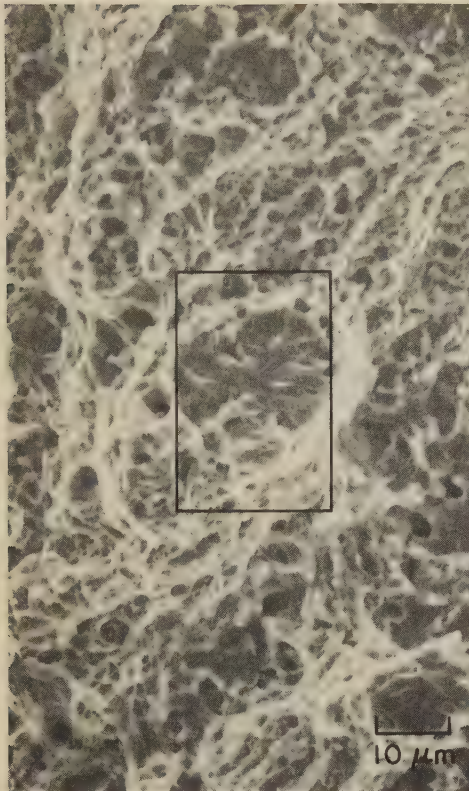


SEM fractograph 1000×
3748 Area in the central final-fracture region in 3747. The range of dimple sizes is similar to that in the unnotched fracture in 3745, but only one secondary crack is evident, and it is of modest size. See fractograph 3749, at right, for a higher-magnification view of the area outlined by the rectangle.

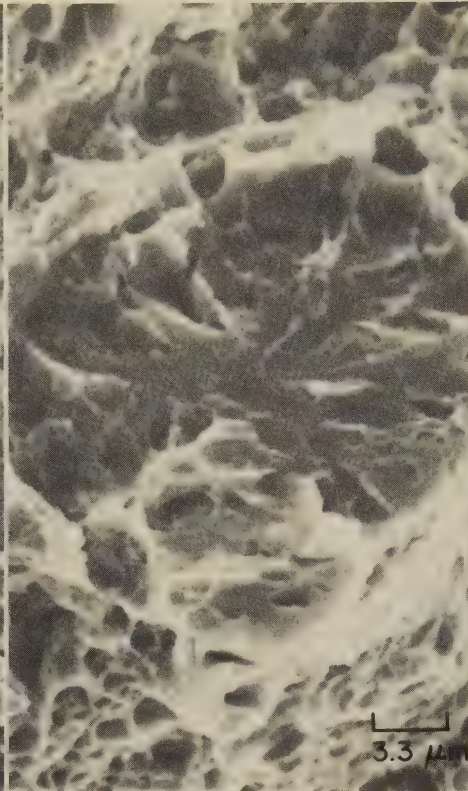


SEM fractograph 3000×
3749 Higher-magnification view of the area in the rectangle in 3748 (left). Range in dimple size is more clearly evident here. Large dimple at upper right was presumably initiated by a large inclusion (not shown). See 3750 and 3751 (next page) for views of the crack-nucleus area at the rim.

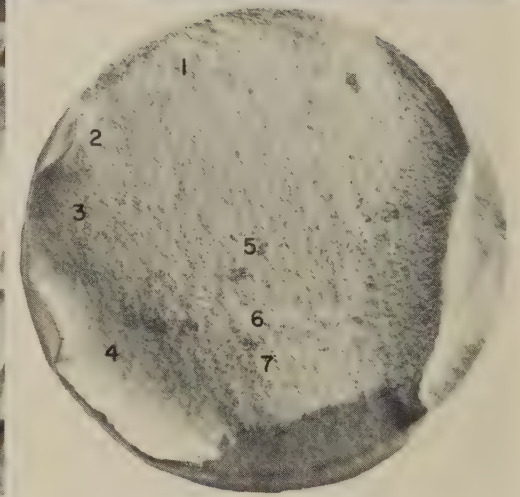
SEM and Light Fractographs: Notched Specimen of 8740 Steel Fractured by Tensile Overload (Continued); 8740 Steel Aircraft Bolt Fractured by Fatigue



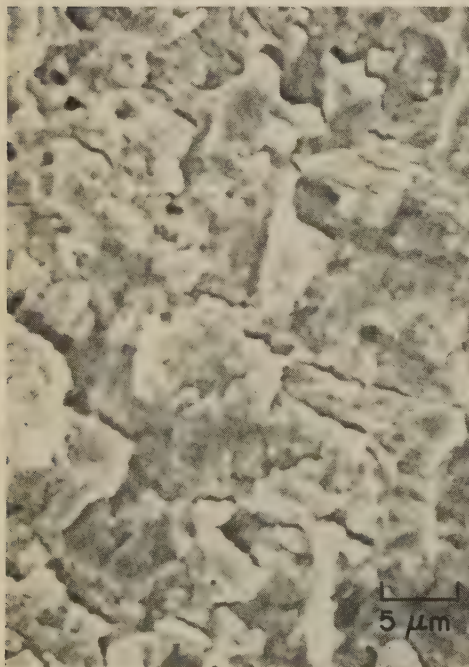
SEM fractograph 1000×
3750 Same fracture surface (8740 steel) as in 3747, showing crack-nucleus area at rim. Compare the radial features in the circular area at center with those in 3744. See 3751 for a higher-magnification view of the area in the rectangle.



SEM fractograph 3000×
3751 A higher-magnification view of the area within the rectangle in fractograph 3750 (at left). The radial pattern visible here bears a superficial resemblance to that shown in 3744, but is the result of local quasicleavage.



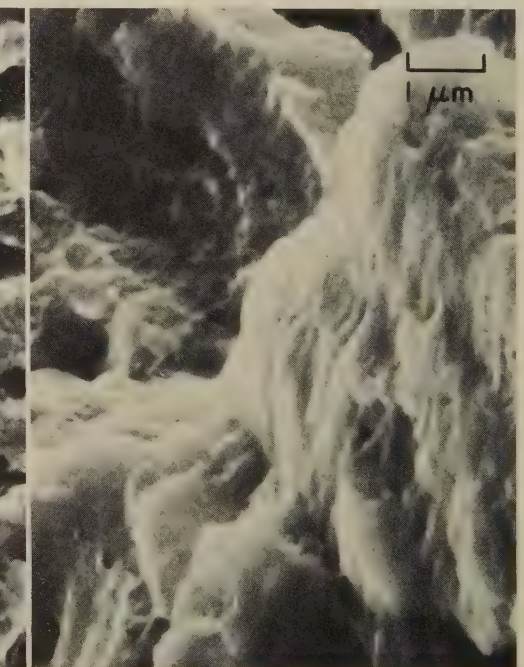
Light fractographs 3 1/3 × (3752); 8 × (3753)
3752 Perspective view (3752) and end-on view (3753) of the surface of a fatigue fracture in an aircraft bolt of 8740 steel. Hardness, Rockwell C 40; tensile strength, 1241 MPa (180 ksi). Numbers in 3753 refer to locations of 3754 to 3762.



SEM fractograph 2000×
3754 View at position No. 1 in 3753, near the origin of the fatigue fracture. Fragmentary fatigue striations are visible, many of which are associated with fissures.

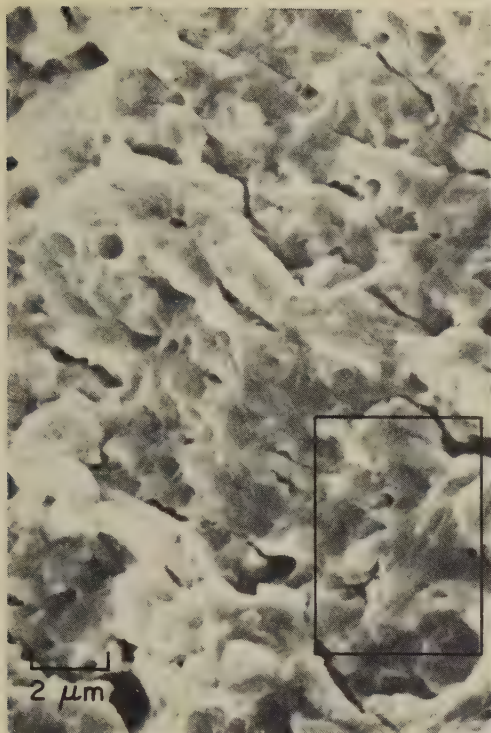


SEM fractograph 5000×
3755 Another view at position No. 1 in 3753, at higher magnification than fractograph 3754 (left), showing scattered voids that have very irregular shapes.

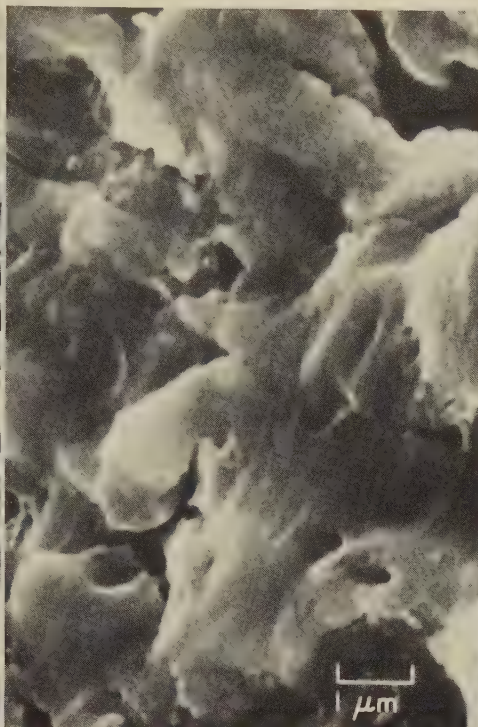


SEM fractograph 10,000×
3756 View at position No. 2 in 3753, farther from the origin than 3754 and 3755 and near (but not affected by) the damage at the surface. A few tiny dimples.

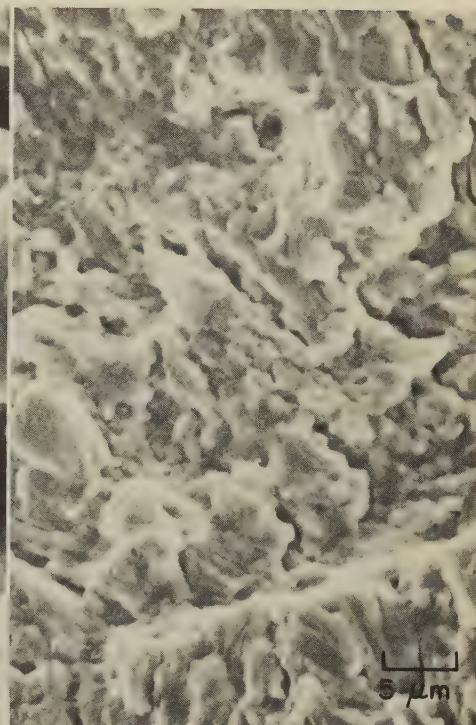
SEM Fractographs: 8740 Steel Aircraft Bolt Fractured by Fatigue
(Continuation of a Series Begun on Facing Page)



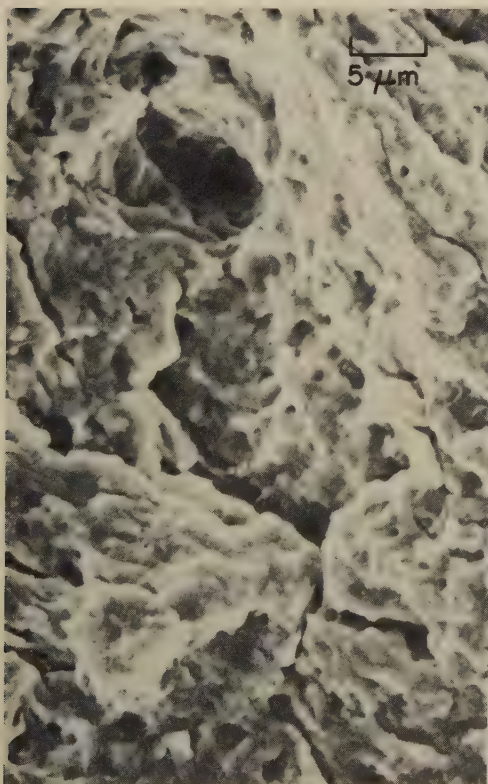
SEM fractograph 5000×
3757 View at position No. 3 in 3753, showing fissures (or striations) that were found to be perpendicular to the marks in 3753 radiating from the crack origin near position No. 1. See 3758.



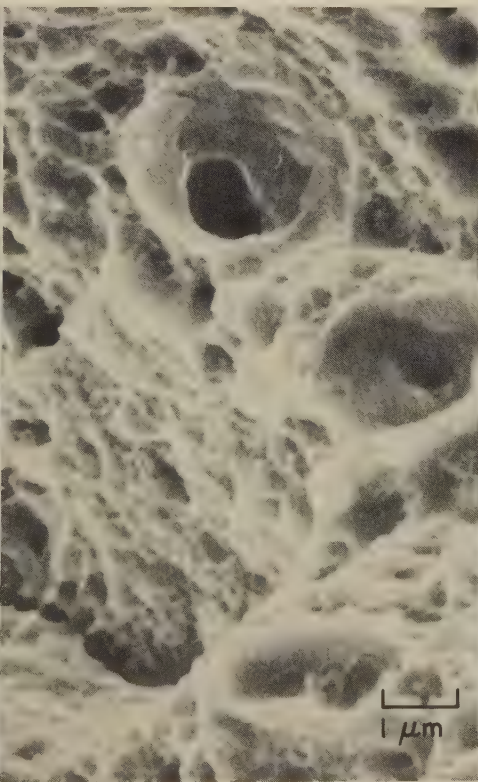
SEM fractograph 10,000×
3758 Higher-magnification view of the area within the rectangle in fractograph 3757 (at left). Note that the facets exhibit striation-like features that are perpendicular to the array of fissures.



SEM fractograph 2000×
3759 View at position No. 4 in 3753. The system of fissures shown in 3757 and 3758 is visible here as well. Although this region is near the shear lip, no evidence of fast fracture can be seen.



SEM fractograph 2000×
3760 View at position No. 5 in 3753 (near center), showing the end of the fatigue portion of the fracture, and the dimples characteristic of fast fracture.



SEM fractograph 10,000×
3761 View at position No. 6 in 3753. No evidence of fatigue. Here, fracture occurred entirely by microvoid coalescence. Note the small, well-defined voids.



SEM fractograph 500×
3762 View at position No. 7 in 3753. This region was produced near the final moment of fracture, but not close enough to the shear lip to show shear dimples.

SEM Fractographs: Fe-3.9Ni Specimen Fractured by Bending at -160 C (-256 F);
Fe-0.3Ni Specimens Fractured by Bending at -130 C (-202 F)



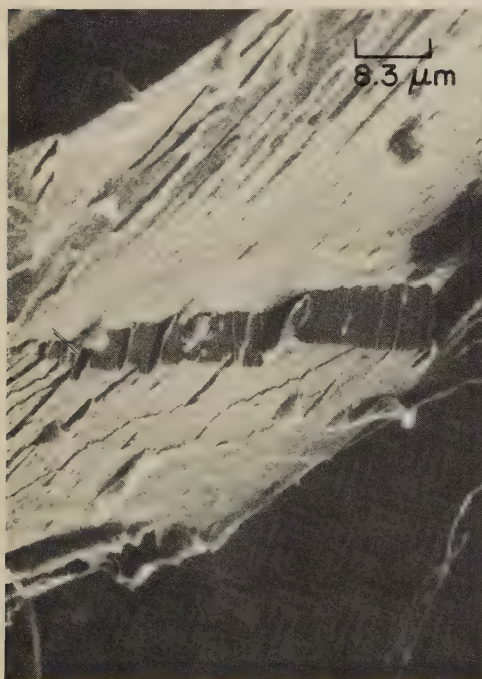
SEM fractograph 250×
3763 Surface of a slow-bending fracture produced at -160 C (-256 F) in Fe-3.9Ni alloy deoxidized with aluminum and titanium, which was forged at 1260 C (2300 F), hot rolled at 1040 C (1904 F), annealed at about 1000 C (1832 F), air cooled. Root of specimen notch is at top. Fracture was by cleavage that began at cracked Ti(C,N) particles (as at arrow). See 3764.



SEM fractograph 1200×
3764 Higher-magnification view of the slow-bending fracture in 3763 (at left). During testing, specimen temperature was controlled by an isopentane bath cooled with liquid nitrogen. Ferrite grain size, 30 μm . The angle of the notch was 45° , and the nominal radius of the root of the notch was 0.01 in . The fracture originated at cracked Ti(C,N) particles (as at arrow).



SEM fractograph 550×
3765 Surface of a slow-bending fracture that was produced at -130 C (-202 F) in an Fe-0.3Ni alloy that had been melted, deoxidized, forged, rolled and heat treated exactly the same as the higher-nickel alloy shown in fractographs 3763 and 3764. See also fractographs 3766 to 3768 (below).



SEM fractograph 1200×
3766 Another view of the slow-bending fracture in 3765, showing a different region of the fracture surface at higher magnification. Here, as in the specimen shown in 3763 and 3764, fracture was by quasicleavage. Also shown is the intersection of a twin boundary with the cleavage plane. See also fractograph 3767 (right).

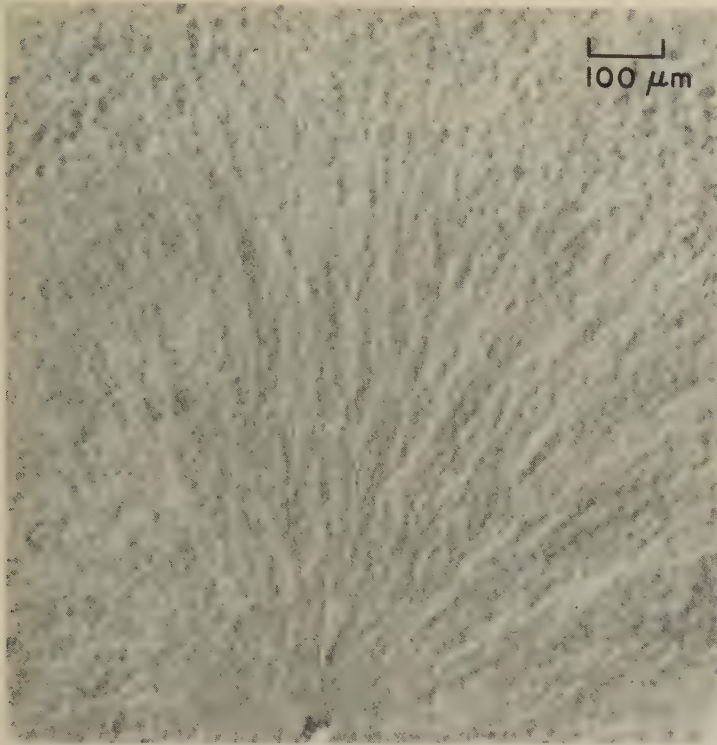


SEM fractograph 750×
3767 Surface of a bending fracture in a specimen of the same alloy and the same history as that in 3765, showing assorted river patterns. Note twist boundary at center, which has generated several cleavage steps. Although the higher nickel content of the alloy in 3763 gave greater strength, the aspects of subzero impact rupture are about the same for both alloys. See 3768.



SEM fractograph 1300×
3768 Another view of the bending fracture in 3767, showing a different region at higher magnification. This region best demonstrates the difference between this Fe-0.3Ni alloy and the Fe-3.9Ni alloy in 3763 and 3764 by displaying many small "tongues", or microtwins, which are characteristic of Fe-0.3Ni, and also of unalloyed (Armco) iron, but not of Fe-3.9Ni.

SEM Fractographs: Carburized 0.20C-1.0Mn-3.05Ni-1.65Cr-0.5Mo Steel Fractured in Rotary-Bending Fatigue; Effect of Test Temperature on Impact Fractures in 3.5Ni-1.5Cr-0.5Mo-0.1V Steel



SEM fractograph

100×

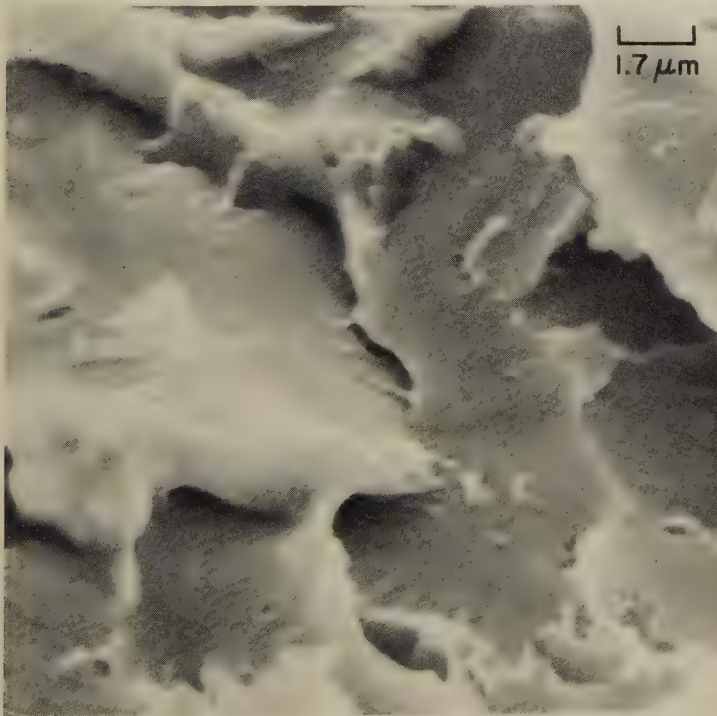
3769 Surface of a fatigue fracture produced in rotary bending in a specimen of 0.20% C, 1.0% Mn, 3.05% Ni, 1.65% Cr, 0.5% Mo steel carburized 5 hr at 925 C (1697 F), heat treated ½ hr at 870 C (1598 F), oil quenched, heat treated ½ hr at 832 C (1530 F), oil quenched, and tempered 1 hr at 150 C (302 F). The crack origin (at bottom) is at an alumina inclusion.



SEM fractograph

3000×

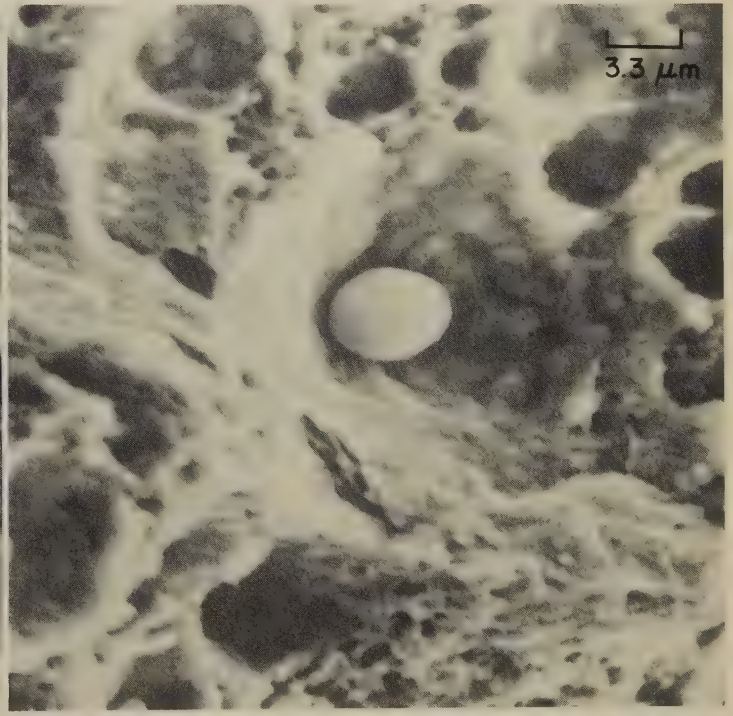
3770 Surface of a Charpy impact fracture in a specimen of 3.5% Ni, 1.5% Cr, 0.5% Mo, 0.1% V steel that had been tempered to a hardness of 260 Bhn. This "rock-candy" intergranular fracture was produced by impact testing at 20 C (68 F) after the specimen had been given an embrittling treatment of 100 hr at 500 C (932 F). See also fractographs 3771 and 3772, below.



SEM fractograph

6000×

3771 Surface of a Charpy impact fracture produced at -120 C (-184 F) in a specimen of the same steel as in 3770, tempered to the same hardness (260 Bhn), but not given the embrittling treatment, showing facets of transgranular quasicleavage separated by very pronounced, irregular steps. Feathery appearance of river patterns is probably due to poor contrast. See also 3772.



SEM fractograph

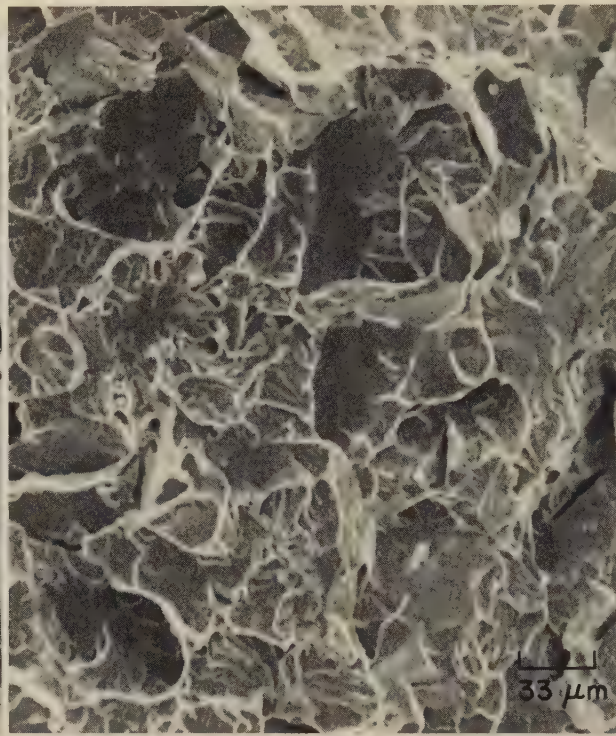
3000×

3772 Surface of a Charpy impact fracture produced at 100 C (212 F) in a specimen of the same steel and hardness as in 3770 and 3771, but also without the embrittling treatment described in 3770. Fracture here was by microvoid coalescence; a very wide range of dimple sizes is evident. Inclusions can be seen within dimples; note the large, egg-shaped inclusion at center.

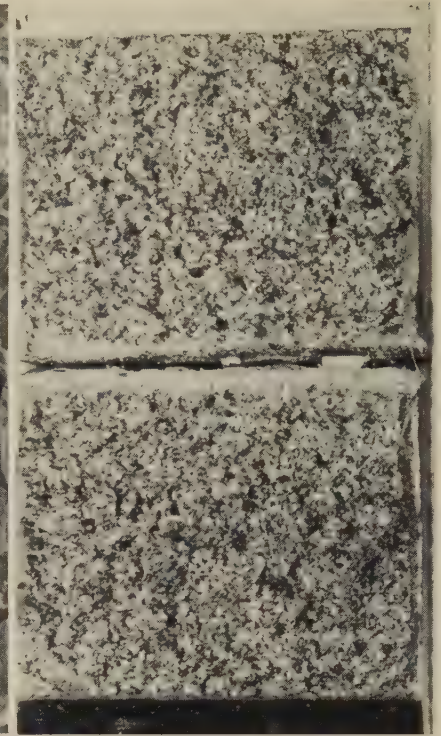
Light Fractographs and SEM Fractographs: Fe-12Ni-0.5Ti Alloy Fractured by Impact at -196°C (-321°F); Series Showing Influence of Aging Temperature



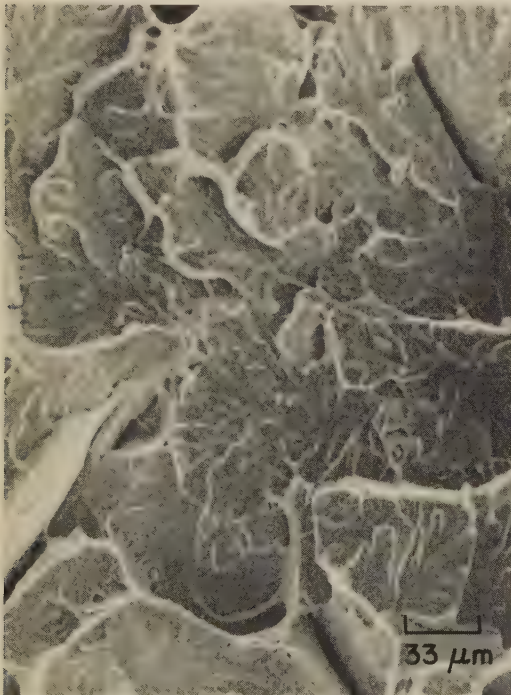
Light fractograph 4.8×
3773 Both fracture surfaces of a specimen that was not aged after austenitizing. See also 3774.



SEM fractograph 300×
3774 This SEM fractograph of the unaged specimen in 3773 shows quasicleavage facets. The impact energy was less than 20 ft-lb.



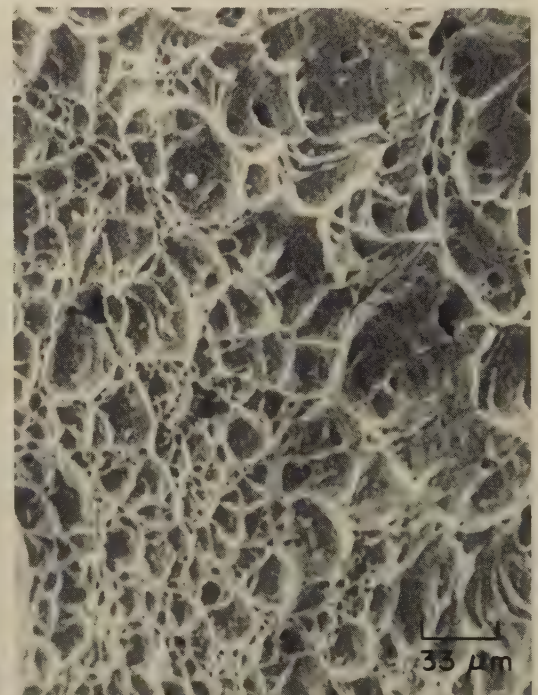
Light fractograph 4.8×
3775 Both fracture surfaces of a specimen aged at 650°C (1202°F) 2 hr and air cooled. See also 3776.



SEM fractograph 300×
3776 This SEM view of the specimen in 3775 shows that aging at 650°C (1202°F) produced almost no change in fracture-surface characteristics from those of unaged specimen in 3774. Impact energy was less than 20 ft-lb.



Light fractograph 4.8×
3777 Both fracture surfaces of a specimen aged at 700°C (1292°F) 2 hr and air cooled. Impact energy was about 150 ft-lb. Much deformation accompanied fracture. See 3778.



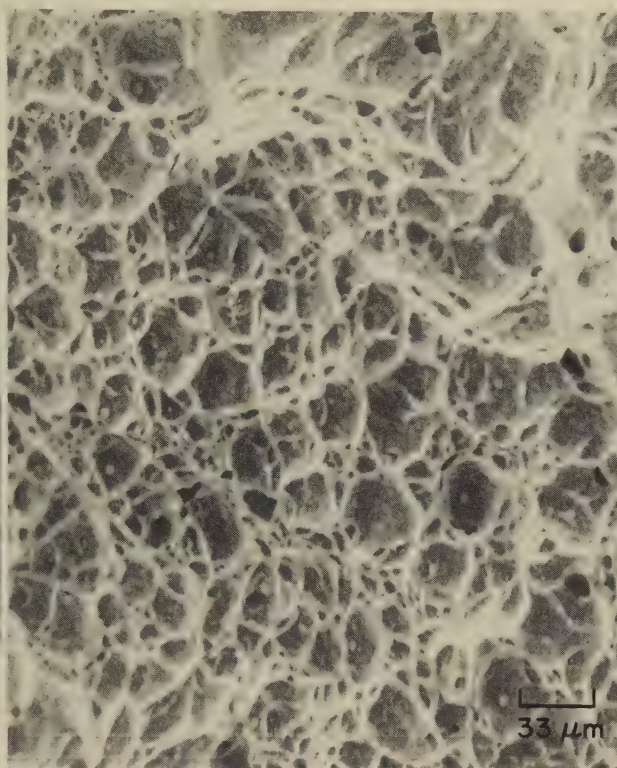
SEM fractograph 300×
3778 This SEM fractograph of the specimen in 3777, which was aged at 700°C (1292°F), shows dimpled rupture instead of the quasicleavage facets observed in the specimens in fractographs 3774 and 3776.

These facing pages present six related pairs of light and SEM fractographs of specimens of an Fe-12Ni-0.5Ti alloy intended for use at cryogenic temperatures. The series shows the effect on Charpy impact energy at -196°C (-321°F), and on fracture-surface characteristics, of the temperature of aging after austenitizing at 900°C (1652°F) for 2 hr and air cooling.

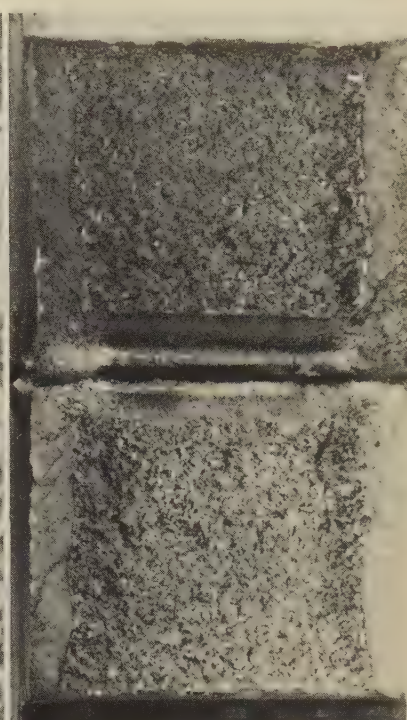
Light Fractographs and SEM Fractographs: Fe-12Ni-0.5Ti Alloy Fractured by Impact at -196°C (-321°F); Series Showing Influence of Aging Temperature (Continued)



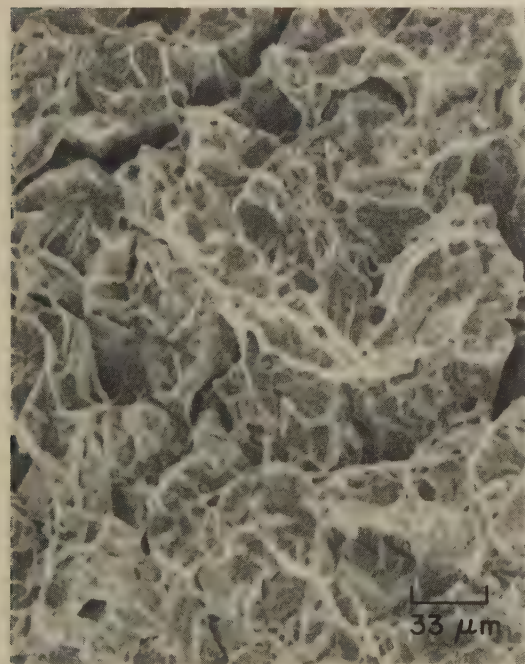
Light fractograph 4.8×
3779 Both fracture surfaces of a specimen aged at 750°C (1382°F) 2 hr and air cooled. Impact energy was about 150 ft-lb; deformation is similar to that in 3777. See 3780.



SEM fractograph 300×
3780 Scanning electron microscope fractograph of the specimen in 3779. This fracture, like that of the specimen in 3778, shows dimpled rupture. 33 μm



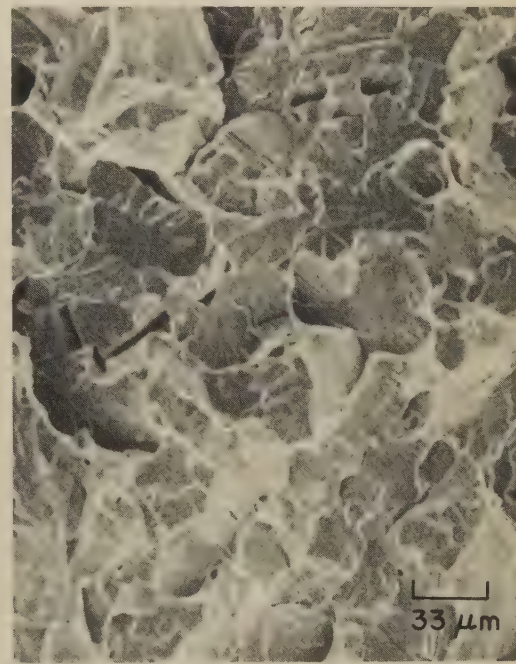
Light fractograph 4.8×
3781 Specimen aged at 800°C (1472°F) 2 hr and air cooled. Unlike 3779, this fracture shows little deformation, and impact energy was less than 20 ft-lb. See also 3782.



SEM fractograph 300×
3782 SEM view of specimen in 3781. Fracture appears to have propagated by a mixture of intergranular separation and cleavage, yet shows indications of some dimples. Note the deep secondary intergranular cracks. 33 μm



Light fractograph 4.8×
3783 Specimen aged at 850°C (1562°F) 2 hr and air cooled. The fracture is much coarser than that of the specimen in 3781, but is similar to it in other respects. See 3784.



SEM fractograph 300×
3784 This SEM fractograph of the specimen in 3783 shows that the fracture, like that in 3782, exhibits cleavage facets and short, deep intergranular cracks. This specimen also had impact energy of less than 20 ft-lb. 33 μm

These facing pages present six related pairs of light and SEM fractographs of specimens of an Fe-12Ni-0.5Ti alloy intended for use at cryogenic temperatures. The series shows the effect on Charpy impact energy at -196°C (-321°F), and on fracture-surface characteristics, of the temperature of aging after austenitizing at 900°C (1652°F) for 2 hr and air cooling.

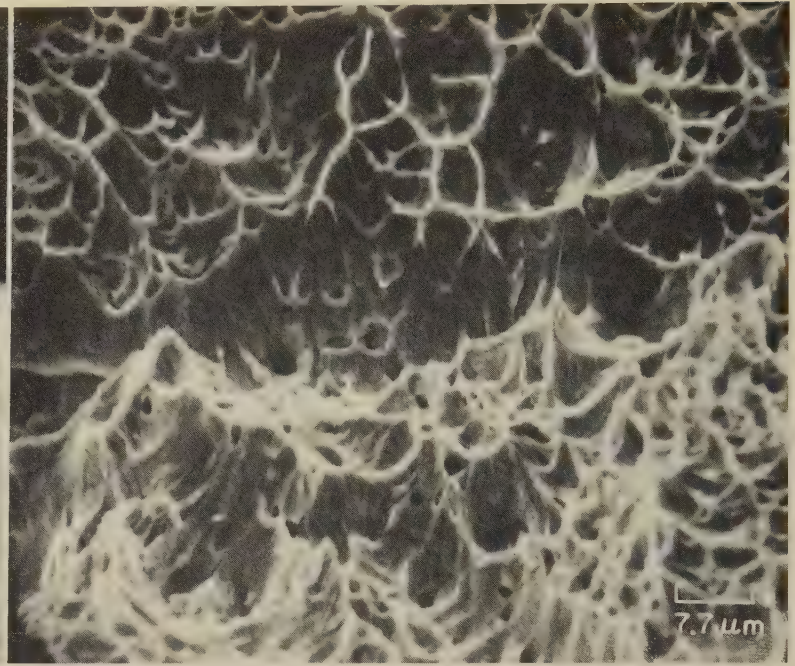
Light and SEM Fractographs: Specimen of 18% Ni, Grade 300, Maraging Steel
Fractured in a Tensile Test at Room Temperature



Light fractograph

26×

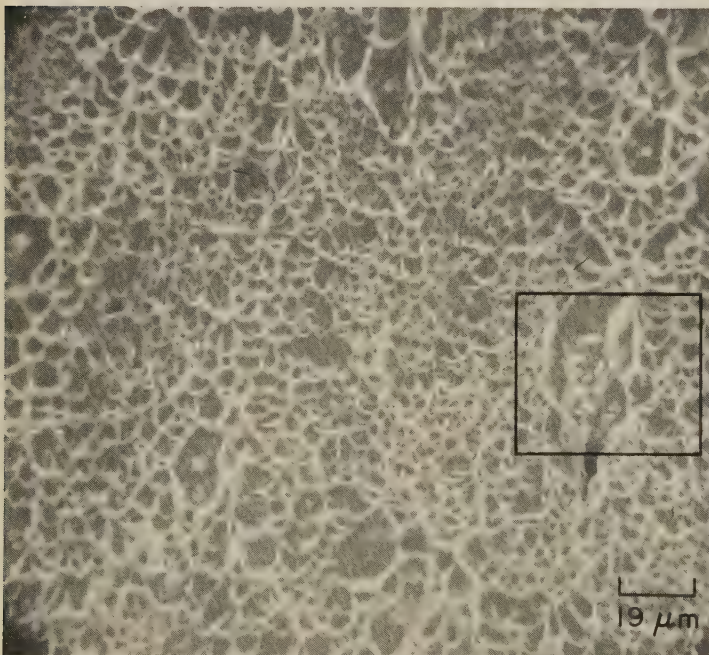
3785 Surface of a fracture in a tensile-test specimen of 18% Ni, grade 300, maraging steel aged 3 hr at 482 C (900 F), broken at room temperature. The crack-initiation zone (at center) is an example of extremely uneven fibrous fracture; there appear to be no radial marks leading to the base of the surrounding shear lip. The shear lip is of the pronounced type that is observed when a large reduction in cross-sectional area accompanies fracture. See also 3786 to 3789.



SEM fractograph

1300×

3786 SEM view of the fracture surface of the specimen of 18% Ni, grade 300, maraging steel in fractograph 3785 (left), showing a region in the area of transition from fibrous fracture in the central zone to fracture by shear in the surrounding lip. Visible in the lower portion of the fractograph are the equiaxed dimples (viewed obliquely) that are characteristic of fracture in pure tension; above are the elongated dimples of the shear lip. Note the horizontal boundary between these two types of fracture. See also fractographs 3787 and 3788, below.



SEM fractograph

520×

3787 View of the shear-lip region of the fracture surface in 3785 (above). Microvoid coalescence here has produced shear dimples with characteristic elongated shape. Note the large voids, which formed at inclusions of Ti(C,N). The matrix did not adhere to these inclusions, which allowed the voids to open early in the fracture process and to grow large. See 3788 (right) for a higher-magnification view of the area within the rectangle.

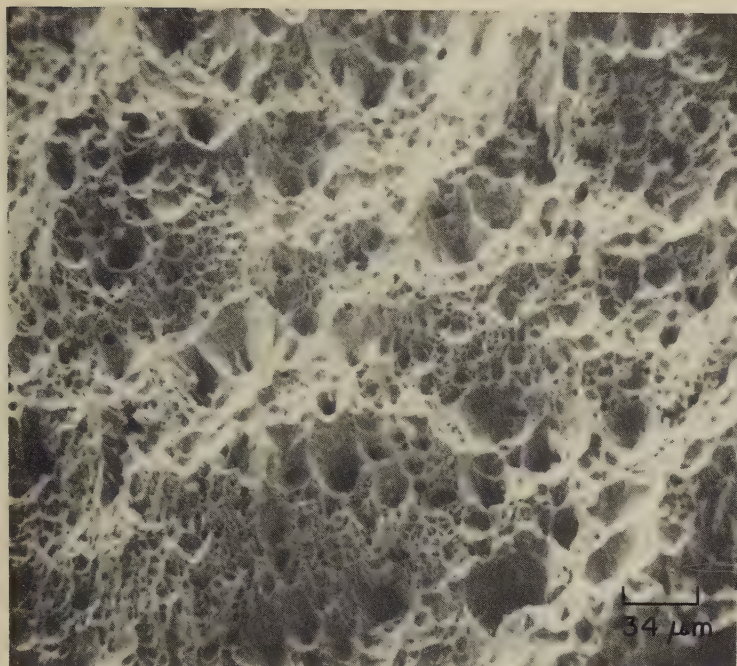


SEM fractograph

2200×

3788 Higher-magnification view of the area in the rectangle in 3787, showing one of the very large voids. Clearly visible is the array of Ti(C,N) inclusions that triggered the formation of this void. These may have been separate particles originally, or they may be segments of one or more larger particles that broke apart before the void opened. Except for a few tiny dimples visible here (lower right), the region in 3787 was found to lack the dispersion of fine dimples normally present in surfaces of tensile-test fractures.

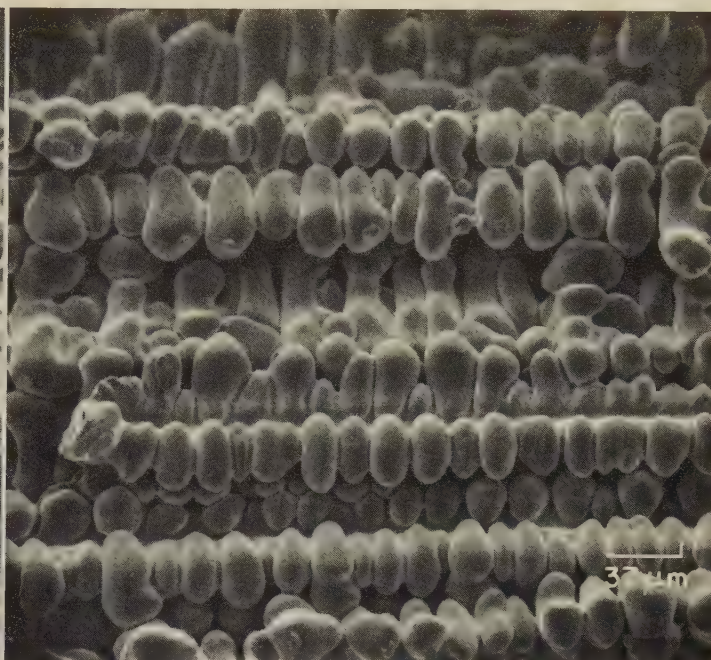
SEM Fractographs: Tensile Fracture in 18% Ni, Grade 300, Maraging Steel (Continued);
Shrinkage Porosity in Tensile Fracture in Cast 18% Ni, Grade 300, Maraging Steel



SEM fractograph

290×

3789 Another view of the surface of the tensile-test fracture in 18% Ni, grade 300, maraging steel in 3785 (facing page), showing a portion of the central zone of the fracture, close to the origin. The surface here is composed of equiaxed dimples of two different sizes. The larger dimples probably formed at Ti(C,N) particles; all of the dimples were caused by particles of some sort.



SEM fractograph

270×

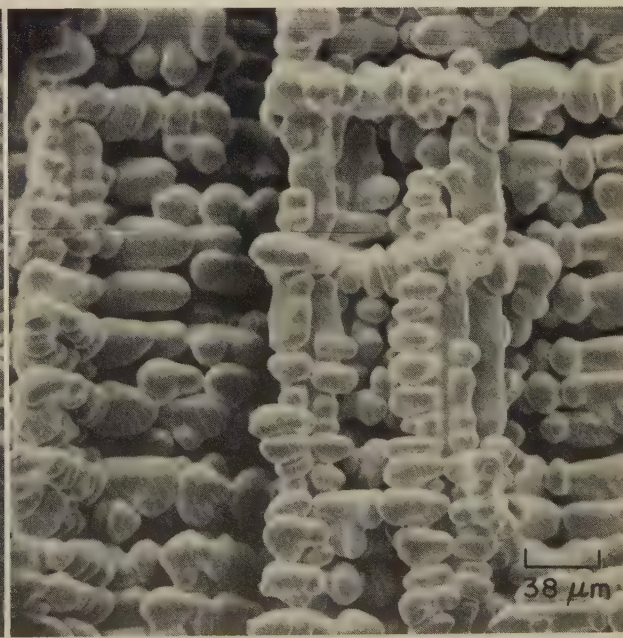
3790 Surface of a tensile-test fracture in a cast specimen of 18% Ni, grade 300, maraging steel, showing a region where the fracture intersected a shrinkage cavity and exposed dendrites whose growth during solidification was arrested by a lack of molten metal within the cavity. In this view, the primary dendrite arms are oriented horizontally. See also 3791 and 3792.



SEM fractograph

130×

3791 Lower-magnification view of the exposed dendrites in the shrinkage cavity in the cast specimen of 18% Ni, grade 300, maraging steel in 3790, showing dendrites that formed at different orientations. Had this casting been properly risered, the channels between the dendrite arms would have been filled, forming continuous metal. See 3792, which shows the area in the rectangle at higher magnification.

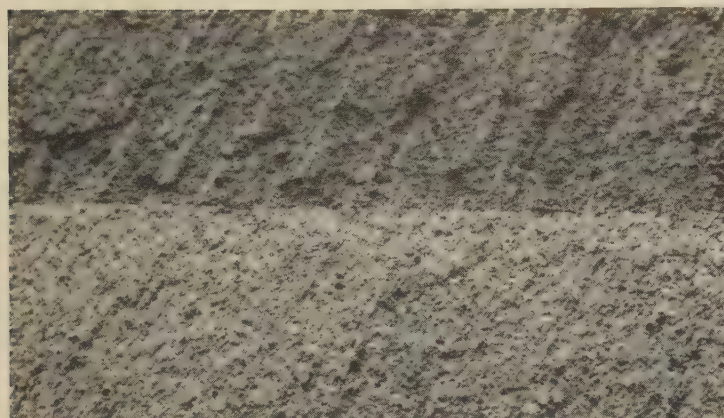


SEM fractograph

260×

3792 Enlarged view of the area outlined by the rectangle in fractograph 3791. Primary dendrite arms are oriented vertically here; secondary arms are at various orientations normal to the primary arms. Appreciable secondary-arm growth is evident, but the higher-order branching often found in castings has not occurred.

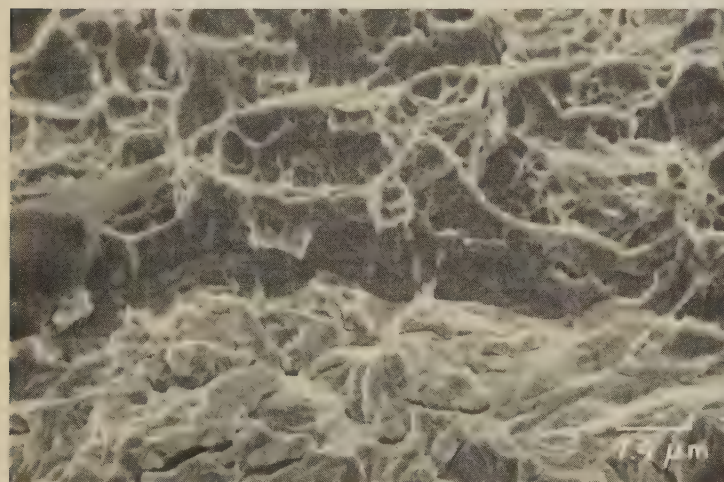
SEM Fractographs: 18% Ni, Grade 300, Maraging Steel Fracture-Toughness Specimens Showing Fatigue Precrack and Tension-Overload Fracture Surfaces



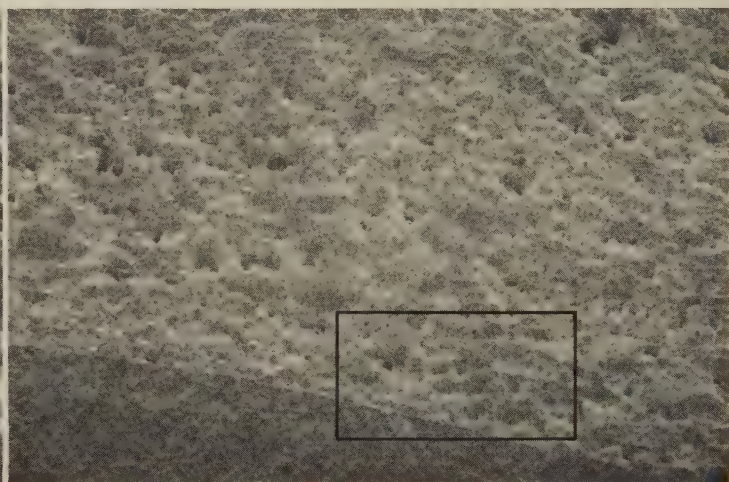
SEM fractograph 26×
3793 Fracture surface of a fracture-toughness specimen of 18% Ni, grade 300, maraging steel; the heat treatment of this specimen was not reported. This view shows entry of the fatigue crack from bottom, and sharp onset of final, fast fracture at center. See also fractographs 3794 and 3795; compare with 3796.



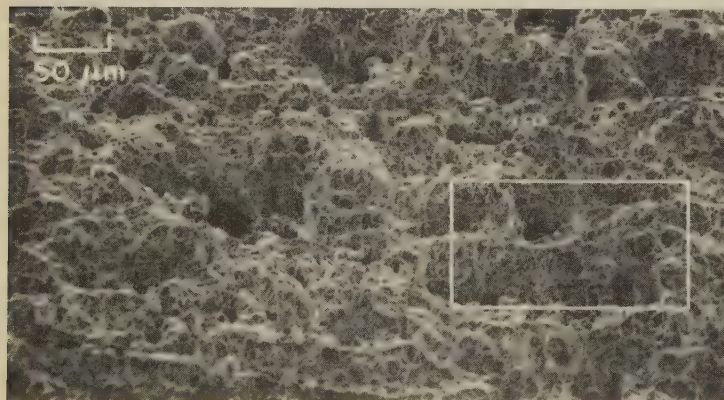
SEM fractograph 300×
3794 A view, at higher magnification, of the fracture surface shown in 3793, with the fatigue-crack surface at bottom and the fast-fracture surface at top. Note the secondary cracks, and lack of clear fatigue striations, in the fatigue area. See also fractograph 3795 (below, at left).



SEM fractograph 1350×
3795 Same fracture surface in 18% Ni, grade 300, maraging steel as in fractographs 3793 and 3794 (above), shown here at still higher magnification. At bottom, fatigue has produced numerous secondary cracks. Note the stretched zone at center, at the transition from fatigue to final, fast fracture.



SEM fractograph 47×
3796 Fracture surface of a fracture-toughness specimen of 18% Ni, grade 300, maraging steel aged 3 hr at 538 C (1000 F) and air cooled. Fatigue crack at bottom; ductile, tension-overload fracture at top. Note ridges, spaced at about 60 microns, in ductile region parallel to crack front. See 3793, 3797 and 3798.



SEM fractograph 200×
3797 Higher-magnification view of the area in the rectangle in 3796. Tension-overload dimples are clearly shown, but no details of the fatigue zone (bottom) are visible. The discontinuous nature of the ridges in the tension-overload region is evident. See 3798 for enlarged, composite view of area in rectangle here.



SEM fractograph 600×
3798 This is a composite of four scanning-electron-microscope fractographs of the plane-strain region of the area of tension-overload fracture in the specimen shown in 3796 and 3797, taken from the area within the rectangle in 3797. This shows more clearly the changes in surface orientation between the ridges.

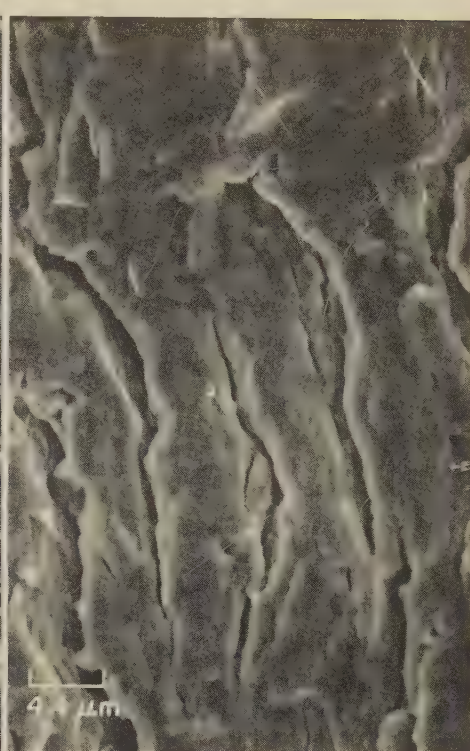
SEM Fractographs: 18% Ni, Grade 300, Maraging Steel Fractured in Low-Cycle Fatigue Tests After Various Heat Treatments



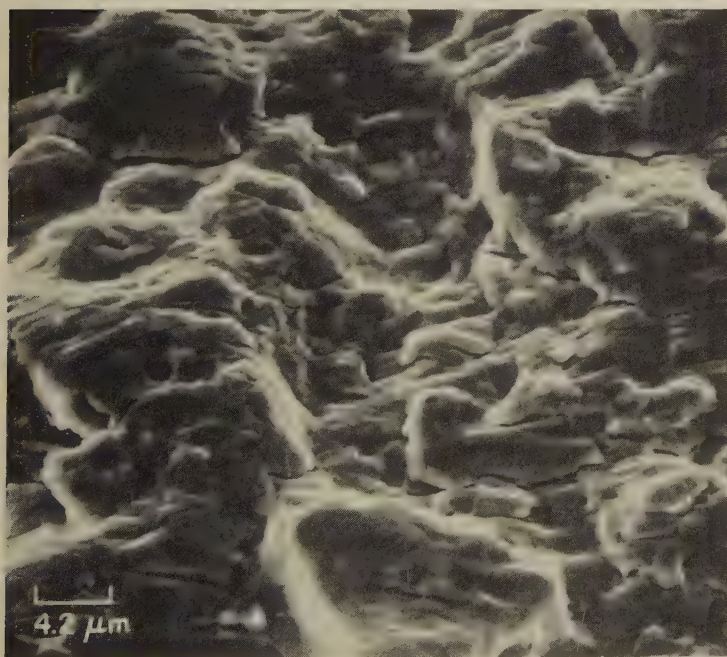
SEM fractograph 640×
3799 A low-cycle fatigue fracture (at about 3000 cycles) of 18% Ni, grade 300, maraging steel that had been annealed 1 hr at 816 C (1500 F) and air cooled. There is no evidence of clearly defined striations, but there is a system of more or less parallel secondary cracks. See also 3800, 3801.



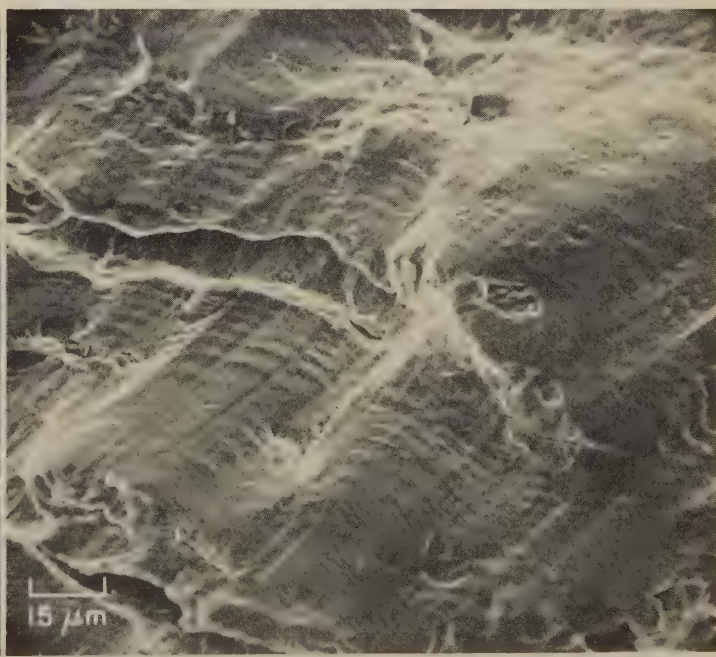
SEM fractograph 1250×
3800 A view of a different area of the fracture in fractograph 3799 (at left). Note that in this area quite regular striations are in evidence, many of them with fissures at their roots (as at A). Note also the several rubbed areas, particularly those at the top. See also 3801, at right.



SEM fractograph 2250×
3801 Same fracture as shown in 3799 and 3800, but an area at still another location, as seen at higher magnification. Here again is a system of repetitive fissures that appear to be quite deep and very irregular. There is little evidence of the conventional type of striations in this area.

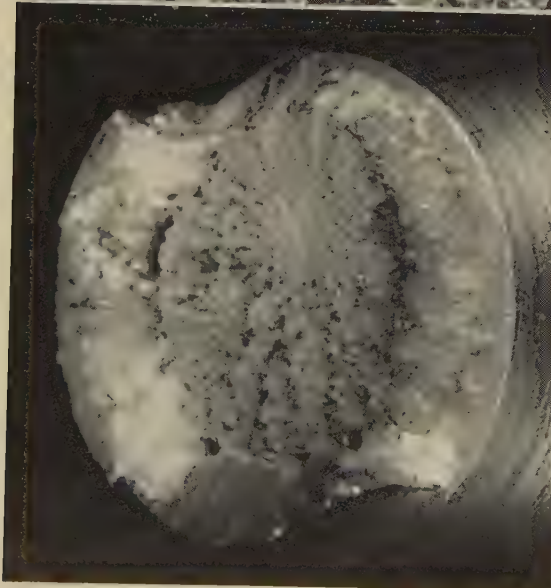


SEM fractograph 2400×
3802 Surface of a low-cycle fatigue fracture (at about 1000 cycles) in 18% Ni, grade 300, maraging steel that had been aged at 482 C (900 F) for 3 hr and air cooled. This fracture surface displays a progression of rather fine but extremely irregular striations, separated here and there by secondary cracks.



SEM fractograph 670×
3803 Low-cycle fatigue fracture of 18% Ni, grade 300, maraging steel (heat treatment not reported). This has relatively uniformly spaced fatigue striations with fewer secondary cracks than are seen in 3799 to 3802. The pattern of striations is similar to that produced by varied loading in service.

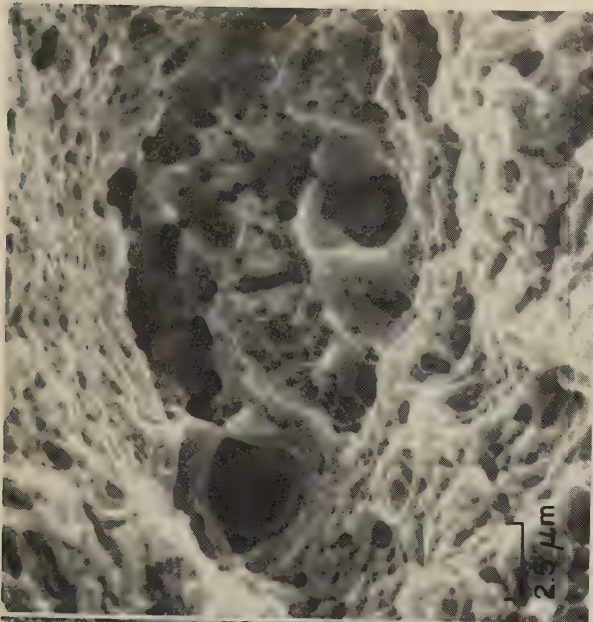
Light Fractographs and SEM Fractographs: Tension-Overload Fractures in Unnotched and Notched Specimens of H11 Tool Steel



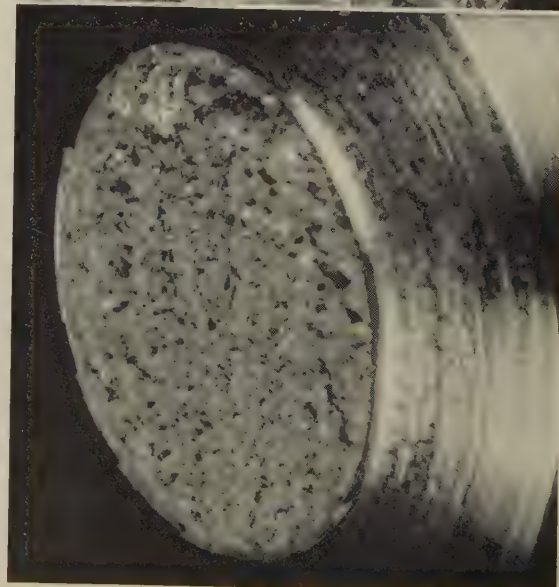
3804 Tension-overload fracture in an unnotched specimen of H11 tool steel heat treated to a tensile strength of 2041 MPa (296 ksi) and 48% reduction in area. Note radial features between fibrous origin (just right of center) and shear lip. See fractographs 3805 and 3806, at right.



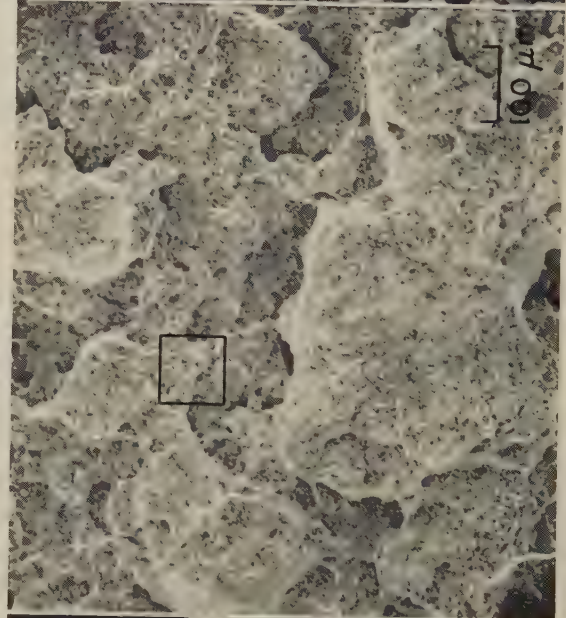
3805 Another view of the fracture surface in 3804, taken in the vicinity of the fracture origin, showing an unusually uneven array of dimpled facets with a scattering of large voids. See 3806 for a higher-magnification view of the area in the rectangle.



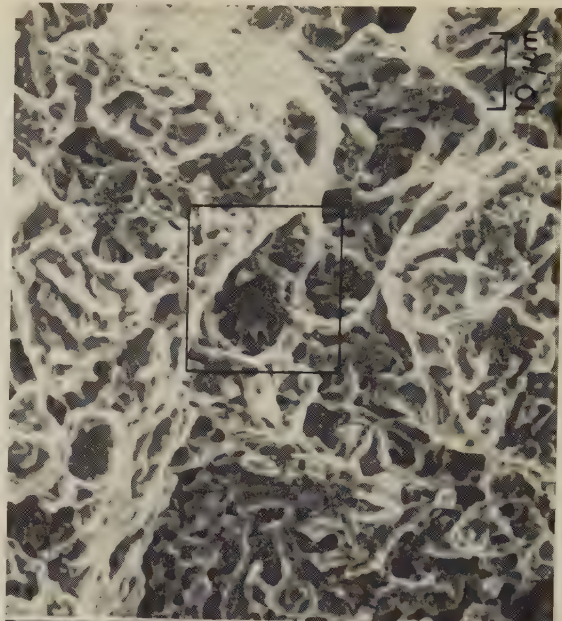
3806 Higher-magnification view of the area in the rectangle in 3805 (left), showing one of the large voids, and clearly revealing dimples of various sizes both at the bottom and along the side walls of the void.



3807 Tension-overload fracture in notched specimen of H11 tool steel (same heat treatment as in 3804). Notched tensile strength ($K_C = 3.5$) is 2665 MPa (386.5 ksi). A flat surface, partly bounded by a hairline shear lip. See also 3808 to 3810.

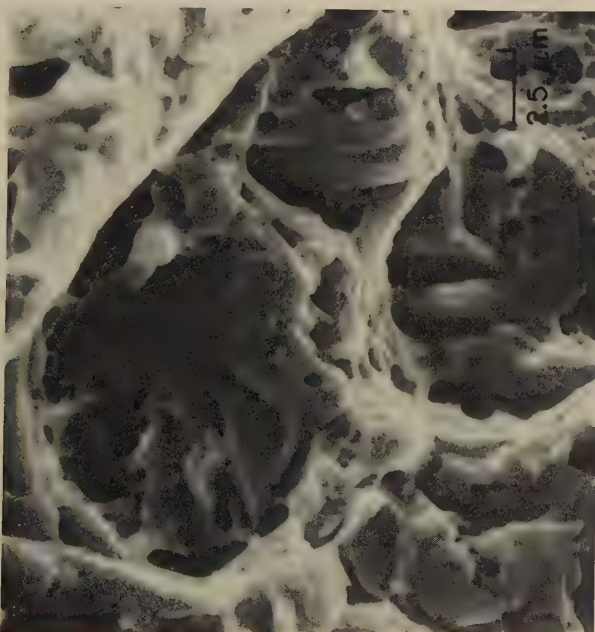


3808 SEM view of the fracture surface in 3807 (left). This surface seems to be generally dimpled, but at this relatively low magnification the features that appear to be dimples are not adequately resolved. See 3809, an enlarged view of area in rectangle.



3809 Higher-magnification view of area in rectangle in 3808 (left), showing dimples that are associated with local quasicleavage. Very little evidence of secondary cracking is present. Area in rectangle is shown at higher magnification in 3810 (next page).

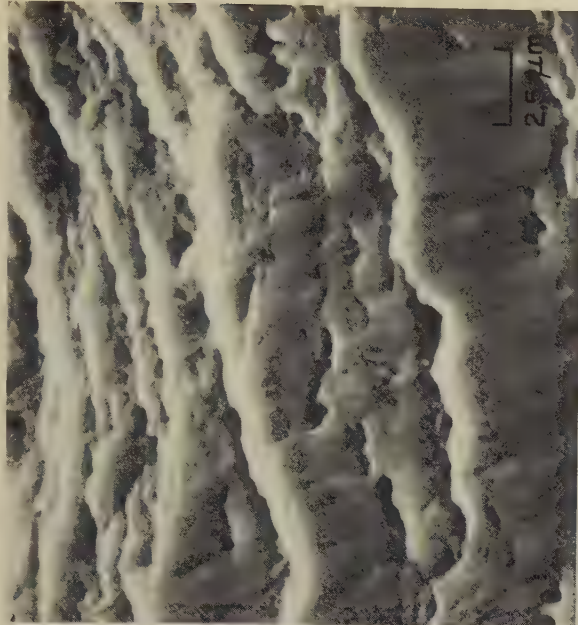
Light and SEM Fractographs: Tension-Overload Fracture in a Notched Specimen of H11 Tool Steel (Continued); Low-Cycle Fatigue Fracture in H11 Tool Steel



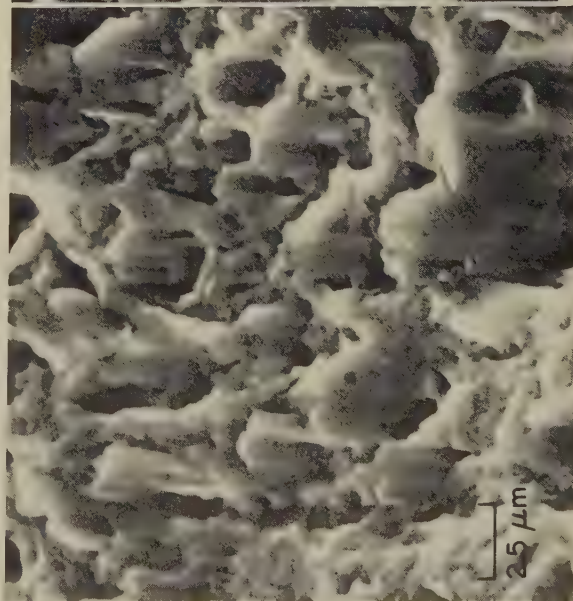
SEM fractograph
3810 Higher-magnification view of the area within the rectangle in fractograph 3809 (facing page). Small quasicleavage facets are visible, both within and adjacent to the larger dimples.



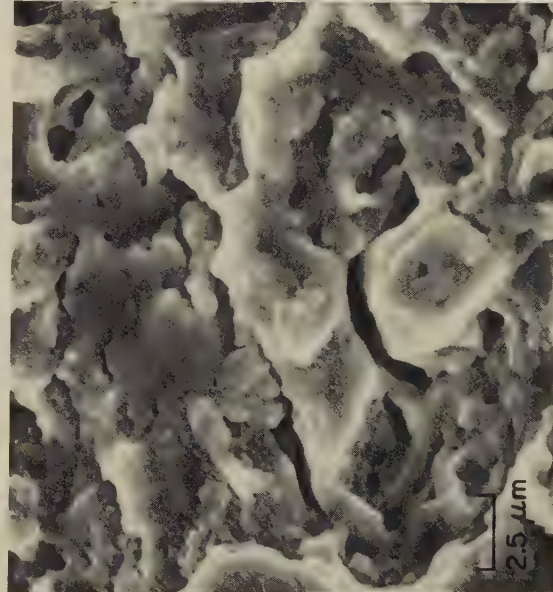
Light fractograph
3811 Low-cycle fatigue fracture in threaded specimen of H11 tool steel (same heat treatment and tensile strength as in 3804) that broke after 21,000 cycles of tension-tension ($R = 0.1$); maximum load, 60% of tensile strength. Dark, crescent-shaped region (A-A) is fatigue portion of fracture. See also 3812 to 3815.



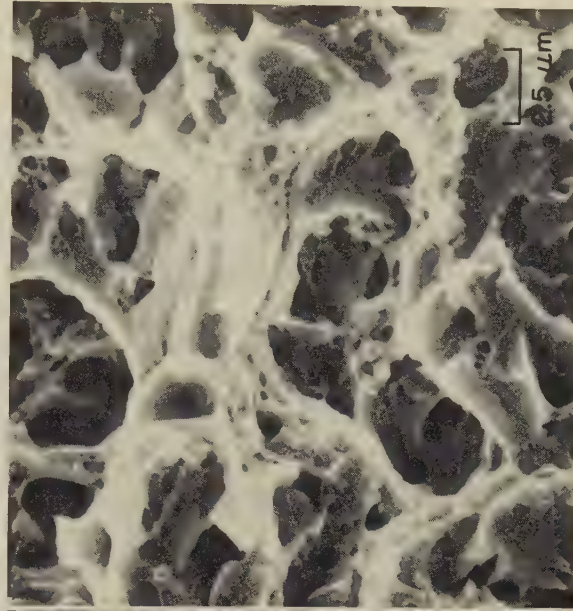
SEM fractograph
3812 SEM view taken near the outer edge of the crescent in 3811. Evident are ridges that are attributed to mechanical damage during shear deformation. In this region, there appear to be no secondary cracks.



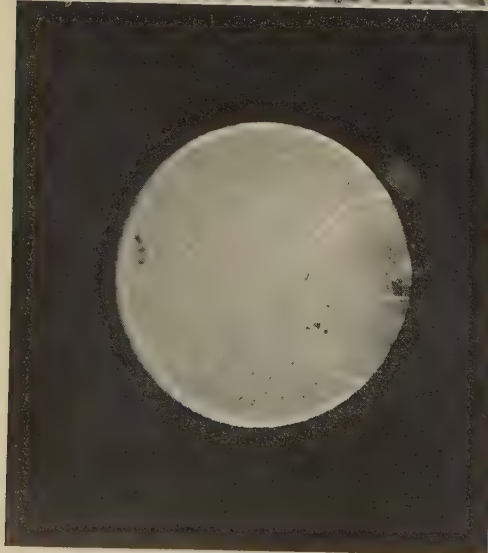
SEM fractograph
3813 View of the crescent in 3811, showing a region farther from the outer edge than 3812 is, and revealing ridges, formed during shear deformation, that have very irregular crests.



SEM fractograph
3814 Another view of the crescent in 3811, showing a region still farther from the outer edge than 3813 is. This region shows little evidence of conventional fatigue striations but reveals small cleavage facets, many of which are separated by secondary cracks.



SEM fractograph
3815 View of the fracture surface in 3811, showing a region in the zone of final fast fracture, and revealing the equiaxed dimples expected in a tension-overload fracture. No secondary cracks are visible.



3816 High-cycle fatigue fracture in H11 tool steel heat treated to a tensile strength of 2041 MPa (296 ksi) and 48% reduction in area, which broke after 775,000 cycles of tension-tension ($R = 0.1$) under a maximum load of 30% of tensile strength. The fatigue-crack origin is at the outer edge of the crescent-shaped region at bottom. See also 3817 and 3818.

Light fractograph



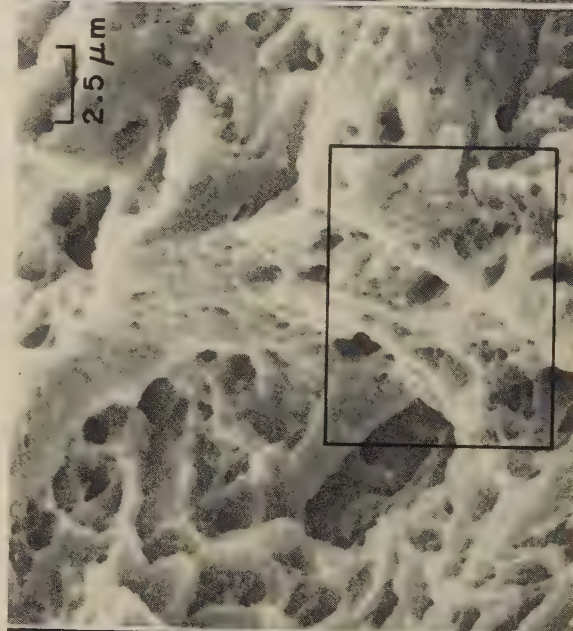
3819 Fracture caused by hydrogen embrittlement in threaded specimen of H11 tool steel (same heat treatment and tensile strength as in 3816). Hydrogen impregnation was by plating. Fracture occurred before the full sustained load could be applied and progressed around the circumference of the specimen. See 3820 to 3823.

Light fractograph



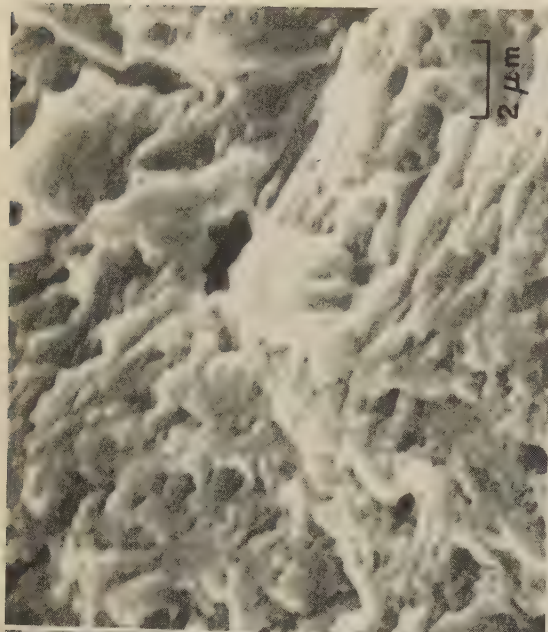
3817 An area within the crescent-shaped (fatigue) region of the fracture surface in 3816. The surface contains many pockmarks, which resemble dimples. There are no suggestions of fatigue striations. See 3818 for an enlargement of area in rectangle.

SEM fractograph



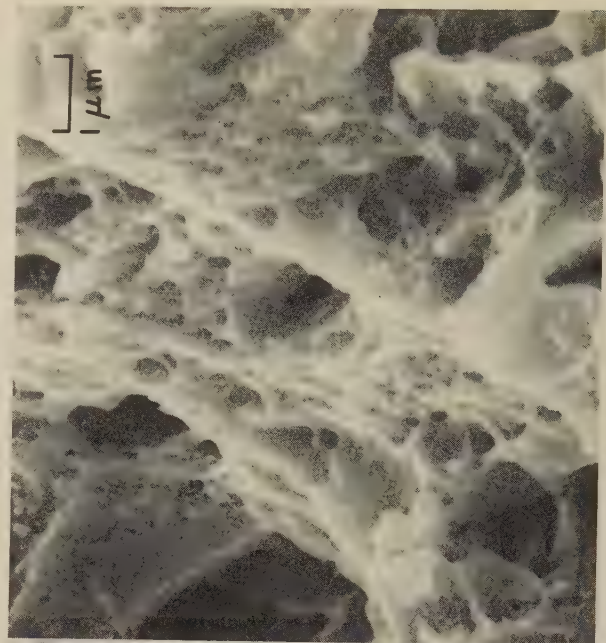
3820 SEM view of the fast-fracture region of the fracture surface in 3819, showing an unusual type of surface for a specimen heavily charged with hydrogen. Fracture occurred mainly by microvoid coalescence; there is no evidence of intergranular rupture. Area in rectangle is shown at higher magnification in 3821.

SEM fractograph



3818 Higher-magnification view of the area within the rectangle in 3817 (left). Some of the contours suggest striations, but they are very localized. Some features resemble cleavage facets but do not have the degree of flatness that is normally expected of cleavage.

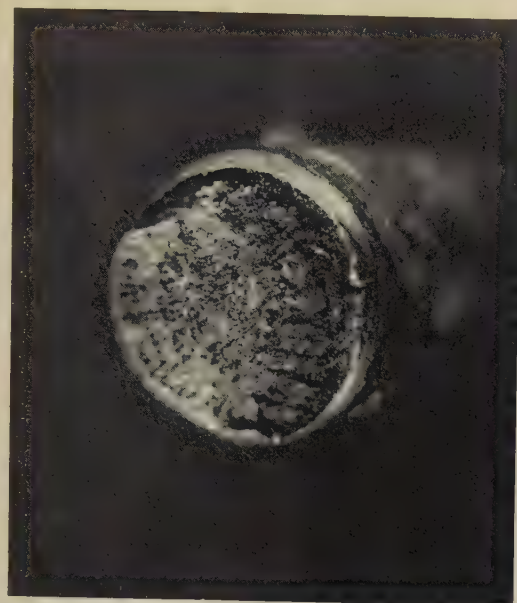
SEM fractograph



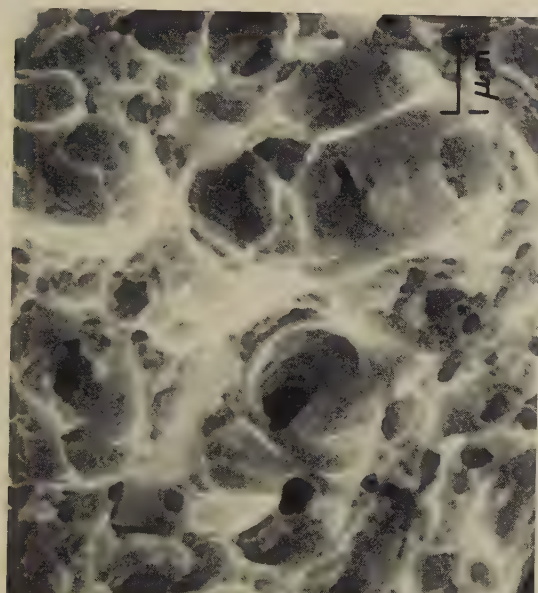
3821 Higher-magnification view of the area in the rectangle in 3820 (left). Very fine dimples and large facets are both present. A few features resemble cleavage facets, but the grain-boundary parting expected in hydrogen-embrittled fractures is absent.

SEM fractograph

Light and SEM Fractographs: H11 Tool Steel Fractured by Hydrogen Embrittlement (Continued);
H11 Tool Steel Fractured by Stress-Corrosion Cracking



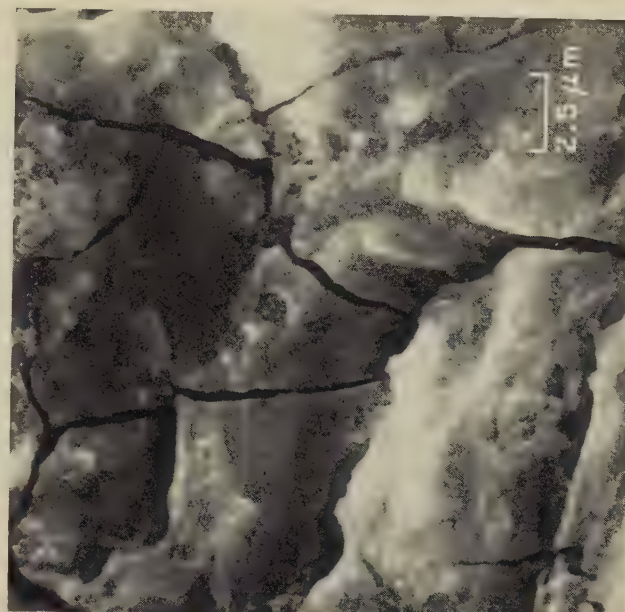
Light fractograph
3824 6× Fracture caused by stress-corrosion cracking in a threaded specimen of H11 tool steel (same heat treatment and tensile strength as in 3816) at a sustained loading of 75% tensile strength in a 3.5% NaCl environment at room temperature. Appreciable corrosion is evident. See also 3825 to 3827.



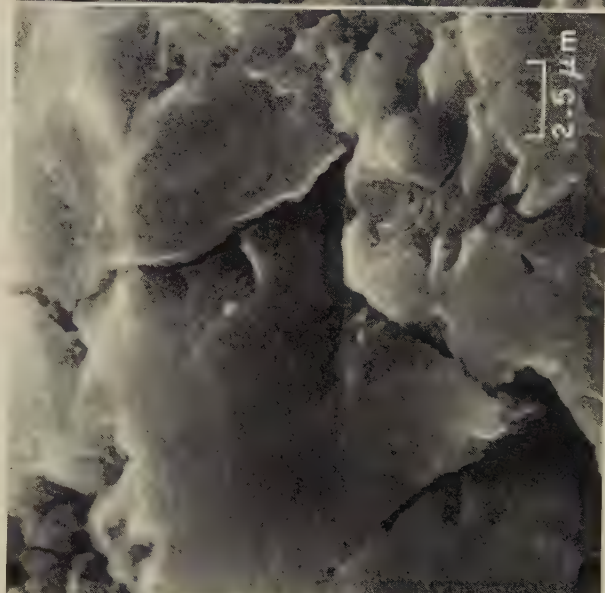
SEM fractograph
3823 10,000× Higher-magnification view of a region of which most is contained within the rectangle in fractograph 3822 (left). This region, like the one shown in 3821, exhibits a considerable range in dimple size and no trace of grain-boundary parting.



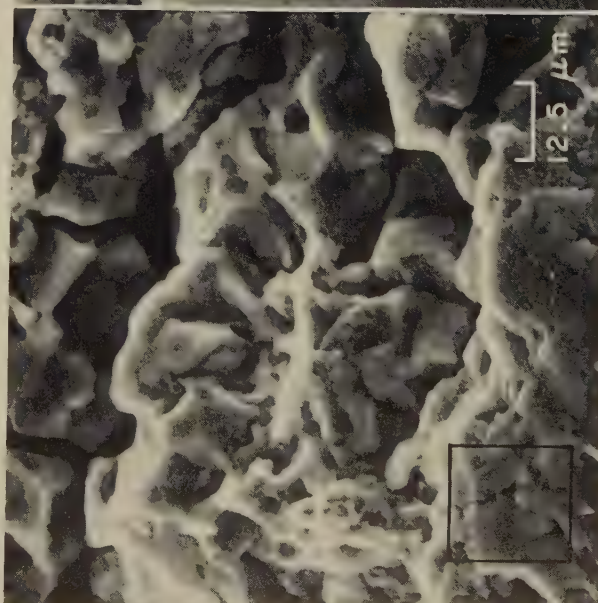
SEM fractograph
3822 4000× Another view of the fracture surface in hydrogen-embrittled H11 tool steel shown in 3819 (facing page). The surface consists almost entirely of dimpled rupture. A few facets are present and suggest possible local cleavage. See 3823.



SEM fractograph
3827 4000× High-magnification view of a region of the fracture in 3824 not shown in 3825, displaying grain-boundary facets and some corrosion. Some of the deep secondary cracks may be transgranular.



SEM fractograph
3826 4000× Higher-magnification view of the area in the rectangle in 3825, showing secondary cracking, which appears to follow some grain boundaries. The large, smooth facets resemble transgranular cleavage more than they resemble grain-boundary rupture.

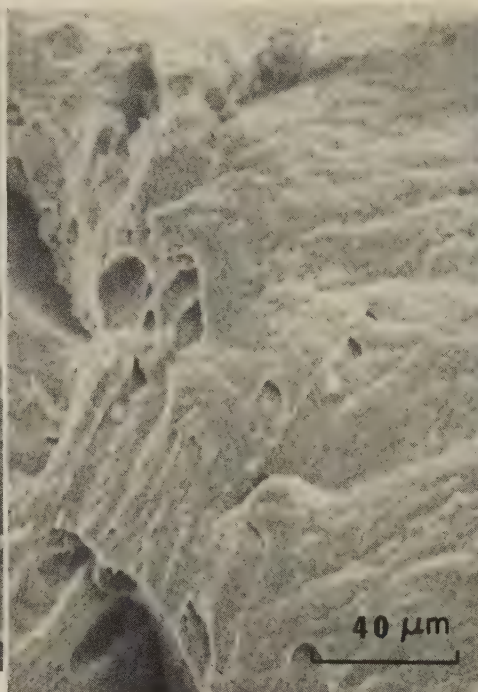


SEM fractograph
3825 800× SEM view of the fracture surface in 3824, showing fracture by grain-boundary cracking under NaCl attack. Some facets show no trace of corrosion. Deep secondary cracks are present. A few facets suggest quasicleavage. See 3826.

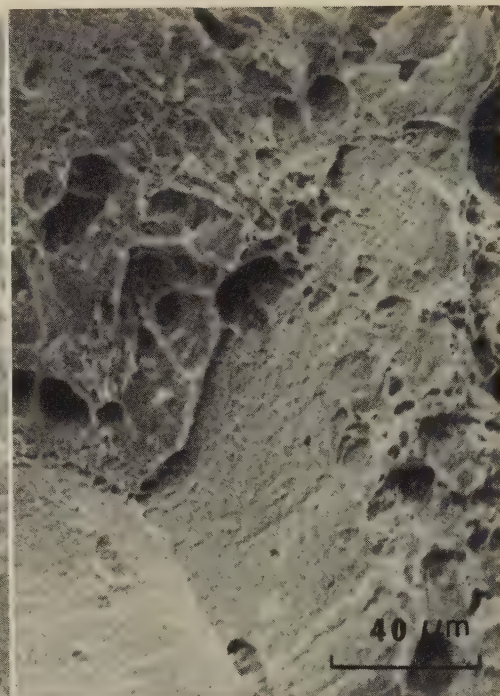
SEM Fractographs: Fe-6.4Cr-3.2Ta Alloy Fractured in Tension (Effect of Test Temperature);
Fe-6.2Ta Alloy Fractured in Tension (Effect of Heat Treatment)



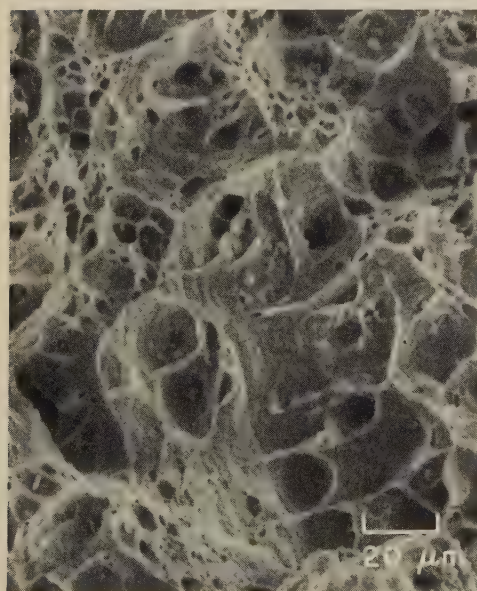
SEM fractograph 100×
3828 Fracture surface in an iron-base alloy containing 7 at. % (6.4 wt %) Cr and 1 at. % (3.2 wt %) Ta, pulled in tension at room temperature after solution treatment for 1 hr at 1320 C (2408 F) and water quenching, then aging at 700 C (1292 F) for 40 min and air cooling. Fracture was by transgranular cleavage believed to have originated at a grain-boundary network of Laves-phase Fe_2Ta precipitate. See 3829-31.



SEM fractograph 500×
3829 Fracture surface in a specimen of the same Fe-Cr-Ta alloy, and with the same heat treatment, as in 3828, but tensile tested at 200 C (392 F). In addition to cleavage, this fracture shows features of quasicleavage, but the higher test temperature provided greater ductility and a number of elongated dimples made their appearance. See also 3830 and 3831.



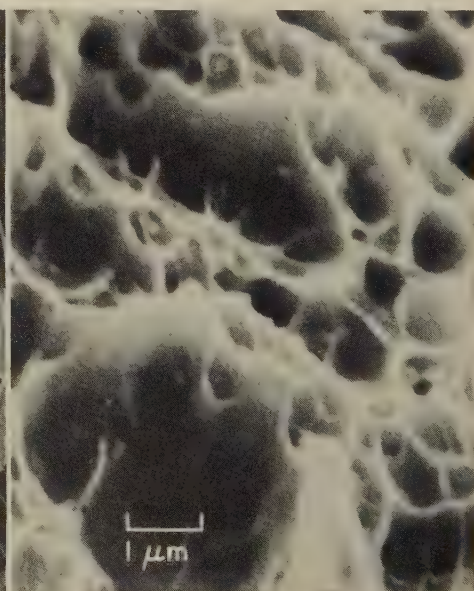
SEM fractograph 500×
3830 Same Fe-Cr-Ta alloy, and with the same heat treatment, as in 3828 and 3829, but fractured by tension overload at 400 C (752 F). Its appearance suggests rupture along two grain boundaries (at bottom center), as well as an increased quantity of dimples compared with the number present in 3829. The dimples here are also much more equiaxed than those in 3829. See 3831.



SEM fractograph 500×
3831 Fracture surface in a specimen of the same Fe-Cr-Ta alloy, and with the same heat treatment, as in 3828, 3829 and 3830, but which was broken in tension at 600 C (1112 F). At this test temperature, the ductility was sufficient to eliminate completely both cleavage and intergranular mechanisms of failure, and fracture occurred entirely by microvoid coalescence.

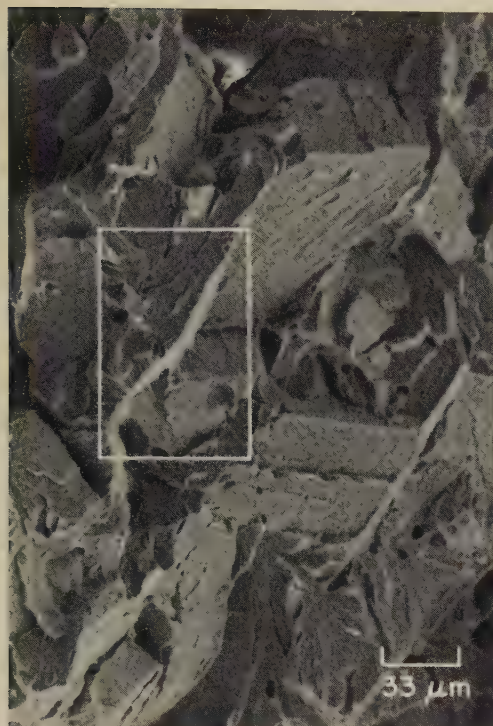


SEM fractograph 100×
3832 A room-temperature tensile fracture by cleavage of an Fe-2 at. % (6.2 wt %) Ta alloy solution treated 1 hr at 1400 C (2552 F), water quenched, aged 1 hr at 700 C (1292 F), air cooled. Laves-phase Fe_2Ta precipitate, uniformly distributed in the matrix and believed present at grain boundaries, caused brittleness (<1% tensile elongation). See also 3833.

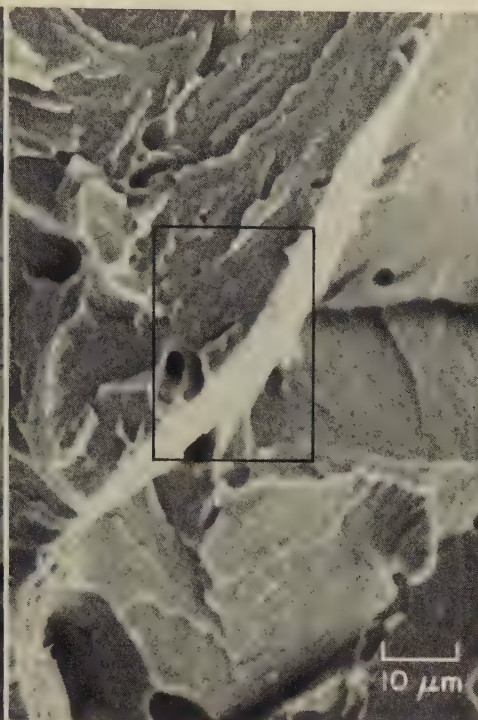


SEM fractograph 10,000×
3833 A room-temperature tensile fracture in a specimen of the same alloy as in 3832, given the same heat treatment plus a spheroidizing treatment of 10 min at 1100 C (2012 F) and air cooling. Spheroidization of precipitates at grain boundaries and within grains, plus a finer grain size than in 3832, resulted in dimpled fracture and 22% tensile elongation.

SEM Fractographs: Comparison of Charpy Impact Fractures in 0.18% C, 3.85% Mo Steel and in 0.41% C, 4.2% Mo Steel, Both With the Same Heat Treatment



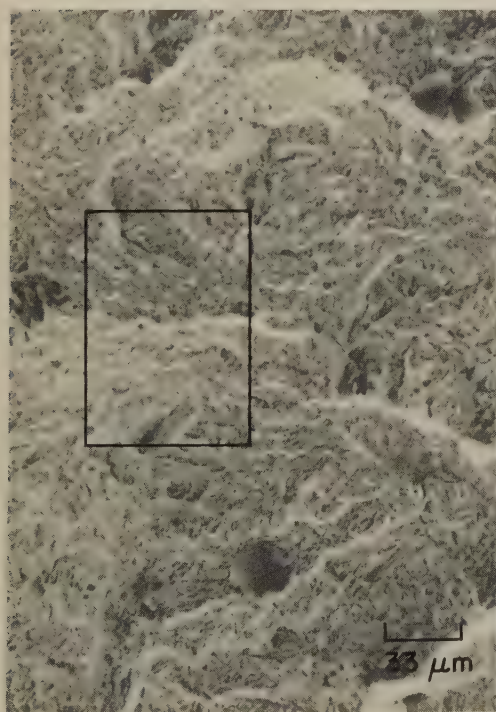
SEM fractograph 300×
3834 Charpy impact fracture in 0.18% C, 3.85% Mo steel after heat treatment in an inert atmosphere at 1200 C (2192 F) for 1 hr, followed by an ice-10% brine quench. Many quasicleavage facets are visible. See fractograph 3835 (an enlargement of the area in the rectangle).



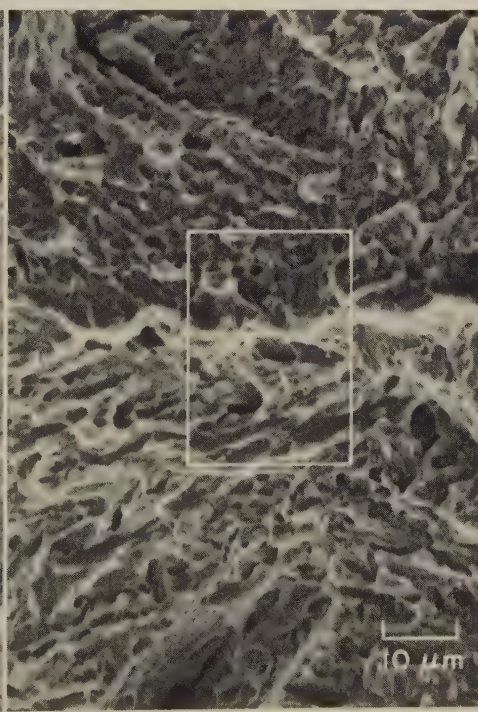
SEM fractograph 1000×
3835 Area outlined by the rectangle in 3834, shown at higher magnification, which makes details of the quasicleavage more clearly evident. A few elongated dimples are present. Area in the rectangle here is shown at higher magnification in fractograph 3836, at right.



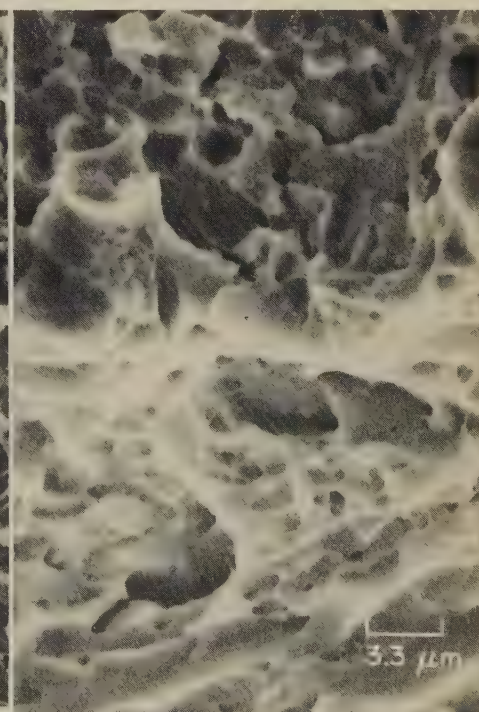
SEM fractograph 3000×
3836 Area outlined by the rectangle in 3835, shown at higher magnification. The bright tilted facet may be a grain boundary or a tear ridge. An inclusion is faintly visible in the dimple about midway along the left edge.



SEM fractograph 300×
3837 Charpy impact fracture in 0.41% C, 4.2% Mo steel after the same heat treatment as that for the specimen in 3834. This fracture occurred by dimpled rupture, although the impact energy was only 1/3 that of 3834. See 3838 and 3839.



SEM fractograph 1000×
3838 This view at higher magnification of the area outlined by the rectangle in 3837 reveals that many of the dimples are highly elongated, exhibiting locally some features suggestive of cleavage. Area in rectangle here is shown enlarged in 3839.



SEM fractograph 3000×
3839 Area outlined by the rectangle in fractograph 3838, shown at triple the magnification. At this enlargement, many extremely fine dimples are visible, formed along the margins of larger voids.

SEM Fractographs: 0.3C-0.6Mn-5.0Mo Secondary-Hardening Steel (Effect of Various Heat Treatments on Results of Plane-Strain Fracture-Toughness Tests)



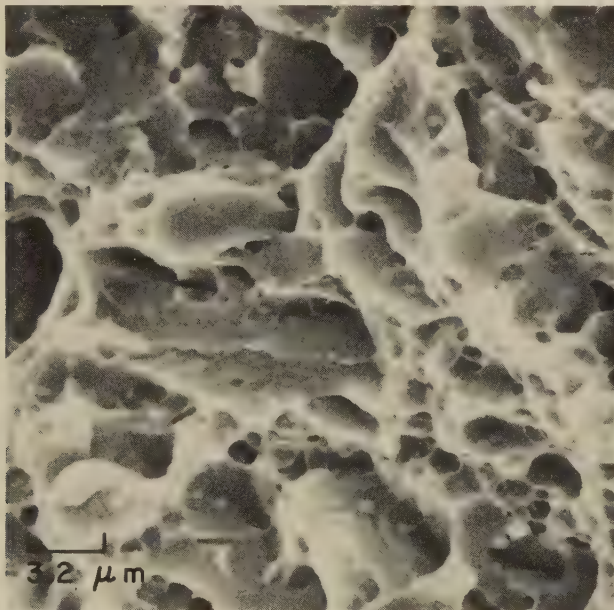
SEM fractograph 290×
3840 This specimen was austenitized at 1204 C (2200 F). Yield strength was 1413 MPa (205 ksi). There appear to be large facets of quasicleavage, such as at A; elsewhere, the surface contains rather large dimples. Note the large void near the center.



SEM fractograph 300×
3841 This specimen was austenitized at 1093 C (2000 F). This fracture, like that in 3840, displays quasicleavage facets; some of them are apparently rather deeply indented. There are also intervening regions showing clusters of equiaxed dimples.



SEM fractograph 1000×
3842 This specimen, austenitized at 982 C (1800 F), shows none of the quasicleavage facets observed in 3840 and 3841. There appear to be many scattered dimples, but most of the surface consists of small facets, seemingly caused by cleavage.



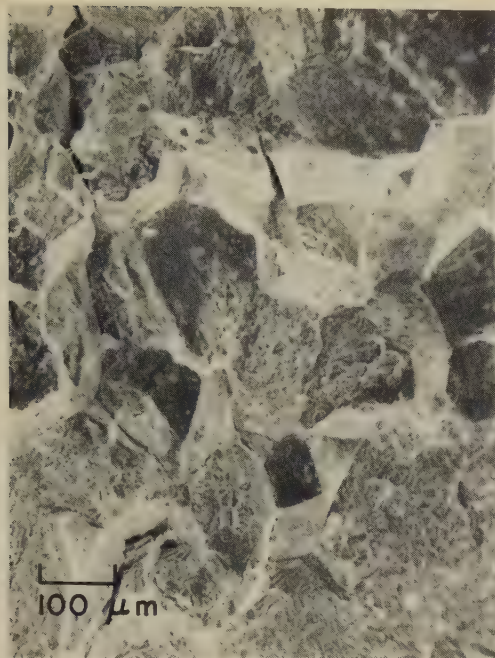
SEM fractograph 3150×
3843 This specimen was austenitized at 871 C (1600 F). Yield strength was 1324 MPa (192 ksi). The fracture surface exhibits a wide range of dimple sizes. The heat treatment resulted in a plane-strain fracture-toughness (K_{Ic}) value of 55 MPa·m^{1/2} (50 ksi·in.^{1/2}); this contrasted with a value of 121 MPa·m^{1/2} (110 ksi·in.^{1/2}) for the specimen in 3840—probably because of incomplete solution of carbide particles at the lower austenitizing temperature for the specimen shown here.



SEM fractograph 300×
3844 The heat treatment of this specimen was altered as follows: austenitize at 1204 C (2200 F) for 1 hr, quench to 871 C (1600 F) and hold for 30 min, ice-brine quench, then refrigerate in liquid nitrogen. Fracture appears to have occurred by a combination of transgranular and intergranular cleavage. The K_{Ic} value for this specimen was even lower than that for the specimen in 3843; the lower value is believed to be the result of a different distribution of carbide particles.

The fractographs on this page show the effects of various austenitizing treatments on characteristics of fractures in an experimental secondary-hardening steel containing 0.3% C, 0.6% Mn and 5.0% Mo. All specimens were austenitized for 1 hr at the temperatures indicated, quenched in ice-brine, and then refrigerated for 30 min in liquid nitrogen. Plane-strain fracture-toughness specimens were then tested at room temperature as part of a program to develop high levels of toughness in steels that also maintain ultrahigh tensile strength.

SEM Fractographs: 0.4C-0.6Mn-5.0Mo Secondary-Hardening Steel Fractured in a Plane-Strain Fracture-Toughness Test; Charpy Impact Fracture in 0.42C-2.1Mo-5.2Co Steel



SEM fractograph 100×
3845 An area of the fracture surface in which the fracture appears to be intergranular, with secondary cracks between the grains. The lower portion of the area may contain dimples.



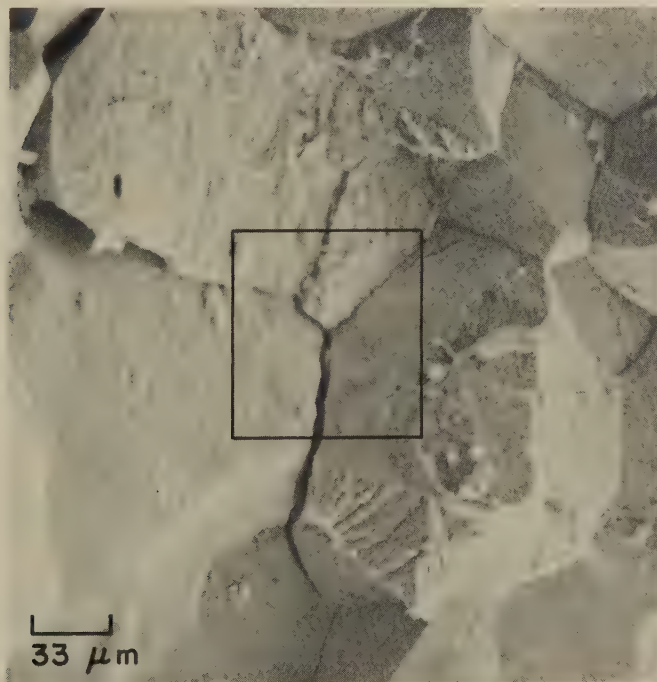
SEM fractograph 300×
3846 Another area of the fracture surface, shown at higher magnification. This area has many characteristics of an intergranular fracture. Grain surfaces exhibit fine dimples but no river patterns.



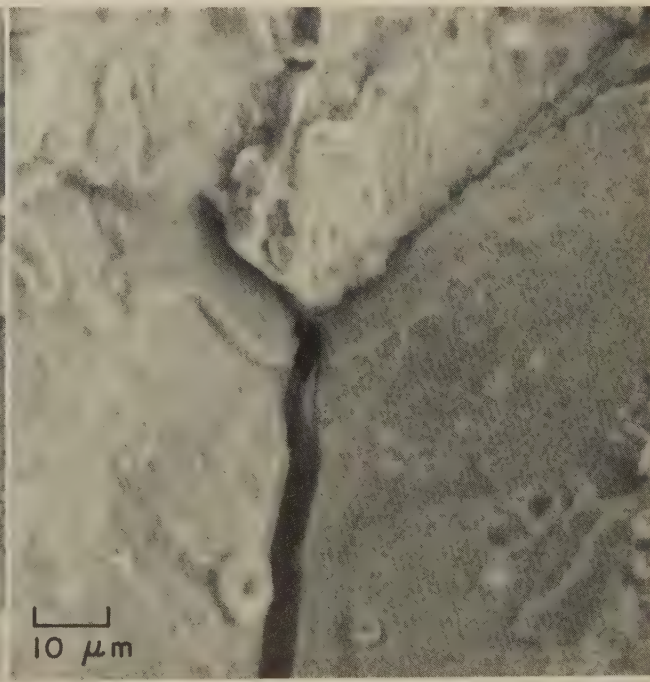
SEM fractograph 1000×
3847 A third area of the fracture surface, at still higher magnification. This area shows a secondary crack penetrating deeply into the grain boundary. Small cleavage steps are evident.

The fractographs above are of a fracture-toughness specimen of 0.4% C, 0.6% Mn, 5.0% Mo secondary-hardening steel that was tested as part of a program to develop fracture toughness in high-strength steel (the same program that yielded the fractographs on the facing page). This specimen was austenitized for 1 hr at 1204 C (2200 F),

ice-brine quenched, and refrigerated for 30 min in liquid nitrogen. Room-temperature yield strength was 1758 MPa (255 ksi). Plane-strain fracture-toughness (K_{Ic}) value was 76 MPa·m^{1/2} (69 ksi·in.^{1/2}) — appreciably less than the value for the lower-carbon (0.3% C) steel in fractograph 3840 (facing page), which was given the same heat treatment.

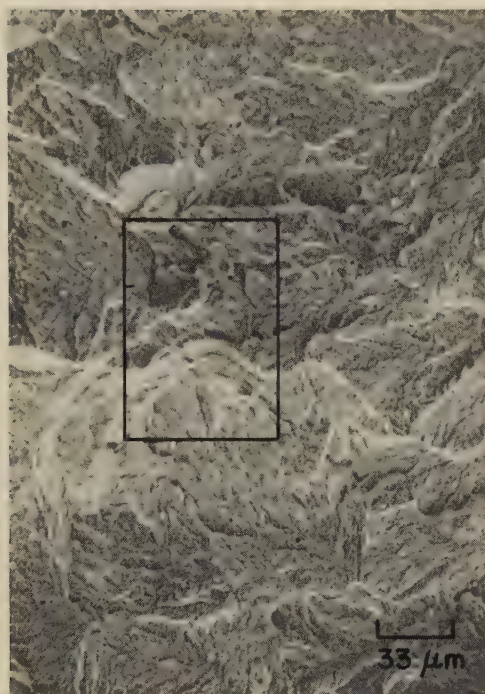


SEM fractograph 300×
3848 A V-notch Charpy impact fracture in a specimen of 0.42% C, 2.1% Mo, 5.2% Co alloy steel that was not as tough as had been expected. The fracture has been largely intergranular, although three facets appear to be transgranular cleavage facets. Note the secondary grain-boundary crack. Area in rectangle is shown enlarged in 3849.



SEM fractograph 1000×
3849 Area outlined by the rectangle in 3848, shown at a higher magnification. The two facets in the lower portion are believed to be grain surfaces; facet in upper portion is believed to be a transgranular cleavage facet. The cause of the low toughness of this specimen was quench cracking. Small rings visible here may be artifacts.

SEM Fractographs: Charpy Impact Fractures in 0.43C-3.85Mo-9.0Co Steel Specimens That Were Given Different Heat Treatments



SEM fractograph 300×
3850 Charpy V-notch impact fracture in alloy steel (0.43% C, 3.85% Mo, 9.0% Co) that was heat treated in an inert atmosphere at 1200 C (2192 F) for 1 hr, then quenched in an agitated solution of ice and 10% brine. It appears that fracture was by a shear process. See 3851.



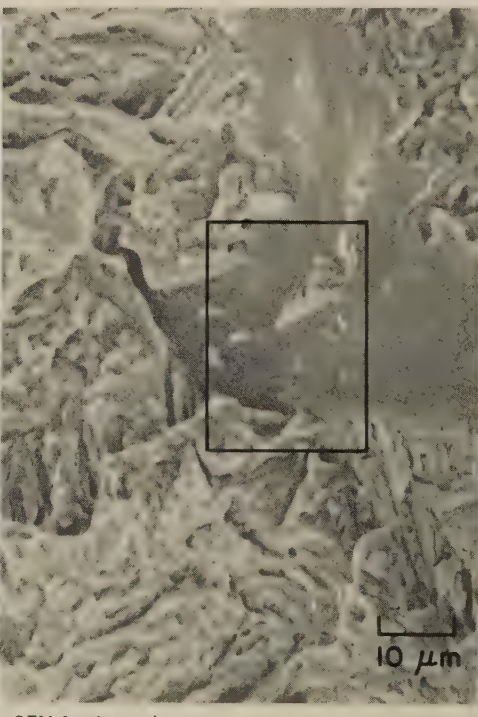
SEM fractograph 1000×
3851 Higher-magnification view of the area within the rectangle in 3850, showing more clearly the shear deformation and some isolated dimples. There appear to be small regions of local cleavage. See 3852 (right) for a higher-magnification view of the area in the rectangle here.



SEM fractograph 3000×
3852 Higher-magnification view of the area within the rectangle in 3851 (left), which reveals additional small dimples that are not readily apparent at the lower magnification. See also fractographs 3853 to 3855, for the effects of tempering on the fracture surface.



SEM fractograph 300×
3853 Charpy impact fracture in a specimen of the same alloy steel, and given the same austenitizing treatment, as in 3850, but then tempered for 1 hr at 600 C (1112 F), which maximized secondary hardening, and air cooled. See 3854.



SEM fractograph 1000×
3854 An enlargement of the area in the rectangle in 3853 (left). This specimen, which had the same yield strength as that of the as-quenched specimen in 3850, fractured mainly by intergranular separation. See 3855 for a higher-magnification view of the area in the rectangle here.

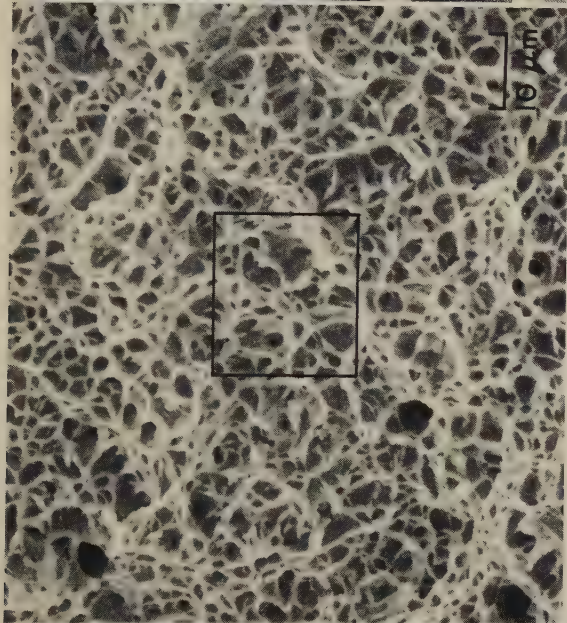


SEM fractograph 3000×
3855 Higher-magnification view of the area in the rectangle in fractograph 3854 (at left). A tonguelike formation is visible (at left center) on the flat surface of a grain. Tempering has produced embrittling networks of carbide particles.

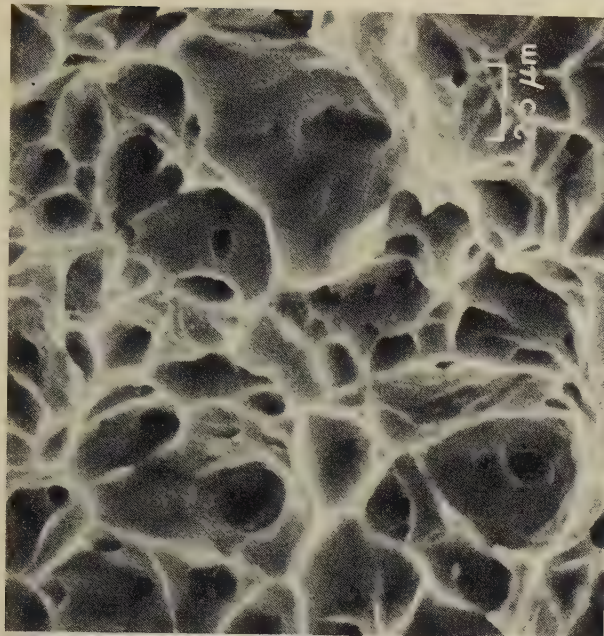
Light and SEM Fractographs: Unnotched and Notched Specimens of 13-8 PH Stainless Steel Fractured by Tension Overload



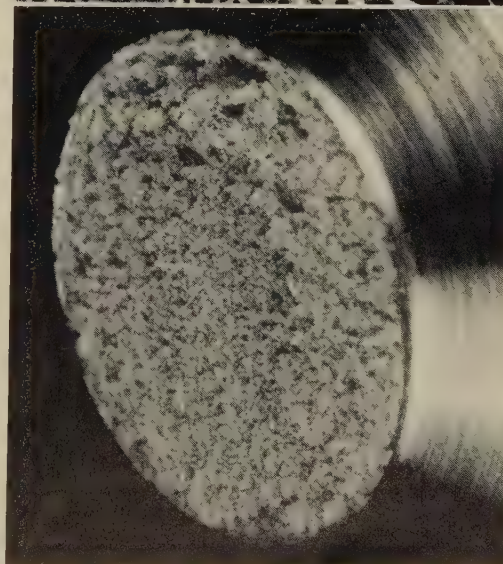
Light fractograph
3856 A classic example of cup-and-cone tension-overload fracture, in an unnotched specimen of 13-8 PH stainless steel with a tensile strength of 1634 MPa (237 ksi) and 47% reduction in area. There are circumferential secondary cracks at the base of the shear lip. See also 3857 (right).



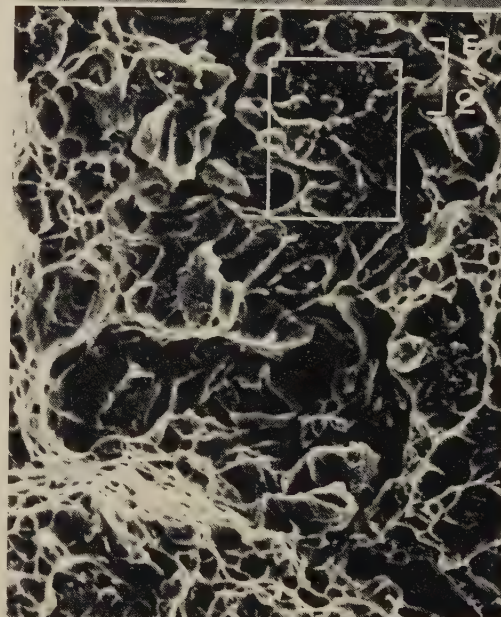
SEM fractograph
3857 SEM view of an area in the flat, central region of the fracture surface in 3856 (left), showing the equiaxed dimples of rather uniform size that are expected in this type of fracture. The scattered ridges produce the fibrous appearance seen at low magnification (3856). See fractograph 3858, a higher-magnification view of the area outlined by the rectangle.



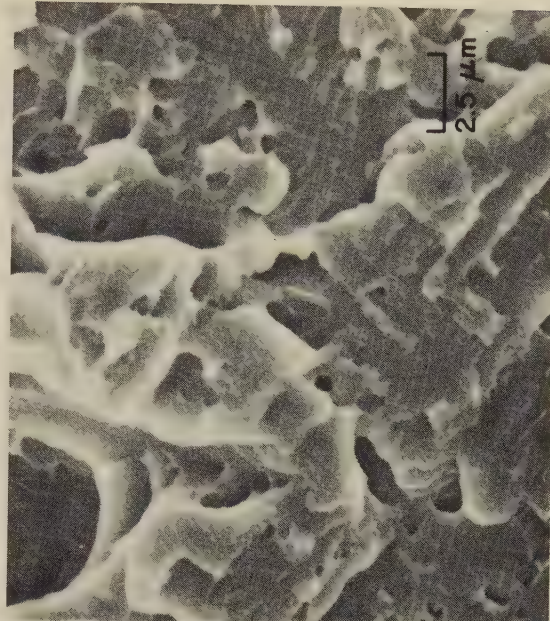
SEM fractograph
3858 Higher-magnification view of the area in the rectangle in fractograph 3857 (left), showing small dimples within dimples of moderate size, as well as very tiny voids in the membranes separating the dimples of moderate size. Note that there are almost no inclusions.



Light fractograph
3859 A typical tension-overload fracture in a notched specimen of 13-8 PH stainless steel with the same properties as those of the specimen in 3856. The fracture surface appears uniformly fibrous, with a hint of a shear lip. See also fractograph 3860 (at right).



SEM fractograph
3860 SEM view of an area of the fracture surface in 3859, showing dimpled rupture in some regions (at left, for example) and, elsewhere, facets that suggest local quasicleavage without evidence of any conventional river patterns. See fractograph 3861 (at right), a higher-magnification view of the area in the rectangle.

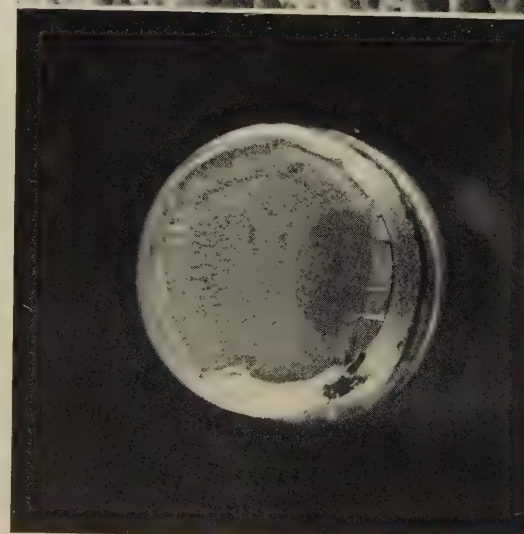


SEM fractograph
3861 Higher-magnification view of the area in the rectangle in 3860 (left). This SEM view shows that in the fine-scale structure there do appear to be some delicate cleavage steps, particularly at right.

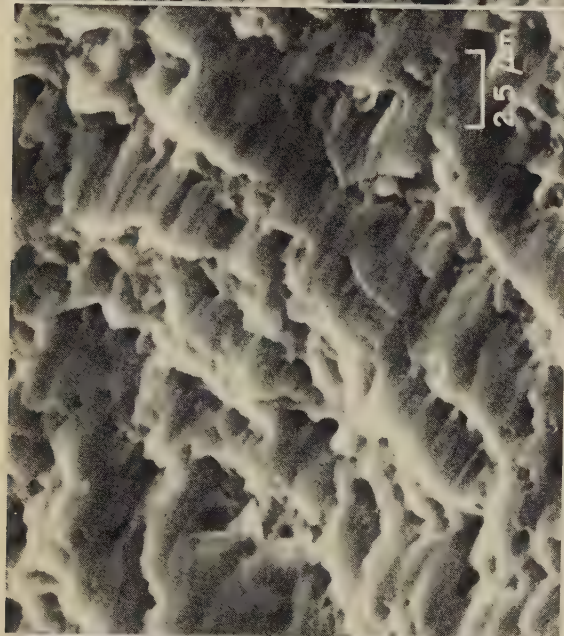
Light and SEM Fractographs: 13-8 PH Stainless Steel Specimens Fractured in Low-Cycle and High-Cycle Fatigue Tests



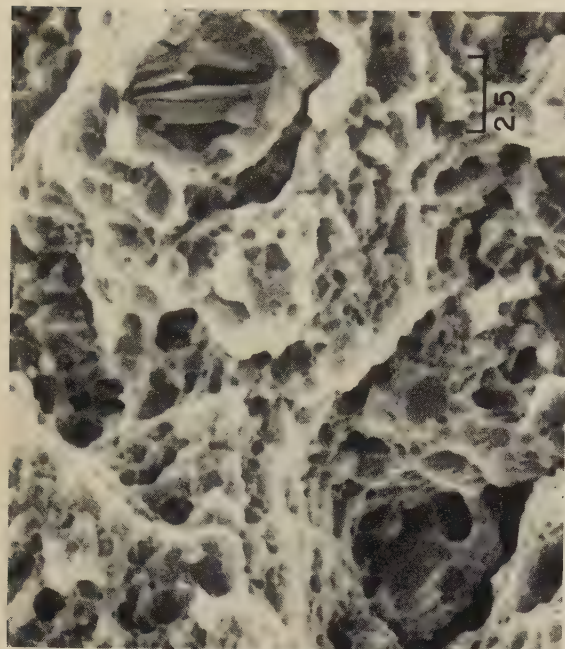
Light fractograph
3862 Low-cycle fatigue fracture in threaded specimen of 13-8 PH stainless steel (tensile strength, 1634 MPa or 237 ksi; 47% reduction in area) tested in tension-tension ($R = 0.1$) with maximum loading at 60% of tensile strength. Fracture, at 16,000 cycles, began at lower edge of crescent-shaped area at bottom.



Light fractograph
3865 High-cycle fatigue fracture in threaded specimen of 13-8 PH stainless steel (same properties as for specimen in 3862) tested in tension-tension ($R = 0.1$) with maximum loading at 30% of tensile strength. Fracture occurred at 959,000 cycles. Note the crescent-shaped crack nucleus. See also 3866 and 3867.



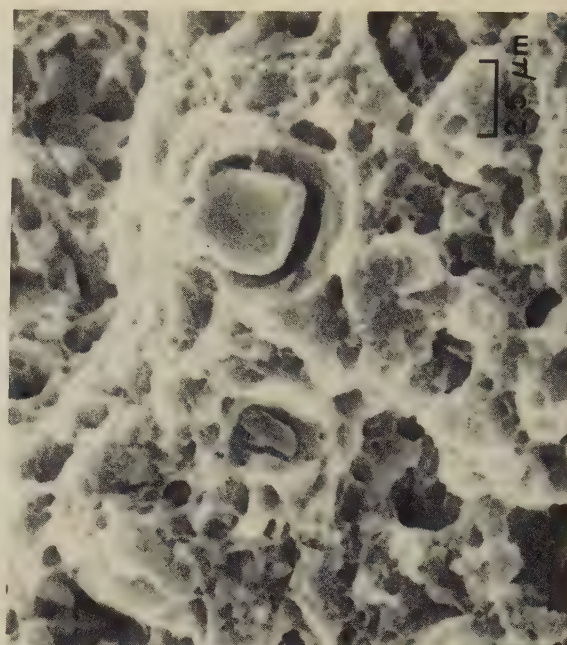
SEM fractograph
3863 SEM view of the fracture surface in 3862 (at left), taken at the rounded lip at the bottom edge of the crescent-shaped area. Even this close to the crack origin there are no fatigue striations. The irregular surface displays ridges formed by a shear process.



SEM fractograph
3864 Another SEM view of the fracture surface in 3862, taken in the region of final fast fracture. Fatigue fracture has given way to dimpled rupture. Two pockets, one at the left and one at the right, contain features that resemble localized quasicleavage.

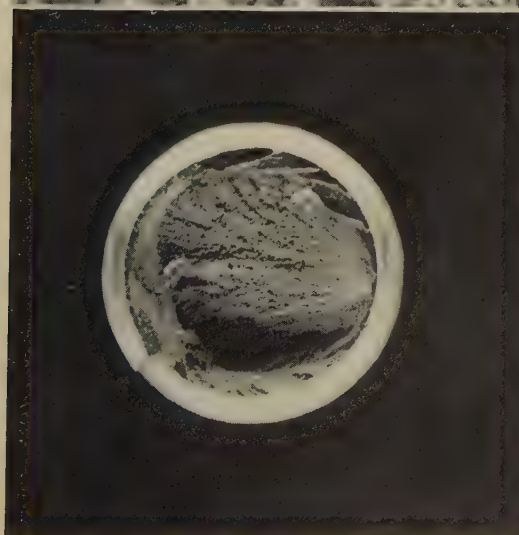


SEM fractograph
3866 SEM view of fracture in 3865 (at left), taken as close as possible to the bottom edge of the origin region. This rough surface does not contain fatigue striations, but instead suggests a shear mechanism of fracture and bears considerable resemblance to 3863.

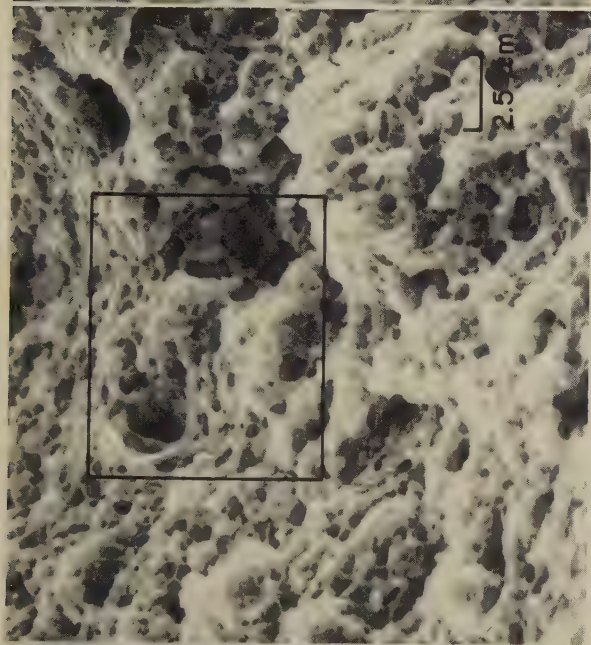


SEM fractograph
3867 View of the fracture surface in the fast-fracture region in 3865, showing basically equiaxed dimpled rupture but also containing scattered features of quasicleavage. Some regions display heavy concentrations of extremely small dimples.

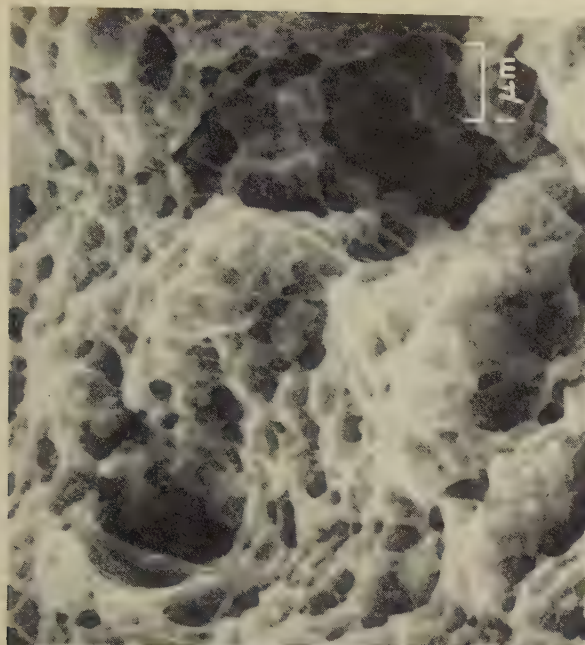
Light and SEM Fractographs: 13-8 PH Stainless Steel Specimens Fractured by Hydrogen Embrittlement and by Stress-Corrosion Cracking



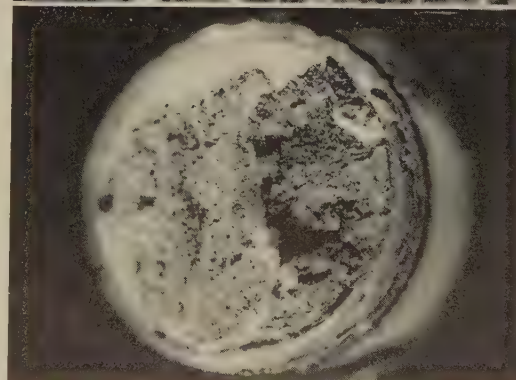
Light fractograph
3868 Surface of a fracture in a threaded specimen of 13-8 PH stainless steel (same properties as for the specimen in 3862) that was heavily charged with hydrogen by plating without subsequent baking. The specimen broke during loading. The crack origin, visible at bottom edge, grew both circumferentially and radially. See also fractograph 3869.



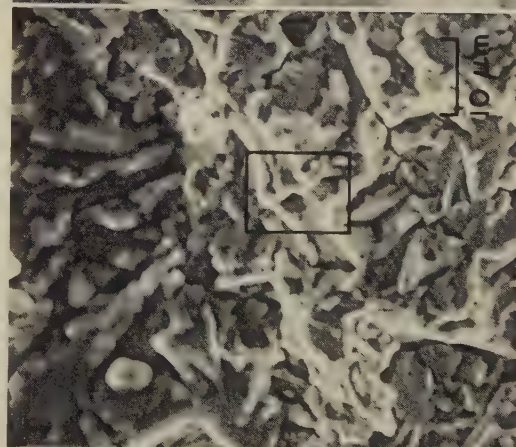
SEM fractograph
3869 SEM view of a region of the fracture surface shown in 3868 (left), revealing none of the intergranular rupture that is characteristic of hydrogen embrittlement but instead showing the equiaxed dimples of tension overload. See 3870 (enlarged view of outlined area).



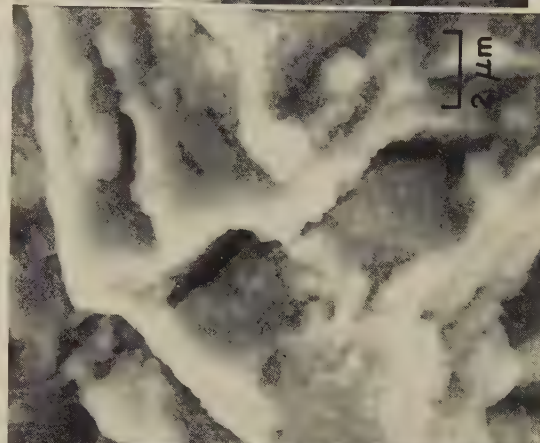
SEM fractograph
3870 Higher-magnification view of the area in the rectangle in fractograph 3869 (left), showing clearly the very dense grouping of very small dimples around larger dimples. There is no evidence here either of grain-boundary facets or of inclusions.



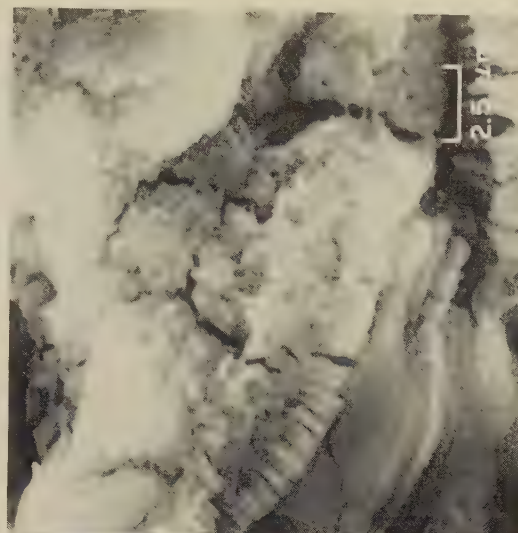
Light fractograph
3871 Stress-corrosion-cracking fracture in threaded specimen of 13-8 PH stainless steel (same properties as in 3862) loaded to 75% of tensile strength in a 3.5% NaCl solution. See 3872.



SEM fractograph
3872 SEM view of crack-origin area of fracture surface in 3871, showing corrosion products that probably are oxides. Secondary cracks may or may not extend into the metal below. See also 3873 and 3874.

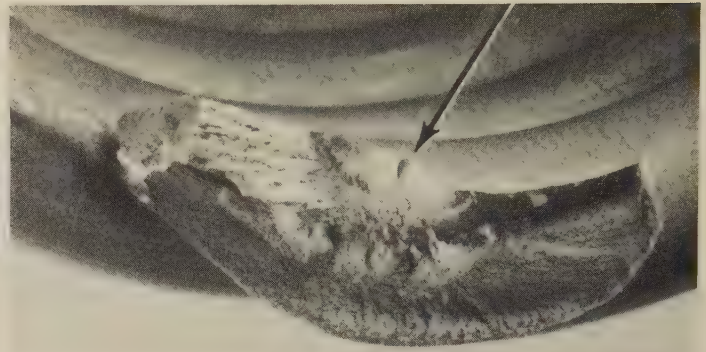
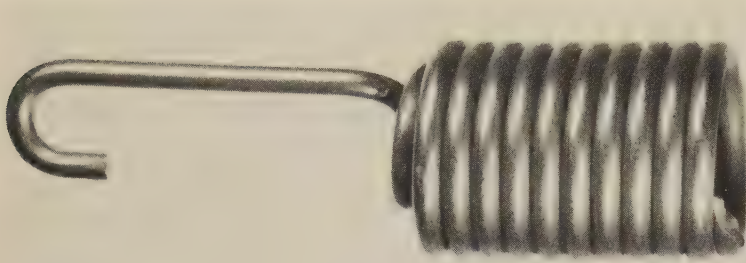


SEM fractograph
3873 Enlargement of the area in the rectangle in 3872 (left). The oxide coating appears to be quite continuous except for the scattered secondary cracks. Compare with 3874 (right).



SEM fractograph
3874 Another view of the crack-origin area of the fracture surface shown in 3871, displaying a coating of a hydroxide corrosion product containing many fine secondary cracks. Compare with the area shown in fractograph 3873 (left).

Photograph, Light Fractograph, Micrograph, TEM Fractographs: 17-7 PH Stainless Steel Aircraft Throttle-Control Spring That Fractured by Fatigue in Service



Photograph

1½×

3875 An aircraft throttle-control spring that broke in fatigue after 274 hr of service. The material was 17-7 PH stainless steel wire, 0.104-in. diam, heat treated to condition CH-900 and a hardness of Rockwell C 51 to 52. Expected tensile strength of the wire was 1889 to 2096 MPa (274 to 304 ksi). Fracture, visible at right, occurred at the third turn from the end of the spring; 3876 shows surface.

Light fractograph

10×

3876 Surface of the fracture in the coil spring shown in 3875 (at left). The crack nucleus is believed to be at the transverse "ledge" (indicated by the arrow) in the upper central portion of the clamshell pattern. See also 3877 to 3881 (below), and 3882 to 3884 (on facing page).



Micrograph (etchant: Marble's reagent)

500×

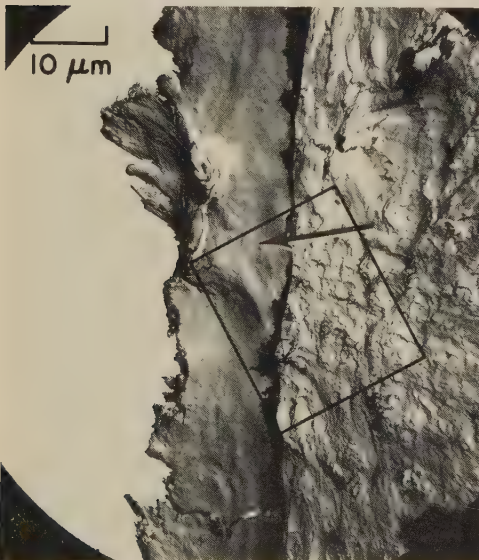
3877 Microstructure of a cross section of the 17-7 PH stainless steel wire in 3875 and 3876, showing the distribution of inclusions (some are indicated by arrows), which in general was acceptable. (Note, however, the two large inclusions at the surface.)



TEM fractograph

3000×

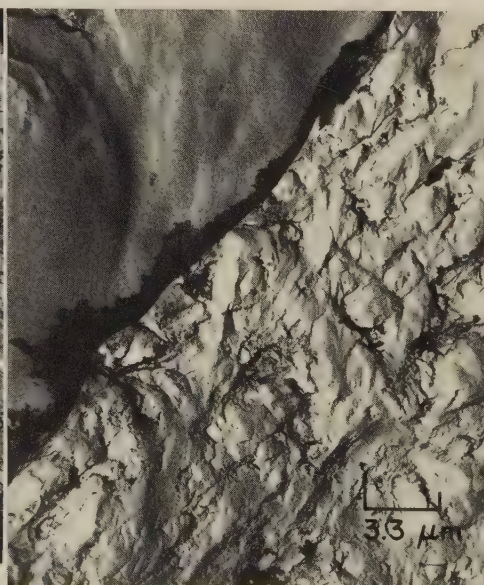
3878 A plastic-carbon replica of a large globular inclusion (arrow) similar to those visible in 3877. This inclusion was exposed by the fracture shown in 3876 and is located near the crack nucleus.



TEM fractograph (p-c replica)

1000×

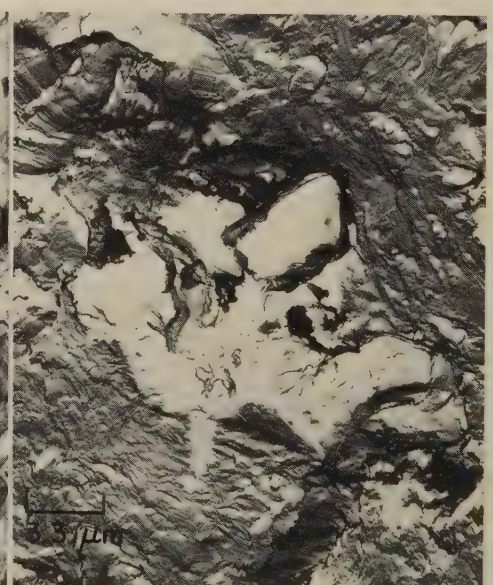
3879 A very long inclusion (arrow) near the crack nucleus of the fracture in 3876 is shown here as a smooth dark surface. Fatigue striations lie parallel with the metal-inclusion interface. Area in rectangle is shown enlarged in 3880.



TEM fractograph (p-c replica)

3000×

3880 Area outlined by the rectangle in 3879, shown at higher magnification. Fatigue striations, which are not well defined, exist as irregular diagonal lines from upper right to lower left in this view.

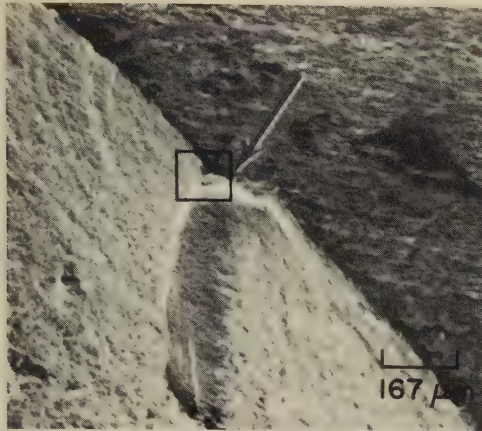


TEM fractograph (p-c replica)

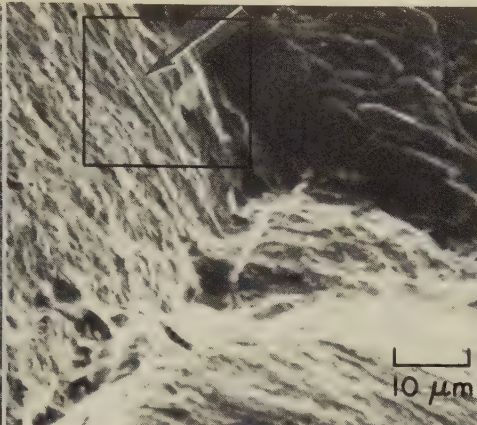
3000×

3881 A view of an area of the fracture in 3876 that was not near the crack nucleus, showing high-stress, low-cycle fatigue striations and (at center) quasicleavage of what is presumed to be an inclusion.

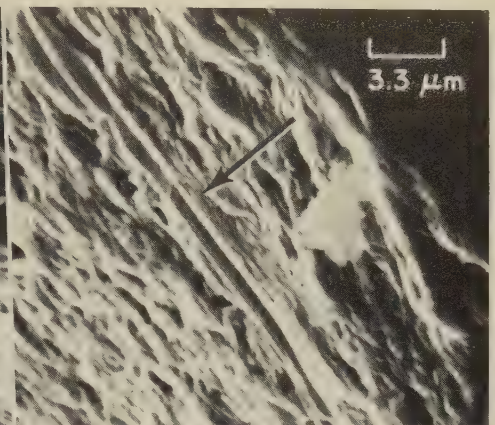
SEM and TEM Fractographs: Service-Fatigue Fracture in 17-7 PH Stainless Steel Throttle-Control Spring (Continued); Type 301 Stainless Steel Specimens Fractured in Fatigue Tests



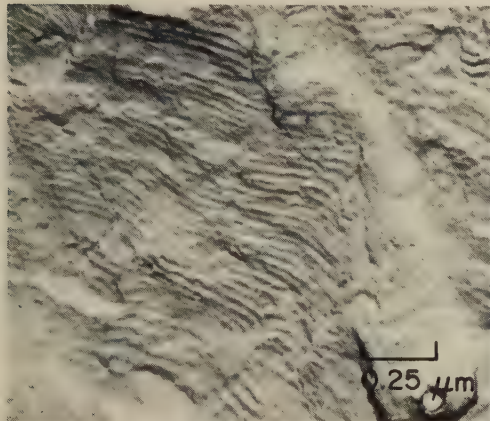
SEM fractograph 60×
3882 A larger view, by SEM, of the "ledge" (at arrow) in fractograph 3876 (facing page). The clamshell pattern of fatigue-crack arrests radiates from the crack nucleus. See fractograph 3883, at right.



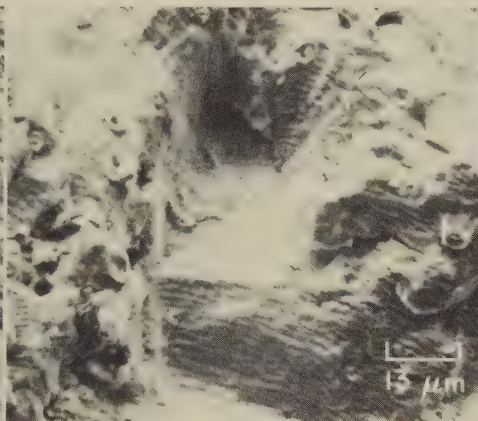
SEM fractograph 1000×
3883 Area outlined by the rectangle in 3882, shown at higher magnification. A slender inclusion stringer (at arrow) is visible in the face of the fracture surface. Rectangle here is shown enlarged in 3884.



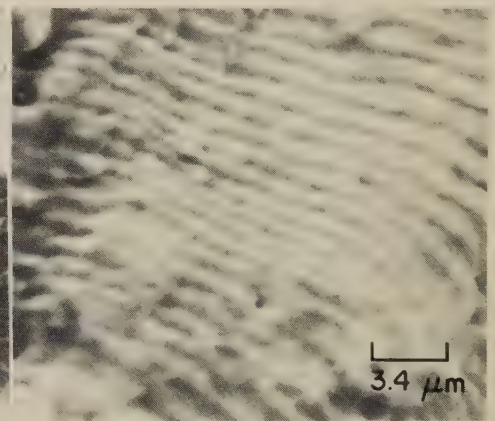
SEM fractograph 3000×
3884 Area in rectangle in 3883, shown at higher magnification. The inclusion stringer (indicated by the arrow) is still more clearly evident. This stringer may have been the crack-initiation site.



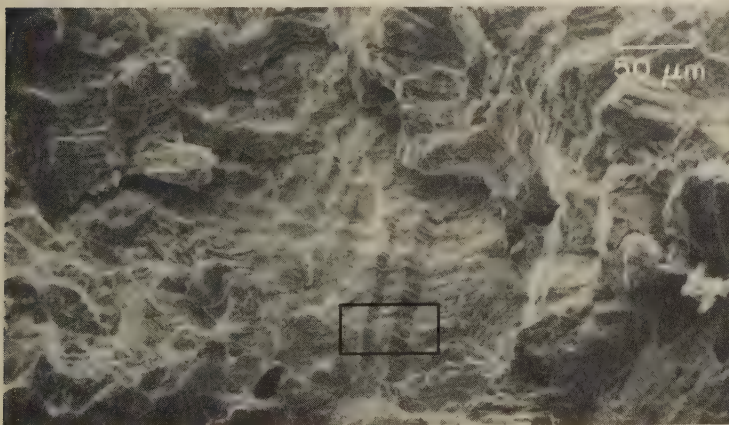
TEM fractograph (p-c replica) 40,000×
3885 Surface of a fatigue crack in type 301 stainless steel, produced at a stress-intensity range (ΔK) at the crack tip of 37.9 MPa·m^{1/2} (34.5 ksi·in.^{1/2}) at 95 C (203 F). Spacing of clearly defined fatigue striations is about 0.04 μm. See also 3886.



SEM fractograph 750×
3886 Surface of a fatigue fracture in type 301 stainless steel, produced at a stress-intensity range (ΔK) at the crack tip of 55 MPa·m^{1/2} (50 ksi·in.^{1/2}) at 95 C (203 F). Fatigue striations and secondary cracks are visible. See also 3885 and 3887.



SEM fractograph 2950×
3887 A portion of the same fracture surface as that in 3886 but at higher magnification, showing occasional inclusion sites among the regular fatigue striations. Spacing of the striations is about 1.3 μm, which is much greater than that in 3885.

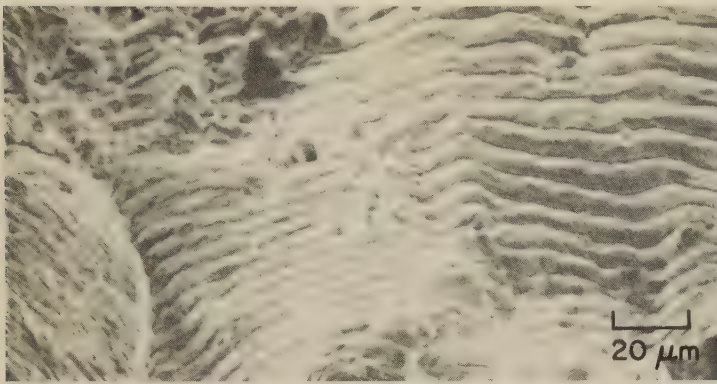


SEM fractograph 200×
3888 Surface of a fatigue-crack fracture in a specimen of type 301 stainless steel that was highly stressed, breaking in 2000 cycles. Crack growth was very irregular, with many pronounced offsets. At center, twin boundaries have affected crack propagation. Area in rectangle is shown at higher magnification in 3889.



SEM fractograph 1400×
3889 A higher-magnification view of the area outlined by the rectangle in fractograph 3888, which includes twin-boundary outlines. Several secondary cracks have formed at the roots of the fatigue striations. The striae, however, are not delineated well enough to permit a confident estimate of the spacing.

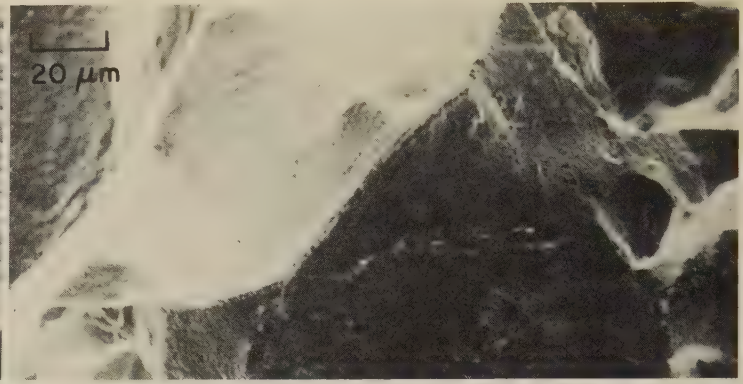
SEM and TEM Fractographs: Type 304 Stainless Steel Fractured in Low-Cycle Fatigue Test;
0.20C-2.0Mn-1.0Si-13.5Cr-8.8Ni-3.0Mo Stainless Steel Fractured in Fracture-Toughness Test



SEM fractograph

500×

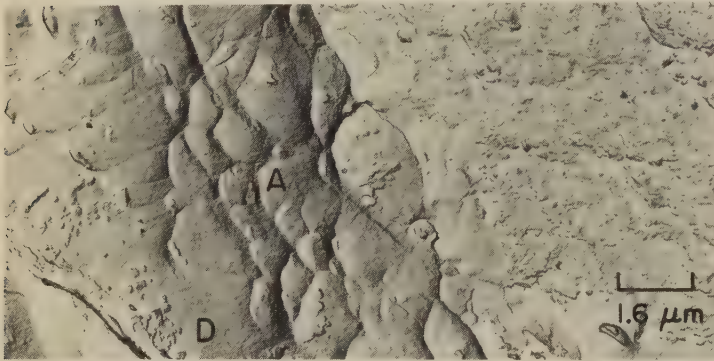
3890 Surface of a fracture in a specimen of type 304 stainless steel that was broken in a controlled-strain low-cycle fatigue test in air at 593 C (1100 F) at 12 cycles per minute. Before being tested, the specimen was solution annealed and then aged for 1000 hr at 593 C (1100 F). Maximum strain was 0.5% tension and compression, producing a maximum saturated stress of about 228 MPa (about 33 ksi) tension and compression. Fracture occurred at 3604 cycles. The fracture surface shows transgranular facets with clearly defined ductile fatigue striations. See also 3891.



SEM fractograph

500×

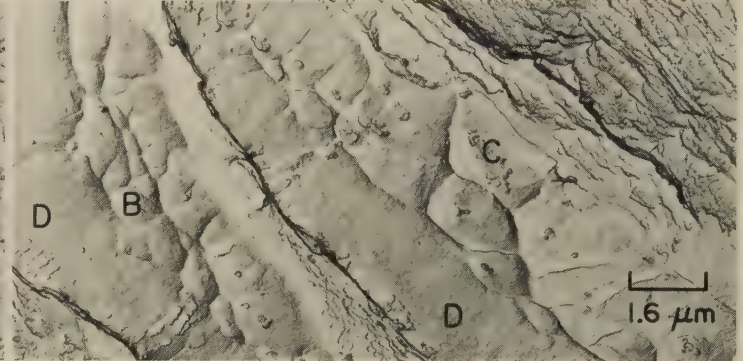
3891 Surface of a fracture obtained in low-cycle fatigue in air at 593 C (1100 F) in a specimen taken from the same heat of type 304 stainless steel as was the specimen in 3890 (at left), and subjected to the same heat treatment and test procedure, but held 10 min at the peak tensile strain of each cycle. Maximum strain was 0.5% tension and compression, which produced a maximum saturated stress of about 228 MPa (about 33 ksi) tension and compression. Fracture occurred at 636 cycles. The features of this fracture surface indicate that the fracture was intergranular.



TEM fractograph (p-c replica)

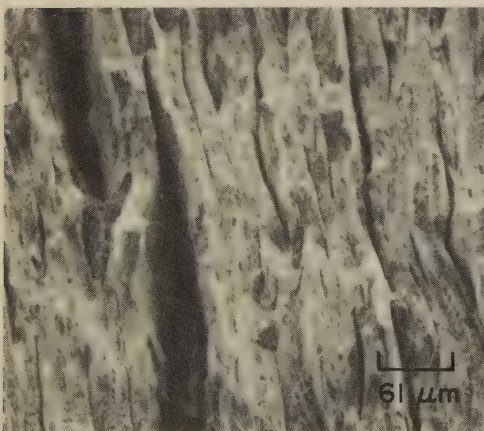
6150×

3892, 3893 Two TEM views of a fracture obtained in a metastable austenitic stainless steel in a fracture-toughness test at -196 C (-321 F) after 80% deformation at 450 C (842 F). The alloy contained 0.20% C, 2.0% Mn, 1.0% Si, 13.5% Cr, 8.8% Ni and 3.0% Mo. The fracture surface was etched in a solution of 5 g CuCl₂ in 100 ml each of H₂O, HCl and CH₃OH, for identification of any martensitic regions. Visible are moderate-size tear dimples in the austenite (around A in 3892 and around B and C in 3893), fine bands of very small dimples in the martensite (upper right in 3893) and areas of stretched metal (at D's). See also 3894 to 3896.



TEM fractograph (p-c replica)

6150×



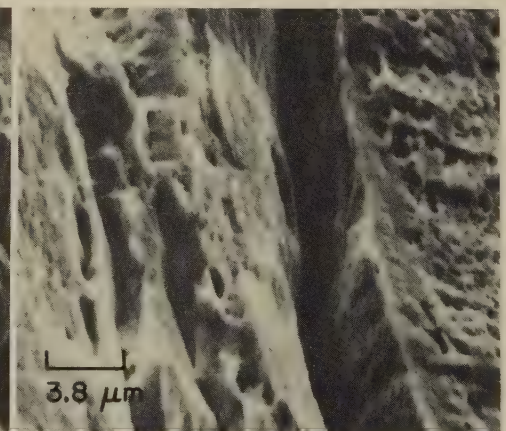
SEM fractograph

165×



SEM fractograph

835×

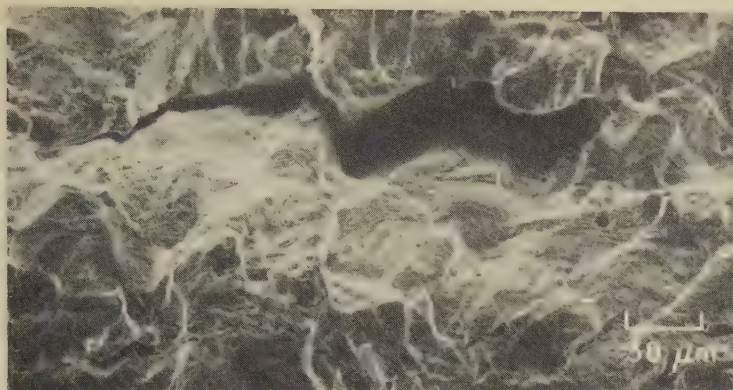


SEM fractograph

2650×

3894, 3895, 3896 Three SEM views of the surface of a fracture that was obtained at -196 C (-321 F) in a specimen of the same austenitic stainless steel as in 3892 and 3893, subjected to the same deformation prior to fracture-toughness testing. No etchant was used here. The rectangle in 3894 (left) indicates the area shown at higher magnification in 3895 (center), and the rectangle in 3895 indicates the area shown at still higher magnification in 3896 (right). The delamination visible in these three views is of the same nature and of the same order of magnitude as the bands of stretched metal shown in 3892 and 3893. The deep furrows are believed to be cracks in regions of martensite. Visible in 3896 are a fracture in martensite (right of center), a stretched region (to right of fracture) and dimples (at far right).

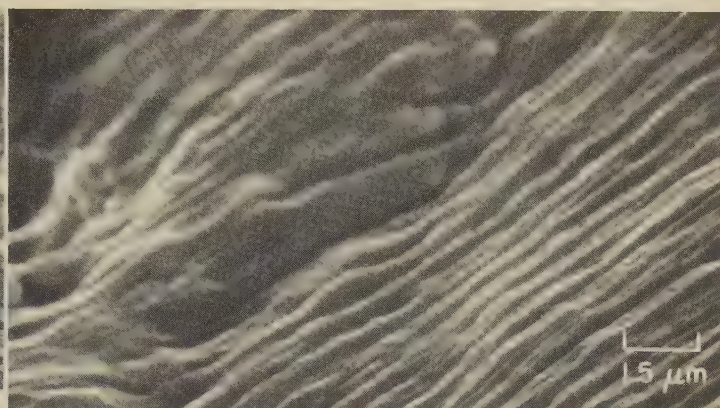
SEM Fractographs: 0.004C-0.01Mn-0.01Si-15.8Cr-12.5Ni Iron Alloy Fractured at 90 C (194 F); 316L and A-286 Austenitic Steels Fractured by Overload; Hastelloy X Fractured at High Temperature



SEM fractograph

260×

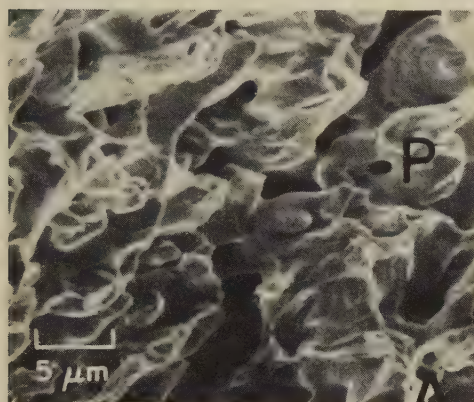
3897 Fatigue-precracked region of a specimen of an iron alloy containing 0.004% C, 0.01% Mn, 0.01% Si, 15.8% Cr and 12.5% Ni, fracture-toughness tested at a stress-intensity range (ΔK) of 35 MPa·m^{1/2} (32 ksi·in.^{1/2}) and at 90 C (194 F). Note pronounced secondary cracks, and that striation spacings just below the large crack are much narrower than elsewhere. See 3898.



SEM fractograph

6600×

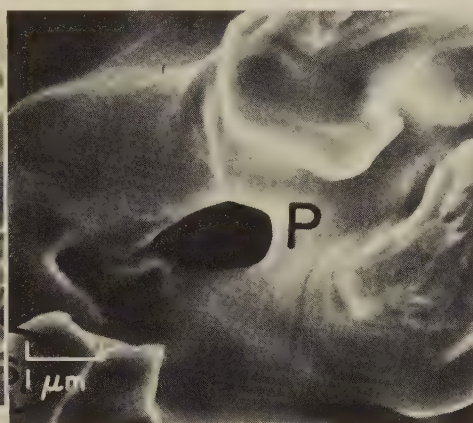
3898 Higher-magnification view of a region near the large secondary crack in the fatigue-fracture surface shown in fractograph 3897 (left). The fatigue striations appear to be remarkably smooth and continuous. At top and at left are suggestions of secondary cracks at the roots of striations.



SEM fractograph

2000×

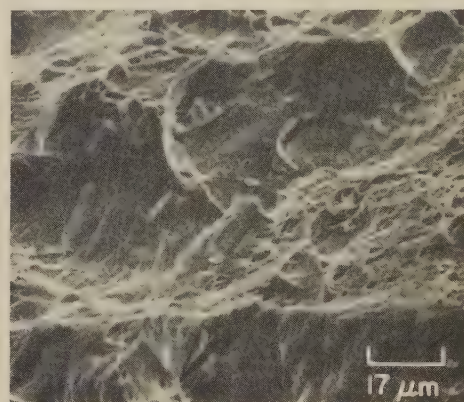
3899 Tensile-overload fracture in a compacted powder metallurgy specimen of type 316L austenitic stainless steel. Note that there are pores that were not closed in pressing. See 3900 for an enlargement of a region near letter P.



SEM fractograph

10,000×

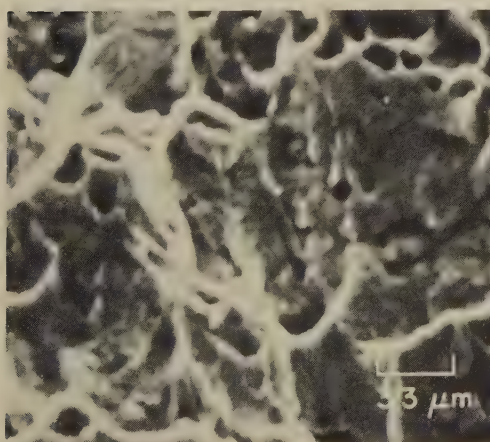
3900 Enlargement of a region near letter P in 3899 (letter P marks a pore that is visible in both views). The flow around the pores appears to be different from that away from them.



SEM fractograph

600×

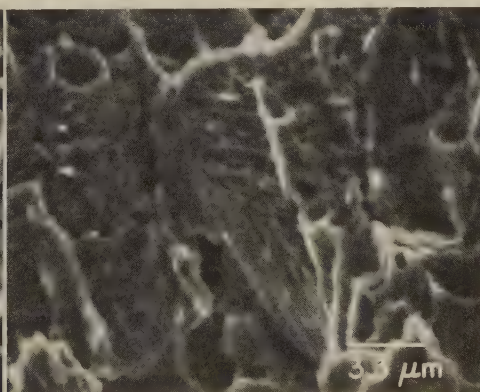
3901 Surface of an overload fracture in A-286 austenitic steel, showing a wide variation in size of tear dimples. Fatigue precracks in specimens of this alloy did not propagate during fracture-toughness testing in bending.



SEM fractograph

3000×

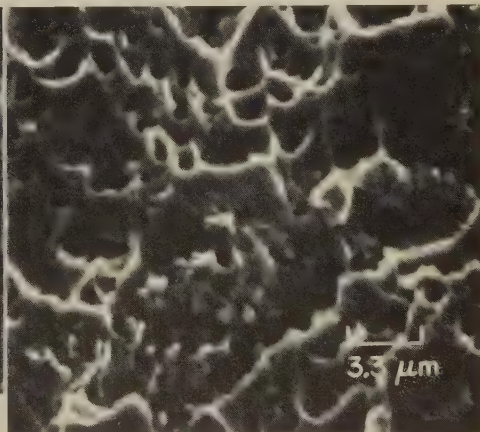
3902 Fracture surface of a specimen of Hastelloy X that was homogenized at 1149 C (2100 F) for 2 hr, water quenched, and then broken in a tensile test at 593 C (1100 F). Reduction in area, 45%. Note the tear dimples in this transgranular fracture. See also 3903 and 3904.



SEM fractograph

3000×

3903 Fracture surface in same alloy, and given same heat treatment, as in 3902. Although this specimen was broken in tension at 649 C (1200 F), reduction in area (29%) was lower than in 3902. This reflects "midrange minimum ductility", which is present in many nickel-base alloys. Tear dimples are present, but are accompanied by flat grain-boundary facets. See also 3904.



SEM fractograph

3000×

3904 Surface of a fracture in another specimen of Hastelloy X, given the same heat treatment as described in 3902, and broken in a tensile test at 760 C (1400 F). Reduction in area, 46%. This fracture is transgranular, and shows pronounced tear dimples. Compare with 3903 (left).

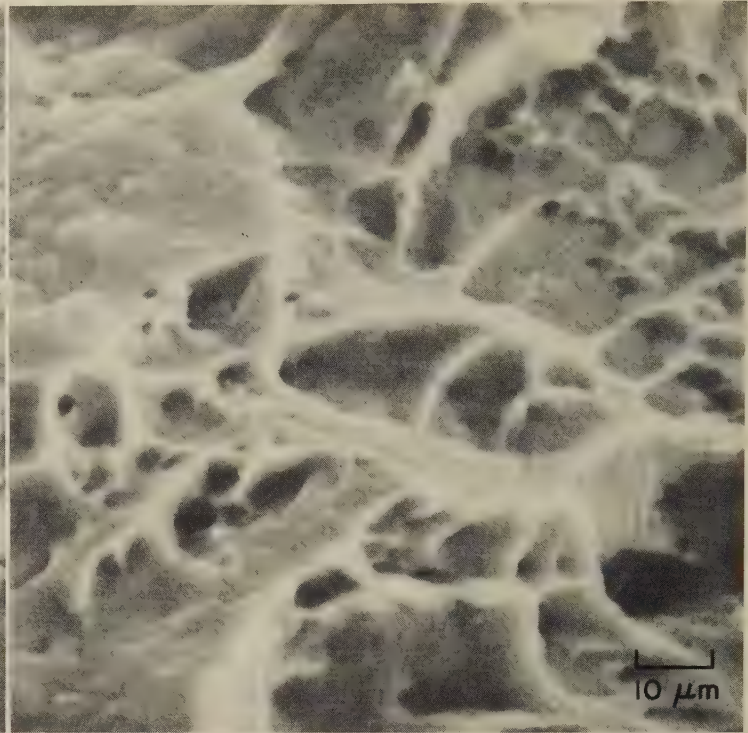
SEM Fractographs: Refractaloy 26 Alloy Fractured by Room-Temperature Impact (Effect of Aging Temperature), and by Stress Rupture at Two Temperatures



SEM fractograph

1000×

3905 An impact fracture at 22 C (72 F) in Refractaloy 26 alloy after solution annealing for 2 hr at 982 C (1800 F) and water quenching, followed by aging for 200 hr at 899 C (1650 F) and air cooling. The hardness was 205 dph. The fracture appears to have occurred by cleavage, with needle-like features reflecting the shape of Ni_3Ti precipitates. See also fractograph 3906, at right.



SEM fractograph

1000×

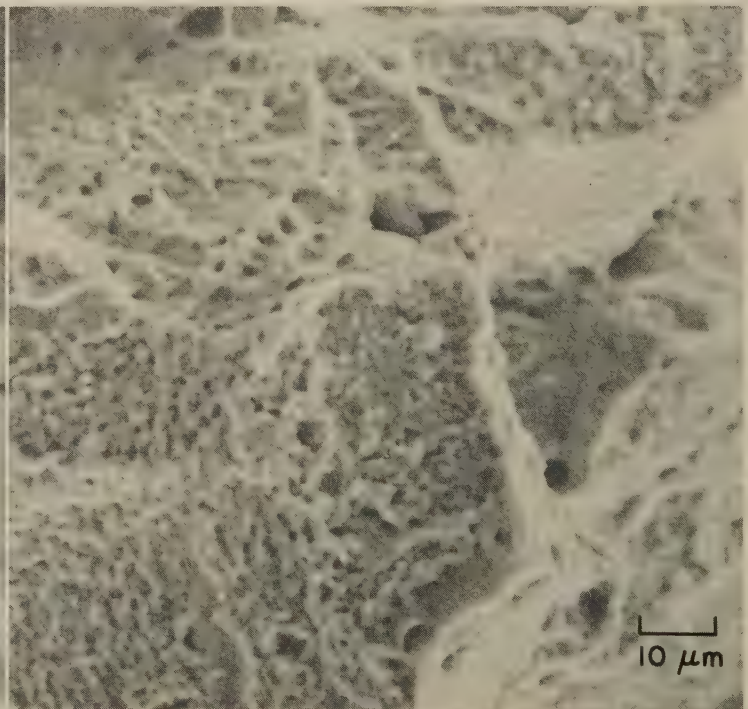
3906 An impact fracture at 22 C (72 F) in a specimen of Refractaloy 26 that was solution annealed same as specimen in 3905 but was then aged for 9 hr at 732 C (1350 F) and air cooled. The hardness was 410 dph. The fracture surface contains shear dimples with perhaps traces of stretched metal—in marked contrast with the fracture surface shown in 3905.



SEM fractograph

1000×

3907 A stress-rupture fracture in Refractaloy 26 alloy that had been solution treated for 2 hr at 982 C (1800 F), water quenched, then aged 9 hr at 732 C (1350 F) and air cooled. Specimen was loaded at a stress of 785 MPa (114 ksi); rupture occurred after 33 hr at 566 C (1050 F). A typical intergranular "rock candy" fracture, with slip bands in the grain facets. See also 3908.



SEM fractograph

1000×

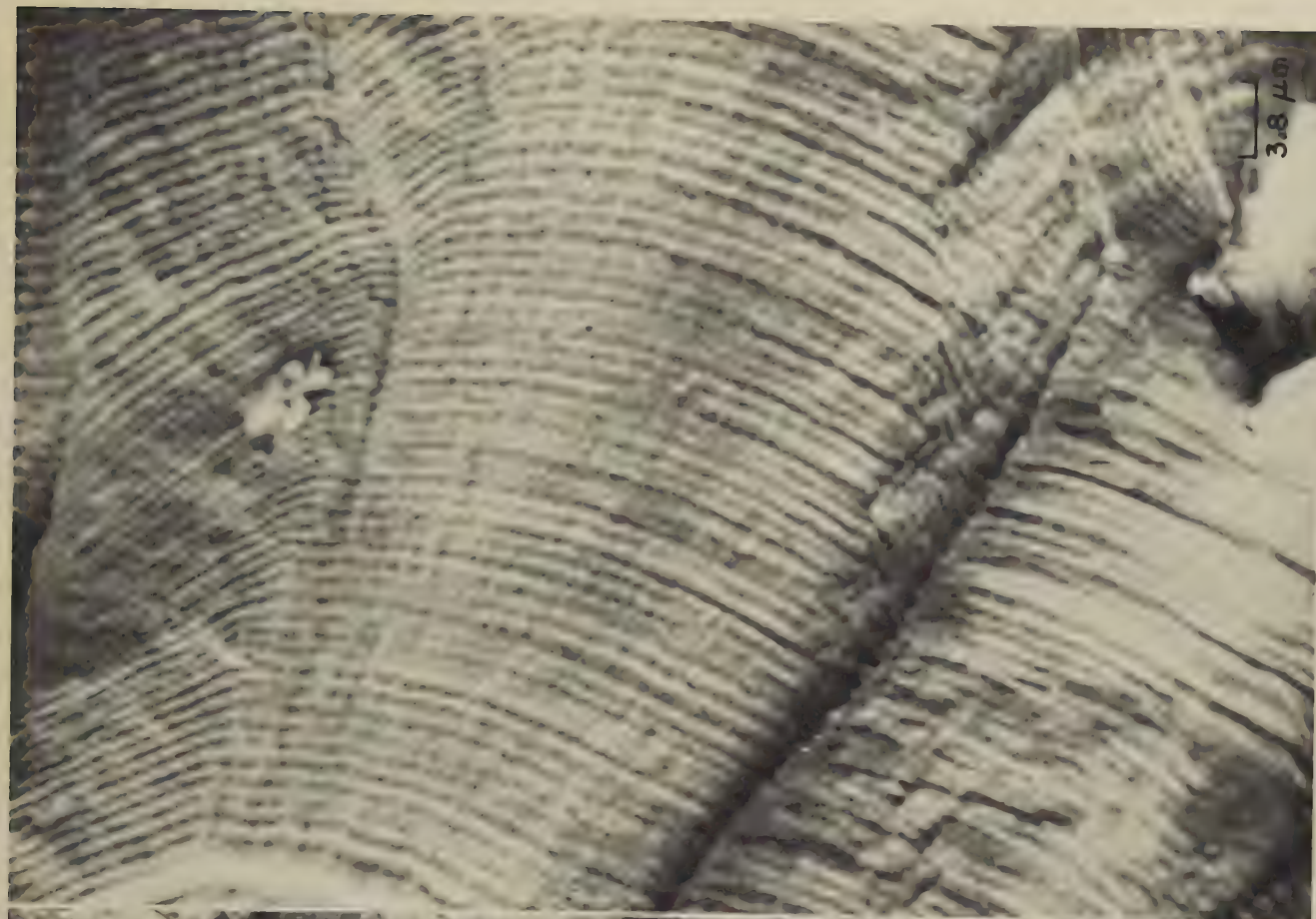
3908 A stress-rupture fracture in a specimen of Refractaloy 26 alloy that had been given the same heat treatment as the specimen in 3907, but for which rupture occurred after 3713 hr at 700 C (1292 F) under a load of 275 MPa (40 ksi). Hardness of both specimens was 430 dph. The higher test temperature here resulted in formation of a myriad of dimples on intergranular surfaces.

SEM Fractographs: Cast Alloy 718 Specimen That Was Fractured in a Fatigue Test at Room Temperature



SEM fractograph

3909 Surface of a fracture in a specimen that was cast from alloy 718, produced in a fatigue test at room temperature. The fatigue striations are clearly visible, defining a number of adjacent fatigue patches in which the cracks advanced on separate fronts. At upper right is a region of shrinkage porosity, encompassed by rounded dendrite arms. See also fractograph 3910.



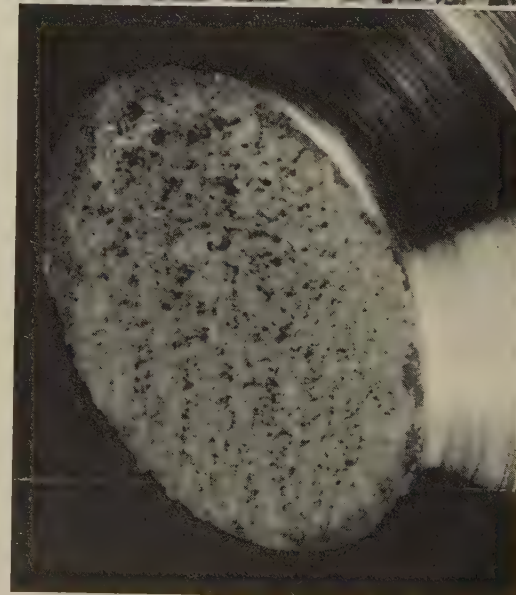
SEM fractograph

3910 A higher-magnification view of the same fracture surface as that shown in 3909, although not from exactly the same area. Here, the direction of fatigue-crack propagation was roughly left to right. The steps separating the fatigue patches are clearly visible, particularly at lower left. The spacing of fatigue striations in the central patch is approximately 1 μm.

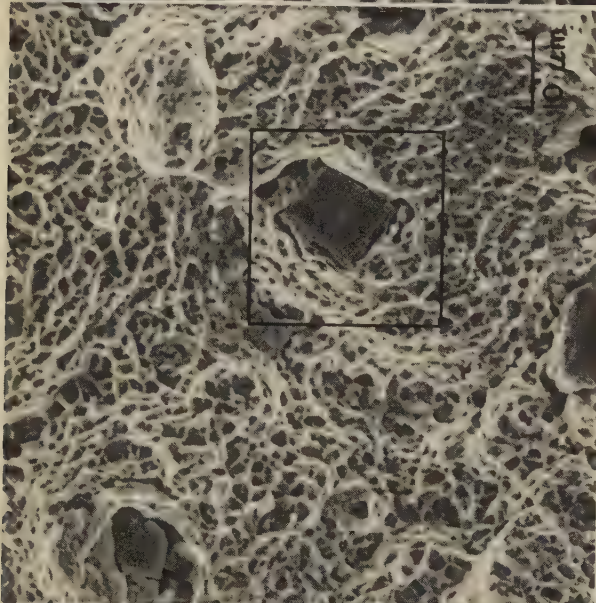
Light Fractographs and SEM Fractographs: Alloy 718 Unnotched and Notched Specimens
Fractured by Tension Overload at Room Temperature



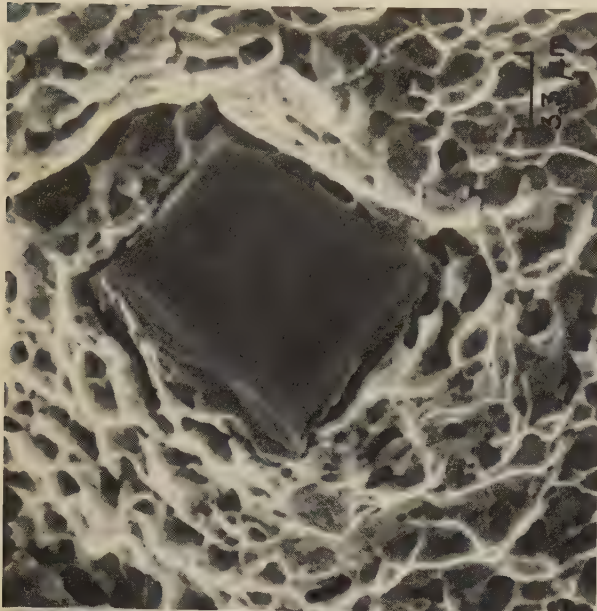
3911 A cup-and-cone fracture produced by overload tension at room temperature in an unnotched specimen of alloy 718 having a tensile strength of 1444.5 MPa (209.5 ksi) and 36% reduction in area. The central, origin zone is extremely rough. The shear lip has a small amount of cracking. See also fractographs 3912 and 3913, at right.



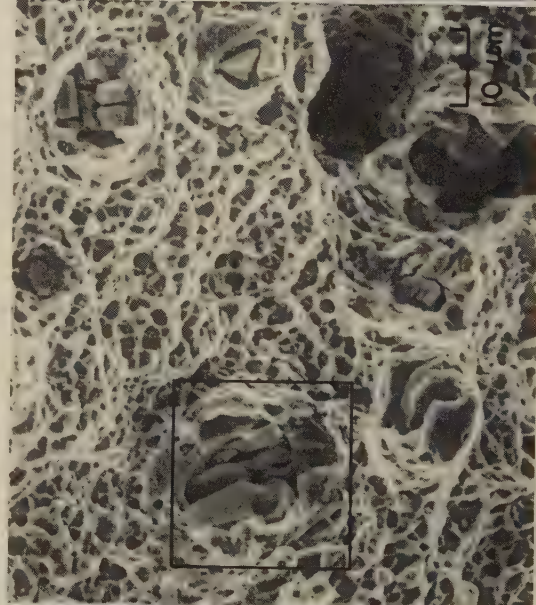
3914 A flat fracture produced by overload tension at room temperature in a notched specimen of alloy 718 having a notched tensile strength of 2048 MPa (297 ksi), and the same mechanical properties before notching as the specimen in 3911. The fracture surface is coarse. See 3915, 3916.



3912 An SEM view of an area in the central zone of the fracture in 3911. This area is composed of equiaxed dimples and a rather uniformly distributed precipitated phase, which is bonded to the matrix generally but is separated from it locally by cracks. See 3913.



3913 Area outlined by the rectangle in 3912, shown at higher magnification. It is evident that, despite the appreciable amount of deformation produced by the tensile test, the particle in the center is still almost completely adherent to the matrix.

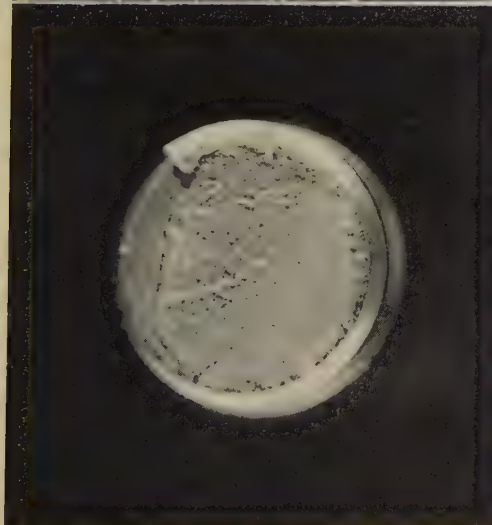


3915 SEM view of the fracture surface in 3914, showing equiaxed dimples in the matrix areas. The precipitated phase, unlike the behavior of this phase in the unnotched specimen in 3911-3913, has fractured into many pieces in nearly every location. See 3916.

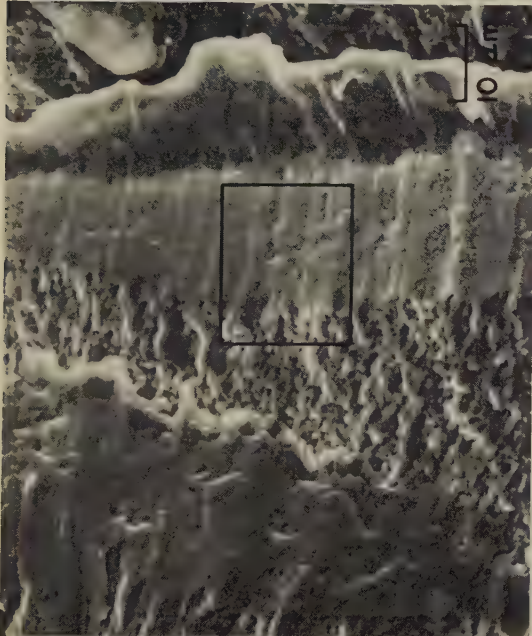


3916 Higher-magnification view of area in rectangle in 3915, showing a large particle of precipitated phase. The complex cracking of the particle is clearly evident. Note, however, that the matrix has not flowed away from the pieces but still adheres to them.

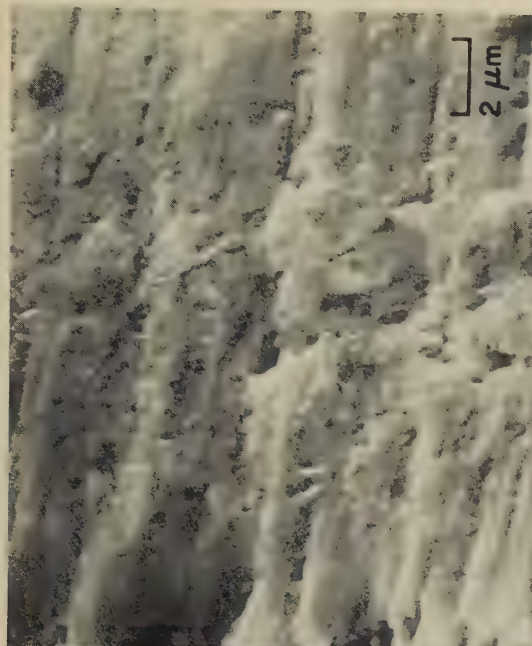
Light Fractographs and SEM Fractographs: Alloy 718 Specimens Fractured in Low-Cycle and High-Cycle Fatigue Tests at Room Temperature



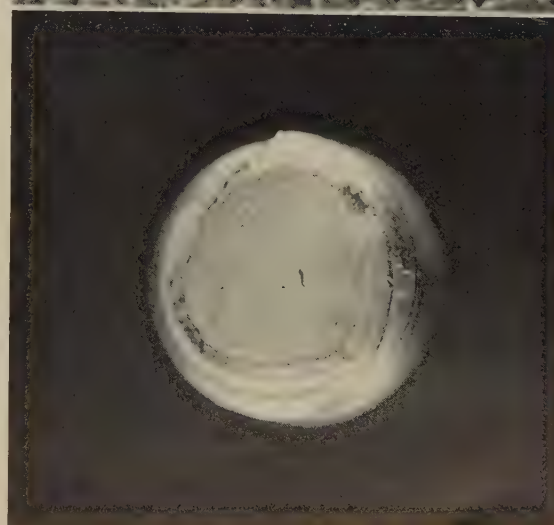
3917 Fracture produced at 33,000 cycles of low-cycle fatigue in a threaded specimen of alloy 718 in tension-tension ($R = 0.1$) at room temperature, maximum load at 862 MPa (125 ksi) — about 60% of the tensile strength. Origin was in the large, smooth crescent in the lower area. See also fractographs 3918 and 3919.



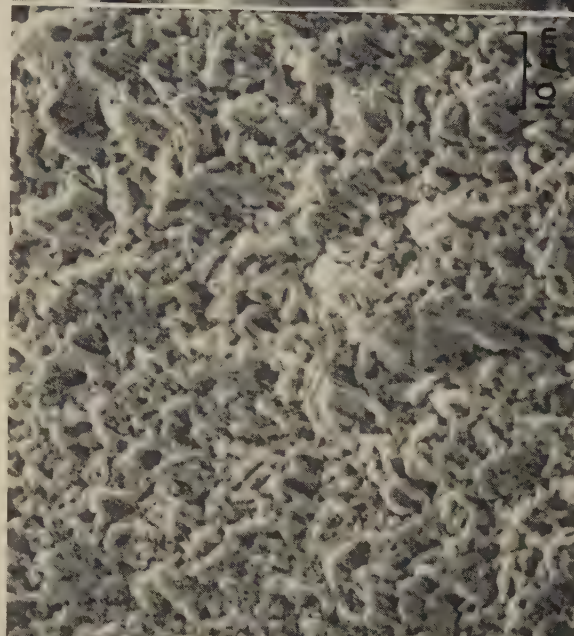
3918 Outer extremity of the fracture in 3917. The striations falsely resemble fatigue striations; actually, they are one order of magnitude larger than true fatigue striations and are considered to be slip steps. See 3919 for a larger view of area in rectangle.



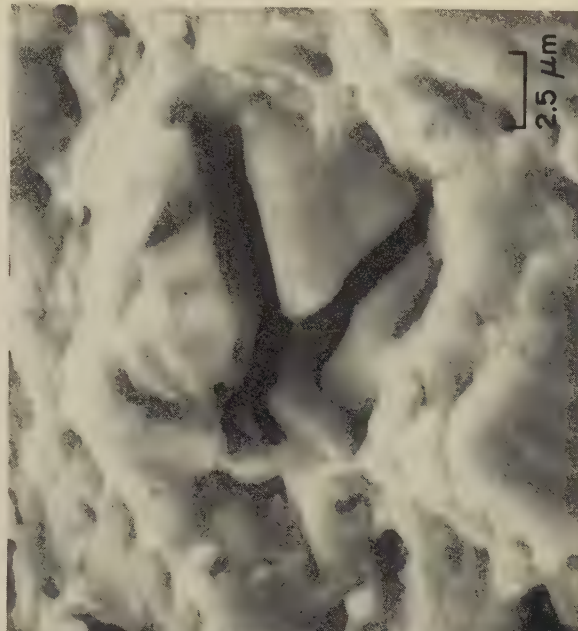
3919 Area in rectangle in 3918, at higher magnification. There are no signs here of the true fatigue striations that are seen in the TEM replicas from this fracture shown in fractographs 4501, 4503 and 4504; however, those TEM replicas are not from this same location.



3920 A high-cycle fatigue fracture in a threaded specimen of alloy 718 in tension-tension ($R = 0.1$) at room temperature, maximum load at 434 MPa (63 ksi) — or about 30% of the tensile strength. Rupture was at 1648 kc. Surface is quite smooth. See 3921, 3922.



3921 This area of the fracture surface in 3920 is of interest in that it is nonorthodox: there are no striations, no dimples and no cleavage facets; instead, small ligaments formed (perhaps by slip) and then snapped off. See also fractograph 3922, at right.



3922 View of another area of the fracture surface in 3920. The features in the lower foreground are possibly fatigue striations, but are too poorly resolved for accurate determination. At center is an inclusion that fractured during rupture of the specimen.

SEM and Light Fractographs: Fractures in U-700 Alloy by Fatigue Testing at 760 C (1400 F), as Influenced by Frequency of Stress Application



SEM fractograph

300×

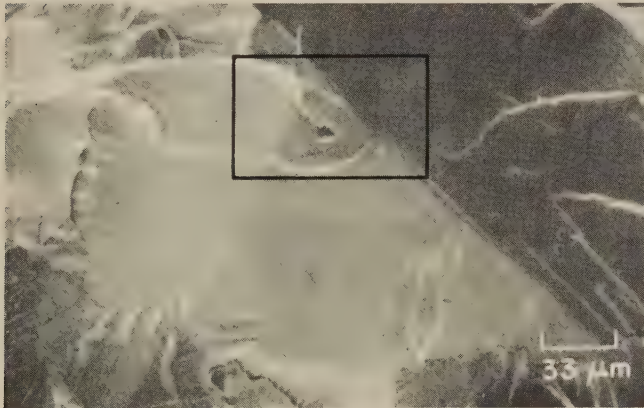
3923 Fatigue-fracture surface of a specimen of U-700 alloy tested at 600 cycles per minute at 760 C (1400 F) under a stress cycling between 34 and 621 MPa (5 and 90 ksi), with fracture at 1800 kc. Arrow designates the subsurface origin of the fatigue crack. See 3924 (enlargement of area in rectangle), and 3925 to 3928.



SEM fractograph

1000×

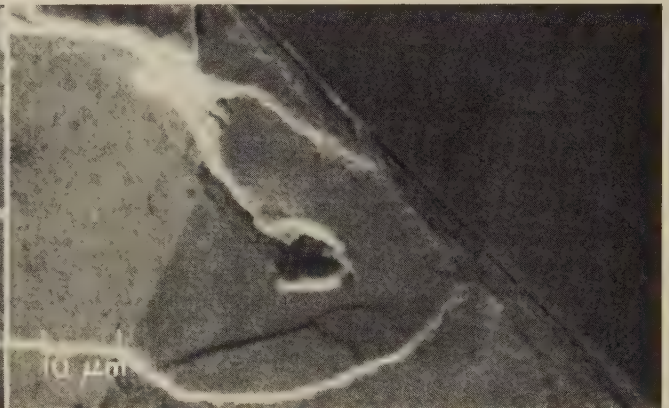
3924 View at higher magnification of the area in the rectangle in 3923. Arrow designates the crack origin, which was at the interface between the matrix and a particle (missing here) at a grain boundary. Crack growth was along {111} planes in two grains, and transverse to the {111} planes in a third (upper right).



SEM fractograph

300×

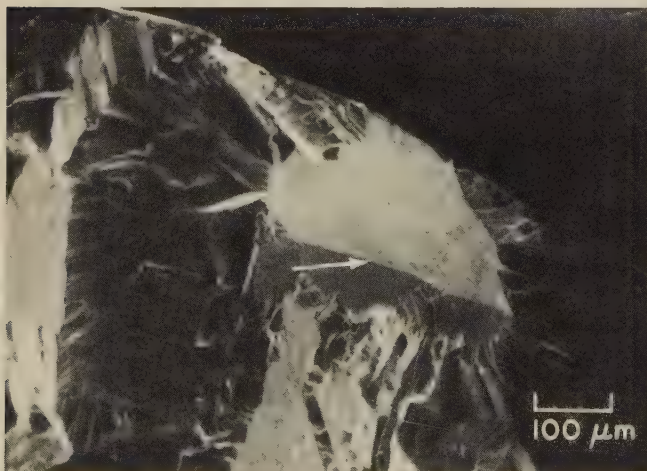
3925 A fatigue fracture in U-700 alloy tested at the same frequency, temperature and stress as for 3923. Fracture was at 347 kc after 8 hr. Crack initiation was at the intersection of two coherent annealing-twin boundaries. Area in rectangle is shown enlarged in 3926.



SEM fractograph

1000×

3926 Area within the rectangle in fractograph 3925, shown here at higher magnification. The particle near the center, which is thought to be TiC, is close to the crack origin. Crack propagation was along the {111} plane of the twins, and thereafter was transverse.



SEM fractograph

100×

3927 A fatigue fracture in U-700 alloy tested at the same temperature and stress as for 3923 and 3925, but at a frequency of 60,000 cycles per minute. Fracture occurred at 240 kc after 4 min. The crack, like that in the fracture shown in 3925, initiated at an intersection of coherent annealing-twin boundaries (arrow).

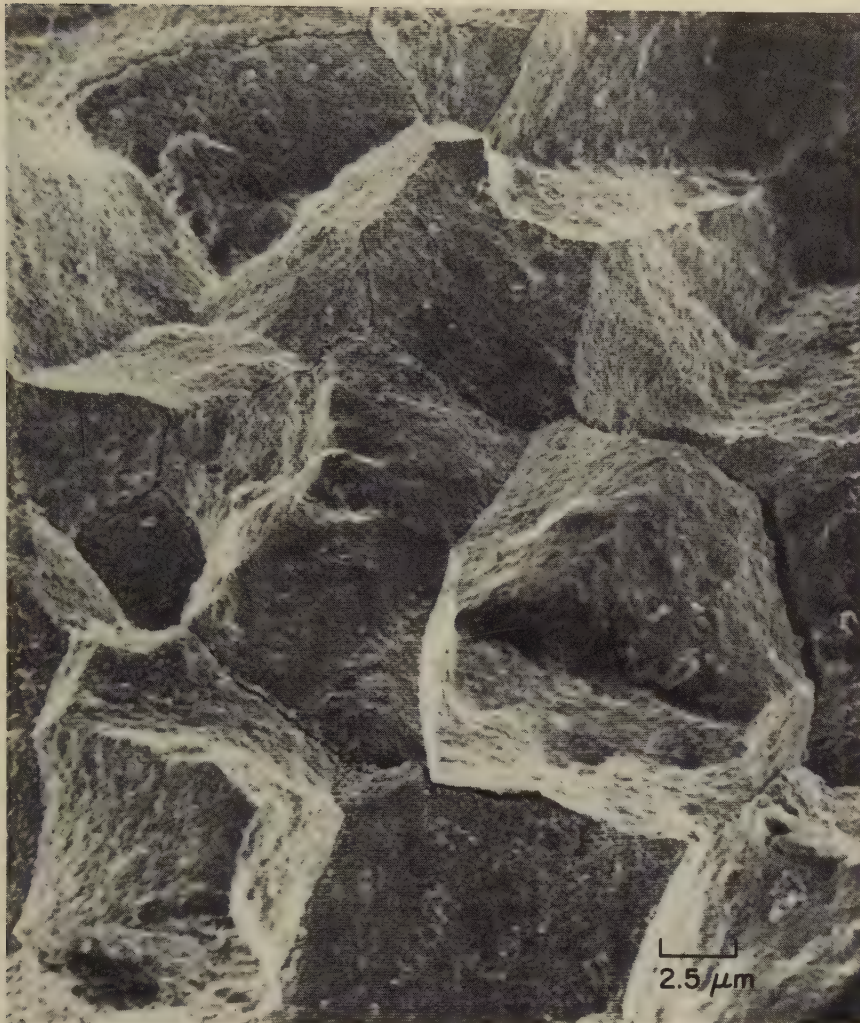


Light fractograph

280×

3928 A {111} facet oriented at an angle of 60° to 70° to the stress axis of a specimen of U-700 alloy fractured in a low-frequency (≤ 20 cycles per minute) fatigue test; other test conditions were same as for 3923. The facet, which lies in the perimeter of the fatigue zone, shows fatigue striations but no river patterns.

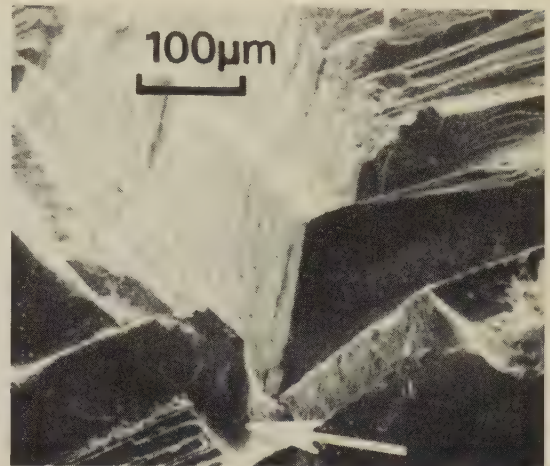
SEM Fractographs and SEM Micrograph: Waspaloy Alloy Fractured by Stress Rupture;
MAR-M 200 Alloy Fractured by Ultrasonic Fatigue at Room Temperature



SEM fractograph

400×

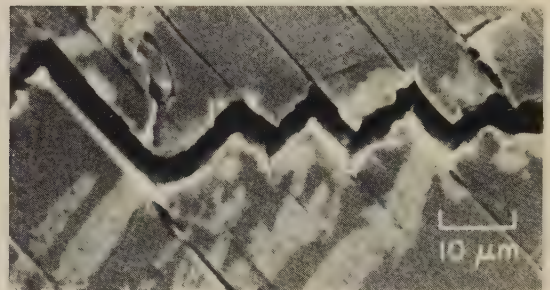
3929 An outstanding example of an intergranular fracture surface. Specimen is wrought Waspaloy that was fractured in a stress-rupture test. Secondary cracks are visible in a number of grain boundaries. The grain facets appear to be coated with oxide; some may have a surface of fine dimples.



SEM fractograph

140×

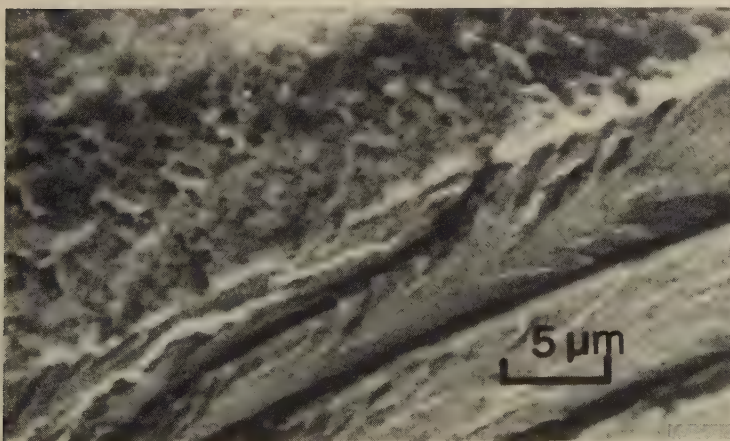
3930 Surface of a cleavage fracture in a unidirectionally cast single crystal of nickel-base alloy MAR-M 200 that was heat treated* and then tested in ultrasonic fatigue at 20,000 cps at room temperature. The fatigue-crack origin was at a surface pore (arrow). See 3931, 3932 and 3933.



SEM micrograph

1000×

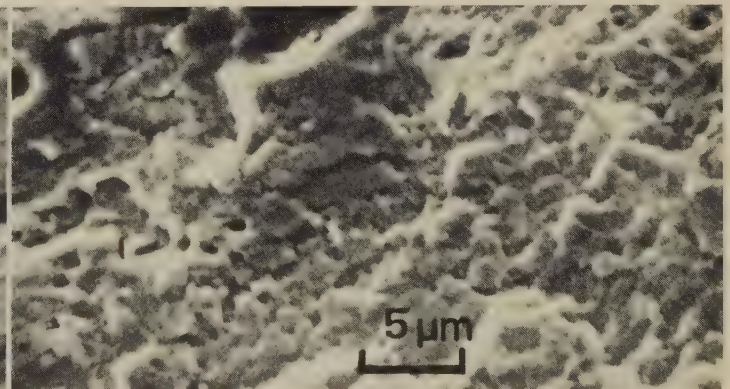
3931 An SEM micrograph of the [100]-oriented free surface of a single crystal of heat treated MAR-M 200 alloy* that was fatigue tested as described for 3930, showing crack propagation. The [001] longitudinal-displacement axis is vertical in this view; slip and crack propagation followed {111} planes.



SEM fractograph

2800×

3932 A surface typical of the fracture near the site of fatigue-crack origin of the MAR-M 200 crystal* in 3930, showing sharply defined cleavage-fracture steps at lower right and, between the steps, systems of river patterns.



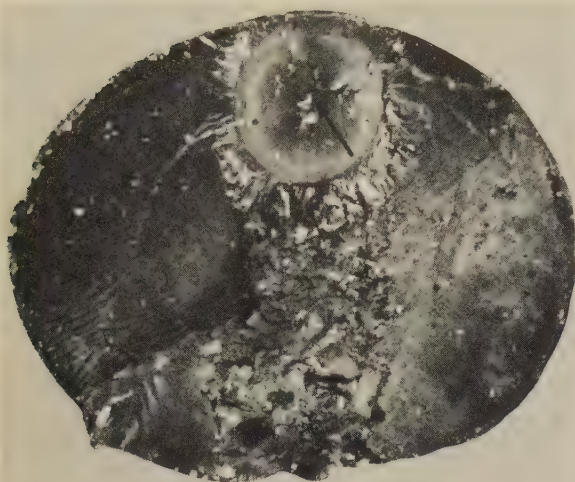
SEM fractograph

2700×

3933 High-magnification view of an area of an ultrasonic fatigue fracture in a crystal of MAR-M 200 heat treated* and tested same as for 3930, showing small, equiaxed dimples associated with late stages of crack propagation at total strain amplitudes of 0.0035 to 0.0055. (Contrast the appearance of the surface here with the blocklike cleavage facets in 3930, at 140×.)

*Prior to fatigue testing, the crystals of MAR-M 200 in 3930 to 3933 were solution treated and aged. Solution treatment: 4 hr at 1232 C (2250 F), water quench; aging: 32 hr at 871 C (1600 F), air cool.

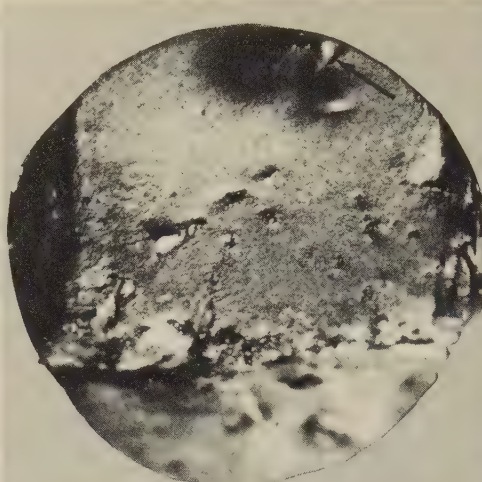
Light, SEM and TEM Fractographs: MAR-M 200 Alloy Fractured by Fatigue in Air and in Vacuum;
Powder Metallurgy Specimen of IN-100 Alloy Fractured by Tension Overload



Light fractograph

16×

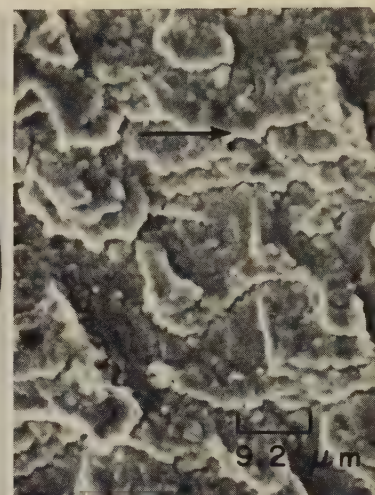
3934 Fatigue-fracture surface of a single crystal of MAR-M 200 nickel-base alloy tested in air at 927 C (1700 F) at a stress range of 515 MPa (75 ksi), and breaking at 950 kilocycles. Origin is at an internal pore (arrow near top). Compare 3935.



Light fractograph

25×

3935 Fatigue fracture in single crystal of MAR-M 200 tested in vacuum at 927 C (1700 F) at a stress range of 275 MPa (40 ksi). Fracture occurred at 1580 kilocycles. Origin is at a surface pore (arrow near top).



SEM fractograph

1080×

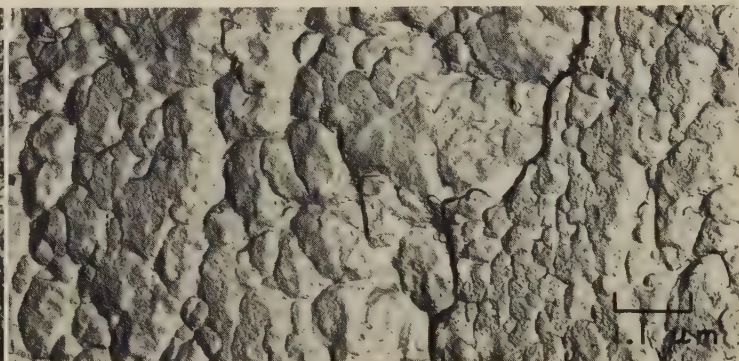
3936 MAR-M 200 fractured in low-stress fatigue at 927 C (1700 F) in air. Rough steps, with edges aligned nearly parallel to crack-growth direction (arrow), are oxide coated.



Light fractograph

125×

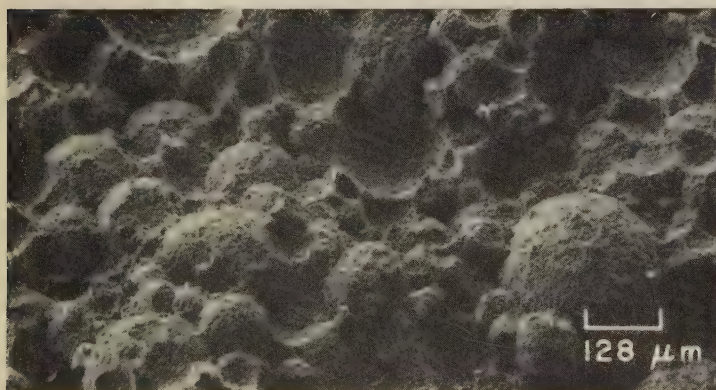
3937 Fatigue fracture in single crystal of MAR-M 200 tested in vacuum at 760 C (1400 F) at a stress range of 515 MPa (75 ksi). Fracture occurred at 2590 kilocycles. Unlike aluminum (see TEM fractograph 5149), this alloy shows clear fatigue striations when tested in vacuum as well as when tested in air. Here, crack propagation was from bottom to top. See fractograph 3938.



TEM fractograph (p-c replica)

9000×

3938 Replication of the surface of a fracture in a crystal of MAR-M 200 alloy that was fatigue tested in vacuum at 760 C (1400 F), showing equiaxed dimples. Visible are suggestions of vertical ledges roughly 4 μm apart; these do not seem to relate to fatigue striations such as those shown in fractograph 3937 (left), which have spacings of 10 μm or more.



SEM fractograph

78×

3939 Tension-overload fracture in a compacted powder metallurgy specimen of IN-100 low-carbon nickel-base alloy, isostatically hot pressed at 1121 C (2050 F) for 2 hr at 172 MPa (25 ksi). The specimen was pulled at 1149 C (2100 F) at a strain rate of 0.0013 per second and broke in 14.3 sec, at a stress of 53.8 MPa (7.8 ksi). Particles are relatively undeformed. See 3940.

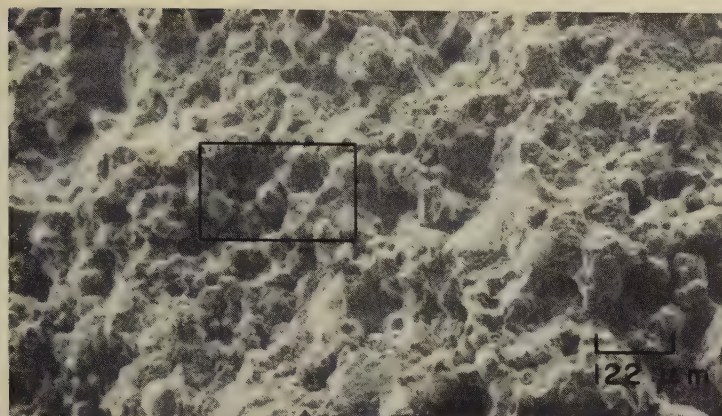


SEM fractograph

278×

3940 Higher-magnification view of the fracture in 3939 (left), showing clearly the dimple-like features of the surface of the powder metallurgy specimen. It should be noted that although the fracture followed the original interfaces between particles, there are no secondary cracks between the particles.

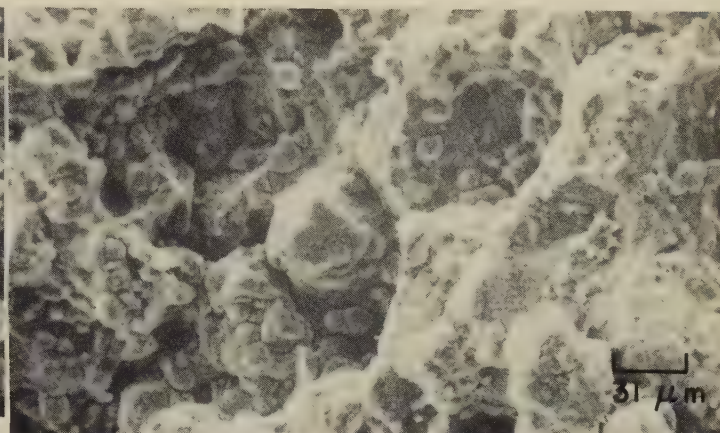
SEM Fractographs: Powder Metallurgy Specimens of IN-100 Alloy Produced Under Different Compacting Conditions and Fractured in Tension at High Temperature



SEM fractograph

82×

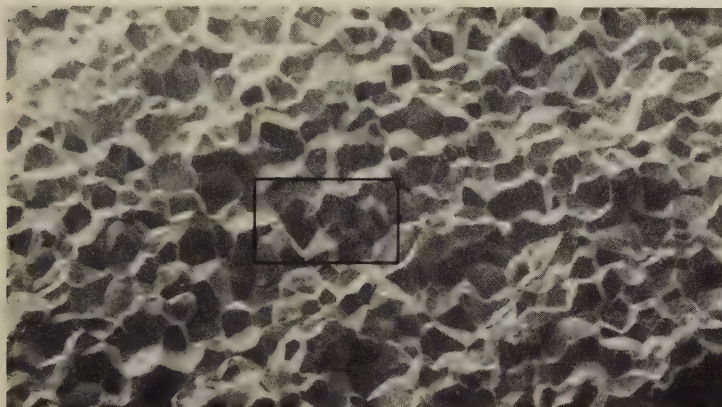
3941 Fracture in a compacted powder metallurgy specimen of IN-100 low-carbon nickel-base powder isostatically pressed for 2 hr at 172 MPa (25 ksi) and 1232 C (2250 F). Specimen was broken in tension at 1149 C (2100 F). Strain rate, 0.0008 per sec; maximum stress, 97.2 MPa (14.1 ksi); test time, 24½ sec. Fracture is partly interparticle, partly transgranular. See also 3942.



SEM fractograph

322×

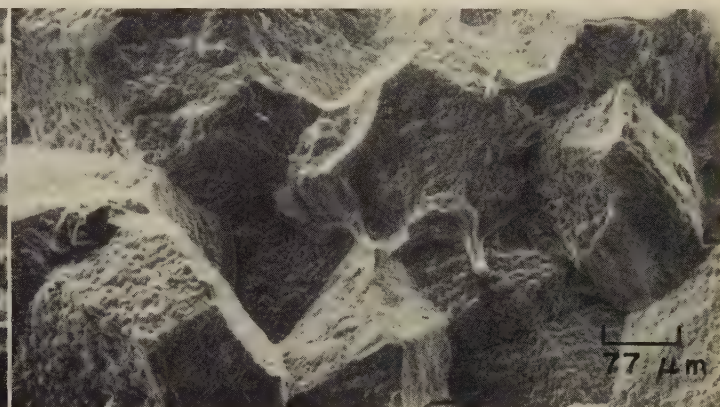
3942 Enlarged view of area in rectangle in 3941. Here, fracture appears mostly, but not completely, interparticle. The small particles (about 1-μm diam) may be powder fines; however, this seems unlikely because fines should have been consolidated by the temperature and pressure used in producing the compact.



SEM fractograph

26×

3943 Fracture in a compacted powder metallurgy specimen of IN-100 low-carbon nickel-base powder processed under the same compacting conditions as described in 3941. Specimen was broken in tension at 1178 C (2152 F). Strain rate, 2.6 per sec; maximum stress, 128.2 MPa (18.6 ksi); test time, 0.005 sec. See also 3944.



SEM fractograph

130×

3944 Higher-magnification view of the area in the rectangle in 3943. Unlike the specimen in 3941, the specimen here underwent recrystallization, either in hot pressing or during preheating at 1178 C (2152 F) before testing. The fracture is completely intergranular. Grain facets have features that may be dimples.



SEM fractograph

28×

3945 Fracture in a compacted powder metallurgy specimen of IN-100 low-carbon nickel-base powder for which the following sequence of temperatures was used, each for 1 hr, during isostatic hot pressing at 172 MPa (25 ksi): 1274 C (2325 F), 1243 C (2269 F), 1274 C (2325 F), 1243 C (2269 F). Specimen was broken in tension at 1149 C (2100 F), with a strain rate of 3.4 per sec and a maximum stress of 13.8 MPa (2.0 ksi). See also 3946 (right).



SEM fractograph

68×

3946 View of the fracture surface of the powder metallurgy specimen shown in fractograph 3945 (left), at a different location and at higher magnification. This specimen, like that in 3943, has undergone recrystallization, and the fracture is totally intergranular. The grain facets contain many small particles about 30 μm in diameter; it seems unlikely that they are powder fines.

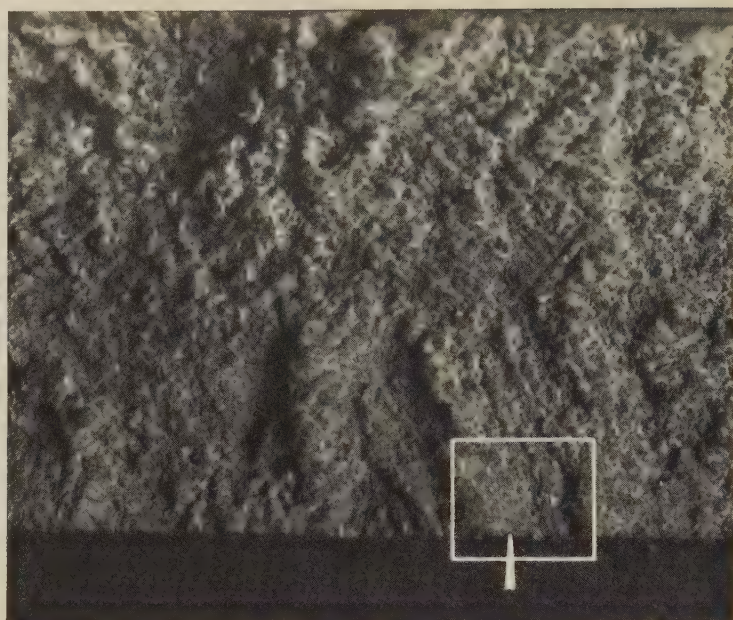
Light Fractographs and SEM Fractographs: Cast Alloy 713C Turbine Wheel That Fractured by Fatigue in Service



Light fractograph

2×

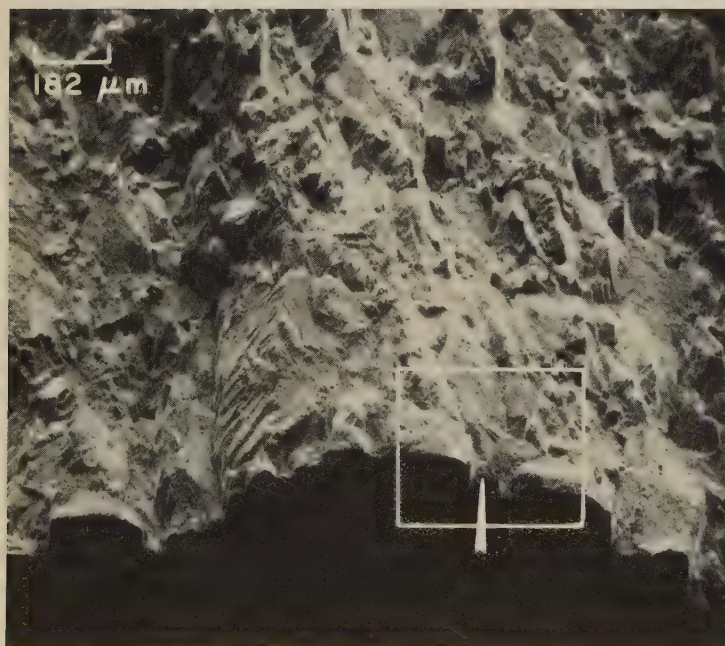
3947 Segment of a fractured second-stage gas-turbine wheel, cast from alloy 713C, that broke from fatigue in service. (About half of the disk portion of the wheel was never recovered.) The fracture origin (at arrow) was in a grinding-relief groove adjacent to the wheel-balancing pad. Additional circumferential cracks, not adjuncts of fracture, were found elsewhere in the grinding-relief groove. See 3948 for area in rectangle, enlarged.



Light fractograph

10×

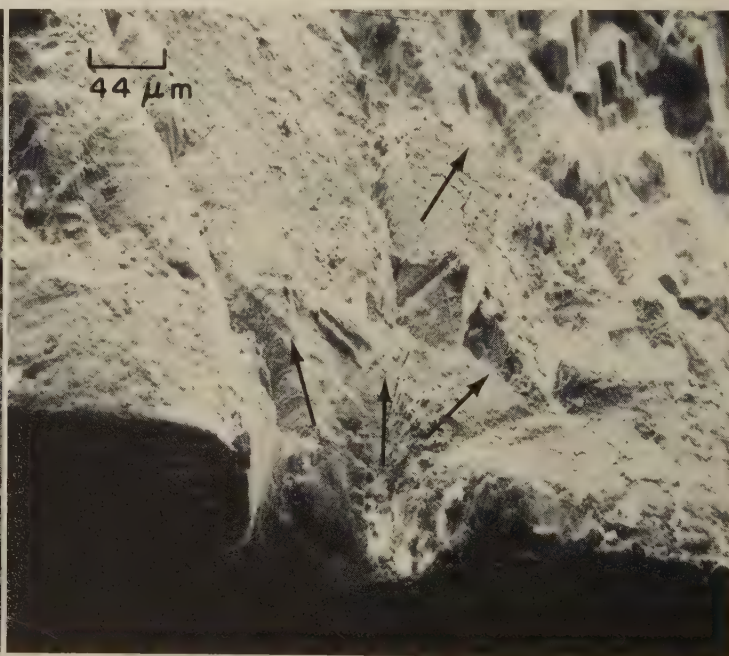
3948 Crack-origin region within the rectangle in 3947, at higher magnification. Arrow marks the probable location of the crack nucleus. The surface of the grinding-relief groove is below the fracture surface. Measurements of the radius at the bottom of the groove gave values that were about 70% of the average desired and about 87% of the minimum. The excessive sharpness of the radius may have been conducive to cracking. See 3949.



SEM fractograph

55×

3949 This SEM view was taken of the outlined area in 3948 after the fracture surface, which contained many white, gelatinous particles as received at the laboratory, was cleaned ultrasonically in 18% HCl solution for 1½ min and then washed in acetone and blown dry. The interface between the fracture and the grinding-relief groove was carefully examined in the origin area, and only one probable crack origin was discovered—that marked by the arrow. Area in rectangle is shown at higher magnification in 3950.

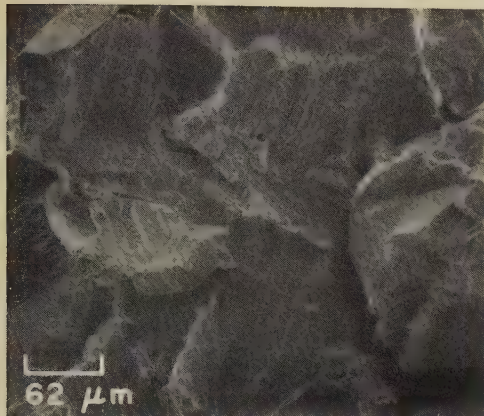


SEM fractograph

225×

3950 A view at higher magnification of the outlined area (containing the probable origin of fracture) in fractograph 3949. Numerous patches of fatigue striations are visible; the arrows indicate the directions of fatigue-crack propagation from what appears to be a surface defect within the grinding-relief groove. The fatigue facets were found to be transgranular, giving way, outside of the dark, crescent-shaped fatigue-crack area visible in macrograph 3947, to ductile dimples.

SEM Fractographs: Duranickel Alloy Fractured by Slow-Bend Fracture-Toughness Testing in Hydrogen, After Various Heat Treatments



SEM fractograph

160×

3951 Fracture surface of a specimen of Duranickel, vacuum solution treated and quenched, aged 1 hr at 500 C (932 F) and cooled in air. The specimen, which was notched, precracked, and slow-bend fracture-toughness tested in hydrogen, broke by combined cleavage and intergranular fracture. See fractograph 3952 at right.



SEM fractograph

1000×

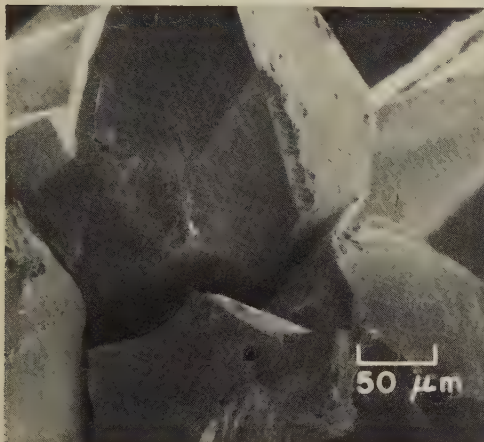
3952 A portion of the same fracture surface as that in 3951, but at higher magnification, showing facets that contain cleavage river patterns (bottom right) and pyramid-shaped tongues (top left).



SEM fractograph

95×

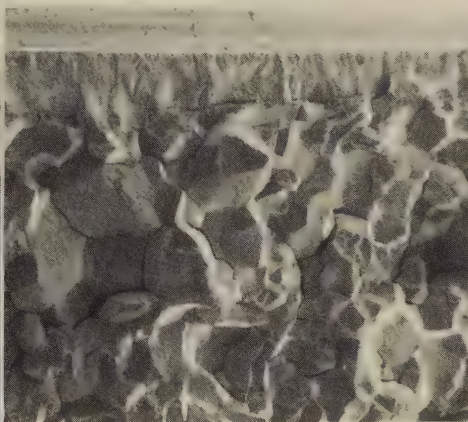
3953 Fracture in Duranickel that, except for being aged 4 hr, was heat treated and tested same as 3951. Fracture here is more completely intergranular, with less cleavage, than 3951. Both fractures show secondary cracks. See also 3954.



SEM fractograph

200×

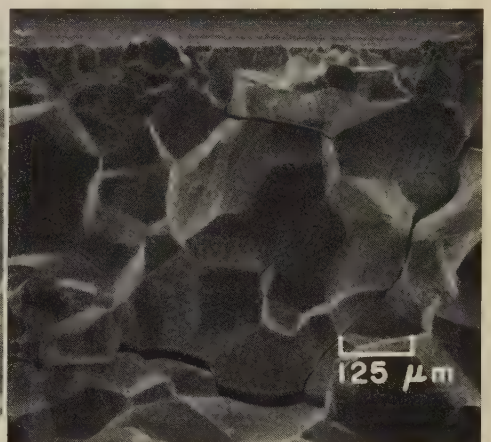
3954 A view at higher magnification of the fracture in 3953, showing it to be also a nearly wholly intergranular fracture, with deep secondary cracks at the grain boundaries.



SEM fractograph

20×

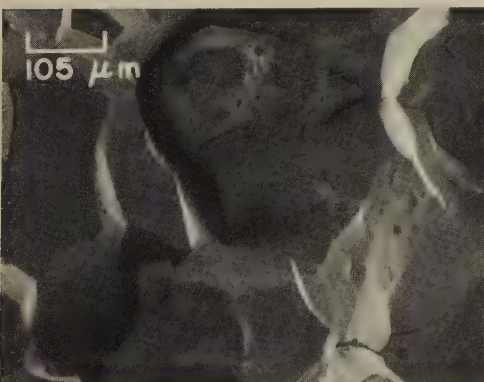
3955 Fracture in Duranickel that, except for being aged 8 hr, was heat treated and tested same as 3951 and 3953. Notch and fatigue precrack are at top. An example of sustained-load intergranular fracture in hydrogen. See 3956 to 3958.



SEM fractograph

80×

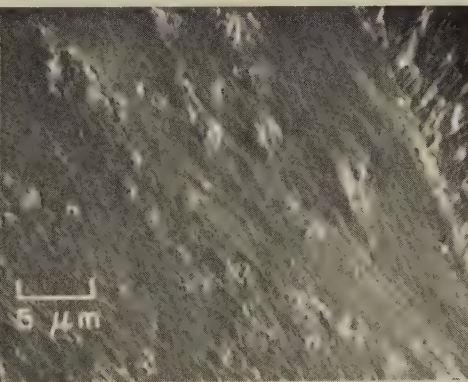
3956 A similar but larger view of the fracture in 3955, showing notch at top but no fatigue crack. Fine grains at notch were presumably cold worked in machining and recrystallized in aging.



SEM fractograph

95×

3957 Same fracture as that shown in 3955 and 3956, but an interior area. One or two cleavage facets are seen. Most of the fracture is intergranular, with large secondary cracks.



SEM fractograph

2000×

3958 A highly magnified view of the fracture in 3955-3957. Striations visible here show crack advances under constant bending deflection in hydrogen; compare with the fatigue striations in 3959.

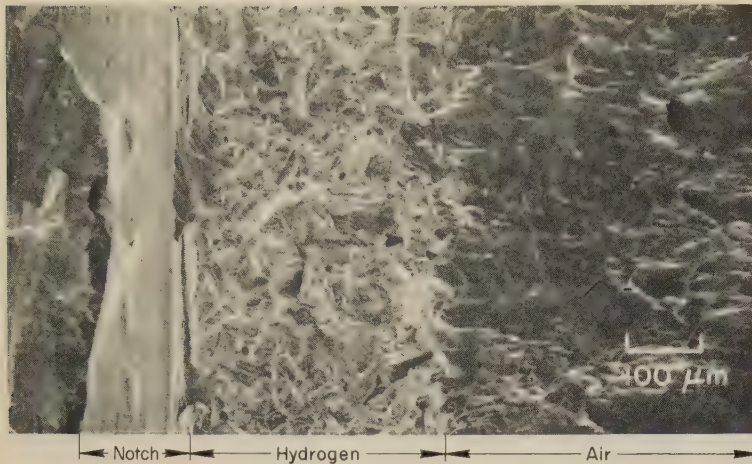


SEM fractograph

2000×

3959 High-magnification view of the fatigue precrack produced in air at base of notch in specimen in 3955. Compare fatigue striations here with crack-advance features in 3958. White marks at A's here are later fissures.

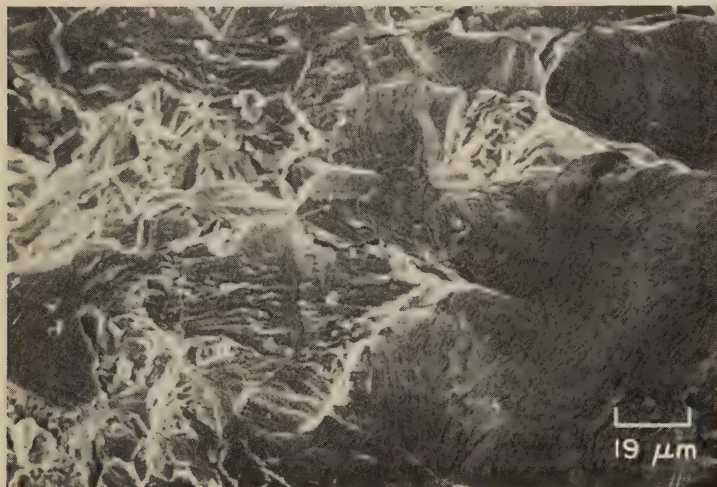
SEM Fractographs: Specimen of Nickel 201 That Was Fractured in a Three-Point Bending Test at Room Temperature in Hydrogen and in Air



SEM fractograph

100×

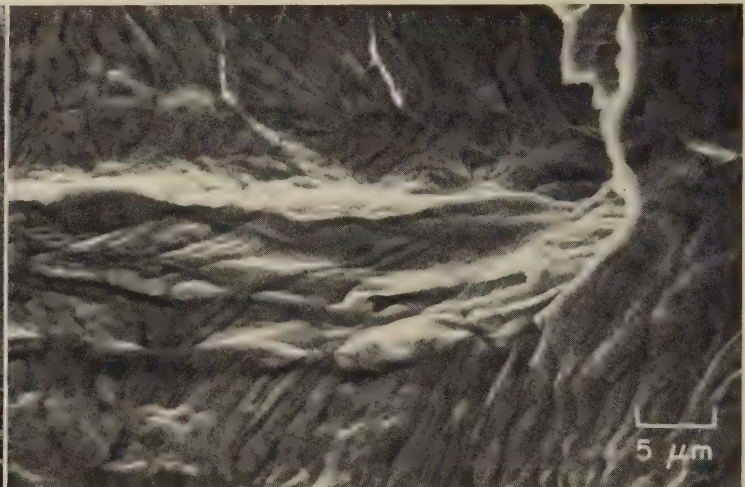
3960 The fractograph at left shows the surface of a fracture in a bend-test specimen of Nickel 201 containing 0.02% C, 0.35% Mn, 0.01% S, 0.35% Si, 0.25% Cu, 0.4% Fe, remainder Ni. After the material had been annealed, a specimen 19 mm wide by 3.17 mm thick was prepared, a notch was machined in the side of the specimen, and a fatigue crack was produced in the root of the notch. The specimen was then loaded in three-point bending (77-mm support span) to give a fixed displacement rate of 0.0015 μm per sec. The test was performed at room temperature in a stainless steel chamber equipped for testing in vacuum, in hydrogen or in air. During the first portion of the test, the chamber was filled with hydrogen; partway through the test, the hydrogen was replaced with air. In this view, the notch is at the left, and just to the right of the root of the notch is a very shallow fatigue crack. The central region (light) is the portion of the fracture that was obtained in hydrogen, and the darker region at right is the portion that was subsequently produced in air. See 3961 to 3964 for higher-magnification views of the portions produced in hydrogen and in air, and of the transition between them.



SEM fractograph

540×

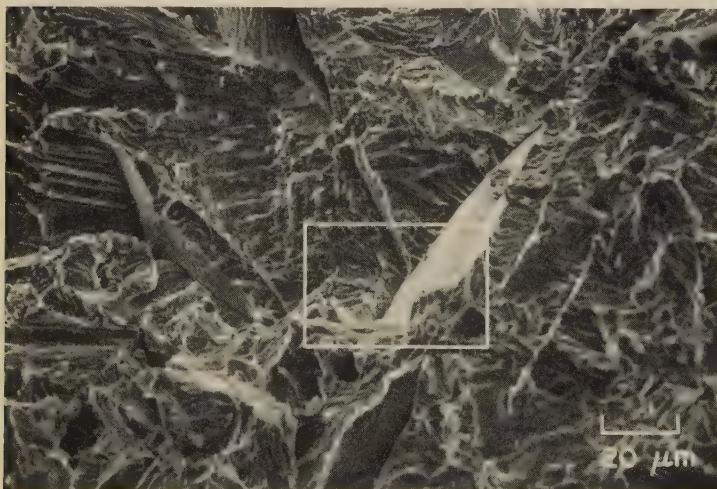
3961 View of an area of the fracture surface in 3960 that shows the transition from fracture in hydrogen (left) to subsequent fracture in air (right). Much of the fracture produced in hydrogen shows transgranular cleavage. In the portion produced in air, flow occurred after the crack front had passed.



SEM fractograph

2000×

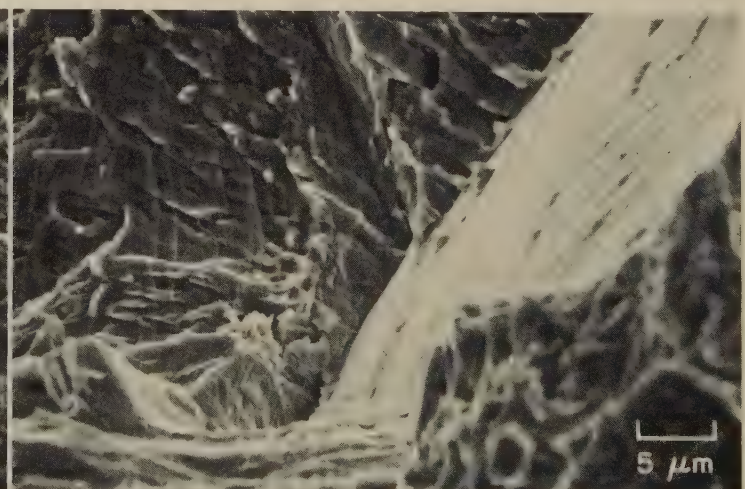
3962 View of the fracture surface in 3960, showing a region from the portion of the fracture that was produced in air. Visible are suggestions of dimples, but these features have been largely obscured by the effects of the secondary flow that occurred in this very ductile metal following passage of the crack front.



SEM fractograph

500×

3963 View of the fracture surface in 3960, showing a region from the portion of the fracture that was produced in hydrogen. As in the left portion of 3961, the fracture here is mainly by transgranular cleavage. Scattered regions of intergranular separation were reported but are not visible here. See also 3964.

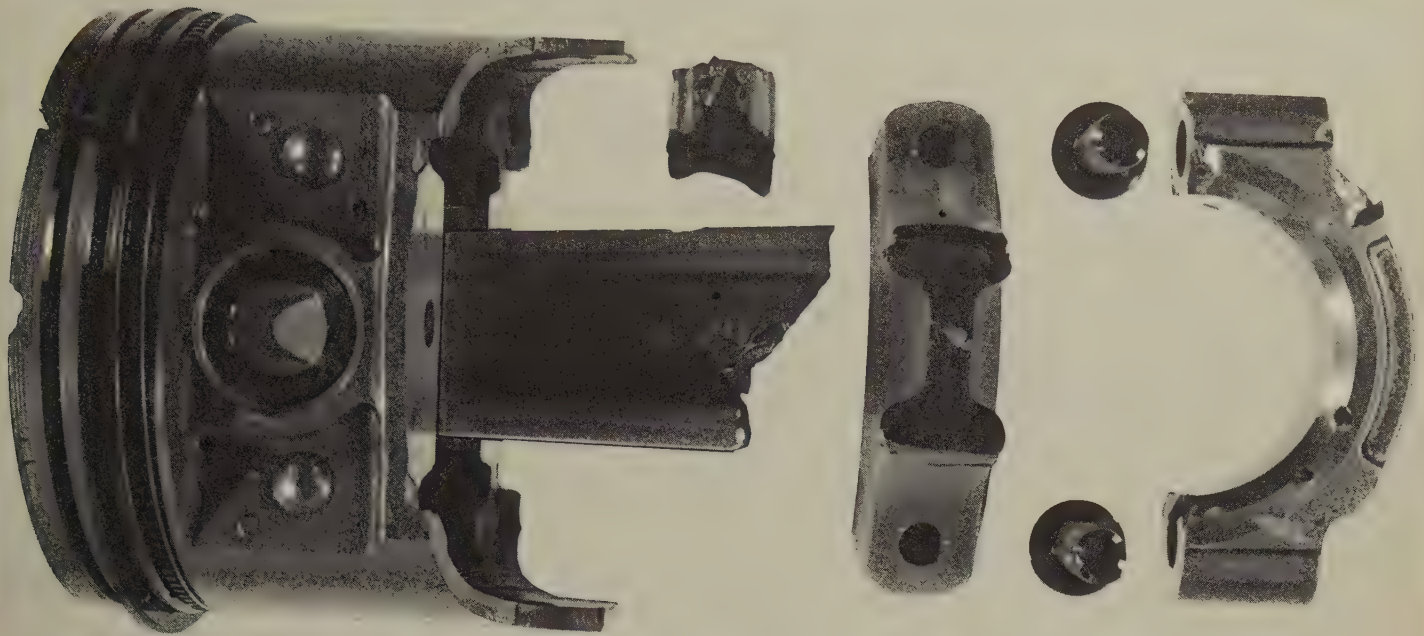


SEM fractograph

2000×

3964 Higher-magnification view of the area outlined by the rectangle in fractograph 3963 (left), showing the ledge-like character of the cleavage facets. In contrast, a suggestion of dimpled rupture is visible at bottom right. Note the small tongues on the bright facet at right.

Photograph, Light Fractograph, SEM Fractograph: Cast Aluminum Alloy 333 Experimental Connecting Rod Fractured by Sudden Overload During a Performance Test



Photograph

3965 Components of an experimental automotive connecting rod that fractured by overload during testing. (Shown also is the piston used in the test.) The rod was cast of aluminum alloy 333. Note that the shaft of the connecting rod suffered a compound fracture; the portion closest to the cap has a relatively straight, transverse fracture surface, and the portion connected to the piston shows a partially diagonal fracture, with the segment that broke away shown above the shaft. It is not known whether both fractures occurred in the shaft at the moment of initial fracture or whether the segment broke away later due to impact within the cylinder before the engine was shut off. The fracture surface visible here bears no features that in any way suggest a fatigue fracture. The 4340 steel bolts (left of cap at far right) also broke; for details of the bolt fractures, see 3678 to 3685. See also 3966 and 3967.

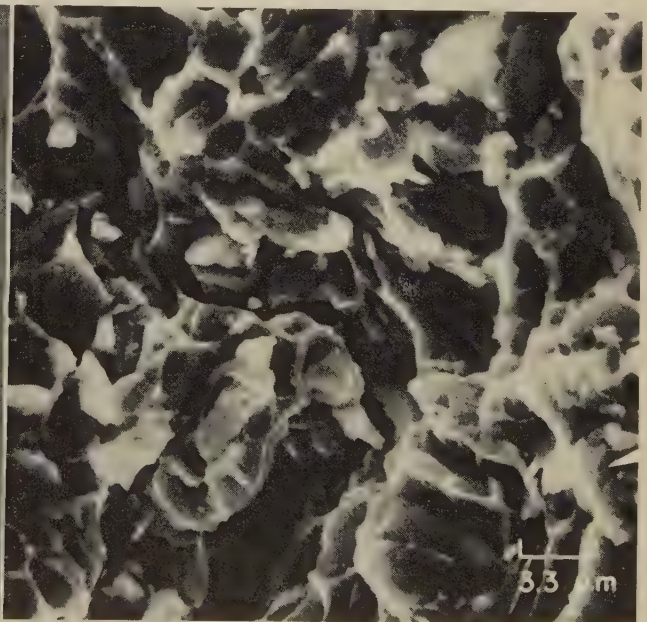
About $\frac{3}{4} \times$



Light fractograph

2×

3966 Fracture surface of the portion of the aluminum alloy 333 connecting rod in 3965 that was still attached to the piston after the test. It appears that each flange contains a chevron pattern, which suggests that there were two crack origins. This supports the theory that two successive fractures occurred in the rod. The mechanical damage in the right fracture surface indicates that the right origin probably led to the initial rupture. There are no indications of the beach marks that are characteristic of fatigue fractures. See also fractograph 3967 (right).

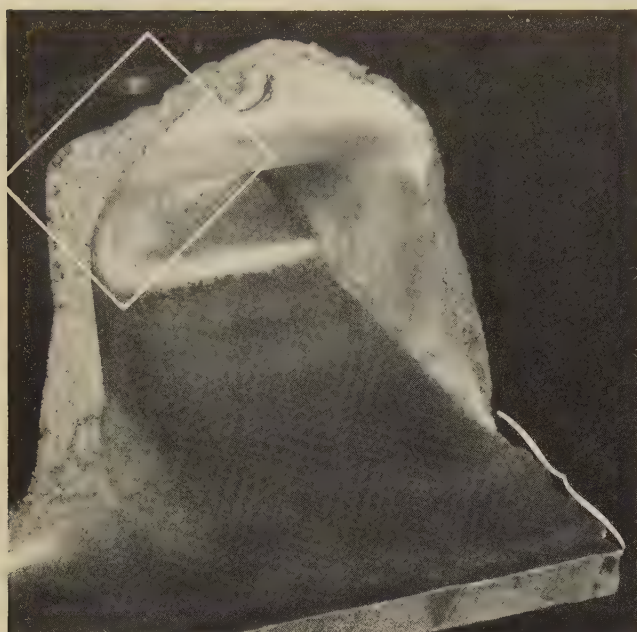


SEM fractograph

3000×

3967 High-magnification view of one of the fracture surfaces of the fractured connecting rod shown in 3965. It is evident that fracture was by dimpled rupture, which indicates that the fracture was caused by sudden overload. As in the views at about $\frac{3}{4} \times$ in 3965 and at 2× in 3966, no indications of fatigue are visible here. The fracture appears quite "clean" with very little evidence of nonmetallic inclusions.

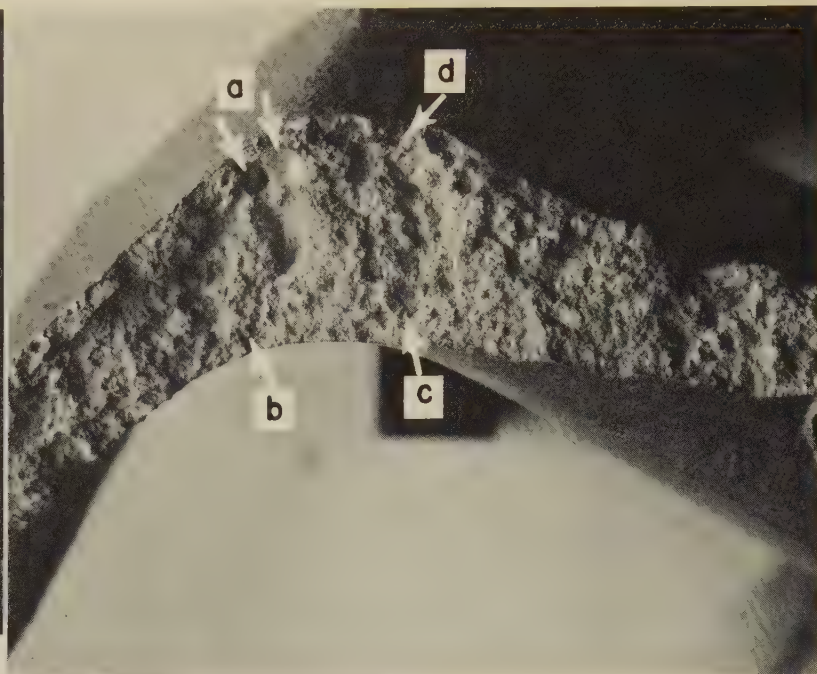
Photograph; Light and SEM Fractographs: Sand Cast Aluminum Alloy 356-T6 (Modified)
Carrier Tray That Fractured in Service in a Brittle Manner



Photograph

Actual size

3968 A portion of a fractured carrier tray sand cast of an aluminum alloy intended to be 356-T6. Chemical analysis revealed that the copper and zinc contents were of an order of magnitude above the specified limits. The silicon content was approximately as dictated by the specification. The hardness measured 82 Bhn — appreciably above the 70 Bhn expected. Tensile strength was 179 to 193 MPa (26 to 28 ksi) — slightly below the specified minimum of 207 MPa (30 ksi). See 3969 for area in rectangle, and 3970 for bracketed area, at a magnification of three diameters.



Light fractograph

3×

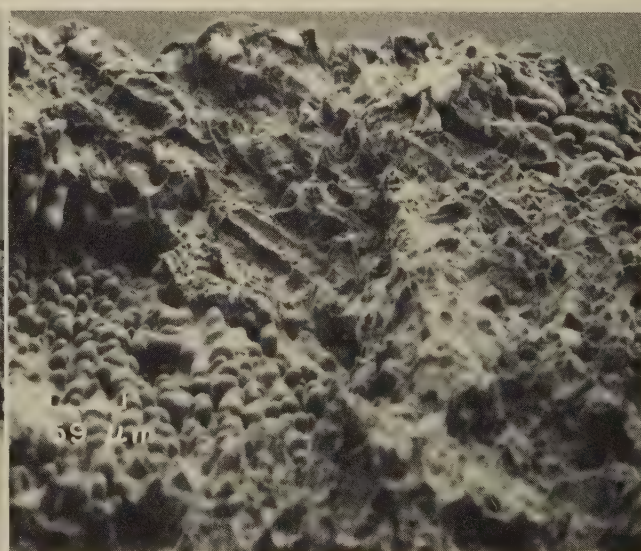
3969 Fracture surface of the rectangle-outlined shoulder of the sand cast carrier tray in 3968. The appearance of this surface suggests that fracture occurred in a brittle manner. The two arrows at "a" indicate two large gas cavities. The arrows at "b", "c" and "d" identify sites that were examined with a scanning electron microscope. (SEM fractographs of these sites are shown in 3971, below, and in 3972 to 3975, on the opposite page.) Note the absence of shear lips on the edges of this fracture surface, indicating a general lack of ductility.



Light fractograph

3×

3970 This fracture surface is from the bracketed edge of the sand cast carrier tray in 3968. Like the surface shown in 3969, the one here also exhibits the characteristics of brittle fracture, there being no sign of a shear lip at any of the edges. Again, there is evidence of porosity; the arrows point to quite large gas cavities. The cavities could have been caused by a reaction between the liquid metal and organic binders in the sand mold, or could have resulted from entrapped air being carried into the mold by undue turbulence in pouring the casting.

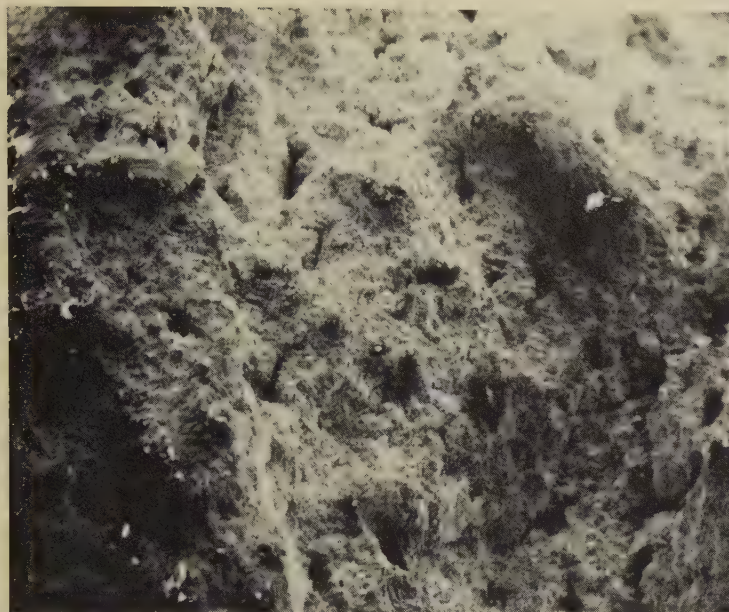


SEM fractograph

170×

3971 Area at the lower edge of the fracture in 3969, as indicated there by arrow at "b". Two regions of shrinkage porosity, at upper right and lower left, contain dendrite lobes, which existed as "free surfaces" within the cavities after the available liquid metal solidified. This behavior can be caused by an excessively high pouring temperature (which exaggerates total contraction in freezing) or by failure to provide proper risers.

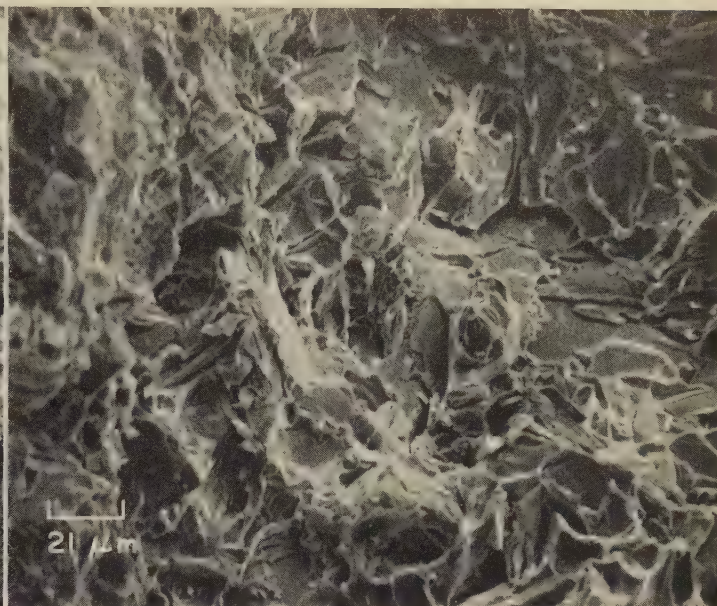
SEM Fractographs: Sand Cast Aluminum Alloy 356-T6 (Modified) Carrier Tray
That Fractured in Service in a Brittle Manner (Continued)



SEM fractograph

18×

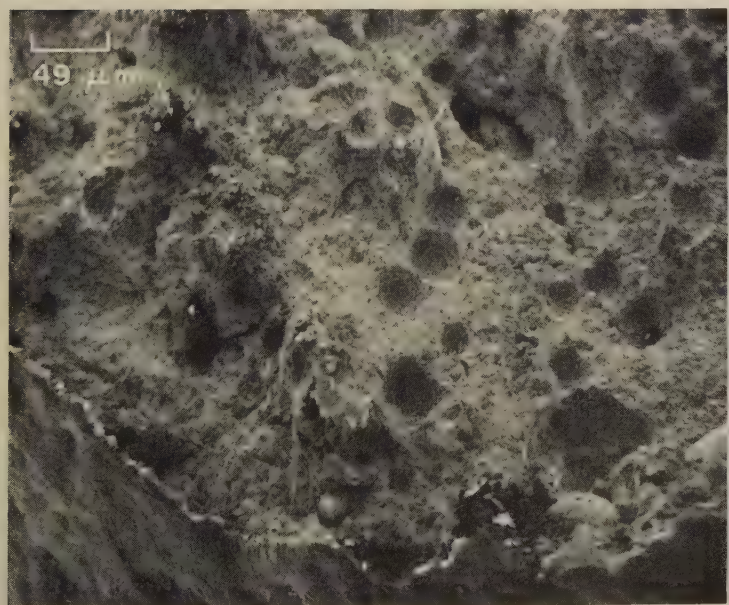
3972 Area at arrow "c" near the lower edge of the fracture in 3969 (opposite page). At the low magnification here, it is not possible to identify details of the mechanisms of fracture. This view, however, does show many cavities, some of them resembling dark slits, indicating quite generally distributed shrinkage porosity. Smeared region at upper left indicates mechanical damage — probably in handling of the carrier tray after fracture occurred. See also fractograph 3973 (at right).



SEM fractograph

475×

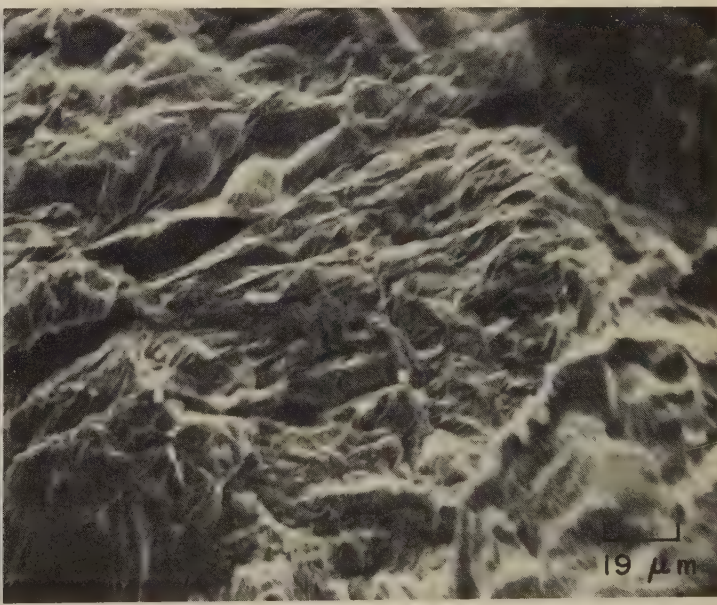
3973 A portion of the same fracture area as that in 3972 (area at arrow "c" in 3969), as seen at higher magnification. This view shows a complicated array of facets separated in many instances by indications of isolated dimples. The degree of flow in microvoid coalescence, however, did not contribute materially to ductility, and over-all fracture was brittle in nature. This region does not contain any of the shrinkage porosity seen elsewhere in this fracture but may contain nonmetallic inclusions.



SEM fractograph

205×

3974 This SEM view was taken in the area marked by arrow "d" in the fracture shown in 3969. This area exhibits a distribution of very small cavities, believed to be gas pockets, that are of a much different order of magnitude from those indicated by arrows at "a" in 3969. The latter were about 1.5 mm in diameter, whereas the cavities here are about 25 μm across. At bottom and left, a small portion of the exterior surface of the casting is visible. See also fractograph 3975, at right, for a view of this same fracture surface area at higher magnification.

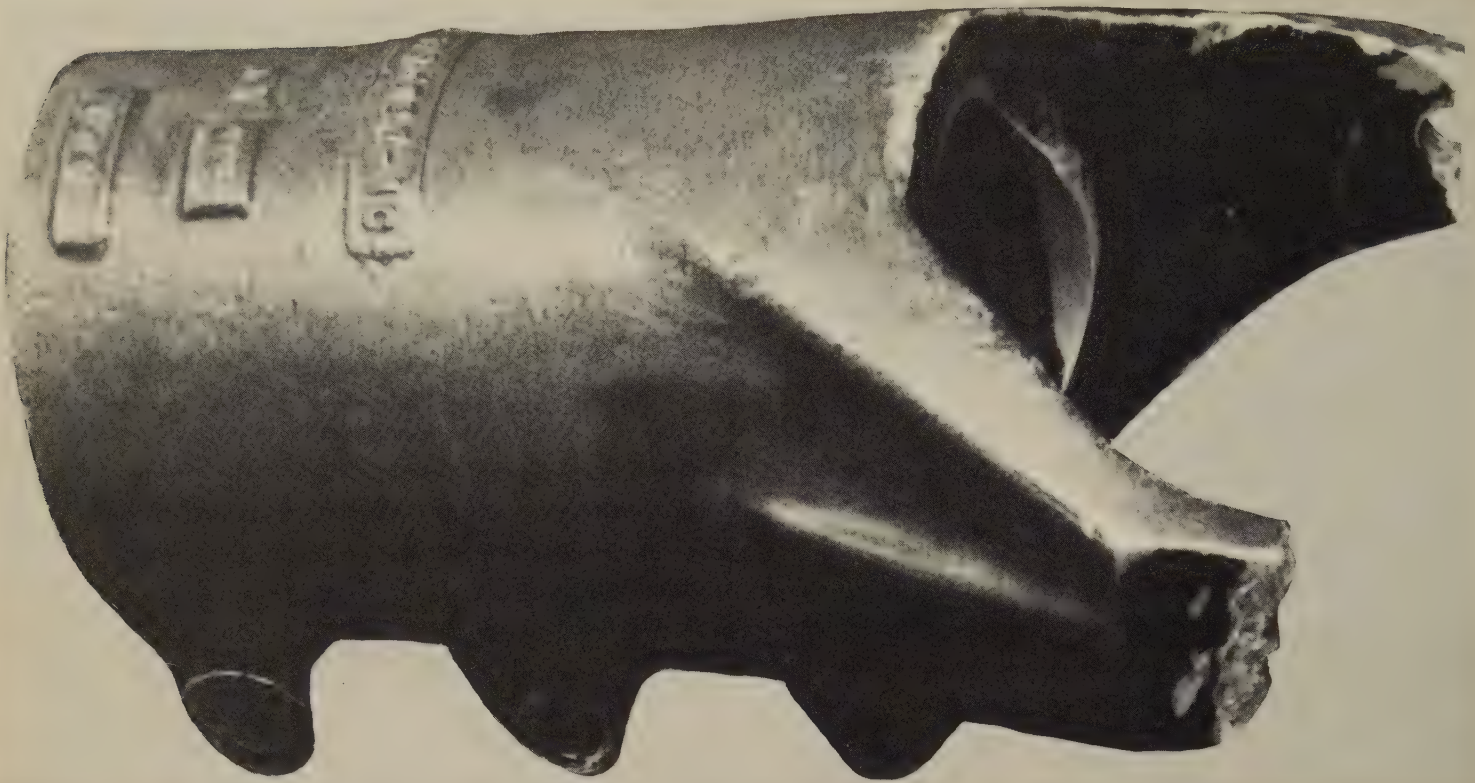


SEM fractograph

520×

3975 Enlarged view of a part of the fracture surface area in 3974. Some features vaguely resemble fatigue striations, but it is doubtful that they were caused by fatigue inasmuch as they do not seem to have been formed in an orderly sequence (and there are no beach marks in fractographs 3969 and 3970). Instead, the surface is very tumbled, with no suggestion of fatigue patches, and many regions bear whiskerlike features resembling some form of cleavage step. Lacking a significant amount of dimples, this surface can be rated as a brittle fracture.

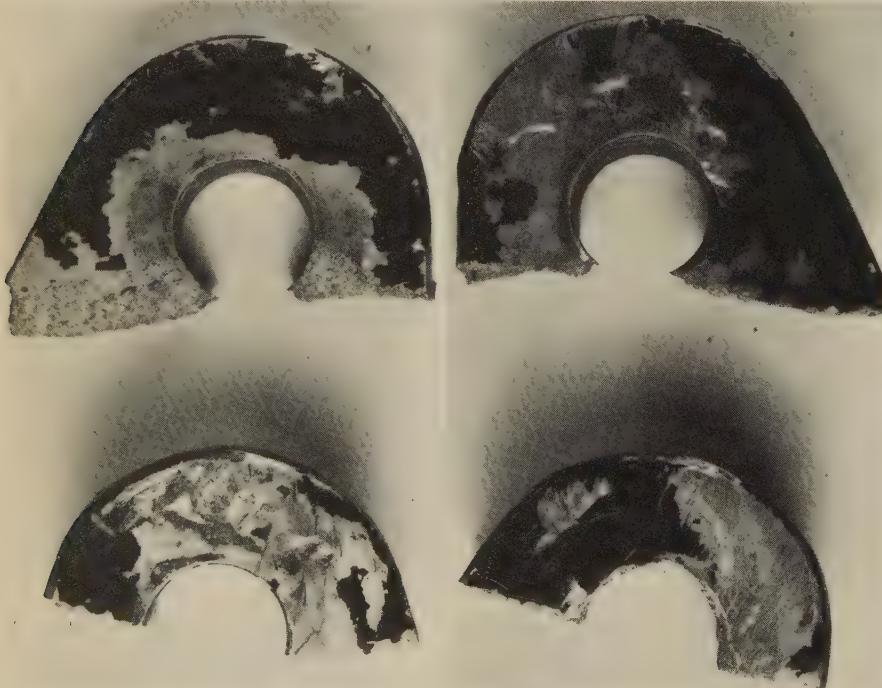
Photographs and Light Fractograph: Cast Aluminum Alloy 356-T6 Yoke, From a Helicopter Tail-Rotor Drive Assembly, That Fractured by Fatigue in Service



Photograph

Actual size

3976 A broken extension-housing yoke, part of a helicopter tail-rotor drive assembly, that fractured by fatigue in service. The fracture occurred through the left and right lugs at the points of attachment to the tail boom. The yoke was cast from aluminum alloy 356 and heat treated to the T6 temper. Chemical analysis showed that the composition of the yoke conformed to specifications except for silicon, which was 0.05% below the required minimum. Hardness measurements ranged from Rockwell B 48 to 52 (or about 81 to 85 Bhn), which was above the required minimum. Details of the fractures are shown in 3977 to 3984 (below, and on the opposite page).



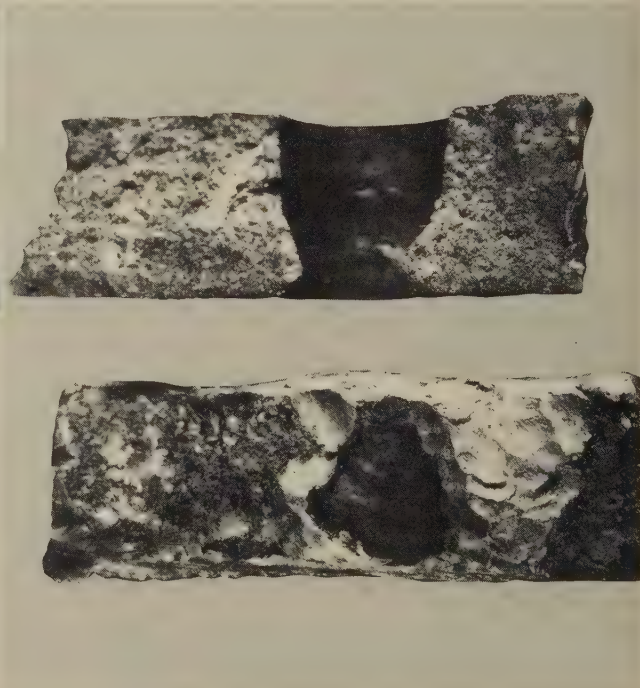
Photograph

2×

Photograph

2×

3977, 3978 Both sides of each of the two lugs that were broken from the extension-housing yoke shown in 3976, above. The inboard sides of the lugs are shown in 3977 (left); the outboard sides, in 3978 (right). Mechanical damage and loss of paint are evident. See 3979, at right, and 3980, on facing page.

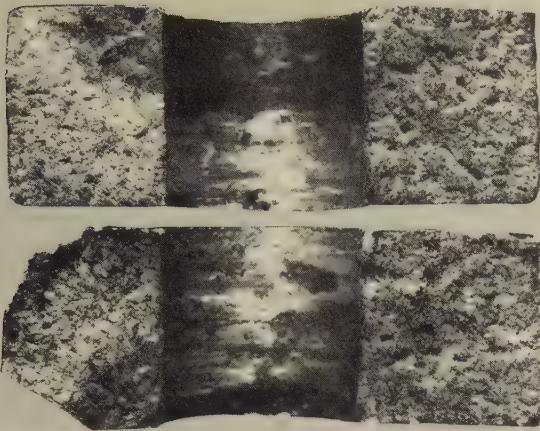


Light fractograph

3×

3979 Views of (at top) fracture surfaces of the upper lug in 3977 and 3978, and (at bottom) the mating surface of the yoke. Yoke surface is greatly deformed by repeated impacts, which obviously occurred after fracture.

Light and SEM Fractographs: Service-Fatigue Fracture of a Cast Aluminum Alloy 356-T6
Yoke From a Helicopter Tail-Rotor Assembly (Continued)



Light fractograph

3980 Views of (at top) fracture surfaces of the lower lug in 3977 and 3978, and of (at bottom) the mating surfaces of the yoke. Note discolored quadrant at top left corner of the bore of the lug (see also 3981), and corresponding area in yoke fracture adjacent to bottom left corner of the bore. Edge of the discoloration is the beach mark of the fatigue crack that was the origin of final fracture.

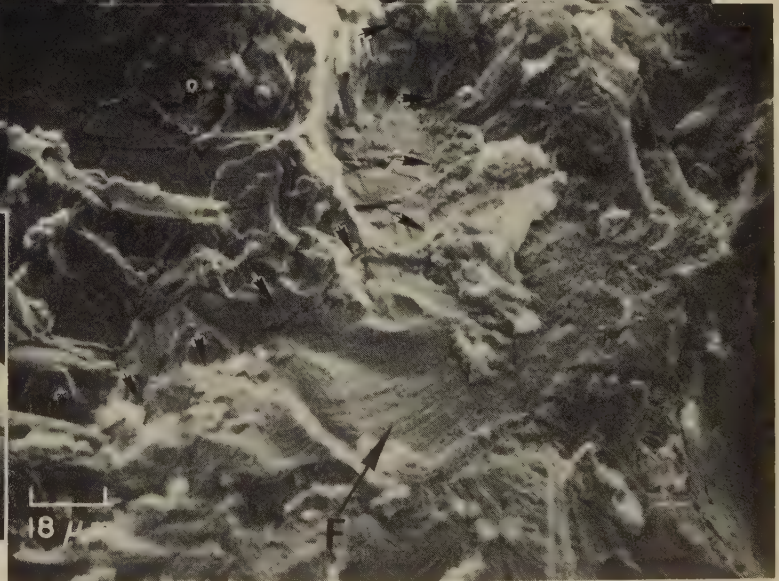
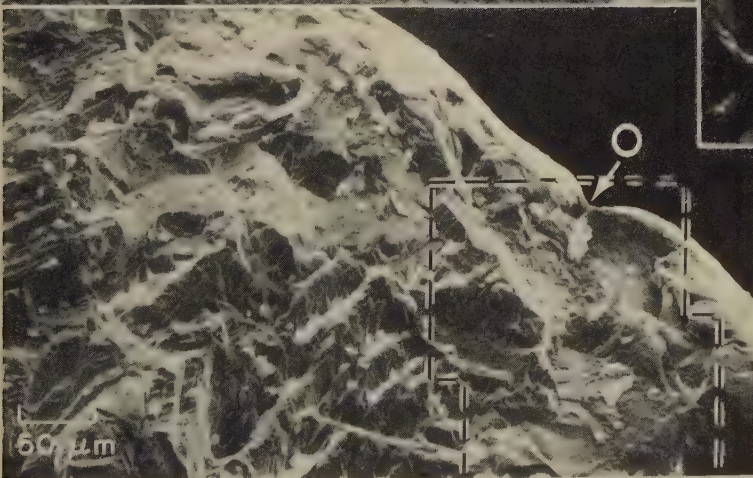
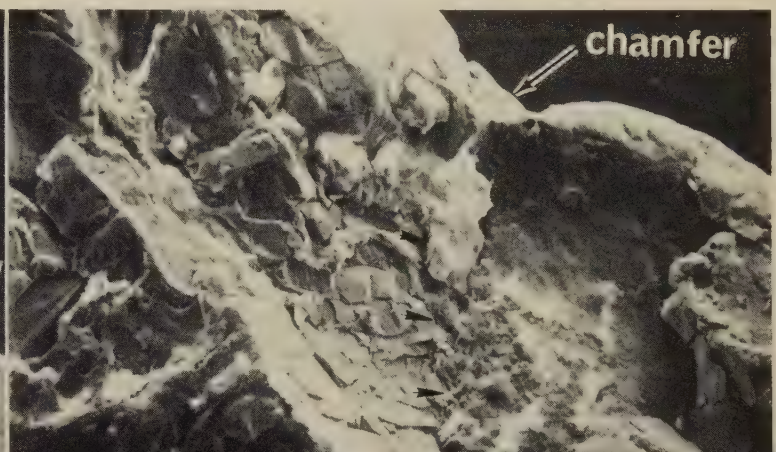
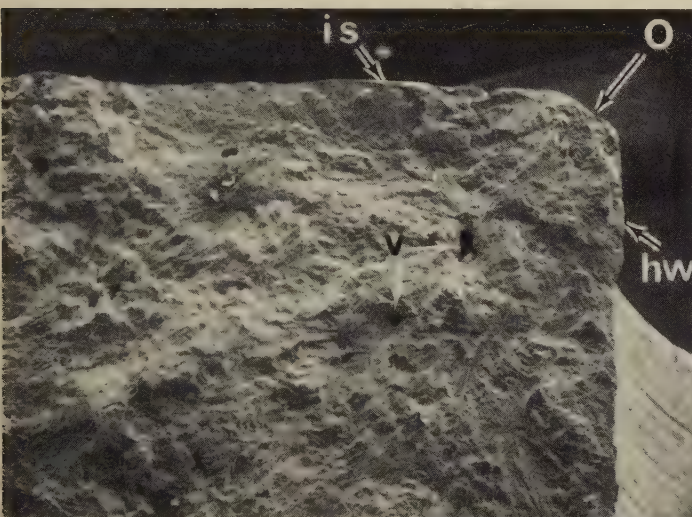


3×

Light fractograph

8×

3981 Enlarged view of one fracture surface of the lug in 3980, more clearly showing the fatigue-crack region at top left corner of the bore. Crack was nucleated at corner marked by arrow at "O". Fatigue area extended approximately to dashed line. See also 3982 and 3983.



SEM fractographs

21× (3982); 200× (3983)

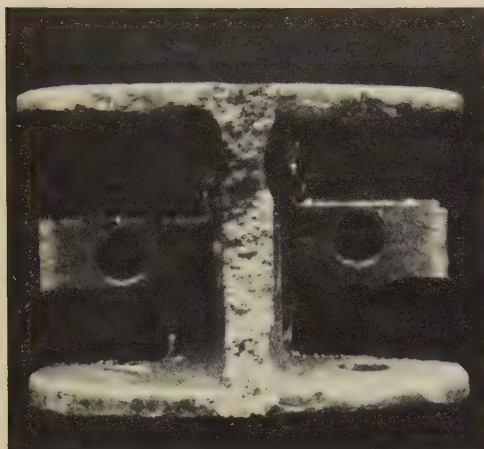
3982 Two views, at higher magnifications, of the fatigue-crack area of the lug fracture surface in 3981. In the upper view (3982), arrow at "O" denotes the crack nucleus in the chamfer, arrow at "is" points to inboard side, arrow at "hw" indicates hole wall, and arrows at "v" point to voids. The lower view (3983) shows the area near the origin of the crack in 3982 at higher magnification. In general, the crack propagated radially from point "O". See also fractograph 3984 (at right).

SEM fractograph

550×

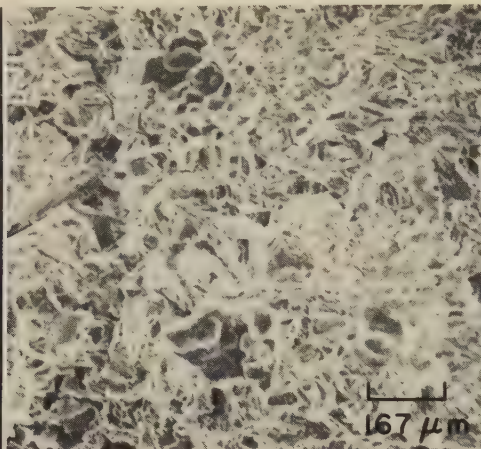
3984 This is the area within the dashed lines in fractograph 3983 (at lower left), shown at higher magnification. The initial crack opened at the chamfer (upper right corner). The onset of fatigue fracture is indicated by the small arrows running from upper middle to lower left. The arrow at "F" points to an area of typical fatigue striations. The initial phase of fracture was brittle.

Photograph, SEM Fractographs: Cast Aluminum Alloy 356-T6 Bell-Crank Fitting
of an Aircraft Rear Horizontal Elevator, Fractured in an Air Crash



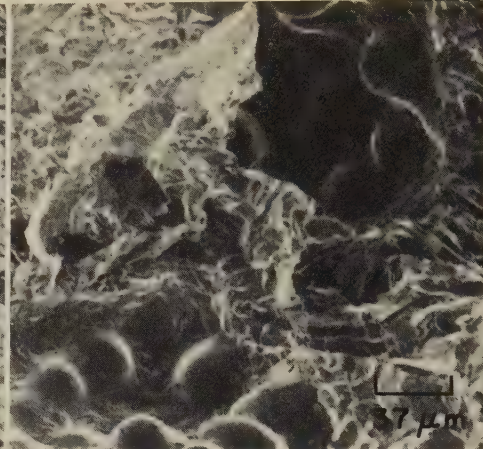
Photograph 1½×

3985 Fractured bell-crank fitting of cast aluminum alloy 356-T6. The fitting, which was from an aircraft rear horizontal elevator, fractured in a crash. No crack origin was found. See also 3986 to 4002.



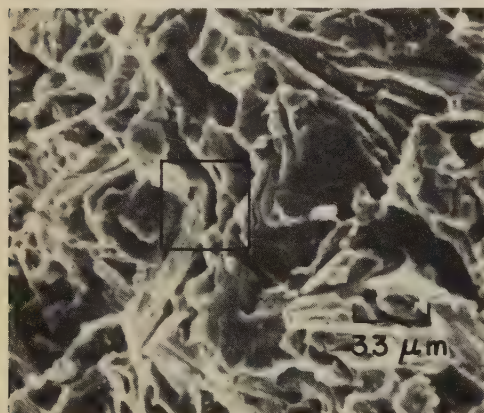
SEM fractograph 60×

3986 A more highly magnified view of the fracture in 3985. The appearance here is typical of the entire fracture surface. There is little evidence of surface flow. See also fractograph 3987 (right).



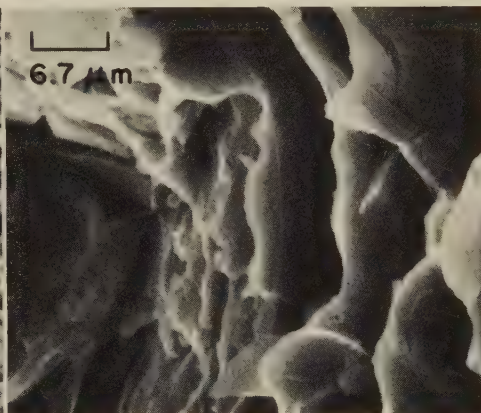
SEM fractograph 270×

3987 Many of the features of the fracture surface in 3986 (left) are associated with shrinkage cavities of the type shown here. The round knobs are exposed secondary arms of dendrites.



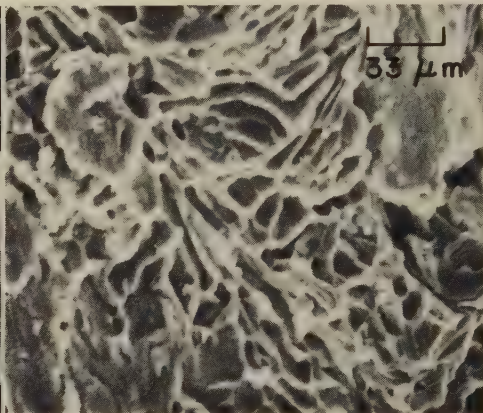
SEM fractograph 300×

3988 A cellular region that was found to be characteristic of the fracture surface in 3985. Although some features faintly suggest dimples, the higher-magnification view in 3989, showing the area in the rectangle here, reveals no dimples.



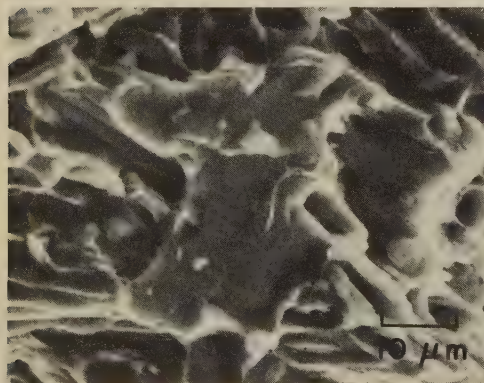
SEM fractograph 1500×

3989 Higher-magnification view of the area outlined by the rectangle in fractograph 3988 (left). There are no suggestions of dimples visible here; instead, the surface exhibits platelets that have been bent and cracked.



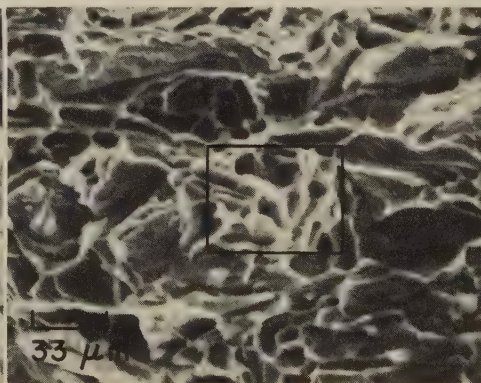
SEM fractograph 300×

3990 View at another location in the fracture surface in 3985. The formation of the cellular structure shown here and in 3988 is attributed to the microstructure that resulted from the freezing patterns and heat treatment of the casting.



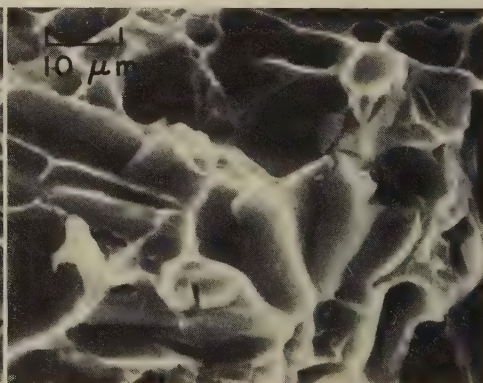
SEM fractograph 1000×

3991 Another view of the fracture surface shown in 3985. As in 3989 and 3990, there is no evidence of true dimples, but cellular structure only. There appear to be many small inclusions on the surface; most are not bonded to the matrix.



SEM fractograph 300×

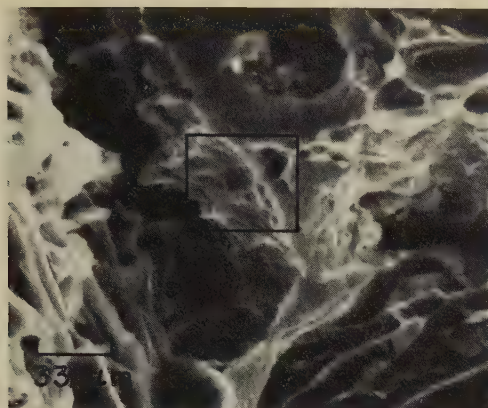
3992 An overload fracture in a miniature tensile-test specimen cut from the fitting in 3985, displaying the same type of cellular surface structure produced by the service fracture. See 3993, a higher-magnification view of the area in the rectangle.



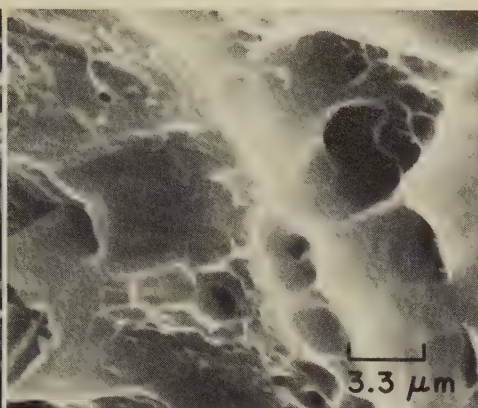
SEM fractograph 1000×

3993 A higher-magnification view of the area outlined by the rectangle in fractograph 3992. Although the features here strongly resemble those shown in 3989, close scrutiny reveals the presence of tiny dimples in the edges of some cells.

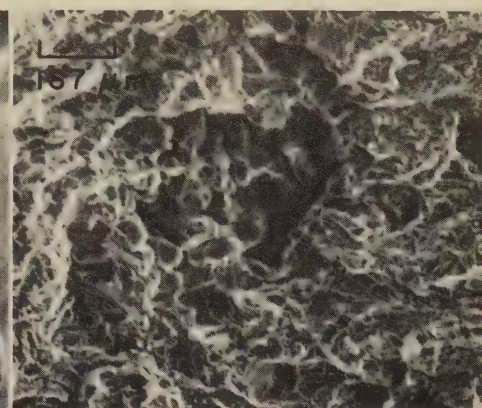
SEM Fractographs, SEM Micrographs: Fractured Cast Aluminum Alloy 356-T6 Bell-Crank Fitting
(Continued): Fractures in Test Specimens Cut From Fitting; Microstructure



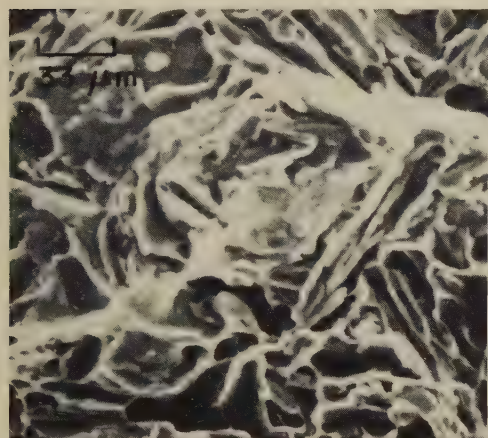
SEM fractograph 300×
3994 View of the fracture surface shown in 3992, but at another location. In this area, there are small, clearly visible dimples clustered in the central, outlined region, which is shown at higher magnification in fractograph 3995 (right).



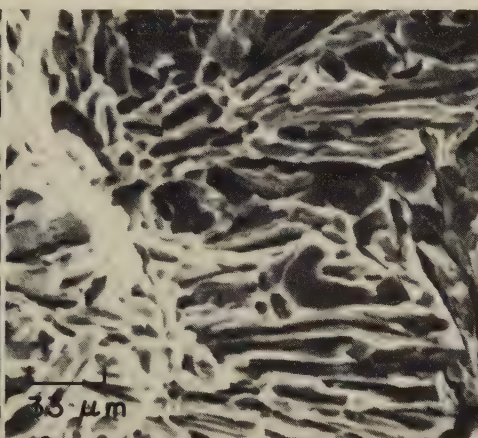
SEM fractograph 3000×
3995 A higher-magnification view of the area in the rectangle in 3994 (at left), showing small dimples of several sizes and suggesting that the service fracture shown in 3985 (with no dimples) was not the result of simple overload.



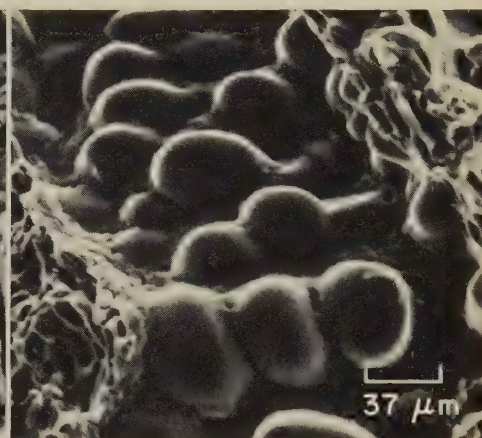
SEM fractograph 60×
3996 Surface of a fracture in a miniature impact-test specimen cut from the broken aluminum alloy 356-T6 bell-crank fitting shown in 3985. The appearance here is very similar to that of the service fracture in 3986, at the same magnification.



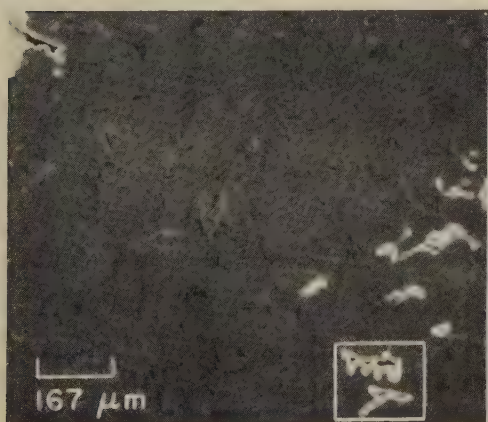
SEM fractograph 300×
3997 View of the fractured test specimen in 3996, but at another location. The appearance here is quite similar to that of the service fracture in 3990.



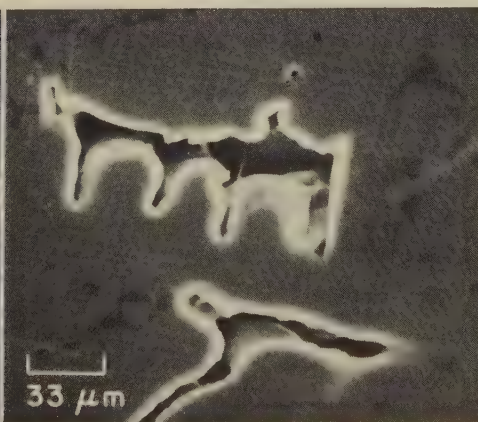
SEM fractograph 300×
3998 Another view of the fracture surface shown in 3996 and 3997. Compare with the view of the service fracture in 3988 and note the marked resemblance.



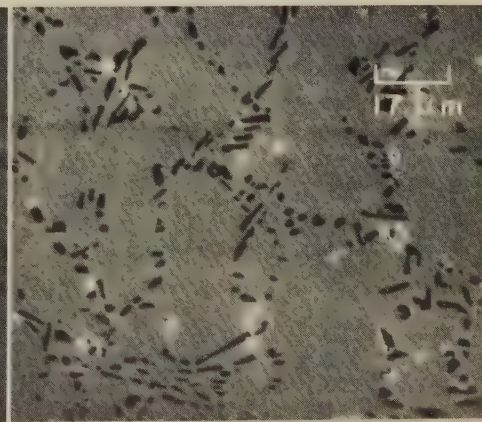
SEM fractograph 270×
3999 View of fracture surface in 3996-3998, displaying a shrinkage cavity. Cavity is somewhat like those in 3987, but with a much coarser dendrite cell structure.



SEM micrograph (as polished; not etched) 60×
4000 A polished but unetched section of the broken fitting in 3985, showing the expected dendritic network of silicon particles (dark features; see 4002) and light shrinkage cavities (see 4001 for a higher-magnification view of the outlined area).

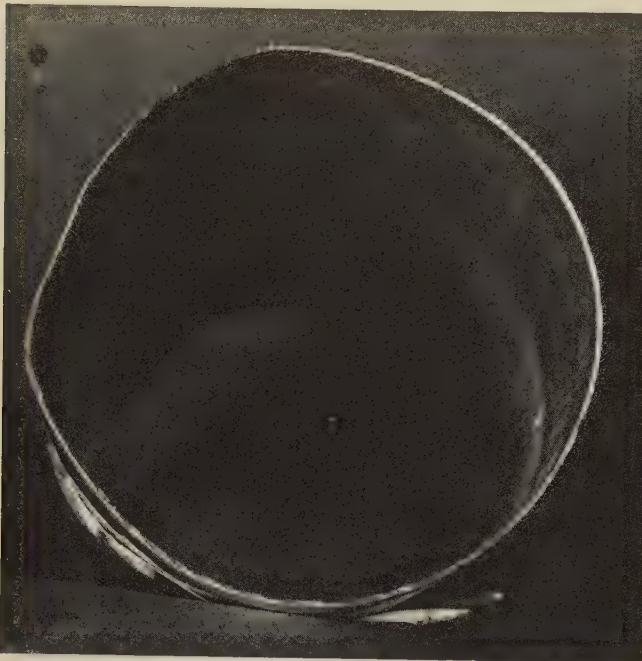


SEM micrograph (as polished; not etched) 300×
4001 A higher-magnification view of the shrinkage cavities shown in the outlined area in micrograph 4000 (left). Note that the shapes of these shrinkage cavities are very conducive to crack propagation with little plastic deformation.



SEM micrograph (as polished; not etched) 600×
4002 Enlarged view of 4000, showing a eutectic structure consisting of a dendritic network of silicon particles in an aluminum matrix. This network and the extensive shrinkage porosity contributed to rupture under the impact of the air crash.

Photograph, SEM Fractographs: Aluminum Alloy 1100 Portable Cylinder for Storage of Pressurized Helium, Which Fractured Explosively Because of Stress Corrosion



Photograph

Actual size

SEM fractograph

40×

4003, 4004 Photograph and SEM fractograph showing the fracture surface of a small portable cylinder used for storage of helium gas under pressure that exploded while at rest in storage. The cylinder was approximately 2 3/4 in. in diameter by 10 in. long and had been formed from a 0.03-in.-thick sheet of aluminum alloy 1100. Normal pressure in the cylinder, when full of helium, was 2 MPa (300 psi); maximum pressure, 4 MPa (600 psi). The cylinder broke when the bottom separated from the sidewall with explosive force, leaving a very even fracture surface; separation was probably at the very bottom of the sidewall. Photograph 4003 (left) shows the entire levels, separated by offsets, containing crack arrests. Rupture began at the inside of the cylinder wall and terminated in a pronounced ductile shear lip (at top in 4004). Note the secondary stress-corrosion cracks in the inside surface of the wall (at bottom in 4004), which are parallel to the fracture surface. See also fractographs 4005 and 4006 (below).



SEM fractograph

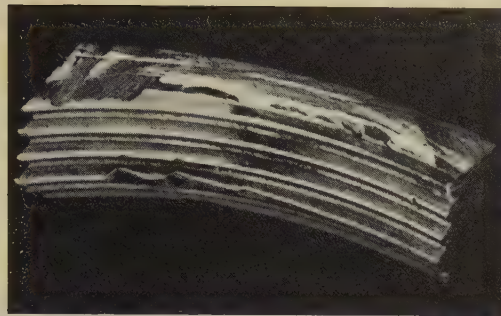
83×

SEM fractograph

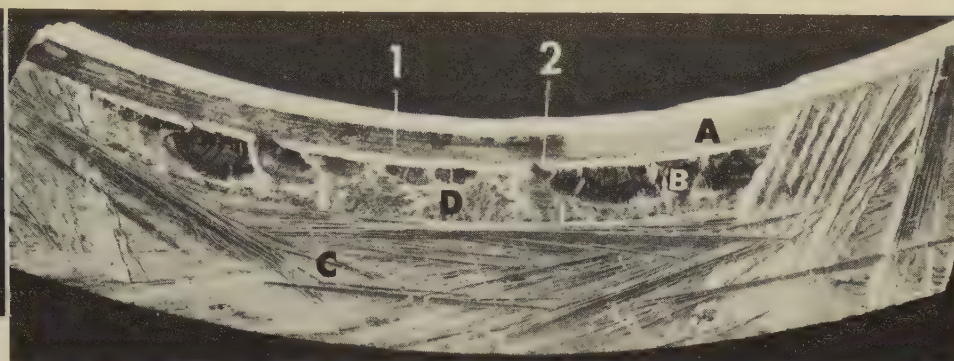
108×

4005, 4006 SEM views of two portions of the fracture surface of the cylinder in 4003 (above, at left). These views, at higher magnification than 4004, also show the crack arrests, the offsets between adjoining stress-corrosion-crack surfaces, and the numerous secondary cracks in the inside surface of the cylinder wall (at bottom) that are parallel to the fracture. In 4006 (right), numerous corrosion pits are visible also. These pits are probably due to condensation of water vapor, at the bottom of the cylinder, that was carried by the helium gas. (Light-microscope examination revealed that cracks formed at bottoms of corrosion pits.) It is likely also that the forming operation created large stress concentrations at the junction between the sidewall and the bottom of the cylinder.

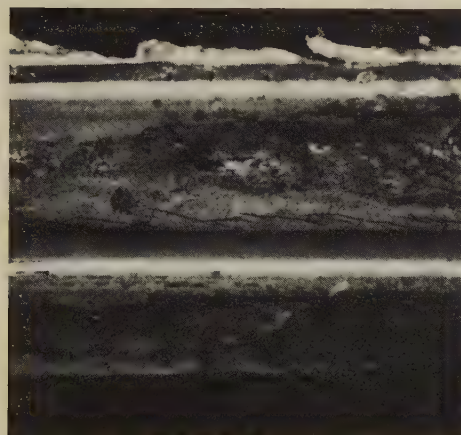
Photographs, Light Fractograph, SEM Fractographs: Aluminum Alloy 2014-T6 Aircraft Propeller Hub That Fractured in Service by Fatigue



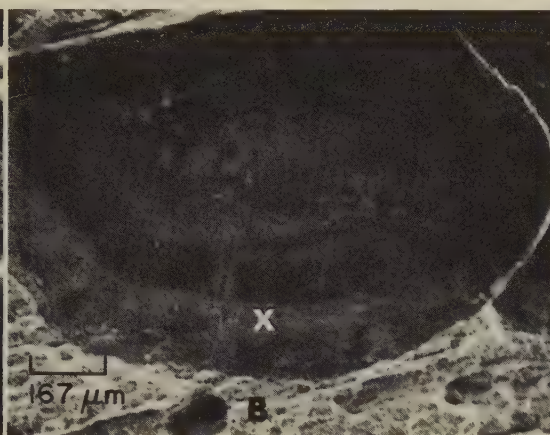
Photograph 2/3×
4007 Segment of a propeller hub, of aluminum alloy 2014-T6, that fractured in service by fatigue. Fracture surface, seen obliquely across the top of the segment here, is shown in a frontal view in 4008, at right. See also 4009 to 4014, below, and 4015 to 4020, on the next page.



Light fractograph 5×
4008 Frontal view of the fracture surface shown obliquely in 4007 (left). The narrow ledge at "A" is the top thread visible in 4007. The dark area at "B" is the surface of one of the original (fatigue) cracks. Saw cuts ("C") were made partway through the hub segment, and the original cracks were then exposed by overload fracture, which produced the surface at "D". See 4010 and 4014 for enlarged views of areas 1 and 2.



Photograph 6×
4009 View of the root of a thread in the propeller-hub segment shown in 4007, revealing that cracks had formed other than those that caused the fracture. Note the layers of corrosion products on thread surfaces. See also fractograph 4020, on the next page.



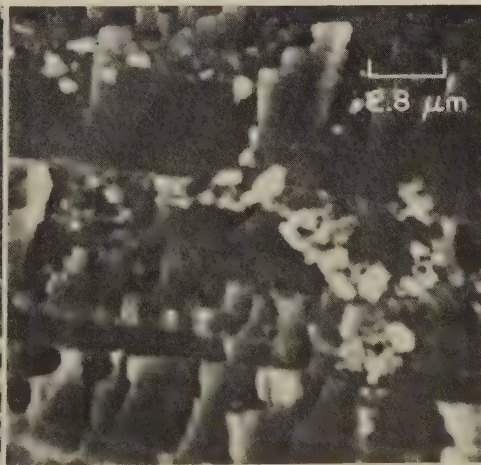
SEM fractograph 60×
4010 Higher-magnification view of the area in 4008 marked 1. The bright region at bottom ("B") is the surface of the overload fracture produced to expose the original cracks. The center region of the fatigue-crack surface (dark) is quite corroded; the outer region at "X" (shown at higher magnification in 4011) is relatively clean.



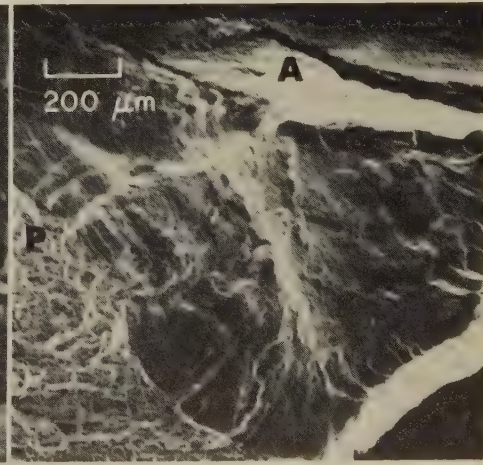
SEM fractograph 360×
4011 Higher-magnification view of the fatigue-crack surface at "X" in 4010. Although some corrosion products are present, fatigue striations are still faintly visible in region "Y". Region "Y" is shown at higher magnification in fractograph 4012, below.



SEM fractograph 1100×
4012 Enlarged view of region "Y" in 4011. At this magnification the fatigue striations are clearly identified by the alignments of corrosion products. See 4013 for an enlarged view of area "Z".

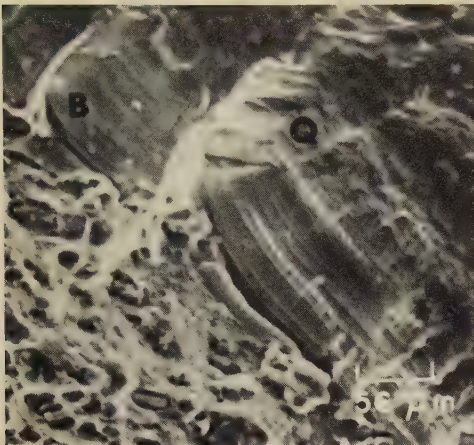


SEM fractograph 3600×
4013 A higher-magnification view of the area at "Z" in fractograph 4012, which shows that the corrosion products have formed shelves at the edges of fatigue striations.

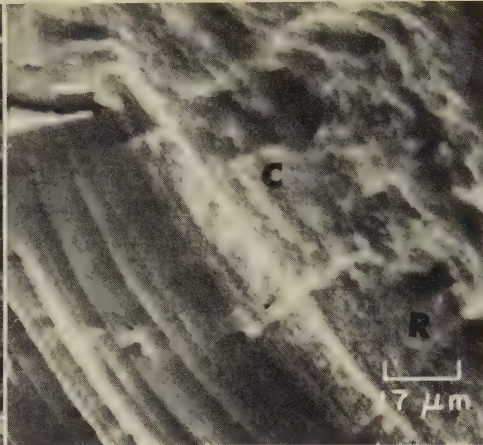


SEM fractograph 50×
4014 Higher-magnification view of area 2 in 4008, showing (at "A") the crack nucleus at the root of the thread. See 4015, on the next page, for a higher-magnification view of the area at "P".

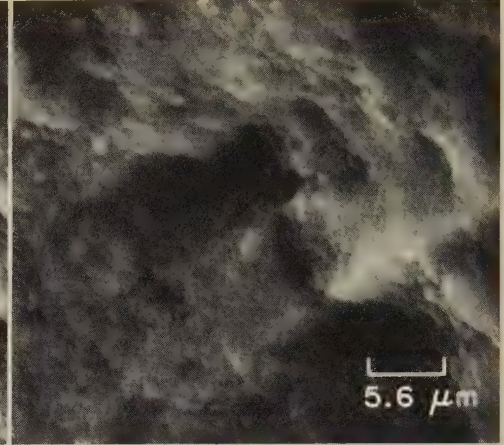
SEM Fractographs: Fracture in Aluminum Alloy 2014-T6 Propeller Hub (Continued);
Aluminum Alloy 2024-T4 Fracture-Toughness Specimen Precracked by Fatigue



SEM fractograph 180×
4015 View of area "P" in fractograph 4014 (preceding page), at higher magnification. Area containing fatigue striations is at "B"; overload fracture that exposed the fatigue crack is at lower left. Area at "Q" is shown enlarged in 4016.



SEM fractograph 600×
4016 Area at "Q" in 4015, at higher magnification, which clearly shows the fatigue striations. Some of the striations (at "C") are partly obscured by the effects of corrosion. The area at "R" is shown at still higher magnification in 4017.



SEM fractograph 1800×
4017 A more distinct view, at higher magnification, of the corroded region at "R" in fractograph 4016 (at left). Some of the corrosion attack was general in nature, although numerous pits were formed by localized corrosion.



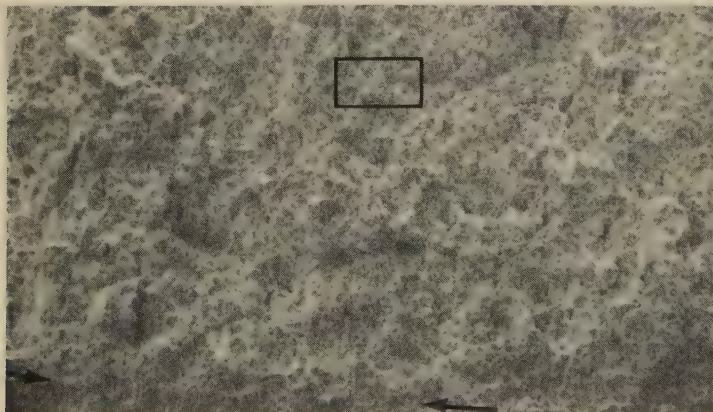
SEM fractograph 36×
4018 A crack in the propeller-hub segment in 4007 not seen in 4008. Fatigue beach marks are visible at uppermost right. The very bright areas at bottom are corrosion debris. See also 4019.



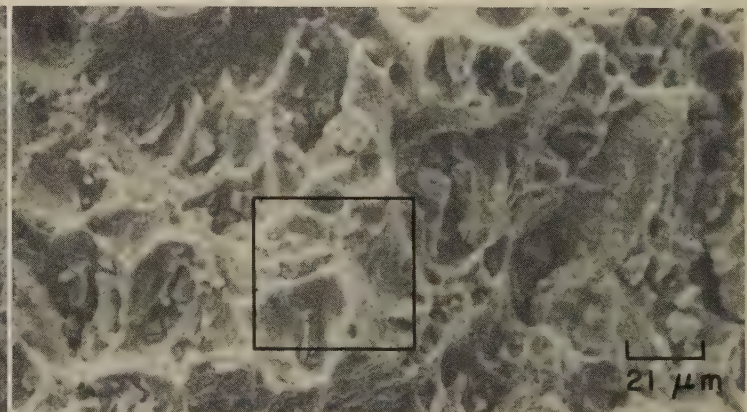
SEM fractograph 60×
4019 Area near site of origin of the fatigue crack in 4018. Note corrosion "spikes" issuing from beach marks. X-ray analysis identified bright debris as silicates of iron, cadmium and aluminum.



SEM fractograph 300×
4020 A view of the thread root in 4009 (preceding page) at considerably increased magnification, which more clearly shows the pitting, spalling, corrosion products, and one of the cracks in the root.

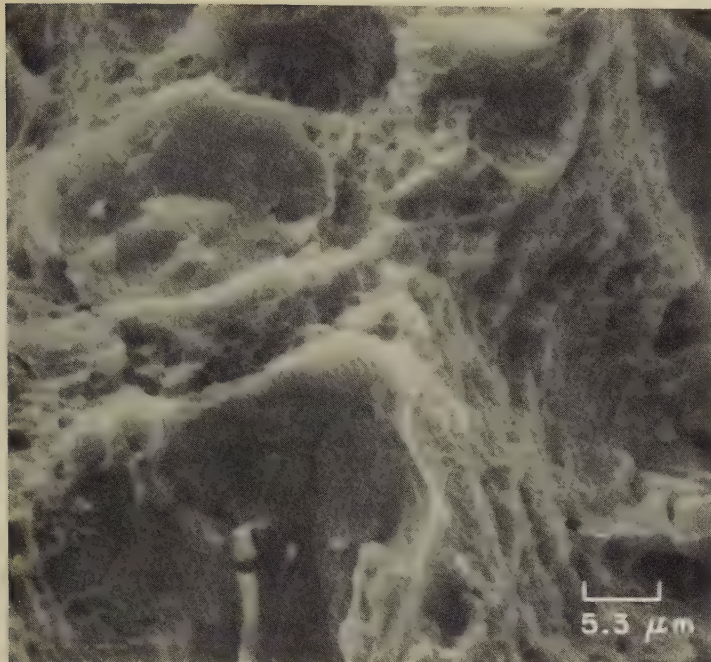


SEM fractograph 49×
4021 Fracture surface of a plane-strain fracture-toughness specimen of aluminum alloy 2024-T4 aged 48 hr at 23 C (73 F) before being tested. Tensile strength was 461 MPa (67 ksi). Termination of the fatigue precrack can be faintly seen across the bottom (arrows); above it is the later overload fracture. See 4022.



SEM fractograph 480×
4022 An enlarged view of the area outlined by the rectangle in 4021, in the overload portion of the fracture. Many areas of small dimples are visible surrounding larger cavities containing broken and cracked inclusions. For a higher-magnification view of the area in the rectangle here, see 4023 (facing page).

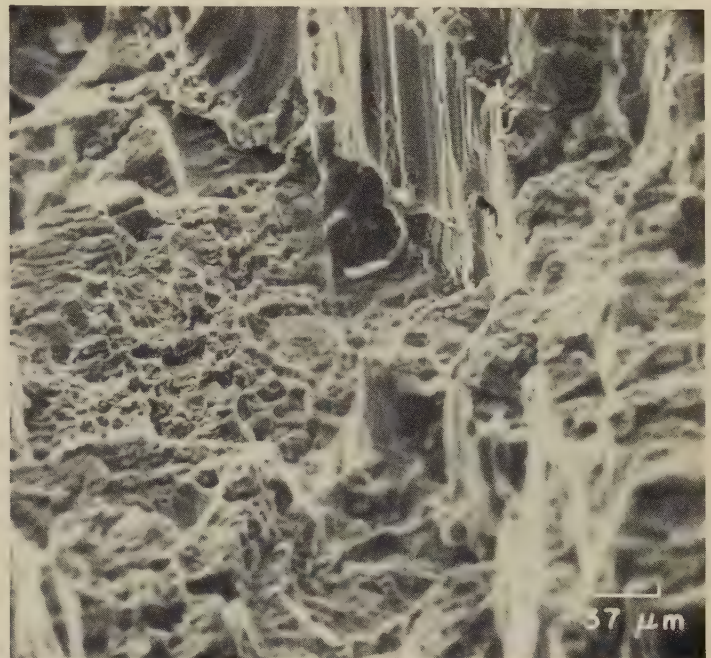
SEM Fractographs: Aluminum Alloy 2024-T4 Fracture-Toughness Specimen (Continued);
Aluminum Alloy 2024-T3 Fatigue-Test Specimen Fractured in Argon



SEM fractograph

1900×

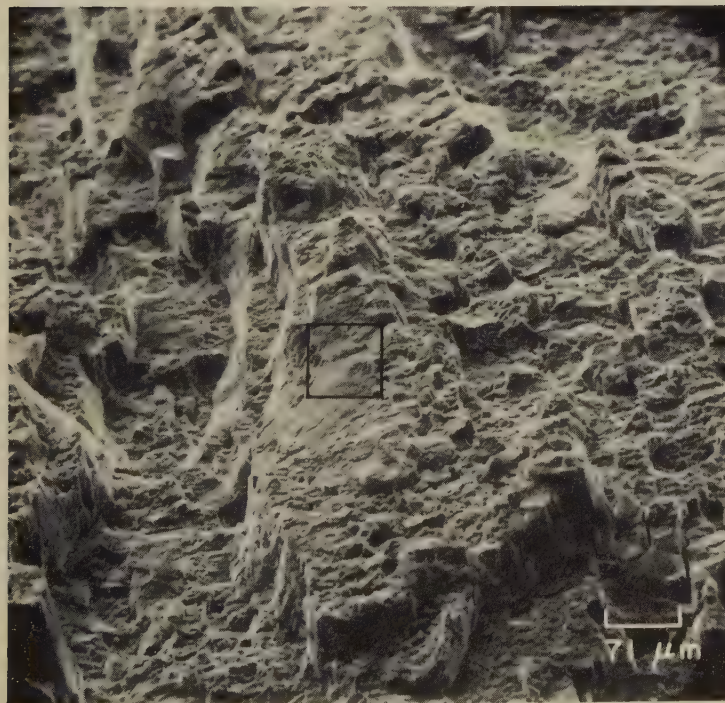
4023 This conclusion of the series begun in fractograph 4021 (opposite page) is a view at higher magnification of the area within the rectangle in fractograph 4022. Here, the small dimples, which are of quite uniform size, can be seen very clearly. At top is an area that appears to be a cleaved facet of an inclusion. At bottom is a large void that has evidently formed by separation from a slablike inclusion of which the edge is still visible at the center of the void.



SEM fractograph

270×

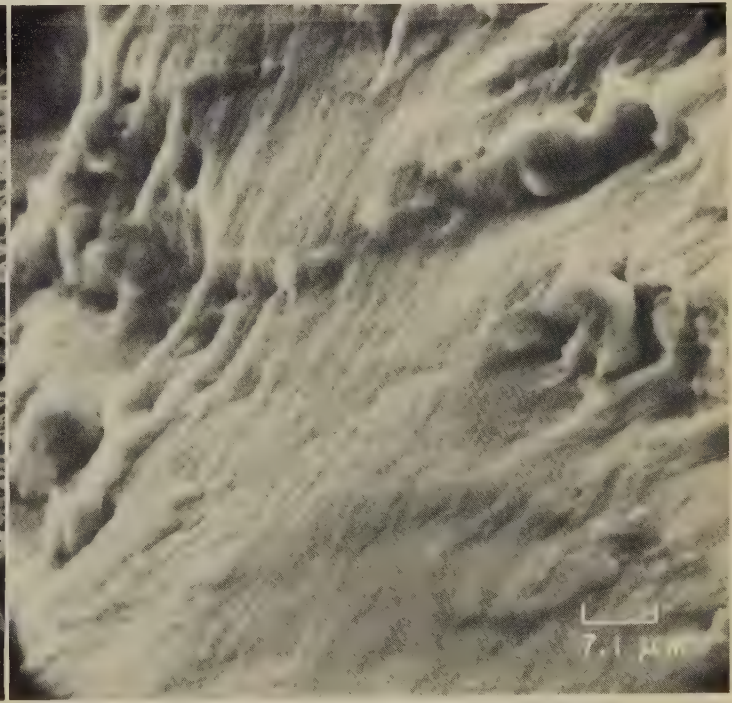
4024 Fracture surface of a fatigue-test specimen of aluminum alloy 2024-T3, showing a portion of the region of final, fast fracture. Stress-intensity range (ΔK) was 21 MPa·m^{1/2} (19 ksi·in.^{1/2}); the stress was applied in an argon atmosphere at room temperature at a frequency of 10 cycles per second. The area has voids that may be moderate-size dimples. The vertical face is apparently a very large tear ridge or cleavage step joining two areas of dimpled rupture. See also 4025, 4026.



SEM fractograph

140×

4025 A different area of the fracture surface shown in 4024. This also exhibits vertical faces that are tear ridges. The surface is covered with voids, but at this low magnification it is not possible to decide whether or not they are dimples. The smooth central area outlined by the rectangle is shown enlarged in 4026.

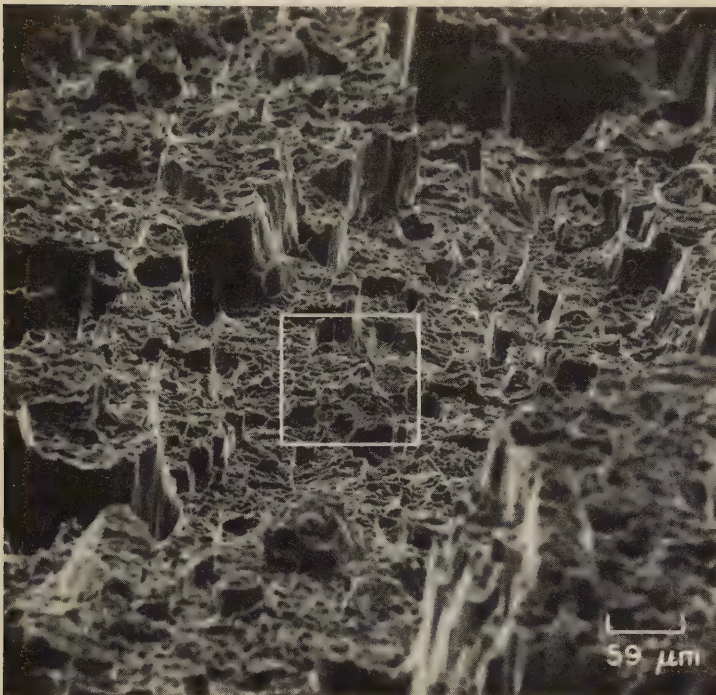


SEM fractograph

1400×

4026 A view of the rectangle-outlined area of the fracture surface in fractograph 4025, at higher magnification. With this enlargement, it is evident that the area is not truly smooth, but rather that it bears a uniform array of extremely fine fatigue striations. Near the right edge is a small area of minute dimples.

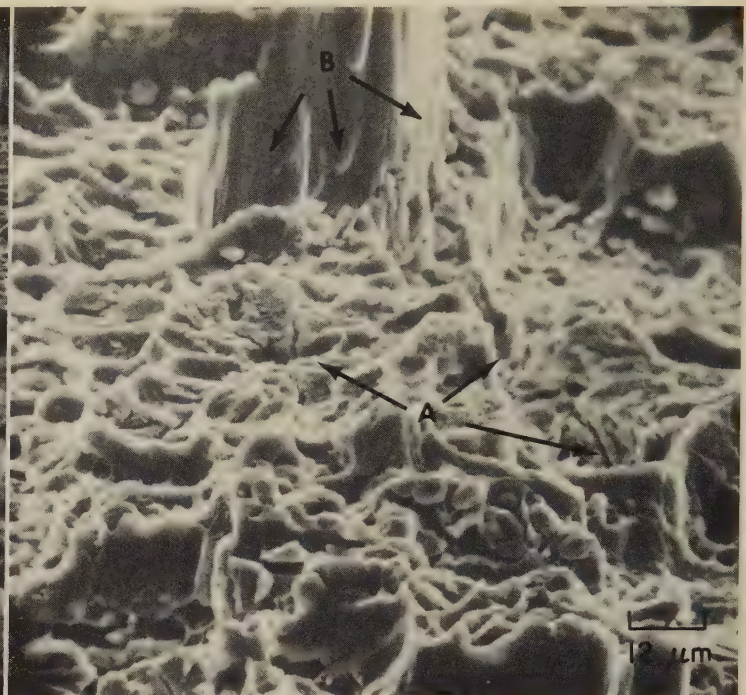
SEM Fractographs: Aluminum Alloy 2024-T3 Fractured in a Fatigue Test in Argon,
and Fractured in a Fatigue Test in a 3.5% NaCl Solution



SEM fractograph

170×

4027 Fracture surface of a fatigue-test specimen of aluminum alloy 2024-T3 tested at 23 C (73 F) in argon. The fatigue crack, similar in appearance to the one in 4025 (preceding page), was produced by a stress-intensity range (ΔK) of 24.8 MPa·m^{1/2} (22.6 ksi·in.^{1/2}) at a frequency of 10 cycles per second. Much of the surface shows features resembling dimples, but the vertical "cliffs" are probably delaminations along grain boundaries. See 4028, a higher-magnification view of area in rectangle.



SEM fractograph

850×

4028 Area outlined by the rectangle in fractograph 4027 (left), as seen at higher magnification. This view provides a much clearer delineation of the fine details of the fracture surface and shows a combination of dimpled rupture and grain-boundary separation. Intergranular secondary fissures such as those marked by the arrows at A led to the formation of the vertical "cliffs" shown here (arrows at B) and in fractograph 4027. Cracked and broken inclusions are visible at many locations.



SEM fractograph

260×

4029 Fracture surface of a fatigue-test specimen of aluminum alloy 2024-T3 that was tested in an environment of a 3.5% solution of NaCl in water. The stress-intensity range (ΔK) was 19.8 MPa·m^{1/2} (18 ksi·in.^{1/2}) at 10 cycles per second. The central region of this view contains patches of well-defined fatigue striations. In adjacent regions, there appear to be faintly defined striae that have been obscured by corrosion. In other regions, it is uncertain whether fatigue or cleavage was active. See 4030 (area in rectangle).

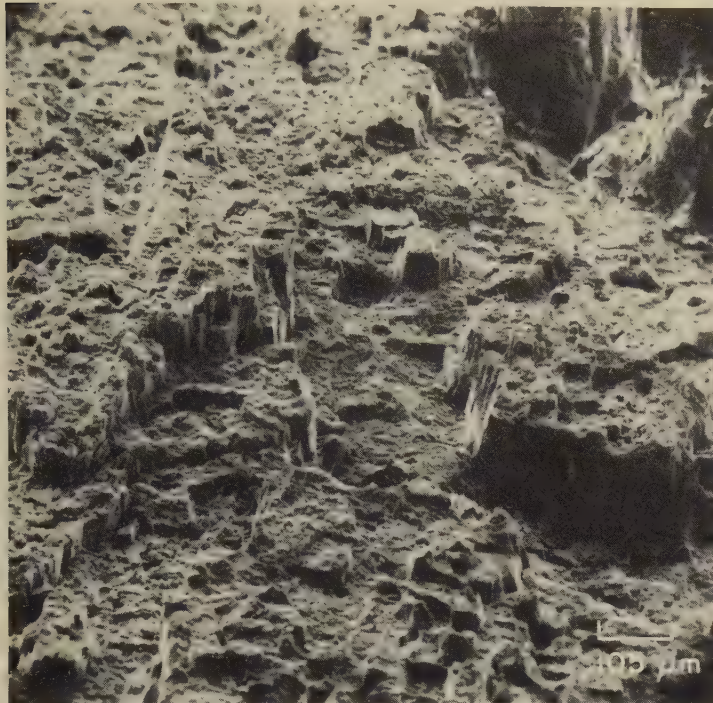


SEM fractograph

1320×

4030 A view at higher magnification of the area outlined by the rectangle in fractograph 4029, showing the fatigue striations in finer detail. Note that superimposed on the fine striations at somewhat irregular intervals is a system of fissures, or perhaps more pronounced striations; the presence of these features may reflect either a repetitive variation in strain amplitude or stress, or periodic interruptions in the applied stress cycle (which allowed locally increased corrosion), or both.

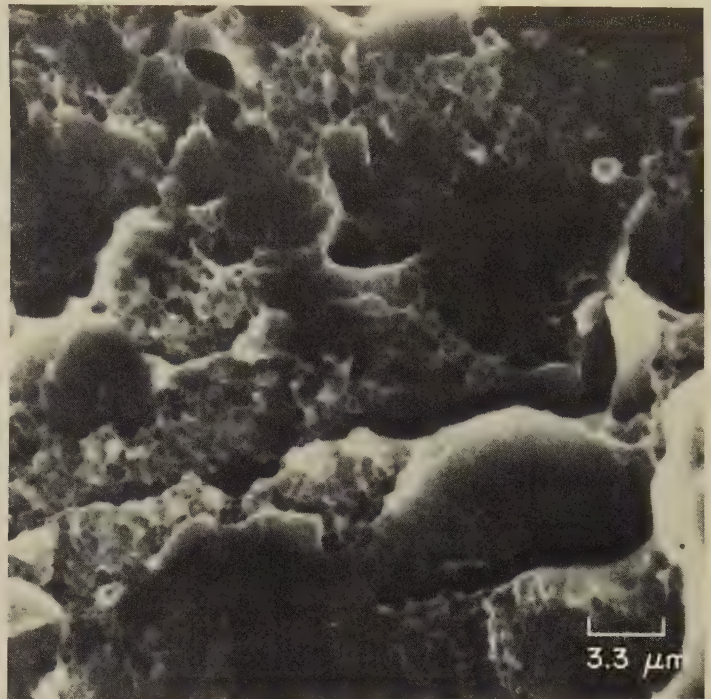
SEM Fractographs: Aluminum Alloy 2024-T3 Fatigue Tested in a 3.5% NaCl Solution (Continued);
Aluminum Alloy 7075-T6 Fractured by Tension Overload



SEM fractograph

95×

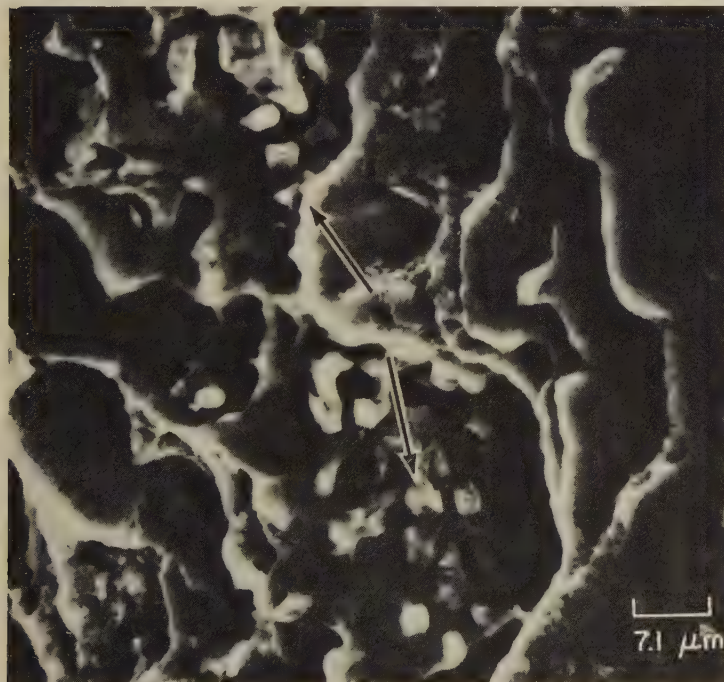
4031 Fracture surface in a specimen of aluminum alloy 2024-T3 that was fatigue tested in a 3.5% NaCl aqueous solution under the same conditions as for the specimen shown in fractograph 4029 except for a higher stress-intensity range of 24.2 MPa·m^{1/2} (22 ksi·in.^{1/2}). One small region (at lower right) may contain fatigue striations; otherwise, the surface appears to be the result of a brittle type of fracture.



SEM fractograph

3000×

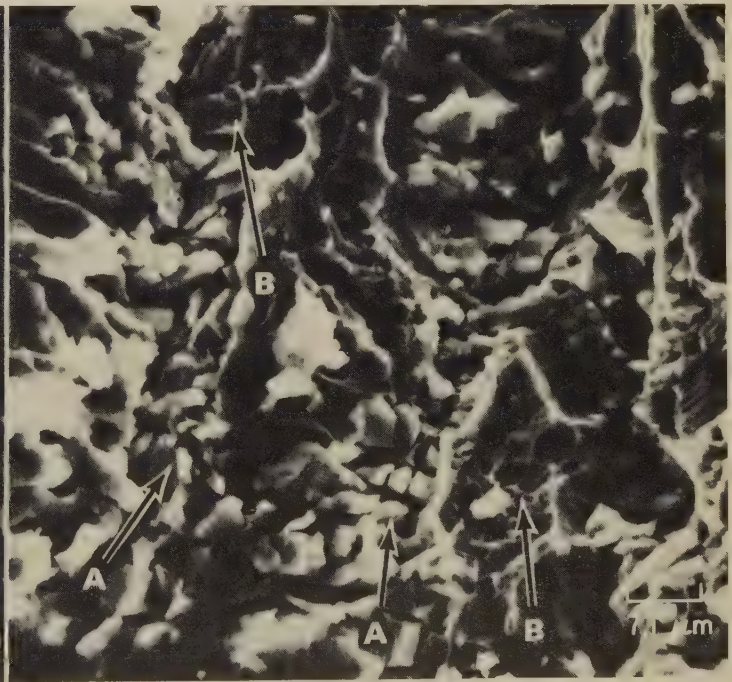
4032 Tension-overload fracture produced at room temperature in a specimen 1/8 in. wide by 1/2 in. long, cut from 0.03-in.-thick sheet of aluminum alloy 7075-T6 that had been solution heat treated at 460 C (860 F) and aged for 24 hr at 121 C (250 F). The material contained about 0.10 vol % of second-phase particles and was quite ductile, as evidenced by the small, equiaxed dimples. Compare with fractographs 4033 and 4034.



SEM fractograph

1400×

4033 Tension-overload fracture produced at room temperature in aluminum alloy 7075-T6 with the same heat treatment and specimen dimensions as described in 4032, but containing 0.54 vol % of second-phase particles. The plastic strain was 8%, which is less than the 13% for the specimen in 4032, but relatively large regions of ductile fracture are visible. Note the larger number of brittle particles here (arrows) than in 4032. See also 4034.

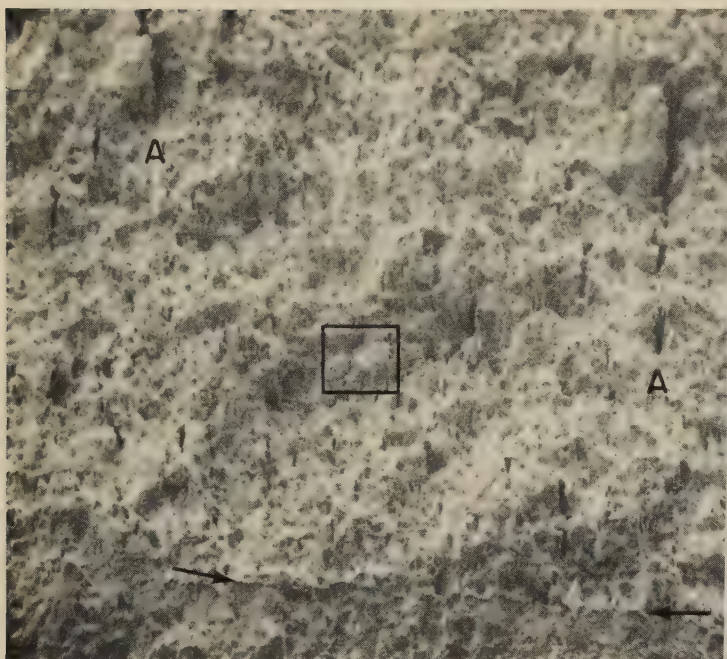


SEM fractograph

1400×

4034 A primarily brittle fracture produced in tension at room temperature in aluminum alloy 7075-T6 with the same heat treatment and specimen dimensions as in 4032 and 4033, but containing a large amount (1.19 vol %) of second-phase particles. Many of the second-phase particles are visible (arrows A). Equiaxed dimples are evident at locations where particles are absent (arrows B). Compare with the fracture surfaces in 4032 and 4033.

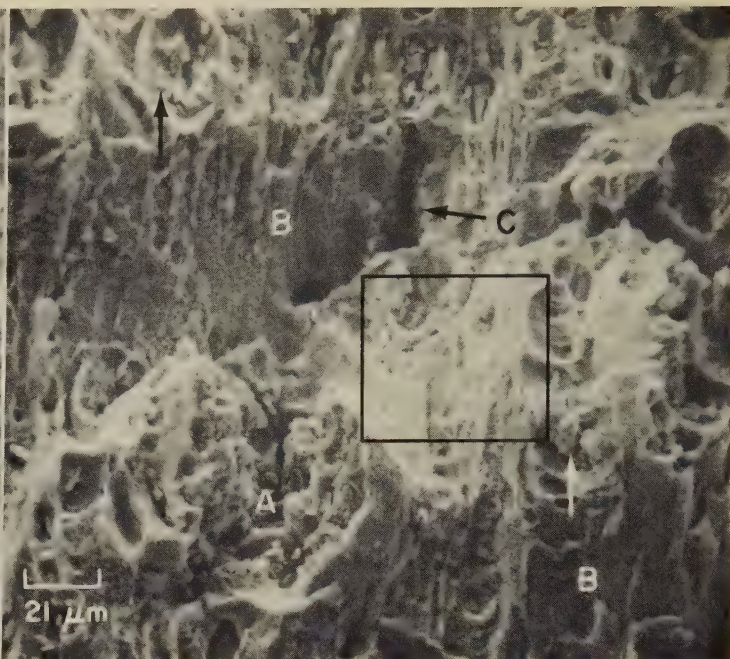
SEM Fractographs: Aluminum Alloy 7075-T6 Specimens Fractured in a Toughness Test and in a Short-Transverse Tension Test



SEM fractograph — gold shadowed

48×

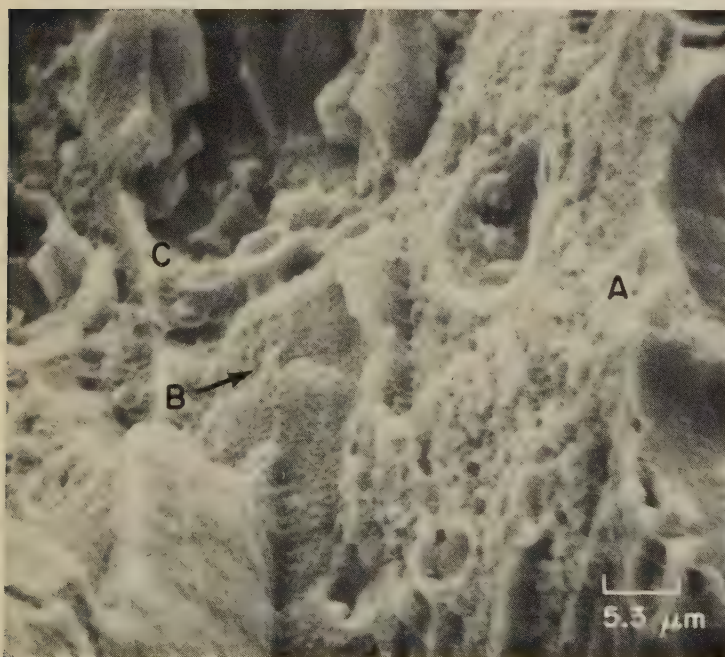
4035 Fracture surface of a fracture-toughness test specimen of aluminum alloy 7075-T6, showing the zone of transition from the fatigue-precrack region (below arrows) to the tension-overload plane-strain fracture region (above arrows). Specimen was aged 24 hr at 121 C (250 F); tensile strength was 593 MPa (86 ksi), and uniform elongation was 13%. Note the appreciable number of vertical delaminations (as at A's), which probably are grain-boundary separations, caused by the transverse tensile stress in the plane-strain region. Area in rectangle is shown enlarged in 4036.



SEM fractograph — gold shadowed

480×

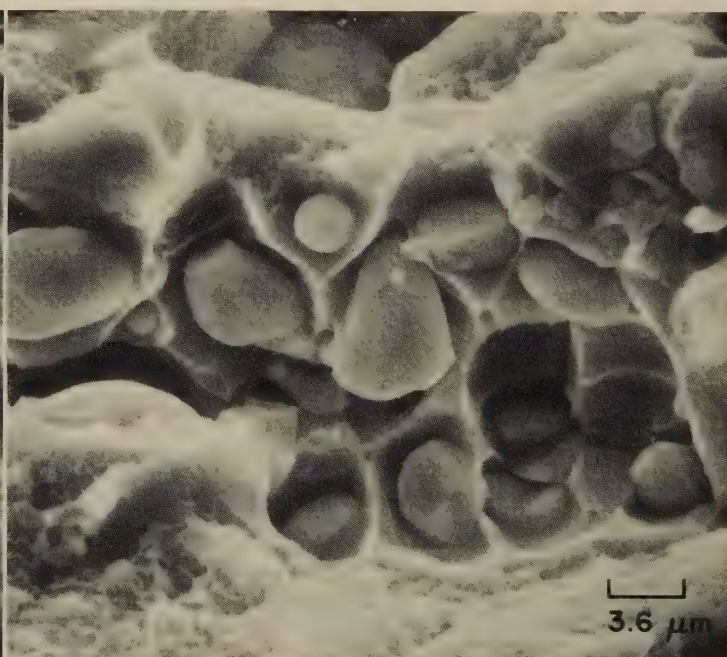
4036 Area outlined by the rectangle in fractograph 4035, as seen at ten times the magnification there. It is apparent that the matrix contained many second-phase particles that have undergone brittle fracture (arrows). The surface is quite complex, with some regions that appear to show clusters of minute dimples (A) and other regions that strongly resemble intergranular fracture (B's). At C is one of the numerous vertical fissures visible in 4035, presumably elongated during tension overload. See 4037 for a higher-magnification view of area in rectangle here.



SEM fractograph — gold shadowed

1900×

4037 Higher-magnification view of the area in the rectangle in fractograph 4036. At A is a region of extremely fine dimples, which are slightly out of focus. At B, there appear to be grain-boundary facets bearing small, very shallow dimples. At C are fragments of a number of second-phase inclusions, many of which have separated from their original pockets in the matrix.

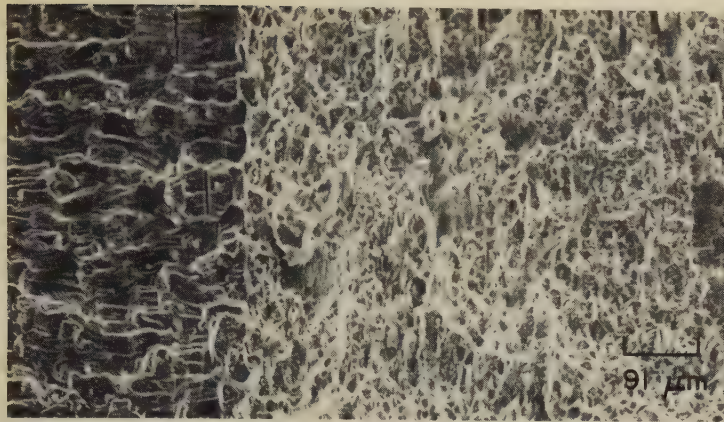


SEM fractograph

2800×

4038 Tension-overload fracture in the short-transverse plane of a specimen of aluminum alloy 7075-T6. At top and bottom are regions of quite small dimples. In the central portion of this view are large pockets in which the cleaved facets of intermetallic inclusions are visible. These inclusions, which are rich in iron and silicon, are only slightly bonded to the walls of the pockets.

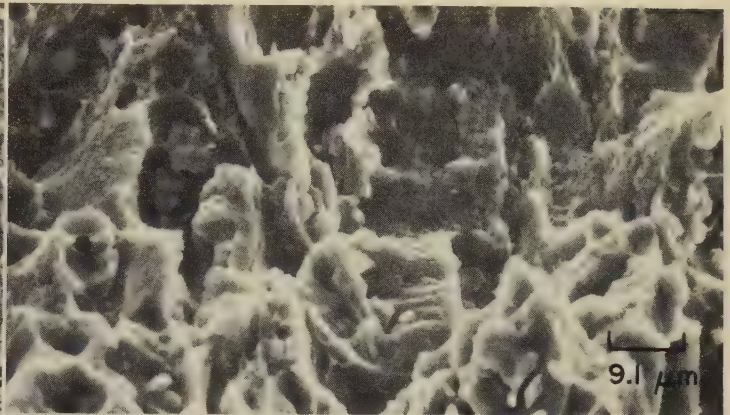
SEM Fractographs: Aluminum Alloy 7075-T6 Specimens Fractured in Slow-Bend Fracture-Toughness Tests in Air and in Mercury Vapor



SEM fractograph

110×

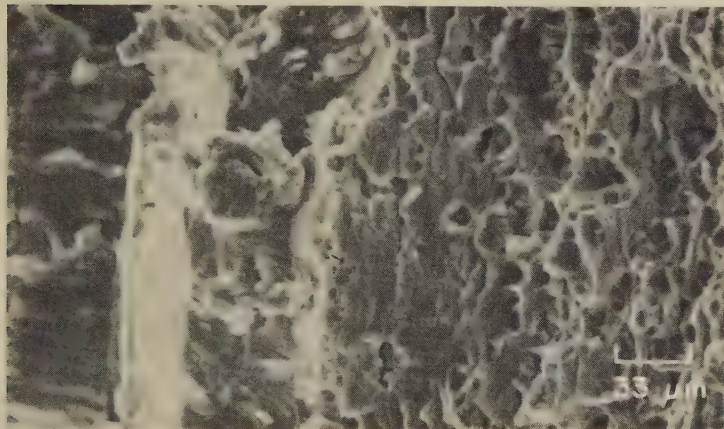
4039 Specimen of aluminum alloy 7075-T6 broken in a slow-bend fracture-toughness test in air. Dark area, at left, is the fatigue-precrack surface, which shows no fatigue striae. At right is the tension-overload fracture surface; here, the surface appears dimpled, although this is uncertain at only 110×. See 4040.



SEM fractograph

1100×

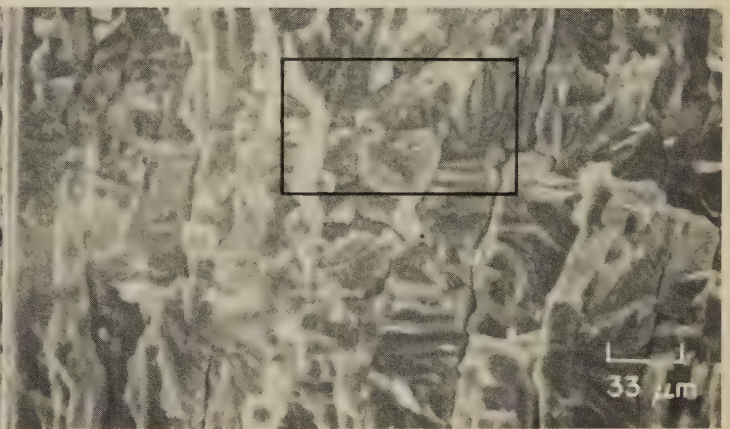
4040 A portion of the tension-overload fracture surface in 4039, as seen at ten times the magnification there, which reveals fine details. A number of medium-size dimples contain inclusions, some of which are broken. In contrast are the minute dimples visible at left and right in the upper portion of this view.



SEM fractograph

300×

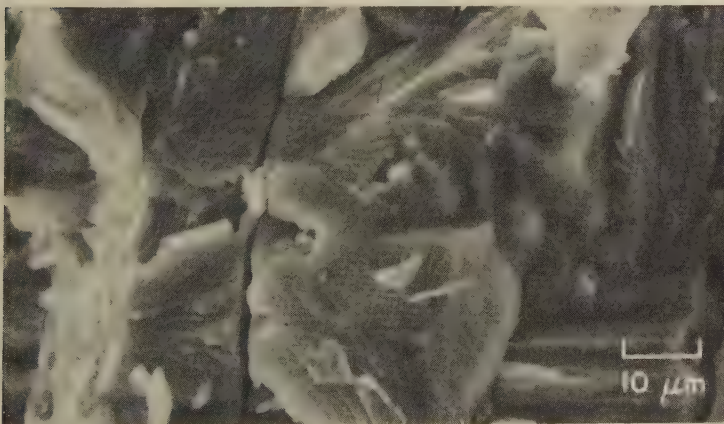
4041 View of the transition between a slow-bend fracture induced in mercury vapor (left of center) and one occurring in air (right of center) in a specimen of aluminum alloy 7075-T6. The fracture induced in mercury vapor appears to have occurred by cleavage; the fracture in air exhibits dimples, which increase in frequency toward the right side of this fractograph.



SEM fractograph

300×

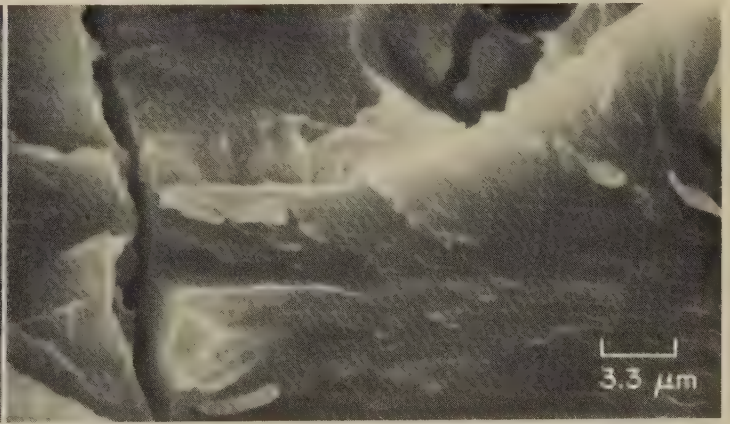
4042 Fracture surface of an aluminum alloy 7075-T6 specimen broken in a slow-bend fracture-toughness test in mercury vapor. Obviously, a completely brittle fracture. Many facets show faint characteristics of quasicleavage. Note the large number of secondary cracks, possibly at grain boundaries, all of which are more or less parallel. Area in rectangle is shown enlarged in 4043.



SEM fractograph

1000×

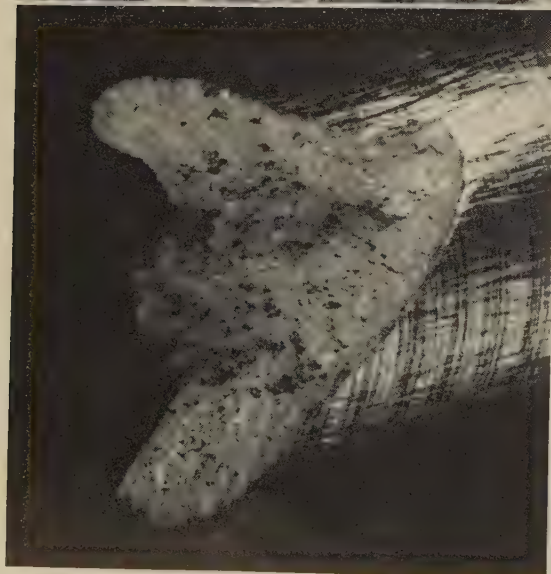
4043 Higher-magnification view of the surface contours outlined by the rectangle in 4042. This reveals the cleavage river patterns quite clearly; note the changes in fracture direction at right. This view also reveals the depth and continuity of the secondary cracks. See also fractograph 4044, at right.



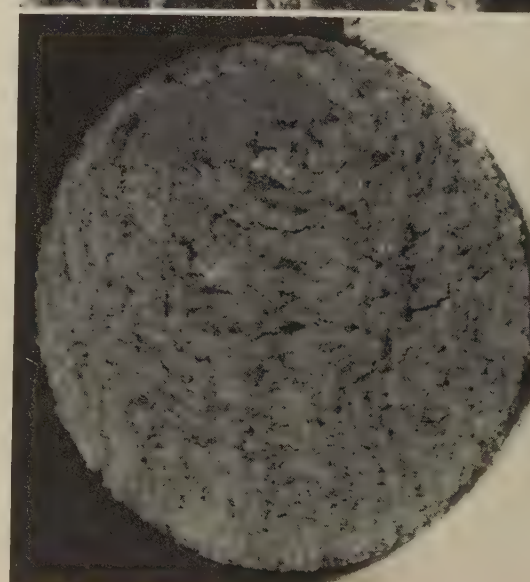
SEM fractograph

3000×

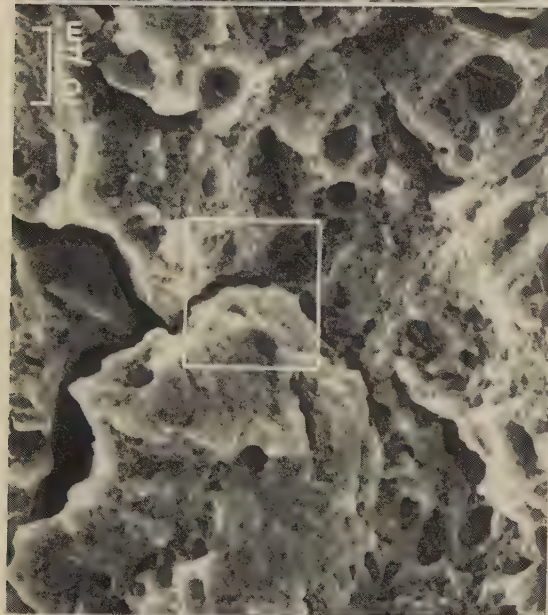
4044 Another view, at still higher magnification, of the fracture surface in 4042 and 4043. At top is what appears to be a pocket holding a cracked inclusion. The remainder of the surface shows cleavage facets plus projections that are somewhat similar to the tongues seen in cold fractures of iron.



Light fractograph
4045 Surface of a tension-overload fracture in an unnotched specimen of aluminum alloy 7075-T6 having tensile strength of 520 MPa (75 ksi), with 22% reduction in area. Surface is coarsely fibrous; shear lip has formed two opposing lobes. See also 4046 and 4047, at right.



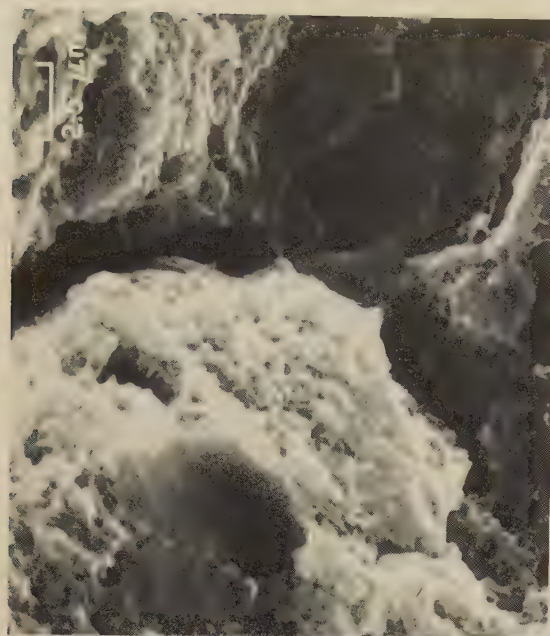
Light fractograph
4048 Tension-overload fracture in notched specimen of aluminum alloy 7075-T6. Notched tensile strength, 750 MPa (109 ksi); unnotched tensile strength, same as 4045. Surface is flat and coarsely fibrous. Considerable secondary cracking is evident, even at this low magnification. See 4049 and 4050.



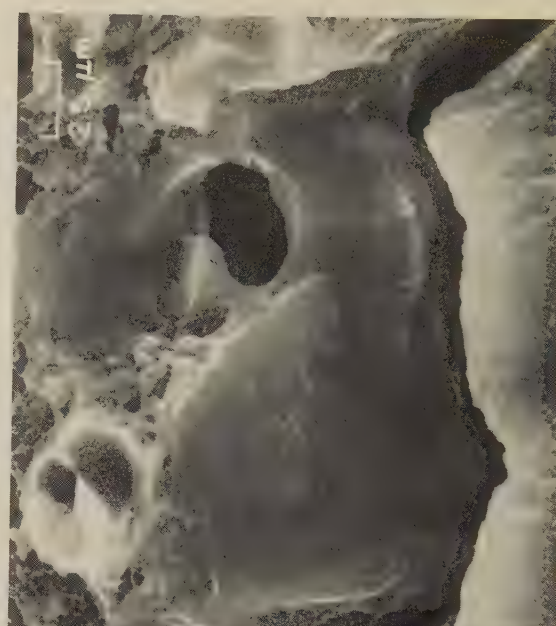
SEM fractograph
4046 A scanning electron microscope view of the central area of the fracture surface in 4045. Although this is a ductile rupture, it contains very deep secondary cracks. The major pores were sites of alloy second-phase particles that are no longer in place. See 4047 for an enlarged view of area in rectangle.



SEM fractograph
4049 A scanning electron microscope view of the interior of the fracture surface in 4048. This shows that in general the secondary cracking is intergranular, although the primary rupture is not. Numerous pores contain alloy second-phase particles. See 4050.



SEM fractograph
4047 Enlarged view of the fracture-surface area outlined by the rectangle in 4046. The higher magnification here makes it possible to observe the fine size of the dimples, which in general is less than half a micron. This is a remarkable uniformity of size in a fracture surface as rough as this one.



SEM fractograph
4050 Higher-magnification view of the area outlined by the rectangle in 4049. This fourfold enlargement makes visible the fine dimples surrounding the particle sites. Note that the surfaces of the secondary grain-boundary cracks are remarkably smooth.

Light Fractographs and SEM Fractographs: Aluminum Alloy 7075-T6 Specimens Fractured in Low-Cycle and in High-Cycle Fatigue Tests



4051 Cone-shaped fracture surface produced by low-cycle fatigue in aluminum alloy 7075-T6 (same mechanical properties as in 4045). Loading was tension-tension with $R = 0.1$ and a maximum loading of 310 MPa (45 ksi). Fracture occurred at 26,000 cycles. See also fractographs 4052 and 4053.

Light fractograph

6×



4054 High-cycle fatigue fracture in aluminum alloy 7075-T6 (same mechanical properties as in 4045) loaded in tension-tension with $R = 0.1$ and a maximum loading of about 159 MPa (23 ksi). Fracture was at 548,000 cycles. Gauge near center is post-test mechanical damage. See also 4055, at right.

Light fractograph

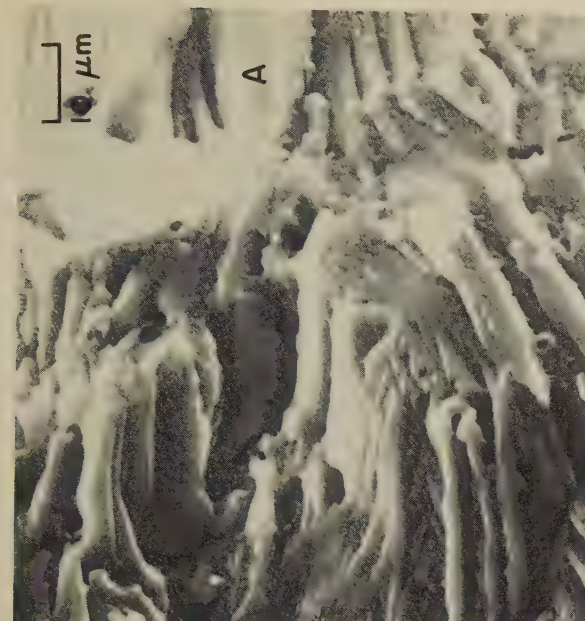
6×



4052 Scanning electron microscope view of a very complex surface found near the outer edge of the fracture in 4051, believed to have formed principally by severe deformation by slip. There appears to be a complete absence of secondary cracks. See 4053.

SEM fractograph

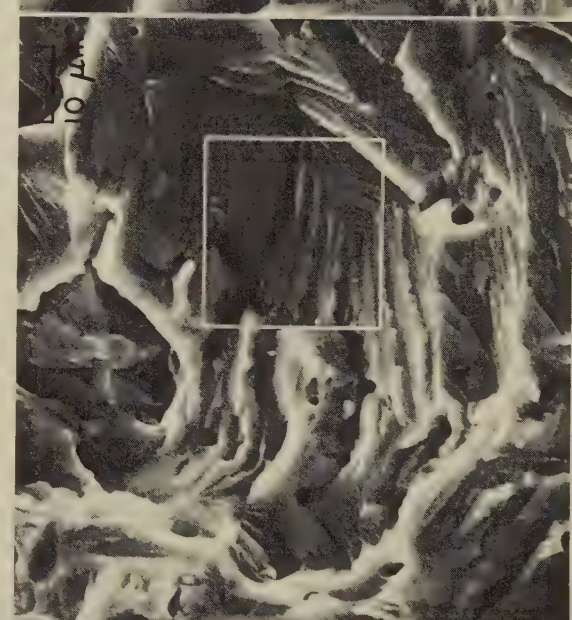
300×



4053 A view at higher magnification of the area in the rectangle in 4052. Fatigue striations with a spacing of about $0.5 \mu\text{m}$ were discerned at region "A" when magnified at 4000 \times , oriented at a slight angle counterclockwise to the vertical edge of this print.

SEM fractograph

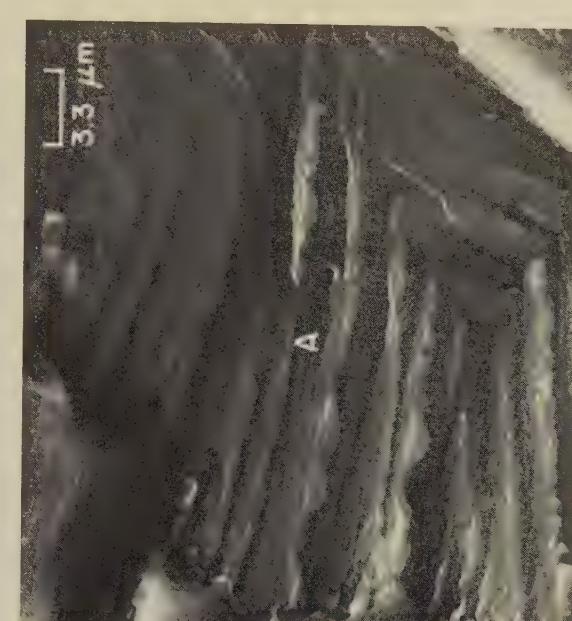
1000×



4055 A view of the fracture surface in 4054 that is very similar to the view of the low-cycle fracture surface in 4053. It is believed that the steplike formations resulted from a slip mechanism. Secondary cracks are not visible. See fractograph 4056.

SEM fractograph

1000×



4056 Area outlined by the rectangle in 4055, as seen at triple the magnification there. Fatigue striations, which are about an order of magnitude smaller than the steplike formations, are faintly visible parallel with the edges of the "steps", as at area "A".

SEM fractograph

3000×

Light and SEM Fractographs: Aluminum Alloy 7075-T6 Wing-Spar Carry-Through Forging That Fractured in Service by Fatigue



Light fractograph

About $3\frac{1}{2}\times$

4057 Surface of a crack in an aircraft wing-spar carry-through forging of aluminum alloy 7075-T6. The crack was discovered during inspection after 5269 hr of service and was opened up. The external surface at edge C-C had been machined after forging. The regions marked "A" contain fatigue features that originated at a flaw (marked B-B) extending the full length of the segment. Area at "O" is shown enlarged in 4058. See also 4059 to 4064.



SEM fractograph

60×

4058 An SEM view, at higher magnification, of the area at "O" in 4057. At left of the boundary (dark line running up from "A") is the surface of the flaw (B-B in 4057); at right of it is a fatigue surface ("A" at right in 4057). Note the beach marks just above mid-height in the fatigue surface (at arrows).



SEM fractograph

400×

4059 A typical region in an area "A" of 4057. Fatigue striations that are nearly vertical (arrow) are faintly visible. These were found to be parallel to the flaw (B-B in 4057) in both "A" areas in 4057. Scattered dimples are evident in locations adjacent to the fatigue striations. See also 4060, at right.

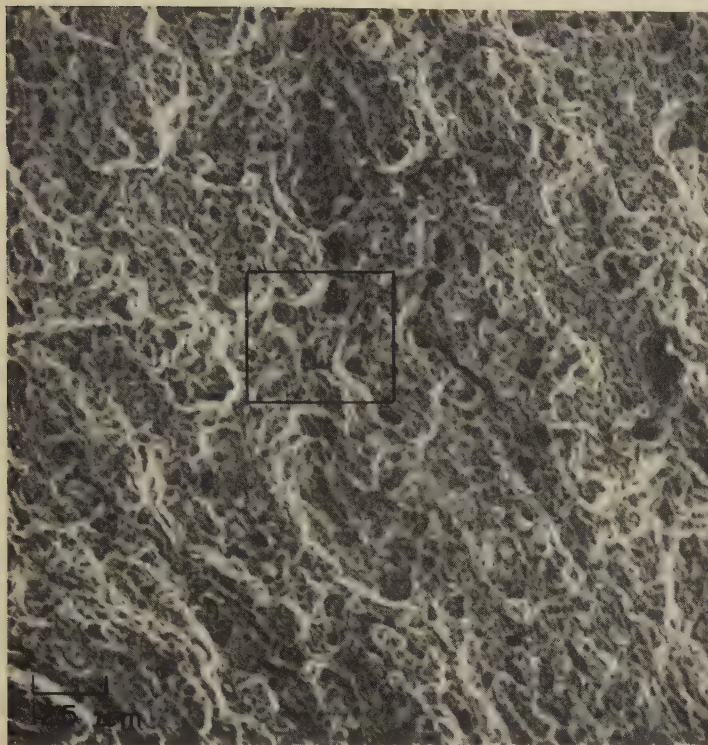


SEM fractograph

3000×

4060 Highly magnified view of fatigue striations typical of those in areas "A" in 4057. In general, these striations were parallel with the flaw B-B. Dimples characterized the remainder of the fracture. Inclusions near the flaw suggested that it was the result of a pipe not cropped from the ingot.

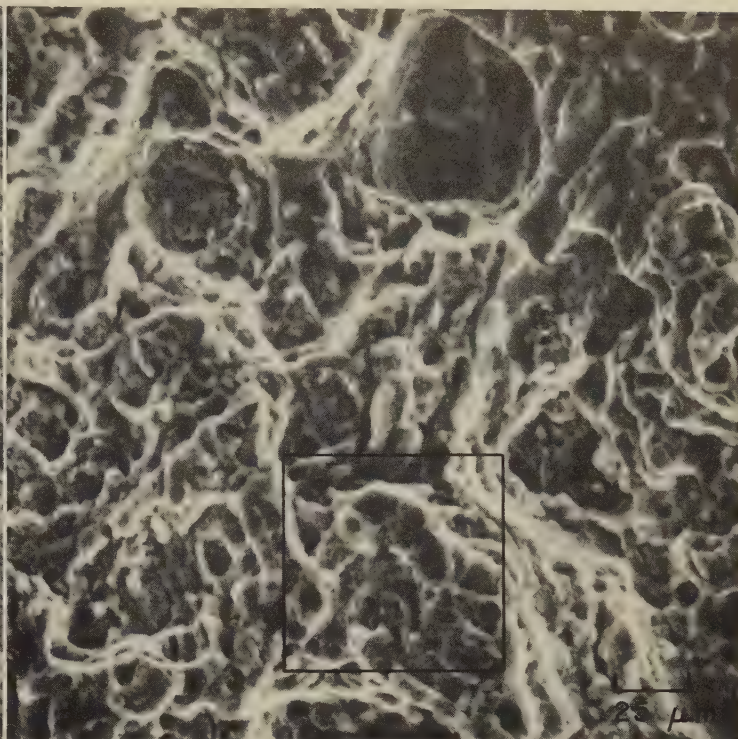
SEM Fractographs: Aluminum Alloy 7075-T6 Wing-Spar Carry-Through Forging That Fractured in Service by Fatigue (Continued)



SEM fractograph

80×

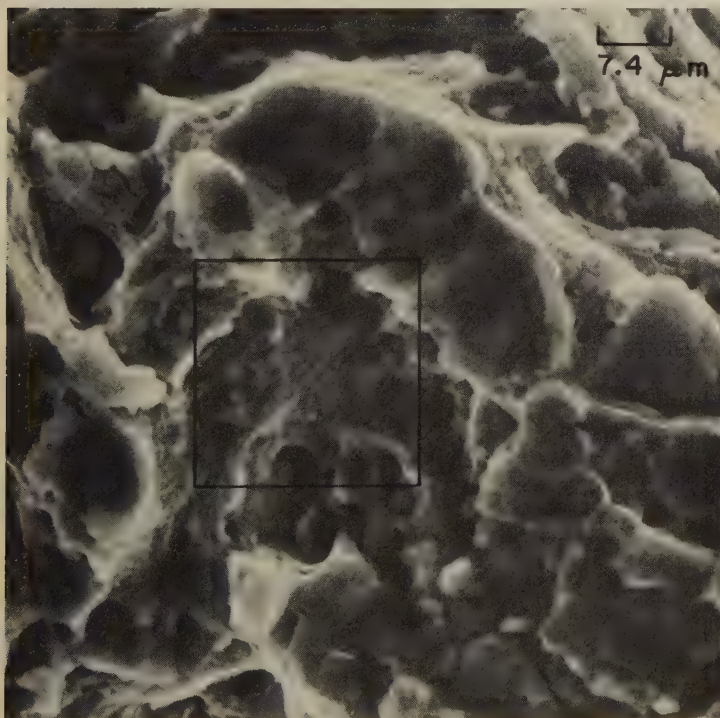
4061 A region of the overload portion of the fracture in 4057 (opposite page). This region, which exhibits the dimples characteristic of ductile rupture, is representative of the entire fracture except for areas "A", and flaw B-B, in 4057. Scattered large dimples contain visible inclusions. See also 4062.



SEM fractograph

400×

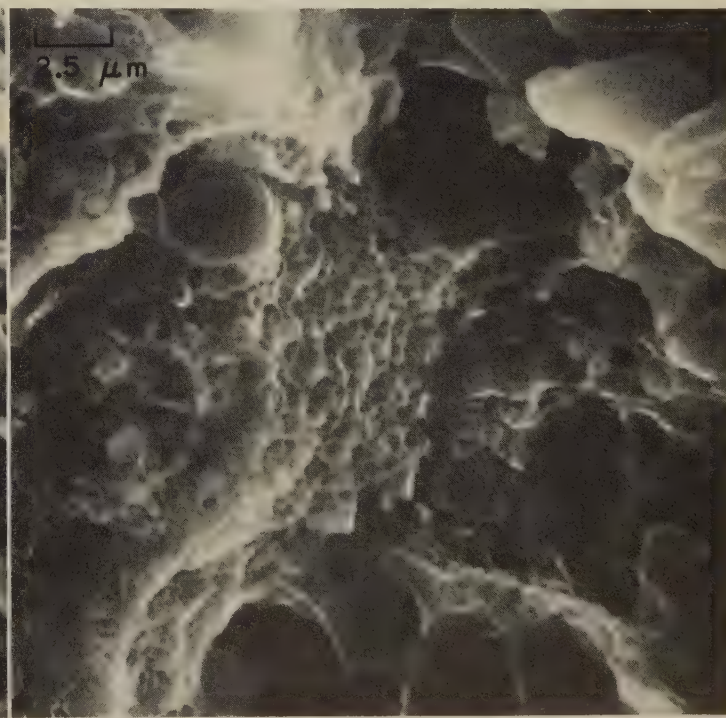
4062 Area outlined by the rectangle in fractograph 4061, as seen at five times the magnification there. Large dimples show the inclusions that initiated them; fine dimples that are too small to be resolved at this magnification exist among the large dimples. See also fractograph 4063 (below, at left).



SEM fractograph

1340×

4063 A view at still higher magnification of the area in the rectangle in 4062. The fine dimples can just be distinguished on the surfaces adjacent to the large dimples. Many alloy second-phase particles are discernible, although some are so deep within the dimples as to be nearly invisible. See also 4064.



SEM fractograph

4000×

4064 A greatly magnified view of the fracture region in 4061, showing the area outlined by the rectangle in 4063. The region at center is made up of equiaxed dimples of quite uniform size. Note that several dimples are too deep for their bottoms to be lighted by an exposure proper for most of the dimples.

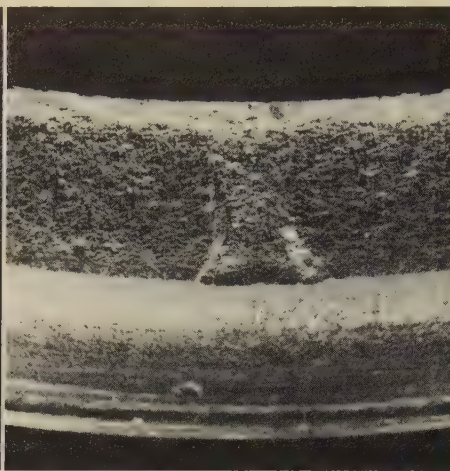
Photograph, Light Fractographs, SEM Fractographs: Aluminum Alloy 7075-T6
Aircraft Shock-Strut Piston That Fractured in Service by Fatigue



Photograph

5/8×

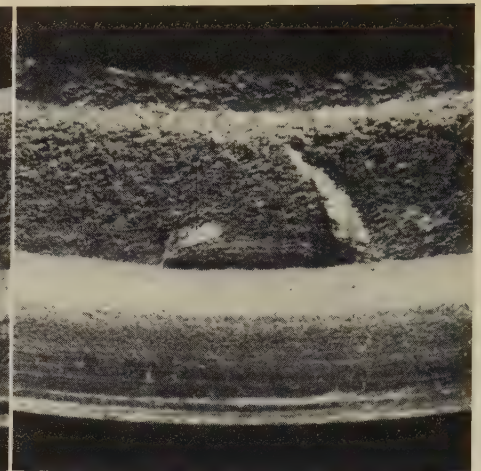
4065 An aircraft shock-strut piston, of aluminum alloy 7075-T6, that fractured by fatigue in service. Hardness was Rockwell B 80. Numerals identify areas that received specific examination. See fractographs 4066 to 4076.



Light fractograph

5×

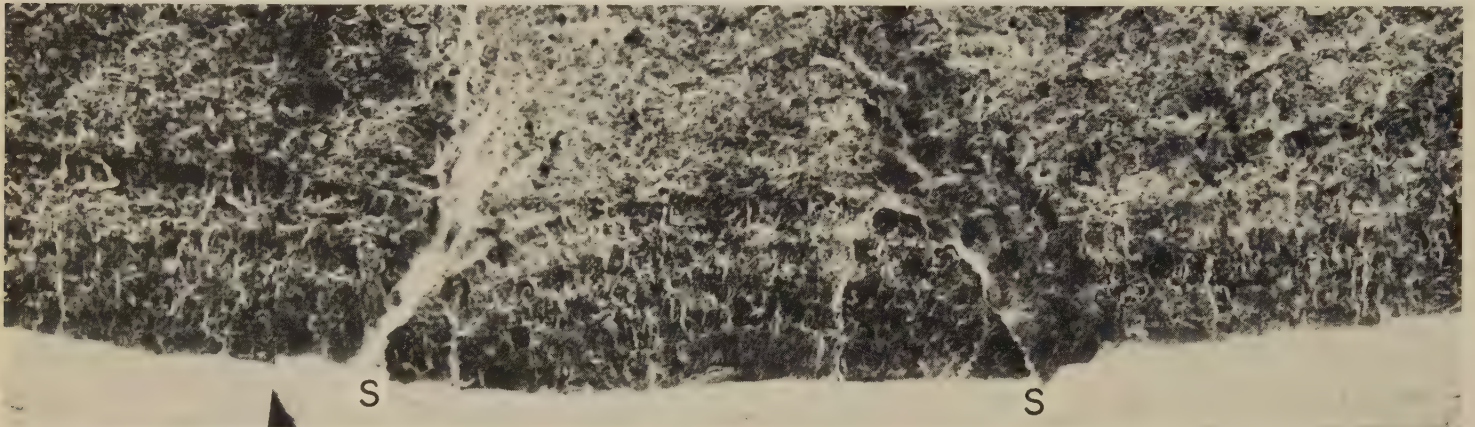
4066 A larger, more detailed view of the fracture in 4065, at area 1. (A brief examination of area 2 of the fracture showed that it had virtually identical characteristics.)



Light fractograph

5×

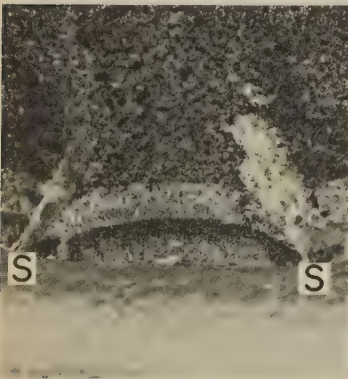
4067 A magnified view of area 3 of the fractured piston in 4065. (Area 4 was also examined, and found to have equivalent characteristics.) More details of area 3 are shown in 4068 to 4076.



SEM fractograph (composite)

27×

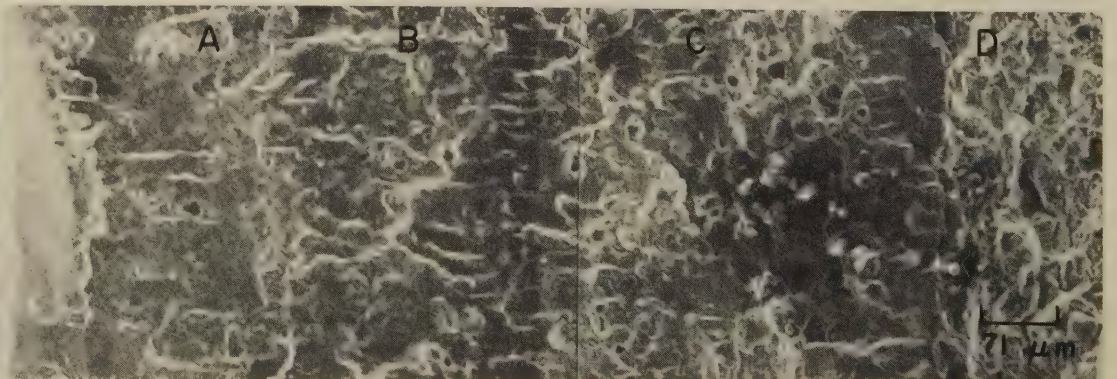
4068 This is a composite of four SEM views that were taken at the location of a suspected fatigue origin in area 3 of the piston fracture in 4065. (The location shown here lies at about the center of the view of area 3 shown in 4067.) The piston had been shot peened to provide compressive surface stresses as a protective measure against fatigue. The peened surface is at bottom in this view. The crescent-shaped area S-S was determined by stereo scrutiny to lie in a plane lower than the fracture face around it. The appearance of the edge of the fracture suggests that fatigue beach marks exist not only within the crescent but also on either side of it. See 4069, 4070.



Light fractograph

12×

4069 Area 3 of fracture in 4065, at a magnification intermediate between those of 4067 and 4068, showing definite marginal zones on either side of crescent (S-S).

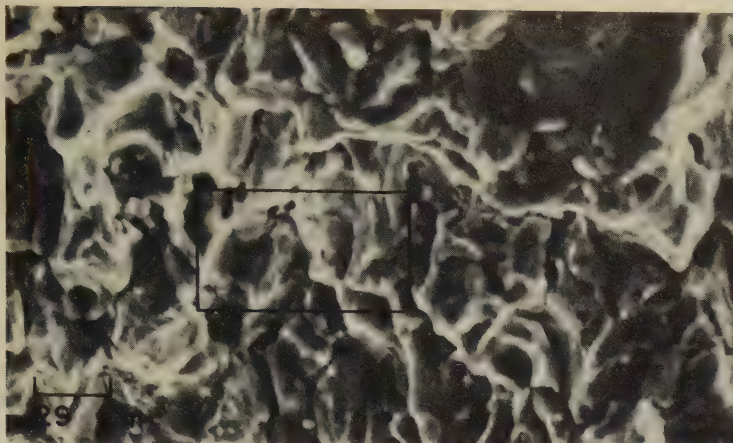


SEM fractograph (composite)

140×

4070 A composite view of the center of the crescent marked S-S in fractograph 4068. Zone A corresponds to the lower light zone of the crescent in 4069, which is adjacent to the shot peened surface. The dark appearance of zone B here (and of same zone in 4069) is due to a film of contamination, which resisted all efforts at removal by ultrasonic cleaning. High magnification revealed fatigue striations in zone C. Zone D is the beginning of the final overload fast fracture. No specific cause of fracture initiation was found other than local areas of inadequate shot peening. See also 4071 to 4076.

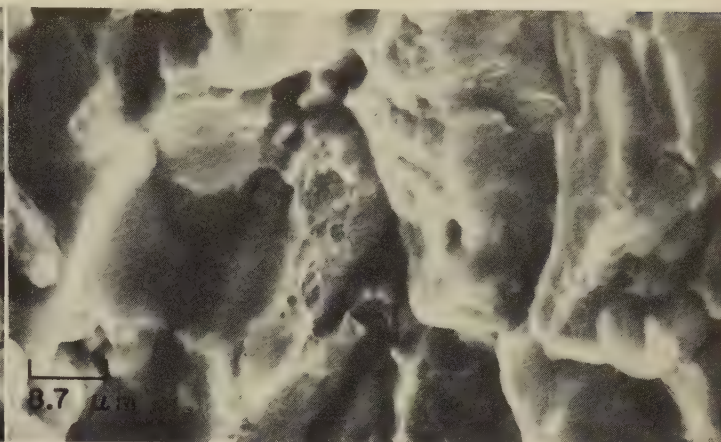
SEM Fractographs: Aluminum Alloy 7075-T6 Aircraft Shock-Strut Piston That Fractured in Service by Fatigue (Continued)



SEM fractograph

350X

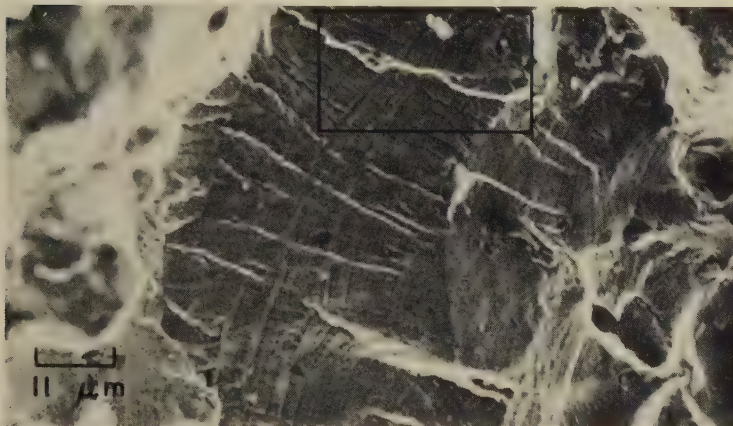
4071 Enlarged view of zone D in 4070, showing features that are typical of that region of final overload fast fracture. Many pores are visible that undoubtedly contained alloy second-phase particles earlier. The rectangle-outlined central region (shown enlarged in 4072) contains barely recognizable fine dimples.



SEM fractograph

1150X

4072 Area outlined by the rectangle in fractograph 4071 (left), as viewed at a higher magnification. Here, tiny dimples are resolved in the facets at upper center. These dimples are of a size very different from that of the large pores visible in the lower portion of the fractograph.



SEM fractograph

935X

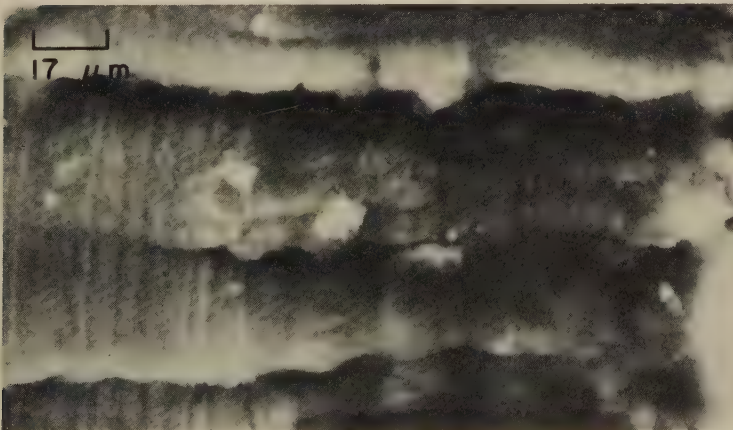
4073 View of zone C in 4070, showing fatigue striations. In general, lines drawn normal to the striations would point to the center of crescent S-S in 4068 and 4069 as the crack origin. Exceptions due to local grain orientations are also visible. Similar striations were on both sides of the crescent. See 4074.



SEM fractograph

3175X

4074 A view at higher magnification of the area in the rectangle in fractograph 4073. This shows the details of the fatigue striations present in zone C of 4070 much more clearly. Note the very small fatigue patches, separated by steps; the crack fronts of these patches merged again after a very few stress cycles.



SEM fractograph

580X

4075 A view of the fracture surface at the line of demarcation between zones B and C in fractograph 4070. Zone B is to the right here, and zone C is to the left. The film of contamination in zone B, which obscured essentially all the fatigue features, is very apparent. See also fractograph 4076, at right.

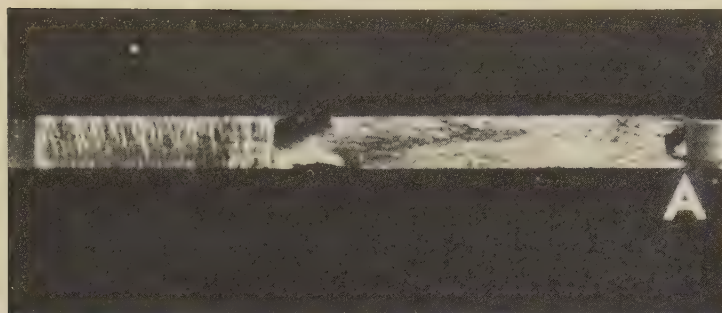


SEM fractograph

7000X

4076 View at another region at the demarcation between zones B and C in 4070, which is even more abrupt than in the view shown in fractograph 4075 (at left). It seems obvious that the source of the corrosion was suddenly eliminated, perhaps by a change of service, since there is no sign of any gradual transition.

Light and SEM Fractographs: Aluminum Alloy 7075-T6 Bomb-Rack Side Plate That Fractured by Fatigue Initiating at a Corrosion Site



Light fractograph

4077 Fatigue-fracture surface of a bomb-rack side plate fabricated of aluminum alloy 7075-T6. Saw marks at left were made in opening up the fatigue crack for study. Crack origin was found to be at the edge of an attachment hole (marked "A", at right). See 4078 for a view of the area near "A" at five diameters.



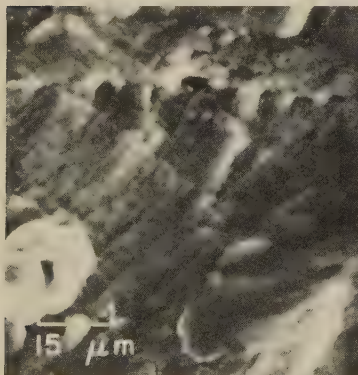
Light fractograph

4078 An enlarged view of the area near "A" in 4077, showing corrosion (in dark area at right end) at the site of crack initiation. The side plate had been used as a fuel-tank support element in a 25-hr ground-level qualification test of the tank in a corrosive environment under spectrum loading. See also 4079.



SEM fractograph (composite)

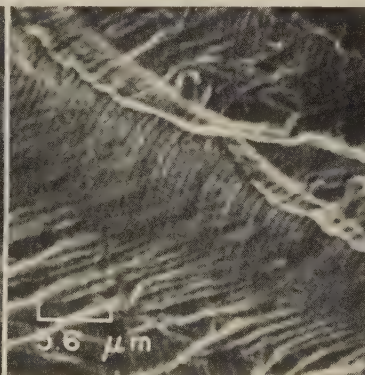
4079 A composite of three low-magnification SEM fractographs of the surface of the fatigue fracture at "A" in 4077 after ultrasonic cleaning. A small portion of the attachment hole is visible along the top of this view. The lack of beach marks here is perhaps due to the brevity of the test (25 hr). Attempts to locate the exact point of crack initiation were not successful, because of the presence of tool marks at the edge of the attachment hole. It is believed, from the orientation of the fatigue striations at "W", "X", "Y" and "Z" (see 4080 to 4083 for enlarged views of these areas), that the crack began at top right, near the edge of the attachment hole.



SEM fractograph

670×

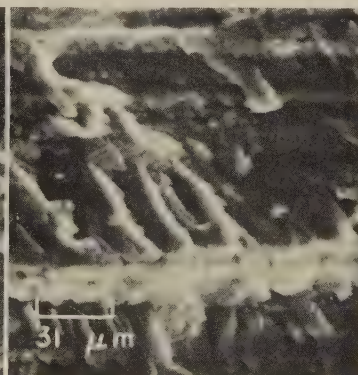
4080 Area Z in 4079, which shows clear, well-defined fatigue striations. Normals to the striations point to the crack origin at the nearby corner of the attachment hole.



SEM fractograph

1800×

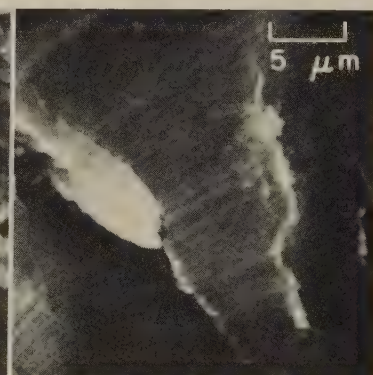
4081 Area W in 4079, showing very regular fatigue striations. Like those in 4080, the striations here are oriented so that normals to them point to the corner near area Z.



SEM fractograph

320×

4082 Area Y in 4079. This area, which is near the midthickness of the side plate, shows a herringbone pattern with ten times the spacing of the fatigue striations in 4081.

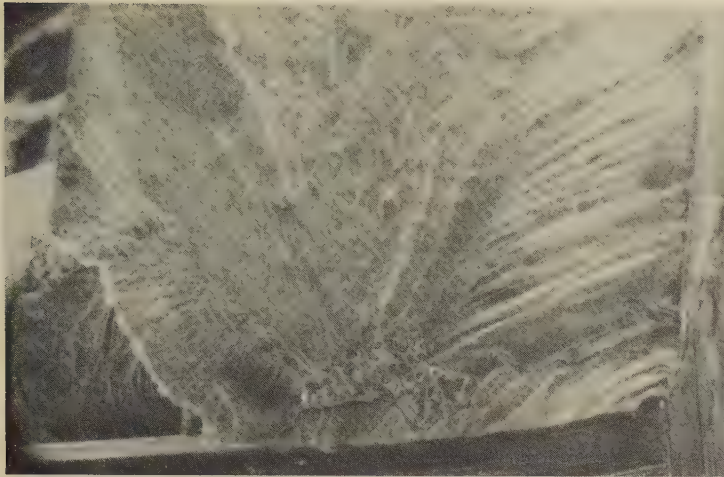


SEM fractograph

2000×

4083 View of area X in fractograph 4079. This area, which is near the top left corner of the attachment hole, shows numerous fatigue facets that contain striations.

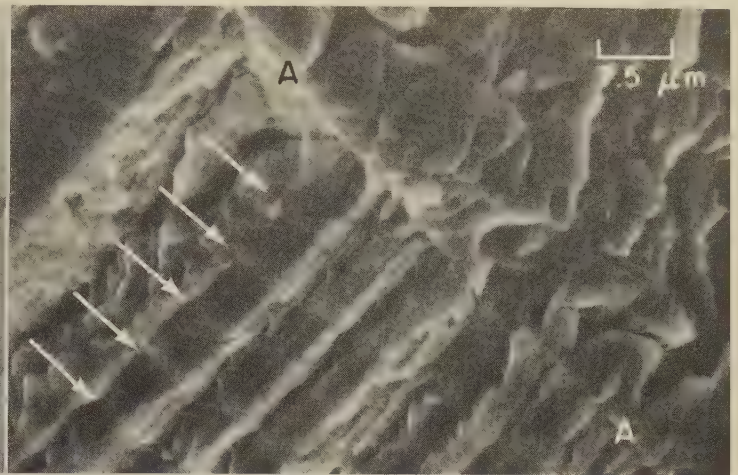
SEM Fractographs: Aluminum Alloy 7075-T6 Specimens Fractured in Fatigue Tests in Air, in Distilled Water, and in a 3.5% NaCl Solution



SEM fractograph

26×

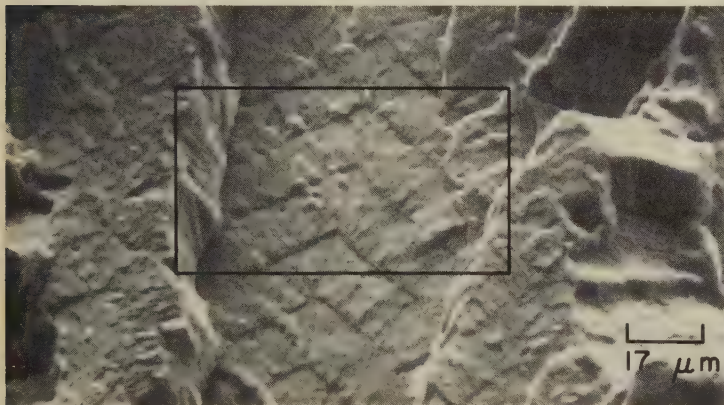
4084 Fatigue fracture in a notched plate specimen of aluminum alloy 7075-T6 subjected to cyclic stresses in air. (Notch is at bottom; sides of plate, at far left and right.) It is apparent that the fracture consists of at least three cracks that formed on various planes and temporarily grew independently.



SEM fractograph

1325×

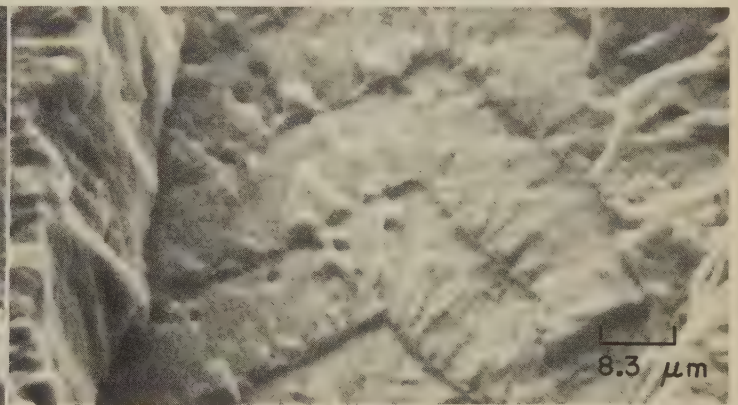
4085 Fatigue fracture in a specimen of aluminum alloy 7075-T6 tested in air. The surface exhibits a pattern of brittle, widely spaced striations (at arrows) that are nearly parallel to a grain boundary (A-A). The tensile component (wide, flat region) of each striation was formed by a cleavage mechanism of fracture.



SEM fractograph

600×

4086 Corrosion-fatigue fracture in a specimen of aluminum alloy 7075-T6 tested in distilled water. Surface exhibits fatigue striations. The unusual sharp angle in the striations defines the location of a nearly vertical grain boundary, in the central grain. Area in rectangle is shown at higher magnification in 4087.



SEM fractograph

1200×

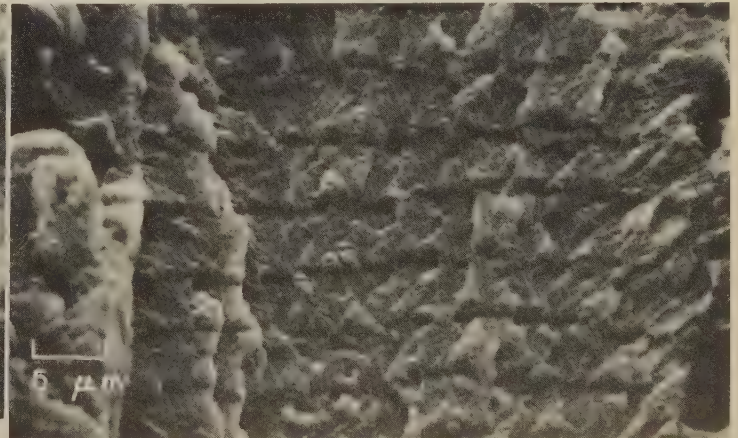
4087 A view of the area in the rectangle in 4086, at double the magnification there. Observe the wide, flat regions of the fatigue striations; these regions have progressed by cleavage. The unusual angled shape of the striations is the result of adherence of the crack fronts to crystallographic directions.



SEM fractograph

500×

4088 Corrosion-fatigue fracture in a specimen of aluminum alloy 7075-T6 that was tested in a 3.5% NaCl solution. Surface shows two types of striations: at left and at lower right are grains with ductile striations, and between them lies a grain with pronounced brittle striations. See also fractograph 4089.

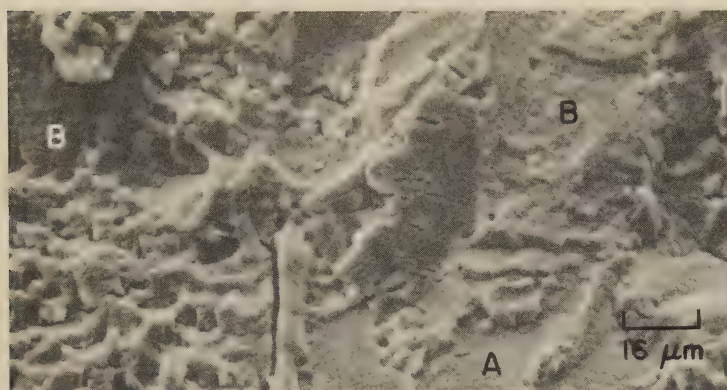


SEM fractograph

2000×

4089 Brittle striations in a corrosion-fatigue fracture in a specimen of aluminum alloy 7075-T6 that, like the specimen in 4088, was tested in a 3.5% NaCl solution. Striations (horizontal here) have very uniform spacing.

SEM Fractographs: Aluminum Alloy 7075-T6 Fatigue Tested in 3.5% NaCl Solution With Different Applied EMF; Cast 7075-T6 Fatigue Tested in 3.5% NaCl Solution



SEM fractograph

625×

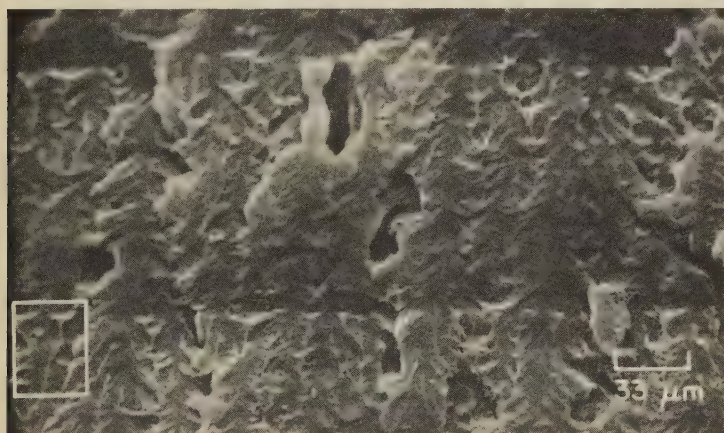
4090 Corrosion-fatigue fracture in aluminum alloy 7075-T6 tested in a 3.5% NaCl solution. During testing, specimen was subjected to an applied electrical potential of -0.700 mv as measured against a standard calomel electrode. A mixture of ductile striations (at A) and brittle striations (at B) is evident, with some fissures. See also fractograph 4091.



SEM fractograph

640×

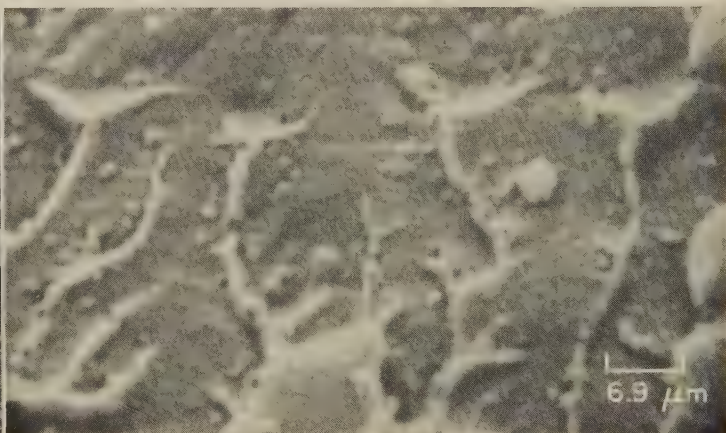
4091 Corrosion-fatigue fracture in a specimen of aluminum alloy 7075-T6 that was tested in a 3.5% NaCl solution and, during testing, was subjected to an applied electrical potential of -1.200 mv (versus -0.700 mv for specimen in 4090). Surface shows brittle striations that exhibit typical topography; there is no evidence of striation fissures here. See also 4092.



SEM fractograph

300×

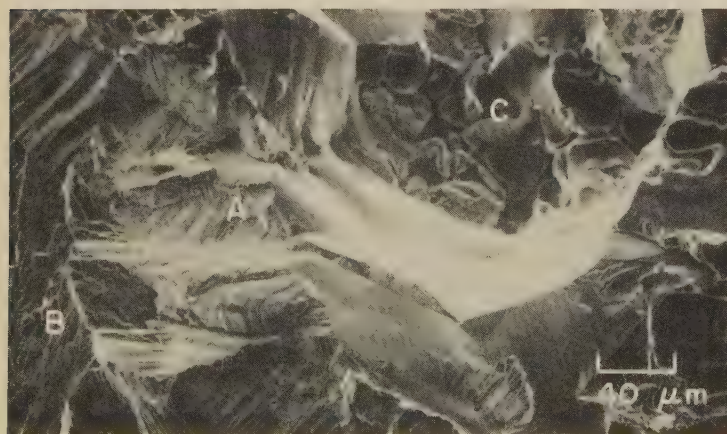
4092 Corrosion-fatigue fracture in a specimen of aluminum alloy 7075-T6 that, like the specimen in 4091, was tested in a 3.5% NaCl solution while subjected to an applied electrical potential of -1.200 mv. Note the extremely large striation spacing; only two readily apparent adjacent brittle-striation peaks are included in this view. See also fractograph 4093, at right.



SEM fractograph

1450×

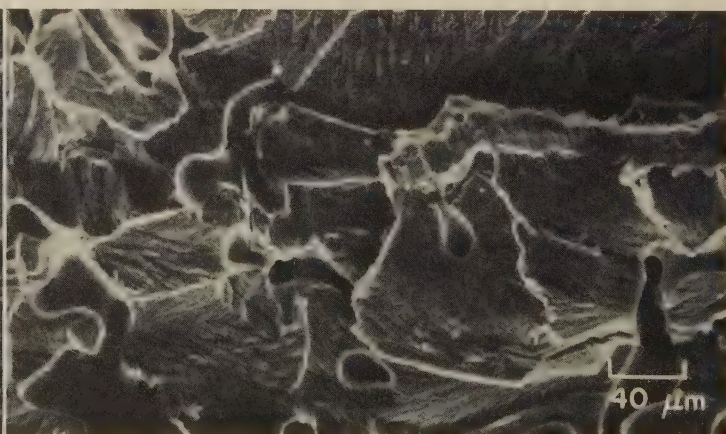
4093 A higher-magnification view of the fracture in 4092, showing an area of which the right half is outlined by the rectangle there. The wide, flat portion of a single striation is visible, beginning at the peak near the top. The surface configuration in this region of cleavage separation suggests a set of river patterns, exaggerated by corrosion products.



SEM fractograph

250×

4094 Fatigue-fracture surface of a test bar cast from aluminum alloy 7075, aged to the T6 temper and then tested in a 3.5% NaCl solution. A diagonal region of fatigue striations is visible at A; this region abuts areas of intergranular fracture (at B) and interdendritic porosity (at C).

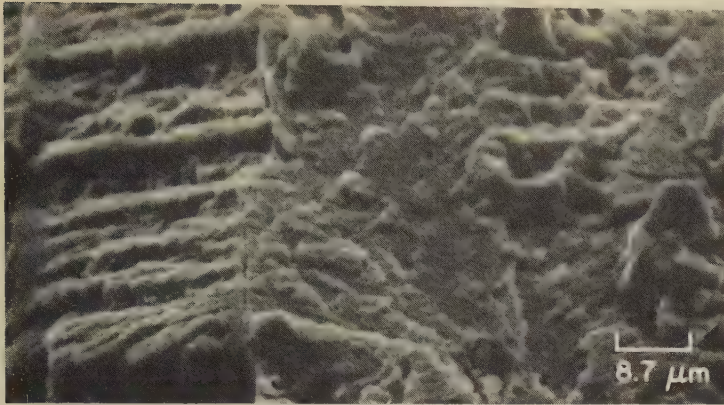


SEM fractograph

250×

4095 Fatigue fracture in a cast single-crystal specimen of aluminum alloy 7075 that was aged to the T6 temper and then tested in a 3.5% NaCl solution. Most of the view is filled with an interdendritic network of solidification porosity, which did not halt or blunt the fatigue crack.

SEM Fractographs: Aluminum Alloys 7075-T6, 7075-T651 and 7475-T6 That Were Fractured in Fatigue Tests in a 3.5% NaCl Solution



SEM fractograph

1150×

4096 Surface of a corrosion-fatigue fracture in a specimen of aluminum alloy 7075-T6 that was tested in a 3.5% NaCl solution. Shown here are portions of two grains that exhibit brittle striations; the difference in appearance of the striations in the two grains is caused by the difference in grain orientation. The vertical dividing line is the boundary between the grains.



SEM fractograph

120×

4097 An area of the corrosion-fatigue fracture surface of an aluminum alloy 7075-T651 specimen that was tested in a 3.5% NaCl solution under a cyclic stress-intensity range (ΔK) of 6.6 MPa·m^{1/2} (6 ksi·in.^{1/2}) at 10 cycles per second. Ductile and brittle striations would be expected in such a fracture but cannot be resolved at this magnification. See also fractograph 4098.



SEM fractograph

110×

4098 Another area of the fracture surface of which a portion is shown in 4097. This possesses similar features, but the surface is flatter, lacking the bluflike cleavage steps present in 4097. Again, fatigue striations are unresolved. See 4099.



SEM fractograph

560×

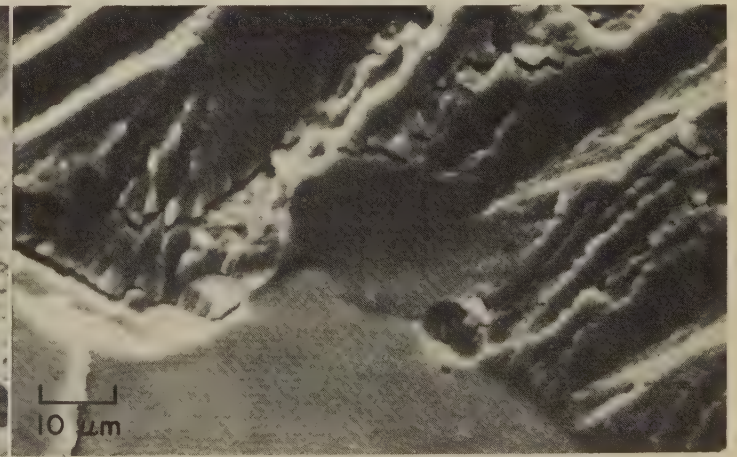
4099 Area in the rectangle in 4098, at higher magnification, showing the edge of the smooth area believed to possess patches of ductile striations. Compare these features with those of the 7475-T6 specimen (also tested in 3.5% NaCl) in 4100, 4101.



SEM fractograph

100×

4100 Corrosion-fatigue fracture in aluminum alloy 7475-T6 tested in a 3.5% NaCl solution under a cyclic stress-intensity range (ΔK) of 13 MPa·m^{1/2} (12 ksi·in.^{1/2}) at 10 cycles per second, showing contrasting features: ductile striations (unresolved) in smooth regions; brittle striations in adjacent grains. See 4101.



SEM fractograph

1000×

4101 Area outlined by the rectangle in fractograph 4100, as seen at ten times the magnification there, which makes the fine fatigue striations in the smooth region clearly visible. Above are brittle striations forming, at a steep incline, what is in effect a cleavage step up to a second fracture level.

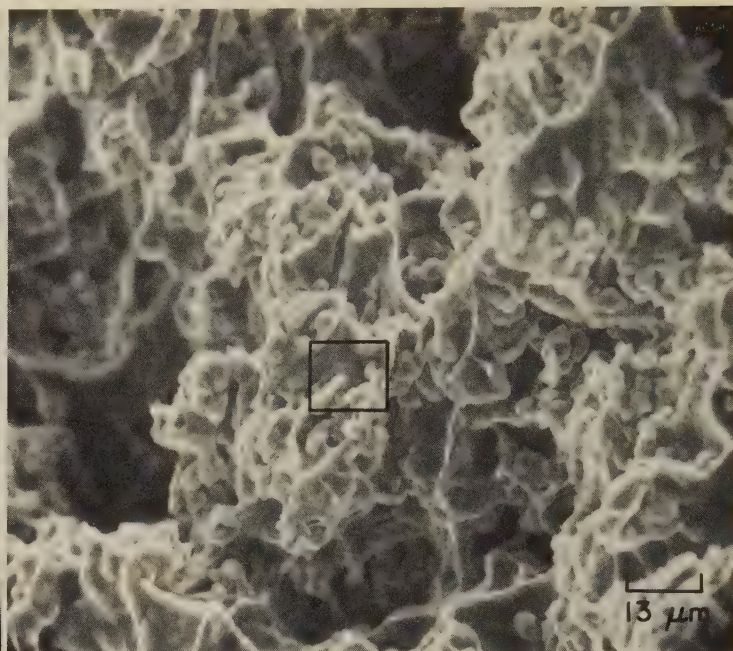
SEM Fractographs: Specimens of 67Al-33Cu Superplastic Eutectic Alloy Having Different Grain Sizes, Fractured by Tensile Overload at 450 C (842 F)



SEM fractograph

70×

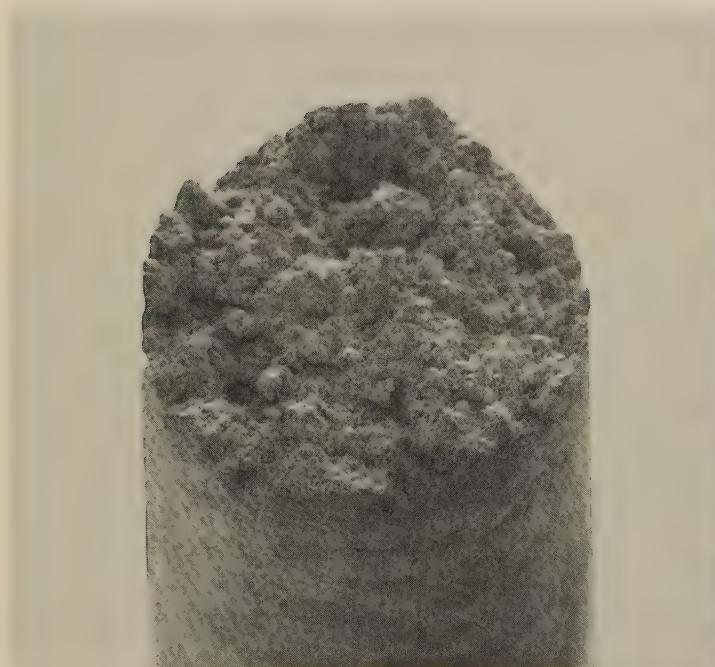
4102 Tensile-overload fracture in a specimen of a superplastic eutectic alloy containing 67% Al and 33% Cu. The material was cast, and the as-cast ingot was extruded at 430 C (806 F). Testing was performed at 0.001 in. per second and at a controlled temperature of 450 C (842 F). The surface shows coarse dimples and an irregular contour. There is some suggestion of a shear lip, but it is not sharply defined. See also 4103 (right).



SEM fractograph

770×

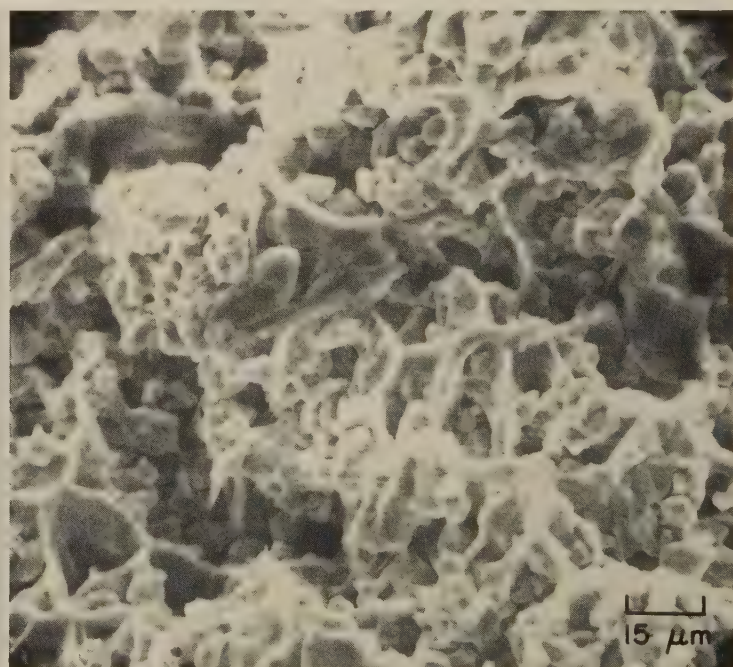
4103 A higher-magnification view of the area in the rectangle in fractograph 4102 (left), showing more clearly the details of the fracture surface. It should be noted that the grain size of this specimen is approximately 7 μm. Note also that a majority of the dimples contain one or more particles — probably particles of the CuAl₂ phase of the eutectic. See 4106 (opposite page), a higher-magnification view of area in rectangle here.



SEM fractograph

26×

4104 Surface of a tensile-overload fracture in a specimen of 67Al-33Cu superplastic eutectic alloy that was cast, extruded and tested exactly the same as the specimen in fractograph 4102 (above). The grain size of this specimen is 10 μm, compared with 7 μm for the specimen in 4102. The fracture surface shown here is fully as rough as that in 4102, but here there is no suggestion of a shear lip. See also fractograph 4105 (right).

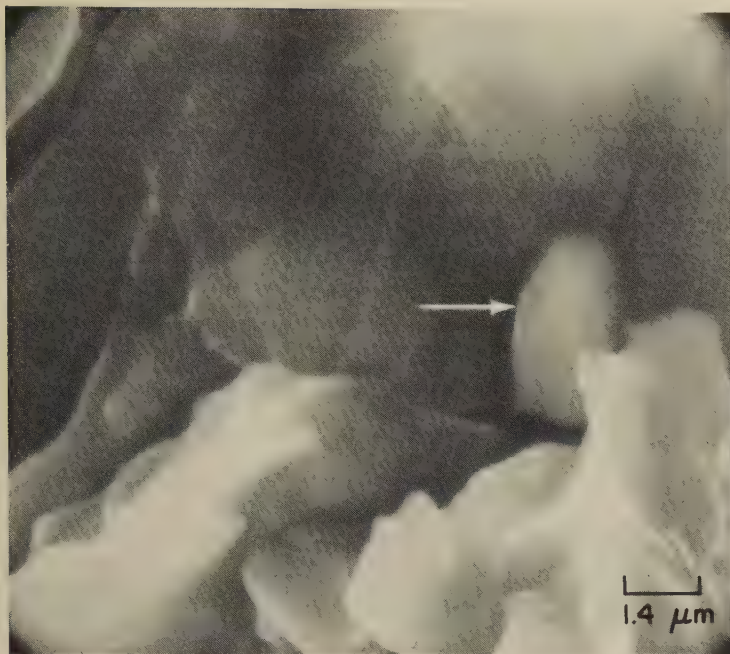


SEM fractograph

670×

4105 View of a region at the center of the fracture surface in 4104, shown at higher magnification. The dimples contain particles of the CuAl₂ phase of the eutectic that are similar in size and, for the most part, in contour to those in 4103. There does not appear to be much adherence of these particles to the matrix. The difference in grain size here and in 4103 is not apparent because of the difference in magnification. See also 4108.

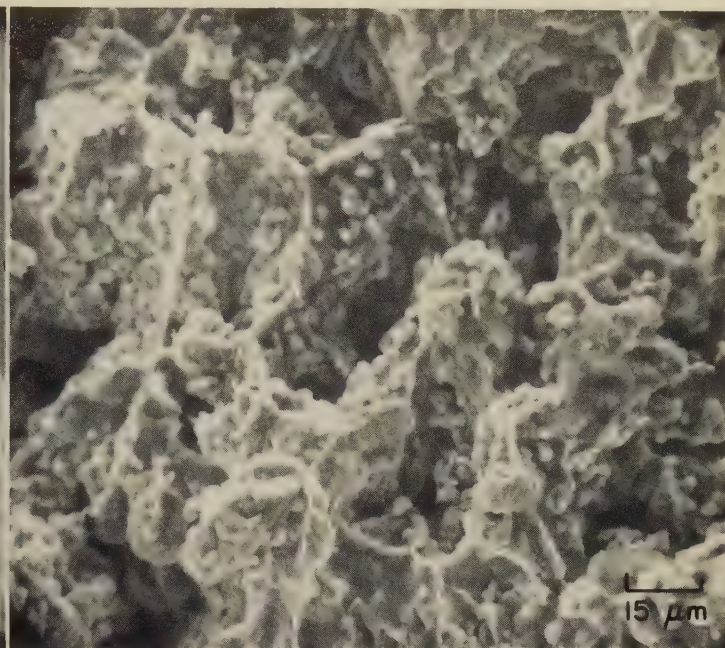
SEM Fractographs: Specimens of 67Al-33Cu Superplastic Eutectic Alloy
Fractured by Tensile Overload at 450 C (842 F), Continued



SEM fractograph

7000×

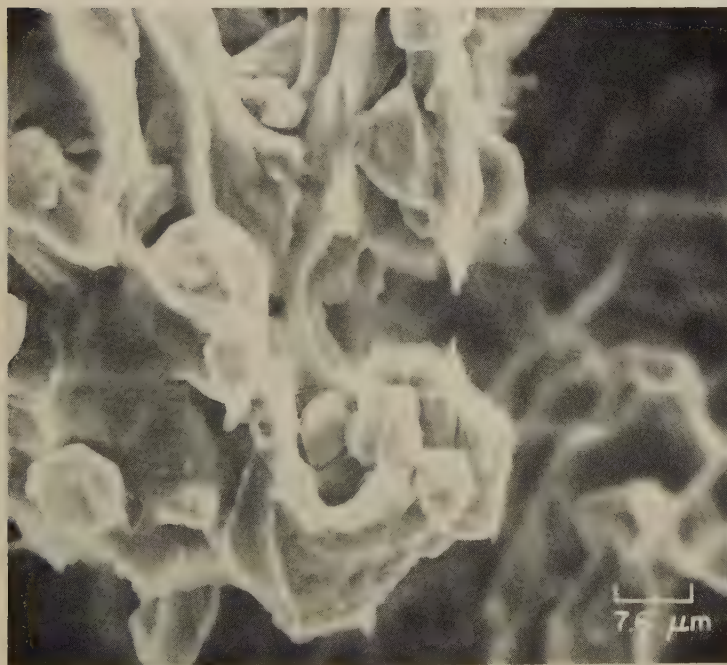
4106 Higher-magnification view of the area in the rectangle in fractograph 4103 (opposite page, top row). The contours of the facets in the right foreground demonstrate that the aluminum solid-solution matrix phase of this eutectic alloy was highly ductile. In the right background, at arrow, is a spheroidal particle that should be of the CuAl_2 phase; most of the surface of this particle appears to be detached from the matrix.



SEM fractograph

670×

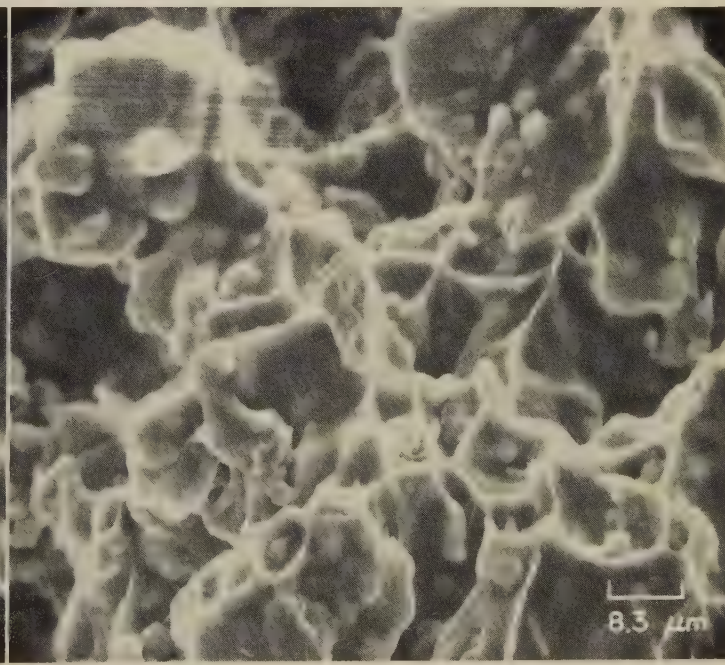
4107 Tensile-overload fracture in a specimen of 67Al-33Cu alloy that was cast, extruded and tested the same as the specimens in 4102 and 4104. In this specimen, the grain size is only 2 μm . It appears that both the large dimples and the CuAl_2 particles here are smaller than those in 4103 and 4105, but certainly greater than one-fifth the size of those in 4105, which shows a specimen with a grain size of 10 μm .



SEM fractograph

1320×

4108 A view of the fracture surface in 4104 (opposite page, bottom row), showing a different area than in 4105, at a still-higher magnification. Note that the aluminum solid-solution matrix phase has undergone a high degree of plastic flow, deforming into many fine points and spicules. Adjacent regions of the fracture surface would be expected to contain some of the very smooth facets that are formed by stretching.

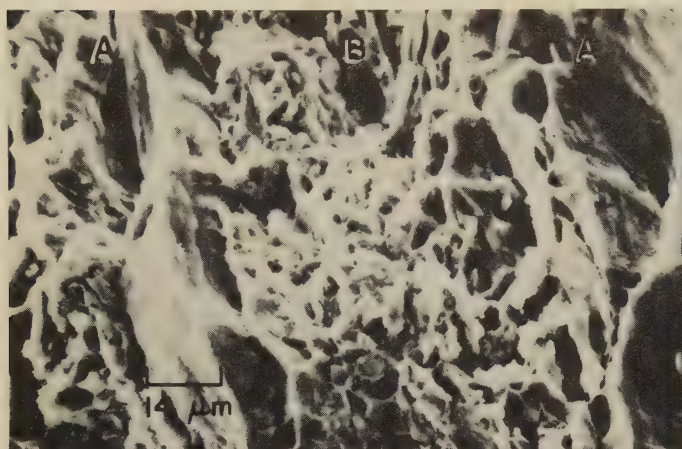


SEM fractograph

1200×

4109 Tensile-overload fracture in a specimen of 67Al-33Cu alloy that was cast, extruded and tested the same as those in 4102, 4104 and 4107; the grain size of this specimen is 5 μm . Compared with 4108 (grain size, 10 μm), this specimen has smaller CuAl_2 particles, about the same degree of plastic flow of the aluminum solid-solution matrix phase, and more complete bonding of many of the particles of CuAl_2 phase to the matrix.

SEM Fractographs: Boron-Fiber, Aluminum-Matrix and Boron-Fiber, Titanium-Matrix Composites Fractured in Transverse Tensile, Transverse Compressive and Longitudinal Tensile Tests



SEM fractograph

725×

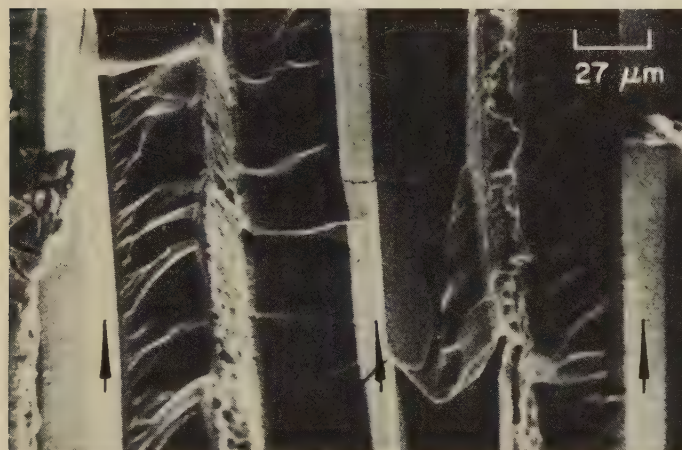
4110 Typical transverse tensile fracture in the aluminum matrix material used in preparing boron-aluminum composites. View shows two layers of aluminum alloy foil (locations A) that were plasma-arc sprayed with aluminum alloy powder (location B) then hot-press bonded.



SEM fractograph

37 1/2×

4111 Surface of a transverse tensile fracture in a sheet of composite consisting of 4.2-mil-diam BORSIC fibers (boron filaments formed by vapor deposition on tungsten cores, then vapor coated with silicon carbide) in a matrix of aluminum alloy 6061 (foil and sprayed powder). The fibers split longitudinally on a diametral plane. See also 4112.



SEM fractograph

375×

4112 Transverse tensile fracture in a sheet of BORSIC-aluminum composite, similar to 4111, but at higher magnification. The aluminum alloy 6061 matrix is indicated by the arrows. At the center of each 4.2-mil-diam BORSIC fiber is its tungsten core. Fracture of the fibers originated at flaws in the fiber surfaces.



SEM fractograph

11×

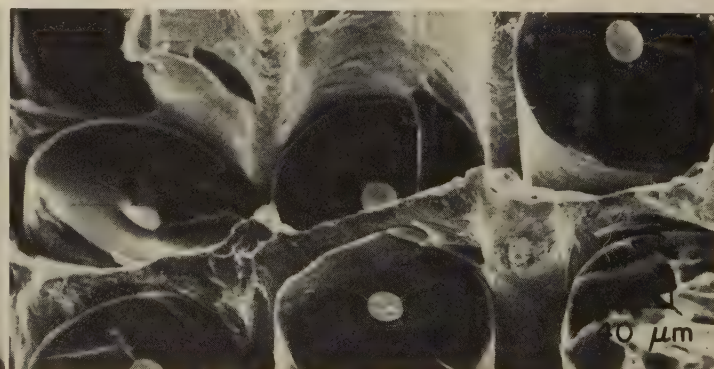
4113 Transverse tensile fracture in a sheet of BORSIC-aluminum composite. The BORSIC fibers are 4.2 mils in diameter; the matrix is foils of aluminum alloy 1145 plasma-arc sprayed with aluminum alloy 1100 powder. Few of the fibers have split, except where specimen edges were damaged during preparation.



SEM fractograph

55×

4114 Surface of a transverse compressive fracture in a sheet of BORSIC-aluminum composite. The BORSIC fibers are 4.2 mils in diameter; the matrix is foils of aluminum alloy 6061 plasma-arc sprayed with powder of the same alloy. Here, as in fractograph 4111, the fibers split longitudinally. Also visible is the result of shear deformation of the matrix.



SEM fractograph

250×

4115 Surface of a longitudinal tensile fracture in a sheet of BORSIC-titanium composite, which may be compared with the transverse tensile fracture in the sheet of BORSIC-aluminum composite shown in 4112. Note the smooth cleavage facets on the BORSIC fibers here, and the manner in which the titanium alloy matrix was deformed by being pulled from the fibers.

SEM Fractographs: Graphite-Fiber, Magnesium-Matrix Composite Fractured in a Longitudinal Tensile Test



SEM fractograph

73×

4116 Surface of a fracture in a longitudinal tensile-test specimen of a carbon (graphite) - magnesium composite having a tensile strength of 640 MPa (93 ksi). The approximate makeup of the composite was 40% graphite fibers (Modmor type I) and 60% magnesium matrix (99.5% pure), by volume. See also fractographs 4117 (at right) and 4118 (below, at left) for higher-magnification views of the areas outlined by the large and small rectangles, respectively. See also fractograph 4120 (below, at right).



SEM fractograph

180×

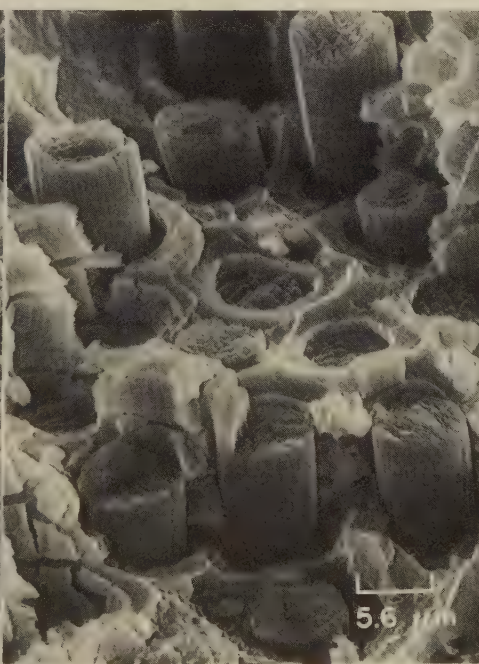
4117 Higher-magnification view of the area in the larger rectangle in 4116 (left). At letter A are two transversely oriented features that appear to be graphite fibers that either are lying loose on the surface or were inadvertently misaligned during manufacture. The feature at B is probably a ridge. Much of the surface exhibits broken fibers, the ends of which are roughly in the same plane as the fracture in the surrounding matrix, but at center are exposed fibers with the appearance of "palisades".



SEM fractograph

450×

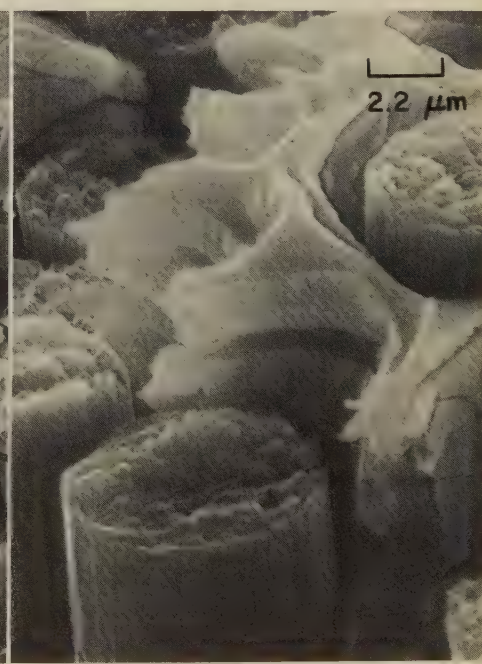
4118 Higher-magnification view of the area in the smaller rectangle in 4116, showing "palisades", some of which are the reverse of those in 4117 in that the fibers have broken at the bottom of the "palisades", exposing the sides of the holes in the matrix. See 4119 (right) for an enlarged view of the area in the rectangle.



SEM fractograph

1800×

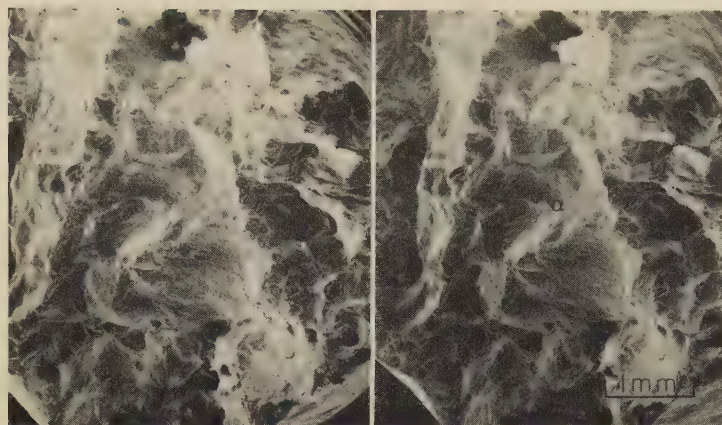
4119 An enlargement of the area in the rectangle in fractograph 4118 (left), showing that the magnesium matrix fractured in a brittle manner; note the many transverse fissures in the sides of the holes. Note also that the surfaces of the holes in the matrix reflect faithfully the fluted contours of the graphite fibers.



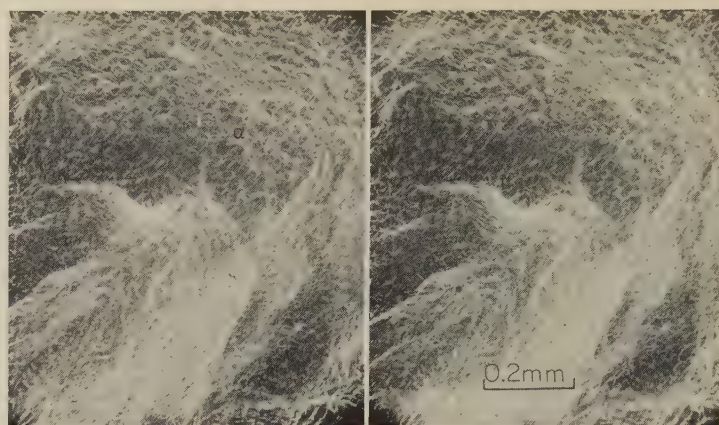
SEM fractograph

4500×

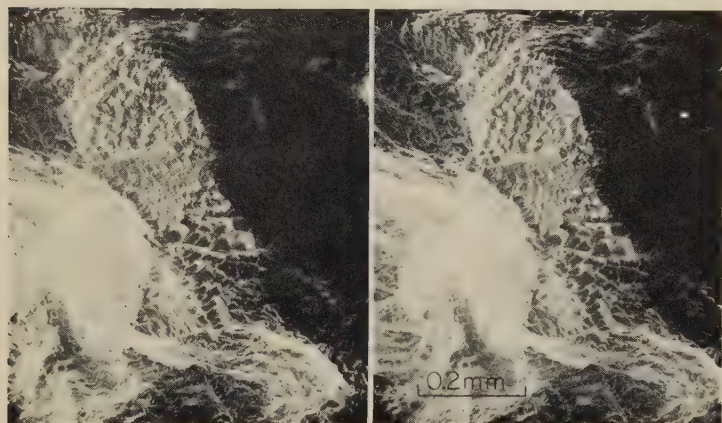
4120 A view at higher magnification of an area of the fracture surface shown in fractograph 4116 (above). The rough surfaces of the broken graphite fibers are clearly visible here. Compare these rough surfaces with the smooth cleavage facets on the broken boron fibers shown in fractograph 4115 (opposite page).



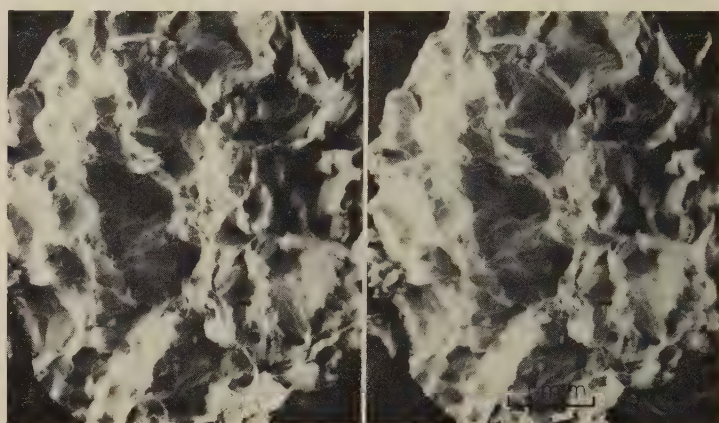
4121 Fracture at 425 C (797 F), 20 MPa (3 ksi) 11½×



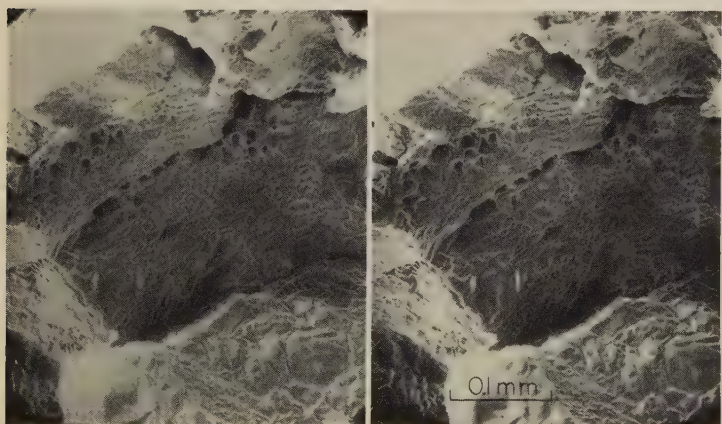
4122 Area at α in 4121, at higher magnification 60×



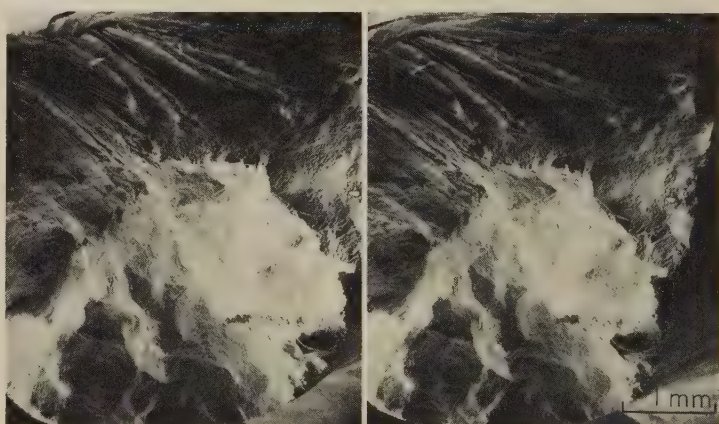
4123 A different area of the fracture in 4121 70×



4124 Fracture at 440 C (824 F), 15.5 MPa (2.25 ksi) 11×



4125 A different area of the fracture in 4124 135×



4126 Fracture at 525 C (977 F), 10.3 MPa (1.5 ksi) 12½×

The stereo pairs of SEM fractographs on these facing pages are of fracture surfaces produced in specimens of high-purity copper (99.999% Cu) by creep testing to rupture at temperatures ranging from 425 to 642 C (797 to 1188 F) and at tensile stresses ranging from 7 to 20 MPa (1 to 3 ksi). The material was continuously cast into ¾-in.-diam rod, swaged down to 0.55-in. diam, then machined into buttonhead specimens with gage sections 1½ in. long and ¼ in. in diameter. Before being tested, each specimen was heat treated in the creep-test furnace, first for 1 hr at 400 C (752 F) in hydrogen and then for 16 hr at 800 C (1472 F) in purified helium. The testing also was done in purified helium.

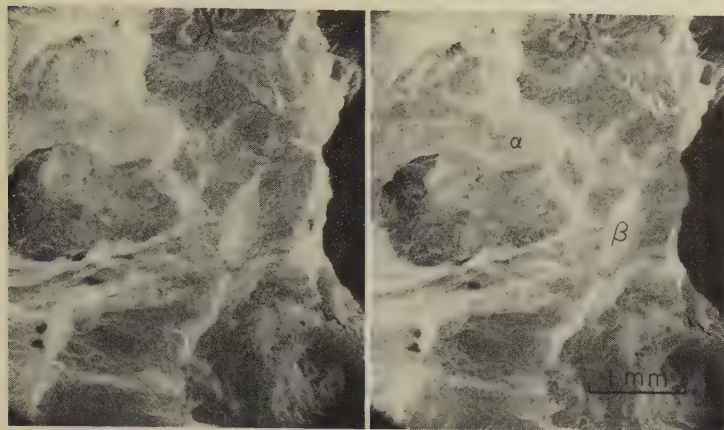
At low temperature or low stress, or both, the main mechanism of fracture was intergranular separation with accompanying microvoid coalescence, and the separated-grain facets were oriented at high angles relative to the tensile axis. At high temperature or high stress, or both, the fracturing was transgranular and highly plastic. At intermediate combinations of test temperature and stress, the main mechanism of fracture was the same as at low temperature or low stress

(intergranular separation with accompanying microvoid coalescence), but the fracture surface was fairly smooth and had a fine texture.

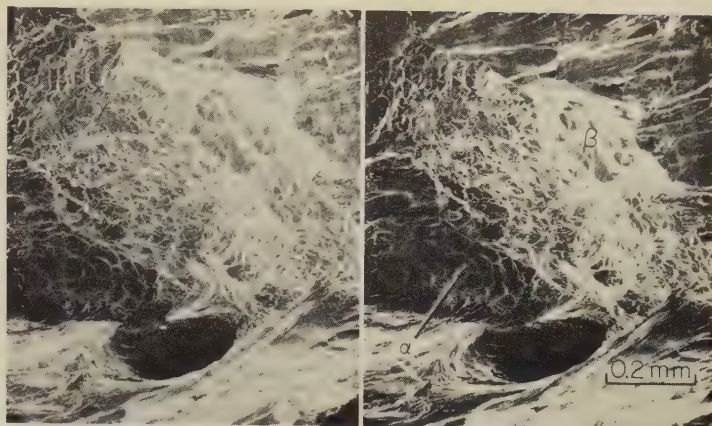
The specimen in fractographs 4121, 4122 and 4123 was tested at 425 C (797 F) and 20 MPa (3 ksi) and attained a steady-state strain rate of 2.0×10^{-6} per minute, fracturing in 76 hr, 54 min. These views show a fine texture of dimples, which resulted from microvoid coalescence, on fairly smooth separated-grain facets. The area at α in the center of the dimples is shown at higher magnification in 4122; note the uniform size of the dimples. Fractograph 4123, which is of an area of the fracture different from that in 4121, shows dimples with shapes that vary depending on orientation of the grain facets relative to the tensile axis.

The specimen shown in fractographs 4124 and 4125 was tested at 440 C (824 F) and 15.5 MPa (2.25 ksi) and attained a steady-state strain rate of 7.0×10^{-7} per minute, fracturing in 308 hr, 30 min. These fractographs show two different areas of the fracture surface. The area shown in 4124 displays separated-grain facets oriented at high angles relative to the tensile axis; the area shown in 4125 (at higher magnification) clearly shows the small dimples on the grain facets.

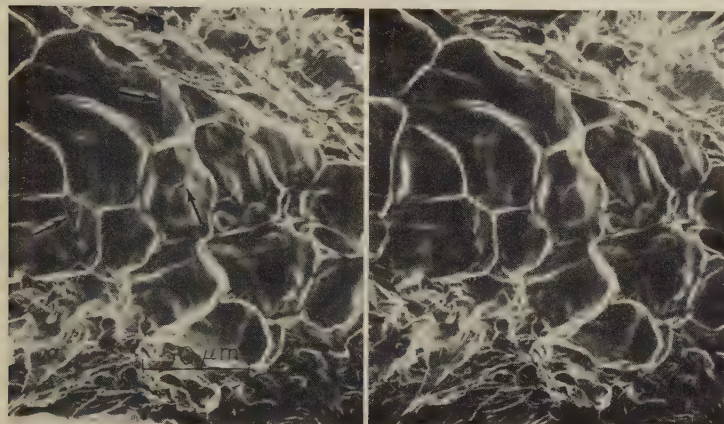
Tested at Six Different Temperatures, Showing Various Fracture Mechanisms



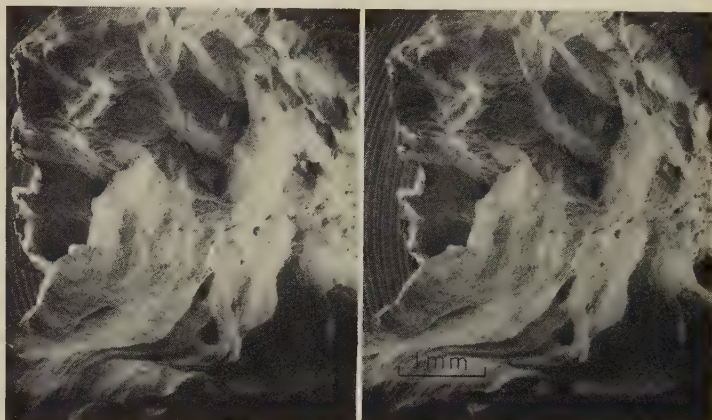
4127 Fracture at 540 C (1004 F), 10.3 MPa (1.5 ksi) 11½×



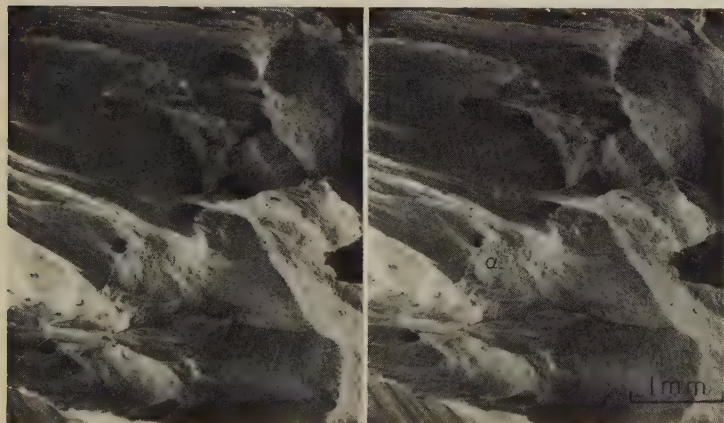
4128 Area at bottom of cavity at left center in 4127 60×



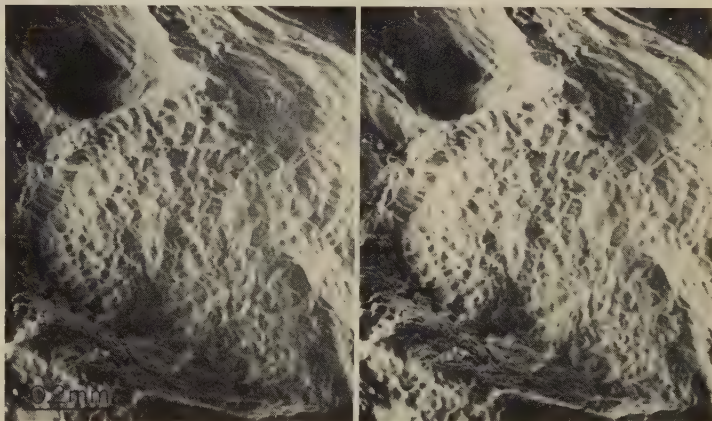
4129 Dimples indicated by arrow marked α in 4128 280×



4130 Fracture at 602 C (1116 F), 10.3 MPa (1.5 ksi) 11½×



4131 Fracture at 642 C (1188 F), 7 MPa (1 ksi) 12×



4132 Region at α in 4131, at higher magnification 60×

The specimen in fractograph 4126 was tested at 525 C (977 F) and 10.3 MPa (1.5 ksi) and attained a steady-state strain rate of 5.0×10^{-7} per minute, fracturing in 300 hr, 6 min; its fracture surface has larger and smoother facets than those in 4124 and 4125. At top in this view is a region that fractured by transgranular rupture accompanied by plastic flow.

The specimen in fractographs 4127, 4128 and 4129 was tested at 540 C (1004 F) and 10.3 MPa (1.5 ksi) and attained a steady-state strain rate of 1.65×10^{-6} per minute, fracturing in 67 hr, 50 min. The fracture surface in 4127 exhibits regions with a fine texture of dimples (such as at α and β), separated-grain facets (at top right) somewhat like those in 4124, and highly plastically deformed features near the bottom edge of the large cavity at left center. Fractograph 4128, from near the cavity in 4127, shows different patterns of small dimples (at α and β) resulting from microvoid coalescence, and a region of extensive plastic flow (at bottom, adjacent to the large dimple). The dimples indicated by the arrow marked α are shown at still higher magnification in 4129. The small arrows in 4129 point to thermally etched

networks of microstructural boundaries, which intersect the dimple boundaries and indicate that there is no relationship here of the dimple surfaces to crystallographic planes.

The specimen in fractograph 4130 was tested at 602 C (1116 F) and 10.3 MPa (1.5 ksi) and attained a steady-state strain rate of 4.8×10^{-6} per minute, fracturing in 40 hr, 54 min; its fracture surface shows a region of intergranular fracture (above the center) similar to that in fractograph 4124. Like the region at top in fractograph 4126, the region in the lower half of 4130 fractured by transgranular rupture accompanied by plastic flow.

The fracture surface of the specimen in fractograph 4131, which was tested at 642 C (1188 F) and 7 MPa (1 ksi), attaining a steady-state strain rate of 2.0×10^{-6} per minute and fracturing in 129 hr, 24 min, displays one region with a fine texture of dimples (at α). Extreme plastic flow, particularly at the grain just to the right of center, is seen in stereo to project out like a knife edge. Fractograph 4132 is a view at higher magnification of the region at α in fractograph 4131, showing patterns of dimples of various sizes.

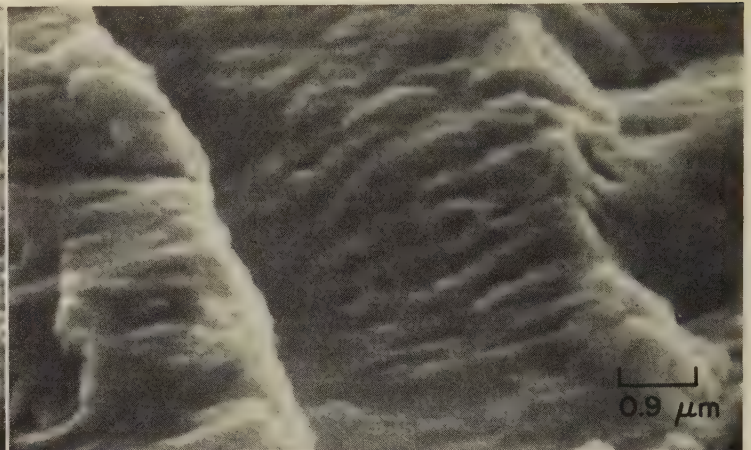
SEM Fractographs: Specimen of OFHC Copper Fractured in a Fatigue Test in Dry Air;
Specimen of Free-Machining Copper (Tellurium Added) Fractured by Tensile Overload



SEM fractograph

2200×

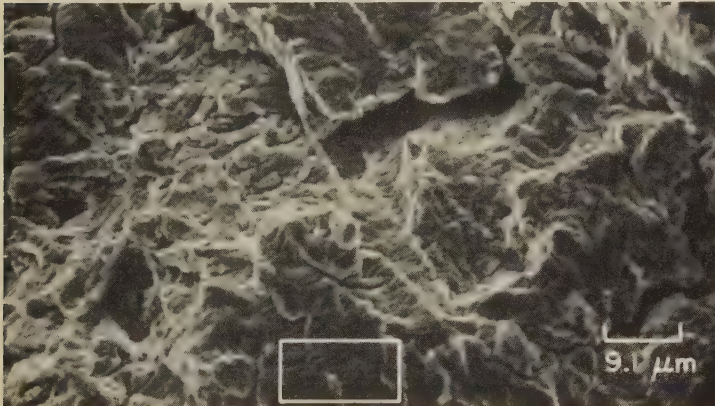
4133 Surface of a fatigue-test fracture in a notched specimen of oxygen-free, high-conductivity (OFHC) copper that had undergone a 67% reduction in cross-sectional area by cold work before being tested in dry air. The region shown here is 3 mm from the notch, where slow crack growth caused irregular striations to form. Note the numerous secondary cracks. See also 4134 to 4137.



SEM fractograph

11,000×

4134 Another region of the surface of the fatigue-test fracture in OFHC copper shown in fractograph 4133 (left), also 3 mm from the notch. At this higher magnification, the irregularity of the fatigue striations is clearly visible. There are no intergranular secondary cracks in this region, and there are no fissures between the fatigue striations.



SEM fractograph

1100×

4135 A region of the surface of the fatigue-test fracture in OFHC copper shown in 4133, 5 mm from the notch, where the rate of crack growth was greater than in the region in 4133. Intergranular secondary cracks are clearly evident. Fatigue striations are not well resolved at this magnification. See 4136 (right) for a higher-magnification view of the outlined area.



SEM fractograph

5500×

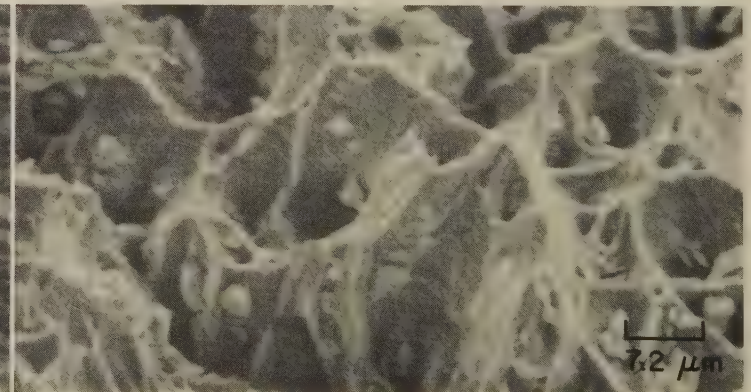
4136 Higher-magnification view of the outlined area at the bottom of fractograph 4135 (left). Here, many of the fatigue striations have resulted in small fissures but show the same irregularity displayed in fractograph 4134 (above); however, the steps visible here (at center and near right edge) appear to be much smaller than the one in 4134.



SEM fractograph

4600×

4137 Region of the fatigue-fracture surface in 4133 to 4136, 20 mm from the notch, where the rate of crack growth had increased considerably. The result of this high rate of crack growth is the array of very regular fatigue striations visible here, which are more typical of aluminum than of copper.

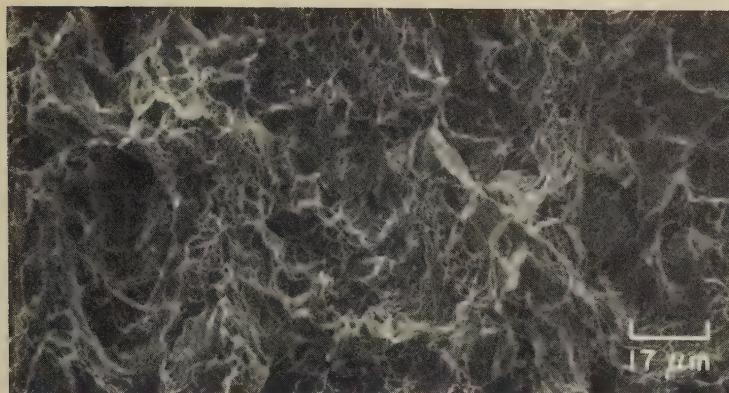


SEM fractograph

1390×

4138 Surface of a tensile-overload fracture in a specimen of free-machining copper, showing large dimples. Scattered throughout the structure are particles of Cu_2Te . The tellurium was added to the alloy to improve machinability (the particles of telluride act as chip breakers).

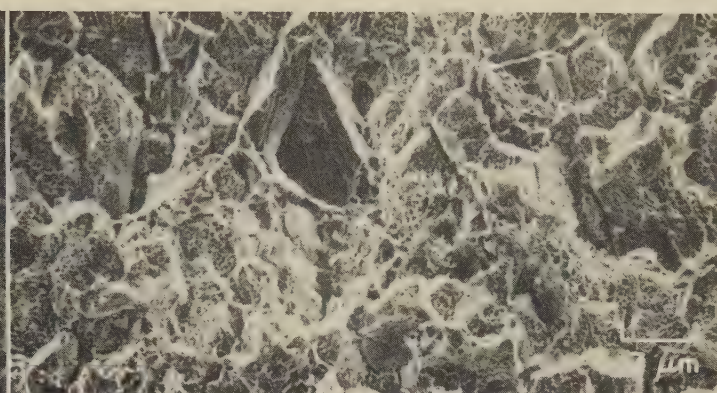
SEM Fractographs: Cu-2.5Be Alloy Fracture-Toughness Tested After Aging at Different Temperatures;
Spinodal 64Cu-27Ni-9Fe Alloy Fracture-Toughness Tested After Different Heat Treatments



SEM fractograph

600×

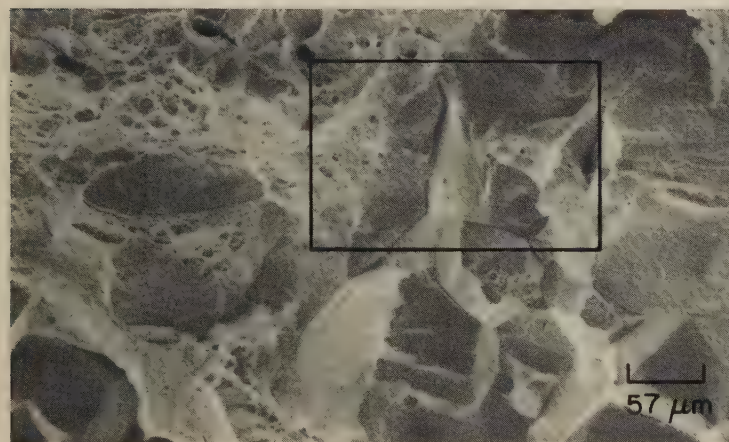
4139 Fracture surface of an underaged fracture-toughness test specimen of Cu-2.5Be alloy that had been aged for 1½ hr at 260 C (500 F) prior to being tested in air. Tensile strength was 930 MPa (135 ksi). Fracture was transgranular and produced the wide variety of dimple sizes shown here. There are some large pores, but there is little evidence of secondary cracking. Compare with fractograph 4140 (at right).



SEM fractograph

600×

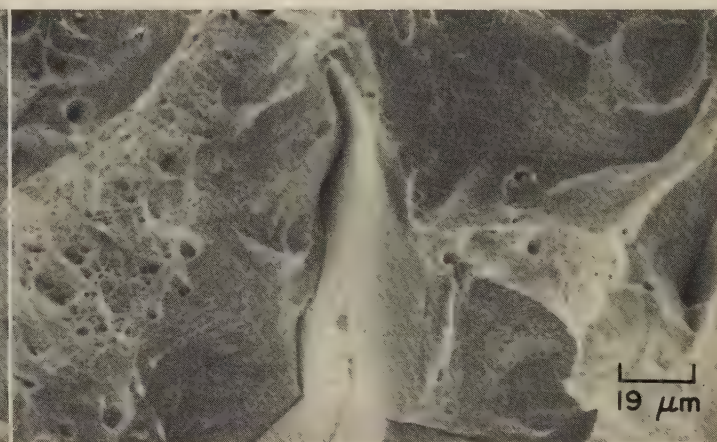
4140 Fracture surface of a fully aged fracture-toughness test specimen of Cu-2.5Be similar to that in 4139 (left) but aged 3 hr at 316 C (600 F) before being tested in air. Tensile strength was 1240 MPa (180 ksi). The dimples on the transgranular facets are much finer than in 4139, and there is a network of secondary cracks that appear to be intergranular. One facet (at top center) appears to have formed by quasicleavage.



SEM fractograph

175×

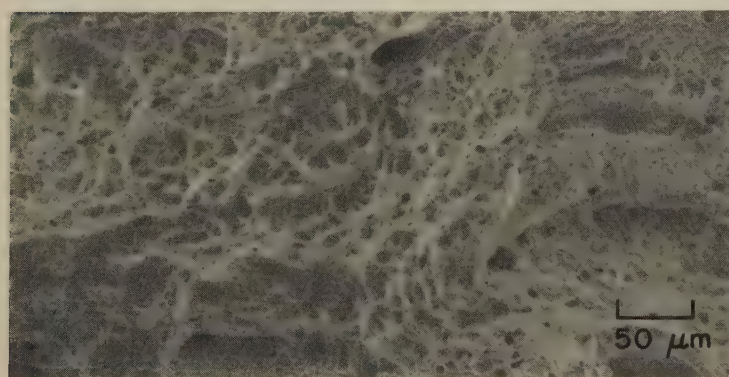
4141 Tensile-overload fracture in a fracture-toughness specimen of 64Cu-27Ni-9Fe alloy that underwent spinodal decomposition during heat treatment for 10 hr at 775 C (1427 F). The surface contains many intergranular facets with intervening regions of dimpled transgranular facets. See fractograph 4142 (right) for a higher-magnification view of the area in the rectangle.



SEM fractograph

525×

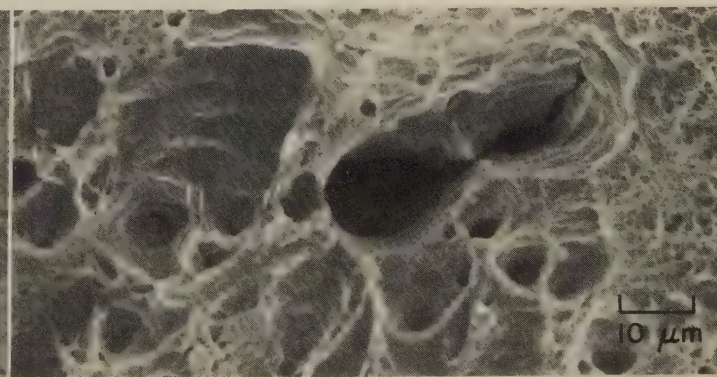
4142 A higher-magnification view of the area outlined by the rectangle in fractograph 4141 (left), revealing a fine structure of dimples, which resulted from microvoid coalescence, on the separated-grain facets. The regions of intergranular fracture here may have been caused by increased coarsening of the spinodal microstructure at the grain boundaries.



SEM fractograph

200×

4143 Tensile-overload fracture in a fracture-toughness test specimen of the same 64Cu-27Ni-9Fe alloy as in 4141, but here spinodal decomposition occurred during heat treatment at 775 C (1427 F) for 100 hr. Only dimpled transgranular facets are visible (no intergranular facets); this may be due to a coarser spinodal structure resulting from the longer heat treatment.

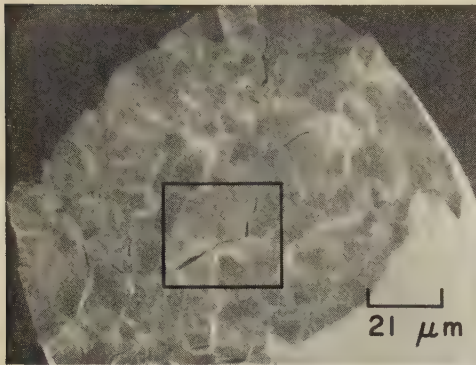


SEM fractograph

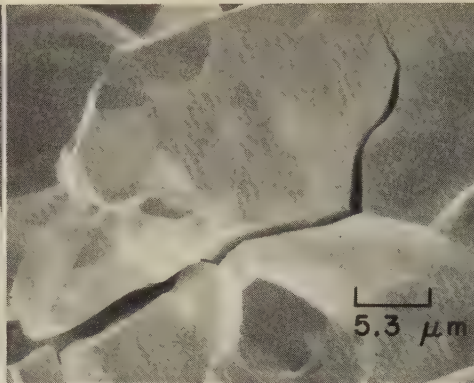
1000×

4144 Surface of the fracture in a fracture-toughness test specimen of the same 64Cu-27Ni-9Fe alloy as in fractographs 4141 to 4143, but which was heat treated at 775 C (1427 F) for 200 hr. Very fine dimples can be seen among the larger ones. The large cavity at the center of this view is believed to have resulted from a localized separation at a grain boundary.

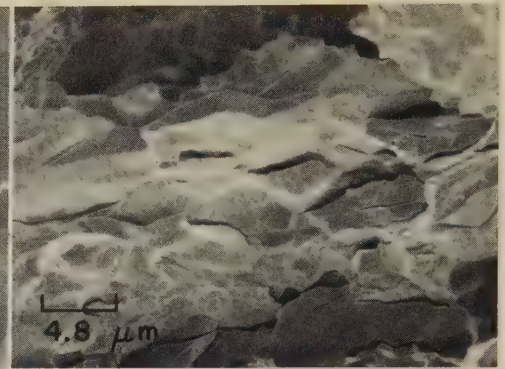
SEM and Light Fractographs, SEM Micrographs: Iridium Wire and Sheet Fractured in Bending; Tensile Peel-Test* Fractures in High-Lead, Low-Tin Solders



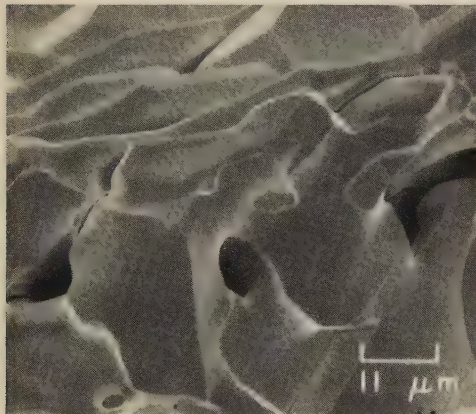
SEM fractograph 470×
4145 Surface of a brittle, intergranular fracture, produced by bending, in a polycrystalline iridium wire (0.127-mm diam) that had been annealed in vacuum for 2 hr at 1200 C (2192 F). See 4146, an enlarged view of the area in the rectangle.



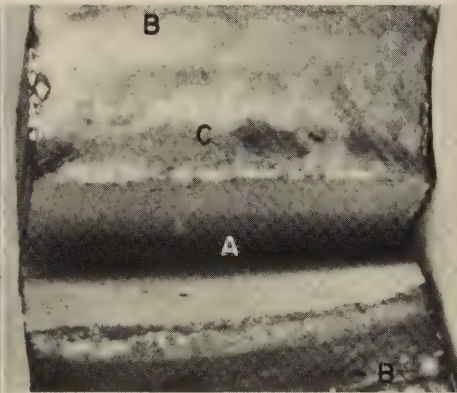
SEM fractograph 1900×
4146 Higher-magnification view of the area within the rectangle in fractograph 4145 (left). This entire area exhibits separated-grain facets and shows no evidence of plastic flow.



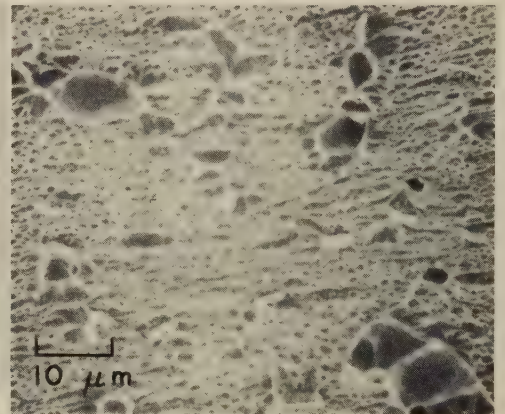
SEM fractograph 2100×
4147 Surface of a brittle, intergranular fracture, produced by bending, in an iridium sheet (rolled to 0.076 mm thick) that had been annealed for 2 hr at 1200 C (2192 F) in vacuum. Note the deep secondary cracks between the elongated grains.



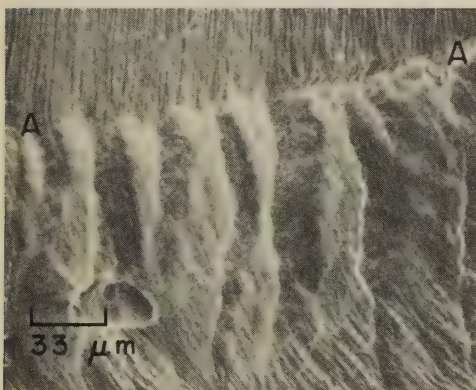
SEM micrograph 875×
4148 Surface of iridium sheet that had been annealed for 50 hr in helium at 1715 C (3119 F) to equilibrate a large grain size, then thermally faceted to permit study of possible impurity segregation.



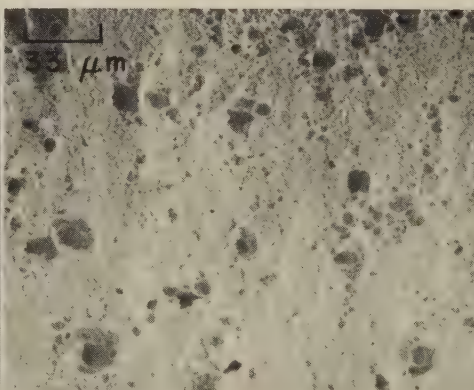
Light fractograph 6×
4149 View of a fracture (A) at the joint between a copper alloy CDA No. 260 (cartridge brass, 70%) strip (B) and a block of solder (C), opened by a tensile peel test*. Strip-to-solder interface between B and C at top did not open.



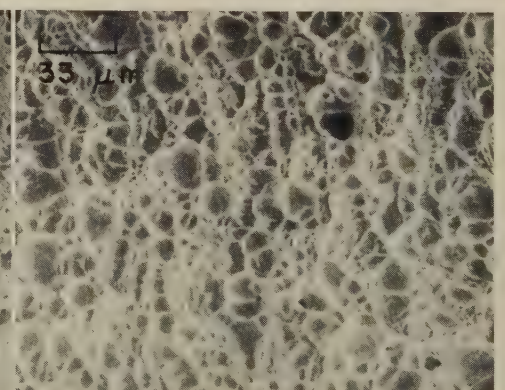
SEM fractograph 1000×
4150 Surface of a tensile peel-test* fracture in a solder joint with good strength and ductility that was made using 97.5Pb-1Sn-1.5Ag. The solder shows a fine continuous structure of dimples.



SEM micrograph 300×
4151 Free bulk-solder surface (perpendicular to fracture surface) of a tensile peel-test* specimen (after testing) prepared using 96.2Pb-3.8Sn-0.03Te alloy. Note flow below the grain boundary A-A.



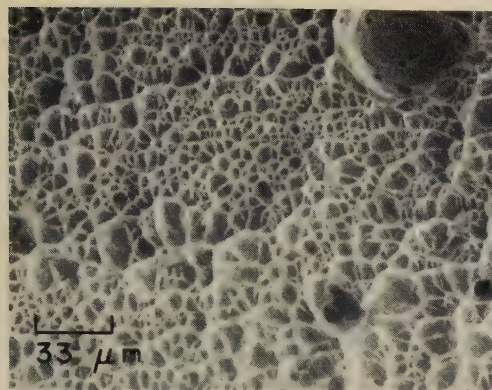
SEM fractograph 300×
4152 Surface of a tensile peel-test* fracture in the same solder alloy as in 4151. The soldered joint was strong and ductile, and the solder has a fine dimpled structure that is mostly unresolved here.



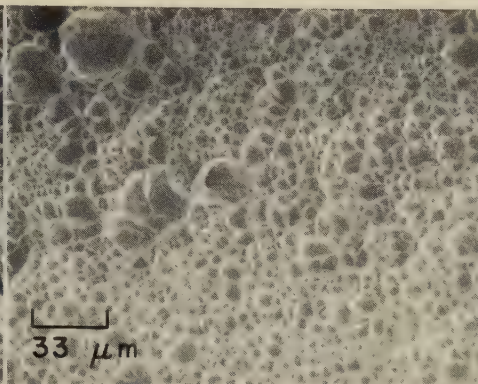
SEM fractograph 300×
4153 Surface of a tensile peel-test* fracture in a specimen prepared using 95.7Pb-3.8Sn-0.5Ag solder alloy. Structure of the solder is uniformly dimpled and is appreciably coarser than that in 4152.

*In tensile peel tests of soldered joints, a strip of copper alloy 7/8 in. long by 3/8 in. wide by 0.005 in. thick is bent to a U shape with a 1/8-in. space between the sides of the U. The bend is dipped for 5 sec in freshly melted solder under a flux and then is removed to allow solidification of the small block of solder retained in the U. The free ends of the copper strip (legs of the U) are then pulled apart in a tensile-test machine to peel the strip from one side of the block of solder.

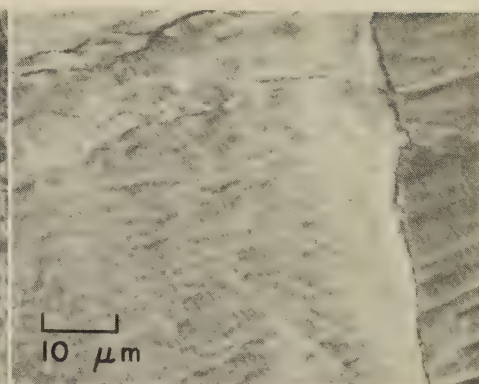
SEM Fractographs, SEM Micrograph: Tensile Peel-Test* Fractures in High-Lead, Low-Tin Solders (Continued), and in 85Pb-15Sn Solder



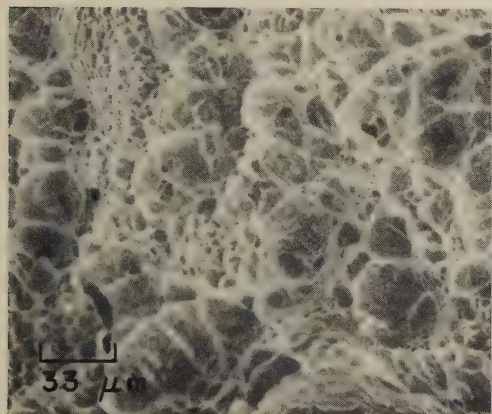
SEM fractograph 300×
4154 Surface of a tensile peel-test* fracture in 95Pb-3.8Sn-1.2Ag solder alloy. This solder is slightly different from that in 4153, but shows a similar array of dimples, most of which are of uniform size.



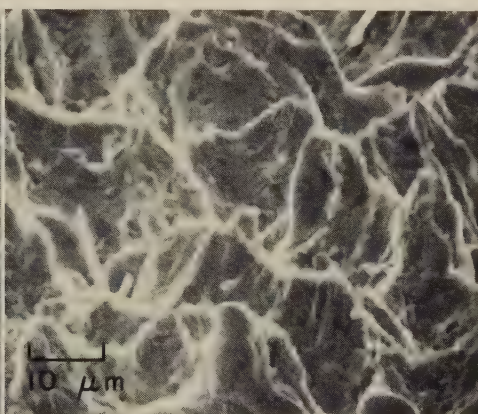
SEM fractograph 300×
4155 Surface of a tensile peel-test* fracture in 94Pb-4Sn-2Ag solder alloy, which contains slightly more silver and tin than the alloys in 4153 and 4154, showing somewhat smaller dimples. See also 4156.



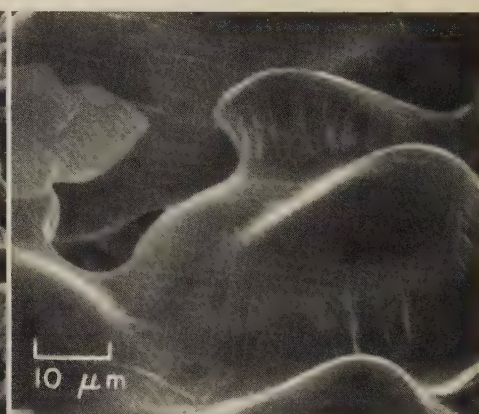
SEM micrograph 1000×
4156 SEM view of the free bulk-solder surface of the tensile peel-test* specimen in fractograph 4155, showing only slight surface slip but revealing both transgranular and intergranular cracks.



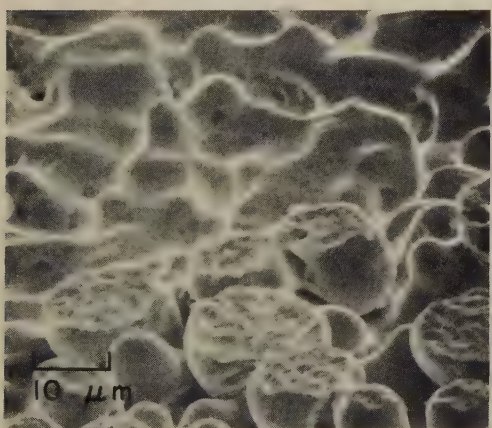
SEM fractograph 300×
4157 Surface of a tensile peel-test* fracture in 92.8Pb-6Sn-1.2Ag solder alloy. This alloy, which contains more tin than the alloy in 4154, shows a wide variation in dimple sizes.



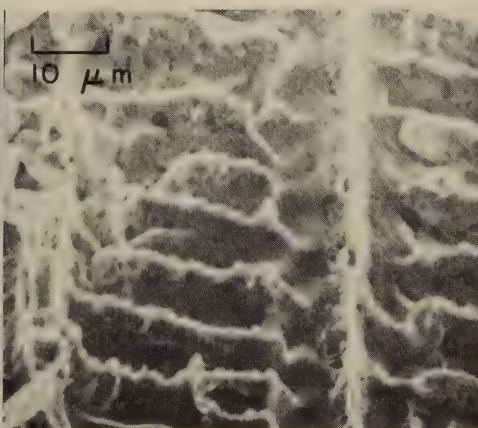
SEM fractograph 1000×
4158 Tensile peel-test* fracture surface of a joint with good strength and ductility, made with 85Pb-15Sn solder, showing a coarse-grained cellular structure. See also fractographs 4159 to 4162.



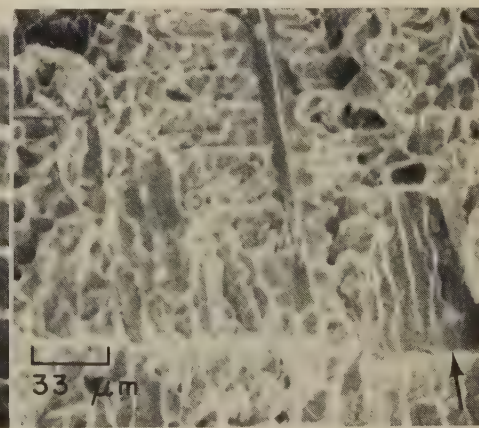
SEM fractograph 1000×
4159 Surface of a tensile peel-test* fracture in a low-strength, porous joint, made with the same solder as in 4158 (left), showing dendrite nodes apparently covered with a film, which has wrinkled.



SEM fractograph 1000×
4160 Surface of a tensile peel-test* fracture in a low-strength, porous joint, made with the same solder as in 4158 and 4159. Note film-covered region (top) similar to 4159, and the cellular, ductile fracture surfaces of the dendrite arms (bottom).



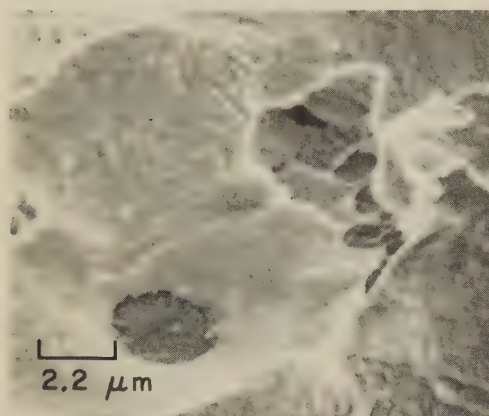
SEM fractograph 1000×
4161 Tensile peel-test* fracture surface of a joint with low strength due to hot tears (not shown) that formed during solidification, made with the same solder as in 4158 to 4160. Here, fracture is parallel to the direction of major dendrite growth.



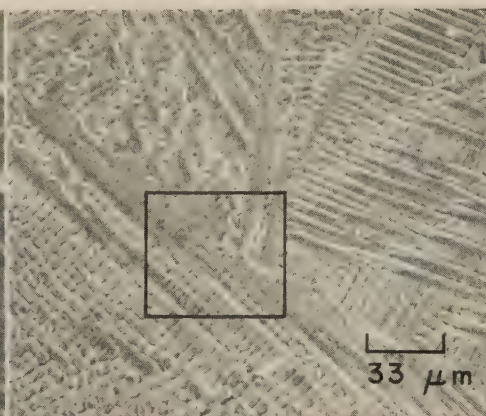
SEM fractograph 300×
4162 Surface of a tensile peel-test* fracture in another joint having low strength due to hot tears (as at arrow), made with the same solder as in 4158 to 4161 (85Pb-15Sn). Here, fracture has followed regions of interdendritic shrinkage. See 4163.

*For a description of tensile peel tests of soldered joints, see footnote on opposite page.

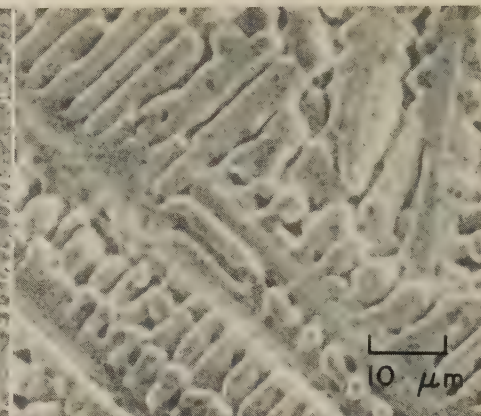
SEM Fractographs and Micrographs: Peel Tests* of 85Pb-15Sn and 70Pb-30Sn Solders; Tension-Overload Fracture in Alloy HM21A (97Mg-2Th-1Mn); Cleavage Fracture in TZM Alloy (Mo-0.5Ti-0.08Zr)



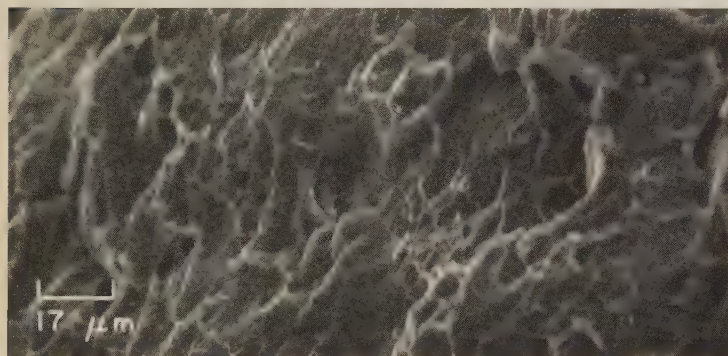
SEM fractograph 4500×
4163 Surface of a tensile peel-test* fracture in 85Pb-15Sn solder. Fracture in the ductile dimple at left began at the dark, round feature, where the bulk of the solder failed to cling to the initial layer.



SEM micrograph 300×
4164 Free bulk-solder surface of a tensile peel-test* specimen soldered with 69.9Pb-29.6Sn-0.5Ag alloy. Note the complete lack of deformation. See 4165, an enlarged view of area in rectangle.



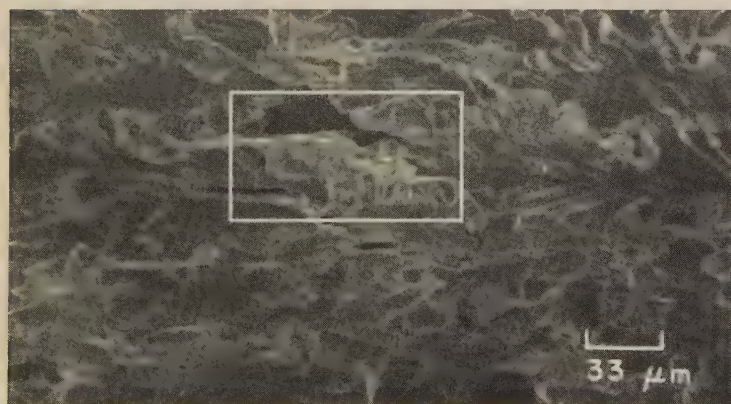
SEM micrograph 1000×
4165 Higher-magnification view of the area in the rectangle in micrograph 4164 (at left), showing more clearly the absence of surface deformation despite the plastic flow at the peeled joint.



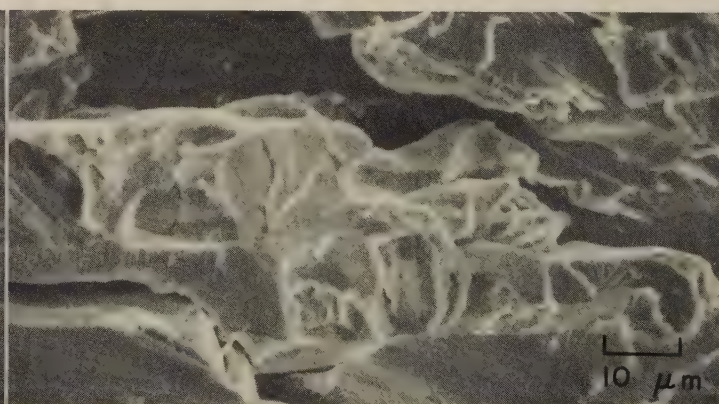
SEM fractograph 600×
4166 Surface of a tension-overload fracture in a specimen of magnesium alloy HM21A (97% Mg, 2% Th, 1% Mn) that broke during measurement of crack-growth rate in a fracture-toughness test. This ductile, dimpled surface is characteristic of magnesium alloys tested either in air or in a hydrogen atmosphere.



SEM fractograph 50×
4167 A low-magnification SEM view of the surface of a fracture produced in fracture-toughness testing of molybdenum alloy TZM (Mo-0.5% Ti-0.08% Zr) in air. The same type of brittle cleavage fracture shown here is obtained when this alloy is fracture-toughness tested in hydrogen. See also 4168.



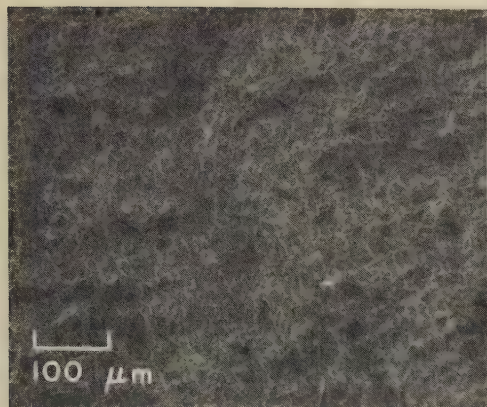
SEM fractograph 300×
4168 Same fracture surface as in 4167, shown at a higher magnification. Here the cleavage facets can be seen more distinctly, and there are no traces of dimples. There are several secondary cracks, which appear to be intergranular. See 4169 for a higher-magnification view of the area in the rectangle.



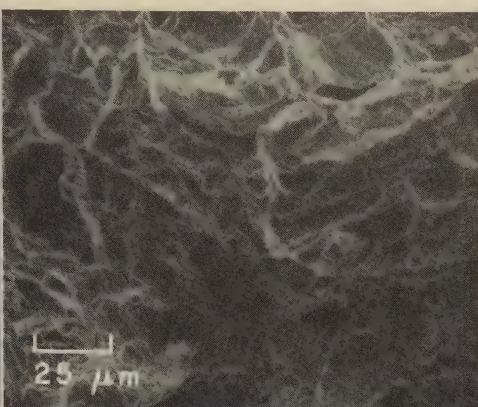
SEM fractograph 1000×
4169 A higher-magnification view of the area in the rectangle in fractograph 4168 (left). In this view, the cleavage steps on the facets are clearly visible. Except for the secondary cracks, this portion of the fracture surface appears to be composed entirely of transgranular facets.

*In tensile peel tests of soldered joints, a strip of copper alloy 7½ in. long by ¾ in. wide by 0.005 in. thick is bent to a U shape with a ¼-in. space between the sides of the U. The bend is dipped for 5 sec in freshly melted solder under a flux and then is removed to allow solidification of the small block of solder retained in the U. The free ends of the copper strip (legs of the U) are then pulled apart in a tensile-test machine to peel the strip from one side of the block of solder.

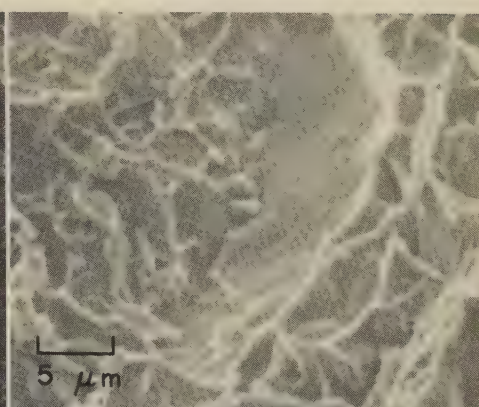
SEM Fractographs: Specimens of Titanium Alloys Ti-5Al-2.5Sn and Ti-6Al-4V That Were Broken in Fracture-Toughness Tests in Air and in Hydrogen



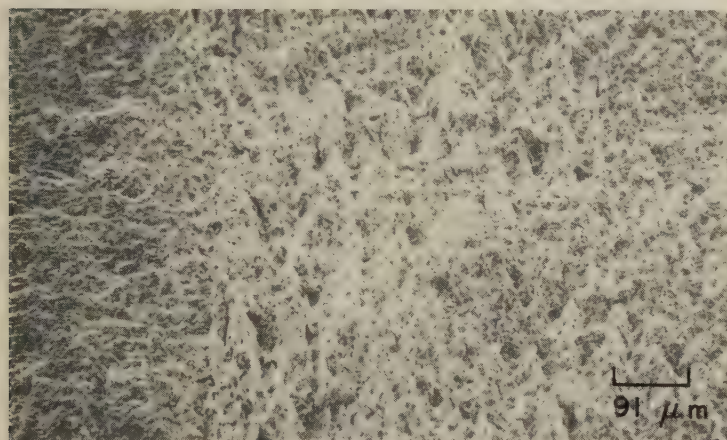
SEM fractograph 100×
4170 Fracture in a double-cantilever-beam, fracture-mechanics specimen of titanium alloy Ti-5Al-2.5Sn solution treated at 1066 C (1950 F), furnace cooled, and wedge-opening loaded in air at 24 C (75 F). See also fractograph 4171 (at right).



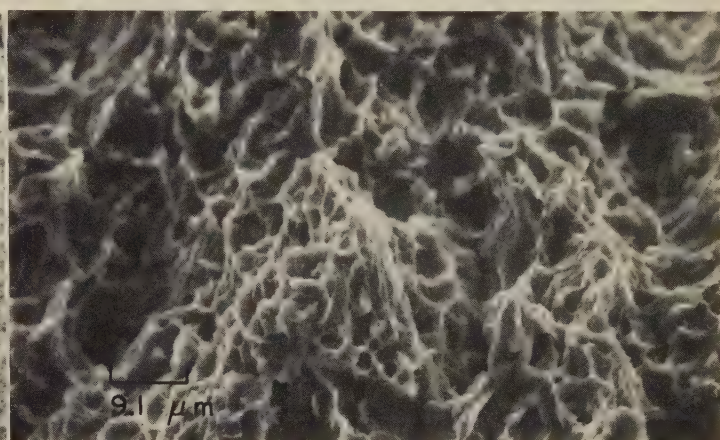
SEM fractograph 400×
4171 Higher-magnification view of the fracture surface shown in 4170. It is evident that this fracture is one of dimpled overload, with suggestions of ledges. See also fractograph 4172 (right).



SEM fractograph 2000×
4172 A view at still higher magnification of the fracture surface shown in fractographs 4170 and 4171. Visible at center is a ledge, which has resulted from step-wise propagation of the crack.



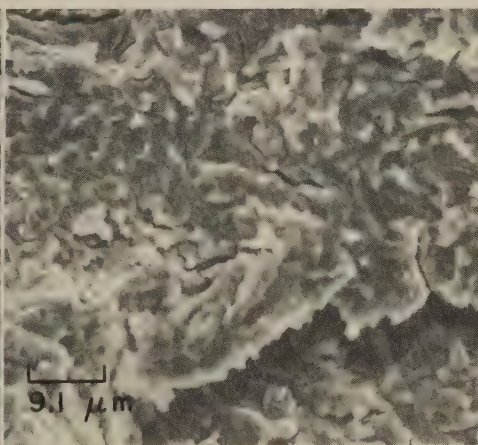
SEM fractograph 110×
4173 Fracture surface of a ductile fracture-toughness specimen of titanium alloy Ti-6Al-4V that was solution treated for 40 min at 829 C (1525 F), water quenched, aged at 510 C (950 F), then loaded in three-point bending (in air). See also 4174 to 4177.



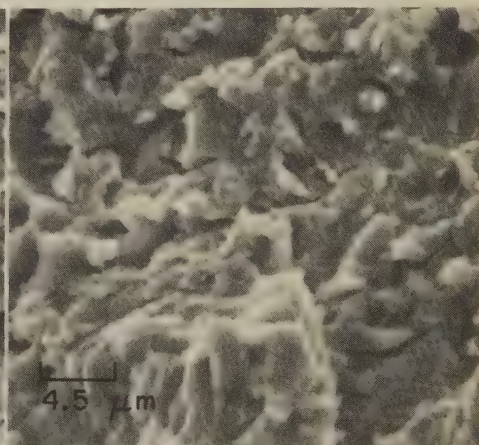
SEM fractograph 1100×
4174 Higher-magnification view of the fracture surface in 4173, typical of fractures produced in this alloy in air after various solution treatments. Entire surface shows dimpled fracture of fine, equiaxed alpha phase that ruptured in ductile shear.



SEM fractograph 110×
4175 Fracture surface of a specimen of Ti-6Al-4V alloy similar to the specimen shown in 4173 and having the same history, but tested in a hydrogen atmosphere. The principal features here are numerous secondary cracks. See also 4176 (right).

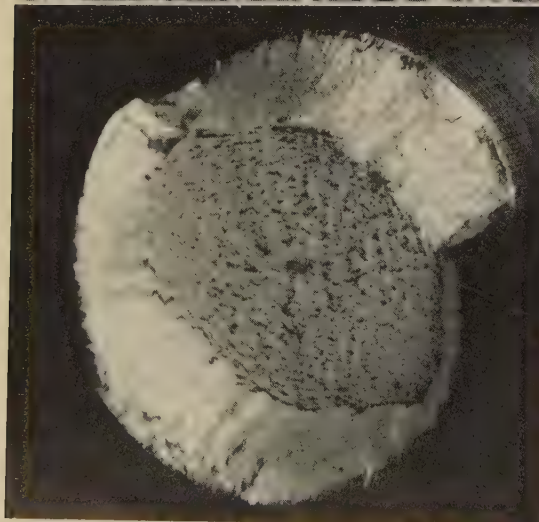


SEM fractograph 1100×
4176 Higher-magnification view of the fracture surface shown in 4175 (at left). The embrittlement of this specimen by hydrogen was slight (about 12%). Fracture was by a mixture of shear rupture and transgranular cleavage. See also 4177.

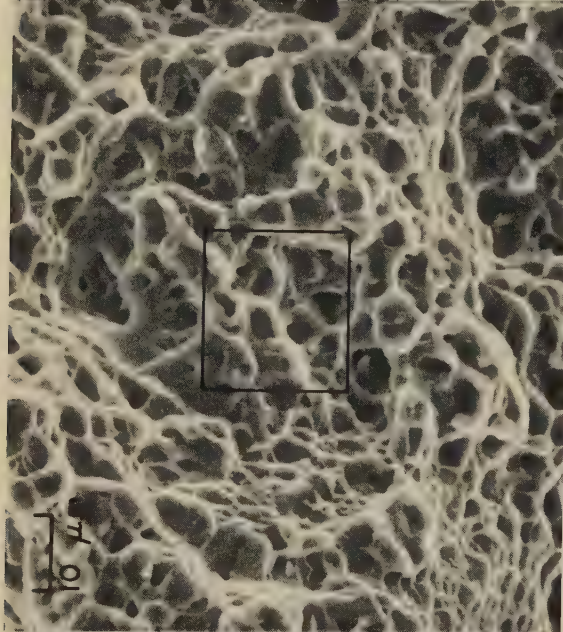


SEM fractograph 2200×
4177 Same fracture surface as in fractographs 4175 and 4176, but shown at even greater magnification. Many small secondary cracks are present among moderate-sized dimples.

Light Fractographs and SEM Fractographs: Titanium Alloy Ti-6Al-4V Unnotched and Notched Specimens Fractured in Tensile-Overload Tests



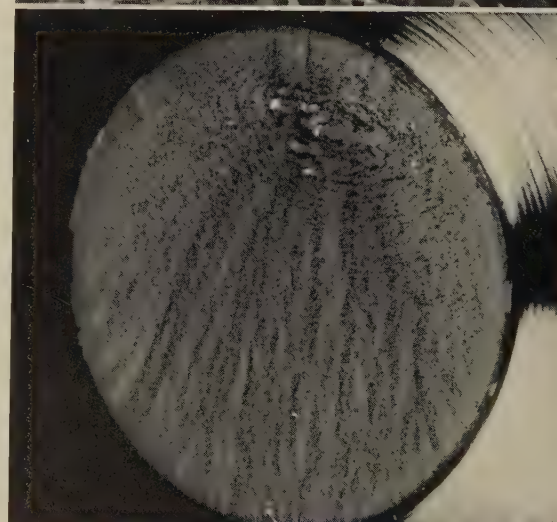
4178 Tensile-overload fracture surface of an unnotched specimen of titanium alloy Ti-6Al-4V heat treated to a tensile strength of 1158.8 MPa (168.5 ksi) and 47% reduction in area. A classic example of cup-and-cone fracture having a flat, fibrous central zone. See 4179.



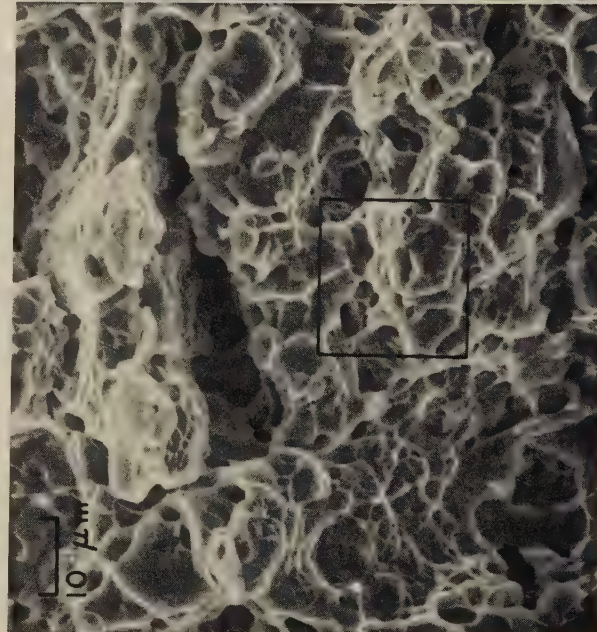
4179 A view of the fibrous central zone of the fracture surface in 4178, showing the equiaxed dimples expected in this region. The dimples are relatively uniform in size, with none being extremely large. A few inclusions are evident. See 4180 (area in rectangle, enlarged).



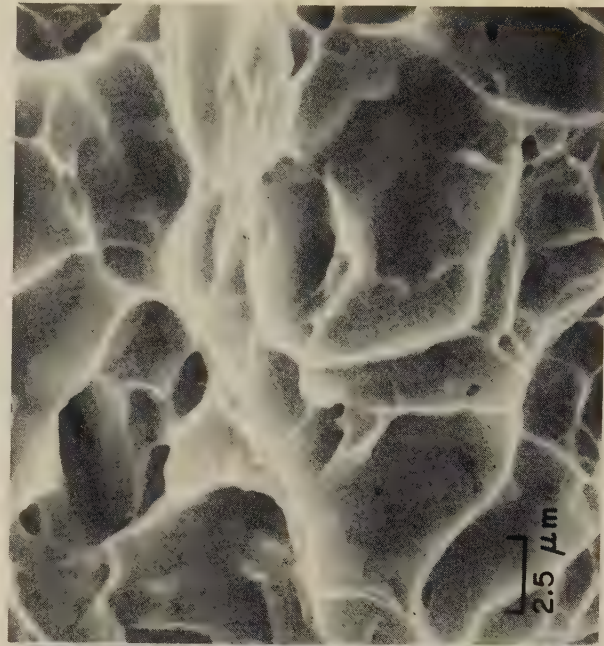
4180 Area outlined by the rectangle in fractograph 4179, as seen at four times the magnification there. Note the numerous small dimples that are situated within the larger dimples. This ductile fracture exhibits no sign of secondary cracking.



4181 Tensile-overload fracture surface of a notched specimen of titanium alloy Ti-6Al-4V heat treated to same mechanical properties as specimen in 4178, and with notched tensile strength of 1696 MPa (246 ksi). Crack nucleus is below center, at right. See 4182.

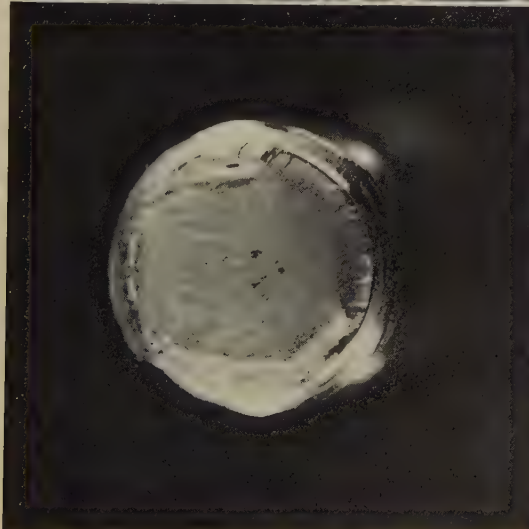


4182 Center of fracture surface in 4181. In contrast to the fracture surface of the unnotched specimen in 4179, dimples of various sizes are displayed here, and some secondary cracking is detectable. Also see 4183.



4183 A view at higher magnification of the area outlined by the rectangle in fractograph 4182. Note the small dimples that are present both at the edges of and within the larger dimples.

Light Fractographs and SEM Fractographs: Titanium Alloy Ti-6Al-4V Specimens Fractured in Low-Cycle and High-Cycle Fatigue Tests



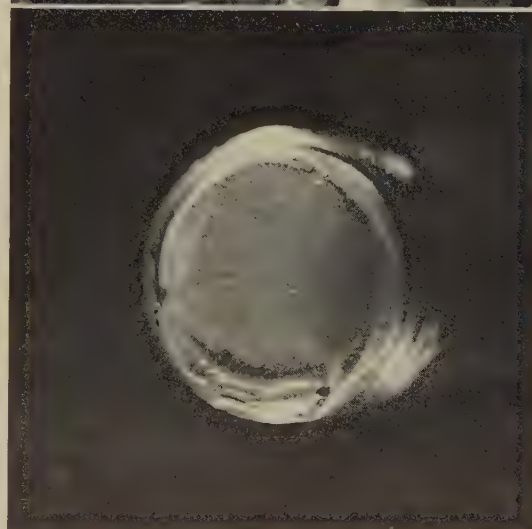
6×
4184 Fracture surface of a specimen of titanium alloy Ti-6Al-4V (same mechanical properties as in 4178, on facing page) broken in low-cycle fatigue (26,000 cycles) in tension-tension ($R = 0.1$) at maximum loading of 689 MPa (100 ksi). Several crack origins are visible at bottom. See also fractograph 4185, at right.



SEM fractograph
1000×
4185 A view of the fracture surface in 4184, showing an area close to the edge of the crack origins. Many small voids, which bear little resemblance to conventional dimples, are visible among the small facets. Area in rectangle is shown enlarged in 4186.



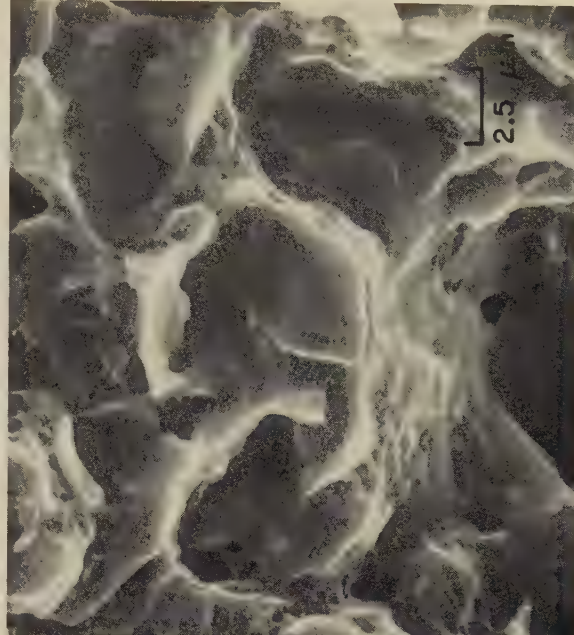
SEM fractograph
3000×
4186 Area outlined by the rectangle in 4185, as seen at triple the magnification there. Note the several small secondary transgranular cracks. The features at upper left are not considered fatigue striations, being too widely spaced (compare with TEM fractograph 4754).



6×
4187 High-cycle fatigue fracture in a specimen of titanium alloy Ti-6Al-4V (same mechanical properties as in 4178, on facing page) that was tested in tension-tension ($R = 0.1$) at maximum loading of 345 MPa (50 ksi), breaking in 937,000 cycles. The curved fatigue beach mark can be seen near bottom. See 4188 and 4189.

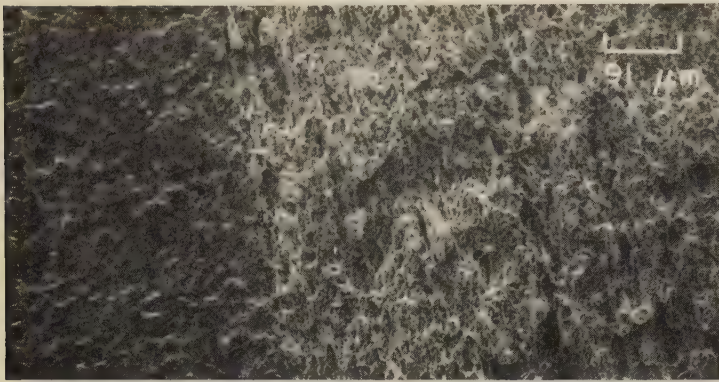


SEM fractograph
4000×
4188 View of fracture surface in 4187 showing an area at the curved beach mark. As in 4186, the parallel fissures are not believed to be striations, because their spacing is at least three times that of the features visible by transmission electron microscopy at the same site (see also TEM fractograph 4759).



SEM fractograph
4000×
4189 Another view of the fracture surface in fractograph 4187, this one showing an area in the rapid-fracture region beyond the fatigue beach mark. Fine tear dimples are distinctly evident on the walls of the larger dimples. No fissures or secondary cracks are visible here.

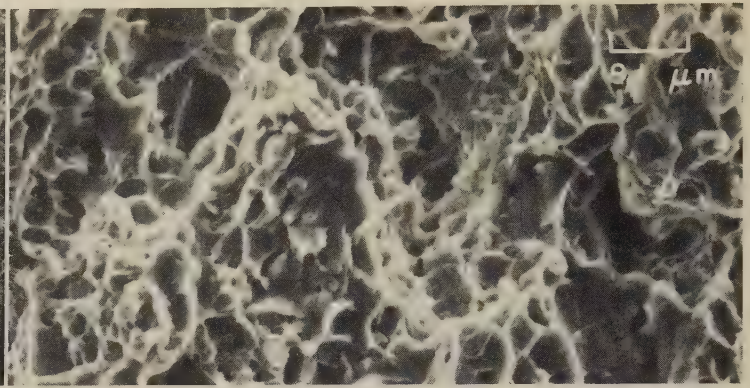
SEM Fractographs: Mill Annealed Titanium Alloy Ti-6Al-4V Fracture-Toughness Tested in Air and in Hydrogen; Heat Treated Ti-6Al-4V Fracture-Toughness Tested in Hydrogen



SEM fractograph

110×

4190 Fracture surface of a specimen of titanium alloy Ti-6Al-4V mill annealed sheet that was fracture-toughness tested in air. At left (dark) is fatigue-precrack region; at right is region of tensile-overload fracture, which is dimpled and has aligned elongated cavities suggesting localized slip. See 4191.

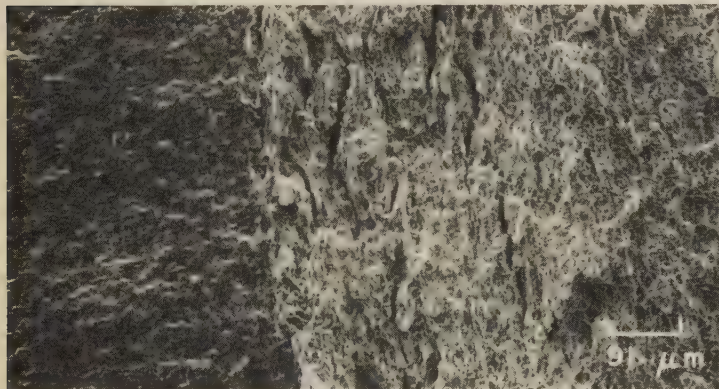


SEM fractograph

1100×

4191 A portion of the tensile-overload-fracture region of the fracture surface in 4190, as seen at ten times the magnification there. This displays a rather uniform size of equiaxed dimples, shows essentially no inclusions, and contains no indication of secondary cracking; in summary: a thoroughly ductile fracture.

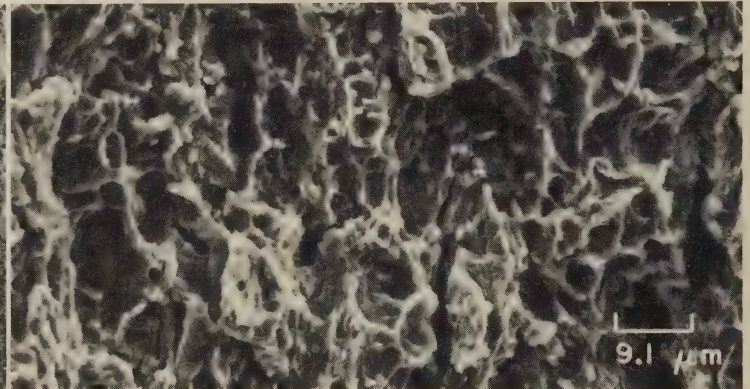
NOTE. All structures shown on this page are continuous alpha phase with dispersed beta phase.



SEM fractograph

110×

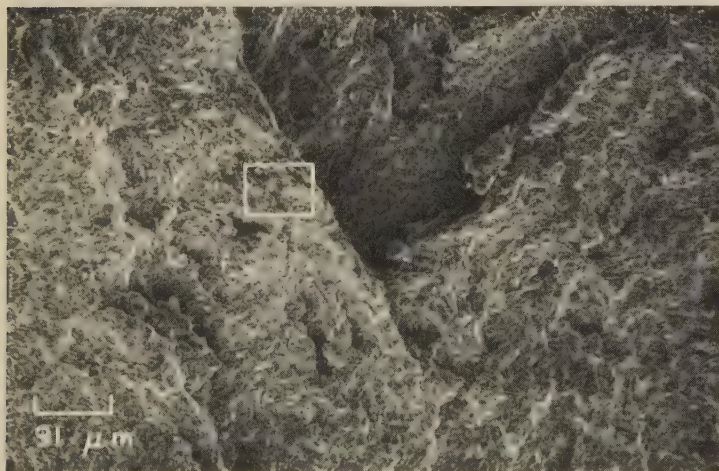
4192 Fracture surface of a specimen of the same material and condition as in 4190 (mill annealed Ti-6Al-4V sheet) but fracture-toughness tested in hydrogen at 1 atm. The fatigue-precrack region (dark area at left), produced in air, is identical with that in 4190, but note the deep cracks among the dimples in the tensile-overload region at right. See also fractograph 4193.



SEM fractograph

1100×

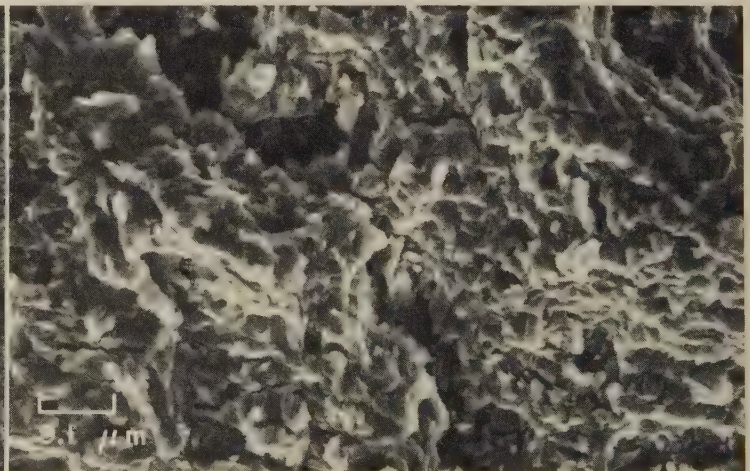
4193 A view of the region of tensile-overload fracture in 4192, at ten times the magnification there. In spite of the effects of hydrogen, this region is quite similar in appearance to the tensile-overload region of the air-tested specimen in 4191. Observe, however, that here there are many fine, parallel secondary cracks scattered throughout the dimpled surface.



SEM fractograph

110×

4194 Same as 4192, except that before being fracture-toughness tested in hydrogen, this specimen was heat treated at 704 C (1300 F) for 2 hr and air cooled. In contrast to the fracture surface shown in 4192, no dimples are evident here. The surface exhibits giant steps. See also fractograph 4195, at right.

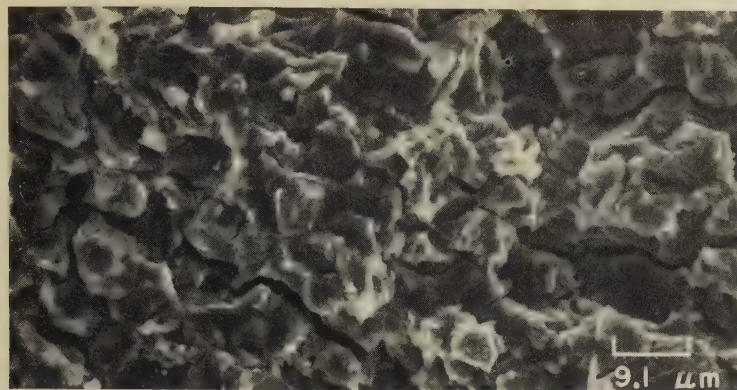


SEM fractograph

1100×

4195 Area outlined by the rectangle in fractograph 4194, as seen at ten times the magnification there. The rim of the central step in 4194 is at top right, and secondary fissures extend diagonally across the view. This surface contains no large cleavage facets, and has been characterized as "feathery".

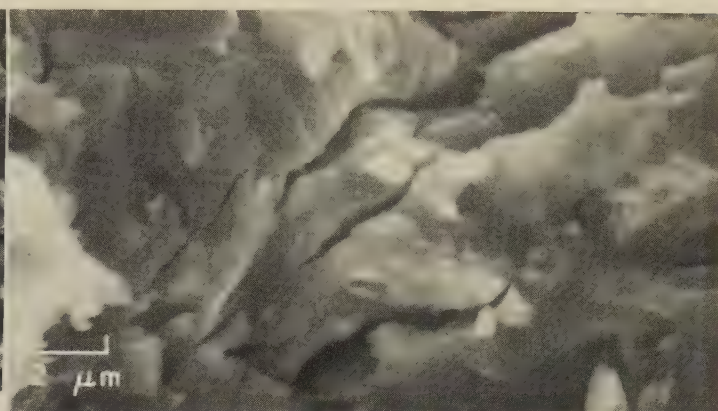
SEM Fractographs: Titanium Alloy Ti-6Al-4V Fracture-Toughness Specimens That Were Fractured in Hydrogen and in Air After Various Heat Treatments



SEM fractograph

1100×

4196 Fracture surface of a fracture-toughness specimen of titanium alloy Ti-6Al-4V that was heat treated for 40 min at 954 C (1750 F), stabilized* and then tested at 25 C (77 F) in hydrogen. The deep secondary cracks are interpreted as following the boundaries between the grains of primary alpha and the beta matrix. See also fractograph 4197, at right.

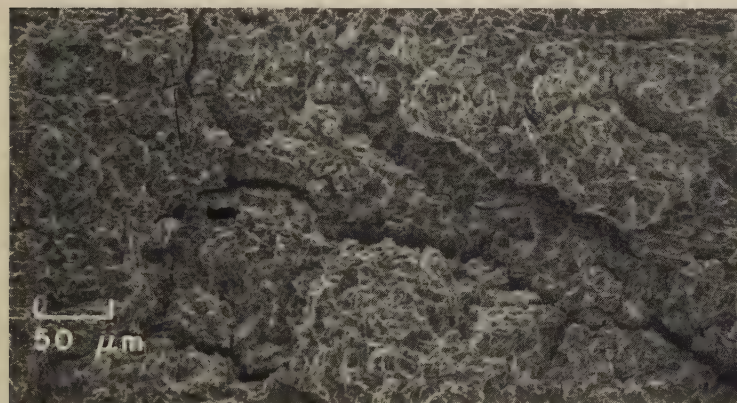


SEM fractograph

5000×

4197 A view of the fracture surface in 4196 as seen at higher magnification, which shows in greater detail the fine secondary cracks; these are transgranular in contrast to the network of major secondary cracks. The fracture is brittle, but the facets are small and irregular and have no detectable river patterns.

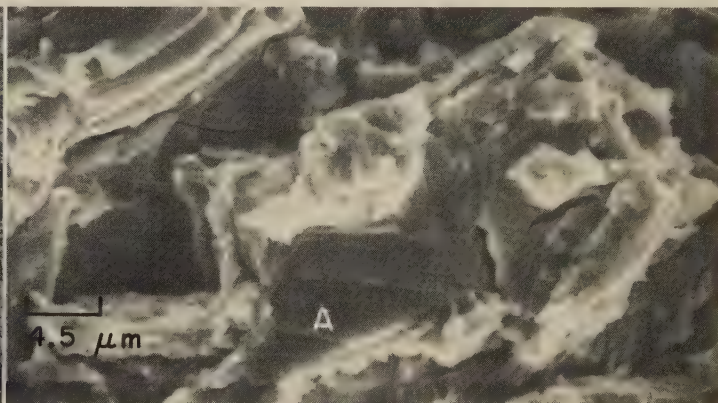
NOTE. All structures shown on this page are continuous beta phase with dispersed alpha phase.



SEM fractograph

200×

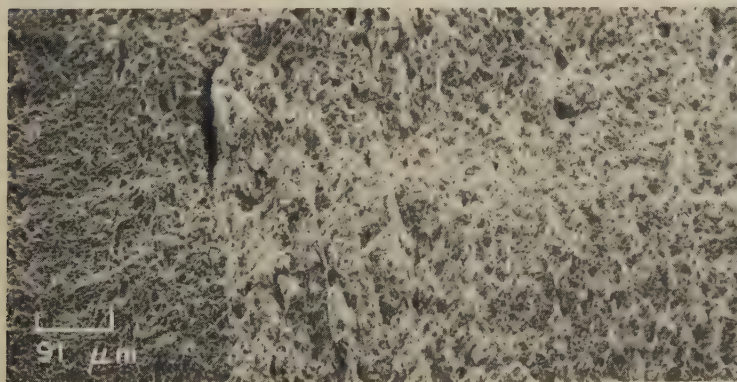
4198 Fracture surface of a fracture-toughness specimen same as in 4196, except this specimen received a 24-hr soak at 954 C (1750 F) before undergoing the stabilizing treatment.* A gross network of secondary intergranular cracks is evident, providing steps that separate different levels of the main crack advance. See also fractograph 4199, at right.



SEM fractograph

2200×

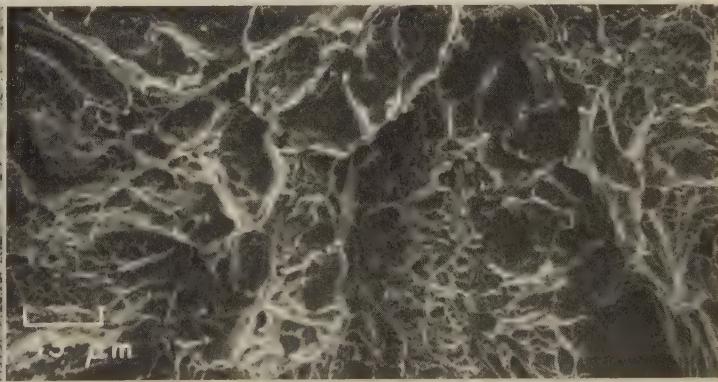
4199 A view of the fracture surface in 4198, at 11 times the magnification there. Note the intricate rupture patterns. Some of the main cracks are believed to follow the interfaces between the continuous beta-phase matrix and the dispersed acicular alpha phase. Observe the "terraced" area at A; similar areas are visible in fractographs 4205 to 4207, on the next two pages.



SEM fractograph

110×

4200 Fracture surface of a fracture-toughness specimen of titanium alloy Ti-6Al-4V heat treated 40 min at 954 C (1750 F) and water quenched, aged at 510 C (950 F), and tested in hydrogen. The fatigue-precrack region is at left. The tensile-overload region, at right, closely resembles that of specimen in 4192.



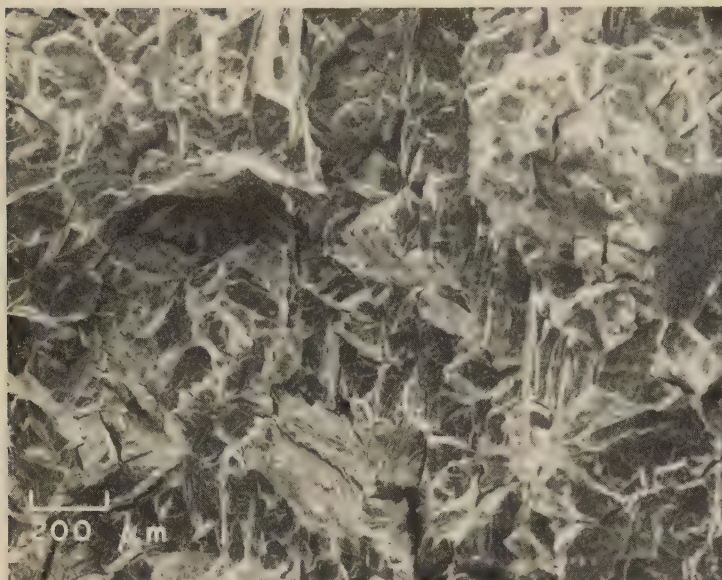
SEM fractograph

230×

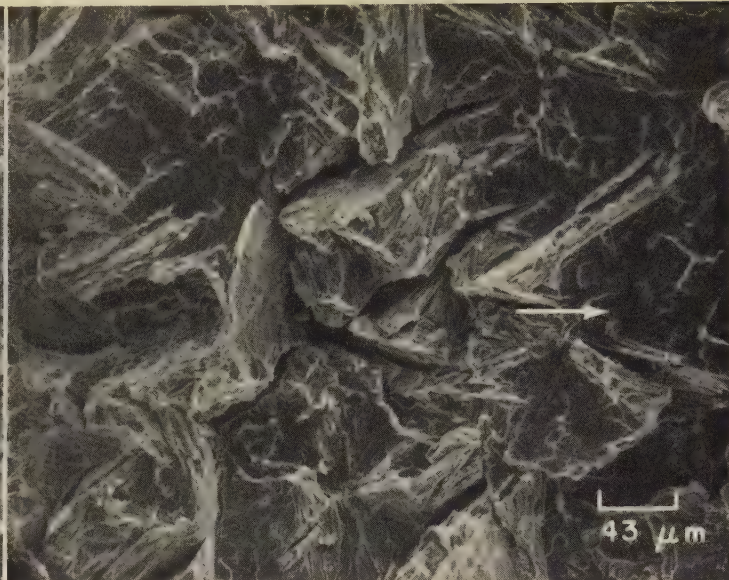
4201 Fracture surface of a fracture-toughness specimen of titanium alloy Ti-6Al-4V that was heat treated 40 min at 1038 C (1900 F), stabilized* and then tested in air at 25 C (77 F). Note the tremendous range in size of the dimples. See also fractographs 4202 through 4205, on the next page.

*Stabilizing consisted of furnace cooling to 704 C (1300 F) from the heat treating temperature, holding 1 hr, furnace cooling to 593 C (1100 F), holding 1 hr, and air cooling. This treatment was used to secure a large grain size to increase the susceptibility of the alloy to slow-strain-rate embrittlement in hydrogen.

SEM Fractographs: Specimen of Titanium Alloy Ti-6Al-4V That Was Broken
in a Fracture-Toughness Test in a Hydrogen Atmosphere

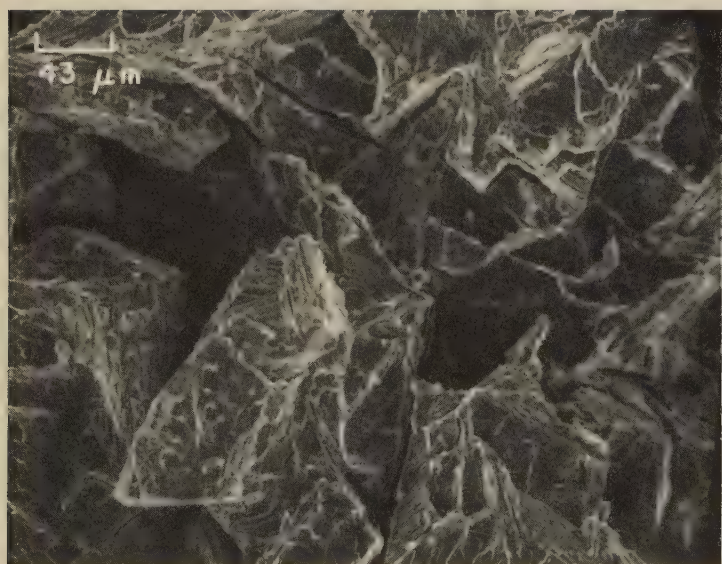


SEM fractograph 50×
4202 A Ti-6Al-4V fracture-toughness specimen identical to that in 4201 (preceding page) except broken in hydrogen at 25 C (77 F). This fracture surface appears to be very brittle, showing intergranular secondary cracks that follow exceedingly angular paths. Note the larger cleavage facets. See also 4203.

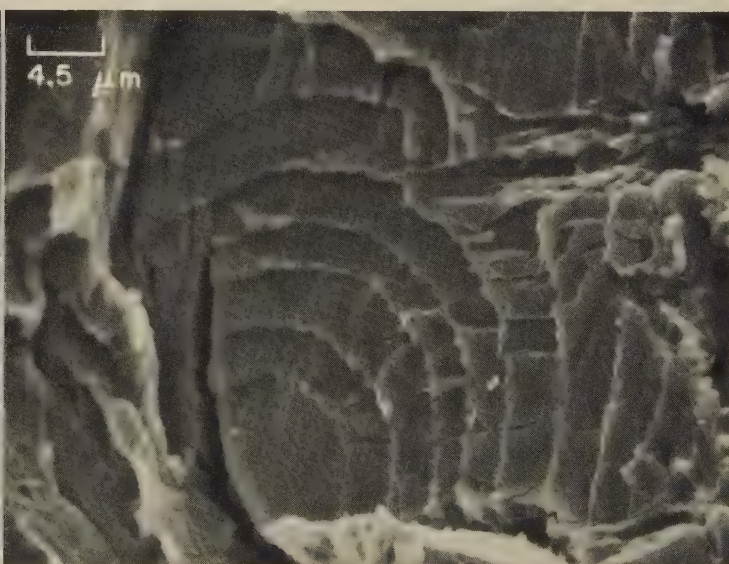


SEM fractograph 230×
4203 Higher-magnification view of the fracture surface in 4202, showing quasicleavage facets and detailed river patterns. Note particularly the unusual concentric pattern of steps at arrow, and compare it with the similar pattern of steps that is shown at higher magnification in 4205 (below).

NOTE. All structures shown on this page are continuous beta phase with dispersed alpha phase.

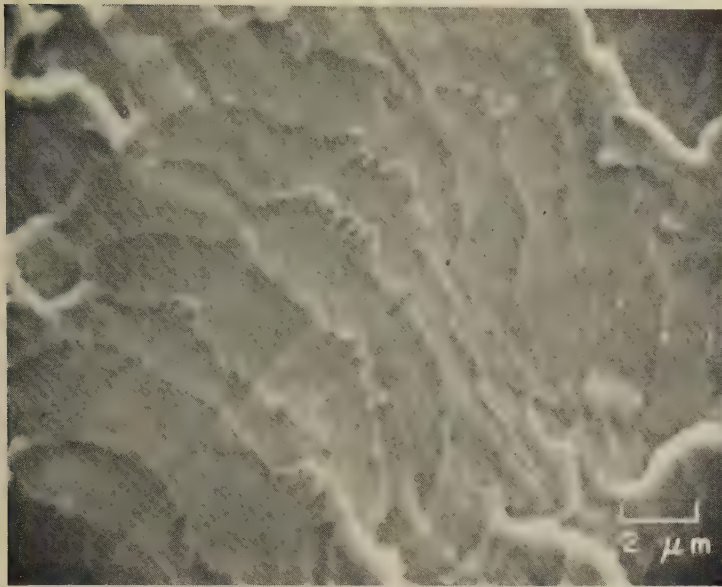


SEM fractograph 230×
4204 Higher-magnification view of the fracture surface in fractograph 4202, showing an area different from that in fractograph 4203. As in 4202, the very angular secondary cracking is noteworthy, and is believed to have been influenced by interfaces between beta phase and acicular alpha phase. Note the fine parallel steps on the angular facets at bottom right.



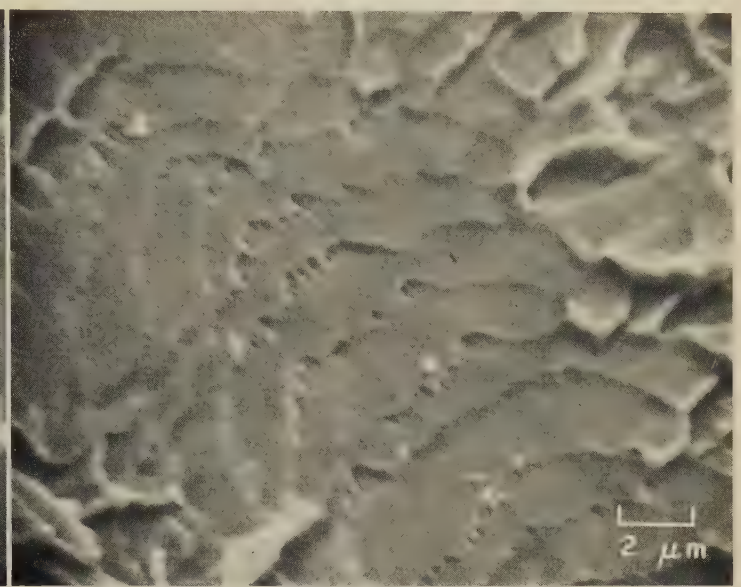
SEM fractograph 2200×
4205 Another view of the fracture surface in fractographs 4202 to 4204, at even higher magnification, showing a region containing a very unusual "terraced" facet that is similar to the area shown and discussed in 4203. It is possible that this relatively flat area was a prior beta grain. Observe also that the "terraces" have cleavage steps of their own.

SEM Fractographs: Titanium Alloy Ti-6Al-4V Fracture-Toughness Tested in Hydrogen (Continued);
Tension-Overload Fracture in a Tungsten-Fiber, Silver-Matrix Composite



SEM fractograph

5000×



SEM fractograph

5000×

4206, 4207 SEM views of the mating surfaces in an area of the fracture shown in 4202 to 4205 that is very similar to the area shown in 4205. This particular type of "terraced" fracture surface was found to be characteristic of all Ti-6Al-4V specimens that have microstructures consisting of beta phase and acicular alpha phase and that have been fracture-toughness tested in a hydrogen atmosphere. Note that the edges of the steps appear to contain small dimples; this seems to be quite unusual in a fracture surface having many of the characteristics of cleavage.

NOTE. The structure shown above is continuous beta phase with dispersed alpha phase.



SEM fractograph

320×

4208 Surface of a tension-overload fracture in a composite consisting of tungsten fibers in a silver matrix. The tungsten fiber marked P has undergone a ductile fracture with necking whereas fiber Q has suffered a sharp, flat, transverse cleavage fracture. See also 4209.



SEM fractograph

10,000×

4209 Higher-magnification view of an area of tungsten fiber P in fractograph 4208 (left). Deformation during fracture has thinned the walls of the dimples to sharp edges, which shows the highly ductile nature of the fracture. Note the uniformity in height of the walls.

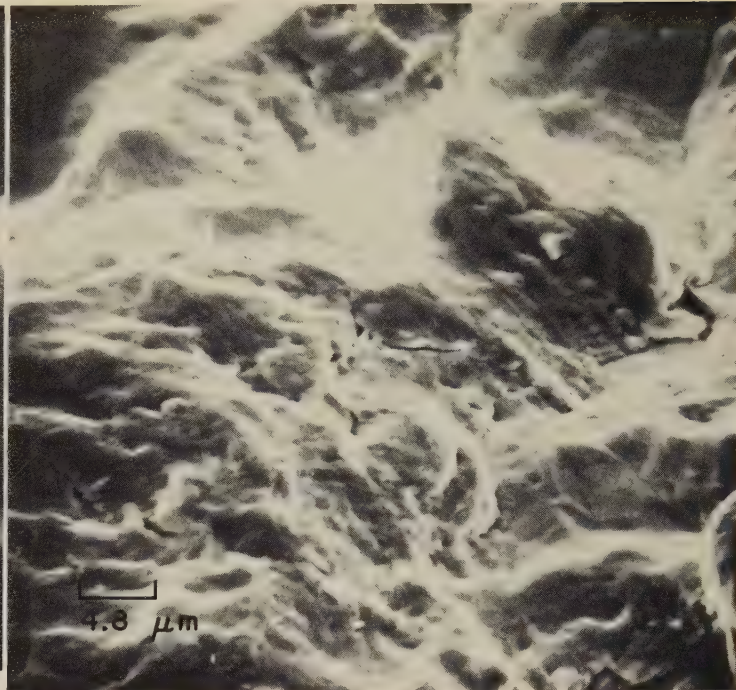
SEM Fractographs; Photograph: Fatigue-Test Fractures in Specimens of Zircaloy-2 and Zircaloy-4



Photograph

6×

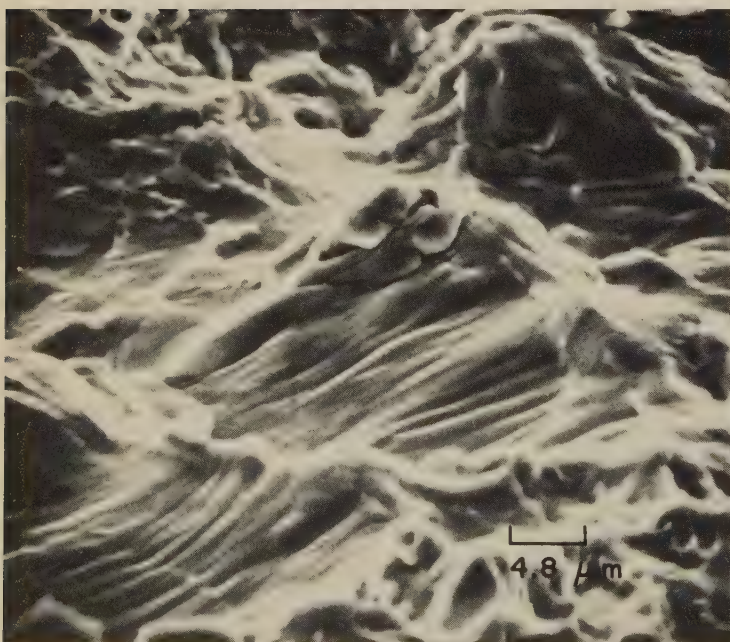
4210 Surface of a partially fractured fatigue specimen of Zircaloy-2 (Zr-1.34% Sn-0.15% Fe-0.10% Cr-0.055% Ni) plate that had been initially annealed and cross rolled at 790 C (1454 F), rolled again at 430 C (806 F), and recrystallized at 625 C (1157 F) for 4 hr. Cracks are located at intersecting slip planes. Total plastic strain was 0.041. See also 4211 and 4212.



SEM fractograph

2100×

4211 Scanning electron microscope view of the surface of a fracture in a specimen similar to that shown in photograph 4210 (left), displaying a combination of dimples and fatigue striations. The applied loading was tension-compression; plastic strain was 0.0185, and failure occurred at 600 cycles.



SEM fractograph

2100×

4212 Same fracture surface as in 4211, but a different area. The axis of the fatigue specimen was in the transverse direction of the plate. Thickness of the plate, 0.525 in. Final minimum specimen diameter was 0.250 in., obtained by longitudinal polishing.



SEM fractograph

25×

4213 Surface of a fracture in a specimen of Zircaloy-4 that was tested in very-low-cycle fatigue. The applied stress was high, producing a very high crack-growth rate in each cycle and the unusually broad fatigue striations visible here.

Comparison of SEM and TEM Stereofractographs

Prepared by John A. Fellows

CONTENTS

Plain carbon steel: impact fracture	282-283
0.65% C, 1.05% Mn steel: impact fracture	284
Class 612 (T2) high speed tool steel: impact fracture	285
4340 steel: tension-overload fracture; high-cycle fatigue fracture	286-287
Aluminum alloy 7075-T6: tension-overload fractures; low-cycle fatigue fracture; stress-corrosion fracture	288-293
Titanium alloy Ti-8Al-1Mo-1V: tension-overload fracture; high-cycle fatigue fracture; stress-corrosion fracture	294-296

THIS SECTION of the Atlas of Fractographs reproduces a portion of "A Comparison Atlas of Electron and Scanning Electron Fractography", a thesis presented by James Lee Hubbard in June, 1971, in partial fulfillment of the requirements for the degree of Master of Science in Metallurgy at Georgia Institute of Technology. These comparisons of SEM and TEM stereofractographs represent the first examples of point-by-point comparison of identical fields of view giving a one-to-one correspondence. They show for the first time that, when properly arranged for stereo viewing (in which hills are hills and valleys are valleys), the contours displayed by the TEM fractographs are the same as those shown by the SEMs despite the difference in appearance of the individual pictures. Even the fact that some of the features in the TEMs lack the true height of the same features in the SEMs (the result of partial collapse of the replica) does not significantly detract from the similarity of contours that can be recognized at once when the fractographs are viewed in 3-D.

The two stereofractographs of each fracture surface presented in the following pages are mounted with the SEM view at the top and the TEM view at the bottom of each set. When viewing in 3-D, the eyes may be shifted from the SEM fractographs to the TEMs and back at will without losing the three-dimensional appearance. It will be observed that the conformity of contour between the SEM and the TEM pairs is surprisingly exact, considering the disparity in appearance between the two types of fractograph.

Method of Preparation

The preparation of these fractographs began in each instance with a careful scan of the fracture surface under a low-power binocular microscope to select an

area of maximum interest. This was then marked by an identifying scratch in the center of the selected area.

A plastic replica of each marked area was prepared using Fullam replica tape No. 1134, which was softened in acetone and then pressed in place to eliminate air bubbles and replicate all crevices. The tape was allowed to harden in place before being stripped from the fracture surface. The first replica of each area, which was made to clean the fracture surface, was discarded, and a second replica was prepared for use in fractographic examination.

Each replica was shadowed with platinum at a 45° angle with a layer about 20 to 30 angstroms thick; this was followed by evaporation of carbon onto the plastic at a 90° angle, to a thickness of about 100 angstroms. Finally, the replica was trimmed to a triangle centered on the identifying scratch mark, with the points of the triangle serving to orient the piece for tilting to produce the stereofractographs. The triangular replica was mounted on a 150-mesh copper grid and immersed in acetone to dissolve the plastic.

Each stereo pair of TEM fractographs was taken at a 6° tilt from the normal to the replica plane, at a selected location acceptably distant from the identifying scratch. The outcome, however, because of the procedure used in preparing the replicas, was a "negative" surface in which each hill was a valley and each valley a hill. This meant that during the shadowing process each valley cast a shadow outside itself. As Hubbard acknowledged, this negative surface made an exact comparison between the TEM and the SEM fractographs difficult, because the SEMs show a positive surface. For the purpose of this Handbook, therefore, it was decided to ignore the nature of the shadowing, and to abandon the original arrangement of the stereo pairs

used by Hubbard by transposing the prints in each TEM pair so that the view originally on the left was moved to become the view on the right. The effect of this was to give a "positive" image in 3-D, with the only strange aspect being the casting of an external shadow by a cavity. This disadvantage is outweighed by providing conformity of contours in the TEM view with those in the SEM, thus making possible a close visual comparison of the two types of fractographs.

After preparation of the replica, the sample was sectioned to produce a specimen suitable for mounting in the scanning electron microscope, with the specimen containing the identifying scratch mark in the center of the fracture area preserved. The specimen was scanned in the microscope to locate the scratch; then, using the TEM fractographs previously prepared, the exact location of the replica was found, and the magnification and orientation adjusted, to give an exact counterpart of the TEMs. The stereo pair of SEM fractographs was taken, tilting the fracture surface to an angle of 6° on both sides of the position normal to the electron beam.

Stereoscopic Viewing

The viewing of stereofractographs is a rewarding experience, well worth the slight effort necessary to acquire the talent. It is reported that 80% of those who try are able to see a three-dimensional image almost at once, 10% will succeed after some effort, and the remaining 10% will probably never be able to acquire the knack. The basis for stereo viewing is the circumstance that if the left eye views one picture and the right eye views a second picture to the right of the first one, and if the two pictures have been taken at a favorable angle of 6° to 7° to each side of "straight ahead", the brain will perceive a single three-dimen-

Comparison of SEM and TEM Stereofractographs: Introduction (Continued); Plain Carbon Steel Fractured by Impact at Room Temperature

sional surface contour. The trick, therefore, is in learning how to make each eye see a separate picture.

There are a number of procedures for undertaking stereo viewing. A simple technique is to roll two sheets of paper to form two tubes 8½ in. long and about 1 in. in diameter, taping the seams to prevent unrolling. Positioning the tubes so that each eye sees only the appropriate print in a stereo pair will at first produce two superimposed views. By relaxing the eyes and concentrating on some prominent feature in the field of view, the two images will drift toward each other and suddenly merge. When that happens, the scene will appear in three dimensions.

The adjustment of the eyes for 3-D viewing is sometimes aided by the use of a special viewer, of which several types are commercially available. A simple but effective stereo viewer, imprinted with appropriate instructions, is contained in the pocket on the inside back cover of this volume. The low-power enlargement provided by the lenses of this viewer appears to assist in encouraging the eyes to "see separately". With a little practice, the attention may be shifted vertically (that is, toward the top or the bottom of the page) without disturbing the three-dimensional image.

A more durable viewer is available for about \$20 (1974 cost) from Abrams Instrument Corp., 606 East Shiawassee St., Lansing, Mich. This viewer (Folding

Pocket Stereoscope, Model CF-8) has the advantage that the distance between the lenses is adjustable to match the spacing between the eyes.

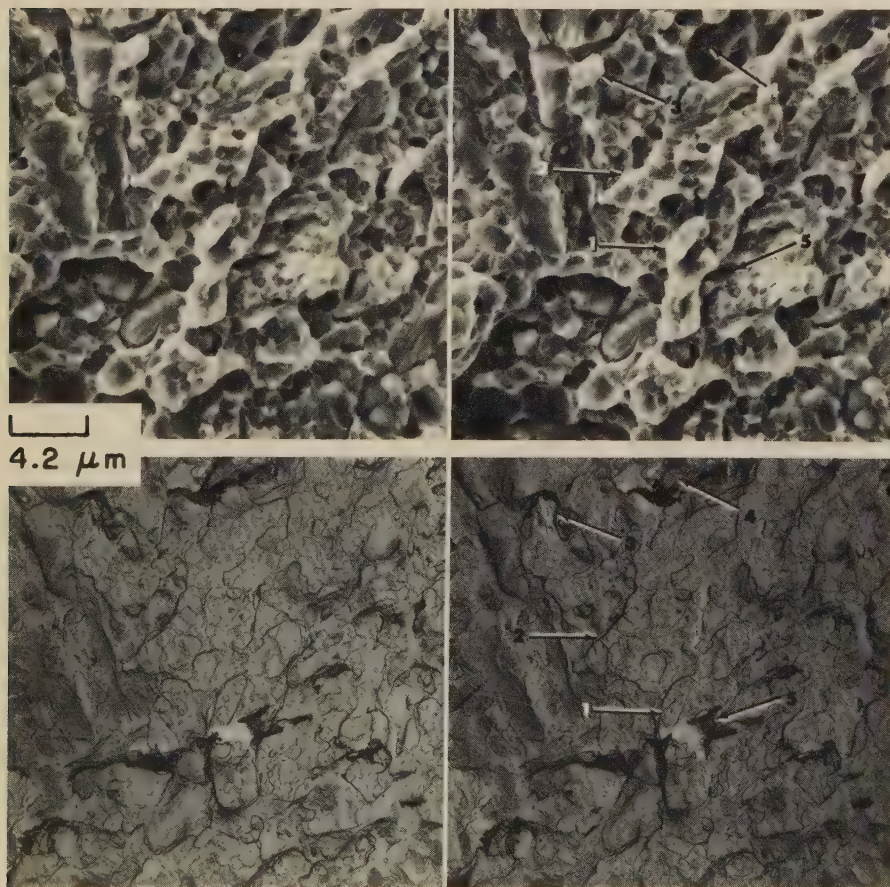
The spacing and therefore the width of stereo-pair pictures are chosen on the basis of the average eye spacing. Beginning at some stereo-pair spacing less than normal, it becomes somewhat more difficult to adjust the eyes for 3-D viewing as that spacing is increased. Obviously, it is not feasible to use a distance between conjugate points of the two prints that is greater than the eye spacing, because that would require the lines of sight of the eyes to diverge. Thus, the maximum width of each print in a stereo pair should not be greater than the spacing selected. It is usual practice to select a less-than-average eye-spacing distance so that all types of eyes can view the stereo pair without difficulty. A frequently used distance is between 55 and 60 mm, but examples of stereo pairs with spacings as small as 40 mm can be found in metallurgical journals.

There are occasions in which the use of large stereoprints is desirable. The means for viewing them in 3-D is a binocular arrangement that permits two lenses to focus on two prints whose common features are at a considerably greater distance apart (as, for instance, two 8-by-10-in. prints), with the images of those lenses transferred by means of prisms to a pair of eyepieces set at a

spacing to match the viewer's eyes. This binocular type of instrument is highly satisfactory for special laboratory use, but expensive for casual viewing (for example, the Wild Heerbrugg viewer of this type, from Switzerland, costs, at present writing, about \$1000).

The ultimate solution for the viewing of ordinary stereo pairs in three dimensions is to induce the unaided eyes to see the two prints separately. The basis for achieving this is focusing the eyes on a distant object, one that is more than 100 ft away, and then transferring attention to the stereo pair held adjacent to the line of sight. One destructive method is to punch a hole at an exact point in each print of a stereo pair used for training, and then hold the pair at arm's length while looking through the holes at a remote scene. Transferring attention to the pictures will provide 3-D vision when the two holes suddenly fuse into one.* A similar procedure is simply to gaze just over the top of the prints at the horizon. It will be found quite promptly (by all but the less fortunate 20%) that the focus of the eyes can be changed from the remote to the near at hand without allowing the eyes to point toward each other as in focusing on a very close object.

*This procedure is discussed, and stereofractographs are provided for practice, in a report by C. D. Beachem, "The Interpretation of Electron Microscope Fractographs", U. S. Naval Research Laboratory, NRL Report 6360, Jan 21, 1966.



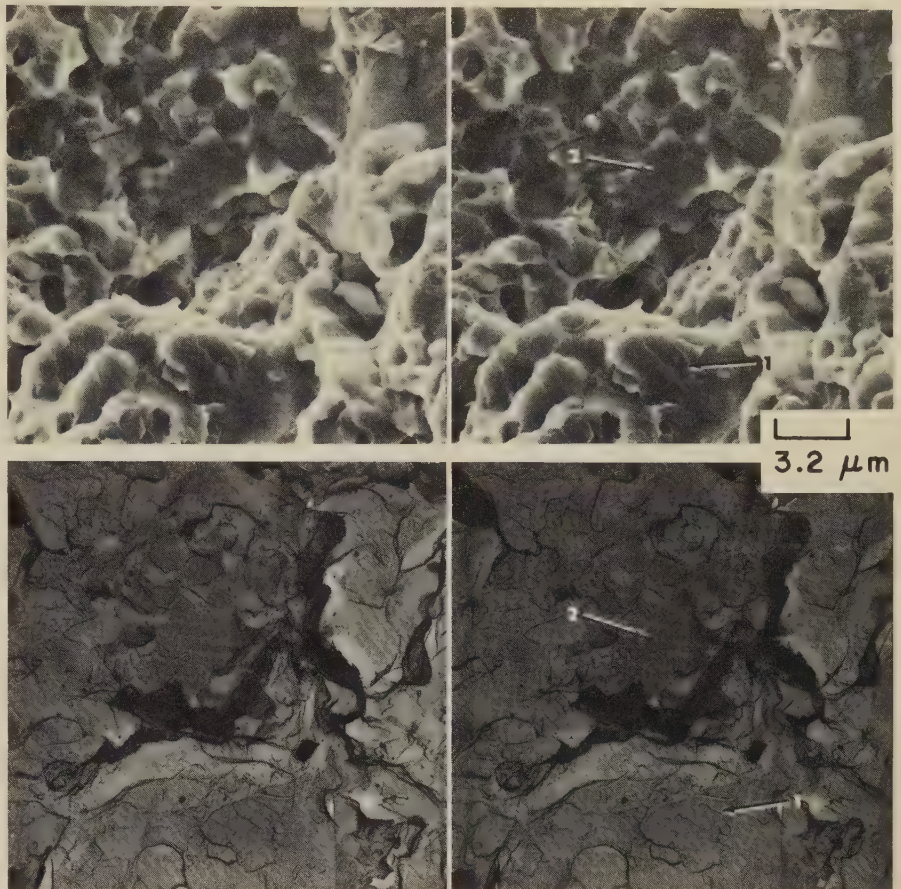
SEM (4214) and TEM (4215) stereofractographs 2400×

4214 Surface of a room-temperature impact fracture in plain carbon steel after heat treatment at 800 C (1472 F) for 5 min and oil quenching. The specimen was fractured untempered, at a hardness of Rockwell C 65. The fracture surface exhibits dimples resulting from microvoid coalescence, and small local areas of quasicleavage facets. Viewing these fractographs in 3-D assists greatly in recognition of the features that are common to both views. For instance, the roughly oval tip of a projection at arrow 1 in the SEM view can easily be identified in the TEM. A feature with a crudely triangular tip pointing to the left (arrow 2) is also readily recognized. The upper portion of this feature, however, appears much flatter in the TEM view than in the SEM, although local marks can be identified in each. Another site of conformance between the SEM and TEM stereofractographs is at arrow 3. Some details are lost at arrows 4 and 5 in the TEM pair, because of local tearing of the replica. See also fractographs 4216-4217 and 4218-4219, on the opposite page.

Comparison of SEM and TEM Stereofractographs: Plain Carbon Steel Fractured by Impact at Room Temperature (Continued)

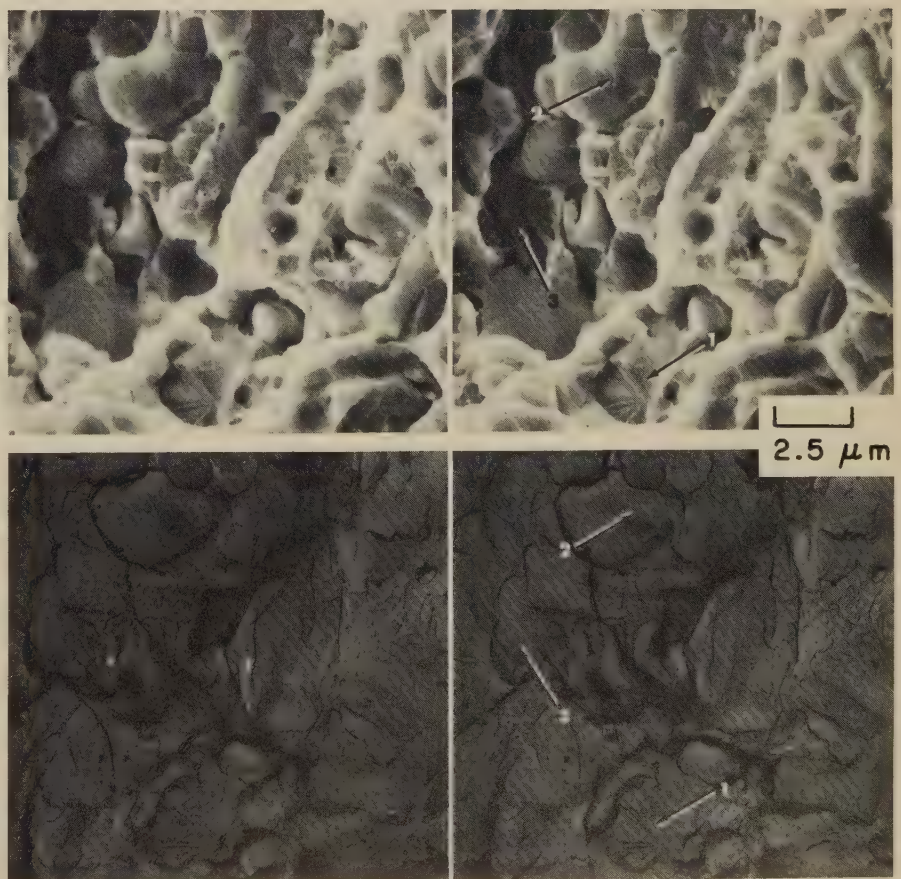
SEM (4216) and TEM (4217) stereofractographs 3100×

4216 A second set of SEM and TEM stereofractographs of the fracture surface in 4214
4217 and 4215 (room-temperature impact fracture in plain carbon steel), showing a different area and at higher magnification. Again, the fracture surface exhibits dimples and quasicleavage facets. Some of the latter are shown with much the same details in each stereo pair. At arrow 1, for example, both the SEM and the TEM stereofractographs display the same cleavage steps; the TEM view shows them more sharply but the SEM presents them in greater three-dimensional relief. Another example is at arrow 2; the facet is clearly recognizable, and has identical shape and orientation, in both reproductions, but the fine detail is more sharply registered in the TEM pair. The deep gulf between arrows 1 and 2 (viewing in stereo is essential to an appreciation of the contours of this gulf) is plainly shown in the SEM pair, but is obscured by tearing of the replica in this area in the TEM. Evidently, the depth of the gulf made stripping difficult. See also 4218-4219, below.

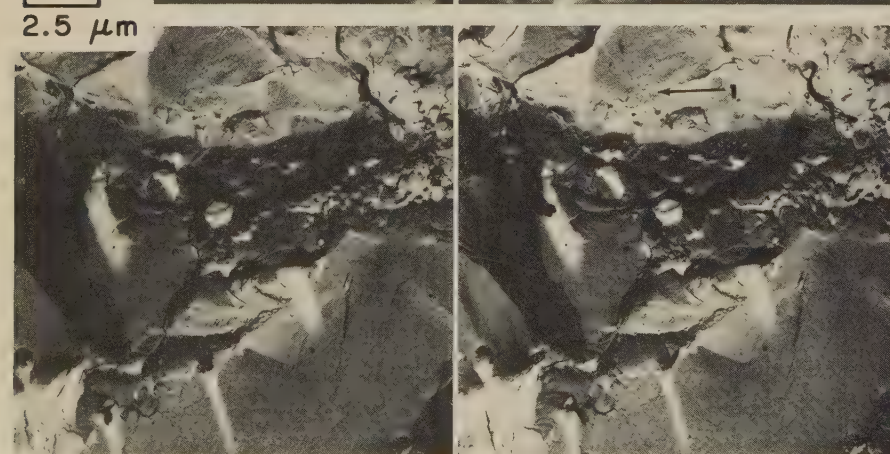
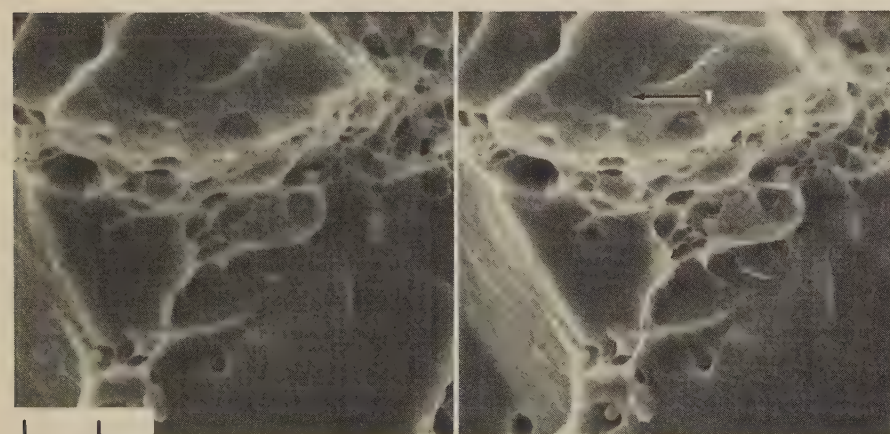
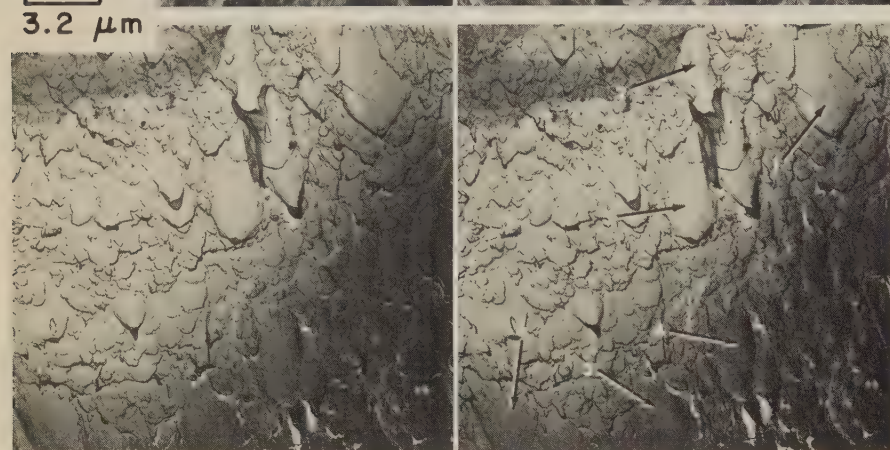
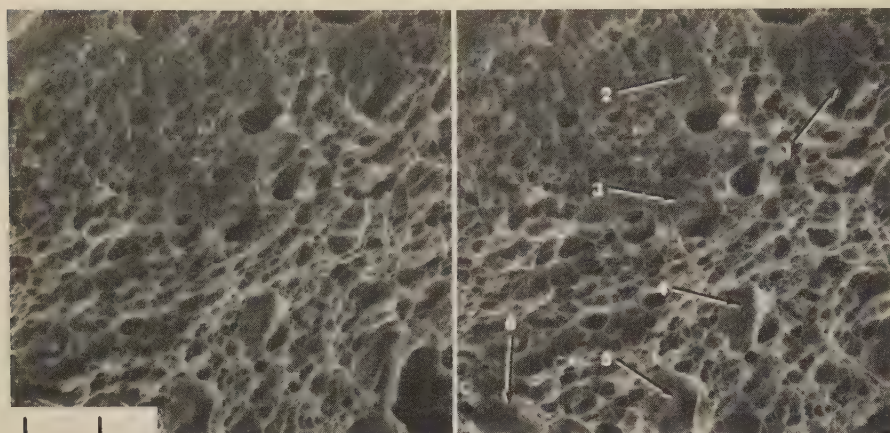


SEM (4218) and TEM (4219) stereofractographs 4000×

4218 A third area in the surface of the impact fracture in plain carbon steel in 4214-4215
4219 and 4216-4217, as presented by SEM and TEM stereofractographs at even greater magnification. The fracture characteristics resulting from microvoid coalescence and quasicleavage are unaltered. In the facet at arrow 1, both the SEM and the TEM views show the distinct, fan-shaped pattern of cleavage steps—again, as in 4216-4217, with the details more sharply outlined in the TEM. The small cavity just to the right in the SEM pair is, however, obscured by what is apparently a replica tear in the TEM. A similar contrast in details is available at arrow 2; both the SEM and the TEM views register the same fracture outlines, with the TEM view giving more fine detail and the SEM view presenting the major details in greater three-dimensional relief. Both pairs record the deep area (arrow 3) completely. One noteworthy item in the SEM pair is the veil-like feature just below arrow 3; this may be some remnant of the replica applied before the SEM fractograph was taken.



Comparison of SEM and TEM Stereofractographs: Low-Alloy Manganese Steel (0.65% C, 1.05% Mn)
Fractured by Impact at Room Temperature After Oil Quenching



SEM (4220) and TEM (4221) stereofractographs 3100×

4220 Surface of a room-temperature impact

4221 fracture in low-alloy manganese steel
(0.60 to 0.70% C, 1.0 to 1.1% Mn) that was
oil quenched from 900 C (1652 F) before

being broken. The surface shows mainly shear dimples, some of which (at upper right in each stereo pair) are large enough to display areas of stretching. (It should be noted that a TEM replica of such large dimples may sag or collapse and, as in this comparison, introduce a very different appearance to the dimples from that displayed in an SEM view.) Specific dimples may be identified without question in each pair of views, and a number of these have been indicated by arrows 1 to 6. Observe, however, that the sense of depth, particularly in the larger dimples in the SEM pair, is quite lacking in the TEM. Nonetheless, the presence of an extremely large range of dimple sizes in this fracture surface is clearly established by the fractographs produced by both techniques. See also 4222-4223, below.

SEM (4222) and TEM (4223) stereofractographs 4000×

4222 Same room-temperature impact fracture

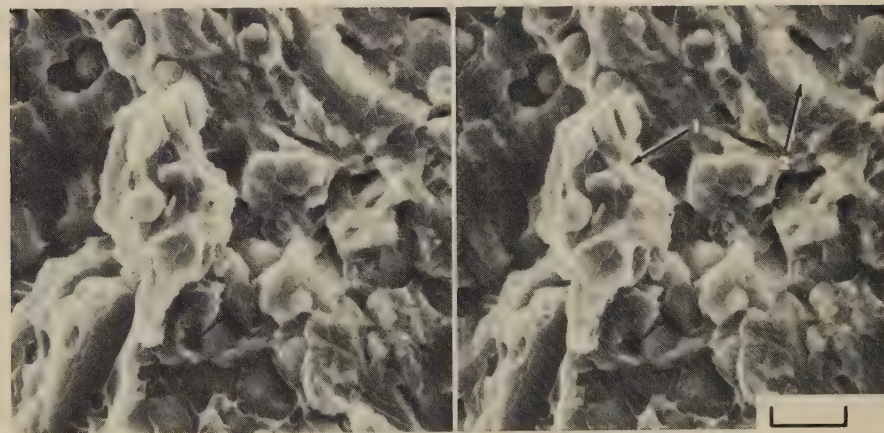
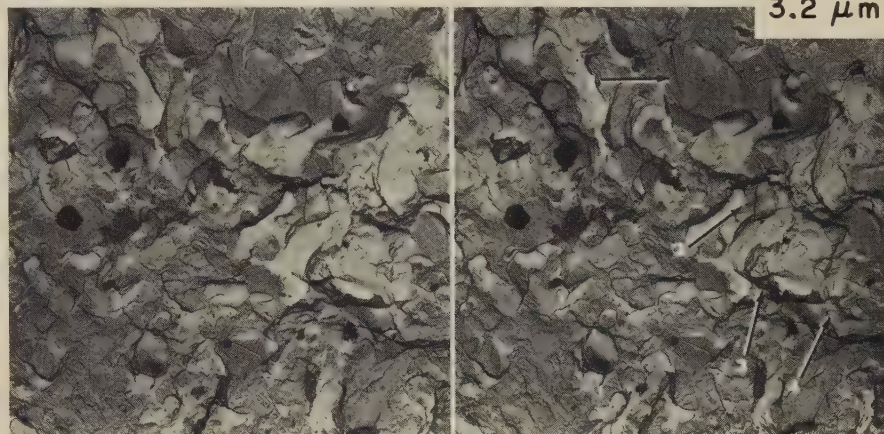
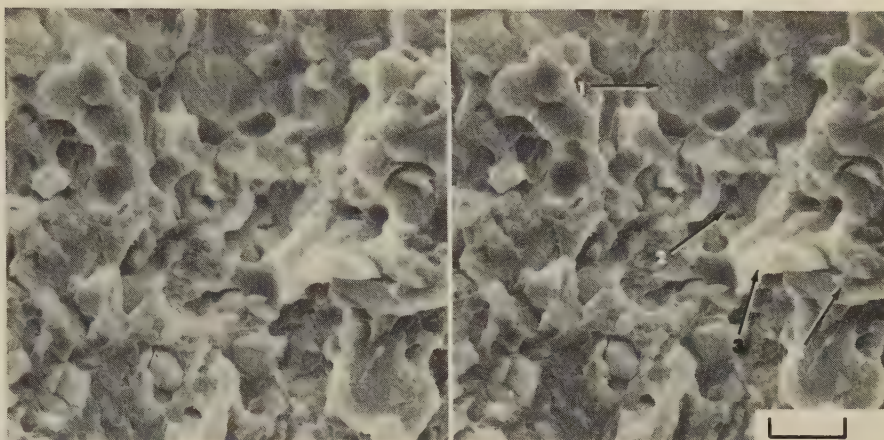
4223 in low-alloy manganese steel as in 4220-4221, but a different area of the fracture

surface and at higher magnification. Visible are large cleavage facets with intervening regions containing dimples. The slightly dish-shaped appearance of the elevated area at arrow 1 shows very exact conformance between the fractographs produced by the two techniques. Observe also that the dimples below this dish-shaped area, on the surface that appears to be nearly vertical in 3-D, have a very similar appearance in both stereo pairs. Note that the shadowing in the TEM pair now appears as "spillage" marks from dimples; this is because the TEM reproduction was prepared as a negative replica but for this presentation has undergone transposition of the stereo pair to give a positive surface view for comparison with the SEM pair. Some of the dimples contain inclusions, which in this instance are better revealed by the SEM pair than by the TEM pair.

Comparison of SEM and TEM Stereofractographs: Class 612 (T2) High Speed Tool Steel Fractured by Impact at Room Temperature

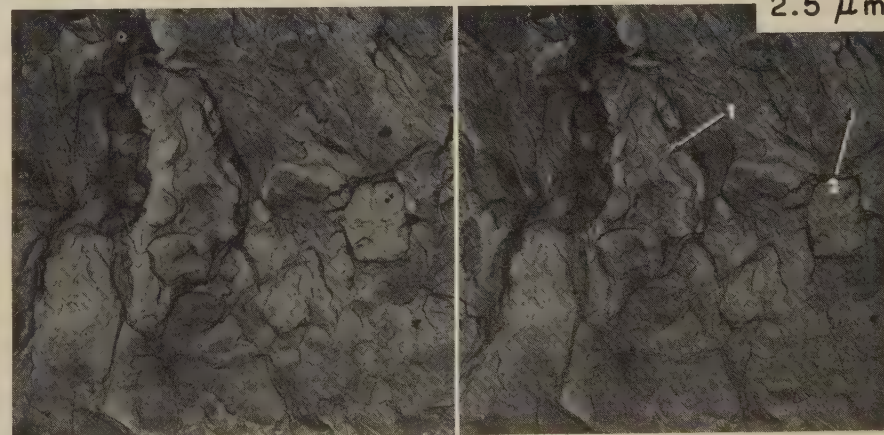
SEM (4224) and TEM (4225) stereofractographs 3100×

4224 Surface of a room-temperature impact fracture in a specimen of class 612 (T2) high speed tool steel having a nominal composition of 18% W, 4% Cr, 2% V and 1% C. The specimen had been heat treated for 5 min at 1200 C (2192 F) and oil quenched, and tempered for ½ hr at 500 C (932 F) and air cooled, yielding a hardness of Rockwell C 64. Surface shows quasicleavage facets and scattered dimples. In some of the features, the two fractographic techniques provide exact duplicates; in others, some details are missing from the TEM view. The region around the quasicleavage facet at arrow 1 is an example of quite good, detailed conformance between SEM and TEM, including the deep hole below (at arrow 2). At arrow 3, stereo viewing of the SEM pair reveals a very high prong that is not found in the TEM; this bears evidence that the replica tore very locally. Compare, however, the fine details that appear in both pairs at arrow 4, as well as at other points of duplication. See also 4226-4227, below.

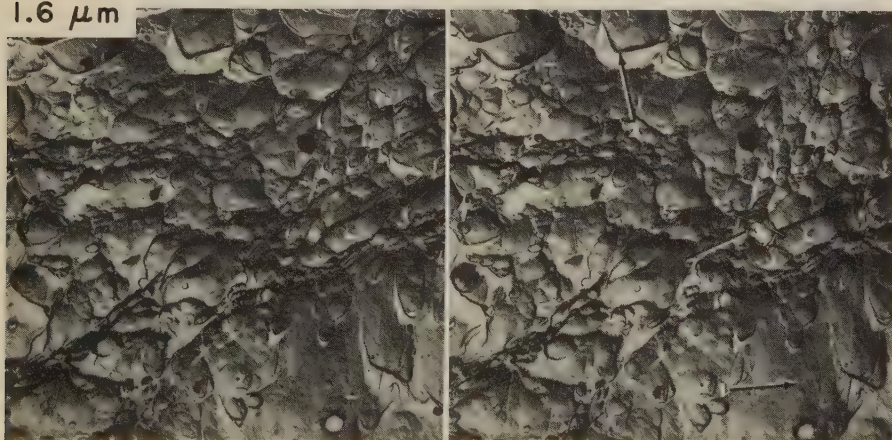
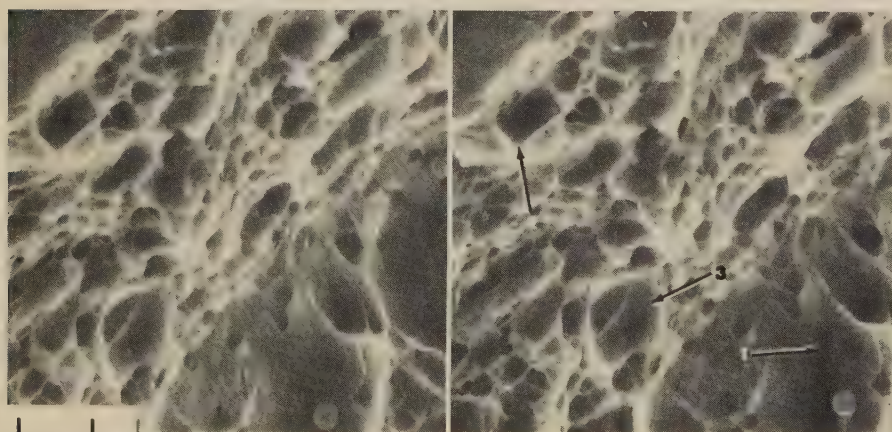
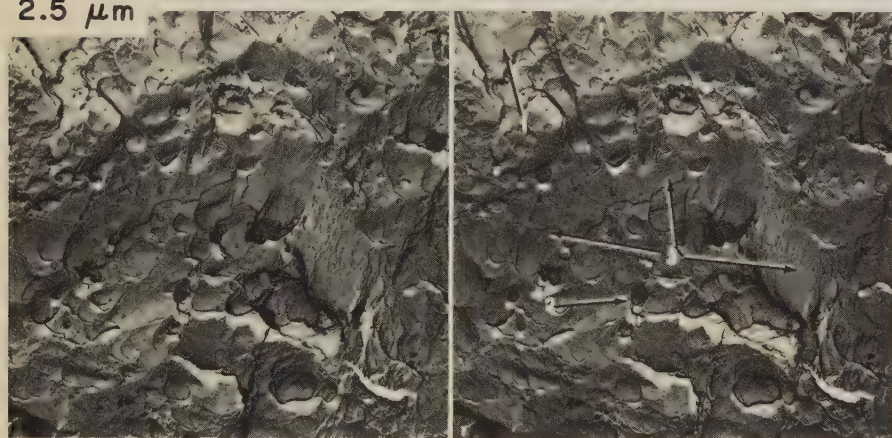
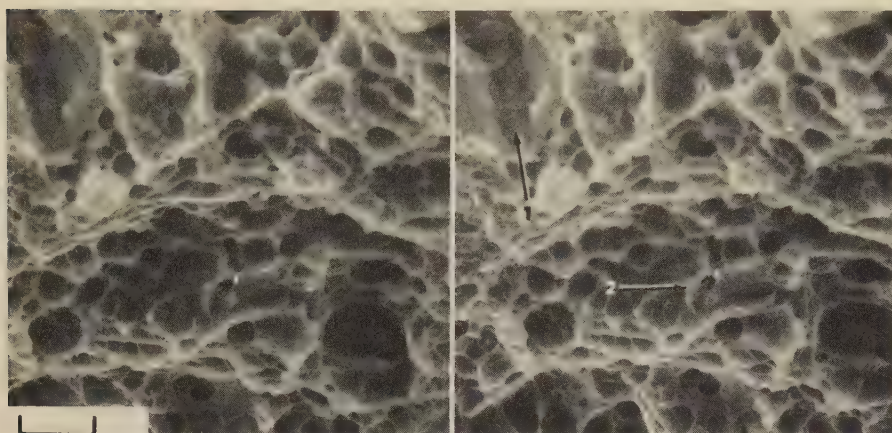


SEM (4226) and TEM (4227) stereofractographs 4000×

4226 Views of a different area, and at higher magnification, of the fracture surface in 4224-4225, above. This is a remarkably complex area, containing many small and varied quasicleavage facets and exhibiting a number of spheroidal inclusions. The most prominent feature is the high peak at arrow 1, which is reproduced in very faithful and identical detail in both stereo pairs. Note that the two inclusions between the twin tips of the peak are shown in both pairs, but that similar inclusions slightly nearer the top of the SEM pair are missing in the TEM because of damage to the replica. The top center area of the SEM view appears to record a greater number of surface complexities than does the same area in the TEM view; at arrow 2, however, the TEM view displays very fine fracture marks that cannot be found in the same location in the SEM view.



Comparison of SEM and TEM Stereofractographs: Notched Specimen of 4340 Steel Fractured by Tension Overload at Room Temperature



SEM (4228) and TEM (4229) stereofractographs 4000×

4228 Fracture surface of a notched specimen of

4229 4340 steel heat treated ½ hr at 816 C (1500 F) and oil quenched, tempered 1 hr at

260 C (500 F) and air cooled to give a hardness of Rockwell C 50, then broken by tension overload at room temperature. The surface is dimpled, with at least one area (at arrow 1) showing some evidence of stretching. At first glance, the TEM pair appears to bear little resemblance to the SEM, but careful scrutiny in 3-D of the sites at arrows 1 and 2 establishes that they are indeed identical. The major area of departure appears to lie in the regions marked 3 in the TEM pair. Study of the SEM pair shows that the direction of observation is essentially tangential to these regions, which are not visible because of overhang. An SEM view of this area taken at a 30° angle (not shown) disclosed stretched regions containing the same dimples as those in the regions marked 3 in the TEM pair. See also 4230-4231, below.

SEM (4230) and TEM (4231) stereofractographs 6400×

4230 A higher-magnification set of views of another area in the tension-overload fracture in the notched specimen of 4340 steel

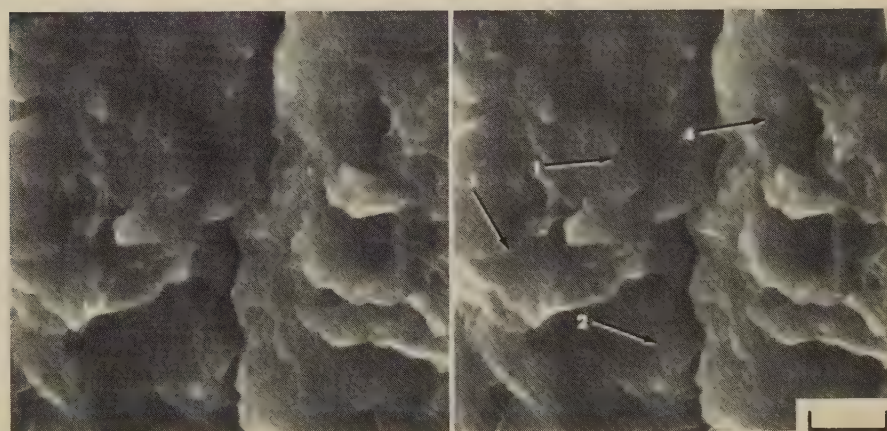
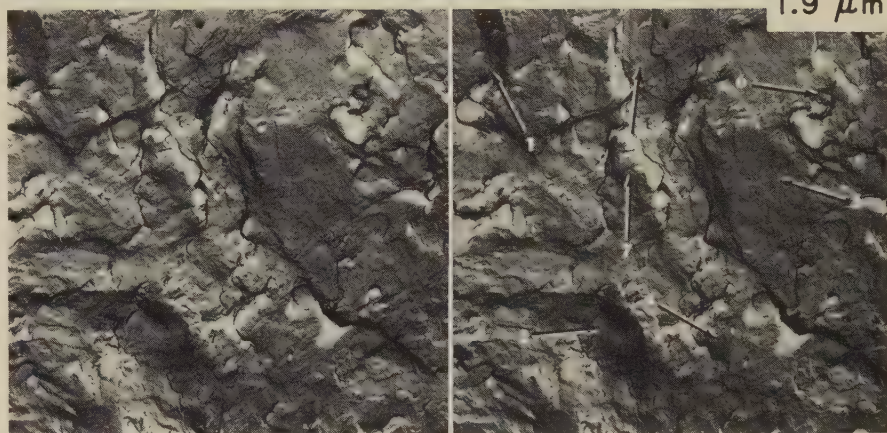
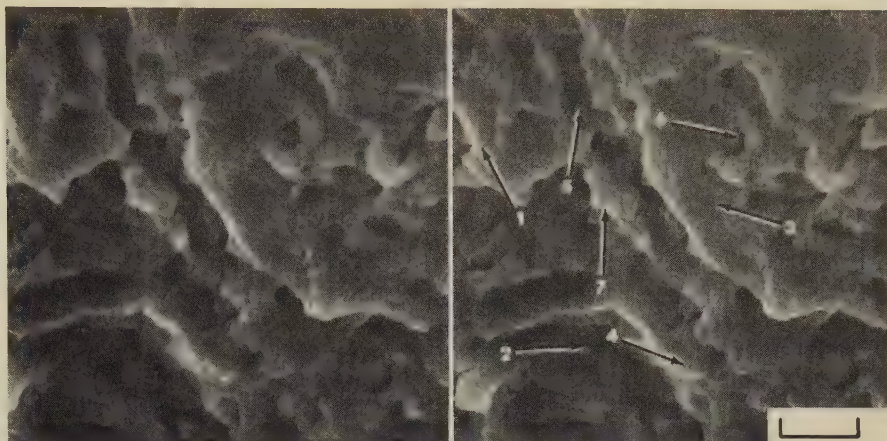
4231 in 4228-4229, showing a somewhat similar fracture surface consisting predominantly of dimples. Unlike 4228-4229, the SEM and TEM pairs here are readily recognized as showing the same fracture contours. The features indicated by arrows 1, 2 and 3, for instance, are obviously the same in both pairs. Even the inclusion at arrow 1 can be seen in both the SEM and the TEM. Note that in the TEM replica, the shapes of both the large and small dimples bear a very close resemblance to those of the dimples in the SEM pair; this is even more apparent when the stereo pairs are viewed in 3-D. Note particularly the features displayed in the stretched dimple at arrow 1; each contour found in one pair can be identified in the other.

Comparison of SEM and TEM Stereofractographs: 4340 Steel Specimen Fractured by High-Cycle Fatigue in Tension

SEM (4232) and TEM (4233) stereofractographs 5250×

4232 Surface of a high-cycle fatigue crack in the same 4340 steel, with the same heat treatment and hardness, as in 4228-4229.

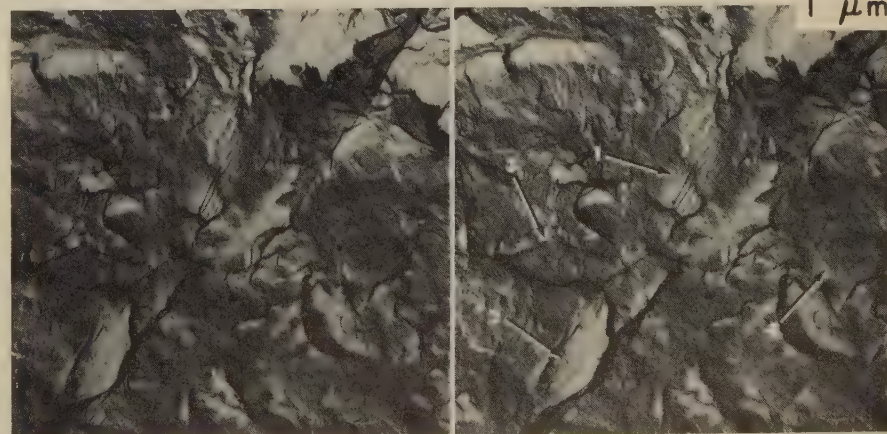
4233 The specimen was tested in tension at a maximum stress of 234 MPa (34 ksi) but was not fractured (a similar specimen broke at 75,000 cycles). This area of the surface is irregular and may have undergone rubbing in being opened up. In regions at arrows 1 and 2, the crack appears partly intergranular. Fatigue striations are faintly visible in the TEM pair at arrows 3 and 4, but none are resolved in the SEM. The match in topographies revealed by the two techniques is excellent; particular attention is called to the matching contours in the two views at arrows 5, 6 and 7. There appear to be several secondary intergranular cracks; some of these cracks, although they are more distinct in the TEM pair, are visible also in the SEM, whereas others can be seen only in the TEM. See also fractographs 4234-4235, below.



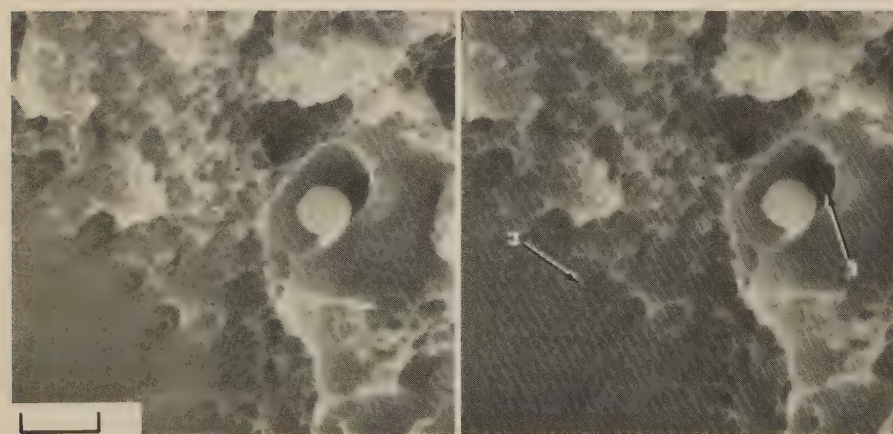
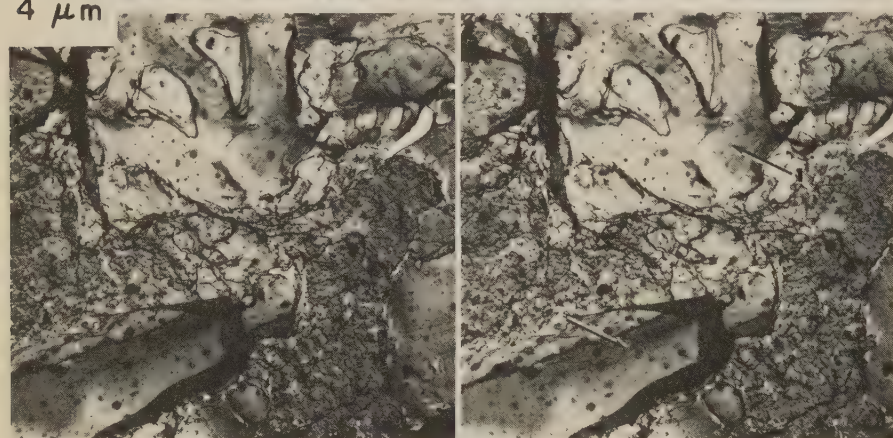
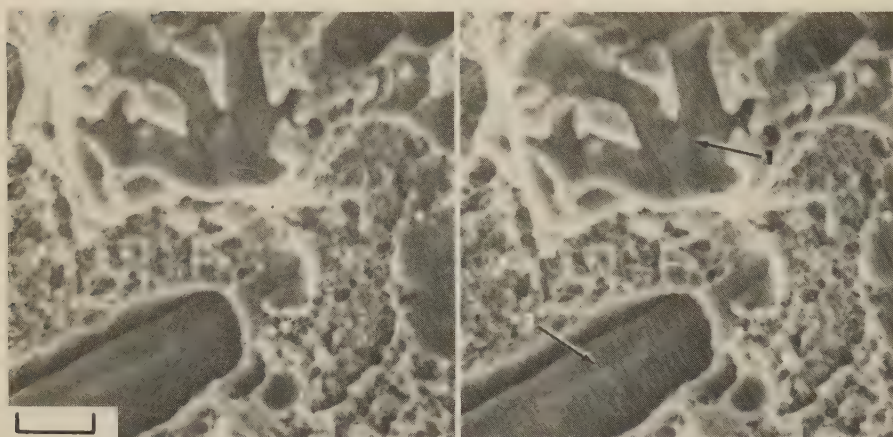
SEM (4234) and TEM (4235) stereofractographs 10,080×

4234 A more highly magnified set of views of another area in the high-cycle fatigue fracture in 4340 steel in 4232-4233. The fracture surface bears a few poorly defined fatigue striations and appears to have received considerable rubbing. A number of secondary cracks are evident, some of which seem to be intergranular.

4235 Comparison between the SEM and the TEM pairs is somewhat difficult, because features in the two views are oriented at different angles. However, careful scrutiny reveals that certain features are indeed common to both pairs, one of them being the patch of what appear to be fatigue striations at arrow 1. These are much more clearly visible in the TEM pair, because those in the SEM lack contrast. Another region of similar marks can be seen at arrow 4 in the TEM but cannot be discerned in the SEM. Other features identifiable in both pairs are marked by arrows 2 and 3.



Comparison of SEM and TEM Stereofractographs: Aluminum Alloy 7075-T6 Notched Specimen
Fractured by Tension Overload at a Crosshead Velocity of 0.002 In. Per Minute



SEM (4236) and TEM (4237) stereofractographs 2500×

4236 Surface of a fracture produced at room temperature in a notched specimen of aluminum alloy 7075-T6 by tension overload at a crosshead speed of 0.002 in. per minute. The tensile strength of the specimen was 592.3 MPa (85.9 ksi). The surface shows quite fine equiaxed dimples surrounding sites of large second-phase particles. The conformity in contour between the SEM and the TEM stereo pairs is excellent, particularly when they are viewed in 3-D. Of especial interest is the area marked by arrow 1 near the top of each pair, which had been in contact with second-phase particles. Near the bottom, at arrow 2, is a second-phase particle in a cavity that has started to open up. Note that the dimples around the perimeter of this large particle show exact correspondence between the SEM and the TEM pairs. Also, the very tiny dimples in the TEM view resemble closely the appearance of those in the SEM. See also 4238-4239, below.

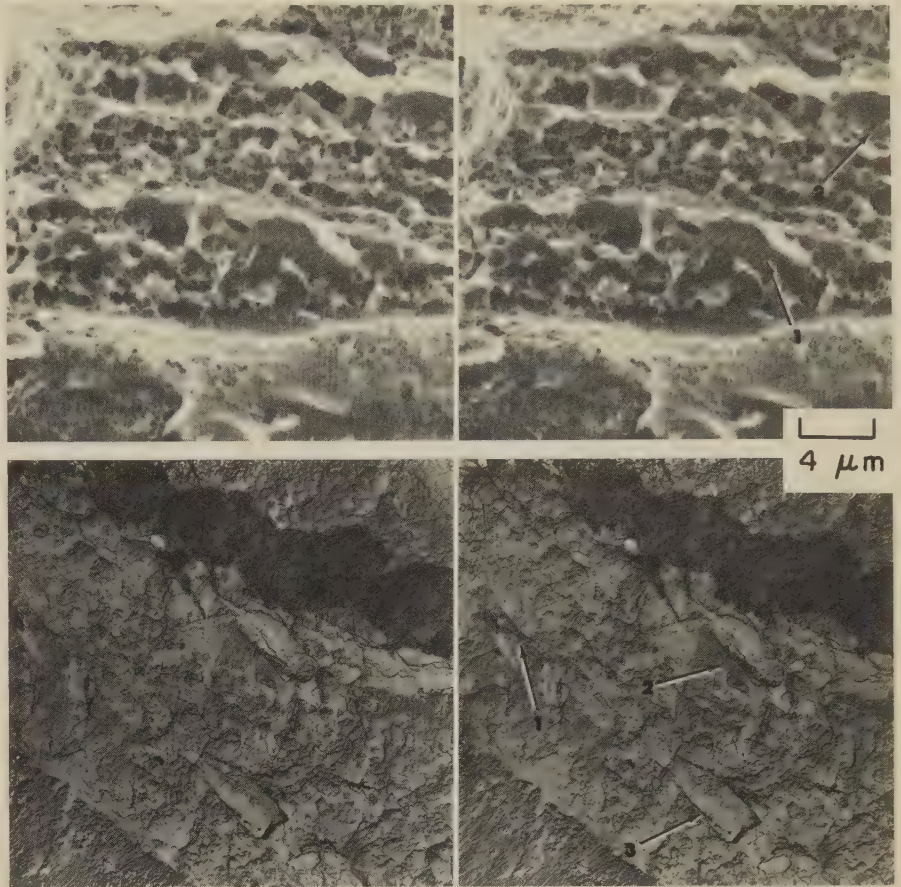
SEM (4238) and TEM (4239) stereofractographs 5250×

4238 Comparison SEM and TEM views of another area in the tension-overload fracture surface of aluminum alloy 7075-T6 shown in 4236-4237, at higher magnification. This surface contains equiaxed dimples, shear dimples, a stretched area, and second-phase particles. The dark spots at arrow 1 in the stretched area of the TEM replica are artifacts that undoubtedly resulted from the deposition of a foreign material during dissolution of the first-stage plastic replica. The SEM stereofractograph gives a better idea of the topography than does the TEM when the members of each pair are viewed individually, but both reproduction techniques afford equivalent perception of the contours when the views are observed in stereo. The TEM stereo pair shows more detail in the hole behind the second-phase particle at arrow 2 than is shown in the SEM. Equivalent detail in the SEM would be produced by a change of exposure. Arrow 3 marks an area where the TEM pair gives much fine detail of the shear dimples, which is not resolved in the SEM.

Comparison of SEM and TEM Stereofractographs: Aluminum Alloy 7075-T6 Notched Specimen Fractured by Tension Overload at a Crosshead Velocity of 0.5 In. Per Minute

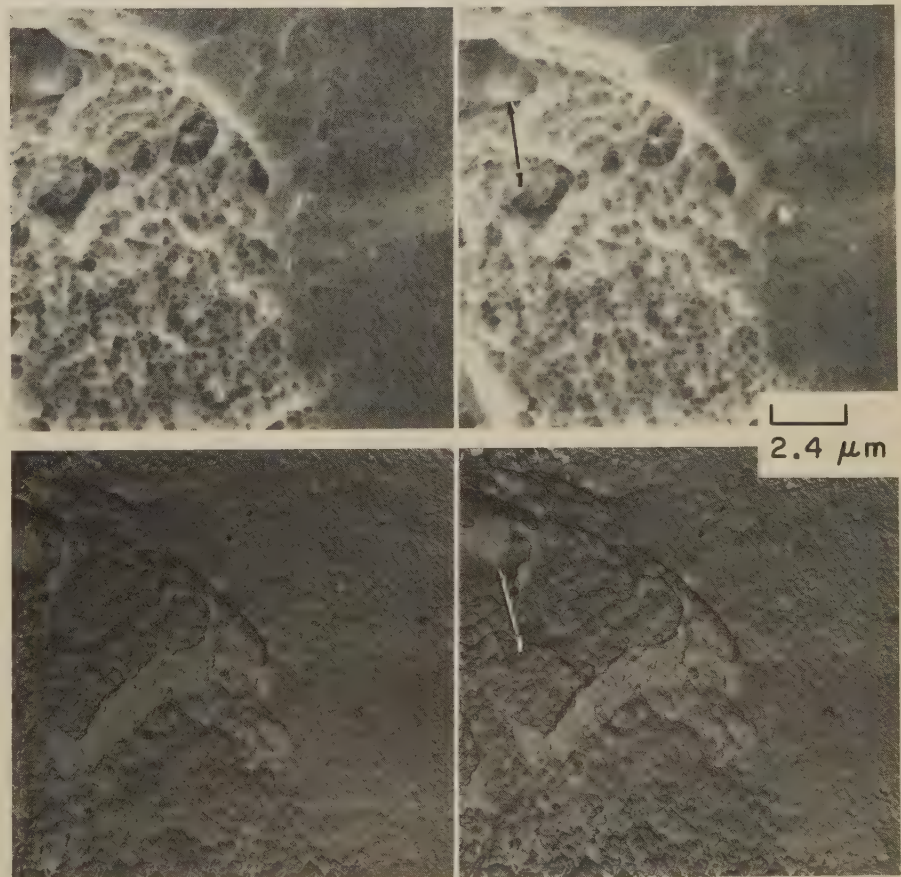
SEM (4240) and TEM (4241) stereofractographs 2520×

4240 Surface of a tension-overload fracture in a notched specimen of aluminum alloy 7075-T6 that, like the specimen shown in 4236-4237 and 4238-4239 (facing page), was tested at room temperature, but at a crosshead speed of 0.5 in. per minute — which is more normal. The surface, however, is somewhat similar to that of the specimen tested at the lower crosshead speed, containing equiaxed dimples and sites where second-phase particles exist or previously existed. Comparison of the SEM pair with the TEM pair is somewhat difficult because the orientation of view in the two pairs is at different angles and thus the two show areas that do not exactly coincide. Also, the dark band near the top of the TEM view (an artifact caused by tearing and overlapping of the carbon replica) alters its appearance. Study of the comparison views in stereo shows that the sharp edge of the abyss at the bottom of the SEM fractograph appears across the lower left corner in the TEM fractograph. Furthermore, it is evident that the sites marked by arrows 1 and 2 are the same features in the two reproductions. The second-phase particle at arrow 3 in the TEM view is not included in the SEM. See also 4242-4243, below.

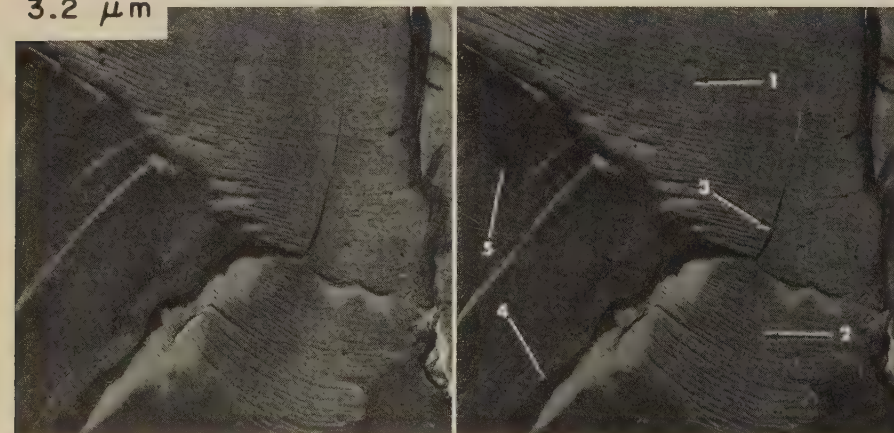
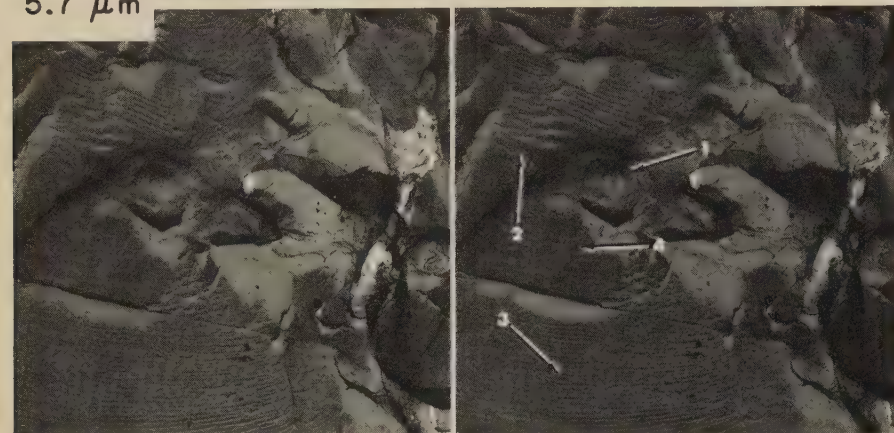
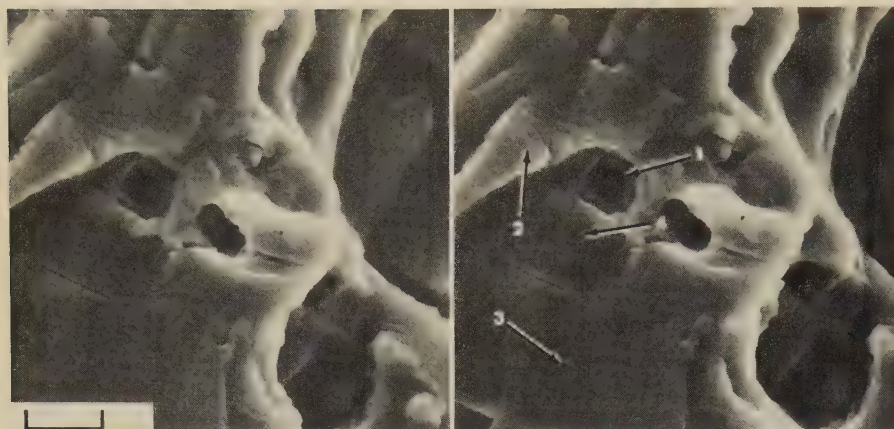


SEM (4242) and TEM (4243) stereofractographs 4200×

4242 Higher-magnification comparison views of another area in the tension-overload fracture of the notched specimen of aluminum alloy 7075-T6 discussed in 4240-4241. Like the surface shown in those stereofractographs, the area here also displays fine equiaxed dimples and, at arrow 1, what is apparently a second-phase particle. A large portion of this area is a relatively smooth incline that may be a previous interface with a very large second-phase particle. The views shown by the SEM and the TEM pairs are in exact agreement, and individual dimples can be identified in the two surface reproductions. As is evident in many of these examples, the heights and depths of the topography as portrayed by the SEM are materially more pronounced than the counterparts portrayed by the TEM.



Comparison of SEM and TEM Stereofractographs: Aluminum Alloy 7075-T6 Fractured by Low-Cycle Fatigue



SEM (4244) and TEM (4245) stereofractographs 1760×

4244 The first of four sets of views, at increasing magnification, showing four areas of the surface of a low-cycle fatigue-test fracture in aluminum alloy 7075-T6 obtained with a maximum loading of 117 MPa (17 ksi) at 1900 cycles per minute. Fracture occurred at 600,000 cycles. The tensile strength of the material was 586 MPa (85 ksi). The fracture surface is characterized by well-defined fatigue striations and prior sites of second-phase particles. There appear to be secondary cracks—possibly of an intergranular nature. The topographic details in the area shown here (for example, the contour at arrow 1) can be easily recognized in both the SEM and the TEM pairs. The fatigue striations show differences that are characteristic of the two reproduction techniques. The striae are readily identified in both fractographs at arrow 2. Careful scrutiny of the SEM fractograph shows the striations that are sharply outlined at arrow 3 in the TEM. At arrow 4, the TEM pair displays very fine striations that are not resolved in the SEM. See also 4246-4247 (below) and 4248-4249, 4250-4251 (next page).

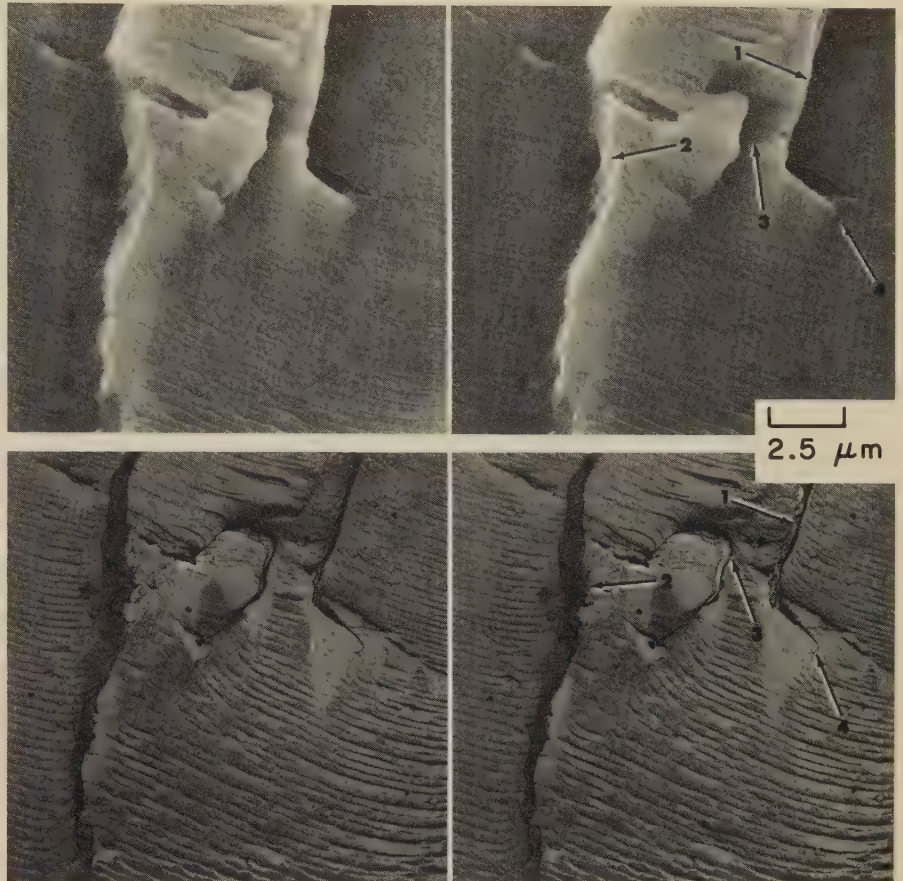
SEM (4246) and TEM (4247) stereofractographs 3100×

4246 A higher-magnification set of views showing another area of the surface of the low-cycle fatigue-test fracture in aluminum alloy 7075-T6 in 4244-4245. The fracture surface here is made up of several fatigue-striation patches. In the regions at arrows 1 and 2, the striations are shown quite clearly in both the SEM and the TEM pairs, but their contours are much more sharply defined in the TEM. Arrows 3 and 4 designate locations where the TEM replica was torn or overlapped. In the narrow fatigue patches at left in these views, the fatigue striations that are easily seen in the TEM pair are seen with difficulty at arrow 5 in the SEM. These striations could be brought out more clearly in SEM reproduction with more favorable contrast and a more desirable angle of illumination by the electron beam. However, the resolution attainable with the SEM technique is not comparable to that attainable with the TEM.

Comparison of SEM and TEM Stereofractographs: Aluminum Alloy 7075-T6 Fractured by Low-Cycle Fatigue (Continued)

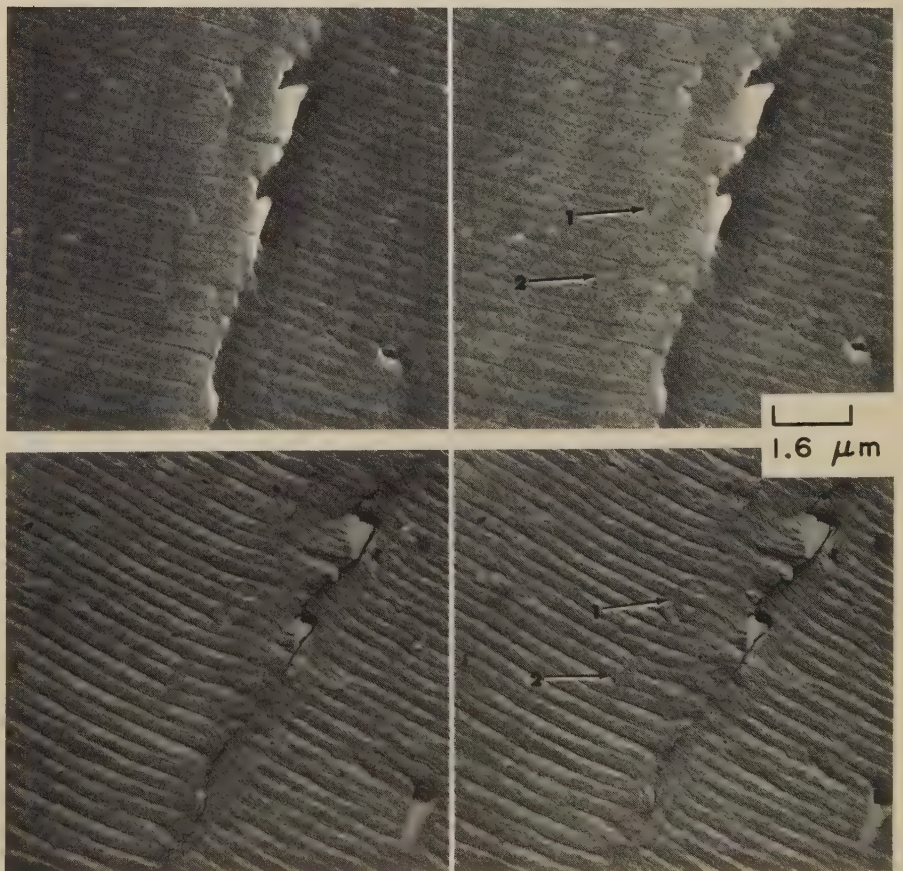
SEM (4248) and TEM (4249) stereofractographs 4000×

4248 A third set of views, at still higher magnification, showing another area of the surface of the low-cycle fatigue-test fracture in aluminum alloy 7075-T6 in 4244-4245 and 4246-4247. In this area the fracture surface shows well-defined fatigue striations that are clearly visible in both the SEM and the TEM pairs but with more detail and contrast in the TEM. Note the excellent match of the reproductions made by the two techniques. The vertical surface at arrow 1 is quite accurately registered in the TEM fractograph, but at the other side (at arrow 2) the replica has been torn. The detail in the crevices marked by arrows 1 and 3 is more clearly displayed in the TEM pair but could be matched in the SEM if the exposure were adjusted for this purpose. The sharp line at arrow 4 in the TEM fractograph bears some resemblance to a replica tear, but it is also visible in the SEM and actually is a secondary crack in the aluminum. See also 4250-4251 (below).

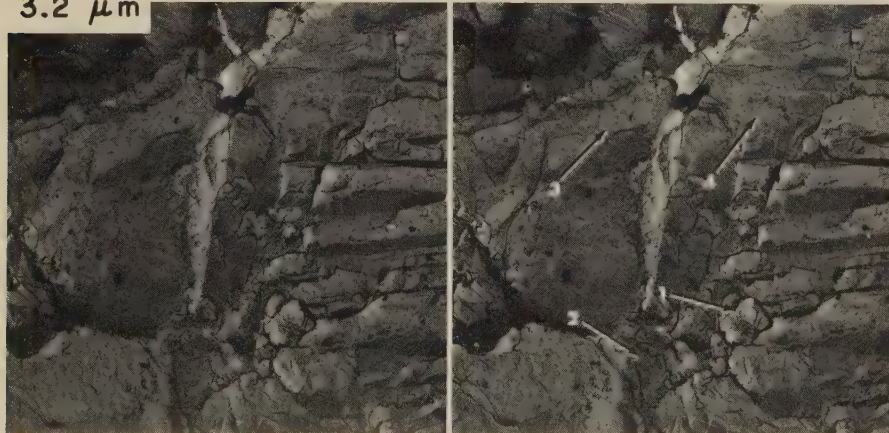
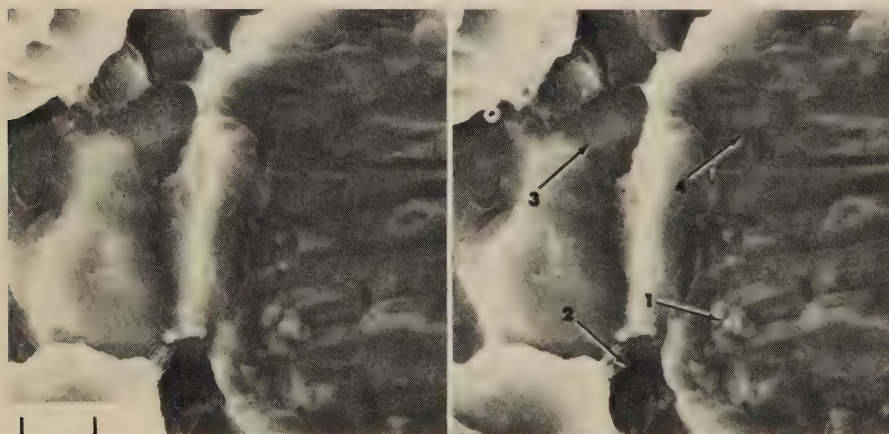
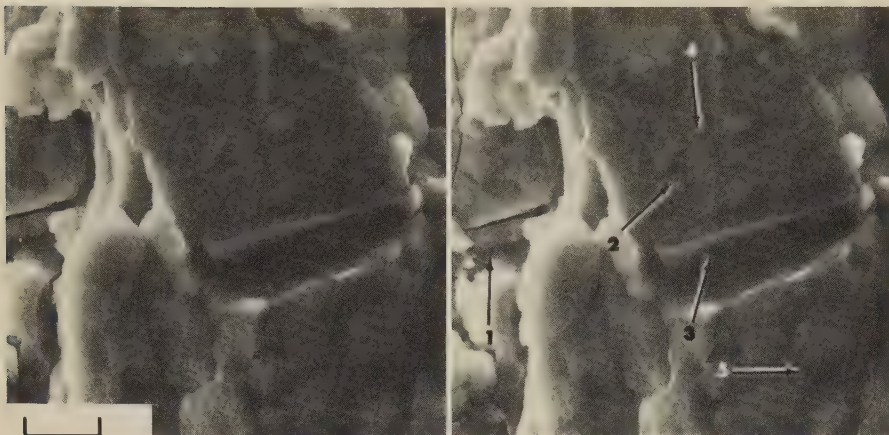


SEM (4250) and TEM (4251) stereofractographs 6400×

4250 A fourth set of views, again at higher magnification, showing a fourth area of the surface of the low-cycle fatigue-test fracture in aluminum alloy 7075-T6 in 4244-4245, 4246-4247 and 4248-4249. This region of the fracture surface shows portions of two fatigue patches separated by a sizable step. At this magnification, much of the detail of the striations is visible in both the SEM and the TEM fractographs. Note the slight indentation marks that can be seen at arrows 1 and 2; these of course are much more clearly defined in the TEM pair. The gray mark below the cavity at lower right in the TEM was produced during shadowing of the replica, a negative surface in which the cavity in the specimen was reproduced as a projection. The height of the step at the juncture of the two fatigue patches is shown to be much greater in the SEM than in the TEM pair; this is the result of replica "collapse".



Comparison of SEM and TEM Stereofractographs: Fracture in Aluminum Alloy 7075-T6 Caused by Stress-Corrosion Cracking in Water at Room Temperature



SEM (4252) and TEM (4253) stereofractographs 1760×

4252 The first of four sets of views, at increasing magnification, of four areas of the surface of a fracture resulting from stress-corrosion cracking in aluminum alloy 7075-T6 exposed to water at room temperature and to stress (maximum not reported) by hydrostatic pressure. The tensile strength of the material was 586 MPa (85 ksi). This region of the fracture surface shows intergranular separation, minute corrosion pits on grain surfaces, second-phase particles, and general freedom from accumulations of corrosion debris. When viewed in 3-D, the SEM pair shows that the left edge of this area is much lower than the central region (compare regions at arrows 1 and 2). This difference in elevation is not apparent in the TEM fractograph, indicating collapse of the replica. Arrow 3 indicates a second-phase particle, and arrow 4 designates a site previously occupied by another. The corrosion pits that are clearly visible in the TEM pair near arrow 5 are not resolved in the SEM. See also 4254-4255 (below) and 4256-4257, 4258-4259 (next page).

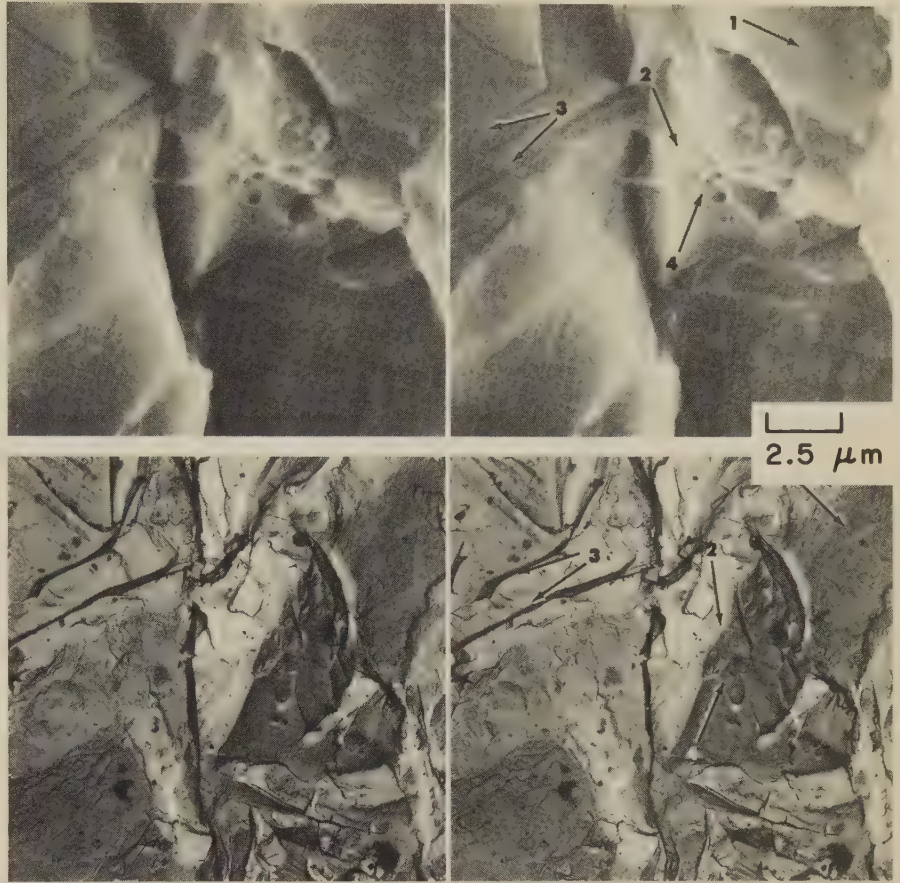
SEM (4254) and TEM (4255) stereofractographs 3100×

4254 A higher-magnification set of views showing a different area of the surface of the fracture resulting from stress-corrosion cracking in aluminum alloy 7075-T6 in 4252-4253 (above). In this area of the surface, fracture is mainly intergranular, complicated by flat facets at the right that are prior interfaces between the matrix and bar-shaped second-phase particles. There appears to be very little corrosion debris. The detail shown in the SEM pair is remarkably identical to that resolved in the TEM. Observe that the fine detail around the tiny prong at arrow 1 can be recognized in both the SEM and TEM pairs; the same conformance is true in the deep depression at arrow 2. Some of the corrosion pits near arrow 3 can be identified in the SEM fractograph, but those in the region of arrow 4 can be seen only in the TEM. Again, the true differences in elevation, which are shown in the SEM pair, are not registered in the TEM because of replica collapse.

Comparison of SEM and TEM Stereofractographs: Fracture in Aluminum Alloy 7075-T6 Caused by Stress-Corrosion Cracking (Continued)

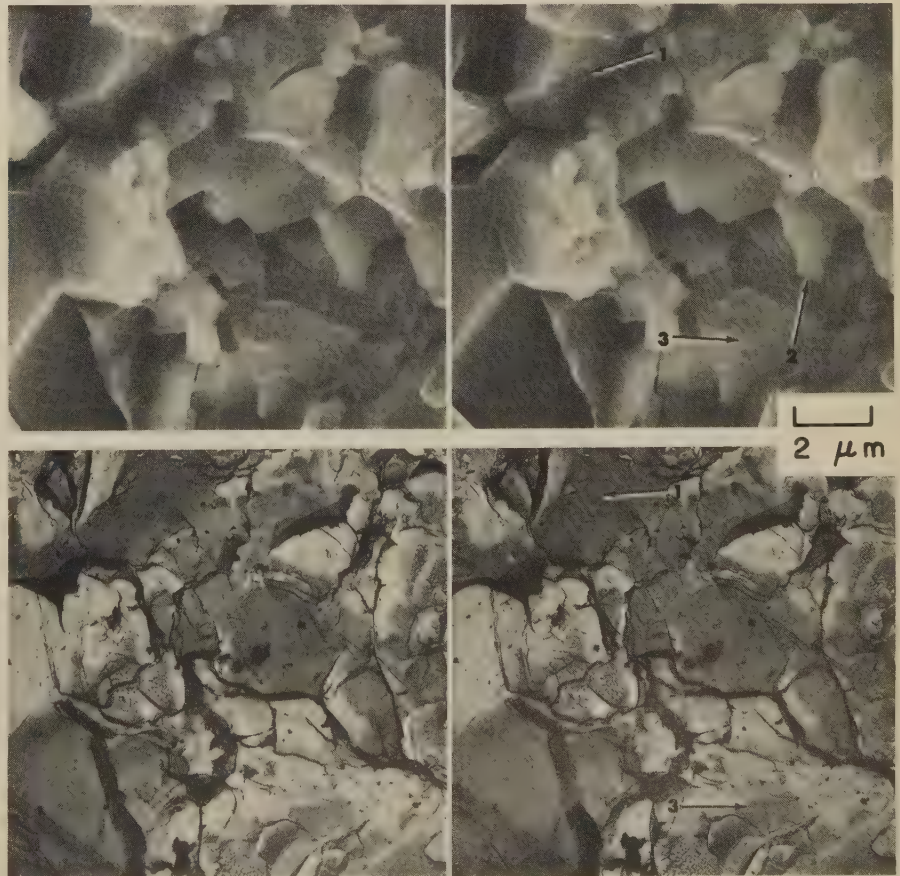
SEM (4256) and TEM (4257) stereofractographs 4000×

4256 A set of views, at even higher magnification, of a third area of the fracture caused by stress-corrosion cracking in aluminum alloy 7075-T6 in 4252-4253 and 4254-4255. In this area, the fracture surface is markedly intergranular, contains several secondary cracks (some of which appear to be transgranular), exhibits some corrosion pits but little corrosion debris, and contains local regions of moderate-size dimples. In general, the reproduction of surface contours in the TEM pair matches very closely that in the SEM. However, mismatch is evident at regions affected by replica collapse; for example, the region at arrow 1 (as viewed in 3-D) appears to be higher than the region at arrow 2 in the SEM pair but lower than the region at arrow 2 in the TEM. Note the excellent agreement between the two techniques in registering the secondary cracks at arrow 3 and the details of the dimples at arrow 4. However, very few corrosion pits are resolved in the SEM pair. See also 4258-4259 (below).

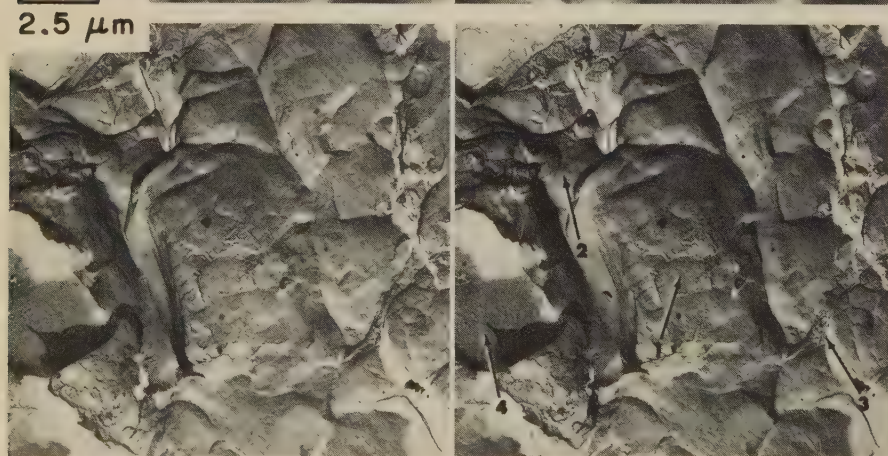
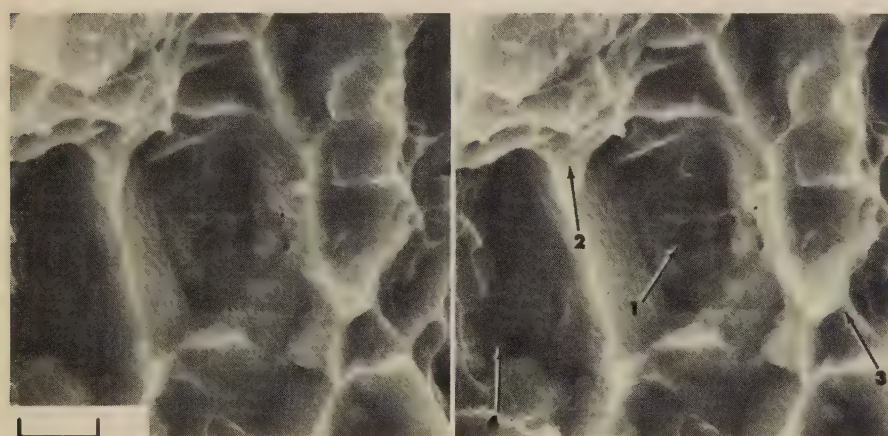
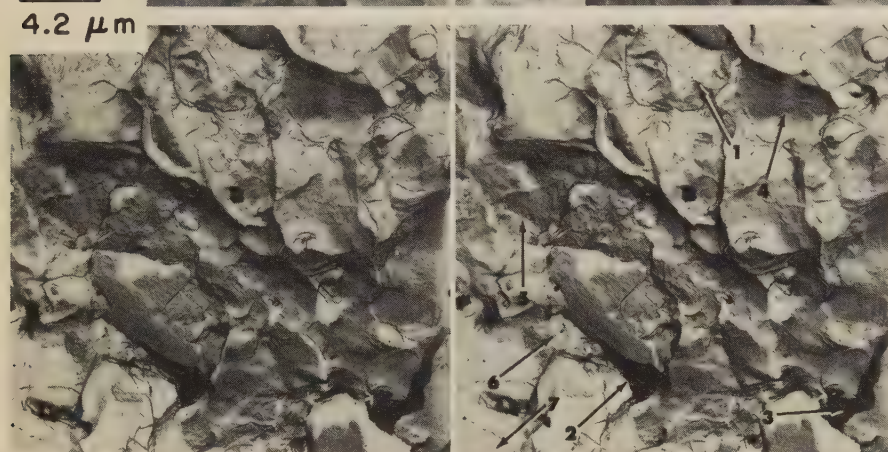
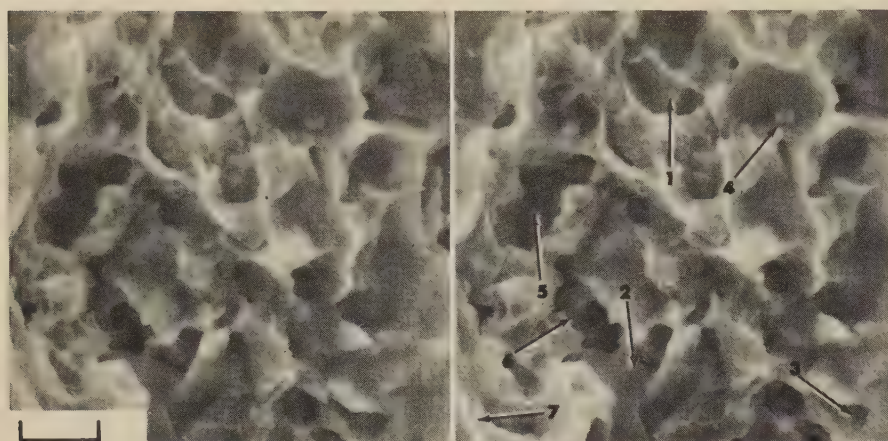


SEM (4258) and TEM (4259) stereofractographs 5000×

4258 A fourth set of views, again at higher magnification, showing another area of the stress-corrosion-cracking fracture in aluminum alloy 7075-T6 shown in 4252-4253, 4254-4255 and 4256-4257. Similar to the three preceding sets, this set of views shows a variety of grain surfaces resulting from intergranular rupture. The TEM fractograph shows many minute corrosion pits on these separated-grain surfaces, none of which are resolved in the SEM pair. The dark zones between grains in the TEM pair are caused by folding of the replica at secondary cracks. Observe the excellent agreement between the SEM and TEM pairs as to contour and detail, particularly in the region at arrow 1. Arrow 2 marks a feature in the SEM that does not appear in the TEM, which is unusual. Again, differences in elevation are minimized in the TEM; the region at arrow 3 appears to be at the same level as the ridge above arrow 1 whereas the SEM shows that the region at arrow 3 is much lower.



Comparison of SEM and TEM Stereofractographs: Notched Specimen of Annealed Titanium Alloy Ti-8Al-1Mo-1V Fractured by Tension Overload at Room Temperature



SEM (4260) and TEM (4261) stereofractographs 2400×

4260 Surface of a tension-overload fracture in a notched specimen of annealed Ti-8Al-1Mo-1V alloy that was broken at room temperature. The tensile strength of the material was 1000 MPa (145 ksi). The fracture surface consists of dimples of various sizes, a few of which show some sidewall stretching. The SEM and TEM pairs are in close agreement as to details of contour; compare, for example, the contours in and around the depression at arrow 1. In the TEM fractograph, tears and folds in the replica obscure the surface in the crevices at arrows 2 and 3. Note that the cube-shaped second-phase particle at arrow 4 in the SEM is missing entirely from the TEM. Many superficial surface features that are clearly visible in the TEM pair are not resolved in the SEM. Some replica collapse is evident when the elevations at arrows 5, 6 and 7 in the TEM fractograph are compared with those in the SEM. See also 4262-4263 (below).

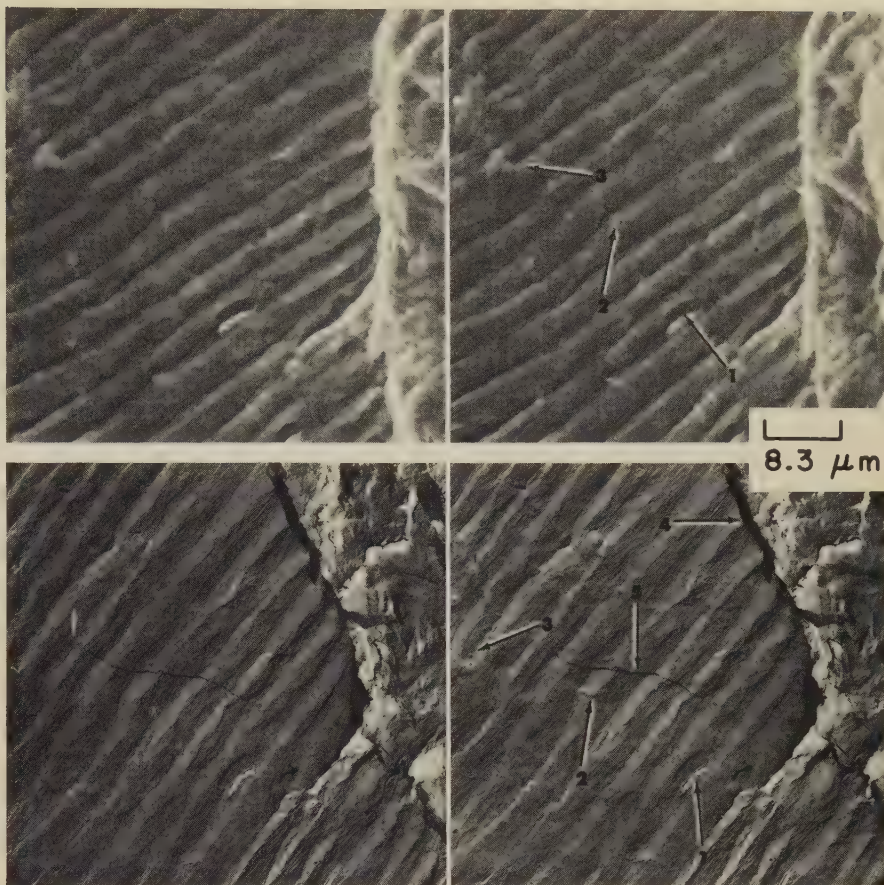
SEM (4262) and TEM (4263) stereofractographs 4000×

4262 A more highly magnified set of views of a different area of the surface of the tension-overload fracture in annealed Ti-8Al-1Mo-1V alloy shown in 4260-4261 (above). This area shows rather large dimples. For the most part, the topographic agreement between the SEM and TEM pairs is very close, as may be seen by comparing the contours at arrows 1, 2 and 3. Note that the stretch marks on the left side of the cavity at arrow 2 are clearly visible in both pairs. Elsewhere, however, similar marks are largely unresolved in the SEM fractograph. The feature at arrow 4 in the TEM is not a fracture contour but is an artifact caused by a bubble entrapped in the plastic replica. The dark regions above and below this artifact are the result of folds in the carbon replica. The SEM fractograph shows the true surface at arrow 4.

Comparison of SEM and TEM Stereofractographs: Annealed Titanium Alloy Ti-8Al-1Mo-1V Fractured by High-Cycle Fatigue at Room Temperature

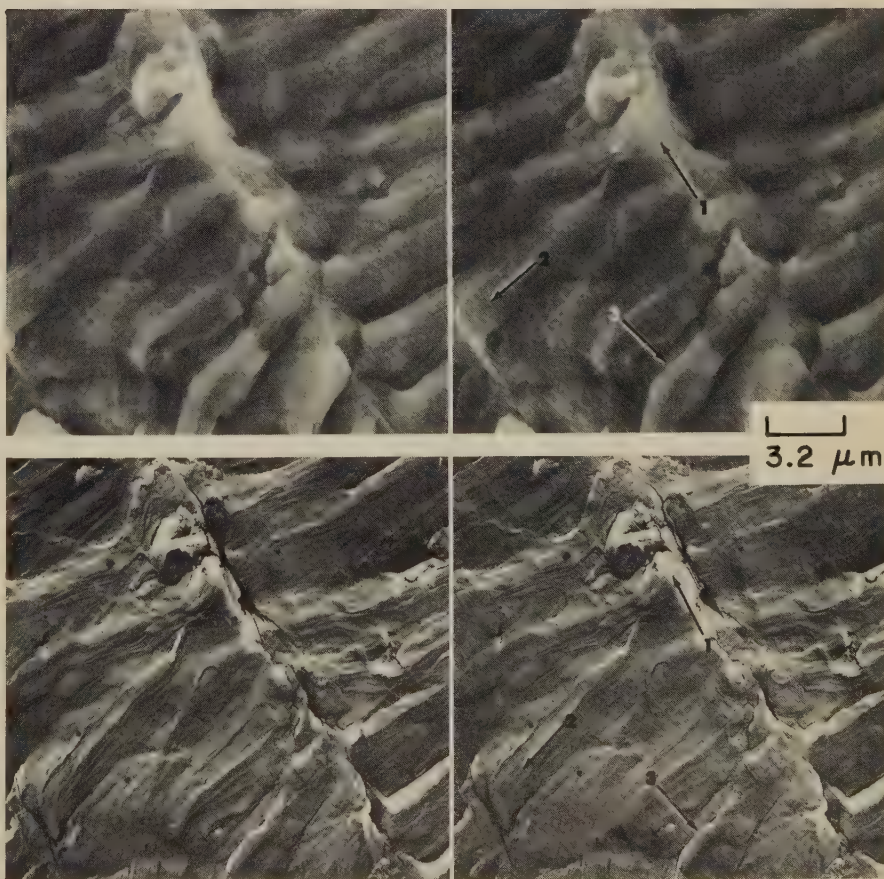
SEM (4264) and TEM (4265) stereofractographs 1200×

4264 Surface of a high-cycle fatigue fracture produced at room temperature in a specimen of the same annealed Ti-8Al-1Mo-1V alloy as in 4260-4261 and 4262-4263. Shown here is a portion of a fatigue patch with widely spaced, well-defined fatigue striations bounded on the right by a high step to the next patch. There is good agreement between the SEM and TEM pairs, as evidenced by the details in the two views at arrows 1, 2 and 3, which are readily recognized in both fractographs. The TEM replica has been torn and folded at the step at right, resulting in the dark band at arrow 4 and the simulation of a crack at arrow 5. The apparent elevation of the step is much reduced in the TEM fractograph compared to the true elevation shown in the SEM. Note also that the contours of the striations appear much flatter in the TEM than in the SEM but that the fine marks on the ridges, which are in sharp focus in the TEM, are not well resolved in the SEM. See also 4266-4267 (below) and 4268-4269 (next page).

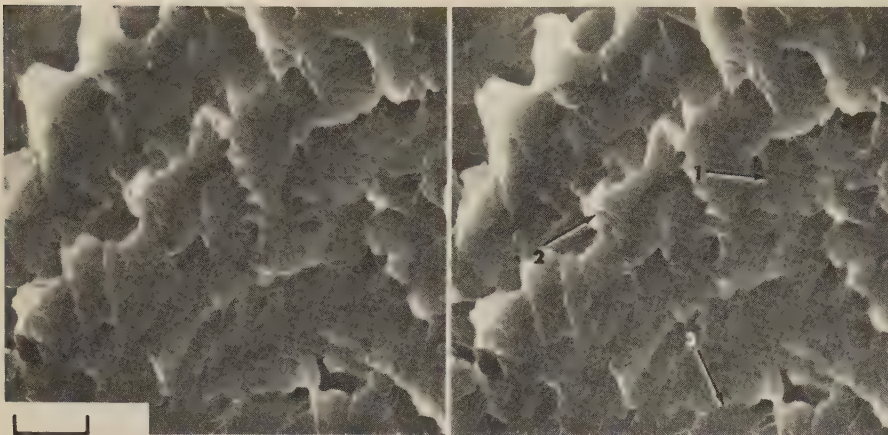


SEM (4266) and TEM (4267) stereofractographs 3100×

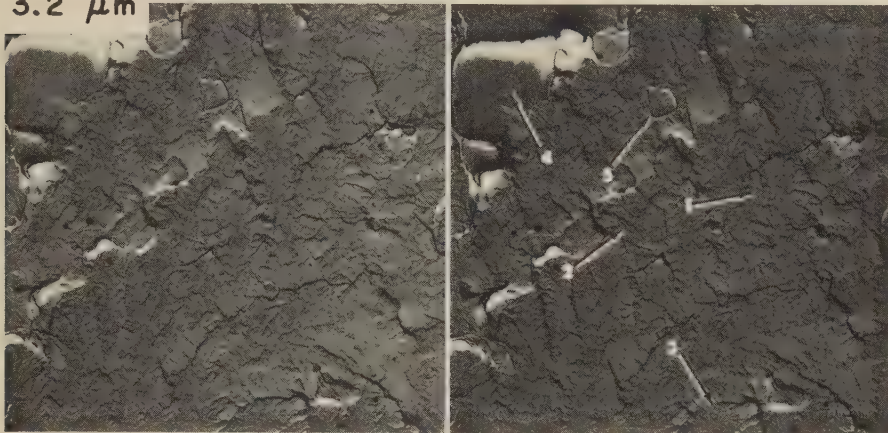
4266 A more highly magnified set of views of another area of the surface of the high-cycle fatigue fracture in annealed Ti-8Al-1Mo-1V alloy in 4264-4265 (above). These stereofractographs show the junction of two adjacent fatigue-striation patches that exhibit considerable irregularity in striation orientation in the neighborhood of the step separating the patches. Comparison of the SEM and TEM pairs shows good agreement in registry of contours, as may be seen at arrows 1, 2 and 3. The fine marks along the ridges of the striae are sufficiently pronounced for many to be shown in the SEM fractograph, but others are not resolved there and are shown much more distinctly in the TEM pair.



Comparison of SEM and TEM Stereofractographs: Titanium Alloy Ti-8Al-1Mo-1V Fractured by Stress-Corrosion Cracking in a 3½% NaCl Solution at Room Temperature



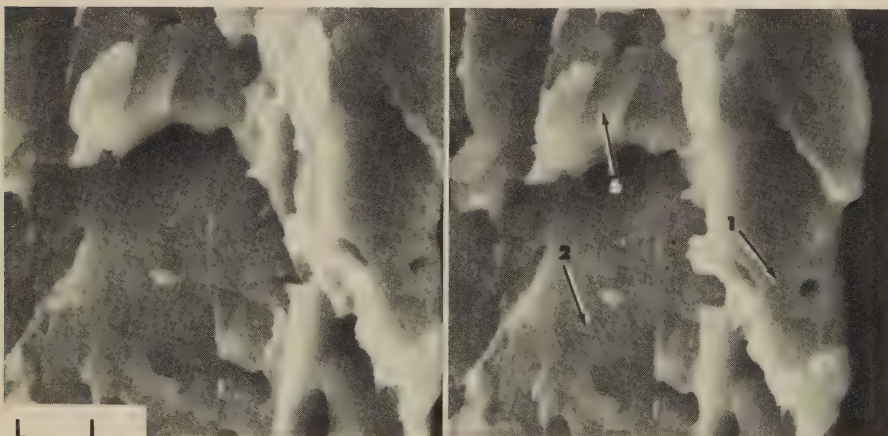
3.2 μm



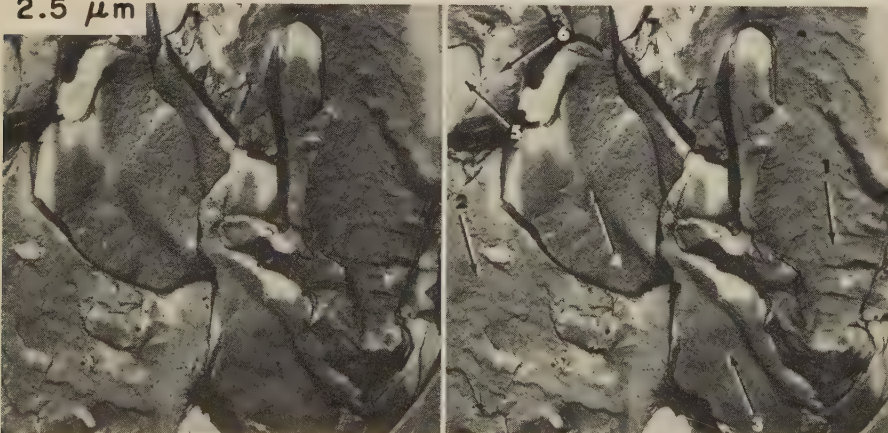
SEM (4268) and TEM (4269) stereofractographs 3100 \times

4268 Stress-corrosion fracture in a specimen of the same annealed titanium alloy Ti-8Al-1Mo-1V as for 4260 to 4267 (preceding two pages). This specimen was subjected to a maximum stress of 170 MPa (25 ksi) while exposed to an environment of 3½% NaCl in water, at room temperature. The fracture surface possesses many small and slightly offset facets, such as those at arrows 1 and 2, that appear to be quasicleavage facets. Many of the features along the edges of these facets, however, show dimple-like characteristics. Serrated ranks of the facets are separated by larger steps, although the fracture-surface area here is not large enough to show how repetitive these tiers may be. Agreement in contour details between the SEM view and the TEM view is very good, as may be seen by comparing the surfaces at arrows 1, 2 and 3. The feature in the upper left corner of the TEM stereo pair, at arrow 4, is an artifact created by entrapment of a gas bubble in the plastic-replica medium. Another feature not common to both the SEM and the TEM views is the apparent artifact at arrow 5 in the TEM. See also 4270-4271, below.

4269



2.5 μm



SEM (4270) and TEM (4271) stereofractographs 4000 \times

4270 A higher-magnification set of views in another area of the stress-corrosion fracture of the annealed Ti-8Al-1Mo-1V specimen of fractographs 4268-4269 (above). This area is somewhat similar to that shown at the lower magnification in 4268-4269, exhibiting rows of modest-size quasicleavage facets at different levels. Some of these facets, as at right, are separated by steps of appreciable height. There is excellent agreement in surface features between the SEM and the TEM pairs in the high-level region at arrow 1 at right, and in the lower-level region at arrow 2. The surface details at arrows 3, 4 and 5 in the TEM view, however, are artifacts resulting either from bubbles or foreign material trapped by the replica. The small facet at arrow 6 is the portion of this region that is common to both the SEM and the TEM fractographs. The surfaces that are real show essentially no accumulation of corrosion debris.

4271

Transmission-Electron-Microscope (TEM) Fractographs From Replicas

Prepared by John A. Fellows

CONTENTS

Armco iron	298-299	Type 431 stainless steel	327	Wrought aluminum alloys:	
Wrought iron	300	Type 633 (AM-350) stainless steel ...	328	2018	352
4130 steel	301	13-8 PH stainless steel	328-330	2024-T3, -T851	352-353
4140 steel	301	17-4 PH stainless steel	330-331	7075-T6	354-361
AMS 6434 steel	302-303	Type 301 stainless steel	331	7079-T6, -T651	362-363
4315 steel	304	Type 302 stainless steel	331-333	Copper-2% Be alloy	364-365
4340 steel	304-315	Alloy 713LC	334	Magnesium alloy AZ81A-T4	366
8740 steel	316-317	Alloy 713C	334-335	TZM molybdenum alloy	367
D-6ac steel	318	IN-100 nickel-base alloy	336	90% Ta-10% W alloy	367
300M steel	318	Alloy 718	336-339	Unalloyed titanium	368
1080 steel	318	Waspaloy	339-342	Titanium alloys:	
Nitralloy G steel	319	René 41 nickel-base alloy	343	Ti-5Al-2.5Sn	369
9310 steel	319	L-605 cobalt-base alloy	343-345	Ti-5Al-3Sn-2Mo-2V	369
Ductile iron	320	U-700 nickel-base alloy	346-347	Ti-6Al-4V	370-373
18% Ni maraging steel	320-321	Alnico alloy	348	Ti-7Al-2Cb-1Ta	373
Type 501 stainless steel	322-323	Aluminum casting alloys:		Ti-8Mn	374
H11 tool steel	323-325	319 (sand cast)	349	Ti-13V-11Cr-4Al	374
Type 410 stainless steel	326	380 (die cast)	350-351	Tungsten	375-376

THE FRACTOGRAPHS presented in this section were provided by the contributors listed on pages 127 and 128, in the Introduction to this Atlas. Most of these fractographs were obtained from replicas of fracture surfaces, by transmission electron microscopy. Many of the TEM fractographs, however, are accompanied by low-magnification light fractographs showing the fracture features evident to the human eye in contrast to the details detectable only by an electron beam at high magnification. In some instances, photomicrographs are also included, to illustrate the microstructure in the vicinity of the fracture.

The arrangement of fractographs here is by alloy type, rather than by type or cause of fracture. Beginning with Armco iron and wrought iron, this section presents examples of fractures of low-alloy steels, high-strength steels, cast iron, maraging steel, tool steel, stainless steels and heat-resisting alloys, and a permanent-magnet material; after these are fractures in nonferrous alloys in alphabetical order, from aluminum to tungsten.

Many of the fractures were produced in a laboratory under various types of applied loading. Others occurred in service; for these, the cause of fracture is reported where it could be deduced. About a fourth of the fractographs are related to fatigue fractures. These display many different types of fatigue-striation shapes at high magnification and beach marks at low magnification. Included also are fatigue fractures exhibiting no striations.

Approximately another fourth of the fractographs are devoted to examples of fracture by tension overload. The dimples that are characteristic of such fracture surfaces are shown to differ widely in appearance depending on the type of alloy, the number of inclusions present, the temperature at which fracture occurred, and the environment of fracture.

The other principal categories of fracture in this section include, in decreasing frequency of presentation: stress-corrosion cracking, hydrogen embrittlement, impact, corrosion fatigue, stress rupture, high-temperature fatigue, and torsion overload—each displaying either its characteristic marks or some modification of them that was induced by the environment of fracture. Each of the remaining types of load application or cause of fracture amounts individually to less than one per cent of the total number of fractographs presented.

Those unfamiliar with the appearance of fracture features revealed by TEM pictures of replicas should refer to the article on Interpretation of TEM Fractographs (page 79), as well as the section of this Atlas on pages 281 through 296. The material presented there provides a basis for understanding the shape and contours of fracture features such as dimples, fatigue striations and cleavage facets (to name a few) and the mechanisms by which they are formed. This material can also familiarize the reader with the aspects of a fracture that reveal where the crack originated, what prob-

ably generated it, and in which directions the crack grew. Such information is useful to an appreciation of what a specific fractograph conveys.

All the recognized categories of fracture features appear in this section—most of them repeatedly and with many variations. Nearly all were reproduced by two-stage plastic-carbon replicas, as indicated by the notation “p-c replica” or “pcr” in the line below the fractograph. The exception is the small number of fractographs that were made from thin, single-stage, direct carbon replicas; each of these is identified by the notation “direct carbon replica”. There are no instances of fractographs prepared from thin, single-stage plastic replicas.

When viewing these fractographs, it should be realized that the shadow areas on direct carbon replicas are deficient in shadowing metal and appear white, thus giving the effect of a negative picture. In two-stage plastic-carbon replicas, the shadowing is usually deposited on the face of the first-stage plastic replica that had been in contact with the fracture surface. The result is that white shadows appear beyond actual valleys on the fracture surface, and actual hills show interior shadows.

The exact metal used for shadowing each replica has not been stipulated for each fractograph, in the interest of conserving space. It may be assumed that the shadowing agent for any particular replica was platinum, palladium, chromium, or platinum-carbon.

Light Fractographs: Three Fracture-Surface Features That Indicate Direction of Crack Propagation;
Annealed Armco Iron Sheet Fractured by Shear Overload at -196°C (-321°F)



Light fractograph

5×

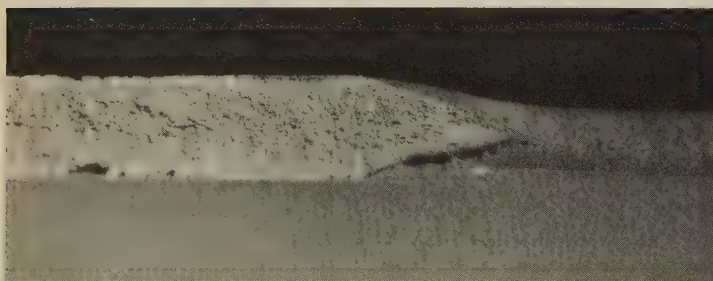
4272 Fracture surface showing an example of "hackle marks", which consistently point in the direction of fracture propagation. By tracing such marks backward, it is possible to locate their common origin, which is the point of fracture initiation. Here, the origin is at the right, and fracture proceeded from right to left. Hackle marks occur during fast fracture.



Light fractograph

5×

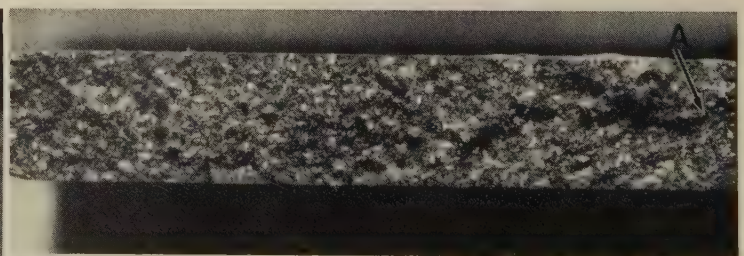
4273 Fracture surface showing an example of "chevron marks", which commonly are seen in overload fast fractures. Chevron marks consistently point toward the origin of fracture. Here, the origin is at the right, and the direction of fracture propagation was from right to left.



Light fractograph

5×

4274 Fracture surface showing a localized zone of plane-strain fracture (at left), the configuration of which indicates that fracture propagated from left to right in this view.



Light fractograph

12×

4275 Fracture surface of a 0.13-in.-thick sheet of annealed Armco iron broken in shear overload at -196°C (-321°F). Tensile strength, 276 MPa (40 ksi). A flat, granular surface. Area at A is shown at higher magnification in 4276 (facing page).

TEM Fractograph, TEM Micrographs, Light Micrograph: Armco Iron Fractured by Shear Overload at -196°C (-321°F) and by Charpy Impact at -196°C (-321°F) and at Room Temperature



TEM fractograph (p-c replica)

5000×

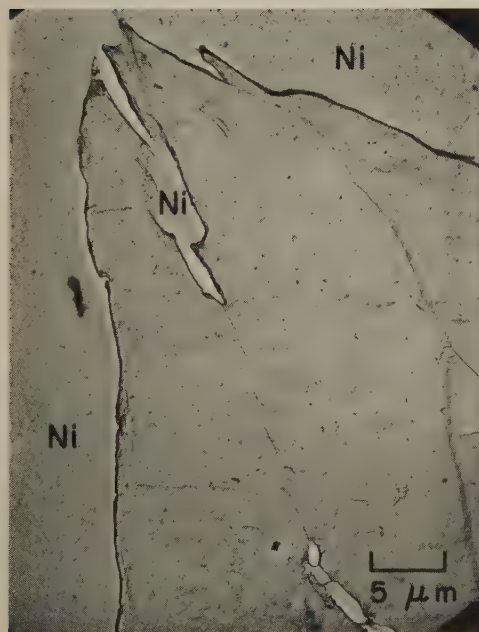
4276 A TEM replica of area A of the surface of the low-temperature shear-overload fracture in Armco iron shown in 4275. This surface exhibits a pattern that is characteristic of cleavage fracture. The local direction of crack propagation was from top to bottom, as suggested by the angle of the tongue below center, which was formed by a local fracture along a twin-to-matrix interface.



TEM micrograph (p-c replica)

2000×

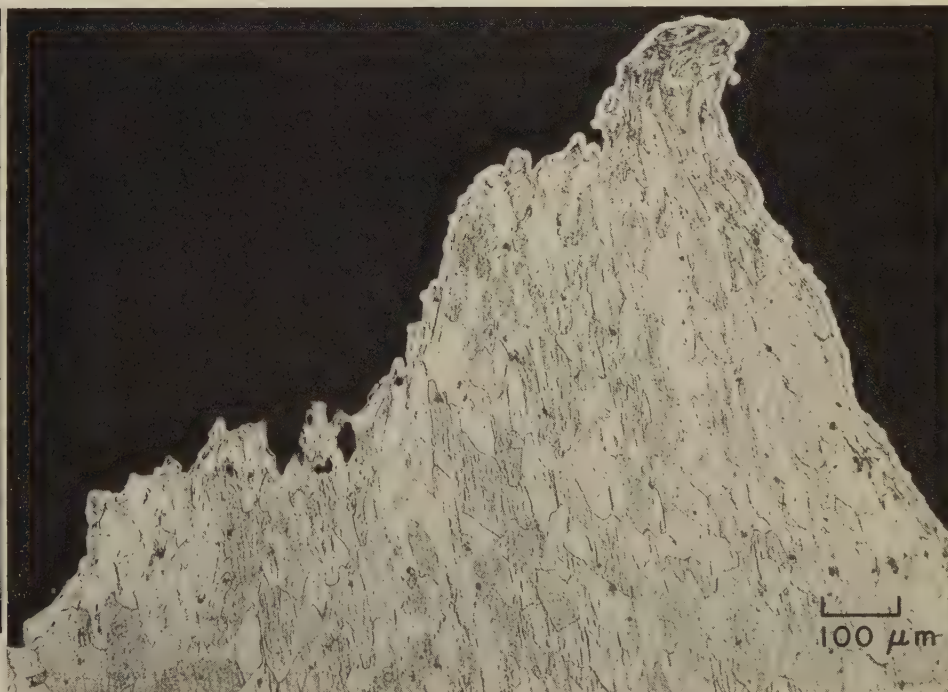
4277 A TEM replica of a polished and etched section through a Charpy impact specimen of Armco iron broken at -196°C (-321°F). Fracture surface, shown in profile (at left, protected by nickel plate), was produced by cleavage. See also 4278.



TEM micrograph (p-c replica)

2000×

4278 A TEM replica of a polished and etched section through a Charpy impact specimen of the same Armco iron as in 4277 but broken at room temperature. Visible at left and at top is a profile of the fracture surface (protected by nickel plate), showing some deformation. See also 4279.



Light micrograph (etchant: nital)

100×

4279 A polished and etched section through the same Charpy impact specimen of Armco iron as shown in micrograph 4278 (at left), which was broken at room temperature. Note that in the region of final fracture (at top right) there has been decided elongation of the grains.

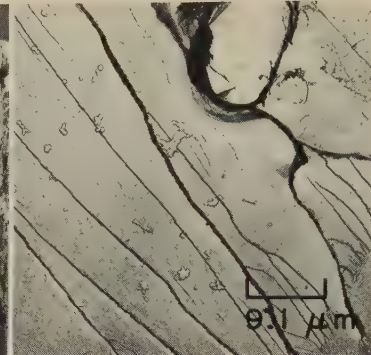
Light and TEM Fractographs: Wrought Iron Fractured by Notch Impact, Showing Effects of Slag-Stringer Orientation and of Test Temperature; Light Micrographs Showing Structure



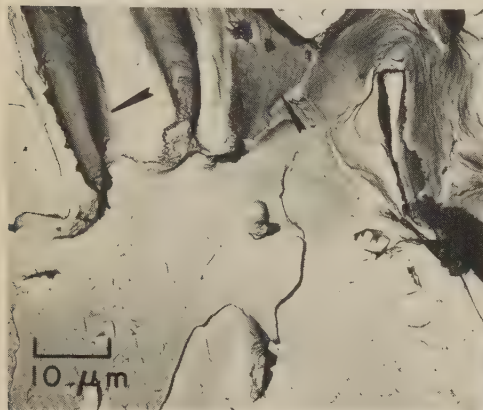
Light fractograph 6×
4280 Surface of an impact fracture in a notched specimen of wrought iron. Here, the longitudinal stringers of slag in the material are parallel to the direction of fracture, which gives the surface this typically "woody" appearance. Compare with fractograph 4281, at right.



Light fractograph 6×
4281 A companion notch-impact fracture to the one shown in fractograph 4280, but here the longitudinal stringers of slag are normal to the fracture surface. Individual particles of slag are not readily visible at this magnification, but they cause the speckled appearance.



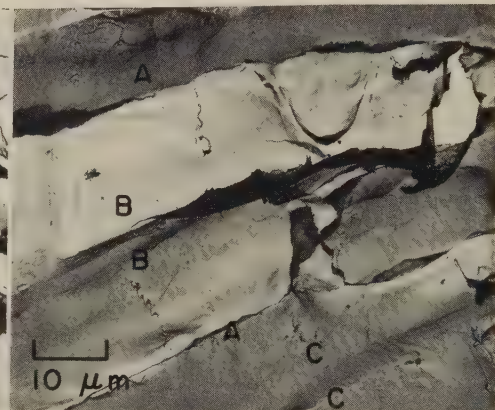
TEM fractograph (p-c replica) 1100×
4282 Charpy impact fracture in wrought iron broken at -59 C (-75 F), showing a cleavage surface normal to slag stringers. Portion of a slag particle is at top. See 4283-4285.



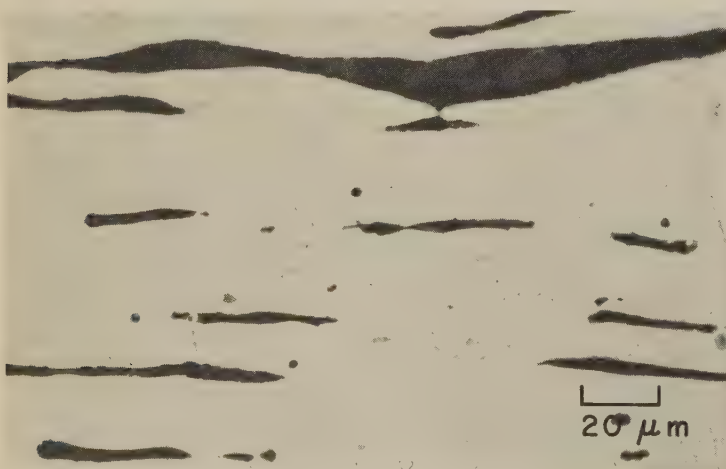
TEM fractograph (p-c replica) 1000×
4283 Surface of a Charpy impact fracture in a second specimen of the same wrought iron as in fractograph 4282, but broken at -32 C (-25 F) and with the slag stringers parallel to the fracture surface. As in 4282, the matrix fractured by cleavage. Note voids, such as at arrows, which were matrix-slag interfaces. Compare with fractographs 4284 and 4285, at right.



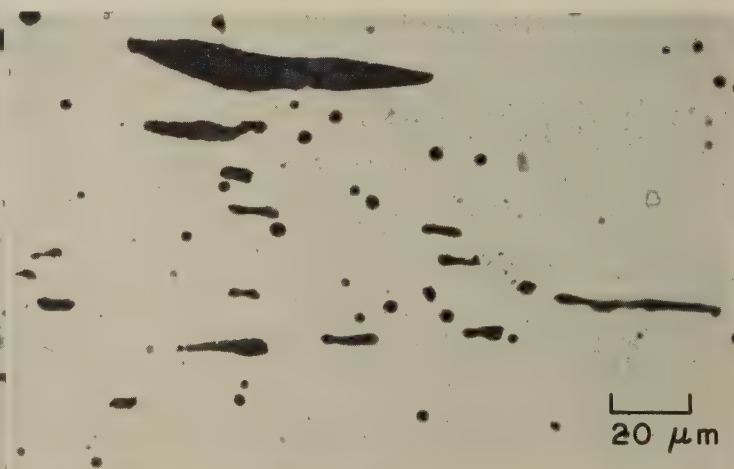
TEM fractograph (p-c replica) 1000×
4284 Surface of a Charpy impact fracture in a third specimen of the same wrought iron as in fractographs 4282 and 4283, but broken at 10 C (50 F). As in 4282, the slag stringers are normal to the fracture surface. Most of this surface formed by coalescence of voids, such as at arrows, which originally formed around slag particles. See also fractograph 4285, at right.



TEM fractograph (p-c replica) 1000×
4285 Charpy impact fracture in a fourth specimen of same wrought iron as in 4282, but broken at 149 C (300 F) and with the slag stringers parallel to the fracture surface. Most of this surface formed by coalescence of microvoids (such as the one at A-A) originally formed around slag particles. The matrix-slag prior interfaces (B-B and C-C) were only slightly deformed.

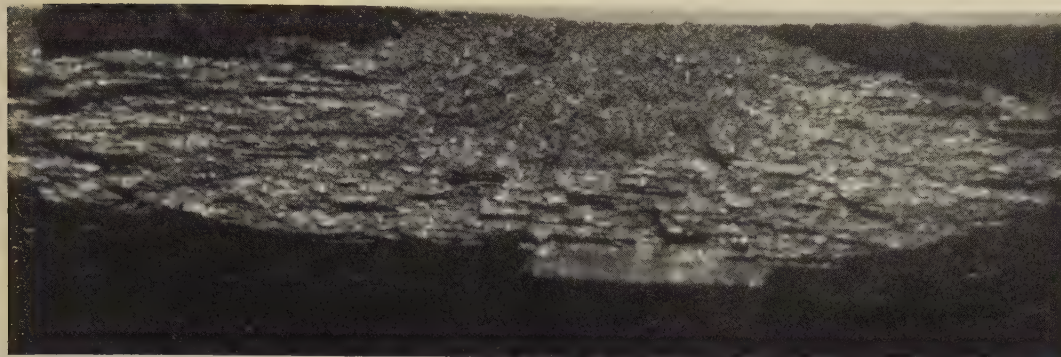


Light micrograph (as polished; not etched) 500×
4286 A polished longitudinal section through a specimen of wrought iron, showing the slag particles, which have been elongated in the direction of rolling. See also 4287, at right.



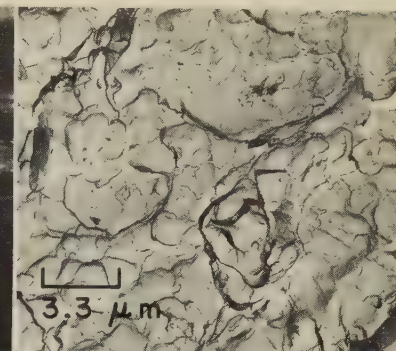
Light micrograph (as polished; not etched) 500×
4287 A polished section through a specimen of wrought iron, taken transverse to the rolling direction. Many slag stringers are round in cross section, but some are slablike.

Light and TEM Fractographs: 4130 Steel Rocket Case Fractured by Sustained Load and Fractured by Impact; 4140 Steel Actuator Rod Fractured by Fatigue



Light fractograph

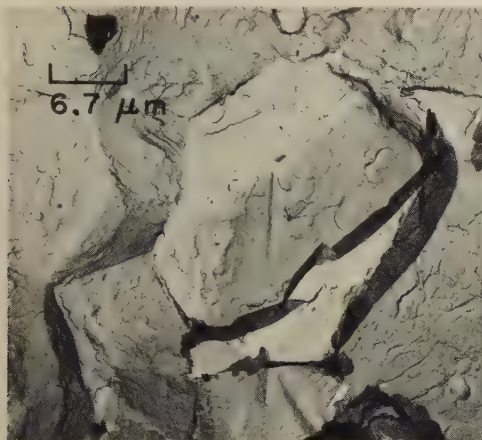
4288 Fracture surface of a rocket-propellant case of $\frac{1}{16}$ -in.-thick 4130 steel with nominal yield strength of 1241 MPa (180 ksi). Fracture occurred after testing for $2\frac{1}{2}$ hr at 182 C (360 F) and internal gage pressure of 6.2 MPa (900 psi), or a hoop stress of about 448 MPa (65 ksi), and originated in a heat-affected zone of a fusion weld that attached a clip. Cracking started in a typical "thumbnail" area (at top center) and continued by flat fracture nearly through the thickness of the sheet; final fracture was of a nearly full shear type. See also 4289 to 4292.



23X

TEM fractograph (p-c replica) 3000X

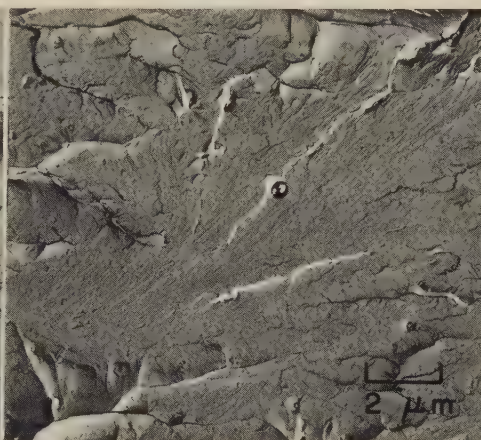
4289 A TEM reproduction of a dull region in the crack-origin area of the fracture in 4288, showing equiaxed dimples, which were produced by tension overload. Compare with 4290.



TEM fractograph (p-c replica)

1500X

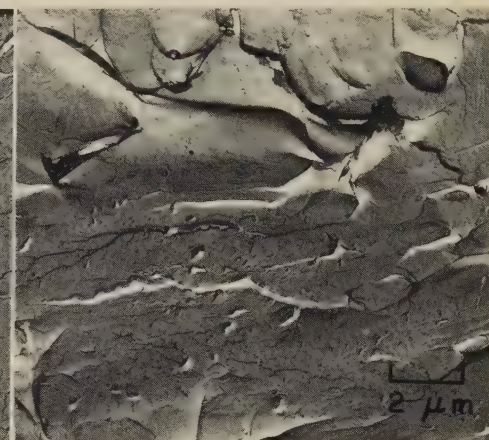
4290 A TEM reproduction of a shiny-faceted region in the crack-origin area of the fracture in 4288. Here, the fracture was intergranular, which suggests the existence of hydrogen embrittlement.



TEM fractograph (p-c replica)

5000X

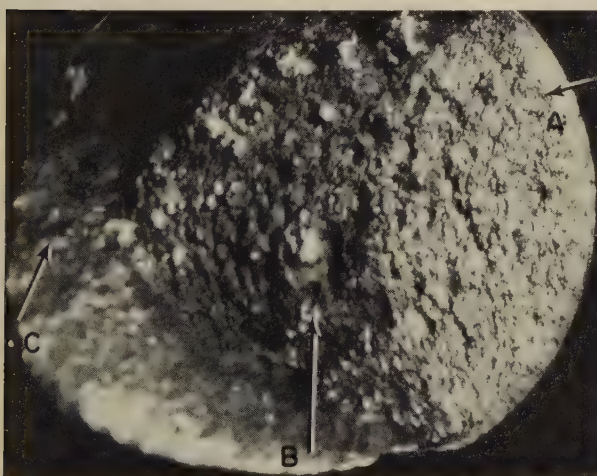
4291 Shiny-faceted region in the crack-origin area of a fracture produced in the rocket case of 4288 by a sharp hammer blow at an adjacent fusion welded clip, showing cleavage facets. See also 4292.



TEM fractograph (p-c replica)

5000X

4292 Another shiny-faceted region in the crack-origin area of the fracture in 4291, showing quasicleavage facets. Like 4291, this shows no intergranular separation, which would require sustained loading.

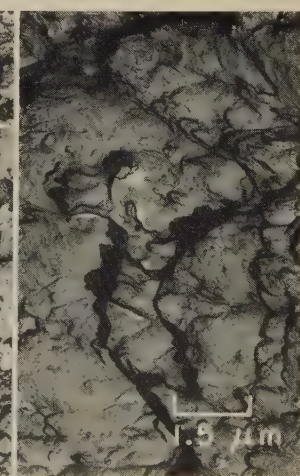
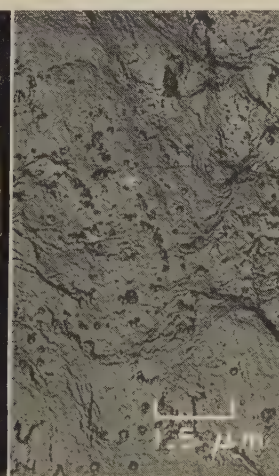


Light fractograph

4293, 4294, 4295, 4296

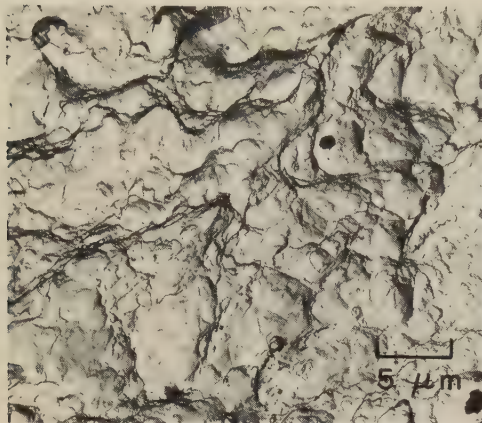
12X TEM fractographs (p-c replicas)

Fractograph 4293 (far left) shows a fracture surface of a helicopter damper-actuator rod made of 4140 steel with tensile strength between 862 and 1000 MPa (125 and 145 ksi). Fracture began as a fatigue crack at A, probably of low-cycle nature, that extended through one-third of the cross section. The crack continued as a fast fracture, ending in the shear lip at left edge. Fractograph 4294 (second from left) is a TEM reproduction taken from zone A in 4293, showing poorly defined fatigue striations. In fractograph 4295 (third from left), which was taken from the fast-fracture area at B in 4293, equiaxed dimples are evident. Fractograph 4296 (far right), obtained from the shear-lip zone at C in 4293, shows the expected shear dimples.

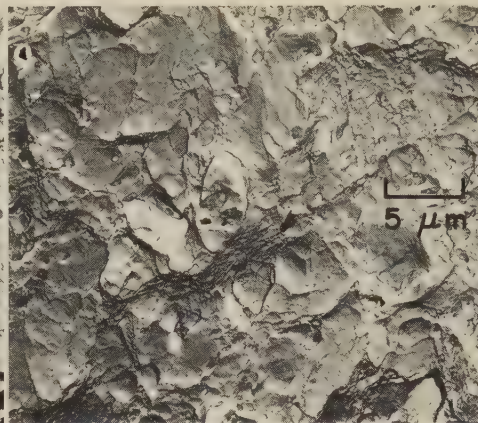


6500X

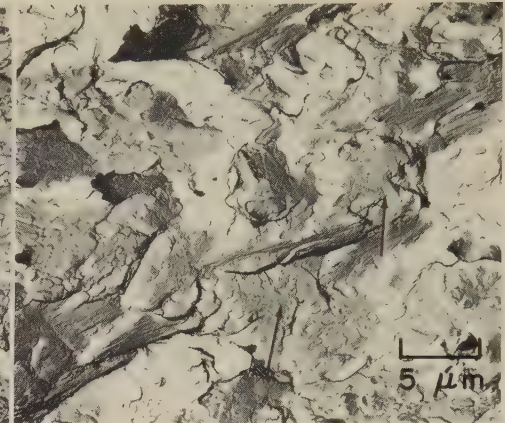
TEM Fractographs, TEM Micrograph: Tension-Overload Fractures at Various Temperatures in Notched and Unnotched Specimens of AMS 6434 Steel; Fractures in AMS 6434 Steel Pressure Vessels



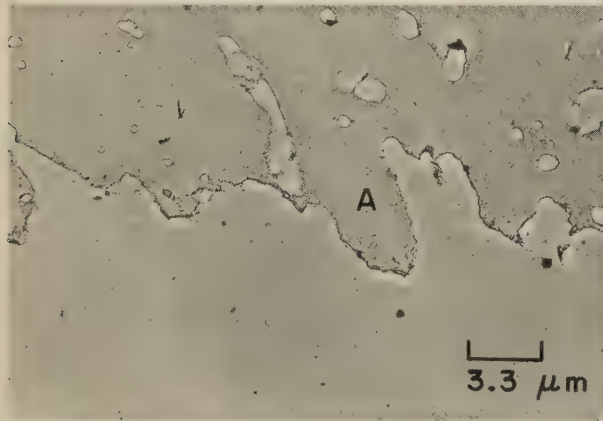
TEM fractograph (p-c replica) 2000×
4297 Surface of a tension-overload fracture in a notched specimen of AMS 6434 steel sheet that was broken at 27 C (81 F), showing small equiaxed dimples. The heavy curved lines are intersections of dimple surfaces. See 4298 and 4299.



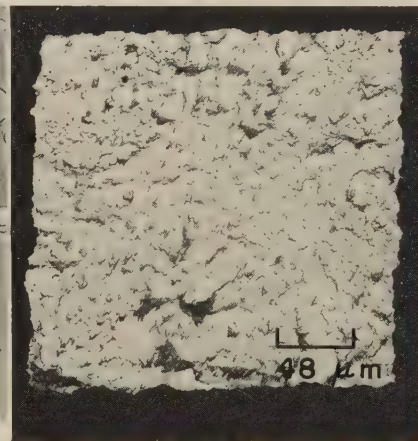
TEM fractograph (p-c replica) 2000×
4298 Surface of a tension-overload fracture in a notched specimen of the same AMS 6434 steel sheet as in 4297, but broken at -73 C (-99 F). The dimples here are of the same size and nature as those in 4297. See also fractograph 4299.



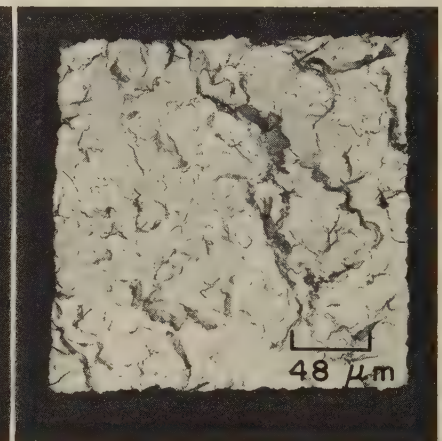
TEM fractograph (p-c replica) 2000×
4299 Surface of a tension-overload fracture in a notched specimen of the same AMS 6434 steel sheet as in fractographs 4297 and 4298, but broken at -190 C (-310 F), showing a mixture of scattered dimples and (at arrows) cleavage facets.



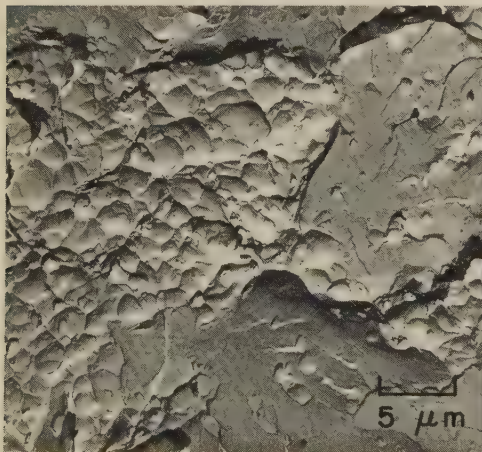
TEM micrograph (p-c replica; nital etch) 3000×
4300 A polished and etched section through an unnotched specimen of AMS 6434 steel broken by tension overload at room temperature, showing a profile of the fracture surface, which is protected by mounting material (at top). Note dimple in profile (A). See 4301.



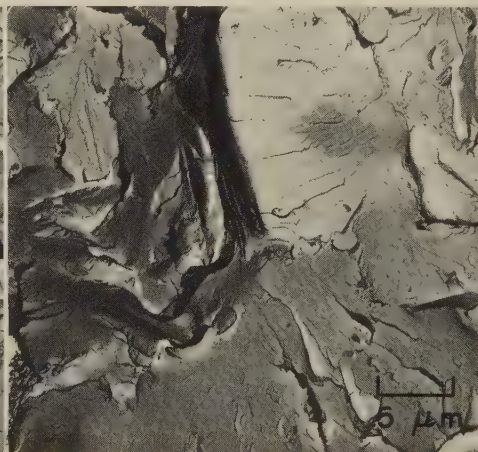
TEM fractograph (p-c replica) 210×
4301 TEM replica of an area of a shear lip in the fracture surface of the specimen of AMS 6434 steel in 4300, showing dimples.



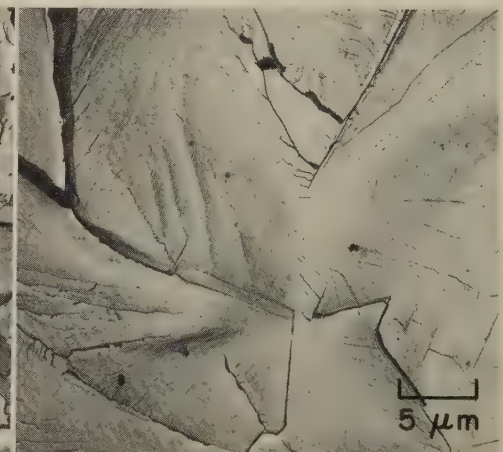
TEM fractograph (p-c replica) 210×
4302 Fracture surface of a specimen of the same AMS 6434 steel as in 4300, but broken at -196 C (-321 F), showing cleavage facets.



TEM fractograph (p-c replica) 2000×
4303, 4304, 4305



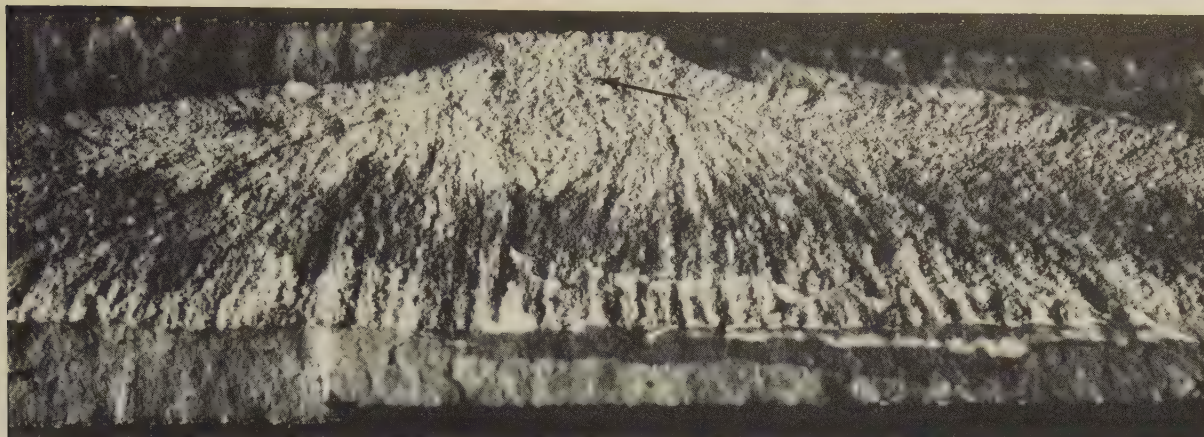
TEM fractograph (p-c replica) 2000×



TEM fractograph (p-c replica) 2000×

Surfaces of fractures in three pressure vessels made of AMS 6434 steel. Fractograph 4303 (left) shows equiaxed dimples, which resulted from tension overload, and quasicleavage facets. Fractograph 4304 (center) shows quasicleavage facets plus (at bottom left) a small region of dimples. Fractograph 4305 (right) shows cleavage facets in large ferrite grains; these facets contain many cleavage steps that originated at twist boundaries.

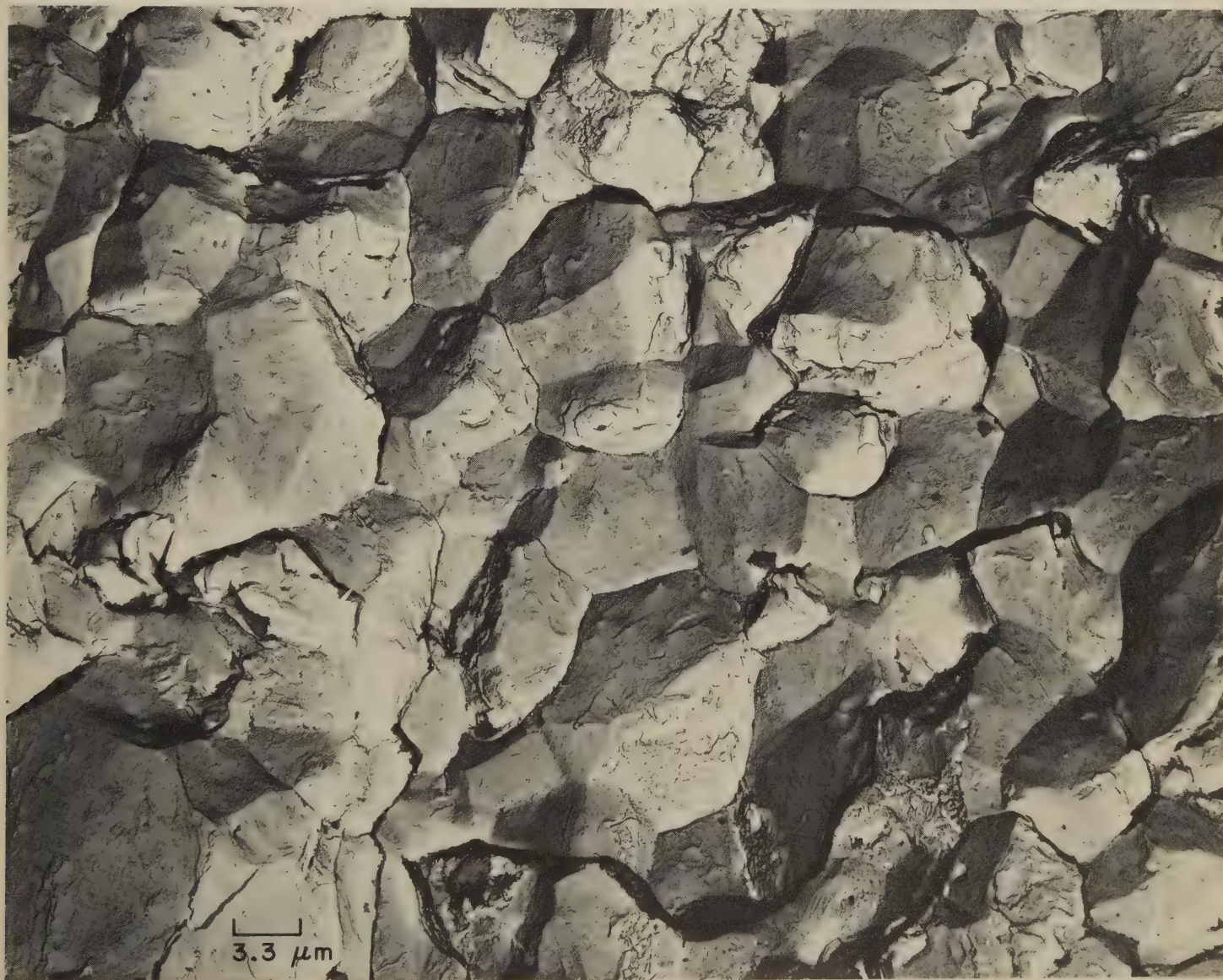
Light Fractograph and TEM Fractograph: AMS 6434 Steel Flask Fractured From Stress-Corrosion Cracking Produced by Stressing During Exposure to Tap Water



Light fractograph

15×

4306 Surface of a fracture in a wall of a flask made of AMS 6434 steel tempered at 204 C (400 F) that was stressed while exposed to tap water, which produced stress-corrosion cracking. See TEM fractograph 4307 (below) for a higher-magnification view of the region at arrow.

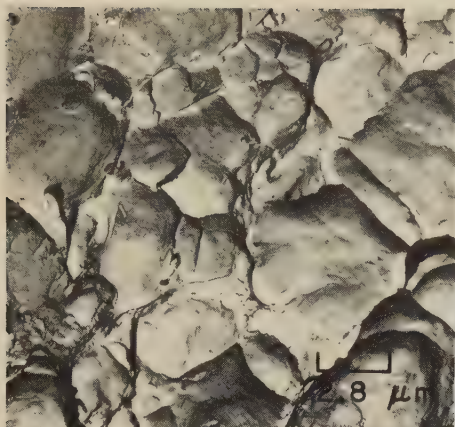


TEM fractograph (p-c replica)

3000×

4307 Higher-magnification view of fracture surface at arrow in 4306, showing clearly the intergranular nature of the fracture, which resulted from stress-corrosion cracking. Grains generally are equiaxed, and the fracture has closely followed grain boundaries.

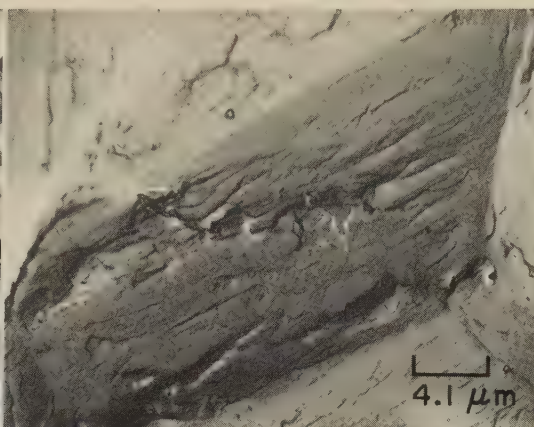
TEM Fractographs: Fractures in 4315 Steel; Fatigue Fracture
in 4340 Steel, Showing Intergranular Cracking



TEM fractograph (p-c replica)

3600×

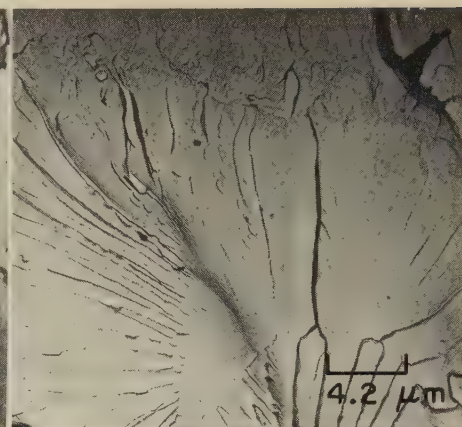
4308 Surface of a tension-overload fracture in a specimen of 4315 steel that was quenched from 982 C (1800 F) and tempered at 316 C (600 F). Note the large, equiaxed dimples.



TEM fractograph (p-c replica)

2450×

4309 Surface of an intergranular fracture, which was caused by hydrogen-embrittlement cracking along grain boundaries, in a specimen of 4315 steel heat treated the same as the specimen in fractograph 4308 (left).



TEM fractograph (p-c replica)

2400×

4310 Surface of a transgranular cleavage fracture, caused by hydrogen embrittlement, in 4315 steel heat treated same as 4308. Note cleavage steps that originated at tilt boundaries.

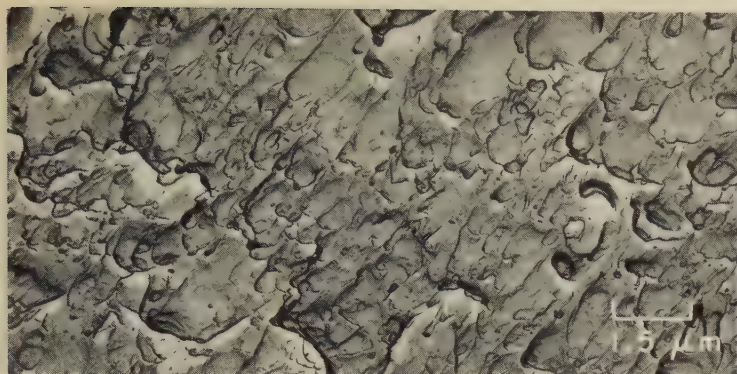


TEM fractograph (p-c replica)

15,000×

4311 A highly magnified view of a fatigue-fracture surface in a specimen of 4340 steel. The specimen was austenitized and quenched, tempered at 204 C (400 F) and then fatigue tested in humid air. Facets at left and at upper right indicate that crack growth proceeded partly by intergranular separation; this implies the possible presence of hydrogen embrittlement or stress-corrosion cracking. No real fatigue striations are discernible.

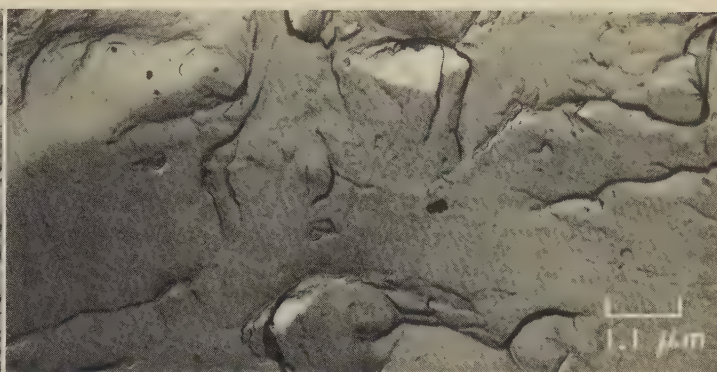
TEM Fractographs and Light Fractograph: 4340 Steel Specimens Fractured by Tension Overload, by Impact, and by Torsion Overload



TEM fractograph (p-c replica)

6500×

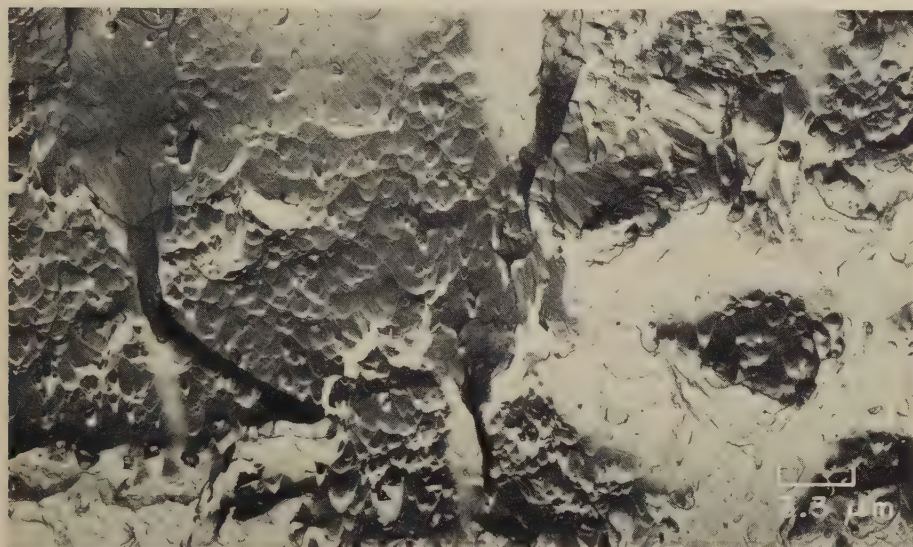
4312 Surface of a fracture in an unnotched specimen of 4340 steel that was broken in tension overload, displaying elongated and quite flat shear dimples. Note that some crude steps have formed, which suggests that there may have been some degree of pulsation in the applied stress during testing.



TEM fractograph (p-c replica)

9300×

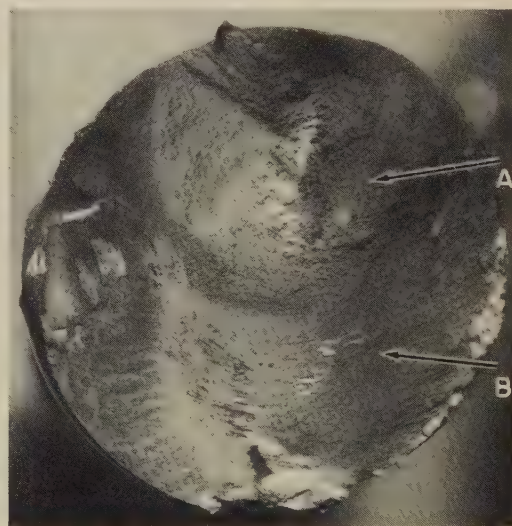
4313 Surface of a fracture in a notched specimen of 4340 steel that was broken in tension overload, showing scattered dimples. It is not certain whether the remainder of the surface in this area consists of quasicleavage facets or of large dimples that have undergone appreciable stretching.



TEM fractograph (p-c replica)

3000×

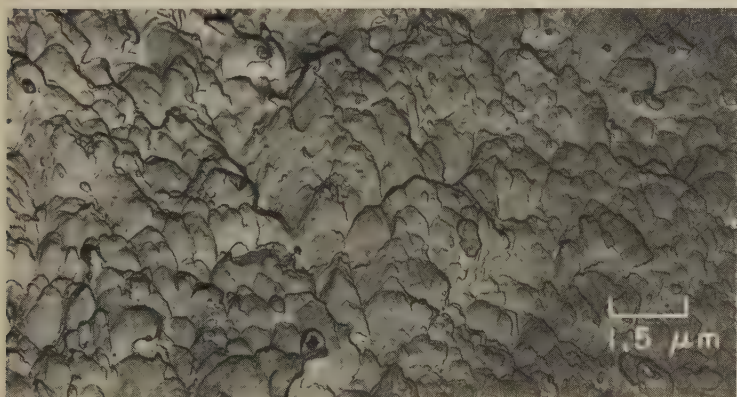
4314 Surface of a fracture in a specimen of 4340 steel that was broken by impact at room temperature, showing small dimples of quite uniform size, some of which (at right) are equiaxed. At left are elongated tear dimples pointing toward a tear ridge (at bottom). At upper left are regions in which considerable local stretching has occurred. Some secondary cracking may be present.



Light fractograph

10×

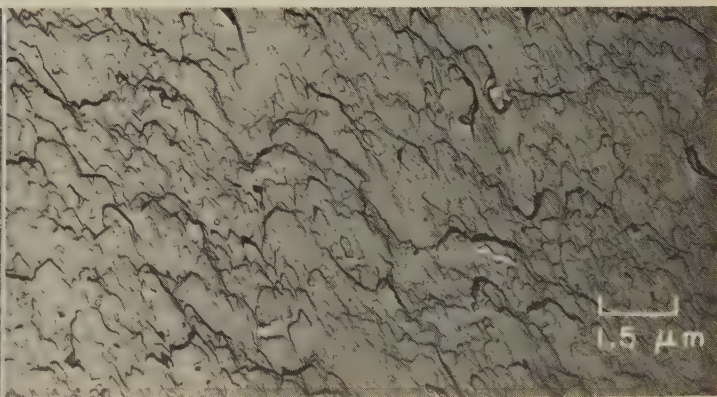
4315 Torsion-overload fracture in 4340 steel oil quenched from 843 C (1550 F) and tempered at 635 C (1175 F) to a tensile strength of 931 MPa (135 ksi). In general, the fracture surface is flat and shiny. See 4316 and 4317 for TEM views of areas A and B.



TEM fractograph (p-c replica)

6500×

4316 TEM replica of an area near letter A (in region of final rupture) in the torsion fracture in fractograph 4315 (above, at right), showing dimples, some of which are slightly elongated but many of which are essentially equiaxed.



TEM fractograph (p-c replica)

6500×

4317 TEM replica of an area near letter B in 4315. The flat and noticeably elongated shear dimples present here are to be expected in this region, which in 4315 (at lower magnification) shows an appreciable amount of torsional deformation.

Light Fractographs: 4340 Steel Unnotched Tensile Specimen With a
Cup-and-Cone Fracture That Originated in a Pinhole



Light fractograph

4×

4318 Matching surfaces of a cup-and-cone fracture in an unnotched tensile specimen of 4340 steel. Before being machined, the specimen had been heat treated to a tensile strength of 1944 MPa (282 ksi). It is evident that rupture originated at a small (but deep) pinhole, which is visible in each fracture surface. A small fibrous area with a zone of radial marks extending from it surrounds the pinhole. See also fractograph 4319 (below).

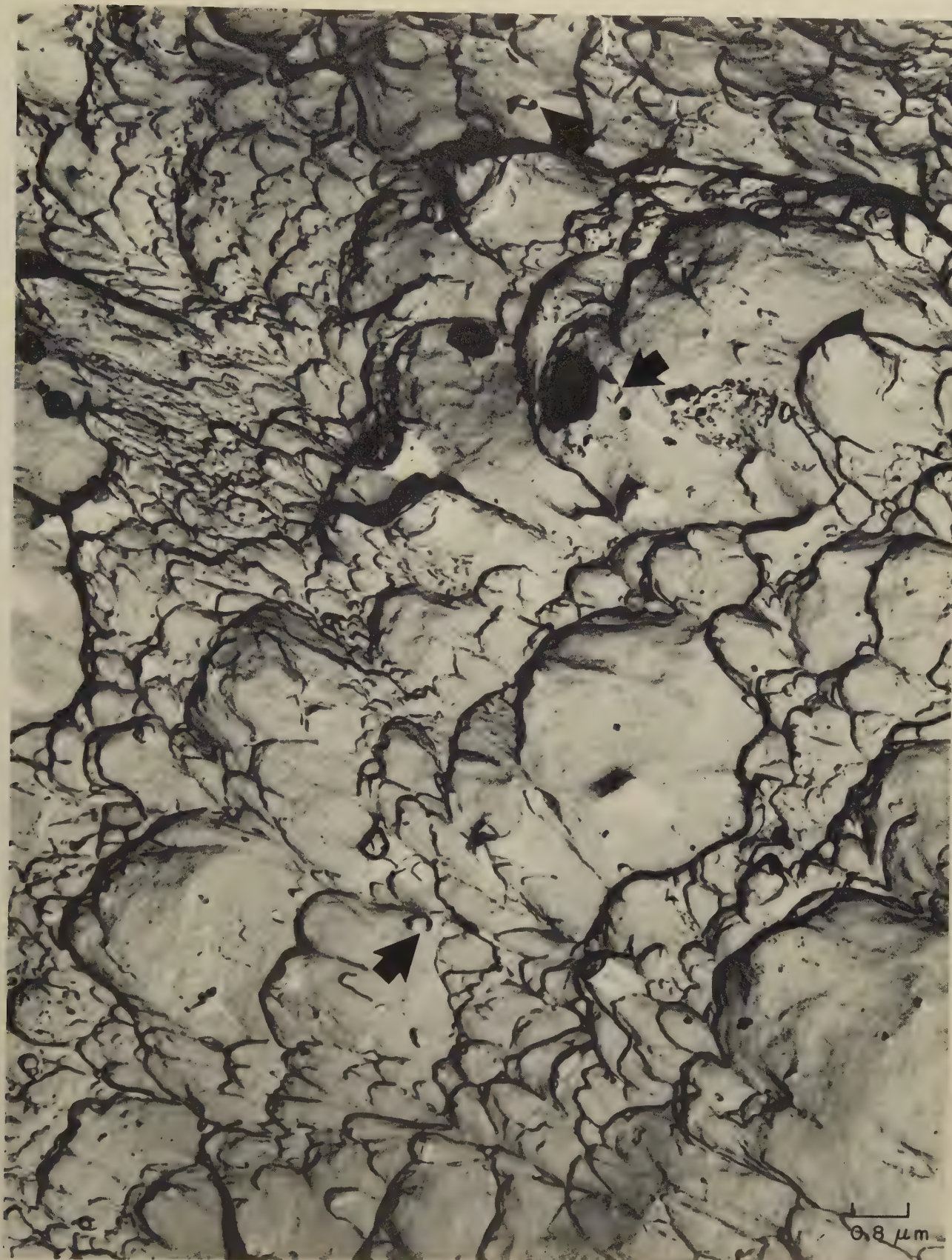


Light fractograph

25×

4319 A more highly magnified view of the fracture-origin area in one of the fracture surfaces in 4318 (above). The pinhole at the crack nucleus is clearly visible just above center. At this magnification it is evident that the region surrounded by the shear lip exhibits characteristics of both fibrous and radial zones (circumferential marks and radial marks). The details of the surface within this area are shown in fractograph 4320 (facing page).

TEM Fractograph: 4340 Steel Unnotched Tensile Specimen With a
Cup-and-Cone Fracture That Originated in a Pinhole (Continued)

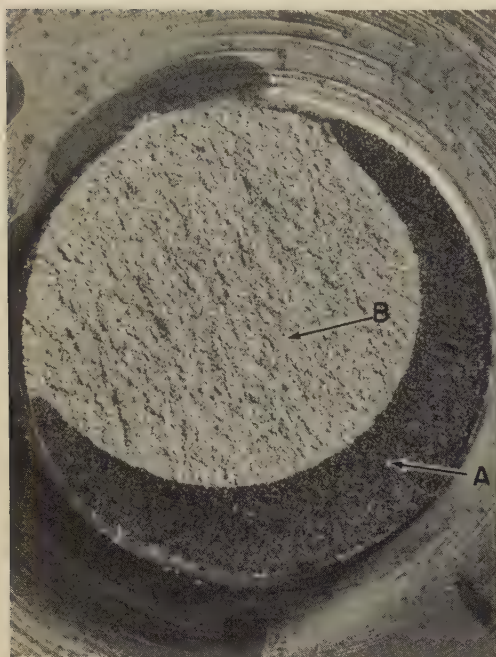


TEM fractograph (palladium-shadowed two-stage carbon replica)

12,000×

4320 A TEM replica of the fracture surface of the 4340 steel tensile specimen in 4318 and 4319 (facing page), showing a region close to the pinhole that nucleated the crack. This region consists mainly of tear dimples of various sizes, formed during early stages of internal rupture. Also visible are small oval tear dimples (indicated by the arrows), each of which was formed at a point where a small subsurface void intersected the surface of an already existing dimple.

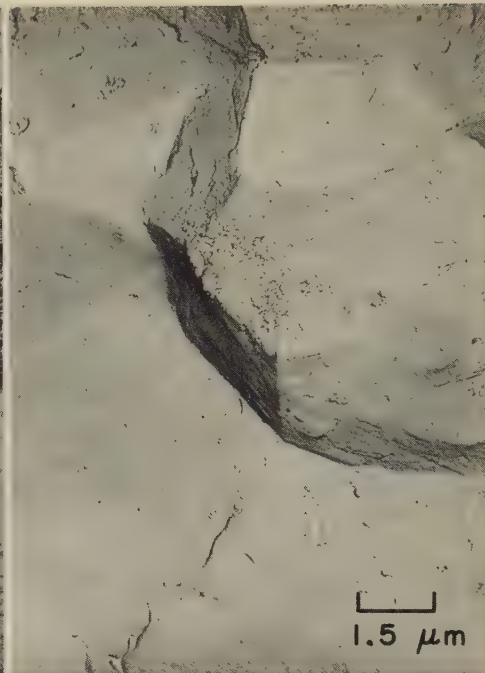
**Light Fractograph and TEM Fractographs: Impact Fracture in a 4340 Steel Cylinder,
Quenched but Not Tempered, That Contained a Quench Crack**



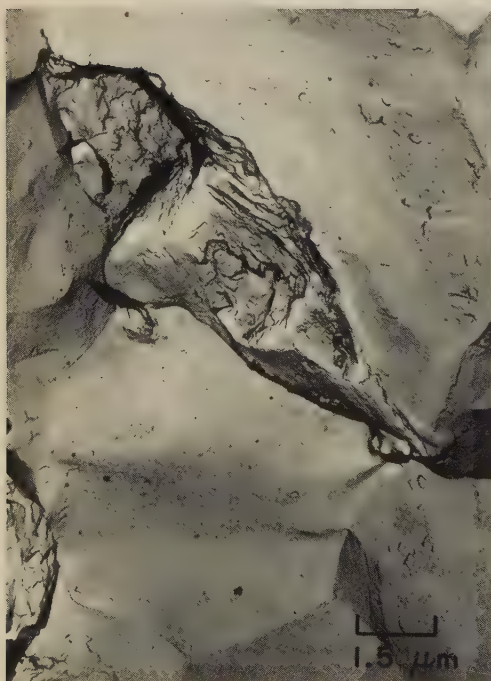
Light fractograph 5×
4321 Impact fracture in 4340 steel machined to a 2-in.-diam, 1½-in.-long cylinder with a ½-in.-diam, 1-in.-long central projection from one end. Specimen was heat treated ¼ hr at 816 C (1500 F) and water quenched, but not tempered; then the projection was broken by hammer blow. The dark crescent (A) is a quench crack; light area (B) is the impact fracture. See 4322-4326.



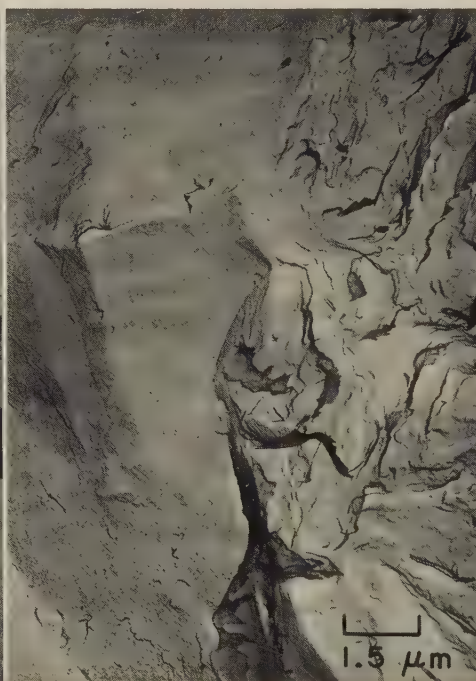
TEM fractograph (p-c replica) 6500×
4322 A TEM replication taken from area A (the quench-crack crescent) in the fracture surface shown in fractograph 4321. Here, the crack is completely intergranular in nature, having faithfully followed the grain interfaces. Traces of oxidation are evident. See 4323, 4324.



TEM fractograph (p-c replica) 6500×
4323 TEM replication from a different region in area A (quench-crack crescent) in the fracture surface in 4321. Here, as in 4322, the crack path has been along the grain interfaces. Scattered marks here resemble the hairline indications associated with either hydrogen embrittlement or stress-corrosion cracking.



TEM fractograph (p-c replica) 6500×
4324 A TEM replication taken near the root of the quench crack, marked A, in fractograph 4321. In addition to separated-grain facets, localized regions of transgranular tearing are visible. The grain facets are clean of oxidation, although they display a few hairline indications.

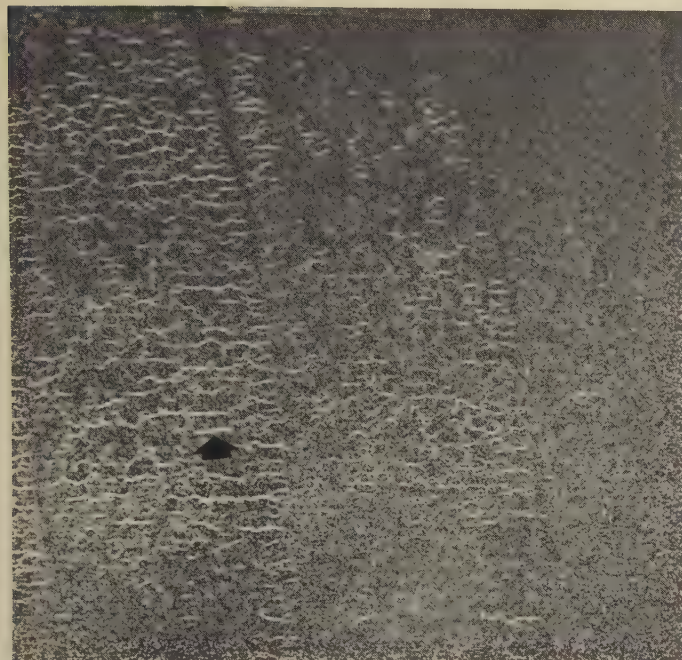


TEM fractograph (p-c replica) 6500×
4325 A TEM replication taken at the root of the quench crack, marked A, in 4321, and the beginning of the impact fracture, marked B there. At left are the last vestiges of intergranular cracking, and at right is the beginning of quasicleavage cracking in this very brittle specimen.



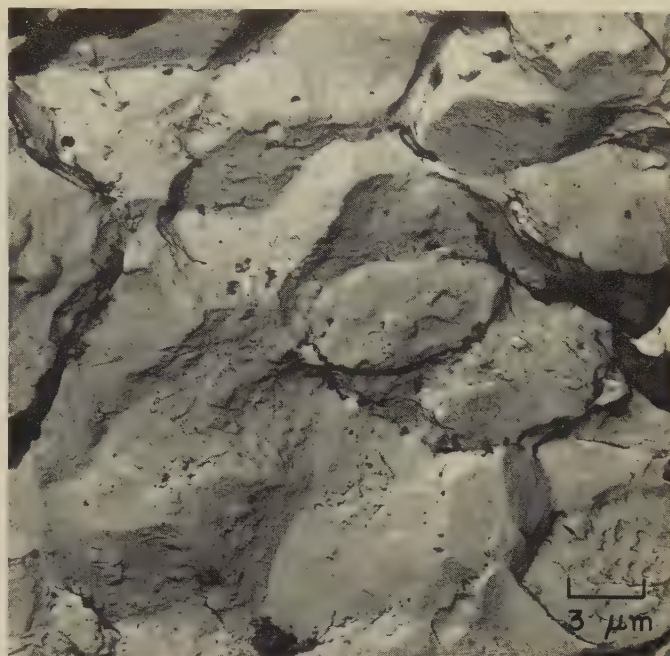
TEM fractograph (p-c replica) 6500×
4326 TEM replica from deep within the impact-fracture area, B, in 4321, showing the quasicleavage characteristics of this brittle, untempered specimen. No large facets are visible; this suggests that the specimen had a fine grain size. Many steps exist in the crack path.

Macrograph and TEM Fractographs of 4340 Steel: Grinding Cracks, and Fractures Originating From or Associated With Grinding Cracks



Macrograph (etchant: 5% nital) 10×

4327 The surface of 4340 steel that was heat treated to a tensile strength of 1793 to 1931 MPa (260 to 280 ksi), showing a network of grinding cracks. These cracks can produce serious stress concentrations leading to early fracture. See 4328 to 4330 for fractures associated with grinding cracks.



TEM fractograph (p-c replica) 3300×

4328 A typical fracture surface arising from rupture of a 4340 steel part possessing grinding cracks such as those shown in macrograph 4327, at left. Both intergranular and transgranular facets are evident; some of the facets show fine dimples. See also fractographs 4329 and 4330, below.



TEM fractograph (p-c replica) 6500×

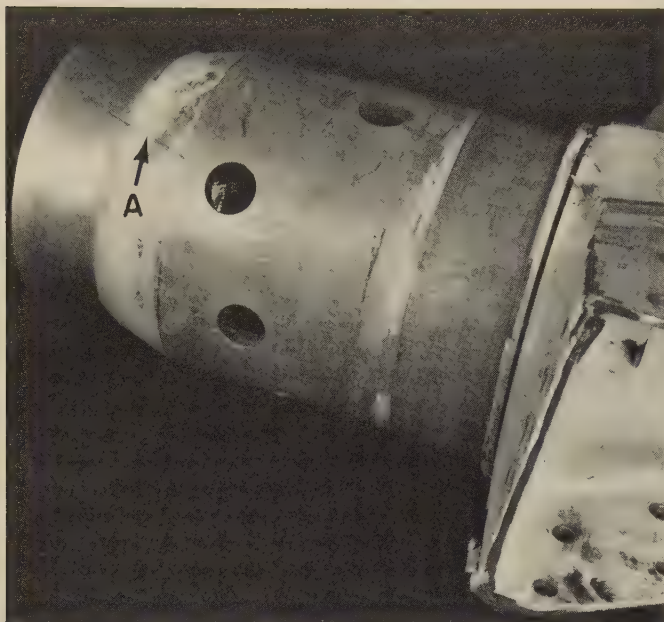
4329 Surface of a fracture in an aircraft nose-landing-gear cylinder made of 4340 steel and heat treated to a tensile strength of 1793 to 1931 MPa (260 to 280 ksi). The surface bears iron oxide resulting from corrosion in grinding cracks. Dimples and a few distinct grain boundaries are present.



TEM fractograph (p-c replica) 6500×

4330 The surface of a crack found beneath chromium plating on a pivot bolt of 4340 steel that was heat treated to a tensile strength of 1793 to 1931 MPa (260 to 280 ksi). Grinding cracks were found in this area, but the completely intergranular nature of this surface suggests subsequent stress corrosion.

Photograph, Light Fractographs, TEM Fractograph: 4340 Steel Aircraft
Horizontal Tail-Actuator Shaft That Fractured in Service



Photograph

$\frac{1}{2} \times$

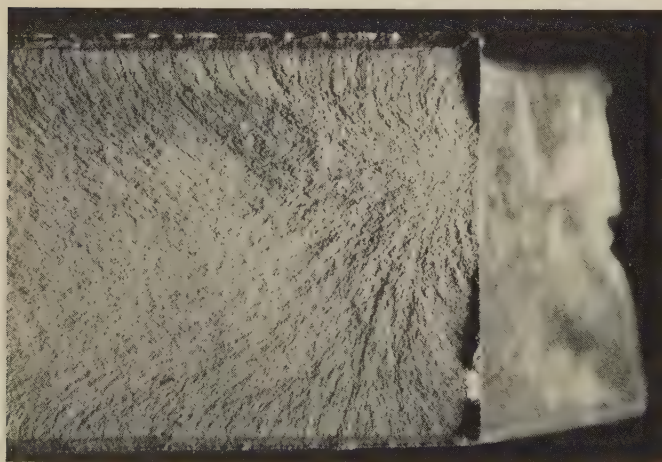
4331 View of an aircraft horizontal tail-actuator shaft that was found during a preflight inspection to contain several cracks (one is shown at A). The shaft was forged from 4340 steel, was heat treated to a minimum tensile strength of 1793 MPa (260 ksi) and a hardness of Rockwell C 50 to 53, and then was vacuum cadmium plated. Cracks were attributed to hydrogen embrittlement. See also 4332 to 4340.



Light fractograph

Actual size

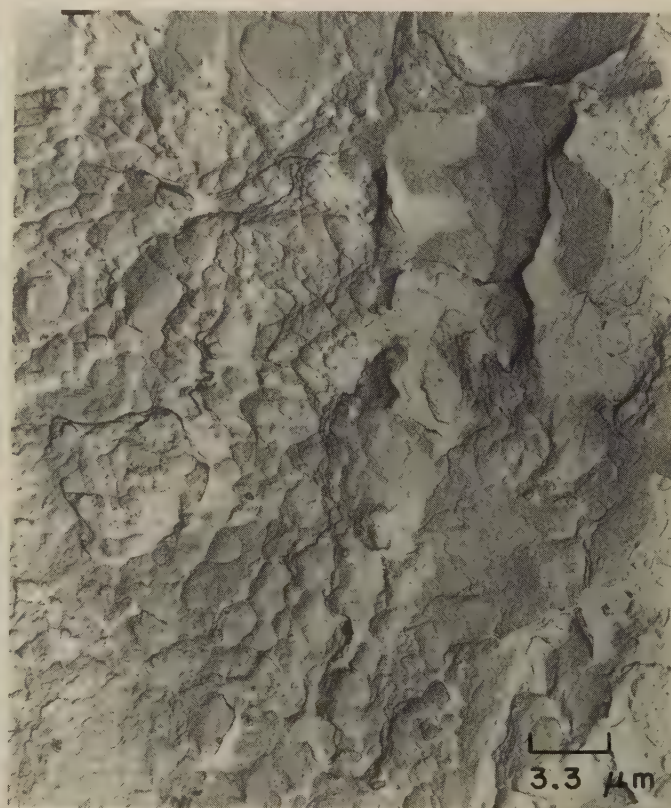
4332 Surface of the crack visible at A in 4331, opened for examination, showing two internal points of crack nucleation, which are marked 1 and 2 and are shown at higher magnification in 4333 and 4334. Neither this crack nor any other crack found in this shaft or in companion shafts showed evidence of the corrosion products (red rust) that would be expected if stress corrosion had been involved.



Light fractographs

$7 \times$

4333 Enlarged views of the internal points of crack nucleation shown in 4332. In fractograph 4333 (above), which includes point 1, chevron marks indicate that direction of fracture was right to left; shear lips are present at the borders. Fractograph 4334 (below), which includes point 2, shows secondary cracking. See 4335-4337.



TEM fractograph (p-c replica)

3000 \times

4335 A TEM replica of a region near the right edge of the fracture surface in 4333, showing a transition from intergranular facets (at right) to dimples (at left). This transition is typical of all cracks in the actuator shaft that originated near holes; in each instance, transition occurred at 0.02 to 0.07 in. from the edge of the hole.

TEM Fractographs, Light Fractographs: 4340 Steel Aircraft
Horizontal Tail-Actuator Shaft That Fractured in Service (Continued)



TEM fractograph (p-c replica)

8000×

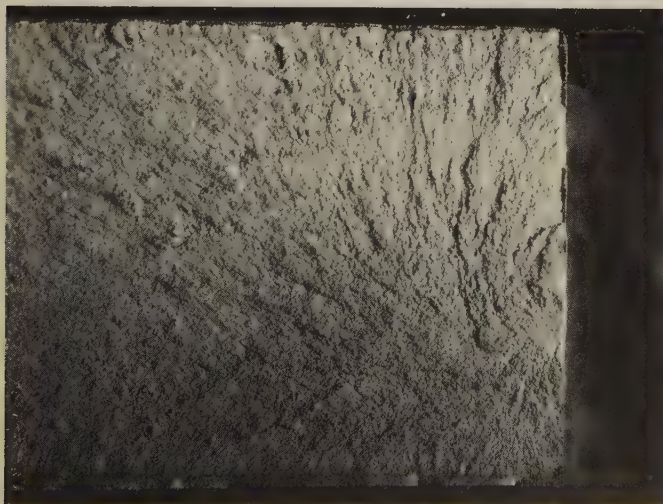
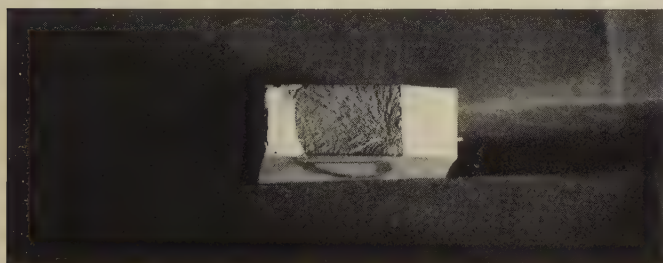
4336 TEM replica of a region centered on the crack-nucleation point visible near the right edge of the fracture surface shown in 4333. The surface is intergranular and free of corrosion products, which is consistent with fracture caused by hydrogen embrittlement.



TEM fractograph (p-c replica)

6000×

4337 TEM replica of a region containing the crack-nucleation site near point 2 in fractograph 4332. The features that are visible in this region are the same as those in the region shown in 4336 (left), which further suggests that hydrogen embrittlement caused the cracks.

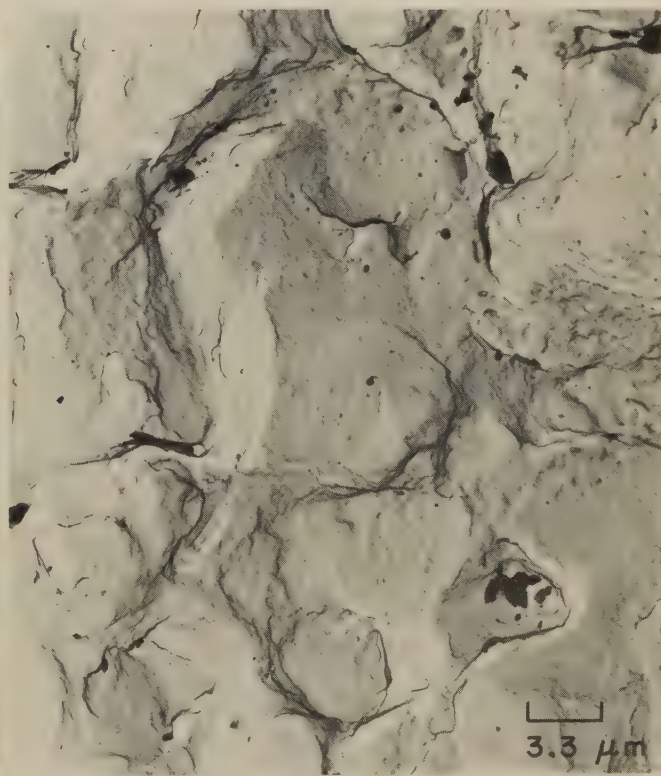


Light fractographs

Actual size (4338); 7× (4339)

4338 Views, at two magnifications, of a crack 135° around the shaft from the crack at A in 4331, opened for examination. Again, the point of crack nucleation was internal. The crack then propagated both inward and outward, as shown by the chevron marks and shear lips.

4339

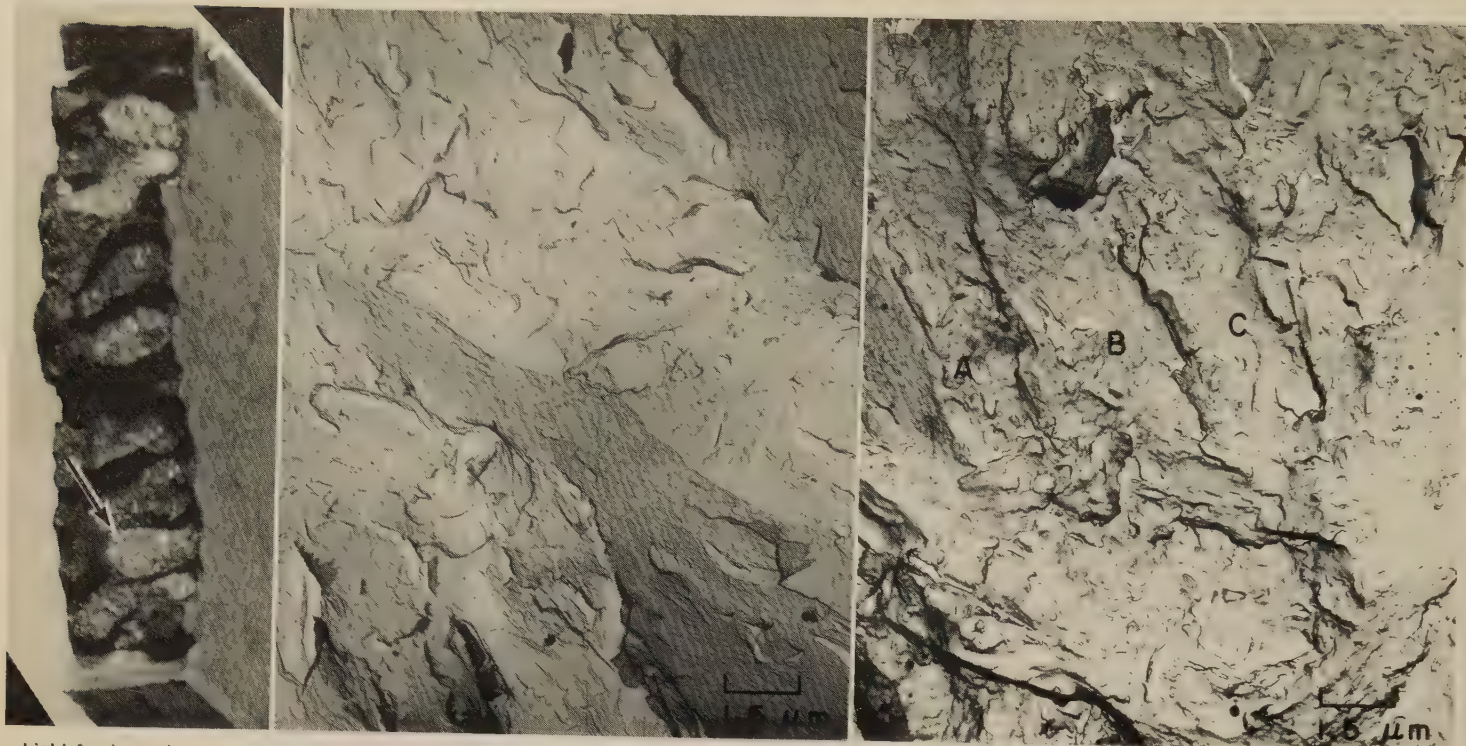


TEM fractograph (p-c replica)

3000×

4340 TEM replica of a region containing a point of nucleation in a crack very similar to those shown in 4332 and 4339, in a companion actuator shaft. This surface shows all of the intergranular characteristics of fracture by hydrogen embrittlement seen in 4336 and 4337.

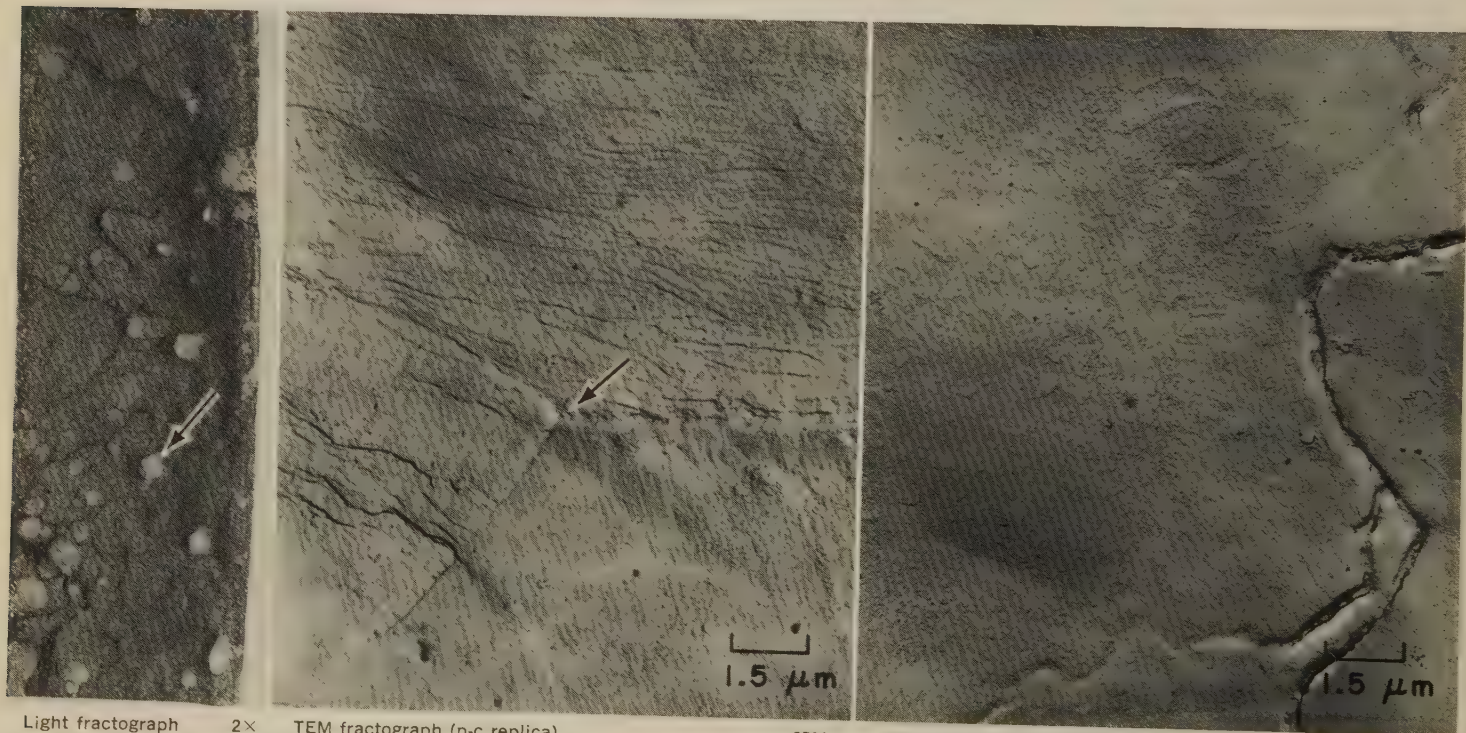
Light and TEM Fractographs: 4340 Steel Fractured in Loading After Being Charged With Hydrogen; Fracture in 4340 Steel Displaying Hydrogen Flakes



Light fractograph 14× TEM fractograph (p-c replica) 6500×

4341, 4342, 4343

Fractograph 4341 (left) shows a fracture surface in a specimen of 4340 steel sheet that was heat treated at 843 C (1550 F), oil quenched, tempered at 482 C (900 F), cathodically charged with hydrogen, and broken in loading to a stress of 689 MPa (100 ksi). The large facets of separated grains in 4341 display the intergranular nature of hydrogen-embrittlement fractures. The crack origin is not identifiable, but it is usually subsurface in fractures of this type. Two areas in the large facet at the arrow are shown in TEM fractographs 4342 (center) and 4343 (right). There is evidence also of quasicleavage in 4343, at A, B and C.

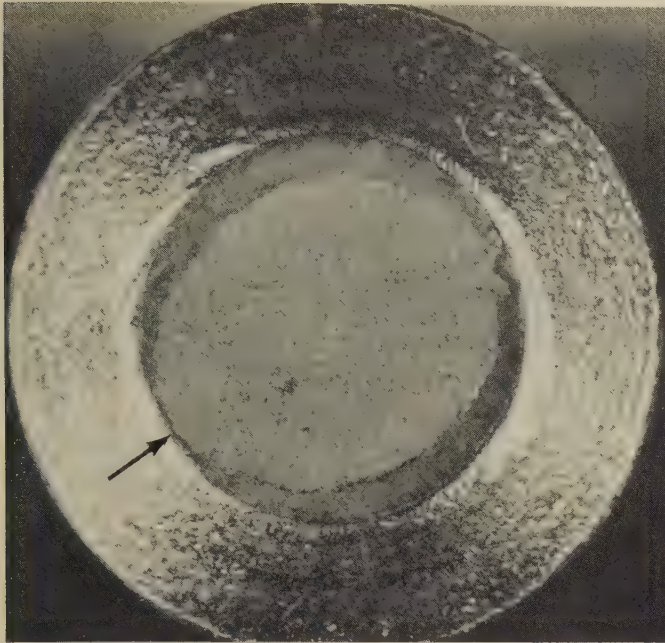


Light fractograph 2× TEM fractograph (p-c replica) 6500×

4344, 4345, 4346

Fractograph 4344 (left) shows a fracture surface in forged 4340 steel (heat treatment not reported), displaying the flat, bright, fine-textured features known as hydrogen flakes or fisheyes. Two areas in the flake at the arrow are shown in TEM fractographs 4345 (center) and 4346 (right). The surface in 4345 is flat and displays a fine, rippled texture that may have been caused by fracture of lamellae of fine pearlite. The speckled appearance may have been caused by corrosion products. The ridges, which may be grain boundaries, form a junction at the arrow. The surface in 4346 is remarkably smooth, with unusual "worm track" marks. The forked ridge at lower right is a deep fault or rift, probably the result of a structural discontinuity.

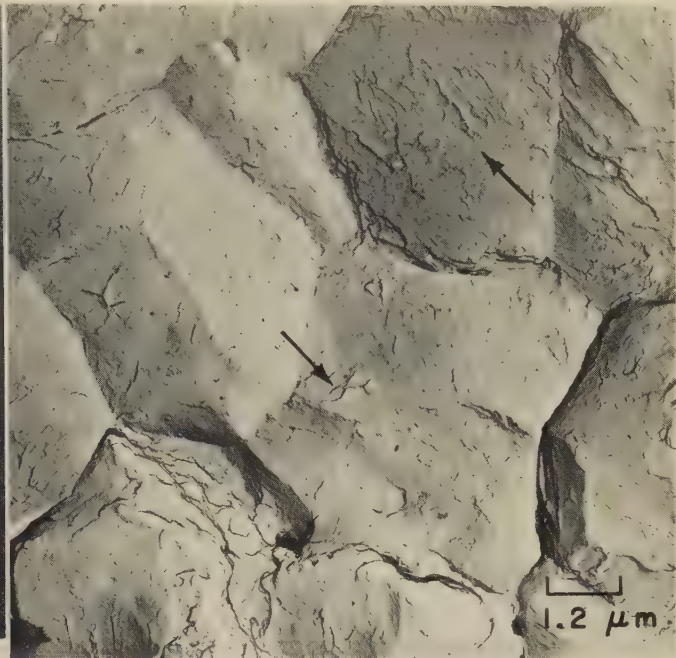
**Light and TEM Fractographs: Hydrogen-Embrittled 4340 Steel Fractured by Sustained Loading;
Cracks in 4340 Steel Landing-Gear Cylinders Due to Hydrogen Embrittlement and Stress Corrosion**



Light fractograph

14×

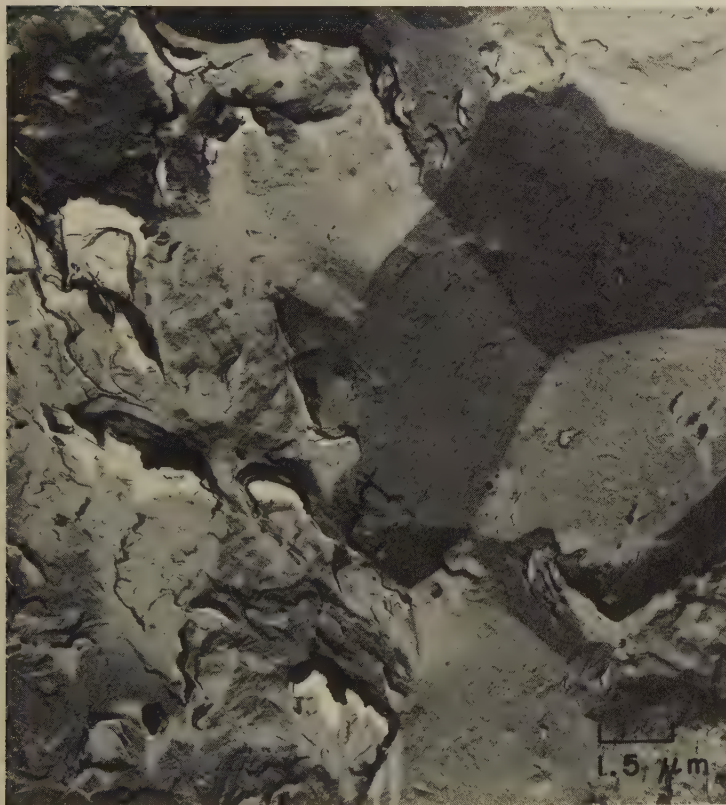
4347 Surface of a sustained-load fracture in a hydrogen-embrittled notched specimen of 4340 steel with tensile strength of 1793 to 1931 MPa (260 to 280 ksi). This type of fracture can result from absorption of too much hydrogen from either acid pickling or metal plating. Area near the crack origin (at arrow) is shown in 4348.



TEM fractograph (p-c replica)

8000×

4348 A TEM replica of the fracture surface in 4347, showing the area near the crack origin. This area displays the intergranular facets that are characteristic of hydrogen embrittlement. The hairline indications (at arrows) serve to distinguish this type of fracture from others.



TEM fractograph (p-c replica)

6500×

4349 Surface of a crack discovered beneath chromium plating on an aircraft main-landing-gear cylinder of 4340 steel having a tensile strength of 1793 to 1931 MPa (260 to 280 ksi). Mainly intergranular in nature, the crack is attributed to hydrogen embrittlement, perhaps as a result of the plating.

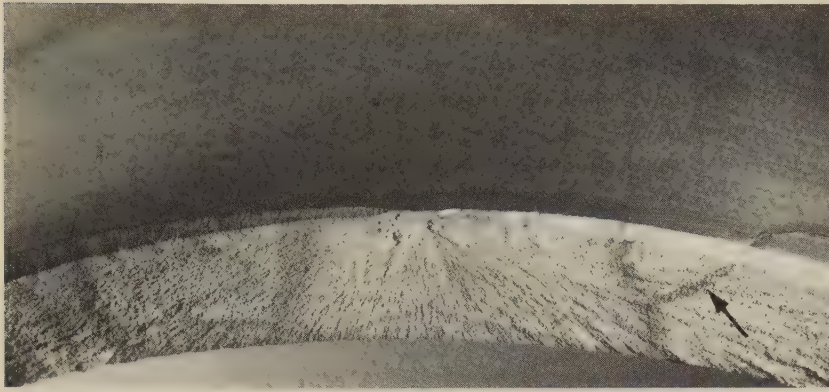


TEM fractograph (p-c replica)

6500×

4350 Surface of a crack that was found in an aircraft nose-landing-gear cylinder made of 4340 steel having a tensile strength of 1793 to 1931 MPa (260 to 280 ksi). The crack originated by stress corrosion at a region of concentrated nonmetallic inclusions beneath a discontinuous chromium plate.

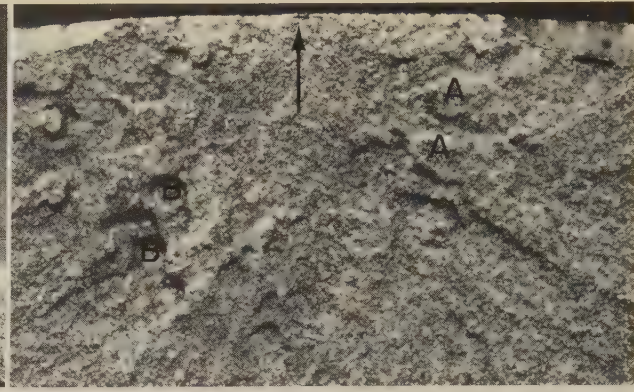
Light and TEM Fractographs: 4340 Steel Aircraft Landing-Gear Cylinder Broken in Low-Cycle Fatigue;
4340 Steel Sheet Exposed to Marine Atmosphere and Fractured by Stress-Corrosion Cracking



Light fractograph

2X

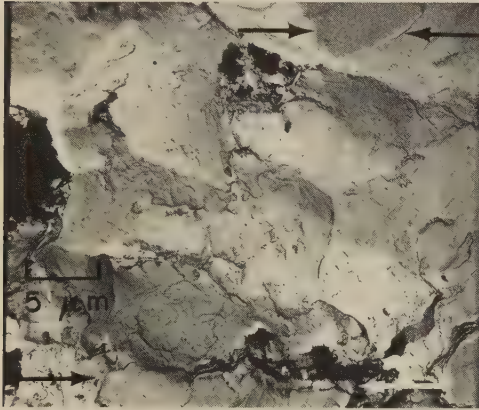
4351 Surface of a low-cycle fatigue fracture in an aircraft landing-gear cylinder made of 4340 steel that was hardened and tempered to a tensile strength of 1793 to 1931 MPa (260 to 280 ksi). The cylinder was stressed in the laboratory to its tensile strength four times and broke at a stress of 1103 MPa (160 ksi) during the final loading. Note the secondary crack (arrow) to the right of the crack origin (at center), representative of many that extended completely through the wall of the cylinder. See also 4352 to 4355.



Light fractograph

14X

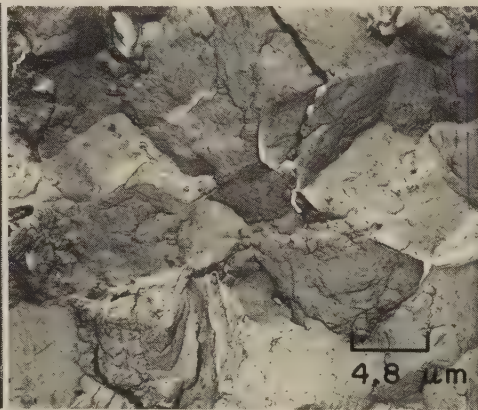
4352 Higher-magnification view of the crack-origin area of the fracture surface in 4351. Fracture originated at a small surface crack (visible at arrow) that was present prior to testing. The small flat-topped projections (at A's) and flat-bottomed depressions (at B's) were not found elsewhere in the fracture surface. See also fractographs 4353 to 4355.



TEM fractograph (p-c replica)

2000X

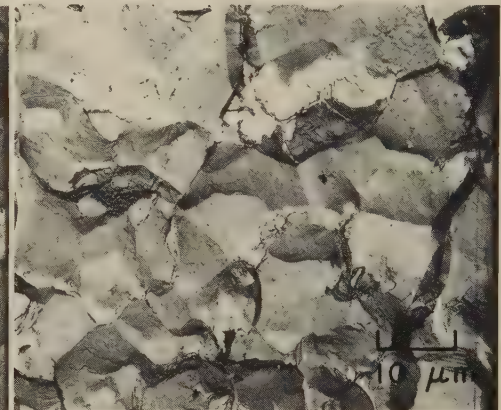
4353 TEM replica of a portion of the surface crack in 4352, where fracture originated. Note rubbed areas between arrows. The facets are intergranular; the opaque particles lie 0.002 to 0.003 in. below the outer surface of the cylinder.



TEM fractograph (p-c replica)

2100X

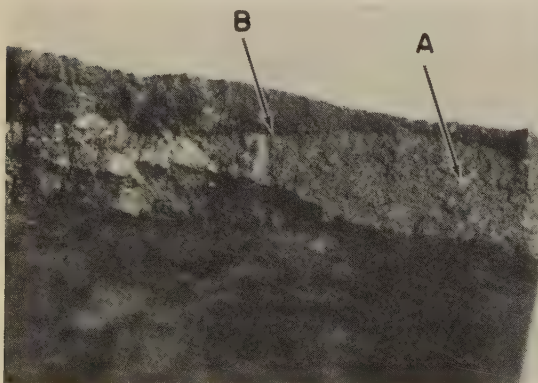
4354 TEM replica of the fracture surface in 4352, showing a region 0.01 in. below the outer surface. The mixture of intergranular facets and dimples shown here is typical of some plane-strain fracture surfaces in 4340 steel.



TEM fractograph (p-c replica)

1000X

4355 TEM replica of the fracture surface in 4352, showing a region at the bottom of a depression directly below the surface crack. In this entire area of projections and depressions (see 4352), fracture was completely intergranular.

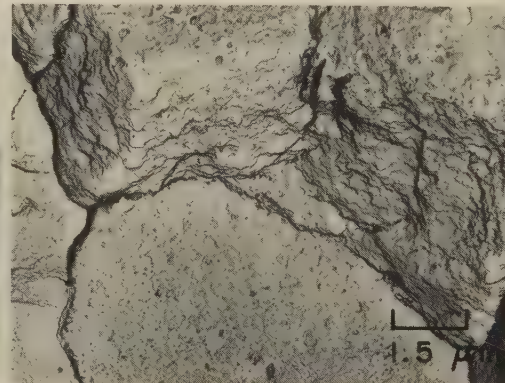


Light fractograph

13X

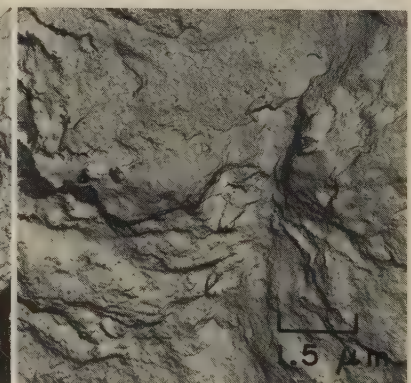
4356, 4357, 4358

Surface of a fracture in 4340 steel sheet that was heat treated at 843 C (1550 F), oil quenched, and tempered at 232 C (450 F). The sheet was loaded to a stress of 1241 MPa (180 ksi) for 27 days in a marine atmosphere and broke as the result of stress corrosion. Fractograph 4356 (left) is a low-magnification view of the entire fracture surface. Stress-corrosion cracking began at the right edge and produced the flat, tongue-shaped area marked A; at B, cracking changed to fast fracture and produced shear lips. Two regions in the area marked A in 4356 are shown at higher magnification in TEM fractographs 4357 (center) and 4358 (right). The facets in 4357 are clearly intergranular and carry an accumulation of corrosion products; this surface is fairly typical of stress-corrosion cracking. The facets in 4358 are too severely corroded for positive identification but probably are intergranular. See also 4359 to 4361.



TEM fractograph (p-c replica)

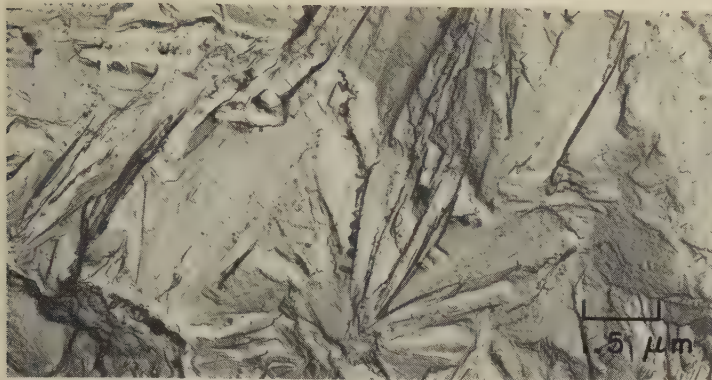
6500X



TEM fractograph (p-c replica)

6500X

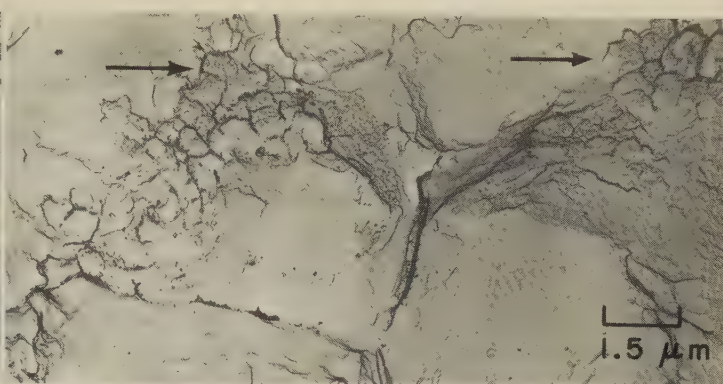
Light and TEM Fractographs: 4340 Steel Sheet Fractured by Stress-Corrosion Cracking (Continued);
Notched 4340 Steel Exposed to Deionized Water and Fractured by Stress-Corrosion Cracking



TEM fractograph (p-c replica)

6500×

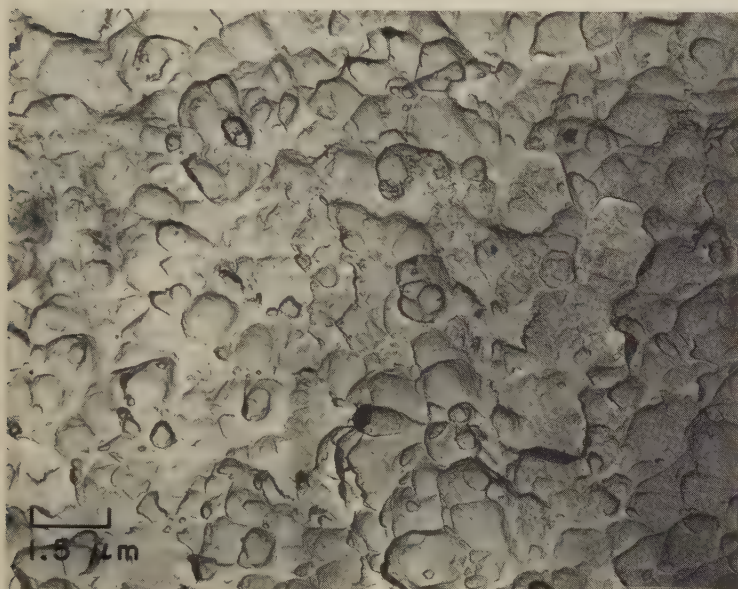
4359 TEM view of another region in the area marked A in 4356. The intergranular facets here carry a complicated array of corrosion products; in some areas, the corrosion products appear to have spalled during rupture.



TEM fractograph (p-c replica)

6500×

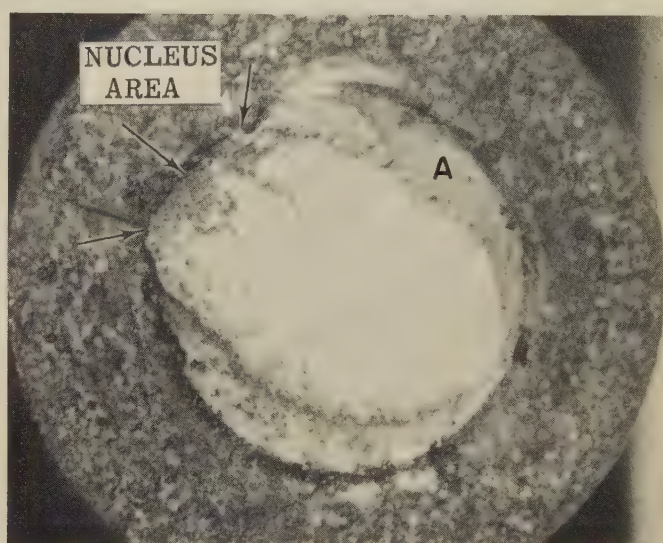
4360 TEM view of still another region in the area marked A in 4356. In addition to intergranular facets, this view shows, in the regions denoted by arrows (near top), another characteristic of stress-corrosion cracking — namely, “mud cracking”.



TEM fractograph (p-c replica)

6500×

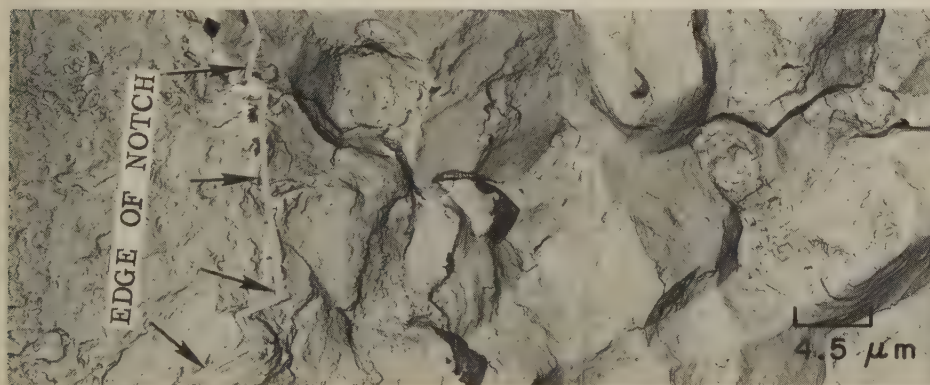
4361 TEM view of a portion of the fast-fracture region to the left of the area marked B in 4356. Shown here are equiaxed dimples, the presence of which indicates that microvoid coalescence occurred under tension overload following the increase in stress-intensity factor caused by growth of the stress-corrosion crack.



Light fractograph

14×

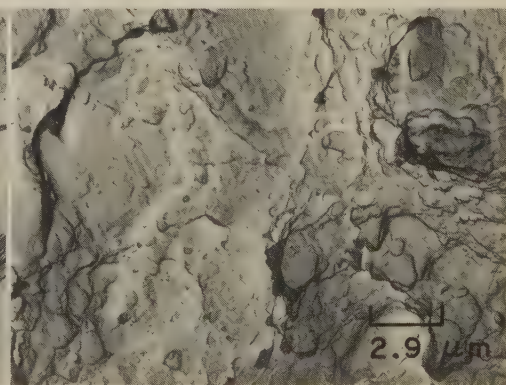
4362 Fracture in a notched specimen of 4340 steel oil quenched from 829 C (1525 F) and tempered at 232 C (450 F). The specimen was alternately exposed to deionized water (10 min) and to air (50 min) while being stressed at 800 MPa (116 ksi), and broke due to stress-corrosion cracking. Corroded perimeter is the notch surface. The region of final, fast fracture is at A. See also fractographs 4363 and 4364, below.



TEM fractograph (p-c replica)

2200×

4363 TEM replica of a region in the crack-nucleation area in the fracture surface in 4362. Crack propagation was intergranular; the exposed grain facets are coated with corrosion products. Secondary cracks are visible at right. All cracks nucleated at, instead of below, the machined surface, regardless of notch sharpness.

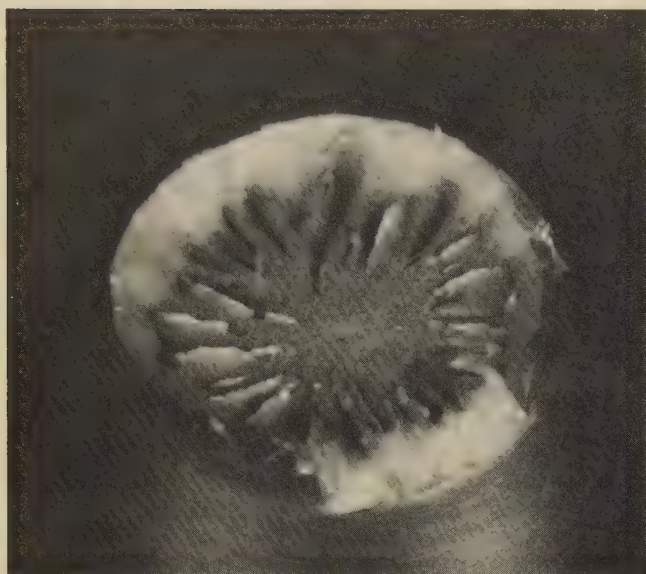


TEM fractograph (p-c replica)

3500×

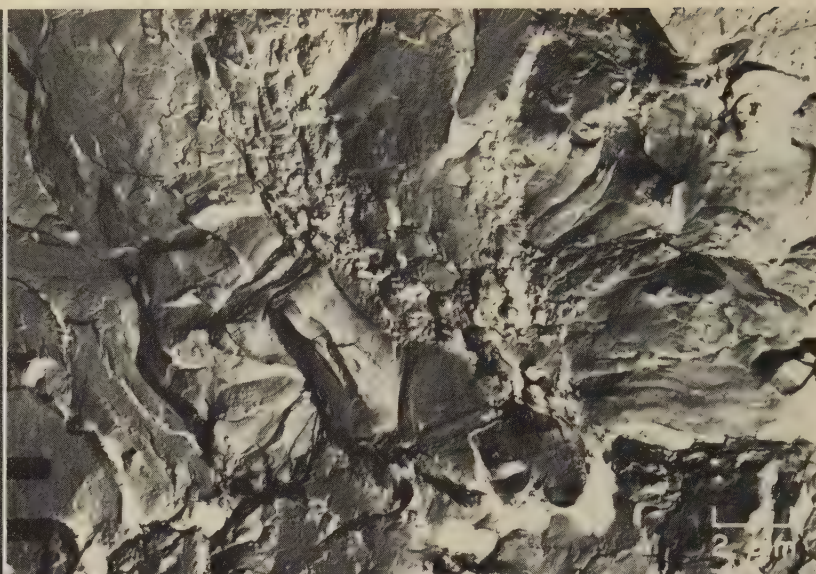
4364 TEM view of a portion of the fast-fracture region (A) of the stress-corrosion fracture surface in 4362. Shown here are dimples and suggestions of cleavage facets.

Light and TEM Fractographs: Unnotched Specimen of 8740 Steel Fractured by Tension Overload



Light fractograph

9×

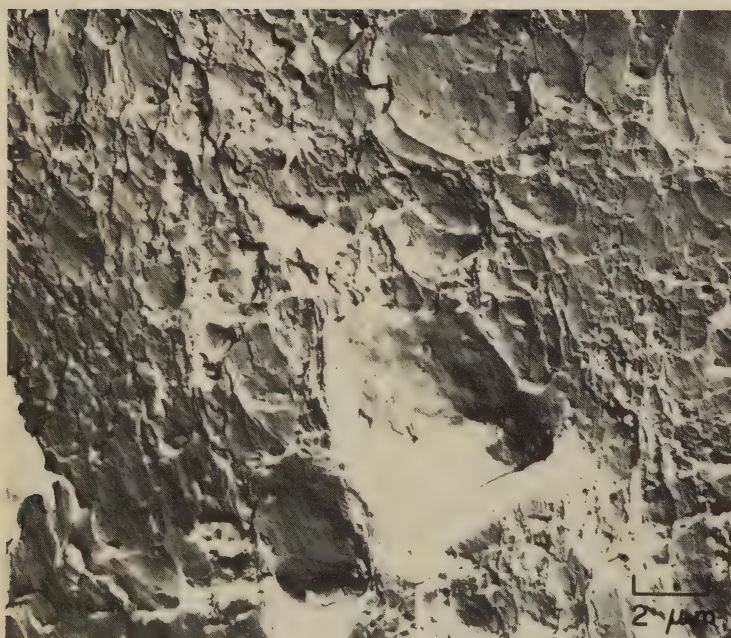


TEM fractograph (p-c replica)

5000×

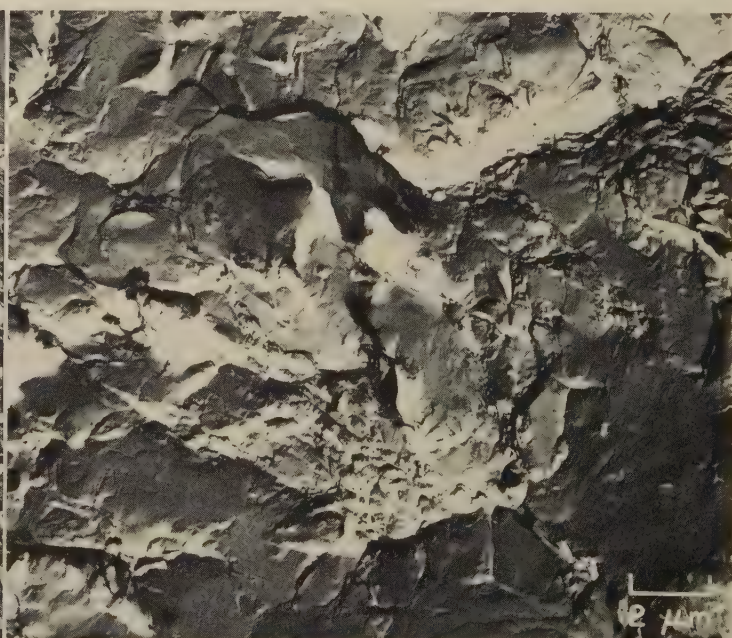
4365 Tension-overload fracture in an unnotched specimen of 8740 steel heat treated to a tensile strength of 1351 MPa (196 ksi); reduction in area, 52%. Note pronounced radial shear marks between central fibrous zone and outer shear lip in this otherwise conventional cup-and-cone fracture surface. See fractographs 4366 to 4368.

4366 TEM replica of an area in the central fibrous zone of the fracture surface in 4365, taken as close as possible to the radial shear marks. The surface contains dimples, in a wide range of sizes, that resulted from microvoid coalescence. There appear to be cleavage facets just below center, and below these facets there is a region with surface characteristics that suggest local quasicleavage. Note secondary cracks.



TEM fractograph (p-c replica)

5000×



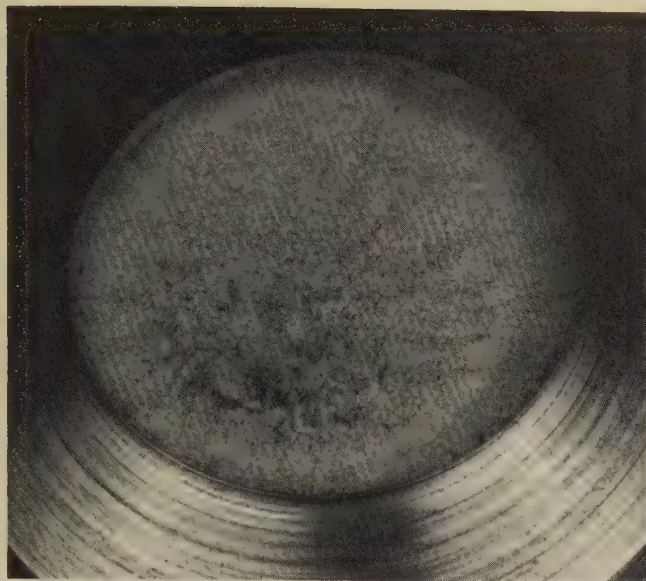
TEM fractograph (p-c replica)

5000×

4367 TEM replica of another area close to the radial shear marks in the fracture surface in 4365. Here, a large number of flat shear dimples are interspersed with a few large dimples. At bottom center is a feature that appears to be a facet of an isolated inclusion rather than a dimple.

4368 TEM replica of a region of the fracture surface in 4365 near those shown in 4366 and 4367. As in 4366, secondary cracks are in evidence. Many of the very fine dimples visible here appear to have formed on the surfaces of larger dimples. Several of the larger facets at bottom appear to be quite flat.

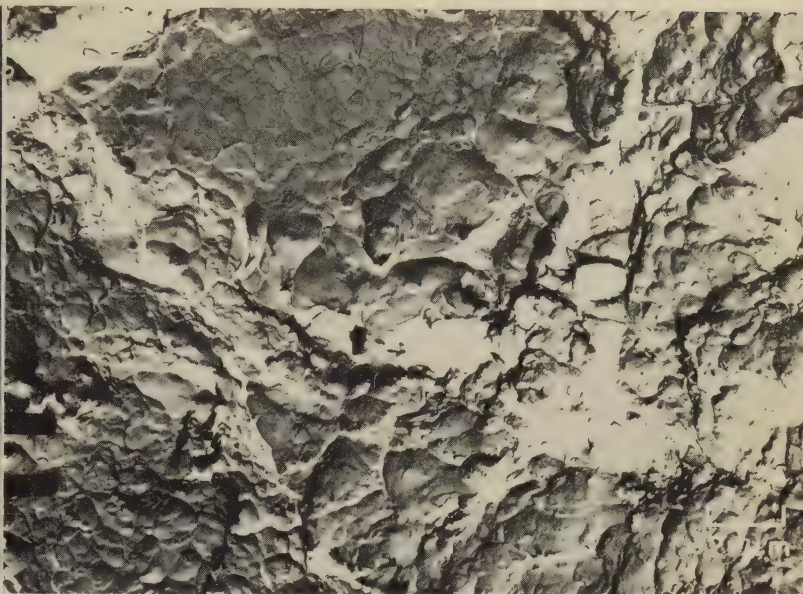
Light and TEM Fractographs: Notched Specimen of 8740 Steel
Fractured by Tension Overload



Light fractograph

9×

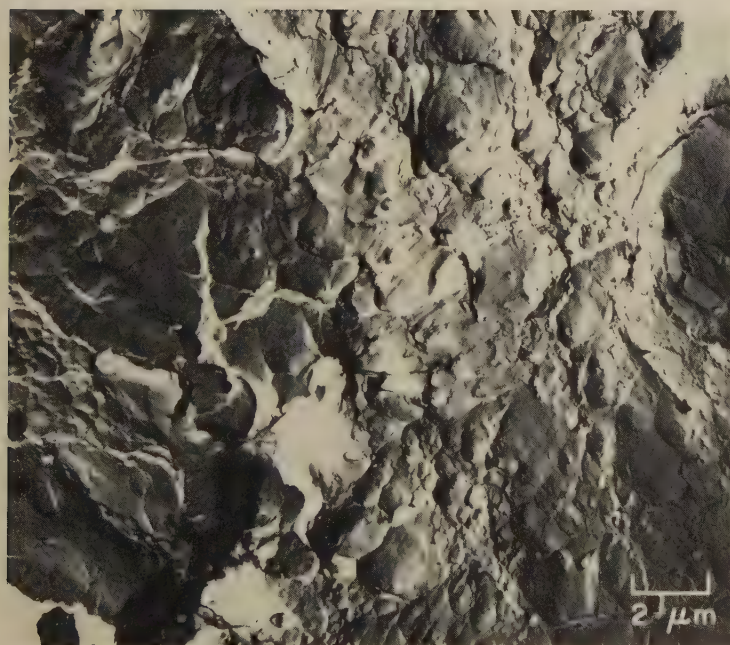
4369 Surface of a tension-overload fracture in a notched specimen of 8740 steel (same properties as in 4365). Notched tensile strength, 2044.3 MPa (296.5 ksi). In the unnotched specimen in 4365 (facing page), rupture began at center; here, the fracture origin was at the root of the notch. A fibrous zone surrounds a central radial fibrous zone. See also fractographs 4370 to 4372.



TEM fractograph (p-c replica)

5000×

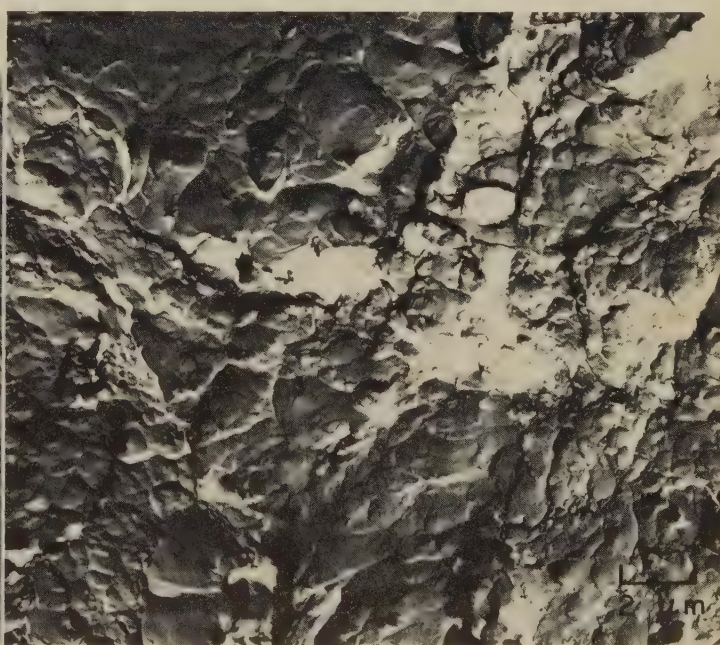
4370 TEM replica of a region in the central radial fibrous zone of the fracture surface in 4369, showing rather small, flat dimples that in general appear quite equiaxed. In an area near top and slightly to the left of center, the dimples are so flat as to present an almost smooth surface. This fracture surface appears to be relatively free of secondary cracks; a few minor ones can be seen at upper right and lower left.



TEM fractograph (p-c replica)

5000×

4371 TEM replica of another area in the central radial fibrous zone of the fracture surface in 4369. The dimples here are very similar to those in 4370. This area does not appear to contain secondary cracks or evidence of local cleavage; there are, however, several marks that are suggestive of tear ridges.

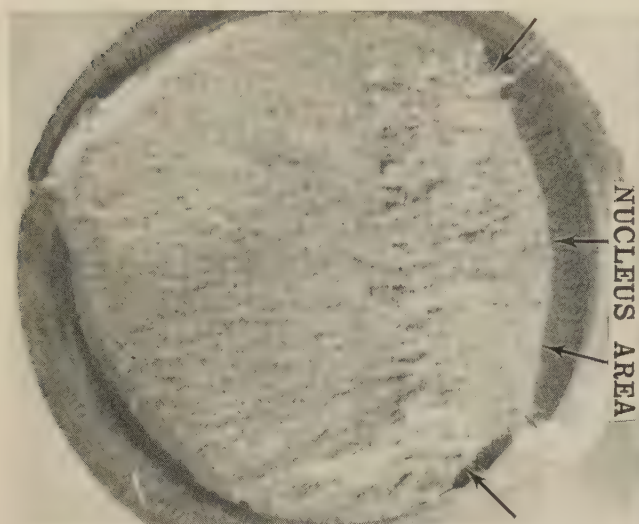


TEM fractograph (p-c replica)

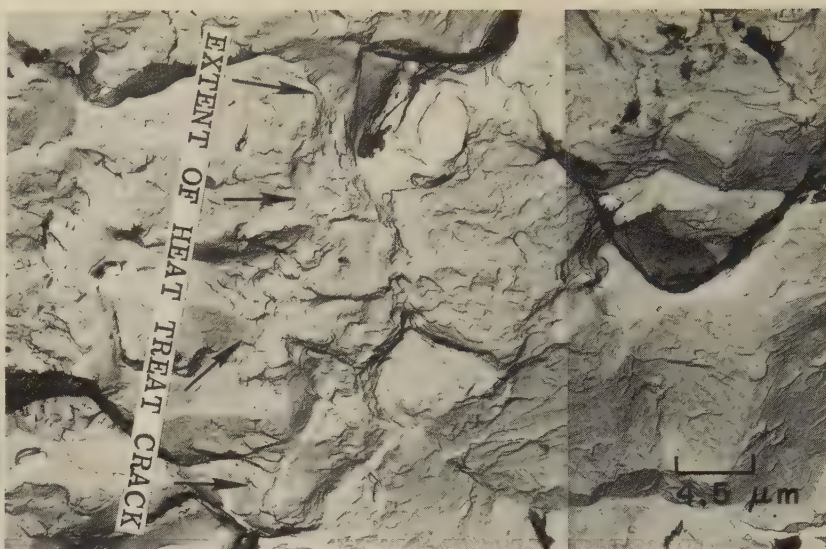
5000×

4372 TEM replica of the tension-overload fracture surface in 4369, showing an area that is only slightly above and to the left of the area seen in fractograph 4370. The two dark marks visible at bottom left cannot be positively identified, but they may be indications of secondary cracks.

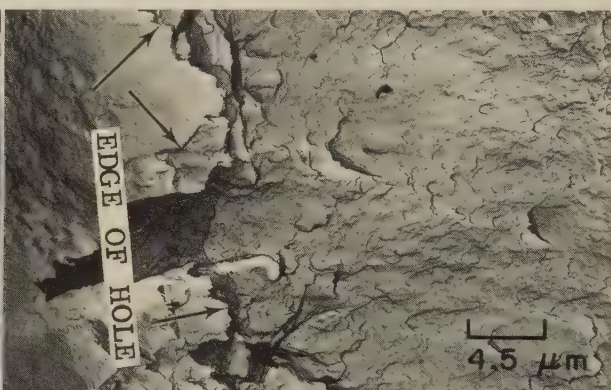
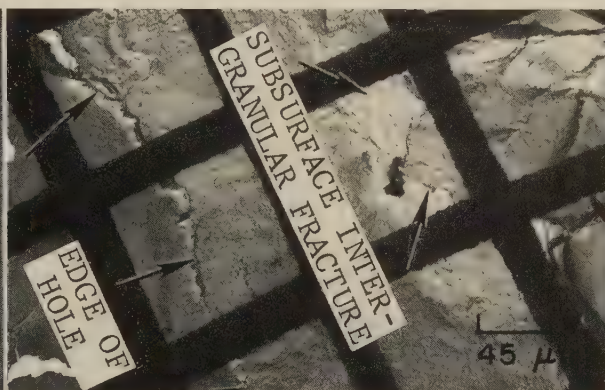
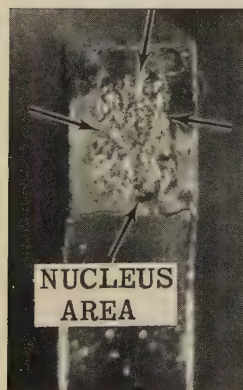
Light and TEM Fractographs: D-6ac Steel Fractured by Stress Corrosion; Fracture in Hydrogen-Embrittled 300M Steel; Fatigue Fracture in a 1080 Steel Transducer Spring



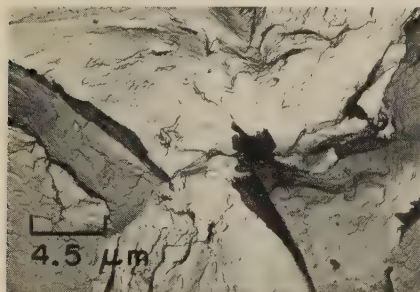
Light fractograph 12×
4373 Surface of a fracture in a specimen of D-6ac steel that broke during a stress-corrosion-cracking test in deionized water. Stress-corrosion cracking originated at the root of a dark heat-treat crack in a thread at right; fast fracture occurred after only 15 hr at a tension of 814 MPa (118 ksi). See also fractograph 4374.



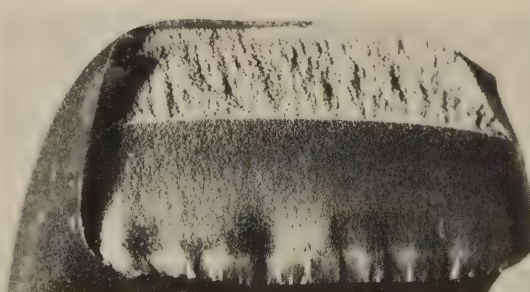
TEM fractograph (p-c replica) 2200×
4374 TEM replica of an area of the fracture surface in 4373 containing the boundary (indicated by arrows) between the heat treatment crack (left) and the stress-corrosion crack (right). At right are intergranular facets, which resulted from stress-corrosion cracking; essentially no corrosion products were formed on these facets during this brief test.



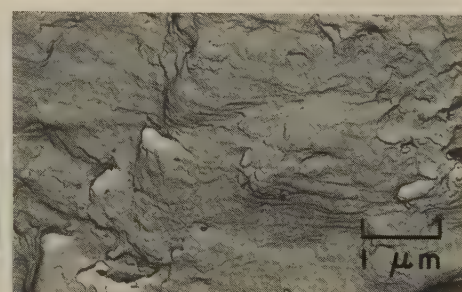
Light fractograph 14× TEM fractograph (p-c replica) 220× TEM fractograph (p-c replica) 2200×
4375, 4376, 4377 Surface of a fracture in a tension-loaded specimen of hydrogen-embrittled 300M steel heat treated 1 hr at 871 C (1600 F) and oil quenched, then double tempered 2 hr plus 2 hr at 302 C (575 F) and air cooled. Tensile strength was 1979 MPa (287 ksi). The nucleus of the crack was below the specimen surface (as indicated in 4375, at left), near a hole with a radius of 0.063 in., which acted as a notch. Fractograph 4376 (center) is a low-magnification TEM view, through a supporting grid, of the edge of the hole and the origins of the subsurface crack, which is intergranular. Fractograph 4377 (right) is a higher-magnification TEM view of the edge of the hole and shows the very flat tear dimples that formed between the crack origins and the hole. See also 4378, below.



TEM fractograph (p-c replica) 2200×
4378 TEM view of the nucleus of the subsurface crack that led to the fracture in 300M steel shown in 4375 to 4377. Separated-grain facets and hairline indications, both of which are typical of hydrogen embrittlement, are clearly evident.

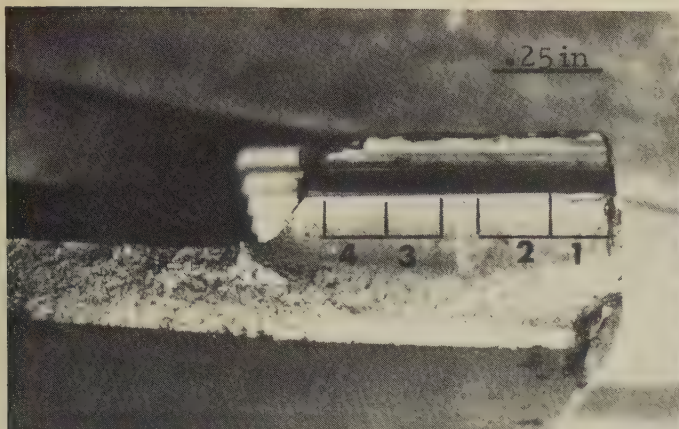


Light fractograph 5×
4379 Surface of a fatigue fracture in a transducer spring made of 1080 steel. The dark zone at bottom is the region of fatigue fracture, and the light zone at top is the region of final, fast fracture. "Ratchet" marks along the lower edge of the fatigue-fracture zone indicate that this fracture had a large number of nuclei. See 4380.



TEM fractograph (p-c replica) 10,000×
4380 High-magnification TEM view of the fatigue zone (dark, at bottom) of the fracture surface in 4379, showing fatigue striations. The fatigue striations are irregular and quite flat, which explains the smooth appearance of this zone in fractograph 4379.

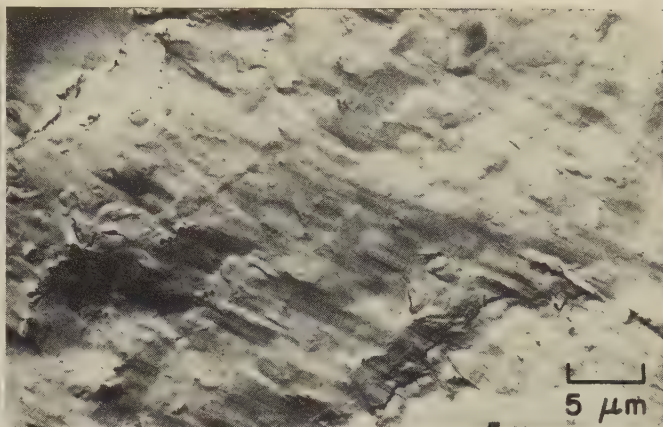
Light and TEM Fractographs: Nitralloy G Steel Ring Gear Fractured by Fatigue;
9310 Steel Planet Gear Fractured by Fatigue



Light fractograph

2¼×

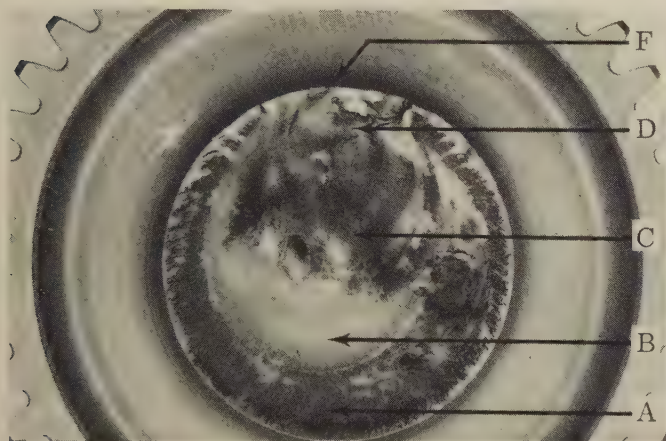
4381 Surface of a fatigue fracture, which originated at the root of a tooth, in a ring gear of Nitralloy G steel. Fracture occurred at full load in service after 2 hr of run-in. Hardness was Rockwell C 34 in the core and greater than Rockwell C 60 in the case. At the crack origin, effective case depth was 30% below specification. See also 4382.



TEM fractograph (p-c replica)

2500×

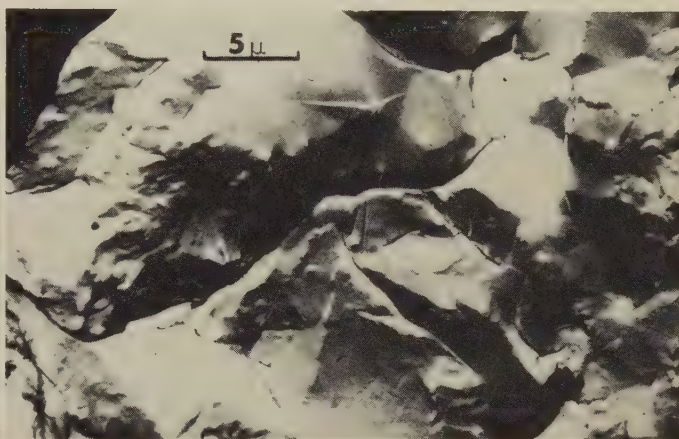
4382 TEM replica of the fracture surface in 4381, showing an area in region 1, which is below the tooth root (fracture origin). This area, from the core of the gear, shows high-cycle fatigue striations (diagonal marks) and is typical of most of the fracture surface. The fracture resulted from inadequate fatigue strength of the thin case at the origin.



Light fractograph

1.35×

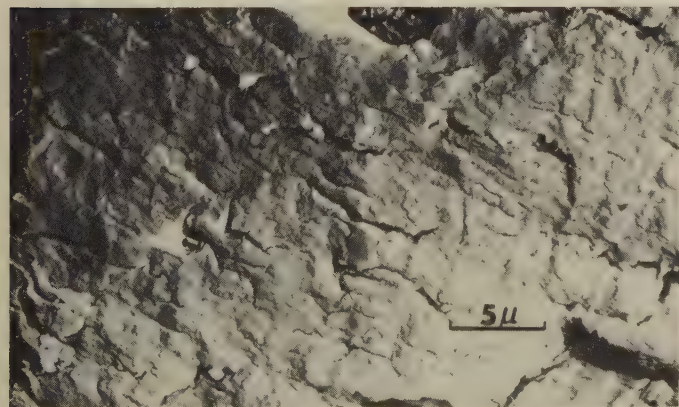
4383 Fatigue fracture in a turbine planet gear of 9310 steel that broke under a light load in service (during run-in). The gear had been heat treated to a hardness of Rockwell C 36.5 to 40 (near the surface). See also 4384 to 4386.



TEM fractograph (p-c replica)

2500×

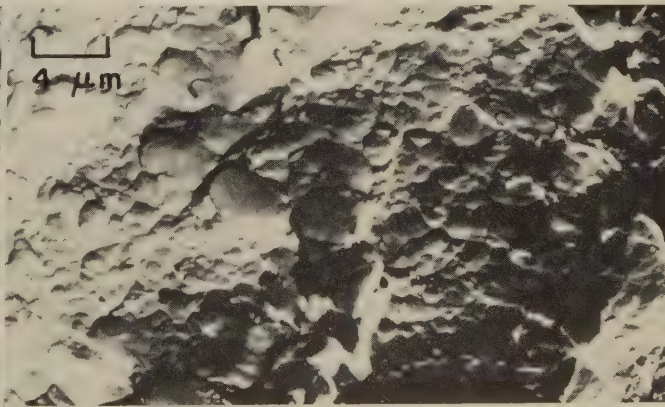
4384 TEM replica of area A in the outer region of the fracture surface in 4383, showing separated-grain facets. This region is believed to have formed a heat-treat crack—the only plausible explanation of its intergranular nature.



TEM fractograph (p-c replica)

2500×

4385 TEM replica of an area representative of fatigue regions B and C in the fracture surface in 4383 (above), between the outer, intergranular zone and the inner, fast-fracture zone, showing striations, formed by torsional stresses during run-in, that are normal to the perimeter of the gear.



TEM fractograph (p-c replica)

2500×

4386 TEM replica representative of areas D and F in the inner, fast-fracture zone in 4383. The numerous equiaxed dimples here indicate that fast fracture resulted from microvoid coalescence under tension overload; termination of fast fracture formed shear dimples (at upper left).

Light and TEM Fractographs: Ductile Iron Planet Gear Fractured by Torsion Overload;
18Ni-9Co-5Mo Maraging Steel Fractured by Corrosion Fatigue in Tap Water



Light fractograph

4387, 4388

Fractograph 4387 (left) shows a fracture surface of a carrier planet gear made of ductile iron (hardness, 146 to 183 Bhn). The gear fractured in service less than 10 hr after installation. Fractograph 4388 (right) is a TEM view of a plastic-carbon replica of the area at the arrow in 4387; the elongated dimples indicate that the gear fractured by torsion overload. Because the mechanical properties of the iron were acceptable, the fracture was attributed to improper installation.



About 1/2×

TEM fractograph

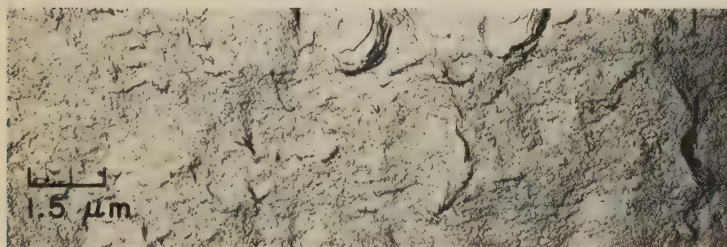
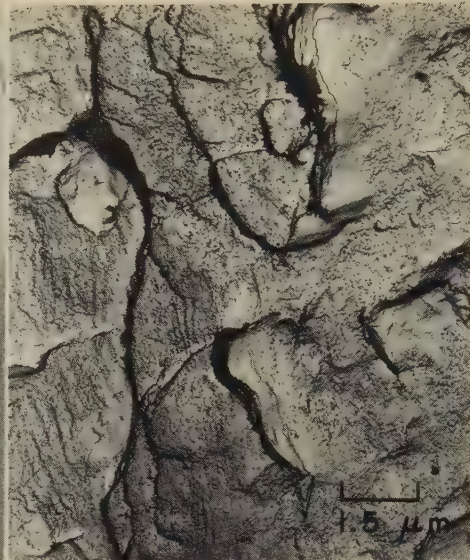
2500×



Light and TEM fractographs

4 1/2×; 6500×

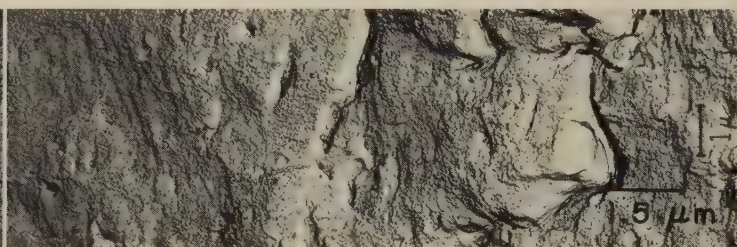
4389, 4390 At left, light fractograph 4389 shows a corrosion-fatigue fracture surface in 18Ni-9Co-5Mo maraging steel with a tensile strength of 2068 MPa (300 ksi), tested in tap water at 1000 cycles per minute to a stress of 862 MPa (125 ksi) max, 172 MPa (25 ksi) min. The maximum load was held 4 hr after each 1000 cycles. At right, TEM fractograph 4390 shows a plastic-carbon replica of a region in the area at A in 4389, which exhibits fatigue striations and corrosion. See 4391 to 4395, below.



TEM fractograph (p-c replica)

6500×

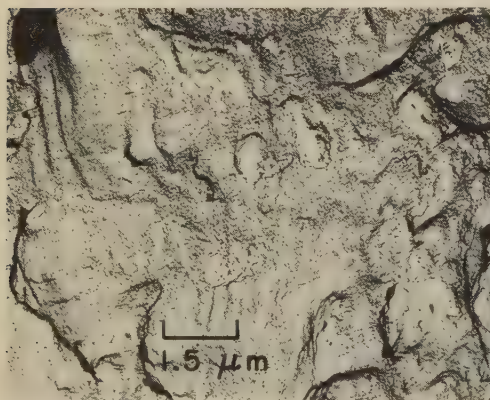
4391 A TEM view of a second region in area at A in fractograph 4389, showing fatigue striations that were very nearly corroded away by the tap water used in the fatigue test. At scattered spots there are suggestions of incomplete dimples.



TEM fractograph (p-c replica)

6500×

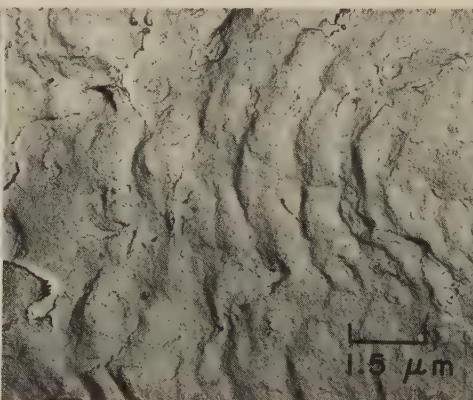
4392 A TEM view of a third region in area at A in fractograph 4389. Here, corrosion has removed nearly all traces of fatigue striations, except for a few scattered marks. There appear to be indications of secondary cracks in grain boundaries.



TEM fractograph (p-c replica)

6500×

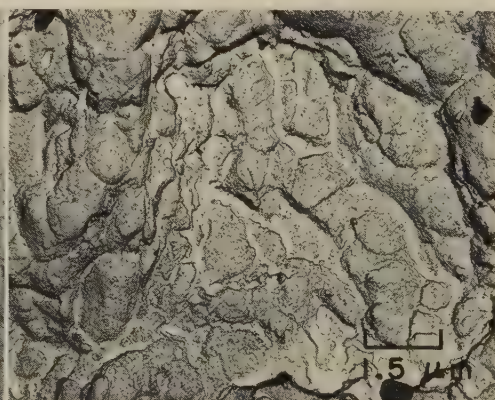
4393 A TEM view of a fourth region in area at A in 4389, showing fatigue striations somewhat more widely spaced than in 4390—the result of an increase in stress as the crack deepened.



TEM fractograph (p-c replica)

6500×

4394 A TEM view of a fifth region in the area at A in fractograph 4389, displaying quite widely spaced, irregular fatigue striations. These striations were evidently formed late in the fatigue test.

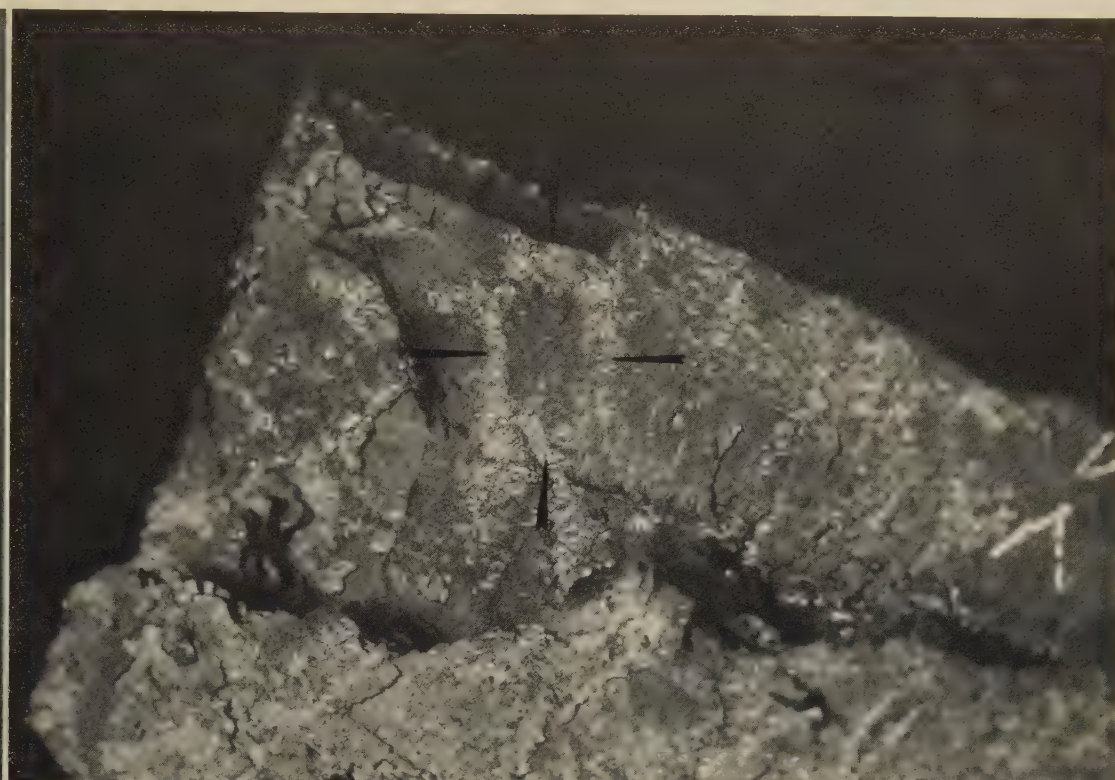
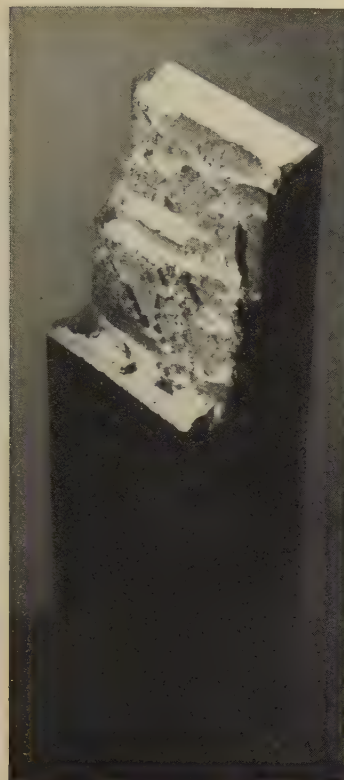


TEM fractograph (p-c replica)

6500×

4395 A TEM view of the area at B in 4389. This area was formed by fast fracture resulting from a planned increase in load after the fatigue test was stopped; it shows the expected dimples.

Light and TEM Fractographs: 18% Ni Maraging Steel Weld Specimen Fractured in Slow Bending, and Companion Weld Specimen Fractured Under Sustained Load After Hydrogen Embrittlement



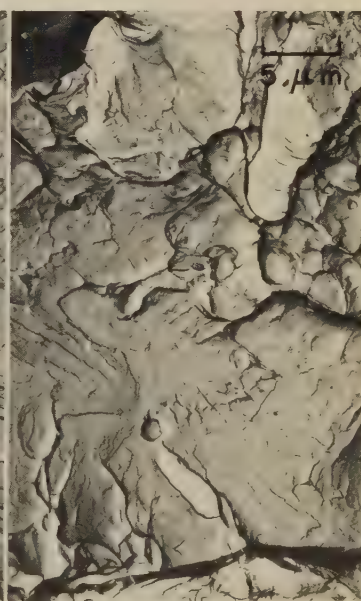
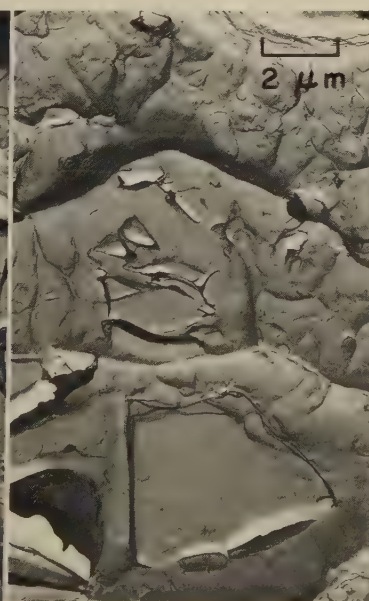
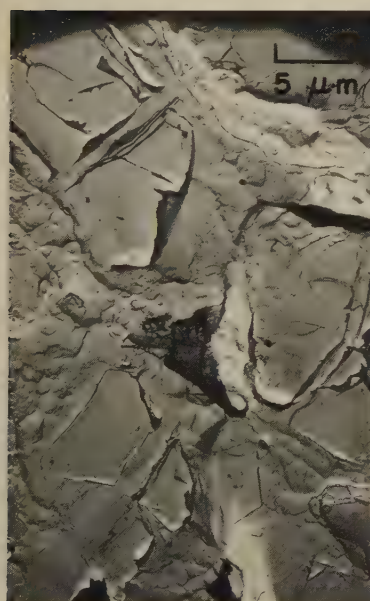
Light fractograph
4396, 4397

Actual size

Light fractograph

8×

At left (4396) is a slow-bend fracture of a weld specimen made by gas tungsten-arc butt welding two $\frac{3}{4}$ -in.-thick plates of 18% Ni maraging steel having a yield strength of 1724 MPa (250 ksi). A specimen $\frac{3}{4}$ in. square by 7 in. long was cut across the weld. After the weld was ground flush, the specimen was notched and then fatigue-cracked in the center of the weld and parallel to the length of the weld. After being aged at 490 C (914 F), the specimen was broken at room temperature in slow, three-point bending. Fracture surface shows steps caused by splitting. A portion of one of these steps is shown at higher magnification in fractograph 4397 (right); the surface here exhibits a network of high-reflectivity areas, one example being identified by the arrows. The remaining areas of the surface were relatively dull. Also see fractographs 4398 to 4401 (below).



TEM fractograph (pcr)

2000×

TEM fractograph (pcr)

5000×

TEM fractograph (pcr)

2000×

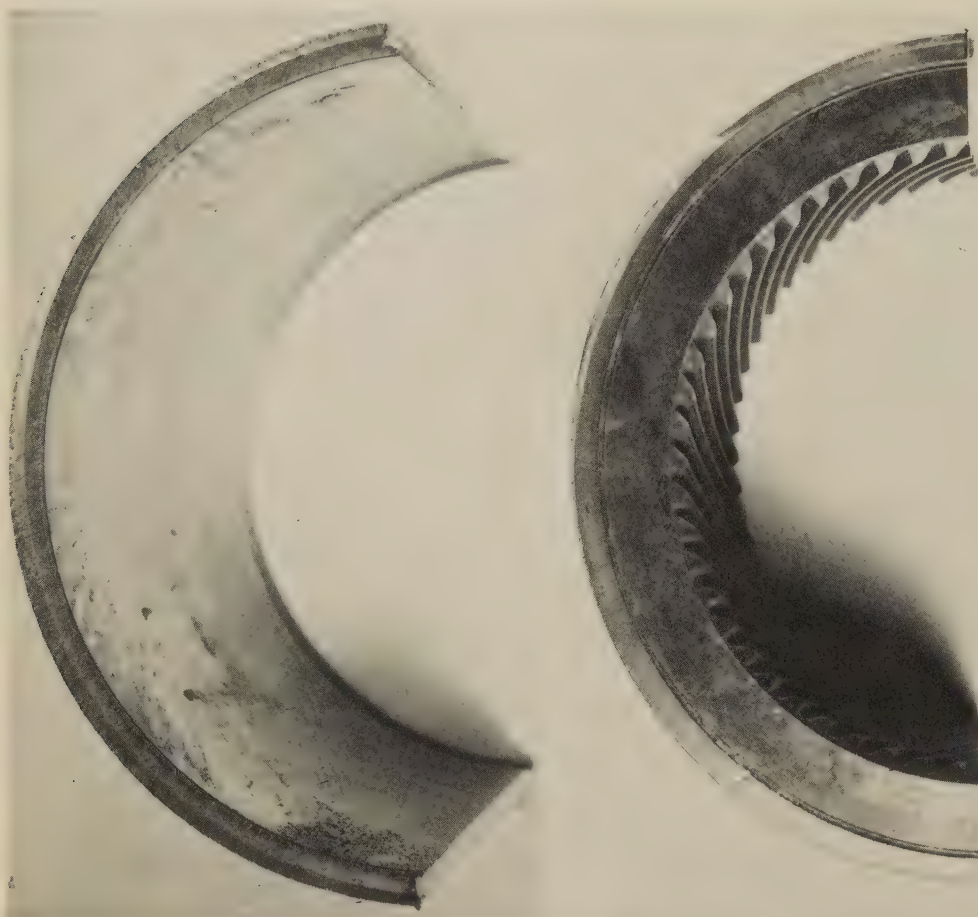
TEM fractograph (pcr)

2000×

4398, 4399, 4400, 4401

Fractographs 4398 and 4399 (left, and left center) are TEM views, at different magnifications, taken from one of the high-reflectivity areas in fractograph 4397. The shiny aspect was due to flat platelets resulting from cleavage of particles of unidentified composition. Note that in both views there are tear dimples between the reflecting facets. Fractograph 4400 (right center) reveals that the structure in the low-reflectivity areas in this fracture surface consists of rather flat equiaxed dimples. Fractograph 4401 (right) is from a companion 18% Ni maraging steel weld specimen to the one in 4396-4400; specimen here was hydrogen embrittled and then fractured by sustained loading at room temperature. This fracture surface shows dimples, together with quasicleavage facets that contain characteristic steps, river patterns and tear ridges.

Photographs; Light and TEM Fractographs: Fatigue Fracture in a Type 501 Stainless Steel Torque Cylinder From the Hub Socket of an Aircraft Propeller



Photograph

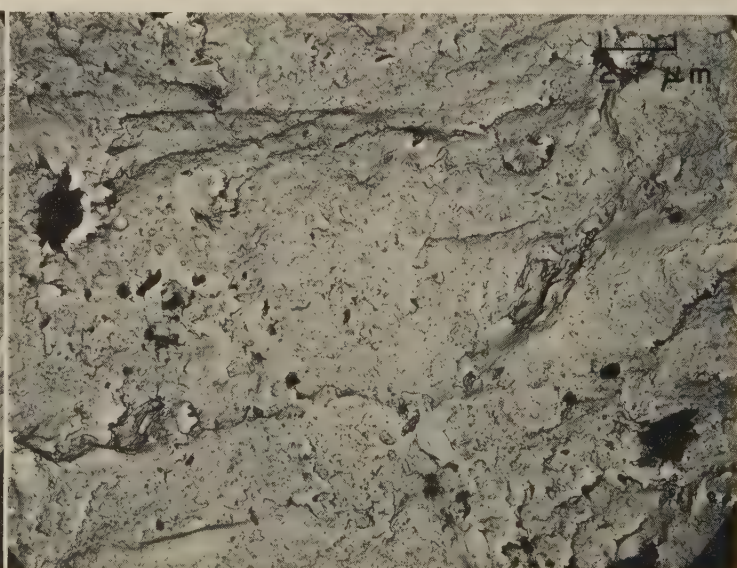
0.8× Photograph

0.8× Light fractograph

10×

4402, 4403, 4404

Photographs 4402 (left) and 4403 (center) show the mating segments of a fractured type 501 stainless steel torque cylinder from the hub socket of an aircraft propeller. Cracking originated at an internal fillet at a shoulder between the smooth bore (4402) and the internal spline (4403). Fractograph 4404 (right) shows clearly the inner fatigue zone and the outer zone of final, tensile-shear fracture. The ratchet marks visible in 4402 (at the bore) are shown more clearly in 4404, a view that reveals many crack nuclei (at arrows). The fatigue cracks that propagated from these nuclei ultimately merged to form a common front. See also fractographs 4405 and 4406 (below), and 4407 and 4408 (opposite page), for TEM views of other regions of this fracture surface.



TEM fractograph (p-c replica)

3750×

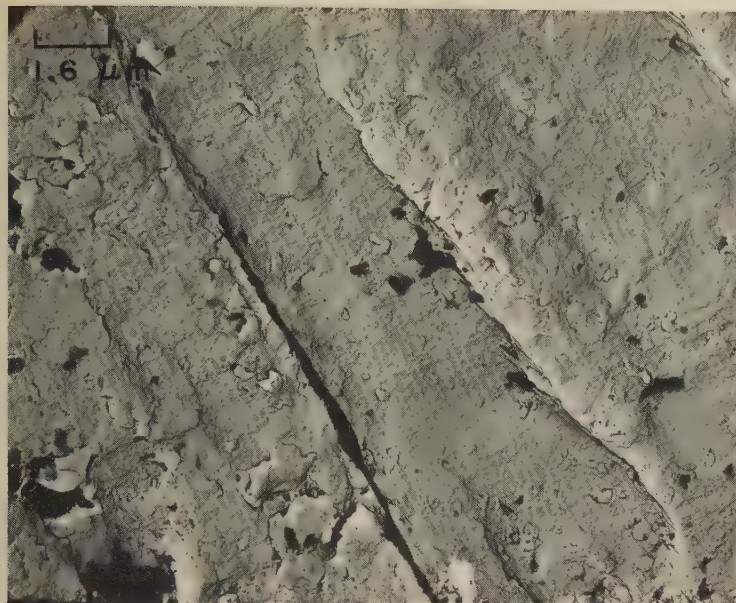
TEM fractograph (p-c replica)

3750×

4405 TEM replica of the fracture surface in 4402, showing a region about 30 μm from a crack nucleus. Visible between the arrows are steps that separate fatigue patches. Fatigue striations are faintly visible within the patches.

4406 TEM replica of the fracture surface in 4403, showing a region about 30 μm from the inner edge. This view shows generally flat fatigue patches that are separated by steps, but no fatigue striations are visible within the patches.

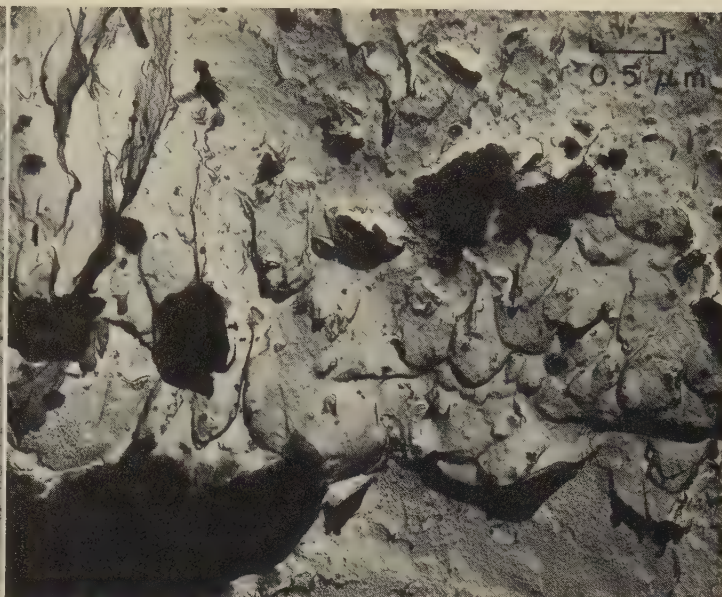
Light and TEM Fractographs: Fatigue Fracture in a Type 501 Stainless Steel Torque Cylinder
(Continued); H11 Tool Steel Specimen Fractured After Hydrogen Embrittlement



TEM fractograph (p-c replica)

6125×

4407 TEM replica of the fracture surface in 4402, showing a region in the fatigue zone but near the zone of final, tensile-shear fracture. This replica reveals fatigue patches separated by steps and containing faint fatigue striations.



TEM fractograph (p-c replica)

18,750×

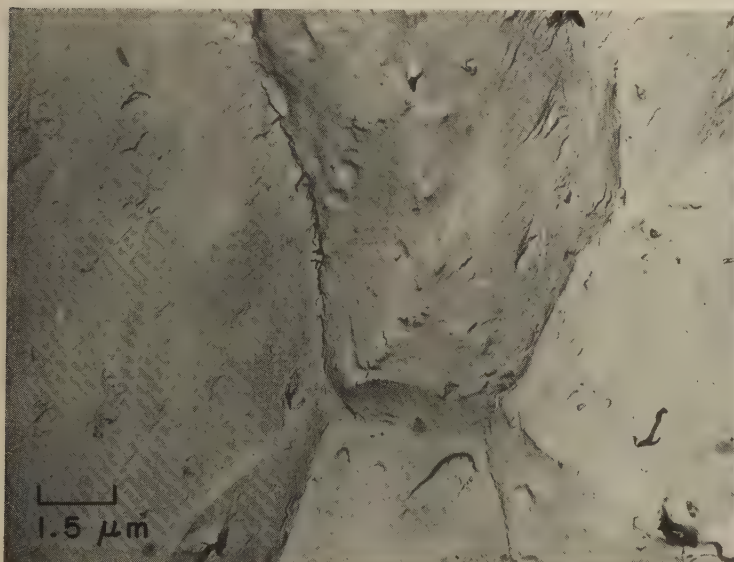
4408 TEM replica of a portion of the shear lip in the fracture surface in 4402, showing shear dimples, which resulted when microvoid coalescence occurred during final, tensile-shear fracture. The dark areas are probably rust or "dirt".



Light fractograph

7.2×

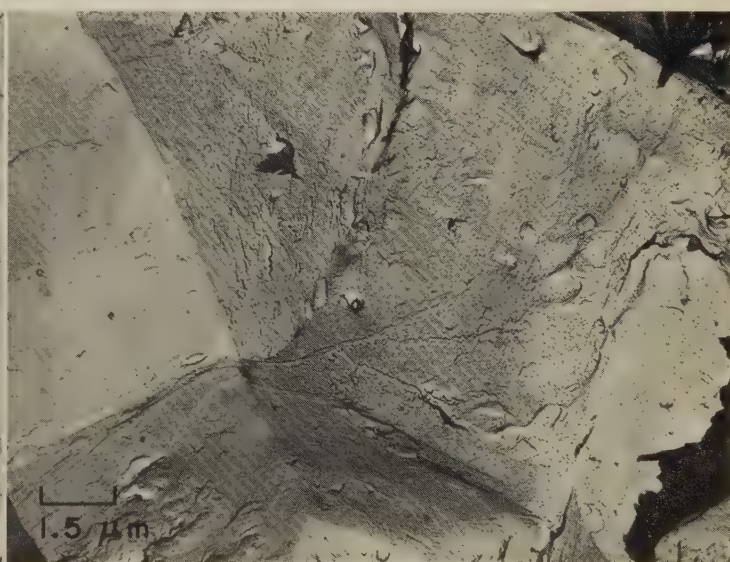
4409 Fracture in a hydrogen-embrittled specimen of H11 tool steel air cooled from 1010 C (1850 F), tempered at 538 C (1000 F), and cathodically charged with hydrogen for 45 min at 1 amp per square inch. The specimen was a hoop with 2-in. ID, 0.050 in. thick and 1 in. long. Fracture occurred during application of static load. See 4410 and 4411 for TEM views of regions at arrow.



TEM fractograph (p-c replica)

6500×

4410 TEM replica of a region at the arrow in 4409, showing the predominantly intergranular fracture surface that is associated with hydrogen embrittlement.

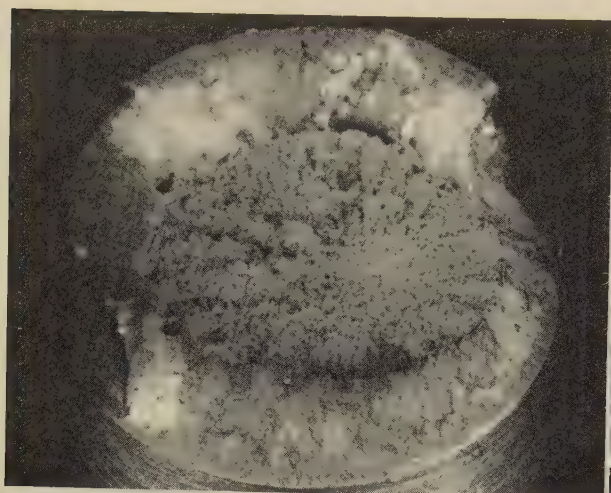


TEM fractograph (direct carbon replica)

6500×

4411 TEM replica of another region at the arrow in 4409, showing an intergranular surface similar to 4410. The grain facets in both 4410 and 4411 are quite free of corrosion products.

Light and TEM Fractographs: Tension-Overload Fractures in Unnotched and Notched Specimens of H11 Tool Steel; Low-Cycle Fatigue Fracture in a Threaded Specimen of H11 Tool Steel



Light fractograph

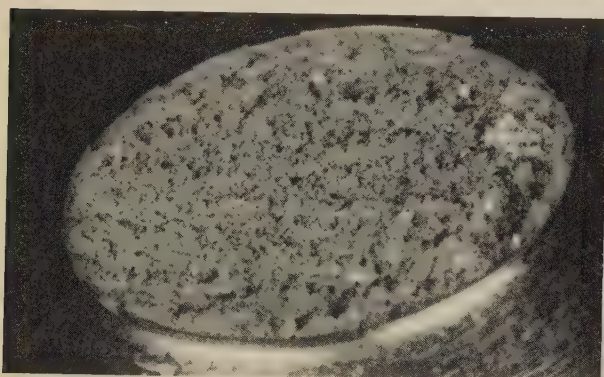


9×

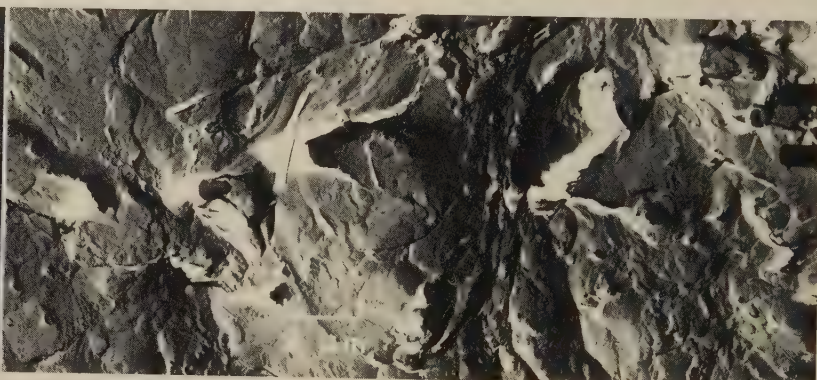
TEM fractograph (p-c replica)

5000×

4412, 4413 Fractograph 4412 (left) shows the surface of a cup-and-cone fracture in an unnotched specimen of H11 tool steel that was heat treated to a tensile strength of 2041 MPa (296 ksi) and broken in tension overload. The fracture originated in the small, central fibrous area contained in the annular radial fibrous zone, and ended at the shear lip. Fractograph 4413 (right) is a TEM replica of an area near the origin of the fracture shown in 4412, exhibiting rather uniformly small, equiaxed dimples surrounding a deep cavity (at right of and above center).



Light fractograph

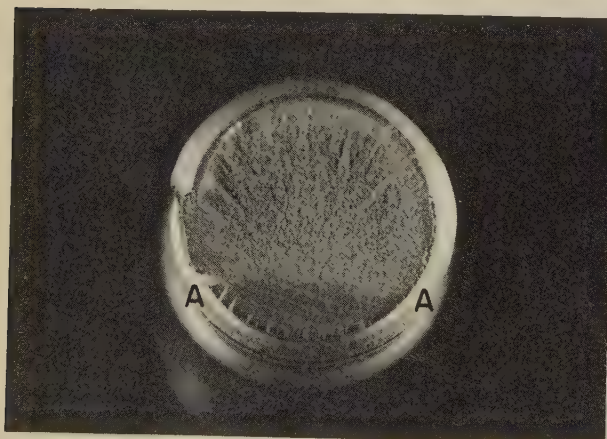


9×

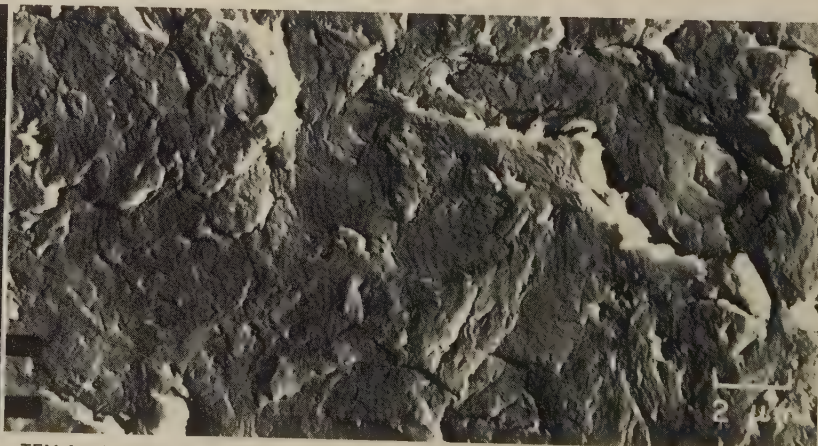
TEM fractograph (p-c replica)

5000×

4414, 4415 Fractograph 4414 (left) shows the surface of a fracture in a notched specimen of H11 tool steel that was broken in tension overload. Unnotched tensile strength was the same as that of the specimen in 4412; notched tensile strength was 2665 MPa (386.5 ksi). Although the illumination here does not permit critical appraisal, the fracture surface appears to be flat and fibrous. Fractograph 4415 (right) is a TEM replica of a region of the fracture surface in 4414, showing many small and medium-size dimples. Also visible are large facets with characteristics that suggest local quasicleavage.



Light fractograph



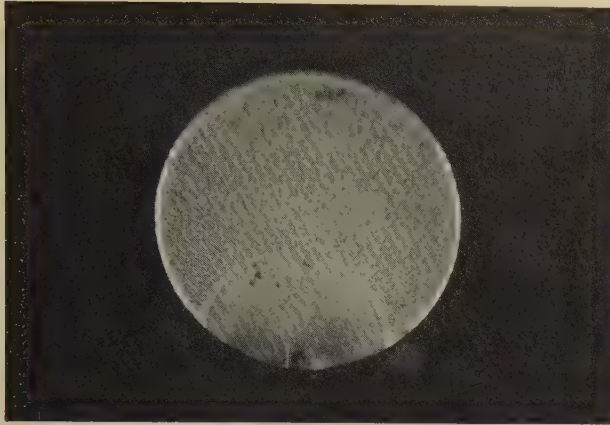
6×

TEM fractograph (p-c replica)

5000×

4416, 4417 Fractograph 4416 (left) shows the surface of a low-cycle fatigue fracture in a threaded specimen of H11 tool steel heat treated to the same tensile strength as the specimen in 4412 and loaded in tension-tension ($R = 0.1$); maximum stress was about 60% of tensile strength. Fracture occurred after 21,000 cycles. At bottom, cracks propagating from several origins merged to form a beach-mark crescent (A-A). Fractograph 4417 (right) is a TEM replica of an area within the beach-mark crescent in 4416. Fine fatigue striations are clearly visible and in general have approximately the same orientation. Several secondary cracks are evident as well.

Light and TEM Fractographs of Fractures in H11 Tool Steel: by High-Cycle Fatigue; After Hydrogen Embrittlement; and by Stress-Corrosion Cracking



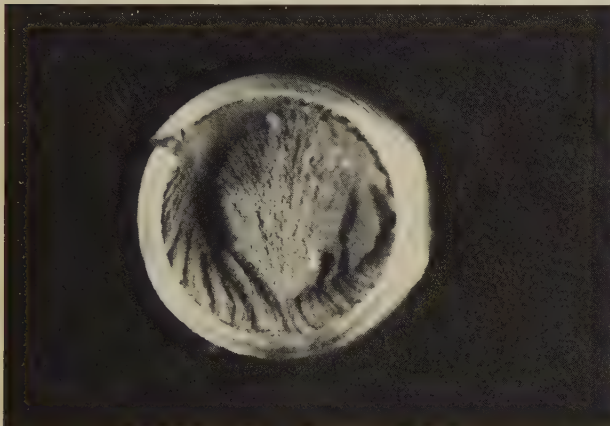
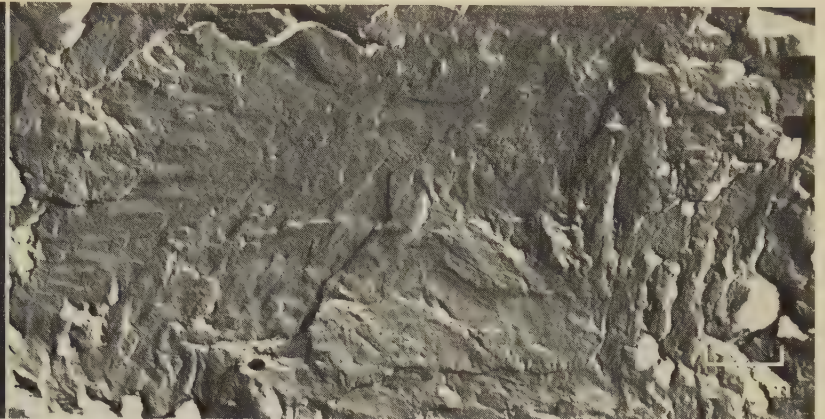
Light fractograph

4418, 4419

Fractograph 4418 (left) shows the surface of a high-cycle fatigue fracture in a specimen of H11 tool steel (same tensile strength as that of the specimen in 4412, on the facing page) that broke after 775,000 cycles. The specimen was loaded in tension-tension ($R = 0.1$), with a maximum stress of about 30% of tensile strength. The beach-mark crescent is clearly evident at bottom. Fractograph 4419 (right) is a TEM replica of a region within the beach-mark crescent in 4418. This extremely smooth fracture surface, which shows little evidence of fatigue striations, suggests some form of cleavage.

6× TEM fractograph (p-c replica)

5000×



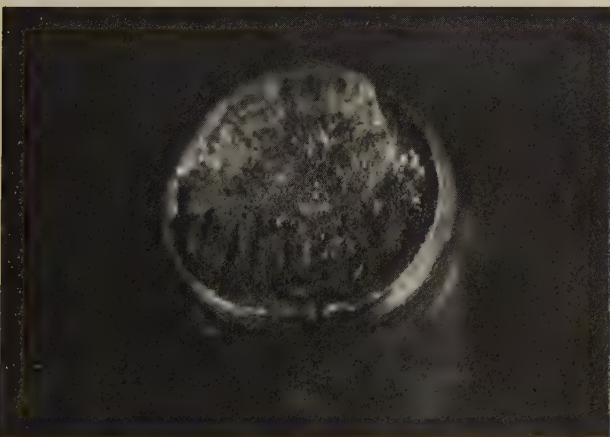
Light fractograph

4420, 4421

Fractograph 4420 (left) shows the surface of a fracture in a threaded specimen of H11 tool steel (same tensile strength as in 4412) hydrogen embrittled as a result of electroplating. This fracture, which occurred during stressing to 75% of tensile strength, originated around nearly the entire circumference of the specimen and yielded a fibrous surface. Fractograph 4421 (right) is a TEM replica of a region of the surface in 4420, showing an array of many very fine dimples on separated-grain facets. At top center is a grain that appears to have been cleaved. There is very little evidence here of secondary intergranular cracking.

6× TEM fractograph (p-c replica)

5000×



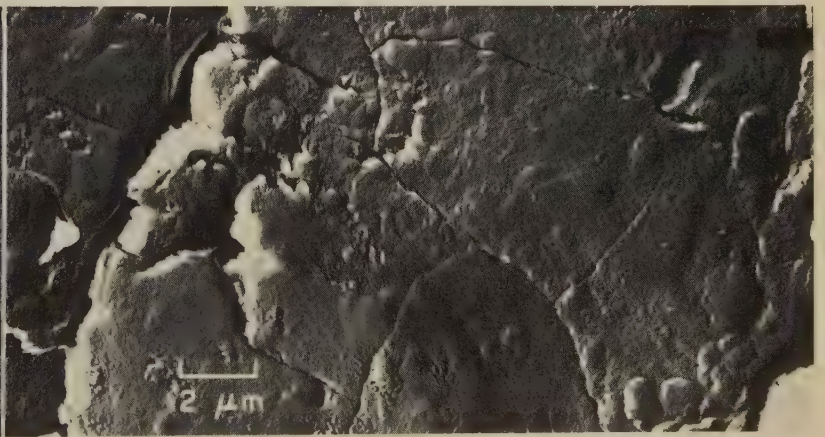
Light fractograph

4422, 4423

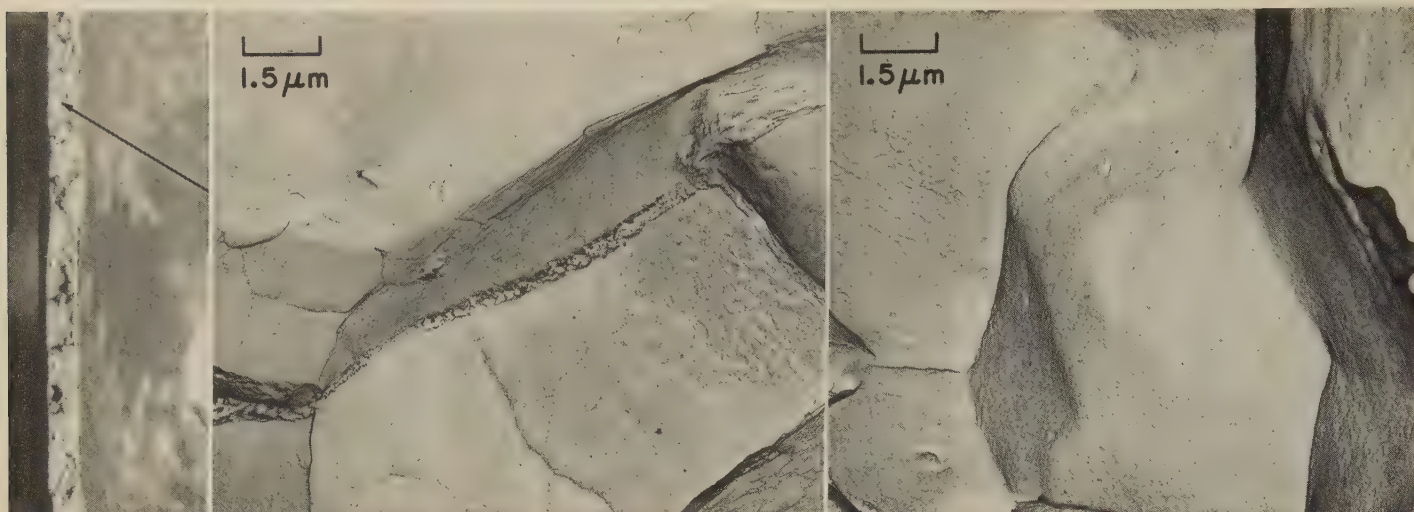
Fractograph 4422 (left) shows the surface of a fracture resulting from stress-corrosion cracking in a threaded bolt of H11 tool steel (same tensile strength as in 4412) stressed to 75% of tensile strength while immersed in a solution of 3.5% NaCl in water. This fracture, which originated around more than 50% of the circumference of the specimen (portion at bottom and at right), yielded a fibrous surface. Fractograph 4423 (right) is a TEM replica of a region in the stress-corrosion portion of the fracture surface in 4422. The features revealed are separated-grain facets containing, in this particular area at least, comparatively little evidence of corrosion products. There are many secondary cracks within the grains and a few large secondary cracks between grains.

6× TEM fractograph (p-c replica)

5000×



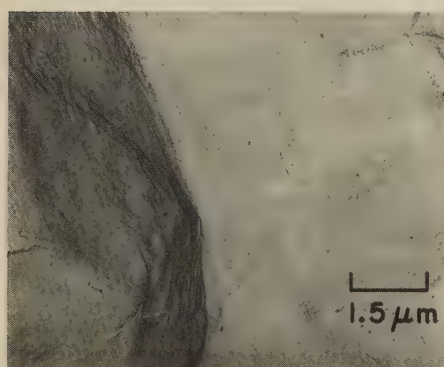
Light and TEM Fractographs: Type 410 Stainless Steel Fractured by Stress-Corrosion Cracking in a Marine Atmosphere; Type 410 Stainless Wire Fractured at a Notch



Light fractograph; two TEM fractographs (p-c replicas)

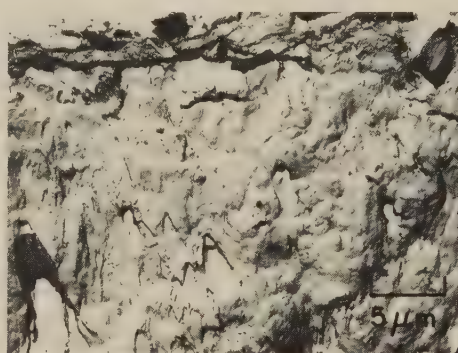
$3\frac{1}{8}\times$ (4424); $6500\times$ (4425, 4426)

4424, 4425, 4426 Fractograph 4424 (left) shows the surface of a fracture that resulted from stress-corrosion cracking in a hoop specimen of type 410 stainless steel air cooled from 982 C (1800 F) and tempered at 371 C (700 F). Tensile strength was 1241 to 1379 MPa (180 to 200 ksi). The specimen was exposed to a marine atmosphere while being stressed at 1055 MPa (153 ksi), and fracture occurred after 10½ months. Fractographs 4425 (center) and 4426 (right) are TEM replicas of two areas at the arrow in the fracture surface in 4424, showing intergranular rupture. In 4425 can be seen a modest amount of corrosion products and some hairline indications that are characteristic of either stress-corrosion cracking or hydrogen embrittlement. In 4426, there are remarkably few features other than separated-grain facets. The lack of considerable corrosion products in 4425 and 4426 after the long marine exposure reflects the slow rate at which this alloy is corrosively attacked. See also 4427.



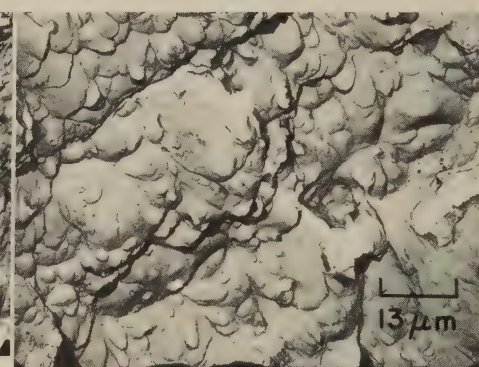
TEM fractograph (p-c replica) $6500\times$

4427 TEM replica of another area at the arrow in the fracture surface shown in 4424. Here, as in 4425 and 4426, very few traces of corrosion products are evident. Note the extreme smoothness of the facets.



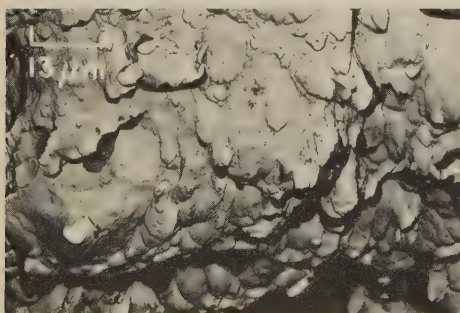
TEM fractograph (direct carbon replica) $2000\times$

4428 Fracture surface of ¼-in.-diam wire, of type 410 stainless steel austenitized ½ hr at 954 C (1750 F), air cooled, and tempered 2 hr at 510 C (950 F), that broke at a notch. Conical dimples at center point toward notch (at top), which shows wavy file marks. See 4429 to 4432.



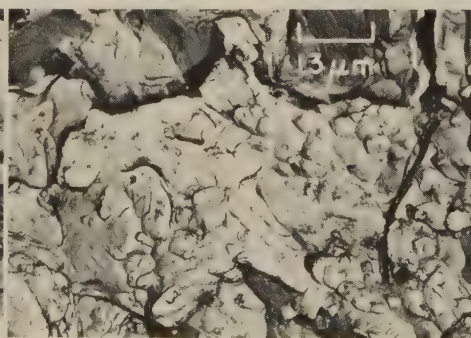
TEM fractograph (direct carbon replica) $750\times$

4429 Another replica of the fracture surface in 4428, but at an area 0.005 to 0.010 in. in from the notch. Here, elongated dimples point to lower right (toward center of notch). The black line indicates a sudden change in surface level.



TEM fractograph (direct carbon replica) $750\times$

4430 TEM replica of the fracture surface in 4428, showing an area the same distance from the notch as the area in 4429 but nearer the surface of the wire. Here, the dimples point downward (toward the notch). The black bands denote sharp changes in surface level.



TEM fractograph (direct carbon replica) $750\times$

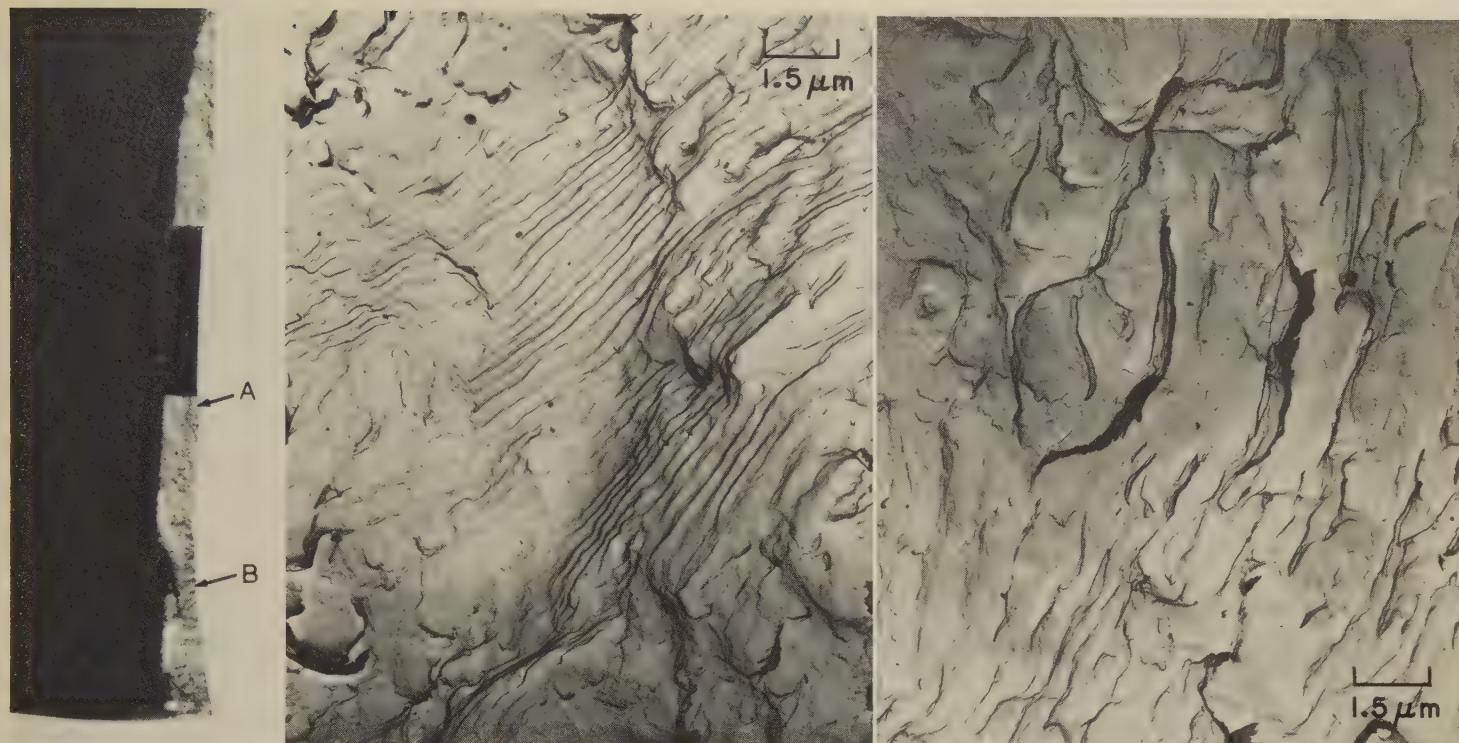
4431 TEM replica of the fracture surface in 4428, showing an area about three times as far from the notch as the areas in 4429 and 4430. Equiaxed dimples are evident at top, bottom and right, but cleavage is present also (at center).



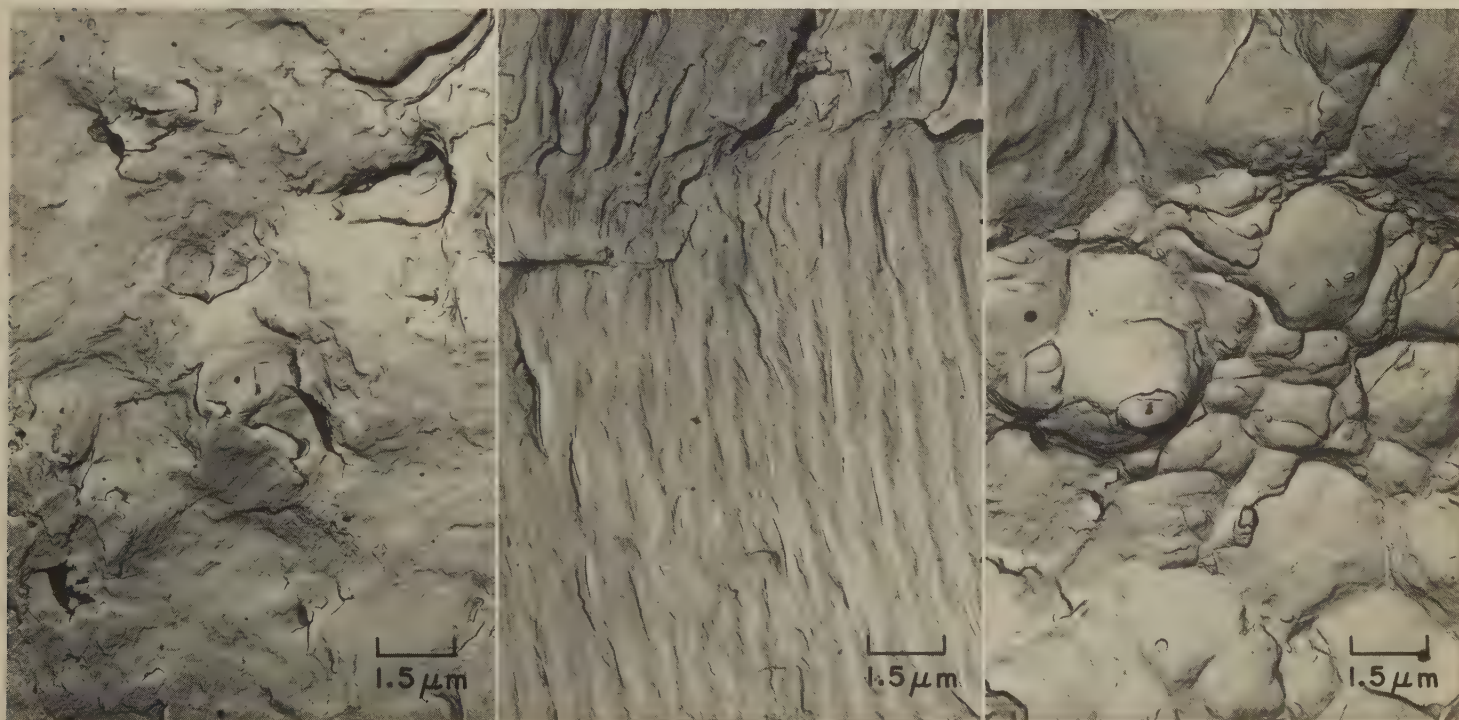
TEM fractograph (direct carbon replica) $750\times$

4432 TEM replica of the fracture surface in 4428, showing an area in the fast-fracture region, about five times as far from the notch as the areas in 4429 and 4430. The features here have resulted largely from cleavage, but small groups of dimples are in evidence also.

Light Fractograph and TEM Fractographs: Type 431 Stainless Steel Notched Specimen Fractured by High-Cycle Fatigue



Light fractograph 4½× TEM fractograph (p-c replica) 6500× TEM fractograph (p-c replica) 6500×
4433, 4434, 4435 Fractograph 4433 (left) shows the surface of a high-cycle fatigue fracture in a 5½-in. by 1-in. by 0.050-in. notched specimen of type 431 stainless steel oil quenched from 1038 C (1900 F) and tempered at 274 C (525 F) to a tensile strength of 1241 to 1379 MPa (180 to 200 ksi). The notch consisted of a center hole 0.01 in. in radius and 0.2 in. long. The specimen was subjected to tensile stress that was cycled from 154.4 to 772 MPa (22.4 to 112 ksi) at 1000 cycles per minute, and fracture occurred after 5700 cycles. Fractographs 4434 (center) and 4435 (right) are TEM replicas of two areas at A in 4433, immediately below the notch. In 4434, fatigue striations are well developed, and suggestions of partly formed dimples are present at a few locations. In 4435, fatigue striations are much less regular than in 4434; again, there are suggestions of partly formed dimples. See also 4436 to 4438, below.



TEM fractograph (p-c replica) 6500× TEM fractograph (p-c replica) 6500× TEM fractograph (p-c replica) 6500×
4436 TEM replica of a third area at A in 4433. This area exhibits faint but quite recognizable fatigue striations with spacings similar to those in 4434.
4437 TEM replica of a fourth area at A in 4433. Regular, widely spaced fatigue striations resulted from increased stress due to reduced cross-sectional area.
4438 TEM replica of an area at B in 4433. The equiaxed dimples visible here resulted from tension overload during final fracture but before final shear rupture.

Light and TEM Fractographs: Type 633 (AM-350) Stainless Steel Fractured by Stress-Corrosion Cracking; 13-8 PH Stainless Steel Unnotched Specimen Fractured by Tension Overload

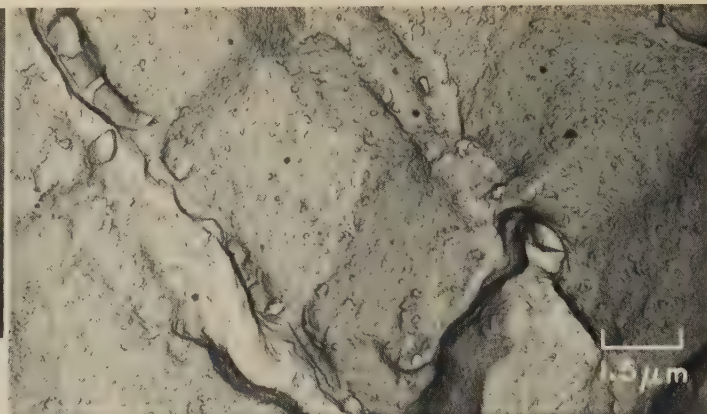


Light fractograph

4439, 4440

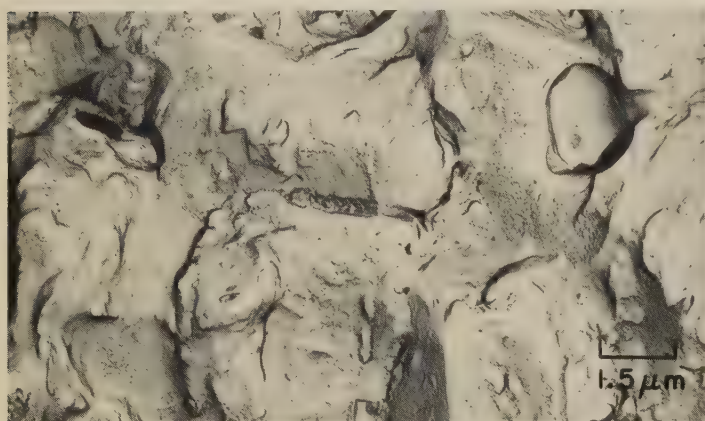
At left (4439) is a stress-corrosion fracture in a sheet specimen (1½-in. by 0.25-in. by 0.025-in. gage section) of type 633 (AM-350) precipitation-hardenable stainless steel solution treated at 932 C (1710 F) and aged at -73 C (-100 F) to a tensile strength of 1448 MPa (210 ksi). Fracture occurred after exposure to marine air under stress of 593.7 MPa (86.1 ksi) for 16 days, originating at one edge of the specimen. Fractograph 4440 (at right) is a TEM view of an area at arrow in 4439. This area is the region of flat, fine-textured fracture produced by stress-corrosion cracking before fracture terminated by shear at the other edge. The fracture surface here is intergranular and contains a moderate amount of corrosion products. See 4441 and 4442.

6×



TEM fractograph (p-c replica)

6500×

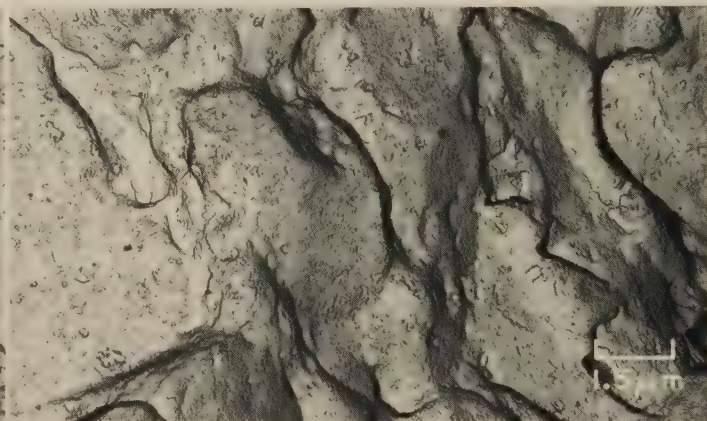


TEM fractograph (p-c replica)

6500×

4441

A TEM view of a second area at the arrow in fractograph 4439. This area, like that in 4440, displays an intergranular surface containing only moderate amounts of corrosion products. A dimple is evident at top right, and features elsewhere suggest very small, embryonic dimples. See also 4442.



TEM fractograph (p-c replica)

6500×

4442

A TEM view of a third area at the arrow in fractograph 4439. Like the areas shown in 4440 and 4441, the one here exhibits an intergranular fracture surface. In this area, however, there appear to be several secondary cracks following grain boundaries between the fracture facets.



Light fractograph

4443

Cup-and-cone fracture in an unnotched specimen of 13-8 PH stainless steel (tensile strength, 1634 MPa, or 237 ksi) broken in tension overload. Central area, where fracture began, appears to be uniformly and finely fibrous. See also 4444, at right.

9×



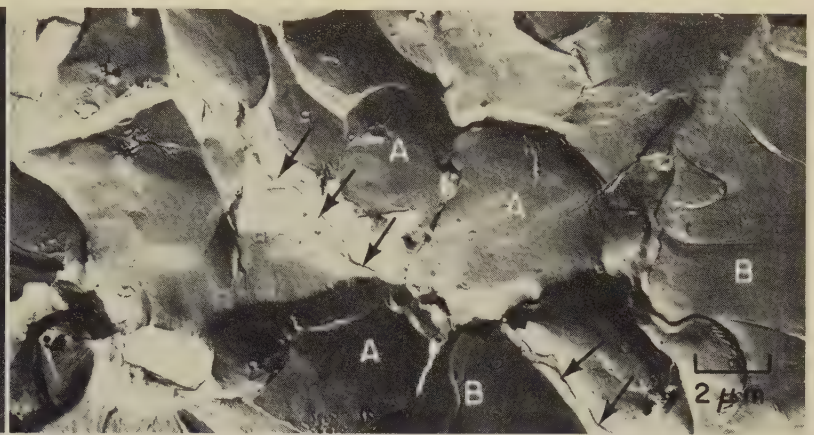
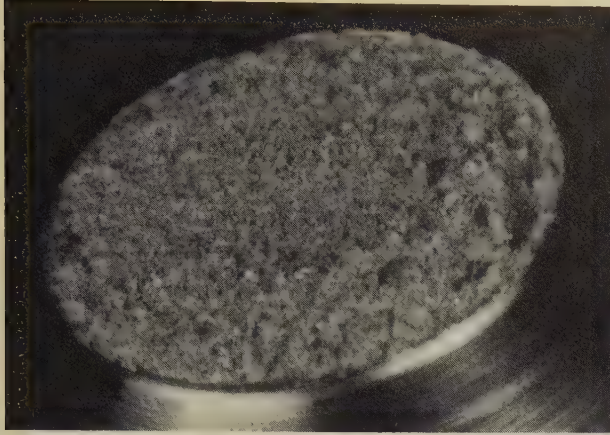
TEM fractograph (p-c replica)

5000×

4444

A TEM view of the central area in the surface of the cup-and-cone fracture in fractograph 4443 (at left), showing dimples that are approximately equiaxed. There appear to be indications of inclusions at the tips of most of the dimples. A few of the dimples are slightly elongated, which suggests proximity to the shear lip.

Light and TEM Fractographs: 13-8 PH Stainless Steel Notched Specimen Fractured by Tension Overload; 13-8 PH Bolts Fractured by Low-Cycle and by High-Cycle Fatigue



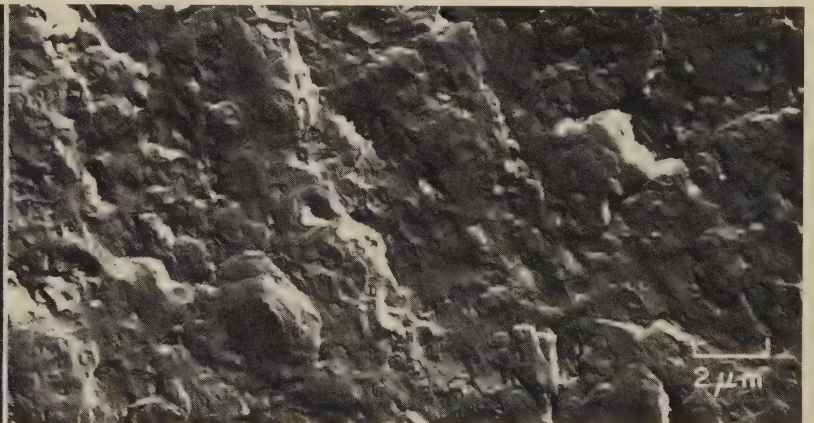
Light fractograph

9× TEM fractograph (p-c replica)

5000×

4445, 4446

Fractograph 4445 (left) shows a fracture in a notched specimen of 13-8 PH stainless steel (same unnotched tensile strength as in 4443), broken in tension overload. Notched tensile strength was 2423.5 MPa (351.5 ksi). The fracture surface is fibrous. Specific sites of fracture origin in the notch root are not visible. Fractograph 4446 (right) is a TEM view of the fracture surface in 4445, showing large dimples (as at A's). The surfaces of the dimples are remarkably smooth, in some instances suggesting stretched areas (B's). A few minor secondary cracks are evident (at arrows). The only inclusions visible here are tiny.



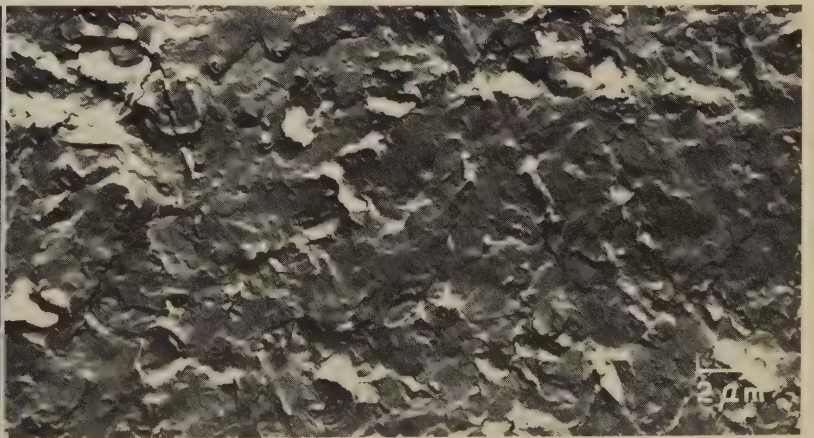
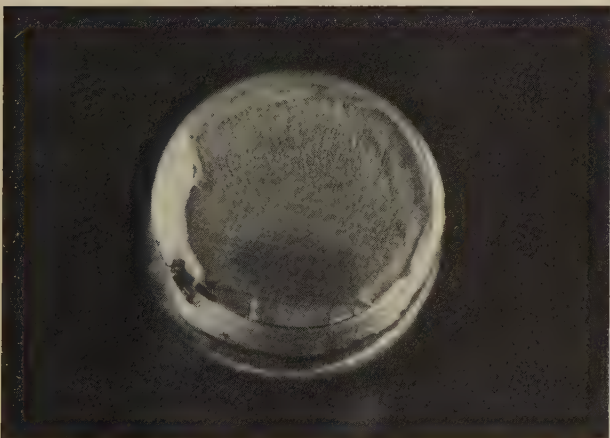
Light fractograph

6× TEM fractograph (p-c replica)

5000×

4447, 4448

At left (fractograph 4447) is a low-cycle fatigue fracture in a threaded bolt of 13-8 PH stainless steel (same tensile strength as 4443) that was loaded in tension-tension ($R = 0.1$) under a maximum stress of 60% of the tensile strength. Fracture occurred at 16,000 cycles. Several crack nuclei are visible along the thread root. Fractograph 4448 (right) is a TEM view within the fatigue crescent at the bottom of the fracture surface in 4447. This view displays very little evidence of identifiable fatigue striations; no dimples are apparent. Instead, the surface bears some resemblance to one resulting from cleavage.



Light fractograph

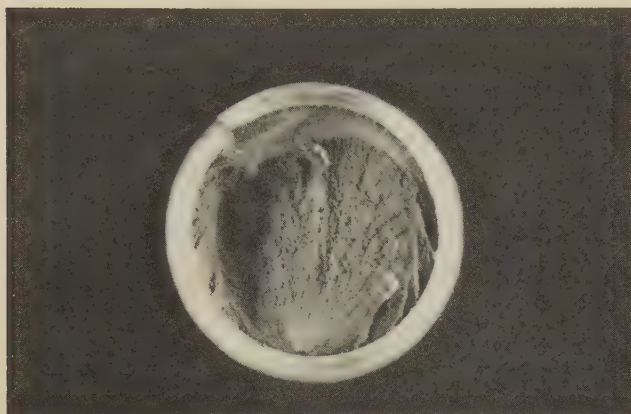
6× TEM fractograph (p-c replica)

5000×

4449, 4450

Fractograph 4449 (left) shows a high-cycle fatigue fracture in a threaded bolt of 13-8 PH stainless steel (same tensile strength as 4443) that was loaded in tension-tension ($R = 0.1$) under a maximum stress of 30% of tensile strength. Fracture occurred at 959,000 cycles. Several crack nuclei are visible in the thread root. Fractograph 4450 (right) is a TEM view of a region well within the fatigue crescent in 4449. This view shows no fatigue striations except for those in one or two tiny wrinkled areas near the top. The surface has angular characteristics suggesting a crystallographic influence on fracture path.

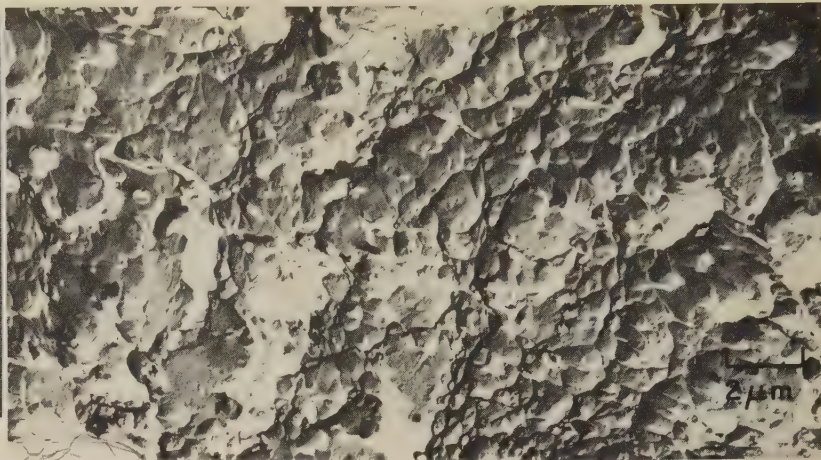
Light and TEM Fractographs: 13-8 PH Stainless Steel Fractured After Hydrogen Embrittlement and by Stress-Corrosion Cracking; 17-4 PH Stainless Steel Fractured by Tension Overload



Light fractograph

6×

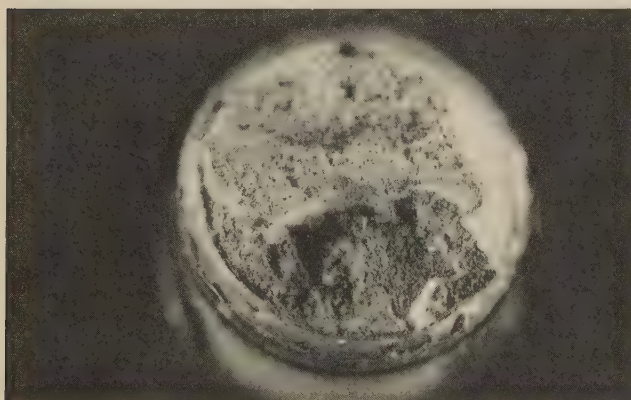
4451 Surface of a fracture in a hydrogen-embrittled, threaded tensile specimen of 13-8 PH stainless steel (tensile strength, 1634 MPa or 237 ksi) that was electrolytically charged with hydrogen and broken without having been baked. Fracture occurred around the thread roots before the specimen was fully stressed to 75% of tensile strength. A radial fibrous surface. See 4452.



TEM fractograph (p-c replica)

5000×

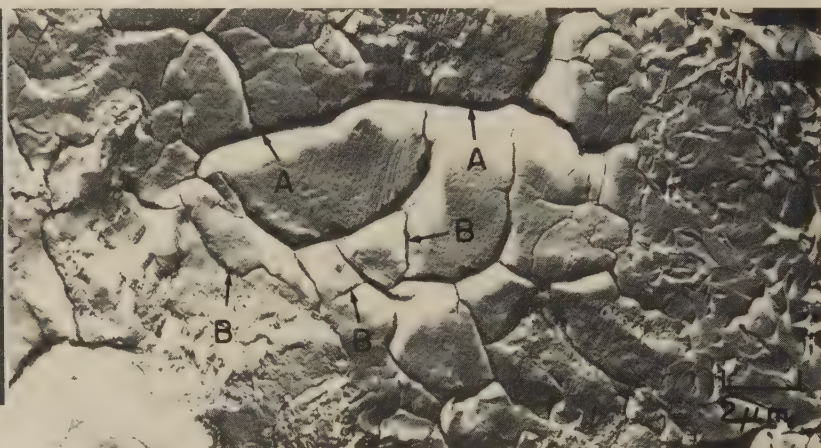
4452 TEM replica of an area in the radial fibrous region of the fracture surface in 4451 (left), showing what apparently are separated-grain surfaces mostly covered with small dimples. In addition, there are larger dimples that may have resulted from microvoid coalescence during local transgranular fracture. A few small facets suggest cleavage.



Light fractograph

6×

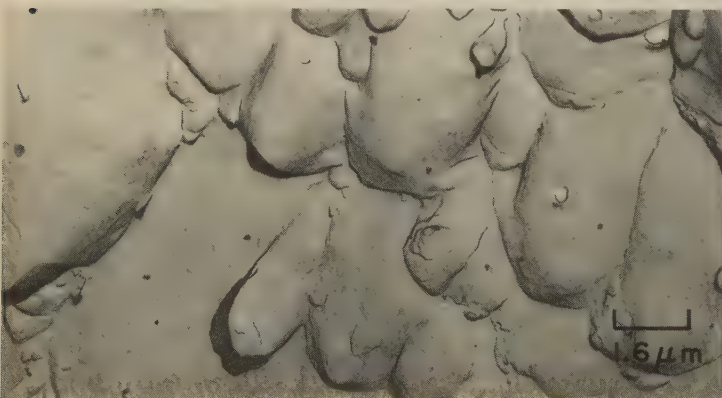
4453 Surface of a fracture that resulted from stress-corrosion cracking in a bolt of 13-8 PH stainless steel (same tensile strength as in 4451) that was stressed to 75% of tensile strength while immersed in a 3.5% solution of NaCl in water. The region of stress-corrosion cracking is at bottom. A coating of corrosion products is evident. See fractograph 4454 (right).



TEM fractograph (p-c replica)

5000×

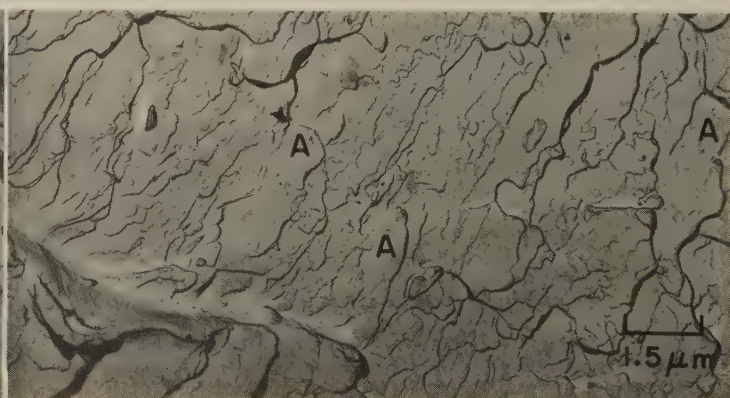
4454 TEM replica of an area in the region of stress-corrosion cracking in the fracture surface in 4453 (left), showing a complicated network of intergranular (arrows A) and transgranular (arrows B) secondary cracks. Some facets are relatively clean; others (at right) show a layer of a corrosion product (probably a hydroxide), which is cracked also.



TEM fractograph (p-c replica)

6450×

4455 Surface of a tension-overload fracture in an unnotched specimen of 17-4 PH stainless steel bar aged at 482 C (900 F) to a tensile strength of 1241 to 1379 MPa (180 to 200 ksi). This TEM replica shows the center of a cup-and-cone fracture surface exhibiting the expected elongated dimples. See 4456.

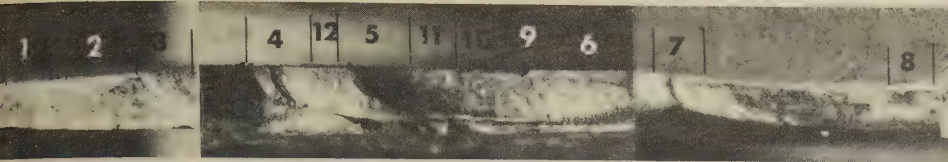


TEM fractograph (p-c replica)

6500×

4456 Surface of a tension-overload fracture in a notched specimen of 17-4 PH stainless steel bar aged same as that in 4455. There appear to be very sharp cleavage steps in this region. Features in scattered areas (as at A's) resemble very flat dimples, but such dimples are rarely found on cleavage surfaces.

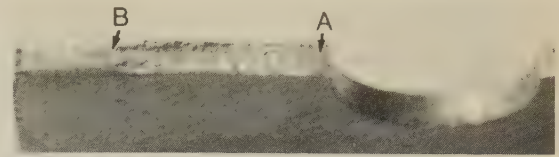
Light and TEM Fractographs: Fatigue Fracture in Cast 17-4 PH Stainless Steel; Tension-Overload Fracture in Type 302 Stainless Steel; Fatigue Fracture in Type 301 Stainless Steel



Light fractograph

13/4×

4457 Composite view of the surface of a low-cycle fatigue fracture in a web of an investment cast compressor rotor of 17-4 PH stainless steel heat treated to a tensile strength of 1096 MPa (159 ksi) and a yield strength of 1069 MPa (155 ksi). Tensile elongation ranged from 6.0 to 11.0%. Hardness was Rockwell C 35.8. The numbers in this view identify areas that were examined by electron microscopy. Fracture, which originated at several nuclei, occurred during shutdown after full-power test run. See 4458, 4459.



Light fractograph

6×

4462 High-cycle fatigue fracture in a notched specimen of type 301 stainless steel sheet subjected at -196°C (-321°F) to tensile stress cycled from 293 to 586 MPa (42.5 to 85 ksi) at 1000 cycles per minute. Fracture occurred after 58,350 cycles. Flat fracture at center hole, which formed the notch, and shear at ends. See fractographs 4463 and 4464, below, for views of areas at A and B.



TEM fractograph (p-c replica)

3000×

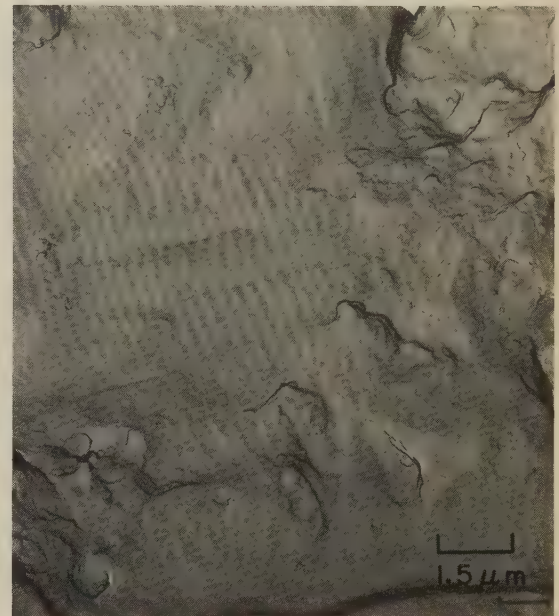
4458 TEM view of the fracture surface in 4457, showing features typical of those in areas 3 to 8. Arrows at left point out fatigue striations, and cleavage marks are visible at right.



TEM fractograph (p-c replica)

2400×

4459 TEM view of the fracture surface in 4457, showing dimples, typical of those in areas 1 and 2, formed by shear overload during final fracture. Fracture occurred at the vibration node in the web.



TEM fractograph (p-c replica)

6500×

4463 TEM replica of an area at A in 4462, showing a smooth surface with regular fatigue striations and with scattered features that resemble partly developed dimples.



Light fractograph

4×

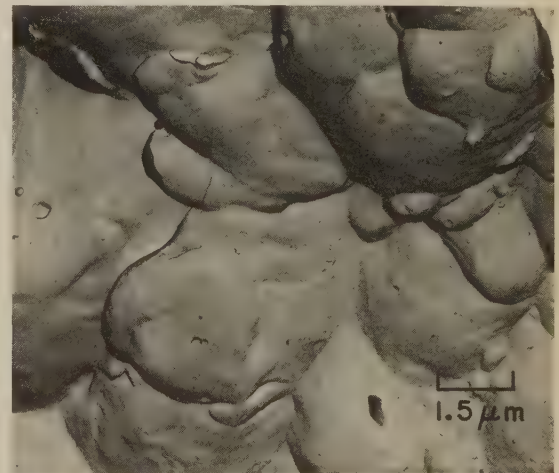
4460, 4461

Fractograph 4460 (left) shows the surface of a tension-overload fracture in an unnotched specimen of type 302 stainless steel tested at room temperature. Tensile strength was 627 MPa (91 ksi). The fracture occurred entirely by shear, with appreciable necking. Fractograph 4461 (right) is a TEM replica of an area at the arrow in 4460, showing the elongated dimples expected in a shear-fracture surface. The dimples are large and well formed.



TEM fractograph (p-c replica)

6500×

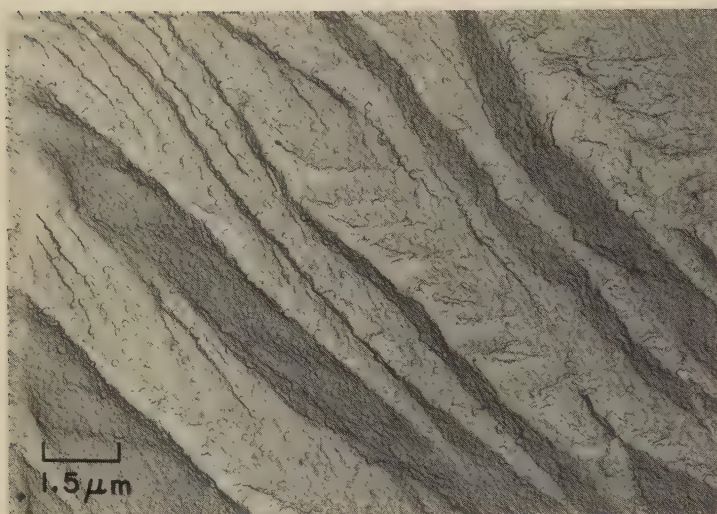


TEM fractograph (p-c replica)

6500×

4464 TEM replica of an area at B in 4462, which is within the region of final, fast fracture. Here, dimples can be seen that are somewhat elongated, which conforms to the shear mechanism of fracture observed in this region.

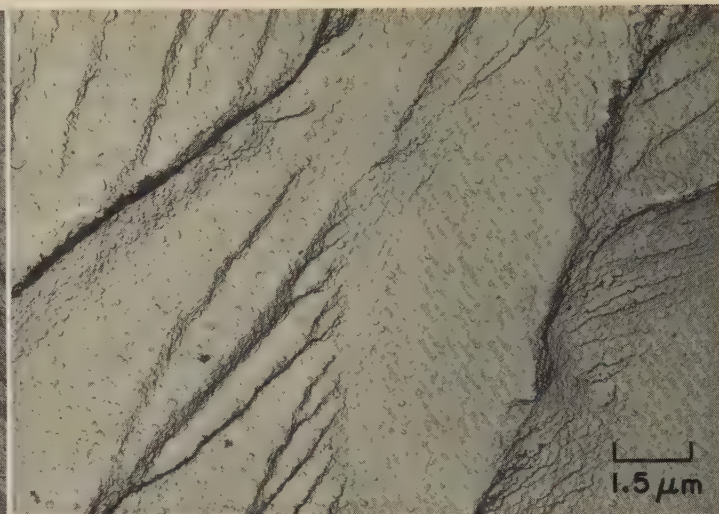
TEM and Light Fractographs: Notched Specimen of Type 302 Stainless Steel Sheet Fractured by High-Cycle Fatigue at 427 C (800 F)



TEM fractograph (p-c replica)

6500×

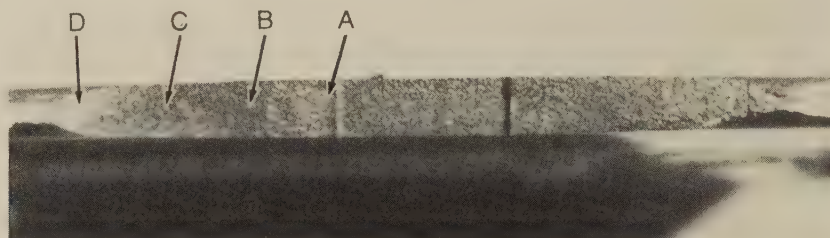
4465 TEM replica of an area near A, close to the notch, in the fracture in 4467 (below), showing definite cleavage steps and essentially no evidence of fatigue striations. A thin oxide film is present. See also fractograph 4466 (right).



TEM fractograph (p-c replica)

6500×

4466 TEM replica of another area near A in 4467, also showing evidence of cleavage steps. The fine marks at right, which are essentially parallel to the cleavage direction, probably are not fatigue striations. See also 4468 to 4475.



Light fractograph

5×

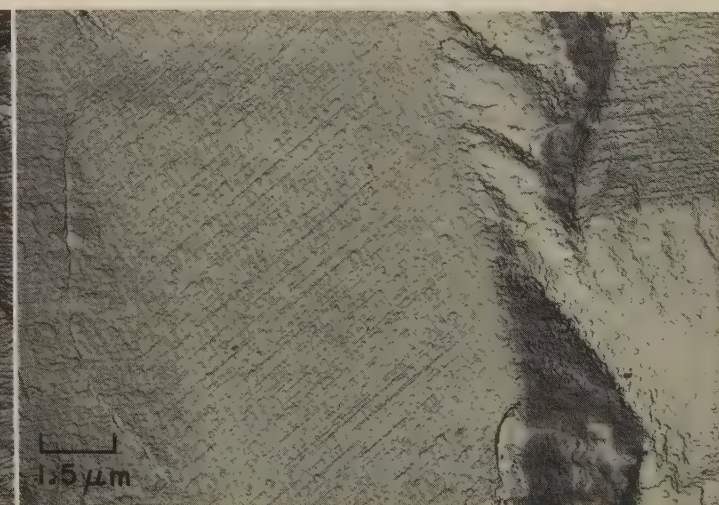
4467 Surface of a high-cycle fatigue fracture in a notched specimen of type 302 stainless steel sheet subjected at 427 C (800 F) to tensile stress cycled from 24.8 to 124 MPa (3.6 to 18 ksi) at 1000 cycles per minute. Fracture occurred after 1,625,450 cycles. The notch in the specimen was a center hole 0.01 in. in radius and 0.20 in. wide. Fatigue area became purple; fast-fracture area became straw colored, with shear and necking. See 4465 and 4466 (above), and 4468 to 4475 (below and on next page), for views at A, B, C and D.



TEM fractograph (p-c replica)

6500×

4468 TEM replica of a third area near A in the fracture surface shown in 4467. Here, fatigue striations are present in rather narrow and somewhat irregular patches. Some evidence of surface oxidation can be seen.

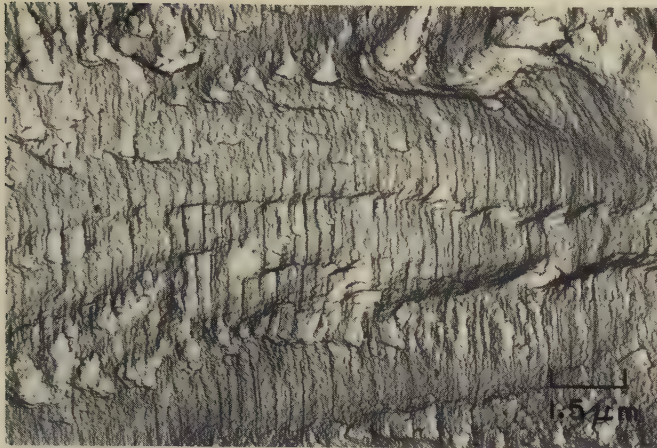


TEM fractograph (p-c replica)

6500×

4469 TEM replica of a fourth area near A in the fracture surface in 4467, showing flat facets quite suggestive of intergranular cleavage. The parallel marks may not be fatigue striations but rather features associated with the oxide film.

TEM Fractographs: Notched Specimen of Type 302 Stainless Steel Sheet
Fractured by High-Cycle Fatigue at 427 C (800 F), Continued



TEM fractograph (p-c replica)

6500×

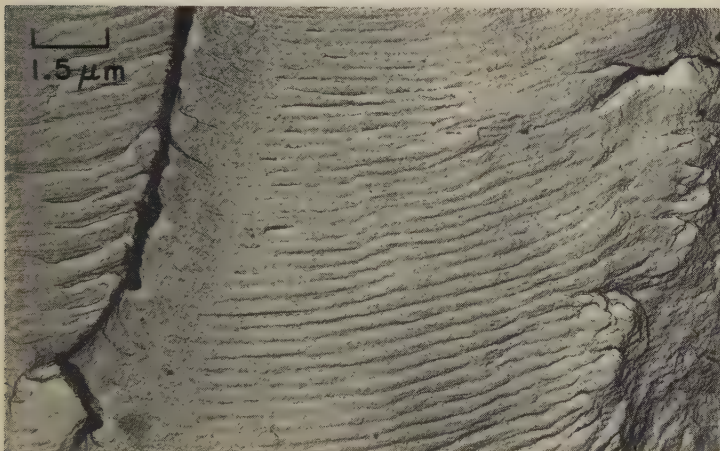
4470 TEM replica of a fifth area near A in the fracture surface in 4467 (facing page). This area is characterized by narrow patches of extremely sharp and distinct fatigue striations. Again, the oxide film is apparent.



TEM fractograph (p-c replica)

6500×

4471 TEM replica of a sixth area near A in the fracture surface in 4467, showing distinct fatigue striations. The markings to the right of the dark region are believed to be cleavage steps, not fatigue striations.



TEM fractograph (p-c replica)

6500×

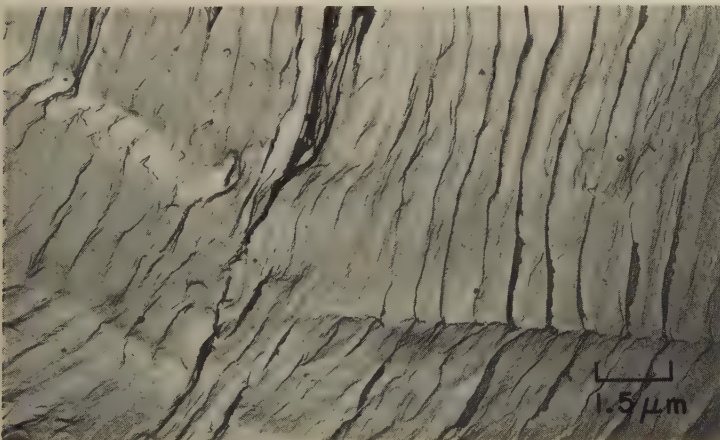
4472 TEM replica of an area at B, approximately 0.09 in. from the notch, in the fracture surface shown in fractograph 4467. The heavy, black mark at left is the result of a sharp difference in level at the junction of two crack fronts. The fatigue striations here are regular and well developed.



TEM fractograph (p-c replica)

6500×

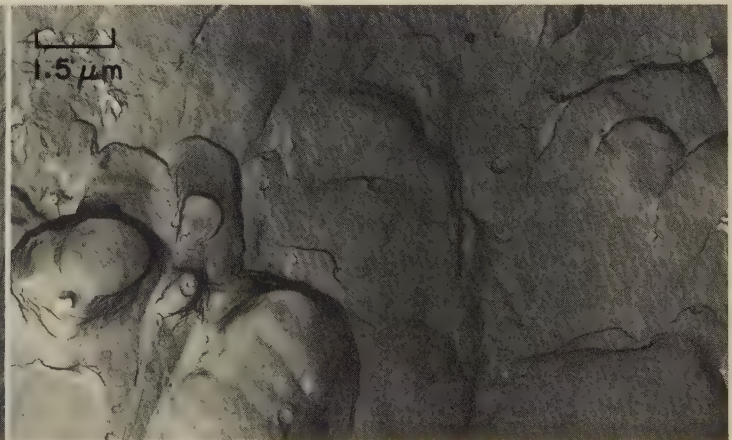
4473 TEM replica of an area at C, about 0.175 in. from the notch, in 4467. Note that the fatigue striations here are more widely spaced than those in 4472, which indicates that the effective stress increased as the crack penetrated into the specimen. Partly formed dimples are visible above and right of center.



TEM fractograph (p-c replica)

6500×

4474 TEM replica of another area near C in 4467, showing a further increase in fatigue-striation spacing. A junction of two crack fronts is visible at lower right. Secondary cracks appear to have formed at some striations.

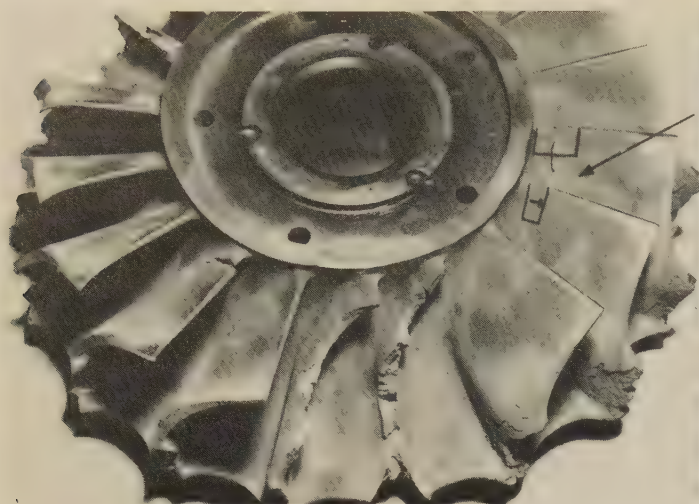


TEM fractograph (p-c replica)

6500×

4475 TEM replica of an area at D, in the region of final, fast fracture and about 0.46 in. from the notch, in 4467. The elongated dimples confirm that final fracture was by shear. Fatigue striations ceased to form when this final stage of fracture began.

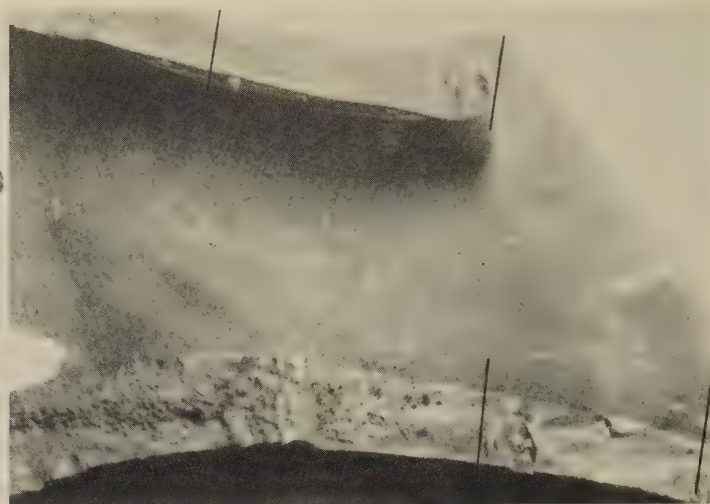
Photograph; Macrograph; Light and TEM Fractographs: Cast Alloy 713LC Rotor Fractured by Corrosion Fatigue; Cast Alloy 713C Unnotched Specimen Fractured by Tension Overload



Photograph

4476 A gas-producer turbine rotor cast of alloy 713LC that fractured after 440 hr of service, as the result of hot corrosion fatigue. Fracture was abrupt, with three blades being thrown off. See 4478 (below) for a view of the area near the arrow. See also fractographs 4477 and 4479.

0.5×



Light fractograph

4477 Fracture surfaces of the two broken turbine-rotor blades at the bottom in photograph 4476. Fatigue beach marks are faintly visible at right on the fracture surface of the lower blade. The region between the parallel black lines on each blade was examined by electron microscopy.

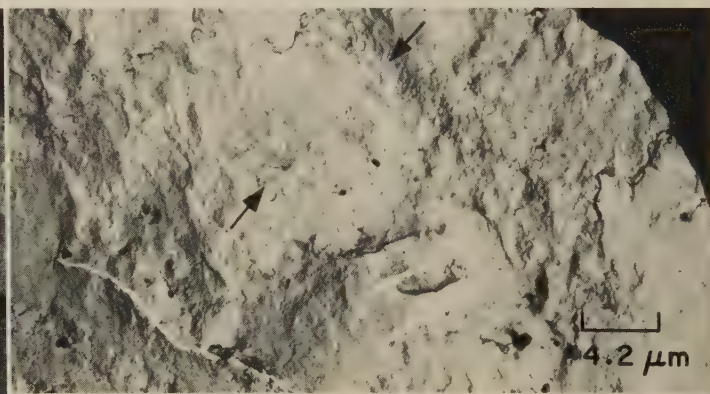
6×



Macrograph (etchant: 95 parts conc HCl, 5 parts 35% H₂O₂)

4478 A macroetched view of a cracked turbine-rotor blade near the arrow in photograph 4476 (above), displaying large columnar grains and a crack that initiated at the trailing edge (at left in this view) of the blade. This crack appears to have followed an intergranular path.

5.5×



TEM fractograph (p-c replica)

4479 A TEM view of a fracture surface of one of the turbine-rotor blades in fractograph 4477 (above). This view is typical of all the areas examined. A patch of fatigue striations is faintly visible at center between arrows. The fatigue crack is believed to have been initiated by hot corrosion, which was shown, by sectioning of blades, to exist at concentrations of lead.

2400×

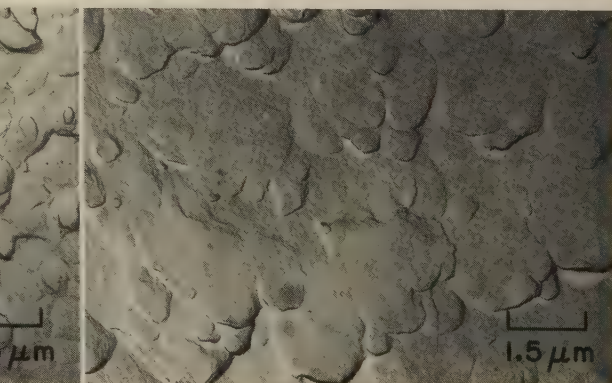


Light fractograph

4480, 4481, 4482



4× TEM fractograph (p-c replica)

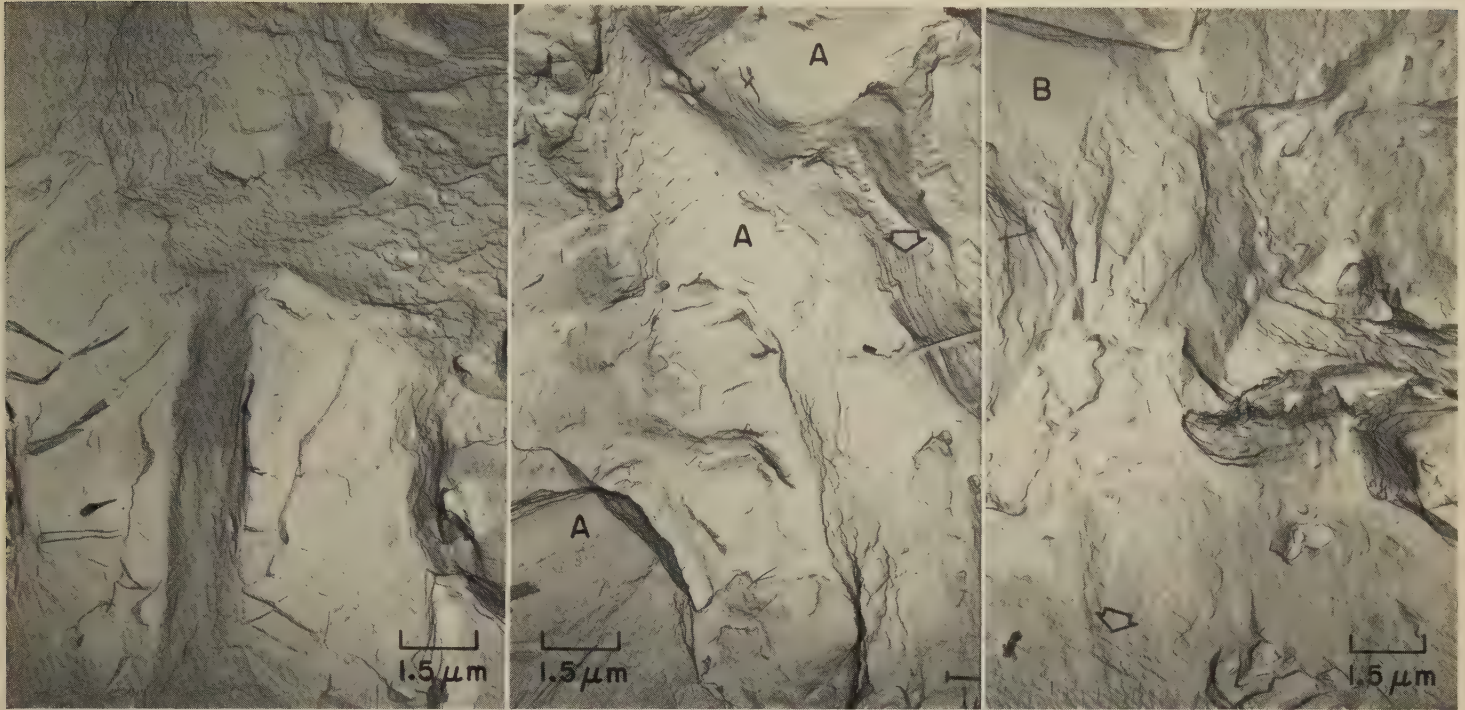


6500× TEM fractograph (p-c replica)

6500×

Fractograph 4480 (left) shows a room-temperature tension-overload fracture in an unnotched specimen of cast alloy 713C annealed at 1149 C (2100 F); tensile strength was 827 MPa (120 ksi). Fractograph 4481 (center) is a TEM view of an area near the arrow in the extremely jagged fracture surface in 4480, showing equiaxed dimples; these were produced by microvoid coalescence during the tension overload. Fractograph 4482 (right) is a TEM view of a second area near the arrow in 4480. This area displays rather flat shear dimples, which are appreciably larger than the equiaxed dimples in 4481.

TEM and Light Fractographs: Cast Alloy 713C Unnotched Specimen Fractured by Tension Overload (Continued); Cast Alloy 713C Fractured by Stress Rupture at 816 C (1500 F)



TEM fractograph (p-c replica)
4483, 4484, 4485

6500×

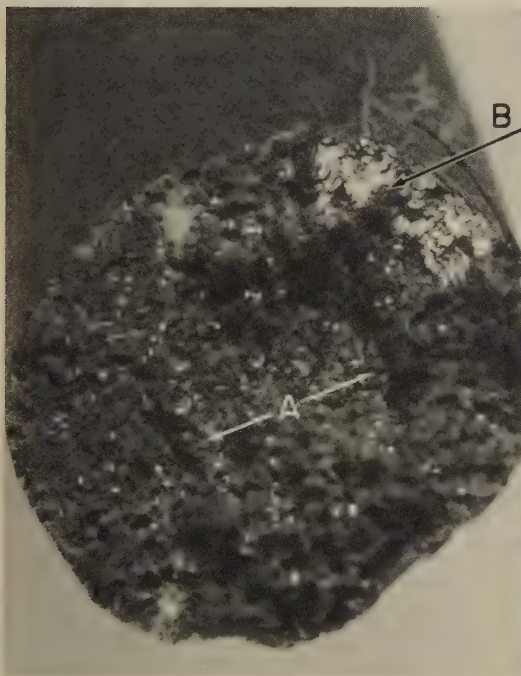
TEM fractograph (p-c replica)

6500×

TEM fractograph (p-c replica)

6500×

TEM views of three more areas near the arrow in fractograph 4480 (facing page). Fractograph 4483 (left) is of an area with features that suggest local rupture by a combination of intergranular separation and microvoid coalescence. There are a number of hairline indications on the separated-grain facets. Fractograph 4484 (center) is of an area in which several very smooth regions (as at A's) show localized stretching. The arrow, at right, indicates a group of slip planes. Fractograph 4485 (right) shows an area that contains a number of examples of slip, one of which is marked by the arrow, at lower left. Stretching is evident in the upper left corner of this view (at B).



Light fractograph

11×

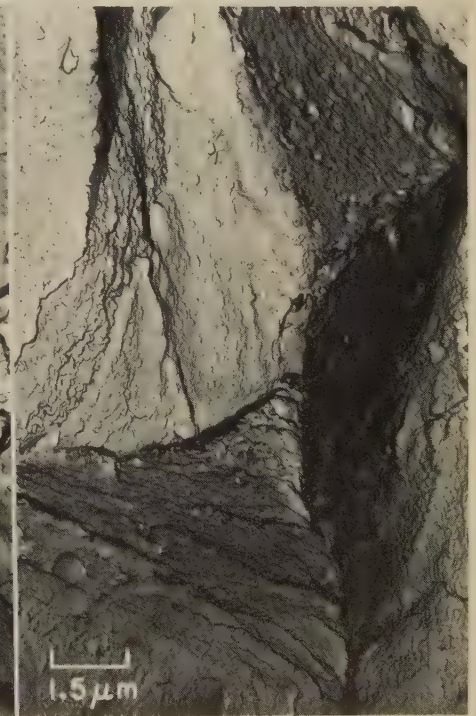
4486 Surface of a stress-rupture fracture in a cast specimen of alloy 713C annealed at 1149 C (2100 F) to a tensile strength of 827 MPa (120 ksi). The test was at 816 C (1500 F) in air, with stress of 276 MPa (40 ksi); fracture occurred at 645 hr. The fracture was jagged and showed secondary cracks (arrows at A). See 4487 and 4488 for views of areas at arrow B.



TEM fractograph (p-c replica)

6500×

4487 A TEM view of an area in the shiny region at arrow B in 4486. Surface here suggests intergranular separation and carries a layer of oxidation products. There are a few suggestions of dimples on separated-grain facets.

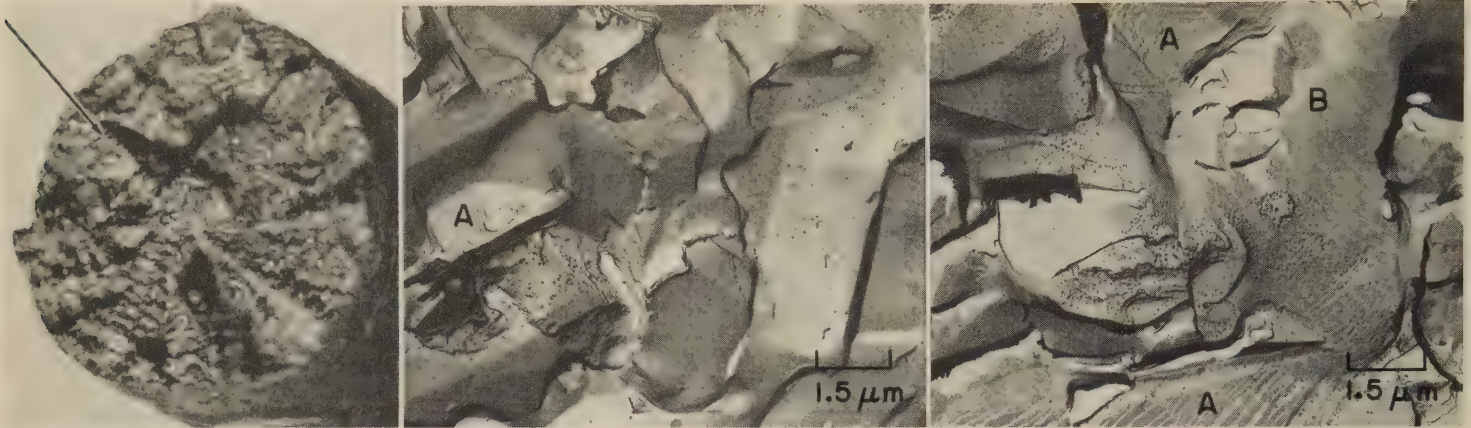


TEM fractograph (p-c replica)

6500×

4488 A TEM view of another area at arrow B in 4486. The intergranular nature of the fracture is more pronounced here. As in 4487, the surface is coated with a layer of oxide, which contributes some of the marks visible.

Light and TEM Fractographs: Cast Specimen of Alloy IN-100 Fractured by Stress Rupture at 982 C (1800 F); Unnotched Specimen of Alloy 718 Fractured by Tension Overload



Light fractograph

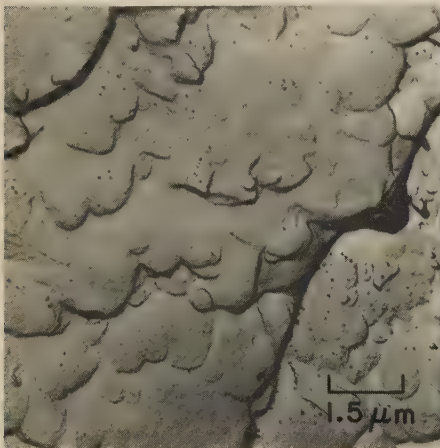
8× TEM fractograph (p-c replica)

6500× TEM fractograph (p-c replica)

6500×

4489, 4490, 4491

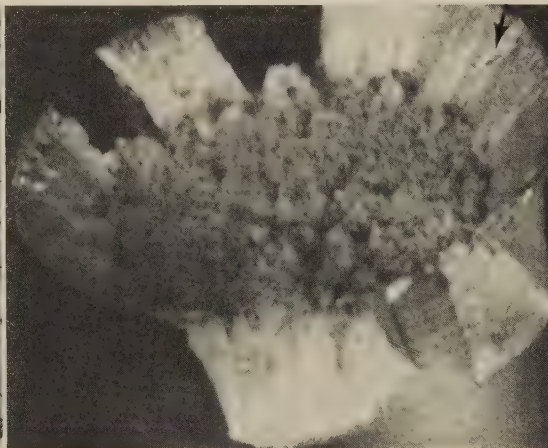
Fractograph 4489 (left) shows the surface of a dendritic stress-rupture fracture in a cast specimen of IN-100 nickel-base alloy that was annealed at 1177 C (2150 F) and loaded at 982 C (1800 F) to a tensile stress of 97 MPa (14 ksi). The specimen broke after 49 hr of testing. Fractograph 4490 (center) is a TEM replica of an area at the arrow in 4489, showing some evidence of intergranular separation and some facets of what appear to be cleaved particles (as at A) of intermetallic compounds. Fractograph 4491 (right) is a TEM replica of another area at the arrow in 4489, showing evidence of glide-plane decohesion (at A's) as well as smooth areas of stretching (as at B). Some surface oxidation apparently occurred after fracture. See also 4492.



TEM fractograph (p-c replica)

6500×

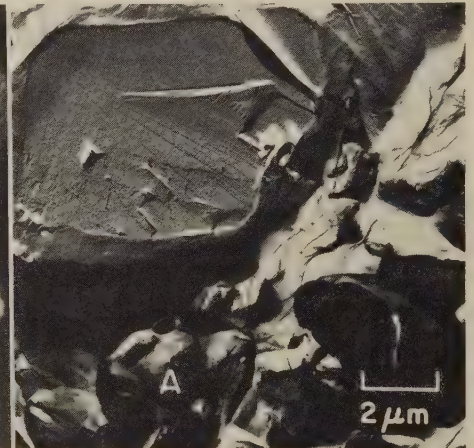
4492 TEM replica of a third area at the arrow in 4489. The elongated dimples here indicate local tearing during fracture, suggesting that multiple ligaments between intergranular separations ruptured by overload.



Light fractograph

9×

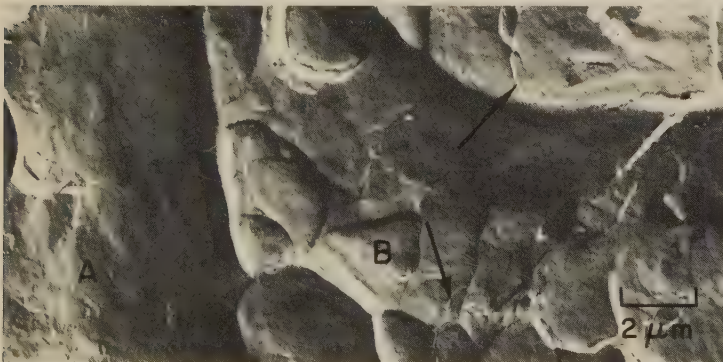
4493 A cup-and-cone fracture in an unnotched specimen of nickel-base alloy 718 that broke by tension overload. Tensile strength was 1450 MPa (210 ksi). The shear lip exhibits a small amount of checking (as at arrow); the central fibrous area is extremely coarse. See 4494 to 4496.



TEM fractograph (p-c replica)

5000×

4494 TEM replica of an area in the central fibrous zone of the fracture surface in 4493. The major feature here is a large cleavage facet of a precipitate particle. Adjacent dimples (as at A) are essentially equiaxed.



TEM fractograph (p-c replica)

5000×

4495 TEM replica of a second area in the central fibrous zone in 4493. The dimples here, which appear to be essentially equiaxed, differ considerably in size (compare dimples at A and B). There appear to be some very minor secondary cracks (at arrows).

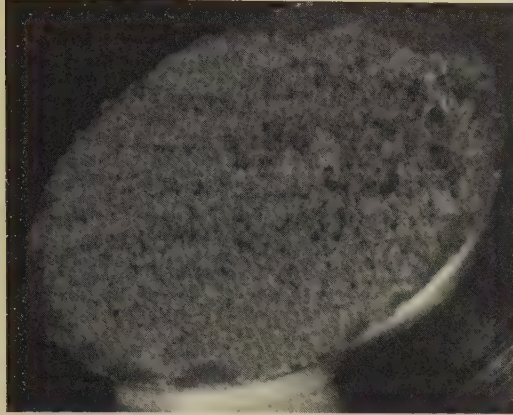


TEM fractograph (p-c replica)

5000×

4496 TEM replica of a third area in the central fibrous zone in 4493. This area must be close to the shear lip, because the dimples here are somewhat directional. There are no signs of cleaved precipitate particles here or in 4495 (left).

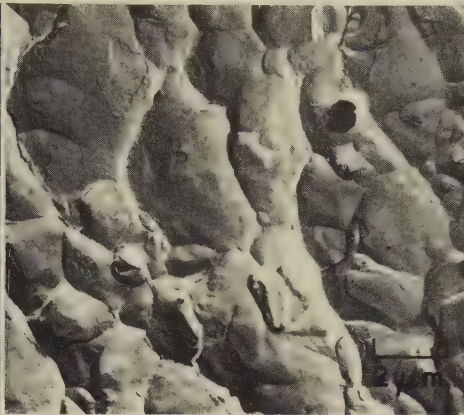
Light and TEM Fractographs: Notched Specimen of Alloy 718 Fractured by Tension Overload;
Threaded Bolt of Alloy 718 Fractured by Low-Cycle Fatigue



Light fractograph

9×

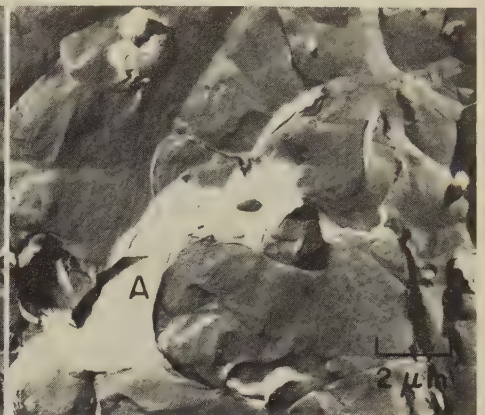
4497 Surface of a tension-overload fracture in a notched specimen of nickel-base alloy 718. Unnotched tensile strength, same as 4493; notched tensile strength, 2048 MPa (297 ksi); $K_t = 3.5$. Fracture surface shows several crack nuclei at the notch. See 4498 to 4500.



TEM fractograph (p-c replica)

5000×

4498 TEM replica of an area of the tension-overload fracture surface in fractograph 4497 (left), showing slightly elongated tear dimples but no sign of precipitate particles such as the one shown in fractograph 4494 (on the opposite page).



TEM fractograph (p-c replica)

5000×

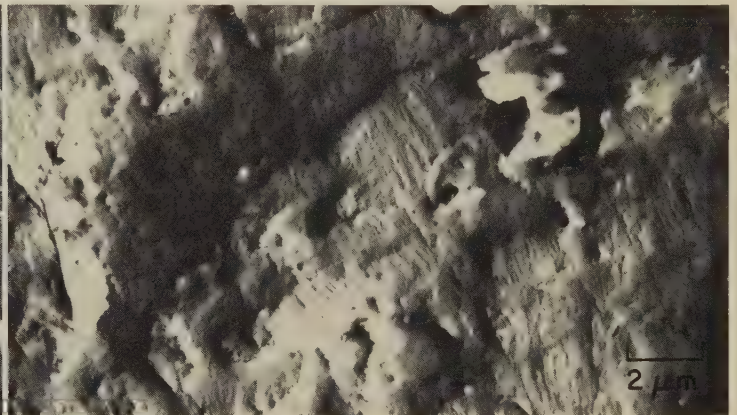
4499 TEM replica of another area of the fracture surface in 4497, showing tear dimples somewhat like those in 4498. White area at lower left (A) could be either a hole in the replica or an area that was shielded from heavy metal shadowing.



TEM fractograph (p-c replica)

5000×

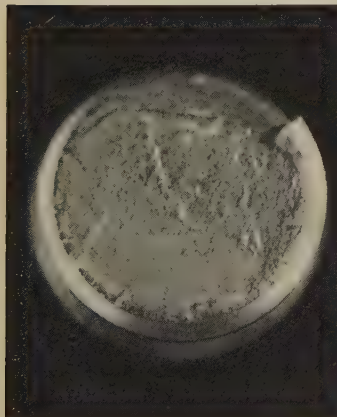
4500 TEM replica of a third area in 4497, showing both large and very small scattered dimples that are all slightly elongated. The bottoms of some of the dimples contain marks (as at arrows) suggesting that the first-stage plastic replica was marred during stripping.



TEM fractograph (p-c replica)

5000×

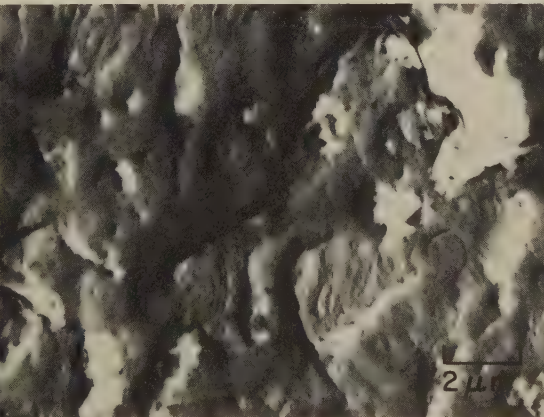
4501 TEM replica of an area in the fatigue zone in 4502 (below, left), near the areas shown in 4503 and 4504. Fatigue striations are clearly evident in some of the fracture facets, but the intervening facets have smooth contours with tiny pockmarks that may be inclusions.



Light fractograph

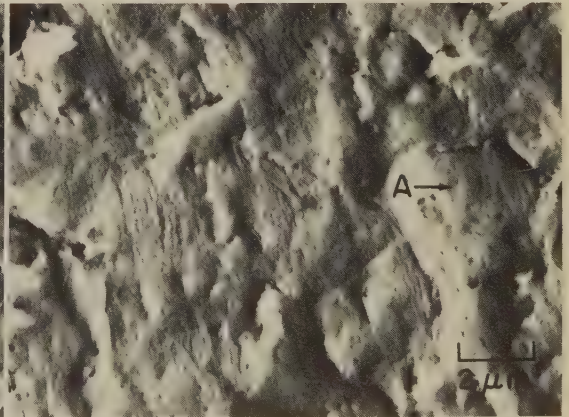
6×

4502, 4503, 4504



TEM fractograph (p-c replica)

5000×

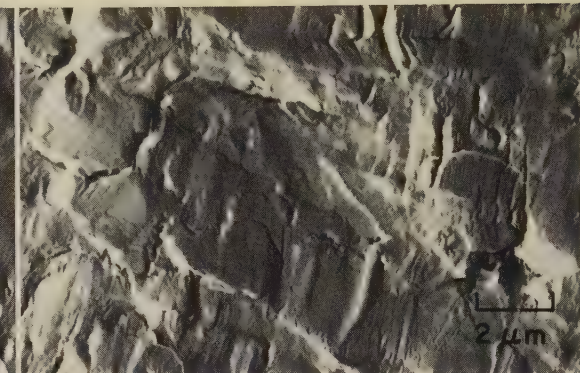
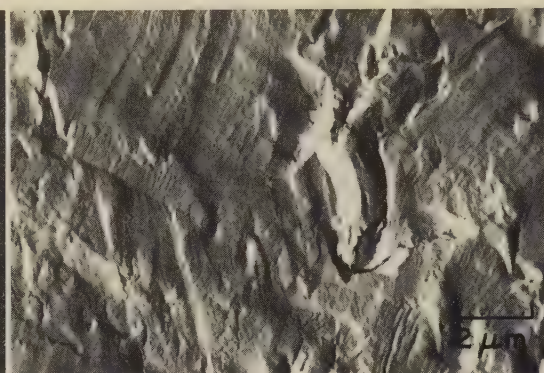
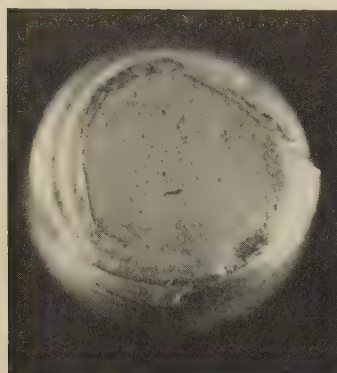


TEM fractograph (p-c replica)

5000×

Fractograph 4502 (left) shows the surface of a low-cycle fatigue fracture in a threaded bolt of nickel-base alloy 718 (same tensile strength as in 4493) that was loaded to a tensile stress of 862 MPa (125 ksi). Fracture occurred after 33,000 cycles. Many crack nuclei are visible in the thread root. Fractograph 4503 (center) is a TEM replica of an area in the fatigue zone at the bottom of the fracture surface in 4502 and shows isolated patches of fatigue striations that are rather indistinct and not uniformly spaced. Fractograph 4504 (right) is a TEM replica of another area in the fatigue zone in 4502 and shows fatigue striations more generally distributed than those in 4503 and present even on rounded features (as at A). See also 4501, above.

Light Fractographs and TEM Fractographs: Alloy 718 Threaded Bolt Fractured by High-Cycle Fatigue; Alloy 718 Notched Specimen Fractured by High-Cycle Fatigue



Light fractograph

6×

TEM fractograph (p-c replica)

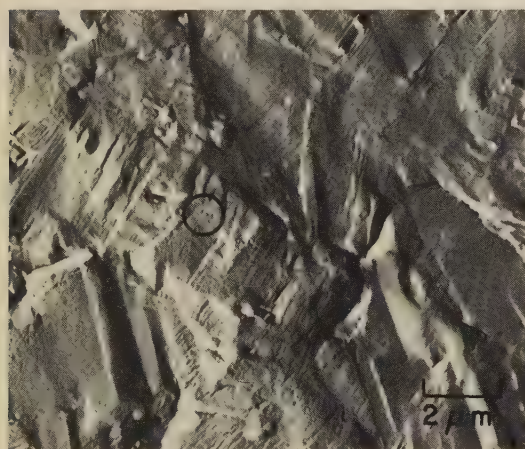
5000×

TEM fractograph (p-c replica)

5000×

4505, 4506, 4507

Fractograph 4505 (left) shows the surface of a high-cycle fatigue fracture in a threaded bolt of nickel-base alloy 718 (tensile strength, 1450 MPa or 210 ksi) that was loaded in tension-tension ($R=0.1$) with a major stress of 414 MPa (60 ksi). Fracture occurred after 1,648,000 cycles. Fractograph 4506 (center) is a TEM replica of an area in the fatigue zone of the fracture surface in 4505, showing well-defined fatigue striations. Note that the striation patterns in certain grains at right show that these grains are oriented at 30° to the general array of grains. Fractograph 4507 (right) is a TEM replica of another area in the fatigue zone in 4505. This replica shows many smooth regions containing extremely faint fatigue striations. Note that at left there are features that resemble both intergranular and transgranular secondary cracks. See also fractograph 4508.

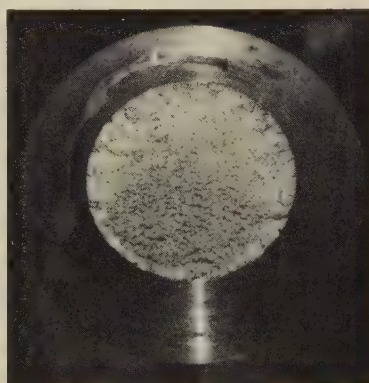


TEM fractograph (p-c replica)

5000×

4508

TEM replica of a third area in the fatigue zone in 4505. Nearly all of the grains here show regular fatigue striations, some of which are oriented 45° to their neighbors. The three small dots in the circle near center may be "tire tracks".

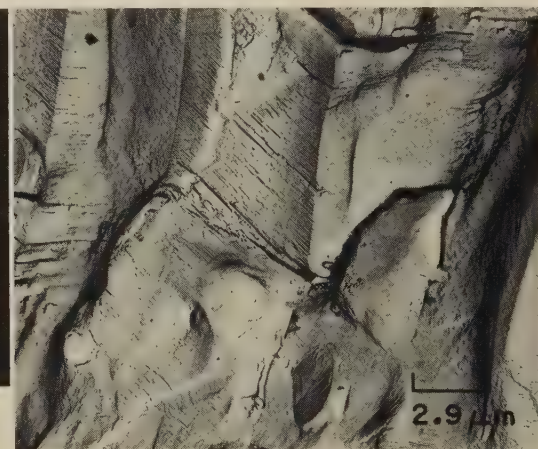


Light fractograph

3.7×

4509

High-cycle fatigue fracture in a notched specimen of alloy 718 solution treated, aged to tensile strength of 1393 MPa (202 ksi), loaded to tensile stress cycled from 138 to 689 MPa (20 to 100 ksi) at 500 cycles per minute, and broken after 11,800 cycles. See 4510 to 4513.

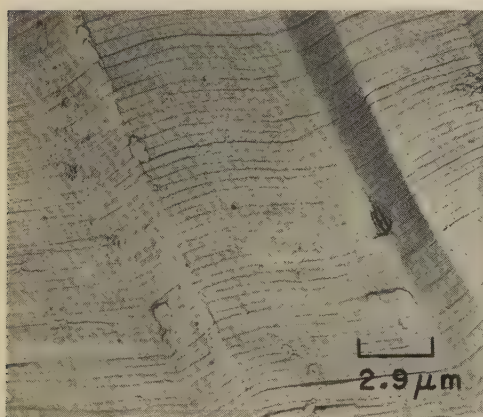


TEM fractograph (p-c replica)

3400×

4510

TEM replica of an area at one of the fatigue-crack nuclei at the notch in 4509. Notch had 60° angle, 0.008-in. root radius, 0.30-in. diameter. Here, fatigue striations meet at sharp angles at twin boundaries. (The striations at bottom center are very faint.)

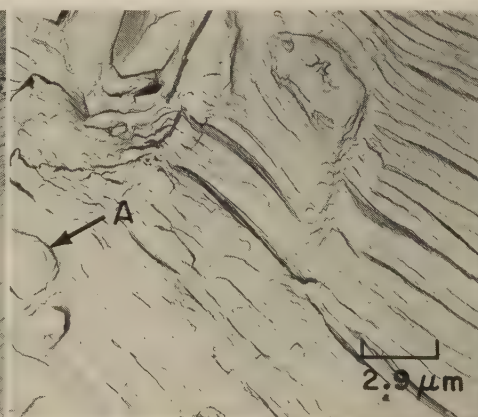


TEM fractograph (p-c replica)

3400×

4511

TEM replica of an area in 4509 near (but not at) a fatigue-crack nucleus. In this area, regular, well-developed fatigue striations show curvature, as well as sharp angles at twin boundaries.



TEM fractograph (p-c replica)

3400×

4512

TEM replica of an area in the fatigue zone of the fracture surface in 4509, but an area well away from any fatigue-crack nuclei. The shape of the feature at A suggests an incipient dimple.



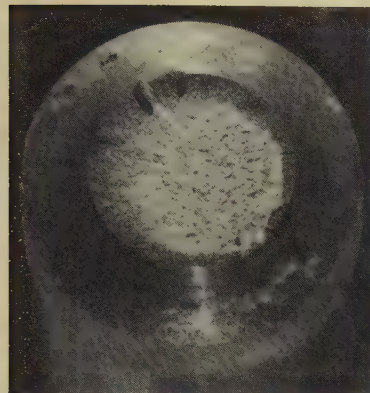
TEM fractograph (p-c replica)

3400×

4513

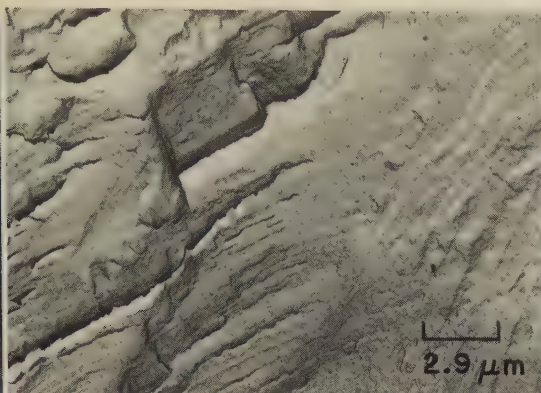
TEM replica of an area in 4509 in the transition zone between fatigue and fast fracture. Note that the spacing of the fatigue striations is considerably wider at top center than elsewhere.

Light and TEM Fractographs: Notched Specimen of Alloy 718 Fractured by Low-Cycle Fatigue;
Unnotched Specimen of Waspaloy Fractured by Tension Overload at Room Temperature



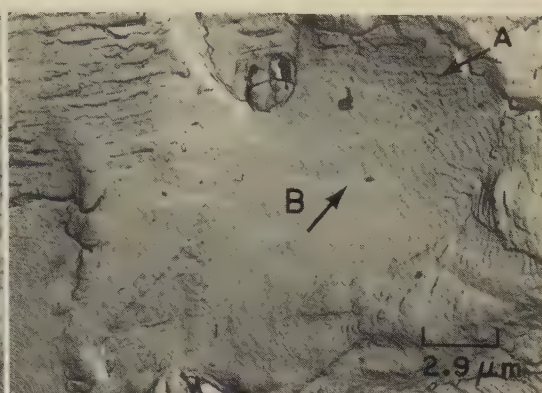
Light fractograph

3½×



TEM fractograph (p-c replica)

3400×

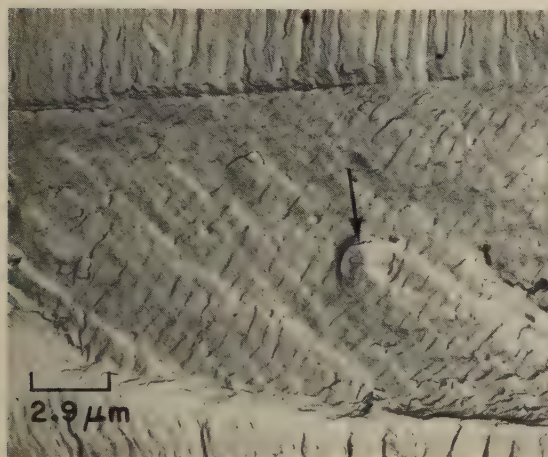


TEM fractograph (p-c replica)

3400×

4514, 4515, 4516

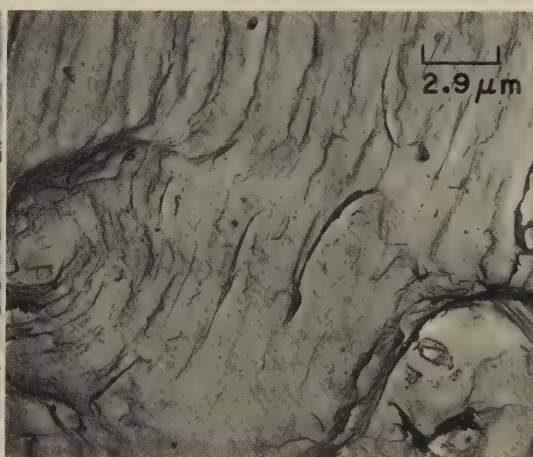
Fractograph 4514 (left) shows the surface of a low-cycle fatigue fracture in a notched specimen (notch same as that in 4510) of alloy 718 solution treated and aged to a tensile strength of 1393 MPa (202 ksi). The specimen was loaded at 593 C (1100 F) to a tensile stress cycled from 117 to 586 MPa (17 to 85 ksi) at 500 cycles per minute. Fracture occurred after 7500 cycles. Fractograph 4515 (center) is a TEM replica of an area at one of many fatigue-crack nuclei around the root of the notch in 4514, showing a faceted, angular surface with very fine fatigue striations. The surface characteristics here have perhaps been affected by oxidation. Fractograph 4516 (right) is a TEM replica of an area near (but not at) another fatigue-crack nucleus in 4514. Some lines (as at A) are present at an angle with the fatigue striations (as at B); these lines are probably slip lines rather than more fatigue striations, because fatigue striations do not cross each other. Some striations appear to contain fissures. See also 4517 and 4518.



TEM fractograph (p-c replica)

3400×

4517 TEM replica of an area of the fracture surface in 4514 well away from any fatigue-crack nucleus. Presence of fatigue patches shows that crack fronts propagated on different levels. Incipient dimple is evident (arrow).



TEM fractograph (p-c replica)

3400×

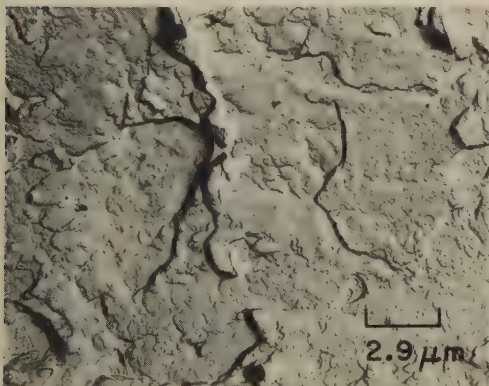
4518 TEM replica of an area in 4514 at the transition between the zone of fatigue and the zone of final, fast fracture. Note that the fatigue striations here are curved, instead of fairly straight as in the area shown in 4517.



Light fractograph

3½×

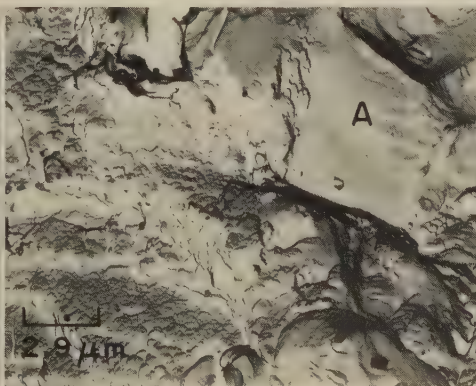
4519 A tension-overload fracture in an unnotched specimen of Waspaloy that was solution treated, aged to a tensile strength of 1230.7 MPa (178.5 ksi), and tested at room temperature. See 4520 to 4522, below.



TEM fractograph (p-c replica)

3400×

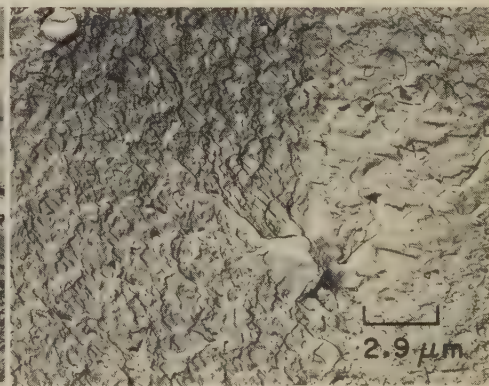
4520 TEM replica of an area at the edge of the fracture surface of the specimen of Waspaloy in fractograph 4519 (above, at right), showing several flat shear dimples and scattered steps or ledges.



TEM fractograph (p-c replica)

3400×

4521 TEM replica of another area of the fracture in 4519, near the area in 4520, showing some very smooth, stretched facets (A), a few normal-size dimples, and regions of extremely fine dimples.



TEM fractograph (p-c replica)

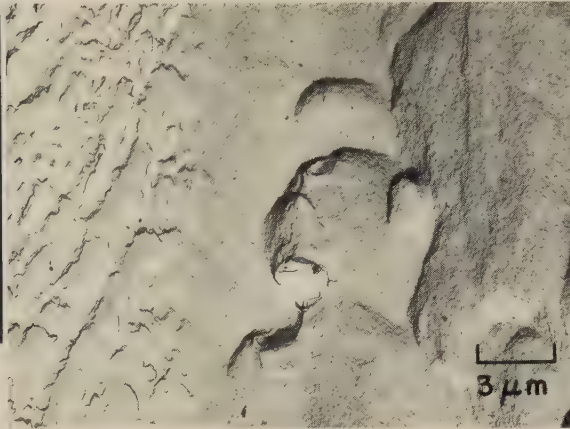
3400×

4522 TEM replica of area at center of fracture surface in 4519, showing a portion of a relatively flat facet covered with very fine dimples. Almost no normal-size dimples were visible near this area.

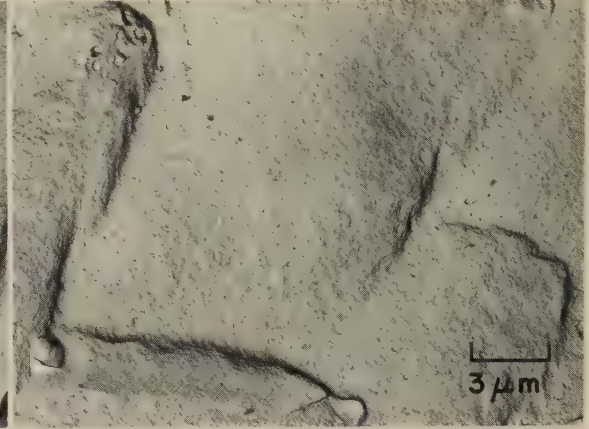
Light and TEM Fractographs of Waspaloy Specimens Fractured by Tension Overload:
Unnotched at 927 C (1700 F); Notched at Room Temperature



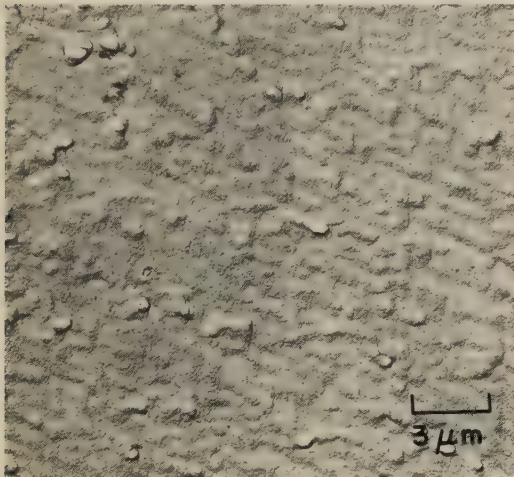
Light fractograph $3\frac{1}{2}\times$
4523 Jagged fracture in an unnotched specimen of Waspaloy that was solution treated, aged to a tensile strength of 1230.7 MPa (178.5 ksi), and broken by tension overload at 927 C (1700 F). See fractographs 4524 to 4526.



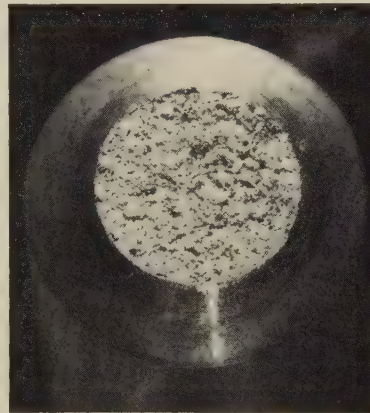
TEM fractograph (p-c replica) $3300\times$
4524 TEM replica of an area in the fracture surface in 4523, showing shear dimples in a wide variety of sizes. In spite of the high temperature of the tension test, only a small amount of surface oxidation is apparent.



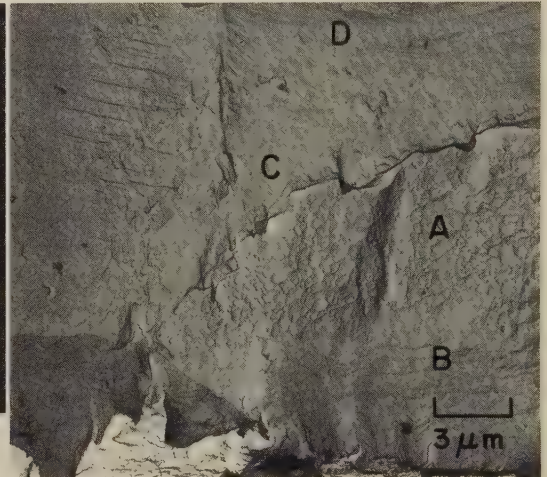
TEM fractograph (p-c replica) $3300\times$
4525 TEM replica of another area in the fracture surface in 4523, showing exceedingly large and very elongated shear dimples. Visible are a few small equiaxed dimples of about the same size as that of the dimples at left in fractograph 4524.



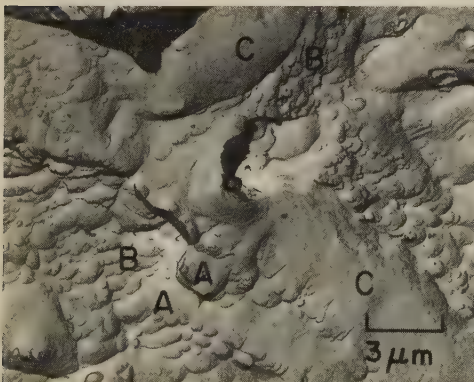
TEM fractograph (p-c replica) $3300\times$
4526 TEM replica of a third area of the fracture surface in 4523, showing a very large flat region containing many small dimples. The surface has a fine graininess that suggests the presence of a high-temperature oxide film.



Light fractograph $3\frac{1}{2}\times$
4527 Tension-overload fracture in a notched specimen of Waspaloy (notch same as that described in 4510) that was solution treated, aged to a tensile strength of 1230.7 MPa (178.5 ksi), and broken at room temperature. See also 4528 to 4531.



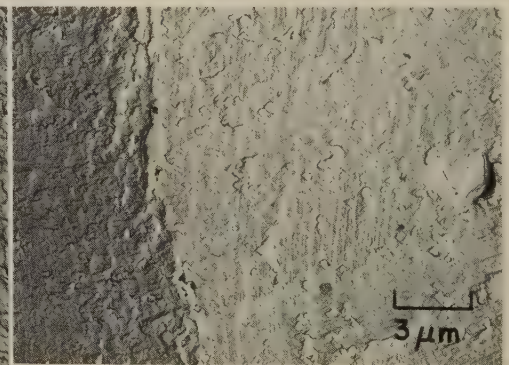
TEM fractograph (p-c replica) $3300\times$
4528 TEM replica of an area at the notch in the fracture surface in 4527, showing extremely flat shear dimples (A), regions of serpentine glide (B), regions of stretching (C), and suggestions of ripples (D).



TEM fractograph (p-c replica) $3300\times$
4529 TEM replica of an area near (but not at) the notch in 4527. A few large, elongated dimples (A's) and many small shear dimples (B's) are evident, as well as several regions of stretching (C's).

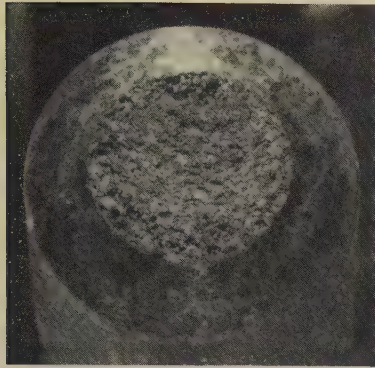


TEM fractograph (p-c replica) $3300\times$
4530 TEM replica of an area near the center of the fracture surface in 4527, showing large facets with fine dimples, a region of stretching (A), and serpentine glide (at lower left). See 4531.

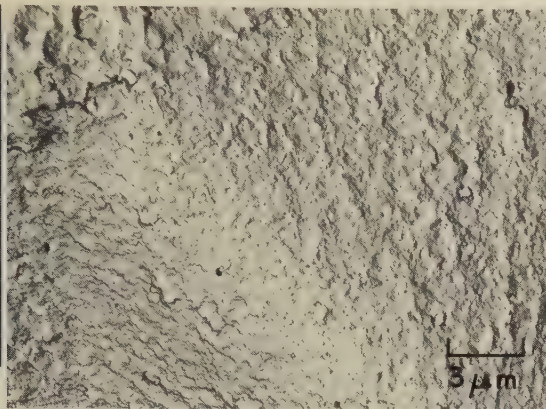


TEM fractograph (p-c replica) $3300\times$
4531 TEM replica of another area near the center of the fracture surface in 4527, showing two large, flat facets. The facet at left contains fine, shallow dimples; the facet at right shows few dimples but perhaps two of many possible systems of slip.

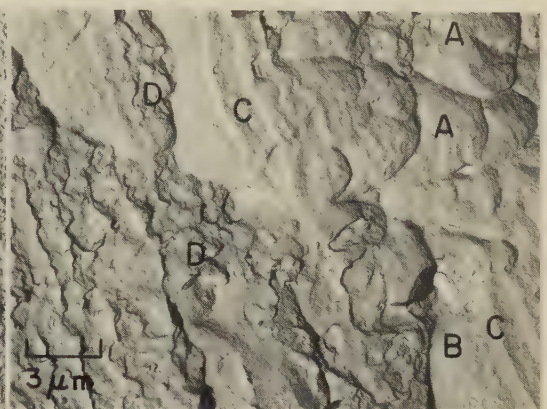
Light and TEM Fractographs: Notched Specimens of Waspaloy Fractured by Tension Overload at 927 C (1700 F) and by High-Cycle Fatigue at Room Temperature



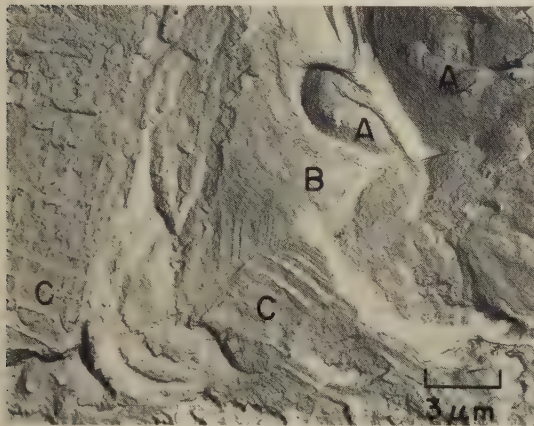
Light fractograph 3½×
4532 Tension-overload fracture in a notched specimen of Waspaloy that was solution treated, aged to a tensile strength of 1230.7 MPa (178.5 ksi), and tested at 927 C (1700 F). A coarsely granular surface. See TEM fractographs 4533 to 4536.



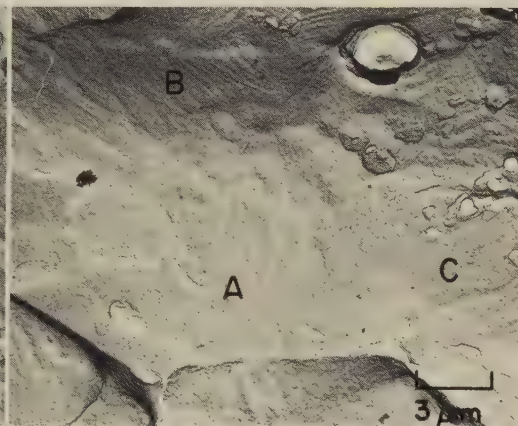
TEM fractograph (p-c replica) 3300×
4533 TEM replica of an area of the fracture surface in 4532, at the notch, which is the same as that in 4510. The topography here resembles that resulting from grain-boundary separation but may have been affected in appearance by the presence of an oxide film.



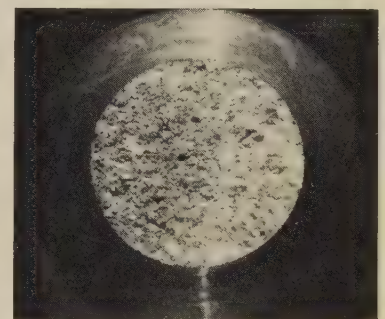
TEM fractograph (p-c replica) 3300×
4534 TEM replica of an area near (but not at) the notch in fractograph 4532. The facets shown here contain large, elongated dimples (at A's), stretched regions (as at B), and some evidence of serpentine glide (at C's). The features at D's do not appear to be dimples.



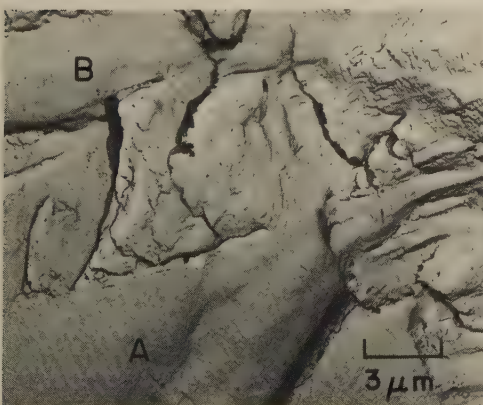
TEM fractograph (p-c replica) 3300×
4535 TEM replica of an area at the center of the fracture surface in 4532, showing dimples (A's) interspersed with regions of stretching (B). Note the unusual array of parallel marks (C's) that resemble fatigue striations; these marks may be glide-plane decohesions or slip, or may be due to microstructure. See 4536.



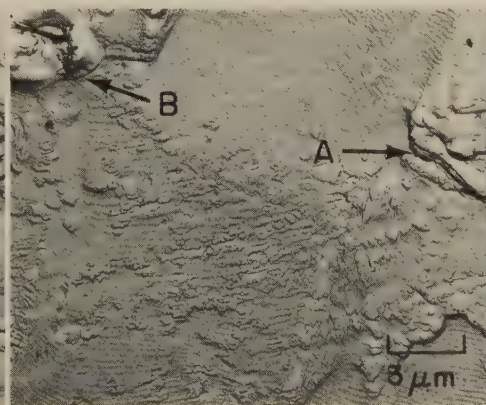
TEM fractograph (p-c replica) 3300×
4536 TEM replica of another area at the center of the fracture surface in 4532. The facets shown here are much larger than those in fractograph 4535. As elsewhere in this fracture, the surface in this area exhibits stretched regions (A) and serpentine glide (B), with occasional suggestions of ripples (C).



Light fractograph 3¾×
4537 Fatigue fracture in a notched specimen of Waspaloy (notch same as in 4510) solution treated, aged to a tensile strength of 1230.7 MPa (178.5 ksi), loaded at room temperature to a stress cycled from 124 to 621 MPa (18 to 90 ksi) at 500 cycles per minute. Fracture occurred after 16,600 cycles. See 4538 to 4546 (below, and on the next page).



TEM fractograph (p-c replica) 3300×
4538 TEM replica of an area at a fatigue-crack nucleus in the root of the notch in the fracture surface shown in 4537 (at right, above). This area exhibits exceedingly fine fatigue striations (at A and B).



TEM fractograph (p-c replica) 3300×
4539 TEM replica of an area in 4537 adjacent to that shown in 4538. Fatigue striations are slightly more widely spaced here than in 4538. Possible inclusions or large precipitates are visible at A and B.

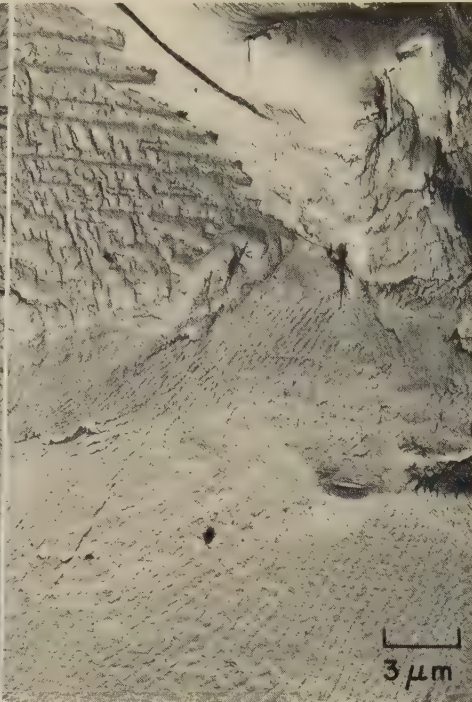


TEM fractograph (p-c replica) 3300×
4540 TEM replica of another area at a fatigue-crack nucleus in 4537, showing very fine fatigue striations at different levels. See also fractographs 4541 to 4546, on the following page.

TEM Fractographs: Notched Specimen of Waspaloy Fractured by High-Cycle Fatigue at Room Temperature (Continued)



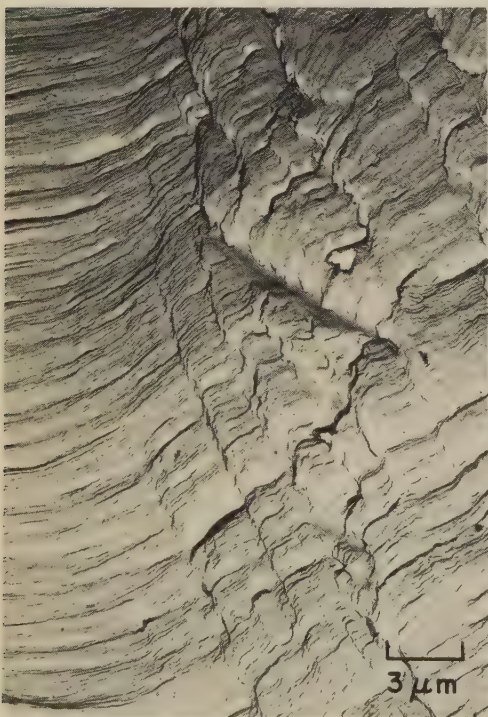
TEM fractograph (p-c replica) 3300×
4541 TEM replica of a fourth area at a fatigue-crack nucleus in 4537 (preceding page), showing fatigue striations at different levels of crack propagation. The features at right are not dimples.



TEM fractograph (p-c replica) 3300×
4542 TEM replica of an area near (but not at) a crack nucleus in 4537. Note the marks at upper left, which certainly are not fatigue striations but perhaps are related to crystal structure.



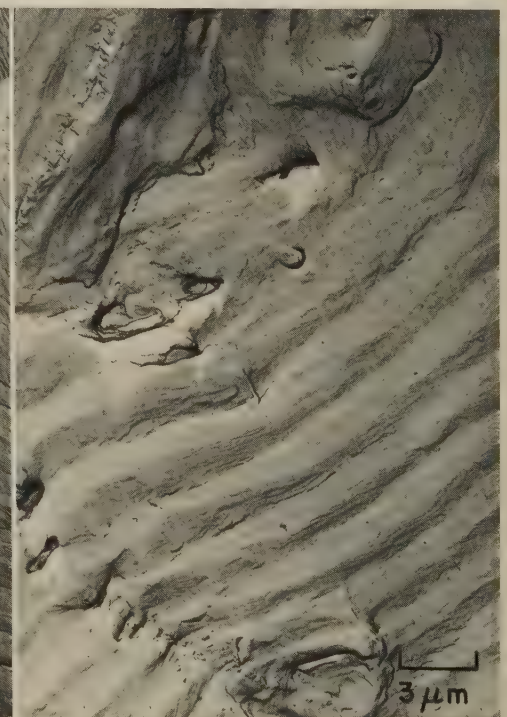
TEM fractograph (p-c replica) 3300×
4543 TEM replica of another area near (but not at) a crack nucleus in 4537. The fatigue striations here are very uniform. Note the additional marks at top left, which may be cleavage steps.



TEM fractograph (p-c replica) 3300×
4544 A third area near (but not at) a crack nucleus in 4537, showing fatigue striations resulting from propagation of several crack fronts on different levels. Irregularity of striation pattern at right may have been caused by microstructure.

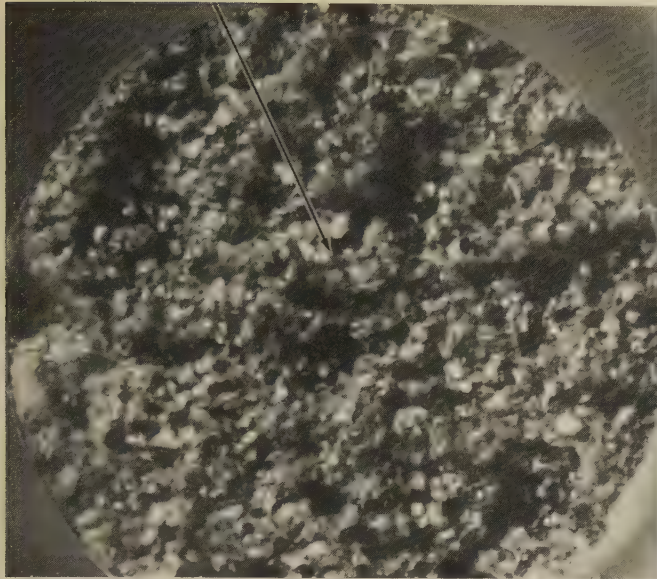


TEM fractograph (p-c replica) 3300×
4545 TEM replica of an area of the fracture surface in 4537 well away from any fatigue-crack nucleus. Fatigue striations along twin boundaries are evident, and the spacing between striations has increased with crack penetration.



TEM fractograph (p-c replica) 3300×
4546 TEM replica of an area at the transition from fatigue fracture to final, fast fracture in 4537. Note that the striation spacing has increased markedly as the cross section has decreased and the effective stress has increased.

Light and TEM Fractographs: Unnotched Specimens of Nickel-Base Alloy René 41 and Cobalt-Base Alloy L-605 Fractured by Tension Overload



Light fractograph

4547, 4548

Fractograph 4547 (left) shows the surface of a "rock candy" type of fracture in an unnotched specimen of nickel-base heat-resisting alloy René 41 that had been solution treated at 1177 C (2150 F) and aged at 899 C (1650 F) to a tensile strength of 1076 MPa (156 ksi). The specimen was broken by tension overload at room temperature. Fractograph 4548 (right) is a TEM view of an area, at arrow, in the center of the fracture in 4547, which appears to be intergranular. This TEM replica reveals flat, elongated dimples, which have formed on what may be large separated-grain facets.



14× TEM fractograph (p-c replica)

6500×



Light fractograph

3×

4549

Tension-overload fracture in an unnotched specimen of solution treated cobalt-base alloy L-605; the tensile strength was 951 MPa (138 ksi). A jagged shear fracture. See also 4550 to 4552, below, for TEM views of three areas of this room-temperature fracture.



TEM fractograph (p-c replica)

3300×

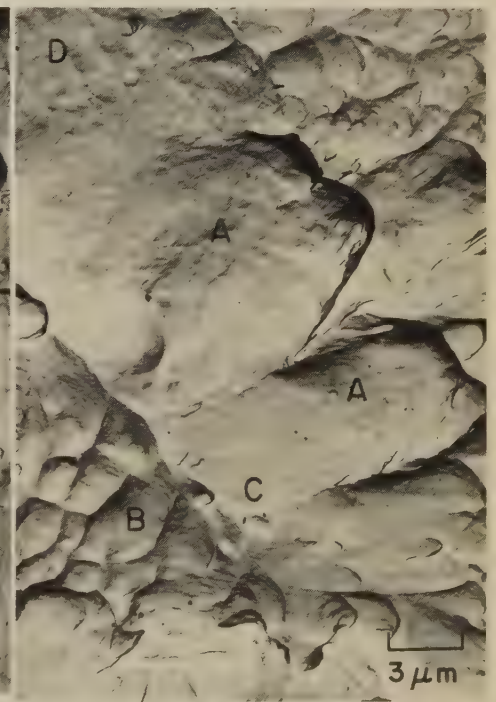
4550 TEM replica of an area at the edge of the fracture surface in 4549 (above, at right), showing shear dimples and several regions of stretching.



TEM fractograph (p-c replica)

3300×

4551 TEM replica of an area near (but not at) the edge of the fracture surface in 4549. Like 4550, this view shows shear dimples and stretched regions; also visible here are suggestions of ripples (at A).

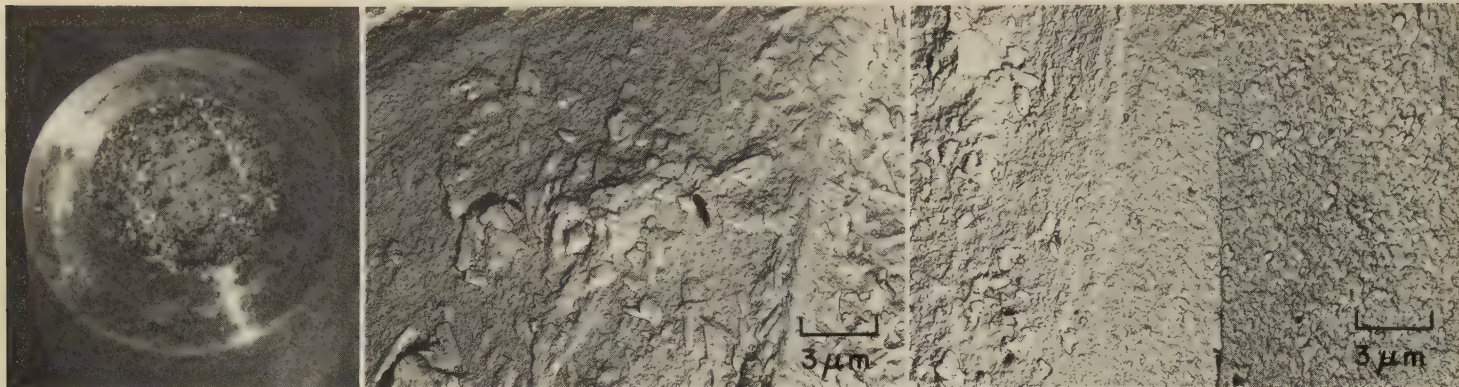


TEM fractograph (p-c replica)

3300×

4552 TEM replica of area at center of fracture in 4549. Large, elongated dimples (A's); essentially equiaxed dimples (B); stretched regions (C); ripples (D).

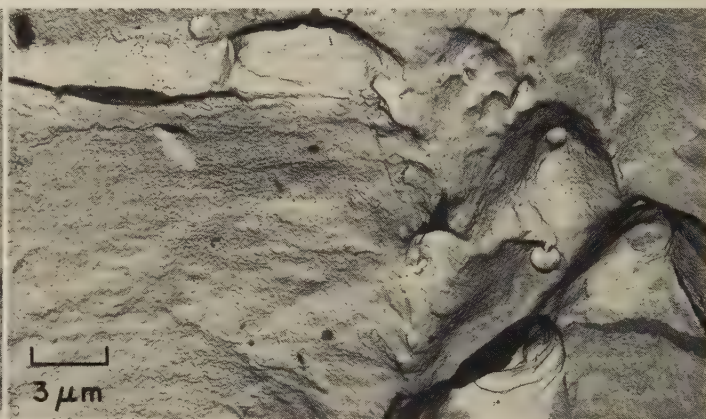
Light and TEM Fractographs: Notched Specimens of Cobalt-Base Alloy L-605 Fractured by Tension Overload and by High-Cycle Fatigue



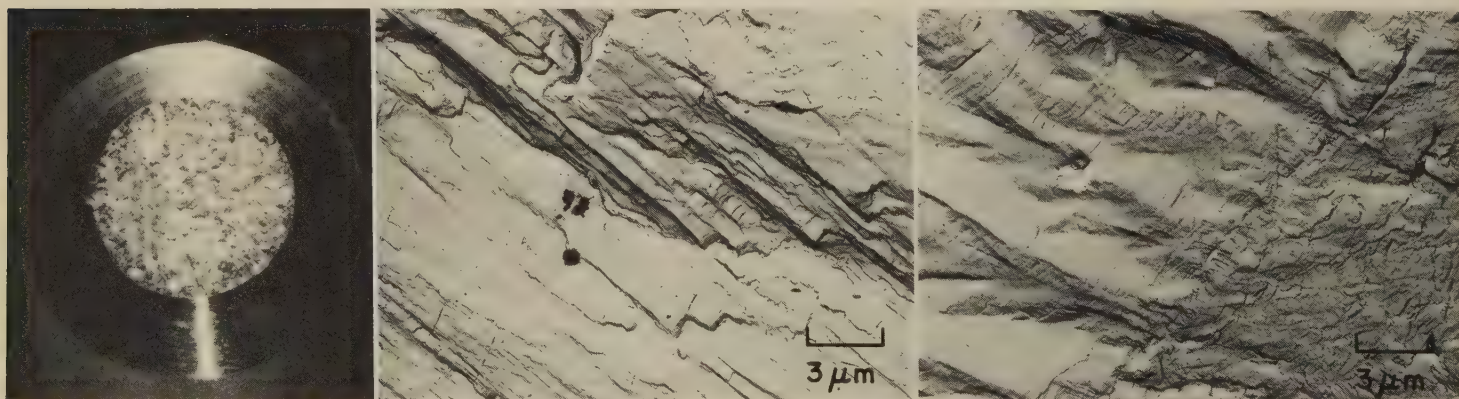
Light fractograph 350× TEM fractograph (p-c replica) 3300× TEM fractograph (p-c replica) 3300×
4553, 4554, 4555 Fractograph 4553 (left) shows the surface of a tension-overload fracture in a notched specimen of cobalt-base alloy L-605 that was solution treated 15 min at 1332 C (2250 F) and air cooled. Unnotched tensile strength was 951 MPa (138 ksi). The notch had a 60° angle, 0.30-in. diam, and 0.008-in. root radius. The specimen was broken at 927 C (1700 F), which produced a coarse, jagged, granular fracture. Notched hot tensile strength was 531 MPa (77 ksi). Fractographs 4554 (center) and 4555 (right) are TEM replicas of two areas near the notch in 4553, each showing portions of two separated-grain facets. Well-developed oxide crystals are visible on the facets in 4554. Oxide particles are also present on the left facet in 4555, but there are fewer of them than in 4554 and they are not as well developed. See also fractographs 4556 and 4557 (below).



TEM fractograph (p-c replica) 3300×
4556 TEM replica of an area at the center of the fracture surface in 4553. This area appears to have formed by transgranular fracture and contains rather flat facets; some portions, as at A, are smooth enough to suggest stretching.



TEM fractograph (p-c replica) 3300×
4557 TEM replica of another area at the center of the fracture in 4553. Both transgranular fracture and intergranular fracture appear to have occurred here; a separated-grain facet is visible at left, and directional dimples at right.

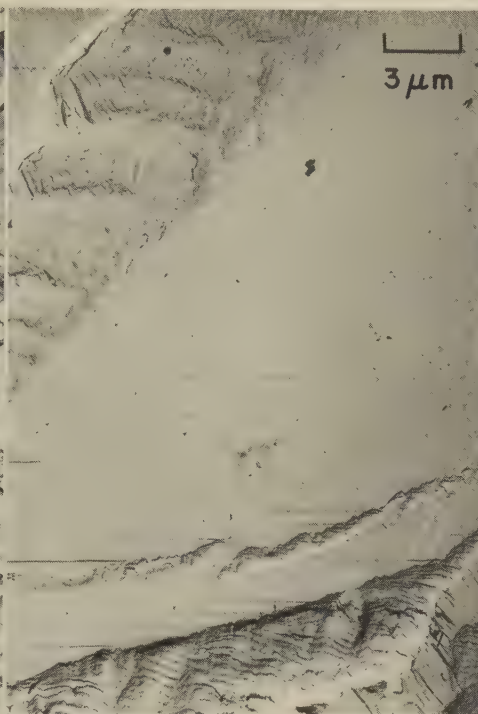


Light fractograph 312× TEM fractograph (p-c replica) 3300× TEM fractograph (p-c replica) 3300×
4558, 4559, 4560 Fractograph 4558 (left) shows the surface of a high-cycle fatigue fracture in a notched specimen of solution treated cobalt-base alloy L-605 (notch and heat treatment same as in 4553). Tensile strength was 951 MPa (138 ksi). The specimen was loaded to a stress cycled from 97 to 483 MPa (14 to 70 ksi) at 500 cycles per minute and broke after 110,000 cycles. Fractograph 4559 (center) is a TEM replica of a region at the fatigue-crack nucleus of the fracture in 4558. Few recognizable fatigue striations are visible here. Instead, there are many angular facets. The faint transverse marks in the lower left quadrant of this view are of unknown origin. Fractograph 4560 (right) is a TEM replica of an area near (but not at) the fatigue-crack nucleus of the fracture in 4558. The fatigue patches at left show an influence of microstructure. The features at lower right are similar to those at upper right in 4559. See also fractographs 4561 to 4566, on the opposite page.

TEM Fractographs: Notched Specimen of Cobalt-Base Alloy L-605
Fractured by High-Cycle Fatigue (Continued)



TEM fractograph (p-c replica) 3300×
4561 TEM replica of a second area near (but not at) the fatigue-crack nucleus in 4558 (facing page). Diagonal band (upper left to lower right) suggests a line of inclusions; otherwise, this area bears some resemblance to the area in 4560.



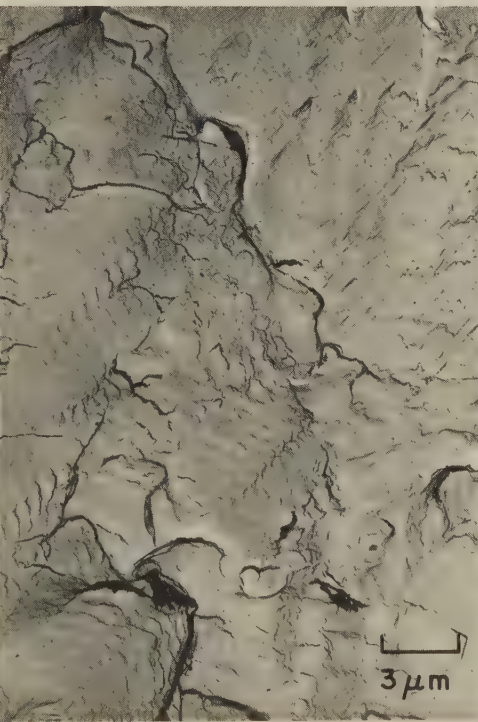
TEM fractograph (p-c replica) 3300×
4562 TEM replica of a third area near (but not at) the nucleus in 4558. Differences in crystal orientation have resulted in some regions being smooth with light striations, others rough with heavy striations. The sharp lines may be steps.



TEM fractograph (p-c replica) 3300×
4563 TEM replica of an area well away from the fatigue-crack nucleus of the fracture in 4558. Diagonal marks (upper left to lower right) are steps separating two adjacent fatigue patches showing regular, well-resolved fatigue striations.



TEM fractograph (p-c replica) 3300×
4564 TEM replica of another area well away from the fatigue-crack nucleus in 4558, showing a particularly strong influence of microstructure on surface pattern, which is quite irregular.

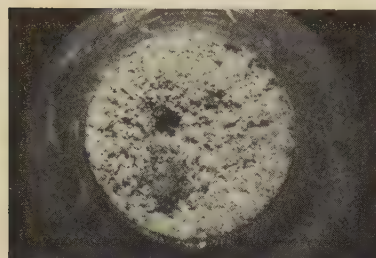


TEM fractograph (p-c replica) 3300×
4565 TEM replica of an area near the transition between fatigue fracture and final, fast fracture in 4558, showing "tire tracks" (at left) and features that suggest scraping (at right).



TEM fractograph (p-c replica) 3300×
4566 TEM replica of another area near the transition between fatigue and fast fracture in 4558. Striation spacing is extremely wide, indicating that this area is very close to the fast-fracture zone.

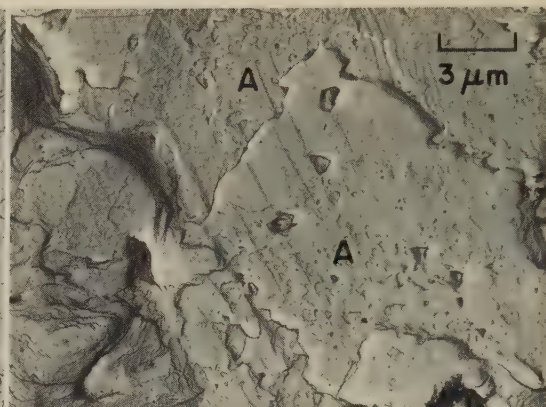
Light and TEM Fractographs: U-700 Alloy Notched Specimen Fractured by Tension Overload at Room Temperature; U-700 Alloy Notched Specimen Fractured by Fatigue at Room Temperature



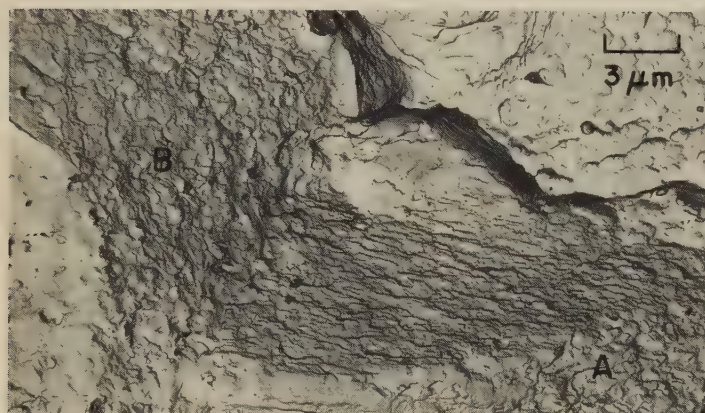
Light fractograph 3.6×
4567 Tension-overload fracture in a notched specimen of U-700 alloy solution treated at 1079 C (1975 F), and aged 24 hr at 843 C (1550 F) and 16 hr at 760 C (1400 F), to tensile strength of 1462 MPa (212 ksi), then broken at room temperature. Notch had a 60° angle, 0.30-in. diam, 0.008-in. root radius. Notched tensile strength, 1731 MPa (251 ksi). See 4568-4571.



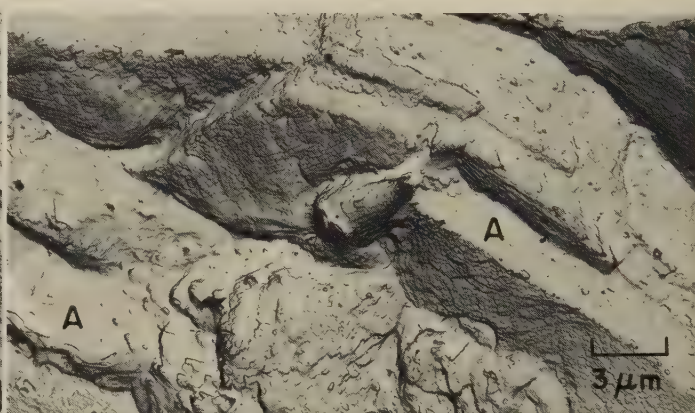
TEM fractograph (p-c replica) 3300×
4568 TEM replica that was taken at the left edge of the tension-overload fracture shown in 4567 (left). The surface in this area is characterized mainly by flat and shallow dimples. Steplike marks are evident between some facets.



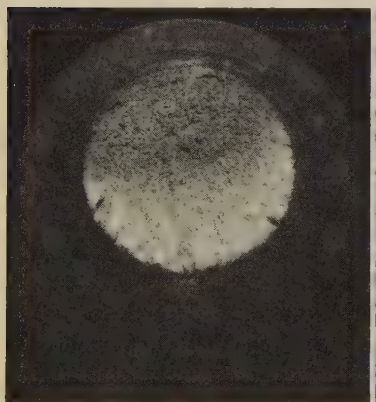
TEM fractograph (p-c replica) 3300×
4569 A TEM replica taken near (but not at) the notch of the fracture in 4567. Facets here are very flat, and there is a sparse sprinkling of tiny depressions (at A's). Steps between facets are evident here, as in fractograph 4568.



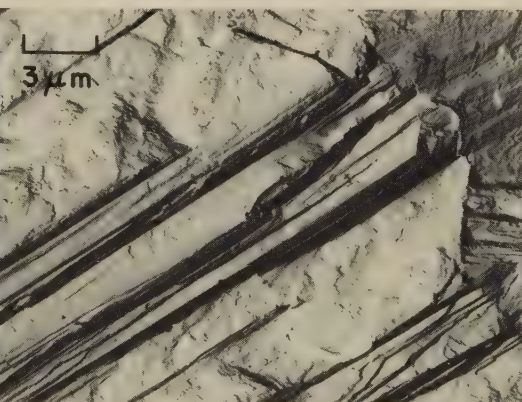
TEM fractograph (p-c replica) 3300×
4570 A TEM replica of an area at the center of the fracture surface shown in 4567. Intergranular rupture, with fine shear dimples visible on the separated-grain facets at A and B.



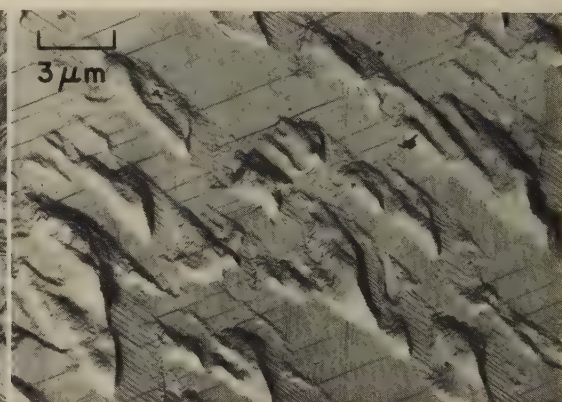
TEM fractograph (p-c replica) 3300×
4571 TEM replica of another area at center of fracture surface in 4567. This area, like that in 4570, displays separated-grain facets, but with intervening stretched regions (A's).



Light fractograph 3.6×
4572, 4573, 4574



TEM fractograph (p-c replica) 3300×

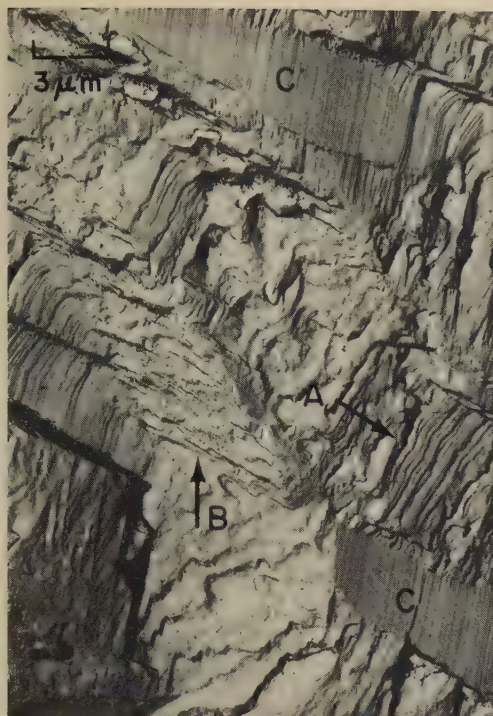


TEM fractograph (p-c replica) 3300×

3300×

Fractograph 4572 (left) shows the surface of a fatigue fracture in a notched specimen of U-700 alloy (notch and heat treatment same as in 4567); tensile strength, 1462 MPa (212 ksi). Tested at room temperature at 500 cycles per minute, at stress of 1379 MPa (200 ksi) max and 138 MPa (20 ksi) min; broke at 12,600 cycles. The fracture had multiple origins and propagated along a crescent-shaped front (light area at bottom and right). Fractograph 4573 (center) is a TEM replica taken at one of the fatigue-crack origins in 4572. The angular, faceted topography here reflects strongly the influence of crystallographic orientation. The straight, fine lines visible in bands are of unknown source. Fine fatigue striations exist in the regions between the bands. Fractograph 4574 (right) is a TEM replica of another area in the nucleus region of the fracture surface in 4572. Angular facets show fatigue striations. The cause of the flat regions is not understood, but repeated replications showed the flatness to be real. The fine parallel lines are believed to represent two systems of slip (vertical, and at 30° to horizontal). See also fractographs 4575 to 4580 (opposite page), for TEM replicas of other areas of this fracture surface.

TEM Fractographs: U-700 Alloy Fractured by Fatigue at Room Temperature
(Continuation of a Series Begun on Facing Page)



TEM fractograph (p-c replica) 3300×

4575 TEM replica of a third area in nucleus region of fracture in 4572. Central area shows what appear to be irregular fatigue striations (at A and B). Fine marks on facets at C's are not artifacts or striations but may have resulted from abrasion by the mating fracture surface.



TEM fractograph (p-c replica) 3300×

4576 A TEM replica taken near (but not at) nucleus in 4572. Note extreme difference in appearance between areas A and areas B. Areas A show what may be very irregular striations. Features in areas B are not artifacts; they may indicate slip, or abrasion by the mating fracture surface.



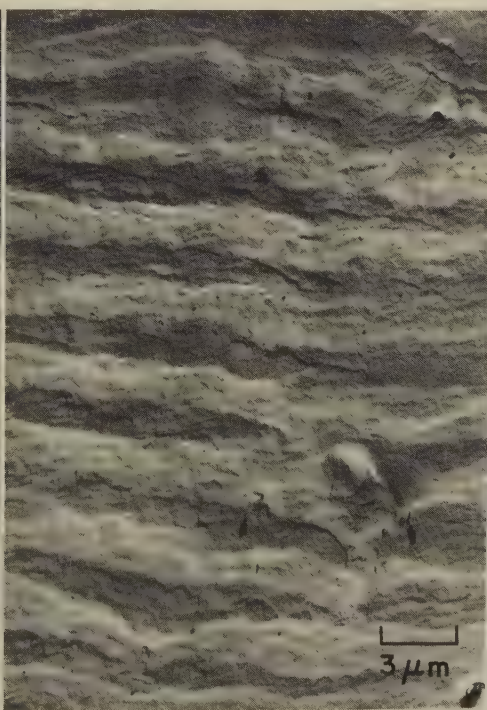
TEM fractograph (p-c replica) 3300×

4577 A TEM replica of an area well away from the fatigue-crack nucleus in 4572. Many fatigue striations here are very deep and distinct, suggesting the generation of secondary cracks; the relatively short length of these deep grooves may be due to microstructural influence.



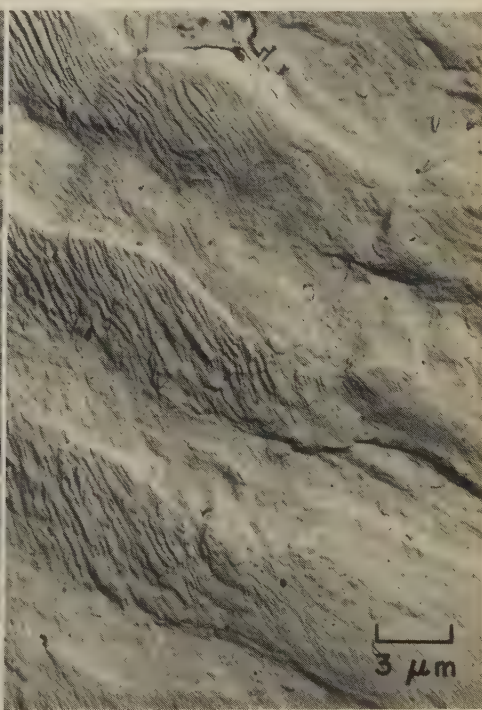
TEM fractograph (p-c replica) 3300×

4578 A TEM replica of another area well away from the fatigue-crack nucleus of the fracture in 4572. Unlike those in 4577, fatigue striations here are quite regular; they are also much more widely spaced, indicating appreciable crack penetration.



TEM fractograph (p-c replica) 3300×

4579 A TEM replica taken near the transition from fatigue to final, fast fracture in 4572. The reduction in remaining cross-sectional area, and the consequent increase in effective stress, has increased the spacing of the striations appreciably.



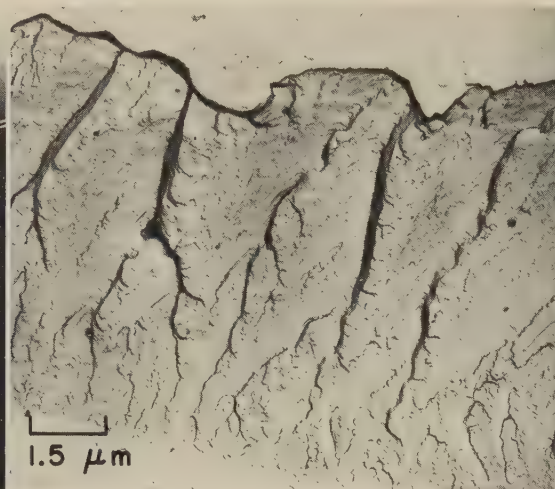
TEM fractograph (p-c replica) 3300×

4580 TEM replica taken at transition from fatigue to final, fast fracture in 4572. Fatigue-striation spacing is very wide. Secondary marks angling across each striation represent slip on a set of favorably oriented crystallographic planes.

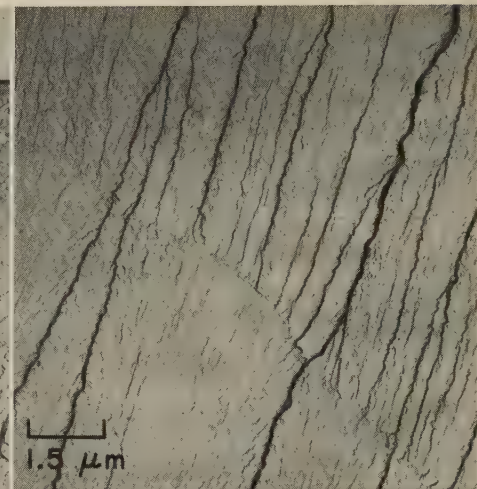
Light and TEM Fractographs: Notched As-Cast Specimen of Alnico Alloy Fractured by Impact at Room Temperature



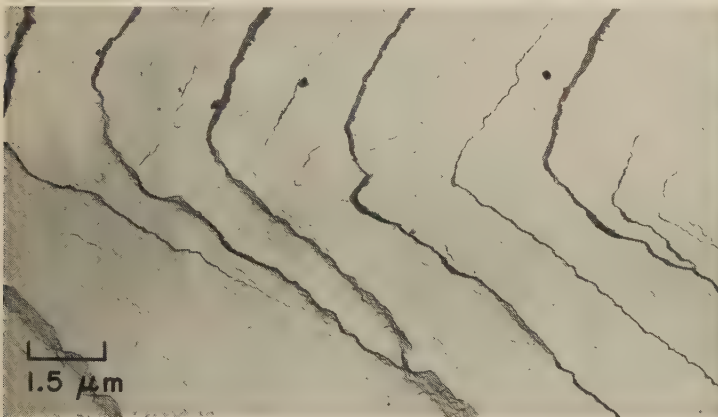
Light fractograph 5½×
4581 Surface of a "rock candy" fracture in a notched as-cast specimen of Alnico alloy broken by impact at room temperature, showing large, shiny facets. The brittle nature of this specimen is reflected in its unnotched tensile strength of only 34 MPa (5 ksi). See also 4582 to 4587.



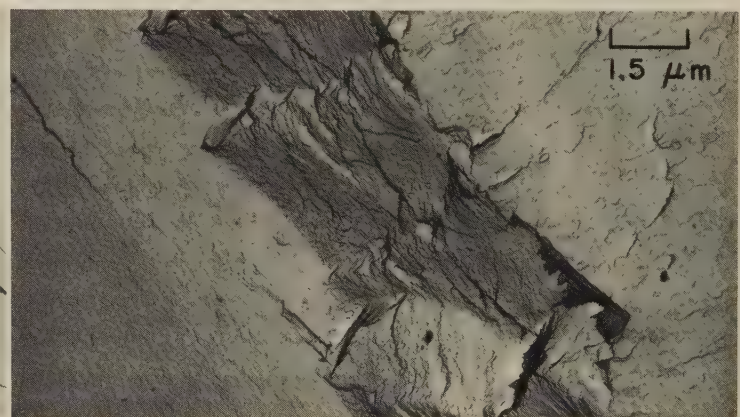
TEM fractograph (p-c replica) 6500×
4582 TEM replica of an area of the facet at the arrow in 4581, showing features resulting from transgranular cleavage. Pronounced cleavage steps in central region indicate that fracture progressed from bottom to top. The margins of this central region are believed to have formed at grain boundaries; the cause of the marked irregularity of the margin at top is not known.



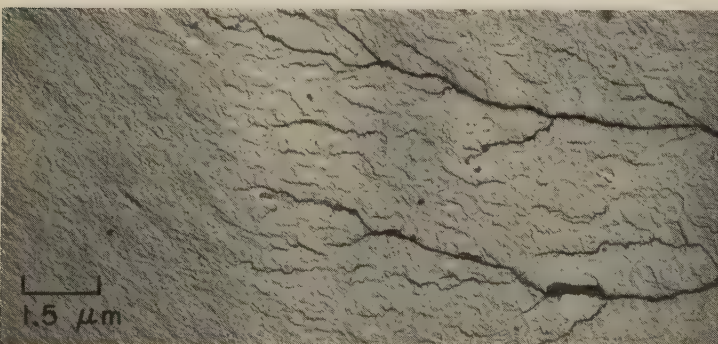
TEM fractograph (p-c replica) 6500×
4583 TEM replica of a second area of the facet at the arrow in 4581, showing features resulting from transgranular cleavage and cleavage steps that cross a tilt boundary extending from lower right to upper left. The approximate direction of crack propagation was from lower left to upper right.



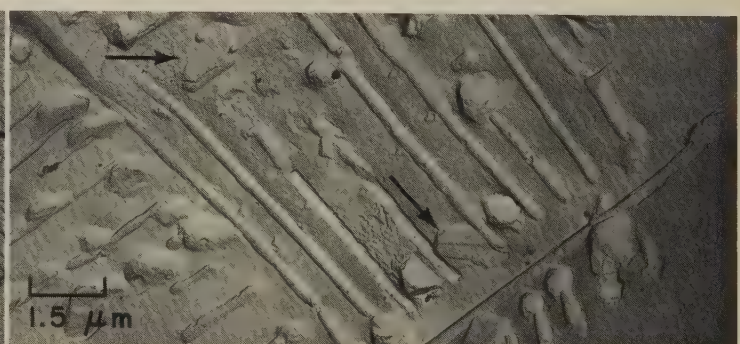
TEM fractograph (p-c replica) 6500×
4584 TEM replica of a third area of the facet at the arrow in the fracture surface shown in 4581. Although no sharp boundary is visible, it appears certain that the cleavage steps, which entered from the top in this view, cross a tilt boundary at mid-height, where they change direction.



TEM fractograph (p-c replica) 6500×
4585 TEM replica of a fourth area of the facet at the arrow in 4581, showing evidence that here fracture occurred in two different directions and on two different levels. The appearance of the fracture region that connects these two levels (diagonal dark band) has been markedly affected by local microstructure.

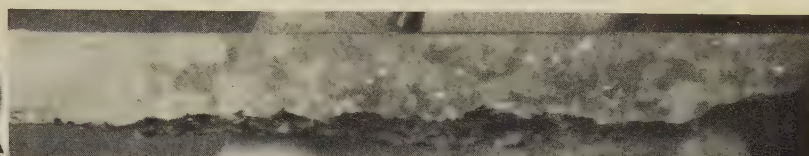
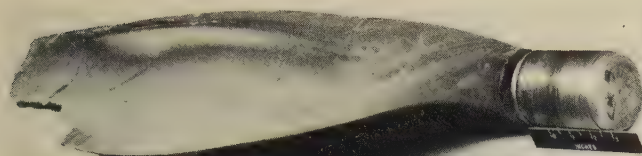


TEM fractograph (p-c replica) 6500×
4586 TEM replica of a fifth area of the facet at the arrow in 4581. The fracture entered this area from the left and, at a tilt boundary, began the formation of cleavage steps, creating a river pattern "flowing" toward the right.



TEM fractograph (p-c replica) 6500×
4587 TEM replica of a sixth area of the facet at the arrow in 4581. This area contains features that could be cleaved second-phase particles or imprints of pulled-out particles. Also visible is a geometric array of rodlike second-phase particles.

Photographs; Light and TEM Fractographs; Macrograph; Micrographs: Sand Cast Aluminum Alloy 319 Cooling-Tower Fan Blade Fractured Because of Stress-Corrosion Cracking



Photographs About 0.1× (4588); 0.4× (4589)

4588 Two photographs of a cooling-tower fan blade of aluminum alloy 319 (as sand cast) that fractured after about 20,000 hr of service in four years. Rated speed was 320 rpm. Fracture was attributed to stress-corrosion cracking that began in areas of shrinkage porosity produced during casting. See 4590 to 4597.

Macrograph — Keller's reagent (4590); light fractograph (4591)

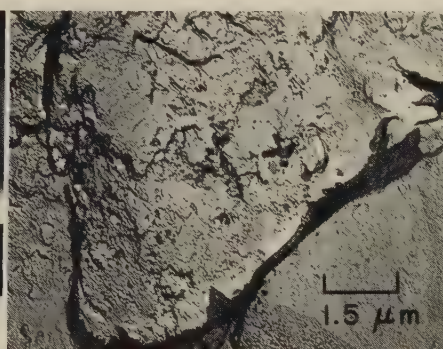
Both at 1½×

4590 Macrograph 4590 (top) shows a polished and etched section of the fan blade in 4588 and 4589, taken perpendicular to the fracture surface, which is shown obliquely at lower edge. Fractograph 4591 (bottom) shows a portion of the fracture surface. The region at right, which appears slightly darker than the region at left, contains casting defects. See 4593 to 4595 for views at A, B and C.



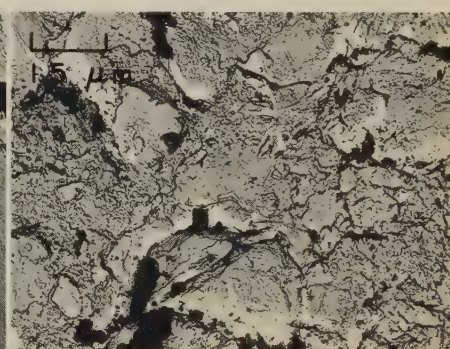
Photograph About 0.4×

4592 A view of the fracture surface of the aluminum alloy 319 fan blade shown in photographs 4588 and 4589. The darker area at top here corresponds to the region at right in 4591. Nominal operating stress (surface tension plus bending) was estimated as 17 MPa (2.5 ksi).



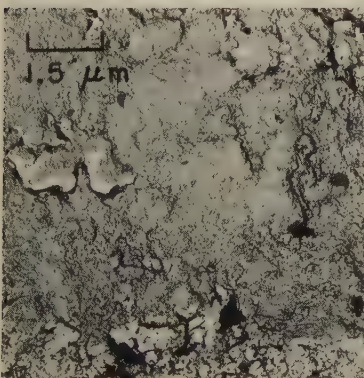
TEM fractograph (p-c replica) 6500×

4593 TEM replica of an area at A in the fracture surface in 4591, showing a casting defect (cold lap). No evidence of fatigue marks, or of impact by foreign objects, is visible.



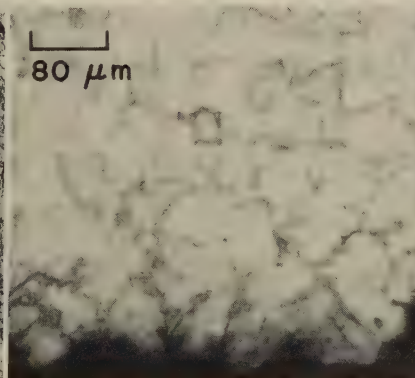
TEM fractograph (p-c replica) 6500×

4594 An area at B in 4591. Here, the surface appears intergranular in part, but also shows transgranular cleavage facets. Note unexplained fine "ripples", both here and in 4593.



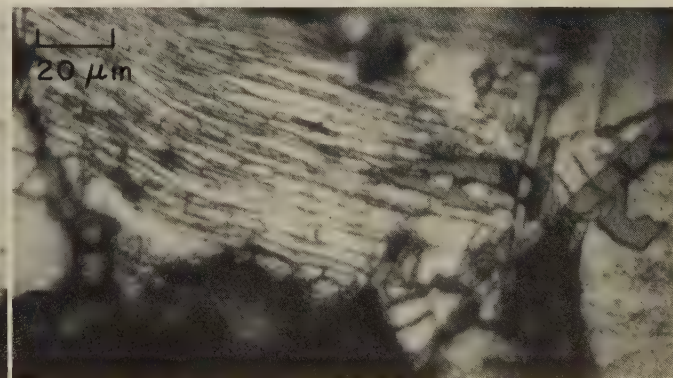
TEM fractograph (p-c replica) 6500×

4595 TEM replica taken from an area at C in 4591. This area is in the lighter region at left in 4591, which was found to be generally flat and to contain both intergranular and transgranular facets.



Micrograph (Keller's reagent) 125×

4596 A polished and etched section of the fan blade shown in 4588 and 4589, taken perpendicular to the fracture surface at C in 4591. The aluminum matrix contains a nearly continuous dendritic network of hard precipitate particles.



Micrograph (Keller's reagent) 500×

4597 Polished and etched section of the fan blade shown in 4588 and 4589, taken perpendicular to the fracture surface in the region at right in 4590, near a large casting defect. The parallel lines are not fatigue striations but rather are a series of parallel straight cracks, which suggest severe local embrittlement of the matrix; these small cracks are believed to have promoted stress-corrosion cracking.

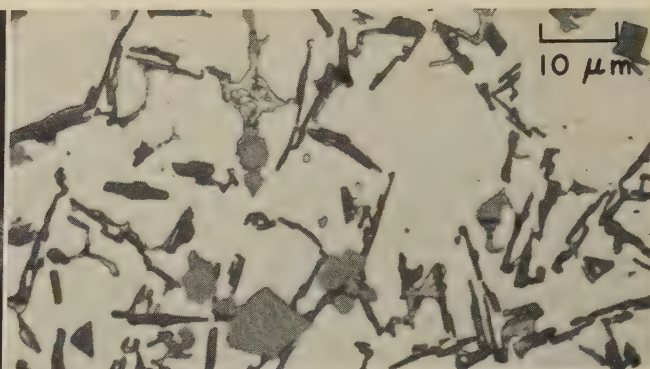
Light and TEM Fractographs, Light and TEM Micrographs: Aluminum Alloy 380 Die-Cast Steering-Gear Covers Fractured in One-Way-Bending Fatigue Tests



Light fractograph

2×

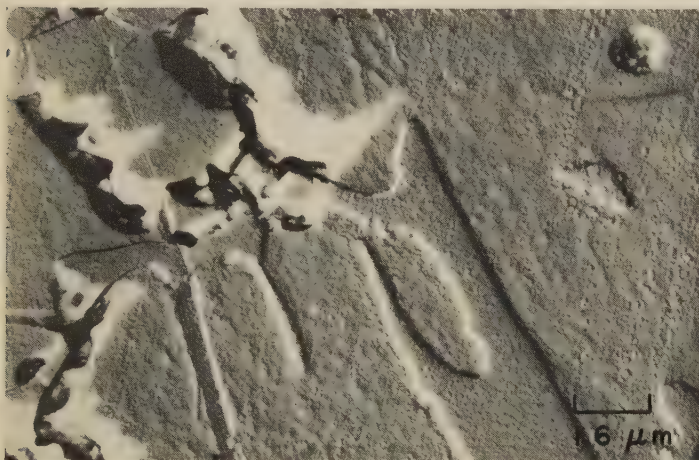
4598 A fatigue-test fracture in a steering-gear upper cover, die cast of aluminum alloy 380. The cover was tested in one-way-bending fatigue with a load of 17,120 newtons (3850 lb) and broke at 13,300 cycles. The fatigue cracks are the lighter areas on the lower side of the fracture surface; four crack origins are visible (arrows). See also 4599 to 4603.



Light micrograph (etchant: 0.5% HF in water)

1000×

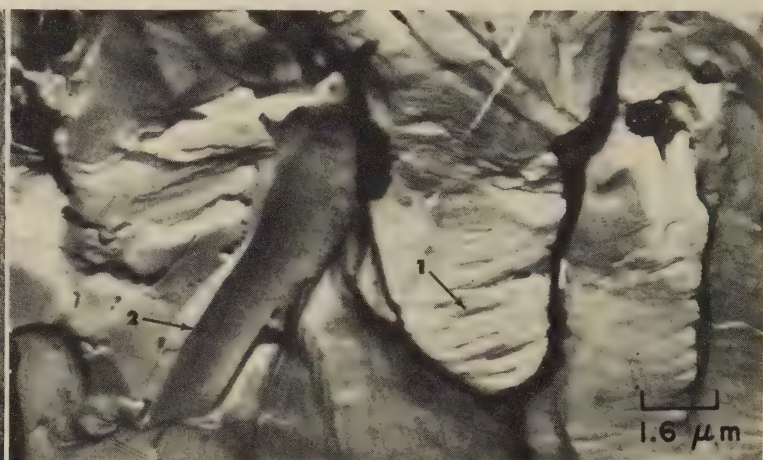
4599 A polished and etched section through a specimen of the die-cast aluminum alloy 380 used for the cover in 4598. The white background is the aluminum matrix. Scattered through it are second-phase particles. See also micrograph 4600.



TEM micrograph (etchant: 0.5% HF in water); p-c replica

6100×

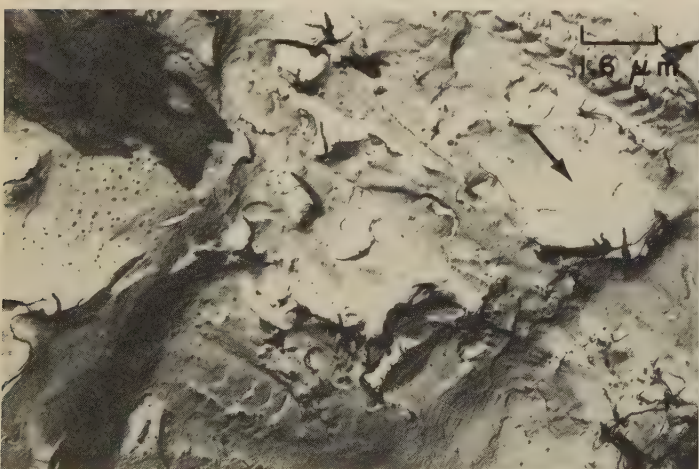
4600 TEM replica of the polished and etched surface of the specimen in 4599. This shows some of the angular second-phase particles in relief, thus permitting comparison of particle size with features in TEM fractographs 4601-4603, which follow.



TEM fractograph (p-c replica)

6100×

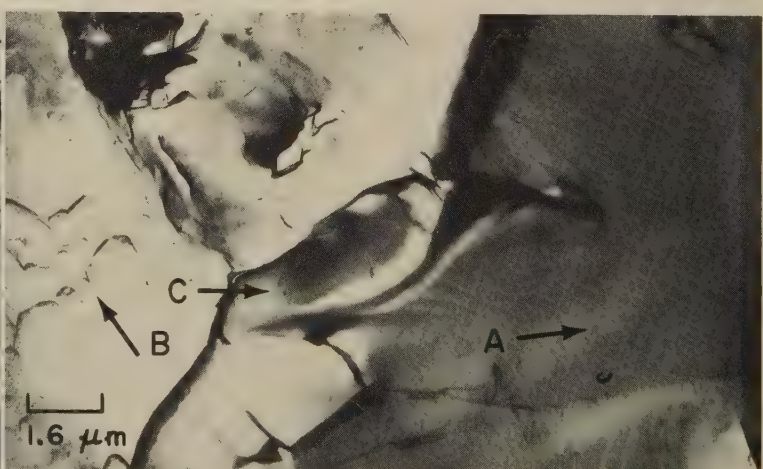
4601 A TEM replica obtained from the fracture surface shown in 4598. Within the aluminum matrix there are the well-defined fatigue striations (arrow 1) of a conventional fatigue fracture. The intermetallic compounds, however, fractured by cleavage (arrow 2).



TEM fractograph (p-c replica)

6100×

4602 A TEM replica of a one-way-bending fatigue fracture in a steering-gear upper cover similar to that in 4598 except tested at a load of 21,740 newtons (4890 lb) and broken at 100 cycles. Typical "tire tracks" are visible at upper right, and slightly below and to left of center. There appear to be stretched areas (as at arrow). Intermetallic compounds fractured by cleavage.

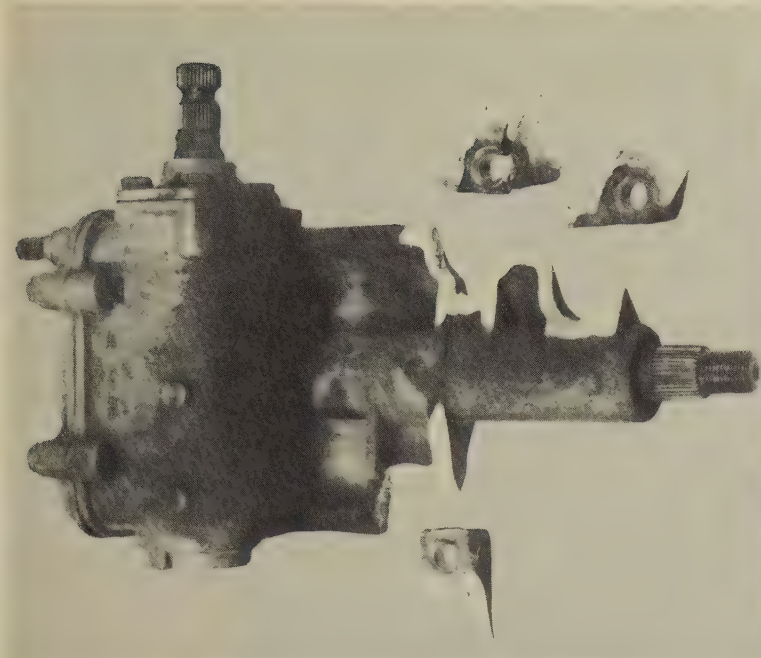


TEM fractograph (p-c replica)

6100×

4603 A TEM replica taken from the fracture surface of a third steering-gear cover, die cast of aluminum alloy 380, which broke on the first cycle of loading at 40,650 newtons (9140 lb). Fracture of the matrix was predominantly intergranular (arrow A), although isolated areas show elongated dimples (arrow B). Second-phase particles fractured by cleavage (arrow C).

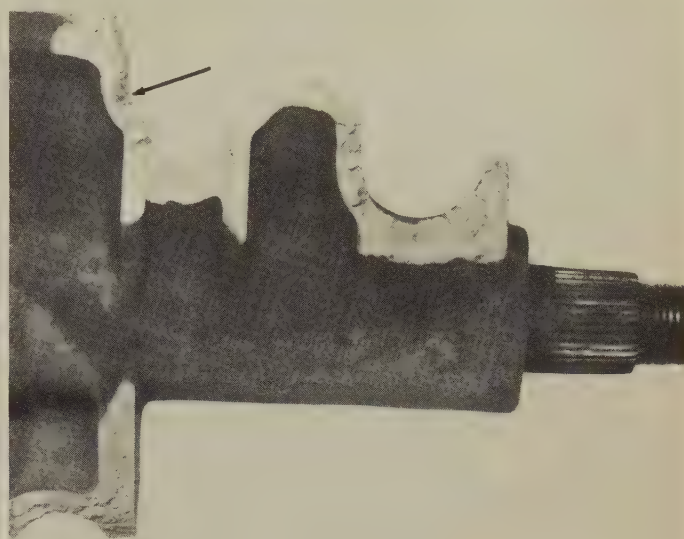
Photograph, Light Fractographs, TEM Fractograph: Aluminum Alloy 380
Die-Cast Steering-Gear Housing Fractured by Impact in Test



Photograph

About $\frac{1}{4} \times$

4604 A steering-gear housing, die cast of aluminum alloy 380, which fractured at the mounting-bolt bosses under a test impact. The steering gear was mounted on a movable sled and rammed into a barricade, tearing the housing from the frame. The three fractured bosses are shown near the locations from which they broke. See also 4605 to 4607.



Light fractograph

$\frac{1}{2} \times$

4605 A half-size view of the fracture surfaces on the steering-gear housing in 4604. This view does not include the mounting-bolt bosses. The arrow marks the mating surface to that of the boss shown in fractograph 4606, below.



Light fractograph

$2 \times$

4606 Fracture surfaces of the mounting-bolt boss that was separated from area at arrow in 4605 by the impact. Note the chevron marks faintly visible along the lower edge of the fracture surface at left; these point diagonally upward to the right toward the fracture origin. See 4607 (right) for a TEM replica of the area containing the chevron marks.

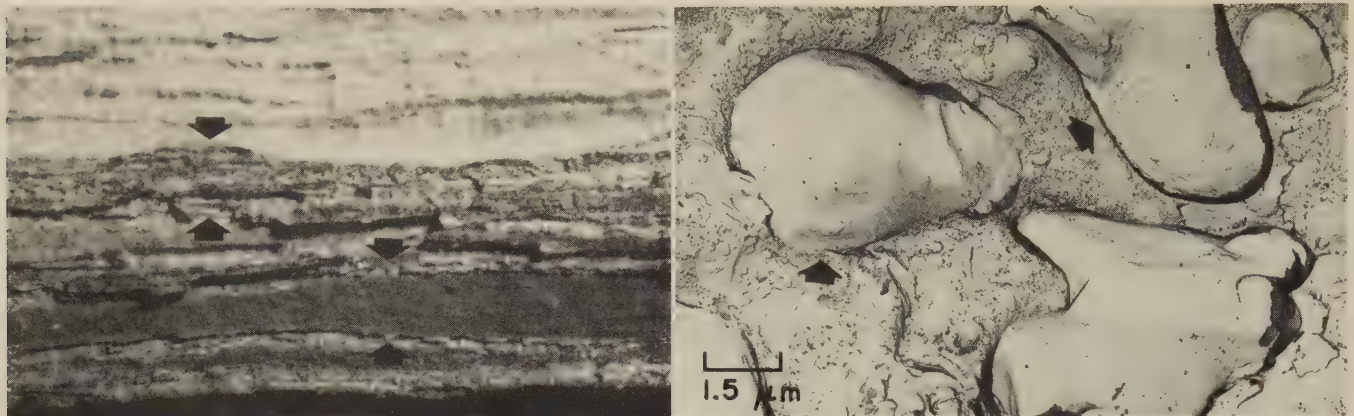


TEM fractograph (p-c replica)

$6100 \times$

4607 A TEM replica of the area containing the chevron marks in 4606. Some features here appear to be artifacts caused by difficulty in stripping the plastic replica. The fracture surface is predominantly intergranular (as at A). Second-phase particles fractured by cleavage (B).

Light and TEM Fractographs: Aluminum Alloy 2018 Forging Fractured Because of Nonmetallic Inclusions; Aluminum Alloy 2024-T3 Fractured by Fatigue at Different Amplitudes



Light fractograph

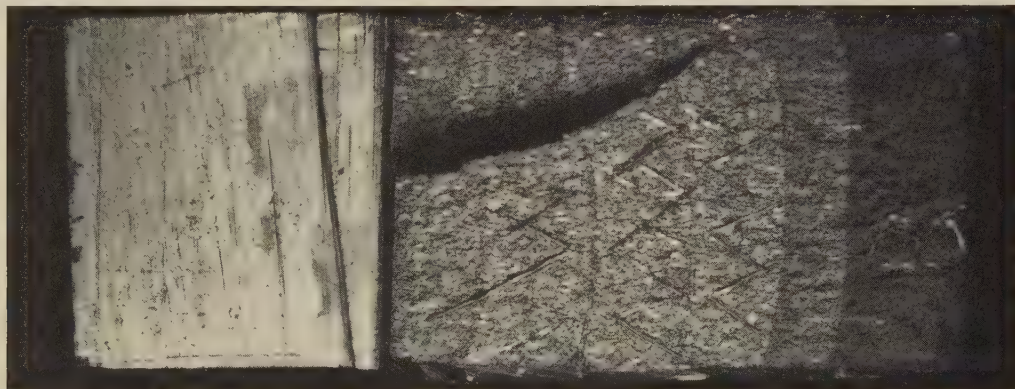
20×

TEM fractograph (p-c replica)

6500×

4608, 4609

Light and TEM views of two areas of the surface of a fracture in a forging of aluminum alloy 2018, showing segregated inclusions. Fractograph 4608 (left) shows bands (between pairs of arrows) containing slag (lower band), and other residue (upper band), entrapped during casting of the forging ingot. Fractograph 4609 (right) is a TEM replica of an area in one of the bands in 4608, showing globular inclusions (as at arrows). Some of these inclusions exhibit conchoidal solidification marks. The areas between the inclusions contain oxide residues and evidence of poor bonding.

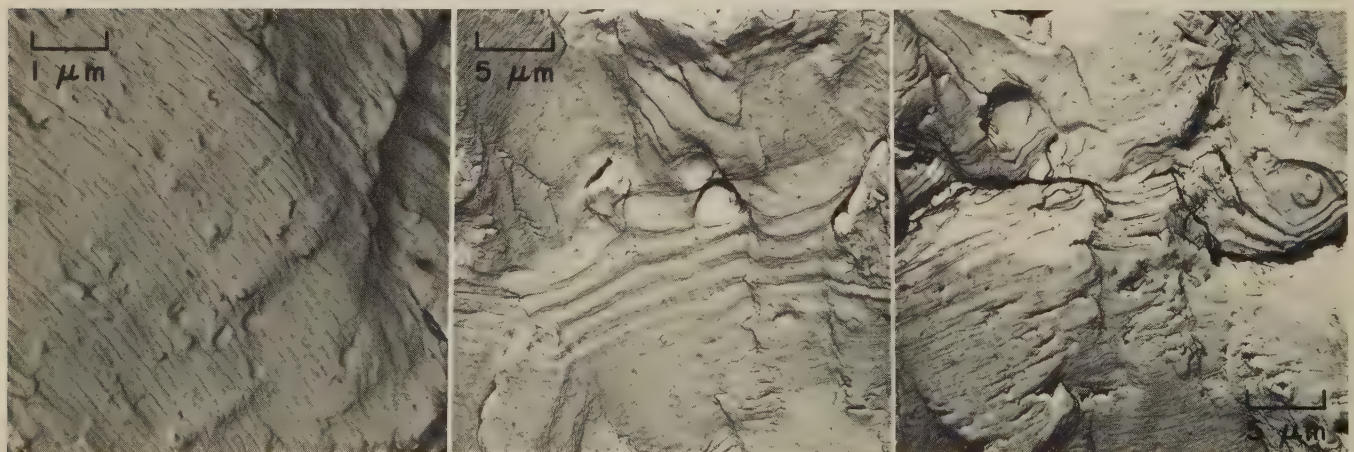


Light fractograph

8×

4610

Surface of a fatigue fracture in a notched specimen of aluminum alloy 2024-T3 that was cracked in stages using different amplitudes. The third zone from right (six zones are visible), for instance, was produced at a low amplitude whereas the second zone from right was formed at a high amplitude. Crack growth (left to right) was produced by cantilever bending, generally at 2.5 cycles per second, with minimum load always zero. See also 4611 to 4615.



TEM fractograph (p-c replica)

10,000×

TEM fractograph (p-c replica)

2000×

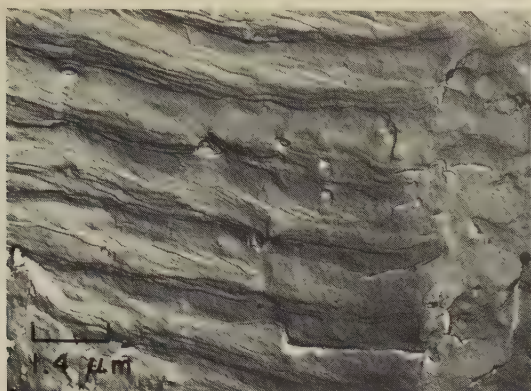
TEM fractograph (p-c replica)

2000×

4611 TEM replica of a low-amplitude area of the fracture surface in 4610. Stress-intensity range (ΔK) was 11 MPa·m^{1/2} (10 ksi·in.^{1/2}). The major portion of each striation is flat or, at most, slightly contoured. The striations are delineated by fissures or crevices.

4612, 4613 TEM replicas of mating areas of the fatigue fracture of which one entire surface is shown in 4610. Fatigue striations generated by five high-amplitude cycles (center) are bounded by striations generated by low-amplitude cycles. Stress-intensity range (ΔK) was 21 MPa·m^{1/2} (19 ksi·in.^{1/2}). The five widely spaced striations are well preserved in fractograph 4612 (left), but 4613 (right) shows only randomly spaced fissures that resulted from extraneous slip, which occurred after the crack front had passed by.

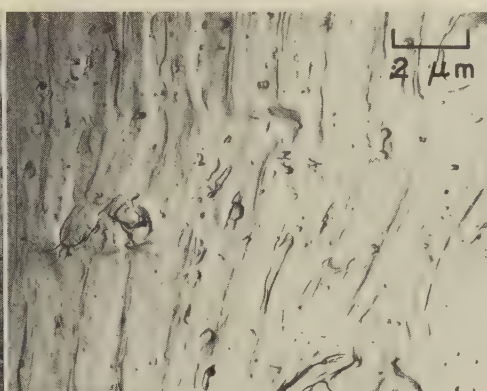
Light and TEM Fractographs: Aluminum Alloy 2024-T3 Fractured by Fatigue (Continued);
Aluminum Alloy 2024-T851 Plate Fractured by High-Cycle Fatigue



TEM fractograph (p-c replica)

7000×

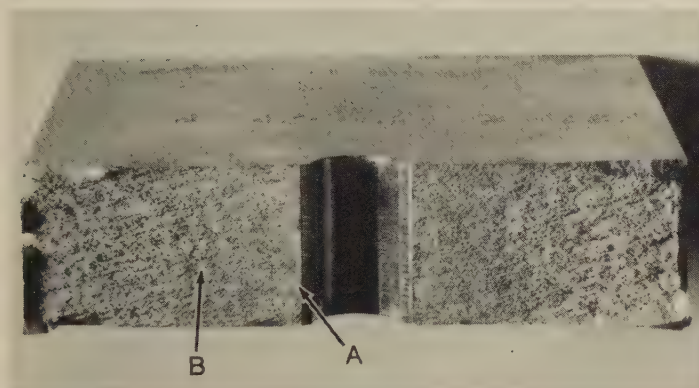
4614 TEM replica of an area in 4610 (facing page) that shows fatigue striations produced at high amplitudes. The center region of each striation is quite smooth, almost as if created by stretching; the regions between these center regions are rumpled and convex (when observed in correct stereoscopic perspective). Also visible are occasional tear dimples, each of which extends across a striation.



TEM fractograph (p-c replica)

5000×

4615 TEM replica of another area in 4610 showing fatigue striations produced at high amplitudes. Here the striations are much less sharply defined than in 4614. Numerous small tear dimples are present. Comparison with the mating surface (not shown) revealed that reverse plastic flow during the closing half of the fatigue cycle modified the two faces independently.

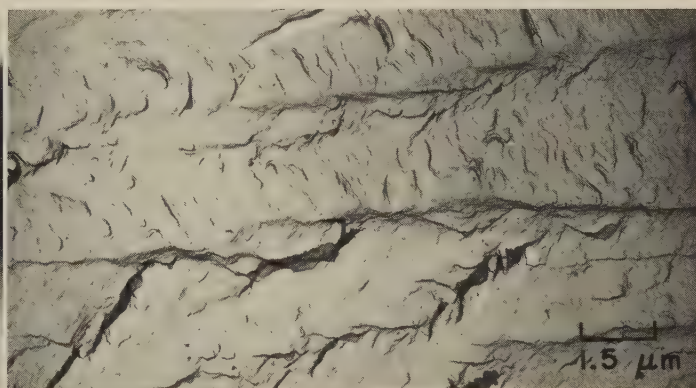


Light fractograph

Actual size

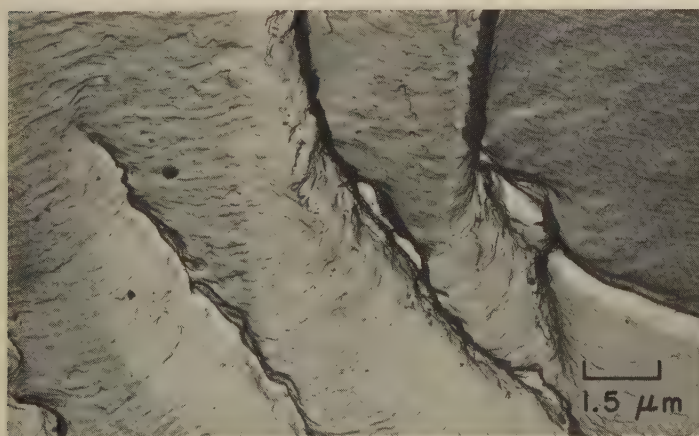
4616, 4617

Fractograph 4616 (left) shows the surface of a high-cycle fatigue fracture in a notched specimen of aluminum alloy 2024-T851 plate with a tensile strength of 490.2 MPa (71.1 ksi). The fracture exposed a hole drilled through the center of the specimen and notches immediately to left and right of the hole. The specimen was loaded in tension transverse to the grain direction, at room temperature, to a stress cycled from 22.7 to 64.8 MPa (3.3 to 9.4 ksi), and broke after 229,700 cycles. The fracture surface is flat and shiny with a shear lip at each end. Fractograph 4617 (right) is a TEM replica of the fracture surface at the notch (marked A) in 4616, showing fatigue patches containing vaguely defined striations. See 4618 and 4619 for TEM replicas of two areas at arrow B in 4616.



TEM fractograph (p-c replica)

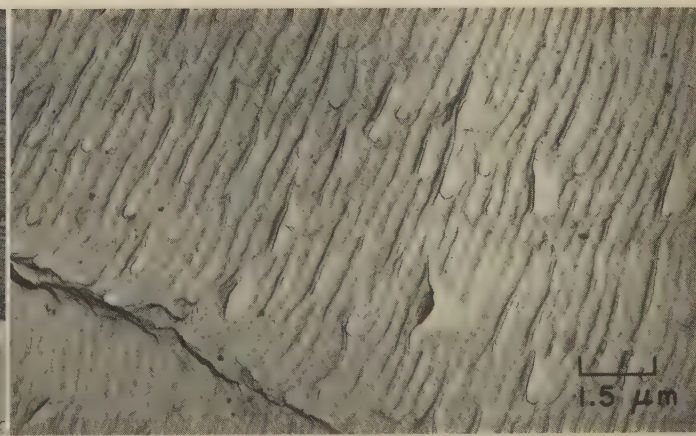
6500×



TEM fractograph (p-c replica)

6500×

4618 TEM replica of an area at arrow B in 4616, showing regular, well-defined fatigue striations in patches created by local crack fronts. These patches occasionally subdivide, as seen at top left, at a discontinuity such as an intermetallic particle.

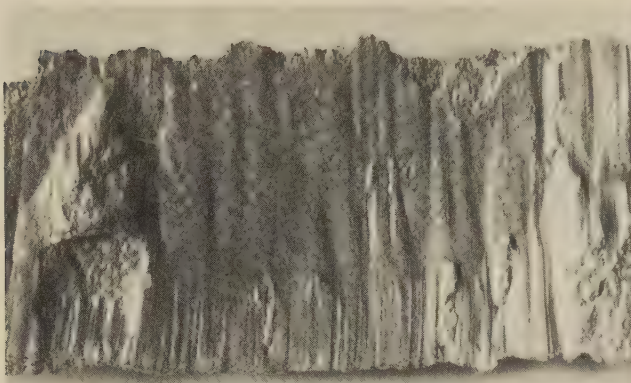


TEM fractograph (p-c replica)

6500×

4619 TEM replica of another area at arrow B in 4616. In this area, there are numerous fissures among the fatigue striations, and it is difficult to distinguish random fissures from crack-closure fissures delineating striations.

Light Fractographs and TEM Fractographs: Three Aluminum Alloy 7075-T6 Forgings That Fractured as a Result of Forging Defects



Light fractograph

4620, 4621



2× TEM fractograph (p-c replica)

6500×

Light and TEM views of the surface of a fracture in a forged part of aluminum alloy 7075-T6. The fracture was caused by internal shearing during the forging operation. Internal shearing, which usually is termed "flow-through", is a defect that frequently extends through the full thickness of the part. The characteristics of the flow induced during forging are visible in 4620 (left). Fractograph 4621 (right) is a TEM replica of an area of the fracture surface in 4620, showing a surface that is flat and virtually featureless, with vague indications of grain boundaries.



Light fractograph

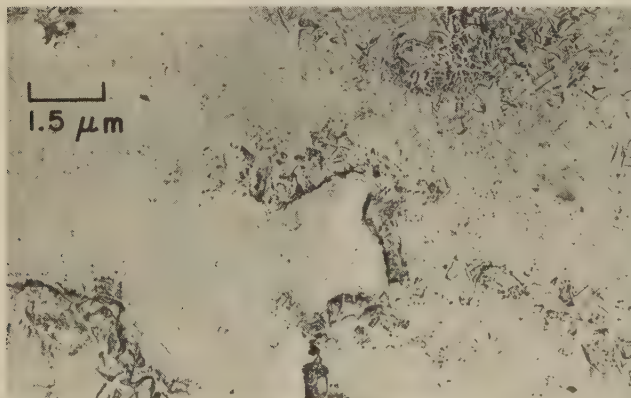
4622, 4623



3× TEM fractograph (p-c replica)

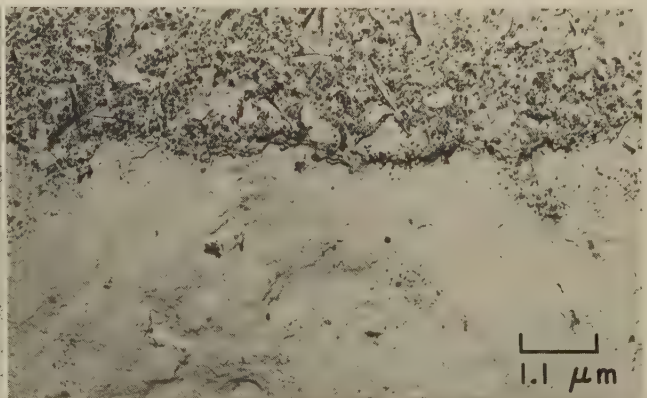
6500×

Light and TEM views of the surface of a fracture in a forged part of aluminum alloy 7075-T6. The fracture originated at cold shuts that resulted from the closing of forging laps. The surface of one cold shut is shown bounded by the arrows in 4622 (left); this surface is fairly flat and bears a layer of oxide particles. Fractograph 4623 (right) is a TEM replica of an area of the cold-shut surface in 4622, showing oxide, and black regions that may be particles picked up from the fracture surface by the replica.



TEM fractograph (p-c replica)

4624, 4625

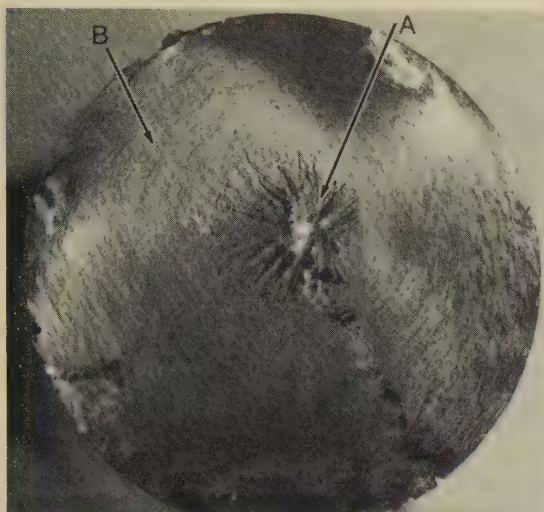


6500× TEM fractograph (p-c replica)

9300×

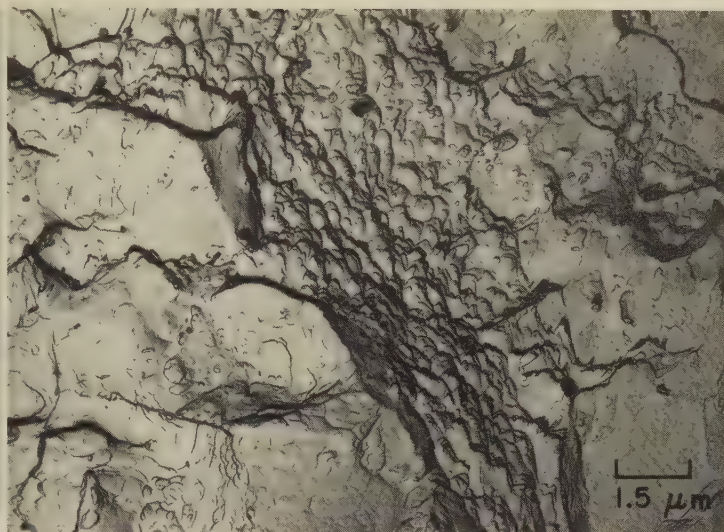
TEM replicas of two areas of the surface of a fracture in a forged aluminum alloy 7075-T6 support for a cargo-door cylinder. The fracture, which originated at a cold shut, formed at an attachment hole that extended above and below the cold shut. These TEM replicas reveal that the fracture surface is flat and encrusted with oxide particles.

Light and TEM Fractographs of Aluminum Alloy 7075-T6: Torsion-Overload Fracture in a Forged Billet; Impact Fracture in an Aircraft Component



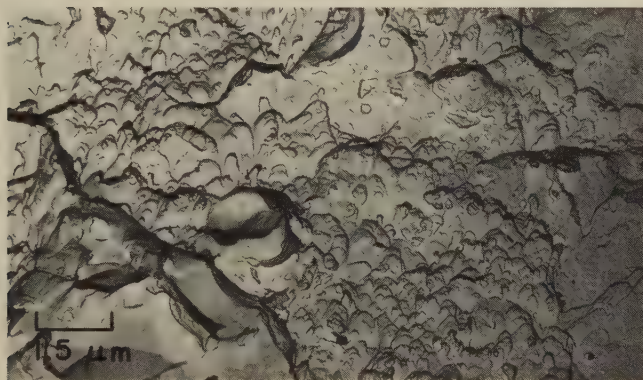
Light fractograph 5×

4626 A torsion-overload fracture in a forged billet of aluminum alloy 7075-T6, with a tensile strength of 572 MPa (83 ksi), that broke at room temperature. Flat, silky outer portion of fracture surface was rubbed in torsion. Note star-shaped pattern at center. See 4627 to 4629.



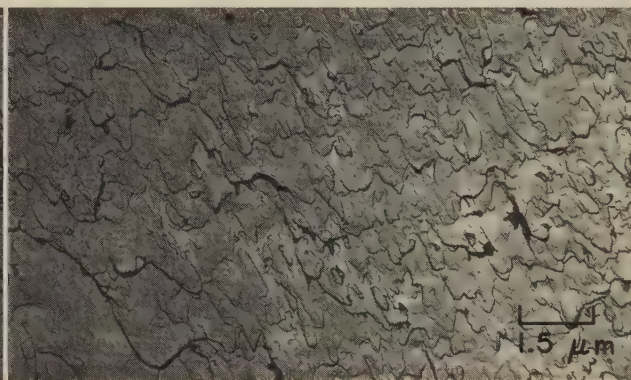
TEM fractograph (p-c replica) 6500×

4627 TEM replica of an area within the star-shaped pattern at arrow A in the center of the fracture surface shown in fractograph 4626. Broad regions containing dimpled separated-grain facets are present, as well as many adjacent flat facets that are suggestive of transgranular cleavage.



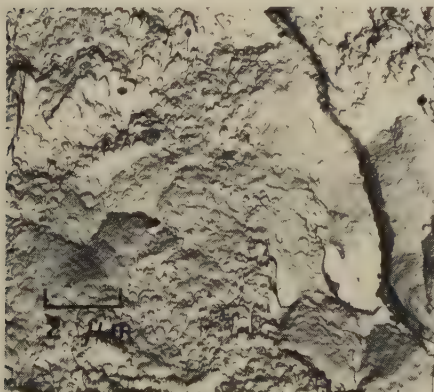
TEM fractograph (p-c replica) 6500×

4628 TEM replica of an area at arrow B in the outer portion of the fracture surface in 4626. Shear dimples such as those shown here were found throughout this portion of the fracture. The feature at bottom left apparently is a cleaved intermetallic particle.



TEM fractograph (p-c replica) 6500×

4629 TEM replica of another area at arrow B in fractograph 4626. This area shows very flat shear dimples, which are interpreted as reflecting in part the rubbing that resulted from the torsional strain that occurred after the crack front had passed by.



TEM fractograph (p-c replica) 5000×

4630 TEM replica of an area of the surface of an impact fracture in an aircraft component of aluminum alloy 7075-T6, showing very fine shear dimples. See also 4631 and 4632.



TEM fractograph (p-c replica) 5000×

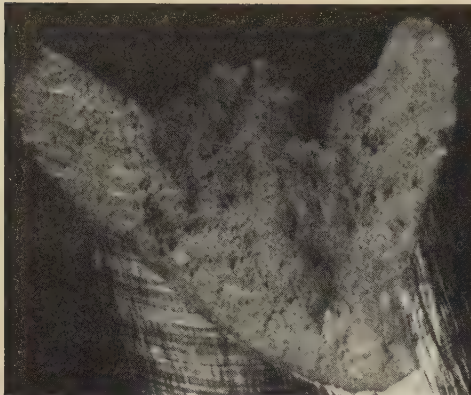
4631 TEM replica of another area of the fracture surface shown in 4630. This area contains rather uniformly sized and uniformly oriented elongated dimples. Crack propagation was from top to bottom.



TEM fractograph (p-c replica) 5000×

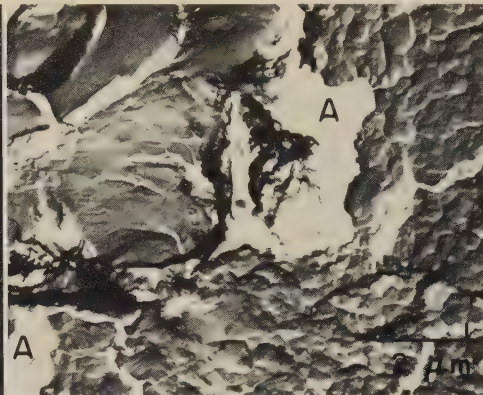
4632 TEM replica of a third area of the fracture surface in 4630 and 4631, showing cleavage facets that may contain fine precipitates. These facets are interspersed with small regions of equiaxed dimples.

Light Fractographs and TEM Fractographs: Aluminum Alloy 7075-T6 Unnotched and Notched Specimens Fractured by Tension Overload

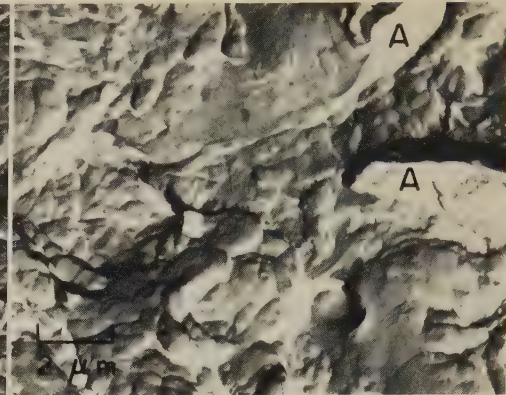


Light fractograph

4633, 4634, 4635



9x TEM fractograph (p-c replica)



5000x TEM fractograph (p-c replica)

5000x

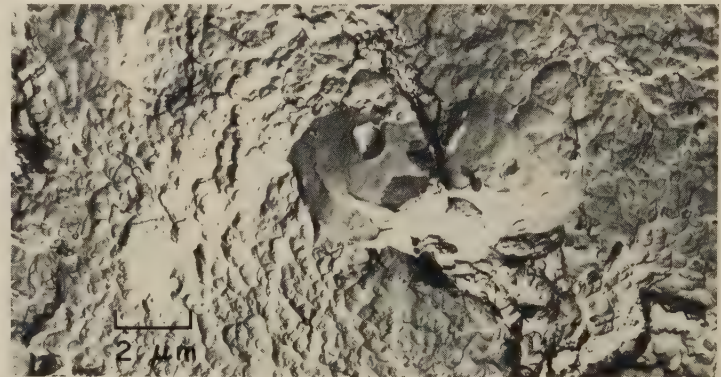
Fractograph 4633 (left) shows the surface of a tension-overload fracture in an unnotched specimen of aluminum alloy 7075-T6 with a tensile strength of 520.6 MPa (75.5 ksi). Fractograph 4634 (center) is a TEM replica of an area in the central region of the fracture surface in 4633, showing uniform fine dimples and exposed surfaces of precipitate particles. Fractograph 4635 (right) is a TEM replica of another area in the central region of the fracture surface in 4633, showing dimples similar in size to those in 4634. In both 4634 and 4635, secondary cracks appear only as voids in the shadowing (white areas marked A). See fractograph 4636 for a TEM view of a third area of this fracture surface.



TEM fractograph (p-c replica)

5000x

4636 TEM replica of an area in the central region of the fracture surface in 4633 nearer the shear lip than the areas in 4634 and 4635, showing small dimples that appear to be slightly elongated. The large feature at center apparently is the surface of a precipitate particle exposed by the fracture.



TEM fractograph (p-c replica)

5000x

4637 TEM replica of an area of the tension-overload fracture surface shown in 4638 (below, left). This area is composed mainly of fine dimples that in general appear to be equiaxed. A large dimple at center appears to contain a stretched-out hole that was left when a precipitate particle was pulled out.



Light fractograph

4638 Tension-overload fracture in a notched specimen of aluminum alloy 7075-T6 with a notched tensile strength of 748.1 MPa (108.5 ksi). Unnotched tensile strength, same as in 4633. The surface is fibrous, with numerous secondary cracks. See also 4637, 4639 and 4640.



TEM fractograph (p-c replica)

5000x

4639 TEM replica of an area of the fracture surface in 4638 showing cleavage facets of precipitate particles (lower right) and a region that appears to have been stretched (far lower right).



TEM fractograph (p-c replica)

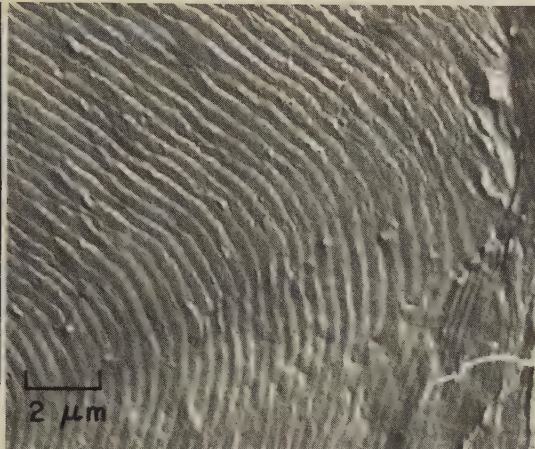
5000x

4640 TEM replica of an area of the fracture surface in 4638 showing small dimples, slightly asymmetrical in some regions. At right of center are two cleavage facets of precipitate particles.

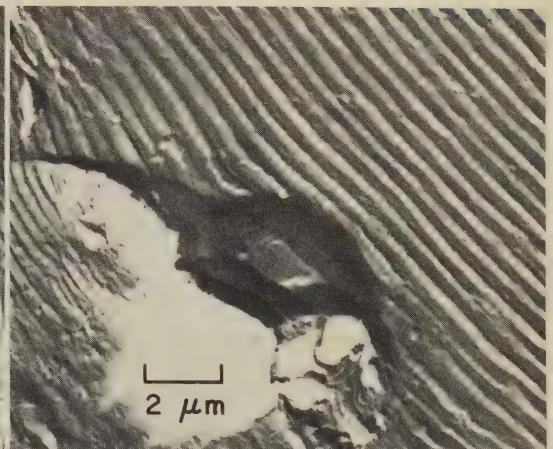
Light and TEM Fractographs: Aluminum Alloy 7075-T6 Specimens Fractured by Low-Cycle and High-Cycle Fatigue



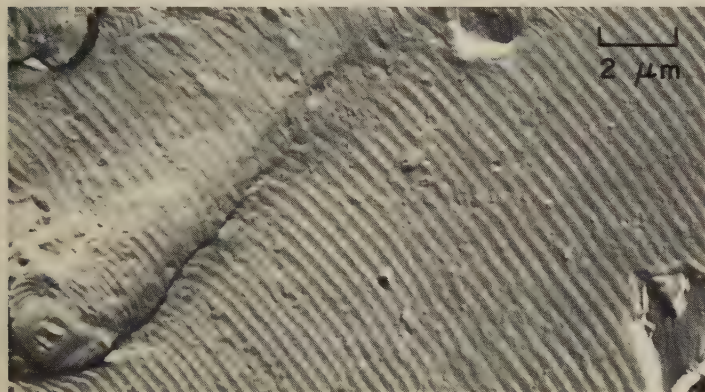
Light fractograph 6×
4641 Surface of a low-cycle fatigue fracture in a specimen of aluminum alloy 7075-T6 (same tensile strength as in 4633) tested in tension-tension ($R = 0.1$) with a maximum stress of 310 MPa (45 ksi). Specimen broke after 26,000 cycles. See fractographs 4642 to 4644.



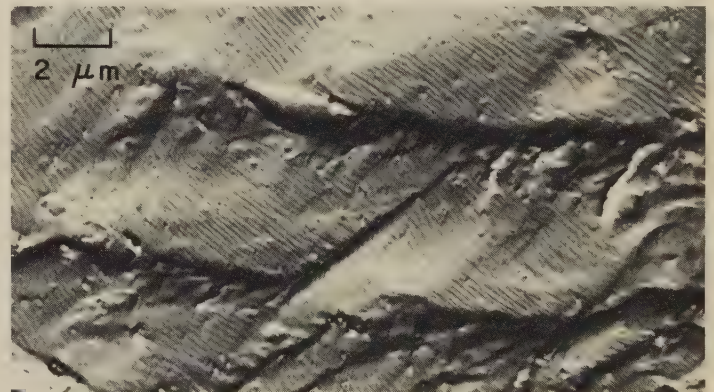
TEM fractograph (p-c replica) 5000×
4642 TEM replica of an area at the edge of the fracture surface in 4641, where fatigue striations apparently continue on the rounded edge of the specimen, which is severely deformed. Note the uniform change in direction of the striations.



TEM fractograph (p-c replica) 5000×
4643 TEM replica of another area of the fracture surface in 4641, showing a pattern of very sharply defined fatigue striations interrupted by a precipitate particle just below center. Note the closer spacing of the striations just to left of the precipitate particle.



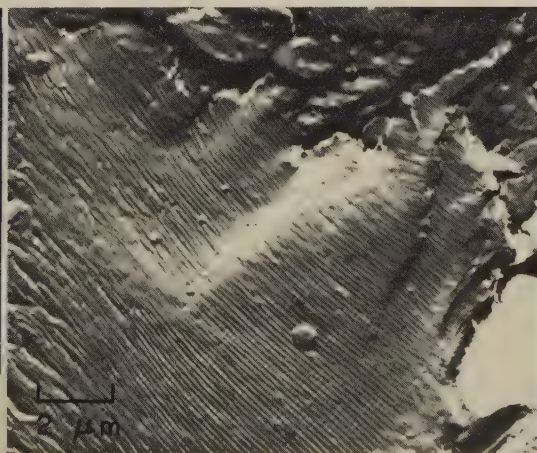
TEM fractograph (p-c replica) 5000×
4644 TEM replica of a third area of the fracture surface in 4641, showing portions of three fatigue-striation patches. Secondary cracks are visible between the patches.



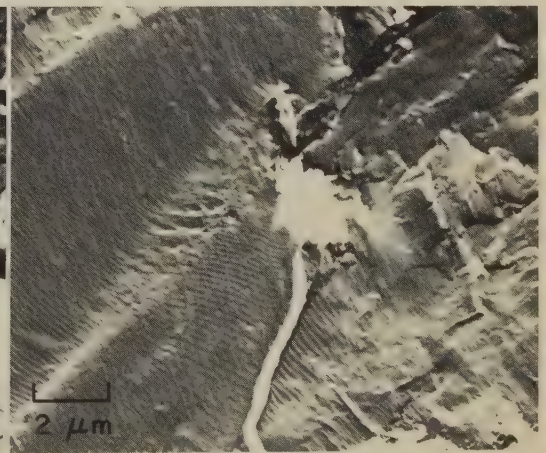
TEM fractograph (p-c replica) 5000×
4645 TEM replica of area near edge of fracture in 4646 (below, left), showing uniform fatigue striations interrupted by local steps where cracks at different levels joined.



Light fractograph 6×
4646 Surface of a high-cycle fatigue fracture in a specimen of aluminum alloy 7075-T6 (same tensile strength as in 4633) tested in tension-tension ($R = 0.1$) with a maximum stress of 152 MPa (22 ksi). Specimen broke after 548,000 cycles. Gouge at center was made after fracture. See 4645, 4647 and 4648.

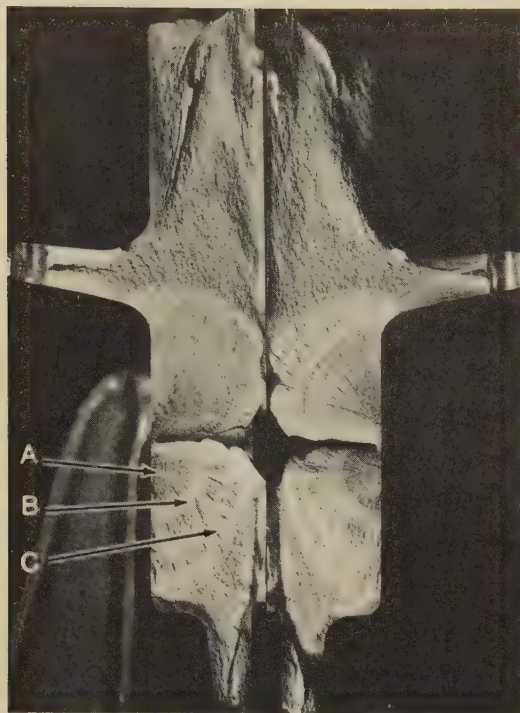


TEM fractograph (p-c replica) 5000×
4647 TEM replica of an area near the edge of the fracture surface in 4646 showing a system of steps (at top). What appears to be a void at lower right more probably is the result of a tear in the replica. The striation spacing here is very similar to that in 4645 and 4648.



TEM fractograph (p-c replica) 5000×
4648 TEM replica of another area near the edge of the fracture surface in 4646, showing several fatigue patches separated by off-sets. The lack of clearly defined striations at upper right indicates that this region may be near a crack origin.

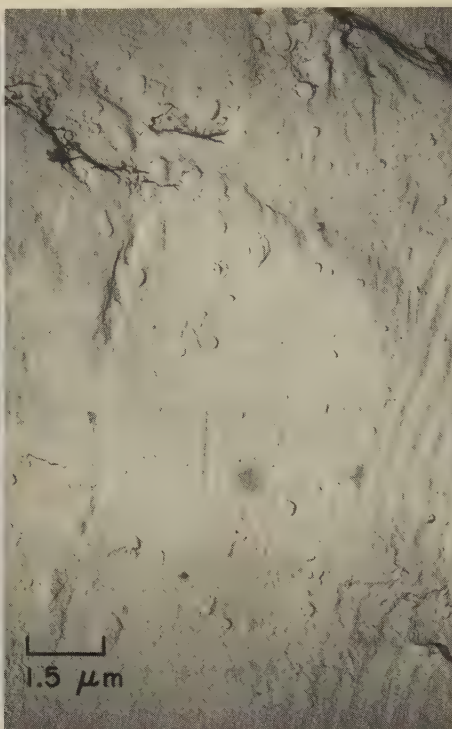
Light and TEM Fractographs of Aluminum Alloy 7075-T6: Extrusion Fractured by High-Cycle Fatigue; Forged Fitting Fractured by Stress Corrosion



Light fractograph

Actual size

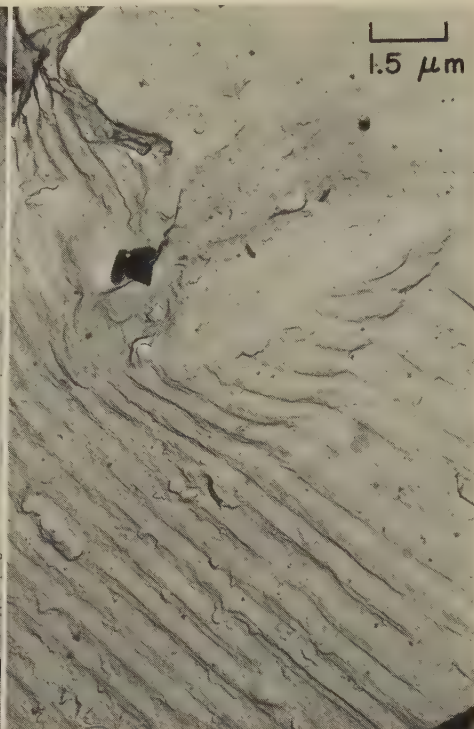
4649 Mating surfaces of a high-cycle fatigue fracture in an aluminum alloy 7075-T6 extrusion (tensile strength, 572 MPa or 83 ksi) subjected to a test program (repeated 16½ times) of 2000 cycles at each of 19 load patterns; fracture occurred after 629,035 cycles. Note "clamshell" marks on both sides of drilled hole. See 4650 to 4652 for TEM views of areas at arrows.



TEM fractograph (p-c replica)

6500×

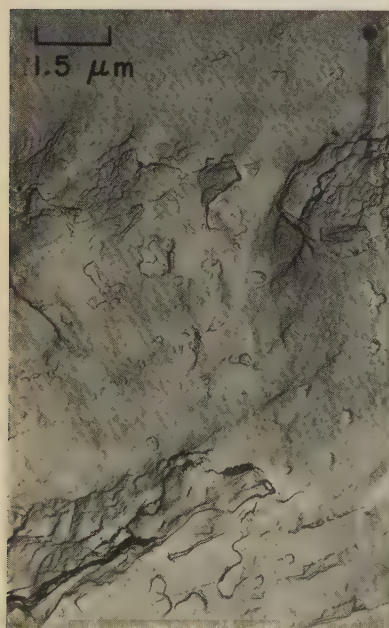
4650 TEM replica taken from an area at arrow A in the fatigue-fracture surface shown in fractograph 4649, near (but not at) the fatigue-crack nucleus. The difference in spacing of the fatigue striations from left to right reflects an increase in loading.



TEM fractograph (p-c replica)

6500×

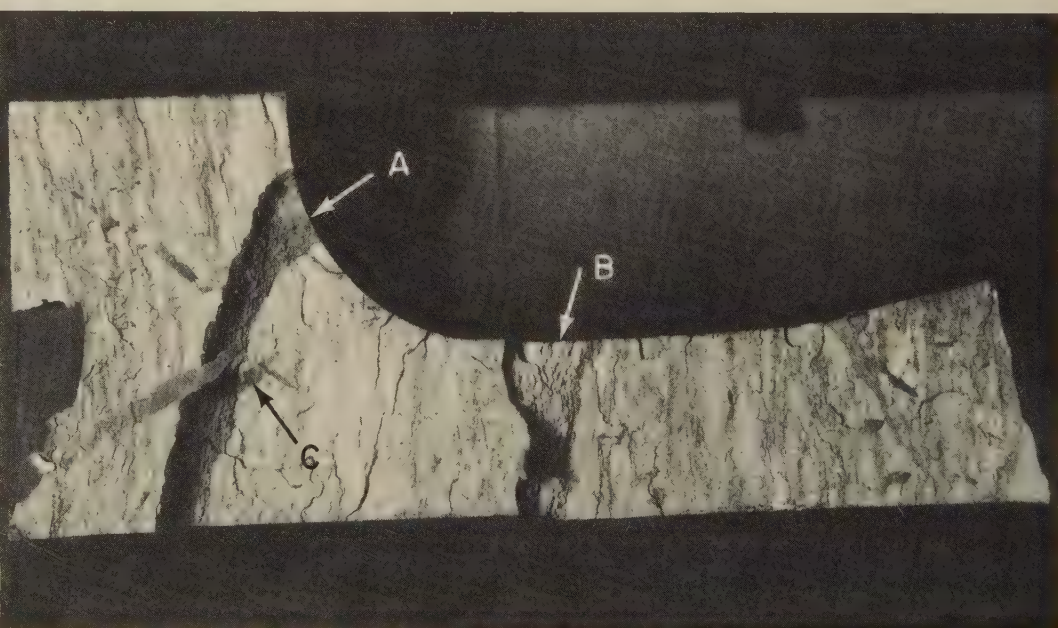
4651 TEM replica of an area at arrow B in 4649, farther from the crack origin than the area in 4650. Note the small change in fatigue-striation spacing at right center. The lines in the striations near bottom suggest slip subsequent to passage of the crack front.



TEM fractograph (p-c replica)

6500×

4652 TEM replica of an area at arrow C in 4649, still farther from the crack origin than the areas in 4650 and 4651, as is indicated by wide striation spacing and patches of dimples.



Light fractograph

3.3×

4653 Surface of a stress-corrosion fracture in a fitting of forged aluminum alloy 7075-T6. During sawing of the fitting to disclose the fracture surface it was found that high residual stresses existed at the centers of the thicker portions of the fitting. Corrosion resulted from exposure to a marine atmosphere. See also micrograph 4654 and fractographs 4655 and 4656 (opposite page), for sectional and TEM views of this fracture. Hardness was Rockwell B 89.5. Areas A and B are offsets in the fracture surface (note the shadow of the sliver at C).

Micrograph, and Light and TEM Fractographs, of Aluminum Alloy 7075-T6: Forged Fitting Fractured by Stress Corrosion (Continued); Forged Hoop Specimen Fractured by Stress Corrosion



Micrograph (Keller's reagent)

50×

4654 Polished and etched section through the fractured aluminum alloy 7075-T6 fitting in 4653; fracture surface is shown in profile at top. The grains are very elongated, which facilitated propagation of both the primary fracture and the secondary cracks shown at midheight.



TEM fractograph (p-c replica)

7800×

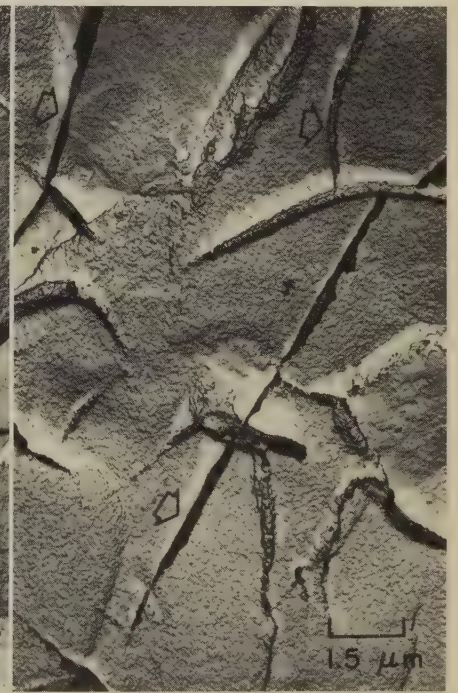
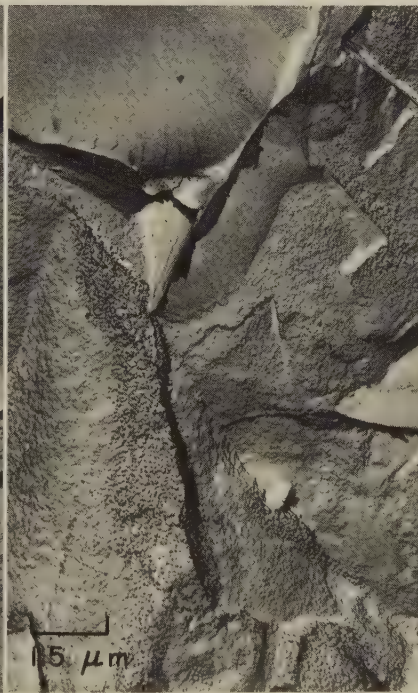
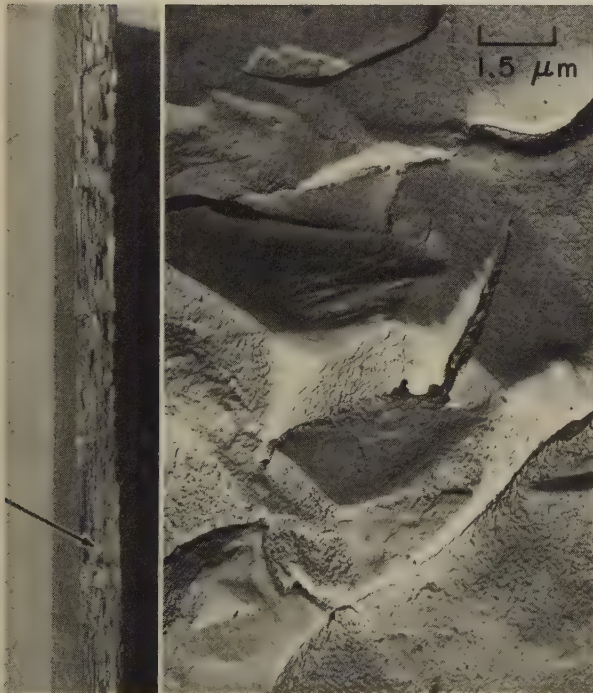
4655 TEM replica of an area of the stress-corrosion fracture surface in 4653, showing characteristic separated-grain facets coated with corrosion products.



TEM fractograph (p-c replica)

7800×

4656 TEM replica of another area in 4653, similar to that in 4655, but also showing secondary cracks between grains, which are also characteristic of stress corrosion.



Light fractograph; three TEM fractographs (p-c replicas)

4× (4657); 6500× (4658-4660)

4657, 4658, 4659, 4660 Fractograph 4657 (left) shows a stress-corrosion fracture in a hoop specimen of forged aluminum alloy 7075-T6 (tensile strength, 614 MPa or 89 ksi) stressed in the short-transverse direction at 372 MPa (54 ksi) while exposed to a marine atmosphere. Fracture occurred after 16 days. Fractographs 4658, 4659 and 4660 show TEM replicas of three areas at the arrow in 4657. Fractograph 4658 (second from left) shows separated-grain facets coated with corrosion products, smooth regions that may be facets of cleaved second-phase particles, and a few "mud cracks". Fractograph 4659 (second from right) shows an area similar to that in 4658, but with longer "mud cracks". The area shown in 4660 (right) lacks the smooth regions visible in 4658 and 4659, contains an even more sharply defined "mud crack" pattern (at arrows), and appears to consist of transgranular facets.

Light Fractograph, Photographs, Micrographs: Extruded Aluminum Alloy 7075-T6
Aircraft Bulkhead Cap Fractured as a Result of Stress-Corrosion Cracking



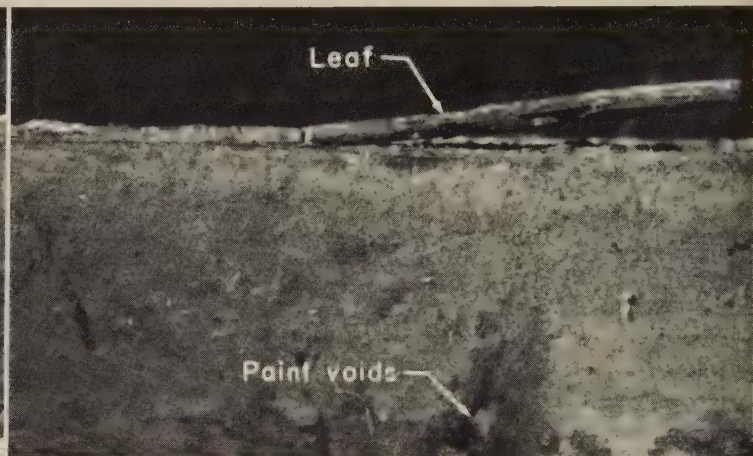
Light fractograph (composite)

4661 Surface of a fracture in an aircraft lower-bulkhead cap fabricated from an extrusion of aluminum alloy 7075-T6. The cap was cut open to expose the fracture for inspection, and evidence of corrosion was found along the edge at which fracture was initiated (bottom edge in this view). Secondary cracks had produced "leaves" (at arrows) in the fracture surface. See also 4662 to 4670 (below, and on facing page).



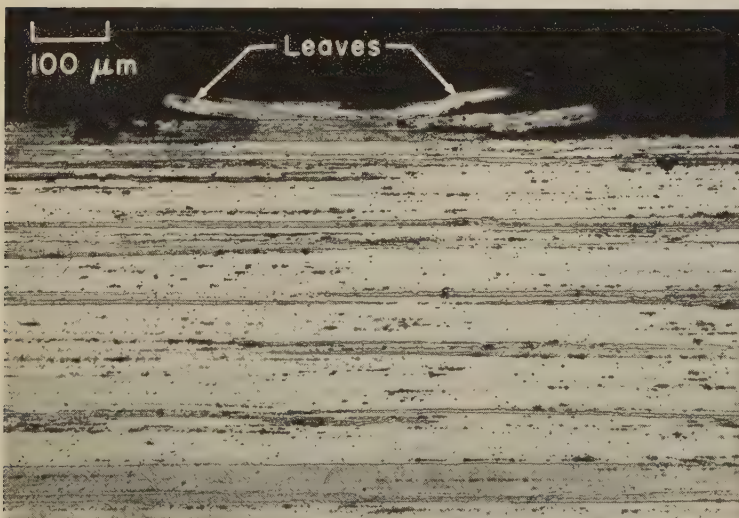
Photograph

4662 A portion of the painted external surface of the fractured aircraft lower-bulkhead cap in fractograph 4661, showing a profile of the fracture surface (at top) and voids in the paint film. Subcracks are evident immediately below and parallel with the fracture surface. Compare with 4663 (right).

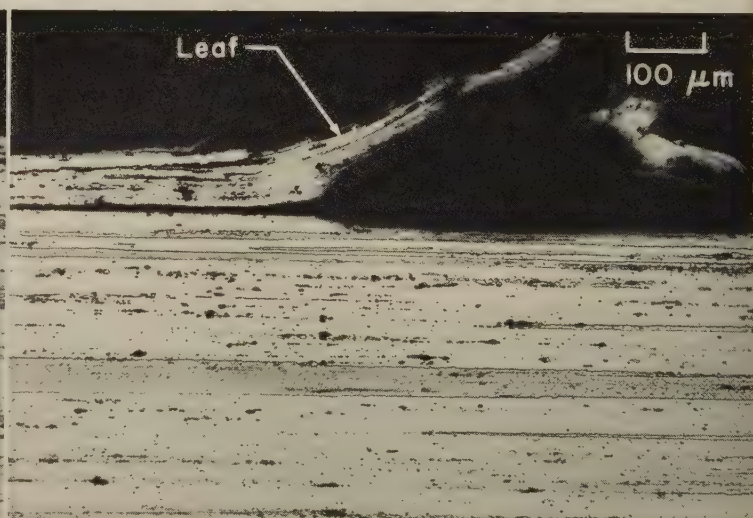


Photograph

4663 Another portion of the painted external surface of the cap in 4661. Fracture surface, shown in profile at top, contains a "leaf"; compare this view of the "leaf" with that in 4661, which is normal to the fracture surface. As in 4662, paint voids are evident.



Micrograph (Keller's reagent)



Micrograph (Keller's reagent)

4664, 4665 Polished and etched sections through two portions of the fractured bulkhead cap in 4661, showing "leaves" in the fracture surface (in profile, at top). Note the elongated grains, which are parallel with the fracture surface. Note also that both the primary and secondary cracks are intergranular. Intergranular corrosion has nearly separated several of the "leaves" from the fracture surface. Stress-corrosion cracking was favored by imposition of tensile stresses in installation and by exposure to a marine atmosphere in service.

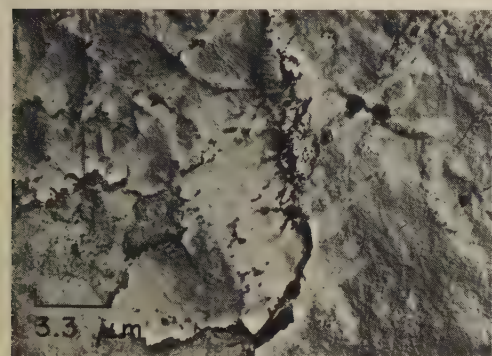
Macrograph and TEM Fractographs of Fractures in Aluminum Alloy 7075-T6: Bulkhead Cap (Continued) and Landing-Gear Component, Both by Stress Corrosion; Fatigue-Cracked Specimen by Impact



Macrograph - composite (Keller's reagent)

20×

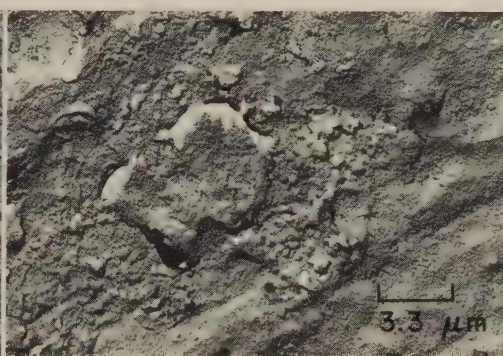
4666 Polished and etched section through the fractured aluminum alloy 7075-T6 bulkhead cap in 4661 (opposite page), showing the fracture surface in profile at left. Note change in grain flow produced during extrusion, from a longitudinal orientation at right to transverse at left; transverse orientation results in grains being parallel to the fracture surface, a condition that aggravates stress-corrosion cracking.



TEM fractograph (p-c replica)

3000×

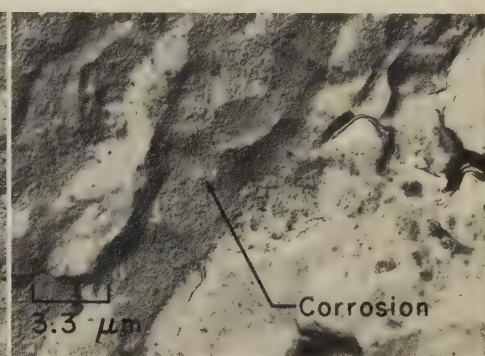
4667 TEM replica of an area of the fracture surface in 4661 near the edge at which fracture was initiated, showing corrosion debris on a very flat intergranular surface. The original separated-grain facets have been corroded away.



TEM fractograph (p-c replica)

3000×

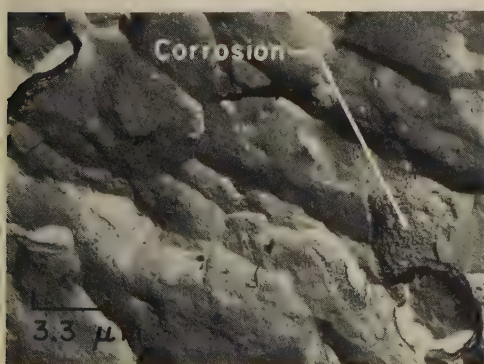
4668 TEM replica taken from another area of the fracture surface in 4661 near the edge at which fracture was initiated. This area, like the one in 4667 (left), shows that cracking was intergranular and was accompanied by severe corrosion.



TEM fractograph (p-c replica)

3000×

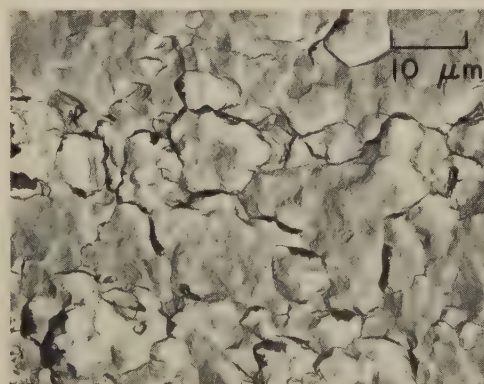
4669 TEM replica of an area of the fracture surface in 4661 deeper into the fracture than 4667 and 4668; here, corrosion of the separated-grain facets is evident, although not as severe as in areas nearer the edge at which fracture was initiated.



TEM fractograph (p-c replica)

3000×

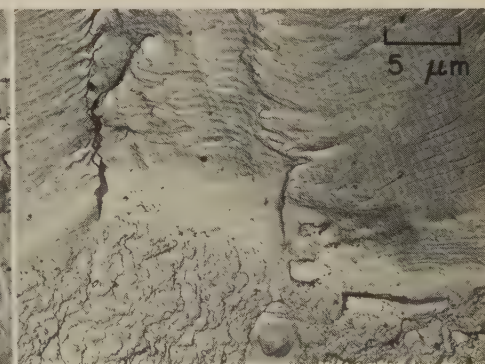
4670 An area of the fracture surface in 4661 still farther from the initiation edge than 4669. This surface, although still intergranular, is relatively free of corrosion products. In a portion of the fracture formed later, evidence of fatigue was found. Final fracture was by shear.



TEM fractograph (p-c replica)

1000×

4671 TEM replica of the surface of an intergranular fracture in an aircraft landing-gear component of forged aluminum alloy 7075-T6 that fractured as the result of stress-corrosion cracking. Note the secondary cracks between the grains.

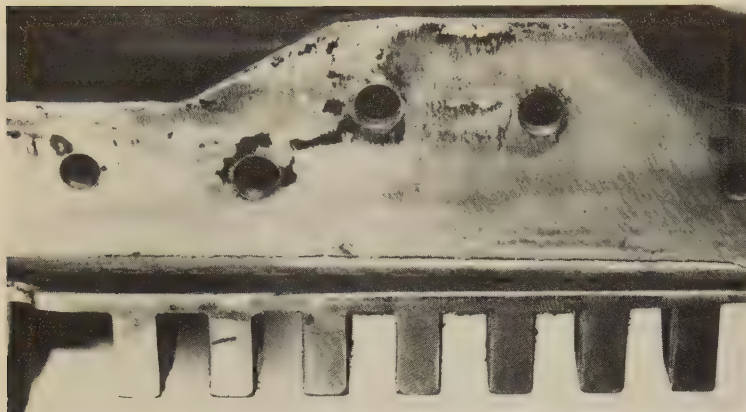


TEM fractograph (p-c replica)

2000×

4672 TEM replica of the surface of a fracture in a specimen of aluminum alloy 7075-T6 that first was cracked by fatigue and then was broken by impact. Stretching and serpentine glide are evident at about mid-height, at the root of the fatigue crack; below are tear dimples formed on impact.

Photograph; Light and TEM Fractographs: Aluminum Alloy 7079-T6 Spar
(Machined From a Forging) That Was Fractured in a Fatigue Test



Photograph

$\frac{3}{4} \times$

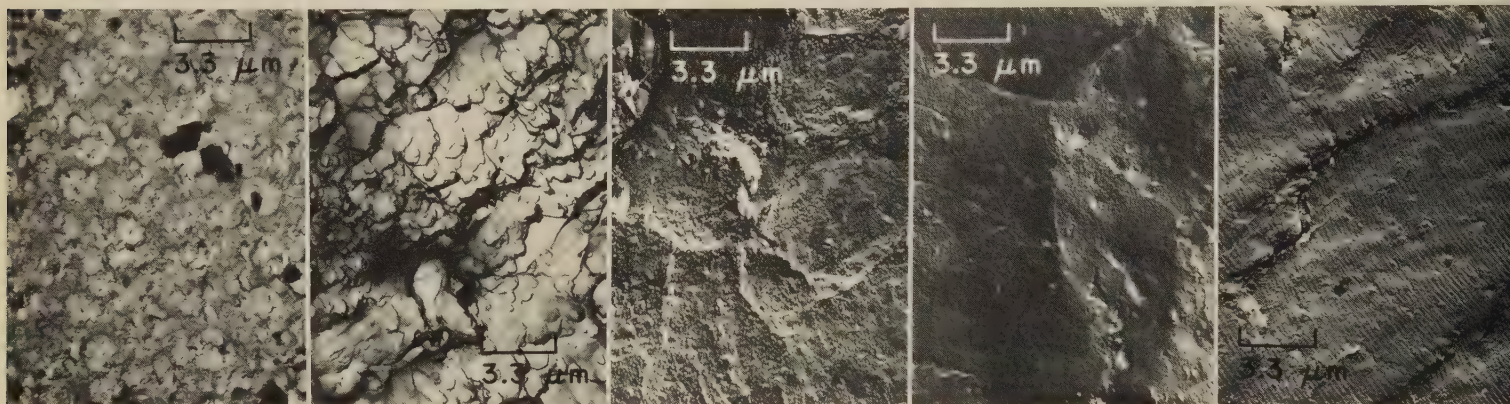
4673 A portion of an aluminum alloy 7079-T6 spar that was machined from a forging. The spar cracked during fatigue testing. The crack is visible as a fine dark horizontal line along the radius of the spar (above nodes). See also fractograph 4674.



Light fractograph

$2\frac{1}{2} \times$

4674 A portion of the surface of the crack in 4673, which was exposed by sectioning. The "clamshell" marks usually observed in fatigue fractures are absent here. See also 4675 to 4684.

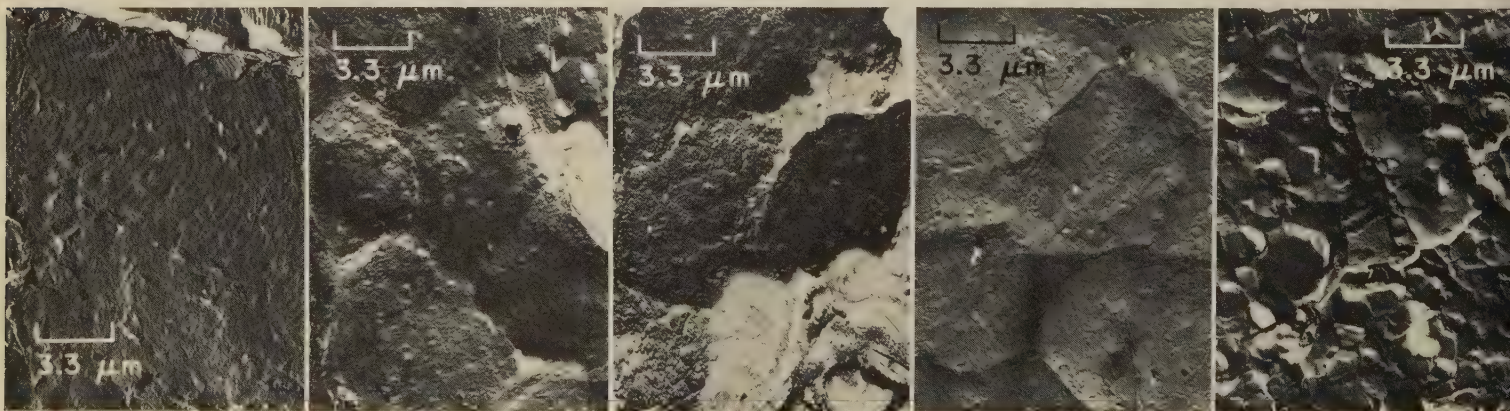


TEM fractographs (p-c replicas)

All at $3000 \times$

4675, 4676, 4677, 4678, 4679

Fractograph 4675 (left) is a TEM replica of an area 0.002 in. from the outer edge of the crack surface in 4674, showing evidence of corrosion on dimples that were formed by tension overload believed to have occurred during straightening; 4676 (second from left) is a replica of an area near that shown in 4675, displaying shear dimples but no corrosion. Fractograph 4677 (center) is a TEM replica of an area 0.003 in. from the outer edge of the crack in 4674 and shows intergranular facets exposed by stress-corrosion cracking; 4678 (second from right) is a replica of an area near that in 4677, showing similar features. Fractograph 4679 (right) is a replica of an area 0.005 in. from the outer edge of the crack in 4674 and shows striations, which indicate fatigue. See also fractographs 4680 to 4684, below, for TEM views of additional areas of the surface of the crack in 4674.



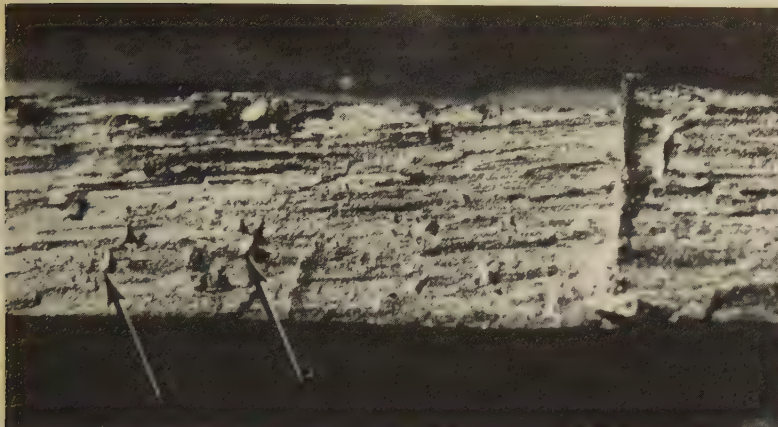
TEM fractographs (p-c replicas)

All at $3000 \times$

4680, 4681, 4682, 4683, 4684

Fractograph 4680 (left) is a TEM replica of an area near that in 4679 (above, right), showing fatigue striations and a region of intergranular facets exposed by stress corrosion. Fractographs 4681 (second from left) and 4682 (center) are replicas of two areas 0.010 to 0.090 in. from the outer edge of the crack in 4674, showing features characteristic of stress-corrosion cracking (separated-grain facets, corrosion products). Fractographs 4683 (second from right) and 4684 (right) are replicas of two areas between the inner crack edge and a point 0.090 in. from the outer edge and show intergranular separation and dimpled transgranular fracture respectively; tension-overload features were observed throughout the remainder of the fracture.

Micrograph; Light and TEM Fractographs: Aluminum Alloy 7079-T6 Spar Fractured by Stress Corrosion; Aluminum Alloy 7079-T651 Notched Plate Fractured by Tension Overload



Light fractograph

10×

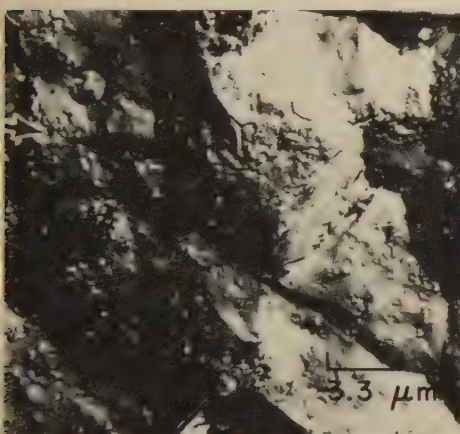
4685 Surface of a stress-corrosion fracture in an aluminum alloy 7079-T6 spar that cracked in service in a marine atmosphere. The arrows at left indicate locations of "leaves" that were formed by intergranular splintering. Hardness was Rockwell B 91. See 4686 to 4688.



Micrograph (Keller's reagent)

50×

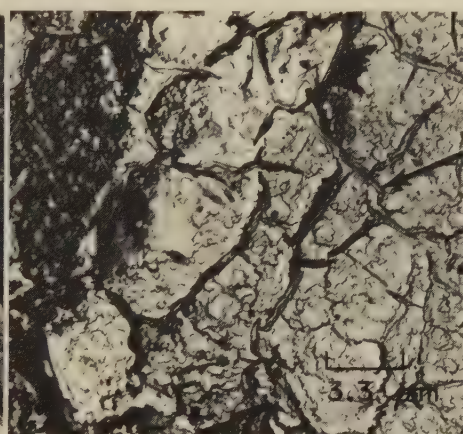
4686 A polished and etched section through the fractured spar in 4685, showing a "leaf" in the fracture surface (at top). The intergranular cracks that formed such "leaves" were 0.002 to 0.010 in. below the main fracture surface.



TEM fractograph (p-c replica)

3000×

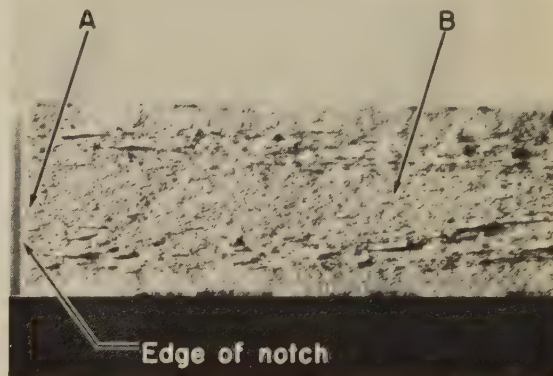
4687 TEM replica of an area of the fracture surface shown in fractograph 4685 (above). This area exhibits intergranular facets that were exposed by stress-corrosion cracking; the facets carry appreciable corrosion products, such as at arrow at upper left edge. See also 4688.



TEM fractograph (p-c replica)

3000×

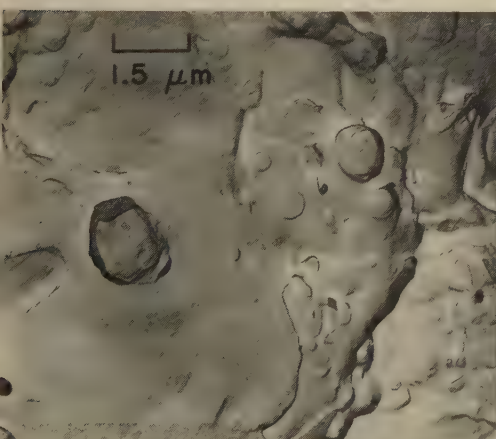
4688 TEM replica of another area of the fracture surface in 4685. Like 4687, this replica shows features of intergranular stress corrosion. Pronounced "mud cracks", such as those at arrow, are evident also. Some local regions of the fracture (not shown) contain dimples.



Light fractograph

Actual size

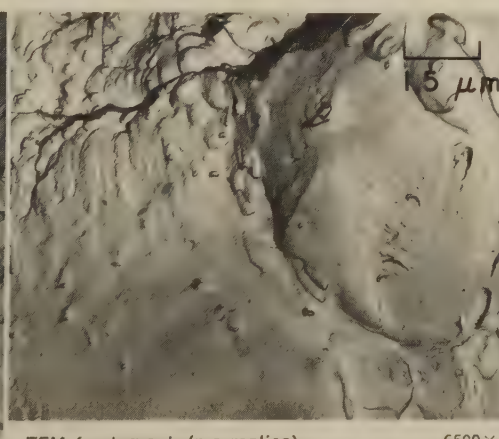
4689 Surface of a tension-overload fracture in a centrally notched plate (64 in. by 20 in. by 1 in. thick) of aluminum alloy 7079-T651. Tensile strength was 565 MPa (82 ksi). Fracture occurred at a net stress of 165 MPa (24 ksi). Notch was 0.005 in. in radius by 7 in. long by plate thickness. The fracture surface is relatively flat but contains jagged features. See 4690 to 4692 for views at A and B.



TEM fractograph (p-c replica)

6500×

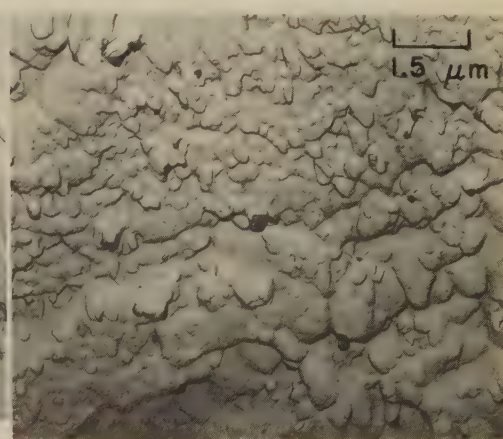
4690 TEM replica of an area at A, at the notch, in 4689, showing dimples of various sizes, large stretched regions, and some serpentine glide. See 4691.



TEM fractograph (p-c replica)

6500×

4691 TEM replica of another area at A in 4689. Like 4690, this replica shows large stretched regions and dimples of various sizes. Two facets near bottom right in this view suggest cleaved second-phase particles.

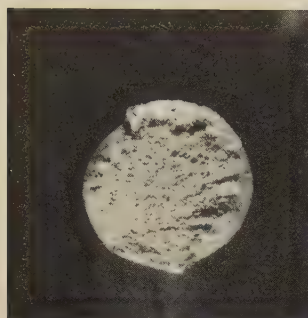


TEM fractograph (p-c replica)

6500×

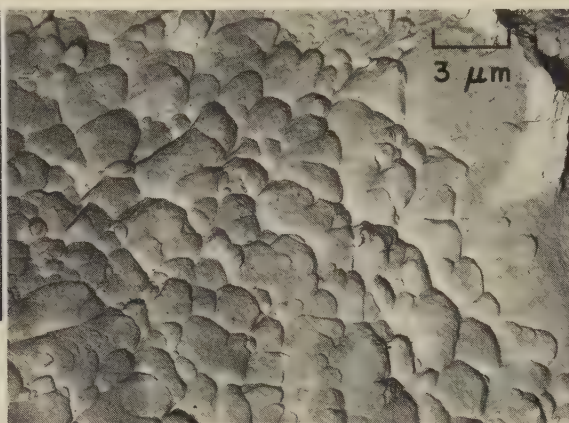
4692 TEM replica of an area at B, about 2 in. from the notch, in 4689. Fracture here shows elongated dimples of various sizes, all oriented in the same general direction.

**Light and TEM Fractographs: Unnotched Specimens of Beryllium Copper (2% Be)
Fractured by Tension Overload at Room Temperature and at 260 C (500 F)**



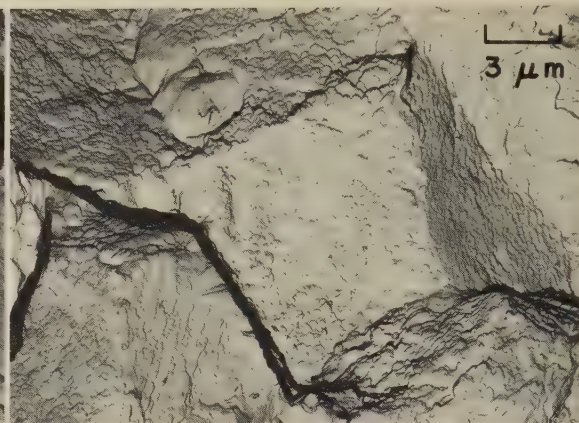
Light fractograph 3½×

4693 Tension-overload fracture in an unnotched specimen of beryllium copper (2% Be) aged at 316 C (600 F) to a tensile strength of 1327.9 MPa (192.6 ksi) and broken at room temperature. A shear lip is visible at top. See also 4694 to 4697.



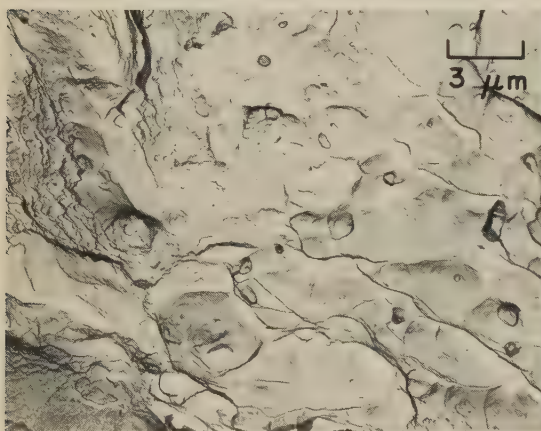
TEM fractograph (p-c replica) 3300×

4694 TEM replica of an area in the shear lip at the edge of the fracture surface in 4693, showing rather uniformly sized shear dimples. There appear to be regions of stretching (top right) and a small region of serpentine glide (right edge).



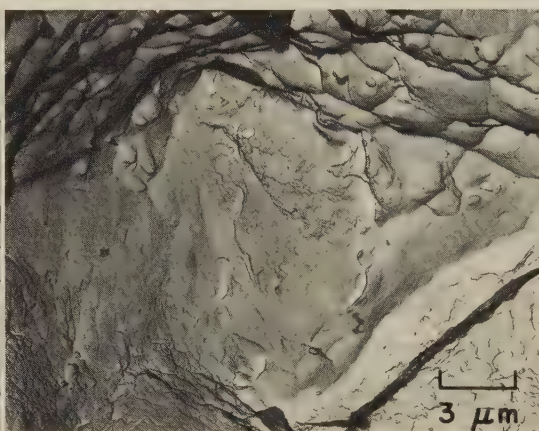
TEM fractograph (p-c replica) 3300×

4695 TEM replica of an area at the center of the fracture surface in 4693, showing rather massive intergranular facets, with very fine dimples on many of the facets. A region containing transgranular facets is visible at top center.



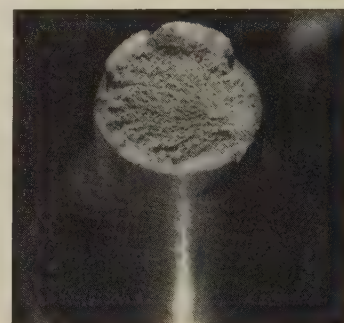
TEM fractograph (p-c replica) 3300×

4696 TEM replica of another area at the center of the fracture surface in 4693, showing dimples on transgranular facets (at right) and on intergranular facets (at left).



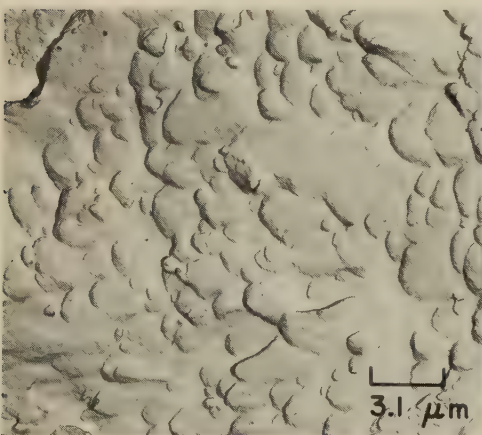
TEM fractograph (p-c replica) 3300×

4697 A third area at the center of the fracture surface in 4693, displaying very large intergranular facets in the lower portion and a region of dimples above.



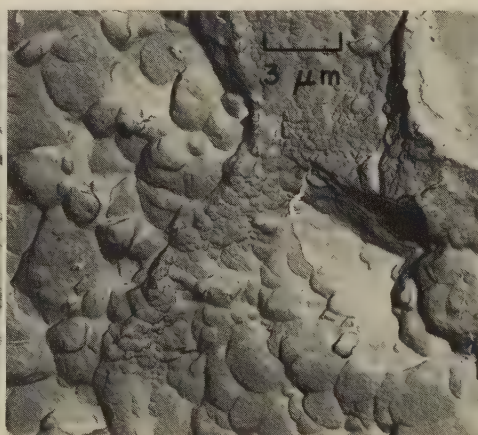
Light fractograph 3½×

4698 Tension-overload fracture in an unnotched specimen of beryllium copper (2% Be) aged at 316 C (600 F) to a tensile strength of 1327.9 MPa (192.6 ksi) and tested at 260 C (500 F). Note shear lip at top. See also 4699 to 4701.



TEM fractograph (p-c replica) 3200×

4699, 4700, 4701



TEM fractograph (p-c replica) 3300×

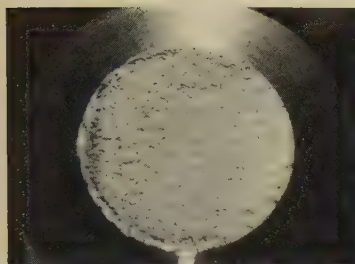


TEM fractograph (p-c replica) 3300×

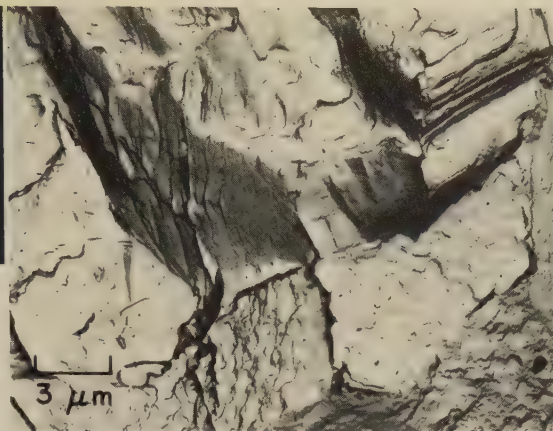
4701

TEM replicas of three areas of the fracture surface in 4698. Fractograph 4699 (left), of an area in the shear lip at the edge of the fracture surface, reveals relatively flat shear dimples and regions of very small dimples. Fractograph 4700 (center), of an area near (but not at) the edge of the fracture surface, shows a mixture of regions of shear dimples and regions of dimpled intergranular facets. Fractograph 4701 (right) is of an area at the center of the fracture surface; except for regions of transgranular shear dimples at lower right, this area shows features of intergranular dimpled rupture and is typical of the entire central zone of the fracture surface.

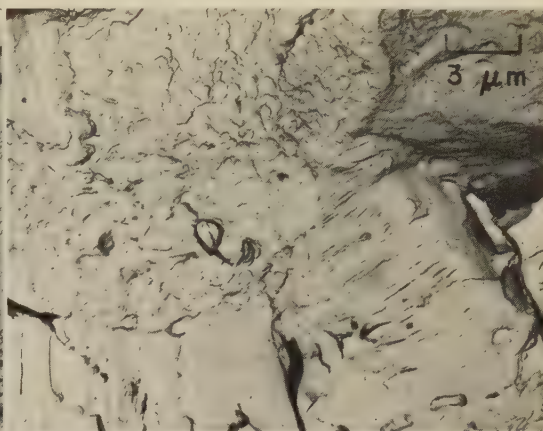
Light and TEM Fractographs: Notched Specimens of Beryllium Copper (2% Be) Fractured by Low-Cycle Fatigue at Room Temperature and by High-Cycle Fatigue at 260 C (500 F)



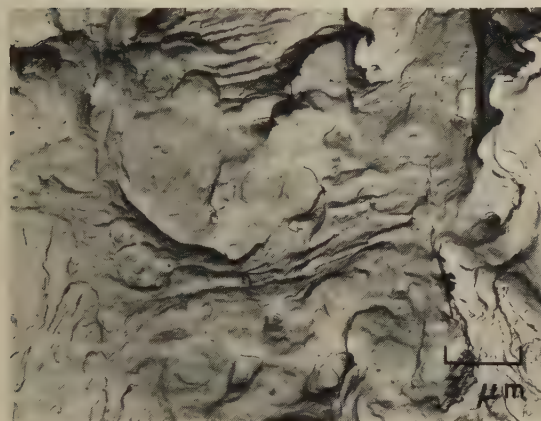
Light fractograph 334×
4702 Low-cycle fatigue fracture in a notched specimen of beryllium copper (2% Be) aged to a tensile strength of 1327.9 MPa (192.6 ksi) and loaded at room temperature to a stress cycled from 83 to 414 MPa (12 to 60 ksi) at 500 cycles per minute. Fracture occurred after 1700 cycles. Notch had a 60° angle, 0.30-in. diam, 0.008-in. root radius. See also 4703 to 4705.



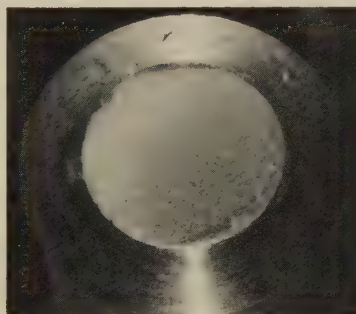
TEM fractograph (p-c replica) 3300×
4703 TEM replica of an area at a crack nucleus at the root of the notch in 4702. Regions of fatigue striations are interspersed with dimpled intergranular facets, some of which show marks that are probably fissures.



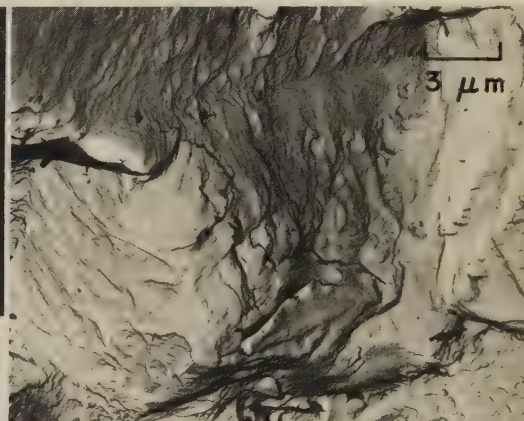
TEM fractograph (p-c replica) 3300×
4704 TEM replica of an area near, but not at, a crack nucleus in the fracture surface in 4702, displaying dimpled intergranular facets (at top), and fatigue patches (below) at strikingly different orientations.



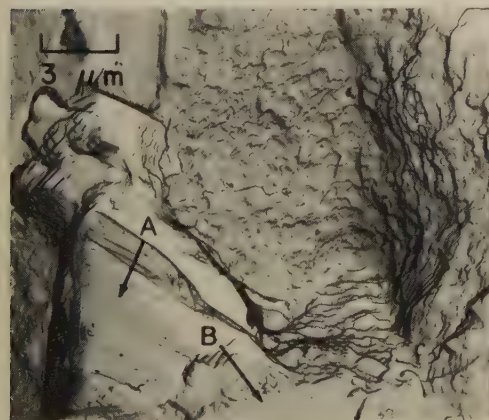
TEM fractograph (p-c replica) 3300×
4705 TEM replica of an area of the fracture surface in 4702, at the transition from fatigue to fast fracture, showing fatigue striations at top, a dimpled intergranular facet at lower right, and rather smooth areas elsewhere.



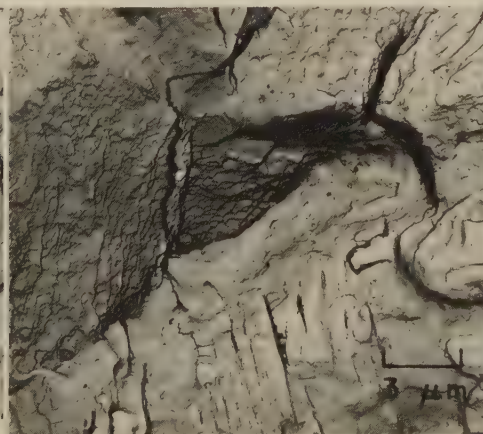
Light fractograph 31/2×
4706 High-cycle fatigue fracture in a notched specimen of beryllium copper (2% Be) loaded at 260 C (500 F) to a stress cycled from 83 to 414 MPa (12 to 60 ksi) at 500 cycles per minute. Fracture occurred after 3200 cycles. Tensile strength and notch same as for 4702. See 4707 to 4710.



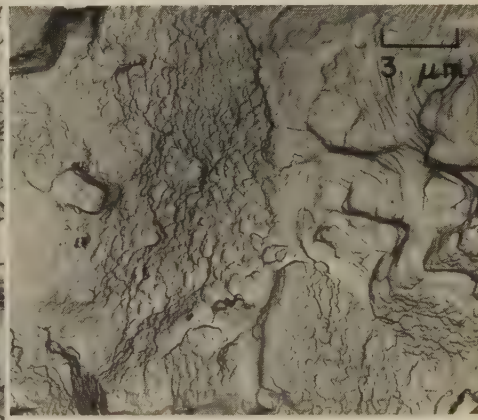
TEM fractograph (p-c replica) 3300×
4707 TEM replica of an area at a crack nucleus at the root of the notch in 4706, showing intergranular facets. Very few of the marks that are visible in this area can be positively identified as fatigue striations.



TEM fractograph (p-c replica) 3300×
4708 TEM replica of an area near, but not at, a crack nucleus in 4706, showing fatigue striations that exhibit striking differences in alignment from A to B and that are interspersed with dimpled intergranular facets.

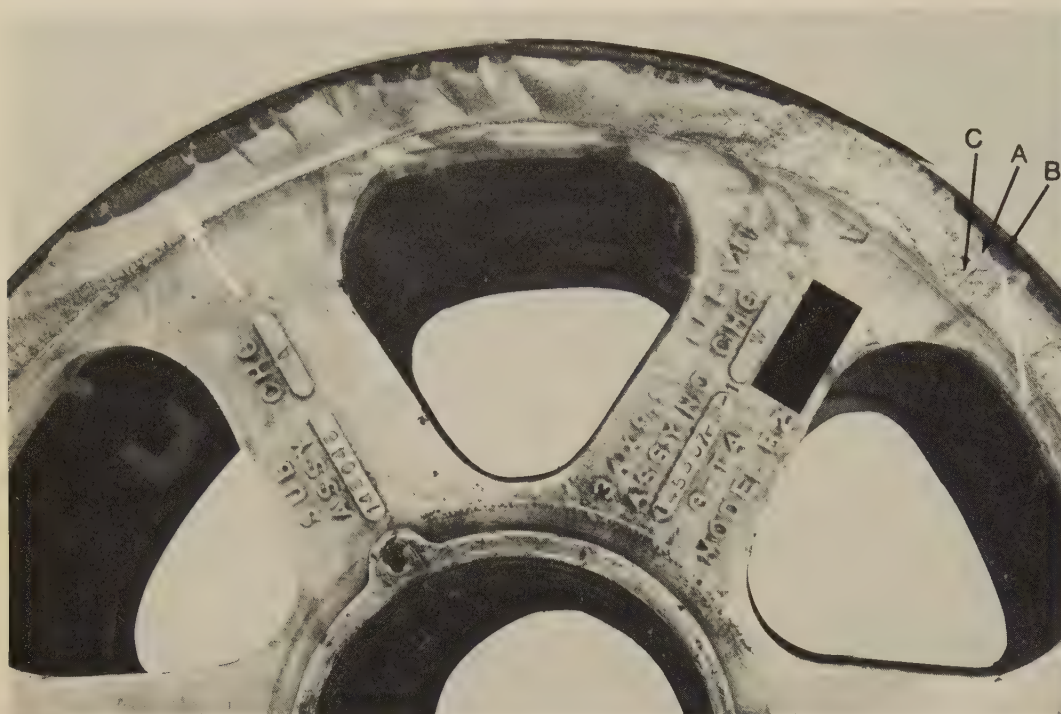


TEM fractograph (p-c replica) 3300×
4709 TEM replica of an area near the transition from fatigue to fast fracture in 4706, showing dimpled intergranular facets in general and suggestions of fissures or striations at bottom.



TEM fractograph (p-c replica) 3300×
4710 TEM replica of an area at the transition from fatigue to fast fracture in 4706. Curved striations with several orientations are visible at upper right; the remainder of the area consists of dimpled intergranular facets.

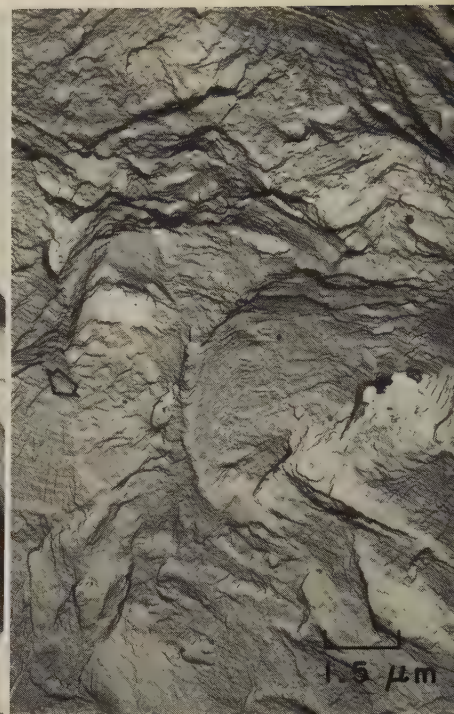
Photograph; TEM Fractographs: Sand Cast Magnesium Alloy AZ81A-T4
Aircraft Landing Wheel Fractured by Corrosion Fatigue



Photograph

4711 Portion of an aircraft landing wheel of sand cast magnesium alloy AZ81A-T4, showing a corrosion-fatigue fracture that occurred in service at the locking-ring channel. Nominal tensile strength was 276 MPa (40 ksi). The fracture extended halfway around the perimeter of the wheel. Many discolored, crescent-shaped fatigue-crack nuclei were found; two are indicated by white arrows. See 4712 to 4715 for TEM views of areas at A, B and C.

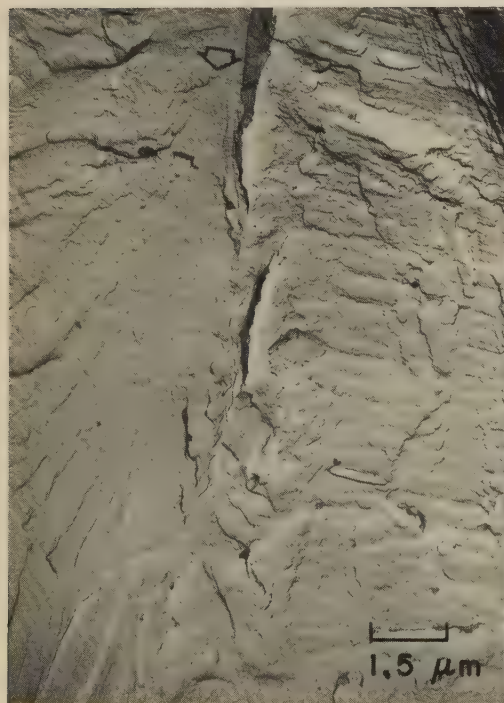
0.3×



TEM fractograph (p-c replica)

6500×

4712 TEM replica of an area at the fatigue-crack nucleus at A in the fracture surface in 4711, showing "brittle" fatigue striations (such as at the arrow at left center).



TEM fractograph (p-c replica)

6500×

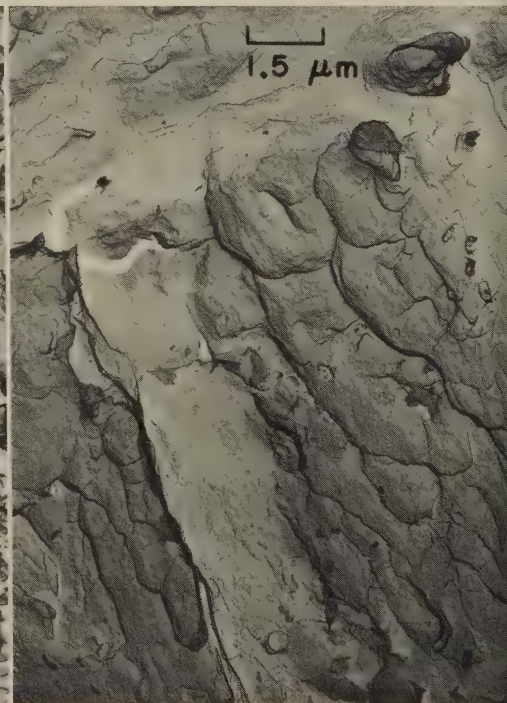
4713 TEM replica of another area at A in 4711. Fine, roughly horizontal striations are visible in a fatigue patch at the arrow at top center; the marks at the right include widely spaced horizontal fissures.



TEM fractograph (p-c replica)

6500×

4714 TEM replica of an area at B in 4711. In this area, the fracture surface is largely obscured by corrosion products. The few facets that are visible have essentially no distinguishable features.

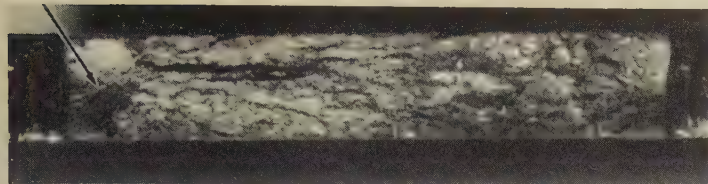


TEM fractograph (p-c replica)

6500×

4715 TEM replica of an area at C in 4711, in the region of final, fast fracture. This area exhibits rather flat, elongated dimples. The region at left center in this view appears to have been stretched.

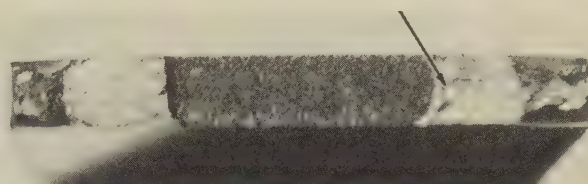
Light and TEM Fractographs: Notched TZM Alloy (Mo-0.5Ti-1.0Zr) Sheet Fractured by Tension Overload; Notched 90Ta-10W Alloy Sheet Fractured by High-Cycle Fatigue



Light fractograph

9×

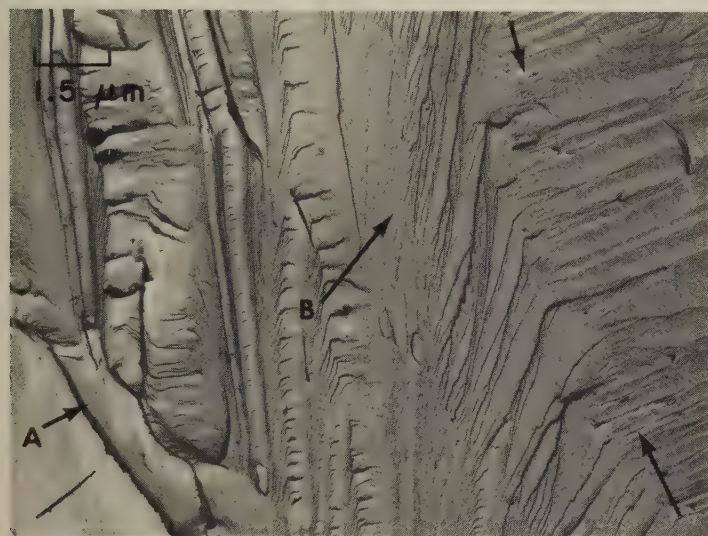
4716 Surface of a tension-overload fracture in a notched specimen of stress-relieved TZM alloy (Mo-0.5Ti-1.0Zr) sheet. Unnotched tensile strength was 972 MPa (141 ksi). The specimen was notched on each edge to a depth of 0.1 in. with a jeweler's saw and broken at room temperature; notched tensile strength was 1007 MPa (146 ksi). Fracture produced distinct flat regions at the origins of each notch. See 4717 and 4718 (below) for TEM replicas of areas at the arrow.



Light fractograph

6×

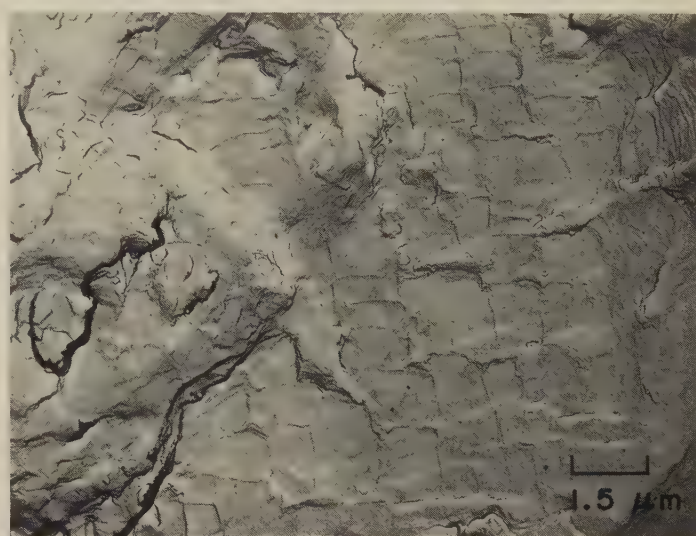
4719 Surface of a high-cycle fatigue fracture in a stress-relieved specimen of 90Ta-10W alloy sheet containing a central transverse notch 0.2 in. wide. Tensile strength was 552 MPa (80 ksi). The specimen was loaded in tension at room temperature to a stress cycled from 80 to 400 MPa (11.6 to 58 ksi) at 1000 cycles per minute and broke after 15,900 cycles. Considerable necking accompanied fast fracture. See also fractographs 4720 and 4721 (below), for TEM replicas of areas at the arrow.



TEM fractograph (p-c replica)

6500×

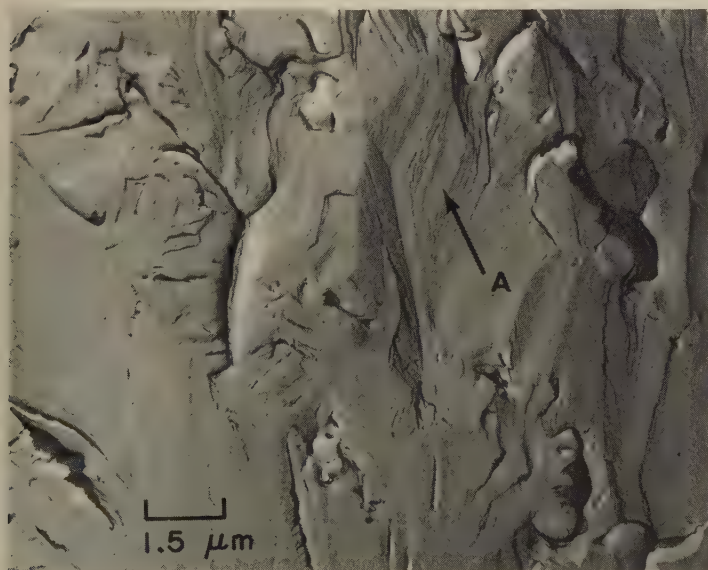
4717 TEM replica of an area at the arrow in 4716 (above). Here, the fracture surface shows transgranular cleavage. A tilt boundary at A; elsewhere, twist boundaries (between arrows) and suggestions of cleavage feather marks (at B).



TEM fractograph (p-c replica)

6500×

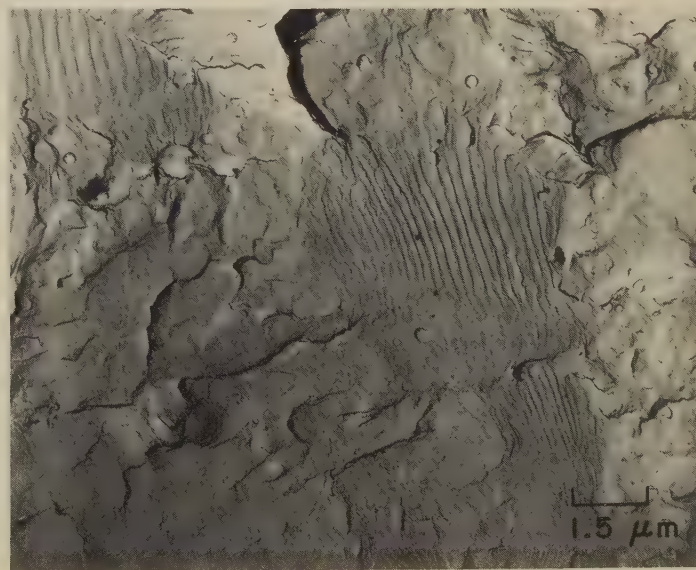
4720 TEM replica of an area at arrow in 4719 (above). A few fatigue striations are visible at top and at right. Remainder of surface here is unusual, consisting of what appear to be very flat-bottomed, shallow dimples.



TEM fractograph (p-c replica)

6500×

4718 TEM replica of another area at the arrow in 4716 (above). The features visible here are cleavage facets with involved steps but few clear river patterns. The features at A bear some resemblance to feather marks.

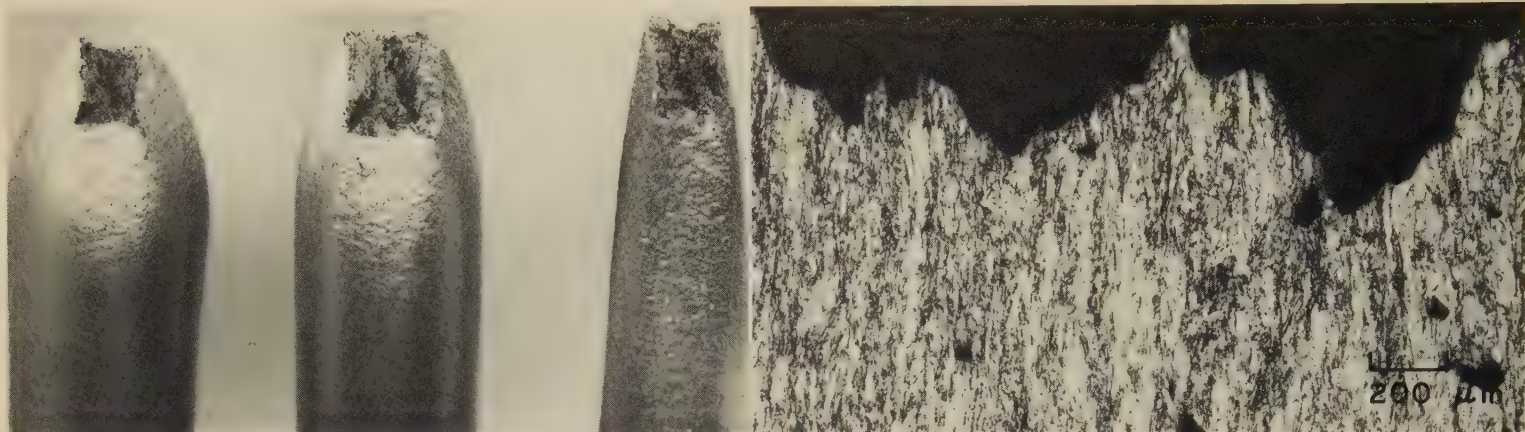


TEM fractograph (p-c replica)

6500×

4721 TEM replica of another area at the arrow in 4719 (above), showing distinct fatigue striations at center and at upper left. Elsewhere, the surface bears scattered and indistinct marks that resemble fatigue striations.

Photograph; Micrograph; TEM and Light Fractographs: Unalloyed Titanium Fractured in a Tension Test; Low-Interstitial Unalloyed Titanium Fractured by Low-Cycle Fatigue



Photograph

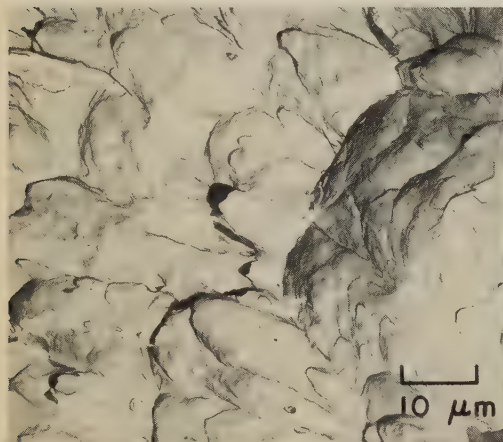
2×

4722 Three specimens of vacuum annealed unalloyed titanium that were broken in a tension test. The specimen at center was tested in air at room temperature; the specimen at left was tested in vacuum at 500 C (932 F); the specimen at right was tested in vacuum at 580 C (1076 F). See also 4723 to 4726.

Micrograph (Kroll's reagent)

50×

4723 Polished and etched section through the tension-test specimen at center in 4722, which was tested in air at 25 C (77 F). The fracture surface is in profile at top. Note marked elongation of grains. The fracture surface is quite rough and appears to be transgranular. The cavities (black areas) are the result of microvoid nucleation.



TEM fractograph (p-c replica)

1000×

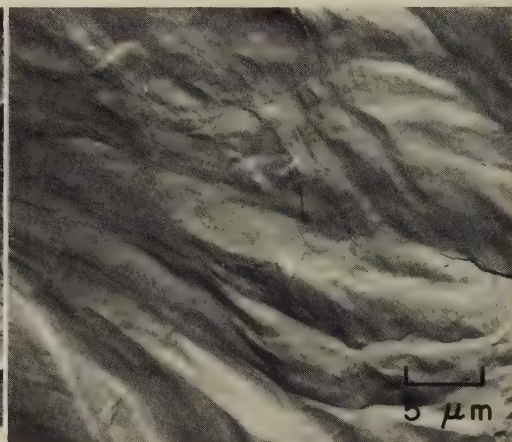
4724 TEM replica of an area of the fracture surface of the specimen at center in 4722, which was broken in air at room temperature, showing a surface composed of elongated shear dimples.



TEM fractograph (p-c replica)

2000×

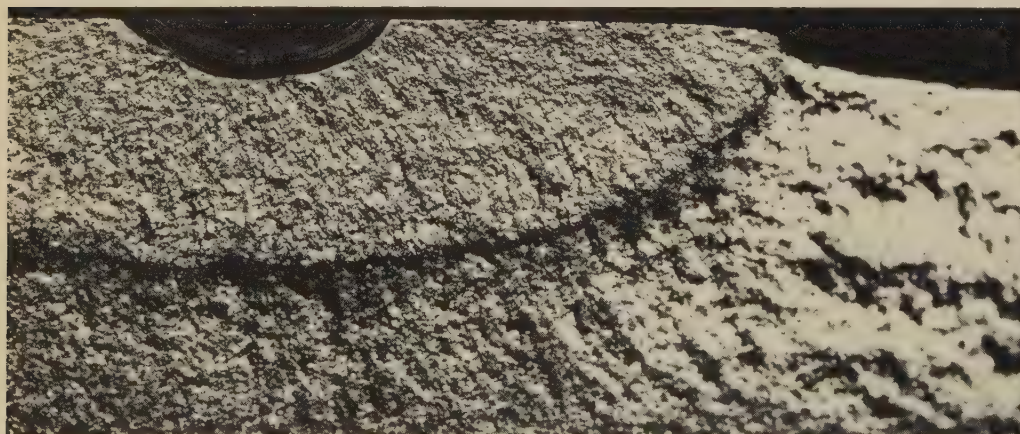
4725 TEM replica of an area of the fracture surface of the specimen at left in 4722, which was tested in vacuum at 500 C (932 F). The dimples here are larger than those in 4724, reflecting the greater ductility at 500 C (932 F) than at room temperature.



TEM fractograph (p-c replica)

2000×

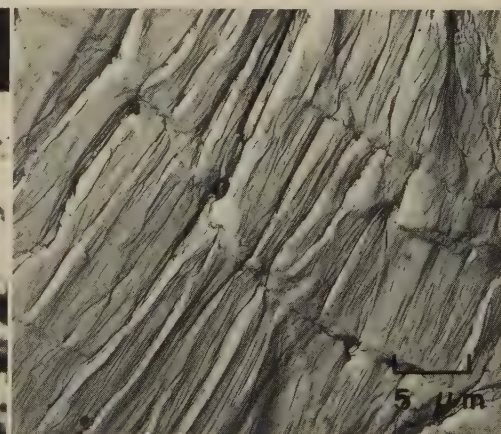
4726 TEM replica of an area of the fracture surface of the specimen at right in 4722, which was tested in vacuum at 580 C (1076 F), showing only serpentine glide — the result of high ductility.



Light fractograph

1½×

4727 Surface of a low-cycle fatigue fracture in a Lehigh-type (notched) specimen of low-interstitial unalloyed titanium, photographed using low-angle illumination to provide maximum contrast. The specimen had been fatigue cracked in preparation for a fracture-toughness measurement, and no measurement of the actual fatigue stress was made. See 4728.

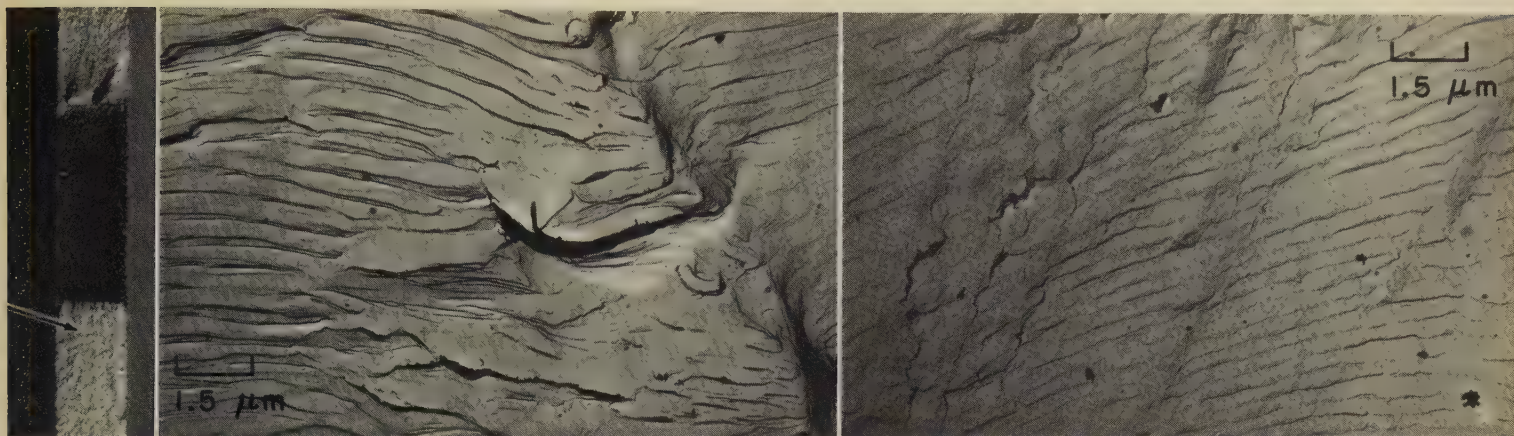


TEM fractograph (p-c replica)

2000×

4728 TEM replica of an area of the fracture surface in 4727, showing typical fatigue striations, many of which exhibit deeply grooved fissures.

Light and TEM Fractographs: Titanium Alloy Ti-5Al-2.5Sn Sheet Fractured by Fatigue;
Titanium Alloy Ti-5Al-3Sn-2Mo-2V Fractured in a Drop-Weight Tear Test

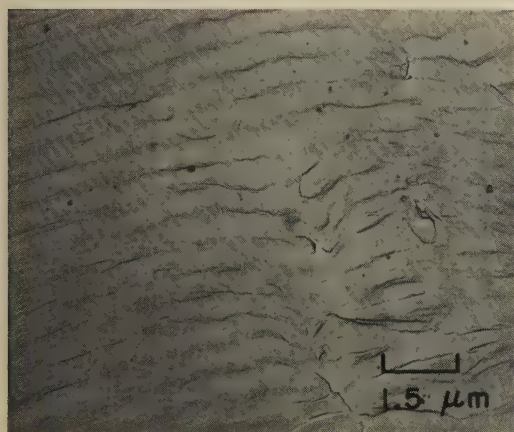


Light fractograph; two TEM fractographs (p-c replicas)

4729, 4730, 4731

Fractograph 4729 (left) shows a portion of the surface of a fatigue fracture in a centrally notched specimen (10 by 1.0 by 0.087 in. thick) of titanium alloy Ti-5Al-2.5Sn sheet annealed to a nominal tensile strength of 862 MPa (125 ksi). The notch was transverse, 0.01 in. in radius, and 0.25 in. long by sheet thickness. The specimen was loaded at room temperature to a stress cycled from 83 to 414 MPa (12 to 60 ksi) at 1000 cycles per minute and broken after 6200 cycles. At center (4730) is a TEM replica of an area at the arrow, adjacent to the notch, in 4729, showing sharply defined fatigue striations; at upper right in this view is a junction between two fatigue patches. At right (4731) is a TEM replica of another area at the arrow in 4729, showing a pattern of long, very regular fatigue striations that resulted from a single crack front. See also fractograph 4732.

41/3 × (4729); 6500 × (4730, 4731)



TEM fractograph (p-c replica)

6500 ×

4732 TEM replica of a third area at the arrow in fractograph 4729, showing striation spacing similar to that in 4730 and wider than that in 4731. Faint suggestions of dimples are visible at right.



Light fractograph

1 1/2 ×

4733

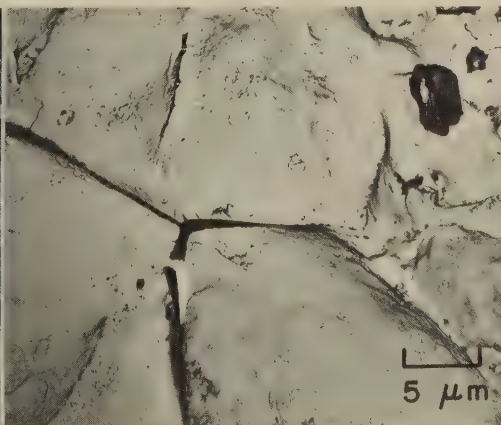
Portion of the fracture surface of a drop-weight tear-test specimen of as-cast titanium alloy Ti-5Al-3Sn-2Mo-2V. It is clearly evident that in many areas fracture was intergranular, exposing the surfaces of some large grains. However, between these separated-grain facets, and particularly near the specimen surface, fracture was transgranular. See also fractographs 4734 to 4736, below.



TEM fractograph (p-c replica)

2000 ×

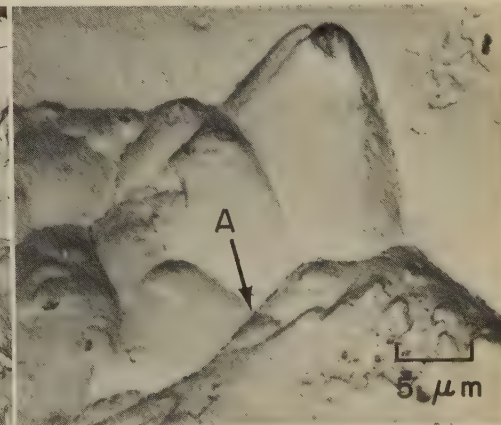
4734 TEM replica of a separated-grain facet in the fracture surface in 4733, showing tear dimples exhibiting relatively little of the elongation expected in such dimples.



TEM fractograph (p-c replica)

2000 ×

4735 TEM replica of a region of transgranular rupture in the fracture surface in 4733. This region exhibits quite large dimples with sharply defined boundaries.

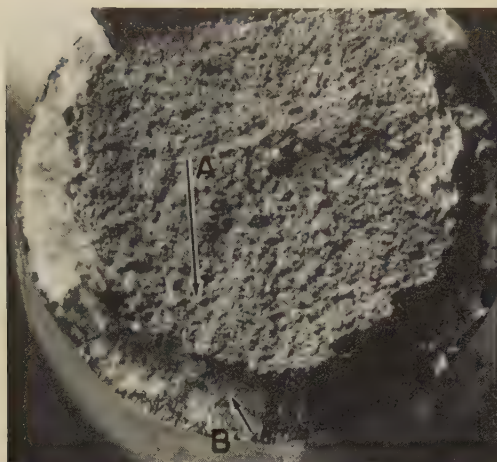


TEM fractograph (p-c replica)

2000 ×

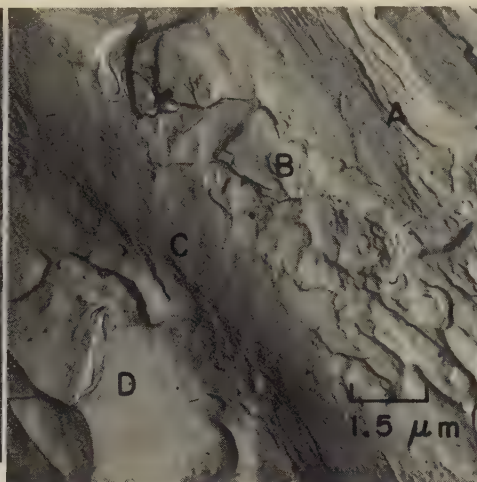
4736 TEM replica of another transgranular region of the fracture surface in 4733, showing tear dimples that do not overlap but that come together at points such as A.

Light and TEM Fractographs: Titanium Alloy Ti-6Al-4V Unnotched Specimens Fractured by Tension Overload at -253 C (-423 F) and by Torsion Overload at Room Temperature



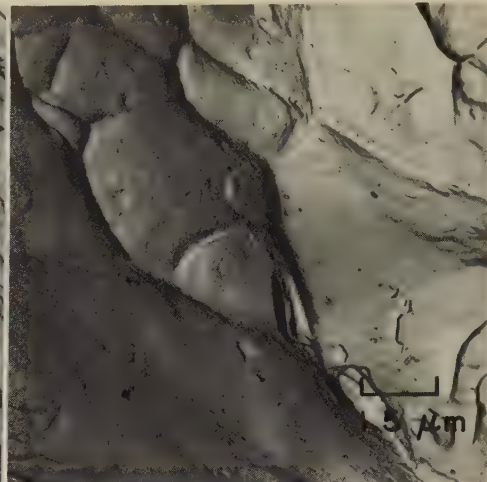
Light fractograph 10×

4737 Tension-overload fracture surface of an unnotched specimen of titanium alloy Ti-6Al-4V annealed to a tensile strength of 1062 MPa (154 ksi) and tested at -253 C (-423 F); fracture stress, 1820 MPa (264 ksi). See 4738 to 4740 for views at arrows.



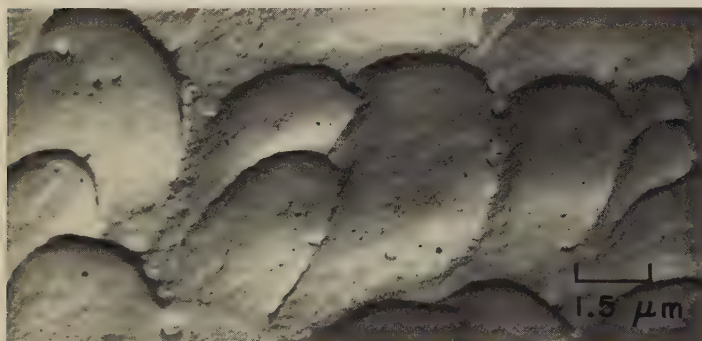
TEM fractograph (p-c replica) 6500×

4738 TEM replica of an area at A in the fracture surface in 4737 (at left). Visible here are ripples (at A), small dimples (in the region marked B), stretched ripples (at C), and large dimples (at D).



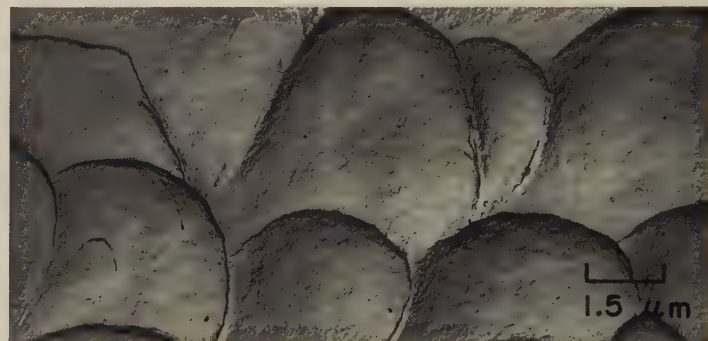
TEM fractograph (p-c replica) 6500×

4739 TEM replica of another area at A in the fracture surface in 4737 (at far left). Dimples of moderate size are present at upper left, adjacent to very much larger dimples below and to the right.



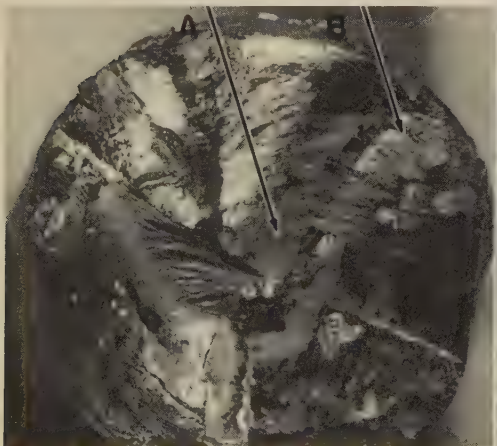
TEM fractograph (p-c replica) 6500×

4740 TEM replica of an area at B in the shear lip of the fracture surface in 4737, showing an array of the large, uniform, well-developed shear dimples that are expected in this portion of the fracture surface.



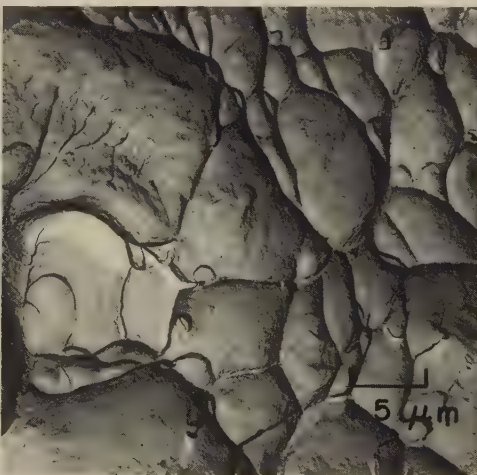
TEM fractograph (p-c replica) 6500×

4741 TEM replica of an area at B near the edge of the fracture surface in 4742 (below, left), showing dimples, the elongation of which reflects the shearing action of the torsion test. See also 4743 and 4744.



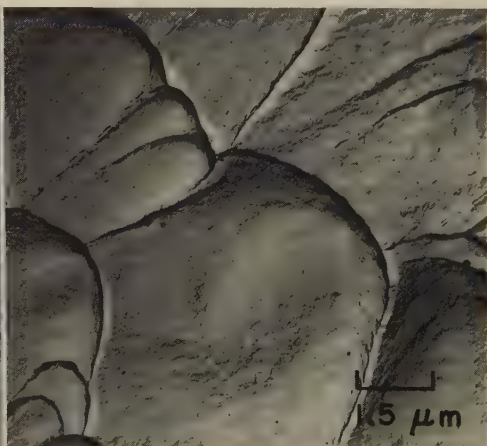
Light fractograph 5×

4742 Surface of a torsion-overload fracture in an unnotched specimen of titanium alloy Ti-6Al-4V solution treated at 954 C (1750 F), aged at 538 C (1000 F) to a tensile strength of 1186 MPa (172 ksi) and tested at room temperature. A jagged fracture surface. See also 4741, 4743 and 4744.



TEM fractograph (p-c replica) 6500×

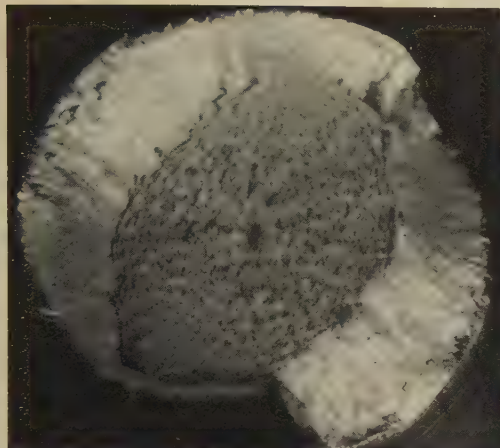
4743 TEM replica of an area at A in the center of the fracture surface in 4742. Equiaxed dimples of widely differing sizes are evident; these dimples are the result of tension that was produced as the final fracture occurred in bending.



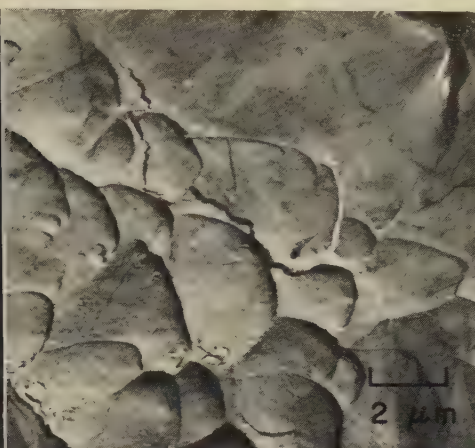
TEM fractograph (p-c replica) 6500×

4744 TEM replica taken from another area at B near the edge of the fracture surface in 4742 (near the area shown in 4741, above). This area, like the one in 4741, exhibits the large and small elongated dimples that are expected in a torsion-overload fracture surface.

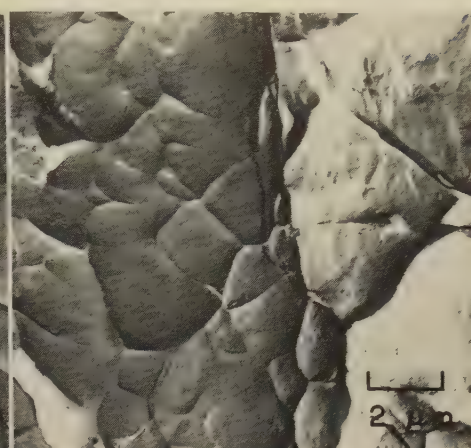
Light and TEM Fractographs: Titanium Alloy Ti-6Al-4V Unnotched and Notched Specimens Fractured by Tension Overload



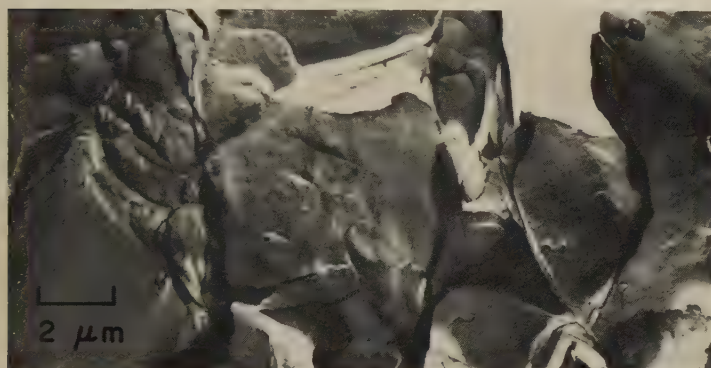
Light fractograph 9×
4745 Surface of a tension-overload fracture in an unnotched specimen of titanium alloy Ti-6Al-4V with a tensile strength of 1162 MPa (168.5 ksi). The flat, central region of the fracture surface is uniformly fibrous. See also 4746 to 4748.



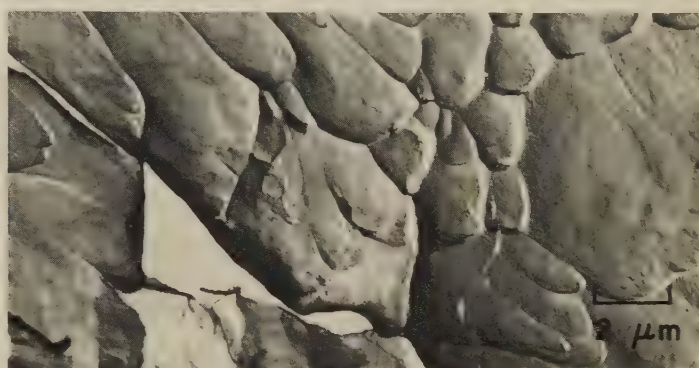
TEM fractograph (p-c replica) 5000×
4746 TEM replica of an area in the outer portion of the flat, central region of the fracture surface in 4745, showing somewhat elongated dimples. The large size and the smoothness of the dimple at top right suggest stretching.



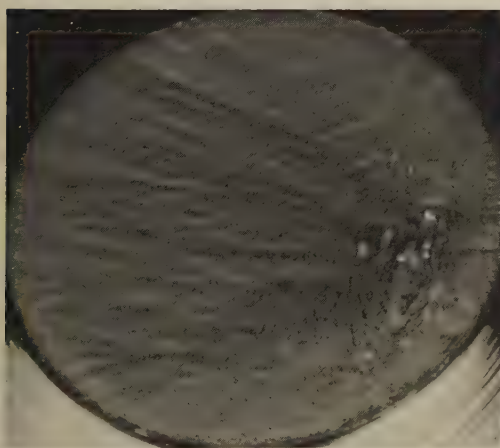
TEM fractograph (p-c replica) 5000×
4747 Another area in the flat, central region in 4745, with dimples more nearly equiaxed than those in 4746. What appears to be a grain boundary crosses the field just right of center; no evidence of secondary cracking at the boundary.



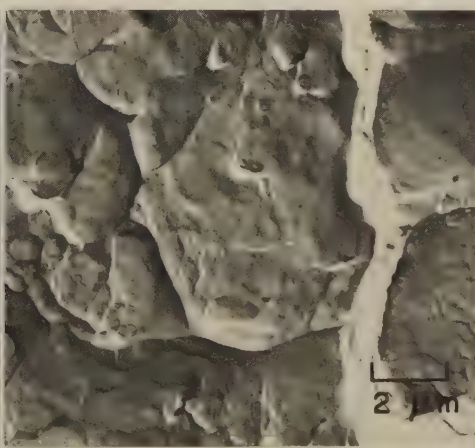
TEM fractograph (p-c replica) 5000×
4748 TEM replica of a third area in the flat, central region of the fracture surface in 4745, showing dimples of various shapes, which exhibit many regions that appear stretched. The white region at top right is a replica tear, not a void.



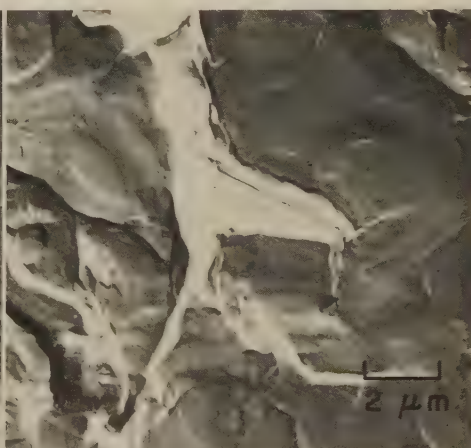
TEM fractograph (p-c replica) 5000×
4749 TEM replica of an area near the center of the fracture surface in 4750 (below, left), showing markedly elongated dimples, many of which are very flat. A secondary crack extends from top left to bottom center.



Light fractograph 9×
4750 Surface of a tension-overload fracture in a notched specimen of titanium alloy Ti-6Al-4V with a tensile strength of 1696 MPa (246 ksi). Unnotched tensile strength, same as in 4745. Fibrous marks radiate from the subsurface fracture origin at right. See 4749, 4751 and 4752.

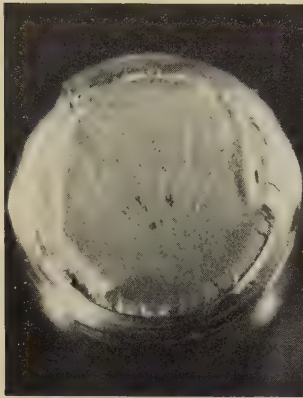


TEM fractograph (p-c replica) 5000×
4751 TEM replica of an area near the center of the fracture surface in 4750 — an area different from the one shown in 4749 (above, at right). The white vertical feature is either a secondary crack or a sharp step. The dimple at top right shows stretching and ripples.

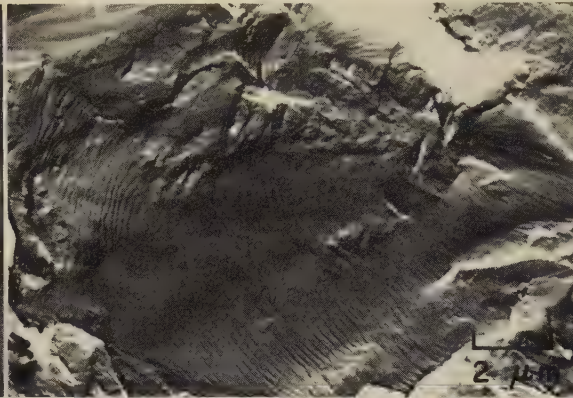


TEM fractograph (p-c replica) 5000×
4752 TEM replica of a third area near the center of the fracture surface in 4750, showing branched secondary cracks (white). The dimples in the upper portion of the field have undergone appreciable stretching and display faint ripples.

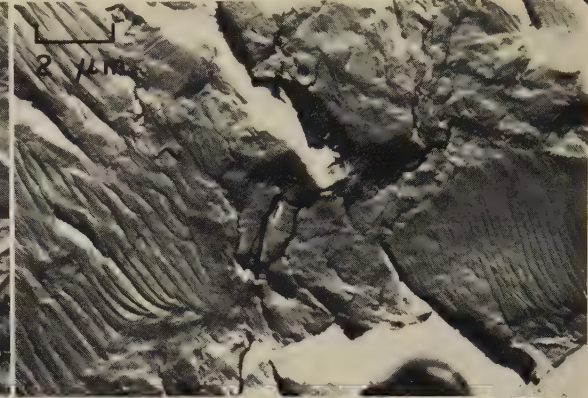
Light and TEM Fractographs: Titanium Alloy Ti-6Al-4V Threaded Bolts Fractured by Low-Cycle Fatigue and by High-Cycle Fatigue



Light fractograph 6×
4753, 4754, 4755

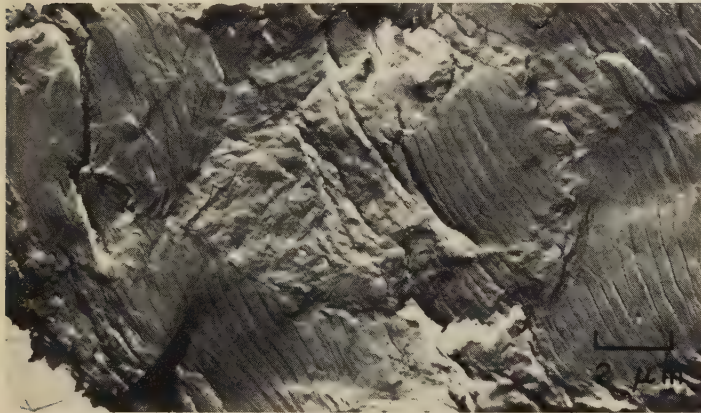


TEM fractograph (p-c replica) 5000×



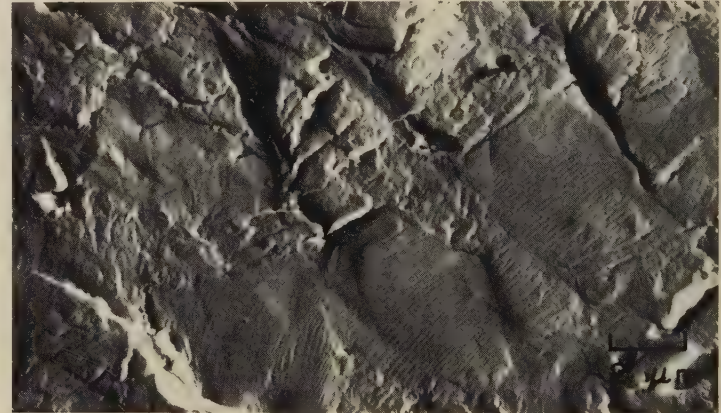
TEM fractograph (p-c replica) 5000×

Fractograph 4753 (left) shows the surface of a low-cycle fatigue fracture in a threaded bolt of titanium alloy Ti-6Al-4V, with a tensile strength of 1162 MPa (168.5 ksi), that was tested in tension-tension ($R = 0.1$) at a maximum stress of 689 MPa (100 ksi) and that broke after 12,000 cycles. The fatigue crack began at several nuclei in the root of the thread. Formation of the smooth fatigue zone at lower right was succeeded by formation of the zone of fibrous fast fracture, in which the fibers are radially oriented. Fractographs 4754 (center) and 4755 (right) are TEM replicas of two areas in the fatigue zone and show sharply defined fatigue striations that vary in orientation. The area shown in 4755 is farther from the crack nuclei than the area shown in 4754 and displays wider striation spacing. See also fractograph 4756 (below, at left).



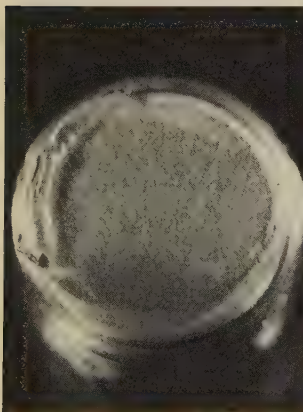
TEM fractograph (p-c replica) 5000×

4756 TEM replica of an area of the fracture surface in 4753 still farther from the fatigue-crack nuclei than the areas in 4754 and 4755 and showing still wider spacing of fatigue striations. The facet at left center is essentially free of striations because of unfavorable crystallographic alignment.

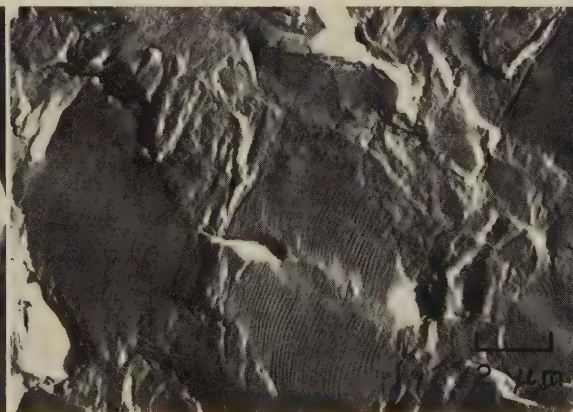


TEM fractograph (p-c replica) 5000×

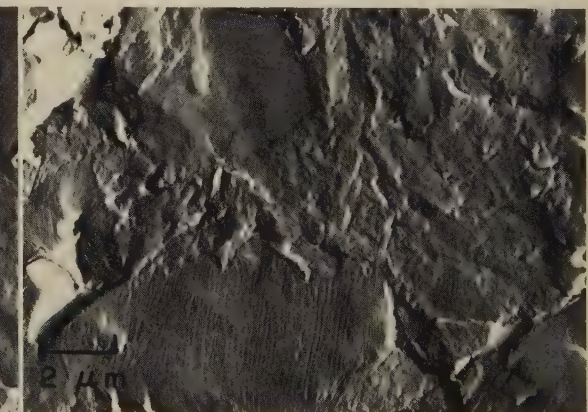
4757 TEM replica of a fatigue-zone area of the fracture in 4758 (below, left). Striations here are much finer than those in the low-cycle fatigue-test specimen in 4753 to 4756, which was broken at higher stress. Numerous facets lack striations because of unfavorable crystallographic orientation.



Light fractograph 6×
4758, 4759, 4760



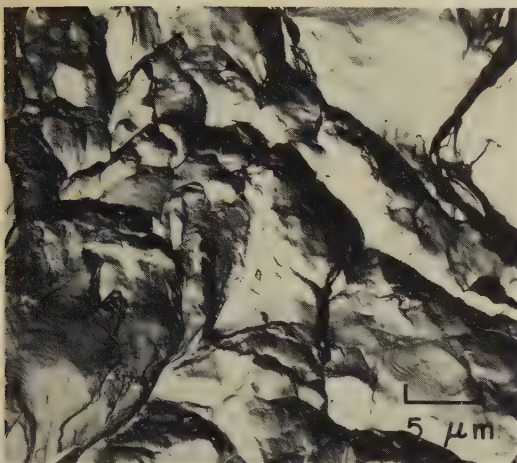
TEM fractograph (p-c replica) 5000×



TEM fractograph (p-c replica) 5000×

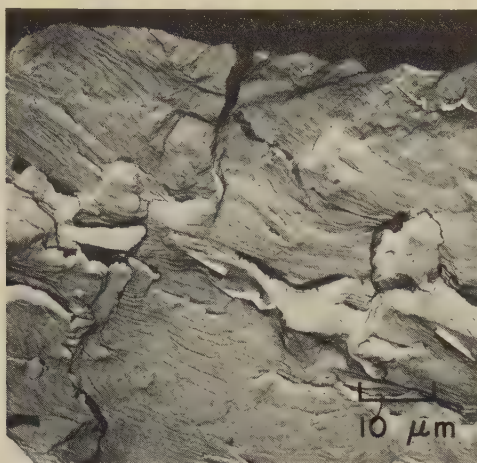
Fractograph 4758 (left) shows the surface of a high-cycle fatigue fracture in a threaded bolt of titanium alloy Ti-6Al-4V, with the same tensile strength as that of the bolt in 4753, that was tested in tension-tension ($R = 0.1$) at a maximum stress of 345 MPa (50 ksi). Fracture occurred after 937,000 cycles. The fatigue crack originated on a broad front at nuclei in the root of the thread. Fractographs at center (4759) and right (4760) are TEM replicas of two areas in the fatigue zone; in both areas, about half of the facets show no striations and the striations in adjacent facets display different orientations. Some secondary cracking has occurred here but is not clearly visible except at top in 4759. See also fractograph 4757 (above, right).

Light and TEM Fractographs of Titanium Alloys: Ti-6Al-4V Fractured by Tension Overload;
Ti-7Al-2Cb-1Ta Fractured by Fatigue in Air, Distilled Water and Salt Water



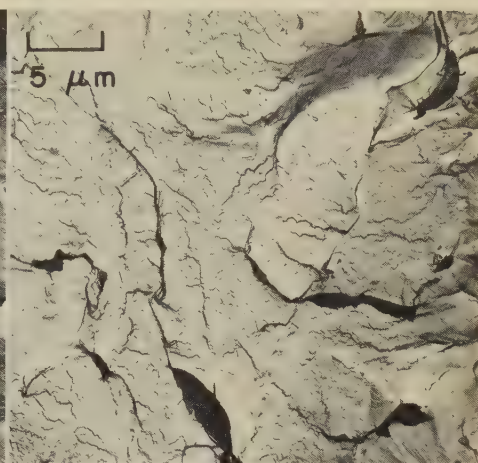
TEM fractograph (p-c replica) 2000×

4761 TEM replica of the surface of a room-temperature tension-overload fracture in a specimen of titanium alloy Ti-6Al-4V, showing dimples in a wide range of sizes. Note ripple marks, throughout, which could be mistaken for fatigue striations.

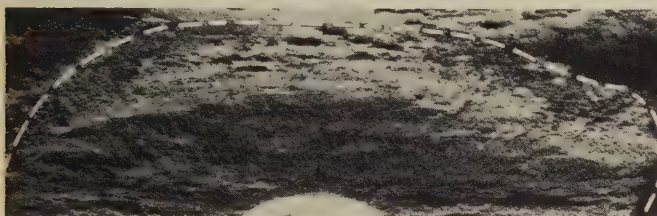


TEM fractograph (p-c replica) 1000×

4762, 4763 TEM replicas of two areas of the fracture surface in 4765 (below, right) — a low-cycle fatigue fracture in titanium alloy Ti-7Al-2Cb-1Ta. Fractograph 4762 (left), of an area at A in the fatigue zone, shows a distorted surface with pronounced fissures between patches of fatigue striations. Fractograph 4763 (right), of an area at B, at the transition between fatigue and tension-overload fracture, shows quasicleavage facets containing small cleavage steps or tear ridges.



TEM fractograph (p-c replica) 2000×



Light fractograph

3 1/2 ×

4764 Surface of a low-cycle fatigue fracture in a center-notched-plate bend specimen of titanium alloy Ti-7Al-2Cb-1Ta, mill annealed, tested in distilled water. The fatigue-crack surface (outlined by dashed line) was exposed by tension overload. See also fractograph 4766 (below, left), for a TEM view of an area of this fracture surface.



Light fractograph

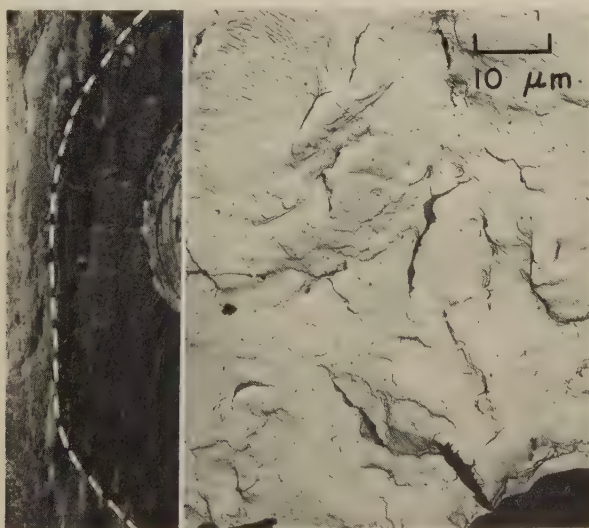
4 3/4 ×

4765 Surface of a low-cycle fatigue fracture in a specimen of Ti-7Al-2Cb-1Ta alloy similar to that in 4764 but tested in ambient air. The rate of crack growth here was lower than that for the specimen in 4764 (tested in distilled water), and the rate for the specimen in 4764 was lower than that for the specimen in 4767 below (tested in salt water). See 4762, 4763 and 4769 for TEM replicas of areas at A, B and C.



TEM fractograph (p-c replica) 1000×

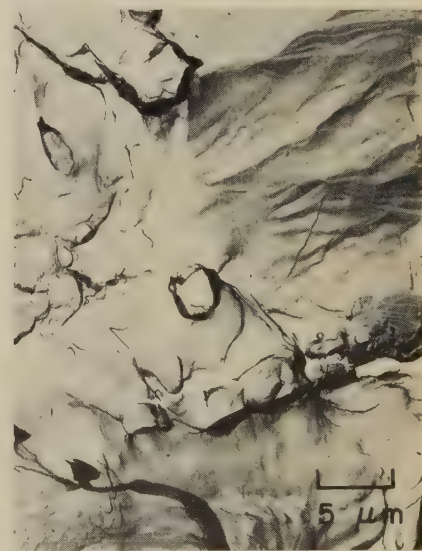
4766 A TEM replica of an area of the surface of the low-cycle fatigue fracture in fractograph 4764 (above), showing quasicleavage facets at left and, at right, facets containing fatigue striations.



Light fractograph; TEM fractograph

4 1/2 ×; 1000×

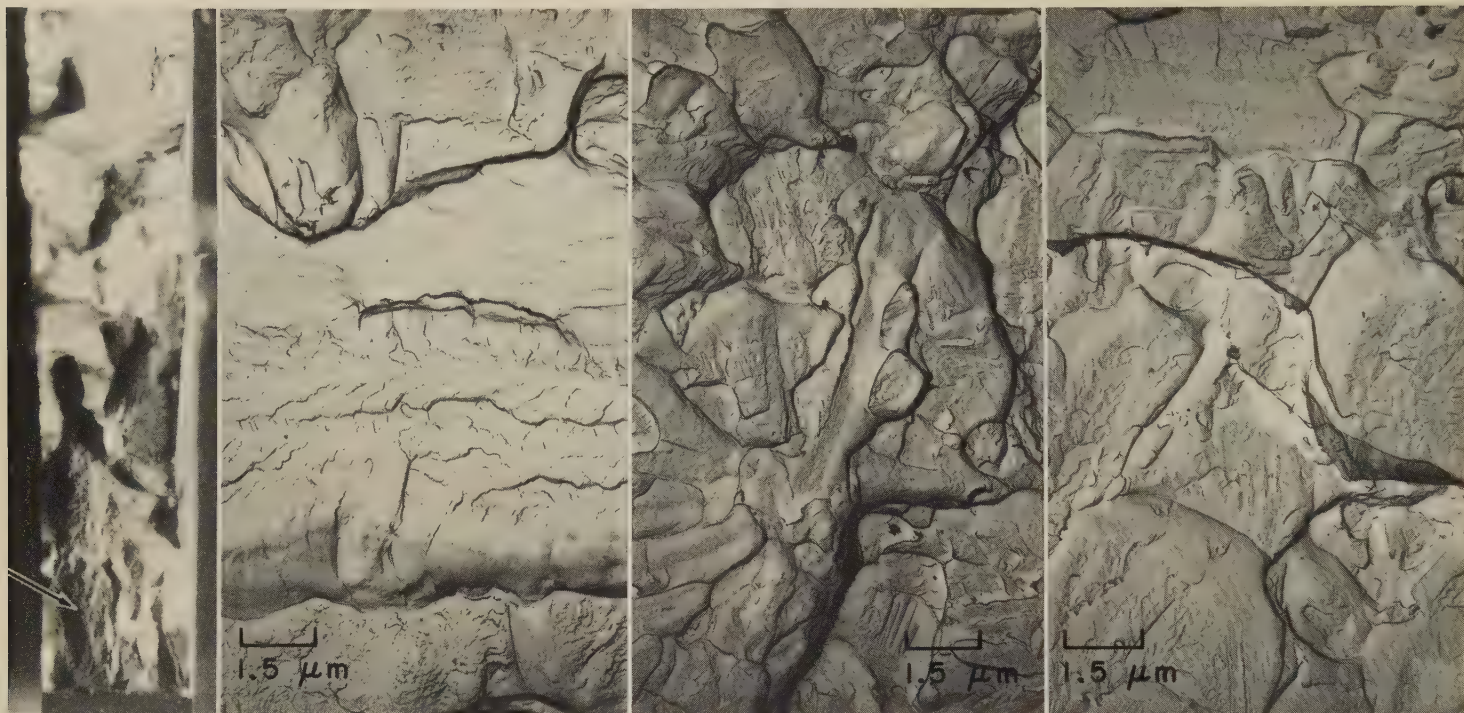
4767, 4768 Fractograph 4767 (left) shows a corrosion-fatigue fracture in a titanium alloy Ti-7Al-2Cb-1Ta specimen similar to those in 4764 and 4765 except tested in salt water. Fractograph 4768 (right) is a plastic-carbon replica of the fatigue zone in 4767 showing fatigue striations at top and quasicleavage facets at bottom.



TEM fractograph (p-c replica) 2000×

4769 TEM replica of an area at C in the tension-overload region of the fracture surface in 4765 (above), showing large and small dimples at left and serpentine glide at top right and bottom right.

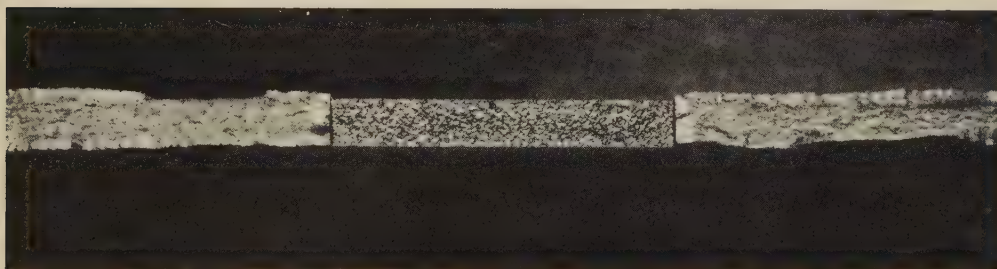
Light and TEM Fractographs of Notched Sheet Specimens of Titanium Alloys:
Ti-8Mn Fractured by Sustained Tension; Ti-13V-11Cr-4Al Fractured by Fatigue



Light fractograph; three TEM fractographs (p-c replicas)

4770, 4771, 4772, 4773 Fractograph 4770 (left) shows the surface of a sustained-tension fracture in a notched specimen of titanium alloy Ti-8Mn sheet (annealed to a tensile strength of 896 MPa or 130 ksi) that was charged with hydrogen at 704 C (1300 F) to 480 ppm and tested at room temperature at a stress of 834 MPa (121 ksi). Fracture occurred after 24 hr. Specimen was notched at both edges, at center of flat gage section ($1\frac{3}{16}$ by 0.25 by 0.045 in.). Notches had angles of 60°, and were 0.05 in. deep and 0.005 in. in radius. Fractographs 4771 to 4773 are TEM replicas of three areas at the arrow (near notch at bottom) in 4770. In 4771 (second from left), a large region of cleavage is bordered by dimple-like features. Fractographs 4772 (second from right) and 4773 (right) show flattened features with aspects of combined cleavage and microvoid coalescence, or "quasicleavage".

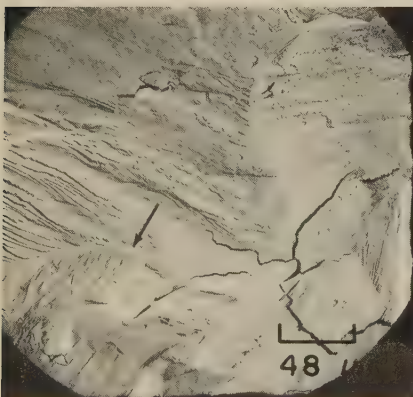
17× (4770); 6500× (4771-4773)



Light fractograph

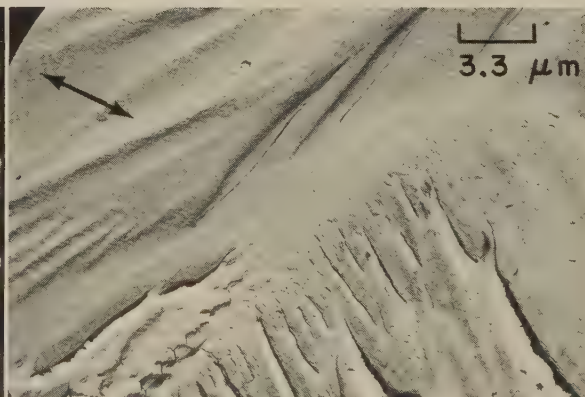
4×

4774 This light fractograph (at left) shows the major portion of the surface of a fatigue fracture in a center-notched specimen of titanium alloy Ti-13V-11Cr-4Al sheet aged at 454 C (850 F) and loaded in tension-tension, at room temperature, to a stress cycled from 62 to 124 MPa (9 to 18 ksi). The specimen broke after 23,000 cycles. See fractographs 4775 and 4776, below.



TEM fractograph (p-c replica)

210×



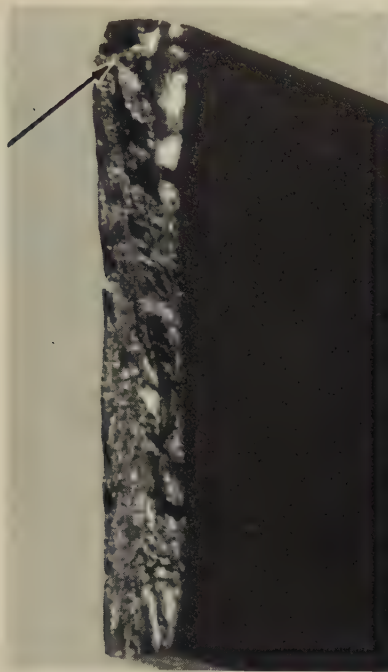
TEM fractograph (p-c replica)

3000×

4775, 4776 Fractograph 4775 (at far left) is a TEM view of a replica of an area of the fracture surface shown in 4774 (at left above). This area exhibits cleavage-like steps, which halt at grain boundaries (arrow). The fatigue striations in this area are much finer than are the more readily visible cleavage-like steps.

Fractograph 4776 (at near left) is a higher-magnification TEM view of a replica of an area at the arrow in 4775, showing extremely fine fatigue striations (parallel with the double-headed arrow), which cross other sets of lines that are analogous to cleavage steps.

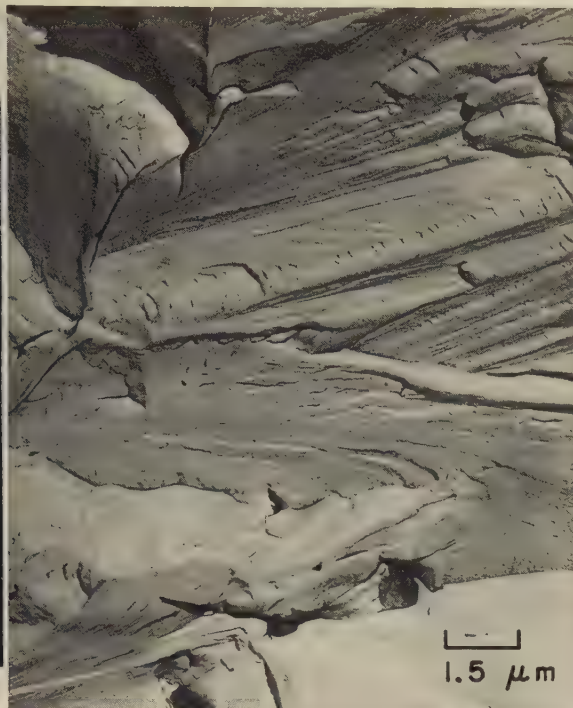
Light Fractograph and TEM Fractographs: Notched Specimen of Commercially Pure Tungsten Sheet Fractured by Tension Overload



Light fractograph

6.7×

4777 Tension-overload fracture in a notched specimen (12 by 0.50 by 0.063 in.) of stress-relieved, commercially pure tungsten sheet (tensile strength, 1103 to 1517 MPa or 160 to 220 ksi) that broke at a stress of 690 MPa (100 ksi), showing jagged, step-like facets. Notch was saw cut to a depth of 0.05 in. See 4778-4780.



TEM fractograph (p-c replica)

6500×

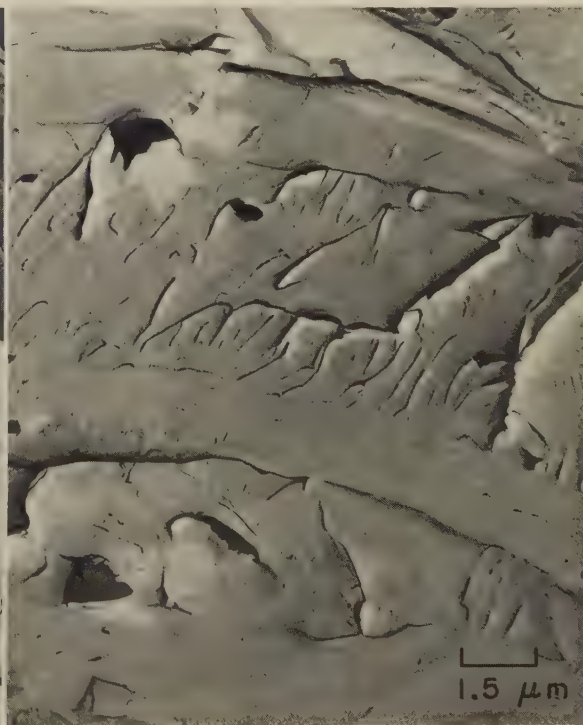
4778 TEM replica of an area at the arrow in the fracture surface in 4777 (left), showing transgranular cleavage facets containing cleavage feathers. The facets at bottom may have resulted from local intergranular rupture.



TEM fractograph (p-c replica)

6500×

4779 TEM replica of a second area at the arrow in the tension-overload fracture surface in 4777. Cleavage facets are evident at top. A region of intergranular rupture is visible at arrow.



TEM fractograph (p-c replica)

6500×

4780 TEM replica of a third area at the arrow in the fracture surface in 4777. Cleavage features are predominant here. However, the narrow facet at top may be a separated-grain facet.

Light and TEM Fractographs; TEM Micrograph: Sintered Tungsten Powder Rocket-Nozzle
Insert That Fractured From Thermal Shock During Test-Stand Firing



Light fractograph

4781 Exposed surface of a crack in a rocket-nozzle insert made of tungsten powder sintered to 70 to 80% of theoretical density. The crack, observed after only 30 sec of test-stand firing, was attributed to thermal shock. The crack was perpendicular to the nozzle axis and extended through about two-thirds of the wall of the insert; shown here is a thin slice of the wall. The crack propagated from left to right in this view, ending at the arrow by the bright facet. The remainder of the fracture was produced in the laboratory to expose the crack surface. See 4782 to 4784, below.

7×



TEM fractograph (p-c replica)

2000×

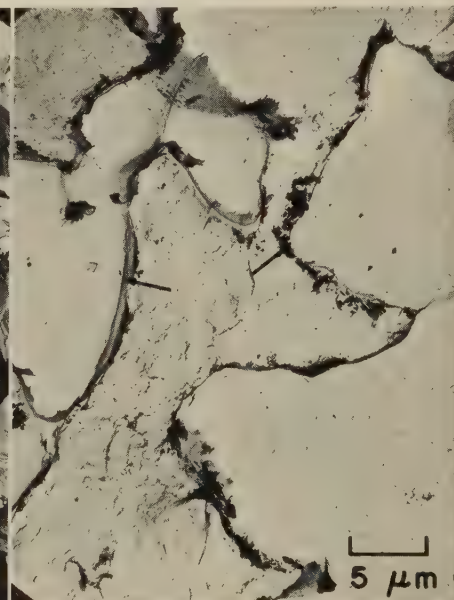
4782 TEM replica of an area in the portion of the fracture in 4781 that occurred during test-stand firing, showing intergranular facets of approximately the same size as the size of the particles of tungsten powder.



TEM fractograph (p-c replica)

2000×

4783 TEM replica of an area in the portion of the fracture in 4781 that was produced in the laboratory. This area, like that in 4782, shows intergranular facets of about the same size as the particles of tungsten powder.



TEM micrograph (Kroll's reagent)

2000×

4784 Plastic-carbon TEM replica of a polished and etched section through the test-stand-firing portion of the crack in 4781. The crack (lower left to upper right) is filled with epoxy resin; crack surfaces (arrows) do not abut because of plastic flow.

Failure-Analysis Fractographs

Prepared by John A. Fellows

CONTENTS

Armco iron; wrought iron	378	4130 steel	413	13-8 PH stainless steel	454
Galvanized steel	379	4140 steel	414-417	15-5 PH stainless steel	454
Low-carbon steel	379-380	4150 steel	415	Types 302, 304, 330 stainless steel	455
1020 steel; cast 0.20% C steel	381-382	0.26C-0.70Mn-0.8Ni-1.00Cr steel	418	Aluminum casting alloy 218	456-457
1030 steel	382	D6B steel	419	Wrought aluminum alloys:	
ASTM A515, grade 70, steel	383-385	AMS 6434 (4335 mod) steel	428	2014-T6	458-461
1033 steel	386	4340 steel	420-425, 427-433	2020-T651; 2024; 2024-T3, -T851	462
1035 steel	387	High-strength low-alloy steel	426, 437	2025-T6	462-464
1038 steel	388, 392	300M steel	434	6061-T6; 7075-T6	465
1039 steel	391	4350 steel	434-435	7079-T6	465-467
1040 steel	388-389	4817 steel; 4820H steel	436	7079-T651; 7106-T63; 7178-T6	467
1041, 1041H, 10B41 (1541, 1541H, 15B41) steels	389-391, 393-394	50B20 steel; 5046 steel	437	Columbium; columbium alloy B-66 ..	468
T-2 nickel steel	393	50B60 steel; 5132 steel	438	99.999% Cu (Pd-coated); tough pitch copper; low-silicon bronze	468
Medium-carbon steel	394-395	5135H steel	439	Phosphor bronze C	468-469
11L40 steel; 1144 steel	396	5145 steel	440	80Cu-20Zn brass + 0.5% Sn	469
1045 steel	397-403	5160 steel	440-441	91-7-2 aluminum-silicon bronze	470
1046 steel	402-404	6150 steel	442	85-5-5-5 leaded red brass	470
1050 steel	405	8617 steel	443	60Cu-37.8Zn manganese bronze	471
1053 steel	406	8620 steel	443-447	48Cu-35Ni-11Sn-6Pb alloy	471
1055 steel	407	8640 steel	446-448	Titanium alloys:	
1060 steel	407-409	8645 steel	449	Ti-2Al-2Zr-2V-1Mo; Ti-2.5Al-16V	471
10B62 (15B62) steel	408	8650 steel	448	Ti-3Al	473
1070 steel	409-411	Ductile iron	450-451	Ti-6Al-4V	472-474
High-carbon steel	410	Gray iron	451	Ti-7Al-2Cb-1Ta; Ti-7Al-1Mo-1V	474
1095 steel	411	Silchrome-1 steel	452	Ti-7Al-3V; Ti-8Al-1Mo-1V	475
4118 steel	412	Type 410 stainless steel	452-453	Tungsten	475
		Cast austenitic steel	454		

THE PREVIOUS sections of this Atlas provide examples of features of fractures in a wide variety of steels, irons and non-ferrous alloys as reproduced by each of three fractographic techniques: light microscopy, scanning electron microscopy, and transmission electron microscopy of replicas. Many of these fractures (except those in the first section, on Light-Microscope Fractographs at Low Magnification) were produced by carefully supervised procedures in research laboratories to illustrate the characteristic features associated with specific fracture mechanisms that were activated in the specimen under scrutiny. The fractures were thus produced under known conditions that could be duplicated at will, but the fractures observed were not necessarily wholly representative of the features that might be encountered in fractures induced in service under more complex conditions of stress and thermal or chemical environment.

The fractographs presented in this section, however, are drawn for the most part from actual service failures due to fracture, in which identification of the cause of fracture had been sought with the aid of fractographic examination and interpretation. The contributors of these fractographs are listed on pages 127 and 128. Here and there, laboratory-produced fractographs are included, usually to provide examples of fracture characteristics not available from in-service failures.

As the Contents List above indicates, the sequence in which the fractographs in this section are presented is by type of alloy, representing essentially the same progression and types of alloys that were treated in four of the previous sections of this Atlas. A large majority of the fractographs in this section were prepared by light microscopy, but in many instances these have been supplemented by SEM or TEM fractographs at high magnification to provide more insight into the fracture mechanisms and causes. Whenever possible, the discussion of the fracture has not only noted the location and identification of the crack origin and the mechanisms by which the crack propagated through the section of the part or component, but has also presented the conclusions as to the cause of the fracture, indicating whether it was a condition of stress, of environment, of surface or interior imperfections, of inadequate design, or of a combination of these factors. Also included, wherever possible, has been a statement of the remedial action taken to avoid a recurrence of the fracture. These assessments of cause and effect thus constitute abbreviated versions of the categories of failure-analysis case histories that involve fracture.

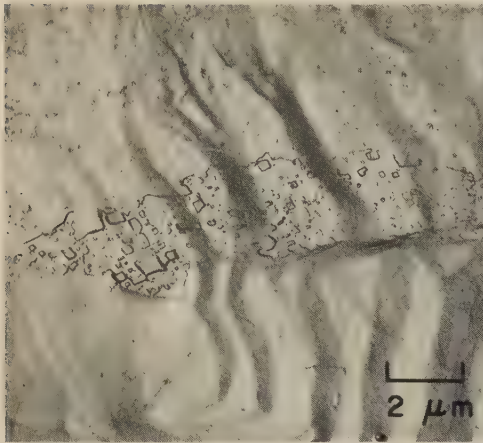
Of the fracture mechanisms illustrated in this section, the predominant type (accounting for about 60% of the total number of fractures reported and fractographs presented) is fatigue. The cate-

gory includes fatigue by reversed bending, rotating bending, cantilever bending, torsion, reversed torsion, tension-tension and spalling. This predominance of fatigue is proportional to experience with fractures in engineering parts and components, in which fatigue is the most common cause of fracture. Among the parts presented here as having exhibited fatigue fractures are aircraft propeller blades and hubs; aircraft landing-gear components, wheels and wing fittings; axles; crankshafts; gear teeth; keyed and splined shafts; and coil and leaf springs.

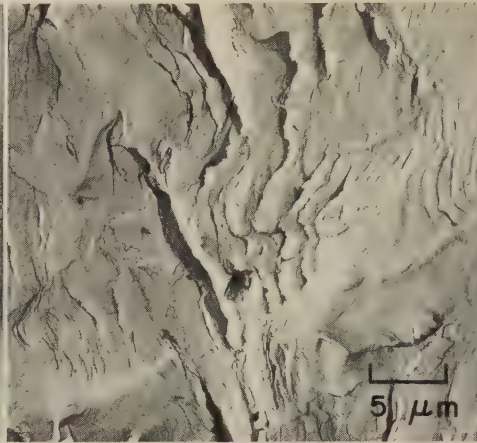
The second most common mechanism of fracture represented in this section may be broadly classed as overload (not including impact fractures). Although the majority of the overload fractures presented are the result of service failures, one group is comprised of fractures by tension-overload tests, of both notched and unnotched specimens, at several test temperatures and after various heat treatments. Examples of fracture causes reported less frequently here include impact, stress-corrosion cracking, weld defects, hydrogen embrittlement, bending, sustained loading and thermal shock.

The fracture features that appear among these fractographs involve all the categories that have been previously discussed in this volume. Fatigue striations, of course, represent the most frequently exhibited feature because of the predominance of fatigue fractures in this section.

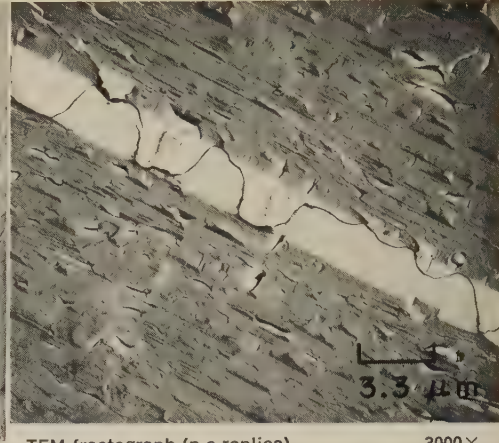
Failure-Analysis Fractographs: Armco Iron (Slip Steps and Slip-Band Cracks; Low-Temperature Cleavage Fractures; Fatigue Fracture); Wrought Iron Link Fractured by Impact



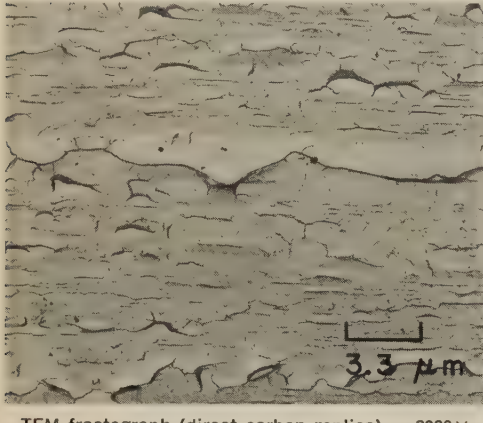
TEM micrograph (p-c replica) 5000×
4785 External surface of a specimen of Armco iron that had been etch-pitted and then subjected to tension during one cycle of a 2.5° bend test. Note the slip steps. See also micrograph 4786.



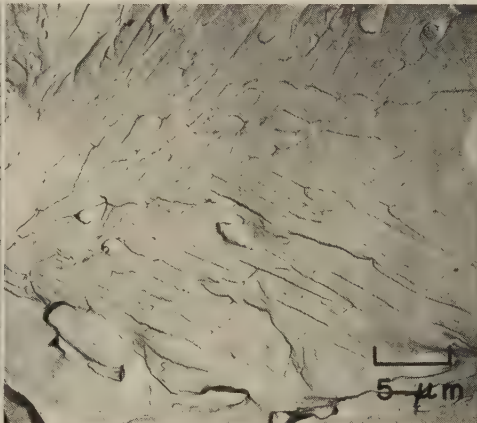
TEM micrograph (p-c replica) 2000×
4786 Same specimen as in 4785 after 5½ cycles of 2.5° bending. At center is the same area as in 4785 (reversed left to right in printing), showing slip-band cracks that have grown at slip steps.



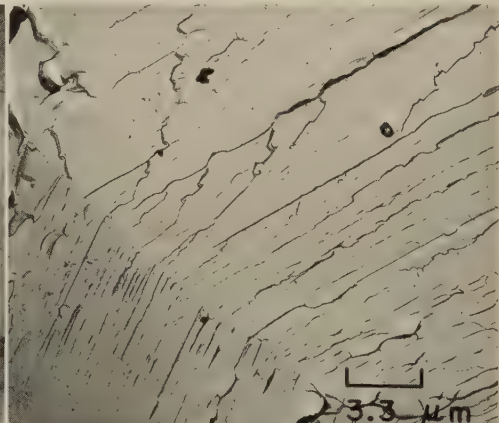
TEM fractograph (p-c replica) 3000×
4787 Cleavage fracture in Armco iron broken at dry-ice temperature (−78.5 C; −109.3 F). The light band shows where cleavage followed a twin-matrix interface. The black meandering line is a shear step through the thickness of the twin.



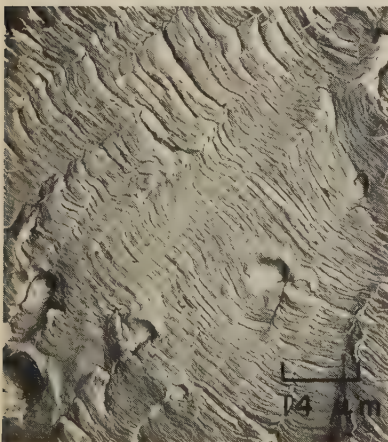
TEM fractograph (direct carbon replica) 3000×
4788 Cleavage fracture in Armco iron broken at dry-ice temperature (−78.5 C; −109.3 F), showing facets of which most have the same orientation. Facets that depart from the general orientation appear lighter or darker than the majority.



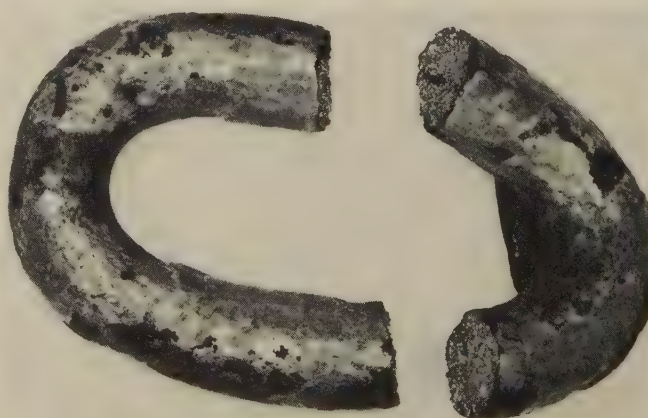
TEM fractograph (p-c replica) 2000×
4789 Cleavage fracture in Armco iron broken at −45 C (−49 F). Instead of cleavage steps, tear ridges (occasionally forming river patterns) were produced here by microscopic plastic flow.



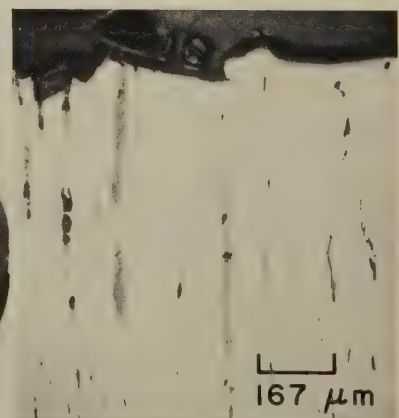
TEM fractograph (p-c replica) 3000×
4790 Cleavage fracture in Armco iron broken at −196 C (−321 F), showing river patterns, tongues and (from bottom right to top left) a grain boundary.



TEM fractograph (p-c replica) 700×
4791 Surface of a fatigue fracture in Armco iron, exhibiting fatigue striations and inclusion-matrix interfaces.



Photograph 1.9×
4792 Wrought iron chain link from a guardrail, fractured by impact in cold weather (2 C; 36 F). Examination of the fracture surfaces disclosed no evidence of prior cracking or of metallurgical defects. See 4793.

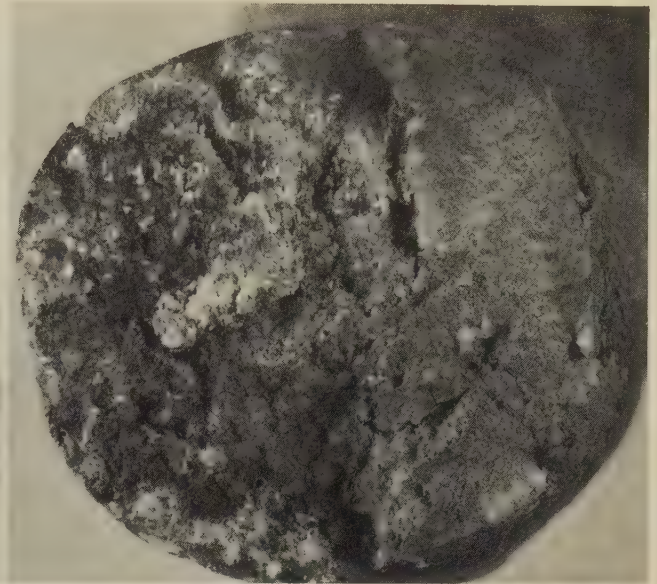


Micrograph (2% nital) 60×
4793 Polished and etched section normal to a fracture surface in 4792, showing the surface in profile at top. Note lack of deformation of cleaved grains.

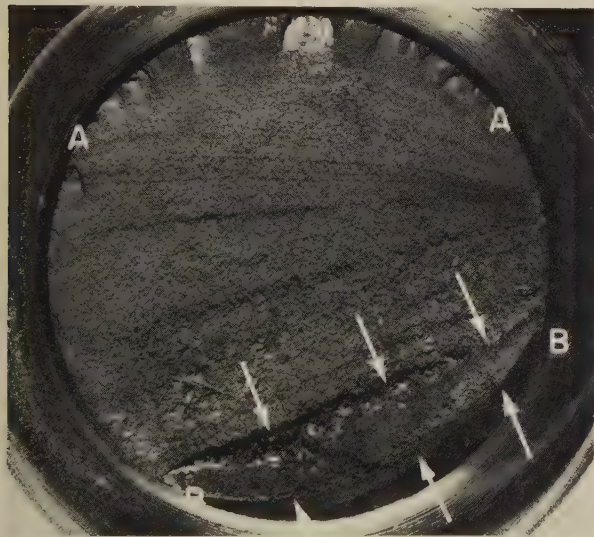
Failure-Analysis Fractographs: Galvanized Steel Link Fractured at Weld; Fatigue Fractures in Low-Carbon Steel Piston Rod and Ship Plate; Fracture in a Low-Carbon Steel Stamping



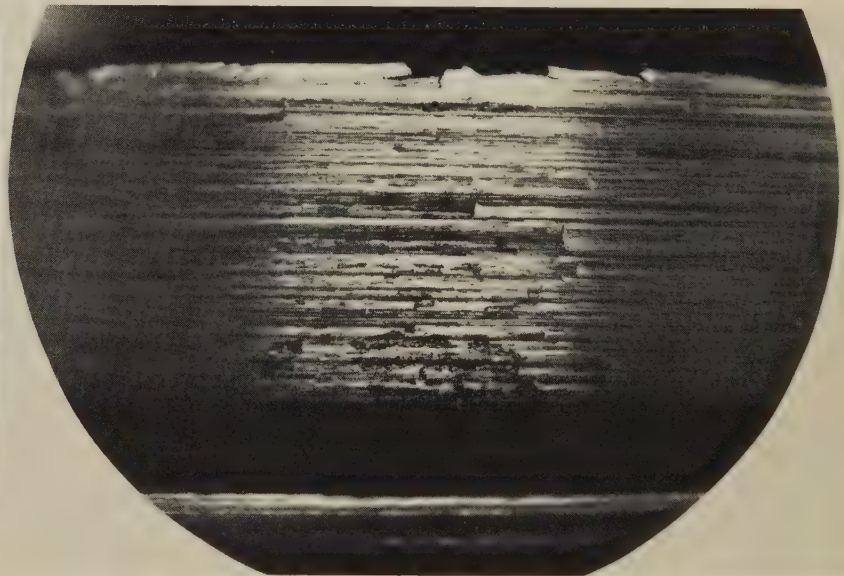
Photograph
4794 A 6-in.-long chain link made of galvanized $\frac{3}{8}$ -in.-diam steel rod that fractured at an imperfectly welded joint. No other defects were discovered. See also fractograph 4795.



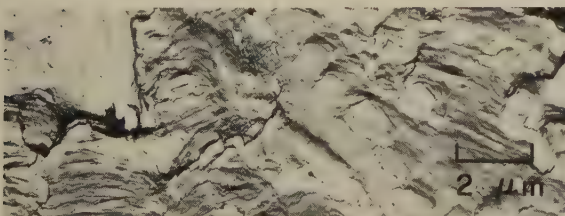
Light fractograph
4795 A view of a fracture surface of the chain link in 4794, showing discolored, undeformed areas indicative of incomplete fusion during welding.



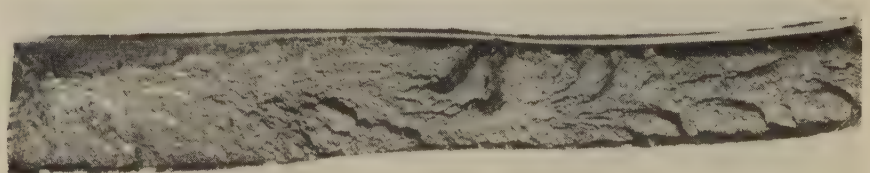
Light fractograph
4796 Surface of a fracture in a lift-truck hydraulic-piston rod of low-carbon steel that broke at a fillet by fatigue. Several fatigue-crack nuclei are evident at top edge (between A's), and there is another at the bottom edge (between B's). Fracture was by reversed bending. Final, fast fracture was in the small region indicated by the arrows. See also 4797.



Light macrograph
4797 A view of coarse machining marks that were found in the fillet in 4796 (left) between the larger-diameter portion of the piston rod and the threaded end. A secondary crack that follows a machining mark is visible at top center. These surface marks are considered to be areas of local stress concentrations, which led to fatigue cracking.

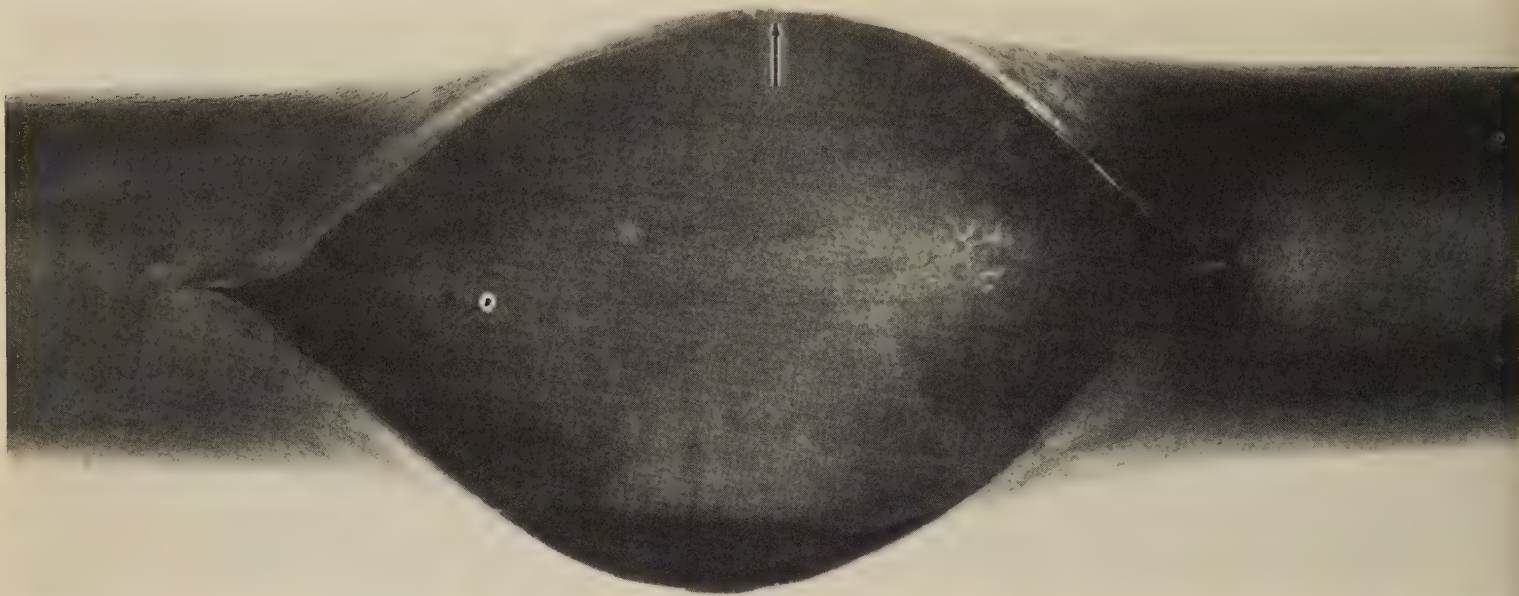


TEM fractograph
4798 Fatigue-fracture surface of a low-carbon steel ship plate broken in a laboratory. Fatigue striations and some signs of dimples.



Light fractograph
4799 Surface of a fracture in a low-carbon steel stamping. Note the chevron marks, which point toward the origin of fracture (out of view to the left); chevron marks are often associated with high-velocity final fracture.

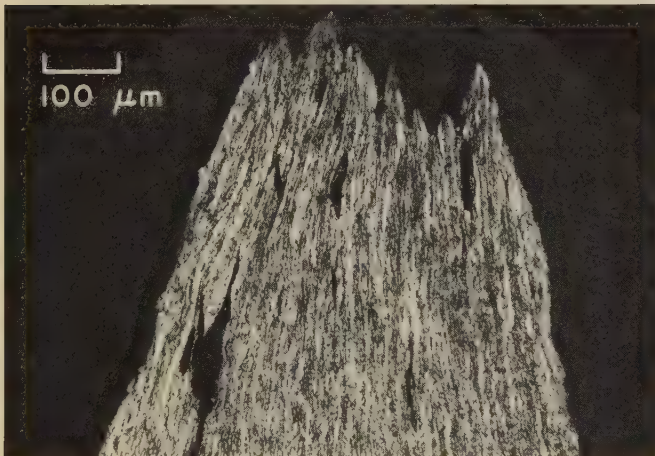
Failure-Analysis Fractographs: Low-Carbon Steel Boiler Tube Ruptured Because of Local Overheating That Resulted From Steam Starvation



Photograph

4800 Rupture in a low-carbon steel boiler tube with a nominal diameter of 3 in. and a 0.130-in.-thick wall. The rupture produced an opening 8 in. in length and 4 in. in maximum width. A slight bulge, which extended outward about $\frac{3}{32}$ in., was discovered about 2 ft below the rupture. Operating temperature was less than 538 C (1000 F), but local overheating occurred because of steam starvation. See also 4801 through 4804.

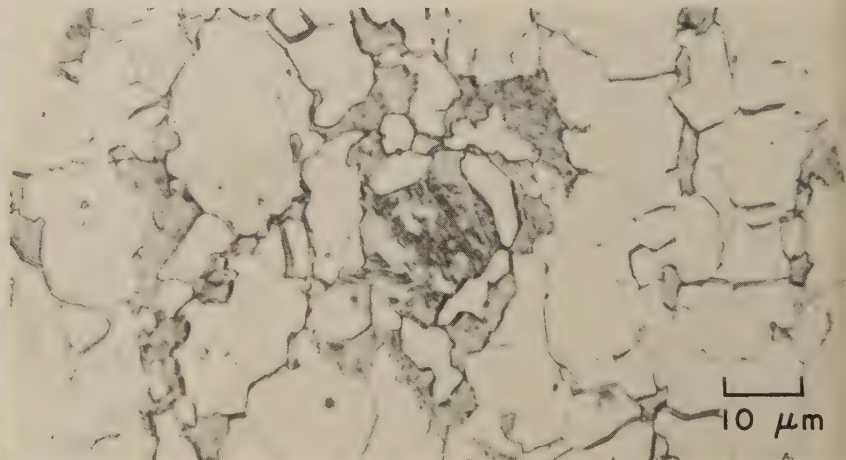
About $\frac{2}{3} \times$



Micrograph (2% nital)

100×

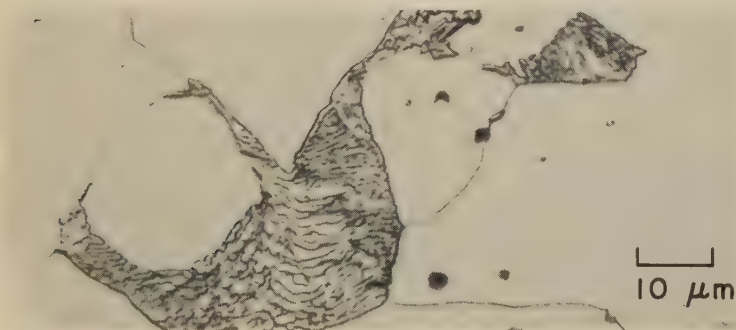
4801 A polished and etched section taken through the highly elongated "knife edge" of the boiler-tube rupture in 4800, showing in profile an area of the rupture surface at the arrow in 4800. See 4802.



Micrograph (2% nital)

1000×

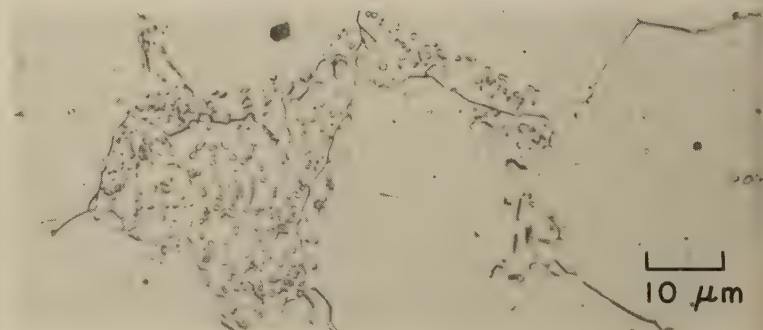
4802 A higher-magnification view of a portion of the section in micrograph 4801, showing ferrite, and low-carbon martensite that was produced at the moment of rupture when steam and water quenched the overheated steel (estimated temperature was 871 C, or 1600 F).



Micrograph (2% nital)

1000×

4803 Section through the tube in 4800, taken diametrically opposite the slight bulge 2 ft below the rupture. Microstructure here is normal, indicating that the temperature gradients that caused the bulge and the rupture were local.

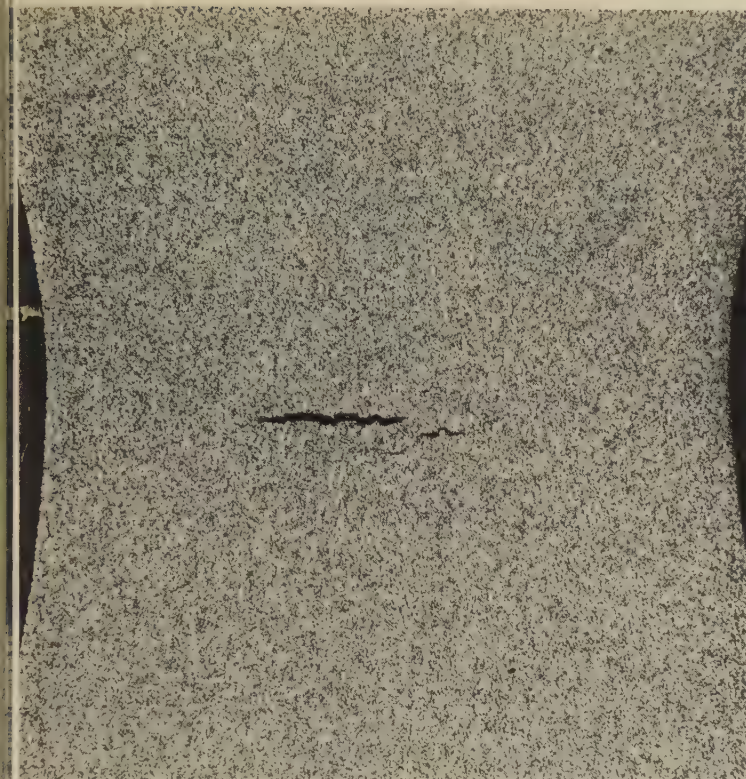


Micrograph (2% nital)

1000×

4804 Section through the tube in 4800, taken at the center of the bulge 2 ft below the rupture, showing that the pearlite normally present was altered to spheroidite—presumably because of overheating to between 538 and 677 C (1000 and 1250 F).

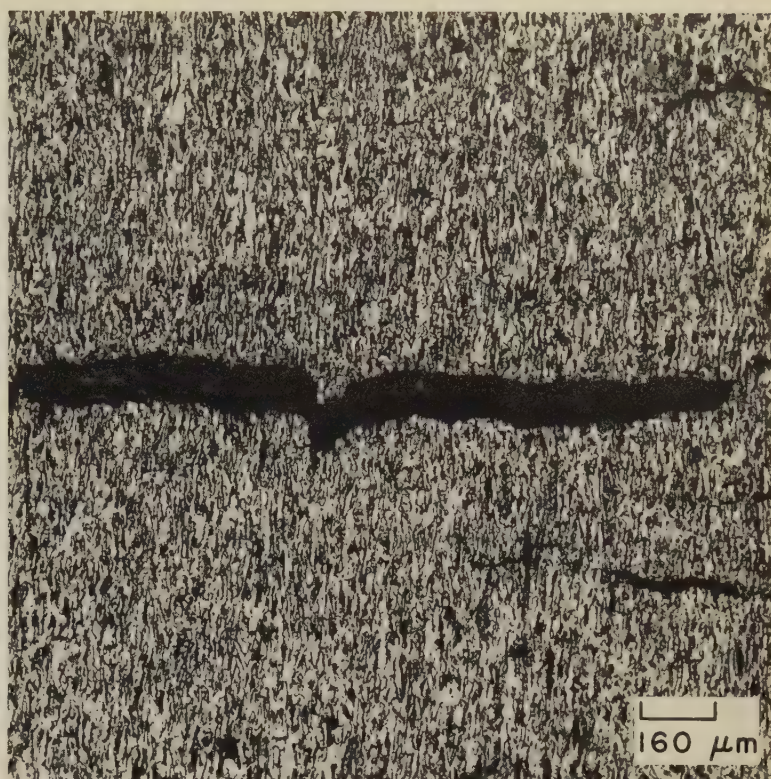
Failure-Analysis Fractographs: Centerline Cracks in 1020 Steel Tensile-Test Specimen;
Fracture in Cast 0.20% C Steel Tensile-Test Specimen, Showing Shear Lips



Macrograph (nital)

10×

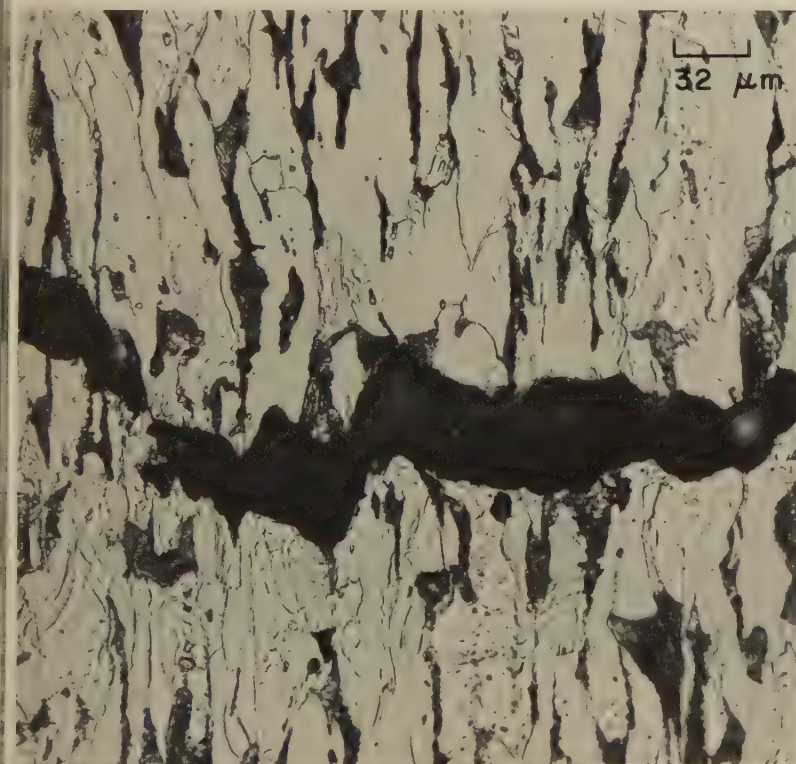
4805 Polished and etched section taken longitudinally through a 0.505-in.-diam tensile-test specimen of 1020 steel. The tensile test was halted after the centerline cracks shown here were formed but before complete fracture occurred. See also 4806 and 4807.



Micrograph (nital)

62½×

4806 Higher-magnification view of one of the centerline cracks in the specimen shown in macrograph 4805 (at left), demonstrating that the cracks are transgranular. Secondary cracks also are visible at right, above and below the main crack. See micrograph 4807.



Micrograph (nital)

312½×

4807 A further enlargement of a centerline crack in the 1020 steel tensile-test specimen shown in 4805 and 4806 (above). Note that the crack crosses alternate plates of ferrite and pearlite; note also the longitudinal deformation of the original equiaxed structure.

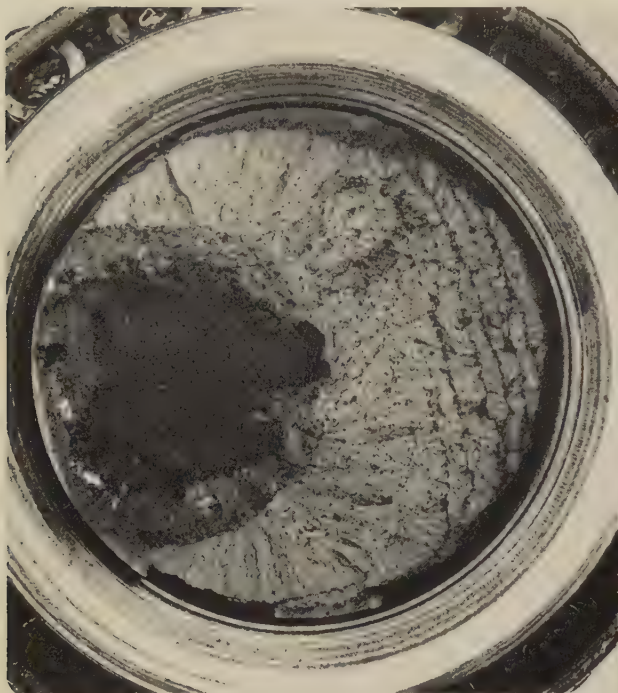


Photograph

7½×

4808 Tensile-test fracture in a 0.505-in.-diam specimen of cast 0.20% C steel with hardness of 255 Bhn. Note that pronounced 45° shear deformation has produced shear lips and also numerous secondary cracks, which formed at pores.

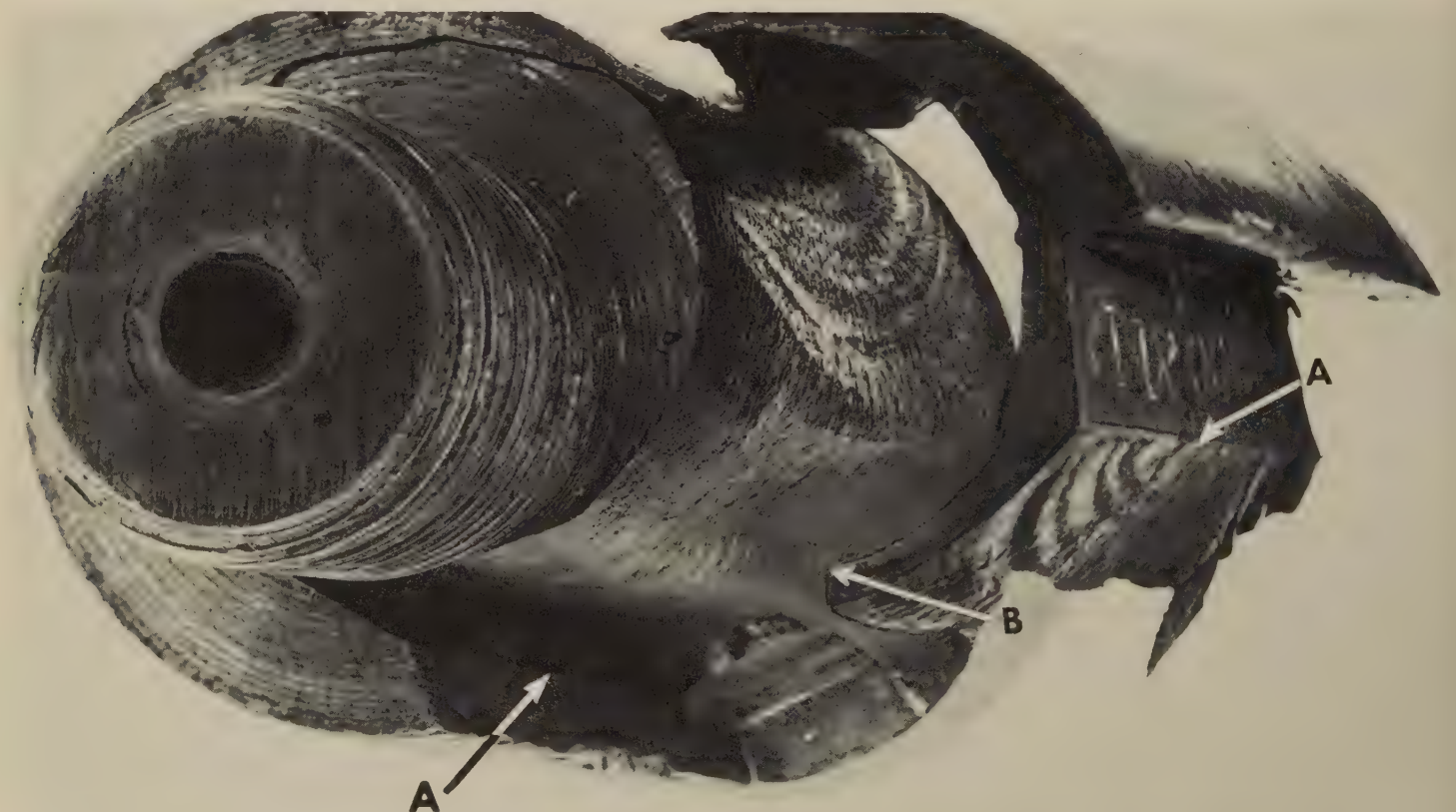
Failure-Analysis Fractographs: Cast 0.20% C Steel Spindle Fractured Through a Shrinkage Cavity; 1030 Steel Keyed Shaft Fatigue Fractured by "Peeling"



Light fractograph 1.3×
4809 Surface of a fracture in a spindle of cast 0.20% C steel; fracture occurred during a static test. The spindle broke through the large shrinkage cavity visible at left, which exhibits a distinctly dendritic structure. See also fractograph 4810 (at right).

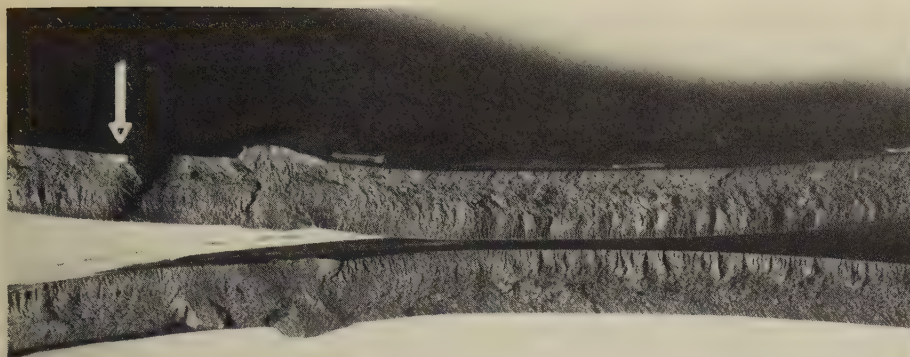


Light fractograph About 4×
4810 Higher-magnification view of the shrinkage cavity in the fracture surface in 4809, showing more clearly the dendritic structure of the cavity. Note the different orientations of the dendrites, as shown by the angles between the various dendritic patterns. Note also the range in size of the dendrites, which indicates different freezing rates.



Light fractograph 1.2×
4811 A complicated fatigue fracture in a 3 3/8-in.-diam keyed tapered shaft of 1030 steel, commonly termed a "peeling" type of fracture. A loose nut had reduced the frictional force on the tapered portion of the shaft, transferring the torsional load to the key. The fatigue crack originated at a corner in the keyway (arrows A) and progressed completely around the shaft in a clockwise circular path, returning beneath the keyway to the location marked by arrow B, where final fracture occurred.

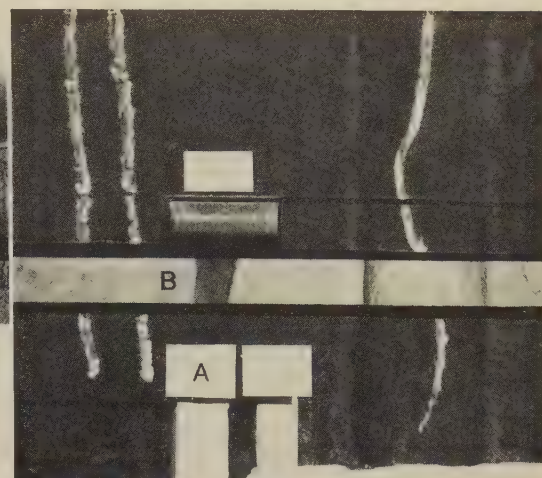
Failure-Analysis Fractographs: ASTM A515, Grade 70, Steel Pressure-Vessel Shell Plate in Which a Fracture Was Originated at Arc Strikes



Light fractograph

4812 Mating surfaces of a crack in a shell plate of an ASTM A515, grade 70, steel pressure vessel used in dehydration of natural gas. Normally, operating pressure was 1.5 MPa (220 psi) and operating temperature was -12 to $+4$ C (10 to 40 F). The crack was exposed by sectioning after a leak was discovered. See 4813 to 4817 for views of the portion near arrow at left.

0.4×



Photograph

0.57×

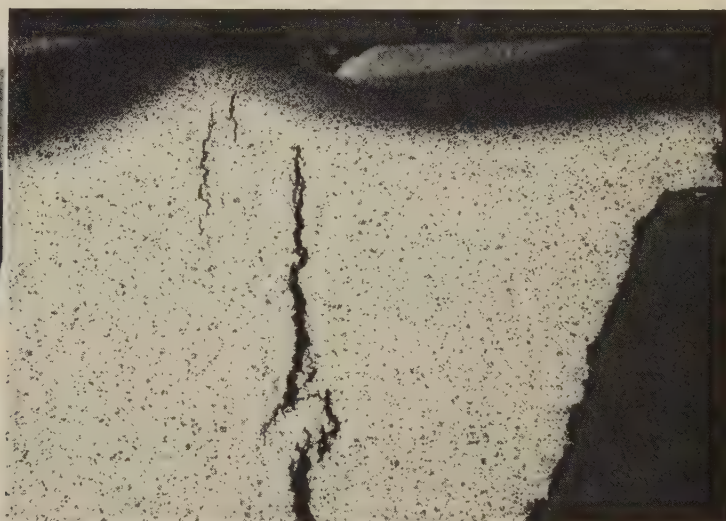
4813 Portion of the fractured shell plate in 4812 near arrow. A and B indicate where sections were cut for further study. Fracture surface is shown in profile at bottom.



Light fractograph

4814 Same portion of the shell plate as in 4813, but before sectioning and at a different orientation. The two dark crescents partly visible at top edge of the fracture surface (at arrows) were caused by arc strikes and served as crack nuclei.

0.7×



Macrograph (nital)

7×

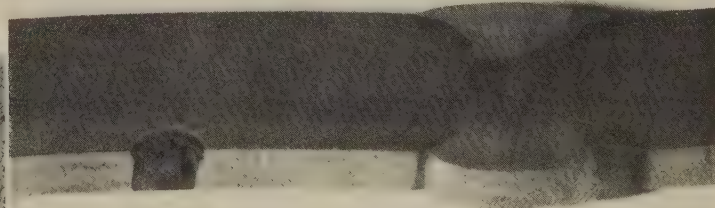
4815 A polished and etched section taken from location A in 4813, showing the arc strike visible at the left arrow in 4814. The large cracks present here are extensions of the fracture, which is visible in profile at right.



Light fractograph

4816 Another view of the fracture surface in 4814, displaying clearly the two dark arc-strike crescents that are indicated in both views by arrows at the top edge of the fracture surface. Chevron marks pointing to these crescents (which are the crack nuclei) are visible both here and in 4812.

0.93×

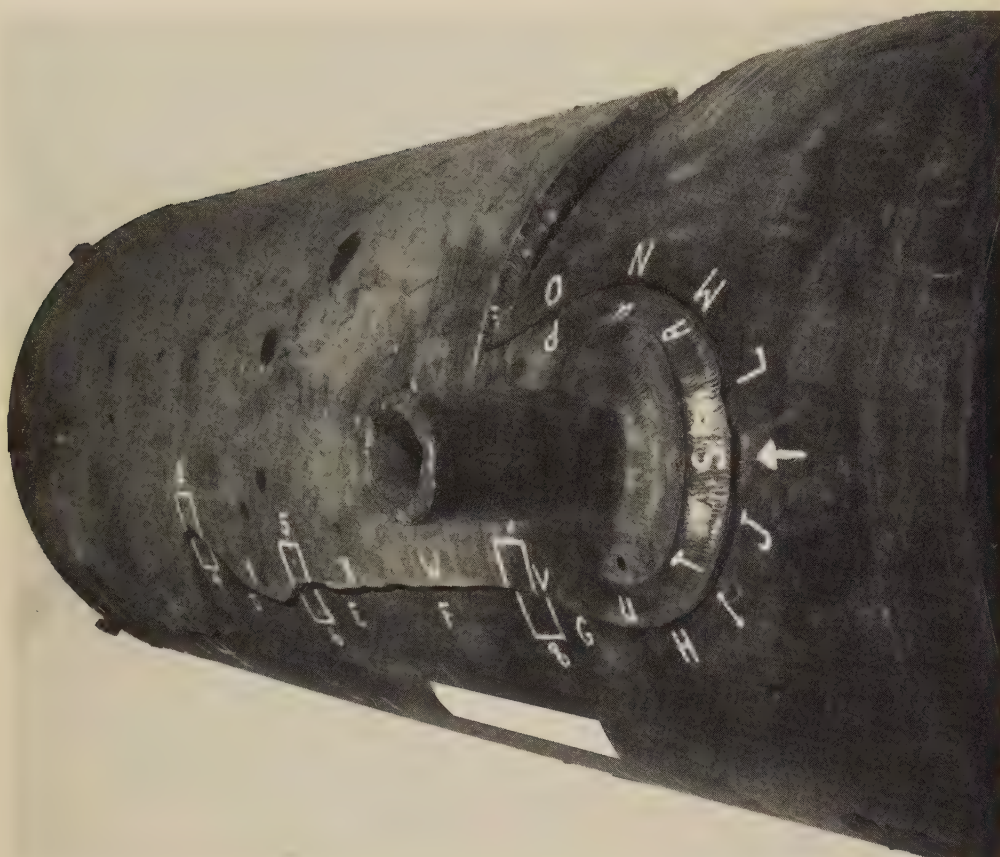


Macrograph (nital)

0.95×

4817 Polished and etched shell-plate section marked B in 4813. Note that the smaller arc strike, visible at the arrow at right in 4814 and 4816, does not extend this far from the fracture. Note also the surface damage caused by the arc strike, in contrast to the excellent condition of the weld deposit.

Failure-Analysis Fractographs: ASTM A515, Grade 70, Steel Pressure-Vessel Shell
in Which a Fracture Originated at the Toe of a Flange Weld



Photograph

4818 Fractured shell of a 34-in.-diam pressure vessel fabricated from a plate (1¼ by 96 by 360 in.) of ASTM A515, grade 70, steel for pressure vessels. The shell broke during testing at an internal gage pressure of 8.3 MPa (1.2 ksi). The fracture, which originated adjacent to a flange (arrow at S), followed a very complex path. See also 4819 to 4827.

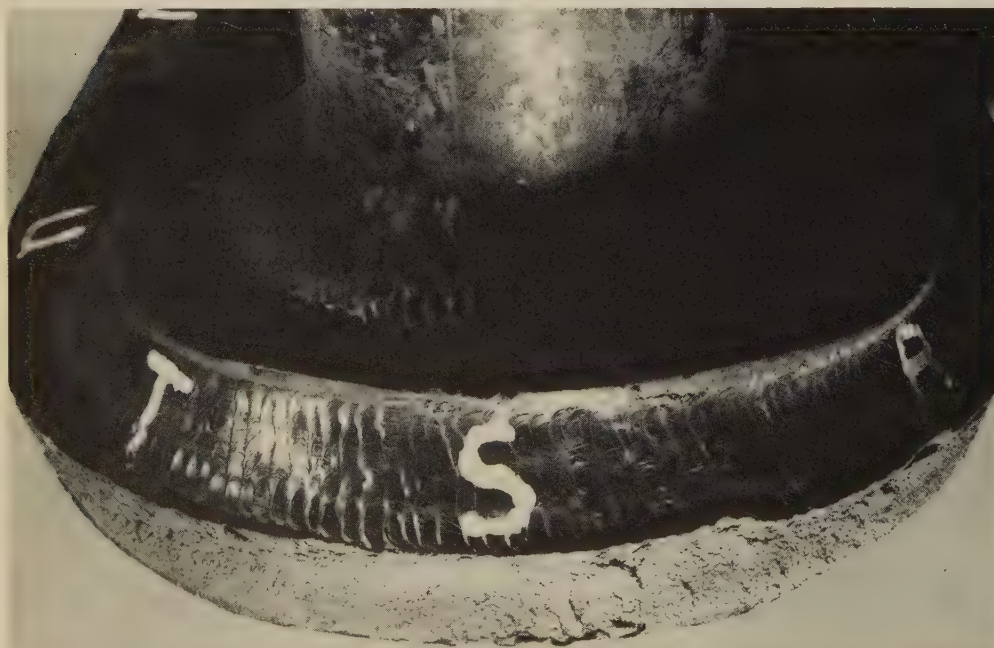
About ⅓ ×



Micrograph (nital)

500 ×

4819 A polished and etched section through the shell in 4818, showing an as-rolled microstructure consisting of a mixture of ferrite and fine pearlite, which resulted in a maximum hardness of Rockwell B 86.



Light fractograph

4820 View of the flange in 4818, showing an adjacent area of the fracture surface of the pressure-vessel shell. Although not as discernible here as in 4825 (next page), chevron marks throughout the fracture surface clearly point toward the area at S, and subsequent examination identified the toe of the flange weld at S as the crack nucleus.

About ⅓ ×

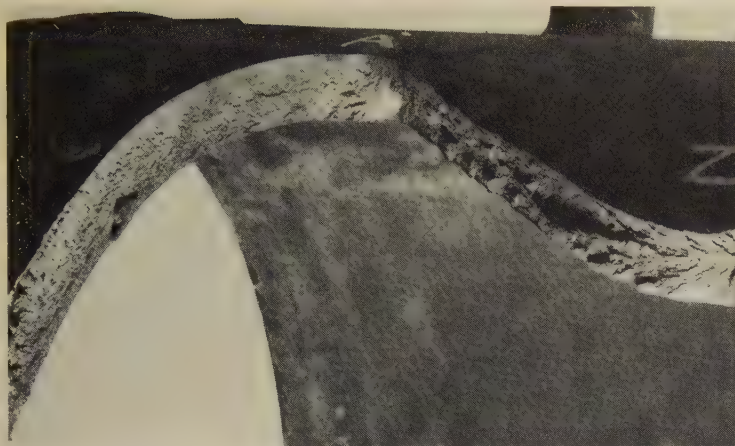


Macrograph (nital)

6 ×

4821 A polished and etched section through the toe of the flange weld at S (crack nucleus) in 4820, taken normal to the fracture surface (at left). The toe of the weld had a maximum hardness of Rockwell C 45.

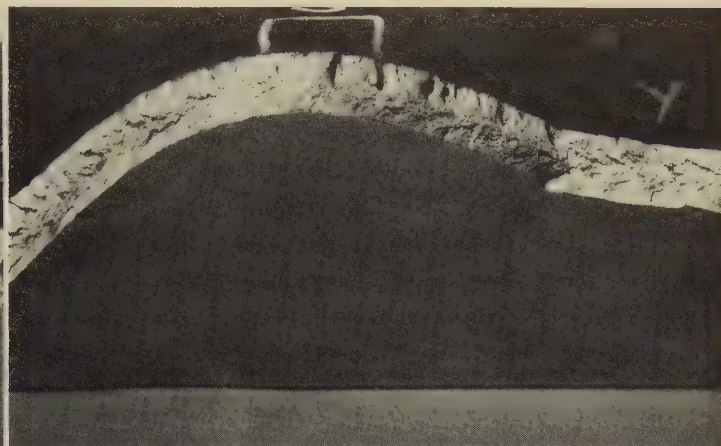
Failure-Analysis Fractographs: ASTM A515, Grade 70, Steel Pressure-Vessel Shell
in Which a Fracture Originated at the Toe of a Flange Weld (Continued)



Light fractograph

0.3×

4822 View of the far left end of the top segment of the fractured pressure-vessel shell in 4818 (facing page), showing chevron marks. The chevron marks were smeared subsequent to fracture but can be clearly identified as pointing to the right.



Light fractograph

0.25×

4823 View of the top segment of the fractured pressure-vessel shell in 4818, showing an area just to the right of the area in fractograph 4822 (at left). Again, chevron marks are visible and consistently point to the right.



Light fractograph

0.45×

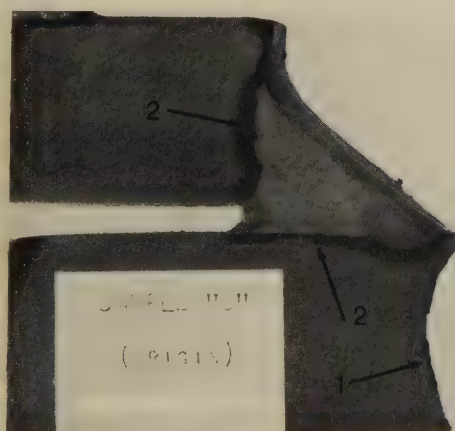
4824 View of the bottom segment of the fractured shell in 4818, showing an area opposite the one in fractograph 4823. This view also reveals sharply defined chevron marks that point to the right.



Light fractograph

0.28×

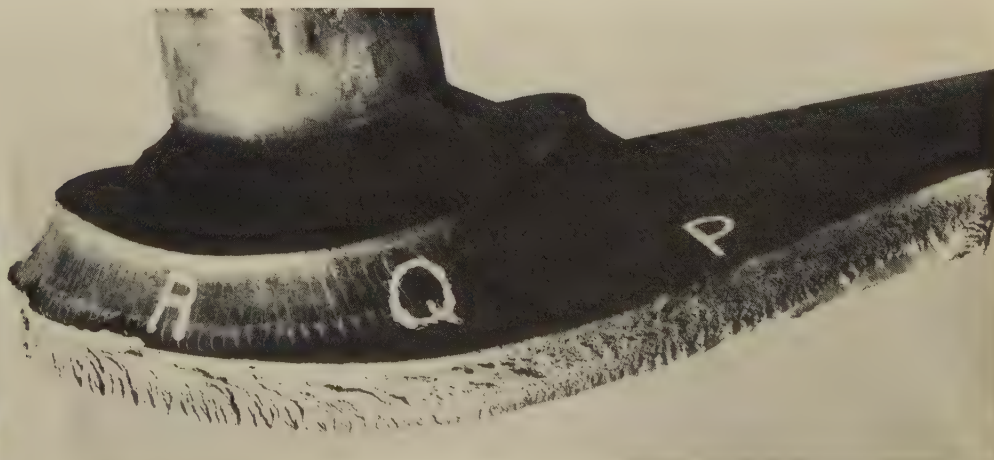
4825 View of the top segment of the fractured shell in 4818, showing an area just to the left of the fracture origin. The continuity of the chevron marks that point toward location S (at right end) is much more perceptible here than in 4820, because of a difference in illumination.



Macrograph

About 0.9×

4826 Section through the flange weld in 4820 and 4825, taken at the fracture origin and normal to the fracture surface, shown in profile at bottom right (arrow 1). Heat-affected zones (arrows 2) appear as shadows here.

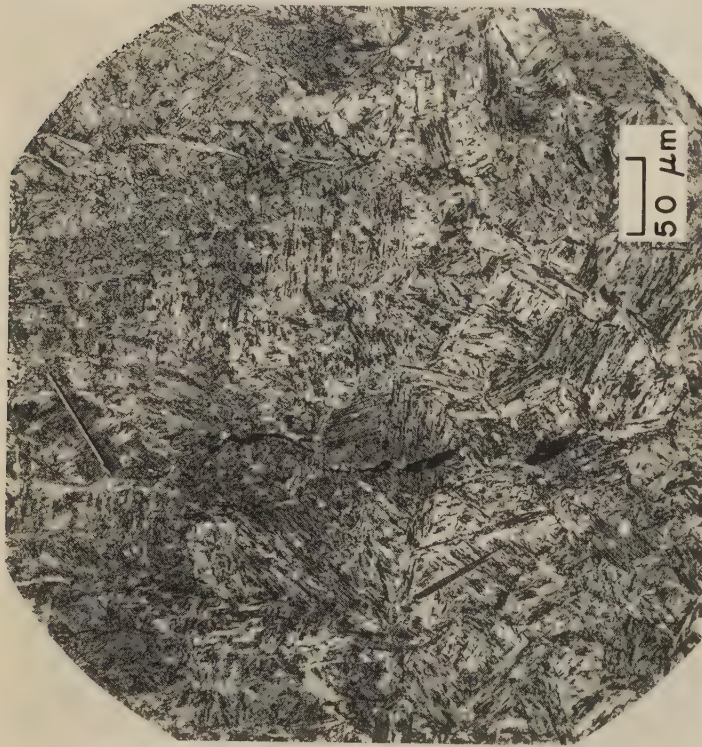


Light fractograph

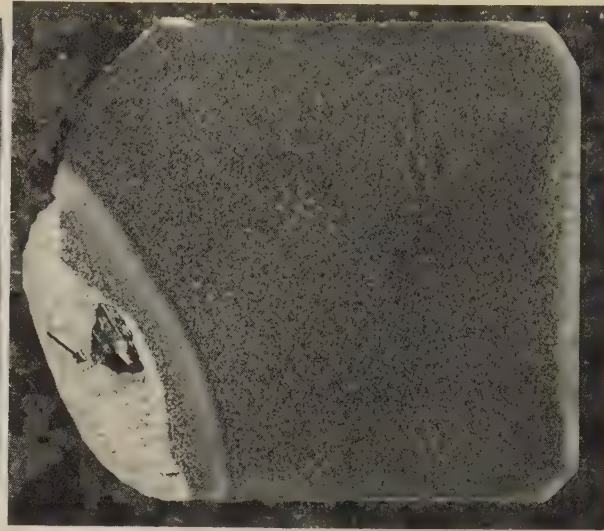
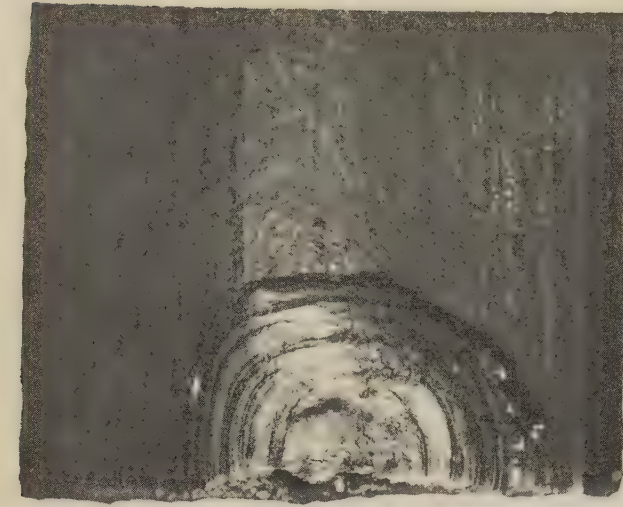
0.28×

4827 View of the top segment of the fractured pressure-vessel shell in 4818, showing an area of the fracture surface just to the right of the crack nucleus. Note that here the chevron marks clearly point to the left, toward the fracture origin. The crack ends at far right, where a section was removed for testing.

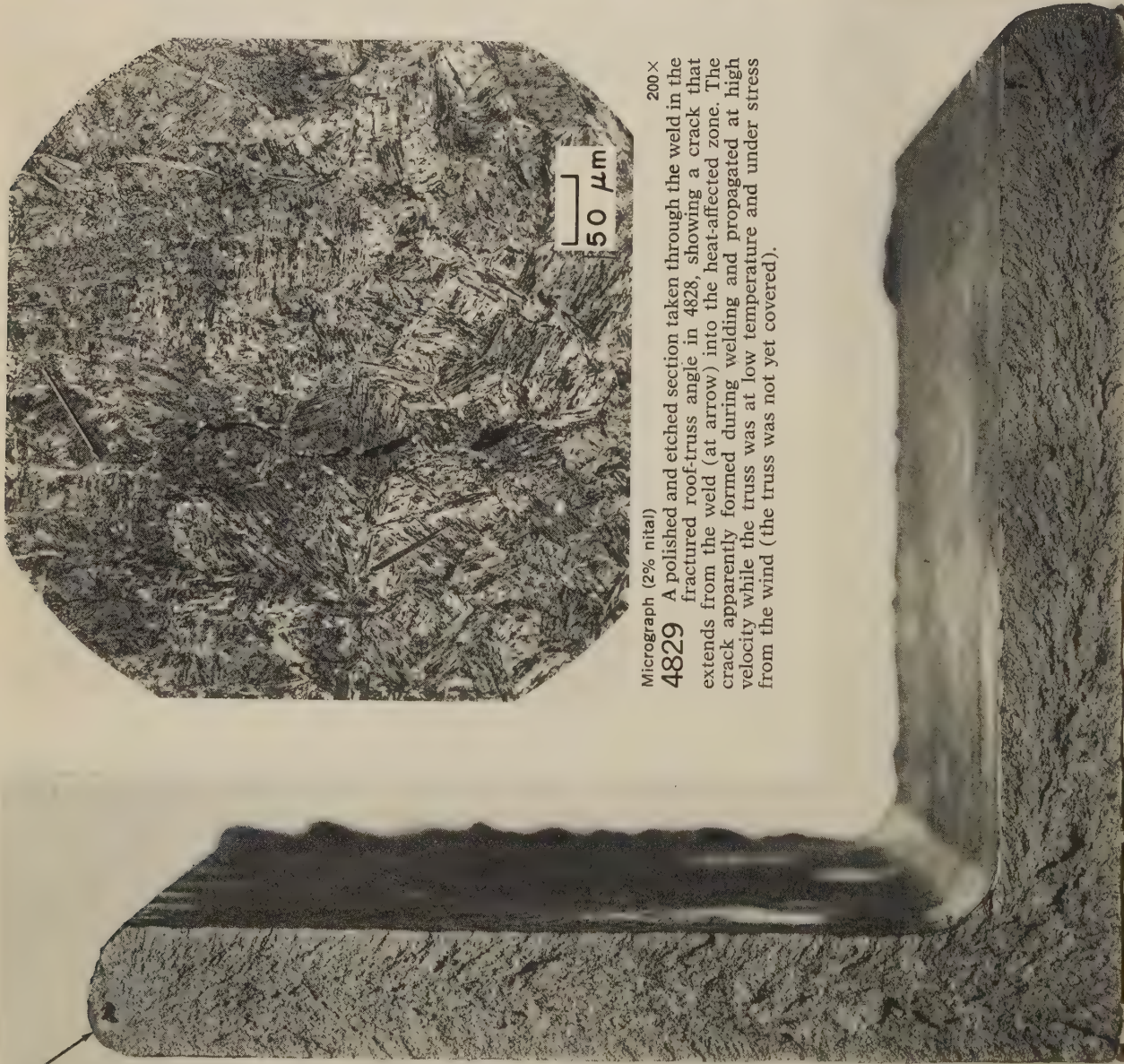
Failure-Analysis Fractographs: 1033 Steel Roof-Truss Angle That Fractured in Service at Low Temperature



Micrograph (2% nital) 200×
4829 A polished and etched section taken through the weld in the fractured roof-truss angle in 4828, showing a crack that extends from the weld (at arrow) into the heat-affected zone. The crack apparently formed during welding and propagated at high velocity while the truss was at low temperature and under stress from the wind (the truss was not yet covered).

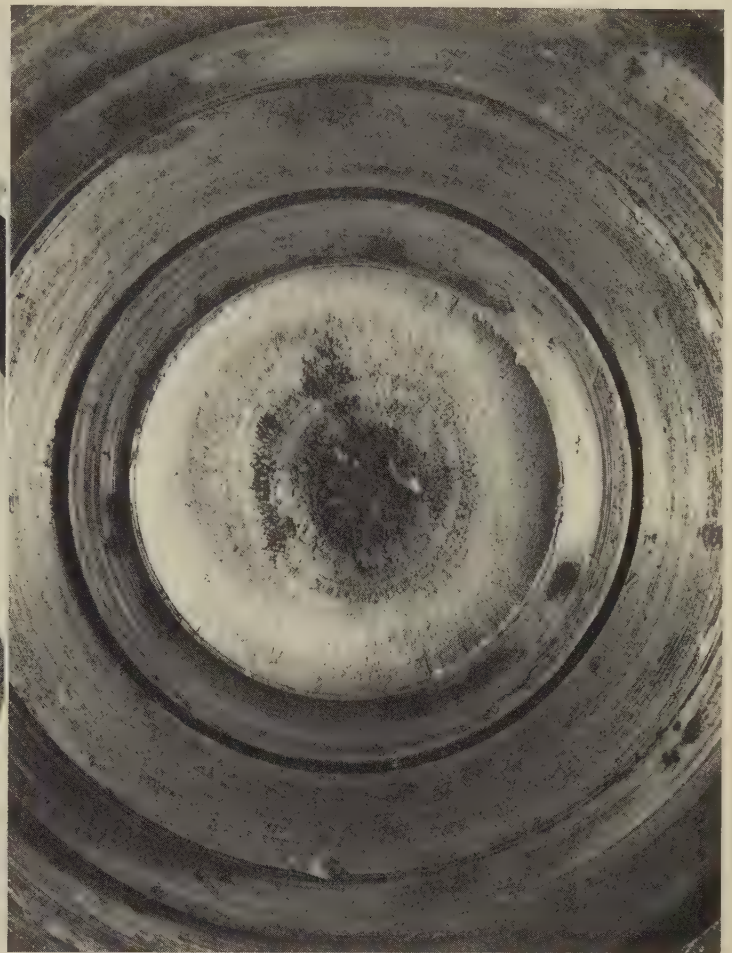
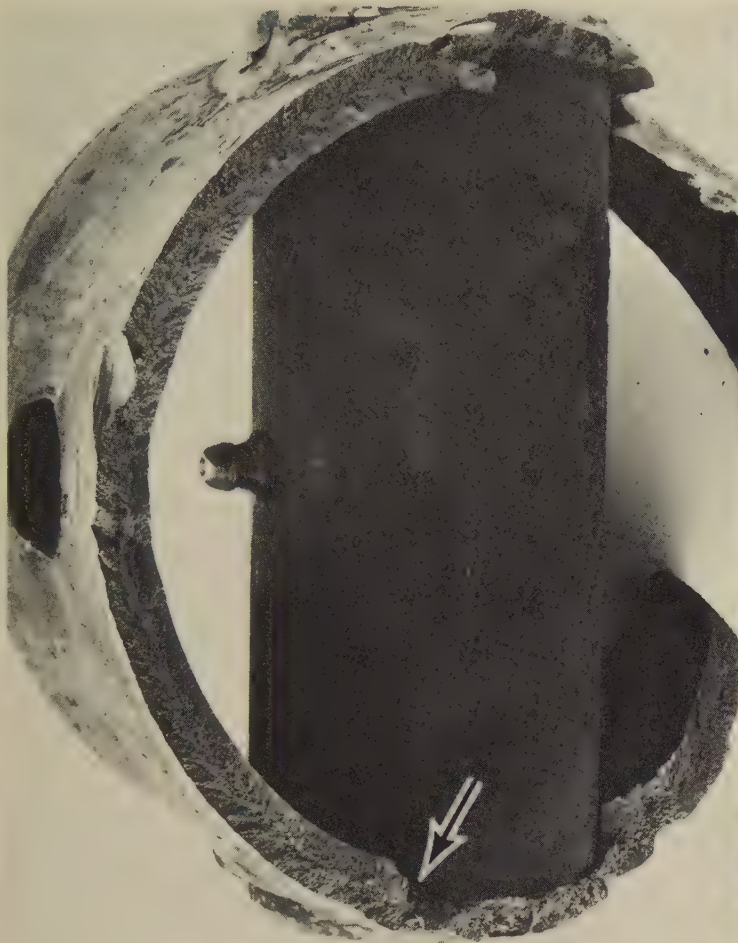


Photograph (4830); macrograph (4831) Both at 5×
4830 Above (4830) is a view of the weld at 5× magnification. Note that the fracture (in profile at left) passes through the center of the weld. Below (4831) is a portion of the fracture surface at the weld, after polishing and etching (2% nital). A crack is visible (at arrow) at the tip of the cavity. Hardness was 187 Bhn in base metal, 516 Bhn in heat-affected zone, 363-534 Bhn in weld.



Light fractograph 1 1/2×
4828 Surface of a fracture in a 1033 steel angle 4 by 1/2 in. that formed part of a roof under construction. Fracture occurred when the temperature was below freezing and the wind velocity was 30 to 40 mph. Visible are chevron marks, which clearly point toward the fracture origin (at arrow) at a weld deposit in the upper edge of the vertical leg. Note the large cavity in the weld zone. See also 4829 to 4831.

Failure-Analysis Fractographs of 1035 Steel: Brittle Fracture in an Axle;
Fatigue Fracture in a Shaft; Torsion-Overload Fracture in a Drive Shaft



Light fractograph

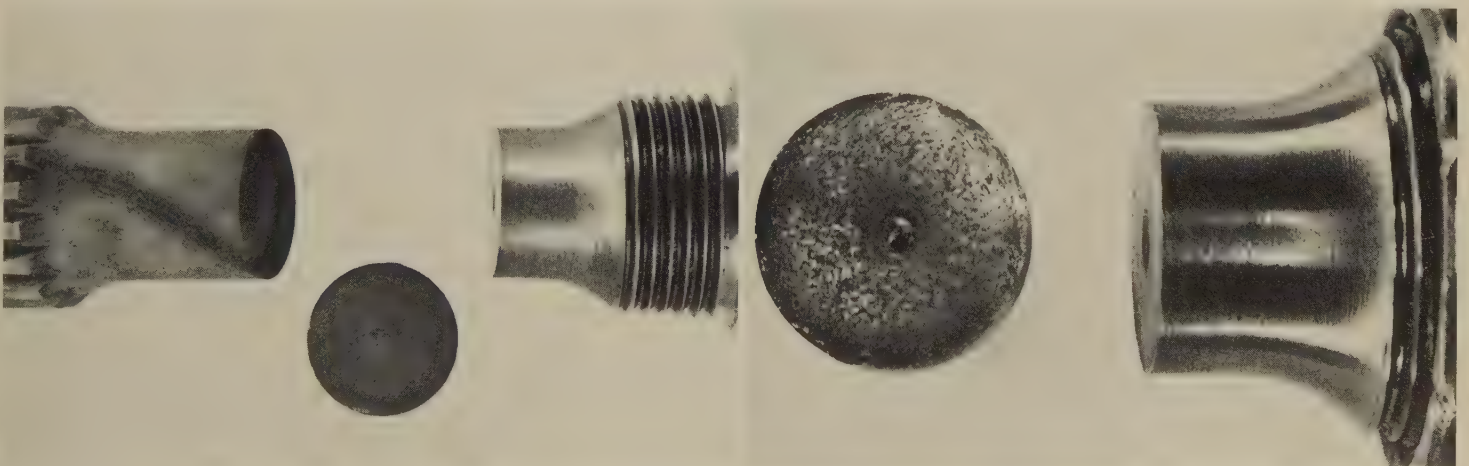
Actual size

4832 Surface of a brittle fracture in an axle made of cold drawn and stress-relieved 1035 steel tubing. Fracture originated at a weld defect (at arrow) during very cold weather. Visible are chevron marks, which show that the fracture progressed clockwise along the left wall before the remainder of the axle wall (cross section shown incompletely here) ruptured in a ductile manner.

Light fractograph

1 1/8 X

4833 Surface of a fatigue fracture in a shaft of medium-carbon steel (composition approximately that of 1035) with a hardness of 143 Bhn. The fracture occurred under rotating bending. Fatigue cracks began at several locations within a sharp tool mark in a fillet that had an adequate radius, and joined around the circumference as they penetrated to the center.



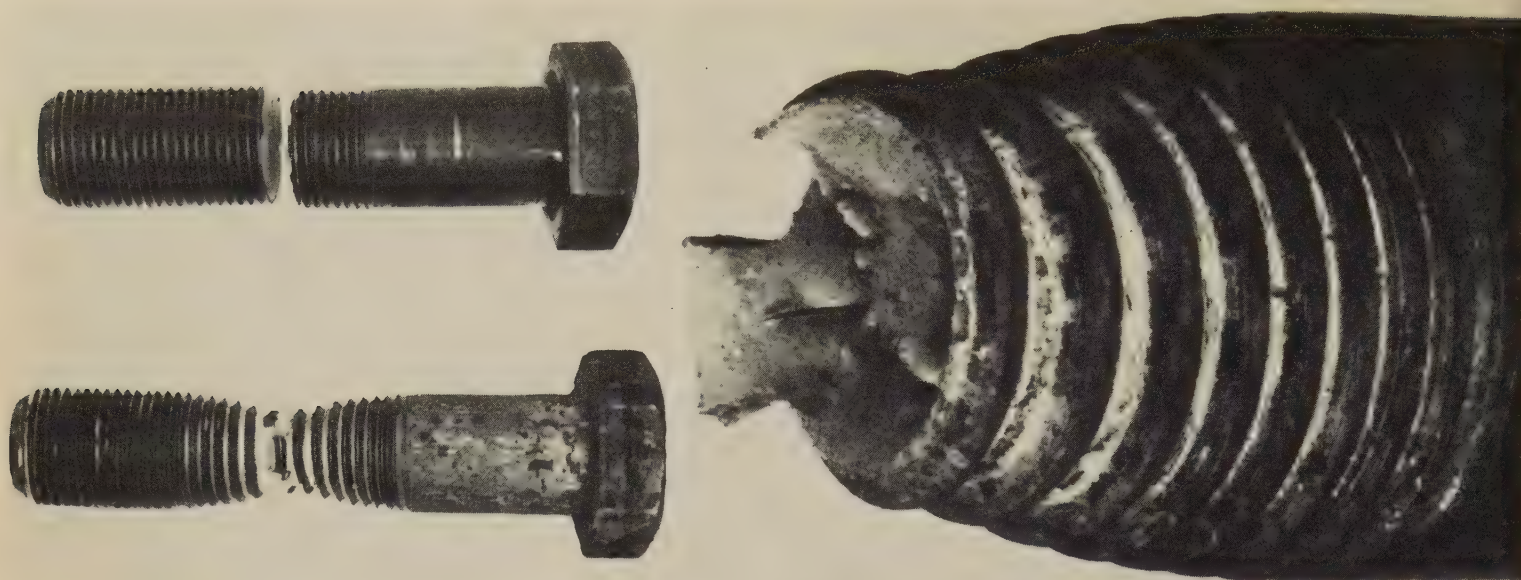
Photograph

Actual size Photograph

2 X

4834, 4835 At left (4834) is a view of a drive shaft of 1035 steel, with a hardness of Rockwell C 34, that fractured under torsion overload, twisting off in a fashion that produced a surface almost as flat as if it had been machined. The threaded portion, at right, contains a fracture surface. A thin slice containing the mating fracture surface was cut from the portion at left; this slice is shown at center, with the fracture surface up. Shaft portion at left, including cut fracture surface, was hot etched in equal parts of hydrochloric acid and water to reveal deformation flow and forging flash lines. The plastic deformation is characteristic of torsion overload in ductile metals and is not typical of rotating fatigue. At right (4835) is a higher-magnification view of the threaded portion of the fractured drive shaft in 4834 and the mating surface of the fracture.

Failure-Analysis Fractographs: 1038 Steel Bolts Fractured by Tension Overload;
1040 Steel Axles Fractured During Stretching and During Straightening



Photograph

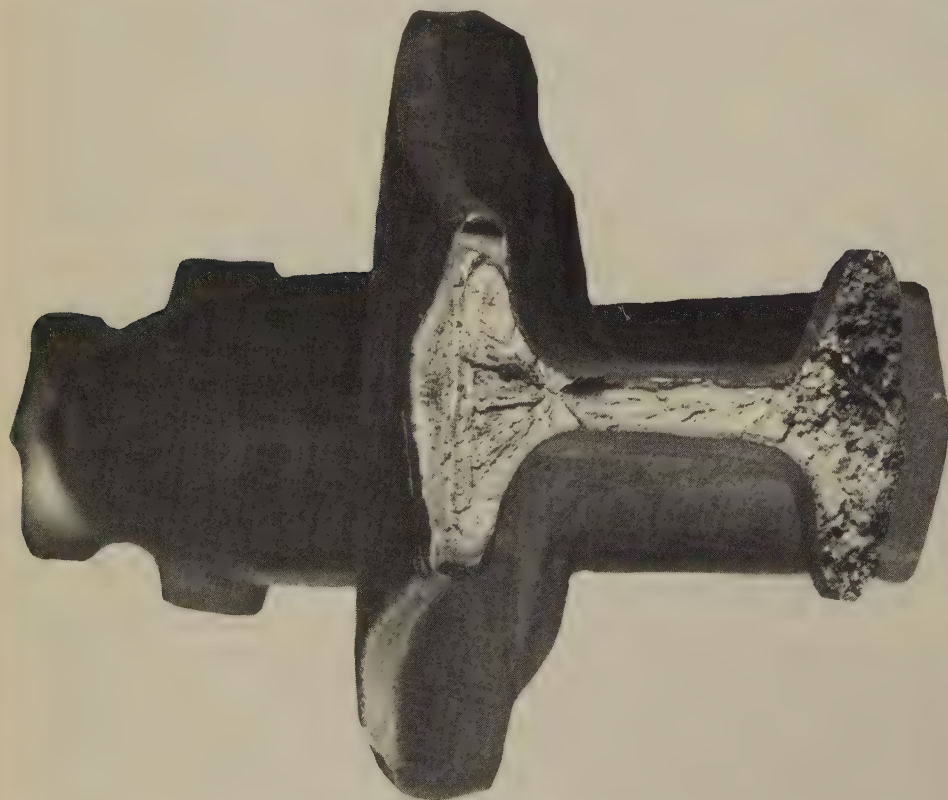
Actual size

4836 Two bolts of 1038 steel that fractured in tension overload, showing the influence of hardness on fracture characteristics. Water-quenched bolt at top had a hardness of Rockwell C 57 and was brittle; annealed bolt at bottom had a hardness of Rockwell C 15 and was ductile. See 4837.

Light fractograph

About $4\frac{1}{2}\times$

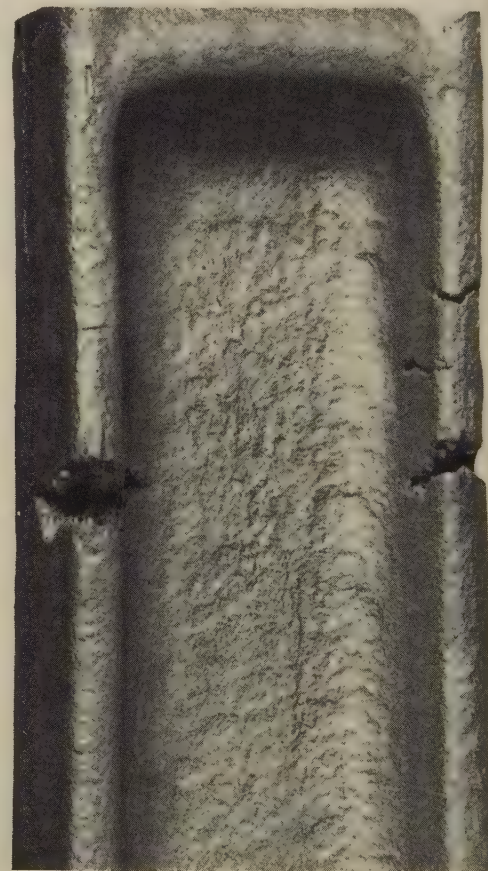
4837 Higher-magnification view of the right-hand segment of the fractured bolt at the bottom in 4836 (left). Note that appreciable reduction in cross-sectional area occurred in this bolt before final rupture took place, which yielded a ductile-fracture surface of the cup-and-cone type.



Light fractograph

1.3 \times

4838 Forged axle of 1040 steel that fractured while being hot stretched prior to quenching. The axle had been severely overheated during the heat treatment, which produced a weak, coarse-grained microstructure with damage at grain boundaries caused by "burning" (incipient melting). "Burning" darkened the areas at right end of the fracture surface.

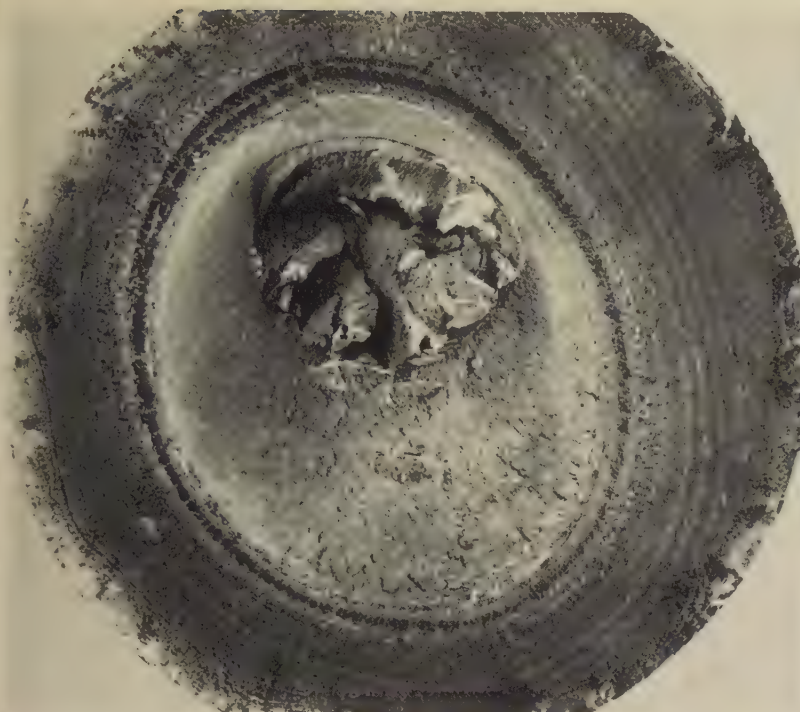


Photograph

About actual size

4839 A forged I-shaped axle section of 1040 steel that experienced tear fractures during a hot straightening operation. This axle, like the one in 4838, had been embrittled by "burning" during severe overheating.

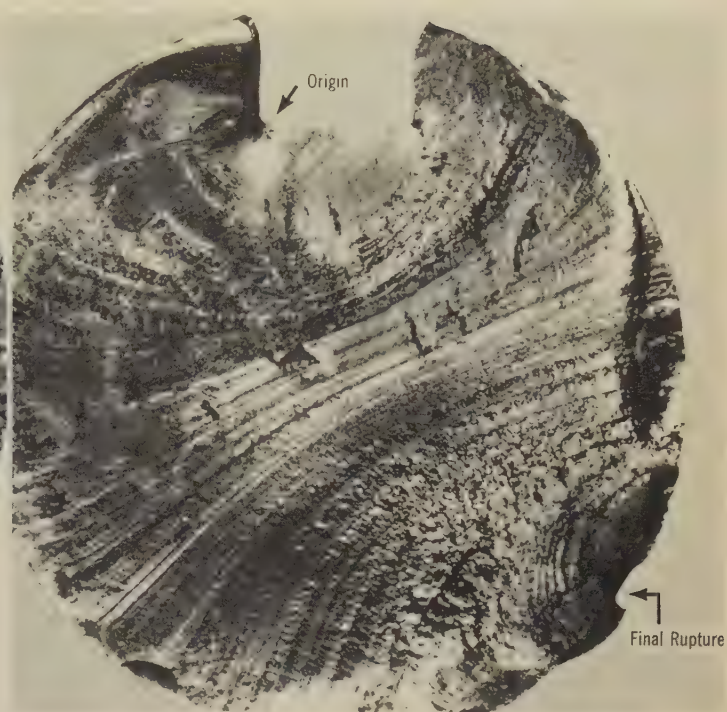
Failure-Analysis Fractographs: Fatigue Fractures in Two 1040 Steel Shafts and Two 1041 (1541) Steel Axles



Light fractograph

4840 Surface of a fatigue fracture in a shaft of 1040 steel with a hardness of approximately Rockwell C 30. The shaft was fractured when subjected to rotating bending. The oval shape of the central region of final, fast fracture indicates that two mutually perpendicular, unequal bending stresses were present. The ratchet marks around the perimeter of the shaft indicate that fracture began at several points.

About 15 \times



Light fractograph

4841 Fatigue-fracture surface of a keyed shaft of 1040 steel (hardness, approximately Rockwell C 30). The fatigue crack originated at the left bottom corner of the keyway and extended almost through the entire cross section before final, fast rupture occurred. Beach marks are visible; these swing counter-clockwise because the direction of rotation was clockwise.

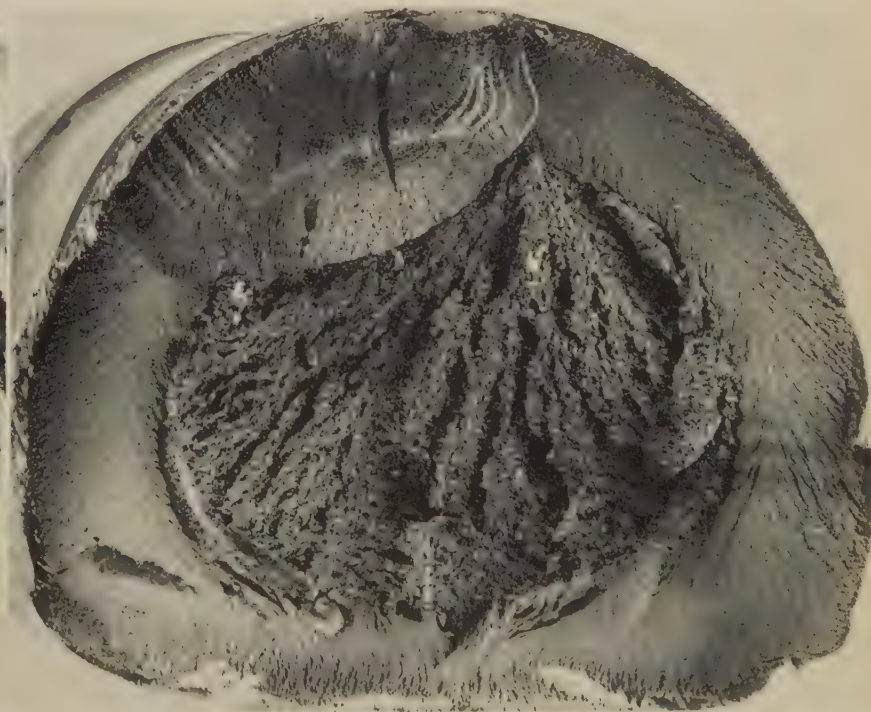
17 \times



Light fractograph

4842 Surface of a fatigue fracture in an induction hardened axle of 1041 (1541) steel with a hardness of Rockwell C 46 in the hardened zone. The fatigue crack originated at a fillet (with a radius smaller than specified) at a change in shaft diameter near a keyway runout. Note the two sets of chevron marks along the hardened perimeter, each set pointing to the crack origin at left.

About actual size

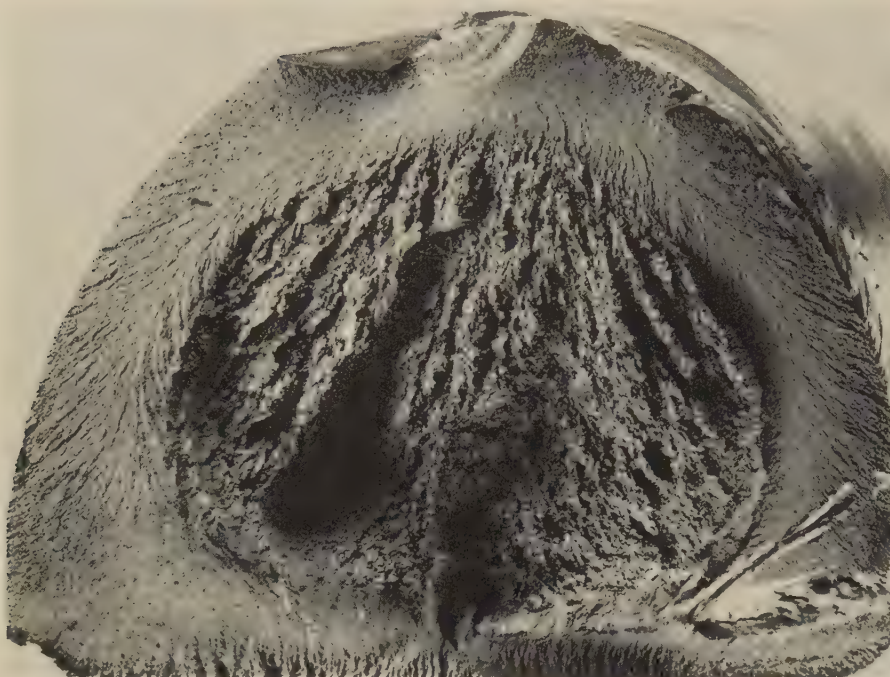


Light fractograph

4843 Surface of a bending-plus-torsional-fatigue fracture in an experimental 3 1/2-in.-diam tractor axle of 1041 (1541) steel that had been induction hardened. Fracture occurred after 1212 hr on an endurance-test track. Note beach marks fanning out from the fatigue-crack origin (slightly to left of center, at top). Beyond the beach marks, cracking progressed by fast fracture along the hardened perimeter, producing two sets of chevron marks pointing toward the crack origin (like the chevron marks in 4842). See also fractograph 4844, on the next page.

11 \times

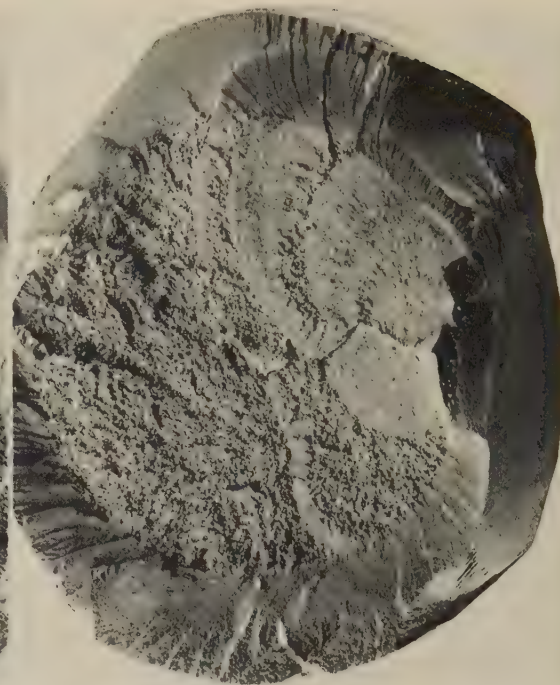
Failure-Analysis Fractographs: Fatigue Fractures in Four Different Induction Hardened 1041 (1541) Steel Axles



Light fractograph

1¼ ×

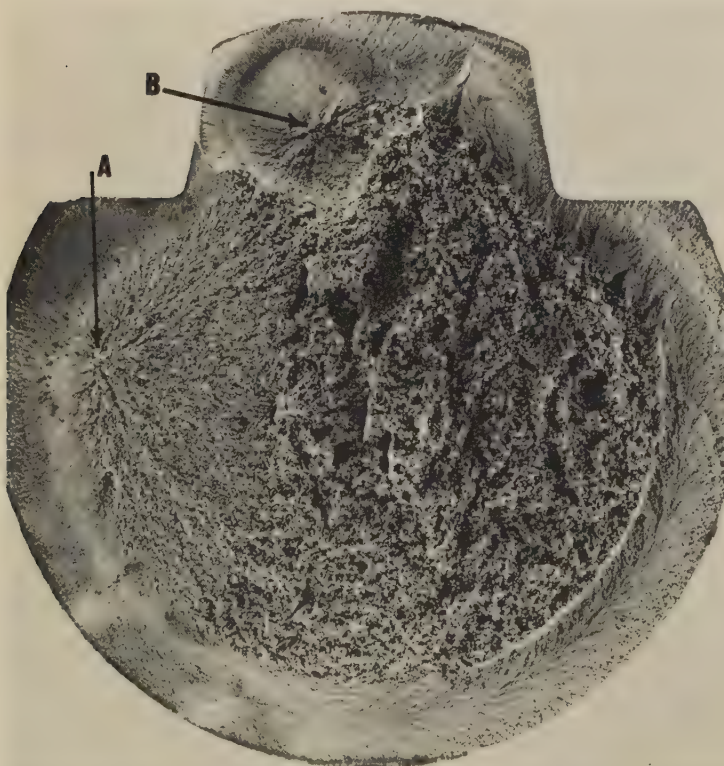
4844 Surface of a torsional-fatigue fracture in an induction hardened 1041 (1541) steel experimental tractor axle same as in 4843 (preceding page). Hardness in the hardened zone was Rockwell C 50 at $\frac{7}{16}$ to $\frac{15}{32}$ in. beneath the axle surface at the crack origin. This axle fractured after 450 hr of endurance testing. In this axle, as in the axle in 4843, crack origin is near top, at a sharp corner of a keyway runout.



Light fractograph

Actual size

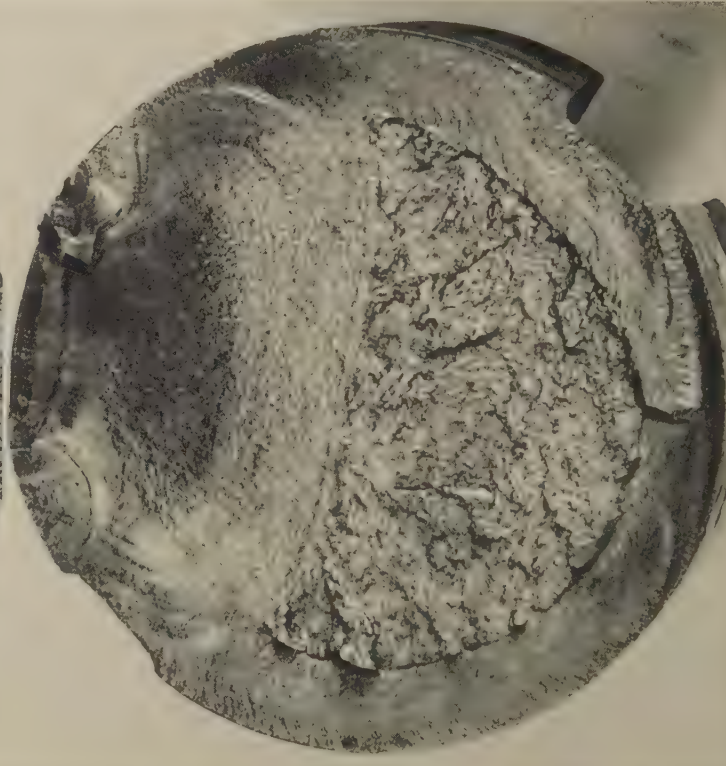
4845 Surface of a fatigue fracture in a truck axle of 1041 (1541) steel induction hardened to Rockwell C 55. The axle broke after 490 hr of service. Crack origin was subsurface, near a keyway. Note that fatigue crack progressed in steps.



Light fractograph

1.2 ×

4846 Fatigue fracture in a 1041 (1541) steel axle induction hardened to Rockwell C 50 and tested in rotating bending. Two cracks are evident; one began at A and progressed around most of the perimeter by fatigue, then by fast fracture, before meeting a smaller crack, which began by fatigue at B. Chevron marks in hardened zone point to both origins. See also Fig. 10(a) on page 16.

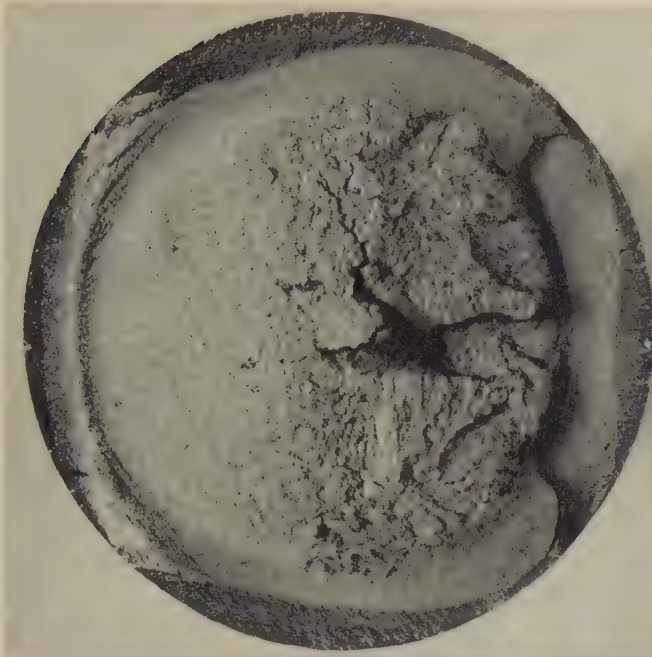


Light fractograph

1½ ×

4847 Surface of a fatigue fracture in a keyed axle of 1041 (1541) steel induction hardened to Rockwell C 50. An accidental arc strike on the axle surface, at left, initiated a fatigue crack, which grew about halfway through the cross section before fast fracture occurred in the hardened zone; fast fracture progressed from both sides of the fatigue crack, as shown by chevron marks.

Failure-Analysis Fractographs: Fatigue Fractures in a Case Hardened 1039 Steel Shaft, in a 1041 (1541) Steel Shaft, and in a 1041 (1541) Steel Keyed Spindle



Light fractograph

2×

4848 Fatigue-fracture surface of a case hardened 1039 steel shaft. Case hardness, Rockwell C 50; core, Rockwell C 19. Note that fracture of the case was nearly complete before the fatigue cracks penetrated into the core.



Light fractograph

2×

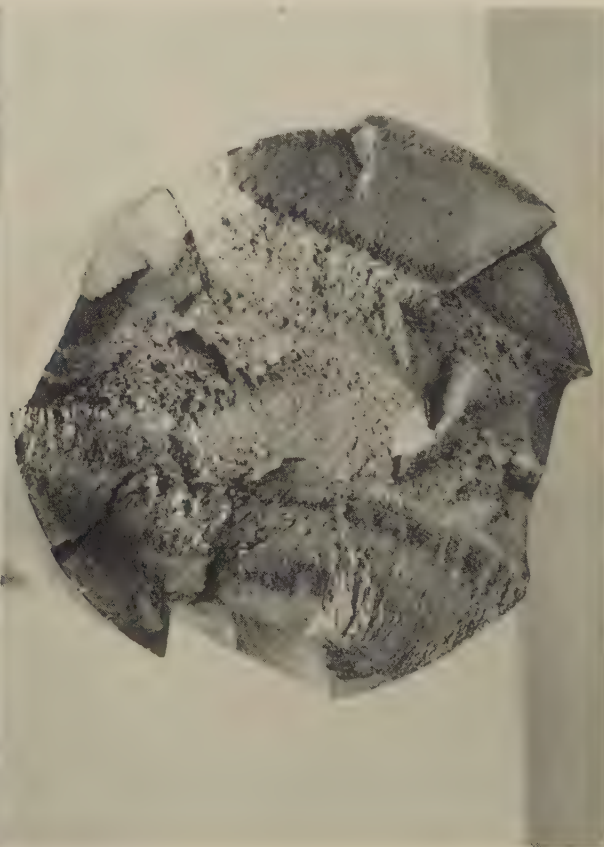
4849 Surface of a fatigue fracture in a shaft of 1041 (1541) steel with a hardness of 302 Bhn. The shaft was broken by reversed stressing. Note the two fatigue-crack origins at right edge and the third origin at left.



Photograph

1½×

4850 View of a broken keyed spindle of 1041 (1541) steel with a hardness of 333 Bhn. A large amount of fretting is visible on both sides of the fracture. Note that the radius of the keyway edge seems small near the fracture. See also fractograph 4851.



Light fractograph

2×

4851 Surface of the fracture in 4850 (left). Note that the radii of the keyway edges have acted as origins for fatigue cracks. A second fatigue zone is visible on the side opposite the keyway. The region between the fatigue zones underwent fast fracture.

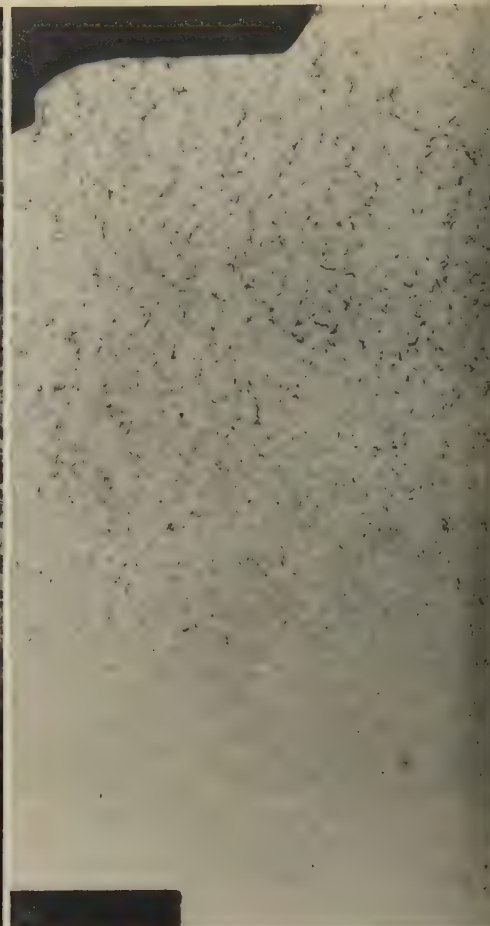
Failure-Analysis Fractographs: 1038 Steel Pump Chamber That Fractured as a Result of "Burning" Caused by Overheating During Forging



Light fractograph

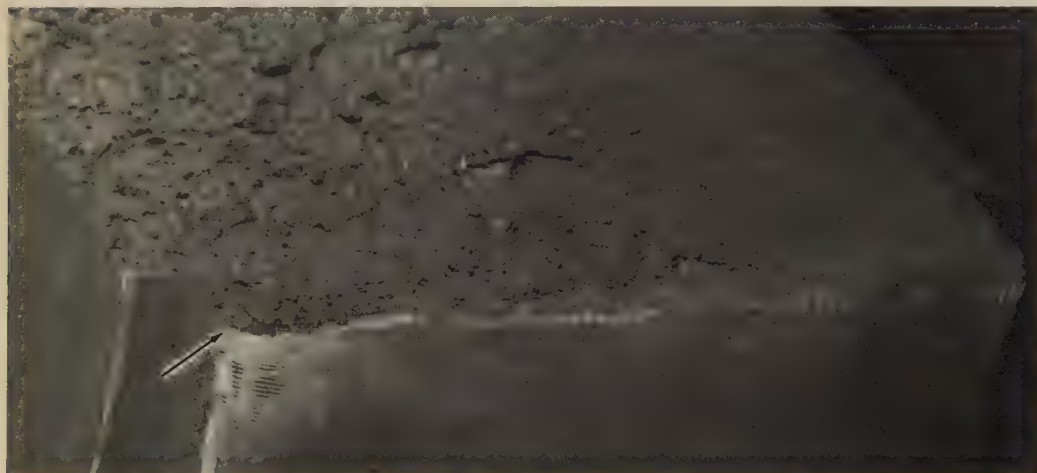
4852 Surface of a fracture in a forged pump chamber of 1038 steel normalized and tempered to a tensile strength of 530 MPa (77 ksi) and 31% elongation. Fracture originated at a radial crack (at arrow) in the plunger bore of the chamber and occurred after only 13 months of service (expected life was 4 to 6 years). Operating pressure in the chamber was 21 to 24.8 MPa (3 to 3.6 ksi). Note coarse, intergranular nature of upper two-thirds of the fracture surface, which was rubbed during propagation of the fracture into the lower portion by fatigue cracking. See also 4853 to 4855.

About actual size



Macrograph (hot HCl + H₂O) About actual size

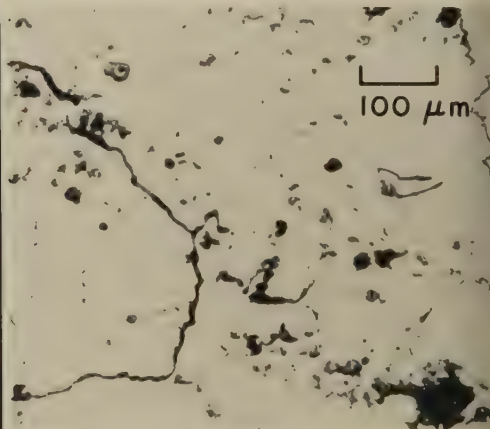
4853 Section taken parallel to the fracture surface in 4852, polished, and etched in equal parts of hydrochloric acid and water at 71 C (160 F). Upper portion, showing an intergranular network formed by "burning" from overheating during forging, coincides with the coarse, intergranular portion of the fracture surface in 4852. The bottom portion here is undamaged.



Light fractograph

4854 An oblique view of the fracture surface in 4852, showing mechanical damage of the plunger-bore surface in the form of regularly spaced grooves (at arrow). It is believed that the crack originated at one of these grooves; however, in view of the marked weakness of the microstructure in the burned upper portion of the fracture surface, it appears that the fracture could have been nucleated anywhere in that portion.

About actual size

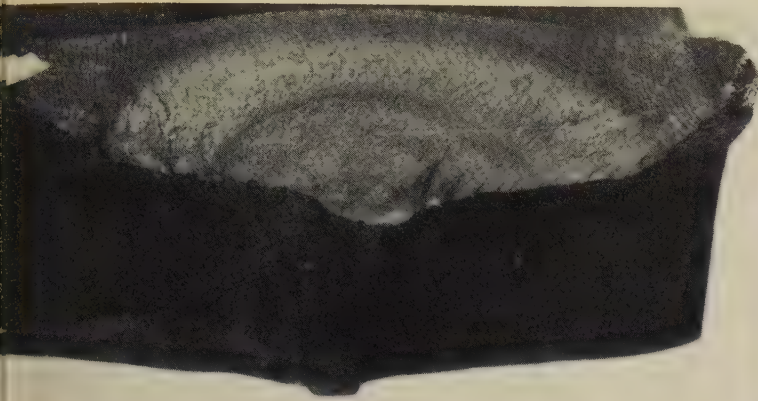


Micrograph (Howarth's reagent)

100×

4855 Polished and etched section taken longitudinally through the center of the coarse portion of the fracture surface shown in 4852 (above, left). Etchant (10 ml HNO₃, 10 ml H₂SO₄, 80 ml H₂O) reveals that burning occurred at boundaries of prior austenite grains during forging.

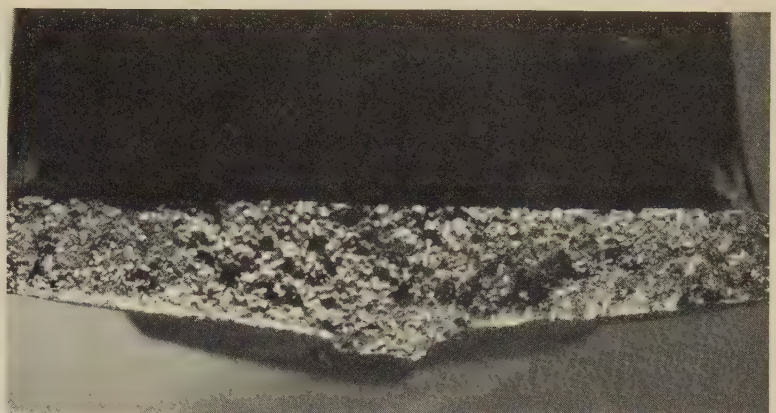
Failure-Analysis Fractographs: 1041 and 1041H (1541 and 1541H) Steel Connecting Rods Fractured by Fatigue and by Single Overload; T-2 Nickel Steel Marine Tailshaft Cracked by Fatigue



Light fractograph

4856 Surface of a fatigue fracture in an experimental connecting rod of 1041 (1541) steel (hardness, Rockwell C 20). The fatigue crack began at bottom, at forging flash line, and penetrated nearly to the bearing surface of the rod before final fracture occurred. See 4857.

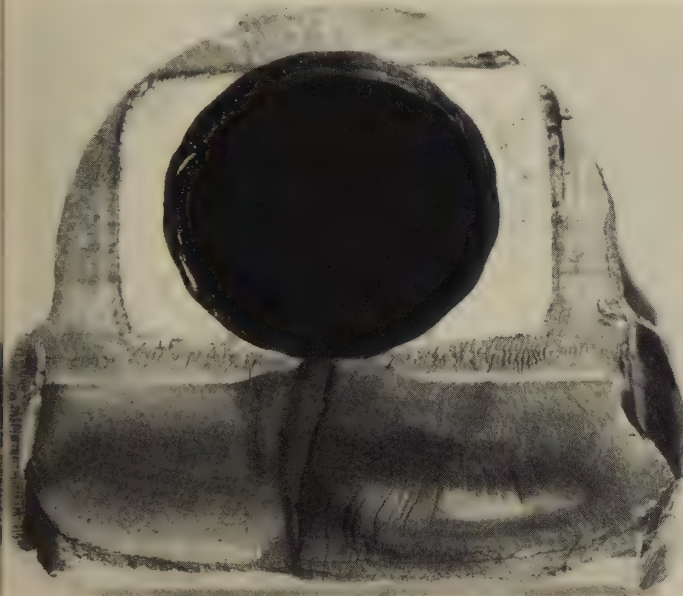
4×



Light fractograph

4857 Surface of a single-overload fracture in a 1041 (1541) steel experimental connecting rod similar to that in 4856. This fracture was caused when the opposite side of the bearing surface ruptured by fatigue. Note that there is no evidence of fatigue marks here.

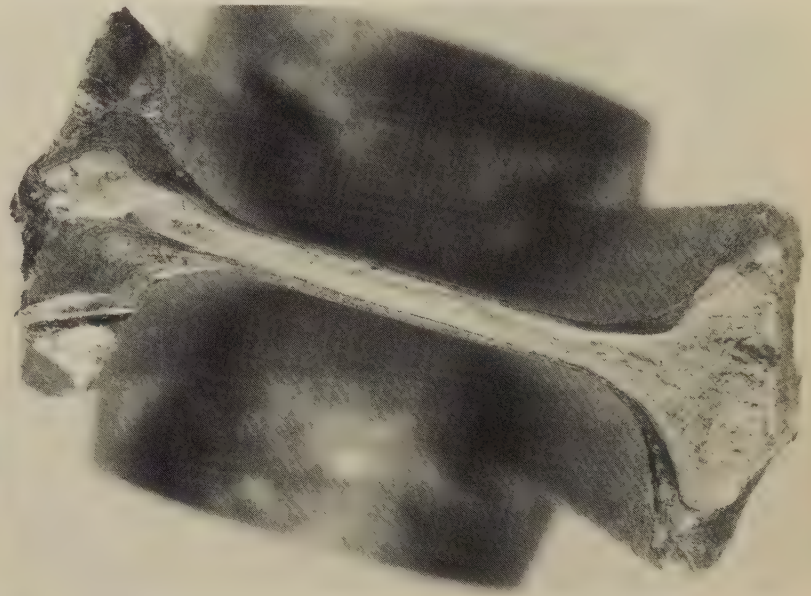
4×



Light fractograph

4858 Surface of a fatigue fracture near the crankshaft bearing in a 1041 (1541) steel experimental connecting rod (hardness, Rockwell C 19). Two fatigue-crack origins are near bolthole. Scuff marks in light area were made by a loose bolt.

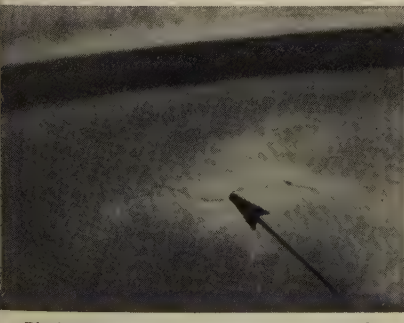
5×



Light fractograph

4859 Surface of a single-overload fracture in an experimental connecting rod of 1041H (1541H) steel with a hardness of Rockwell C 25 to 26. Note the shear lip, which extends almost completely around the perimeter of the fracture surface.

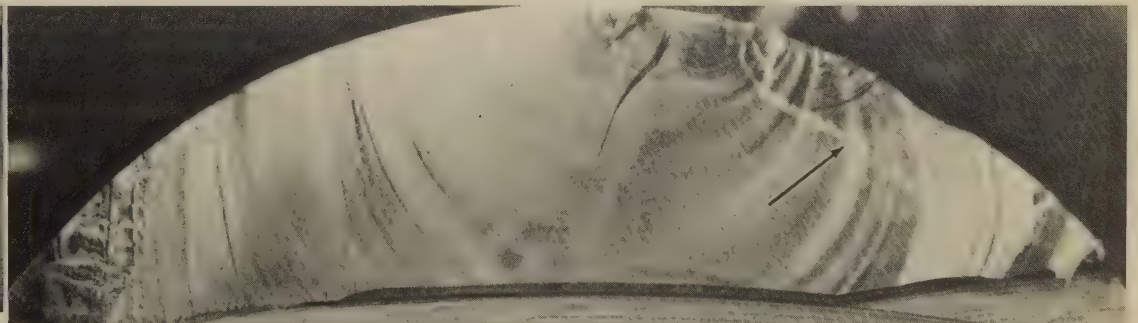
4×



Photograph

0.38×

4860 Crack in a marine tailshaft of T-2 nickel steel (0.27 C, 0.67 Mn, 0.18 Si, 2.8 Ni). Crack occurred after 20 months of service; origin is at arrow. Surface appears defect-free. See 4861.



Light fractograph

4861 Surface of the crack in 4860, exposed by sectioning, showing characteristics that are typical of fatigue. The crack had penetrated to a depth of $4\frac{1}{2}$ in. before it was discovered. The cause of the crack is not known. The external surface of the shaft visible in 4860 displays no identifiable defect. Chalk line (at arrow) indicates the location of a keyway. The stress-concentration effect of the keyway produced a level of operating stress that was higher than the endurance limit of the material.

$\frac{1}{3}$ ×

Failure-Analysis Fractographs: Fatigue Fractures in a 10B41 (15B41) Steel Splined Axle,
a 1041 (1541) Steel Suspension Bar, and a Medium-Carbon Steel I-Beam



Light fractograph

1½×

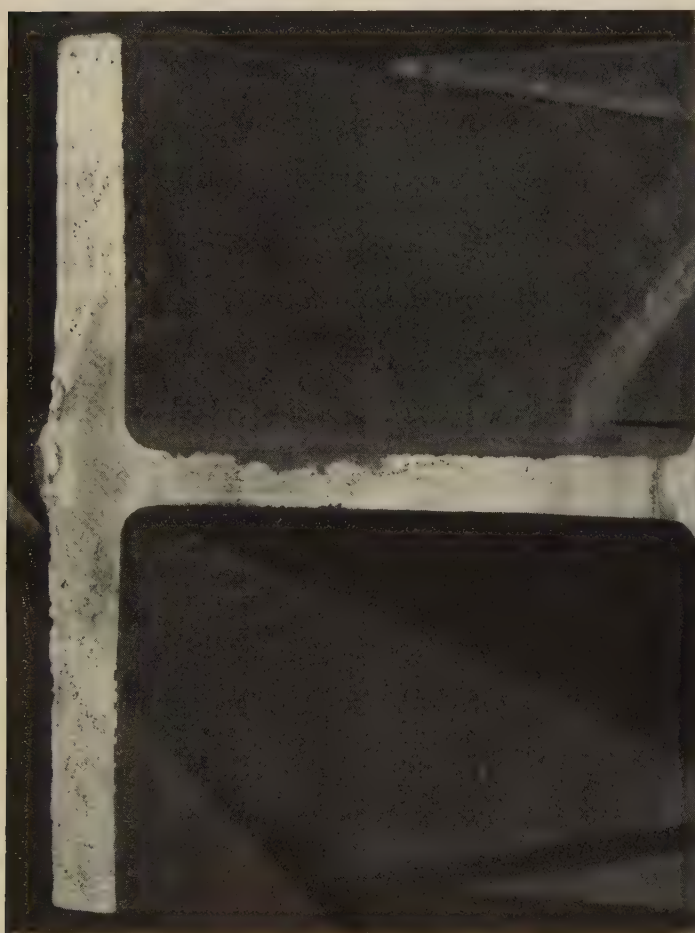
4862 Fracture surface of a large, splined axle of 10B41 (15B41) steel. Rockwell C hardness was 54 at surface, 53 at ⅓ radius and 42 at ½ radius. Fracture resulted when torsional stresses induced a circumferential fatigue crack. The axle was induction hardened to a considerable depth.



Light fractograph

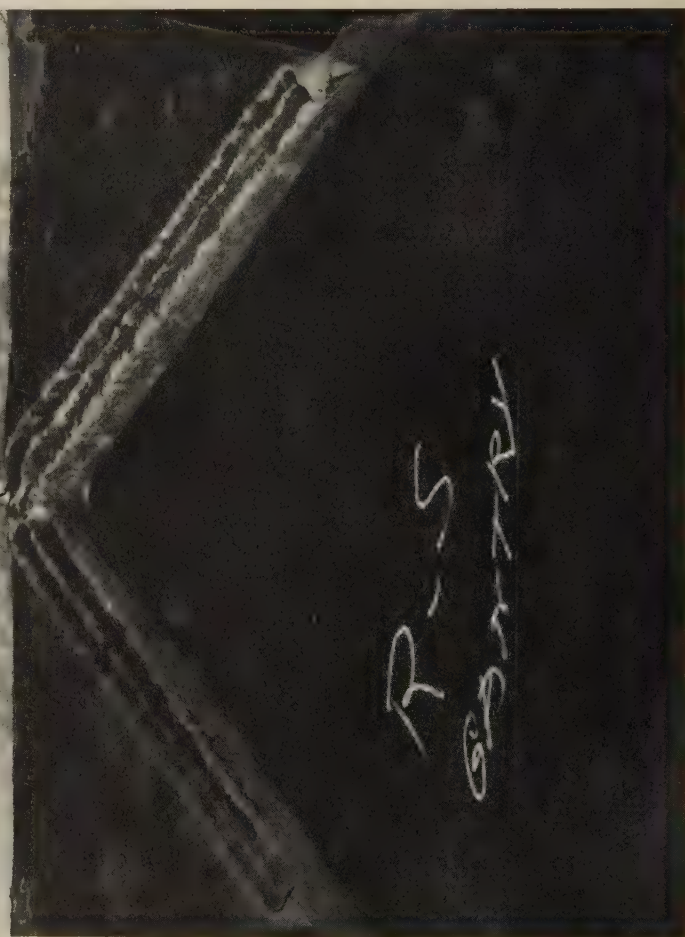
3×

4863 Fracture surface of an experimental suspension bar of 1041 (1541) steel. The fracture origin is clearly visible in the fatigue zone at top right corner. The remainder of the fracture surface contains features that resemble cleavage river patterns.



Light fractograph

4864 Surface of a fatigue fracture in a medium-carbon steel I-beam, with a flange 15¾ by 15¾ by 1⅞ in. and a 1-in.-thick web, that was part of a dragline-excavator A-frame. Each flange of the I-beam was reinforced by a plate (such as that at right) joined to the flange by a double-pass weld. There are two fatigue-crack nuclei, separated by a cleavage step, at the toe of the weld at the outer edge of the flange at right. See also 4865 through 4867 (facing page).



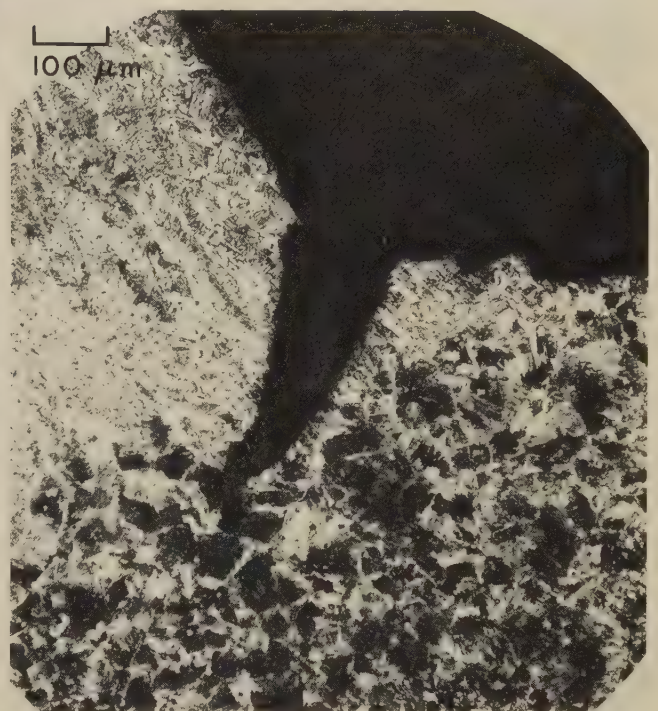
0.3×



Light fractograph

2×

4866 A view of the weld joining the flange and reinforcement plate at top in 4865, showing a crack at the toe of the weld. This crack was present before the fatigue crack, which led to fracture, formed at the toe of the weld in the other flange. See also 4867, at right.



Micrograph (2% nital)

100×

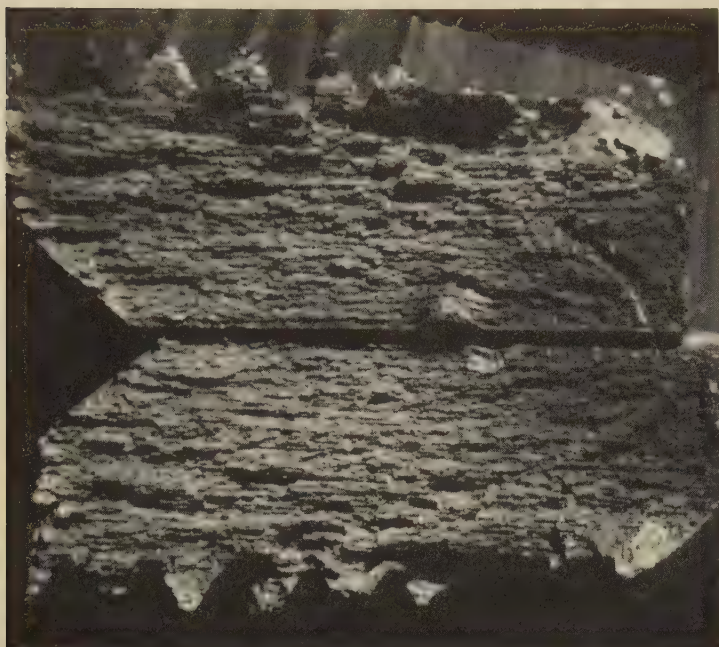
4867 A polished and etched section through the weld in 4866, at a position just to the left of the area shown there. Like that in 4866, the crack shown here was present prior to formation of the fatigue crack in the opposing flange. The weld metal (light) is at upper left.

Light fractograph

1/2×

4865 Another view of the fatigue-fracture surface of the medium-carbon steel I-beam in fractograph 4864 (on preceding page). The fracture origins are clearly evident in the flange at bottom, where two nuclei are situated at the toe of the weld joining a reinforcement plate to the flange. It is remarkable that the fatigue crack penetrated the entire flange at bottom, the entire web, and part of the flange at top before final, fast fracture occurred. See also fractograph 4866 and micrograph 4867, at left and right above.

Failure-Analysis Fractographs: Woody Fracture in an 11L40 Steel Stud Nut; "Tapered Plug" Fracture in an 1144 Steel Idler Shaft; Fatigue Fracture in an 1144 Steel Forging-Hammer Shaft



Light fractograph

10×

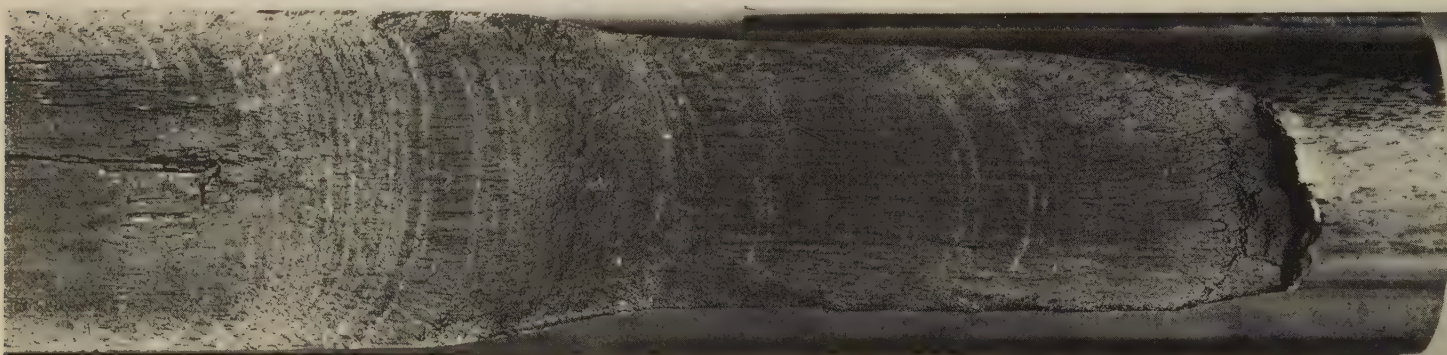
4868 Mating surfaces of a fracture in a stud nut that was machined from 11L40 steel (0.15% Pb) heat treated to a hardness of Rockwell C 31 to 32. Note the very woody nature of the fracture surfaces, which is a result of adding lead to improve the machinability of the steel.



Photograph (4869); macrograph (4870)

About $\frac{1}{2} \times$ (4869); $1\frac{1}{2} \times$ (4870)

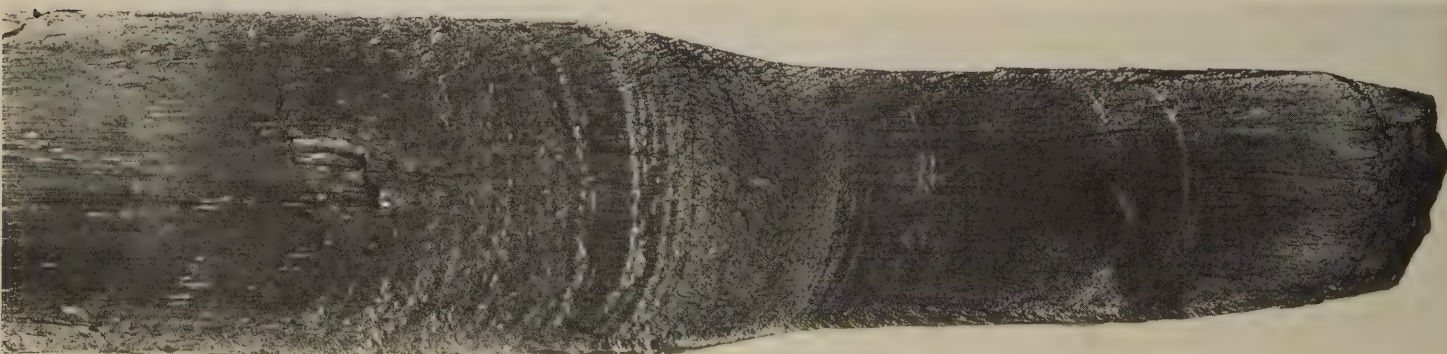
4869 At top (4869) is a "tapered plug" fracture in a splined idler shaft of 1144 steel containing 0.33% S. At bottom (4870) are sections, heavily etched in warm hydrochloric acid, through both the bearing and spline ends of the shaft; patterns of light and dark etching here suggest alloy segregation.



Light fractograph

About $\frac{1}{2} \times$

4871 Fatigue-fracture surface of the shaft of a forging hammer of 1144 steel containing 0.45% C, 1.60% Mn and 0.28% S. The fatigue crack began at a heavily abraded surface area (out of view to the left), penetrated to the center of the shaft, then turned 90° and propagated longitudinally to the point of termination at right (about 25 in.). See also 4872.

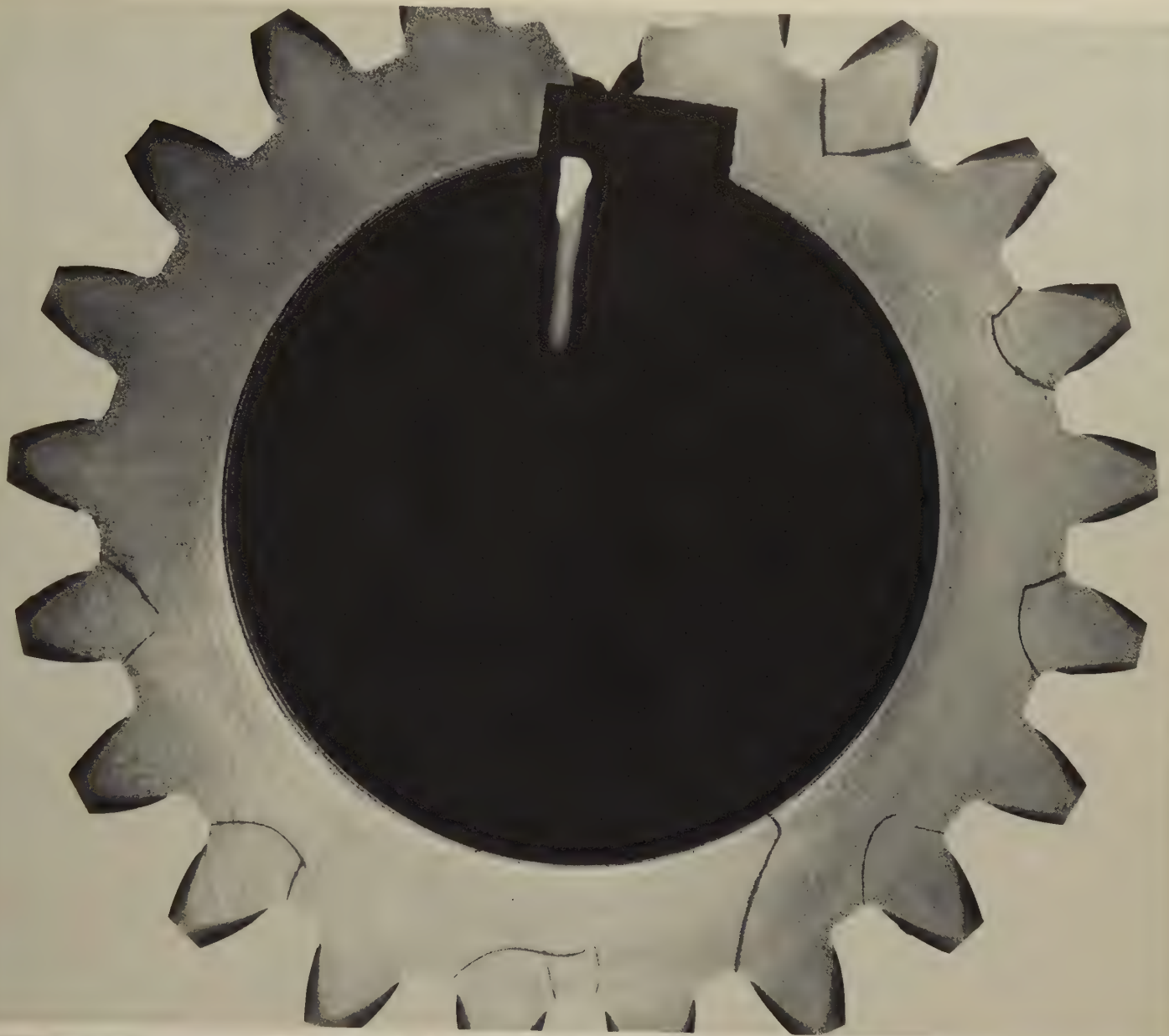


Light fractograph

About $\frac{1}{2} \times$

4872 Mating fracture surface to the one shown in fractograph 4871 (above). This piece of the shaft broke away during service. It is believed that the crack propagated a long distance in the longitudinal direction because of weaknesses associated with the presence of longitudinal bands of elongated manganese sulfide inclusions.

Failure-Analysis Fractographs: Partially Flame Hardened 1045 Steel Crane Gear
in Which Fatigue Cracks Formed at the Roots of Many Teeth



Macrographs (etchant: 5% nital)

- 4873 At top (4873) is a polished and etched cross section of a partially flame hardened crane gear of 1045 steel in which fatigue cracks formed at the roots of many teeth after one year of service. The cracks have been sharply delineated by etching. Note that hardening did not extend even to the root fillet of any tooth. At bottom (4874) is a polished and etched cross section of a portion of a gear that was subjected to full-contour flame hardening; note the better tooth form, with fully radiused tooth roots.
- 4874

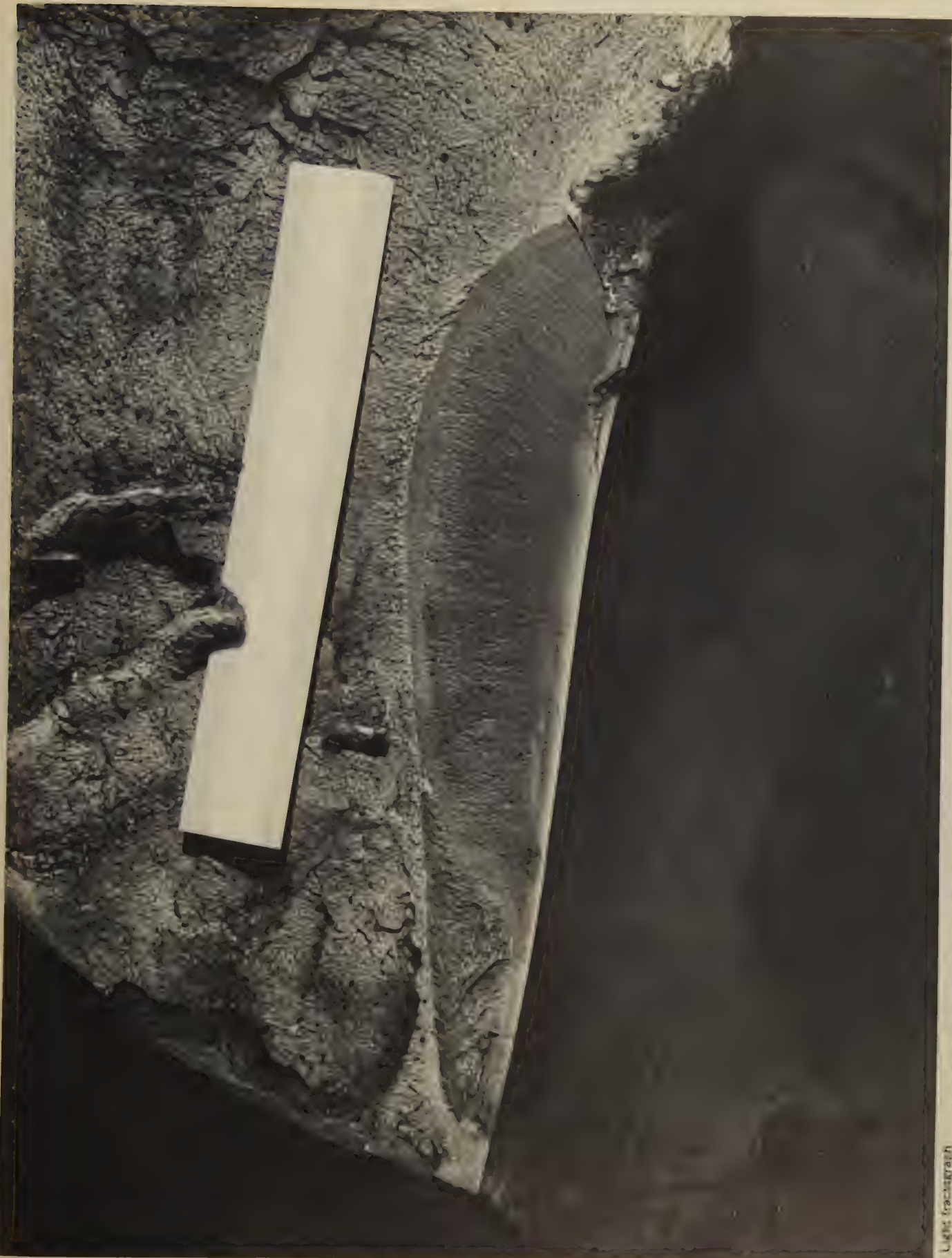
About actual size (4873); about 2× (4874)

Failure-Analysis Fractographs: Forged 1045 Steel
Blooming-Mill Spindle Fractured by Fatigue



Light fractograph

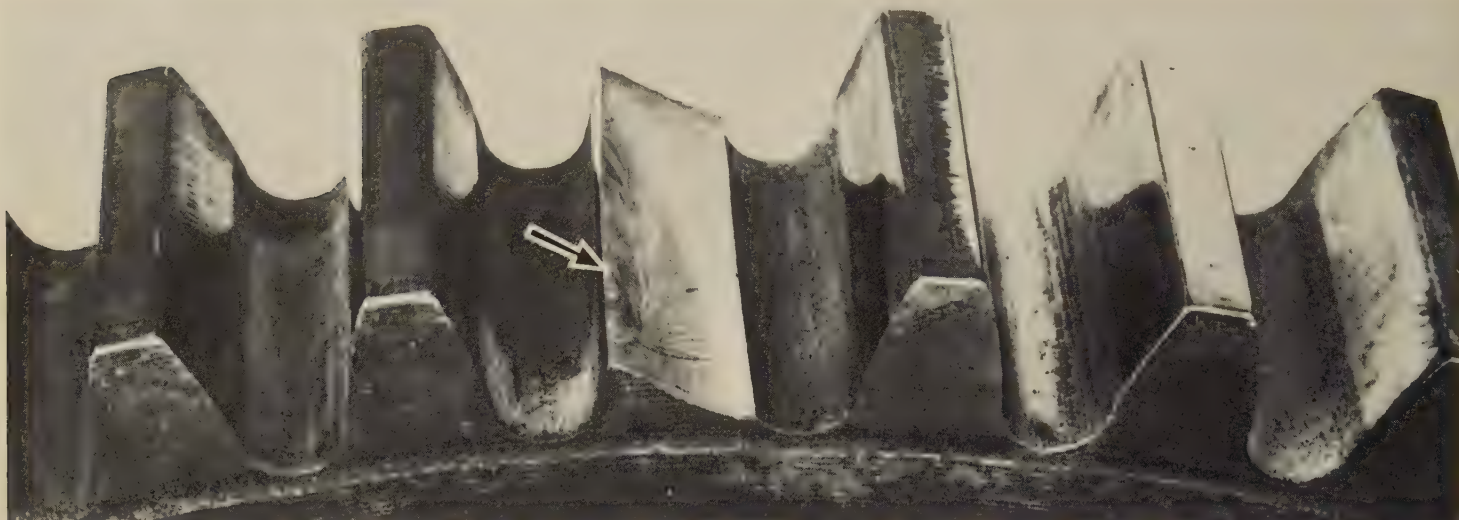
0.4 ×
4875 A fracture surface in the jaw end of a blooming-mill spindle of forged 1045 steel. This spindle was 27 ft long, 35 in. in diameter at the jaw end, and 42 in. in diameter at the drive end. The white six-inch rule at top indicates the massive size of the spindle. After the spindle had been normalized, the inner surface of the jaw was flame hardened. The fracture originated at the jaw surface, at the lower edge of the fatigue zone (left of center). See also fractograph 4876 (on facing page).



Light fractograph

4876 Enlarged view of the fatigue zone of the 1045 steel blooming-mill-spindle fracture shown in fractograph 4875 (opposite page). Note the radial marks originating at the surface of the jaw. A few beach marks are faintly visible at the top edge of the fatigue zone. Note the sharpness of the terminating edge of the fatigue zone, at the transition to final, fast fracture. Note also the tongues of metal near the rule in the zone of final, fast fracture.

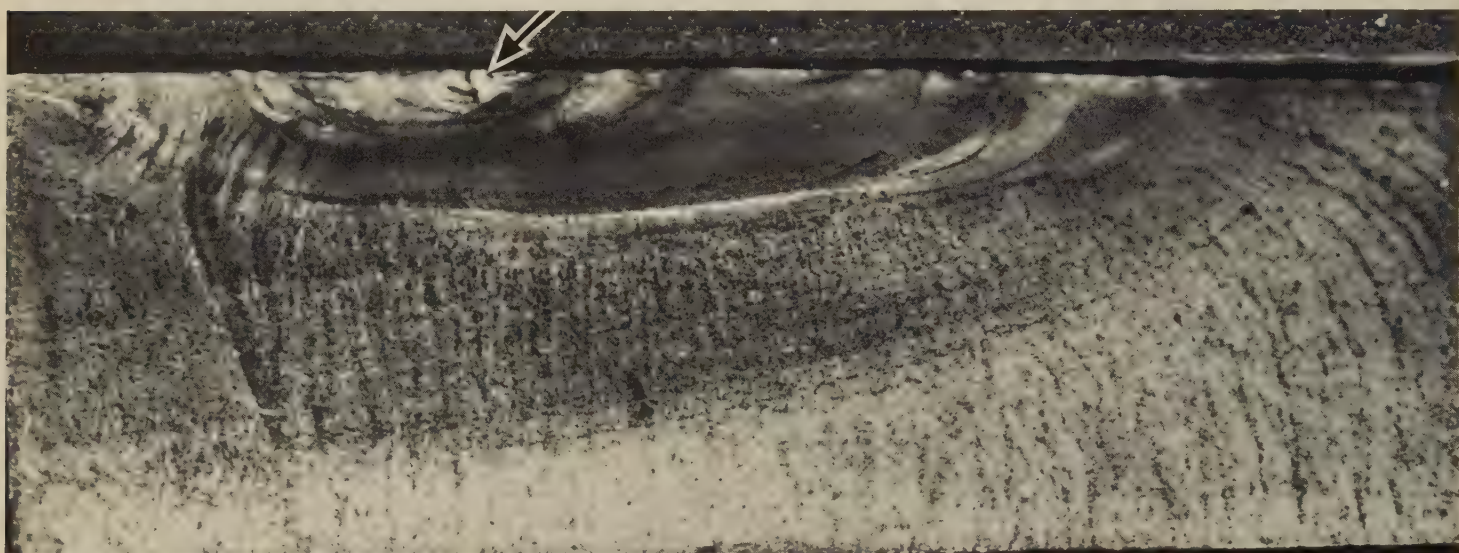
Failure-Analysis Fractographs: Bending-Fatigue Fractures in a 1045 Steel Transmission Gear and a 1045 Steel Crankshaft



Photograph

4877 A bending-fatigue fracture in a $\frac{7}{8}$ -in. constant-mesh transmission gear of 1045 steel, induction hardened to Rockwell C 55 at the surface. The arrow indicates the crack origin at the left edge of the fracture, where a small pit existed near the base of the contact area on the pressure side of the tooth. See also fractograph 4878, below.

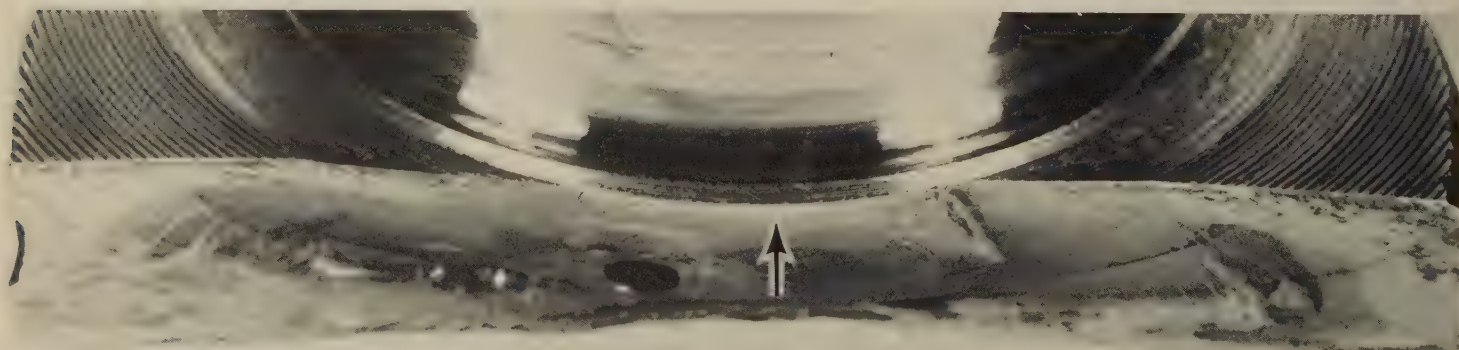
About $1.9\times$



Light fractograph

4878 A view of the fracture surface of the broken gear tooth shown in 4877, above. The area immediately adjacent to the crack origin (at arrow) is well rubbed, which indicates that the crack progressed slowly at first. The loading apparently was fairly well-distributed, although the crack grew somewhat more rapidly toward the left.

About $9\frac{1}{4}\times$

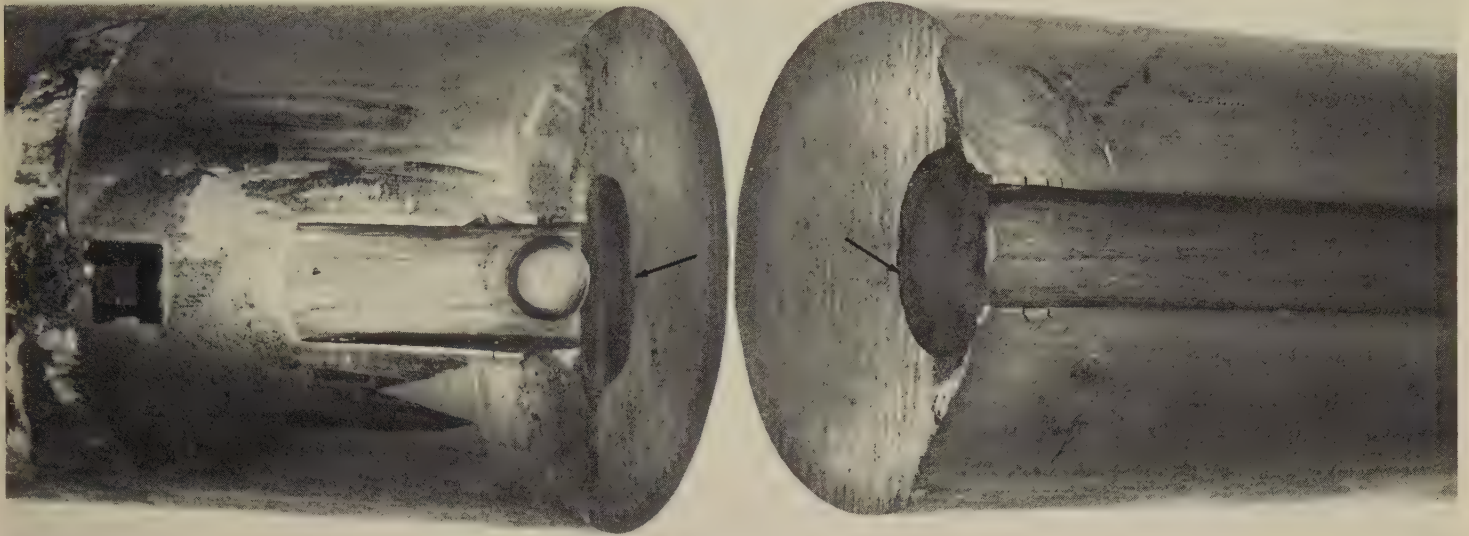


Light fractograph

4879 A bending-fatigue fracture originating at a stress concentration in a fillet of a crankshaft of 1045 steel. The fillet was poorly shaped and contained a sharp tool mark. The crack started at the point marked by the arrow and followed the tool mark for some distance in each direction.

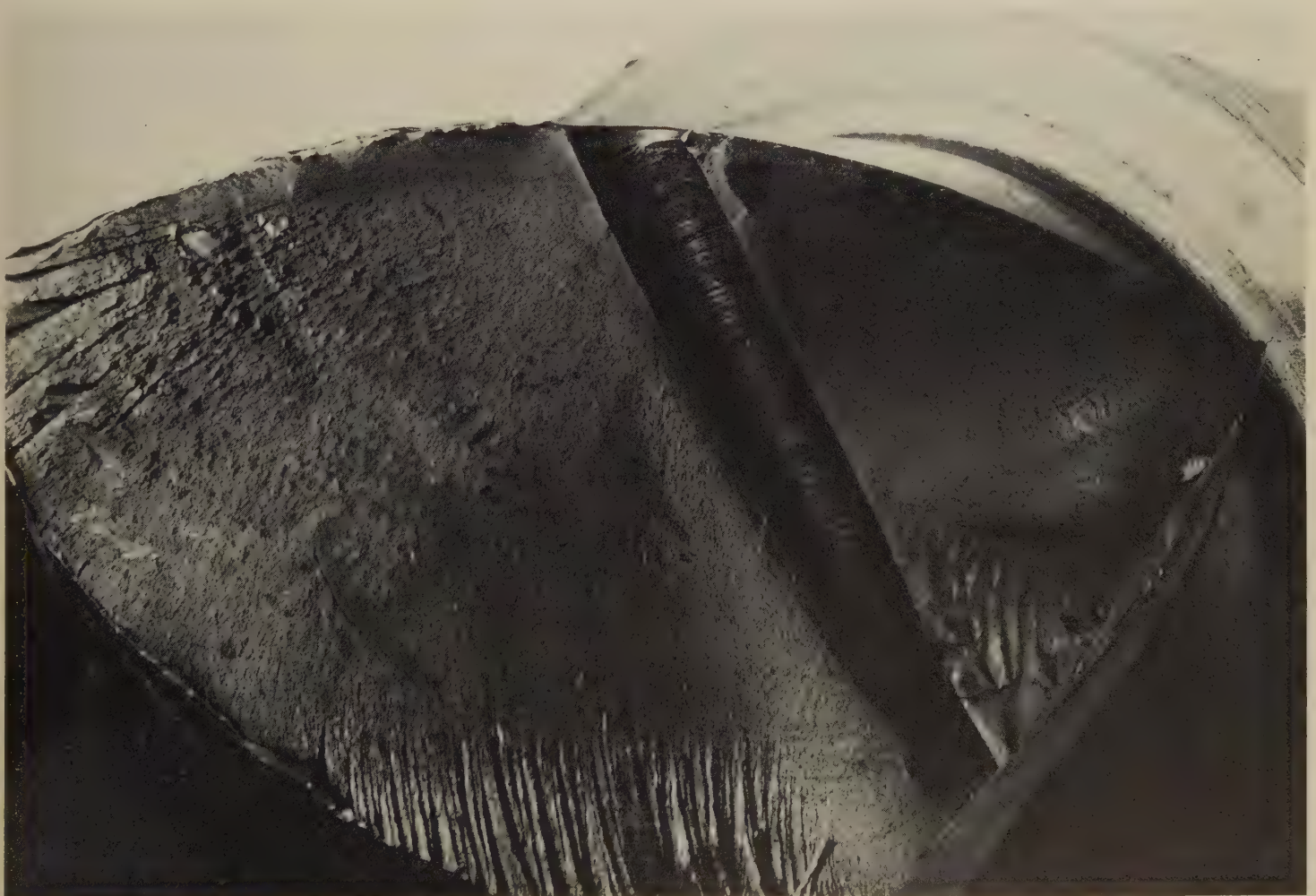
Actual size

Failure-Analysis Fractographs: 1045 Steel Shaft Fatigue-Cracked at a Keyway-Stop
Weld Deposit; 1045 Steel Crankshaft Fractured by Torsional Fatigue at an Oil Hole



Photograph

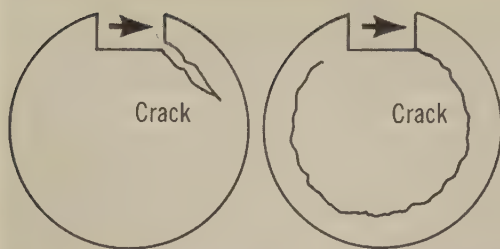
4880 A view of the mating surfaces of a fatigue crack (dark areas) exposed by sectioning a 1045 steel shaft quenched and tempered to a hardness of approximately Rockwell C 40. The crack, which was discovered before it could penetrate the entire cross section of the shaft, originated at a weld deposit that served as a stop in a keyway. 1 $\frac{2}{3}$ ×



Light fractograph

4881 Surface of a torsional-fatigue fracture in a 1045 steel crankshaft induction hardened to Rockwell C 55. The crack originated at the edge of an oil hole. Although it is not clearly evident in this view, the crack grew at a 45° angle to the axis of the crankshaft because of tensile-stress components caused by the torsional loading. About 2 $\frac{1}{2}$ ×

Failure-Analysis Fractographs: "Peeling" Fatigue Fracture in 1045 Steel
Keyed Shaft; Bending-Fatigue Fracture in 1046 Steel Crankshaft



Photograph

About 2.3×

4882 At top right are the mating segments of a keyed shaft of cold drawn 1045 steel that was broken by fatigue, resulting in a "peeling" type of fracture; a complete shaft is shown at bottom. The fatigue crack began in the bottom corner of a keyway in which, because of a loose fit, the key transmitted nearly all the torque. The fracture progressed in shear parallel to the shaft surface, as shown at top left, traveling completely around the shaft.

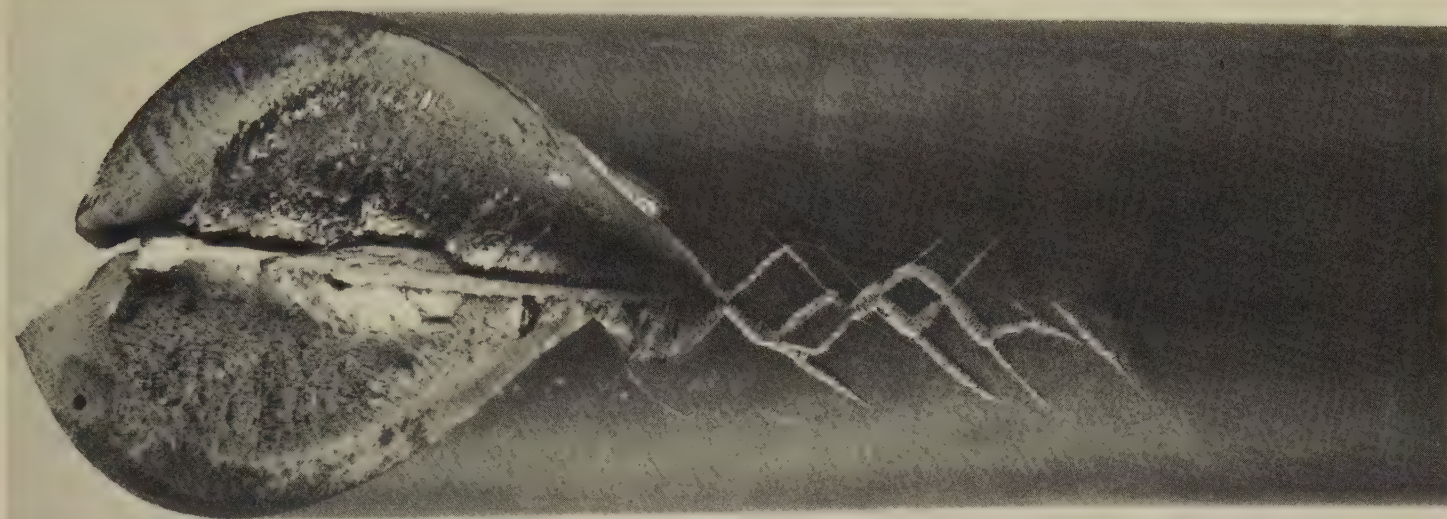


Light fractograph

About $\frac{3}{4}$ ×

4883 Surface of a fatigue fracture in a crankshaft of 1046 steel with a hardness of Rockwell C 25 in the region of fracture. Two cracks were generated under a bending stress; one crack started in the journal fillet at the arrow and progressed through the cheek until it met the second crack, which began in the fillet on the opposite side of the cheek. Note the sharply defined beach marks in the upper portion of the fracture surface.

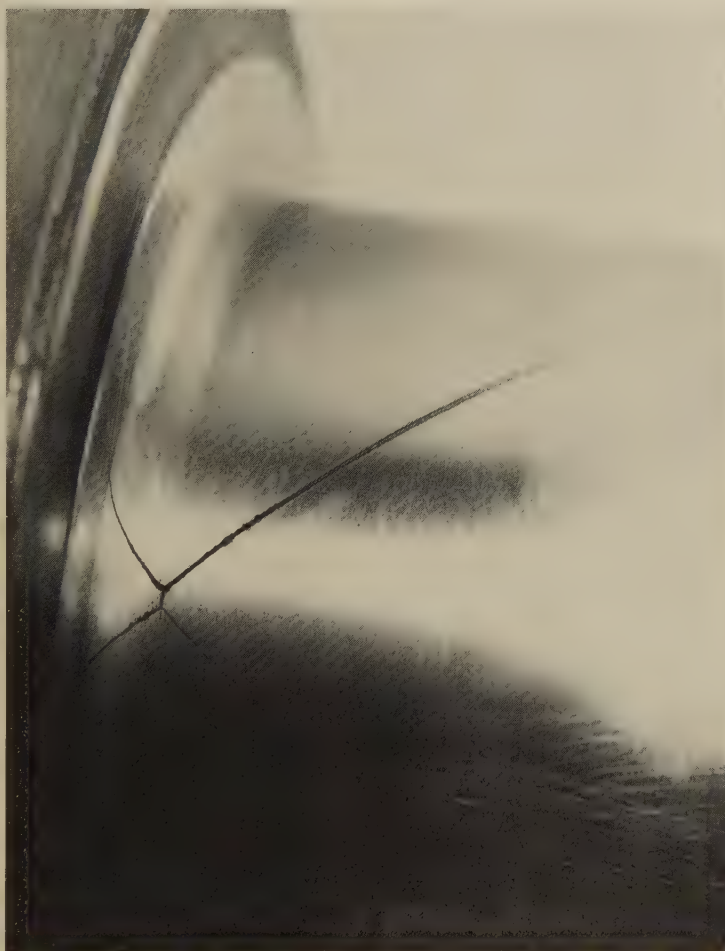
Failure-Analysis Fractographs: 1045 Steel Axle and Crankshaft Fractured by Fatigue in Reversed Torsion; 1046 Steel Shaft Fractured by Fatigue in Reversed Cantilever Bending



Photograph

About $1\frac{2}{3}\times$

4884 Fatigue fracture in a 1.5-in.-diam axle of 1045 steel induction hardened and tempered to Rockwell C 52 and tested in reversed torsion, showing fatigue cracks on the diagonal planes of maximum tension stress. Secondary cracks revealed by the iron-powder patterns on the axle, which was magnetized, are symmetrical, indicating that the stresses applied during the test were fully reversed.



Photograph

$1.35\times$

4885 Fatigue fracture in a 1045 steel crankshaft, with a hardness of Rockwell C 23, that was tested in reversed torsion. Visible at the base of a fillet is a fatigue crack that originated in the transverse direction (rather than in the longitudinal direction, as is most common) and that branched in four directions along the diagonal planes of maximum tension stress.

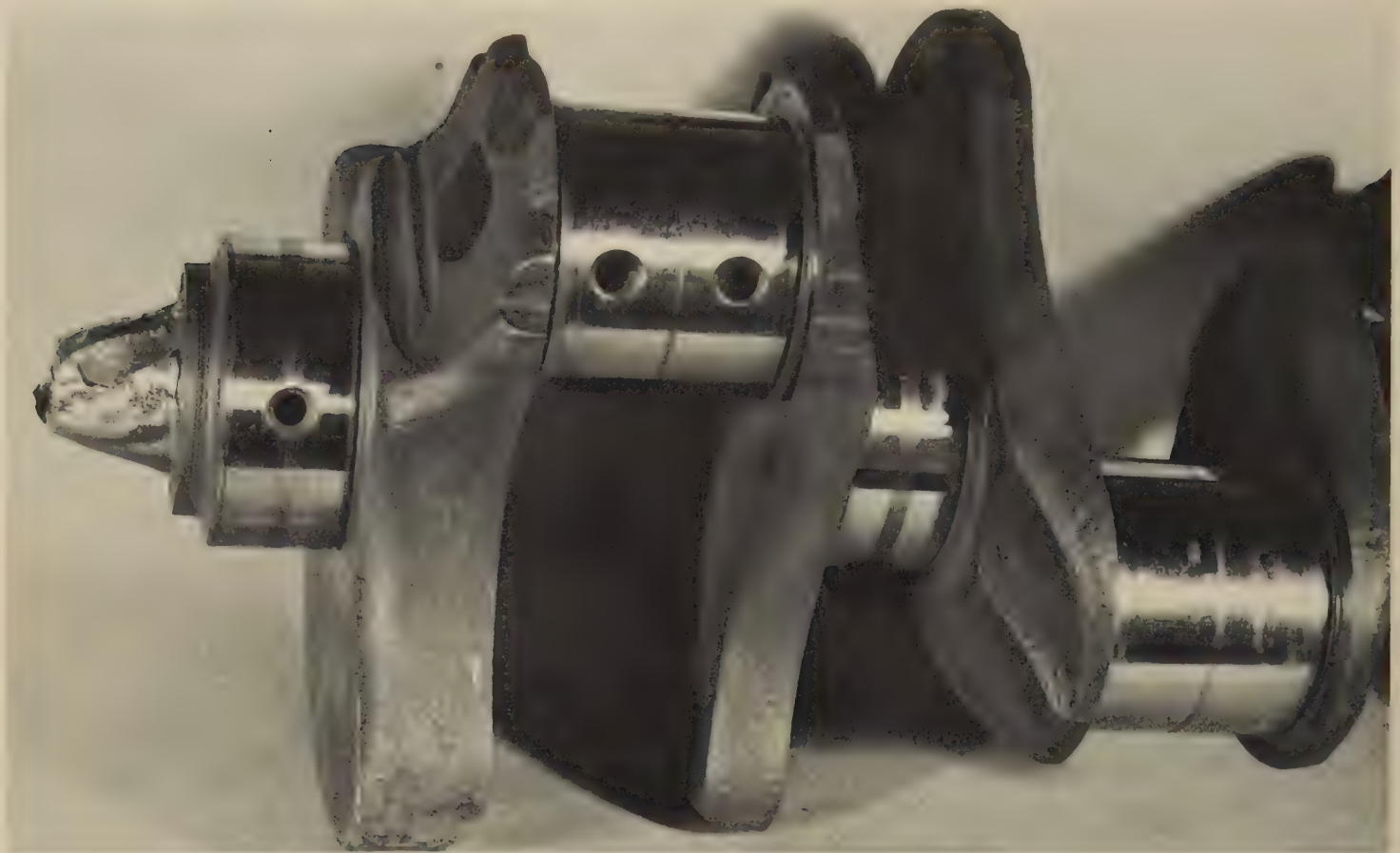


Light fractograph

About $2\frac{1}{6}\times$

4886 Surface of a fatigue fracture in a 1.6-in.-diam shaft of 1046 steel with a hardness of approximately Rockwell C 30. The shaft was tested in reversed cantilever bending. It is evident from the symmetrical fatigue pattern here that each side of the shaft was subjected to the same maximum stress and to the same number of load applications.

Failure-Analysis Fractographs: 1046 Steel Marine-Engine Crankshaft That Was Fractured by Fatigue



Photograph

4887 Marine-engine crankshaft of 1046 steel, quenched and tempered to a hardness range of 229 to 269 Bhn, that broke by fatigue at the timing-gear end, at left. The fracture surface, which is tapered, underwent severe battering at the time of final rupture. See also fractographs 4888 and 4889, below, for views of the fracture surface.

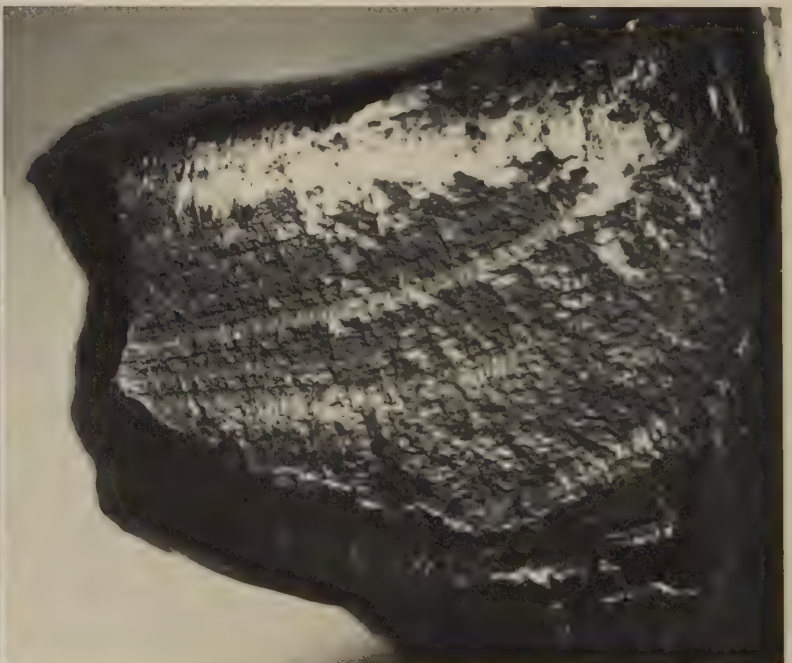
2/3x



Light fractograph

4888 End view of the tapered fracture surface in 4887, showing a counterbored longitudinal oil hole. Note the very rough machining marks and tears, which were sources of stress concentration.

3x



Light fractograph

4889 Higher-magnification side view of the tapered fracture surface of the crankshaft shown in 4887. Although the fracture surface underwent considerable battering during final rupture, the marks of progressive fatigue cracking are clearly evident.

3x

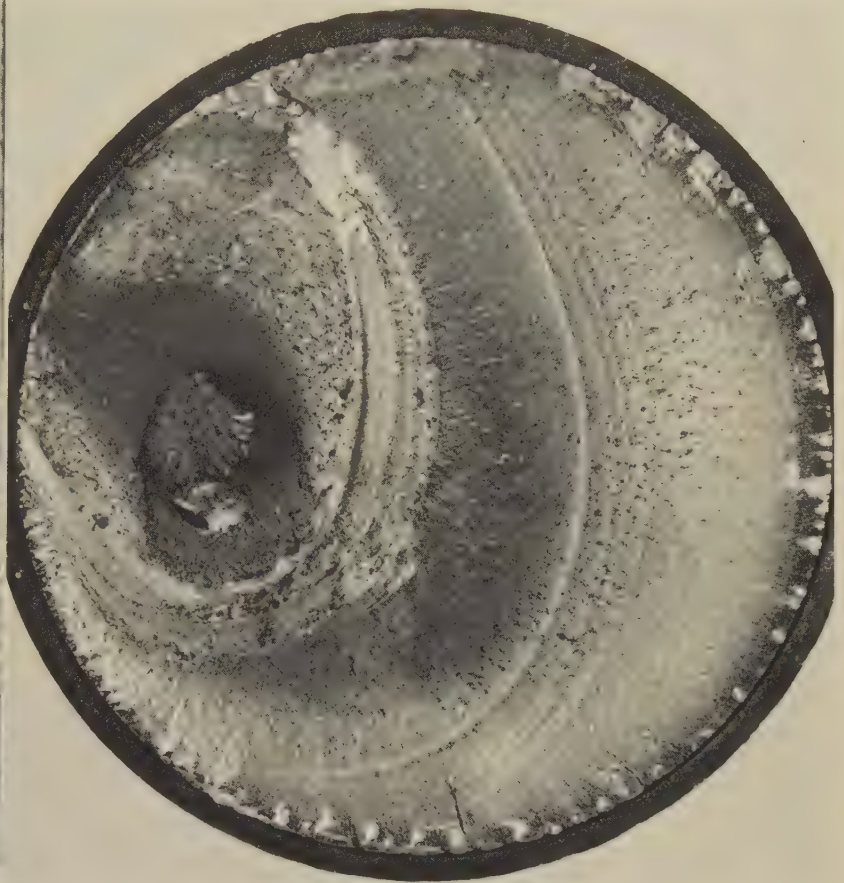
Failure-Analysis Fractographs of Fatigue Fractures in 1050 Steel: Gear Tooth at a Forging Defect; Shaft by Rotating Bending; Axle by Reversed Torsion



Light fractograph

About $2\frac{1}{2}\times$

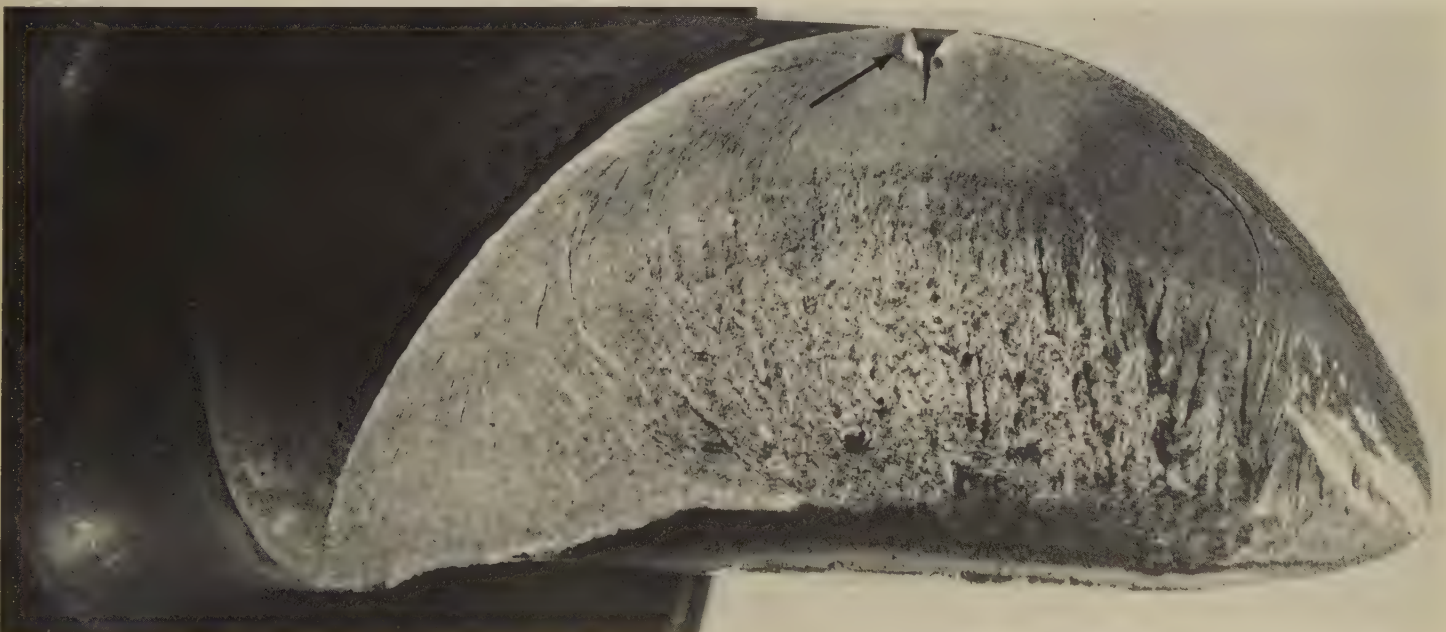
4890 Surface of a fatigue fracture in a tooth of a 1050 steel gear with a hardness of Rockwell C 55. The fatigue crack originated at a forging defect (at arrow). Fatigue beach marks are visible near the fatigue-crack origin. Beyond these marks are the steps of a river pattern, caused by cleavage.



Light fractograph

About $2.4\times$

4891 Surface of a fatigue fracture in a 1050 steel shaft, with hardness of about Rockwell C 35, that was subjected to rotating bending, showing ratchet marks indicating that fatigue cracks were initiated at many locations along a sharp snap-ring groove. Visible is an eccentric pattern of oval beach marks, the presence of which suggests an imbalance in loading.

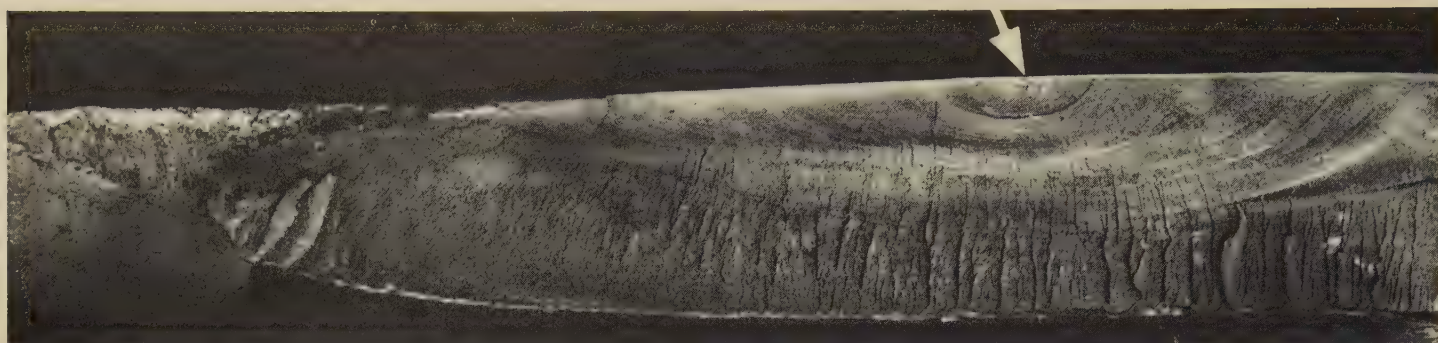


Light fractograph

About $2\times$

4892 Surface of a fatigue fracture in a full-floating axle of 1050 steel induction hardened to about Rockwell C 50. The axle was tested in reversed torsion. The arrow indicates the origin of the fatigue crack, which grew by shear fatigue to the small, circular beach mark. Subsequent crack growth was by tension fatigue until final fracture (brittle tensile) occurred under a single torsional load.

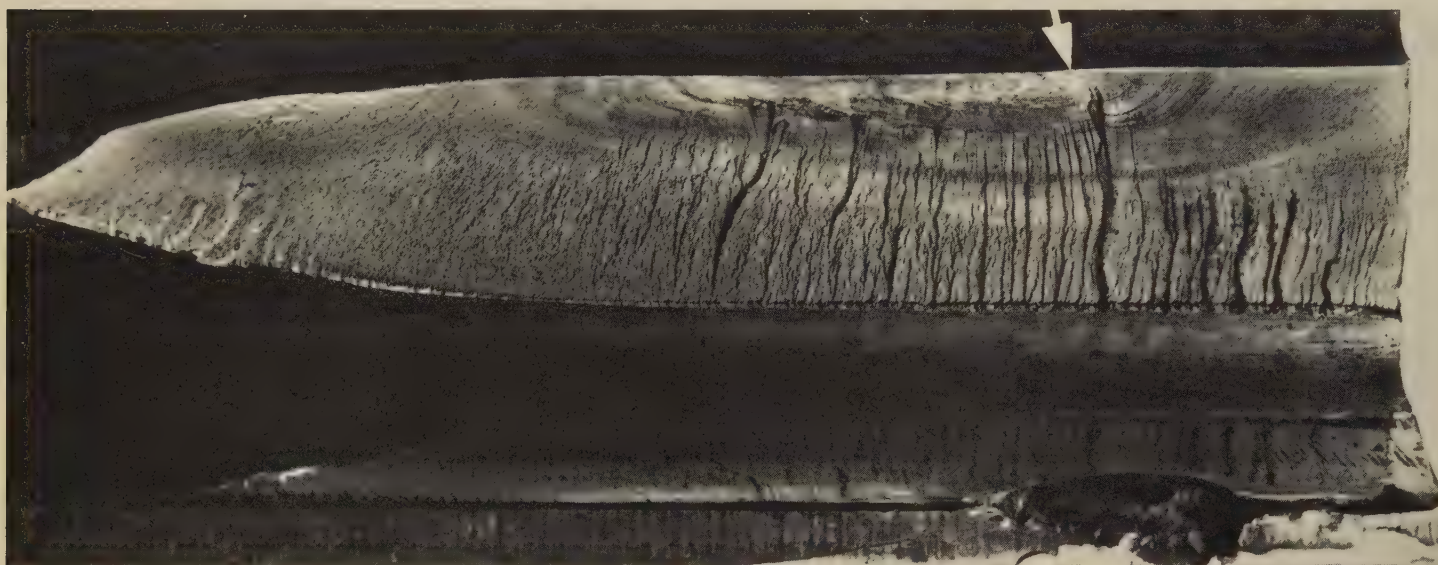
Failure-Analysis Fractographs: Induction Hardened 1053 Steel Tractor Bull Gears Fractured by Fatigue in Service



Light fractograph

About 2½×

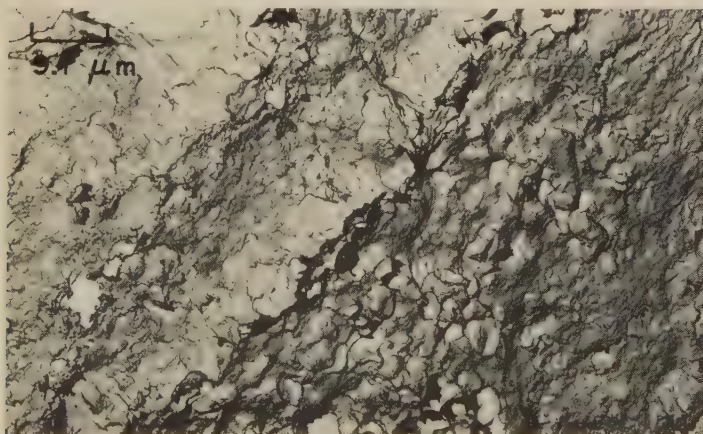
4893 Surface of a fatigue fracture that occurred, after 732 hr of service, in a tooth of the induction hardened 1053 steel left-side bull gear of a tractor. Hardness of the tooth was Rockwell C 57 at the tip and Rockwell C 50 at a depth of 13.3 mm. Hardness in the root fillet was about Rockwell C 56 near the surface and Rockwell C 50 at a depth of 11.5 mm. The arrow indicates the origin of the fatigue crack. See also fractographs 4894, 4895 and 4896, below.



Light fractograph

About 2½×

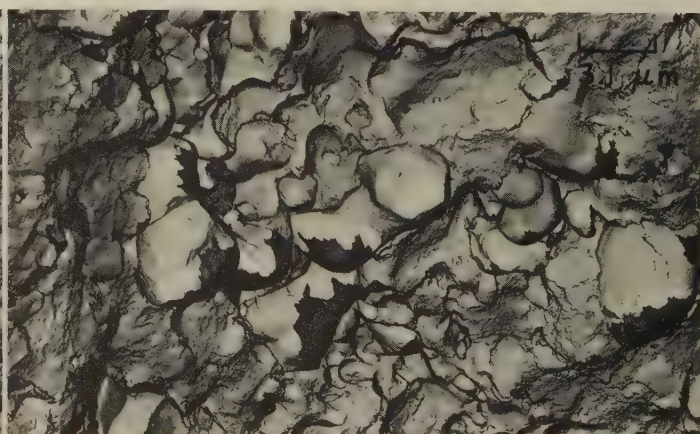
4894 Surface of a fatigue fracture (similar to that in 4893) that occurred, after 841 hr of service, in a tooth of the right-side bull gear of the same tractor. This gear also was made of 1053 steel and induction hardened. Hardness of this gear was similar to that of the gear in 4893 except that the depths at which hardness was Rockwell C 50 were 12.2 mm below the tip of the tooth and 9.5 mm below the surface of the root fillet. The arrow indicates the fatigue-crack origin. The damage to the tooth just below the one that fractured probably resulted from jamming by a fragment from the fracture.



TEM fractograph (p-c replica)

1100×

4895 TEM replica of an area of the fracture surface of the left-side bull gear in 4893, taken near the fatigue-crack origin. Visible are several inclusions believed to have contributed to the formation of the fatigue crack. See 4896.

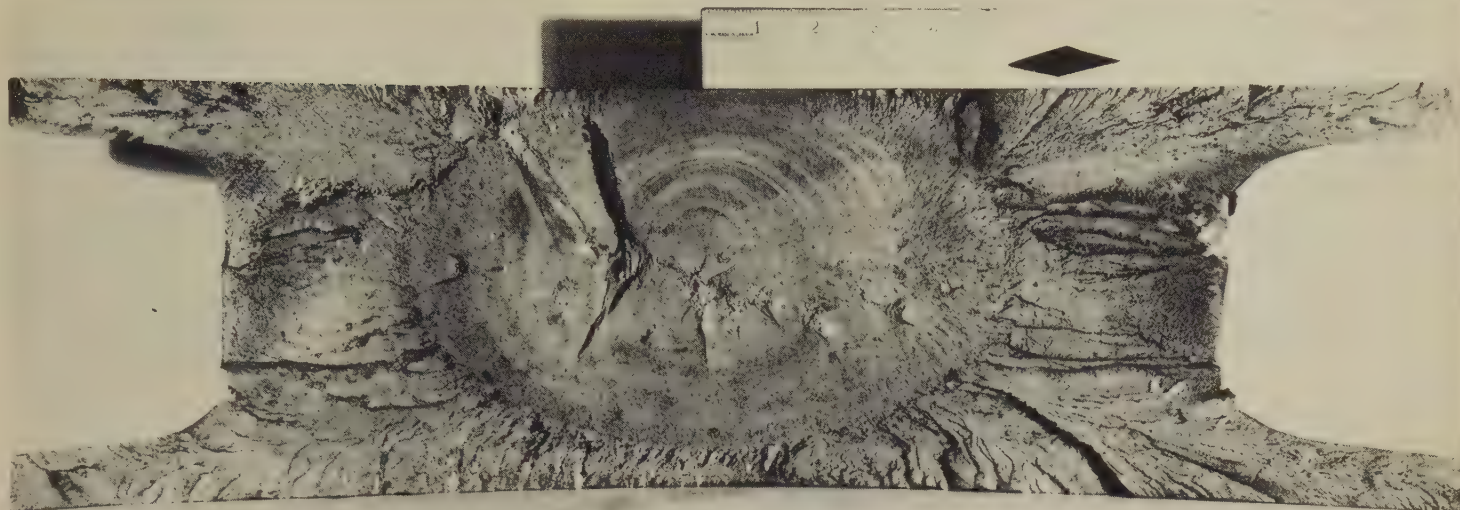


TEM fractograph (p-c replica)

3200×

4896 TEM replica of a portion of the area in 4895 (at left), but at higher magnification, showing the inclusions more clearly. Similar inclusions were found near the crack origin in the fracture surface of the right-side bull gear in 4894.

Failure-Analysis Fractographs: 1055 Steel Crane Wheels Fractured by Fatigue in Service; 1060 Steel Spring Wires Fractured by Fatigue



Light fractograph

0.3×

4897 Surface of a fatigue fracture that occurred, after approximately one year of service, in a 1055 steel wheel of a 600-ton stripper crane. Visible in the center of the fracture is a fatigue zone showing beach marks that are concentric around the fatigue-crack origin, which evidently was an internal flaw approximately 1½ in. beneath the wheel-tread surface. The chemical analysis of the steel was 0.60% C, 0.82% Mn, 0.009% P, 0.024% S and 0.24% Si, which was acceptably close to specification. Note the chevron patterns in the area of final, fast fracture that surrounds the fatigue zone.



Light fractograph

7/16×

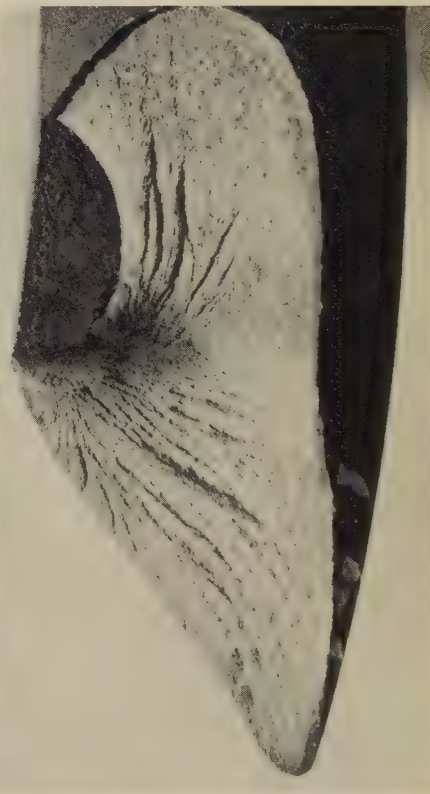
4898 Surface of a fatigue fracture that developed in the flange of a 1055 steel wheel of an open-hearth crane after nearly 20 years of service. The fracture surface was exposed by arc cutting the adjacent metal. This fatigue fracture, like the one shown in 4897 (above), was initiated by an internal flaw and propagated outward radially; no external defect was found to be involved in either this fracture or the fracture in 4897.



Light fractograph

7×

4899 Complex fatigue fracture in 1060 steel spring wire, 0.18-in. diam, originating at two or more crack nuclei at and above lower shoulder at left edge.



Light fractograph

About 3×

4900 Surface of a fatigue fracture in 5/8-in.-diam spring wire of 1060 steel. The crack origin, which undoubtedly was a surface flaw, generated a fatigue zone (dark area at upper left). The fatigue crack grew very slowly, and beach marks became obscured by oxide.



Light fractograph

3×

4901 Fatigue fracture in a $\frac{5}{16}$ -in.-diam suspension spring of 10B62 (15B62) steel wire. The fatigue crack probably originated at a surface defect and grew so slowly that oxidation occurred (note darkness of fatigue zone at left).

Photograph

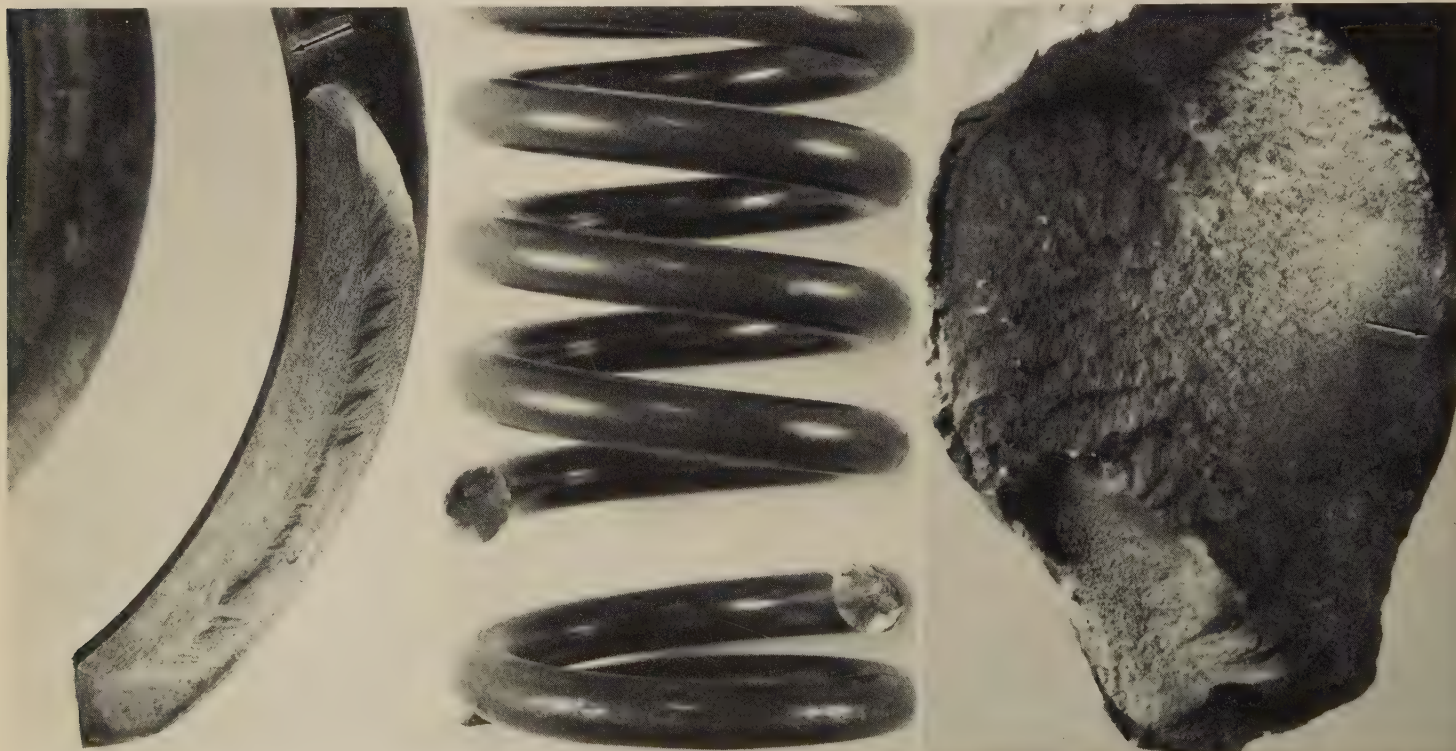
2×

4902 Fractured $\frac{1}{2}$ -in.-diam spring of 10B62 (15B62) steel wire with a hardness of 477 Bhn. Note the spiral gouges, which are screw marks that were generated during coiling. See also 4903, at right.

Light fractograph

3×

4903 Fracture surface of the spring in 4902. The crack originated at a screw mark. The small size of the fatigue zone (at left) indicates that final, fast fracture occurred soon after crack initiation.



Light fractograph

2×

4904 Fatigue-fracture surface of a suspension spring of 10B62 (15B62) steel wire with a hardness of 460 Bhn. Note the fine seam (at arrow), which is the fatigue-crack origin.

Photograph

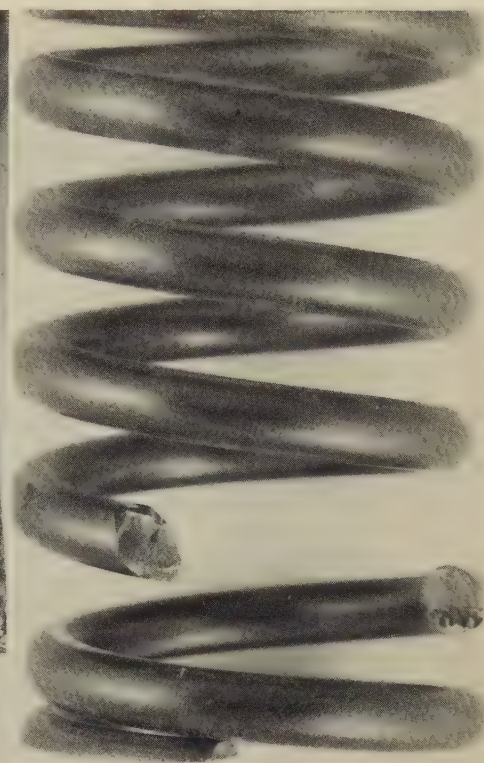
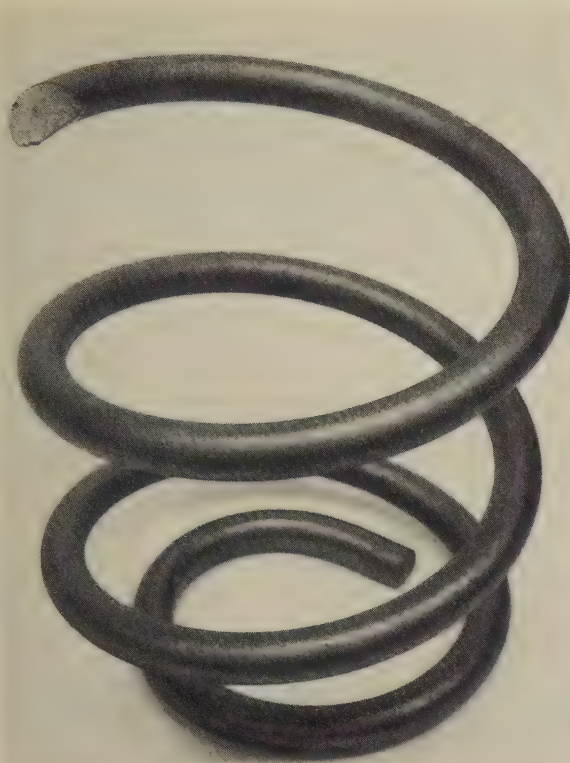
2×

4905 Fatigue-fractured valve spring of $\frac{3}{16}$ -in.-diam 1060 steel wire. The wire appears to be free of surface defects, a conclusion that is supported by the evidence in fractograph 4906 (at right).

Light fractograph

15×

4906 Higher-magnification view of fracture surface at right in 4905. The fatigue crack began at a subsurface origin (at arrow), not at a surface defect. Final, fast fracture formed shear lips at top, at left and at bottom.



Photograph
4907 Fatigue-fractured spring formed from $\frac{3}{4}$ -in.-diam 1060 steel wire. The seam on the back side of the top turn enters the fracture surface at the dark spot at left edge. See fractograph 4908, at right, for a view of the fracture surface.

Light fractograph
4908 Fracture surface of the spring in 4907 (left). The fatigue-crack origin is at the seam at left edge. The surface of the wire was gouged after fracture.

Photograph
4909 Fatigue-fractured spring of 0.200-in.-diam 1060 steel wire (hardness, Rockwell C 43 to 48). This fracture, unlike that of the similar spring in 4905, originated at the surface (see 4910, at left below).

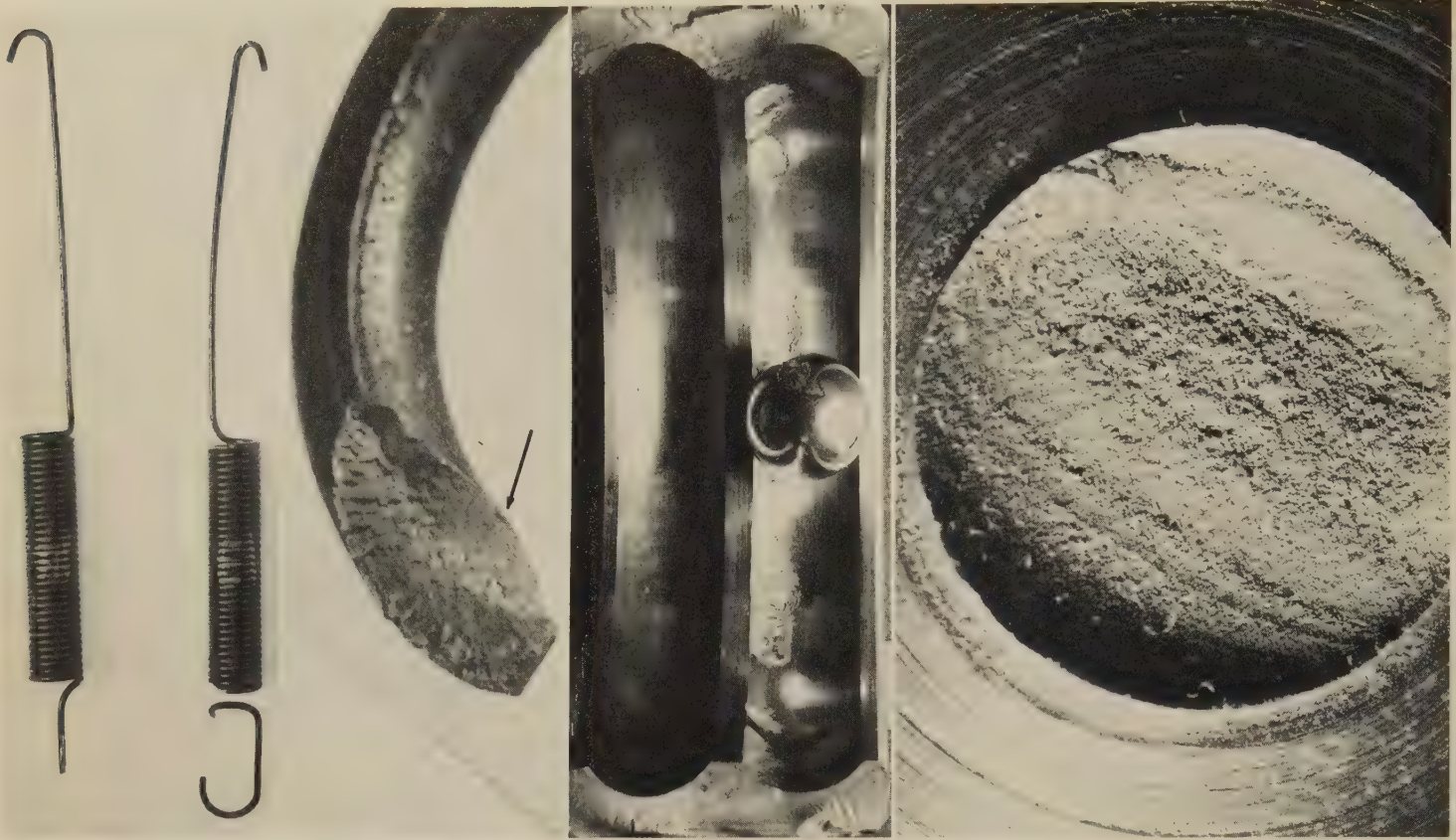


Light fractograph
4910 Fracture surface at right in 4909, shown at higher magnification. The nucleus of the fatigue crack is clearly visible on the wire surface at top, with a succession of beach marks fanning out below it. The surface of the zone of final, fast fracture appears to be quite woody.

Light fractograph
4911 Surface of a complex fatigue fracture in a valve spring formed from 1070 steel wire, showing two facets at right angles.

Photograph
4912, 4913 Fatigue fracture in a spring of 1070 steel wire with a hardness of Rockwell C 54. At left (4912) is a side view of one fracture surface, deep etched to show a long seam (at arrow). At right (4913) is a frontal view of the mating fracture surface, showing the fatigue-crack origin (at right), which is at a second seam.

Failure-Analysis Fractographs: Fractures in 1070 Steel Wire Springs,
High-Carbon Steel Bearing Race and Valve Spindle, and 1070 Steel Torsion Bar



Photograph $\frac{3}{4} \times$ Light fractograph $15 \times$
4914, 4915 At left (4914) are two fatigue-fractured springs of 0.050-in.-diam cold drawn 1070 steel music wire. Coil diameter was about $\frac{3}{8}$ in. At right (4915) is a fracture surface of one of the springs in 4914, showing a fatigue-crack origin at right edge (arrow).

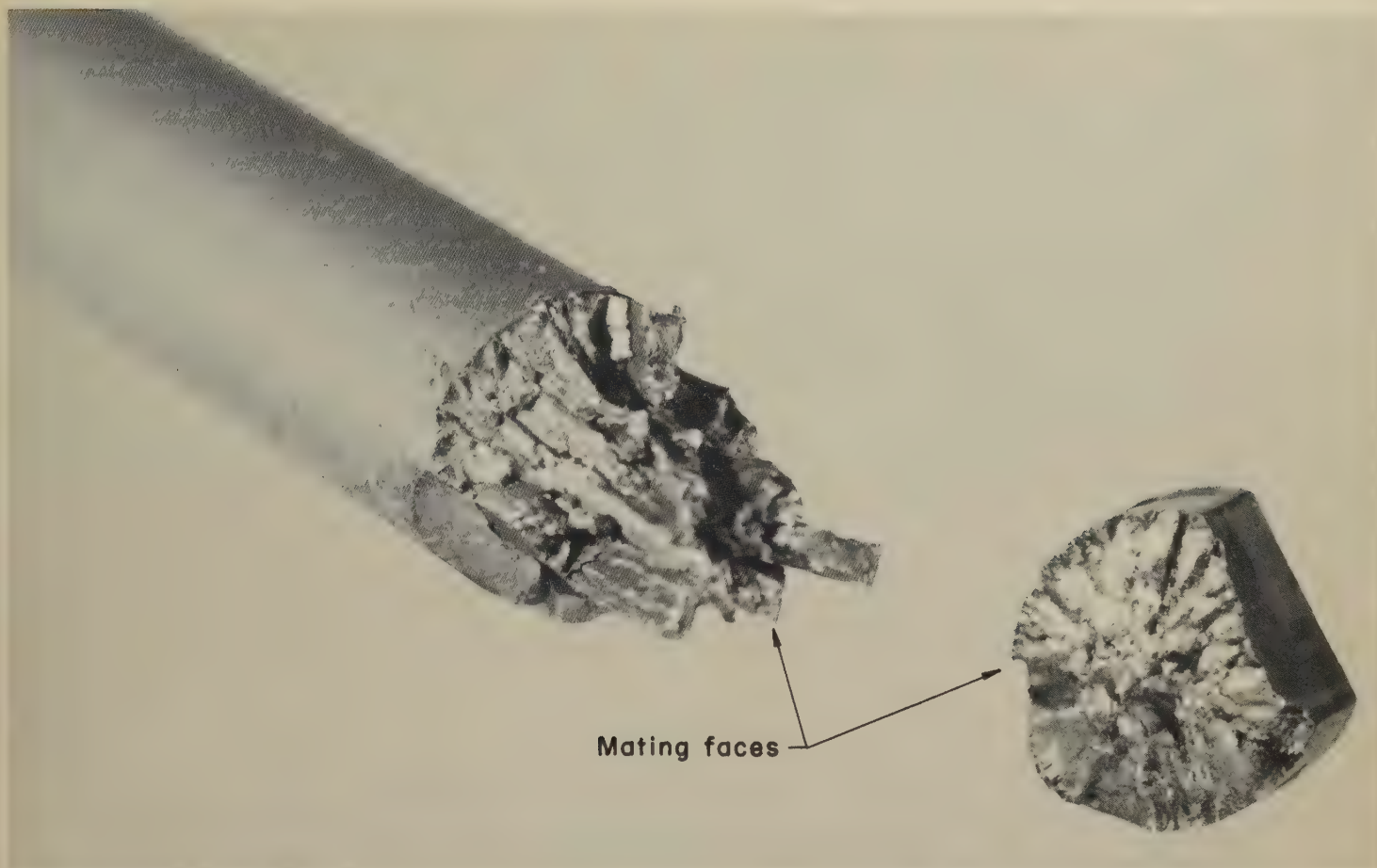
Photograph $0.95 \times$
4916 Fracture in the outer race of a high-carbon steel bearing of a forced-lubrication pump. Flaking of the ball bearing suggests overloading.

Light fractograph $2.1 \times$
4917 Surface of a fatigue fracture in a high-carbon steel spindle of an air-pump valve. Fatigue beach marks are clearly visible. The coarse machining marks on the surrounding shoulder indicate that machining produced notches that were deep enough to cause stress concentrations.



Photographs $5 \times$
4918 Two sides of a fractured $\frac{5}{16}$ -in.-diam 1070 steel torsion bar that had been quenched, and tempered to a hardness of Rockwell C 45. The bar fractured in a torsional fatigue test, cracking along both longitudinal and transverse shear planes. The test was halted before the fracture was complete. The fracture occurred at a machined flat, which fitted into the test-machine grip. Compare with the torsion-bar fracture shown in fractograph 4920, on the facing page.

Failure-Analysis Fractographs: 1070 Steel Torsion Bar Fractured by Torsional Fatigue; 1095 Steel Spring Fractured by Fatigue



Mating faces

Light fractographs

5.6×

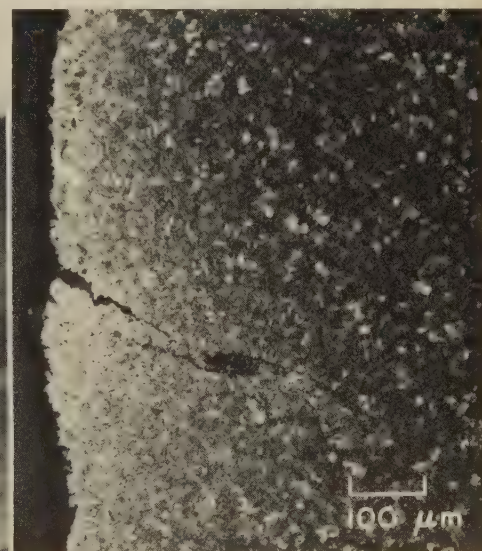
4920 Torsional fatigue fracture in a $\frac{5}{16}$ -in.-diam torsion bar of 1070 steel that was quenched, and tempered to a hardness of Rockwell C 45. This fracture is similar to that in 4818 and 4819 (facing page) except that complete separation occurred here; the same pattern of fatigue cracks along longitudinal and transverse shear planes is evident.



Light fractograph

About actual size

4921 Surface of a fatigue fracture, which occurred after about one year of service, in a 1095 steel spring of a 250-ton shear. A fatigue zone is evident at the inner (right) edge of the fracture surface (at arrow). This is a normal location for a fatigue-crack origin in a coiled spring, and the fracture may be rated as typical. The fatigue crack penetrated a distance of approximately $\frac{1}{2}$ in. into the spring before final, fast fracture occurred. See also micrograph 4922, at right.

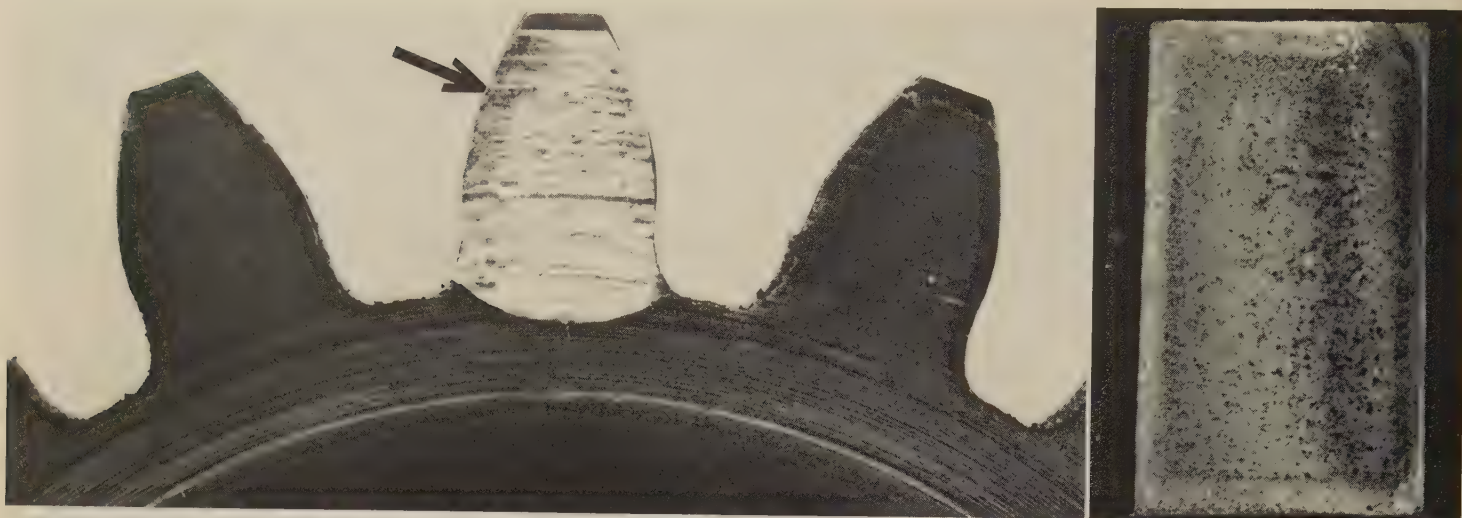


Micrograph (nital)

100×

4922 Polished and etched section through the spring in 4921, taken adjacent to the fracture. Visible is a crack-like defect that probably nucleated the fatigue crack. Decarburization (white zone) around the defect indicates that the defect is a seam, which existed prior to service.

Failure-Analysis Fractographs: Carburized 4118 Steel Gears in Which Teeth Fractured by Fatigue



Photograph

35/8 X

Light fractograph

4 1/2 X

4923, 4924 At left (4923) is a side view of a carburized gear of 4118 steel in which a tooth fractured by fatigue. (The tooth fragment was whitened to provide contrast with the remainder of the gear and was repositioned on the gear for this photograph.) The arrow indicates the point at which the major cantilever-bending load was exerted on the tooth, producing tensile stress in the root fillet below, where the fatigue crack originated. Fractograph 4924 (right) shows the fracture surface of the broken gear tooth, with a very fine texture at left edge (where the crack originated) and a rougher texture at right.

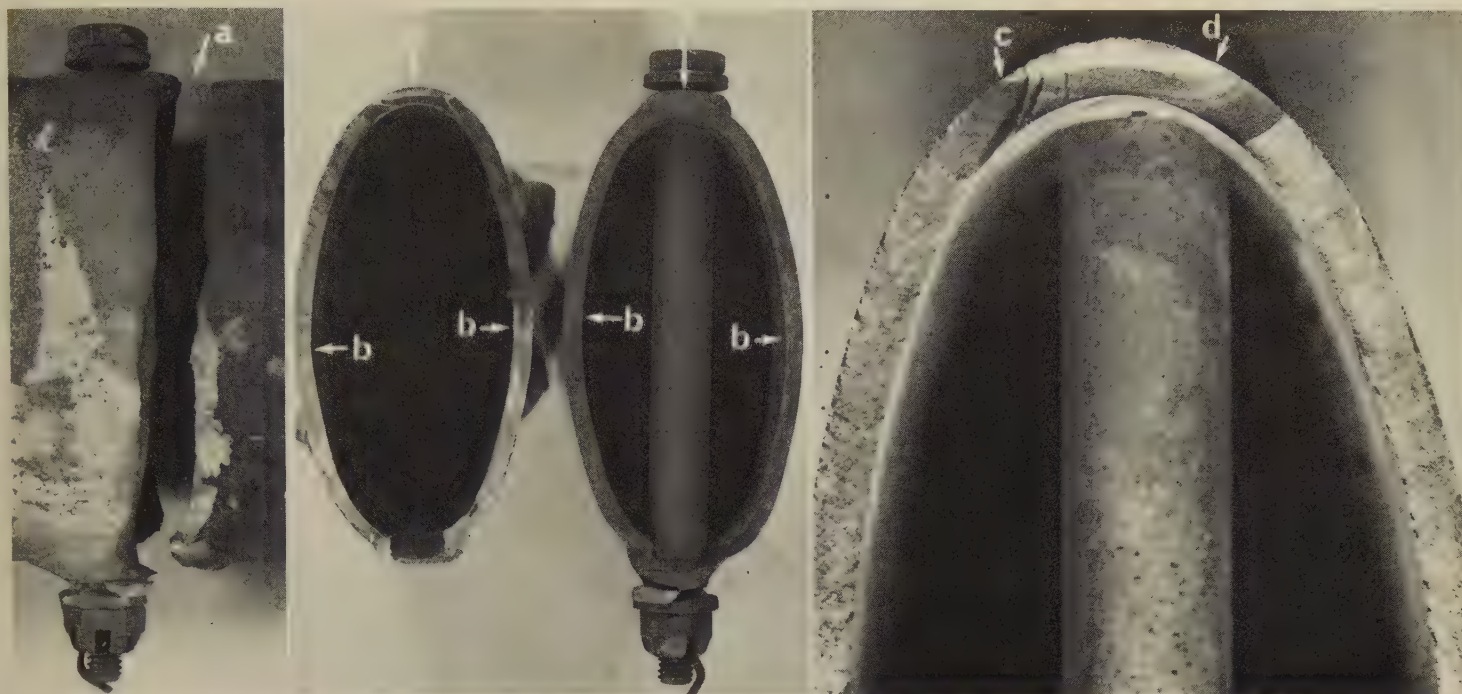


Light fractograph

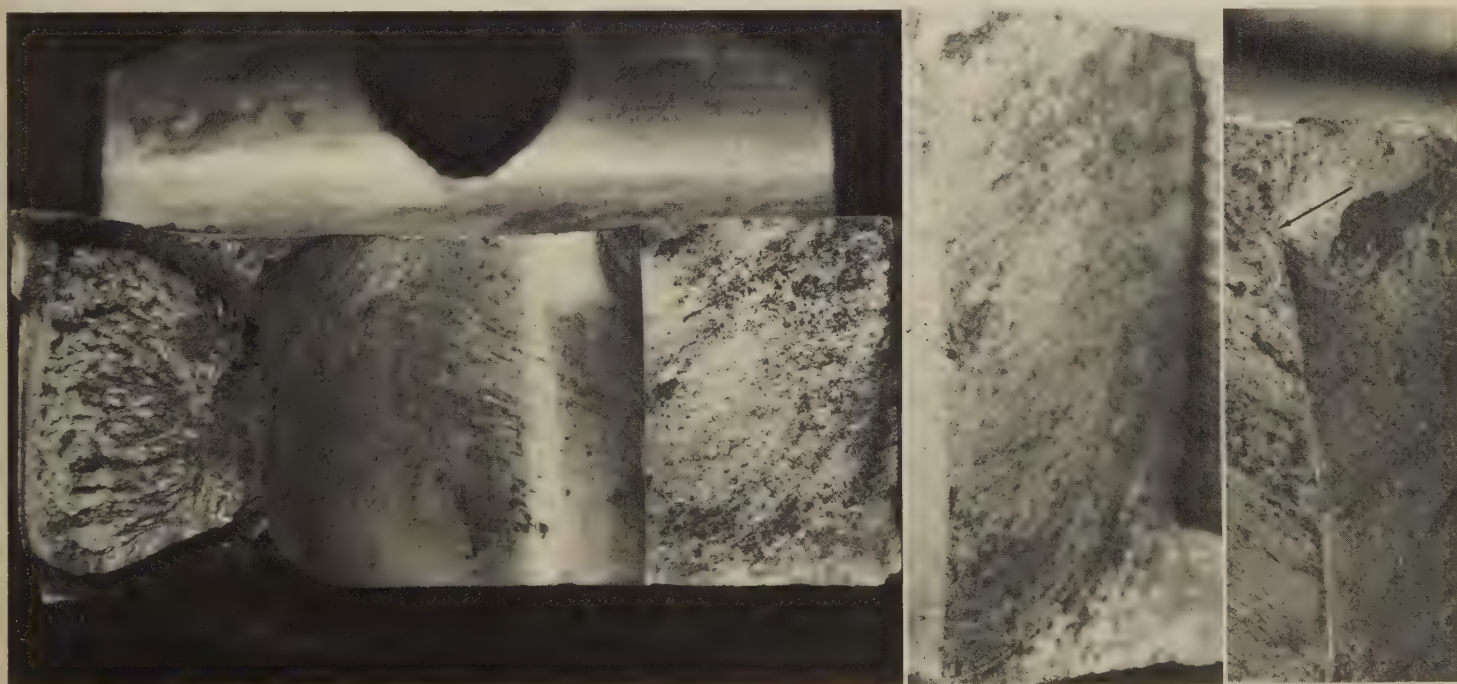
About 3.1 X

4925 A planet gear of 4118 steel in which most of the tips of the teeth broke off after brief service. The gear was carburized and heat treated to a case hardness of about Rockwell C 60. The case extended, however, to an excessive depth, which created a high residual tensile stress at the interface between the case and the core. The additional stresses from service loading initiated cracks at this interface; ultimately, these cracks propagated, probably by fatigue, to the surfaces of teeth.

Failure-Analysis Fractographs: 4130 Steel Aircraft Wing-Spar Cap Fractured by Fatigue;
4130 Steel Aircraft Wing-Attachment Fitting Fractured by Fatigue



Photograph Actual size Light fractograph Actual size Light fractograph 5×
4926, 4927, 4928 At left (4926) is a view of a fatigue fracture in the lower cap of an aircraft wing-spar assembly. The cap was formed of 4130 steel elliptical tubing, with a 0.10-in.-thick wall, heat treated to a tensile strength of 1138 to 1344 MPa (165 to 195 ksi). A skin-attachment bolt, contained in a tube passing through and welded to the cap, was close to the fracture, which originated at "a" (top). At center (4927) is a view of the surfaces of the fracture in 4926; again, the fatigue-crack origin is at "a" (top). The points at which final, fast fracture began are marked "b". At right (4928) is a higher-magnification view of the top portion of the fracture surface at right in 4927, showing the area of initiation of the fatigue crack, which originated at a welding crack formed during attachment of the bolt tube prior to heat treatment. The region between "c" and "d" appears light because of rubbing by the mating surface before final, fast fracture occurred.

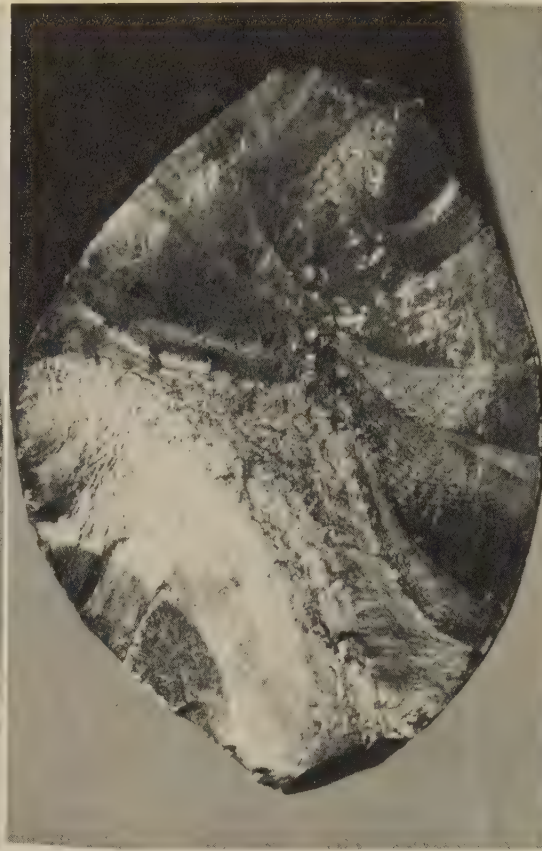


Light fractograph 2× Light fractograph 4× Light fractograph 10×
4929, 4930, 4931 Three views of a fracture in an aircraft lower wing-attachment fitting, which originated at a fatigue crack in an area of fretting and corrosion at a bolthole. The fitting was made of 4130 steel and heat treated to a tensile strength of about 1034 MPa (150 ksi). The fracture face at right in fractograph 4929 (left) was produced 95% by fatigue and contains a shear lip (bottom right); the fracture face at left in 4929 was produced by bending overload after the right side of the fitting had fractured. At center (fractograph 4930) is an oblique view of the fracture face at right in 4929, displaying the shear lip more clearly. At right (fractograph 4931) is a higher-magnification view of the area at upper left in 4930, showing the fatigue-crack origin (at arrow) and the fretting and corrosion in the bolthole (at left).

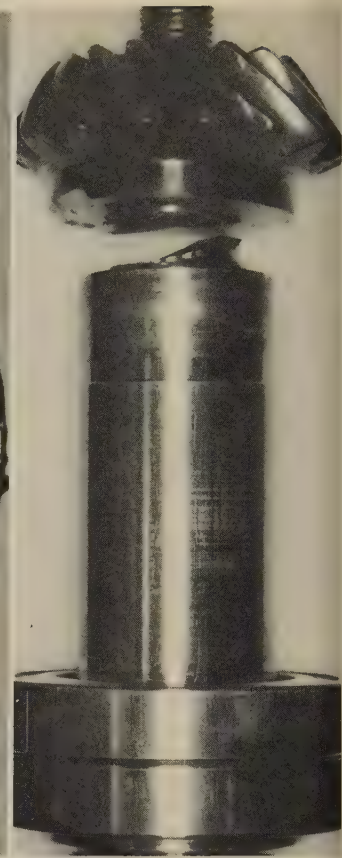
Failure-Analysis Fractographs: Fatigue Fractures in 4140 Steel Stud, Suspension Component, and Helicopter Tail-Rotor Drive-Pinion Shaft



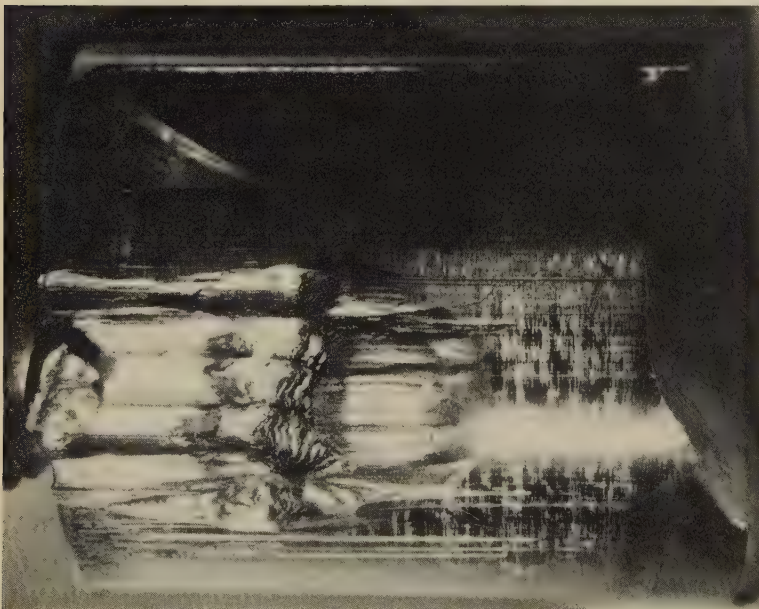
Light fractograph 2×
4932 Surface of a fatigue fracture in a stud of 4140 steel with hardness of Rockwell C 34 in the core and Rockwell C 45 at the surface. The crack originated at bottom in this view, in a well-rubbed fatigue zone, and penetrated nearly 90% of the cross section of the stud before final, fast fracture occurred.



Light fractograph 5×
4933 Surface of a fatigue fracture in a suspension component of 4140 steel heat treated to a hardness of 273 Bhn. Two fatigue zones are evident, at lower left and at upper right; the remainder of the fracture surface is the zone of final, fast fracture.



Photograph Actual size
4934 Fatigue fracture in a 4140 steel tail-rotor drive-pinion shaft of a helicopter, heat treated to a hardness of Rockwell C 35. See also 4935 through 4938.



Photograph
4935, 4936

At left (4935) is a view of the threaded end of the fractured shaft in 4934, after removal of the pinion gear. At right (4936) is a view of the bore of the pinion gear. Both photographs display severe galling damage of the contacting surfaces, which resulted in the gear being frozen on the shaft; the gear was removed by cutting through it from both sides. The appearance of the gouge marks indicates that most of the galling damage was done in forcing the gear onto the shaft. Photograph 4935 (left) shows also a keyway and an oblique view of a fracture surface; the fracture originated at a location on the keyway edge that is not visible here.



5× Photograph

5×

Failure-Analysis Fractographs: Fatigue Fractures in 4140 Steel Tail-Rotor Drive-Pinion Shaft (Continued) and 4150 Steel Splined Shaft



Light fractograph

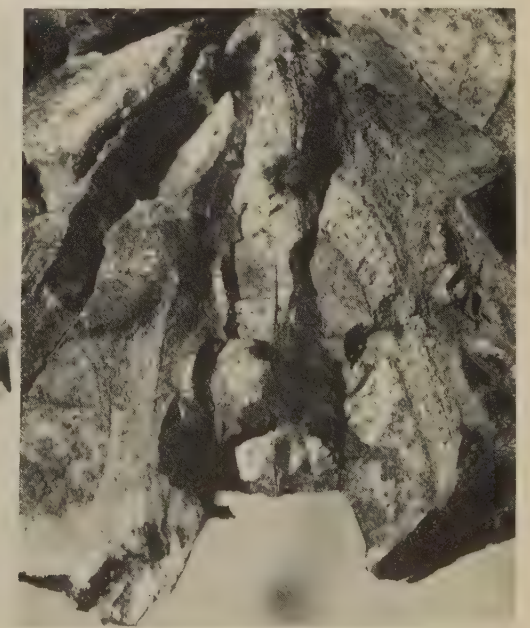
2×

Light fractograph

10×

4937, 4938

Two views of a surface of the fatigue fracture in the tail-rotor drive-pinion shaft in 4934, taken with the key and the pinion gear in place. The fatigue-crack origin (arrows) is in the keyway, slightly to the right of the corner formed by the edge of the keyway and the outside surface of the shaft. Not visible here are deep tool marks and machining tears on the inside of the keyway, which were the sources of the stress concentrations responsible for initiation of the fatigue crack. The smooth fracture surface shown in these views is typical of those produced by high-cycle fatigue in combined bending and torsion.



Photograph

1/2×

Light fractograph

1 1/2×

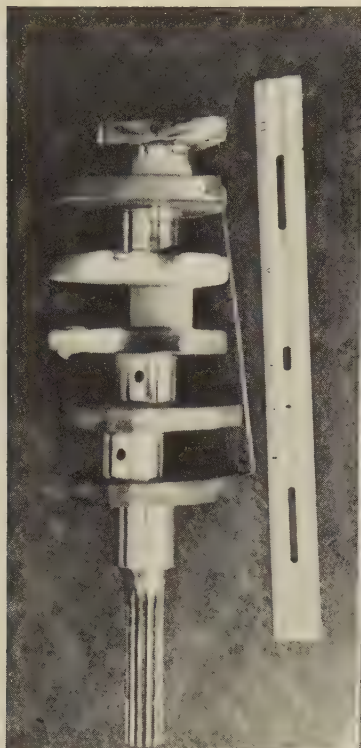
Light fractograph

3 1/2×

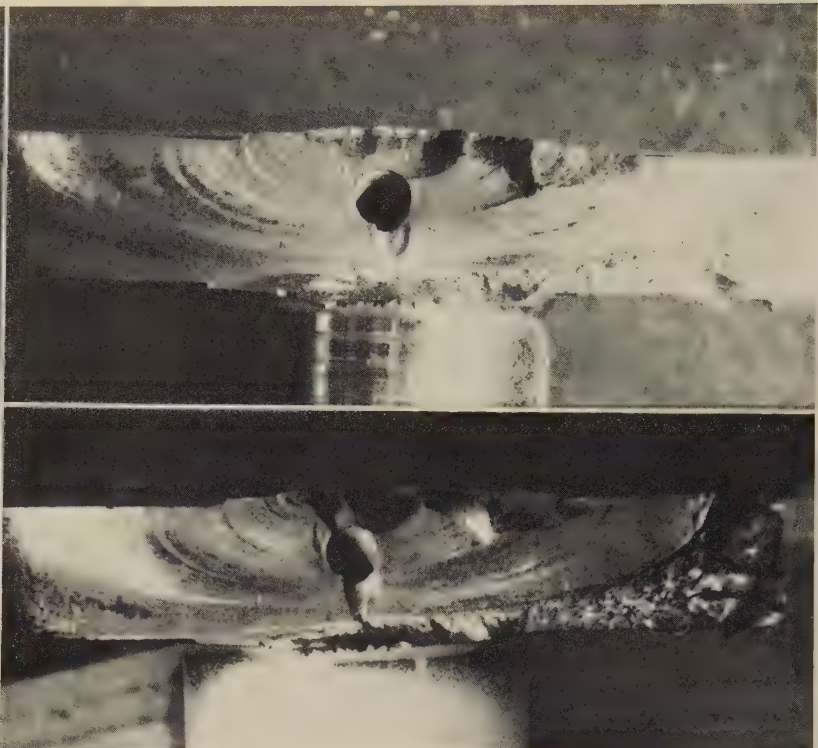
4939, 4940, 4941

Photograph 4939 (at left) shows a fractured 4150 steel splined shaft heat treated to a hardness of Rockwell C 43. Note that there is a secondary transverse crack below the main fracture. At center (fractograph 4940) is a view of one surface of the fracture in 4939, showing a very complicated starlike pattern. Close examination of the many arms of the "star" reveals the presence of fatigue beach marks produced by crack fronts that propagated separately but simultaneously. Particularly evident are the beach marks on the arms at bottom, which are shown at higher magnification in fractograph 4941 (right). Sharp radii at the bases of the splines appear to have been the origins of the fatigue cracks.

Failure-Analysis Fractographs: Fatigue Fractures in 4140 Steel Outboard-Motor Crankshafts



Photograph About $\frac{1}{4} \times$
4942 Outboard-motor crankshaft, forged of 4140 steel and heat treated to a hardness of Rockwell C 35 to 40, that fractured in service through a throw (at top). Chromium plating had been used to build up worn journals. See also 4943 to 4953.



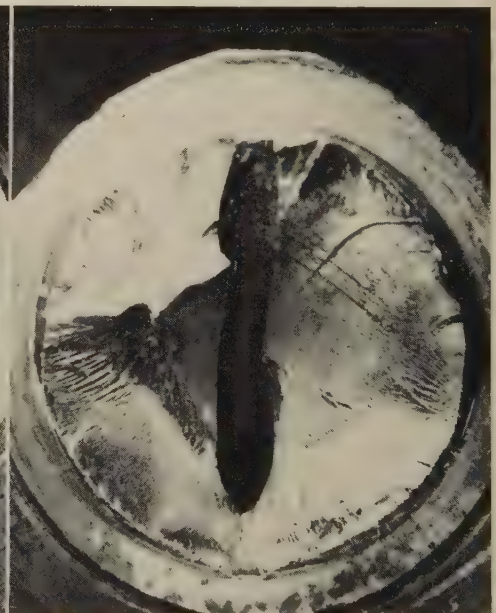
Light fractographs About $1.7 \times$ (4943); about $1.3 \times$ (4944)
4943 Fractograph 4943 (at top) is a view of the surface of the fracture in 4942, showing several small crack nuclei above the oil hole. Fatigue cracks from these nuclei merged to form a single crack front, which nearly penetrated the entire cross section of the throw before final, fast fracture occurred. Fractograph 4944 (at bottom) is another view of the surface of the fracture in 4942, photographed using illumination that reveals more of the details of the area of final, fast fracture than does 4943. The fatigue crack was initiated at a bottom fillet of the No. 2 main-bearing journal, which was chromium plated.



Light fractograph



About $1.6 \times$



Light fractograph

About $1.6 \times$

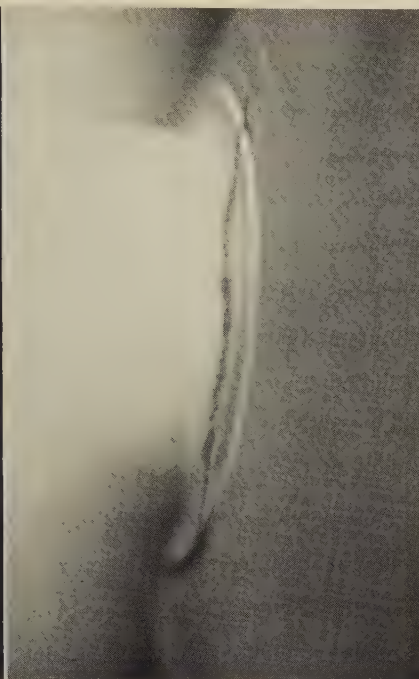
4945, 4946, 4947 Surfaces of three fatigue fractures in crankshafts the same as that in 4942; in each of these crankshafts, however, fracture progressed through a plated connecting-rod journal, rather than through a throw as in 4942. Each of these fractures originated at multiple nuclei along a fillet. Fatigue cracks began at these nuclei and then joined to form a single crack front along a portion of the journal periphery. Final separation was by fast fracture. In the fracture at left (4945), there are three or four crack nuclei at the right edge; the fatigue-crack front penetrated past the oil hole before final, fast fracture occurred. In the fractures at center (4946) and right (4947), fatigue cracks formed at many nuclei at the bottom edge, and the fatigue-crack front followed the oil hole toward the opposite edge. In 4947, a second crack front, independent of the main front, advanced from upper left.

Failure-Analysis Fractographs: Fatigue Fractures in 4140 Steel Outboard-Motor Crankshafts (Continued)



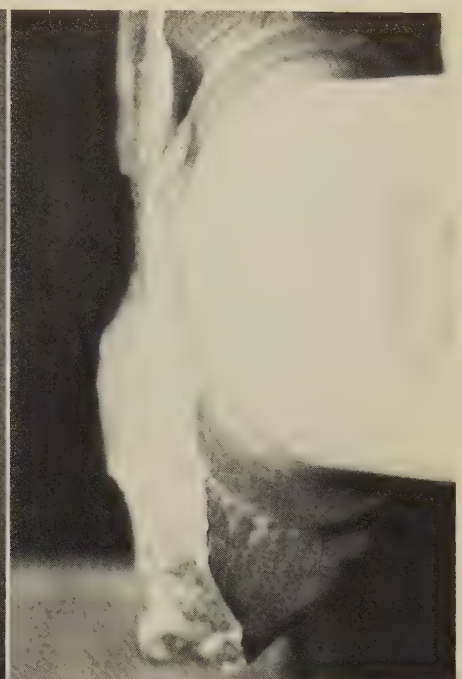
Light fractograph

4948 Surface of a fatigue fracture through a chromium-plated connecting-rod journal in a crankshaft the same as those in 4942 to 4947 (opposite page), showing many brittle cracks, which originated in the chromium plating and converged to create four large, deeply penetrating fatigue cracks having very different facet angles.

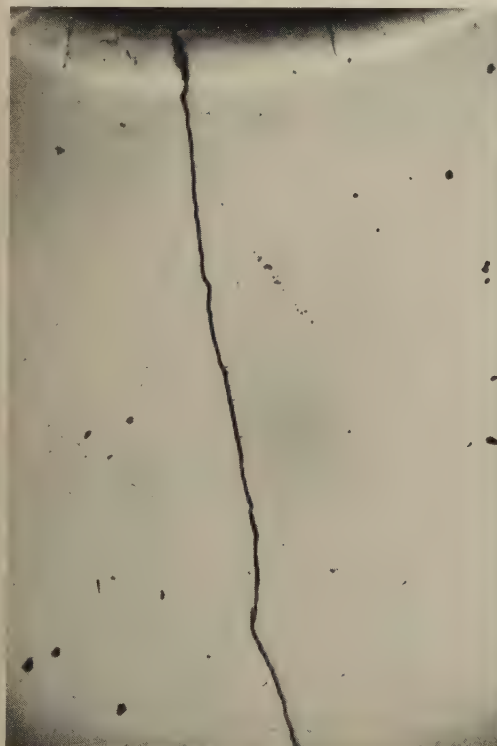


Photograph

4949, 4950 At left (4949) is a view of a fillet of a chromium-plated connecting-rod journal in a crankshaft the same as those in 4942 to 4948, showing a crack revealed by magnetic-particle inspection. This crack is typical of those that grew to form the fractures shown on this page and on the facing page. (A similar secondary crack is visible at right in 4944.) Photograph 4950 (right) shows such secondary cracks in a fillet, immediately adjacent to a fracture in a throw of a companion crankshaft; see also 4951 and 4952.



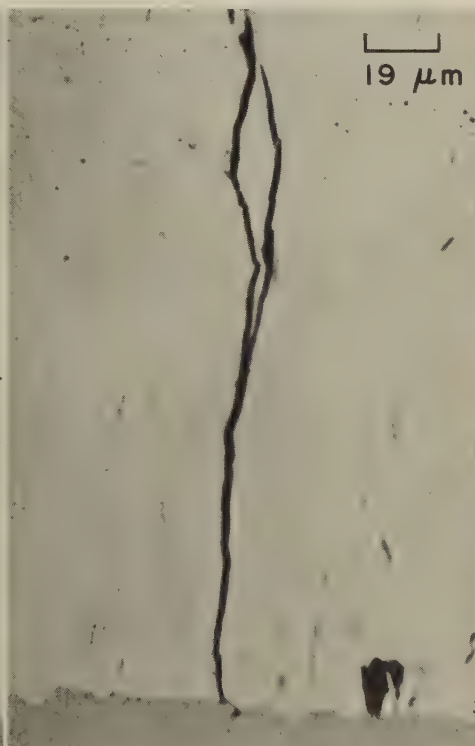
Photograph



Micrograph (as polished; not etched)

30×

4951 Longitudinal section taken, at mid-height, through the fillet in 4950. Note the cracks in the chromium plating at top, one of which extends 0.185 in. into the base metal. Hardness of plating here and in 4952 and 4953 was Rockwell C 60 to 70.

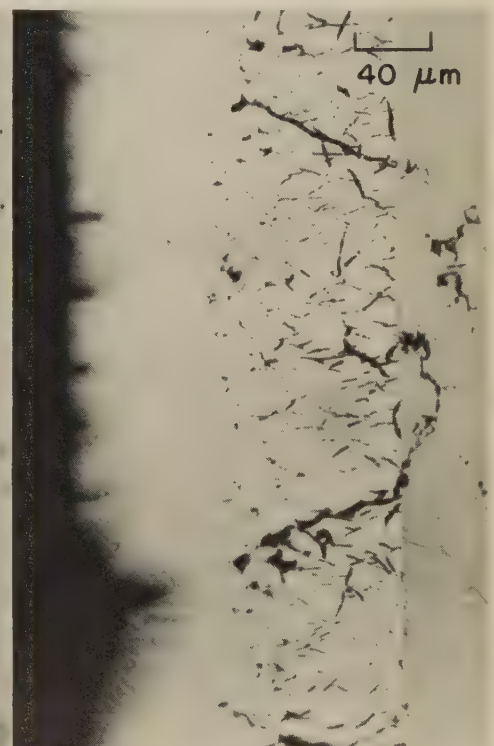


19 μm

Micrograph (as polished; not etched)

525×

4952 Higher-magnification view of the first crack to the right of the deep crack in the chromium plating in 4951. Note that this crack had just begun to penetrate the base metal (at bottom).



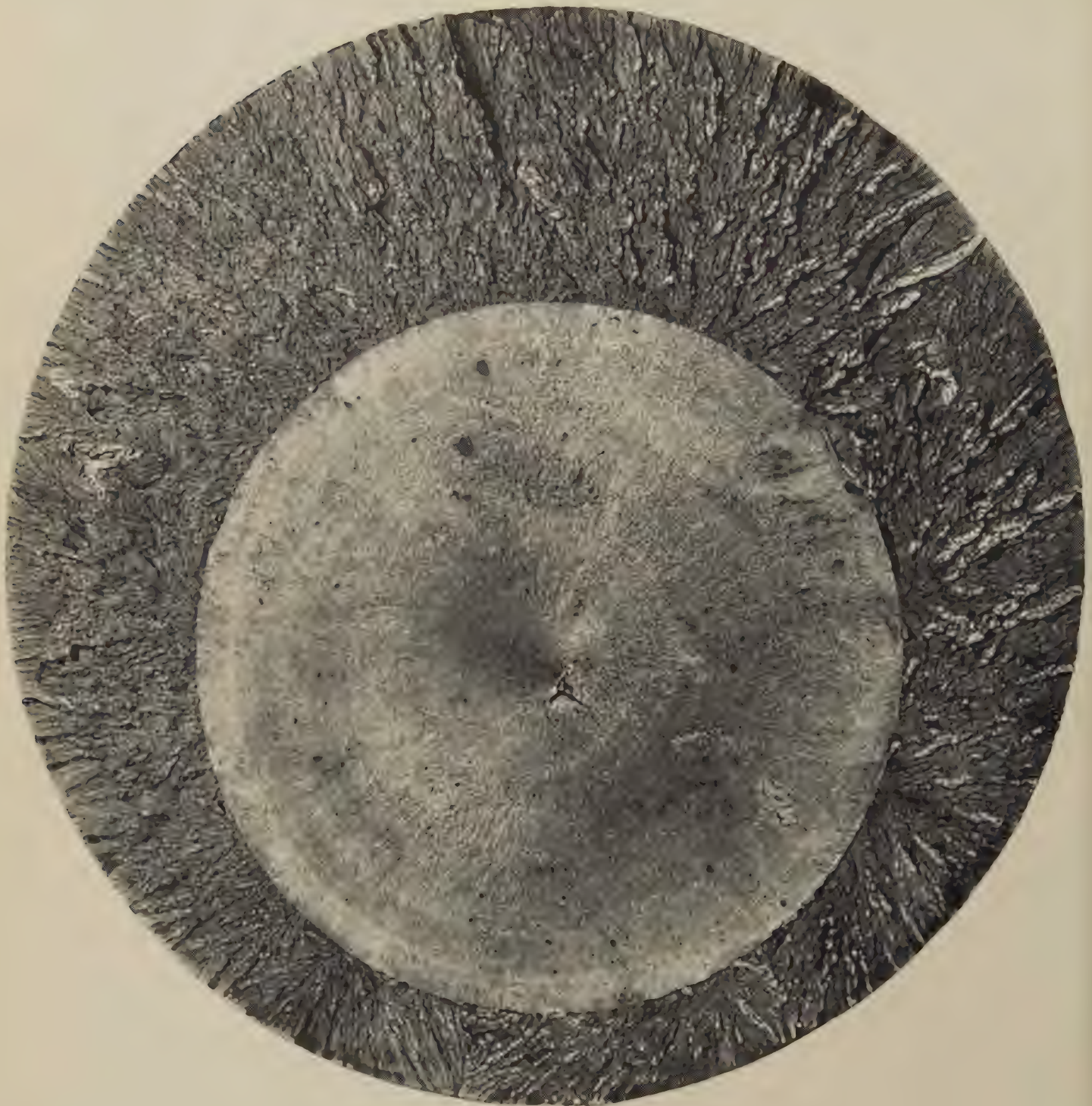
40 μm

Micrograph (as polished; not etched)

250×

4953 Section through a chromium-plated journal typical of those in the crankshafts on these facing pages, showing cracks and considerable porosity, both of which contributed to fracture.

Failure-Analysis Fractographs: Tensile Fatigue Fracture in a Forging-Hammer
Piston Rod of 0.26C-0.70Mn-0.87Ni-1.00Cr Steel



Light fractograph

0.93×

4954 Surface of a fatigue fracture in an 8-in.-diam piston rod of a steam hammer for forging. The rod was fabricated from 0.26% C, 0.70% Mn, 0.87% Ni, 1.00% Cr steel and heat treated to a hardness of Rockwell C 24 at the surface and Rockwell C 17 at the center of the section. This is an example of fracture caused by pure tensile fatigue, in which surface stress concentrations are absent and a crack may start anywhere in the cross section. In this instance, the initial crack formed at a forging flake slightly below center, grew outward symmetrically, and ultimately produced a brittle fracture without warning.



Light fractograph

About $1\frac{1}{4} \times$

4955 Surface of a fracture in an equalizer bar, which supports the front end of a tractor, fabricated from D6B steel and heat treated to a hardness of Rockwell C 45 to 47. The bar was put into service for 200 hr and then returned to the laboratory, where it was flexed in fatigue to fracture at 60,000 cycles. Note the very fine texture of the fatigue-crack zone at the upper left corner. It is concluded that because there are no beach marks beyond that small corner zone, the remainder of the fracture occurred in a catastrophic manner. Shear lips are evident along the top and right edges, and may also be present around the lower left corner. (D6B steel contains 0.45% C, 0.80% Mn, 1.00% Cr, 0.50% Ni, 1.00% Mo, 0.10% V.)

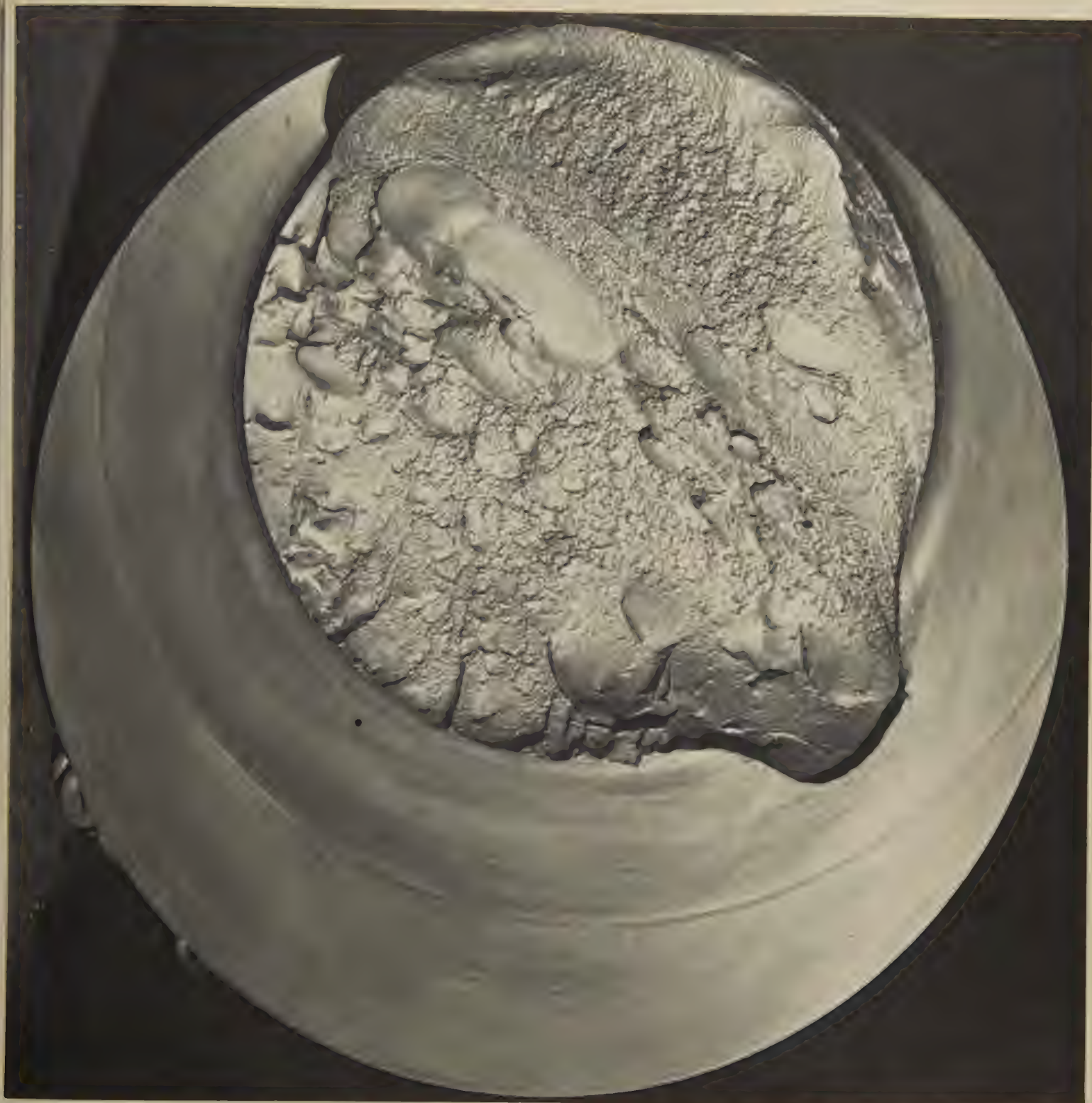
Failure-Analysis Fractographs: 4340 Steel Upsetting-Machine Crankshaft
Fractured by Fatigue



Light fractograph

Actual size

4956 Surface of a fatigue fracture through a journal of a crankshaft for a 6-in. upsetting machine. The crankshaft was forged of 4340 steel and was normalized to a yield strength of 593 MPa (86 ksi), a tensile strength of 807 MPa (117 ksi), 20.5% elongation and a hardness of 232 Bhn. Specimens cut from the crankshaft and reheat treated in exact accordance with prescribed practice had tensile strength of 945 MPa (137 ksi), 18% elongation and a hardness of 277 Bhn. The increased tensile strength and hardness indicate that the original heat treatment of the crankshaft was improper and led to a short fatigue life. See 4957 (facing page) for a view of the mating fracture surface.

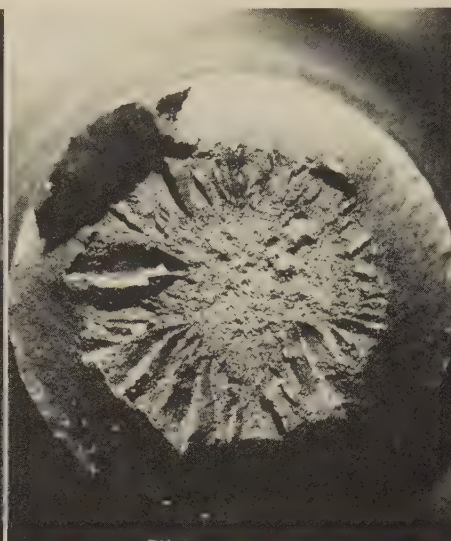
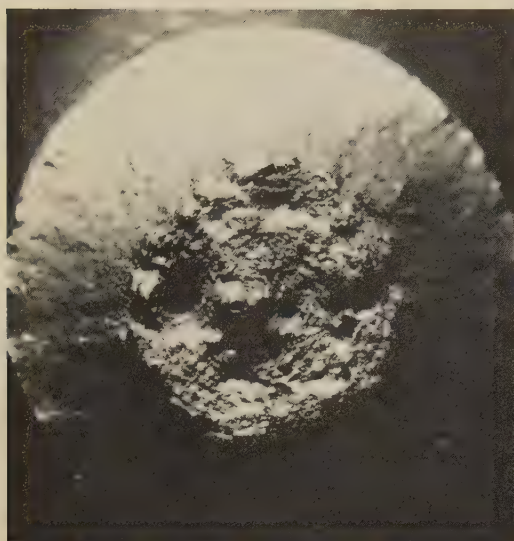


Light fractograph

$\frac{7}{8}\times$

4957 A view of the mating fracture surface to that shown in 4956 (facing page). The illumination here is at a different angle from that in 4956, with the result that in some locations it is difficult to determine which of the features are projections and which are depressions. It appears likely that there were several fatigue-crack nuclei around the journal perimeter; the principal nucleus probably was in the rubbed area at upper right here (upper left in 4956). There is a possibility that the crankshaft contained forging flakes and that some of these flakes were exposed during machining of the journal and initiated the fatigue cracks.

Failure-Analysis Fractographs: Unnotched and Notched Specimens of 4340 Steel Fractured by Tension Overload at Different Test Temperatures



Light fractograph

15×

Light fractograph

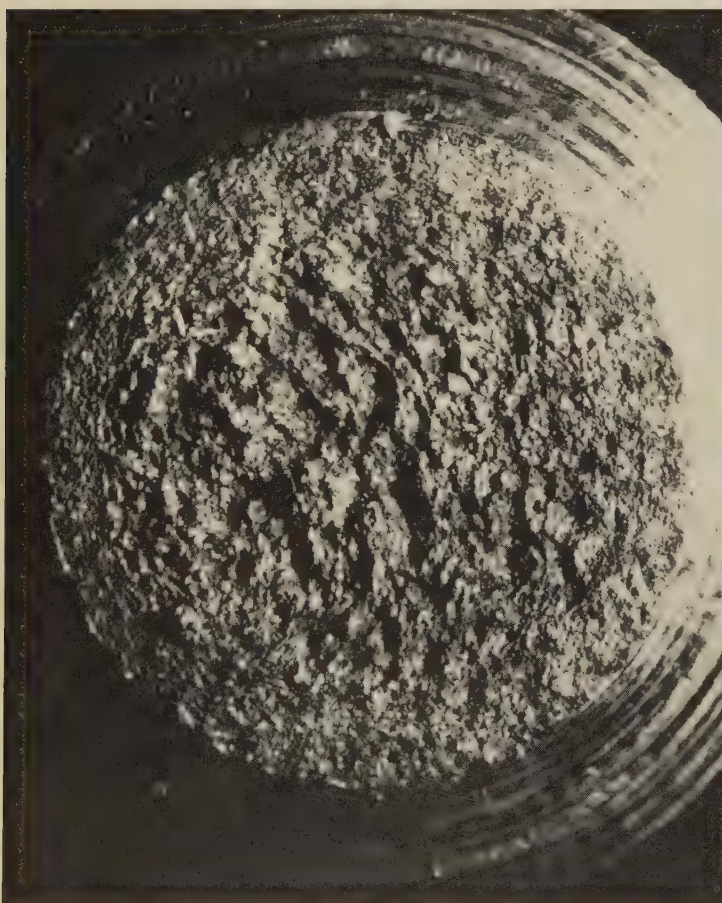
15×

Light fractograph

15×

4958, 4959, 4960

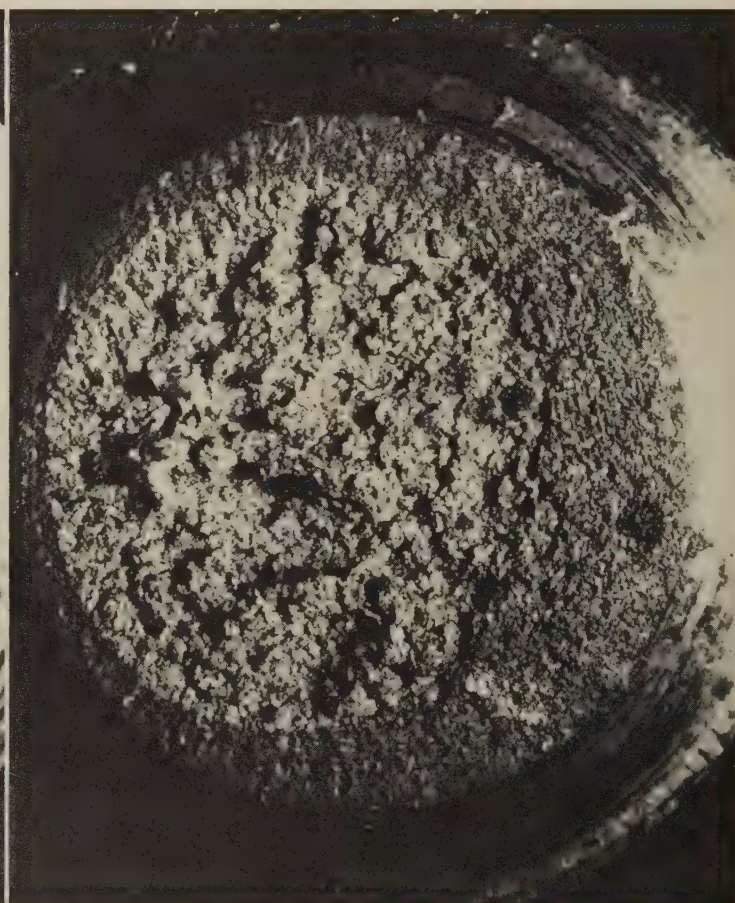
Surfaces of tension-overload fractures produced at different temperatures in three unnotched specimens of 4340 steel, heat treated to a hardness of Rockwell C 35. The specimen in 4958 (left) was tested at 160 C (320 F). A shear lip is visible, surrounding a fibrous region. The specimen in 4959 (center) was tested at 90 C (194 F). At this lower test temperature, a radial fracture zone formed around the fibrous region, which formed first; also, the shear lip here is smaller than that in 4958. The specimen in 4960 (right) was tested at -80 C (-112 F). At this still lower test temperature, no fibrous region formed. Instead, fracture formed a radial zone that extends nearly to the specimen surface and terminates in a narrow shear lip.



Light fractograph

17×

4961 A tension-overload fracture in a notched specimen of 4340 steel, heat treated to a hardness of Rockwell C 27 and tested at -40 C (-40 F), showing a completely fibrous surface. See 4962 and 4963 (right, and on facing page) for fractures in similar specimens tested at different temperatures.

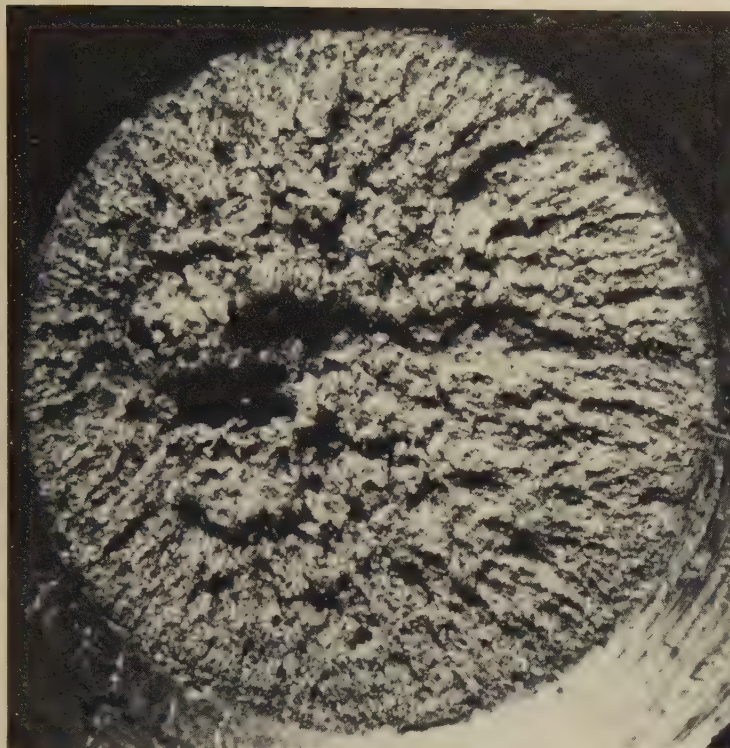


Light fractograph

17×

4962 Surface of a tension-overload fracture in another notched specimen of 4340 steel, the same as in 4961 but tested at -120 C (-184 F). Two distinctly different fracture-surface zones are visible; a fibrous zone, which originated at the notch, surrounds a radial region of final, fast fracture.

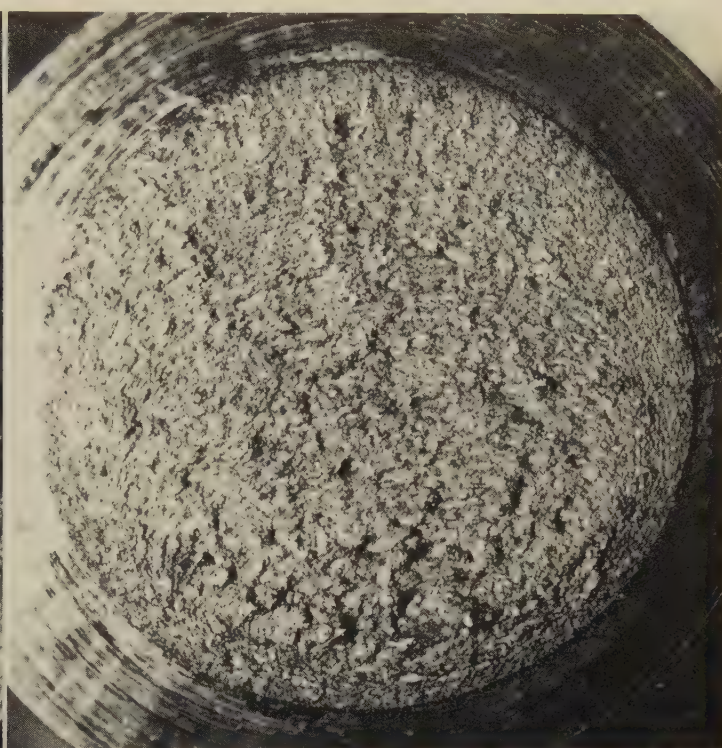
Failure-Analysis Fractographs: Notched Specimens of 4340 Steel Fractured
by Tension Overload at Different Test Temperatures (Continued)



Light fractograph

17×

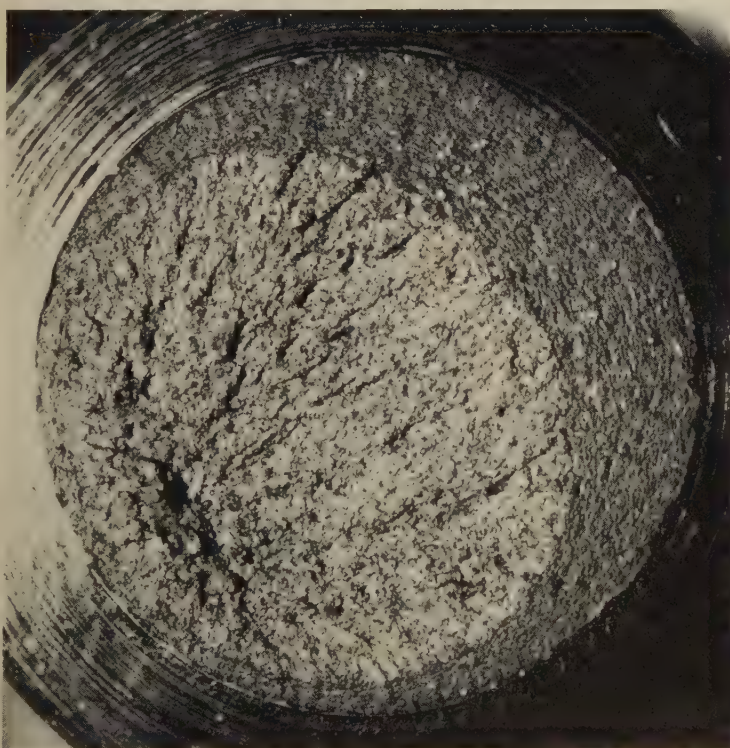
4963 Surface of a tension-overload fracture in a third notched specimen of 4340 steel, the same as those in 4961 and 4962 but tested at -155°C (-247°F). At this low test temperature, a completely radial fracture was produced. The surface shows no fibrous zone, only radial marks.



Light fractograph

17×

4964 A tension-overload fracture in a notched specimen of 4340 steel similar to those in 4961 to 4963 but heat treated to a hardness of Rockwell C 35. Tested at -40°C (-40°F). The surface shows only fibrous marks. See 4965 and 4966, below, for surfaces of fractures in similar specimens at different test temperatures.



Light fractograph

17×

4965 Surface of a tension-overload fracture in a notched specimen of 4340 steel the same as the specimen shown in fractograph 4964, but tested at -80°C (-112°F). A fibrous zone, which originated at the notch, surrounds a radial zone, which is off-center because of nonsymmetrical crack propagation.



Light fractograph

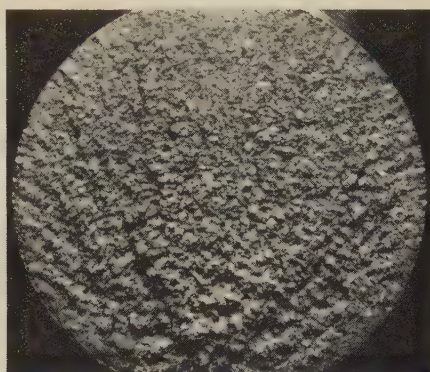
17×

4966 Tension-overload fracture in a notched 4340 steel specimen same as in 4964 and 4965, but tested at -155°C (-247°F). Even at this very low temperature, a small annular zone of fibrous fracture was formed next to the notch. Final, fast fracture produced the radial marks in the central region.

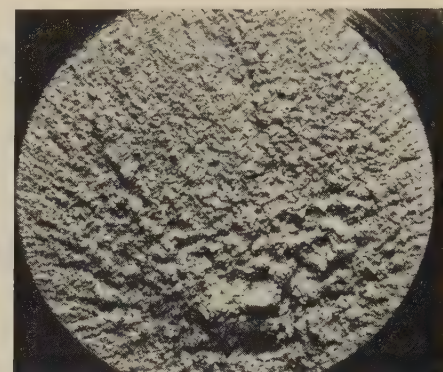
Failure-Analysis Fractographs (Light Fractographs): 4340 Steel Notched Specimens Fractured by Tension Overload, Showing Effects of Heat Treatment and Test Temperature



4967 180 C (356 F) 8×

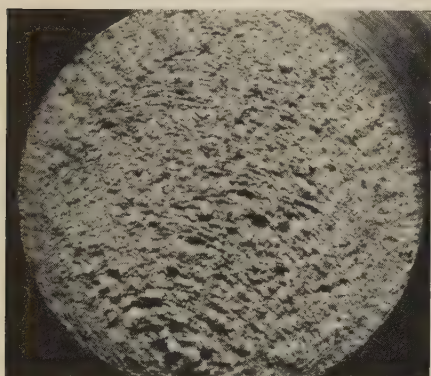


4968 90 C (194 F) 8×



4969 26 C (79 F) 8×

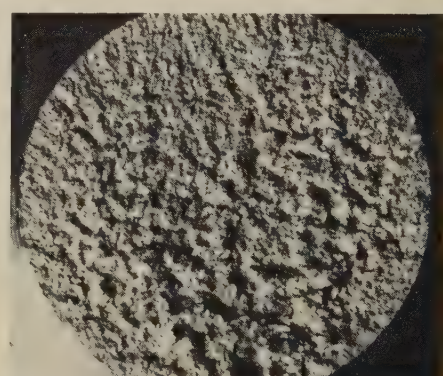
Shown above are fracture surfaces of three notched tensile-test specimens prepared from 4340 steel that had been austenitized, quenched, and tempered at 315 C (600 F) to provide the following room-temperature properties: yield strength of 1558 MPa (226 ksi), unnotched tensile strength of 1758 MPa (255 ksi), and notched tensile strength of 1765 MPa (256 ksi). The specimens were broken by tension overload at the temperatures indicated beneath the fractographs. The fracture surface shown in 4967 is completely fibrous. Lowering the test temperature from 180 C (356 F) to 90 C (194 F) resulted in the formation of a very narrow, obscure fibrous rim enclosing a zone of radial marks (see 4968). Lowering the test temperature further, to 26 C (79 F), produced a fracture made up entirely of radial features (see 4969).



4970 0 C (32 F) 8×

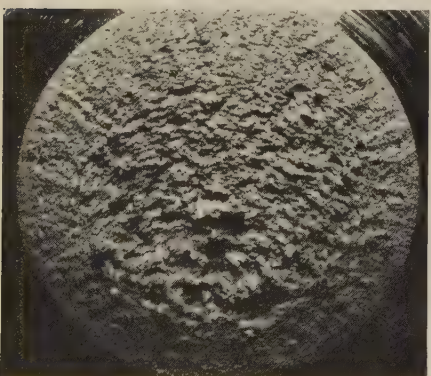


4971 -80 C (-112 F) 8×

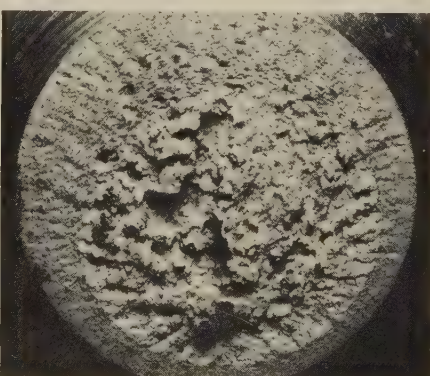


4972 -196 C (-321 F) 8×

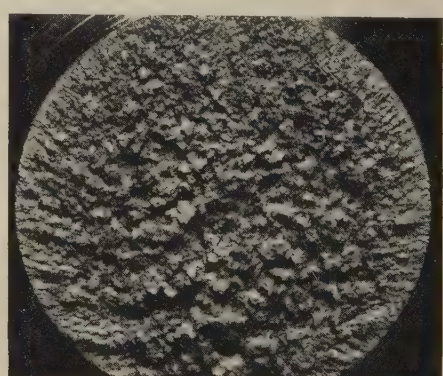
Shown above are fracture surfaces of three notched tensile-test specimens prepared from 4340 steel that had been austenitized, quenched, and tempered at 480 C (896 F) to provide the following room-temperature properties: yield strength of 1234 MPa (179 ksi), unnotched tensile strength of 1310 MPa (190 ksi), and notched tensile strength of 1903 MPa (276 ksi). The specimens were broken by tension overload at the temperatures indicated beneath the fractographs. The specimen shown in 4970 was broken at 0 C (32 F) but, in contrast to the specimen in 4969, which was tempered at 315 C (600 F), yielded a completely fibrous fracture. The fracture shown in 4971, which was produced at -80 C (-112 F), shows a fibrous rim surrounding a zone of radial marks. The fracture shown in 4972, which was produced at -196 C (-321 F), shows only radial marks.



4973 -60 C (-76 F) 8×



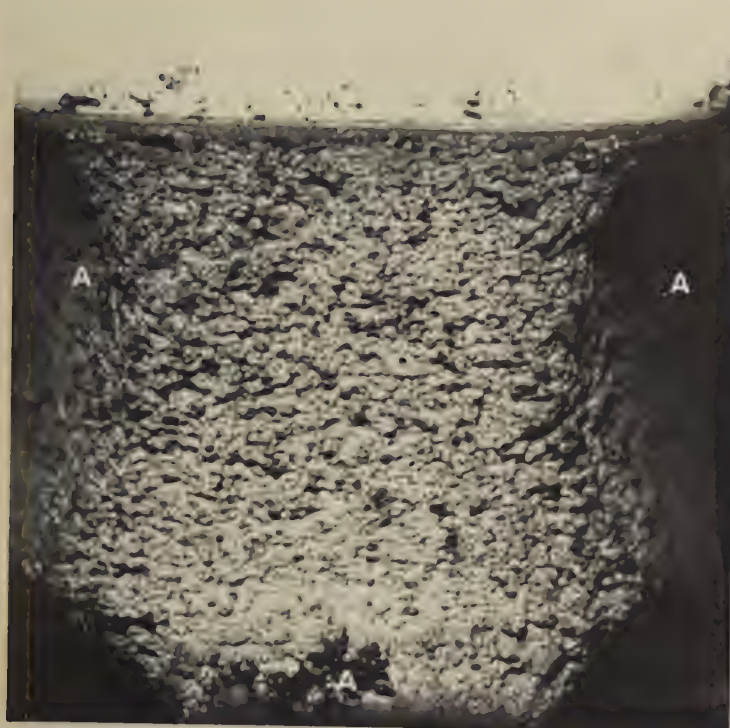
4974 -130 C (-202 F) 8×



4975 -196 C (-321 F) 8×

Fracture surfaces of three notched tensile-test specimens prepared from 4340 steel that had been austenitized, quenched, and tempered at 650 C (1202 F) to provide the following room-temperature properties: yield strength, 917 MPa (133 ksi); unnotched tensile strength, 1014 MPa (147 ksi); notched tensile strength, 1489 MPa (216 ksi). The specimens were broken by tension overload at the temperatures indicated beneath the fractographs. The specimen in 4973 was broken at -60 C (-76 F) but displays a completely fibrous surface. The fracture in 4974 was produced at -130 C (-202 F); note the appreciable increase in the size of the fibrous zone, compared with that in 4971, caused by the lower strength that resulted from tempering at 650 C (1202 F). The specimen in 4975, which was broken at -196 C (-321 F), exhibits a fracture surface containing only radial marks.

Failure-Analysis Fractographs: 4340 Steel Specimens Fractured in Charpy Impact Tests,
Showing Effect of Decreasing Test Temperature



4976

-80 C (-112 F)

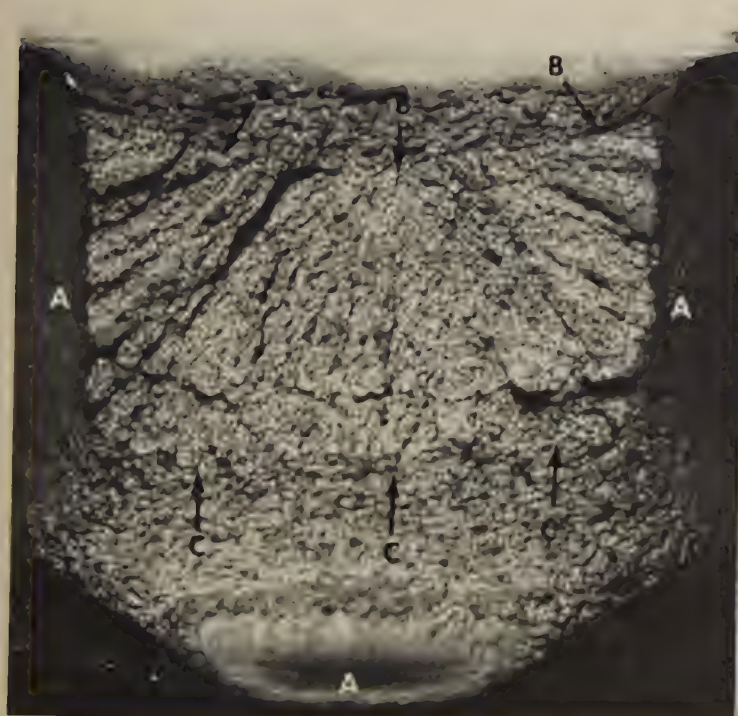
10×



4977

-90 C (-130 F)

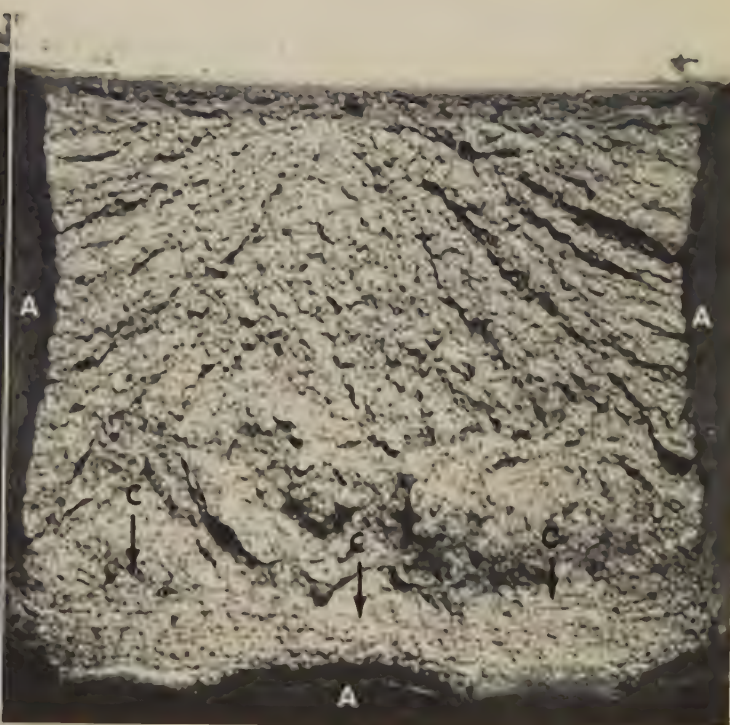
10×



4978

-100 C (-148 F)

10×



4979

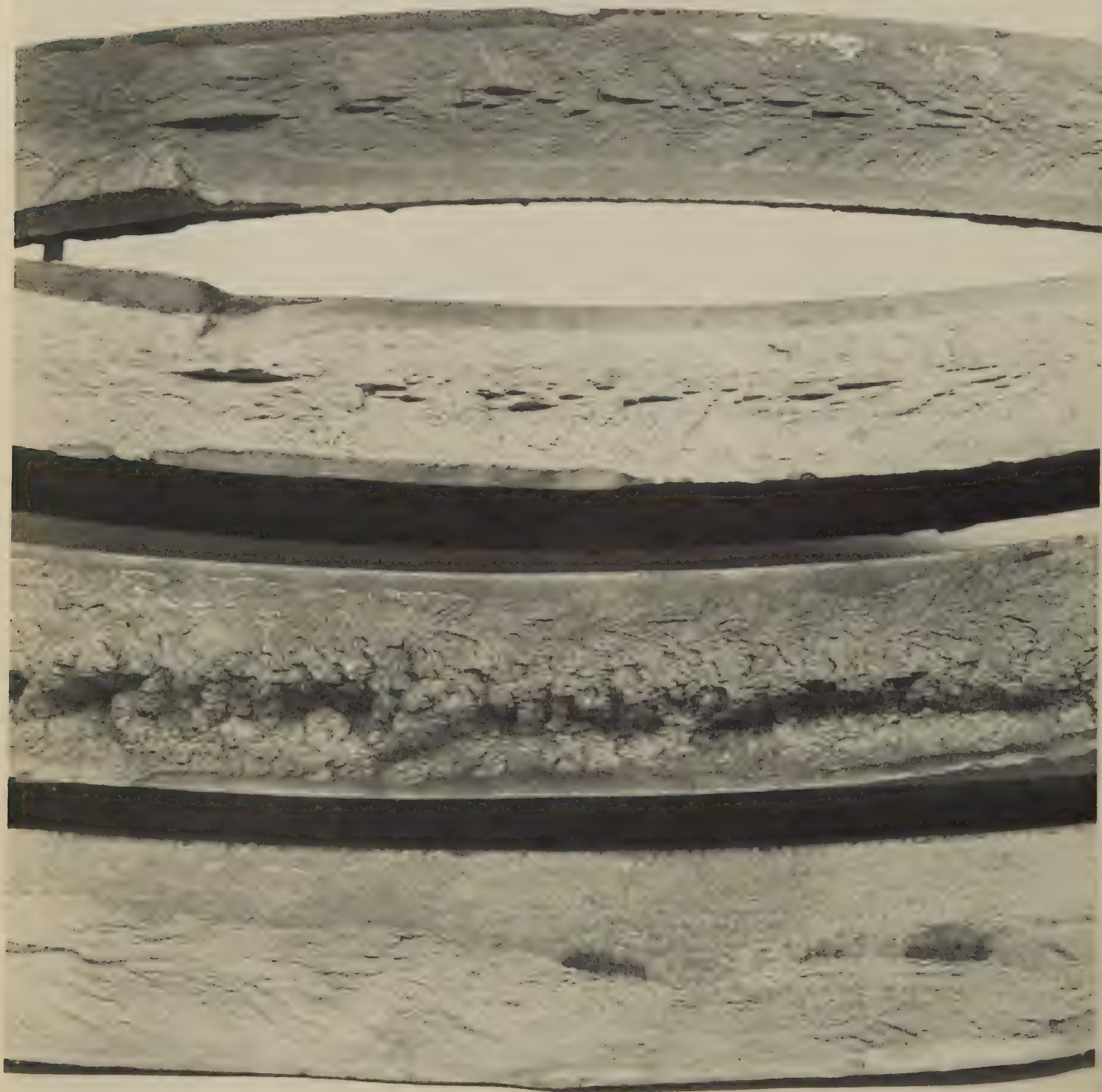
-120 C (-184 F)

10×

The four light fractographs on this page show the surfaces of impact fractures in Charpy specimens of 4340 steel heat treated to a hardness of Rockwell C 27, and depict the changes in surface characteristics as test temperature was decreased. The specimen in fractograph 4976, which was broken at -80 C (-112 F), shows a fibrous fracture surface containing shear lips (at A's). The specimen in fractograph 4977 was broken at -90 C (-130 F). This temperature is close to the ductile-brittle transition temperature, as indicated by the presence of a small area of radial marks (between arrows B and arrows C) in the center of the otherwise fibrous fracture sur-

face. Shear lips are present here also (at A's). The specimen in fractograph 4978 was broken at -100 C (-148 F) and shows an area of radial marks (between arrows B and arrows C) much larger than that in 4977 while retaining fibrous regions above arrows B (near the notch) and below arrows C. The shear lips here (at A's) are comparable to those in 4976 and 4977. The specimen in 4979 was broken at -120 C (-184 F); its fracture surface contains a radial zone larger than that in 4978 but still shows a small area of fibrous fracture below arrows C (opposite the notch). Also, the shear lips here (at A's) are appreciably smaller than those in 4978.

Failure-Analysis Fractographs: High-Strength Low-Alloy Steel Hemispherical Accumulator Head
Fractured During Pressure Testing at Room Temperature

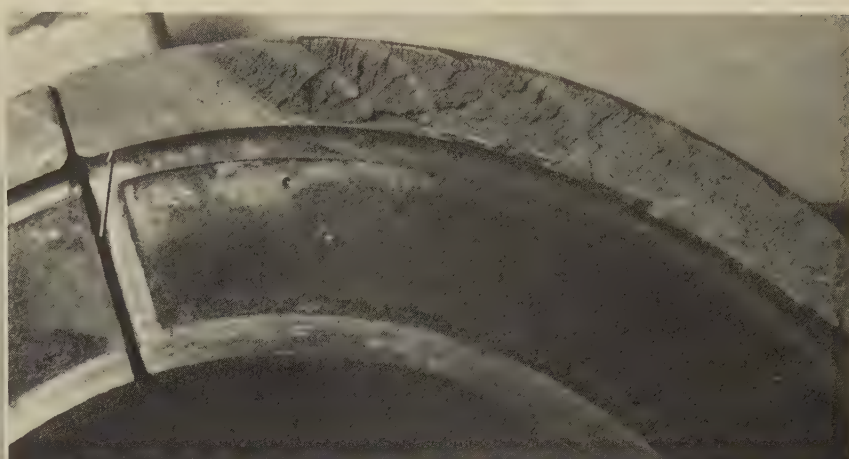


Light fractograph (four surfaces)

4980 Four fracture surfaces of a hemispherical accumulator head of high-strength low-alloy steel (0.15% C, 0.8% Mn, 0.6% Cr, 0.85% Ni) that broke into several pieces during pressure testing at room temperature. Hardness ranged from Rockwell C 28 to Rockwell C 39. Fracture originated at a thin spot in the wall, where banding was present also. At top are mating surfaces of a fracture near the room-temperature cleavage. The fracture surface third from the top is very coarse-grained, whereas the surface at bottom is fine-grained and silky; the difference in appearance between these two surfaces may have resulted from a difference in rate of crack propagation.

Actual size

Failure-Analysis Fractographs: 4340 Steel Aircraft-Propeller Hub Clamp Fractured by Fatigue



Photograph

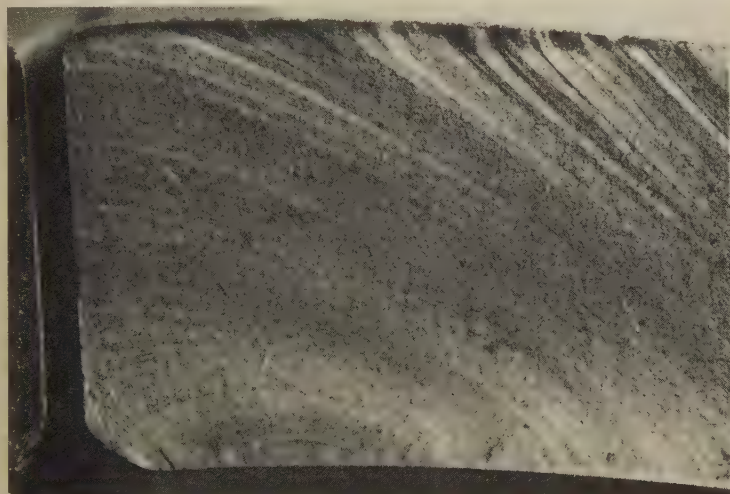
About 0.4×

4981 A view of a broken aircraft-propeller hub clamp of 4340 steel heat treated to a hardness of Rockwell C 40, showing a circumferential fatigue fracture. Fracture began at two origins in a fillet of an inner sidewall. See also 4982 to 4986.

Light fractograph

2×

4982 A portion of the fracture surface of the broken clamp in 4981. One fatigue-crack origin is marked by an arrow; the other is just to the left of the clamp parting line. The crack that began at the origin at the arrow propagated to the right by continuous fatigue cracking for about $\frac{3}{8}$ in. and then continued alternately by rapid tearing and slow fatigue cracking.



Light fractograph

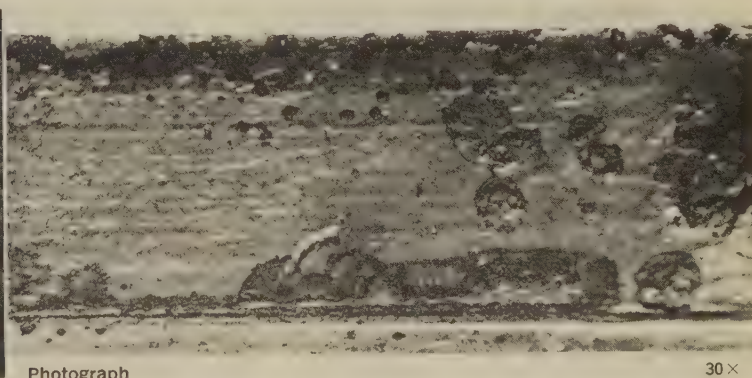
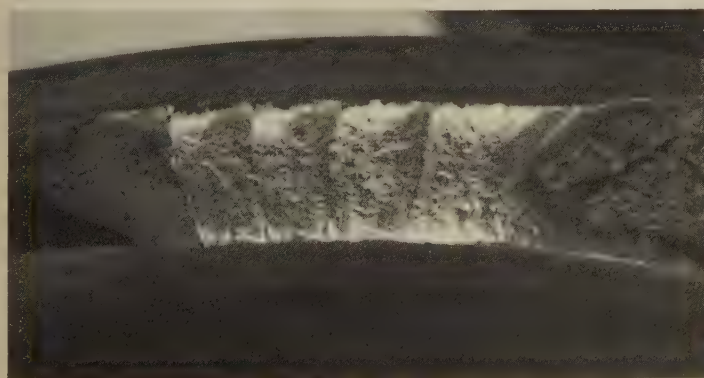
10×

4983 Higher-magnification view of the fatigue-crack origin at arrow in 4982. In the fillet beneath the lower edge of the fracture, several corrosion pits are faintly visible in an area where cadmium plating was required but was found to be missing.

Light fractograph

10×

4984 Area just to the right of the zone of continuous fatigue cracking in 4982, showing intermittent zones of rapid tearing and slow fatigue cracking. Sharply defined beach marks are visible in the fatigue zones.



Light fractograph

4½×

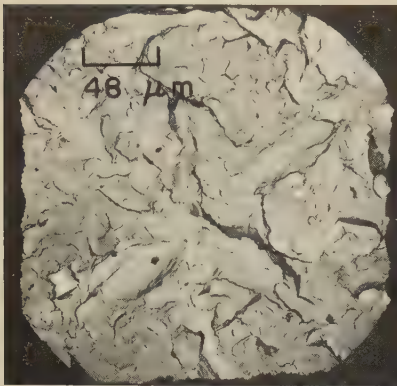
4985 A view of the fracture in 4981, showing an area near the onset of final, fast fracture. About 45% of the fracture surface shown here is composed of fatigue patches interspersed among regions of rapid tearing, which suggests that the hub clamp underwent periodic changes in load amplitude.

Photograph

30×

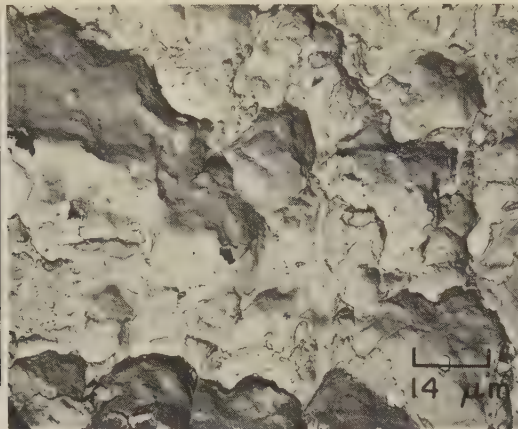
4986 A view of the inside surface of the broken clamp in 4981, clearly displaying the corrosion pits that are dimly visible in 4983 in the fillet below the edge of the fracture, near the fatigue-crack origin. The many small pits along the edge of the fracture surface (shown in profile at top) are believed to have been mainly responsible for the initiation of the fatigue cracks.

Failure-Analysis Fractographs: AMS 6434 (4335 Mod) Steel Impact and Service Fractures;
4340 Steel Stress-Corrosion Fractures, and Impact Fractures After Hydrogen Embrittlement



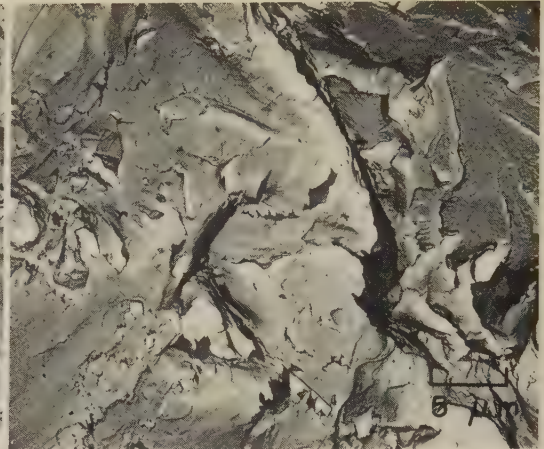
TEM fractograph (p-c replica) 210×

4987 Impact fracture in a specimen of AMS 6434 (4335 mod) steel quenched and then tempered at 204 C (400 F) to a yield strength of about 1550 MPa (225 ksi) and broken at -196 C (-321 F), showing a woody type of cleavage-fracture surface.



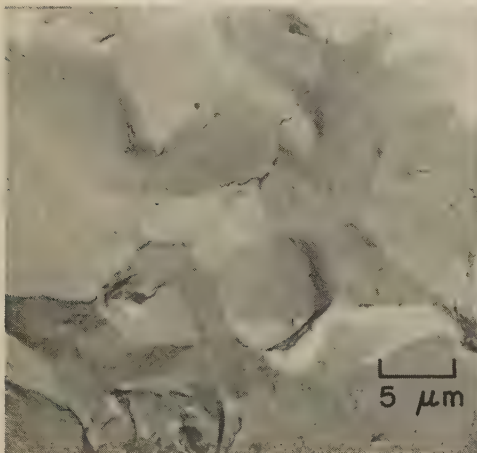
TEM fractograph (p-c replica) 700×

4988 Impact fracture in a specimen of AMS 6434 (4335 mod) steel (same properties as 4987) broken at room temperature, showing fairly large equiaxed dimples, which are characteristic of tension-overload fractures.



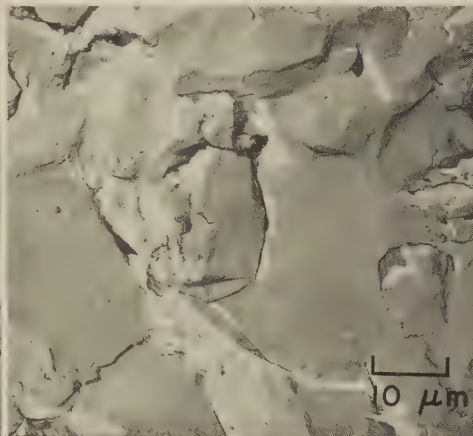
TEM fractograph (p-c replica) 2000×

4989 Fracture surface of an air flask of AMS 6434 (4335 mod) steel that was broken in service. This complicated surface contains several quasicleavage facets.



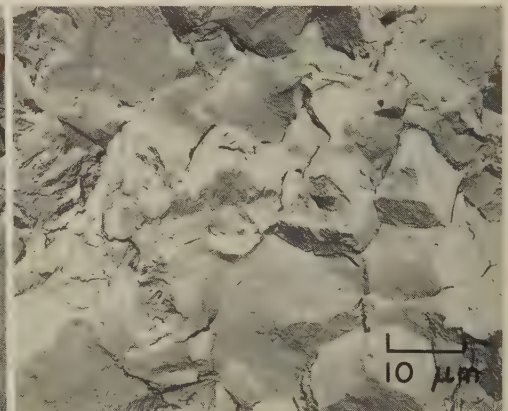
TEM fractograph (p-c replica) 2000×

4990 Stress-corrosion fracture surface of a specimen of 4340 steel that was stressed in distilled water, which resulted in clean intergranular facets plus a small number of fine tear ridges.



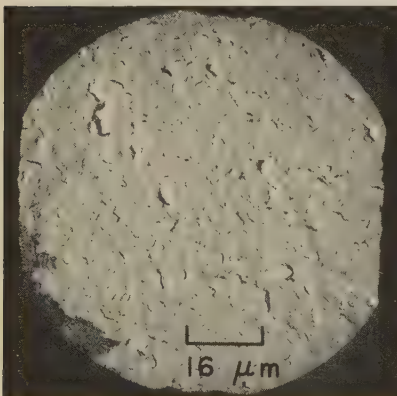
TEM fractograph (p-c replica) 1000×

4991 Surface of a stress-corrosion fracture in a specimen of 4340 steel that was hardened and tempered, then stressed in a 3½% NaCl solution. Intergranular facets, tear ridges and quasicleavage facets are evident. Compare with 4992.



TEM fractograph (p-c replica) 1000×

4992 Impact-fracture surface of a specimen of hardened and tempered 4340 steel embrittled by charging with hydrogen. The crack mechanism here is hydrogen cracking, not stress-corrosion cracking, yet this fracture surface resembles that in 4991. (See also 4993 through 4998.)



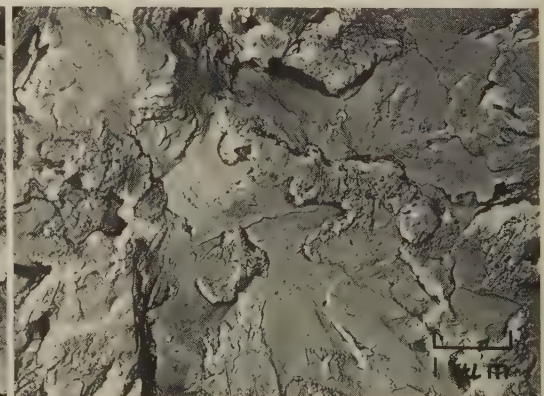
TEM fractograph (p-c replica) 630×

4993 Surface of a second impact fracture in hydrogen-embrittled 4340 steel; an excellent example of a surface composed of transgranular, cleavage facets.



TEM fractograph (p-c replica) 2000×

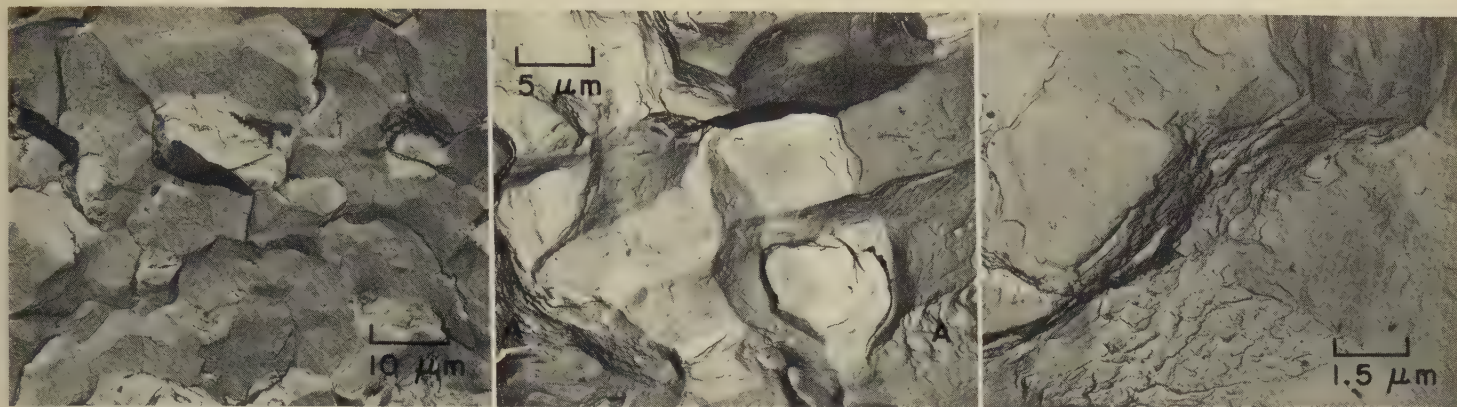
4994 Surface of a third impact fracture in hydrogen-embrittled 4340 steel, showing intergranular facets. Between the intergranular facets, however, are regions of dimples that were produced by microvoid coalescence.



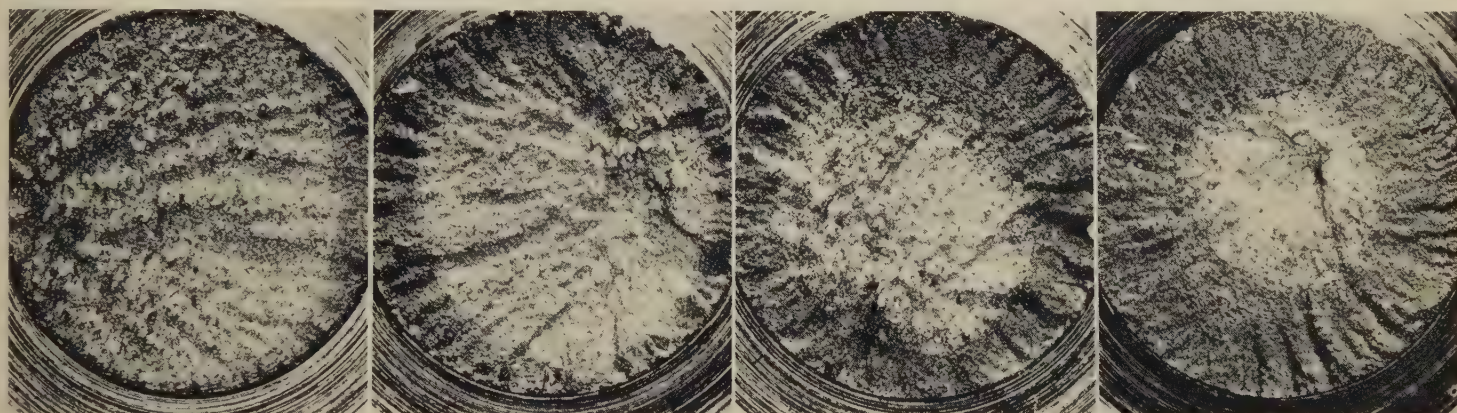
TEM fractograph (p-c replica) 10,000×

4995 Surface of a fourth impact fracture in hydrogen-embrittled 4340 steel, showing the intergranular facets expected of hydrogen cracking plus many areas of transgranular, quasicleavage facets. See also 4996-4998.

Failure-Analysis Fractographs: 4340 Steel, With and Without Hydrogen Embrittlement, Fractured by Impact, Tension (Overload and Sustained), Fatigue; Micrograph of Hydrogen-Embrittled Structure



TEM fractograph (p-c replica) 1000× TEM fractograph (p-c replica) 2000× TEM fractograph (p-c replica) 6500×
4996, 4997, 4998 Fractographs 4996 (left) and 4997 (center) show surfaces of impact fractures in two specimens of hydrogen-embrittled 4340 steel (continuation of a series begun in 4992, on the opposite page). The fracture in 4996 bears a considerable resemblance to those shown in 4991 and 4992, except that fewer quasicleavage facets are visible here. The fracture in 4997 exhibits intergranular facets containing many fine tear ridges; two areas of fine dimples (at A's) are visible also. Fractograph 4998 (right) shows the surface of a fracture in a specimen of hydrogen-embrittled 4340 steel that was broken under sustained load, exhibiting intergranular facets, and dimples that resulted from microvoid coalescence.



Light fractograph About 8× Light fractograph About 8× Light fractograph About 8× Light fractograph About 8×
4999, 5000, 5001, 5002 Surfaces of four tension fractures, which illustrate the effect of decreasing stress on the fracture-surface characteristics of notched specimens of 4340 steel broken at room temperature. Notch radius was 0.001 in. Microstructure of all four specimens was tempered martensite. The specimen at far left (4999) was broken by tension overload (notched tensile strength was 2006 MPa, or 291 ksi) and shows a relatively small fibrous zone at the right edge. The three other specimens were charged with hydrogen and then were subjected to sustained loading. The specimen at left center (5000) broke in 1.65 hr under a stress of 1379 MPa (200 ksi). The specimen at right center (5001) broke after 5.35 hr under a stress of 1034 MPa (150 ksi). The specimen at far right (5002) fractured after 5.5 hr under a stress of 689 MPa (100 ksi). Note that the progressive decrease in fracture stress from 4999 to 5002 was related to a progressive increase in the size of the fibrous zone.



TEM micrograph (nital) 2000× TEM fractograph (p-c replica) 4275× TEM fractograph (p-c replica) 3000×
5003 A plastic-carbon TEM replica of a polished and etched section through a specimen of 4340 steel containing internal grain-boundary cracks caused by hydrogen embrittlement.
5004 Tension-overload fracture in 4340 steel notched specimen. Fracture occurred both by microvoid coalescence (see fine dimples at upper left, large dimples at lower right) and by quasicleavage through pearlite colonies (see facet at center). Arrows show directions of crack propagation.
5005 Fatigue fracture in 4340 steel that was tested in humid air, exhibiting an intergranular surface similar to one caused by stress corrosion and showing no conventional characteristics of fatigue.

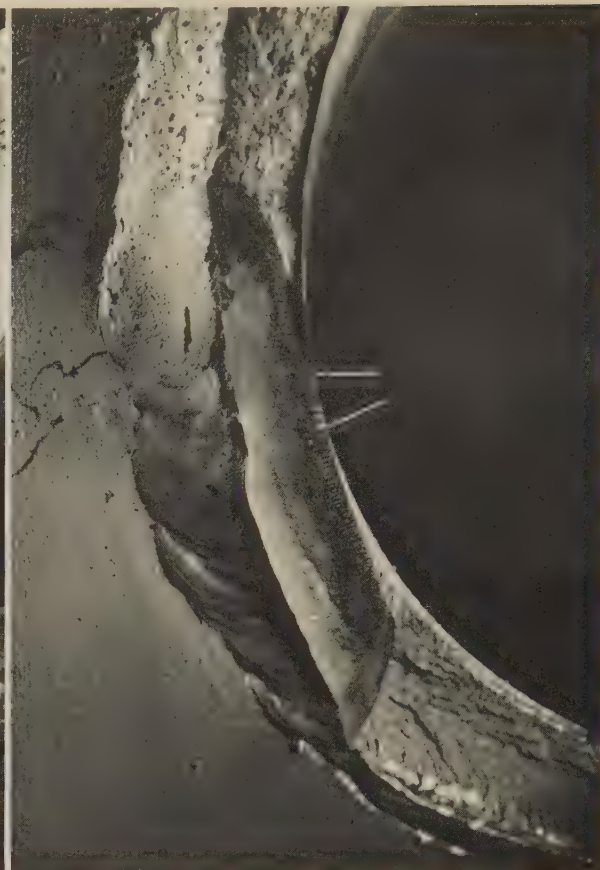
Failure-Analysis Fractographs: 4340 Steel Aircraft Propeller Hub Fractured by Fatigue Originating at a Weld Overlap



Photograph

1/2×

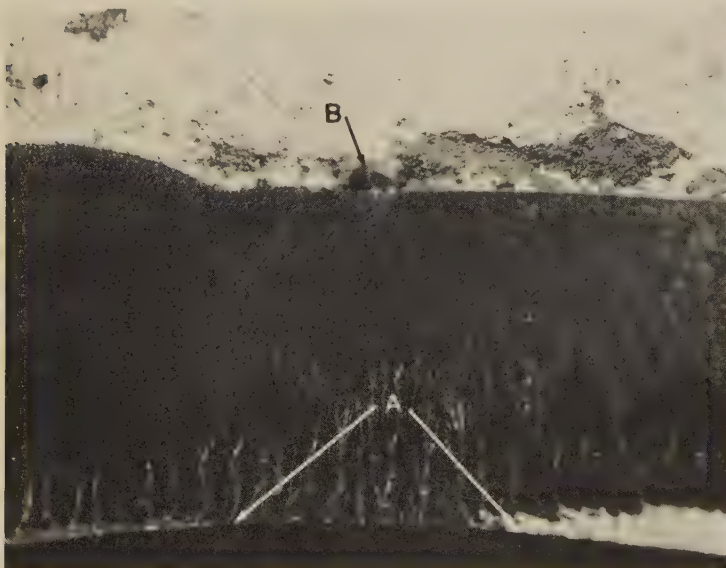
5006 Mating segments of an aircraft propeller hub of quenched and tempered 4340 steel that broke by fatigue, showing both surfaces of the fracture, which occurred at the welded joint between the barrel of the hub and the fitting for attachment of the hub to the hydraulic cylinder. Arrows indicate on each fracture surface the location of the fatigue-crack origin—at the toe of the weld bead, where a slight weld overlap had formed. See also 5007 to 5009.



Light fractograph

2×

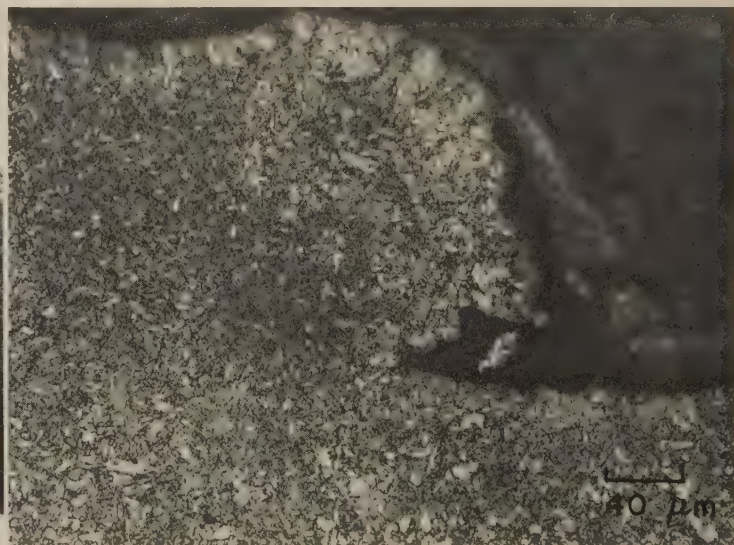
5007 Fracture surface of the barrel portion of the broken hub in 5006, showing the fatigue-crack origin. The fatigue crack was about 1 3/4 in. long but had penetrated the hub wall completely for only about 1/8 in. (arrows). Note shear lip at inside of hub wall on either side of the fatigue crack.



Light fractograph

8×

5008 A higher-magnification view of the fatigue-crack origin in fractograph 5007, showing clearly the beginnings of the shear lips (arrows at A) on each side of the zone of complete penetration of the fatigue crack. At the upper edge of the fatigue crack, a small piece of protruding weld metal is visible (arrow B) at the crack nucleus.

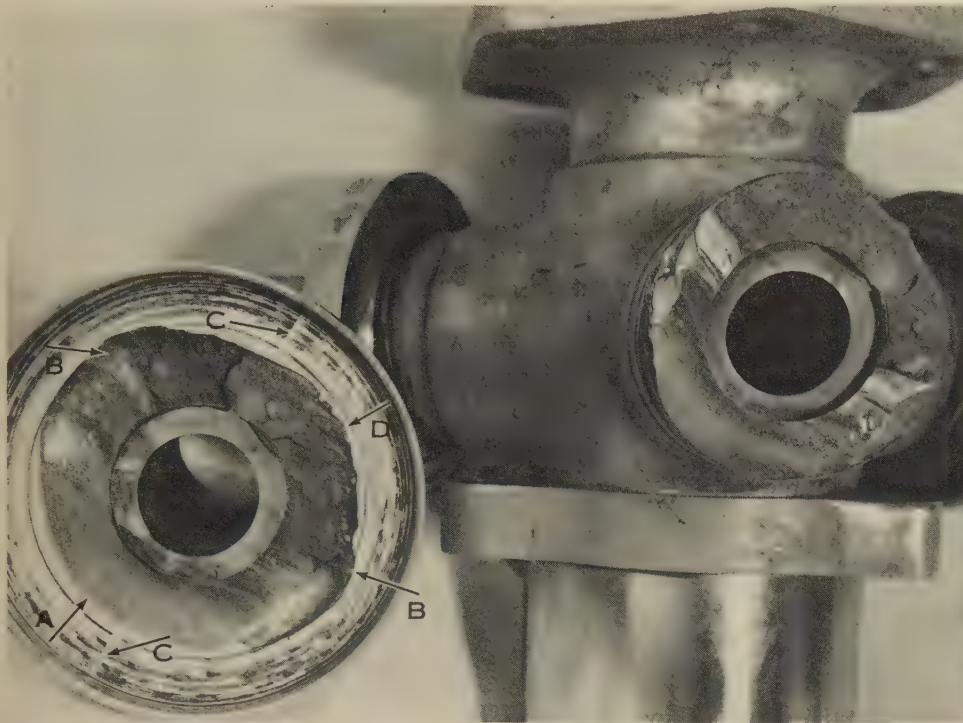


Micrograph (1% nital)

250×

5009 Polished and etched section through the weld and base metal of the fitting portion of the broken hub in 5006, at a point near (but not at) the fracture surface, showing a weld overlap, which forms a crevice. It was at a similar crevice that the stress caused by the heat of welding opened a crack in the hub wall. Otherwise, the weld was sound and well bonded. Hardness: Rockwell C 23 to 43 in the weld; Rockwell C 35 to 44 in the base metal.

Failure-Analysis Fractographs: Forged 4340 Steel Aircraft Propeller-Hub Spider
Fractured by Fatigue; 4340 Steel Worm-Gear Shaft Fractured by Fatigue



Light fractograph

0.6×

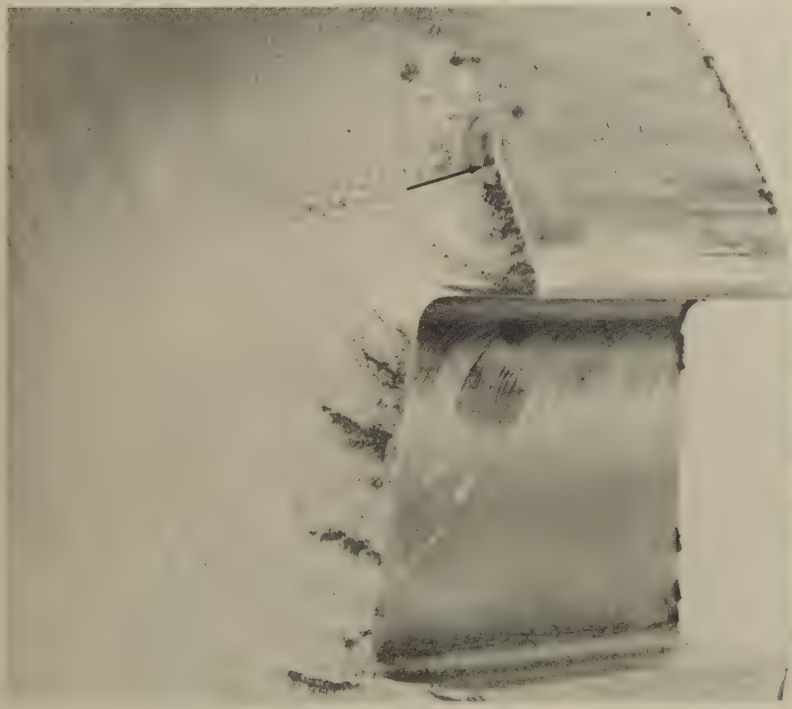
5010 Mating surfaces of a fatigue fracture in a blade arm of a forged aircraft propeller-hub spider of 4340 steel and through the central pilot tube of the arm. The fatigue crack originated in the fillet between the bearing-retention flange and the blade arm. Hardness of the forging was Rockwell C 35. The origin is at arrow A (lower left), at an inclusion. The fatigue crack penetrated as far as the locations indicated by arrows B before final, fast fracture occurred. Alignment of the bearing-race parting line (arrows C) was not as specified. See fractograph 5011, at right, for a view at arrow D.



Light fractograph

10×

5011 A view of an area at arrow D in 5010, in the region of final, fast fracture. Fatigue patches are interspersed among areas of rapid crack advance, indicating that final fracture occurred in stages.



Light fractograph

About actual size

5012 Surface of a fatigue fracture in the worm-gear shaft of a 400-ton open-hearth stripper crane, which broke after 18 months of service. The material was 4340 steel heat treated to a hardness of 280 Bhn. The fatigue-crack origin is visible at the arrow at upper right, above the keyway, in an area that had been grooved and abraded when the worm gear was pressed onto the shaft. See also 5013.



Micrograph (nital)

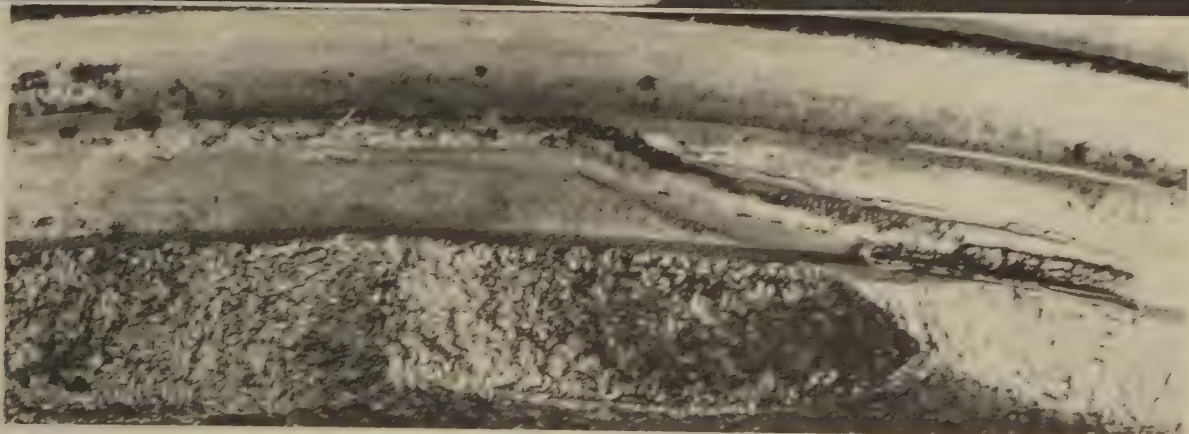
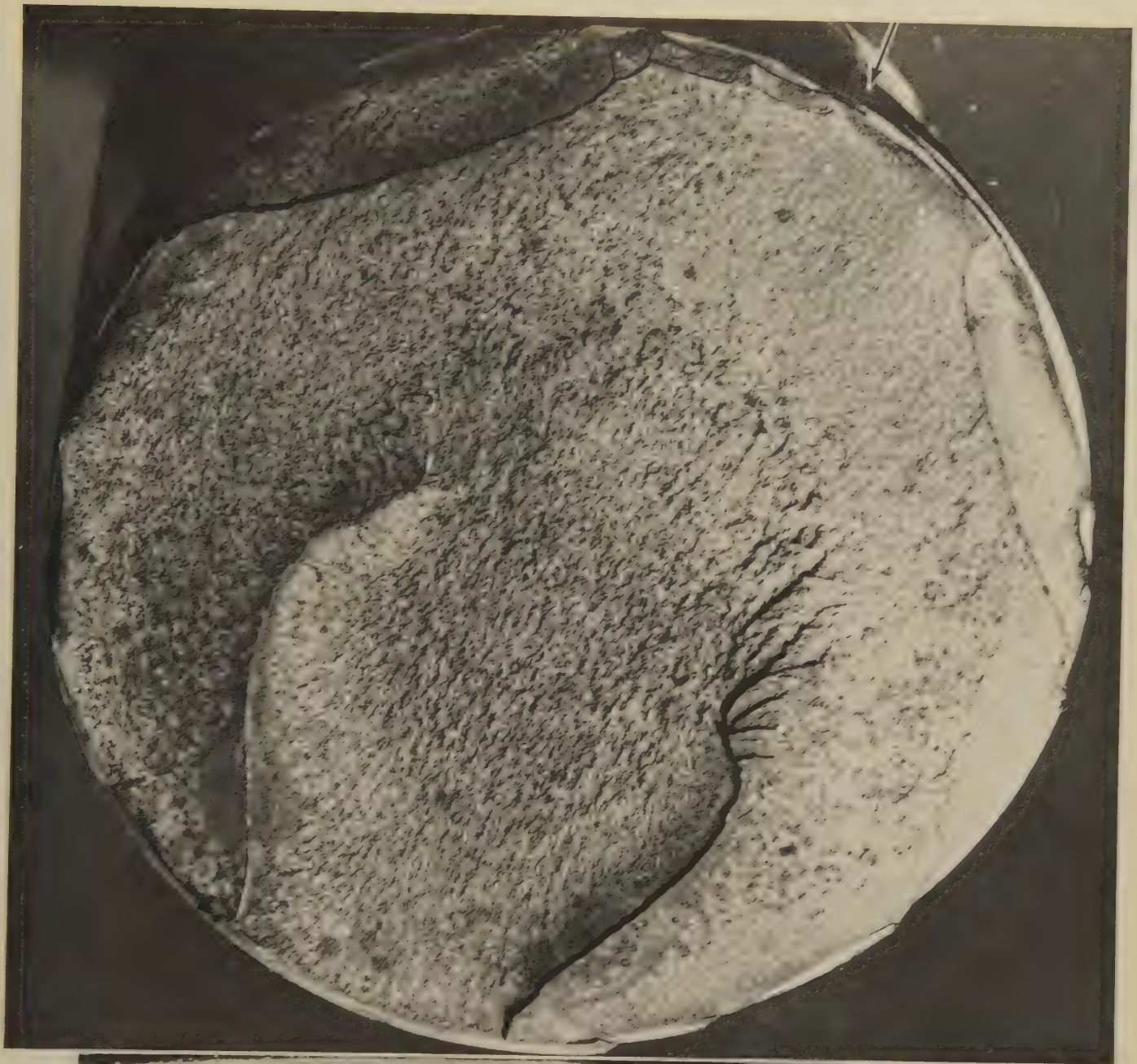
100×

5013 Polished and etched section taken longitudinally through the broken worm-gear shaft in 5012, adjacent to the fracture surface, showing transverse cracks that originated at the heavily cold worked surface of the shaft (at top). A similar crack initiated the fatigue fracture.



Two light fractographs

5014, 5015 At top (5014) is a view of a service fracture in a 5-in.-diam suspension strut of a missile silo. Actual size (5014); $1\frac{1}{2} \times$ (5015) treated to tensile strength of 1612.7 MPa (233.9 ksi), 11% elongation, and Charpy V-notch impact strength of 17.3 joules (12.8 ft-lb). The fracture origin (arrow) is at a thread root, two full threads deep into the coupling. At bottom (5015) is a view of the origin in the mating fracture surface (shown in 5016, on facing page). Note that two wedge-shaped pieces had been broken from the strut perimeter at symmetrical locations on either side of the origin (arrows A); one remained in the coupling and is visible in 5014.

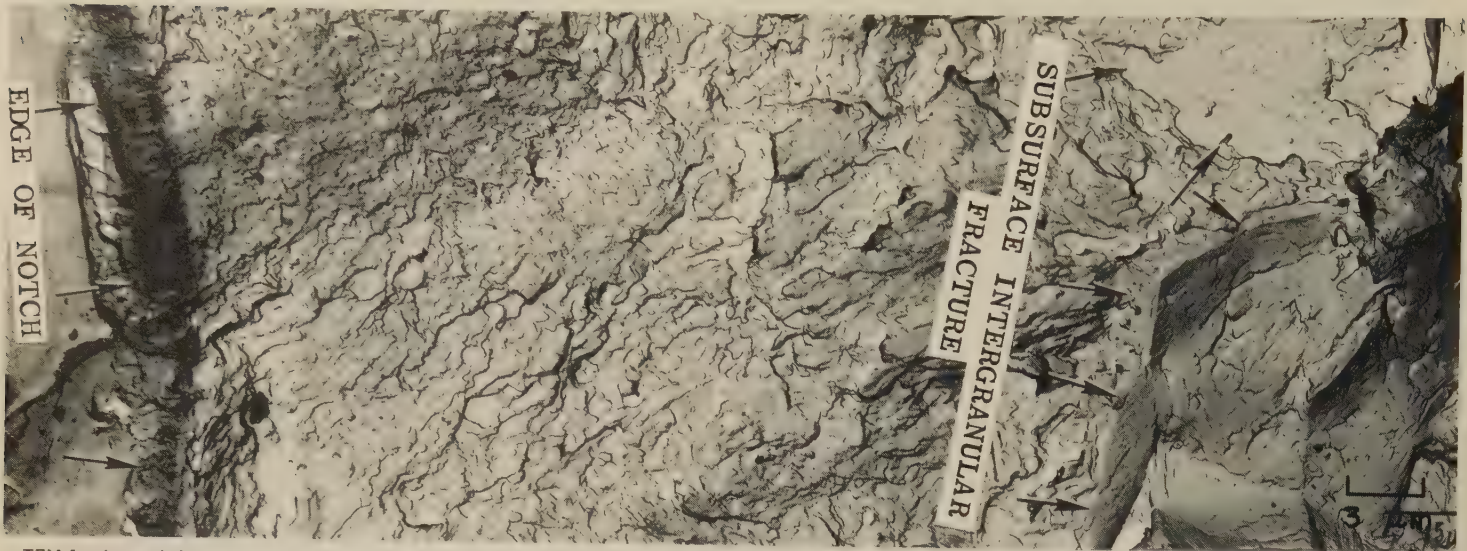


Two light fractographs

5016, 5017 At top (5016) is the mating fracture surface of the strut in 5014 (facing page). The fracture (origin at arrow) penetrated the strut at an angle, starting at the second thread within the coupling and emerging six threads lower on the opposite side. In both fracture surfaces, in the area opposite the origin, is a crudely circular crater with shear-lip borders. At bottom (5017) is a view of the threads near the origin. Note that the thread behind the fracture surface is partly stripped and there are corrosion pits on the threads. Fracture was ascribed to thread defects, corrosion, and excessive strength with low toughness.

14x (5016) 7x (5017)

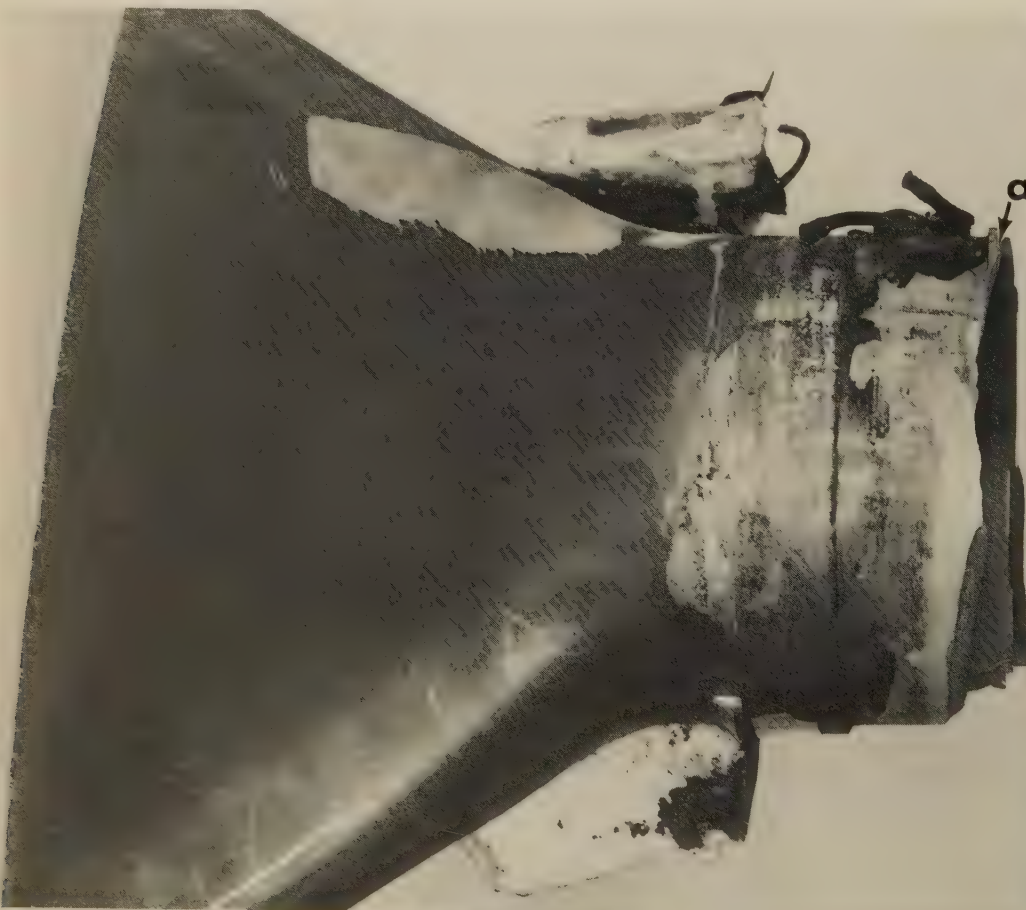
Failure-Analysis Fractographs: 300M Steel Notched Specimen Fractured by Hydrogen Embrittlement; 4350 Steel Aircraft Propeller Blade Fractured by Fatigue



TEM fractograph (p-c replica)

5018 Surface of an intergranular fracture in a hydrogen-embrittled notched specimen of 300M steel. The specimen was hydrogen embrittled during cadmium plating in a cyanide bath after being heat treated to a tensile strength in the range of 1862 to 2068 MPa (270 to 300 ksi); fracture occurred during testing at a sustained stress of 858 MPa (124.5 ksi). It has been observed in hydrogen-embrittled steels that when a sharp notch is present, nucleation of intergranular fracture occurs close to the notch, and when an extremely sharp notch (such as a heat-treat crack) is present, intergranular fracture occurs as a continuous extension of that notch. Here, where the notch was relatively blunt (0.005-in. radius), the fracture had a subsurface origin.

3300×



Photograph

5019 A portion of an aircraft propeller blade of 4350 steel that fractured in fatigue after about 1250 hr of service. The fracture occurred in the root section of the blade; the location of the origin is indicated by arrow "a", in the fillet at the inboard side of the cuff ring. The fracture was initiated by a crack that had been oxidized by exposure to air while the steel was at high temperature (as, for example, in forging or in heat treatment without atmosphere control). See also 5020 through 5024 (at right, and on the opposite page).

1/2×



Light fractograph

5×

5020 View of the fatigue-crack origin at arrow "a" in 5019, visible here at the right edge of the dark, oxide-covered granular crack indicated by arrows marked "c".

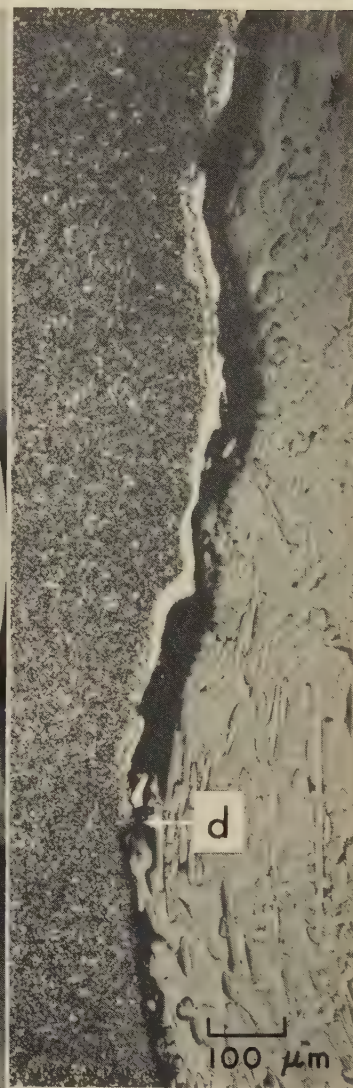
Failure-Analysis Fractographs: 4350 Steel Aircraft Propeller Blade
Fractured by Fatigue (Continued)



Light fractograph

Actual size

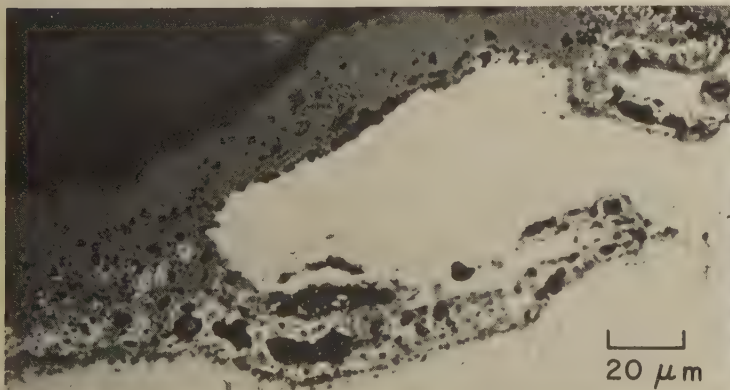
5021 View of the surface of the propeller-blade fatigue fracture in 5019 (facing page). The dark, oxidized surface of the crack that initiated the fatigue fracture is at "a" (top right). The fatigue crack penetrated the blade wall at "a" and then progressed in both directions along the wall to the points marked "b" before final, fast fracture took place. The extremely fine beach marks visible here and in 5020 are typical of very high-cycle fatigue.



Micrograph (1% nital)

100×

5022 Polished and etched section through fracture origin in 5019, showing oxide layer (light) on initial crack above "d", fatigue crack below "d", blade metal at left.



Micrograph (as polished; not etched)

500×

5023 A polished but unetched section through the fracture-initiating crack in 5019, showing an oxide layer, which penetrated the blade metal (light gray areas) at a few locations. Dark surface at top left is the specimen-mounting material.

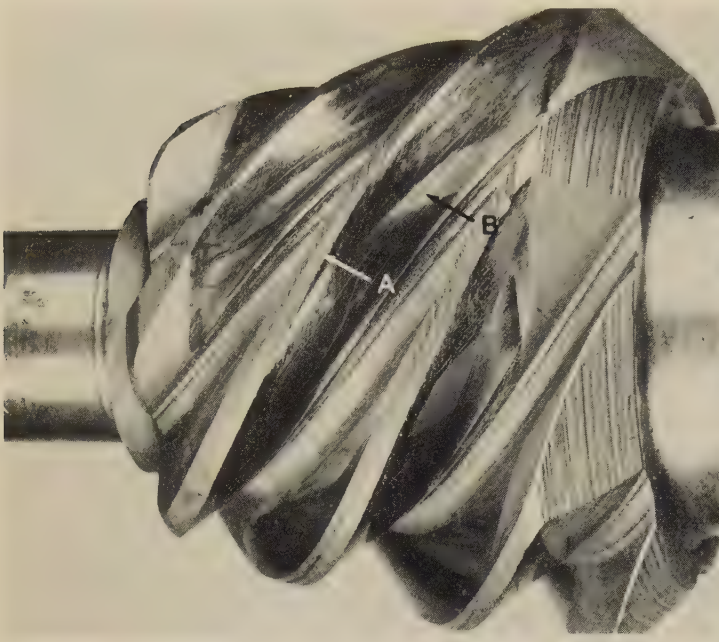


Micrograph (1% nital)

100×

5024 A polished and etched section through the fracture-initiating crack in 5019, showing the microstructure of the blade metal. Note the shallow zone of decarburization below the oxide layer; both the decarburization and the oxide were caused by high-temperature exposure to air.

Failure-Analysis Fractographs: Fatigue Fractures in Carburized 4817 Steel Spiral Gears, Carburized 4817 Steel Shaft, and Case-Hardened 4820H Steel Spiral Bevel Pinion Gear



Photograph
5025 View of a carburized spiral gear of 4817 steel, showing fine subcase fatigue cracks in the gear-tooth tips (such as at arrow A) and flanks (such as at arrow B); these cracks are evidence of the first stages of spalling fatigue, which originated near the case-core interface because the load-carrying capacity of the gear was exceeded. Compare with photograph 5026 (at right).



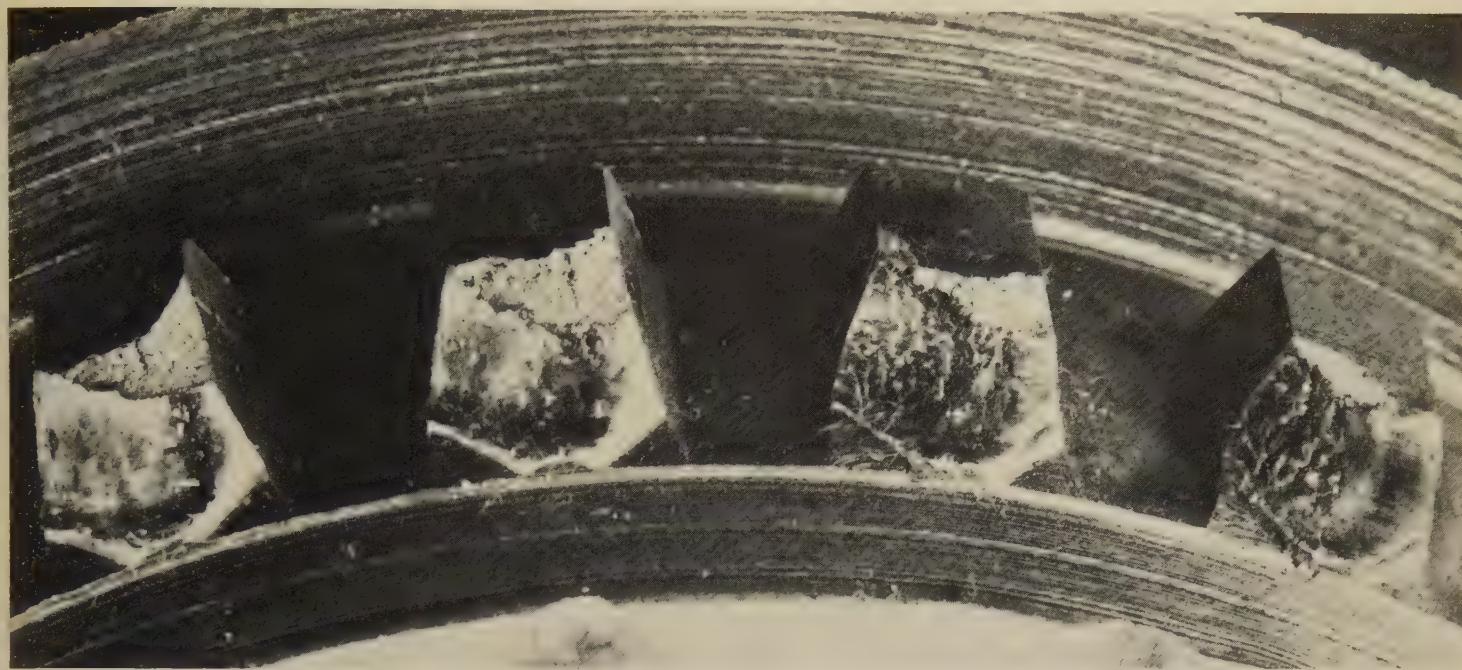
Photograph
5026 A companion gear to that in 5025, also of 4817 steel and carburized, showing subcase fatigue fractures initiated by fine cracks similar to those in 5025. Note that large fragments have spalled away from the teeth. Fatigue beach marks can be seen in these complex fracture surfaces, especially at upper right.



Light fractograph
5027 Surface of a fatigue fracture that began at six fillet areas around the periphery of a shaft, near the runouts of spiral grooves. The material is 4817 steel; the shaft was carburized and heat treated to a surface hardness of Rockwell C 60. The fatigue cracks penetrated equally, indicating that stress concentrations at the six fillet areas were essentially equal.



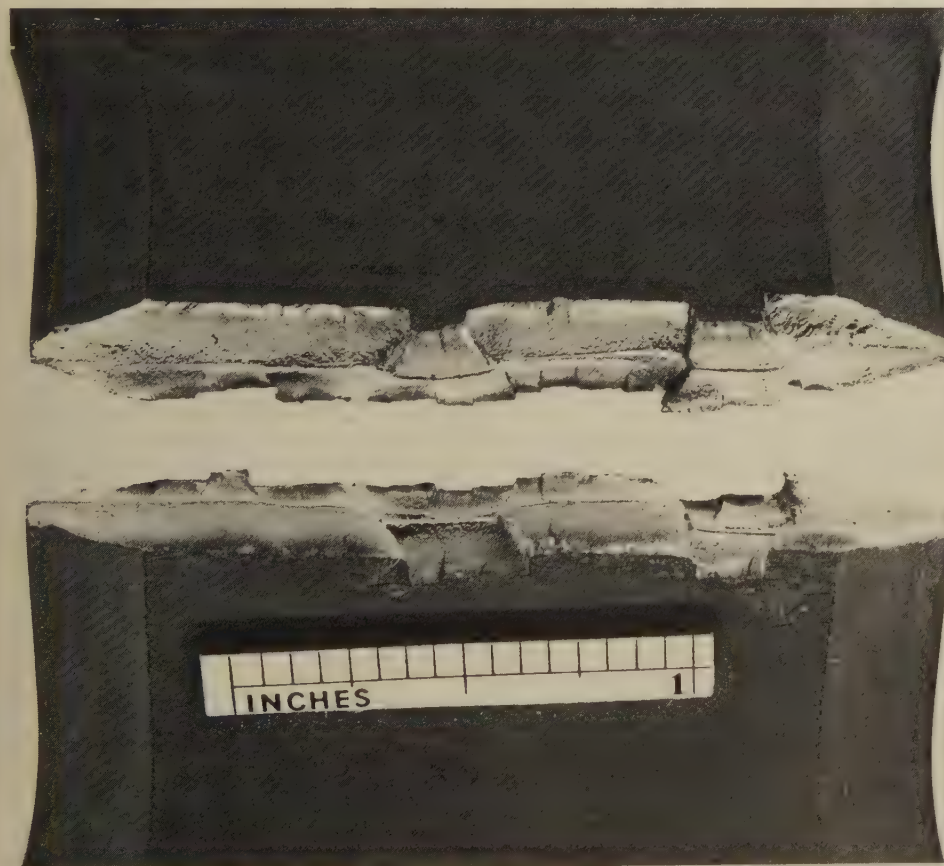
Light fractograph
5028 Fatigue fractures in a spiral bevel pinion gear of 4820H steel, case hardened to a depth of 0.045 to 0.080 in. Case hardness, Rockwell C 56; core hardness, Rockwell C 30. Fatigue cracks began in tooth roots (which were not shot peened), often forming on either side of a tooth (arrows) and meeting in the middle of the tooth. A deeper case, and shot peening of the entire gear, were recommended.



Light fractograph

4×

5029 Fractures in teeth of a carburized gear of 50B20 steel, heat treated to a surface hardness of Rockwell C 60, and subjected to 10,000 impact blows, which chipped and battered the corners of the teeth as shown here. Repeated blows subsequent to fracturing have obscured many of the fracture-surface characteristics in the two teeth at right. In the two teeth at left, large fragments were removed late in the test, exposing fracture surfaces that were generally untouched by subsequent battering.



Light fractograph

About 2.4×

5030 Oblique view of the mating surfaces of a fatigue fracture produced in reversed bending in a 1/4-in.-thick specimen of high-strength low-alloy steel plate with a yield strength of about 345 MPa (about 50 ksi). Multiple fatigue cracks originated at both surfaces of the specimen. Note the centerline neutral axis.

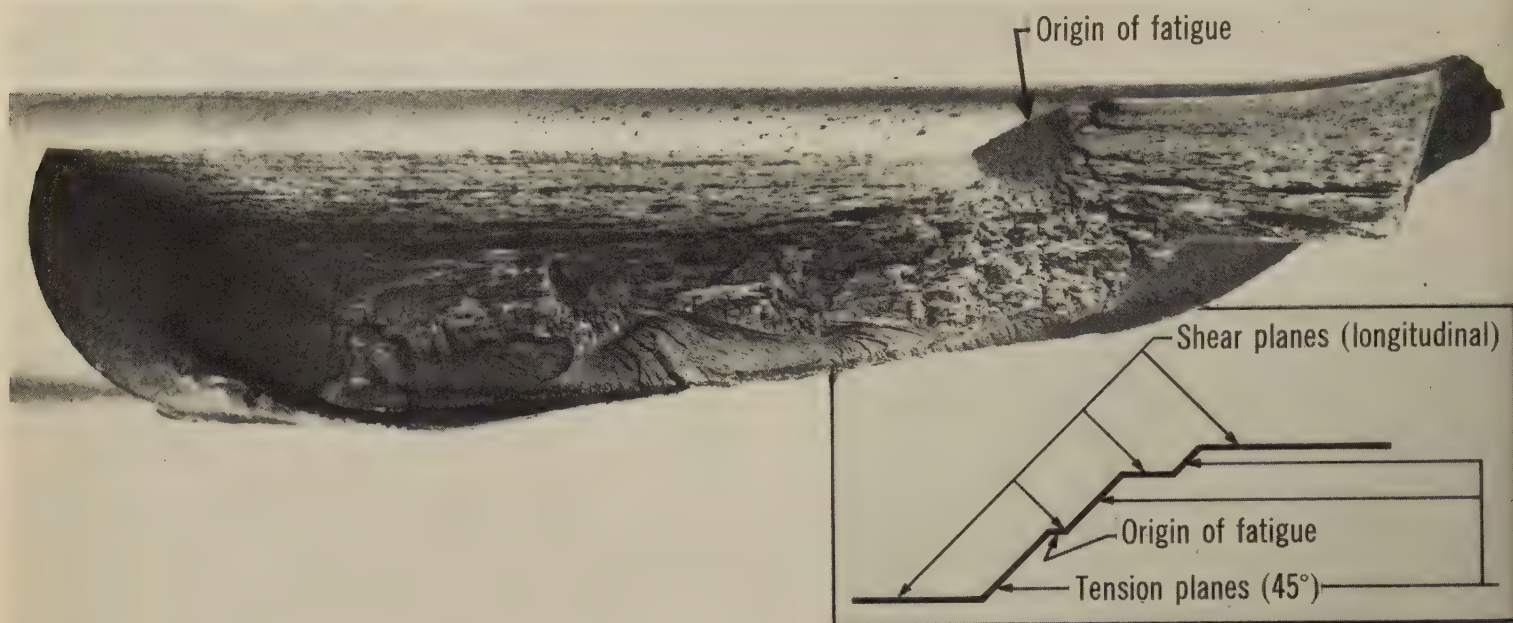


Light fractograph

2 1/4×

5031 Case-hardened pin of 5046 steel with a hardness of Rockwell C 61 in the case, 248 Bhn in the core, showing fatigue zone (right). The pin was cut (at left), then broken (light area at center). Sectioning of the pin revealed subcase fatigue cracking.

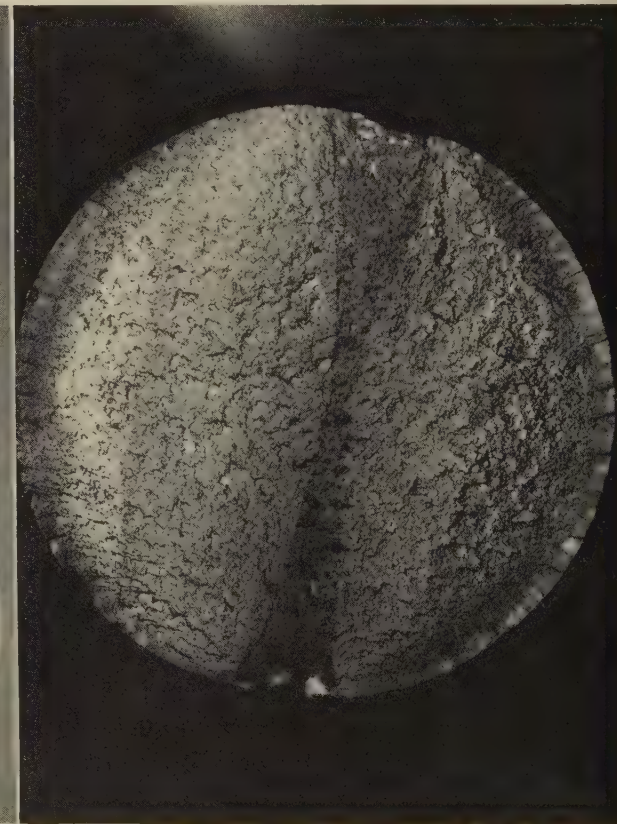
Failure-Analysis Fractographs: Fatigue Fractures in 50B60 Steel Torsion-Bar Spring, 5132 Steel Suspension Component, and 5132 Steel Spindle (in Reversed Bending)



Light fractograph

5032 Surface of a torsional-fatigue fracture in the cylindrical portion of a 1½-in.-diam torsion-bar spring of 50B60 steel heat treated to a hardness of Rockwell C 53. The fatigue crack originated in a very small (0.015 in. long) facet (labeled "Origin of fatigue") on a longitudinal shear plane and progressed alternately on 45° tension planes and longitudinal shear planes, as indicated in the diagram. Note that the semicircular fatigue patch surrounding the origin lies in the 45° plane.

1¼×



Light fractograph

5033, 5034

Views of the mating fracture surfaces of a suspension component that was fabricated of 5132 steel and that broke in a fatigue test. Note the two fatigue-crack origins, one at arrows A (top) and the other at arrows B (bottom). The crack that was initiated at the origin at arrows B is the earlier crack, as indicated by the well-rubbed surface near that origin.

3×

Light fractograph

3×

Light fractograph

5035

Surface of a laboratory reversed-bending fatigue fracture in a spindle of 5132 steel heat treated to a hardness of 262 to 321 Bhn. Fatigue cracks from multiple surface origins joined to form two main crack fronts, which nearly met at center.

2×

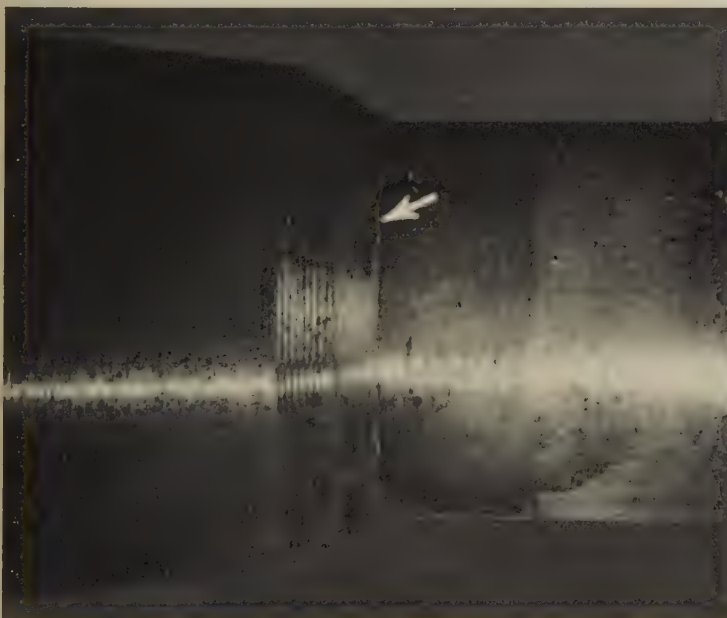
Failure-Analysis Fractographs: 5135H Steel Steering-Knuckle Spindle That Fractured Because of Fatigue Cracking, and an Identical Intact Spindle With a Fatigue Crack



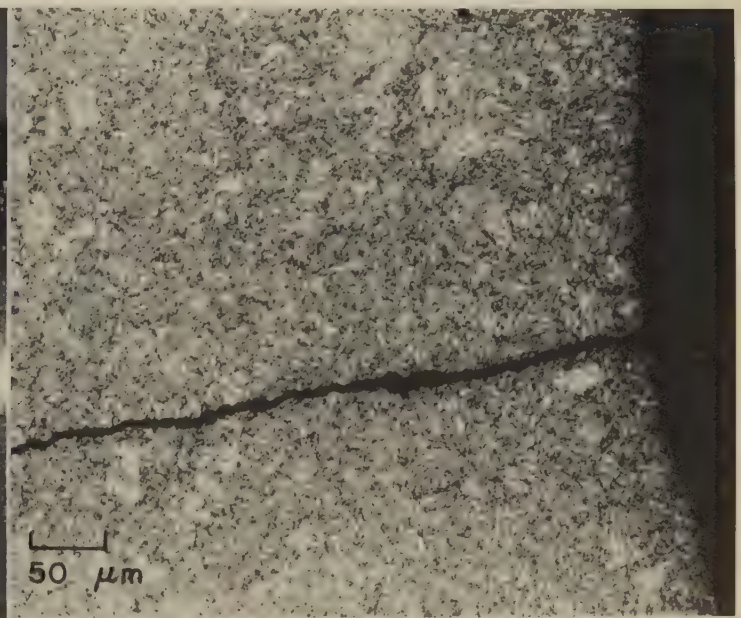
Photograph 3/4×
5036 Fracture in the spindle of a steering knuckle fabricated of 5135H steel and heat treated to a uniform hardness of Rockwell C 29. Fracture was caused by fatigue cracks that formed on opposite sides of the spindle, at the root of a fillet in the straight section adjacent to the threads. See also 5037 to 5039.



Light fractograph 5×
5037 View of the fracture surface of the steering-knuckle spindle in 5036. Several fatigue cracks originated at the surface of the spindle, at both top and bottom. These cracks began in slightly different planes but, after penetrating a short distance, joined to form two continuous crack fronts.

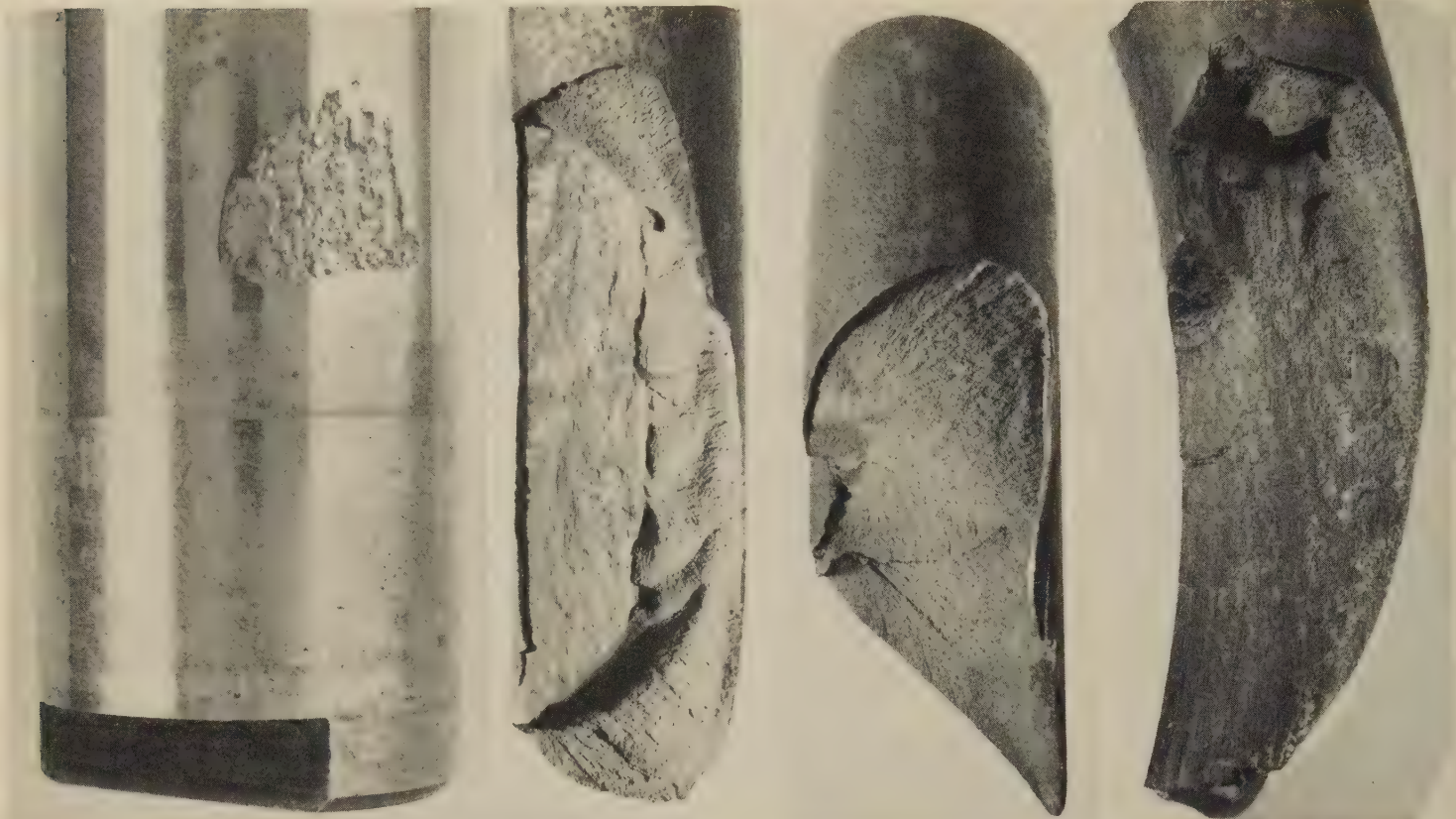


Photograph 3×
5038 View of a steering-knuckle spindle identical to the one shown in photograph 5036 (above). The arrow points to a fatigue crack that formed in exactly the same location as did the fatigue crack that caused the fracture in 5036. Note the deep tool marks on the tapered portion of the spindle. See 5039.



Micrograph (2% picral) 200×
5039 Polished and etched section through the crack in the spindle shown in 5038 (left). The crack, which appears to be transgranular, originated in the root of a fillet in which transverse machining or grinding marks were found. Fracture in 5036 was attributed to stress concentrations caused by such marks.

Failure-Analysis Fractographs: 5145 Steel Shaft Fretted by Friction and Corrosion;
5160 Steel Coiled Springs and Rectangular-Section Spring Fractured by Fatigue



Photograph

5040 Fretting, caused by a combination of friction and corrosion, on a shaft of 5145 steel that was heat treated to a case hardness of Rockwell C 62 and a core hardness of Rockwell C 55.

5×

Light fractograph

5041, 5042, 5043

Surfaces of three fatigue-test fractures in coiled springs for lightweight trucks, fabricated of $\frac{3}{8}$ -in.-diam 5160 steel wire with a hardness of Rockwell C 46 to 50. The fracture at left (5041) was initiated by a long seam. At center (5042), a small fatigue-crack origin is visible at left, probably at a surface defect. The fracture at right (5043) was probably initiated by a seam.

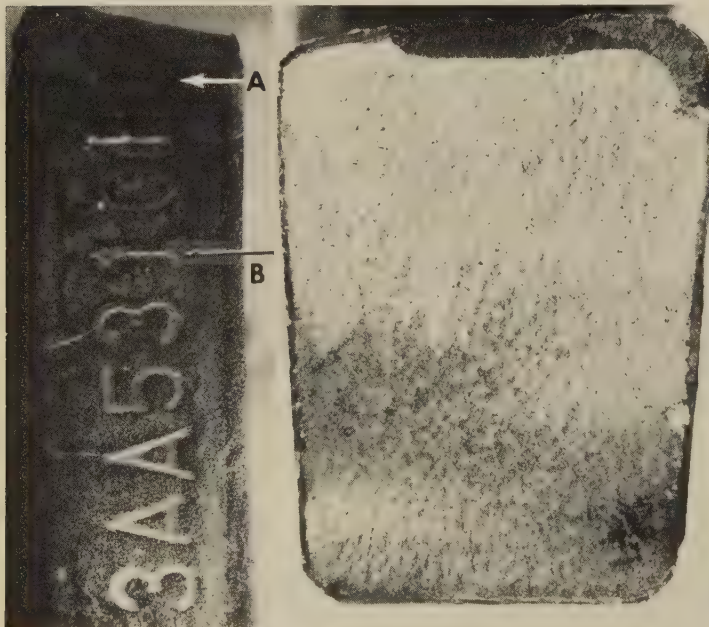
2×

Light fractograph

2×

Light fractograph

2×



Photograph

5044, 5045, 5046

Fatigue fracture in an experimental spring of 5160 steel with a hardness of Rockwell C 47.5 to 51.5. The spring had been fabricated to a roughly rectangular cross section and was broken in testing. The fine white lines in 5044 (left) are magnetic-particle traces of cracks caused by stamping of the identifying symbols. At top in 5044 is the surface of the fracture, which began at a crack that formed at the stamped numeral at arrow A. The fracture surface is shown also in 5045 (center), with stamped surface in profile at top; the fatigue zone (dark) is visible at top edge. At right (5046) is a section through the stamped numeral at arrow B in 5044. Note the crack, which formed at the numeral, in the steel below a protective nickel plate (light).

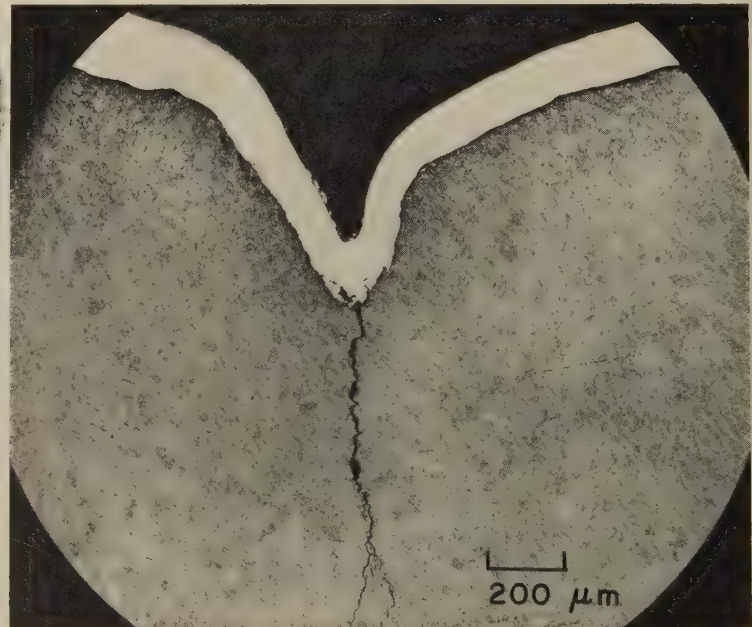
1½×

Light fractograph

3×

Micrograph (nital)

50×

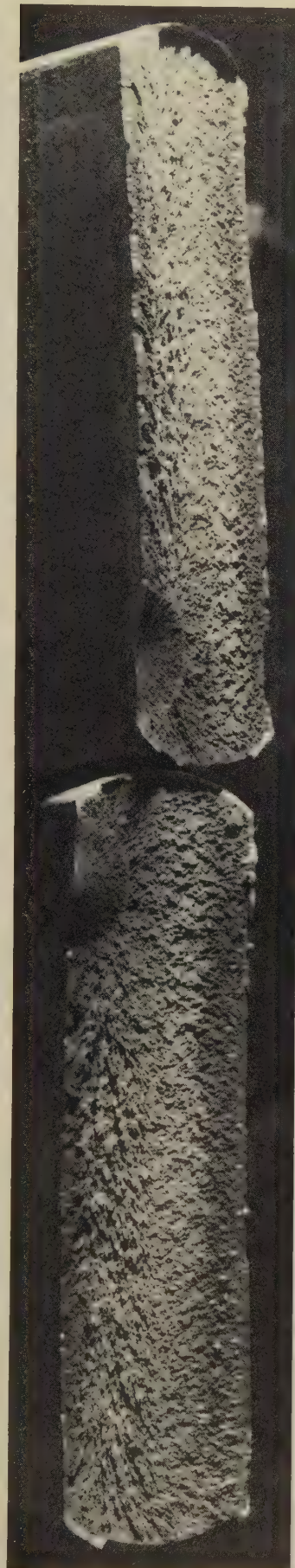


Failure-Analysis Fractographs: 5160 Steel Leaf Springs That Were Fractured by Fatigue



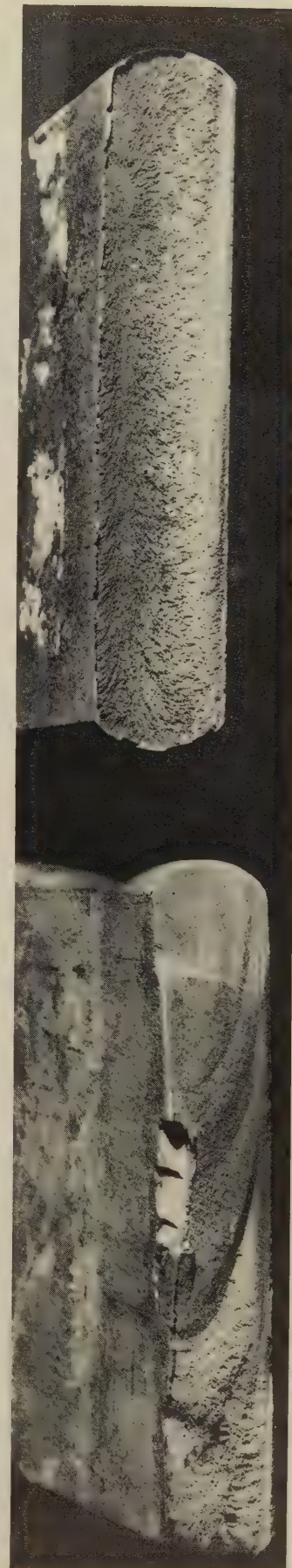
Photograph (a); two light fractographs (b and c)

5047 At top left (a) is a view of one of the fracture surfaces of that broken leaf, showing a large fatigue zone. Although no fatigue marks are clearly visible, the fatigue-crack origin appears to lie at the lower edge, just to the left of the light triangular facet. Note the shear lip along the upper edge. At right (c) is a fracture surface of a similar but thicker leaf, also of 5160 steel, with a hardness of 415 Bhn. Two fatigue-crack origins are visible at the lower edge, one near each end. The dark region at upper right is a shadow of a shear lip.



Light fractograph

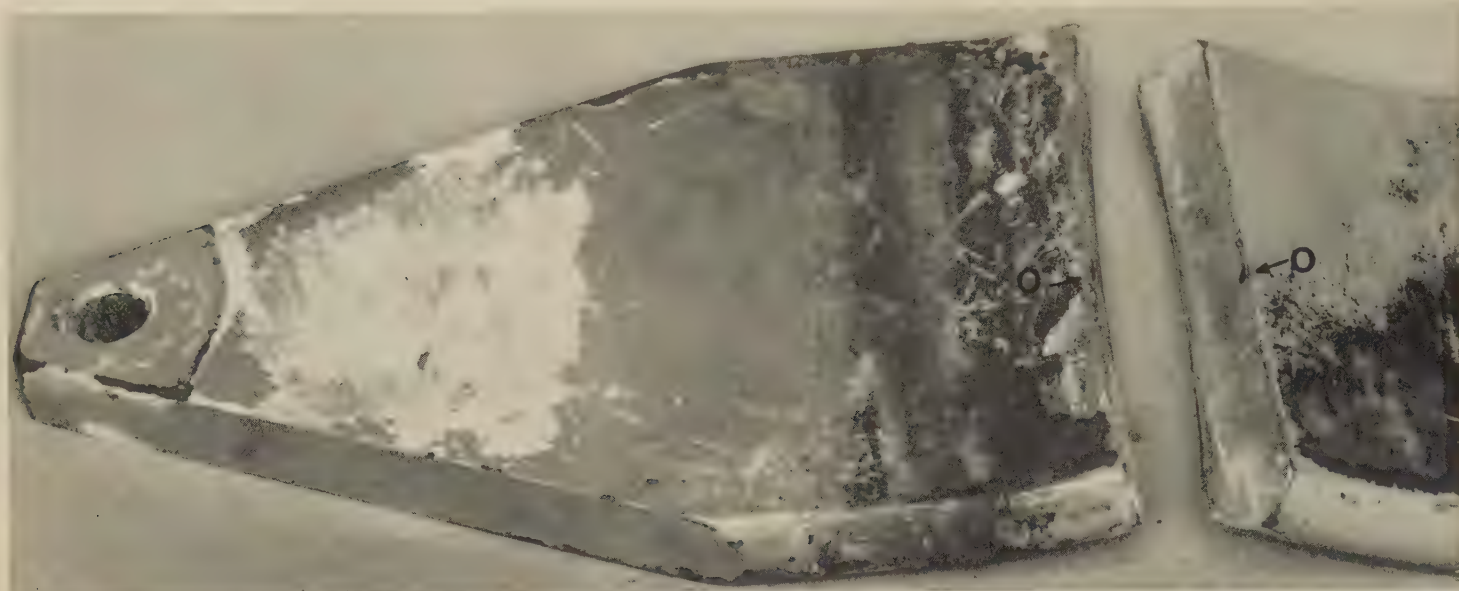
5048 Mating surfaces of a fatigue fracture in a leaf of a 5160 steel leaf spring with a hardness of 415 to 429 Bhn. The two segments of the leaf appear to have different thicknesses because the fracture surface of the segment at left is shown less obliquely due to the upward curve in that segment. The fatigue-crack origin is visible at the top of each fracture surface, near the edges shown adjacent here. A gouged region was found on the upper (tension) surface, in the area of the origin; the gouging was attributed to foreign material between this and an adjacent leaf. Metallographic examination disclosed a heavy concentration of globular oxide inclusions surrounding the origin.



Light fractograph

5049 Surfaces of fatigue fractures in leaves from two 5160 steel rear-bogie leaf springs. The leaf shown at left had a hardness of 371 to 381 Bhn, and the leaf at right had a hardness of 442 to 452 Bhn. The fracture surface of the leaf at left shows a fatigue-crack origin near the upper right corner, apparently at a surface defect. Beach marks show that the fatigue crack achieved nearly complete penetration before final, fast fracture occurred. The fracture surface of the leaf at right also exhibits a small fatigue zone at upper right, which is believed to have been initiated by deep-penetrating surface corrosion. Final, fast fracture occurred early, creating a very complete pattern of chevron marks.

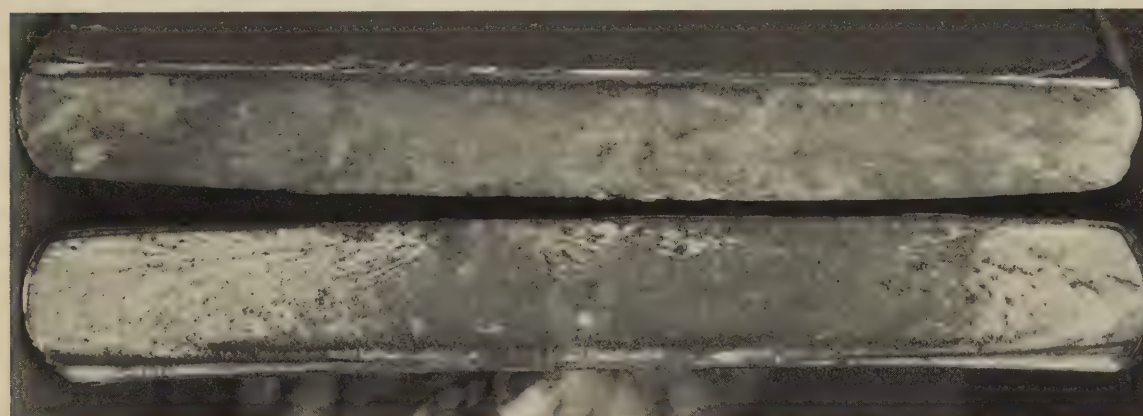
Failure-Analysis Fractographs: Fatigue Fracture in a 6150 Steel Spring Leg of an Aircraft Main Landing Gear



Photograph

5050 Fatigue fracture in a 6150 steel spring leg of an aircraft main landing gear, heat treated to a minimum tensile strength of 1550 MPa (225 ksi) and a hardness of Rockwell C 49. Visual inspection of the fracture surfaces showed that the fatigue crack originated at the location marked by arrows O. The appearance of the external surface of the spring leg indicated that the part had been shot peened but that peening had been inadequate. The dimensions of the spring leg conformed to specifications. See also 5051 to 5055.

3/4 X



Light fractograph

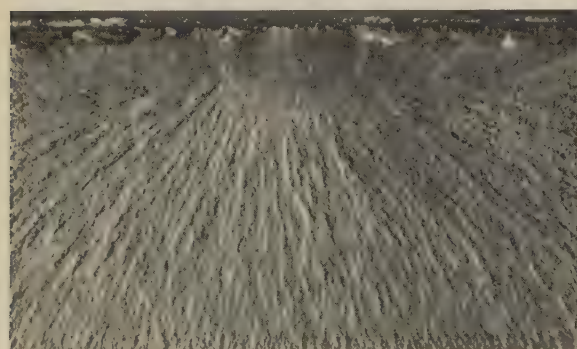
Actual size

5051 Mating fracture surfaces of the broken main-landing-gear spring leg in 5050. A small fatigue zone can be seen just to the left of center, at the edges shown adjacent here. This zone grew to a length of only about 0.2 in., and to a depth of slightly more than 0.1 in., before final, fast fracture occurred. The remainder of each fracture surface shows features typical of rapid tearing.



Micrograph (1% nital) 250 X

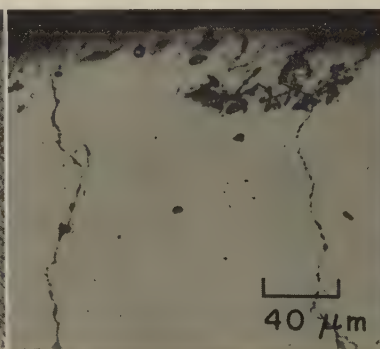
5052 Section through the spring leg in 5050, showing the irregular profile of the fast-fracture surface, at right.



Light fractograph

4 X

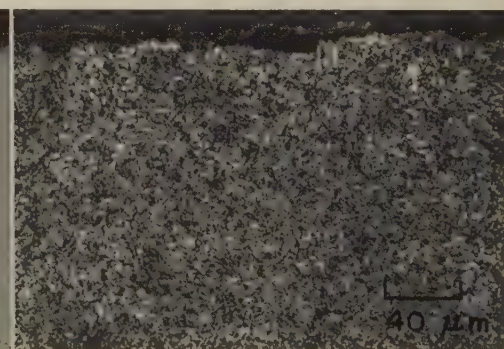
5053 A view of the fracture surface at bottom in 5051, showing the fatigue zone at top center. Metallographic study of this region revealed partial decarburization to a depth of 0.028 in., which contributed to fracture.



Micrograph (unetched)

250 X

5054 Section through the spring leg in 5050, near the fracture origin. Secondary cracks extend inward from the shot-peened surface (at top).

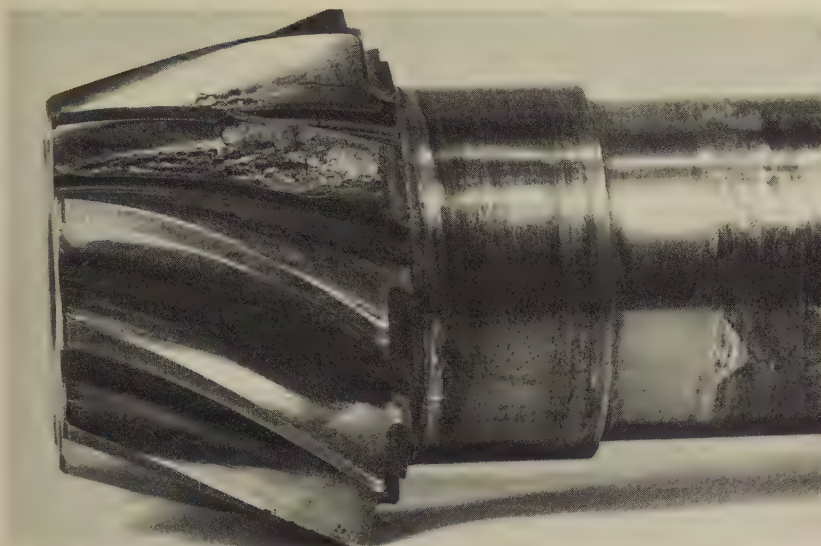


Micrograph (1% nital)

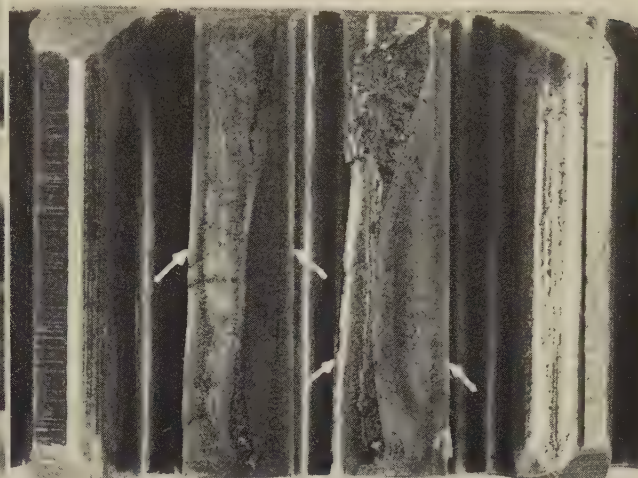
250 X

5055 Another section through the spring leg in 5050, showing a profile of the fatigue-crack surface, at top. Compare the smoothness of this surface with the irregularity of the fast-fracture surface in 5052.

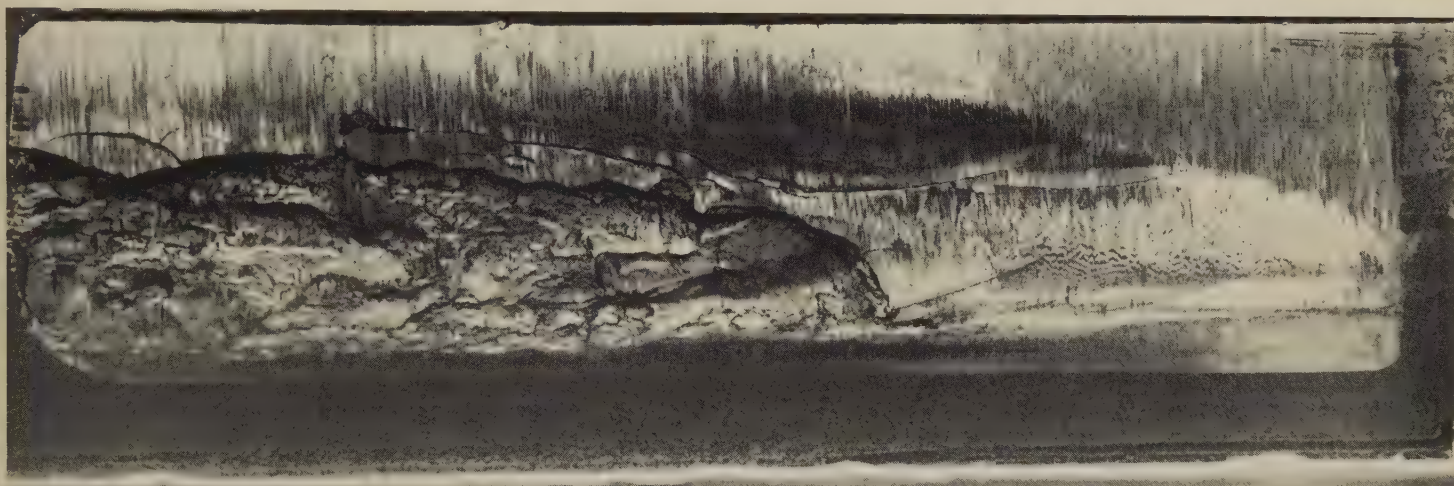
Failure-Analysis Fractographs: Carburized 8617 and 8620 Steel Pinions and Gears Fractured by Bending Fatigue and by Spalling Fatigue



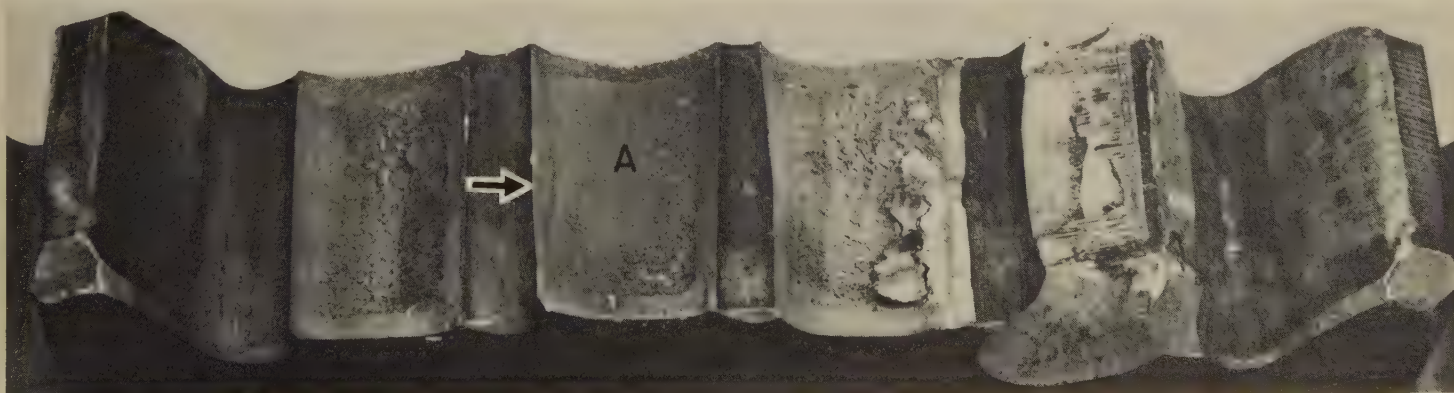
Photograph 3/4×
5056 Bending-fatigue fracture in the heel of one tooth of a spiral bevel pinion of 8617 steel, carburized and hardened to Rockwell C 57 in the case. Fracture resulted from severe pitting. Note that pitting had begun in an adjoining tooth (near top).



Photograph About 2×
5057 Bending-fatigue fracture in two teeth of a reverse idler gear of 8617 steel, carburized and hardened to Rockwell C 60 in the case. Arrows point to root fillets on both sides of each tooth, where fracture began because of excessive stress in these locations.



Light fractograph About 4×
5058 Surface of a spalling-fatigue fracture in a single tooth of a heavily loaded final-drive pinion of 8620 steel, carburized and hardened to Rockwell C 60 in the case, showing vertical scratches, which indicate that appreciable abrasive wear took place also. The surface ripples at right suggest that a small amount of plastic flow occurred under the applied load.



Photograph 2×
5059 Bending-fatigue fractures in several teeth of a spur gear of 8620 steel, carburized and hardened to Rockwell C 60 in the case. The tooth marked A apparently broke first, as the result of a fatigue crack that originated in the fillet to the left of the tooth (arrow). After this tooth broke off, fracturing of the teeth on each side of it was accelerated.

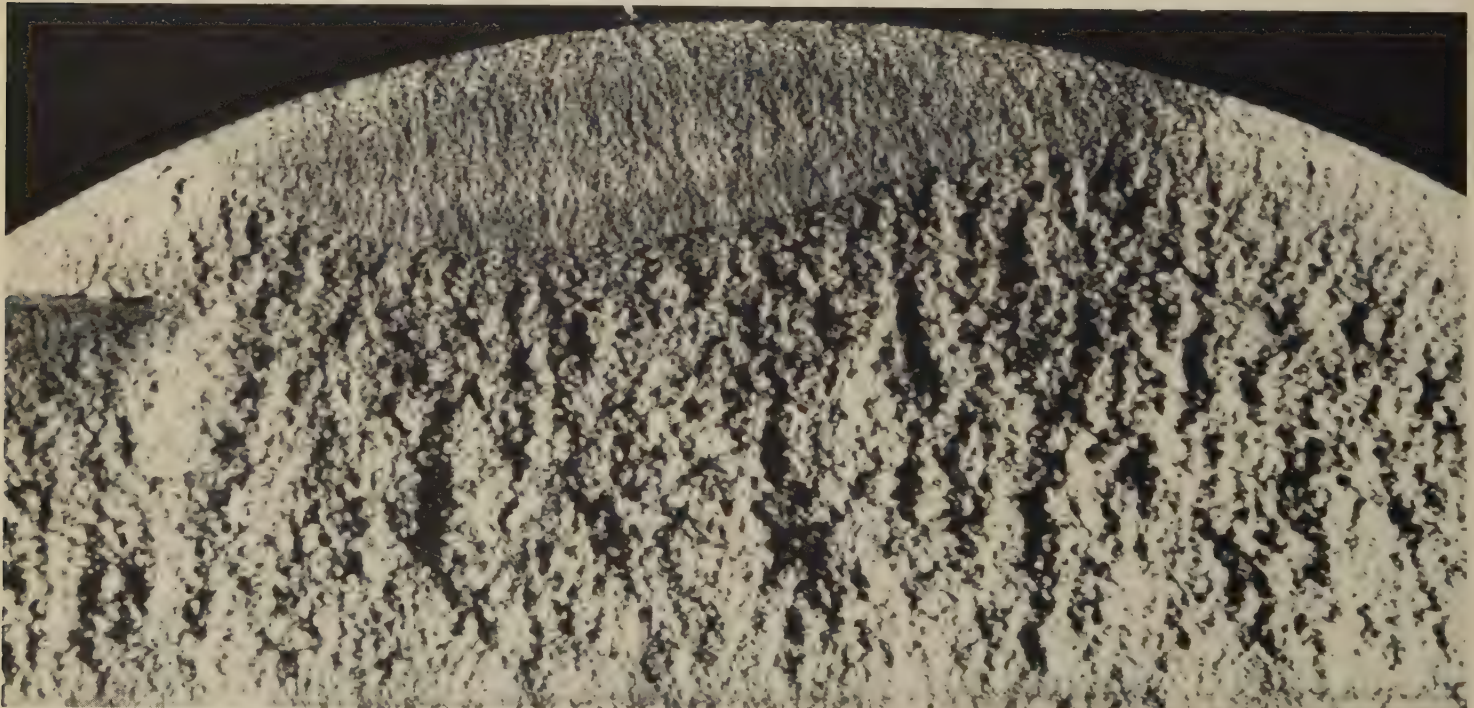
Failure-Analysis Fractographs: 8620 Steel Carburized Kingpins
Fractured by Single Overload and by Fatigue Plus Overload



Light fractograph

About 22×

5060 Fracture surface of a 1¼-in.-diam kingpin of 8620 steel, carburized and case hardened to Rockwell C 57 to 63, then broken in a laboratory by a single overload. Chevron marks are faintly visible in the case and point to the fracture origin, at top center (indicated by pointer). Compare with the fracture surface in 5061 (below).

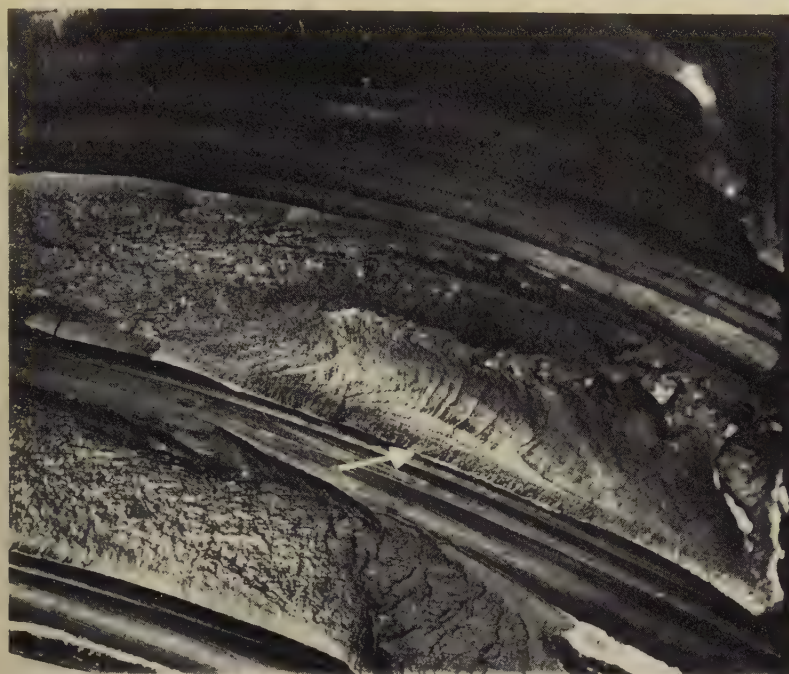


Light fractograph

About 10×

5061 Fracture surface of a 1½-in.-diam kingpin of 8620 steel, carburized and case hardened to Rockwell C 57 to 63. Laboratory bending-fatigue testing resulted in a fatigue crack, which was then broken open by a single overload. Note that the fatigue zone (at top) has a texture much smoother than that of the overload region, which constitutes the remainder of the fracture surface.

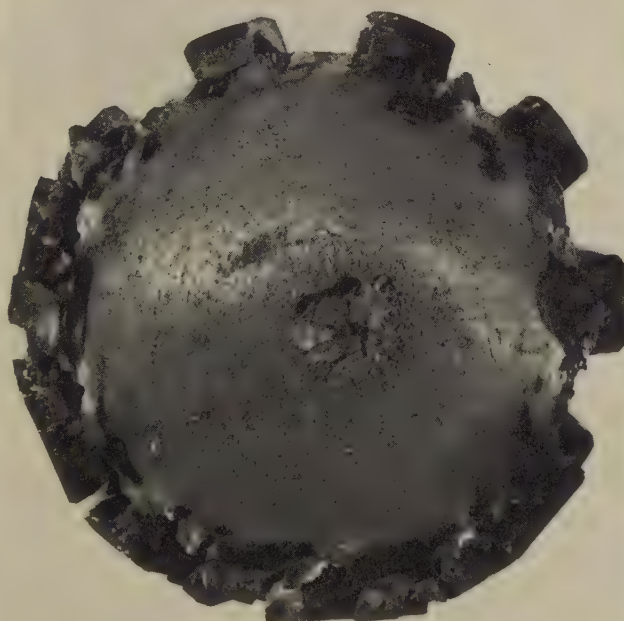
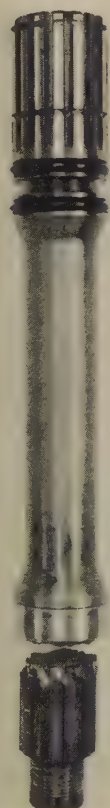
Failure-Analysis Fractographs of Carburized 8620 Steel Parts: Spiral Bevel Pinion Fractured by Bending Fatigue; Splined Shafts Fractured by Torsional Fatigue and by Torsion Overload



Light fractograph 1.65×
5062 Surface of a bending-fatigue fracture in a tooth (upper tooth in this view) of a large spiral bevel pinion of 8620 steel carburized and hardened to Rockwell C 60 at the surface. The arrow marks the fatigue-crack origin, in the root fillet. The absence of this tooth resulted in fracture of the tooth below by overload.



Light fractograph 2×
5063 Surface of a torsional-fatigue fracture in a splined shaft of 8620 steel that was carburized and case hardened. Multiple fatigue cracks evidently formed at the roots of the splines and then joined to penetrate much of the case before final, fast fracture occurred.



Photograph 1/4× Light fractograph 1 1/2× Photograph 1 1/2×
5064, 5065, 5066 At left (5064) is a view of a broken splined shaft of 8620 steel, surface carburized to a case depth of 0.042 in. and hardened to Rockwell C 63 to 65; core hardness was Rockwell B 96. Specified case hardness was Rockwell C 57 to 62. The fracture resulted from torsion overload. At center (5065) is a view of a surface of the fracture in 5064. Brittle fracture of the splines occurred first; later, the soft, ductile core fractured in the transverse shear plane. At right (5066) is a view of the O-ring region of the shaft in 5064. A 45° torsion crack is visible (at A) at the edge of an oil hole; this crack is proof of the torsional nature of the loading that was imposed on the shaft.

Failure-Analysis Fractographs: Cast 8620 Steel Coil-Grab Arm Fractured by Fatigue; 8640 Steel Boom-Point Pin Fractured by Fatigue



Photograph

5067, 5068, 5069

0.1X

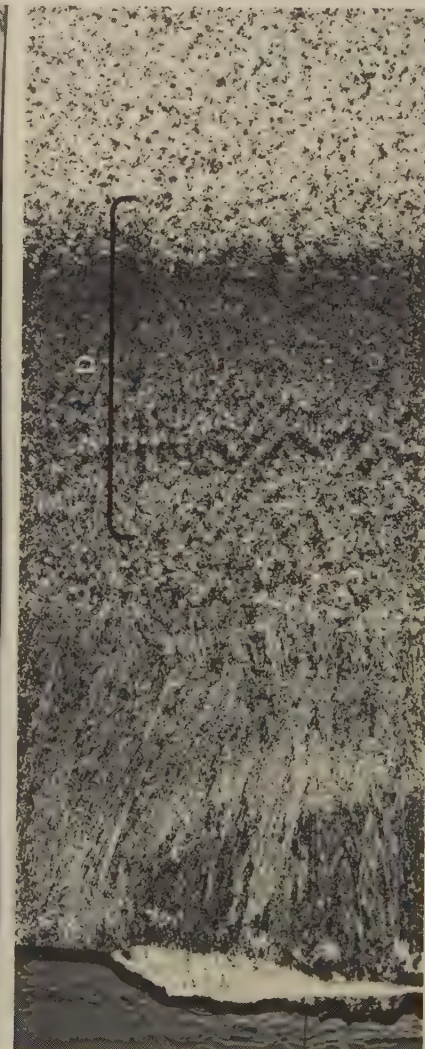
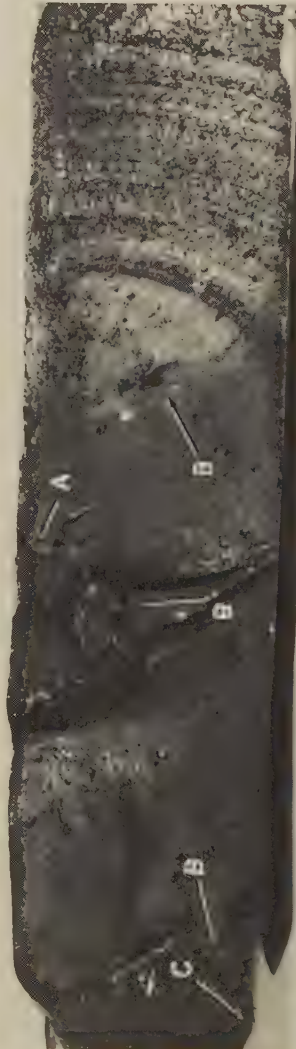
Photograph

0.025X

Photograph

0.08X

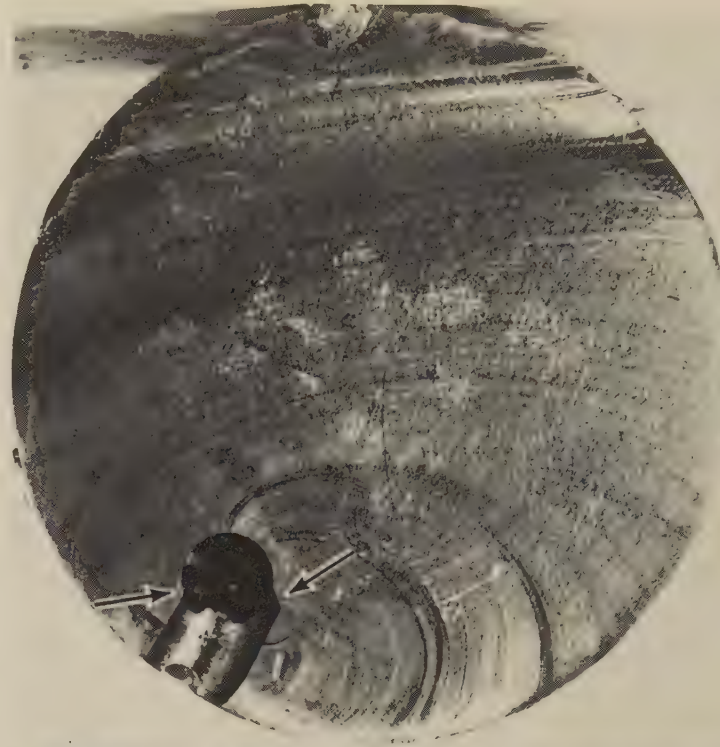
A fatigue fracture in the arm of a coil grab that broke after seven years of service. The arm had been cast of 8620 steel, quenched, and tempered to a hardness of Rockwell C 25. Magnetic-particle inspection of the arm had been performed annually during six years of service, so the crack must have developed sometime during the final year of service. At left (5067) is a view of one segment of the broken arm, with a flexible shoe (left) still attached. Clearly visible on the larger flange is the fatigue zone, which originated at the arrow, at sand pockets near the surface that acted as stress raisers. At center (5068) is a view of the coil grab minus the arm segment in 5067. The fatigue-crack origin is at the bottom in this view. At right (5069) is a view of both segments of the broken arm, showing the fracture surface in 5068. Not visible is a repair weld on the underside, as viewed here, near the crack origin. See also 5070 and 5071.



Light fractograph (5070); macrograph - 2% nital (5071)

Actual size (5070); 25X (5071)

At top (5070) is the portion of the fracture surface in 5068 and 5069 that includes the fatigue-crack origin (at arrow A). This portion was sliced from the outer edge of the larger flange of the broken arm; the cut surface is in profile at bottom here. Sand pockets exist near the origin and elsewhere (at arrows B). The repair weld (at arrow C) was made after the casting had been heat treated, as shown by the presence of a dark heat-affected zone at D in 5071 (at bottom), which is a polished and etched section through the weld.

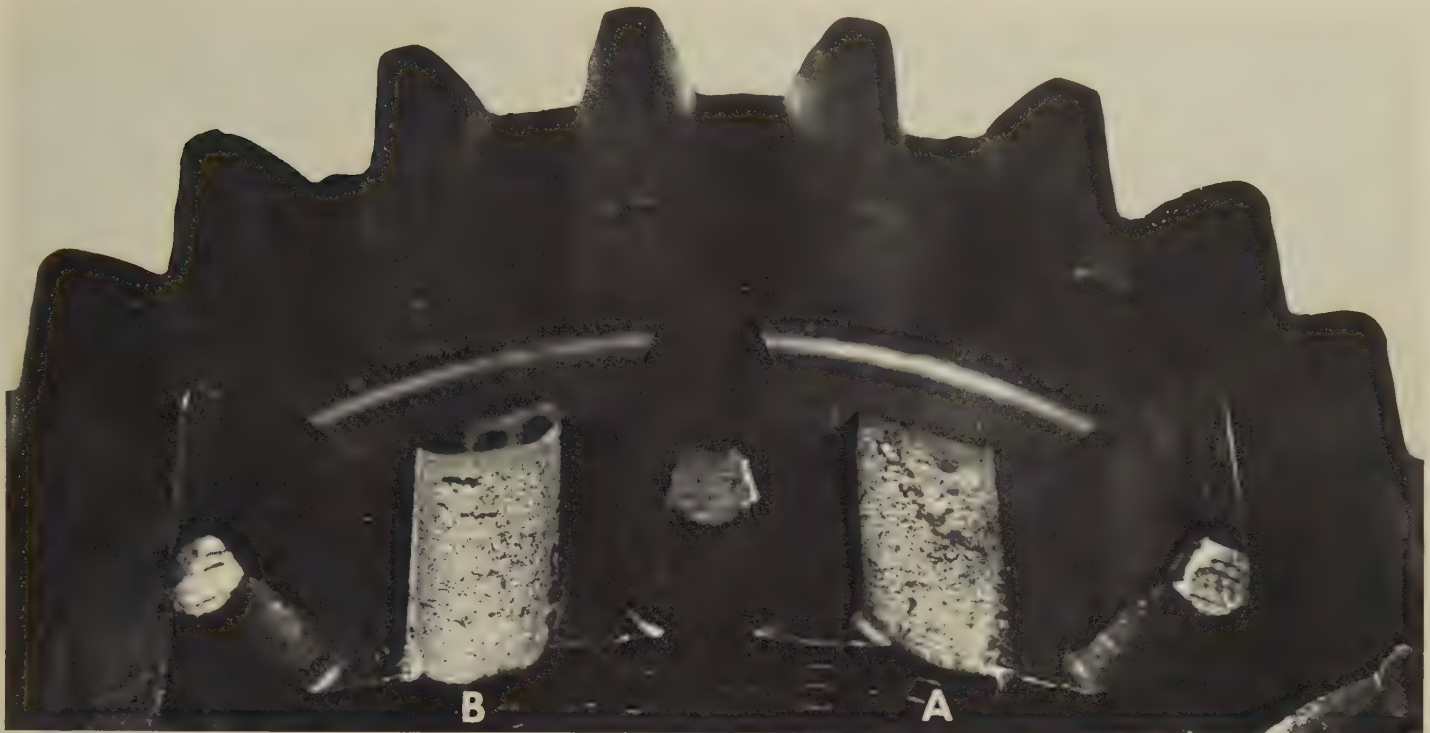


Light fractograph

5072

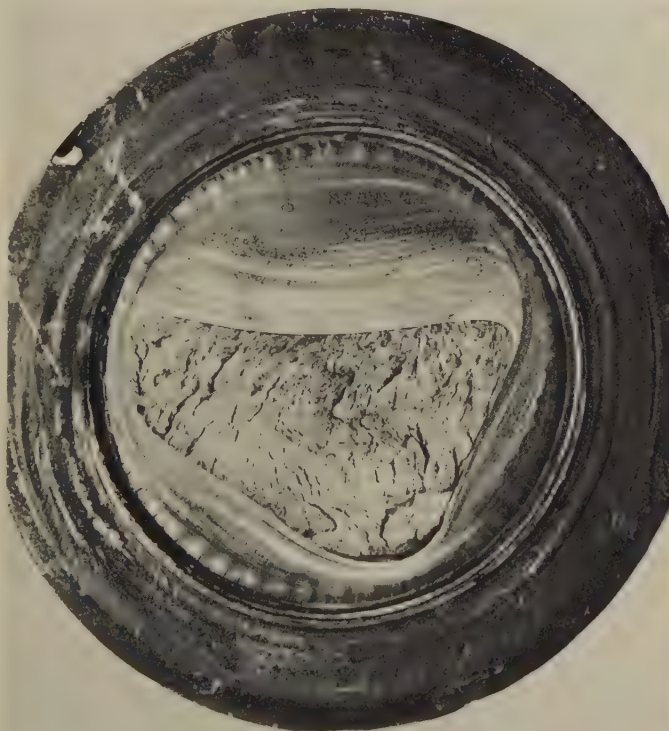
About actual size
Surface of a fracture in a boom-point pin that broke during service. The material is 8640 steel that was quenched and then tempered to a hardness of 269 Bhn. Sharp corners of mismatched transverse grease holes provided stress concentrations that generated two fatigue cracks (arrows). The front that was formed by the merging of these two cracks nearly penetrated completely across the pin before final, fast fracture occurred.

Failure-Analysis Fractographs: Carburized 8620 Steel Cluster Gear Fractured by Overload;
8640 Steel Axles Fractured by Fatigue



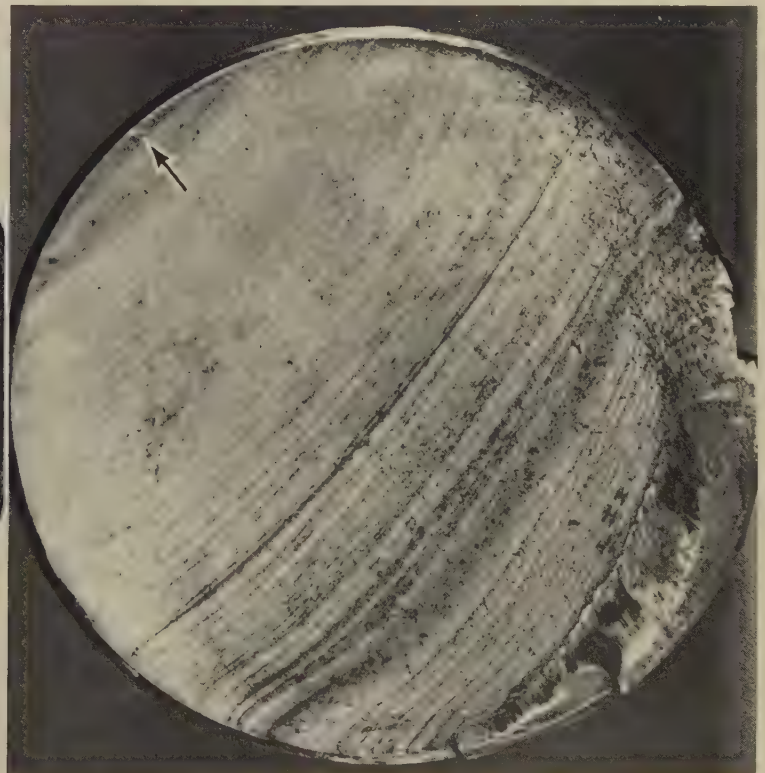
Photograph

5073 Fractured cluster gear of 8620 steel, carburized and hardened to Rockwell C 60 in the case. The tooth at A fractured in service. The tooth at B was broken later, in a laboratory, by overload caused by the impact of a 100-lb weight dropped from several feet. The fracture surfaces of both teeth exhibit characteristics of cleavage and are very similar to each other, indicating that the fracture of the tooth at A was also caused by a sudden overload. 1½×



Light fractograph

5074 Surface of a fatigue fracture in a 4-in.-diam axle of 8640 steel with a hardness of about Rockwell C 30. Contained within a shrink-fitted collar (visible here), the non-rotating axle was subjected to bending stresses in three directions, which produced this unusual pattern of beach marks. 0.65×



Light fractograph

5075 Surface of a fatigue fracture in a nonrotating axle of 8640 steel with a hardness of approximately Rockwell C 30. Visible are beach marks, which indicate that the fatigue crack penetrated across more than 90% of the axle before final, fast fracture occurred. The origin (arrow) was at a discontinuity in a cut thread. About 0.95×

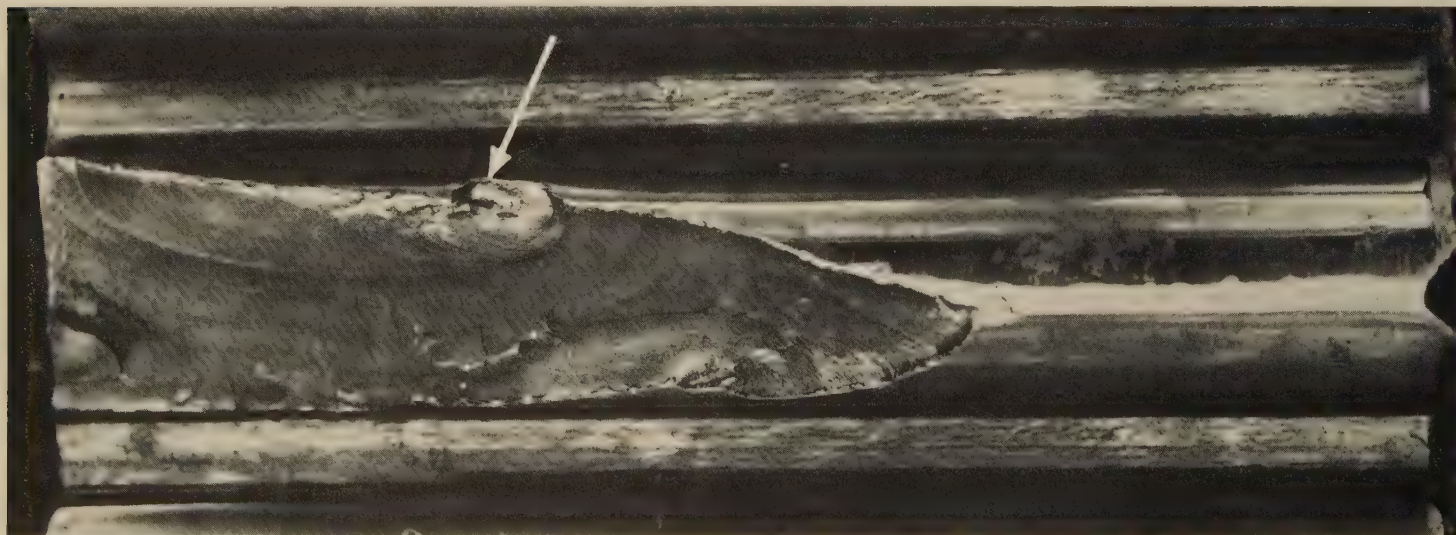
Failure-Analysis Fractographs: 8640 Steel Forged Connecting Rod Fractured by Fatigue;
8650 Steel Sprocket-Drive Pinion Fractured by Bending Fatigue



Light fractograph

About 7×

5076 Surface of a fatigue fracture in a forged connecting rod of 8640 steel with a hardness of Rockwell C 26 to 27 throughout. The rod broke after approximately 52,000 miles of service. The fatigue-crack origin is at the left edge, at the flash line of the forging, but no unusual roughness of the flash trim there was discovered. No metallurgical cause of the fracture was detected. The fatigue crack progressed about halfway around the oil hole at left before final, fast fracture occurred. Note the pronounced shear lip at the right edge.



Light fractograph

1.6×

5077 Surface of a bending-fatigue fracture in a tooth of a sprocket-drive pinion of 8650 steel induction hardened to Rockwell C 58 to 60. The fatigue-crack origin is at a deep pit (arrow) in the tooth surface. Severe end loading produced other, smaller pits in the surfaces of the teeth. Beach marks indicate that the fatigue crack penetrated a large portion of the tooth before a piece broke off.

Failure-Analysis Fractographs: 8645 Steel Splined Main Drive Shaft for a Lift Truck, Fractured by Fatigue



Photograph

5078, 5079

At left (5078) is a fatigue fracture in the splined main drive shaft of a lift truck. The material is heat treated 8645 steel. Hardness was Rockwell C 44 throughout, except at the surfaces of some of the splines, where the hardness was Rockwell C 38. There was no apparent reason for the low hardness of these splines; decarburization, which was suspected originally, was not revealed by metallographic examination. Note the longitudinal cracks in the portion at left. Experimentally broken longitudinal sections of the shaft showed very "woody" fracture surfaces. At right (5079) is a view of the fracture surface of the right portion of the shaft in 5078. Sharpness of fillets is evident, such as at the arrows in 5078 and 5079. See also 5080 through 5082.

114x Light fractograph

114x



Light fractograph

5080

Fracture surface of the left portion of the shaft in 5078 showing the badly mangled splines separated by longitudinal cracks, which are evident also in 5078 (above).

114x



Micrograph (2% nital)

5081

Longitudinal section through a spline of the shaft in 5078, showing inclusions, banding, and some free ferrite. The cause of the fracture was improper design; corners at bases of splines had adequate radii for most of the spline length, but these radii were reduced, forming sharp angles, at points near where the splines blended with the shaft.

100x

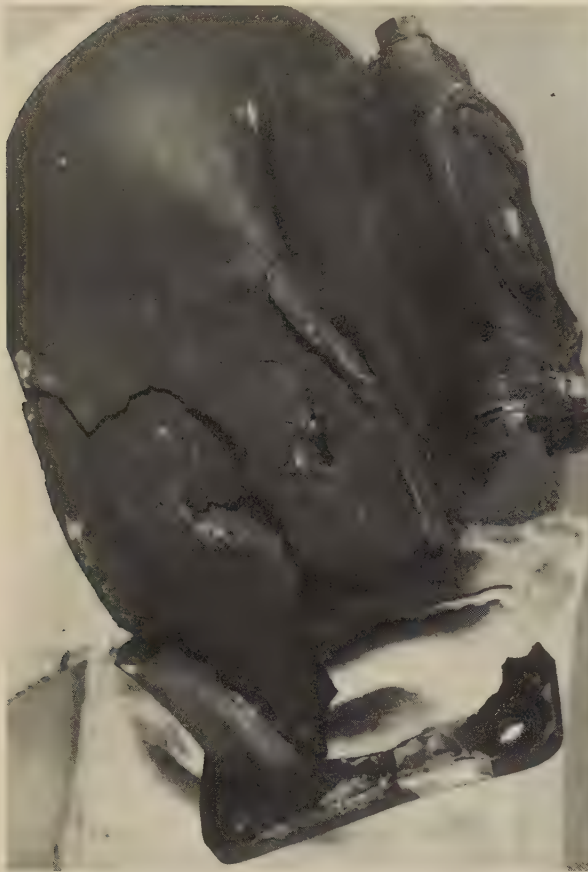


Macrograph (1 part HCl, 1 part H₂O)

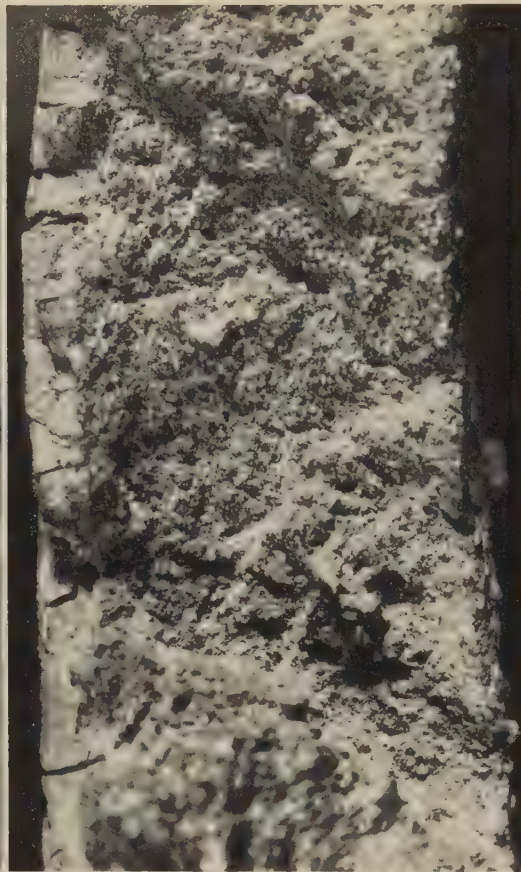
2x

5082 Longitudinal section through the same spline as in 5081, displaying the size and even distribution of the inclusions in the steel. Some of the inclusions were found to be as long as 1/16 in.

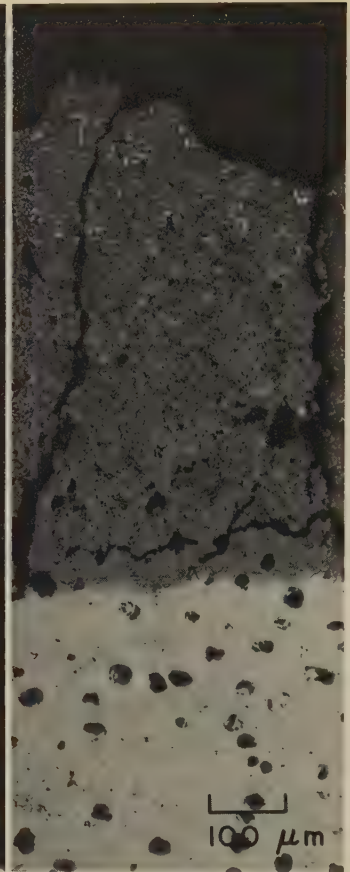
Failure-Analysis Fractographs: Ductile Iron Turbocharger Housing Fractured by Impact;
Ductile Iron Experimental Bracket Fractured by Fatigue



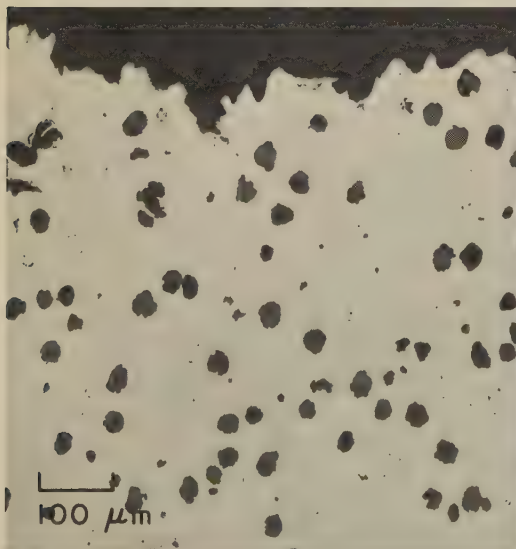
Photograph $\frac{1}{2} \times$
5083 View of a broken turbocharger housing, showing several pieces fitted together (the remaining pieces are missing). The material is ductile iron. The outer wall of the housing was crushed inward against the inner wall. Impact by a foreign object was suspected as the cause of the fracture. See also 5084 through 5087, at right and below.



Light fractograph $10 \times$
5084 A portion of a fracture surface of the wall of the housing in 5083, showing an appearance that is typical of the entire fracture surface. The inner surface of the housing wall (at left) has a heavy layer of scale, which was caused by high operating temperature; the fracture surface has only a film of oxide.



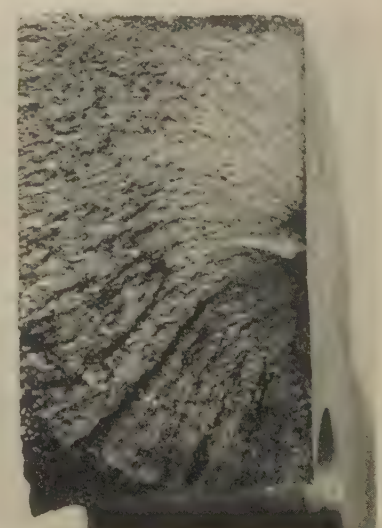
Micrograph (unetched) $100 \times$
5085 A polished section through the layer of scale visible at left in 5084, on the inside surface of the housing. Area at bottom shows spheroidized graphite nodules in a matrix of ferrite.



Micrograph (unetched) $100 \times$
5086 Polished section through the fractured housing in 5083 (taken in the region shown in 5084), with the fracture surface in profile at top. The lack of appreciable scale on the fracture surface indicates only brief exposure to hot gases after fracture.

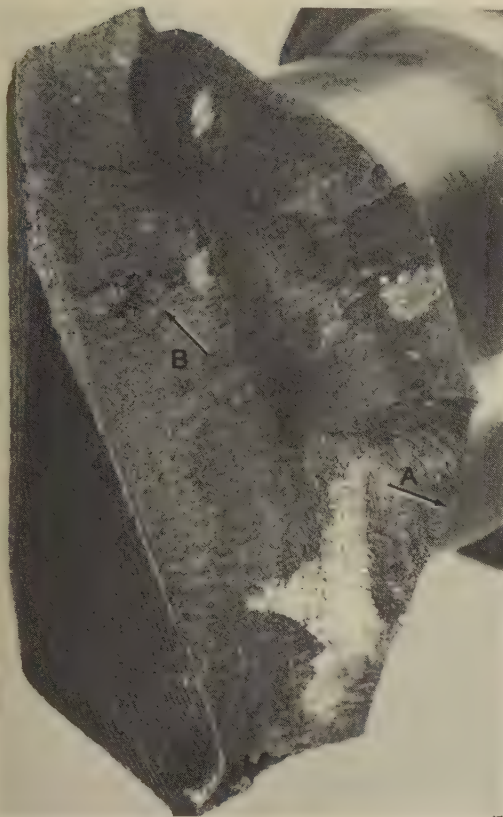


Photograph Actual size
5087 A view of a hole, which formed during service, in the housing of a turbocharger similar to that shown in 5083. Appreciable scale, which was caused by escaping hot exhaust gases, is evident in the area immediately surrounding the hole.



Light fractograph $2 \times$
5088 Fatigue-fracture surface of an SAE D4018 ductile iron experimental bracket (hardness, 170 Bhn max) that was broken in a laboratory. Note fan-shaped fatigue zone, and fatigue-crack origin (right edge, midheight).

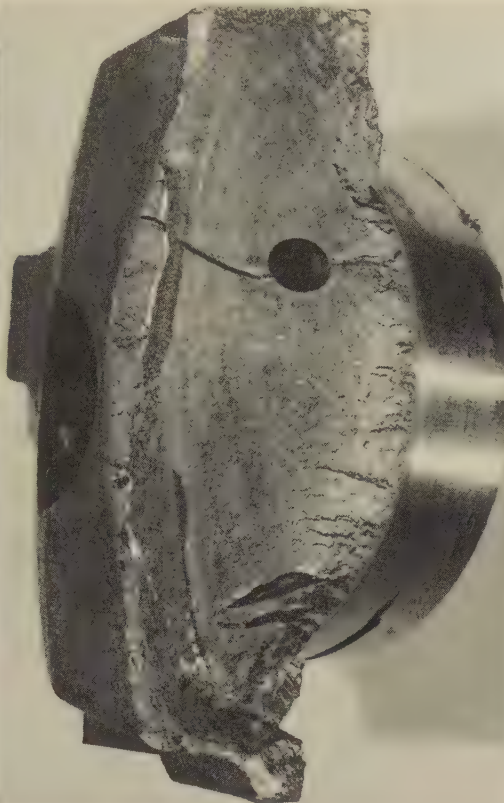
Failure-Analysis Fractographs: Ductile Iron Experimental Crankshafts Fractured in Fatigue Tests; Gray Iron Pipe Flange Fractured Because of Improper Bolting



Light fractograph

2½ ×

5089 Surface of a fatigue-test fracture in an experimental crankshaft of induction hardened 80-60-03 ductile iron with a hardness of 197 to 225 Bhn. Fatigue-crack origin is at arrow A. Note porosity at arrow B, which was unrelated to fracture initiation.



Light fractograph

Actual size

5090 Surface of a fatigue-test fracture in an experimental crankshaft of ductile iron with a hardness of 241 to 255 Bhn. Note the multiple fatigue-crack origins at the journal edge (at right). Fatigue beach marks are evident, which is unusual in cast iron.



Light fractograph

Actual size

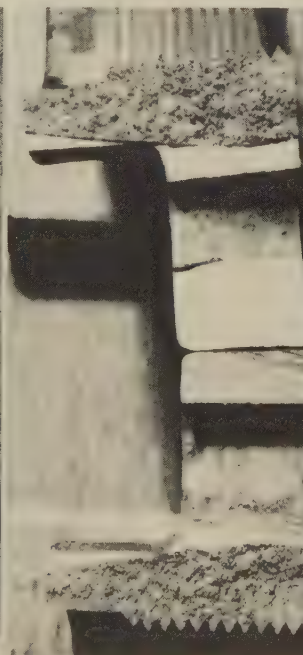
5091 Surface of a fatigue fracture in an experimental crankshaft broken in a fatigue test. The material is ductile iron with a hardness of 241 Bhn. The origin of the fatigue crack is at the edge of the journal, at arrow.



Photograph

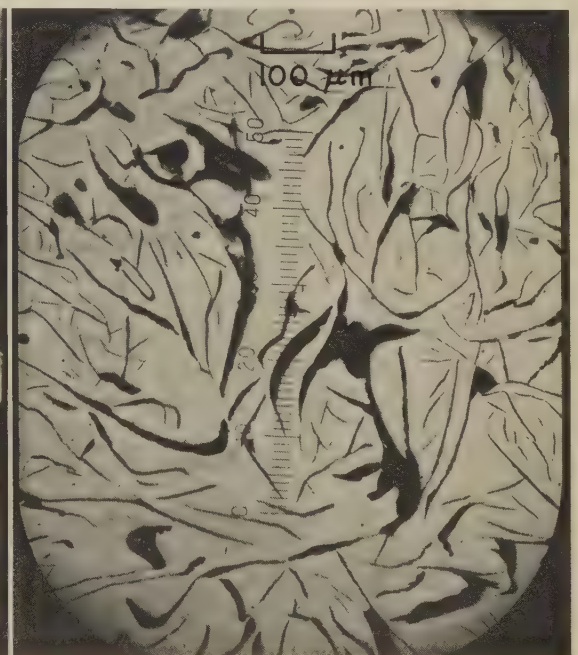
¼ ×

5092 View of a broken gray iron pipe flange. The fracture was attributed to stresses caused by misalignment with the pipe and by improper bolting (two bolts had to be seated partly on raised cast numerals), and to very inferior strength. See also fractograph 5093 and micrograph 5094.



Light fractograph About 2/3 ×

5093 Two of the coarse fracture surfaces of the pipe flange in 5092. No porosity or shrinkage cavities were discovered.

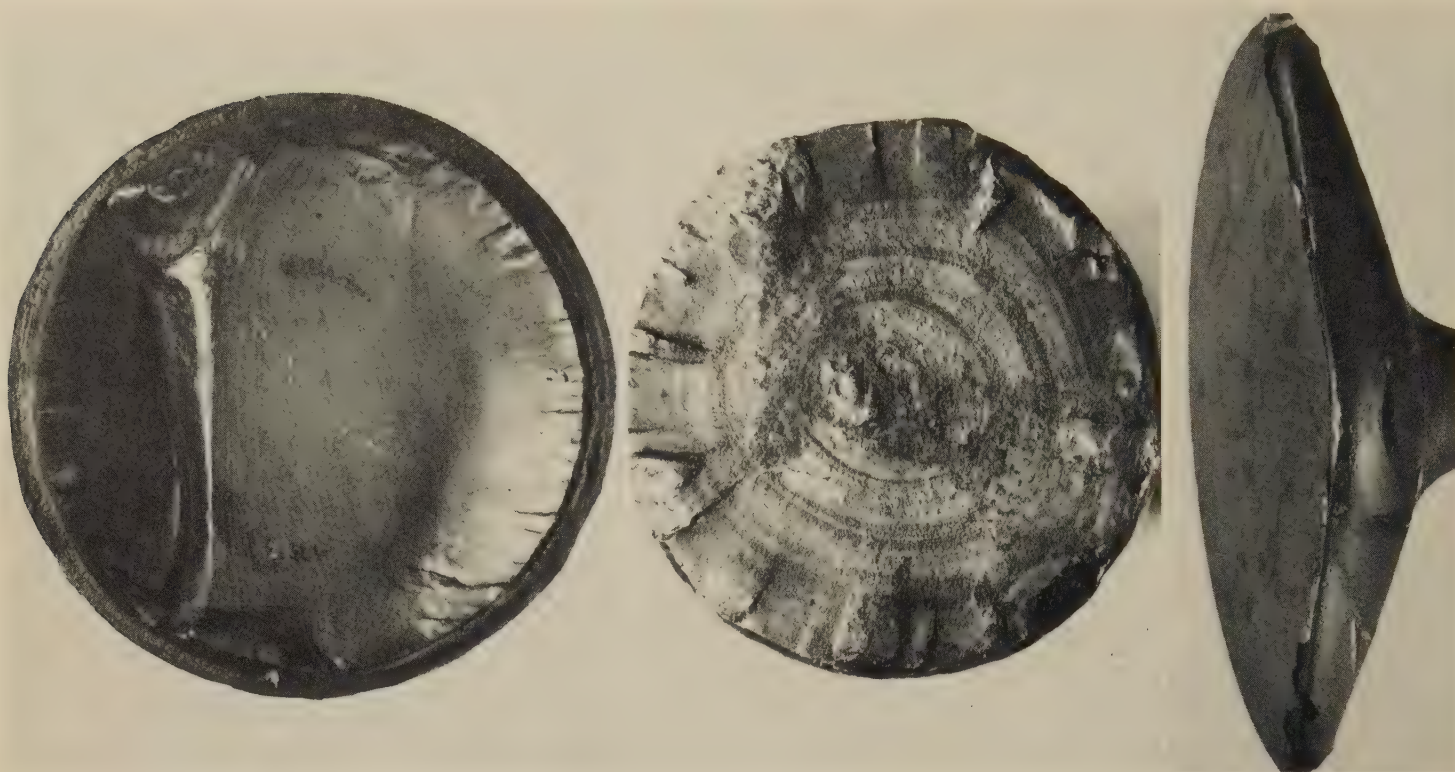


Micrograph (unetched)

100 ×

5094 A polished section through the gray iron pipe flange in 5092, showing very coarse and irregular graphite flakes; these graphite flakes, together with the low hardness of the flange (108 to 122 Bhn), resulted in low strength.

Failure-Analysis Fractographs: Silcrome-1 Steel Automotive Intake Valves Fractured by Fatigue; Type 410 Stainless Steel Wire Fractured in Tension



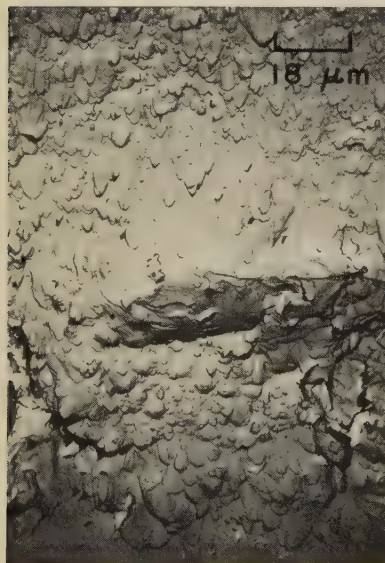
Light fractograph

10× Light fractograph

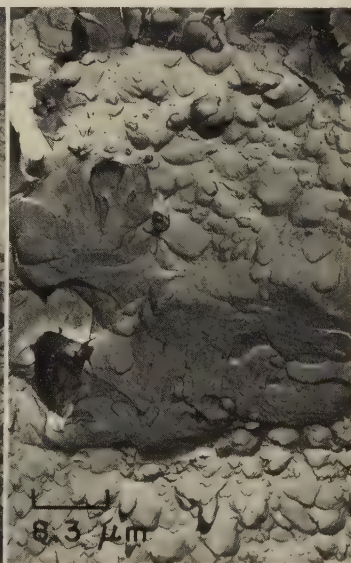
10× Light fractograph 2×

5095, 5096, 5097

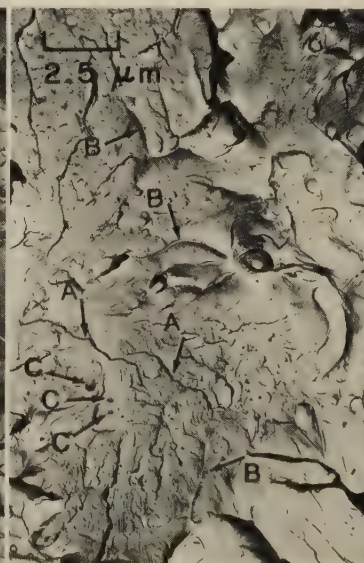
Surfaces of fatigue fractures in three automotive intake valves forged of Silcrome-1 steel (0.45% C, 3.25% Si, 8.5% Cr) and heat treated. At left (5095) is a transverse fracture in the stem of a valve with a hardness of Rockwell C 37. The stem rocked within the valve retainers, initiating many fatigue cracks around the periphery of the stem; these cracks later joined to form two main crack fronts. Very well-defined beach marks are visible in the fatigue zone at right. At center (5096) is a transverse fracture in the stem of a valve with a hardness of Rockwell C 38. The stem rotated in the valve retainers, which initiated many fatigue cracks around the periphery of the stem; these cracks penetrated nearly a third of the way to the center of the stem before uniting into a single circumferential crack front. At right (5097) is a fracture in the head of a valve with a hardness of Rockwell C 37. The fatigue-crack origin is at right, at the head-stem juncture. Note the peeled surface layer.



TEM fractograph (p-c replica) 550×
5098 View, at a shear lip, of a fracture surface of type 410 stainless steel wire that had been austenitized, quenched, tempered at 204 C (400 F), then broken in tension at room temperature. Shear dimples below quasicleavage area at center are less flat than those elsewhere. See also 5099.



TEM fractograph (p-c rep.) 1200×
5099 A view of the mating fracture surface to that shown in fractograph 5098 (at left), but at a different area of the shear lip, turned 180°, and at a higher magnification, clearly exhibiting a quasicleavage facet surrounded by shear dimples.

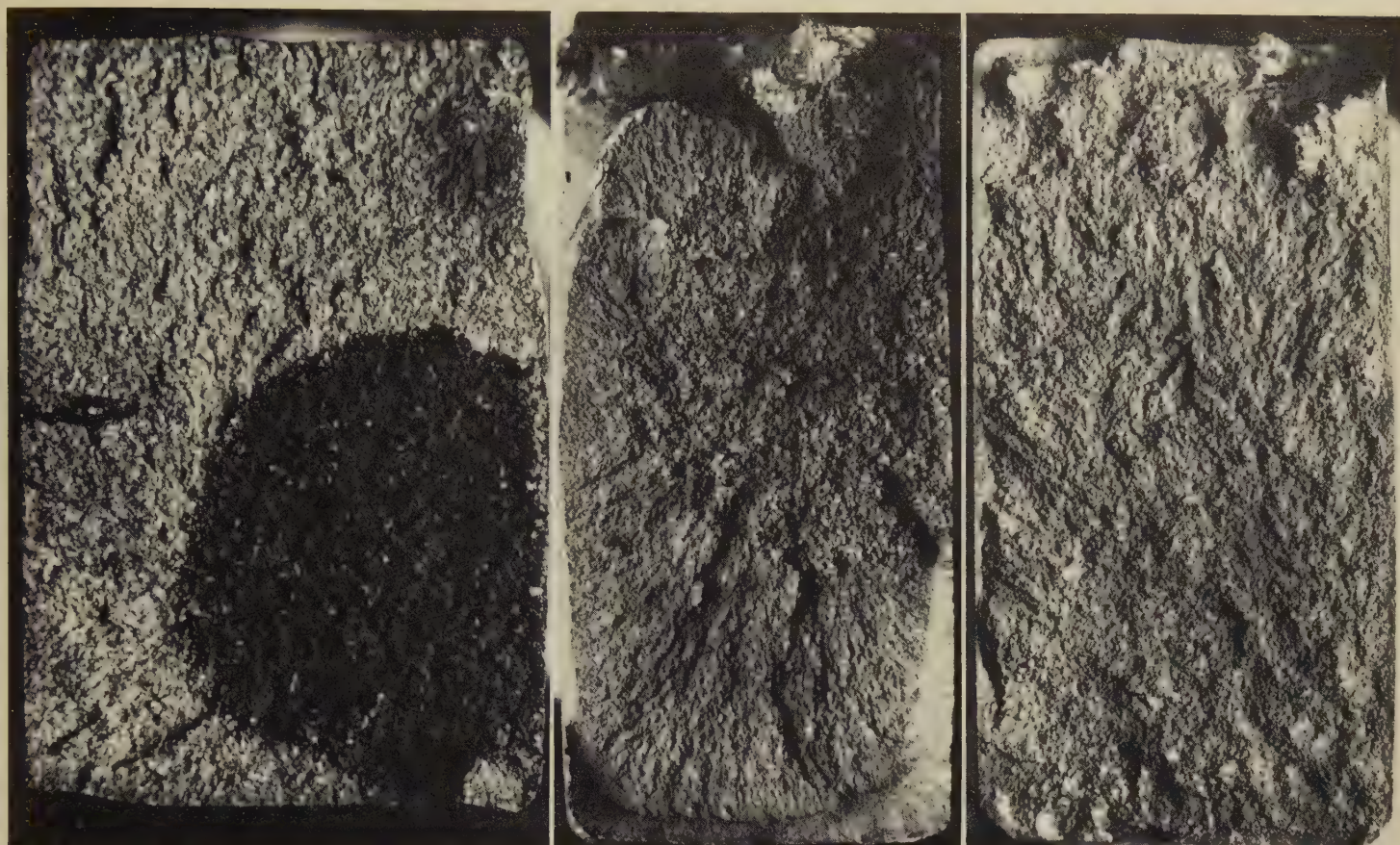


TEM fractograph (p-c replica) 4000×
5100 Quasicleavage facets in the surface of a fracture in type 410 stainless steel wire hardened, tempered, and then broken in tension at 10 C (50 F). Arrows A point to steps such as those found in true cleavage; arrows B, to tear ridges; arrows C, to tongues.



TEM fractograph (p-c replica) 750×
5101 Quasicleavage facets in the surface of a fracture in type 410 stainless steel wire that had been air cooled from 954 C (1750 F), tempered 2 hr at 510 C (950 F), notched, then broken in tension at room temperature. A few dimples are present also.

Failure-Analysis Fractographs: Type 410 Stainless Steel Conveyor-Chain Links in Which Fractures Were Initiated by Heat-Treat Cracks



Light fractograph

8×

Light fractograph

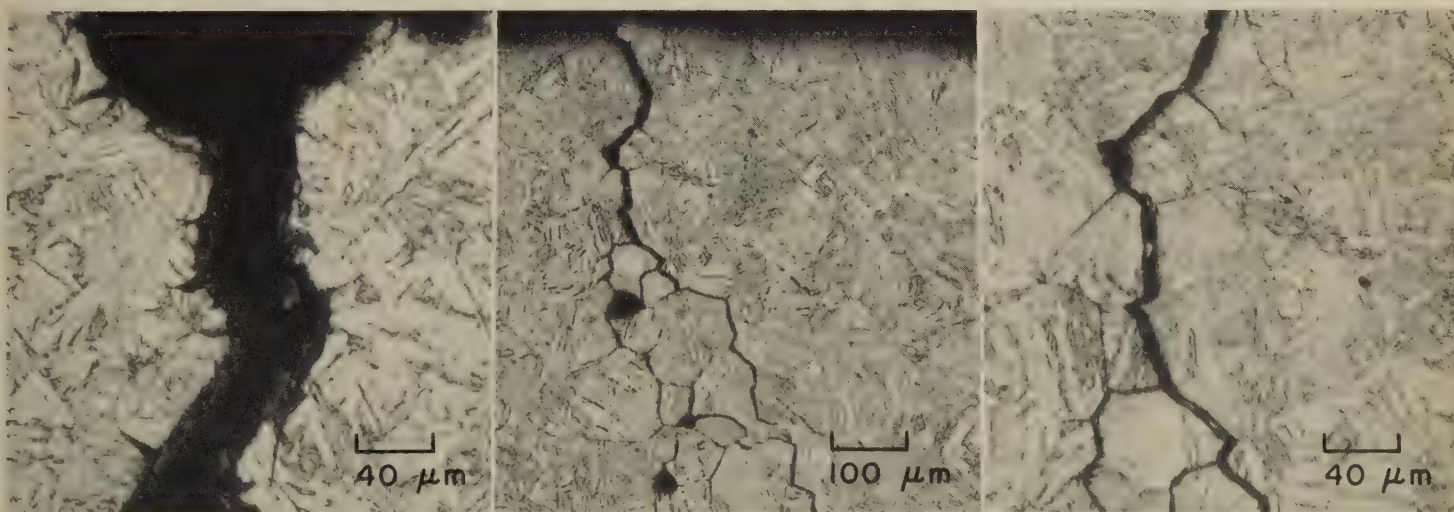
8×

Light fractograph

8×

5102, 5103, 5104

Surfaces of fractures in three type 410 stainless steel links of a conveyor chain used in a food-processing operation. Heat treatment of the links had included box annealing at 996 C (1825 F) for 1 hr, oil quenching, and tempering between 260 and 371 C (500 and 700 F) for 2 hr. Measured hardness was Rockwell C 37 to 44. Service conditions included cleaning in water containing 2 ppm of chlorine at 70 C (158 F), cleaning in saturated steam at 120 C (248 F), cleaning in air at 120 C (248 F), and water cooling at 20 to 32 C (68 to 90 F). At left (5102) is the dark, oxidized surface of a heat-treat crack; the remainder of the fracture surface is brittle and shows no shear lip. At center (5103) is a heat-treat crack (at top edge) and a shear lip (at bottom edge), with fast fracture between them. At right (5104) is a very small heat-treat crack (right side of top edge) and portions of a shear lip (at left edge and at top edge left of crack). See also micrographs 5105 through 5107 (below).



Micrograph (super picral)

250×

Micrograph (super picral)

100×

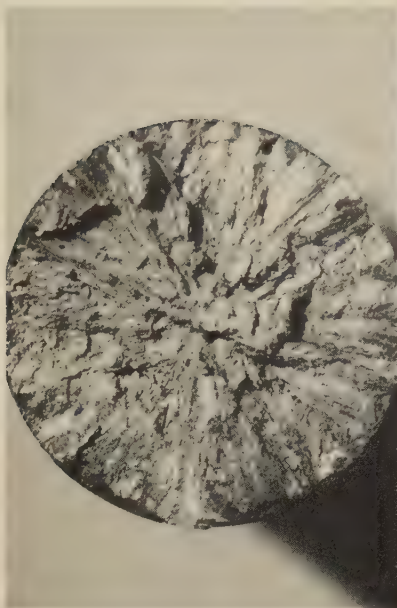
Micrograph (super picral)

250×

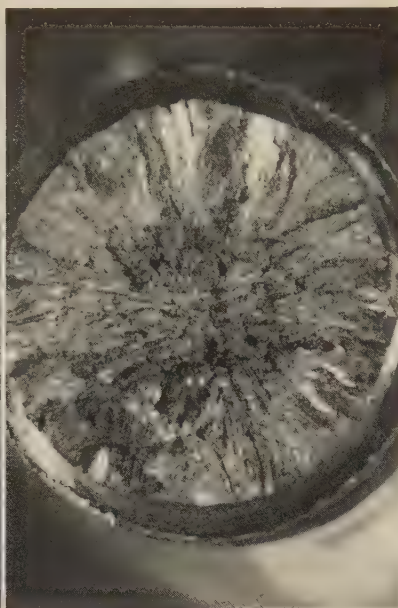
5105, 5106, 5107

Polished and etched sections through secondary heat-treat cracks branching from the primary fractures in the conveyor-chain links in 5102 and 5104 (above), showing the intergranular nature of the cracks. At left (5105) is a crack in the link in 5102. Note that the surfaces of this crack have oxide coatings; the short cracks branching from it were oxide induced. At center (5106) and at right (5107) are views, at different magnifications, of a secondary crack in the link shown in 5104. Again, oxide is present within the crack, as can be seen somewhat obscurely in 5107. Note that this crack has branched to connect with nonmetallic inclusions. It is evident, from the presence of oxide on all crack surfaces, that both primary and secondary heat-treat cracks formed before the links were oil quenched from the annealing temperature.

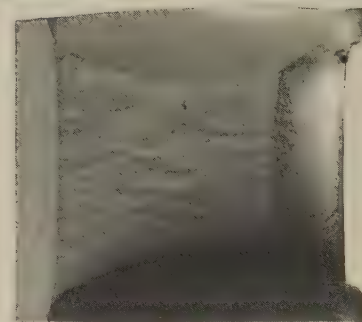
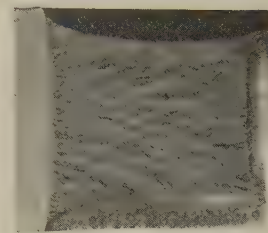
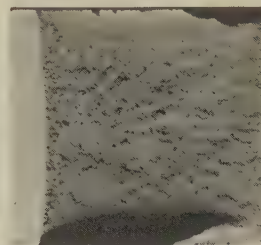
Failure-Analysis Fractographs: Fractures in Cast Austenitic Steel Valves;
Fractures in 13-8 PH Stainless Steel; Fatigue Fracture in 15-5 PH Stainless Steel



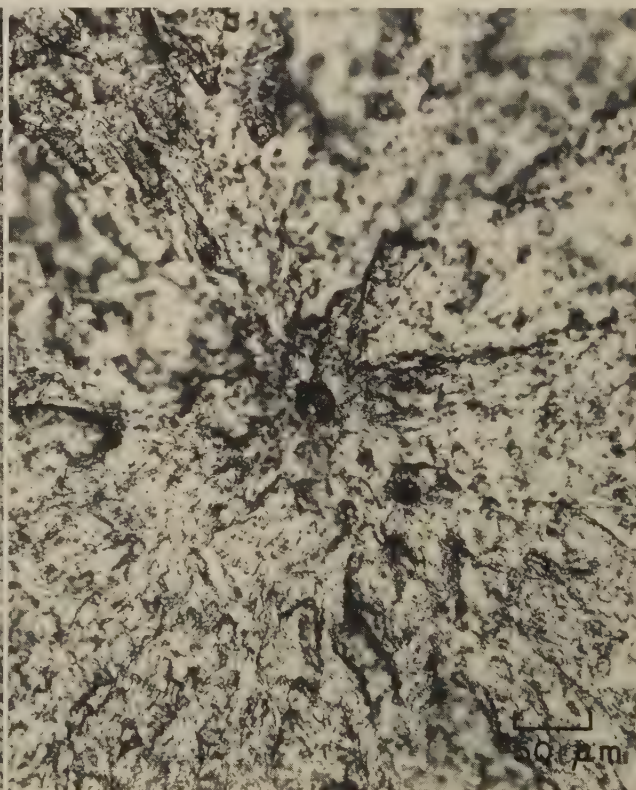
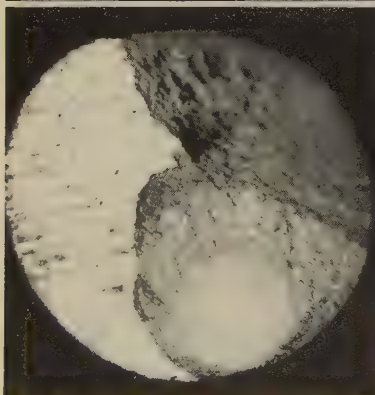
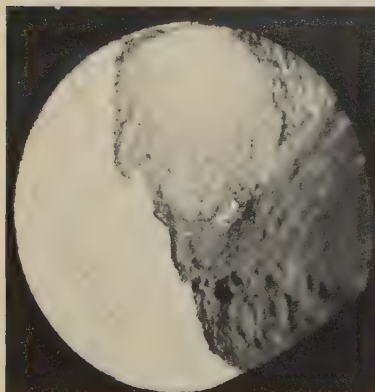
Light fractograph 7×
5108 Surface of a fracture in the stem of an automotive valve cast of austenitic steel (0.85 C, 2.5 Si, 16.5 Cr, 14.5 Ni, 1.0 max Mo, 1.0 max Cu, 3.0 max Co). Note woody appearance, which is characteristic of fractures in castings.



Light fractograph 7×
5109 Surface of a fracture in the stem of an automotive valve that was cast of the same austenitic steel as in fractograph 5108. The hardness of the valve was Rockwell A 59. Note the shrinkage porosity and dendrites at center.



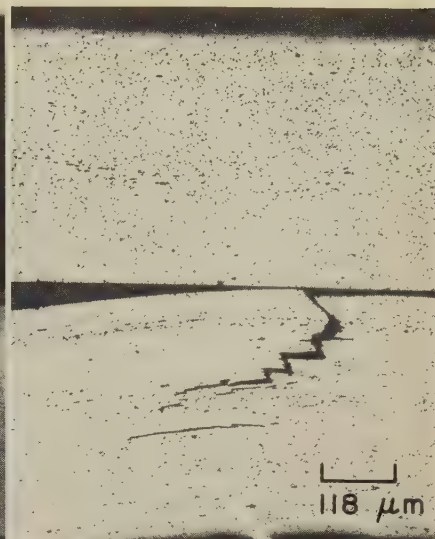
Light fractographs All at about 1 1/3×
5110, 5111, 5112 Fractures in three 13-8 PH stainless steel fracture-toughness specimens aged 4 hr at 538 C (1000 F) to a yield strength of 1379 MPa (200 ksi). Specimens in 5110 and 5111 (from 10-in.-square stock), at top, and specimen in 5112 (from 6-in.-square stock), at bottom, had K_{Ic} of 120 and >142 MPa·m^{1/2} (109 and >129 ksi·in.^{1/2}), respectively.



Light fractographs
5113, 5114, 5115, 5116

8× Light fractograph 80× Light fractograph 200×
At left (5113 at top, 5114 at bottom) are the mating fatigue-fracture surfaces of a specimen of 15-5 PH stainless steel heat treated to a yield strength of 1103 MPa (160 ksi). The specimen was tested in tension ($R=0.1$) to a maximum stress of 896 MPa (130 ksi); fracture occurred after 8.7 million cycles. At left in each view is a light area containing grinding marks, where a jagged portion of the region of final, fast fracture was removed to facilitate photography. The fatigue crack originated at the center of the light, circular zone visible in each fracture surface. Fractographs 5115 (center) and 5116 (right) are higher-magnification views of the fracture surface in fractograph 5114. These views show that the fatigue crack originated at an inclusion.

Failure-Analysis Fractographs of Fractures in Stainless Steels: Type 302 Spring (Fatigue);
Type 304 Sheet Tensile-Test Specimen; Type 330 Welded Fan Blade (Fatigue)



Photograph

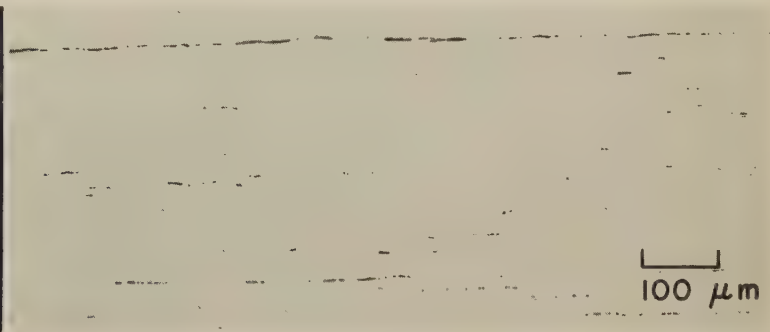
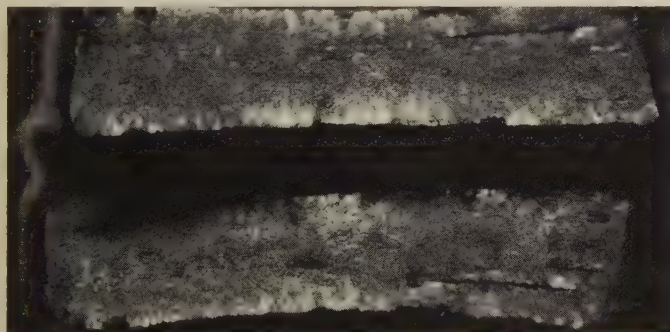
5117, 5118, 5119

About 3× Light fractograph

7× Micrograph

80×

At left (5117) is a view of a broken spiral instrument spring of cold worked type 302 stainless steel flat wire. Hardness at the surface was Rockwell C 45; internal hardness was Rockwell C 53. All fractures in the spring originated at outer, or tension, surfaces. The initial fracture, which was by fatigue and which occurred at the first or second innermost turn, placed point-contact pressure on the adjacent turn, which then broke, producing consecutive fractures in the remaining turns. At center (5118) are two surfaces of the spring — a tension surface (top) and a compression surface (bottom). The tension surface shows vertical ripple marks (which are superficial and can be removed by light polishing), a fracture surface in profile at left, and an incipient fracture at right. The compression surface shows a fracture containing fatigue beach marks. At right (5119) are two polished and electrolytically etched (10% oxalic acid) sections through the spring — a transverse section (top), and a longitudinal section (bottom) showing centerline microcracks. No definite metallurgical cause of fracture was discovered; however, higher hardness in the interior than at the surface is very unusual, and the centerline microcracks may have been a contributing factor.



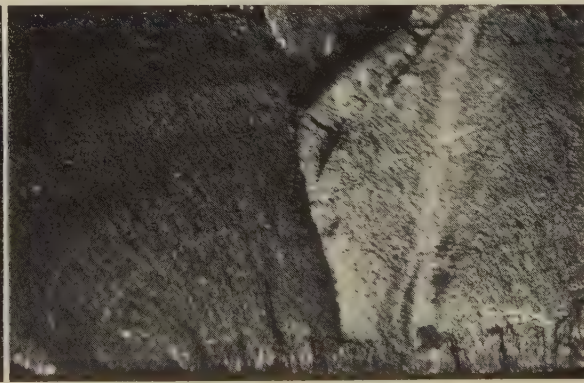
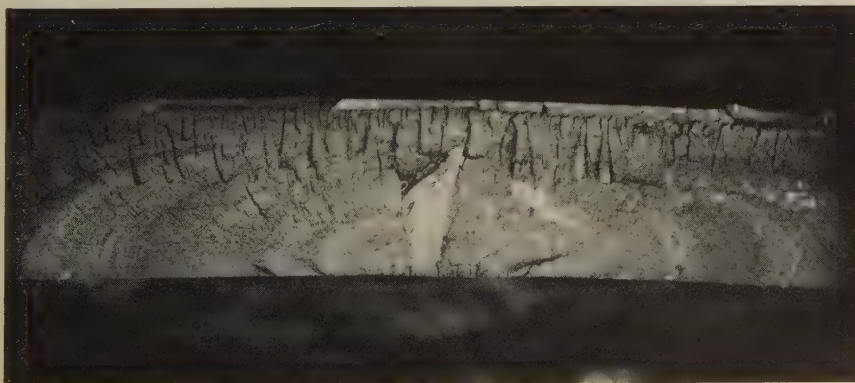
Light fractograph

5120, 5121

6× Micrograph (unetched)

100×

At left (5120) are the mating surfaces of a fracture in a transverse tensile-test specimen of annealed type 304 stainless steel sheet, showing longitudinal cracks. The cracks were attributed in part to laminations caused by severe forming and in part to the stringers of nonmetallic inclusions visible in the polished longitudinal section in 5121 (right).



Light fractograph

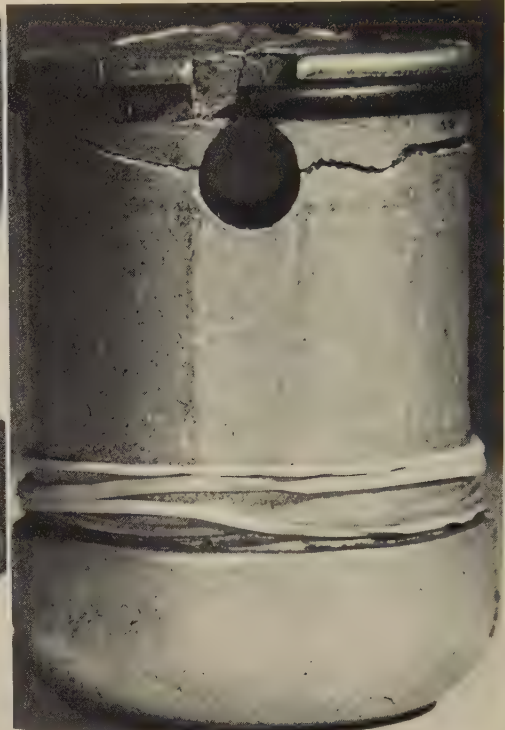
5122, 5123

3½× Light fractograph

12×

Views, at different magnifications, of the surface of a fatigue fracture in a welded fan blade of type 330 stainless steel. Clearly evident are beach marks typical of fatigue. Multiple fatigue cracks, which were initiated by columnar cracks in the weld area at the center of the bottom edge, penetrated a short distance into the blade before uniting to form a single crack front. The columnar cracks in the weld area were attributed to microfissures, which had resulted from improper welding practice.

Failure-Analysis Fractographs: Die Cast Aluminum Alloy 218 Housing of a Chain-Hoist Hook Fractured by Overload in Service



Photograph

About 1.1×

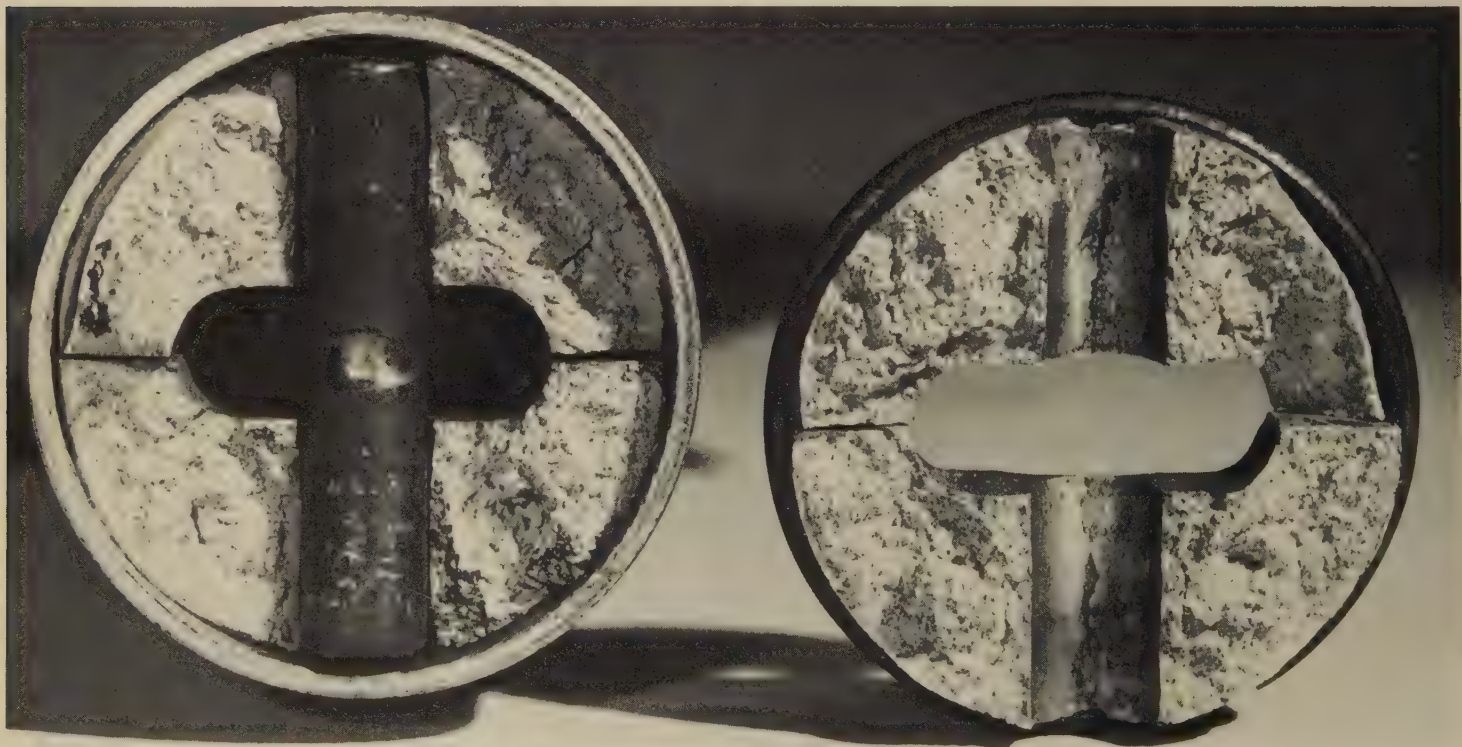
Photograph

1.7×

Photograph

2.4×

5124, 5125, 5126 Fractures in a die cast aluminum alloy 218 housing of a chain-hoist hook, which is believed to have broken by overload in service. At left (5124) is a view of the reassembled hook components, showing a transverse fracture (arrows) in the top surface of the housing. This fracture, which preceded and instigated final fracture of the housing, was above and parallel to a steel retaining pin (shown in 5126, at far right), which secured the hook to the hoist chain. At center (5125) is a side view of the housing, which consisted of two pieces held together by the retaining ring visible at top, showing the final fracture (roughly horizontal), the deformed retaining-pin hole (elongation of about 3% is indicated — a reasonable value for this alloy), and one end of the fracture in the top surface. See also fractographs 5127 (below) and 5128 (on facing page).



Light fractograph

About 2 3/4 ×

5127 Mating surfaces of the fracture in the side of the housing in 5125. At right is the upper surface, with the retaining ring (shown at top in 5125) still in place; visible in the bore of the retaining-pin hole is the fracture in the top surface of the housing (see 5124). At left is the lower surface, with the retaining pin in place inside a collar.



Light fractograph

5128 Enlarged view of the lower left portion of the top fracture surface (shown at right in 5127) of the broken die cast housing in 5124. Note gas cavities (at arrows), which are common interior features of satisfactory die castings. Bending of the retaining pin (see 5126) is believed to have occurred after the transverse fracture of the top surface of the housing caused relocation of the load-bearing points on the pin. Low-cycle fatigue would have been a likely cause of fracture, but no fatigue beach marks could be found.

7½×

Failure-Analysis Fractographs: Aluminum Alloy 2014-T6 Aircraft Main-Landing-Gear Wheel That Was Fractured by Fatigue



Photograph

5129, 5130

Hub portion of the outer half of a broken aircraft main-landing-gear wheel forged of aluminum alloy 2014-T6, which fractured by fatigue. The hardness of the wheel measured 133 Bhn (500-lb load). At left (5129) is a view showing the fracture surface. Beach marks at top identify two fatigue-crack origins (at arrows). A section (polished but unetched) through the origin at arrow "b" is shown in 5130 (right), with the fracture surface at top and the inner surface of the wheel at right. The fatigue crack began in the area at "o"; this area, and the area at "c", show evidence of intergranular surface corrosion. See 5131 (below), 5132 (facing page).

1/3x Micrograph

100x

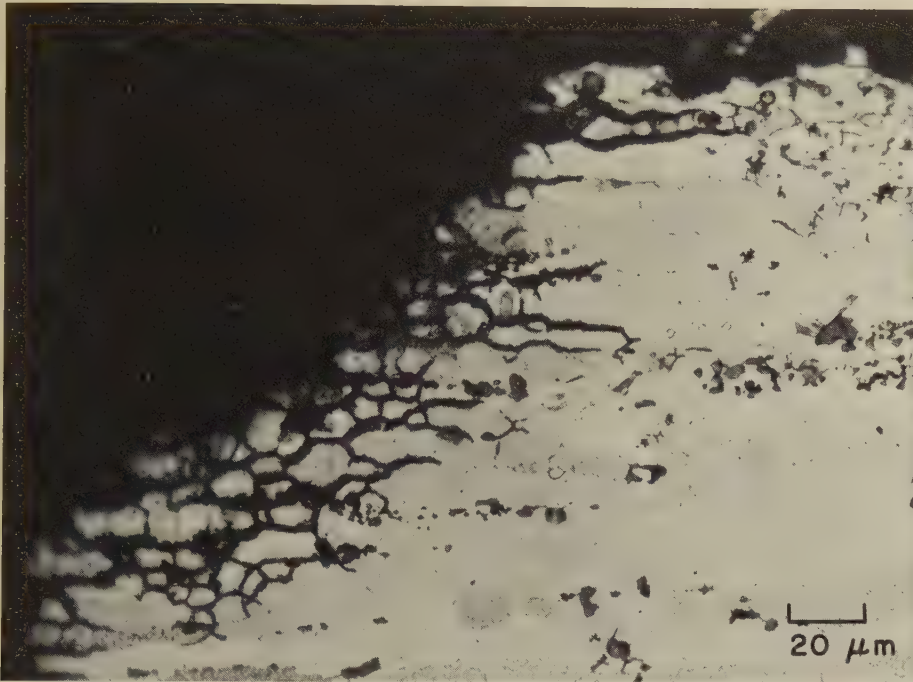


Light fractograph

5131

Higher-magnification view of the fractured main-landing-gear wheel half in 5129, showing the two fatigue-crack origins. The fatigue cracks penetrated almost the entire section before final, fast fracture occurred, producing shear lips. Beach marks emanating in both directions from each origin can be distinguished to the limits of this view. Numerous areas of corrosion damage were found on the inner surface of the wheel (not distinguishable here because of the angle of illumination), any of which could have caused stress concentration sufficiently severe to initiate a fatigue crack.

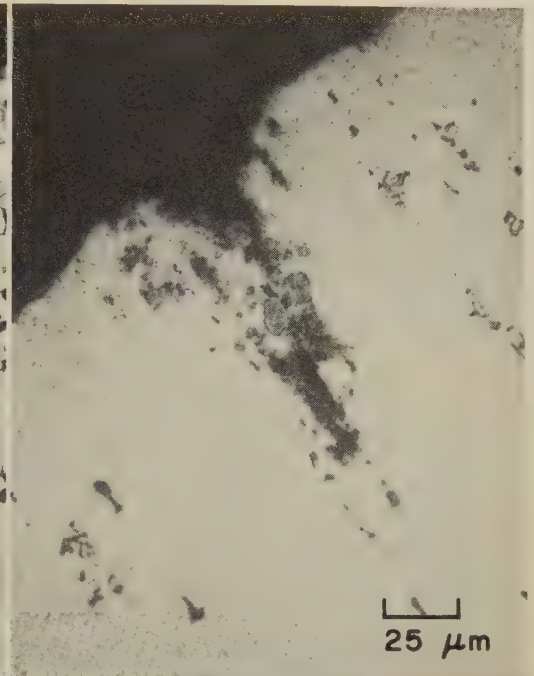
About 1 1/3x



Micrograph (Keller's reagent)

500×

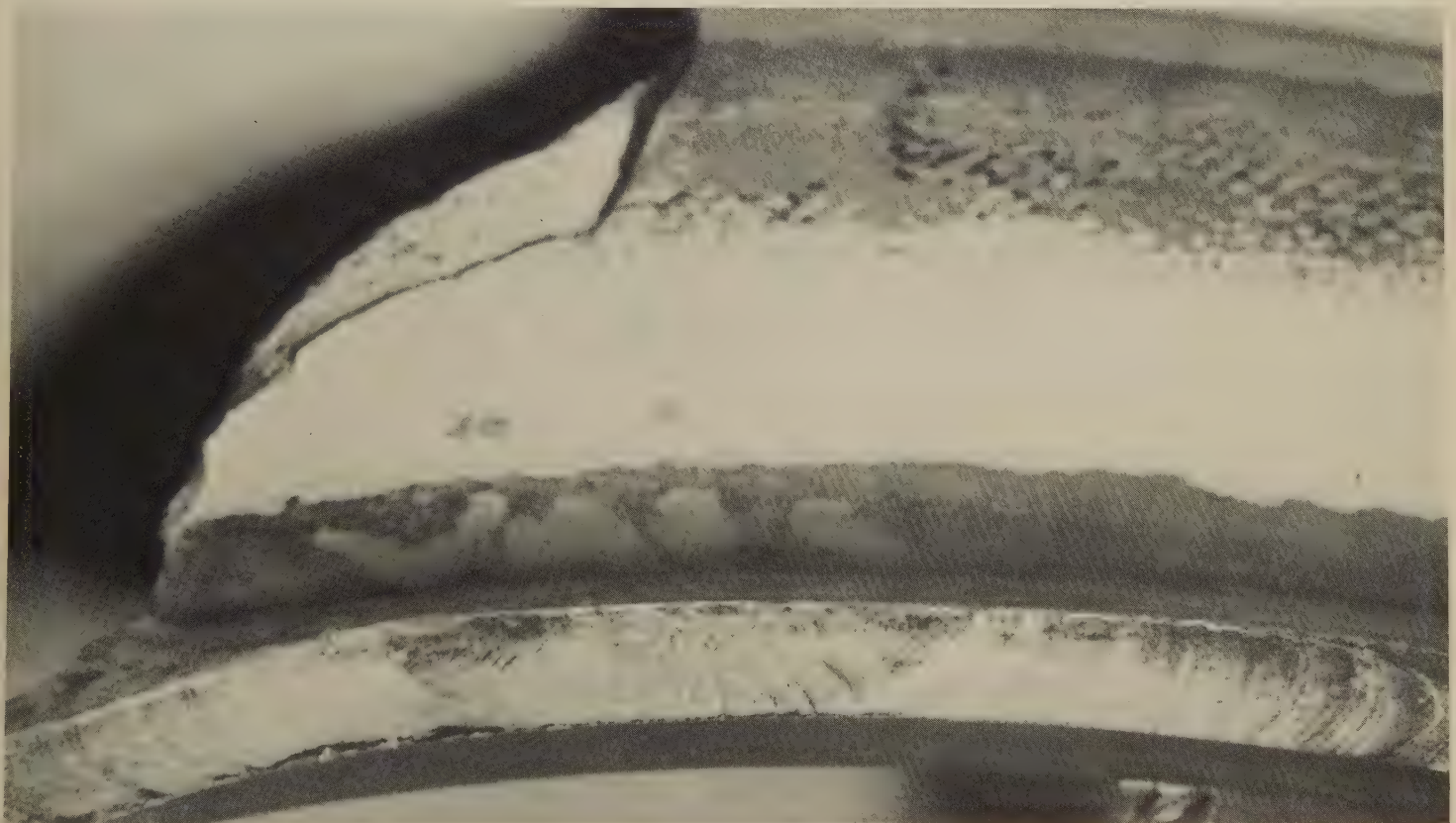
5132 Higher-magnification view of the area in 5130 marked "o", after etching, clearly showing that the corrosive attack of the inner surface of the wheel had produced intergranular cracks typical of those caused by stress corrosion. Such cracks are well-known sources of stress concentrations, which quite often result in the generation of fatigue cracks.



Micrograph (Keller's reagent)

400×

5133 A section through a fatigue fracture in an aluminum alloy 2014-T6 aircraft main-landing-gear wheel similar to that in 5129, showing a corrosion pit typical of several believed to have initiated the fracture.

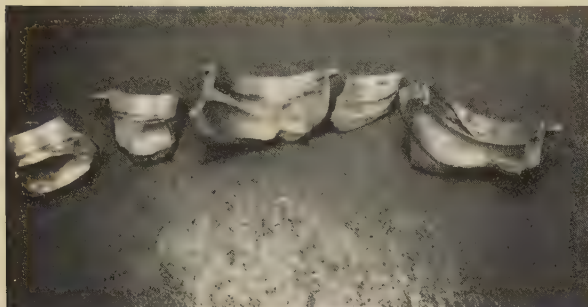


Light fractograph

2¼×

5134 A fragment of the flange portion of a broken half of a forged aluminum alloy 2014-T6 aircraft main-landing-gear wheel similar to that in 5129 (facing page), showing the nucleus of a fatigue fracture caused by corrosion pits similar to the pit shown in 5133 (above, at right). Beach marks are very clearly visible in the fatigue zone. The fracture propagated completely around the wheel in the tube-well area, separating the flange portion from the hub portion.

Failure-Analysis Fractographs: Aluminum Alloy 2014-T6 Aircraft Main-Landing-Gear Wheel-Half Hubs Fractured by Fatigue



Photograph

About $\frac{1}{10} \times$

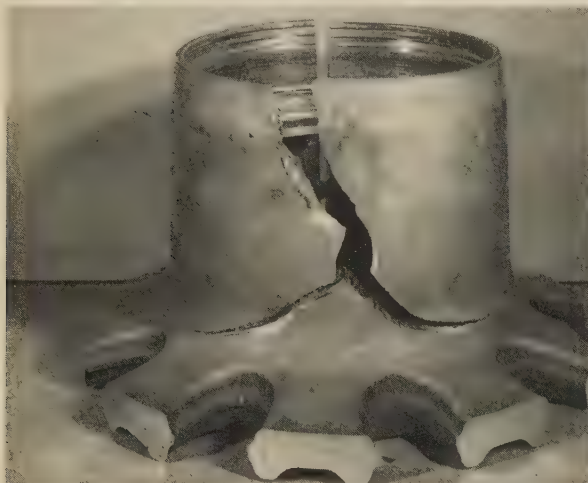
5135 Pieces of the hub of a forged aircraft main-landing-gear wheel half, which broke by fatigue. The material is aluminum alloy 2014-T6. Tensile specimens from elsewhere in the wheel had tensile strength of 493.7 MPa (71.6 ksi) and 8.9% elongation in the transverse direction, and tensile strength of 466.1 MPa (67.6 ksi) and 8.0% elongation in the longitudinal direction. See also 5136.



Light fractograph

1.8 \times

5136 View of an area of one fracture surface of the broken hub in 5135 (at left), showing the fatigue-crack origin. Visible are beach marks, which suggest that the origin is at the location marked by the arrow, presumably at one of several corrosion pits that were found on the surface of the hub. After having penetrated a short distance, the fatigue crack developed a step (dark facet); a second fatigue crack originated at one end of the step.



Photograph

About $\frac{1}{8} \times$

Light fractograph

Actual size

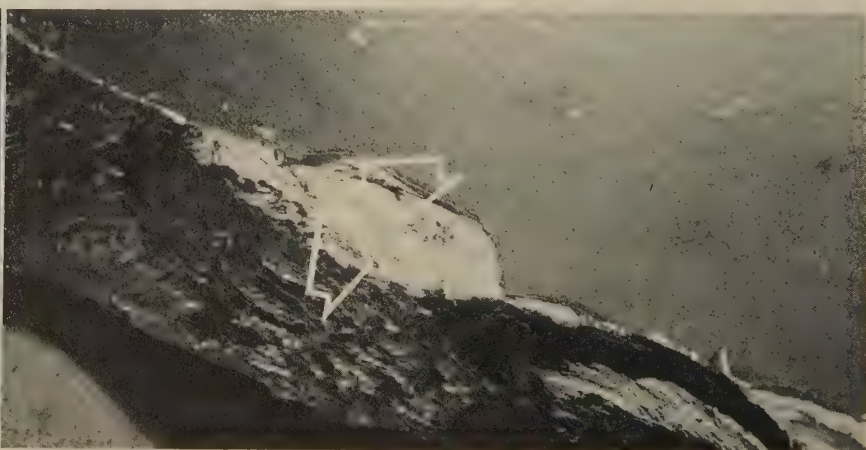
5137, 5138 At left (5137) is the hub of a forged aluminum alloy 2014-T6 aircraft main-landing-gear wheel half, which broke in fatigue. A tensile specimen machined from the hub had tensile strength of 499.2 MPa (72.4 ksi), 12.1% elongation, and hardness of 143 to 150 Bhn, which are acceptable. The fatigue crack originated at the inside surface of the hub. At right (5138) is a fracture surface of the broken hub, showing the fatigue-crack origin. Clearly visible are beach marks, which indicate that the fracture began as a radial fatigue crack, in a plane containing the axis of the wheel. Later, the crack turned to form a circumferential separation between the hub and web of the wheel half, as shown in 5137. See also fractographs 5139 and 5140, below.



Light fractograph

About 5 \times

5139 Enlarged view of the fatigue-crack origin in 5138, which plainly shows the region of initial penetration (light area). At arrow is a forging defect usually known as a bright flake. Note that grain flow is approximately parallel to the flake.

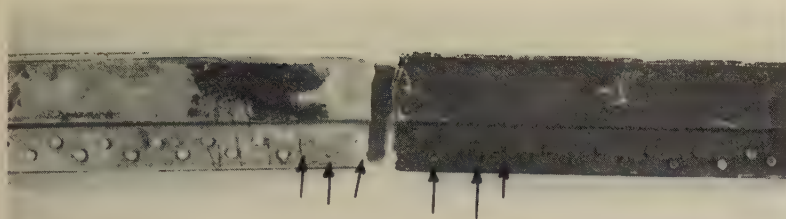


Light fractograph

Actual size

5140 A fracture surface of the broken hub in 5137, showing an area of the circumferential separation between the hub and web. Bright flakes, similar to the defect that initiated the fatigue crack in 5139, are visible at the arrows. These defects have been attributed to hydrogen damage.

Failure-Analysis Fractographs: Aluminum Alloy 2014-T6 Aircraft Wing-Spar Bottom Cap Fractured by Fatigue



Photograph

1/4 ×

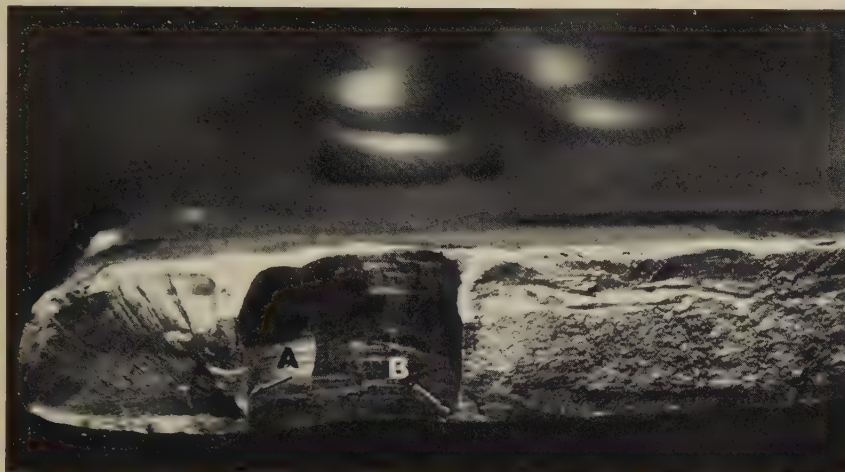
5141 Top surface of an extruded aluminum alloy 2014-T6 bottom cap of an aircraft wing spar, showing a fatigue fracture, at center, which intersected one of the rivet holes indicated by the arrows. Hardness tests near the fracture gave an average value of Rockwell B 85, which is acceptable. See also 5142 through 5146.



Light fractograph

1 1/8 ×

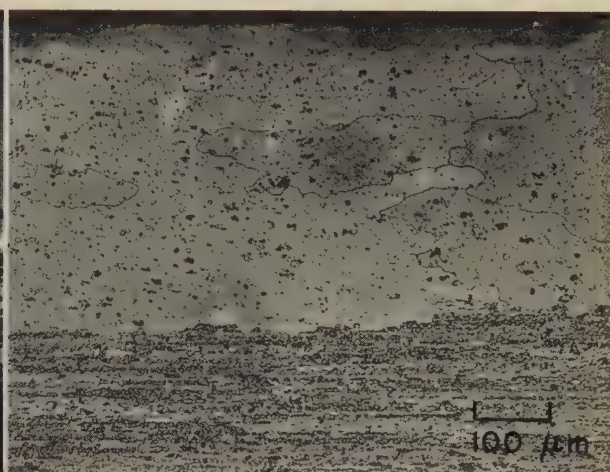
5142 A view of the fracture surface at left in 5141. The rivet hole intersected by the fracture is abnormal, consisting of two overlapping holes (see 5143). Beach marks, which are clearly visible, indicate that the fatigue crack began at the double-drilled rivet hole.



Light fractograph

5 ×

5143 A higher-magnification view of the rivet-hole area of the fracture surface shown in fractograph 5142. The double-drilled nature of the rivet hole is shown quite clearly here. Two fatigue cracks originated at this hole — one beginning at arrow A and growing to the left, and the other beginning at arrow B and growing to the right.



Micrograph (Keller's reagent)

100 ×

5144 Polished and etched section through the cap in 5141. At bottom is a fibrous interior structure typical of aluminum alloy extrusions. At top is one of the coarse-grained, recrystallized layers, 0.018 to 0.037 in. thick, at the top and bottom surfaces of the cap.



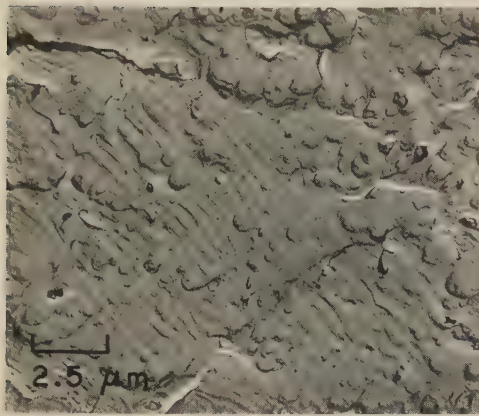
Photograph

5 ×

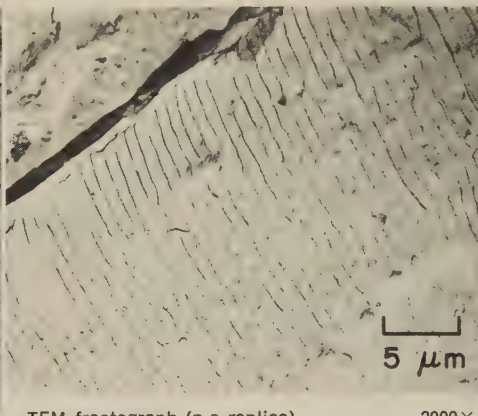
Photograph

5 ×

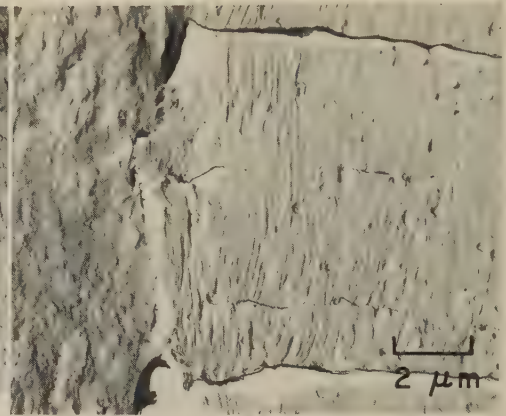
5145, 5146 Views of the top surface (5145, left) and bottom surface (5146, right) of the wing-spar cap in 5141, with the mating fracture surfaces fitted together. The segment at right in each view was deformed after fracture, causing the gap. The double drilling of the rivet hole, noted in 5142 and 5143, is clearly shown (arrows). The edge distance, "e", was measured for each hole (as shown in 5146 for the hole closer to the edge). Edge distance for the hole farther from the edge is about 5/16 in. — the minimum allowed for rivets of the size used here (5/32 in. diam). For the closer hole, edge distance is about 75% of the minimum value, which increased the stresses in that section to excessive levels.



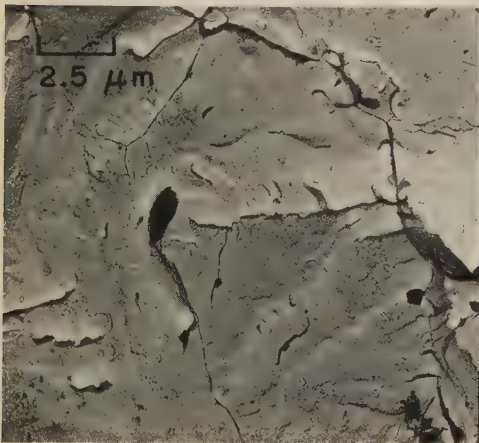
TEM fractograph (p-c replica) 4000×
5147 Surface of a fracture in a specimen of aluminum alloy 2024, showing tear dimples, resulting from microvoid coalescence, scattered among somewhat irregular fatigue striations.



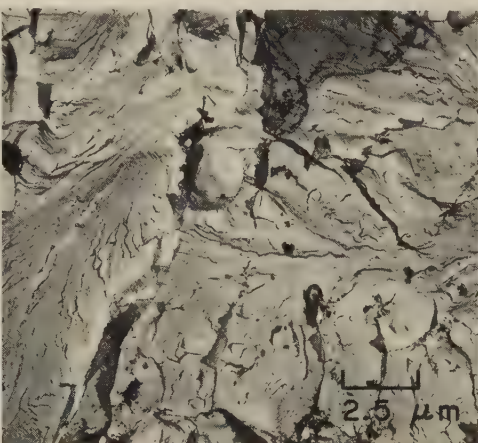
TEM fractograph (p-c replica) 2000×
5148 Surface of a fracture in a fracture-toughness specimen of aluminum alloy 2024-T851, showing a portion of the precrack area, which contains evenly spaced, gently curved tension-tension fatigue striations.



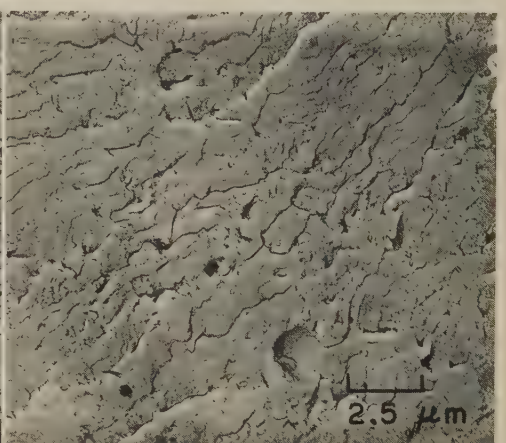
TEM fractograph (p-c replica) 5000×
5149 Surface of a fracture in a specimen of aluminum alloy 2024-T3 fatigue tested alternately *in vacuo* and in air. The nondescript surface at left formed *in vacuo*; conventional striations at right, in air.



TEM fractograph (p-c replica) 4000×
5150 Surface of an intergranular fracture in aluminum alloy 2024-T3 caused by attack by liquid amalgam under minimal tensile stress. This type of attack can lead to very rapid fracture.



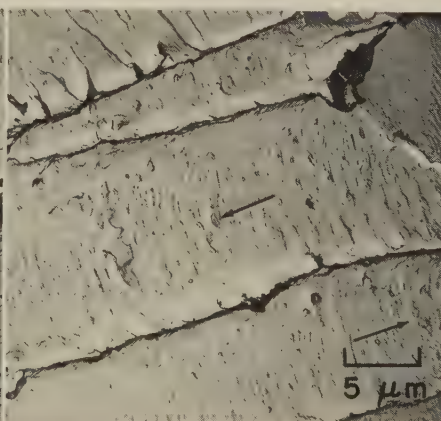
TEM fractograph (p-c replica) 4000×
5151 Surface of a transgranular fracture in aluminum alloy 2024-T3 that was induced by liquid amalgam as in fractograph 5150. The distinct river patterns visible here suggest some form of cleavage.



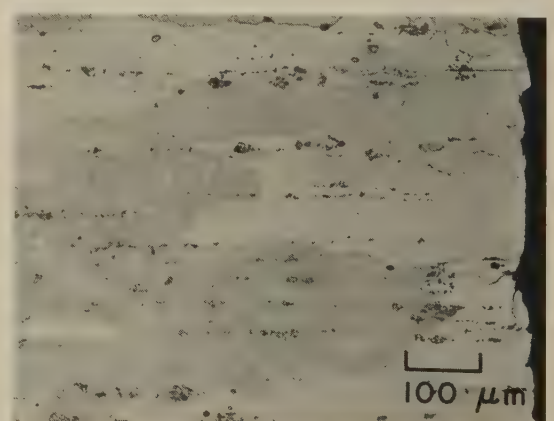
TEM fractograph (p-c replica) 4000×
5152 Surface of a transgranular fracture in plate of aluminum alloy 2024-T3, induced by liquid amalgam as in 5150 and 5151. Visible here are features suggestive of cleavage, but no river patterns.



TEM fractograph (p-c replica) 2000×
5153 Tension-tension fatigue fracture in plate of aluminum alloy 2020-T651, which was stressed in the range of 14 to 34 MPa (2 to 5 ksi) at 36,000 cycles per minute. Fatigue striations interspersed with tear dimples.

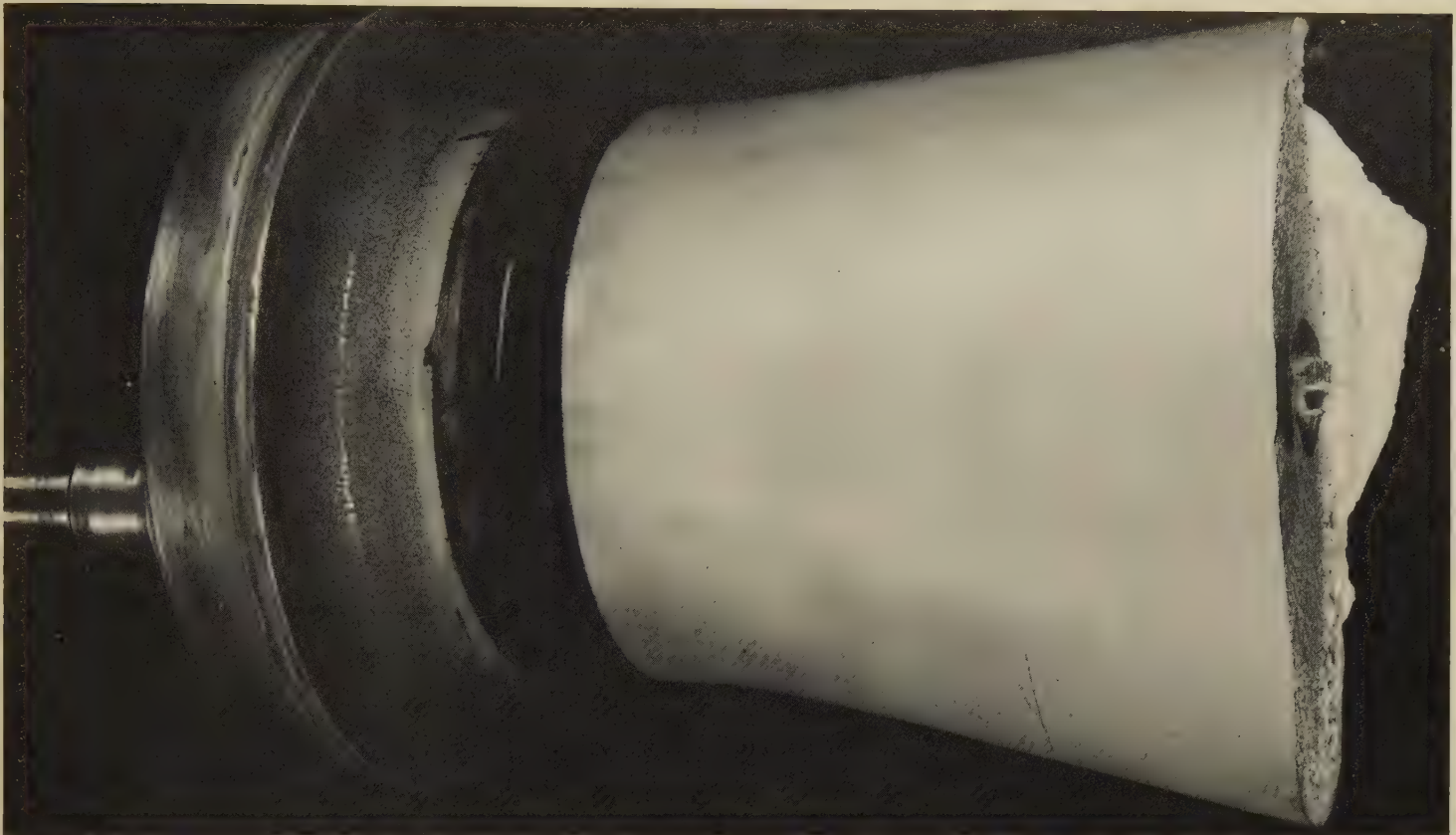


TEM fractograph (p-c replica) 2000×
5154 Surface of a tension-tension fatigue fracture in a second specimen from the same plate as in 5153, showing several patches of rather vague striations, and tongue-shaped intrusions (at arrows) along some striations.



Micrograph (Keller's reagent) 100×
5155 A polished and etched section through the fatigue-fractured aluminum alloy 2025-T6 propeller blade shown in 5156 and 5157 (on the opposite page). This fracture is transgranular, as demonstrated by the profile of the fracture surface, at right.

Failure-Analysis Fractographs: Aluminum Alloy 2025-T6 Aircraft Propeller Blade
Fractured by Fatigue (Continued)



Photograph

Actual size

5156 A view of the shank end of a fractured aircraft propeller blade fabricated of aluminum alloy 2025-T6. The blade broke by fatigue, which originated at an interior cavity that was provided to contain a balance weight comprised of compacted lead wool. Chemical analysis established that the blade was within specified composition limits. Hardness measurements (500-kg load) yielded an average value of 107 Bhn, which was above the required minimum of 100 Bhn. See also 5155 (facing page) and 5157 (below).

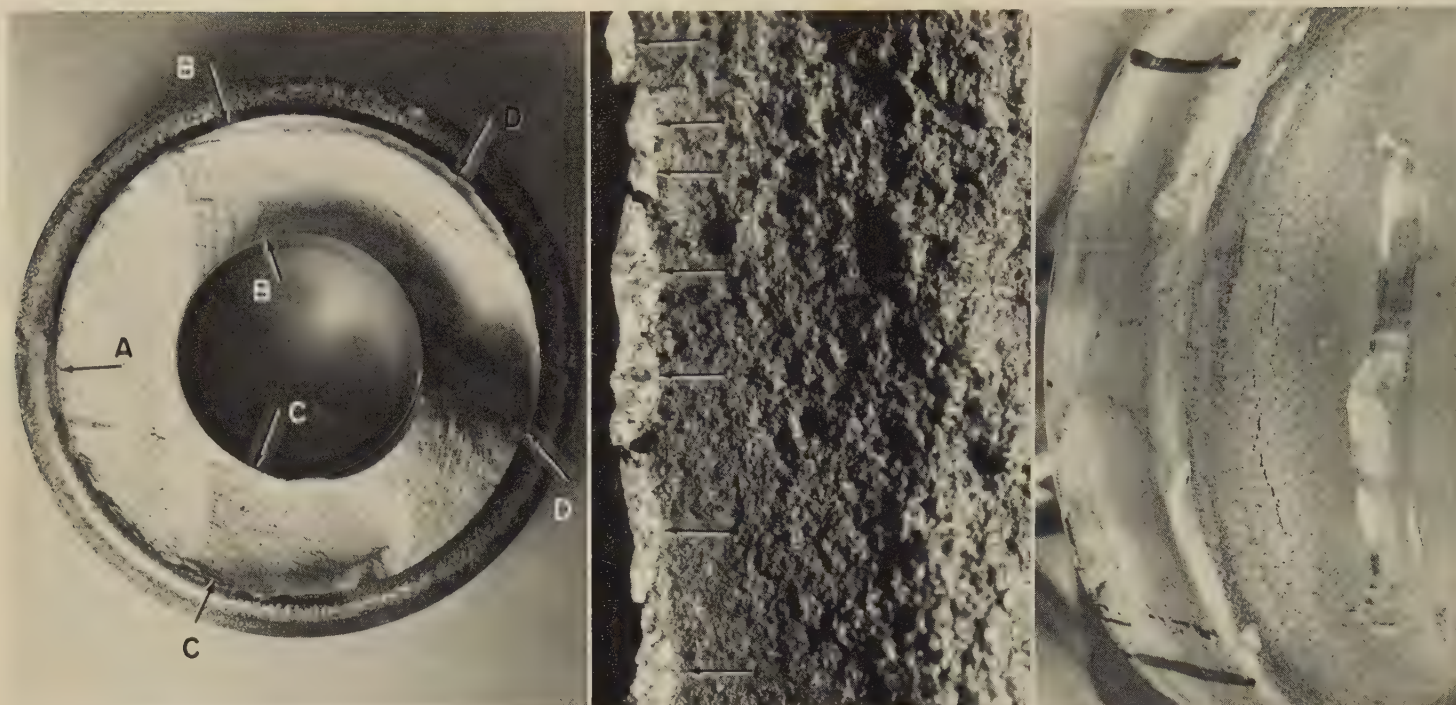


Light fractograph

134X

5157 Fracture surface of the shank end of the broken aircraft propeller blade in 5156. The balance-weight cavity is visible at center, with the fatigue-crack origin at the upper edge (arrow). The fracture originated at the beginning of the radius that formed one end of the cavity. Examination of the cavity surface revealed severe roughness caused by tool marks and by corrosion pits. The combined effect of these tool marks and corrosion pits was considered to be the cause of crack initiation.

Failure-Analysis Fractographs: Aluminum Alloy 2025-T6 Aircraft Propeller Blade Fractured by Fatigue



Light fractograph

3/4×

Light fractograph

20×

Photograph

Actual size

5158, 5159, 5160

At left (5158) is the surface of a fatigue fracture near the hub of an aluminum alloy 2025-T6 aircraft propeller blade. The fracture originated in a shot peened fillet. Small fatigue cracks joined to form the main crack at A, which propagated to B-B and C-C before final, fast fracture occurred. At center (5159) is a portion of the outside edge of the fracture surface in 5158, between the arrows marked D, showing small, distinct fatigue cracks (at arrows) that had been present before final, fast fracture. At right (5160) is a view of the shot peened fillet of a companion propeller blade, showing small fatigue cracks. Depth of the cold worked layer produced by shot peening was nonuniform and averaged about 0.0015 in., instead of the stipulated 0.0055 in. minimum, which afforded inadequate surface fatigue strength. See also 5161 through 5163 (below).



Macrograph

20×

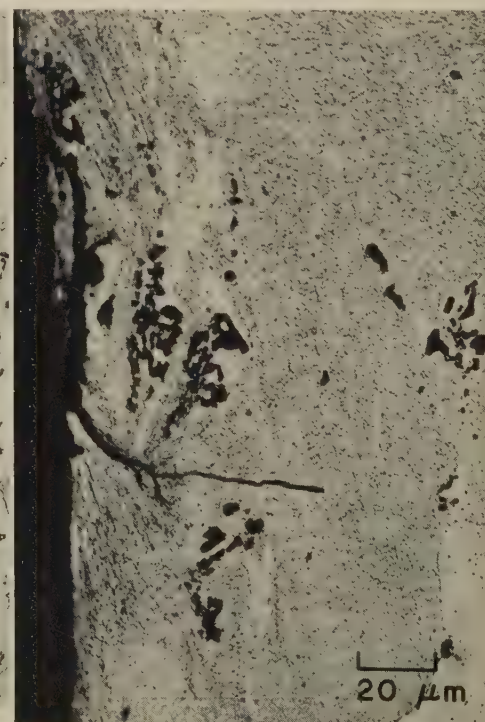
5161 Surface of the shot peened fillet of another companion propeller blade to that in fractograph 5158, showing the same type of fatigue cracks as those in the propeller blade in 5160. These cracks were present in large numbers in the fillet area.



Micrograph (Keller's reagent)

100×

5162 A polished and etched section through the shot peened fillet of the fractured blade in 5158, showing two small fatigue cracks pulled open and blunted by plastic deformation. Note slip bands, which indicate that a slight amount of plastic flow occurred near cracks.

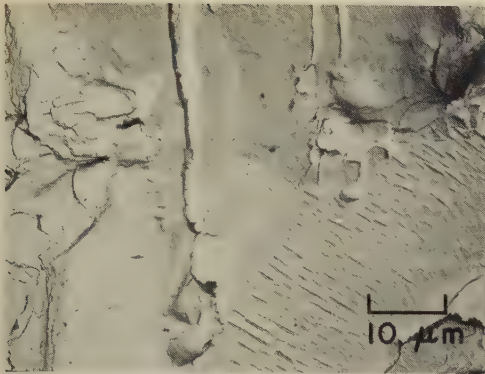


Micrograph (Keller's reagent)

500×

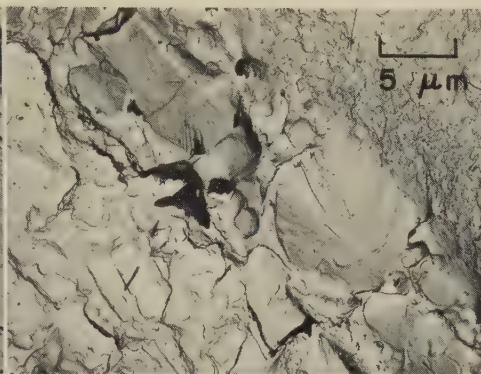
5163 Another polished and etched section through the shot peened fillet of the fractured blade in 5158, showing a fatigue crack that grew from a surface flaw. The structure indicates that only very superficial shot peening occurred here.

Failure-Analysis Fractographs of Aluminum Alloys: 6061-T6 (Fatigue); 7075-T6 (Tension Overload); 7079-T6 Bogie Beam (Stress-Corrosion Cracking)



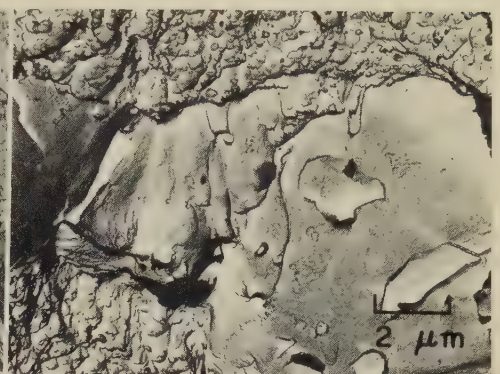
TEM fractograph (p-c replica) 1000×

5164 Surface of a fatigue fracture in aluminum alloy 6061-T6. Fissures or secondary cracks with a spacing of $1\text{ }\mu\text{m}$ are superimposed on low-amplitude fatigue striations with a spacing of $0.15\text{ }\mu\text{m}$.



TEM fractograph (p-c replica) 2000×

5165 Tension-overload fracture surface of a 1-in.-thick plate of aluminum alloy 7075-T6, showing very fine dimples, together with cleavage facets of several large intermetallic particles.



TEM fractograph (p-c replica) 5000×

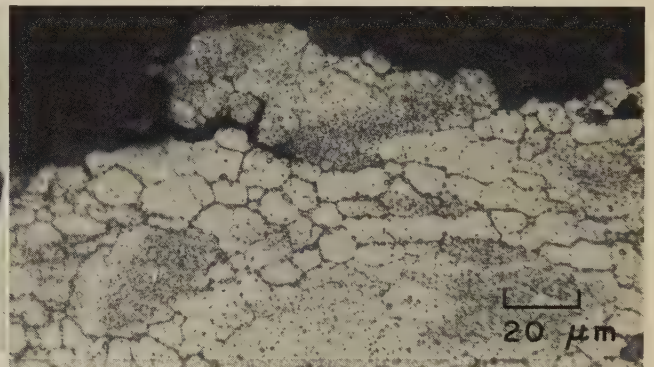
5166 Surface of a tension-overload fracture in an aircraft component of aluminum alloy 7075-T6, exhibiting a large region of stretching that contains several intermetallic particles.



Photograph

$\frac{1}{4}\times$

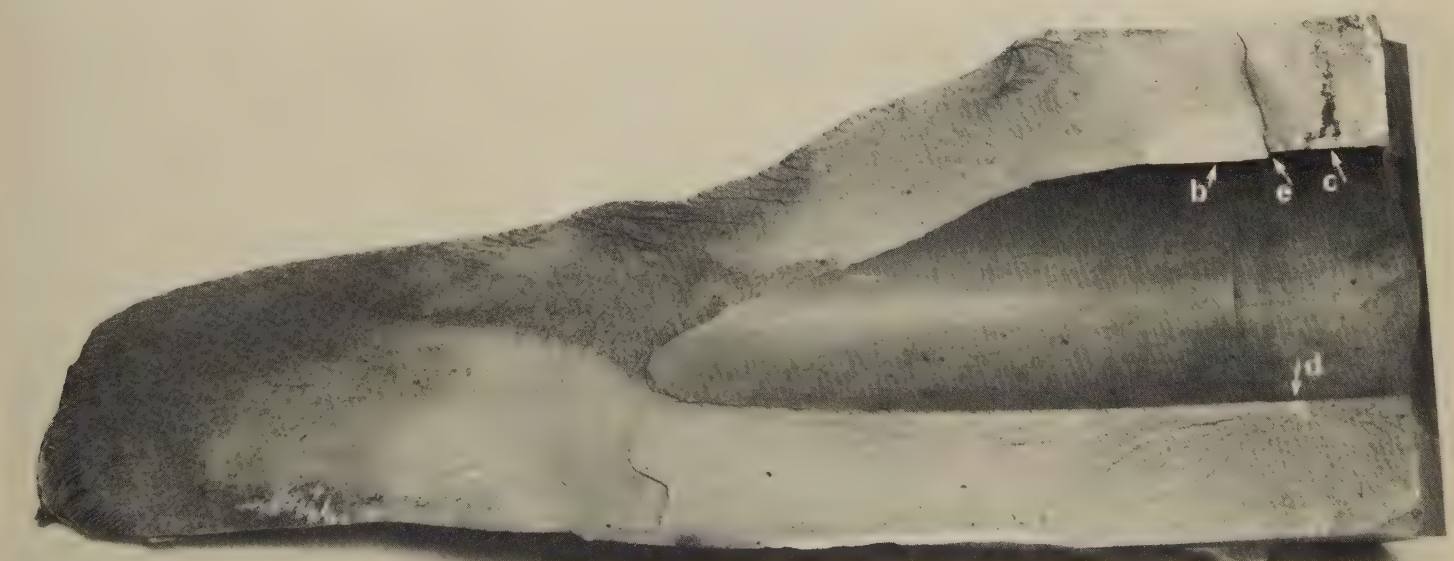
5167 A side view of a piece of a fractured aluminum alloy 7079-T6 bogie beam of an aircraft main landing gear. The fracture surface is at top, in profile. The very straight edge at lower right is a saw cut that was made to separate the fracture area from the remainder of the beam to facilitate inspection. Hardness of the beam was Rockwell B 84. See also micrograph 5168 (right) and fractograph 5169 (below).



Micrograph (Keller's reagent)

500×

5168 Polished and etched section through the light region at arrow "d" in 5169 (below). At top in this view is the profile of the fracture surface. Note that the fracture usually followed grain boundaries. Cracks branching from the fracture surface are evident also.



Light fractograph

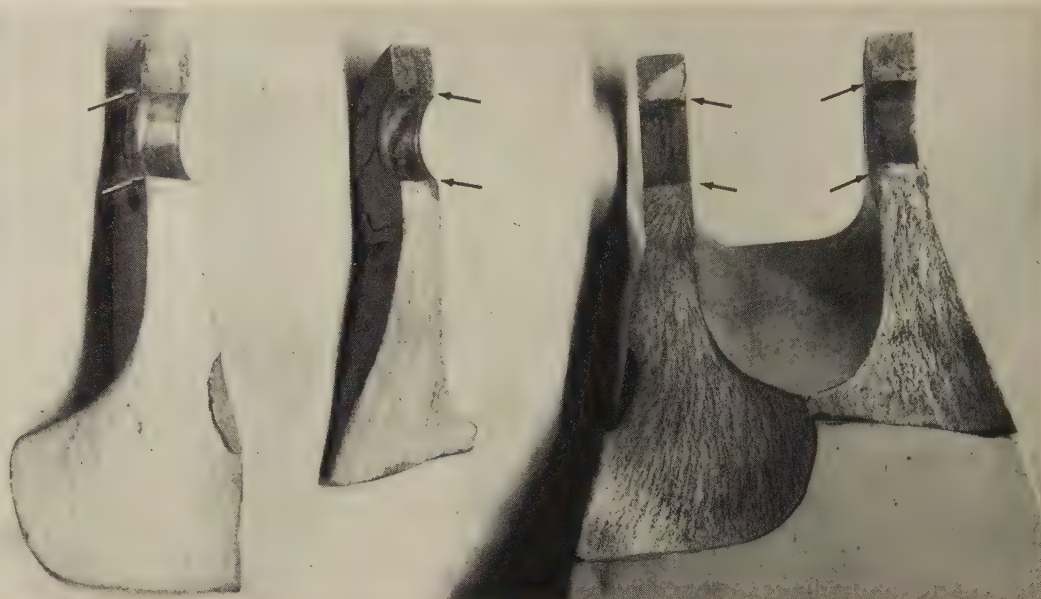
About $0.4\times$

5169 Surface of the fracture in the bogie beam shown in 5167 (above, left). Three stress-corrosion cracks caused the final, fast fracture, which was a tearing type of rupture. The intergranular attack characteristic of stress corrosion is shown in 5168 (above). The three stress-corrosion cracks are the light areas marked by arrows "b", "c" and "d". The crack surfaces appear flat but contain many small steps. Some of these steps were found to have been pulled away from the fracture surface in a leaf fashion, indicating overlapping or branching cracks. At arrow "e" is a pronounced step, which hides a portion of area "b".

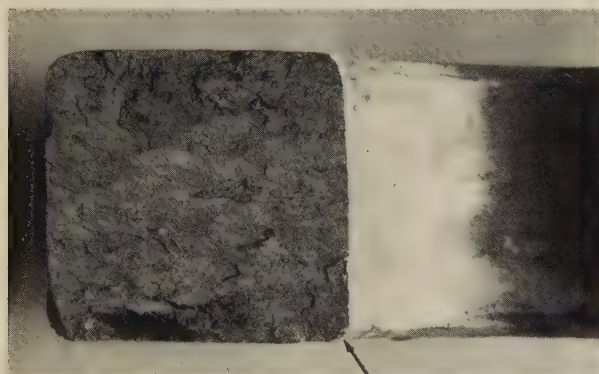
Failure-Analysis Fractographs: Aluminum Alloy 7079-T6 Aircraft Landing-Gear Actuator Beam Fractured Because of Stress-Corrosion Cracking



Photograph $\frac{1}{8} \times$
5170 Portion of a broken aircraft landing-gear actuator beam of aluminum alloy 7079-T6, showing stress-corrosion fractures (at arrow). See also 5171 to 5177.



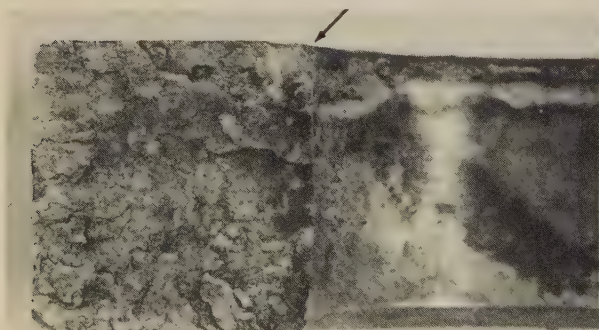
Light fractograph $\frac{5}{8} \times$
5171 A higher-magnification view of the surfaces of the stress-corrosion fractures shown in photograph 5170 (left). These fractures originated at the interior edges of boltholes in clevis-attachment lugs, at the locations designated by the arrows. An appreciable amount of evidence of both corrosion and secondary cracking was found at these origins. Visible are chevron marks, which also confirm these locations as the origins of fracture.



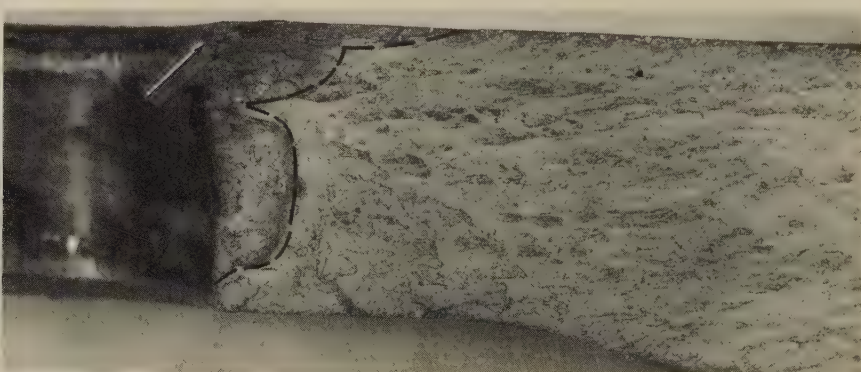
Light fractograph $4 \times$
5172 Fracture surface outboard of the bolthole in the clevis-attachment lug at right in 5171. Entire surface is typical of stress-corrosion cracking. Origin is at arrow (lower right corner of surface).



Light fractograph $4 \times$
5173 Fracture surface inboard of the bolthole in the clevis-attachment lug in 5172 (left). The primary stress-corrosion crack, which originated at arrow, is within the area enclosed by the dashed line (lower left). The remainder of this surface shows chevron marks typical of final, fast fracture.

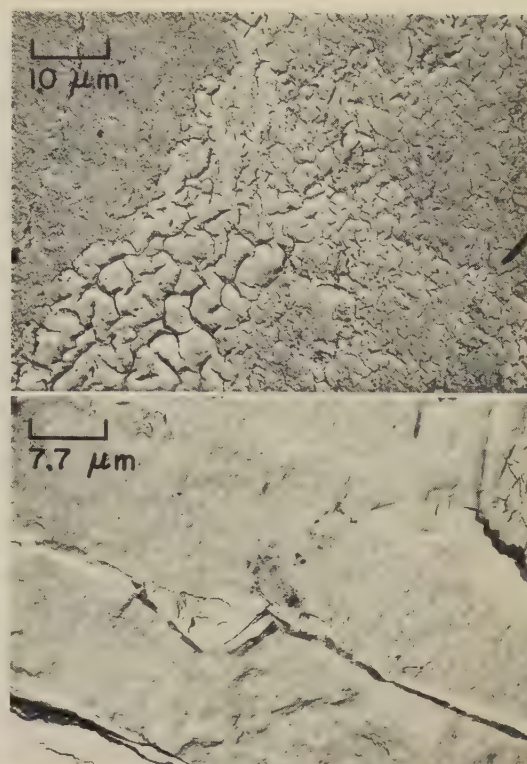


Light fractograph $4 \times$
5174 Fracture surface outboard of the bolthole in the lug at left in 5171. Here, as in 5172, the entire surface is typical of stress-corrosion cracking. Origin is at arrow (upper right corner of surface).



Light fractograph $4 \times$
5175 Fracture surface inboard of the bolthole in the clevis-attachment lug in 5174. The primary stress-corrosion crack, which originated at the arrow, and which is enclosed by the dashed line, is larger than that in 5173. This actuator beam had hardness normal for 7079-T6: 152-157 dph (10-kg load).

Failure-Analysis Fractographs of Aluminum Alloys: 7079-T6 Actuator Beam
(Continued); 7079-T651 Wing Spar; 7106-T63 and 7178-T6 Specimens



Light fractograph

10× Micrograph (unetched) 100×

5176, 5177

At left (5176) is a view, at higher magnification and rotated 90° clockwise, of the fracture surface in 5172 (facing page), showing more clearly the fracture-surface details resulting from stress-corrosion cracking. At right (5177) is a polished section through one of the stress-corrosion-crack origins at the arrows in 5171. The fracture surface is shown in profile at left, and the bolthole is shown in profile at bottom. Note that the crack penetrated parallel to longitudinal flow lines.

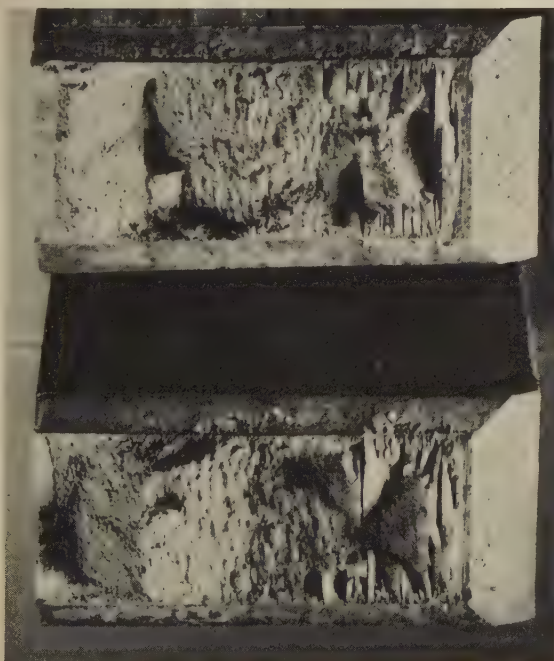
TEM fractographs

1000× (5178); 1300× (5179)

5178

5179

TEM views of plastic-carbon replicas of two areas of the surface of a fracture in an aircraft wing spar of aluminum alloy 7079-T651 subjected to stress-corrosion cracking (in 3.5% NaCl), showing a mud-crack pattern in 5178 (top) and a corroded area in 5179 (bottom).

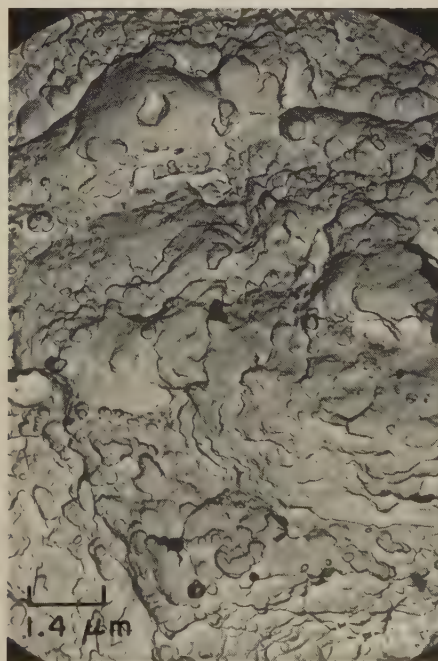


Light fractograph

2 1/2×

5180

Mating fracture surfaces of a stress-corrosion-cracked specimen of aluminum alloy 7106-T63 that was broken under a constant sustained stress near the tensile strength of the material (no step loading was employed). Note the cracks and steps in the fracture surfaces.



TEM fractograph (p-c replica)

7000×



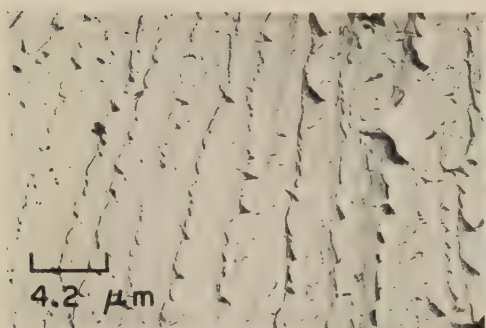
TEM fractograph (p-c replica)

7000×

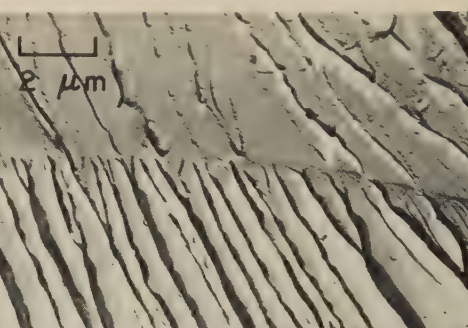
5181, 5182

TEM views of replicas of two areas of the surface of a plane-strain fracture in a specimen of aluminum alloy 7178-T6 that was broken in monotonic (continuously increasing) tension overload at room temperature. Both of these areas exhibit dimples that are characteristic of microvoid coalescence. The long, smooth bands extending diagonally from lower left to upper right in fractograph 5182 (right) are stretched regions.

Failure-Analysis Fractographs: Columbium; Cb Alloy B-66; Pd-Coated 99.999% Cu;
Tough Pitch Copper; Low-Silicon Bronze; Phosphor Bronze C Wire Cloth



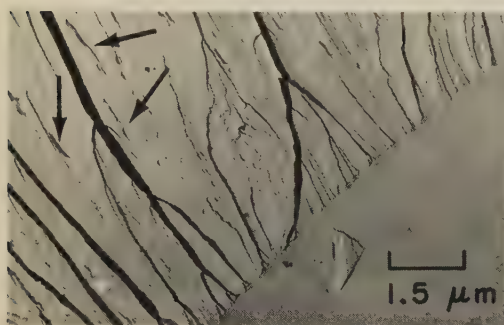
TEM fractograph (p-c replica) 2400×
5183 Cleavage fracture in a specimen of columbium bar that was broken by impact at -196 C (-321 F), showing a system of surface irregularities that resemble the tongues in specimens of Armco iron broken by impact at or below -78.5 C (-109.3 F).



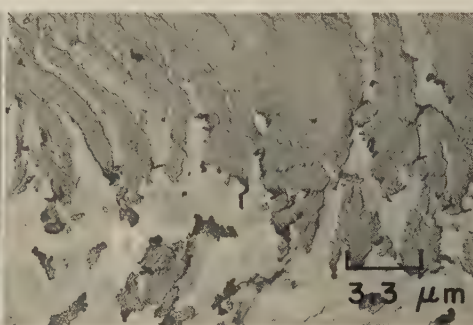
TEM fractograph (p-c replica) 5000×
5184 Cleavage fracture in a specimen of cast columbium nicked with an arc and broken by impact at room temperature, showing cleavage steps. New steps formed at the horizontal tilt-twist boundary; joining of steps occurred below the boundary.



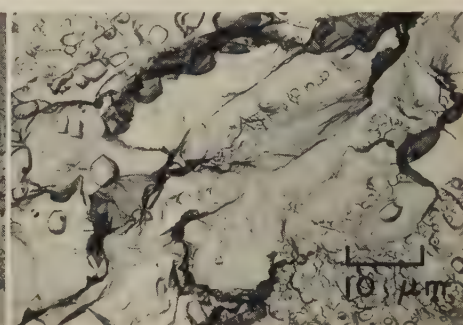
TEM fractograph (p-c replica) 18,000×
5185 Cleavage fracture in a specimen of cast columbium that was broken by the same procedure as for the specimen in 5184, but viewed at much higher magnification. The contours of the features suggest influence of a dendritic microstructure.



TEM fractograph (p-c replica) 6500×
5186 Cleavage fracture in columbium alloy B-66 sheet 0.045 in. thick, broken by impact. Direction of fracture, bottom right to top left. Cleavage steps originate at the grain boundary extending diagonally across the field. Note feather marks (at arrows) between steps.



TEM micrograph (direct carbon replica) 3000×
5187 Surface of a specimen of 99.999% copper that was coated with palladium and then stretched. In stretching, the palladium coating (dark gray) fragmented instead of conforming to the deformation of the copper base metal.



TEM fractograph (direct carbon replica) 1000×
5188 A tension-overload fracture in tough pitch copper. This area of the surface was produced by final, fast fracture in a room-temperature fatigue test. Small dimples surround cleavage facets of copper oxide inclusions.



Light fractograph 2.3×
5189 Fatigue fracture in an antenna post of low-silicon bronze (~1.5% Si, ~0.5% Mn). The fatigue crack originated in the root of a very sharp V thread.



Photograph About 50×
5190 View of bottom of a Fourdrinier wire cloth used in papermaking. Material is phosphor bronze C. The warp wires, which are horizontal in this view, show very heavy wear where they cross the shuttle (or weft) wires. The wire cloth is a continuous belt that operates under high tension and severe reverse bending, which explains the fatigue fractures visible in at least eight locations where the warp wires have been thinned by wear. See 5191 to 5194 (facing page) for other fractures in Fourdrinier wire.

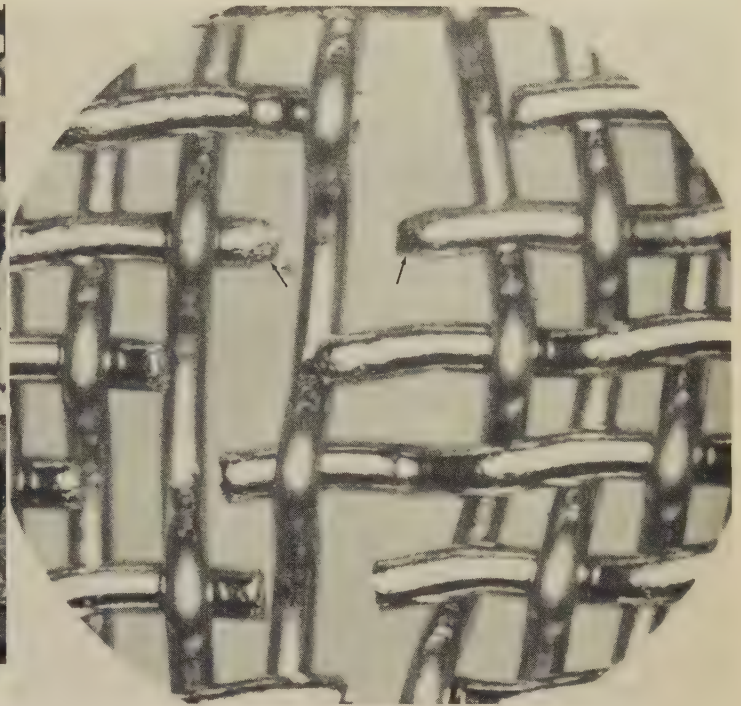
Failure-Analysis Fractographs: Phosphor Bronze C Wire Cloth Fractured by Wear,
by Fatigue, and by Tension; 80Cu-20Zn Brass Wire Cloth Fractured by Fatigue



Photograph

10×

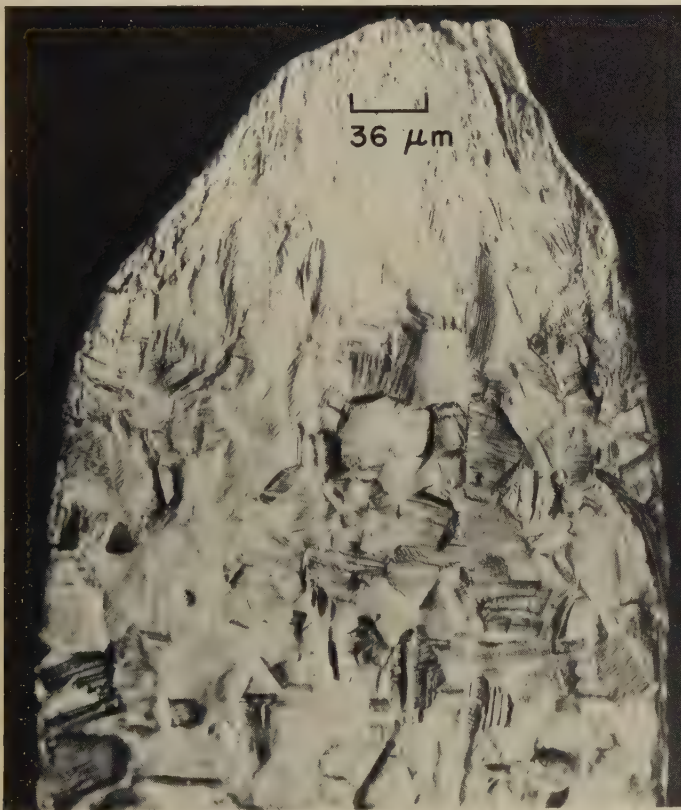
5191 View of bottom of a Fourdrinier wire cloth of phosphor bronze C that was removed from service after 14 days of operation. Heavy wear had occurred on both warp and shute (weft) wires. The fractures in the wires apparently occurred when the wires had worn almost completely through. The warp wires are shown horizontal in this view.



Photograph

About 50×

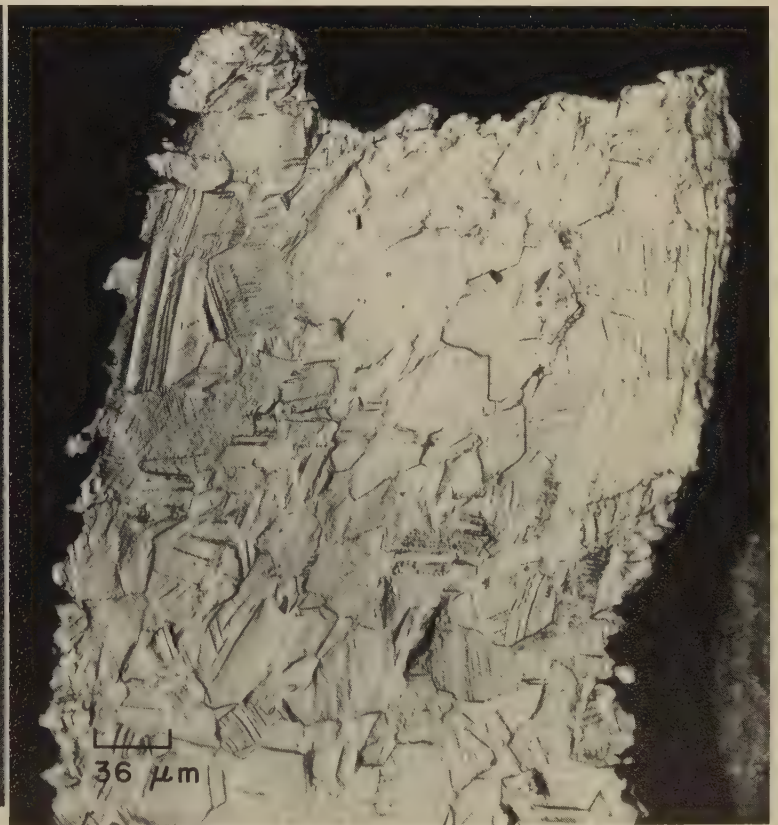
5192 Top view of a break in a Fourdrinier wire cloth of phosphor bronze C, showing fractures in shute (weft) wires. All but one of the fractures occurred by fatigue; the exception (at arrows) shows the necked-down profile of a tension fracture.



Micrograph (ferric chloride)

267×

5193 Longitudinal section through a tension fracture in a warp wire of a Fourdrinier wire cloth of phosphor bronze C. Slip lines are visible throughout the microstructure. The plastic flow and the reduction in area at the fracture (top) were attributed to excessive warp tension.

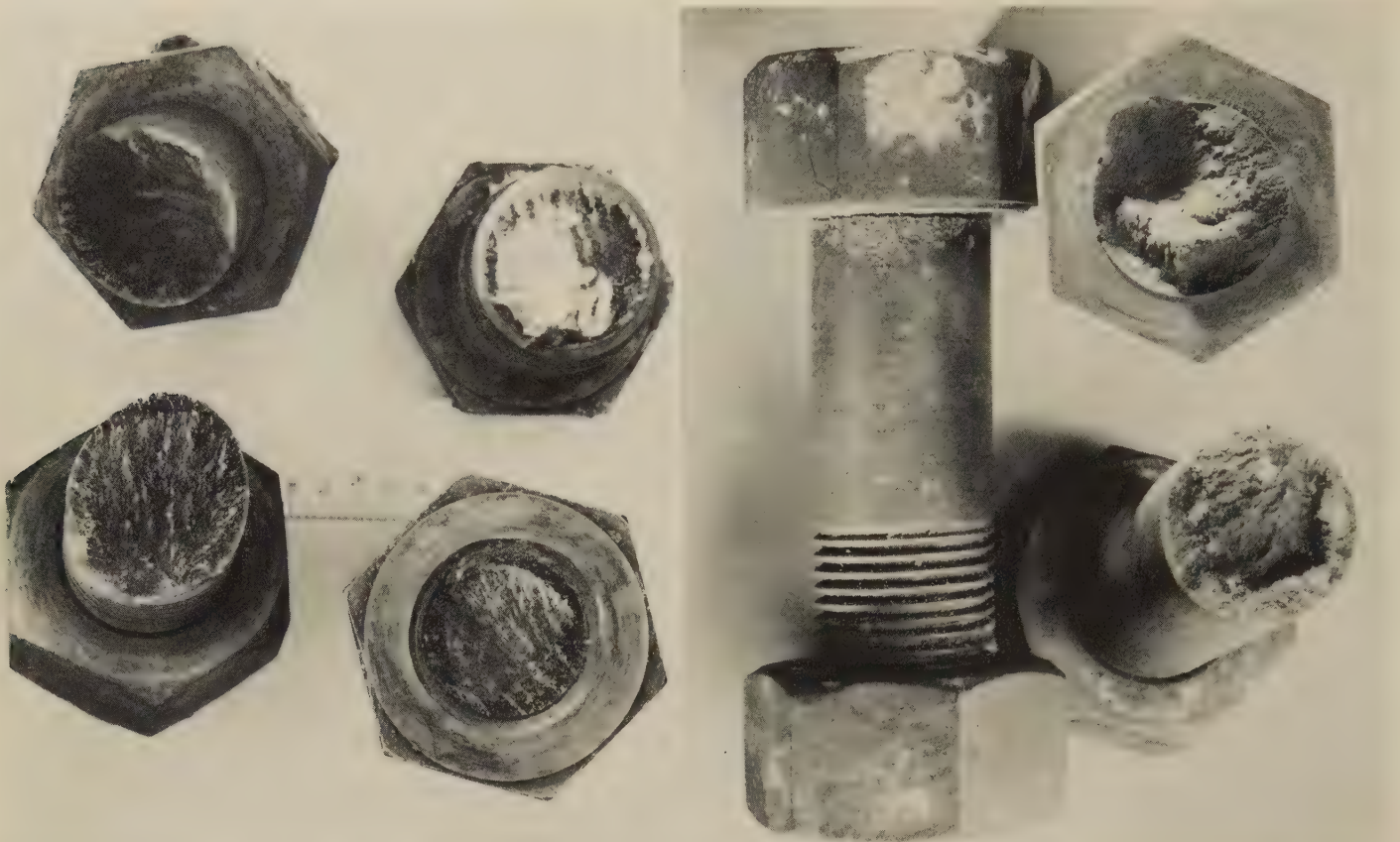


Micrograph (ferric chloride)

267×

5194 Longitudinal section through a fatigue fracture in a shute (weft) wire of a Fourdrinier wire cloth of 80Cu-20Zn brass with 0.5% Sn added. The profile of the fracture is shown at top. Note corrosion pitting visible on the wire surface at left and at right.

Failure-Analysis Fractographs: 91-7-2 Aluminum-Silicon Bronze Bolts Fractured by Stress Corrosion; Cast 85-5-5-5 Lead Red Brass Valve Fractured Because of Porosity



Light fractograph

1.35× Light fractograph

1.35×

5195, 5196 Fractures resulting from stress-corrosion cracking in 91Cu-7Al-2Si aluminum-silicon bronze bolts from the cover of a de-aeration pump that had been subjected to a marine atmosphere. At left (5195) are the surfaces of fractures in four fitted bolts. At right (5196) are the mating fracture surfaces of a broken standard bolt, and a standard bolt (with nut) that contains a stress-corrosion crack in the fillet beneath the bolt head. Although the aluminum contents of the fitted and standard bolts were low (7.5% and 6.5% respectively), the silicon contents were high (2.0% and 3.0% respectively), which resulted in a two-phase (alpha-plus-beta) microstructure. A single-phase alloy might have been more resistant to corrosion.

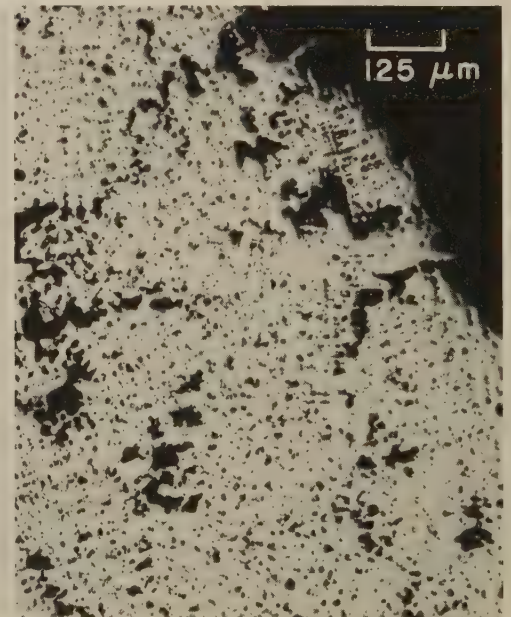


Light fractograph

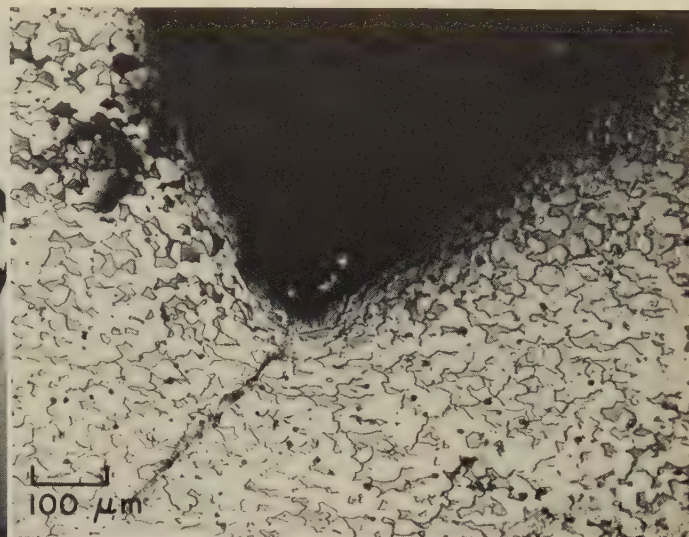
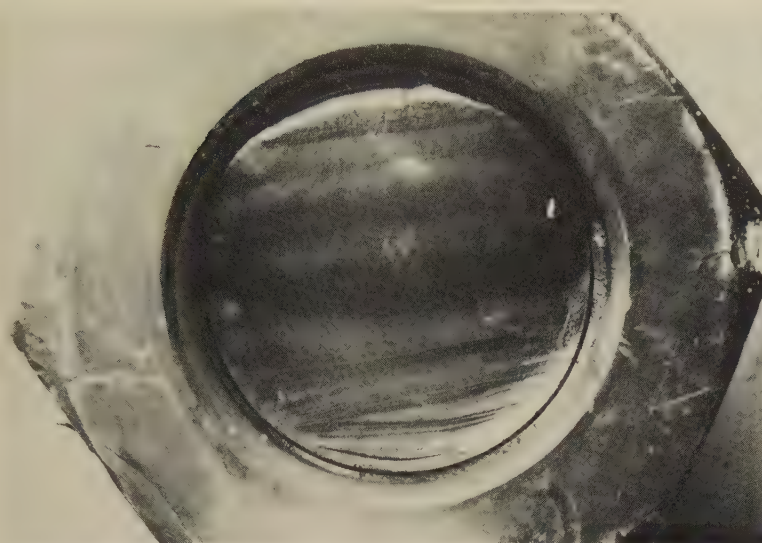
Actual size Micrograph (as polished; not etched)

80×

5197, 5198 At left (5197) is a view of a fractured cock valve that parted in the threads. The valve had been cast of 85Cu-5Zn-5Sn-5Pb lead red brass, which normally provides a very sound structure. At right (5198) is a section through the valve in 5197, adjacent to the fracture, showing an excessive amount of shrinkage porosity scattered throughout the structure. Fracture was attributed to stress concentrations that were generated by the shrinkage pores.



Failure-Analysis Fractographs: 60Cu-37.8Zn-0.7Mn-1.5Fe Manganese Bronze Pump Rod;
48Cu-35Ni-11Sn-6Pb Spindle; Titanium Alloys Ti-2Al-2Zr-2V-1Mo and Ti-2.5Al-16V



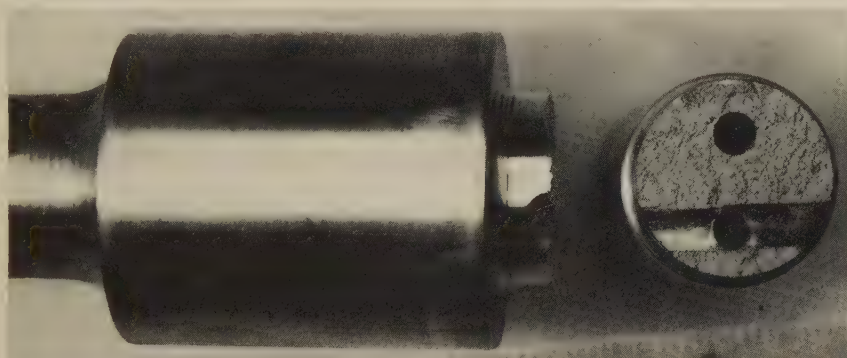
Light fractograph

Actual size Micrograph (etchant: $\text{FeCl}_3 + \text{HCl}$)

100×

5199, 5200

At left (5199) is the surface of a fatigue fracture in an air-pump rod that broke in service. The material is 60Cu-37.8Zn-0.7Mn-1.5Fe manganese bronze. The fatigue crack originated in the root of a sharp V thread and penetrated nearly the entire bolt (shown inside its nut) before final, fast fracture occurred. At right (5200) is a longitudinal section through the broken pump rod in 5199, showing the beginning of a second fatigue crack in the thread root next to that in which the fracture occurred.



Photograph

Actual size

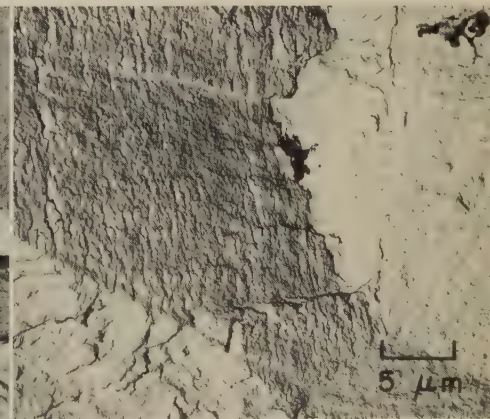
Micrograph (as polished; not etched)

230×

5201

Cleavage fracture in a cast 48Cu-35Ni-11Sn-6Pb alloy valve spindle from a pump. The apparent cause of fracture was internal porosity combined with the presence of three drilled holes, which weakened the section and provided stress raisers. See also micrograph 5202 (right).

5202 A section through the fractured cast valve spindle shown in photograph 5201 (left), taken at a region adjacent to the fracture. Scattered porosity is plainly evident.



TEM fractograph (p-c replica)

2000×

5203

Surface of a fracture produced at room temperature, in a drop-weight tear test, in a specimen of titanium alloy Ti-2Al-2Zr-2V-1Mo, showing a long stringer (arrow) that was broken apart and stretched.

TEM fractograph

2000×

5204

Direct carbon replica (Pd-shadowed) of the surface at the root of an intentionally formed fatigue crack in a titanium alloy Ti-2.5Al-16V specimen, showing tear dimples (at arrows) that formed during the early stages of crack growth.

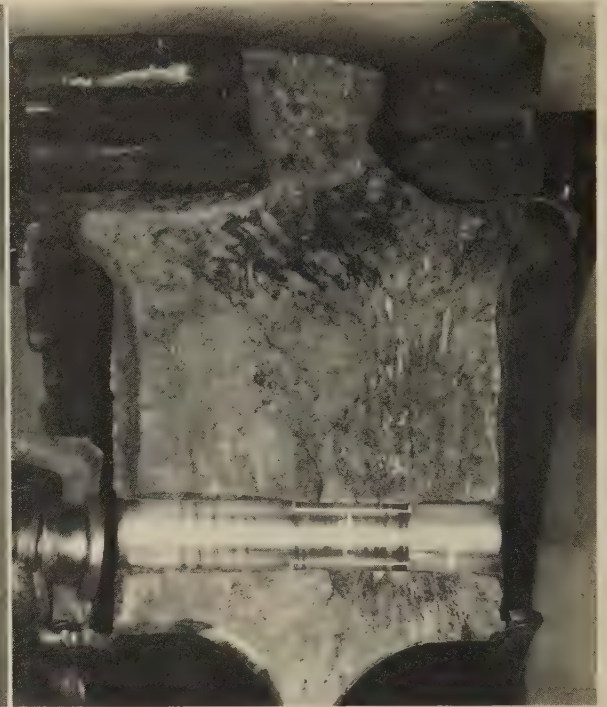
TEM fractograph (p-c replica)

2000×

5205

Replication of the surface of a fatigue fracture in a specimen of titanium alloy Ti-2.5Al-16V, showing fatigue striations. The striations exhibit noticeable changes in orientation where they intersect grain boundaries.

Failure-Analysis Fractographs: Titanium Alloy Ti-6Al-4V Jet-Engine Compressor Disk Fractured by Fatigue



Photograph

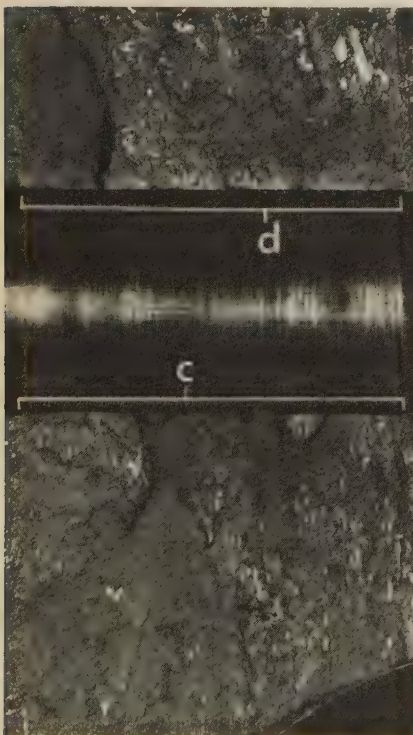
0.2×

Light fractograph

0.9×

5206, 5207

At left (5206) are two portions of a fractured titanium alloy Ti-6Al-4V second-stage compressor disk from a jet engine. Of the three radial fractures, the one at upper right, which passes through the bolthole marked "a", was found to be the primary fracture, exhibiting several fatigue-crack origins adjacent to the hole. The two other fractures showed no sign of fatigue. At right (5207) is a surface of the fracture through the bolthole at arrow "a" in 5206. Several fatigue cracks originated at locations within brackets "c" and "d". Deep tool marks in the bore of the hole are visible between arrows "e" and "f"; a section through the hole marked "b" in 5206 showed no such deep tool marks. Average tensile properties of two specimens cut from the disk were 1007 MPa (146 ksi) tensile strength, 17.5% elongation and 39% reduction of area. See also 5208 and 5209 (below), and 5210 to 5213 (facing page).

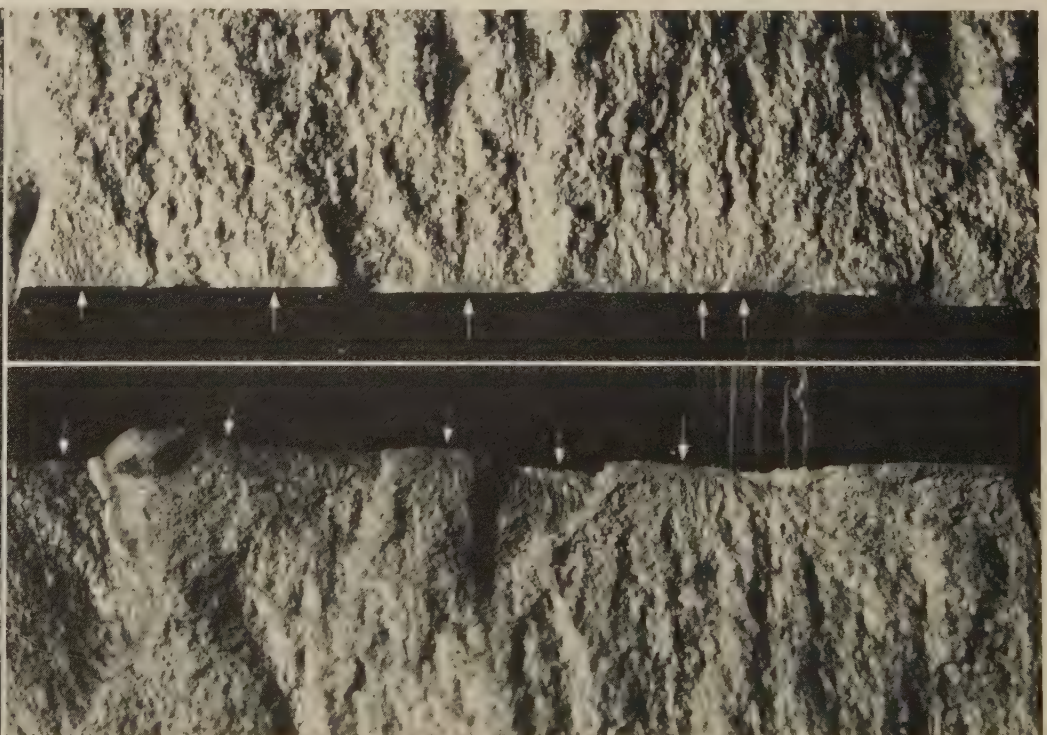


Light fractograph

3×

5208

Enlarged view of the fatigue-crack regions (marked by brackets) at the edges of the bolt-hole in 5207. The cracks grew in both directions from the hole.



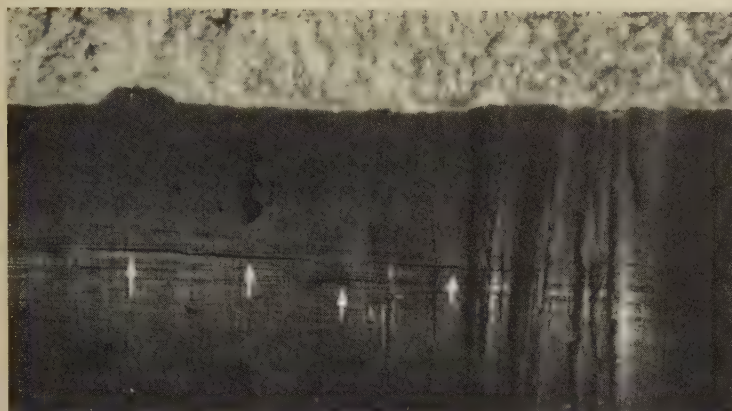
Light fractograph

8×

5209

Separate, higher-magnification views of the bracketed regions of the edges of the compressor-disk bolthole in 5207 and 5208, shown correctly aligned opposite each other. Visible are beach marks in several fatigue-crack zones (at arrows). These separate cracks penetrated only a short distance before joining to form common fronts, which then advanced toward both the rim and the bore of the disk.

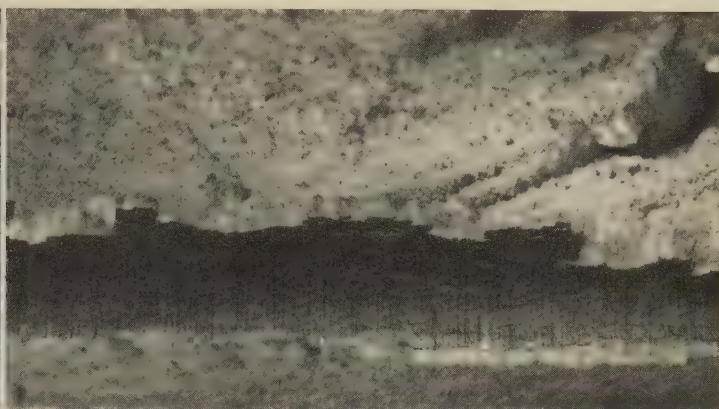
Failure-Analysis Fractographs of Titanium Alloys: Ti-6Al-4V Compressor Disk (Continued);
Ti-6Al-4V (Tension-Overload Fracture); Ti-3Al Drop-Weight Tear-Test Specimen



Macrograph

15×

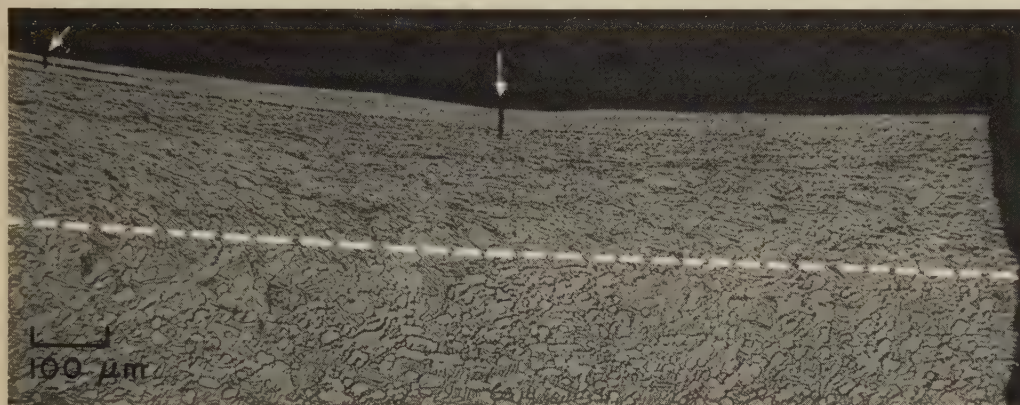
5210 A view of the bore of the bolthole at arrow "a" in the fractured titanium alloy Ti-6Al-4V compressor disk in 5206 (facing page), showing more clearly the deep tool marks faintly visible in 5207 to 5209. The arrows mark locations of longitudinal secondary cracks in the bore of the hole.



Light fractograph

4×

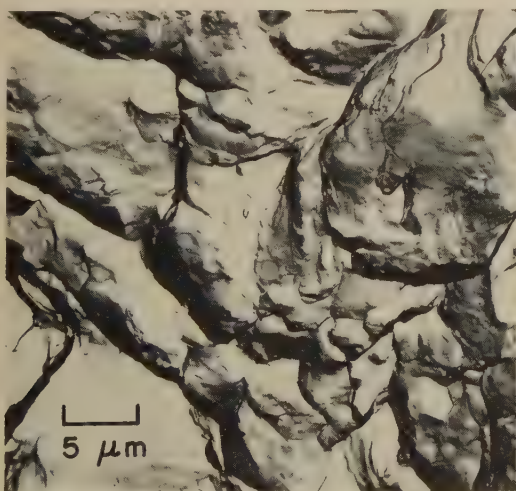
5211 A view of the edge of the bolthole through which passed one of the secondary radial fractures (at left or at bottom) in the compressor disk in 5206. Note the irregular shear-overload cracks at the edge of the hole, which show no characteristics of fatigue, and the irregular secondary cracks in the bore.



Micrographs (etchant: HF plus HNO₃, in H₂O)

5212, 5213 At left (5212) is a section through one of the fatigue-crack zones at one of the bolthole edges in 5209, taken transversely to the hole. The fracture surface is shown in profile at right, and the bore of the hole is shown in profile at top. Note the layer of cold worked metal above the dashed line. At right (5213) is a section through the same general area as that in 5212, but taken longitudinally to the hole. Here, as in 5212, a cold worked layer can be seen (at top); severe surface flow in the bore of the hole is visible also. This damaged condition of the bore surface, and the deep tool marks shown in 5210, probably caused the fatigue fracture.

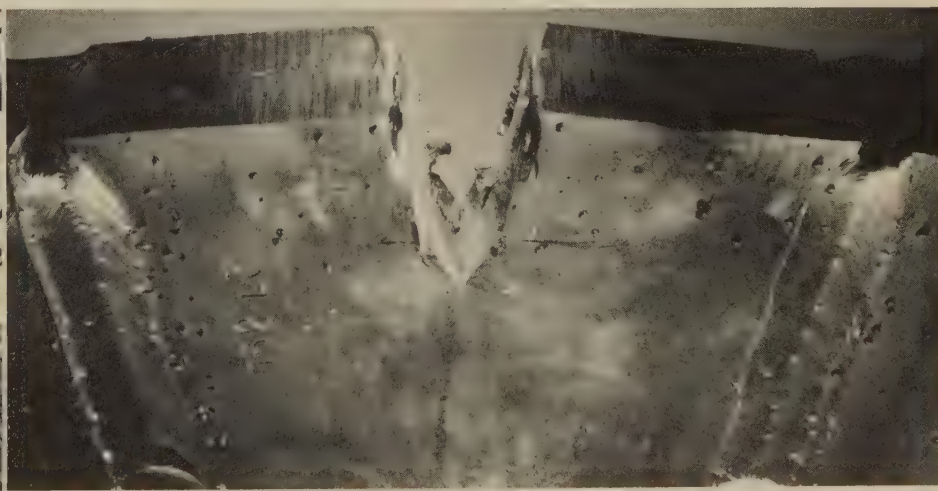
Both at 100×



TEM fractograph (p-c replica)

2000×

5214 Surface of a tension-overload fracture in a specimen of titanium alloy Ti-6Al-4V. Both large and small dimples are present. The large dimples exhibit surface ripples that formed during flow.

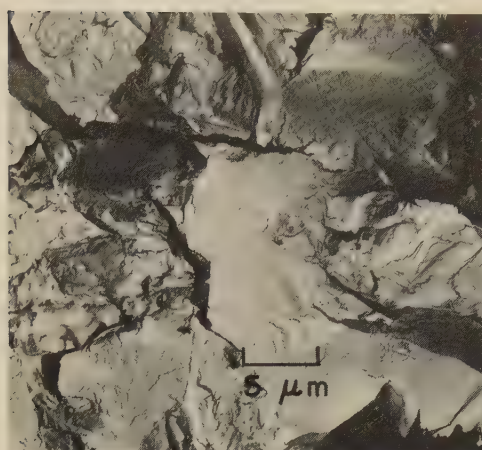


Photograph

3/4×

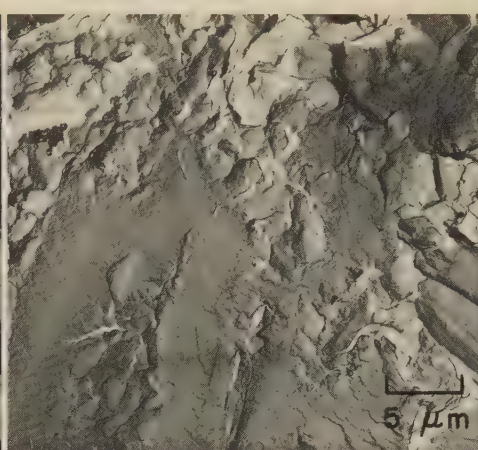
5215 A drop-weight tear-test specimen of titanium alloy Ti-3Al that absorbed the energy of a 10,000-ft-lb blow by bending with little propagation of the fatigue crack previously prepared at the notch root. The crack merely widened as the metal at the root of the crack flowed plastically as in a simple tension test. Electron fractography disclosed that stretching was the predominant feature in the surface of the crack.

Failure-Analysis Fractographs of Titanium Alloys: Ti-6Al-4V (Stress Corrosion); Ti-7Al-1Mo-1V (Drop-Weight Tear Test); Ti-7Al-2Cb-1Ta (Tension Overload, Stress Corrosion)



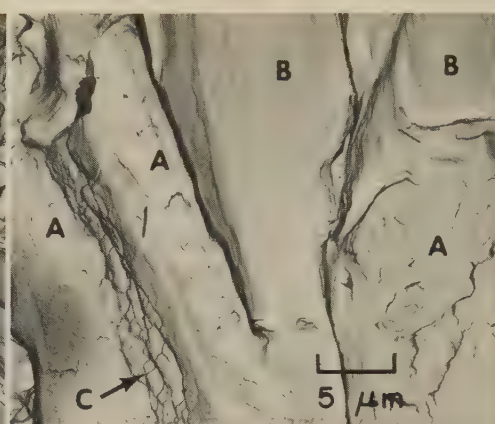
TEM fractograph (p-c replica) 2000×

5216 Fracture resulting from stress-corrosion cracking in a specimen of titanium alloy Ti-6Al-4V that was stressed in methanol. The crack path is transgranular (by cleavage). See also 5217 (right).



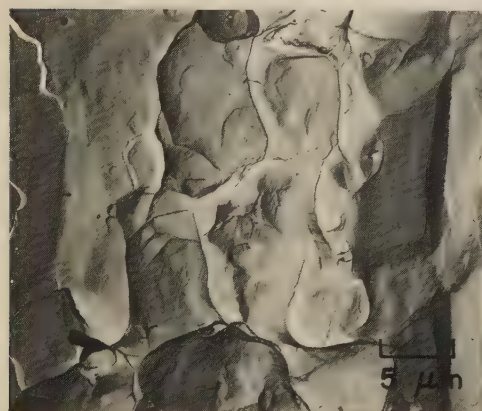
TEM fractograph (p-c replica) 2000×

5217 A companion fractograph to that in 5216, from the same specimen of titanium alloy Ti-6Al-4V, but showing an area farther from the fracture origin. Visible are what appear to be a few small dimples.



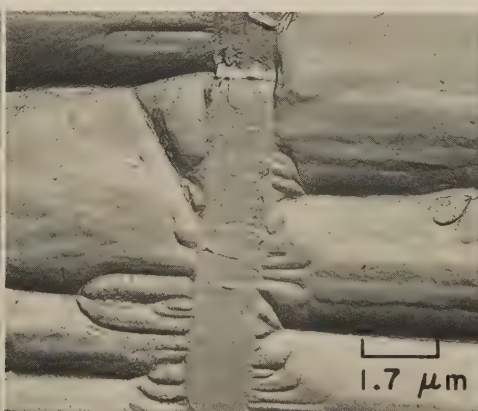
TEM fractograph (p-c replica) 2000×

5218 Bending fracture in a specimen of titanium alloy Ti-6Al-4V that broke by stress-corrosion cracking in 3½% NaCl (areas A) but that also exhibits regions of stretching (areas B) and a step containing what appear to be dimples (arrow at C).



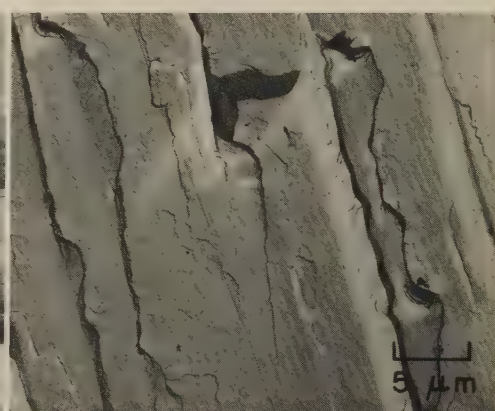
TEM fractograph (p-c replica) 2000×

5219 Surface of a fracture in a specimen of titanium alloy Ti-7Al-1Mo-1V that was broken in a drop-weight tear test, consisting mostly of dimples. A feature that apparently is a tear ridge (vertical) is visible at far right.



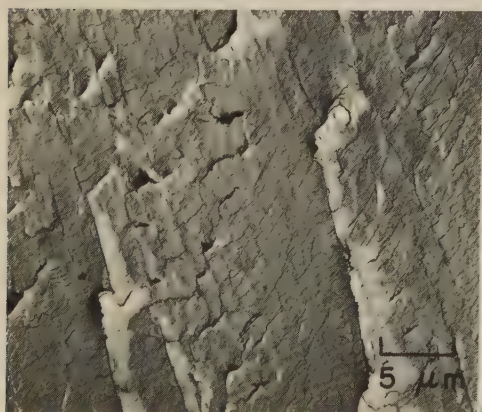
TEM fractograph (p-c replica) 6000×

5220 Fracture produced by tension overload in a specimen of titanium alloy Ti-7Al-2Cb-1Ta, showing staining and very large dimples. Vertical band at center is where a crack initiated at a second-phase region and propagated to left and right.



TEM fractograph (p-c replica) 2000×

5221 Fracture resulting from stress-corrosion cracking in a chill cast specimen of titanium alloy Ti-7Al-2Cb-1Ta that was stressed in distilled water, exhibiting facets that were produced by essentially pure cleavage.



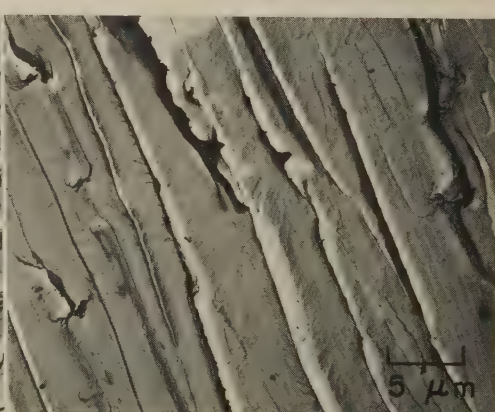
TEM fractograph (p-c replica) 2000×

5222 Cleavage fracture in a specimen of titanium alloy Ti-7Al-2Cb-1Ta, produced by stress-corrosion cracking in methanol. Note the regular array of fissures, which are parallel to the crack front. See also fractograph 5223 (right).



TEM fractograph (p-c replica) 2000×

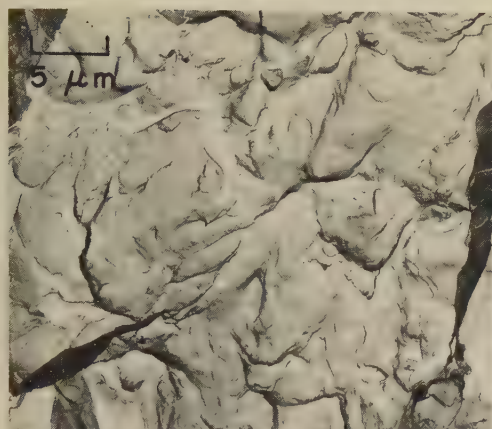
5223 Companion fractograph to that in 5222, from the same specimen, but taken at the stress-corrosion-crack front. In general, the facets here show features of cleavage; in contrast, the facets at top center show what apparently are ripples.



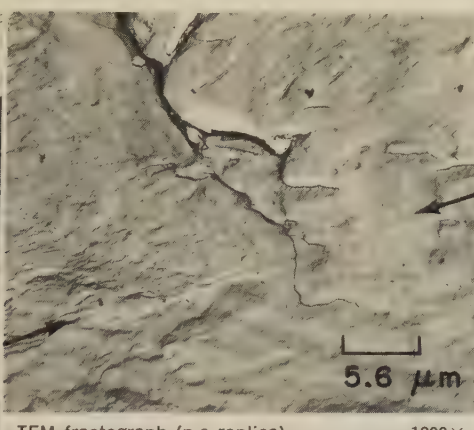
TEM fractograph (p-c replica) 2000×

5224 Cleavage fracture in another specimen of titanium alloy Ti-7Al-2Cb-1Ta, also produced by stress-corrosion cracking in methanol. Note the similarity of the cleavage facets here to those in 5221, which were produced in distilled water.

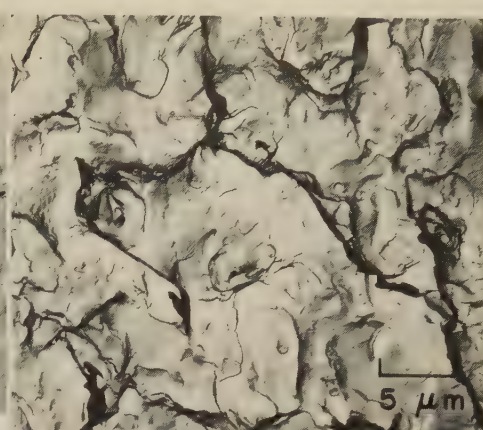
Failure-Analysis Fractographs: Titanium Alloy Ti-7Al-3V (Tension Overload); Titanium Alloy Ti-8Al-1Mo-1V (Fatigue; Impact After Stress Corrosion); Tungsten (Impact)



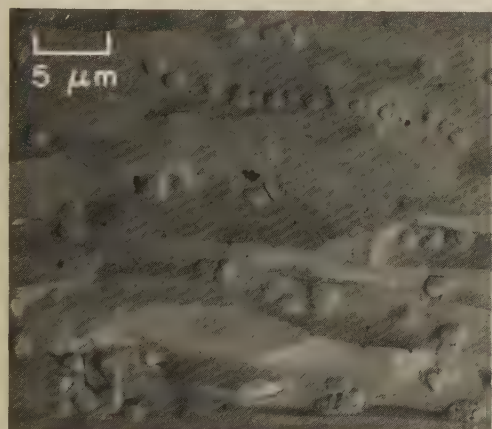
TEM fractograph (p-c replica) 2000×
5225 Surface of a tension-overload fracture in a specimen of titanium alloy Ti-7Al-3V, displaying assorted large to small dimples. Dark lines suggest deep fissures. The two black areas (at lower left and at right) are artifacts.



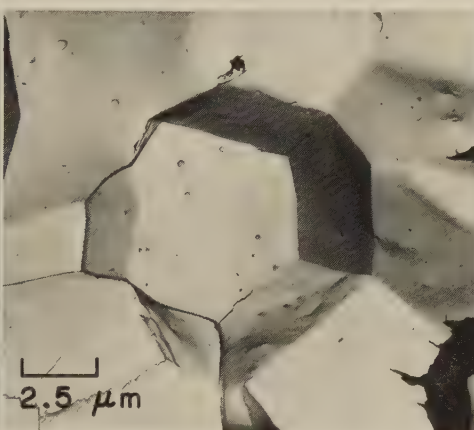
TEM fractograph (p-c replica) 1800×
5226 Fatigue fracture in a specimen of titanium alloy Ti-8Al-1Mo-1V tested in air, then in vacuum. Fine fatigue striations from testing in air are evident above the demarcation indicated by the arrows. Below this demarcation, crack growth occurred in vacuum and no striations were formed.



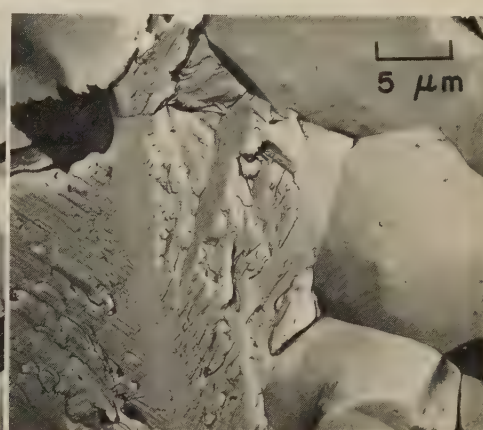
TEM fractograph (p-c replica) 2000×
5227 Fracture in a specimen of titanium alloy Ti-8Al-1Mo-1V broken by impact after stress-corrosion cracking. This area, which is from the fast-fracture region, shows dimples that were formed by microvoid coalescence.



TEM fractograph (p-c replica) 2000×
5228 Surface of an impact fracture in a broken rod of sintered tungsten, showing that separation of the rod was intergranular. Evident are numerous sintering pores that resemble second-phase particles.



TEM fractograph (p-c replica) 4000×
5229 A very clean intergranular fracture in sintered tungsten that was broken by impact. Note the several very flat separated-grain facets; small sintering pores can be seen in several of the facets.



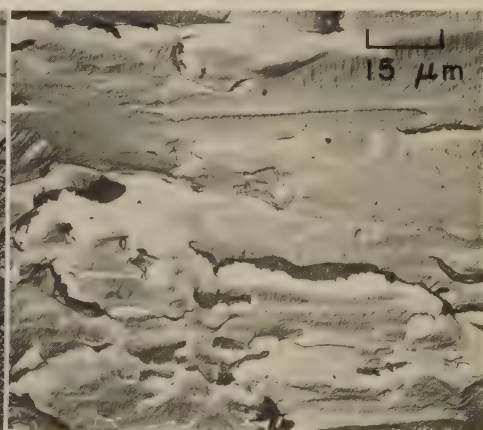
TEM fractograph (p-c replica) 2000×
5230 Impact fracture in sintered tungsten that had been recrystallized, showing separated-grain facets (at right) and cleavage facets (at left); the cleavage facets exhibit twins in the {112} plane.



TEM fractograph (p-c replica) 2000×
5231 Surface of an impact fracture in a single crystal of tungsten that was etched with H₂O₂ after fracture. Cleavage along both the {100} and {113} planes is evident. See also fractographs 5232 and 5233.



TEM fractograph (p-c replica) 2000×
5232 Impact fracture in a tungsten specimen etched with H₂O₂ after fracture. Cleavage facets are evident, showing pits with two distinctly different appearances due to different grain orientations.



TEM fractograph (p-c replica) 650×
5233 Impact fracture in a specimen of tungsten, showing cleavage steps. The fracture surface has been only lightly etched with H₂O₂ and appears very different from those in 5231 and 5232 (at left).

Some Abbreviations and Symbols Used in This Volume

Å, A	angstrom (units)
amp	ampere
AMS	Aerospace Material Specification
AREA	American Railway Engineering Association
ASA (ANSI)	American Standards Association (American National Standards Institute)
ASTM	American Society for Testing and Materials
~	approximately
at. %	atomic per cent
bcc	body-centered cubic
Bhn	Brinell hardness number
C	Centigrade; Celsius
CDA	Copper Development Association
cm	centimeter
σ_3	compressive stress component
CP	chemical purity
°	degree (angular)
diam	diameter
×	diameters (magnification)
dph	diamond pyramid hardness
EDM	electrical discharge machining
ev	electron-volt
F	Fahrenheit
fcc	face-centered cubic
ft	foot
ft-lb	foot-pound
g	gram
gal	gallon
hcp	hexagonal, close-packed
hr	hour
in.	inch
in. ^{1/2}	square root of inches
K	stress-intensity factor
ΔK	range of stress-intensity factor during cyclic loading
K_c	critical plane-stress-intensity factor (plane-stress fracture toughness)
K_{max}	maximum stress-intensity factor
K_t	theoretical stress-concentration factor
K_{Ic}	critical plane-strain stress-intensity factor (plane-strain fracture toughness)
kc	kilocycle
kg	kilogram
kgm/cm ²	kilogram-meter per square centimeter
ksi	kilopounds per square inch
kv	kilovolt
lb	pound
<	less than
≤	less than or equal to
m ^{1/2}	square root of meters
max	maximum
σ_{max}	maximum stress
micro-in.	micro-inch
μm	micron
min	minimum; minute
ml	milliliter
mm	millimeter
mod	modified
MPa	megapascal
mv	millivolt
>	more than
OFHC	oxygen-free high-conductivity (copper)
p-c replica	plastic-carbon replica
P-F	Shepherd hardenability standard
pH	hydrogen-ion concentration (acidity)
ppm	parts per million
R	stress ratio
rpm	revolutions per minute
SAE	Society of Automotive Engineers
sec	second
SEM	scanning electron microscope
τ	shear stress
SLR	single-lens reflex
σ_1	tensile stress component
3-D	third dimension
TEM	transmission electron microscope
vol %	volume per cent
wt %	weight per cent

Index

The symbols used in this index indicate that the information or feature cited in specific entries is as follows: A, the subject of an article; E, in an example; F, in a figure (line illustration or graph); L, in a light fractograph; M, in a micrograph or macrograph; P, in a photograph; S, in a scanning-electron-microscope fractograph; and T, in a transmission-electron-microscope fractograph. The abbreviations SEM and TEM are used in several places to indicate scanning electron microscope and transmission electron microscope, respectively.

Major entries include fracture-surface features, fracture mechanisms, fractographic procedures, parts that fractured, and materials. Subentries under material designations indicate the features that can be seen on the fractographs and the fracture mechanisms.

A

A-286 alloy
 overload fracture (S)225
 quasicleavage (T) 84
 tear dimples (S)225
Abbreviations476
Accumulator head
 failure analysis (L)426
 fracture (L)426
Acid cleaning of fracture surfaces 10
Actuator arm, fatigue fracture
 (L,M,P,S)189
Actuator beam
 failure analysis (L,M,P)466-467
 stress-corrosion-cracking
 fracture (L,M,P)466-467
Actuator rod, fatigue fracture (L,T)301
Actuator shaft, hydrogen-embrittlement
 cracking (L,P,T)310-311
Agricola, Georgius 2
Air-blast cleaning of fracture surfaces9-10
Aircraft parts. See under part name, such
 as *Landing-gear cylinders; Landing*
wheels.
Air flask, fracture (T)428
Air-pump rod
 failure analysis (L,M)471
 fatigue fracture (L,M)471
Air-turbine blade
 fracture, effect of inclusion (L,S) 97
 impact-overload fracture, effect of
 porosity (S)99, 100
Alclad aluminum, fatigue-fracture
 propagation (L) 45
Alkaline cleaning of fracture surfaces 10
Alligator fracture (L)136
Alloy 713C
 cleaning fracture surface (S)234
 dimples (T)234, 334, 335
 elevated-temperature fracture (L,T)335
 fatigue fracture (L,S)234
 fatigue striations (S)234
 hairline indications (T)335
 intergranular fracture (T)335
 oxidation of fracture surface (T)335
 secondary cracks (L)335
 slip planes (T)335
 stress-rupture fracture (L,T)335
 stretching (T)335
 tension-overload fracture (L,T)334-335
Alloy 713LC
 beach marks (L)334
 corrosion-fatigue fracture (L,P,T)334
 creep-to-rupture testing (L,T)112, 113
 elevated-temperature fracture
 (L,M,P,T)334
 fatigue striations (T)334

Alloy 713LC (continued)
 fracture-surface oxidation (T)112
 inclusions (T)112
 powder metallurgy compact,
 intergranular fracture (L,T)112, 113
Alloy 718
 cleavage facet (T)336
 cup-and-cone fractures (L,M,S,T)228, 336
 dendrite arms (S)227
 dimples (S,T)228, 336, 337, 339
 elevated-temperature fracture (L,T)339
 fatigue-crack progression (T)338, 339
 fatigue fractures (L,S,T)227, 229, 337-339
 fatigue striations (S,T)227, 337, 338, 339
 notched
 fatigue fracture (L,T)337, 338, 339
 tension-overload fracture
 (L,M,S,T)228, 337
 precipitate-particle cleavage (T)228, 336
 secondary cracks (T)336, 338
 shrinkage porosity (S)227
 slip lines (T)339
 slip steps (S)229
 tension-overload fractures
 (L,M,S,T)228, 336-337
 twin boundaries (T)338
Alloy steels. See also specific steel
 under *Steels, specific types.*
 carburized
 fatigue fracture (S)203
 tearing plus intergranular fracture
 (S)74, 75
 chevron pattern (L)426
 cleavage facets, stereo views (S,T)284
 dimples (S)203
 stereo views (S,T)284
 elevated-temperature fracture (S)203
 fatigue fractures (L)418, 437
 fatigue striations 87
 fracture toughness, effect of heat
 treatment (S)216-217
 impact fractures (S)133, 203, 215, 217-218
 effects of heat treatment (S)218
 stereo views (S,T)284
 inclusions (S)203
 stereo views (S,T)284
 low-temperature fracture (S)203
 quasicleavage facets (S)203
 river patterns (S)203
 rock candy fracture (S)203
 rotary-bending fatigue fracture (S)203
 tongues (L)426
 torsional-fatigue fracture (L)132
 voids (S)203
Alnico
 cleavage facets (T)348
 cleavage steps (T)82, 348
 fracture, effect of microstructure (T)348

Alnico (continued)
 impact fracture (L)348
 river pattern (T)82, 348
 rock candy fracture (L)348
 second-phase particles (T)348
 tilt boundary (T)348
Alpha-beta titanium alloys
 microvoid coalescence (T) 81
 mixed-mechanism fractures (S)71-72
 stepped fracture surface (T) 88
Alpha titanium alloys, cleavage plus
 fatigue-striation formation (S)72, 73
Aluminum alloy castings
 brittle fracture (L,P,S)238-239
 cellular structure (S)242
 dendritic structure (S)100
 fatigue fracture (L,P,S,T)240-241, 350
 impact fracture (L,P,T)351
 porosity (L,M,S)99-100
 stress-corrosion cracking (L,M,P,T) 349-351
 sudden-overload fracture (L,P,S)237
Aluminum alloy die casting, overload
 fracture (L,P)456-457
Aluminum alloy extrusions
 fatigue fracture (L,T)358, 461
 grain flow (M)361
 stress-corrosion fracture (L,M,P,T) 360-361
 structure (M)461
Aluminum alloy forgings
 fatigue fracture
 (L,M,P,S,T)254-255, 362, 458-459, 460
 fracture involving forging defects (L,T) 354
 fracture originating at inclusions (L,T) 352
 stress-corrosion-cracking fracture
 (L,T)358-359, 361
 torsion-overload fracture (L,T)355
Aluminum alloy plate, tension-overload
 fracture (L,T)363
Aluminum alloys
 banded structures (L,T)121, 122, 123
 effect on fracture mechanism112
 cleaning fracture surfaces 10
 eutectic melting (L,T)101-103
 oxide-film production 58
 oxide-replica removal 58
 stress-corrosion-cracking
 fractures, appearance 90
Aluminum alloys, specific types
 218
 gas cavities (L)457
 overload fracture (L,P)456-457
 220-T6
 fracture (L,M) 99
 microporosity (M) 99
 319
 casting defects (M,T)349
 cleavage facets (T)349
 cold lap (T)349

Aluminum alloys, specific types (continued)

319 (continued)	
precipitate particles (M)	349
stress-corrosion-cracking fracture (L,M,P,T)	349
333	
chevron pattern (L)	237
dimpled-rupture fracture (S)	237
sudden-overload fracture (L,P,S)	237
355	
fracture (M,P)	137-138
gas porosity (M)	137-138
356-T6	
beach marks (L)	241
cellular structure (S)	242
dendrite arms (S)	242
dendrite-cell structure (S)	243
dimples (S,T)	80, 242, 243
eutectic structure (M)	243
fatigue fractures (L,P,S)	240-241
fatigue striations (S)	241
geometric pattern (T)	89
impact fracture (P,S)	242-243
inclusions (S)	242
platelets (S)	242
second-phase particle, fracture (T)	80
shrinkage cavities (S,M)	242, 243
tension-overload fracture (S)	242, 243
voids (S)	241
356-T6 (mod)	
brittle fracture (L,P,S)	238-239
dendrite lobes (S)	238
dimples (S)	239
shrinkage porosity (L,S)	238, 239
A356-T6, Wallner lines (T)	83, 84
A357	
impact-overload fracture (S)	100
porosity (S)	100
A357-T6	
dendritic structure (S)	100
effect of inclusions on fracture (L,S)	97
effect of porosity on fracture (S)	100
shrinkage void (S)	100
380	
bending-fatigue fracture (L,M,T)	350
bending-overload fracture (T)	350
chevron marks (L)	351
cleavage fracture (T)	350, 351
dimples (T)	350
fatigue fracture (L,M,T)	350
fatigue striations (T)	350
impact fracture (L,P,T)	351
microstructure, effect on fracture (M,T)	350
second-phase particles (M)	350
stretching (T)	350
tire tracks (T)	350
1100	
corrosion pits (S)	244
crack arrests (S)	244
elevated-temperature fracture (S)	76
fatigue fractures (T)	22, 87
fatigue fractures, stereo views (L)	22
intergranular fracture (S)	76
secondary cracks (S)	244
stress-corrosion fracture (P,S)	244
stress-rupture fracture (S)	76
2014	
eutectic melting (T)	102, 103
geometric patterns on fracture surface (T)	101
oxidized fracture surface (T)	101
porosity, effect on fracture (L,T)	101
separated-grain facets (T)	102
tension-overload fracture (L,T)	102
weld metal, gas cavities (L,T)	100
weld metal, geometric pattern (T)	89

Aluminum alloys, specific types (continued)

2014-T6	
beach marks (L,M,S)	246, 458, 459, 460, 461
bright flakes (L)	460
cleavage steps (E,T)	119
corrosion on fracture surface (P,S)	245, 246
corrosion pits (M)	459
elevated-temperature fracture (T)	102
eutectic melting (T)	101-103
fatigue fractures (L,M,P,S,T)	86, 118, 119, 123, 124, 245, 458-459, 460-461
fatigue striations (E,S,T)	118, 119, 245, 246
intergranular cracks (M)	459
river patterns (E,T)	119
tearing fracture with fatigue fracture (T)	86
weld metal, interdendritic fracture (T)	89
2018	
fracture (L,T)	352
inclusions (L,T)	352
2020-T651	
dimples (T)	462
fatigue fracture (T)	462
fatigue striations (T)	462
2024	
dimples (T)	462
fatigue striations (T)	462
2024-T3	
amalgam attack (T)	462
cleavage fracture (T)	462
cleavage steps (S)	247
corrosion-fatigue fracture (T)	91
corrosion of fracture surface (S)	248
dimples (S,T)	247, 248, 249, 353
ductile fatigue fractures (S)	69
fatigue-crack propagation (S)	68
fatigue fractures (E,L,P,S,T)	68, 69, 91, 120, 122, 247-249, 352-353, 462
fatigue fractures, effect of crystallography (S)	69
fatigue striations (S,T)	69, 121, 247, 248, 249, 352-353, 462
fracture, effect of environment (T)	462
fracture appearance, effect of environment (S)	247-249
fracture propagation (L,T)	352-353
inclusions (S)	69, 248
intergranular fracture (T)	462
macroscopic vs microscopic crack-growth rate (F)	86
notched, fatigue fracture (L,T)	352
river pattern (T)	462
secondary cracks (S)	69
tear ridges (S)	247
transgranular fracture (T)	91, 462
2024-T4	
dimples (S)	246, 247
fatigue fracture (L,F,T)	84, 138
fracture-toughness-test fracture (S)	246-248
inclusions (S)	246, 247
void (S)	247
2024-T5	
dimple sizes (S)	68
fracture-toughness-test fracture (S)	68
2024-T6	
fatigue fracture (T)	118
fatigue striations (T)	118
2024-T851	
dimples (S)	74
fatigue fractures (L,T)	353, 462
fatigue striations (F,S,T)	74, 84, 353, 462
microvoid coalescence plus fatigue-striation formation (S)	74
notched, fatigue fracture (L,T)	353

Aluminum alloys, specific types (continued)

2025-T6	
fatigue fractures (L,M,P)	462-464
slip bands (M)	464
2124-T851, fracture, effect of inclusions (T)	96
2219-T87	
fatigue fractures (S)	85
fatigue striations (S)	85
shear steps (S)	85
6061, flux inclusions (S)	98
6061-T6	
fatigue-crack propagation (T)	86
fatigue fractures (T)	84, 86, 465
fatigue striations (T)	84, 86, 465
shear steps (T)	84
tire tracks (T)	86
7075 single crystal	
fatigue fracture (S)	260
solidification porosity (S)	260
7075-T6	
beach marks (S)	254, 256
brittle striations (S,T)	69-70, 87, 259, 260
clamshell marks (L)	358
cleavage facets (S,T)	251, 355, 356
cold shuts (L,T)	354
cone-shape fracture (L,S)	253
corrosion-fatigue fractures (S,T)	70, 87, 259-260, 261
corrosion leaves (M,P)	360
corrosion of fracture surface (S,T)	257, 258, 260, 359, 361
crack-growth bands (L)	120, 122
dimples (S,T)	68, 249, 250, 251, 252, 254, 255, 257, 355, 356, 358, 361, 465
dimples, sizes (S)	68
dimples, stereo views (S,T)	288, 289, 293
ductile striations (S)	259, 260
fatigue-crack propagation (S)	68
fatigue fractures (L,P,S,T)	32, 68, 85, 86, 87, 88, 120, 253-261, 357-358
fatigue fractures, stereo views (S,T)	290, 291
fatigue striations (S,T)	74, 85, 86, 87, 253, 254, 257, 258, 259, 260, 357, 358
fatigue striations, effect of corrosion (S)	70
fatigue striations, stereo views (S,T)	290-291
fracture propagation (T)	361
fractures, effect of environment (S)	251
fractures, effect of second-phase particles (S)	249, 250
fracture-toughness-test fractures (S)	250, 251
grain-boundary facets (S)	250
herringbone pattern (S)	258
impact fracture (T)	355
inclusions (S)	70, 250, 251, 254, 255
interdendritic porosity (S)	260
intergranular corrosion (M,P)	360-361
intergranular fractures (S,T)	89, 252, 260
intergranular separation, stereo views (S,T)	292, 293
intermetallic particles, cleavage (T)	465
internal-shearing fracture (L,T)	354
lap (L,T)	95
low-cycle fatigue striations (T)	86
mud cracks (T)	359
notched, fatigue fracture (S)	259
notched, tension-overload fractures (L,S,T)	252, 356
notched, tension-overload fractures, stereo views (S,T)	288-289
oxidation (L,T)	354
plane-strain fracture (L)	47

Aluminum alloys, specific types (continued)

- 7075-T6 (continued)
 plane-stress fracture (L) 47
 pores (S) 252, 257
 precipitate particles (T) 355, 356, 357
 quasicleavage facets (S) 251
 ratchet marks (L) 32
 reversed-bending fracture (S) 68
 river patterns (S) 251
 rubbing (T) 88, 355
 secondary cracks
 (L,S,T) 251, 252, 356, 357, 359, 360, 361
 second-phase particles (S) 250, 251, 255
 second-phase particles, cleavage
 (T) 355, 359
 second-phase particles,
 stereo views (S,T) 288, 289, 290, 291
 separated-grain facets (T) 355, 359
 serpentine glide (T) 361
 shot peened, fatigue fracture
 (L,P,S) 256-257
 slow-bend fracture (S) 251
 spectrum loading, fatigue-
 striation spacing (T) 85
 stereo views of fractures (S,T) 288-293
 stress-corrosion-cracking
 fracture (L,M,T) 358-361
 stress-corrosion-cracking fracture,
 stereo views (S,T) 292-293
 stretching (T) 356, 361, 465
 stretching, stereo views (S,T) 288
 tearing plus fatigue-striation
 formation (S) 74
 tear ridges (S) 74
 tension-overload fractures
 (L,S,T) 249, 250, 251, 252, 356, 465
 tension-overload fractures, effect
 of crosshead velocity (S,T) 288-290
 tension-overload fractures,
 stereo views (S,T) 288-289
 torsion-overload fracture (L,T) 355
 transgranular facets (T) 355, 359
 voids (S) 100
 weld, fatigue fracture (S) 100
 weld, shrinkage cavities (S) 100
 clad 7075-T6, fatigue-fracture
 propagation (L) 45
 7075-T651
 cleavage steps (S) 261
 corrosion-fatigue fracture (S) 261
 fatigue striations (L,S) 31, 261
 7075-T73
 beach marks (L) 31
 fatigue fracture (L) 31
 7076-T6
 fatigue fractures (L) 152
 fatigue striations (L) 139, 152
 impact fracture adjacent to
 fatigue fracture (L) 152
 notched, impact fracture (L) 152
 reversed-bending fracture (L) 152
 7079-T6
 chevron marks (L) 466
 corrosion leaves (L,M) 363, 465
 corrosion of fracture surface (T) 363
 corrosive environment, effect
 on fatigue striations (T) 88
 dimples (T) 362
 fatigue fracture (L,P,T) 362
 fatigue striations (T) 362
 forgings, intergranular fractures (T) 89
 fracture, change of mechanisms (L) 45
 fracture propagation (T) 362
 intergranular fractures (T) 89
 intergranular splintering (L) 363
 mud cracks (T) 363
 separated-grain facets (T) 362

Aluminum alloys, specific types (continued)

- 7079-T6 (continued)
 stress-corrosion-cracking
 fractures (L,M,P,T) 362-363, 465-467
 tension-overload fracture (T) 362
 7079-T651
 dimples (T) 363
 fatigue fracture (T) 87
 fatigue striations (T) 87
 mud-crack pattern (T) 92, 467
 notched, fracture (L,T) 363
 serpentine glide (T) 363
 stress-corrosion-cracking
 fracture (T) 467
 stretching (T) 363
 tension-overload fracture (L,T) 363
 7106-T63, stress-corrosion-cracking
 fracture (L) 467
 7178-T6
 brittle striations (L) 32
 dimples (T) 467
 ductile striations (L) 32
 stretching (T) 467
 tension-overload fracture (T) 467
 7475-T6
 cleavage step (S) 261
 corrosion-fatigue fracture (S) 261
 fatigue striations (S) 261
Aluminum - boron-fiber composite,
 fracture (S) 264
Aluminum brass, arsenical
 stress-corrosion fracture (S) 77
 transgranular fracture (S) 77
Aluminum-copper alloys
 dimples (S) 262, 263
 elevated-temperature fracture (S) 262-263
 grain-size differences (S) 262, 263
 intergranular fracture (S) 112, 113
 second-phase particles (S) 262, 263
 tensile-test fracture (S) 112
 tension-overload fractures (S) 262-263
Aluminum-silicon bronze, stress-
 corrosion-cracking fracture (L) 470
Amalgam, attack on aluminum alloy (T) 462
Angle shapes
 failure analysis (L,M,P) 386
 low-temperature fracture (L,M,P) 386
Antenna post, fatigue fracture (L) 468
Antimony
 cleavage fracture (L) 153
 impact fracture (L) 153
 secondary crack (L) 153
 trigonal symmetry (L) 153
 twins (L) 153
Antimony-bismuth alloy
 cleavage fracture (L) 155
 cleavage steps (L) 155
 dendritic segregation (L,M) 8
 impact fracture (L) 155
 microstructure (M) 8
 river patterns (L) 8
Arc strikes, cracking initiated from
 (L,M,P) 383, 390
AREA rails, fatigue fractures (L) 131
Armco iron
 bending fracture (T) 378
 cleavage fracture (L,M,T) 140, 141, 299, 378
 cubic fracture pattern (L) 142
 fatigue fracture (T) 378
 fatigue striations (T) 378
 fracture appearance
 effect of cold work (L) 141
 effect of hydrogen embrittlement
 (L) 141-142
 effect of inclusions (L) 142
 effect of temperature 129
 glide-plane decohesion (T) 81

Armco iron (continued)

- impact fractures (L,S) 140-142, 167
 intergranular fracture (S) 167
 low-temperature fractures
 (L,T) 83, 140-141, 298-299, 378
 microstructure (M) 299
 notch-impact fracture (L) 142
 oxygen-embrittlement fracture (S) 167
 quasicleavage (L) 140
 river patterns (L,S,T) 141, 142, 167, 378
 secondary cracks (L,S) 141, 142, 167
 serpentine glide (T) 81
 shear-overload fracture (L,T) 298-299
 sheet, fracture origin determination
 (L) 298
 slip steps (M,T) 81, 378
 tear ridges (T) 378
 tongues (T) 83, 299, 378
 twins (L) 140, 142
Armor plate, impact fracture (L) 133
Arrest marks (L,T) 29, 40, 42, 85-86, 117
Artifacts
 corrosion debris on replicas (T) 92
 in replicas (T) 61-63, 288, 289,
 291, 294, 295, 296, 354, 475
 in SEM fractograph (S) 217
 introduction in specimen preparation
 (E,S) 106, 107
 tearing in replicas (T) 371
Atlas of fractographs 129-475
Auger electron spectrometer 26, 52
Austenitic stainless steels
 austenitic structure (T) 224
 dimples (S,T) 224
 fracture features 114
 fracture-toughness-test fractures (S,T) 224
 low-temperature fractures (S,T) 224
 martensitic structure (S) 224
 oxide-film replicas 58
 stress-corrosion-cracking fractures
 (S) 76, 77, 115-117
 stretching (S,T) 224
Austenitic steels, cast
 dendrites (L) 454
 fracture (L) 454
 porosity (L) 454
Automobile parts. See under part name,
 such as *Pistons*.
Axles
 beach marks (L) 447
 bending-fatigue fracture (L) 447
 brittle fracture (L) 387
 failure analyses (E,L,M,P,S,T) 109, 110,
 178-179, 387, 388, 389, 390, 394, 403, 405
 fatigue fractures
 (L,P) 103, 390, 394, 403, 405, 447
 fracture during straightening (P) 388
 fracture during stretching (L) 388
 impact fracture (L,S) 178-179
 induction hardened, fatigue fracture
 (L) 389
 reversed-torsion fatigue fracture (L) 405
 rotating-bending fracture (L) 390
 tear fracture (P) 388
 torsional-fatigue fracture (L) 389-390

B

B-66 alloy
 cleavage-crack propagation (T) 82, 83
 cleavage steps (T) 468
 feather marks (T) 468
 impact fracture (T) 468
 tilt boundaries (T) 82
Background paper for photography
 (L) 11, 16, 17

Backscattered electrons (F) 49, 50
 penetration (F) 50
 resolution with 50
 use for fractography 50

Bainite
 in 1090 steel (S) 180
 in 4070 steel (M) 184

Barley shell pattern (L) 150

Beach marks (L) 29-30
 See also under specific metal.
 relation to fracture origin (L) 38, 41, 42

Bearing, fracture (P) 410

Bell-crank fitting
 failure analysis (M,P,S) 242-243
 impact fracture (M,P,S) 242-243

Bellows for cameras 12

Bells, fracture for quality control 2

Belts, fracture (M,P) 468-469

Bending fractures. See also under specific metal.
 stress states 37

Bend tests 104

Bernard, R. 49

Beryllium, cleavage facets 82

Beryllium copper
 dimples (T) 364, 365
 elevated-temperature fracture (L,T) 364-365
 fatigue fracture (L,T) 365
 fatigue striations (T) 365
 fracture propagation (T) 364
 intergranular facets (T) 364, 365
 notched, fracture (L,T) 365
 serpentine glide (T) 364
 stretching (T) 364
 tension-overload fracture (L,T) 364
 transgranular facets (T) 364

Billets, woody fracture (L) 136

Binocular stereo viewers 282

Biringuccio, Vannoccio 2

Bismuth
 cleavage steps (L) 154
 dendrite boundaries (L) 154
 impact fracture (L) 154
 ripples (L) 154
 secondary cracks (L) 154
 twins (L) 154

Bismuth-antimony alloys
 cleavage steps (L) 155
 impact fracture (L) 155

Bismuth-zinc alloys
 dendritic structure (L) 155
 impact fracture (L) 155
 low-temperature fracture (L) 155
 secondary cracks (L) 155
 trigonal symmetry (L) 155

Black-and-white film 18
 corrections in exposure 21
 developing 22-23

Blisters, de Réaumur's illustration (F) 3

Blooming-mill fractures (L) 136, 137

Blooming-mill spindle
 failure analysis (L) 398-399
 fatigue fracture (L) 398-399

Blooms, rock candy fracture (L) 137

Blowholes, in cast iron (S) 166

Bogie beam
 failure analysis (L,M,P) 465
 stress-corrosion-cracking fracture (L,M,P) 465

Boiler tube
 failure analysis (M,P) 380
 high-temperature fracture (M,P) 380

Boltholes
 effect on fatigue fracture (L,M,P) 393, 413, 472-473
 effect on stress-corrosion-cracking fracture (L,M,P) 466-467

Bolts
 cup-and-cone fracture (L) 388
 failure analysis (L,P,S) 200-201, 388, 470
 fatigue fracture (L,P,S,T) 45, 188, 200-201, 329, 337, 338, 372
 fracture-surface interpretation (L) 45
 notch-bend fracture (L) 132
 stress-corrosion-cracking fracture (L,T) 42, 325, 330, 470
 tension-overload fracture (L,P) 388

Bolt-torque link, stress-corrosion-cracking fracture (L,S) 194-195

Bomb-rack side plate
 failure analysis (L,S) 258
 fatigue fracture (L,S) 258

Boom-point pin, fatigue fracture (L) 446

Boron-fiber - aluminum composite
 cleavage facets (S) 264
 longitudinal tensile fracture (S) 264
 shear deformation of matrix (S) 264
 transverse compressive fracture (S) 264
 transverse tensile fractures (S) 264

Boron-fiber - titanium composite, longitudinal tensile fracture (S) 264

BORSIC composites (S) 264

Bourdon tube, failure analysis (E,T) 116, 117

Bracket, fatigue fracture (L) 450

Brake-cylinder pipe, failure analysis (E,L,P,T) 108

Brass, 80-20
 corrosion pits (M) 469
 fatigue fracture (M) 469

Brass ingots
 fracture (L) 138
 interdendritic surfaces (L) 138
 segregation (L) 138

Brazing flux, entrapment, effect on fracture (S) 98

Bright flakes, in aluminum alloy forging (L) 460

Brinell, Johann Augustus 4, 5

Brittle fractures 139
 crack propagation 28
 deformation 28
 features (F,L) 27
 radial zone 28
 relation to microstructure 7-8
 shear-lip zone 28
 stress states 36

Brittleness, fractographic evidence 109

Brittle striations (L) 32
 revealed by TEM (T) 87

Bromine - alcohol solutions, safety precautions 59

Bronze, fatigue fracture (L,M,P) 468-469

Bruchlinien 4

Bubble artifacts (T) 61, 62

Bulkhead cap, stress-corrosion-cracking fracture (L,M,P,T) 360-361

Bull gears
 failure analysis (L,T) 406
 fatigue fracture (L,T) 406

Burning
 effect on fracture of steel axle (L) 388
 effect on fracture of steel pump chamber (L,M) 392

C

Cadmium embrittlement (T) 92

Cameras 11-13
 focusing 13
 lenses 13

Camera stands 23

Cannon barrels, failure analysis 3, 4

Carbide particles, at fracture origins (S) 65

Carbon, use for shadowing replicas 24

Carbon replicas
 single-stage 58
 two-stage (F) 58, 59
 artifacts (T) 61-63
 thickness 59

Carbon steel castings, impact fracture (L) 131

Carbon steels. See also specific steel.
 beach marks (L) 130
 cleavage steps, stereo views (S,T) 283
 corrosion (L,M) 130
 corrosion-fatigue fracture (L,M) 130
 dimples, stereo views (S,T) 282-283
 fatigue cracks (L) 131
 hydrogen-induced flakes (L) 131
 impact fracture (L) 131
 stereo views (S,T) 282-283
 microvoid-coalescence fractures, stereo views (S,T) 282-283
 quasicleavage facets, stereo views (S,T) 282, 283
 segregation (L) 131

Carbon steel weld deposits
 cleavage fracture (L) 144
 hydrogen pickup (L) 144
 impact fracture (L) 144
 effect of electrode coverings (L) 144
 low-temperature fracture (L) 144
 river patterns (L) 144

Carburized steels
 bending-fatigue fracture (L) 33, 443
 fatigue fractures (L,P) 15, 412, 436
 impact-overload fracture (L) 41
 overload fractures (L) 444, 447
 spalling-fatigue fracture (L) 443
 tearing plus intergranular fracture (S) 74, 75

Cargo-door-cylinder support, fracture (T) 354

Carrier tray
 brittle fracture (L,P,S) 238-239
 failure analysis (L,P,S) 238-239

Case-hardened steels. See also *Carburized steels; Induction-hardened steels.*
 fatigue fractures (L) 134, 412, 436-437
 crack origins (L) 41
 fracture changes with change in structure (L) 16, 44-45, 110
 fracture propagation 40
 fretting fracture (L,P) 440
 tearing plus intergranular fracture (S) 74, 75
 torsional-overload fracture (L,P) 445

Castings
 dendrite patterns (L) 136, 138
 geometric patterns (T) 89
 interdendritic fractures 89
 porosity (L,M,S) 99-100

Cast iron
 bending fractures (S) 166
 blowhole (S) 166
 dimples (S) 166
 fracture, de Réaumur's analysis (F) 4
 inclusions (S) 166
 lamellar structure (S) 166

Cathode-ray tubes 50
 image buildup 50

Cathodoluminescence (F) 49, 50, 52

Cb-752 alloy, cleavage plus intergranular fracture (S) 73

Cellulose acetate
 removal from fracture surfaces 9
 use for coating fracture surfaces 9
 use for replicas 24, 57

Centerline crack (M) 381

Centerline segregation (L,M) 34, 136

Chain-hoist-hook housing
 failure analysis (L,P)456-457
 overload fracture (L,P)456-457

Chain links
 failure analysis (L,M,P)378, 379, 453
 fracture at welded joint (L,P)379
 impact fracture (M,P)378

Chalk, torsional fracture (F)37

Chemical analysis of fracture surfaces26
 attachments for scanning-electron microscope51-52

Chemical environments
 effect on fracture
 (E,P,T)45, 76-78, 90-92, 110-112
 fractures resulting (E,L,P,S,T)114-118

Chernoff, D. K.4

Chevron pattern (L)28-29, 30, 298, 310
 See also under specific metal.
 in fractured axles (L)387, 390
 in fractured roof-truss angle (L,M,P)386
 in fractured steel plate (L)383, 384, 385
 in fractured steel shaft (L)389
 in low-carbon steel (L)379
 relation to crack origin (L)40, 41
 relation to crack-propagation velocity (F)40, 41

Chilled white iron, fracture appearance,
 effect of microstructure44

Chromium-nickel-iron alloy
 fatigue striations (S)225
 secondary cracks (S)225

Chromium-plated steel, fatigue
 fracture (L,M)416-417

Chromium steel
 impact-overload fracture (L)40
 notched, impact-overload fracture (L)40

Clamp
 failure analysis (L,P)427
 fatigue fracture (L,P)427

Clamshell marks (L,M,S)29, 222, 223, 358

Cleaning fracture surfaces9-10
 for replication56
 for SEM viewing (S)234

Cleavage cracks, fracture origin (L,T)95

Cleavage fractures. See also under specific metal.
 characteristics139
 crack origins (S)65
 crack propagation (F,T)82, 83
 features revealed by light microscope32
 features revealed by SEM (S)64-65
 features revealed by TEM (F,T)82-84
 metals in which they occur64, 82
 plus fatigue-striation formation (S)72, 73
 plus intergranular fracture (S)72-73
 plus microvoid coalescence (S)71-72
 plus tearing (S)72
 relation to microstructure7-8
 stress states36

Cleavage steps (L)141
 See also under specific metal.
 in quasicleavage (F)84
 revealed by SEM (S)64-65
 revealed by TEM (T)82, 83

Cleavage tongues. See *Tongues*.

Clevis, failure analysis (E,L,P,T)108

Close-up lenses12

Cluster gears
 failure analysis (P)447
 overload fracture (P)447

Clutch-assembly spring, fatigue
 fracture (S)183

Clutch shaft, fatigue fracture (L,S)183

Coating of fracture surfaces9

Coating of replicas51, 60

Cobalt-base heat-resisting alloys,
 fractures (L,T)343-345

Cobalt-molybdenum steels
 cleavage facets (S)217
 dimples (S)218
 impact fractures (S)217-218
 effect of heat treatment (S)218
 intergranular separation (S)218
 secondary grain-boundary cracks (S)217

Cock valve, failure analysis (L,M)470

Coil-grab arm
 failure analysis (L,M,P)446
 fatigue fracture (L,M,P)446

Coil springs
 failure analysis (L,M,P,S,T)222-223, 440
 fatigue fracture (L)440

Cold finger56

Cold lap (T)349

Cold microscope stages52

Cold shuts
 fracture origins93
 in aluminum alloy forging (L,T)354

Color film18
 corrections in exposure21

Columbium
 cleavage steps (T)468
 impact fracture (T)468
 low-temperature fracture (T)468
 tilt-twist boundary (T)468

Columbium alloys
 cleavage-crack propagation (T)82, 83
 cleavage plus intergranular fracture (S)73
 tilt boundaries (T)82

Columbium alloys, specific types
 B-66
 cleavage-crack propagation (T)82, 83
 cleavage steps (T)468
 feather marks (T)468
 impact fracture (T)468
 tilt boundaries (T)82
 Cb-752, cleavage plus intergranular fracture (S)73

Columnar fracture
 Percy's description4
 Tiemann's description5

Composites, fracture (S)264-265, 279

Compression fractures, stress states
 (F)36, 37

Compressor disks
 failure analyses (E,L,M,P,T) 118, 119, 472-473
 fatigue fractures
 (E,L,M,P,T)118, 119, 472-473

Compressor rotor, fatigue fracture (L,T)331

Conchoidal marks (T)29, 352
 See also *Beach marks*.

Condenser lenses54

Condenser tube, stress-corrosion-cracking
 fractures (S)77, 78

Conductive coatings, on replicas51, 60

Connecting-rod bolts, fatigue
 fractures (L,P,S,T)188

Connecting-rod journals, chromium
 plated, fatigue fracture (L,M)417

Connecting rods
 failure analyses (L,P,S)237, 393, 448
 fatigue fractures (L)393, 448
 single-overload fracture (L)393
 sudden-overload fracture (L,P,S)237

Constant-mesh transmission gear,
 failure analysis (L,P)400

Continuous belts
 failure analysis (M,P)468-469
 fracture (M,P)468-469

Controlled fracture1

Control-system clevis, failure analysis
 (E,L,P,T)108

Conversion-oxide-film replicas58-59

Conveyor-chain links, failure
 analysis (L,M)453

Cooling-tower fan blade, stress-corrosion-
 cracking fracture (L,M,P,T)349

Copper. See also *High-purity copper*.
 creep-rupture fractures (S)266-267
 stereo views (S)266-267
 dimples (S)266, 267
 elevated-temperature fractures (S)266-267
 fracture for quality control2
 intergranular fracture (S)266, 267
 palladium coated, stretching (M)468
 separated-grain facets (S)266, 267
 tension-overload fracture (T)468
 transgranular fracture (S)266, 267

Copper alloys. See specific alloy, such as
Copper nickel, 30%.

Copper alloys, specific types
 360
 corrosion pitting (S)78
 stress-corrosion fracture (S)78
 687
 stress-corrosion fracture (S)77
 transgranular fracture (S)77
 715
 elevated-temperature fracture (S)76
 intergranular fracture (S)76

Copper-beryllium alloys. See also
Beryllium copper.
 dimples (S)269
 fractures, effect of aging temperature
 (S)269
 fracture-toughness-test fractures (S)269
 pores (S)269
 secondary cracks (S)269
 transgranular fracture (S)269

Copper nickel, 30%
 elevated-temperature fracture (S)76
 intergranular fracture (S)76

Copper-nickel-iron alloys
 dimples (S)269
 fracture-toughness-test fractures (S)269
 separated-grain facets (S)269
 spinodal microstructure (S)269
 tensile-overload fractures (S)269

Corrosion-fatigue fractures. See
 also under specific metal.
 fracture features (E,L,P,T)114-115, 116
 revealed by TEM (T)91-92

Corrosion leaves (M,P)360, 363, 465

Corrosion pits (E,M,S)78, 106,
 107, 180, 244, 459
 stereo views (S,T)292-293

Corrosion products
 on fracture surfaces (S,T)78, 92, 93,
 94, 95, 111, 193, 194, 221, 248, 257, 258,
 260, 309, 314, 315, 332, 333, 336, 359, 361
 on stress-corrosion cracks (M)35

Corrosive environments
 effect on fatigue fracture
 (L,P,T)87, 88, 427, 429, 459, 460, 463
 effect on fracture (E,P,T)110-112
 fractures resulting from
 (E,L,P,S,T)114-117, 118

Crack arrests29
 in case-hardened parts40
 in spectrum loading (T)85-86
 in stress-corrosion fractures (T)117
 relation to crack origins (L)40, 42

Crack-growth bands (E,F,L,P,T)118-124

Crack-growth rate
 effect of environment (L,T)373
 fatigue cracks (E,F,L,T)118-124

Crack origins (F,L)38-42
 arc strikes (L,M,P)383, 390
 cleavage fractures (S)65
 determination (E,L,P,T)106-107
 from chevron marks (L)28-29, 30, 40-41
 from fracture profiles24

Crack origins (continued)

- determination (continued)
 - from radial marks (L) 39, 40
- discontinuities at (L,M,T) 93, 314, 379
- effect of notches (F) 38
- fatigue fractures (S) 68-69
- fractographic mapping (F) 42
- importance in failure analysis
 - (E,L,P,T) 106-107
- revealed by SEM (S) 65, 68
- revealed by visual examination
 - (F) 38
- shear lip at (L) 39
- tensile fractures (L) 28
- Crack propagation (F,L)** 42-44
- bands (L) 120, 122
- cleavage fractures (F,S,T) 65, 68-69, 82, 83
- determination
 - from chevron patterns
 - (L) 28-29, 30, 298, 310
 - from fracture profiles (M) 24, 25, 26
 - from hackle marks (L) 298
 - from tongues (T) 299
- fatigue fractures (S,T) 68-69, 338, 339
- importance in failure analysis
 - (E,P) 106-107, 108
- mixed mechanisms (S) 71-75, 192
- rectangular specimens (F) 38, 39
- relation of macroscopic to local
 - direction 83
- revealed by SEM (S) 65, 68-69
- revealed by visual examination (F) 38
- Cracks**
 - effect on fracture origin (L,M,P) 434
 - nondestructive inspection 10
 - opening (L,P,S) 10, 189, 194, 258
 - revealed by fractography 109
- Crane gears**
 - failure analysis (M) 397
 - fatigue cracking (M) 397
- Crane wheels**
 - failure analysis (L) 407
 - fatigue fracture (L) 407
- Crankshafts**
 - bending-fatigue fracture (L) 400
 - failure analyses (L,M,P) 400, 401, 402, 403, 404, 416-417, 420-421
 - fatigue fractures (L,M,P) 93, 404, 416-417, 420-421, 451
 - induction hardened, torsional-fatigue
 - fracture (L) 401
 - reversed-torsion fatigue fracture
 - (P) 403
 - torsional-fatigue fracture (L) 401
- Creep-to-rupture fractures** 112-113
- Crewe, A. V.** 49
- Cryogenic-temperature fractures,**
 - characteristics 111-112
- Crystalline fractures**
 - Brinell's description 5
 - Percy's description 4
 - Tiemann's description 5
- Crystallographic orientation, effect**
 - on fracture appearance (T) 372
- Cubic cleavage, in pure iron (M)** 26
- Cup-and-cone fractures**
 - first treatment 4
 - in 13-8 PH stainless steel (L,T) 328
 - in 17-4 PH stainless steel (T) 330
 - in 1038 steel (L) 388
 - in 4340 steel (L,T) 306-307
 - in 8740 steel (L) 316
 - in alloy 718 (L,T) 228, 337
 - in H11 tool steel (L) 324
 - in L6 tool steel (L) 134
 - in Ti-6Al-4V (L) 274
- Cutting fracture specimens** 10

Cyclic-loading spectrums, crack-growth

- rate (E,F,L,P,T) 85, 118-124
- Cylindrical specimens, fracture**
 - marks (F,L) 27-28, 43

D**D-6ac steel**

- beach marks (L) 31
- fatigue fracture (L,T) 31, 87
- fatigue striations (T) 87
- secondary cracking (M) 35
- stress-corrosion-cracking fracture
 - (L,M,T) 35, 318

D6B steel, fatigue fracture (L) 418**Damper-actuator rod, fracture (L,T)** 301**Davoine, F.** 49**Decarburization**

- effect on fatigue fracture (M) 435, 442
- effect on fracture appearance (L,M) 145
- effect on impact fracture (S) 179

Deep-field photographic microscope 26**Defects. See Discontinuities and specific**
type, such as *Inclusions; Laps.***Deformation**

- effect of applied stress 109
- measuring technique 25

Deformation twins. See Twins.**Dendritic structure** 33

- de Réaumur's illustration (F) 4
- in 1015 steel (S) 171
- in alloy 718 casting (S) 227
- in antimony-bismuth alloy (L,M) 8
- in maraging steel casting (S) 207
- in steel castings (L) 131, 382
- de Réaumur, R. A. F. (F) 2-3, 4

Developing film 21**Dies, fatigue fracture (L)** 134**Dimples. See also under the specific**

- metal.
 - classification (F) 105
 - formation (F) 79-80
 - at inclusions (T) 96
- growth (S) 66-67
- indication of stress orientation 109
- in fatigue fractures (T) 86
- initiation (S) 66, 67
- revealed by light fractographs (L) 33-35
- revealed by SEM (S) 34, 35, 66-68
- revealed by TEM (T) 79-81
- shapes (F,S,T) 66-67, 79, 80
- sizes (S,T) 66-68, 80, 81
- stereo views (S,T) 286, 288, 293, 294

Direct carbon replicas 58**fractographs from**

- (T) 56, 81, 101, 323, 326, 378, 468, 471

Discontinuities. See also the specific

- type, such as *Stringers; Inclusions.*
 - effect on fracture (A) 93-103
 - revealed by light microscope (L) 32-33, 34, 94, 95, 97, 99, 100, 101, 102, 103
 - revealed by SEM (S) 94, 95, 97, 98, 99, 100
 - revealed by TEM (T) 94, 95, 96, 99, 101, 102

Dislocation-density measurements 26**Dispersive spectrometers** 26, 51-52**Dragline-excavator I-beam, fatigue**

- fracture (L,M) 394-395

Drills, fatigue fracture (L) 133**Drive shafts**

- corrosion-fatigue fracture (L,M) 130
- failure analysis (P) 387
- torsion-overload fracture (P) 387

Ductile-brittle fracture transition,

- in 4340 steel (L) 425

Ductile fractures

- effect of inclusions (T) 96
- features (F,L) 27

Ductile fractures (continued)

- features revealed by SEM (S) 66-68
- relation to microstructure 7
- stress state 36

Ductile iron

- beach marks (L) 451
- dimples (T) 320
- fatigue fracture (L) 450, 451
- impact fracture (L,M,P) 450
- induction hardened, fatigue
 - fracture (L) 451
- oxidation of fracture surface
 - (M,P) 450
- spheroidized-graphite structure (M) 450
- torsion-overload fracture (L,T) 320

Ductile striations (L,T) 32, 87**Ductility, fractographic evidence** 109**Duranickel**

- cleavage facets (S) 235
- fatigue striations (S) 235
- intergranular fractures (S) 235
- river patterns (S) 235
- slow-bend fracture in hydrogen (S) 235
- tongues (S) 235

E**Electron emission, in scanning electron**

- microscope (F) 50

Electronic-flash lights 14**Electron microprobe analyzer** 52**Electron-microscope fractography**

- preparation of specimens (A) 9-10
- preservation of specimens (A) 9-10
- transmission vs scanning (S,T) 61
- use for failure analysis (A) 106-124
- uses other than failure analysis (A) 103-105

Electron microscopes

- scanning (F) 49-50
- transmission (F) 54-56

Electroplating, effect on fracture

- (L,M) 45, 189, 310-311

Elevated-temperature fractures

- characteristics 112
- fracture mechanisms (L) 46, 47
- in 301 stainless steel (S,T) 223
- in 302 stainless steel (L,T) 332-333
- in 304 stainless steel (S) 224
- in 430 stainless steel (L) 145
- in 446 stainless steel (L) 147
- in 4130 steel weld (L,T) 301
- in 4340 steel (L) 27, 422, 424
- in 5155 steel (S) 196
- in alloy 713C (L,T) 335
- in alloy 713LC (L,P,T) 334
- in alloy steels (S) 203
- in aluminum-copper alloy (S) 262-263
- in beryllium copper (L,T) 364-365
- in Hastelloy C-276 (E,S) 118
- in Hastelloy X (S) 225
- in high-carbon steels (S) 180-183
- in high-purity copper (S) 266-267
- in IN-100 (L,S,T) 232-233, 336
- in iron (S) 168
- in L-605 alloy (T) 344
- in low-carbon steels (M,P,S) 170, 173, 380
- in titanium (M,P,T) 368
- in U-700 alloy (L,S) 230
- in Waspaloy (L,T) 340-341
- in wrought iron (T) 300

Embrittling phases, fracture

- origins (T) 100-102

Energy-dispersive spectrometers 52**Environments**

- consideration in failure analysis
 - (E,P,T) 106, 110-112, 114-117

Environments (continued)

- effect on fatigue-striation formation (T) 30, 87-88, 91-92
- effect on fracture (L,S,T) 236, 247-249, 259-261, 273, 276-279, 373
- crack-origin location (L) 42
- effect on fracture features, revealed by SEM (S) 75-78
- effect on fracture mechanisms (F,L) 45-47
- Equalizer bar**
 - failure analysis (L) 418
 - fatigue fracture (L) 418
- Equiaxed dimples**
 - revealed by SEM (S) 66-67
 - revealed by TEM (T) 79, 80
- Ercker, Lazarus** 2
- Etch pitting** 26
- Eutectic aluminum-copper alloy, tension-overload fracture (S)** 262-263
- Eutectic melting, fracture origins (L,T)** 100, 101-102
- Exhaust-valve stem, fracture (L)** 16
- Exposure meters** 18-19
- Exposures for photography**
 - computation 19-21
 - test exposures (L) 21
- Extension-housing yoke**
 - failure analysis (L,P,S) 240-241
 - fatigue fractures (L,P,S) 240-241
 - fracture propagation (L,S) 241
- Extension tubes** 12
- Extraction replicas (T)** 102

F

- Facets.** See also *cleavage facets* and *quasicleavage facets* under specific metals.
 - de Réaumur's illustration (F) 3
- Failure analysis (A)** 106-124
 - corrosion-fatigue fractures (E,L,P,T) 114-115, 116
 - effect of environment (E,P,T) 106, 110-112
 - effect of loading 106, 107-109
 - effect of material condition 106, 109
 - effect of size and shape of part 106, 109-110
 - failure causes 377
 - fatigue-crack-growth rate (E,F,L,P,T) 118-124
 - fatigue fractures (E,L,P,T) 108, 118-124
 - fractographs (A) 377-475
 - from test fractures 48
 - intergranular fractures (L,M,S,T) 112-114
 - record keeping 60-61
 - specimen preparation (E,S) 9-10, 106, 107
 - visual examination 106
- Fan blades**
 - failure analysis (L) 455
 - fatigue fracture (L) 455
 - stress-corrosion-cracking fracture (L,M,P,T) 349
- Fan-shaped patterns (L)** 135
- Faraday cage (F)** 50, 51
- Fatigue cracks**
 - definition 29
 - growth rate (E,F,L,T) 118-124
- Fatigue fractures.** See also under specific metal.
 - beach marks (L) 29-30
 - clamshell marks (L,M,S) 29, 222, 223, 358
 - conchoidal marks (T) 29, 352
 - crack growth (E,F,L,T) 108, 118-124
 - crack origins (L,S) 41-42, 68, 108
 - dimpled bands (T) 86
 - effect of environment (T) 91-92

Fatigue fractures (continued)

- effect of stress intensity (L,S) 45, 69, 70
- features revealed by light microscope (L) 30-31, 32
- features revealed by SEM (S) 68-70
- features revealed by TEM (T) 84, 85-89
- fracture propagation (F,S,T) 41, 42-44, 68-69, 84, 85-88
- high-amplitude vs low-amplitude cycles (T) 85, 352-353
- macroscopic features (L) 120
- macroscopic vs microscopic crack-growth rate (F) 86
- microscopic features 120
- plus cleavage (S) 72, 73
- plus intergranular fracture (S) 75, 77
- plus microvoid coalescence (S) 73-74
- plus tearing (S) 74, 75
- ratchet marks (L) 30-31, 32
- spectrum loading (E,F,L,P,T) 85-86, 118-124
- stages (S) 68-69, 85
- stress states 36
- striations. See *Fatigue striations*.
- surface marks (F) 43, 44
- tearing (T) 86
- Fatigue striations (L)** 30, 31, 32
 - See also under specific metal.
 - causes 85
 - masking 108
 - relation to loading (E,F,L,T) 118-124
 - revealed by SEM (S) 68-70, 85
 - revealed by TEM (F,T) 84, 85-88
 - shadowing to reveal 60
 - similar structures (T) 88-89
 - spacing 68
 - stereo views (S,T) 287, 290, 291, 295
- Feather marks**
 - in molybdenum (L) 157
 - in tungsten (T) 83, 375
 - in TZM alloy (T) 367
 - revealed by TEM (T) 83
- Ferrite-pearlite structure**
 - in ASTM A36 steel (M) 175
 - in low-carbon steel (S) 173
- Ferrite structure**
 - in low-carbon iron (S) 168
 - in low-carbon steel (M) 380, 381
- Ferrochromium alloys**
 - cleavage fracture (L) 148, 149
 - impact fractures (L) 148, 149
 - effect of high nitrogen (L) 148
 - effect of low carbon (L) 148
 - river patterns (L) 148, 149
- Fibrous fractures (L)** 136
 - Brinell's description 5
 - de Réaumur's illustration (F) 2, 3
 - Kirkaldy's analysis 3
 - marks, relation to crack origin 38-39
 - Percy's description 4
 - ridges (S) 104
 - Tiemann's description 5
- Fibrous zone**
 - in cylindrical specimens (F,L) 27-28
 - in rectangular specimens (F,L) 28-29
- Filletts, effect on fracture (L)** 389, 402, 403, 431, 434, 439, 443, 464, 470
- Film-flash guide number** 19-21
- Film for photography** 12, 18
 - corrections in exposure 21
 - developing 21
 - identification 21
 - printing 22-23
- Final-drive pinion, spalling-fatigue fracture (L)** 443
- Firing fracture (L,T)** 376
- Fisheyes (L)** 6, 139, 312
- Fishing technique** 59

Fitting, stress-corrosion-cracking

- fracture (L,M,T) 358-359
- Fixing film** 21
- Flame cutting fracture specimens** 10
- Flame-hardened steels, fracture (M)** 397, 398, 399
- Flash lights**
 - exposure computations 19-21
 - flash distance from subject 20
- Flask, stress-corrosion-cracking fracture (L,T)** 303
- Flow lines, fractures at** 103
- Flow-through, in aluminum alloy forging (L,T)** 354
- Fluorescent lights** 13, 14
- Flux inclusions, effect on fracture (S)** 98
- Focal lengths of lenses** 13
- Focusing cameras** 13
- Folds**
 - de Réaumur's illustration (F) 3
 - fracture origins (L,S,T) 93, 94
- Folsom find (P)** 1
- Forging defects, effect on fracture (L,S,T)** 95, 97, 100, 101, 103, 109, 405, 460
- Forging-hammer piston rod**
 - failure analysis (L) 418
 - fatigue fracture (L) 418
- Forging-hammer shaft**
 - failure analysis (L) 396
 - fatigue fracture (L) 396
- Fourdrinier wire cloth**
 - failure analysis (M,P) 468-469
 - fatigue fracture (M,P) 468-469
 - tension fracture (M,P) 469
 - wear (P) 468-469
- Fractographic mapping (F)** 42
- Fractography**
 - definition 1
 - historical background (A) 1-9
 - procedures for study of fracture paths 103, 104
 - recording examination steps 10, 11
 - relation of fractographs to microstructure (L,M) 7-8
 - use in failure analysis (A) 106-124
 - uses other than failure analysis (A) 103-105
- Fractured parts**
 - cleaning 9-10
 - cutting 10
 - opening secondary cracks 10
 - photography (A) 11-24
 - preservation 9, 106
 - sectioning (M) 10, 24-25, 26
 - shape, consideration in failure analysis 106, 112
 - size, effect on fracture mechanism 112
 - visual examination 11, 106
- Fracture mechanisms.** See also *Cleavage fractures; Microvoid-coalescence fractures; Quasicleavage fractures; Fatigue fractures; Tearing fractures.*
 - change during crack propagation (F,L) 44-48
 - effect of size and shape of part 112
 - mixed-mechanism fractures (S) 71-75
- Fracture origins (F,L)** 37, 38-42
 - cleavage fractures (S) 65
 - determination (E,L,P,T) 106-107
 - from beach marks 38
 - from chevron marks (L) 28-29, 38, 298, 310
 - from fracture profiles 24
 - from hackle marks (L) 298
 - discontinuities at (L,M,T) 32-33, 93, 306, 308, 309
 - fatigue fractures (S) 68-69
 - fractographic mapping (F) 42

Fracture origins (continued)

- importance in failure analysis (E,L,P,T) 106-107
- Martens' treatment 4
- notched compared with unnotched specimens (L,T) 39, 316-317
- Fracture profiles (M)** 24-25, 26
- Fracture propagation (F,L)** 42-48
- bands (L) 120, 122
- cleavage fractures (S) 65, 68-69
- determination
 - from chevron marks (L) 298
 - from hackle marks (L) 298
 - from shape of local zones of fracture (L) 42-44, 298
 - from tongues (T) 299
- effect of chemical environment (L) 45
- effect of impact energy (F,L) 47
- effect of microstructure (L) 16, 44-45
- effect of stress-intensity factor (L) 44-45
- effect of stress state (F,L) 47-48
- fatigue fractures (S) 68-70
- fractographic sequences (L,T) 338, 339, 346-347, 352-353
- Kirsh's treatment 4
- mechanism changes (F,L) 44-48
- mixed mechanisms (S) 71-75, 192
- paths (S) 103-104
- procedures for studying 103, 104
- relation of macroscopic to local
 - direction 83, 86
 - surface marks (F) 42-44
- Fracture strain analysis** 26
- Fracture-surface matching** 25
- Fracture surfaces**
 - characteristics (F,S,T) 104-105
 - chemical damage 9
 - cleaning 9, 56
 - coating 9
 - corrosion (T) 9, 92
 - interpreting
 - with light fractography (A) 36-48
 - with SEM fractography (A) 64-78
 - with TEM fractography (A) 79-92
 - mechanical damage (L) 9, 253
 - photography (A) 11-24
 - stereo-pair photographs (F,L,S,T) 22, 23, 98, 104, 111, 266-267, 281-296
 - visual examination 11
- Fracture tests**
 - fracture-toughness tests 104
 - tensile tests (L) 27-28
 - use for distinguishing iron from steel 2, 3
 - use for rating prior austenite grain size 5
- Free-cutting brass**
 - corrosion pitting (S) 78
 - stress-corrosion fracture (S) 78
- Free-machining copper**
 - copper-tellurium particles (S) 268
 - dimples (S) 268
 - tensile-overload fracture (S) 268
- Full-slant shear fractures (F,M)** 37, 39
- crack propagation (M) 39, 40

G

- Galvanized steel, fracture at welded joint (L,P)** 379
- Gas cavities (L)** 33, 457
- Gas porosity (L,M)** 99-100, 137-138
- Gas-turbine wheel**
 - failure analysis (L,S) 234
 - fatigue fracture (L,S) 234
- Gear boxes**
 - failure analysis (E,L,P,T) 109-110
 - fatigue fracture (E,L,P,T) 109-110

Gear housing, overload fracture, effect

- of porosity (S) 100
- Gears**
 - bending-fatigue fracture (P) 443
 - failure analyses (L,M,P) 397, 400, 405, 406, 412, 436, 437, 443, 447
 - fatigue cracking (M) 397
 - fatigue fractures (L,P,T,S) 198, 319, 405, 406, 412, 436
 - crack origin (L) 41
 - fracture originating at inclusion (L) 33
 - impact fracture (L) 437
 - spalling (P) 436
- Gellert, C. E.** 3
- Generator gear box, failure analysis (E,L,P,T)** 109-110
- Geometric patterns**
 - fractures in aluminum alloy forgings (L,T) 100, 101
 - fractures in weld metal (L,T) 100
 - revealed by TEM (T) 89-90
- Glass, fractures** 129
- Glassy fractures, ferrochromium alloy (L)** 149
- Glide, fracture by (F,T)** 81
- Glide-plane decohesion (T)** 66, 81
- Glossy photographs** 22-23
- Gold**
 - aggregate size of vapor-deposited (T) 56
 - shadowing fracture surfaces (S) 26, 250
- Grain-boundary discontinuities, fracture origins (L,T)** 100-101
- Grain-boundary separation**
 - revealed by SEM (S) 69-70, 71
 - revealed by TEM (T) 89-90
- Grain facets** 31-32
- Grain flow**
 - effect on fracture (L) 103
 - lighting to show (F,L) 17
- Grain-size determination**
 - in SEM fractographs (S) 64, 69
- Granular crystalline fractures, Brinell's description** 5
- Granular fracture**
 - de Réaumur's illustration (F) 3
 - Percy's description 4
 - Tiemann's description 4-5
- Graphite-fiber - magnesium composites, longitudinal tensile fracture (S)** 265
- Gray iron**
 - fractographic features 42
 - fracture, de Réaumur's analysis (F) 4
 - fracture-origin determination 42
 - graphite flakes (M) 451
 - pearlite platelets (T) 88
- Grinding cracks, effect on fracture (M,T)** 309
- Grinding relief, effect on fatigue fracture (L,S)** 234
- Grinding-wheel fractures** 129

H

H11 steel. See Tool steels, specific types, H11.

- Hackle marks (L)** 298
- Hackly fracture**
 - Brinell's description 5
 - Tiemann's description 5
- Hairline indications (T)** 90, 318
- Halide flux, entrapment, effect on fracture (S)** 98
- Halted fracture (L)** 133, 138
- Hammer-burst fractures (L)** 135
- Hastelloy C-276**
 - elevated-temperature fracture (E,S) 118
 - intergranular fracture (E,S) 118

Hastelloy X

- dimples (S) 225
- elevated-temperature fractures (S) 225
- grain-boundary facets (S) 225
- tensile fractures (S) 225
- transgranular fractures (S) 225
- Heat exchangers, intergranular fracture (S)** 76
- Heat-treat cracks**
 - effect on fracture (L,T) 318
 - fracture origins (L,M) 93-94, 95, 109, 453
 - temper colors 94
- Heat treatments, effect on fracture (E,L,M,S,T)** 109, 110, 176-177, 214
- Height measurements, use of shadow casting** 26
- Herringbone patterns (L)** 28-29
- revealed by TEM (T) 83-84
- High-carbon steels. See also specific steel.**
 - beach marks (L) 410
 - fatigue fractures (L,P) 410
 - impact-overload fractures, crack origins 40
- High-cycle fatigue fractures** 84, 85
- High-inertia collision fractures** 112
- High-lead low-tin solders, tensile peel-test fractures (L,S,M)** 270-271
- High-magnification fractography. See Microfractography; Electron-microscope fractography; Light-microscope fractography.**
- High-oxygen high-sulfur iron, bending fractures (S)** 165-166
- High-oxygen low-carbon iron**
 - fatigue fracture (S) 167
 - tensile fractures (S) 164-165
- High-purity copper**
 - creep-rupture fractures (S) 266-267
 - intergranular fracture (S) 266, 267
 - transgranular fracture (S) 266, 267
- High-purity iron**
 - brittle fracture (S) 169
 - cleavage steps (S) 162, 169
 - dimples (S) 163
 - impact fracture (S) 162
 - inclusions (S) 163
 - low-temperature fractures (S) 162, 169
 - notch-bend fracture (S) 162, 169
 - river patterns (S) 162
 - tensile fractures (S) 163
 - tongues (S) 162
 - twins (S) 162
- High-purity zinc, impact fracture (L)** 160
- High-silicon steels, impact fracture (S)** 179
- High speed steel**
 - impact fractures (L) 135
 - stereo views (S,T) 285
- High-strength low-alloy steels. See also specific steel.**
 - fatigue fracture (L) 437
 - hydrogen-embrittlement fracture 90
 - intergranular fractures (T) 90
 - pressure-test fracture (L) 426
 - stress-corrosion-cracking fracture (T) 90
 - transgranular fracture (T) 90
- High-strength steel**
 - corrosion products on fracture surface (S) 193
 - dimples (S) 193
 - overload fracture (S) 193
 - stress-corrosion-cracking fracture (S) 193
- High-sulfur high-oxygen iron**
 - bending fractures (S) 165-166
 - effect of manganese addition (S) 166
 - shrinkage cavity (S) 165

- High-temperature fractures.** See also *Elevated-temperature fractures.*
 characteristics112
 fracture mechanisms (L)46, 47
- High-velocity fractures (L)**29
- Hillier, J.**54
- Holes**
 effect on fracture (L,M,P) 318, 353, 354, 401, 416, 448, 456, 461, 466-467, 471, 472-473
 effect on fracture appearance (F)39
 effect on fracture mechanism (T)310-311
- Hollow drills, fatigue fractures (L)**133
- Hooked fracture**5
- Hoop specimens**
 hydrogen-embrittlement fracture (L,T) 323
 stress-corrosion-cracking fracture (L,T)326, 359
- Hot microscope stages**52
- Hot tears (L)**33
- Housings**
 failure analysis (L,M,P)450, 456-457
 overload fractures (L,P)456-457
 effect of porosity (S)100
- Hubbard, James Lee**281
- Hubs**
 failure analyses (L,M,P,S)245-246, 430, 460
 fatigue fractures (L,P,S)245-246, 430, 460
- Hydraulic-piston rods, fatigue fracture (L,M)**379
- Hydraulic radiator assembly, failure analysis (E,T)**118
- Hydrogen embrittlement**
 effect on fracture appearance (L)6, 7
 effect on microstructure7
 intergranular nature (S)70, 71, 76-77
- Hydrogen-embrittlement cracking (P)** 310-311
- Hydrogen-embrittlement fractures**
 compared with stress-corrosion fractures (E,P,T)111
 crack origins42
 effect of notch radius (T)434
 features (E,P,S,T)76, 90-91, 111
 propagation90
- Hydrogen flakes**139
 in 4340 steel (L)312
- Hydrogen porosity, fracture origins (L,M)**99-100
- Hypercompressor packing retainers, failure analysis (E,L,P)**115
- Hypercompressor valve blocks, failure analysis (E,L,P,T)**114-115, 116
- I**
- I-beam**
 failure analysis (L,M)394-395
 fatigue fracture (L,M)394-395
- Idler gear, bending-fatigue fracture (P)**443
- Idler shaft**
 failure analysis (M,P)396
 tapered-plug fracture (M,P)396
- Illumination for photography (F,L)**13-18
- Impact fractures.** See also under specific metal.
 crack origins (F,L)40-41
 features (S)64-66, 67, 68
 laboratory tests139
- Impeller**
 failure analysis (E,S)106, 107
 solidification shrinkage (M)137-138
- Imperfections.** See *Discontinuities.*
- IN-100 alloy**
 dimples (T)336
 elevated-temperature fractures (L,S,T)232-233, 336

- IN-100 alloy (continued)**
 glide-plane decohesion (T)336
 intergranular fractures (S)233
 oxidation of fracture surface (T)336
 powder metallurgy compacts, tension-overload fracture (S)232-233
 stress-rupture fracture (L,T)336
 stretching (T)336
 tension-overload fractures (S)232-233
- Incident-light exposure meters**19
- Inclusions (L)**33
 effect on fracture (L,M)352, 406, 431, 441, 449, 454, 455
 extraction of105
 fracture origins (L,S,T) 33, 94, 96-99, 191, 396
 in 1090 steel (S)181
 in 4130 steel (S)185
 in 4340 steel (S)191
 stereo views (S,T)286
 in 7140 steel (S)198
 in 8620 steel (L,M)15, 25
 in alloy steel (S)203
 in aluminum alloys, cast (S)242
 in aluminum alloys, wrought (S)246, 247, 248, 250, 251, 254, 255
 in Armco iron (L)142
 in high speed steel, stereo views (S,T)285
 in iron (S)163-167
 in iron-silicon alloy (L)151
 in low-carbon steel (S)173
 in manganese steel, stereo views (S,T)284
 in maraging steel (S,T)104, 206
 in molybdenum (L)156, 157
 in molybdenum steel (S)215
 in rolled steel (S)177
 in stainless steel (M,S,T)222, 223
 in titanium alloys (S)274
 in tough pitch copper (T)468
 in tungsten (L)158-159
 relation to dimple formation (S)67, 68
 stereo views (S,T)284, 285, 286
- Induction-hardened steels**
 bending-fatigue fractures (L,P)400, 448
 fatigue fractures (L,P,T)16, 25, 389, 390, 391, 403, 406
 reversed-torsional-fatigue fracture (L)405
- Ingot iron**
 cleavage fracture (L,T)140, 141, 378
 cubic fracture pattern (L)142
 fracture appearance (L)129, 141-142
 hydrogen-embrittlement fracture (L)7
 impact fractures (L)140-142
 low-temperature fractures (L)140-141
 Neumann bands (L)7
 notch-impact fracture (L)142
 quasicleavage (L)140
- Ingots**
 segregation (L)138
 woody fracture (L)136
- Instrument springs, failure analysis (L,M,P)**455
- Intake valves**
 failure analysis (L)452
 fatigue fracture (L)452
- Intercrystalline fractures**5
 See also *Intergranular fractures.*
- Intergranular fractures (L,M,S,T)**112-114
 See also under specific metal.
 conditions for occurrence70, 89
 effect of grain-boundary properties (S)112, 113
 fatigue fractures41
 hydrogen-embrittlement fractures (S)70, 71, 76
 plus cleavage (S)72-73

- Intergranular fractures (continued)**
 plus fatigue-striation formation (S)75, 77
 plus microvoid coalescence (S)74
 plus tearing (S)74, 75
 revealed by SEM (S)70-71, 72
 revealed by TEM (T)89-90
 stress-corrosion fractures (S)70, 72, 76-78
 stress-orientation determination109
 Tiemann's description4-5
- Internal-shearing fracture (L,T)**354
- Ion microprobe analyzer**26, 52
- Ion-scattering spectrometer**26, 52
- Iridium**
 bending fractures (S,M)71, 270
 intergranular fracture (S)70, 71
 secondary cracks (S)270
 separated-grain facets (S)270
- Iron.** See also *Armco iron; Wrought iron.*
 bending fractures (S)165-166
 cleavage steps (S)162, 169
 conversion to steel, fracture appearance (F)3
 dimples (S)163
 fracture for quality control2
 fracture types, de Réaumur's classification (F)2-3
 impact-bend fracture (M)26
 impact fractures (S)162, 168
 inclusions (S)163
 low-temperature fractures (M,S) 26, 162, 169
 notch-bend fracture (S)162, 169
 tensile fractures (S)163, 164-165
- Iron-base heat-resisting alloys, fractures (L,T)**225, 346-347
- Iron-chromium-aluminum alloy, herringbone pattern (T)**83
- Iron-chromium-tantalum alloys**
 cleavage (S)214
 dimples (S)214
 Laves-phase precipitate (S)214
 quasicleavage (S)214
 tensile fractures (S)214
 effect of test temperature (S)214
- Iron-nickel alloys**
 bending fractures (S)202
 cleavage steps (S)202
 low-temperature fractures (S)202
 quasicleavage (S)202
 river patterns (S)202
 tongues (S)202
 twin boundary (S)202
 twist boundary (S)202
- Iron-nickel-titanium alloys**
 cleavage facets (S)205
 dimples (S)204, 205
 impact fractures (L,S)204-205
 deformation (L)204, 205
 effect of aging temperature (L,S)204-205
 intergranular cracks (S)205
 low-temperature fractures (M,S)204-205
 quasicleavage facets (S)204
- Iron-silicon alloys**
 cast structure (M)150
 cleavage (L)149
 cleavage of epsilon phase (L)151
 impact fractures (L)149-151
 effect of microstructure (L,M)150-151
 inclusions (L)151
 Neumann bands (L)150
 river patterns (L)149, 150
 spines (L)151
 twins (L)150
- Iron-tantalum alloys**
 dimples (S)214
 Laves-phase precipitate (S)214
 tensile fractures (S)214
 effect of heat treatment (S)214

J

- Jernkontoret fracture test** 5
Jet-engine compressor disk
 failure analysis (L,M,P)472-473
 fatigue fracture (L,M,P)472-473
Journals, fatigue fracture (L,M)417
Jousse, Mathurin 2

K

- Keyed axles, fatigue fracture (L)**390
Keyed shafts
 failure analyses (L,P)382, 389, 402
 fatigue fracture (L)389
 peeling fracture (L,P)382, 402
Keyed spindle, failure analysis (L,P)391
Keyways, effect on fracture (L,P)389, 390, 391, 393, 402, 414-415
Kingpins
 bending-fatigue fracture (L)444
 overload fracture (L)444
Kink bands (L)160
Kirkaldy, D. 3
Kirsh, B. 4

L

- L-605 alloy**
 dimples (T)343, 344
 elevated-temperature fracture (L,T)344
 fatigue fracture (L,T)344-345
 propagation (T)344-345
 fatigue striations (T)345
 intergranular fracture (T)344
 microstructure, effect on fracture
 surface (T)345
 notched, fatigue fracture (L,T)344
 notched, tension-overload fracture (L,T)344
 oxidation of fracture surface (T)344
 ripples (T)343
 separated-grain facets (T)344
 shear fracture (L,T)343
 stretching (T)343, 344
 tension-overload fracture (L,T)343-344
 tire tracks (T)345
 transgranular fracture (T)344
Lamellar structure
 in cast iron (S)166
 resemblance to fatigue striations (T)88
Laminated fracture (L)135
Landing gear, stress-corrosion fracture (S)72
Landing-gear actuator beam
 failure analysis (L,M,P)466-467
 stress-corrosion-cracking fracture (L,M,P)466-467
Landing-gear axles, fatigue fractures (L)103
Landing-gear bolt-torque link, stress-corrosion-cracking fracture (L,S)194-195
Landing-gear component, stress-corrosion-cracking fracture (T)361
Landing-gear cylinders
 fatigue fracture (L,T)314
 fracture originating at grinding cracks (T)309
 hydrogen-embrittlement fracture (T)313
 stress-corrosion-cracking fracture (T)313
Landing-gear piston assembly
 failure analysis (L,P,S)190
 fatigue fracture (L,P,S)190
Landing wheels
 corrosion-fatigue fracture (P,T)366
 failure analysis (L,M,P)458-459

Landing wheels (continued)

- fatigue-crack growth rates (E,F,L,T)123-124
 fatigue fracture (L,M,P)458-459
Laps
 fracture origins (L,S,T)93, 94
 revealed by fractography (L)32, 109, 409
Latch arm, tension-overload fracture (M,S)175
Laves-phase precipitate
 in iron-chromium-tantalum alloy (S)214
 in iron-tantalum alloy (S)214
Lead red brass, fracture from porosity (L,M)470
Lead-tin-silver solders
 dimples (S)270-271
 tensile peel-test fractures (S,M)270-271, 272
Lead-tin solders
 cellular structure (S)271
 ductile fracture of dendrite arms (S)271
 interdendritic shrinkage (S)271
 tensile peel-test fractures (S)271-272
Lead-tin-tellurium solder
 dimples (S)270
 tensile peel-test fractures (S,M)270
Leaf springs
 failure analysis (L,P)441
 fatigue fracture (L,P)441
Leaves, corrosion (L,M,P)360, 363
Lenses
 focal lengths13
Light fractographs (A)129-138, 139-160
 discontinuities revealed (L)93-103
 features revealed (A)27-35
 interpretation (A)36-48
 stereo views (L)22, 23
Lighting techniques for photography (F,L)13-18
 angle of lighting (L)14, 15, 150
 diffusion16-17
 etched sections (M)17
 fractured parts (F)13, 14, 15-17
 fracture surfaces (F,L)14-17
 reflective parts (F)17
Light-microscope fractographs (A)129-138, 139-160
 beach marks (L)29-30, 31
 chevron patterns (L)28-29, 30
 cleavage facets32
 dimples (L,S)33-35
 discontinuities (L)32-33, 34
 fatigue fractures (L)29-31, 32
 features revealed (A)27-35
 grain facets31-32
 herringbone patterns (L)28-29
 interpretation (A)36-48
 secondary cracks (L,M,P)32
 striations (L)30, 31, 32
Light-microscope fractography
 applications7
 deep-field microscopes26
 historical background (A)1-9
 limitations139
 magnification determination13
 magnification limits1, 139
 photography (A)11-24
 preparation of specimens (A)9-10
 preservation of specimens (A)9-10
 shadow casting25-26
 special techniques (A)24-26
 stereo pairs (L)22, 23
 use of replicas (L)24, 25, 56, 57
 Zapffe's techniques (F)6-7
Light microscopes (F)55
Lights for photography13-14

Liquid-penetrant inspection, effect on

- fracture appearance10
Load cell
 failure analysis (L,S)187
 sudden-overload fracture (L,S)187
Loading
 consideration in failure analysis 106, 107-109
 determination by failure analysis (E,L,P,T)108
 effect on surface features (F)43, 44
 types129
Longitudinal torsional fractures (L)37
Low-alloy steels. See also High-strength low-alloy steels; and specific steel.
 carburized, tearing plus intergranular fracture (S)74, 75
 cleavage facets, stereo views (S,T)284
 dimples, stereo views (S,T)284
 fatigue striations87
 impact fractures (L)133
 stereo views (S,T)284
 inclusions, stereo views (S,T)284
 torsional-fatigue fracture (L)132
Low-carbon high-oxygen iron
 dimples (S)164, 165
 fatigue fracture (S)167
 fatigue striations (S)167
 oxide inclusion (S)167
 tensile fractures (S)164-165
Low-carbon iron
 cleavage steps (S)168
 dimples (S)168
 ductile tearing (S)168
 elevated-temperature fracture (S)168
 ferrite structure (S)168
 impact fractures (S)168
 low-temperature fracture (S)168
 river pattern (S)168
 secondary cracks (S)168
 tongue (S)168
 transgranular fracture (S)168
 twin (S)168
Low-carbon steels
 cleavage fractures (M,T)82, 83
 dimples (S)170, 171
 effect of temperature on fracture mechanism75
 elevated-temperature fracture (M,P,S)170-171, 380
 fatigue fractures (E,L,M,P,T)108, 379
 ferrite (M)82, 380
 fracture, stereo views (L)23
 impact-overload fractures, crack origin (L)40, 41
 intergranular fracture (S)170-171
 martensite (M)380
 rotary-bending fatigue fractures (S,T)172
 spheroidite (M)380
 tensile fractures (M,S)170-171
 effect of manganese-sulfur ratio (M,S)170-171
 reductions in area (M)170
 torsional-fatigue fracture (L)132
 transgranular fracture (M,S)170, 381
Low-cycle fatigue fractures (T)85, 86
Low-magnification fractography. See Macrofractography.
Low-power stereomicroscopes, application to failure analysis106
Low-silicon bronze, fatigue fracture (L)468
Low-temperature fractures
 characteristics111-112
 in 301 stainless steel (L,T)331
 in 1040 steel (S)64, 65
 in 4335 (mod) steel (T)428
 in 4340 steel (L,S)28, 66, 422-424
 in 5155 steel (S)196

Low-temperature fractures (continued)

- in alloy steels (S)203, 204
- in AMS 6434 steel (T)302
- in Armco iron (L,T) ..83, 140-141, 298-299, 378
- in bismuth-zinc alloys (L)155
- in carbon steel weld metal (L)144
- in columbium (T)468
- in high-carbon steels (S)180-182
- in iron (S)168, 169
- in iron-nickel alloys (S)202
- in low-carbon steels (S)173, 175
- in maraging steels, effect of stress-intensity factor (T)82
- in medium-carbon steels (S)179
- in nickel-chromium-molybdenum steel (L)30
- in pure iron (M)26
- in ship-plate steel (L)143
- in Ti-6Al-4V (T)370
- in wrought iron (T)300
- mechanisms (L)46, 47

M**Machining marks. See Tool marks.****Macrofractography**

- fatigue marks (L)29-31, 32
- features revealed (F,L)27-33
- historical background (A)1-8
- magnification determination (F) ..13, 19-20
- magnification limits1
- photography (A)11-24
- ratchet marks (L)30-31, 32
- stereo pairs (F,L)22, 23

Macrographic lenses

- lighting techniques (M)17
- photography, exposures18-19

Macroscopic crack growth, relation to

- microscopic crack growth (F)86

Magnesium alloys, specific types

- AZ81A-T4
 - corrosion-fatigue fracture (P,T)366
 - corrosion of fracture surface (T)366
 - dimples (T)366
 - fatigue striations (T)366
- AZ91-T6
 - fatigue fracture (E,L,P,T)87, 109-110
 - fatigue striations (T)87, 110
- HM21A
 - dimples (S)272
 - fracture-toughness-test fracture (S)272
 - tension-overload fracture (S)272

Magnesium chloride solutions, effect on

- fracture of stainless steel (L,T)115, 116, 117

Magnesium-graphite-fiber composites,

- longitudinal tensile fracture (S)265

Magnetic lenses

- Magnetic-particle inspection, effect on examination in the SEM10

Magnifications

- determination for light-microscope fractography13
- determination from film-to-lens distance (F)19-20
- limits with scanning electron microscope49, 51, 63
- limits with transmission electron microscope (F)54, 55, 63

Main-landing-gear bogie beam

- failure analysis (L,M,P)465
- stress-corrosion-cracking fracture (L,M,P)465

Main-landing-gear cylinder, hydrogen-

- embrittlement fracture (T)313

Main-landing-gear spring leg, failure

- analysis (L,M,P)442

Main-landing-gear wheel-half hub

- failure analysis (L,P)460
- fatigue fracture (L,P)460

Main-landing-gear wheels

- failure analysis (L,M,P)458-459
- fatigue fracture (L,M,P)458-459

Main spar web

- failure analysis (E,F,P,T)120, 121, 122
- fatigue fracture (E,F,P,T)120, 121, 122

Mallet, R.

-3

Manganese bronze

- crack-arrest lines (L)42
- fatigue fracture (L,M)471
- stress-corrosion fracture (L)42

Manganese steel

- cleavage facets, stereo views (S,T)284
- dimples, stereo views (S,T)284
- impact fractures, stereo views (S,T)284
- inclusions, stereo views (S,T)284

Maraging steel

- beach marks (L)42
- hydrogen-embrittlement fracture (T) ...91
- intergranular fracture (T)91
- stress-corrosion fracture (L)42

Maraging steel, 18% Ni

- bending fracture (L,T)321
- corrosion-fatigue fracture (L,T)320
- corrosion of fracture surface (T)320
- dendrites (S)207
- dimples (S,T)206, 207, 208, 320, 321
- embrittling phases, effect on fracture (T)100-101, 102
- fatigue fractures (S)70, 208, 209
- effect of heat treatment (S)209
- fatigue striations (S,T)209, 320
- fissures (S)209
- hydrogen-embrittlement fracture (T)321
- inclusions (S,T)96, 104, 206
- effect on fracture (T)96
- quasicleavage facets (T)321
- river patterns (T)321
- rubbing (S)209
- secondary cracks (S)71, 208, 209
- shrinkage porosity (S)207
- stretching (S,T)81, 82, 208
- tear ridges (T)321
- tensile fracture (L,S)206-207
- tension-overload fracture (S)208
- welds
 - bending fracture (L,T)321
 - hydrogen-embrittlement fracture (T)321
 - porosity (L,T)101

Maraging steel, grade 200, stretching

- in fracture (T)82

Maraging steel, grade 250

- fatigue fracture (S)69-70
- secondary cracking (S)70

Maraging steel, grade 300

- fatigue fractures (S)209
- shrinkage porosity (S)207
- tensile fracture (L,S)206-207
- tension-overload fracture (S)208

Marine-engine crankshaft

- failure analysis (L,P)404
- fatigue fracture (L,P)404

Marine tailshaft

- failure analysis (L,P)393
- fatigue fracture (L,P)393

MAR-M 200

- cleavage steps (S)231
- crack propagation (L,M)231, 232
- dimples (S,T)231, 232
- fatigue fractures (M,S,T)231-232
- fatigue striations (L)232
- oxide-coated steps (S)232

MAR-M 200 (continued)

- river patterns (S)231
- ultrasonic-fatigue fractures (S,M)231

MAR-M 200 single crystal, fatigue

- fracture (S,M)231-232

Martens, Adolf

-4

Martensite

- in 1042 steel (S)176
- in 1090 steel (S)181
- in 4070 steel (M)184
- in 50100 steel (M)197
- in low-carbon steel (M)380

Martensitic stainless steels

- fracture features114
- stress-corrosion-cracking fracture (T)113-114

Materials

- consideration in failure analysis ..106, 109
- properties revealed by fractography109

Mechanical fibering (F,L)

-29, 30

Mechanical twins. See Twins.**Medium-carbon steels. See also specific**

- steel
 - fatigue fracture (L,M)394-395
 - fracture types, Brinell's classification ..5
 - impact-overload fractures, crack origins40
 - single-overload fracture (L)41

Metallographic stages (F)

-7

Metallography

- examining fracture profiles (M) ..24-25, 26
- use in failure analysis109, 111

Microfractographs (L)

- relation to microstructure (L,M)7-8

Microfractography

- applications7
- historical background6-8
- magnification limits1
- specimen holders (F)7
- Zapffe's techniques (F)6-7

Micrography, use in failure analysis

-109

Microprobe analyzers

-52

Microscopes

- deep-field type26
- light (F)55
- scanning electron (F)49-50
- stereo11, 12, 22, 23
- application to failure analysis106
- transmission electron (F)54-56
- use in photographing fracture surfaces12-13

Microscopic crack growth, relation to

- macroscopic crack growth (F)86

Microstructure

- effect on crack propagation (L) ...16, 44-45
- relation to fracture surface139
- aluminum alloy (M,T)350
- iron-silicon alloy (L,M)150
- stainless steels (L,M)146, 148

Microtwins. See Twins.**Microvoid coalescence fractures. See also**

- specific metal
 - dimple classifications (F)105
 - features revealed by SEM (S)66-68
 - features revealed by TEM (T)79-81
 - occurrence79
 - plus cleavage (S)71-72
 - plus fatigue fracture (S)73-74
 - plus intergranular fracture (S)74, 89
 - plus tearing (S)73

Microvoids. See also Dimples.

- coalescence66-68, 79-81
- initiation66, 79-80

Missile-silo suspension strut

- failure analysis (L)432-433
- fracture (L)432-433

Mixed-mechanism fractures (S) 71-75**Molybdenum**

- cleavage facets (L) 156
- feathers (L) 157
- fractures 139
- impact fracture (L) 156-157
 - effect of cold work (L) 156
 - effect of oxygen content (L) 156
- inclusions (L) 156-157
- intergranular fracture (L) 157
- secondary cleavage cracks (L) 156
- transgranular fracture (L) 157
- twins (L) 156
- vacuum-arc cast (L) 156-157

Molybdenum alloy TZM

- cleavage facets (S) 272
- cleavage steps (S) 272
- fracture-toughness-test fracture (S) 272
- secondary cracks (S) 272
- tension-overload fracture (L,T) 367

Molybdenum steels

- cleavage facets (S) 216
- cleavage steps (S) 217
- dimples (S) 215, 216
- fracture-toughness-test fractures (S) 216-217
 - effect of carbon content (S) 216, 217
 - effect of heat treatment (S) 216-217
- impact fractures (S) 215
- inclusions (S) 215
- intergranular fracture (S) 216, 217
- quasicleavage facets (S) 215
- secondary-hardening type, fractures (S) 216-217

Monel

- tearing plus intergranular fracture (S) 74, 75
- tear ridges (S) 75

Monel 400

- elevated-temperature fracture (S) 77
- fatigue striations (S) 77
- intergranular fracture (S) 77, 78
- reversed-bending fracture (S) 77

Monocular microscopes

- Motor case, proof testing, crack propagation (L) 39

Mounting-bolt boss, impact fracture

- (L,P,T) 351

Mud-crack pattern

- in 4340 steel (T) 315
- in aluminum alloys (T) 92, 359, 363, 467
- revealed by TEM (T) 92

Multiple-origin cracks (L) 30, 132, 140**Mushet, David** 3**Mushroom-head closure, failure analysis**

- (E,P,T) 111

Music-wire springs

- fatigue fractures (L,P) 410
- torsional-fatigue fracture, beach marks (L) 41

N**Negative replicas** 56

- transposition for stereo viewing (T) 281, 284

Neumann bands

- in ingot iron (L) 7
- in iron-silicon alloys (L) 150

Nickel 201

- cleavage facets (S) 236
- fracture, effect of atmosphere (S) 236
- notch-bend fracture (S) 236
- three-point-bending fracture (S) 236
- tongues (S) 236
- transgranular cleavage (S) 236

Nickel alloys

- fracture surfaces (S) 75, 77, 78, 236
- oxide-film production and removal 58

Nickel-base heat-resisting alloys,

- fractures (L,P,S,T) 227-234, 334-343

Nickel-chromium-molybdenum-cobalt

- steel, fibrous fracture (S) 104

Nickel-chromium-molybdenum steel

- chevron pattern (L) 30
- dimple formation at sulfide inclusions (T) 96
- fracture-toughness-test fracture (L) 30
- low-temperature fracture (L) 30
- sulfide inclusions (T) 96

Nickel-cobalt steel

- crack branching (M) 32
- stress-corrosion cracking (M) 32

Nickel plating, of fracture profiles

- (M) 24-25, 26

Nickel steel, fatigue cracking (L,M) 393**Nitralloy G**

- fatigue fracture (L,T) 319
- fatigue striations (T) 319

Nodular iron. See Ductile iron.**Nondestructive inspection**

- effect on fracture appearance 10
- lighting of indications for photography 17-18

Nondispersive spectrometers 26, 52**Nose-landing-gear cylinders**

- fracture originating at grinding cracks (T) 309
- stress-corrosion-cracking fracture (T) 313

Notched specimens

- crack origins (F) 38, 39
- crack propagation (F) 43, 45
- effect of temperature on fracture mechanisms (L) 46
- fatigue-fracture marks (F) 43
- fracture features (L) 30
- fracture zones (F) 38
- stress states (L) 47-48
- woody fractures (F) 30

Notches

- effect on crack initiation (F) 38, 39, 109
- effect on fatigue fractures (L,T) 327, 332, 333, 337, 338, 339, 342, 352, 353, 365
- effect on fracture appearance (L) 46
- effect on stress-corrosion-cracking fracture (T) 315
- effect on tension-overload fractures (T) 302, 305, 317, 324, 329, 330, 341, 344, 346, 363

Nuts

- failure analysis (L) 396
- woody fracture (L) 396

O**Oatley, C. A.** 49**Objective lenses (F)** 49, 54, 55**Oblique lighting (L)** 13, 14, 15, 16

- lights (F) 13, 14
- of etched surfaces (M) 17
- of fracture surfaces (L) 14, 15

OFHC copper

- elevated-temperature fracture (S) 76
- intergranular fracture (S) 76
- notched, fatigue fracture (S) 268
- secondary cracks (S) 268
- stress-rupture fracture (S) 76

Open-header dies, fatigue fracture (L) 134**Open-hearth crane wheel, fatigue**

- fracture (L) 407

Opening secondary cracks

- Operation (surgical) microscopes 13

Optical microscopes (F) 55**Optical stereomicroscope (F)** 22, 23**Orthogonal markings (L)** 145**Outboard-motor crankshafts**

- failure analysis (L,M,P) 416-417
- fatigue fracture (L,M,P) 416-417

Outdoor photography 11, 14**Oxidation**

- effect on fracture (M,P,S) 76, 450
- of fatigue crack surface (M) 434-435
- of fracture surfaces (L,M,S,T) 102, 190, 344, 354, 407, 408, 453

Oxide-film replicas 58-59

- applications 58
- fractographs from (T) 116, 117
- production 58
- stripping 58-59

Oxide inclusions

- in irons (S) 163-167
- in molybdenum (L) 156, 157

Oxygen-free high-conductivity copper

- elevated-temperature fracture (S) 76
- fatigue fractures (S) 268
- fatigue striations (S) 268
- intergranular fracture (S) 76
- notched, fatigue fracture (S) 268
- secondary cracks (S) 268
- stress-rupture fracture (S) 76

P**Packing retainers, failure analysis**

- (E,L,P,T) 115

Palisades (S) 265**Palladium, use for shadowing (M)** 56**Parallel lighting (F,L)** 13, 15**Pearlite**

- colonies, fracture (S) 67
- in 1020 steel (M) 381
- in 1090 steel (S) 180, 182, 183
- in 4070 steel (M) 184
- platelets, resemblance to fatigue striations (T) 88

Peeling fatigue fractures (P) 402**Peening, effect on fatigue fracture (L,M,P)** 464**Perchloric acid - alcohol solutions,**

- safety precautions 58

Percy, J. 3-4**P-F test** 5**Phosphor bronze C**

- fatigue fracture (M,P) 468-469
- slip lines (M) 469
- tension fracture (M,P) 469

Photoflood lights

- lighting fracture surfaces (L) 15

Photography (A) 11-24

- accessory equipment 23-24
- cameras 11-13
- developing film 21
- exposure meters 18-19
- exposures 18-21
- film 18
- focusing the image 13
- in the transmission electron microscope 55
- lenses 13
- lighting techniques (F) 12, 13, 14-18
- lights 13-14
- printing photographs 22-23
- setups for (F) 11, 23-24
- shadowless lighting (F) 12, 15
- stereo pairs (F,L) 22, 23
- tripods 23

Pinhole porosity (L,T) 306-307**Pinions**

- bending-fatigue fracture (L,P) 443, 445, 448
- failure analysis (L) 436

- Pinions (continued)**
 fatigue fracture (L) 436
 spalling-fatigue fracture (L) 443
Pins, fracture (L) 437
Pipe flange, failure analysis (L,M,P) 451
Piston rods
 failure analyses (L,M) 379, 418
 fatigue fractures (L,M) 132, 379, 418
 reversed-bending fracture (L,M) 379
Pistons, failure analysis (L,P,S) 256-257
Pits. See also Corrosion pits.
 effect on fracture (P) 443
 revealed by light fractography 33, 448
Pivot bolt, fracture originating at
 grinding cracks (T) 309
Plane-strain fracture (L) 47
Plane-stress fracture (L) 47, 48
Planet gears
 failure analysis (L) 412
 fatigue fracture (L,T) 319, 412
 torsion-overload fracture (L,T) 320
Plastic-carbon replicas (F) 58, 59
 artifacts (T) 61-63
 dissolution of plastic 59
 preparation 59
 thickness of carbon film 59
Plastic coatings for fracture surfaces 9
 removal 9
Plastic-deformation studies 104
Plastic-plastic replicas 59
Plastic replicas (F) 56-58
 artifacts (T) 61-63
 plastic-solvent combinations 57
 preparation 56-58
 stripping 57
Plastic tape (L) 39, 57, 281
Plate metal
 fatigue-fracture marks (F) 44
 fracture propagation (F) 80
Plating
 effect on fracture (L,M) 45, 189, 310-311
 fracture profiles (M) 24-25, 26
Platy fracture (L) 135
Polycrystalline antimony, cleavage
 fractures (L) 153
Porcelanic fractures 5
Porosity
 de Réaumur's illustration (F) 3
 effect on fracture
 (L,M,S,T) 89-90, 99-100, 101, 470, 471
Powder metallurgy compacts
 crack propagation (L,T) 376
 impact fracture (T) 475
 intergranular fracture (L,T) 112, 113, 376
 tension-overload fractures (S) 225, 232-233
Prebus, A. 54
Precipitate particles
 cleavage (T) 228, 336
 dimple formation at (S) 66, 67-68
Precipitation-hardening stainless steels,
 fractures (L,S,T) 219, 223, 328-331
Preparation of fracture specimens (A) 9-10
Preservation of fracture specimens (A) 9-10
Press-type cameras 12
Pressure cylinder
 failure analysis (P,S) 244
 fatigue fracture (P,S) 244
Pressure-gage Bourdon tube, failure
 analysis (E,T) 116, 117
Pressure vessels
 fracture propagation (L) 39
 stress-corrosion fracture (S) 76, 77
 tension-overload fracture (T) 302
Pressure-vessel shell plate, failure
 analysis (L,M,P) 383-385
Primary cracks (F) 38
 opening 10
Printing photographs 22-23
 exposures 22
 fixing 22
 papers 22
Proof testing (L) 39
Propeller blades
 failure analyses (L,M,P) 434-435, 462-464
 fatigue fractures (L,M,P) 434-435, 462-464
Propeller-hub clamp
 failure analysis (L,P) 427
 fatigue fracture (L,P) 427
Propeller hubs
 failure analyses (L,M,P,S) 245-246, 430
 fatigue fractures (L,M,P,S) 245-246, 430
Propeller-hub spider
 failure analysis (L) 431
 fatigue fracture (L) 431
Propeller torque cylinder, fatigue
 fracture (L,P,T) 322-323
Pump chamber
 failure analysis (L,M) 392
 fracture caused by overheating (L,M) 392
Pump impeller, failure analysis (E,S) 106, 107
Pump rod, failure analysis (L) 471
Pure iron
 cubic cleavage (M) 25, 26
 fracture profile (M) 26
 impact-bend fracture (M) 26
 low-temperature fracture (M) 26
- Q**
- Quality control, fracture for** 2
Quasicleavage fractures. See also
 under specific metal.
 features revealed by SEM (S) 65-66
 features revealed by TEM (F,T) 84-85
 in embrittled materials 85
 study 105
Quench cracks
 fracture origin (L) 93, 95, 109
 in 4340 steel (L,T) 308
 in 50100 steel (S) 197
 oxidation 77
- R**
- Radial marks (F)** 27-28
 for fast subsurface crack
 propagation (F) 40, 41
 for fast surface crack propagation (F) 40, 41
 Martens' treatment 4
 relation to crack origin 38
Radial shear 27
Radial zone
 in cylindrical specimens (F,L) 27-28
 in rectangular specimens (F,L) 28-29, 30
Radiator assembly
 failure analysis (E,T) 118
 fatigue fracture (E,T) 118
Radioactive metals, fracture
 examination 26
Railroad rail, fatigue fracture (L) 131
Ratchet marks (L) 30-31, 32
 in 1040 steel (L) 389
 in 1080 steel (L) 318
Reactor system, failure analysis (E,S) 117, 118
Rear-bogie leaf springs, failure
 analysis (L) 441
Recording cathode-ray tubes 50
Rectangular specimens
 fracture marks (F,L) 28-29, 30, 44
 fracture propagation (F) 44
 notched, fracture zones (F) 38, 39
Reflected-light exposure meters 18-19
Refractaloy 26
 cleavage fracture (S) 226
 dimples (S) 226
 impact fractures (S) 226
 effect of aging temperature (S) 226
 rock candy fracture (S) 226
 slip bands (S) 226
 stress-rupture fractures (S) 226
René 41
 dimples (T) 343
 rock candy fracture (L) 343
 tension-overload fracture (L,T) 343
Replica grids 55
 size 59
 use for indexing replicas 60-61
Replicas
 advantages 63-64
 artifacts (T) 61-63, 354
 caused by corrosion products (T) 92
 scratch marks (T) 88
 stereo views (T) 282, 283, 285, 288,
 289, 291, 294, 295, 296
 tearing (T) 337, 371
 carbon 58
 coating
 for light-microscope fractography
 (L) 24, 25
 collapse (T) 291, 292, 294
 determination of direction of
 fracture propagation (F) 80
 fishing technique for placement 59
 indexing 60-61
 oxide 58-59
 plastic-carbon (F) 58, 59
 plastic-plastic two-stage 59
 plastic-solvent combinations 57
 preparation (F) 24, 56-59, 281
 shadowing (F) 59-60, 281
 single-stage (F) 56-59
 two-stage (F) 58, 59
 uses 56
 cleaning fracture surfaces 10
 light-microscope fractography (L) 24
Replica tape (L) 39, 57, 281
Replicating plastics
 types 57
 use for coating fracture surfaces 9
Resin-coated photographic papers 22-23
Resolution
 with scanning electron microscope 49, 50, 63
 with transmission electron
 microscope 55-56, 63
Resonant vibration, fatigue fracture from
 (E,L,P,T) 108
Retained austenite structures, in
 4070 steel (M) 184
Reticulation of shadowing metal (T) 62, 63
Reverse chevron patterns 38
Reversed-bending fractures. See also
 under specific metal.
 effect of loading on fracture
 features (F) 43
Reverse idler gear, bending-fatigue
 fracture (P) 443
Ridge-and-groove marks (L) 151
Rifles (L) 154
Ring gear, fatigue fracture (L,T) 319
Ring lighting (F,L) 13, 14, 15
 of fracture surfaces (L) 14, 15, 16
Ripples 81, 87-88
 in L-605 alloy (T) 343
 in stainless steel (T) 81
 in Waspaloy (T) 340, 341
River patterns. See also under
 specific metal.
 revealed by SEM (S) 64-65
 revealed by TEM (T) 82, 83

- Rivet-heading tool, fatigue fracture**
(L)134
- Rivet holes, effect on fatigue**
fractures (L,M,P)461
- Rock candy fractures**32
in 302 stainless steel (L)137
in 4340 steel (T)89
in Alnico (L)348
in Refractaloy 26 (S)226
in René 41 (L)343
- Rocket-motor case, fracture initiating**
at weld imperfection (L)33
- Rocket-nozzle insert, fracture**
(L,M,T)376
- Rocket-propellant case, failure**
analysis (L,T)301
- Roof-truss angles**
failure analysis (L,M,P)386
low-temperature fracture (L,M,P)386
- Rotating-bending fracture. See also**
under specific metal.
effect of loading on fracture
features (F)43
fracture propagation43
- Rotor fittings, failure analysis**
(E,L,P,T)107
- Rotors, hydrogen-embrittlement**
fracture (S)71
- Rubbing (L)**392
effect on fracture surface (L)132
in bending-fatigue fracture (L,P)400
in fatigue fractures
(L,S,T)117, 209, 413, 420-421
revealed by TEM (T)88
- Ruska, E.**54

S

- Sand castings, defects (L,M,T)**349
- Savot, Louis**2
- Saw-teeth fractures (M)**39
- Scanning-electron-microscope**
fractographs (A)161-280
cleavage features (S)64-65
dimples (S)34, 35, 66-68
vs transmission-electron-microscope
fractographs (S,T)61
discontinuities revealed (S)94-95, 96-99, 100
elevated-temperature fractures (S)75-76
fatigue striations (S)68-70
intergranular fractures (S)70-71, 72
interpretations (A)64-78
mixed-mechanism fractures (S)71-75
quasicleavage fractures (S)65-66
stress-corrosion-cracking
fractures (S)76-78
tearing fractures68
- Scanning-electron-microscope**
fractography
chemical analysis of surface51-52
cleaning specimens (S)9-10, 234
coating of replicas51, 60
historical background49
production of fractographs53
replicas for (S)56, 57, 61
specimens51
demagnetizing10
for transmission mode of operation52
preparation (A)9-10
stereography51
compared with transmission-electron-
microscope fractography
(S,T)63, 281-296
use for failure analysis (A)106-124
uses other than failure analysis (A) 103-105
viewing of fractographs53
- Scanning electron microscopes (A)**49-53
accelerating voltage49
advantages51, 63-64, 68
area of specimen covered64
attachments51-52
backscattering-electron mode of
operation (F)50, 51
cathode-ray tubes50
cold stages52
components (F)49
depth of field49
features54
fidelity63
hot stages52
image buildup50
limitations for fractography63
magnification limits49, 51, 63
magnification methods51
operation (F)50-51
resolution49, 50, 63
secondary-electron mode of
operation (F)50, 51
solid-pair-detector attachment (F)52, 53
specimen contamination50
specimen stages51, 52
tensile stages52
transmission mode of operation52
vacuum system50-51
- Scraping artifacts (T)**62
- Scratches, effect on fracture (L)**443
- Scratch-mark artifacts (T)**88
- Screw dislocations**65
- Seams**
effect on fatigue fracture
(L)408, 409, 411, 440
fracture origins (L)93
revealed by fractography (L)32, 109, 409
- Secondary cracks. See also under**
specific metal.
opening10
revealed by light fractographs
(L,M,P)32
revealed by SEM (S)64, 65, 77
revealed by TEM (T)87
- Secondary-electron collector (F)**50, 51
- Secondary electrons (F)**50
penetration (F)50
resolution with50
- Secondary-hardening steels, fracture**
toughness, effect of heat treatment
(S)216-217
- Secondary stresses**38
- Sectioning fractured parts,**
techniques (M)10, 24-25, 26
- Segregation (L)**33, 34
fracture origins (L,M)100, 101
in low-carbon steel (S)171
revealed by fractography109
- SEM. See Scanning electron microscopes.**
- SEM fractographs (A)**161-280
interpretations (A)64-78
- SEM fractography. See Scanning-**
electron-microscope fractography.
- SEM stereofractographs**51, 266-267
compared with transmission-electron-
microscope stereofractographs
(S,T)281-296
viewing281
- Separated-grain facets**31-32
- Separated-grain fractures**
revealed by SEM (S)70-71, 72, 76-77
revealed by TEM (T)89-90
- Serpentine glide (T)**81
in aluminum alloys (T)361, 363
in beryllium copper (T)364
in titanium and titanium alloys (T) 368, 373
in Waspaloy (T)340, 341

- Service failures**
failure analysis (A)106-124, 377-475
interpretation from test fractures48
- Shadowing of fracture surfaces**25-26, 58
for determining heights of features26
techniques25-26
to reveal fatigue striations68
- Shadowing of replicas (F)**58, 59-60
advantages59
metals used60
thickness of deposits60
use for indexing61
vaporization of heavy metals60
- Shafts**
bending-overload fracture, crack
origin (L)41
failure analyses (L,M,P)387, 389,
396, 401, 402, 403, 405, 415, 431, 445, 449
fatigue cracking (P)401
fatigue fractures (L,M,P,S)41, 45,
183, 387, 389, 391, 396, 415, 431, 436, 449
fracture-surface interpretations (L)45
fretting corrosion (P)440
induction hardened, fatigue fracture (L) 41
induction hardened, torsional
fracture (L)37
peeling fracture (L,P)382, 402
ratchet marks30
reversed-cantilever-bending fatigue
fracture (L)403
reversed-stressing fracture (L)45, 391
rotating-bending fracture (L)45, 389
torsional-fatigue fractures (L,P)132, 445
torsional fracture (L)37
torsion-overload fractures (L,P)36, 387
woody fracture (L)30
- Shape of parts**
consideration in failure analysis106, 112
effect on fracture mechanism112
- Shear blades, impact fracture (L)**134
- Shear dimples (S)**67
revealed by SEM (S)67
revealed by TEM (F)79, 80
- Shear fractures (F,L)**37, 38
dimple shapes (F)79
- Shear-lip zone**
in cylindrical specimens (F,L)27, 28
in rectangular specimens (F,L)28-29, 30
- Sheet metal**
fracture-origin determination (L)298
fracture propagation (F,M)39, 80
plastic zone at crack tip (F)47, 48
- Shell plate**
cracking (L,M,P)383
failure analysis (L,M,P)383-385
fracture (L,M,P)384-385
- Shepherd, B. F.**5
- Ship-plate steels**
dimples (T)379
fatigue fracture (T)379
fatigue striations (T)379
impact fractures (L)143
effect of manganese content (L)143
low-temperature fracture (L)143
notch-impact fractures (L)143
river patterns (L)143
- Shock-strut piston**
failure analysis (L,P,S)256-257
fatigue fracture (L,P,S)256-257
- Shot peening, effect on fatigue**
fracture (L,M,P)464
- Shrinkage cavities**33
fracture origins (L)99, 100
fracture through (L)382
- Shrinkage porosity**
effect on fracture (L,M,P,S,T)227, 349, 470
revealed by fractography109

Silcrome-1 steel, fatigue fracture (L)452
Silicon irons (L,M)149-151
 See also *Iron-silicon alloys*.
Silky fracture
 Percy's description 4
 Tiemann's description 5
Silver, fracture for quality control 2
Single-lens reflex cameras 12
 accessories 12
Single-stage direct carbon replicas 58
 artifacts (T)61-62
 fractographs from
 (T)56, 81, 101, 323, 326, 378, 468, 471
 preparation 58
 thickness control 58
Single-stage plastic replicas (F)56-58
Single-stage replicas (F)56-59
 for light-microscope fractography 24
Sintered tungsten
 impact fracture (L,T)159, 475
 intergranular fracture (S)70-71
 pore size and shape (T)104
Size of parts, effect on fracture
 mechanism112
Slag inclusions (L,T)352
Slag stringers (L,M,T)300
Slant fractures (F)37
Slip
 in alloy 718 (S,T)229, 339
 in U-700 alloy (T)347
Slip bands
 in aluminum alloy 2025-T6 (M)464
 in Refractaloy 26 (S)226
Slip planes, in alloy 713C (T)335
Slip steps, in Armco iron (M)378
SLR cameras12
Small-bubble artifacts (T)61, 62
Sockets, fatigue fracture (L)42
Sodium chloride solutions
 effect on fracture of aluminum
 alloys (S)92, 248-249, 259-261
 effect on fracture of steels (T)90, 91, 428
 effect on fracture of titanium alloys
 (S)78, 91-92
Soldered joints, tensile-peel-test
 fractures (L,M,S)270-272
Solid-metal embrittlement (T)92
Solid-pair detectors (F)52-53
Solid-propellant rocket-motor case,
 fracture (L)33
Solvent cleaning of fracture surfaces10
Spar cap, fatigue fracture (T)120
Spars
 fatigue fracture (L,P,T)362
 stress-corrosion-cracking fracture
 (L,M,T)363
Spar web
 failure analysis (E,F,P,T)120, 121, 122
 fatigue fracture (E,F,P,T)120, 121, 122
Specimen holders (F)7
Specimens
 for scanning-electron-microscope
 fractography51
 contamination50
 for transmission mode of operation51, 52
 for transmission-electron-microscope
 fractography54
 contamination56
 thinning26
 preparation (A)9-10, 51
 artifacts (E,S)106, 107
 preservation (A)9-10
Specimen stages
 for light microscopes (F)7
 for scanning electron microscopes51, 52
 for transmission electron microscopes54
Spectrometers51-52

Spectrum fatigue loading (T)85
 striation counting (E,F,L,T)120-124
Spheroidite, in low-carbon steel (M)380
Spider, propeller hub
 failure analysis (L)431
 fatigue fracture (L)431
Spiegeleisen
 fracture appearance (F)4
 microstructure (F)4
Spindles
 cleavage fracture (M,P)471
 failure analyses (L,M,P)382, 438, 439, 471
 fatigue fractures
 (L,M,P)398-399, 410, 438, 439
 fracture through shrinkage cavity (L)382
 reversed-bending fatigue fracture (L)438
Spindle shaft, fracture (L)99
Spine structures
 in 446 stainless steel (L)147
 in iron-silicon alloys (L)151
 in ship-plate steel (L)143
Spinodal copper-nickel-iron alloy,
 fracture (S)269
Spiral-bevel pinion, bending-fatigue
 fracture (P)443, 445
Spiral gears
 failure analysis (L,P)436
 fatigue fracture (L,P)436
Splined axle
 failure analysis (L)394
 fatigue fracture (L)394
Splined idler shaft, failure analysis
 (M,P)396
Splined shafts
 failure analyses (L,M,P)415, 449
 fatigue fractures (L,M,P)415, 449
 torsional-fatigue fractures (L,P)132, 445
 torsion-overload fracture (L,P)36
Spotlights14
Spot welds, porosity (S)100
Spring legs
 failure analysis (L,M,P)442
 fatigue fracture (L,M,P)442
Springs
 failure analyses (L,M,P,S,T)222-223,
 408-410, 411, 438, 440, 441, 455
 fatigue fractures (L,M,P,S,T)183, 222-223,
 318, 408-410, 411, 438, 440, 441, 455
 fracture originating at stamped
 numeral (L,M,P)440
 fracture origins (L,P)408-409
 torsional-fatigue fracture, beach
 marks (L)41
Spring wire, fatigue fracture (L)407-410, 411
Sprocket-drive pinion
 bending-fatigue fracture (L)448
 failure analysis (L)448
Spur gear, bending-fatigue fracture
 (P)443
Stages
 for scanning electron microscopes51, 52
 for transmission electron microscopes54
 metallographic (F)7
Stainless steels. See also specific
 stainless steel.
 banded structures, effect on fracture
 mechanism112
 cleavage fracture (L)146
 dimples (T)114
 grade determination from fracture
 features114
 heat treated structure (M)146
 impact fracture (L)146
 intergranular fractures (M,T)113, 114
 quasicleavage facets (T)114
 stress-corrosion-cracking fractures
 (M,T)113, 114

Stainless steels, specific types

13-8 PH
 cleavage steps (S)219
 corrosion of fracture surface
 (L,S,T)221, 330
 cup-and-cone fractures (L,S,T)219, 328
 dimples (S,T)219, 220, 221, 328, 329, 330
 fatigue fractures (L,S,T)220, 329
 fracture-toughness-test fractures (L)454
 hydrogen-embrittlement fracture
 (L,S,T)221, 330
 inclusions (T)328, 329
 intergranular fracture (L,T)330
 notched, tension-overload fracture
 (L,T)329
 quasicleavage (S)219, 220
 ridges (S)220
 secondary cracks (L,S,T)219, 221, 329, 331
 stress-corrosion-cracking
 fracture (L,S,T)221, 330
 tension-overload fractures
 (L,S,T)219, 328-329
 voids (S)219
 15-5 PH, fatigue fracture (L)454
 17-4 PH
 cleavage (T)331
 cleavage steps (T)330
 cup-and-cone fracture (T)330
 dimples (T)81, 330, 331
 fatigue fracture (L,T)331
 fatigue striations (T)331
 notched, tension-overload fracture
 (T)330
 quasicleavage (T)84
 second-phase particles (T)81
 tension-overload fracture (T)330
 17-7 PH
 clamshell pattern (M,S)222, 223
 fatigue fracture (L,M,P,S,T)222-223
 fatigue striations (S,T)222
 inclusions (M,S,T)222, 223
 stringer (S)223
 201
 corrosion on fracture surface (S)78
 stress-corrosion-cracking fracture (S)78
 301
 dimples (T)331
 elevated-temperature fracture
 (L,S,T)223, 332-333
 fatigue fractures (L,S,T)223, 331
 fatigue striations (S,T)223, 331
 low-temperature fracture (L,T)331
 notched, fatigue fracture (L,T)331
 secondary cracks (S)223
 twin boundaries (S)223
 302
 cleavage steps (T)332, 333
 dimples (T)81, 331, 333
 fatigue fractures (L,M,P,T)332-333, 455
 fatigue striations (T)332, 333
 intergranular fracture (L)137
 notched, fatigue fracture (L,T)332-333
 oxidation of fracture surface
 (T)332, 333
 ripples (T)81
 rock candy fracture (L)137
 secondary cracks (T)333
 tension-overload fracture (T)331
 302B
 casting, dendrite patterns (L)136
 woody fracture (L)136
 303(Se)
 centerline segregation (L)136
 notch-bend fracture (L)136
 304
 corrosion-fatigue fracture (E,T)115, 116
 dimples (T)81

Stainless steels, specific types (continued)

- 304 (continued)
 elevated-temperature fracture (S)224
 fatigue fractures (E,S,T) ..70, 115, 116, 224
 fatigue striations (S)224
 intergranular fractures (S)77, 224
 secondary cracks (S)70, 77
 stress-corrosion cracking (E,T) ..115, 116
 stress-corrosion-cracking fracture (S) 77
 stretching (T)81
 tensile-test fracture (L,M)455
 transgranular facets (S)224
 weld, stress-corrosion-cracking
 fracture (S)77
- 309
 alligator fracture (L)136
 segregation (L)136
 woody fracture (L)136
- 316
 fatigue fracture (E,T)117
 feather marks (S)117
 river patterns (S)76, 77
 rock candy fracture (S)117
 rubbing (E,T)117
 stress-corrosion-cracking fractures
 (E,S)76, 77, 116, 117
 tear ridges (S)76
- 316L
 pores in powder metallurgy
 compact (S)225
 tension-overload fracture (S)225
- 330
 beach marks (L)455
 fatigue fracture (L)455
- 405
 cleavage crack (L)145
 decarburization (L)145
 grain size (M)145
- 410
 cleavage fracture (T)326
 dimples (T)326, 452
 fracture originating at heat-treat
 cracks (L,M)453
 hairline indications (T)326
 intergranular fracture (L,T)326
 notched, crack propagation (T)326
 quasicleavage facets (T)452
 stress-corrosion-cracking
 fracture (L,T)326
 tear ridges (T)452
 tensile fractures (L,T)136, 452
 tongues (T)452
 wire, fracture (T)326
- 430
 cleavage fracture (L)145
 elevated-temperature fracture
 (L)145, 147
 impact fracture (L)146
 impact fracture, effect of
 microstructure (L,M)146
 notch-impact fracture (L)145
 orthogonal markings (L)145
 quenched structure (M)146
 river patterns (L)146
 secondary cracks (L)146
- 431
 corrosion products on fracture
 surface (T)111
 dimples (T)327
 fatigue fracture (L,T)327
 fatigue striations (T)327
 hydrogen-embrittlement fracture
 (E,P,T)111
 impact fracture (L)136
 intergranular fracture (T)111
 intergranular separation, stereo
 views (S)111

Stainless steels, specific types (continued)

- 431 (continued)
 notched, fatigue fracture (T)327
 tensile fracture (L)136
 transgranular cleavage (T)111
- 440C
 chevron pattern (L)136
 radial marks (L)136
 torsion fracture (L)136
- 446
 annealed structure (M)148
 elevated-temperature fractures (L)147
 impact fractures (L)147-148
 impact fractures, effect of
 heat treatment (L)148
 impact fractures, effect of
 impact velocity (L)147
 spine structure (L)147
- 501
 dimples (T)323
 fatigue fracture (L,P,T)322-323
 fatigue striations (T)322, 323
 ratchet marks (L)322
- 633
 corrosion products on fracture
 surface (T)328
 dimples (T)328
 intergranular fracture (T)328
 secondary cracks (T)328
 stress-corrosion-cracking
 fracture (L,T)328
 AM-350, stress-corrosion-cracking
 fracture (L,T)328
 CN-7M, corrosion-produced pits
 (E,S)106, 107
- Stainless steel wire, fracture (T)326, 452**
Stamping, failure analysis (L)379
**Steam-hammer piston rod, failure
 analysis (L)418**
**Steam-line tubing, intergranular
 fracture (S)77**
Steel. See also specific steel.
 conversion of iron to, fracture
 appearance (F)3
 fracture
 Brinell's analysis5
 de Réaumur's classification (F)2-3
 for quality control2
 Martens' treatment (F)5, 6
 hydrogen embrittlement6, 139
 radial marks27-28
- Steel castings**
 dendritic structure (L)99
 fracture through shrinkage cavity (L)382
 hot tears (L)33
 impact fracture (L)131
 porosity, effect on fracture (L)99
 river patterns (L)33
 shrinkage porosity (L)454
- Steel pipe, fracture profile (M)25**
Steel plate
 chevron pattern (L)29
 fatigue-fracture surface marks (F)44
 full-slant fracture (F)37
 shear-fracture propagation direction (F) 80
 ship-plate steels, fracture (L,T)143, 379
- Steels, specific types**
 21-4N, fracture (L)16
 300M
 cleavage crack (L,T)93, 95
 corroded fracture surface
 (L,S,T)93, 94, 95, 194
 dimples (S,T)195, 318
 grain-boundary cracks (S)194, 195
 hairline indications (T)318
 hydrogen-embrittlement fractures
 (L,T)318, 434

Steels, specific types (continued)

- 300M (continued)
 intergranular fractures
 (S,T)72, 94, 194-195, 434
 laps (L,S)94
 notches, effect on fracture
 origin (T)434
 stress-corrosion cracking (L,S,T) ..93, 94
 stress-corrosion-cracking
 fracture (L,S)72, 194-195
- 1015
 intergranular fracture (S)171
 secondary cracks (S)171
 segregation (S)171
 tensile fracture (S)171
- 1018
 dimples (T)80
 fracture surface (T)80
 macrostructure (M)17
- 1020
 centerline crack (M)381
 dimples (L,S)34, 35
 fatigue fracture in high-cycle
 rotary bending (S,T)172
 fatigue fracture in low-cycle
 rotary bending (S)172
 fatigue striations (S,T)172
 ferrite (M)381
 pearlite (M)381
 rubbing (T)172
 secondary cracks (M,S)172, 381
 tear ridges (T)172
 tire tracks (T)172
 transgranular fracture (M)381
- 1021
 cleavage facets (S)173
 dimples (S)173
 elevated-temperature fracture (S) ..173
 ferrite-pearlite structure (S)173
 inclusions (S)173
 low-temperature fracture (S)173
 notched, impact fractures (S)173
 river pattern (S)173
- 1022
 cleavage fracture (S)174, 175
 dimples (S)174
 equiaxed grain structure (M)174
 impact fracture, effect of
 forged structure (L,M,S)174
 impact fractures (S)174, 175
 low-temperature fracture (S)175
 transition from ductile fracture
 to cleavage fracture (L,M,S)174
- 1025
 cleavage fracture (S)175
 impact fracture (S)175
 microvoid coalescence (S)175
- 1030
 fatigue fracture (L)382
 peeling fracture (L)382
- 1033
 low-temperature fracture (L,M,P)386
 welded, fracture (L,M,P)386
- 1035
 brittle fracture (L)387
 fatigue fracture (L)387
 rotating-bending fracture (L)387
 torsional-overload fracture (P)387
- 1038
 ductile vs brittle fracture (P)388
 fatigue fracture (L,M)392
 overheated structure (M)392
 tension-overload fracture (L,P)388
- 1039
 case hardened, fatigue fracture (L) ..391
 fatigue fracture (L)391
 illumination of fracture surface (L) ..14

Steels, specific types (continued)

- 1040
carbide particles (S) 65
cleavage facets (S) 66
cleavage steps (S) 64
dimples (S) 66, 67
fatigue fracture (L) 389
fracture during straightening (P) 388
fracture during stretching (L) 388
impact fractures (S) 64, 65, 66, 67
incipient melting (L,P) 388
low-temperature fractures (S) 64, 65
notched, impact fractures (S) 64, 65, 66
river patterns (S) 64-65
rotating-bending fracture (L) 389, 390
tongues (S) 64, 65
- 1041
fatigue fractures (L) 389, 390, 391, 393, 394
induction hardened, fatigue
fractures (L) 389, 390, 391
induction hardened, torsional-fatigue
fracture (L) 389-390
reversed-stressing fracture (L) 391
single-overload fracture (L) 393
torsional-fatigue fracture (L) 389-390
- 1041H, single-overload fracture (L) 393
- 10B41, fatigue fracture (L) 394
- 1042
cleavage steps (S) 176
dimples (S) 176, 177
elevated-temperature fractures
(S) 176, 177
fractures, effect of heat treatment
(S) 176-177
fractures, effect of test
temperature (S) 176-177
fracture-surface flow (S) 176
impact fractures (S) 176-177
intergranular facets (S) 176
low-temperature fractures (S) 176, 177
martensite (S) 176
river patterns (S) 177
secondary cracks (S) 177
segregation (S) 177
stringer-type inclusions (S) 177
- 1045
beach marks (L) 399
bending-fatigue fracture (L,P) 400
fatigue cracking (M,P) 397, 401
fatigue fractures (L) 400, 402
flame hardened, fatigue
cracking (M) 397
flame hardened, fatigue
fracture (L) 398, 399
induction hardened, bending-
fatigue fracture (L,P) 400
induction hardened, fatigue
fracture (P) 403
peeling-fatigue fracture (P) 402
reversed-torsion fatigue fracture (P) 403
torsional-fatigue fracture (L) 401
- 1046
beach marks (L) 402
bending-fatigue fracture (L) 402
fatigue fractures (L) 402, 403, 404
reversed-bending fatigue fracture (L) 403
- 1046 (mod), fatigue fracture,
effect of seam (L) 93
- 1050
beach marks (L) 405
chevron marks (L) 178
dimples (S) 178, 179
fatigue fractures (L) 45, 405
fracture-surface interpretation (L) 45
impact fracture (L,S) 178-179
induction hardened, reversed-
torsion fatigue fracture (L) 405

Steels, specific types (continued)

- 1050 (continued)
reversed-torsion fatigue fracture (L) 405
river pattern (L) 405
rotating-bending fatigue
fracture (L) 405
secondary crack (S) 179
- 1053
bending-fatigue fracture (L) 33
fatigue fracture (L,T) 406
inclusion (L) 33
induction hardened, fatigue
fracture (L,T) 406
- 1055
beach marks (L) 407
chevron pattern (L) 407
fatigue fracture (L) 407
- 1060
beach marks (L) 409
cleavage facets (S) 179
decarburized, impact fracture (S) 179
fatigue fractures (L,P) 407, 408-409
impact fracture (S) 170
low-temperature fracture (S) 170
river patterns (S) 179
woody fractures (L) 409
- 10B62, fracture (P) 408
- 1070
fatigue fractures (L) 409-410
torsional-fatigue fracture (L,P) 410-411
- 1075
beach marks (L) 131
fatigue fracture (L) 131
hydrogen embrittlement (L) 131
segregation (L) 131
- 1080
cold drawn wire (M,S) 180
corrosion pits (M) 180
dimples (S) 180
fatigue fracture (L,T) 318
fatigue striations (T) 318
ratchet marks (L) 318
stress-corrosion-cracking fracture (S) 180
- 1090
bainite (S) 180
cleavage facets (S) 180, 181, 182
cleavage steps (S) 180, 182
dimples (S) 180, 181, 182
elevated-temperature fractures
(S) 181-183
impact fractures, effect of heat
treatment (S) 181-183
impact fractures, effect of test
temperature (S) 181-183
inclusion (S) 181
intergranular fracture (S) 181
low-temperature fractures (S) 181-182
martensite (S) 181
pearlite (S) 180, 182, 183
secondary cracks (S) 181, 182, 183
spheroidized carbide (S) 182
- 1095
fatigue fractures (L,M,S) 183, 411
fatigue striations (S) 183
- 1115
dimples (S) 183
fatigue striations (S) 183
fracture surface (S) 183
- 11L40, woody fracture surfaces (L) 396
- 1144
fatigue fracture (L) 396
tapered-plug fracture (M,P) 396
- 15B28
illumination of fracture surface (L) .. 15
induction hardened, fatigue
fractures (L) 25
surface hardened, fatigue crack (L) .. 15

Steels, specific types (continued)

- 1541
fatigue cracks (L) 16
fatigue fractures (L) 389, 390, 391, 393, 394
induction hardened, fatigue
fracture (L) 16, 389, 390
induction hardened, rotating-
bending fracture (L) 16
induction hardened, torsional-
fatigue fracture (L) 389-390
reversed-stressing fracture (L) 391
rotating-bending fracture (L) 16
single-overload fracture (L) 393
torsional-fatigue fracture (L) 389-390
- 1541H, single-overload fracture (L) 393
- 15B41, fatigue fracture (L) 394
- 15B62, fatigue fracture (L) 408
- 3340
dimples (S) 74
intergranular fracture (S) 74
microvoid coalescence plus
intergranular fracture (S) 74
- 4070
cleavage step (S) 184
manganese-sulfide stringers (M) 184
microstructure (M) 184
quasicleavage fracture (S) 184
- 4118
bending-fatigue fracture (L,P) 33, 412
carburized, bending-fatigue
fracture (L) 33
carburized, fatigue fracture (L,P) 412
fatigue fracture (L,P) 412
inclusion (L) 33
- 4130
bending fracture (L) 413
cleavage facets (S,T) 185, 301
crack arrests (S) 186
crack propagation (L) 39
dimples (S,T) 184-186, 301
fatigue fracture (L,P) 413
fractures, effect of heat
treatment (S) 184-185
fracture-toughness-test fractures
(S) 184-185
fracture-toughness-test fractures
in air (S) 185
fracture-toughness-test fractures
in hydrogen (S) 186
hydrogen embrittlement (S) 186
inclusions (S) 185
intergranular fractures (S,T) 184, 186, 301
quasicleavage facets (S,T) 184, 301
secondary cracks (S) 186
tension-overload fracture (L,T) 301
voids (S) 185
- 4140
dimples (S,T) 187, 301
fatigue fractures
(L,M,P,S,T) 187, 301, 414-417
fatigue striations (T) 301
secondary cracks (S) 187
sudden-overload fracture (L,S) 187
sulfide stringers (S) 187
transgranular fracture (S) 187
- 4150
beach marks (L,P) 415
fatigue fracture (L,P) 415
- 4315
cleavage steps (T) 304
dimples (T) 90, 91, 304
effect of stress intensity
on fracture (T) 90, 91
hydrogen-embrittlement fracture
(T) 304
intergranular fracture (T) 304
secondary cracks (T) 90

Steels, specific types (continued)

- 4315 (continued)
 stress-corrosion-cracking
 fracture (T) 90, 91
 tear ridges (T) 90
 tension-overload fracture (T) 304
 tilt boundaries (T) 304
 tongues (T) 90
 transgranular fractures (T) 90, 304
 4335 (mod)
 dimples (S,T) 61, 428
 impact fracture (T) 428
 low-temperature fracture (T) 428
 quasicleavage facets (T) 428
 4340
 beach marks (L) 42, 132, 427
 beach marks, from stress-corrosion
 cracking (L) 31
 change of fracture mechanism with
 temperature (L) 46-47
 chevron marks (L) 310, 311
 corrosion-fatigue fracture
 (E,L,P,T) 114-115, 116
 corrosion products on fracture
 surface (T) 309, 314, 315
 crack-growth rate (E,L,T) 123
 cup-and-cone fracture (L,T) 306-307
 dimples (S,T) 191, 192, 305, 307, 309,
 310, 314, 315, 428, 429
 dimples, formation at inclusions (T) 96, 98
 dimples, stereo views (S,T) 286
 ductile-brittle fracture transition (L) 425
 electroslag remelt grade,
 fracture (S) 191
 elevated-temperature fractures
 (L) 27, 46, 47, 422, 424
 fatigue fractures (E,L,M,P,S,T) 42,
 103, 107, 122, 123, 132, 188, 189, 190, 304,
 314, 420-421, 427, 430-431
 fatigue fractures, effect of
 corrosion (T) 429
 fatigue striations (L,T) 107
 fatigue striations, stereo views (S,T) . 287
 fracture, origin (L) 39
 grain-boundary cracks (M) 429
 grinding cracks (M,T) 309
 hairline indications (T) 308, 313
 hydrogen-embrittlement fractures
 (L,S,T) . 71, 192, 310-311, 312, 313, 428, 429
 hydrogen flakes (L) 312
 illumination of fracture surface (L) . 14
 impact fractures (S,T) 66, 305, 308, 428, 429
 impact fractures, effect of
 temperature (L) 425
 inclusions (S) 191
 inclusions, effect on fracture (T) . 96, 98
 intergranular facets (S) 192
 intergranular fractures (E,L,T) 71,
 89, 90, 107, 110, 308, 309, 310, 311, 313, 314,
 315, 428, 429
 intergranular fractures, stereo
 views (S,T) 287
 low-temperature fractures
 (L) 28, 46, 66, 422-424, 425
 mixed-mechanism fracture (T) 429
 mud cracks (T) 315
 notch-bend fracture (L) 132
 notched, effect of root radius on
 fracture appearance (L) 48
 notched, hydrogen-embrittlement
 fracture (L,T) 313
 notched, low-temperature fracture (L) 46
 notched, stress-corrosion-cracking
 fracture (L,T) 315
 notched, tension fractures (L) 429
 notched, tension-overload fracture
 (L,T) 305, 422-424

Steels, specific types (continued)

- 4340 (continued)
 notched, tension-overload fracture,
 stereo views (S,T) 286
 oxidation of fracture surface (L,S) . 190
 quasicleavage (S,T) 66, 190, 191,
 308, 428, 429
 quench cracks (L,T) 308
 rock candy fracture (T) 89
 rubbing, stereo views (S,T) 287
 secondary cracks (L,S,T) . 192, 314, 315
 secondary cracks, stereo views (S,T) . 287
 shear lips (L) 310, 311
 stress-corrosion cracking (L,S) 95, 114-115
 stress-corrosion-cracking fractures
 (L,T) 31, 90, 313, 314-315, 428
 stretching (T) 305
 stretching, stereo views (S,T) 286
 stringers, effect on fracture (S) . 98-99
 stringer troughs (S,T) 98, 99
 tearing (L) 427
 tear ridges (L,T) 132, 305, 428, 429
 tensile fractures (L) 27, 28
 tensile fractures, effect
 of microstructure (L) 28
 tensile fractures, effect of stress (L) . 429
 tensile fractures, fracture zones (L) 27, 28
 tension-overload fractures
 (L,T) 305, 422-424, 429
 tension-overload fractures,
 effect of hardness (L) 422-423
 tension-overload fractures,
 effect of heat treatment (L) 424
 tension-overload fractures,
 effect of temperature (L) 422-424
 tension-overload fractures, stereo
 views (S,T) 286
 torsion-overload fracture (L,T) 305
 transgranular fractures
 (S,T) 187, 308, 309, 428
 voids (S) 192
 weld, intergranular fracture (E,T) 109-110
 woody fracture (L) 103
 worm-track marks (T) 312
 4340 (mod)
 hydrogen-embrittlement fracture
 (S) 71
 intergranular fracture (S) 71, 76
 quench cracks 77
 secondary cracks (P,S) 32, 76
 stress-corrosion-cracking fracture (S) 76
 4350
 beach marks (L) 434-435
 fatigue fractures (L,M,P) . 94, 95, 434-435
 quench crack (L) 94, 95
 4817
 carburized, fatigue fracture (L,P) . 436
 fatigue fracture (L,P) 436
 4820H
 case hardened, fatigue fracture (L) . 436
 fatigue fracture (L) 436
 50B20
 carburized, impact fracture (L) 437
 impact fracture (L) 437
 5046, case hardened, fracture (L) 437
 50B60
 fatigue fracture (L) 438
 torsional-fatigue fracture (L) 438
 50100
 fracture (M,S) 197
 microstructure (M) 197
 quench crack (S) 197
 secondary grain-boundary cracks (S) 197
 voids (M) 197
 5132
 fatigue fracture (L) 438
 reversed-bending fatigue fracture (L) 438

Steels, specific types (continued)

- 5135H, fatigue fracture (L,M,P) 439
 5145
 case hardened, fretting corrosion (P) 440
 fretting corrosion (P) 440
 5155
 dimples (S) 196
 elevated-temperature fracture (S) . 196
 impact fractures (S) 196
 low-temperature fracture (S) 196
 reversed-torsion fatigue fracture (S) 196
 tire tracks (S) 196
 5160
 beach marks (L) 441
 fatigue fractures (L) 440, 441
 52100
 cleavage facets (S) 197
 dimples (S) 197
 fracture, effect of heat
 treatments (S) 197
 low-temperature fractures (S) 197
 notch-impact fractures (S) 197
 6118, torsion-overload fracture (L,P) . 36
 6150
 fatigue fracture (L,M,P) 442
 stringer trough (S) 99
 sulfide stringer (S) 99
 7140
 beach marks (L) 198
 dimples (S) 198
 fatigue fracture (L,P,S) 198
 inclusions (S) 198
 nitrided, fatigue fracture (L,S) 198
 8617
 bending-fatigue fracture (P) 443
 carburized, bending-fatigue
 fracture (P) 443
 8620
 bending-fatigue fracture
 (L,P) 443, 444, 445
 bending-overload fracture, crack
 origin (L) 41
 carburized, bending-overload
 fracture (L) 41
 carburized, fatigue fracture (L) 15
 carburized, inclusion (L) 15
 carburized, overload fracture (L) 444, 447
 case hardened, spalling-fatigue
 fracture (L) 443
 case hardened, torsional-fatigue
 fracture (L,P) 445
 cast, fatigue fracture (L,P) 446
 chevron pattern (L) 444
 fatigue fracture (L,M,P) 446
 fracture profile (M) 25
 impact fracture (P) 447
 inclusions (M) 25
 overload fracture (L,P) 444, 447
 spalling-fatigue fracture (L) 443
 torsional-fatigue fracture (L,P) 445
 8640
 beach marks (L) 447
 bending-fatigue fracture (L) 447
 fatigue fracture (L) 446, 447, 448
 8645, fatigue fracture (L,M,P) 449
 8650
 beach marks (L) 448
 bending-fatigue fracture (L) 448
 induction hardened, bending-
 fatigue fracture (L) 448
 8740
 cleavage facets (T) 316
 cup-and-cone fracture (L,S) 199
 dimples (S,T) 199, 200, 316, 317
 fatigue fracture (L,S) 200-201
 fatigue striations (S) 200, 201
 fissures (S) 200, 201

Steels, specific types (continued)

- 8740 (continued)
 notched, tension-overload fracture (L,S,T)199-200, 317
 quasicleavage (S)200
 secondary cracks (S,T)199, 316
 tension-overload fracture (L,S,T)199, 316-317
 voids (S)200, 201
- 9310
 carburized, impact fracture (L) 30
 case hardened, effect of inclusions on fracture (S) 97
 dimples (T)319
 fatigue fractures (L,T) 88, 319
 fatigue striations (T)319
 impact fracture (L) 30
 inclusions, effect on fracture (S) 97
 intergranular fracture (T)319
 rubbing (T) 88
 single-overload fracture (T) 88
 tension-overload fracture (T)319
 woody fracture (L) 30
- AMS 6265
 fatigue fracture (T) 88
 rubbing (T) 88
 single-overload fracture (T) 88
- AMS 6434
 cleavage facets (T)302
 cleavage steps (T)302
 dimples (T)302, 428
 impact fracture (T)428
 intergranular fracture (T)303
 low-temperature fractures (T)302, 428
 microstructure (M)302
 notched, tension-overload fracture (T)302
 quasicleavage facets (T)302, 428
 stress-corrosion-cracking fracture (L,T)303
 tension-overload fracture (T)302
- ASTM A36
 cleavage facets (S)175
 dimples (S)175
 ferrite-pearlite microstructure (M)175
 river patterns (S)175
 tension-overload fracture (M,S)175
- ASTM A302, grade B
 cleavage fractures (S)103, 104
 microvoids (S)103, 104
- ASTM A514, type F
 crack branching (L) 32
 impact fracture (L) 32
- ASTM A515, grade 70
 cracking (L,M,P)383
 fracture (L,M,P)384-385
 microstructure (M)384
- D-6ac
 beach marks (L) 31
 fatigue fractures (L,T)31, 87
 fatigue striations (T) 87
 fracture originating in a heat-treat crack (L,T)318
 intergranular facets (T)318
 secondary cracks (M) 35
 stress-corrosion-cracking fractures (L,M,T)35, 318
- D6B, fatigue fracture (L)418
- HY-180
 dimples (S)192
 mixed-mechanism fracture (S)192
 tension-overload fracture (S)192
- SAE EV 8, fracture (L) 16
- Silchrome-1, fatigue fracture (L)452
- Steel stampings**
 chevron pattern (L)379
 fracture (L)379

- Steering-gear cover, bending-fatigue fracture (L,M,T)350**
- Steering-gear housing, impact fracture (L,P,T)351**
- Steering-knuckle spindle, failure analysis (L,M,P)439**
- Step in part, effect on fracture appearance 37**
- Step-wedge photography 21**
- Stereofractographs (L,S,T) 22, 23, 98, 104, 111, 162, 165, 266, 267, 281-296**
 macro views (L)22, 23
 scanning-electron-microscope stereo pairs (S)51, 161, 162, 165
 compared with transmission-electron-microscope stereo pairs (S,T) 63, 281-296
 transmission-electron-microscope stereo pairs (T)281-296
 compared with scanning-electron-microscope stereo pairs (S,T)63, 281-296
 specimen preparation281
 viewing stereo pairs165, 281-282
- Stereo microscopes (F)11, 12, 22, 23**
 application to failure analysis106
- Stereo pairs (L,S,T) 22, 23, 98, 104, 111, 162, 165, 266, 267, 281-296**
 viewing281-282
- Stewart, A. D. G. 49**
- Stone, fracture (P)1-2**
- Stone implements, fracture (P) 1**
- Stress concentrations, effect on fracture (S)107**
- Stress-corrosion cracking (M) 35**
 fracture origins (S)93, 95
- Stress-corrosion-cracking fractures**
 beach marks (L)31
 compared with hydrogen-embrittlement fractures (E)111
 corrosion products111
 crack branching (M) 32
 features (E,S,T)72, 76-77, 90-91, 111, 116-117
 fracture origins (L) 42
 fracture propagation (L)45, 90
 intergranular fractures (S)72, 76-77
 revealed by SEM (S)72, 76-77
 revealed by TEM (T)90-91
 stress states 36
 transgranular fractures (S)76, 77
- Stresses**
 determination by failure analysis (E,L,P,T)107-109
 effect on dimple shape (F)79, 80
 effect on fracture propagation (F)43-44
 magnitude, revealed by fractography109
 orientation, revealed by fractography109
- Stress-intensity factor, effect on crack propagation (L)44-45**
- Stress raisers109**
- Stress state**
 effect on fracture appearance (F,L)47-48
 revealed by light fractography (F,L)36-38
- Stretching in fracture**
 effect of plane-strain stress-intensity factor (T)81, 82
 in 4340 steel (S,T)286, 305
 in alloy 713C (T)335
 in aluminum alloys (S,T)288, 350, 356, 361, 363, 467
 in beryllium copper (T)364
 in IN-100 (T)336
 in L-605 (T)343, 344
 in magnesium alloy AZ81A-T4 (T)366
 in maraging steel (S)208
 in Refractaloy 26 (S)226
 in stainless steel (S,T)224
 in Ti-6Al-4V (T)370, 371

Stretching in fracture (continued)

- in U-700 alloy (T)346
 in Waspaloy (T)339, 340, 341
 revealed by TEM (T)81, 82
- Striations (L)30, 31, 32**
 See also *Fatigue striations*.
 counting, to determine loading (E,F,L,T)118-124
 lamellar structures (T)88-89
 Wallner lines (T)83, 84, 88
- Stringers (L)131**
 formation 98
 fracture origins (S,T)98-99
 in 4070 steel (M)184
 in 4140 steel (S)187
 in 4340 steel (S) 98
 in wrought iron (L,M,T)300
- Stringer troughs (S,T)98-99**
- Stripper-crane wheel, fatigue fracture (L)407**
- Struts, missile silo**
 failure analysis (L)432-433
 fracture (L)432-433
 impact fracture (L,M,S)174
- Stud head**
 failure analysis (L,S)192
 hydrogen-embrittlement fracture (L,S) 192
- Stud nuts**
 failure analysis (L)396
 woody fracture (L)396
- Studs**
 centerline segregation (M) 34
 failure analysis (M,T)113-114
 fatigue fracture (L)414
 laps (L,S)93, 94
 overload fracture (S)193
 stress-corrosion crack (L,S,T)93, 94
 stress-corrosion-cracking fractures (L,M,S,T)42, 113-114, 193
- Subcracks (P)360**
- Subsurface crack origins39-40, 43**
- Sulfide inclusions, dimple formation at (T)96, 97**
- Superplastic aluminum-copper alloy, tensile-overload fracture (S)262-263**
- Surface crack origins (L)38-40, 43**
- Surgical microscopes 13**
- Suspension bar**
 failure analysis (L)394
 fatigue fracture (L)394
- Suspension component**
 failure analysis (L)438
 fatigue fracture (L)414, 438
- Suspension spring, fatigue fracture (L)408**
- Suspension strut**
 failure analysis (L)432-433
 fracture (L)432-433
- Symbols476**

T

- Tail-actuator shaft, hydrogen-embrittlement cracking (L,P,T)310-311**
- Tail-rotor drive-pinion shaft**
 failure analysis (L,P)414-415
 fatigue fracture (L,P)414-415
 stress concentrators415
- Tailshaft**
 failure analysis (L,M)393
 fatigue fracture (L,M)393
- Tantalum alloy 90Ta-10W, fatigue fracture (L,T)367**
- Tantalum-tungsten alloy**
 dimples (T)367
 fatigue fracture (L,T)367
 fatigue striations (T)367

Tapered-plug fracture, in splined idler shaft (M,P) 396

Tear dimples 67
 revealed by SEM (S) 67
 revealed by TEM (F) 79, 80

Tearing fractures 72
 plus cleavage (S) 72
 plus fatigue-striation formation (S,T) 74, 75, 86
 plus intergranular fracture (S) 74, 75
 plus microvoid coalescence (S) 73
 revealed by SEM 68
 revealed by TEM 81-82
 stress-orientation determination 109

Tear ridges 84
 in quasicleavage (F) 84
 relation to crack origin 38

Tear tests 104

TEM fractographs. See *Transmission-electron-microscope fractographs*.

TEM fractography. See *Transmission-electron-microscope fractography*.

Temperature 28
 effect on fracture appearance 28
 effect on fracture mechanisms (L) 46
 elevated-temperature fractures (L,S) 46, 47, 75-76, 112
 low-temperature fractures (L,S,T) 26, 28, 46, 47, 66, 83, 140-141, 168, 169, 180-182

Temper colors of heat-treat cracks 94

Tensile fractures. See also under specific metal.
 dimple shapes (F) 79
 early treatment 4
 stress states (F) 36
 surface marks (F,L) 27-29

Tensile peel tests (S) 270-272
 description 270
 fractures (L,M,S) 270-272

Tensile specimens 27-29
 fracture features (F,L) 27-29
 notched, fracture zones (F,L) 30, 38, 39

Tensile stages 52

Tension-compression loading, effect on fracture-surface features (F) 43, 44

Tension-overload fractures. See under specific metal.

Tension-tension loading, effect on fracture-surface features (F) 43, 44

Tension tests 104

Tent lighting (F) 17

Thermal environments 111-112
 effect on fracture 111-112
 effect on fracture appearance 28
 effect on fracture mechanisms (L) 46
 elevated-temperature fractures (L,S) 46, 47, 75-76, 112
 low-temperature fractures (L,S,T) 26, 28, 46, 47, 66, 83, 140-141, 168, 169, 180-182

Thermal-shock fracture (L,T) 376

Thick single-stage plastic replicas (F) 57-58
 preparation 57
 thickness 57

Thinning specimens 26

Thin single-stage plastic replicas (F) 56-57
 stripping 57
 thickness 57

Thoriated nickel 80
 dimples (T) 80
 dispersed particles (T) 80

Threads 432-433, 471
 effect on fatigue fractures (L,M) 432-433, 471
 effect on fractures (L,M,P,S,T) 94, 194-195, 245, 246, 470, 471
 source of fatigue cracks (L,P,S,T) 188

Three-dimensional viewing (S,T) 281-282
 fractographs for (L,S,T) 22, 23, 98, 104, 111, 162, 165, 266, 267, 282-296

Throttle-control spring 222-223
 failure analysis (L,M,P,S,T) 222-223
 fatigue fracture (L,M,P,S,T) 222-223

Tiemann, H. P. 4-5

Tilt boundaries 304
 in 4315 steel (T) 304
 in Alnico (T) 348
 in columbium alloy B-66 (T) 82
 in TZM alloy (T) 367

Tilting stages 54

Tilt-twist boundary (T) 468

Tire tracks 86
 causes 86
 in 1020 steel (T) 172
 in 5155 steel (S) 196
 in aluminum alloy 380 (T) 350
 in aluminum alloy 6061-T6 (T) 86

Titanium 72
 cleavage-plus-tearing fracture (S) 72
 dimples (T) 368
 elevated-temperature fracture (P,T) 368
 fatigue fracture (L,T) 368
 fatigue striations (S,T) 75, 368
 notched, fracture (L,T) 368
 serpentine glide (T) 368
 tearing plus fatigue-striation formation (S) 75
 tear ridges (S) 75
 tension fracture (M,P,T) 368

Titanium alloys 10
 cleaning fracture surfaces 10
 cleavage plus fatigue-striation formation (S) 72, 73
 cleavage plus microvoid coalescence (S) 71-72
 fracture features 75
 fracture mechanism, effect of temperature 75
 microvoid coalescence plus tearing (S) 73
 stress-corrosion fracture (T) 90

Titanium alloys, specific types

Ti-2Al-2Zr-2V-1Mo 471
 fracture (T) 471
 stringers (T) 471

Ti-2.5Al-16V 471
 dimples (T) 471
 fatigue fracture (T) 471
 fatigue striations (T) 471

Ti-3Al, bending under impact (P) 473

Ti-5Al-2.5Sn 369
 dimples (T) 369
 fatigue fracture (L,T) 369
 fatigue striations (T) 369
 fracture-toughness-test fracture (S) 273
 ledges (S) 273
 notched, fracture (L,T) 369

Ti-5Al-3Sn-2Mo-2V 369
 dimples (T) 369
 drop-weight-tear-test fracture (L,T) 369
 intergranular fracture (L,T) 369
 separated-grain facets (T) 369
 transgranular fracture (T) 369

Ti-6Al-2Sn-4Zr-6Mo 72
 cleavage facets (S) 72
 dimples (S) 72
 mixed-mechanism fractures (S) 72
 stress-corrosion fracture (S) 72

Ti-6Al-4V 275, 472
 beach marks (L) 275, 472
 cleavage facets (T) 90
 cleavage steps (S) 278
 corrosive environment, effect on fatigue striations (T) 87

Titanium alloys, specific types (continued)

Ti-6Al-4V (continued) 274
 cup-and-cone fracture (L) 274
 dimples (S,T) 80, 90, 273, 274, 275, 276, 279, 370, 371, 373, 473, 474
 fatigue-crack propagation (T) 87
 fatigue fractures (E,L,M,P,S,T) 86, 87, 108, 275, 372, 472-473
 fatigue striations (L,T) 86, 87, 108, 372
 feathery fracture surface (S) 276
 fissures (S) 275, 276
 fracture appearance, effect of crystallographic orientation (T) 372
 fracture propagation (L,T) 370-372
 fractures, effect of environment (S) 273, 276-279
 fractures, effect of heat treatment (S) 277
 fractures, effect of hydrogen environment (S) 273, 276-279
 fractures, effect of porosity (L,M) 100, 101
 fracture-toughness-test fractures (S) 273, 276-279
 inclusions (S) 274
 low-cycle fatigue striations (T) 86
 low-temperature fracture (L,T) 370
 microcracking (L,M) 101
 notched, fracture (L,T) 371
 notched, tension-overload fracture (L,S) 274
 nucleation sites for microvoids (T) 80
 quasicleavage facets (S) 278
 ripples (T) 370, 371, 373, 473
 river patterns (S) 278
 secondary cracks (S,T) 87, 273, 274, 276, 277, 278, 371
 segregation (L,M) 100, 101
 shear fracture (M) 39, 40
 shear fracture, crack propagation (M) 39, 40
 solid-metal embrittlement (T) 92
 stabilizing heat treatment 277
 stress-corrosion-cracking fracture (T) 90, 474
 stretching (T) 370, 371, 474
 tension-overload fracture (L,S,T) 274, 276, 277, 370, 371, 373, 473
 terraced fracture surfaces (S) 278
 three-point-bending fractures (S) 273
 torsion-overload fracture (L,T) 370
 voids (S) 275

Ti-7Al-2Cb-1Ta 474
 cleavage facets (T) 474
 dimples (T) 373, 474
 fatigue fractures (L,T) 373
 fatigue striations (T) 373
 fracture, effect of environment (L,T) 373
 quasicleavage facets (T) 373
 ripples (T) 474
 serpentine glide (T) 373
 stress-corrosion-cracking fracture (S,T) 78, 474
 tension-overload fracture (L,T) 373, 474
 transgranular fracture (S) 78

Ti-7Al-1Mo-1V 474
 dimples (T) 474
 fracture from drop-weight tear test (T) 474
 tear ridges (T) 474

Ti-7Al-3V 475
 dimples (T) 475
 tension-overload fracture (T) 475

Ti-8Al-2Cb-1Ta, troughs (T) 81

Ti-8Al-1Mo-1V 91-92
 corrosion-fatigue fracture (T) 91-92
 dimples, stereo views (S,T) 294
 fatigue fractures (T) 91-92, 475

Titanium alloys, specific types (continued)

- Ti-8Al-1Mo-1V (continued)**
 fatigue fractures, effect of stress amplitude (T) 91-92
 fatigue fractures, stereo views (S,T) 295
 fatigue striations (T) 475
 fatigue striations, stereo views (S,T) 295
 impact fracture (T) 475
 notch-tensile fracture, stereo views (S,T) 294
 quasicleavage facets, stereo views (S,T) 296
 stress-corrosion-cracking fracture (T) 475
 stress-corrosion-cracking fracture, stereo views (S,T) 296
 tension-overload fracture, stereo views (S,T) 294
 transgranular fracture (T) 91-92
- Ti-8Mn**
 dimples (T) 374
 notched, fracture (L,T) 374
 sustained-tension fracture (L,T) 374
- Ti-8Mo-8V-2Fe-3Al, microvoid coalescence plus tearing (S)** 73
- Ti-13V-11Cr-4Al**
 cleavage steps (T) 374
 fatigue fracture (L,T) 374
 fatigue striations (T) 374
 notched, fatigue fracture (L,T) 374
- Titanium - boron-fiber composite, longitudinal tensile fracture (S)** 264
- T-junction method of crack-origin location (F)** 38
- Tongues (S,T)** 65, 83
 in Armco iron (T) 299, 378
 in Duranickel (S) 235
 in fast-fracture zone (L) 399
 in high-purity iron (S) 162
 in iron-nickel alloy (S) 202
 in low-carbon iron (S) 168
 in Nickel 201 (S) 236
 in room-temperature testing of alloy steel (L) 426
 in steel (L,S) 64, 65, 398-399
- Tool marks**
 crack origins at (L,M) 379, 387
 effect on fatigue fractures (E,L,M,P,T) 109-110, 400, 404, 410, 414-415, 439, 454, 463, 472-473
 effect on impact fracture (L,S) 178
- Tool steels, specific types**
 A4N, tensile fracture (L) 133
- H11**
 beach marks (L) 324, 325
 corrosion of fracture surface (S) 213
 cup-and-cone fracture (L) 324
 dimples (S,T) 210, 211, 212, 324, 325
 electroplated, fracture (L,T) 325
 fatigue fractures (L,S,T) 211-212, 324-325
 fatigue striations (S,T) 211, 324
 grain-boundary cracking (S) 213
 hairline indications (T) 323
 hydrogen-embrittlement fracture (L,S,T) 212-213, 323, 325
 intergranular fracture (L,T) 323, 325
 notched, tension-overload fracture (L,S,T) 210, 324
 quasicleavage facets (S,T) 210, 211, 324
 ridges (S) 211
 secondary cracks (S,T) 211, 213, 324, 325
 stress-corrosion-cracking fracture (L,S,T) 213, 325
 tension-overload fracture (L,S,T) 210, 324
 voids (S) 210

Tool steels, specific types (continued)

- L6**
 cup-and-cone fracture (L) 134
 impact fracture (L) 134
 tensile fracture (L) 134
- M3, class 1**
 fan-shaped pattern (L) 135
 impact fracture (L) 135
- S1**
 beach marks (L) 134
 fatigue fracture (L) 134
- T1**
 impact fracture (L) 135
 Wallner lines (L) 135
- T2**
 dimples, stereo views (S,T) 285
 impact fractures, stereo views (S,T) 285
 inclusions, stereo views (S,T) 285
 quasicleavage facets, stereo views (S,T) 285
- W1**
 fatigue fracture (L) 133
 notch-bend fracture (L) 133
 reversed-bending fracture (L) 133
- W2**
 case hardened, fatigue fracture (L) 134
 fatigue fracture (L) 134
 class 110, fatigue fracture (L) 133
 class 120, fatigue fracture (L) 134
 class 234, impact fracture (L) 134
 class 241, tensile fracture (L) 134
 class 244, tensile fracture (L) 134
 class 320, fatigue fracture (L) 134
 class 610, impact fracture (L) 135
 class 612, impact fractures, stereo views (S,T) 285
 class 651, impact fracture (L) 135
- Tooth roots, effect on fracture (L,M)** 397, 436
- Torn-plastic artifacts (T)** 62
- Torque cylinder, fatigue fracture (L,P,T)** 322-323
- Torsional-fatigue fractures (L)** 37
 beach marks (L) 41
 in steels (L,P) 389-390, 393, 401, 410-411, 438, 445
- Torsion bars**
 failure analyses (L,P) 410-411, 438
 torsional-fatigue fractures (L,P) 410, 411, 438
- Torsion fractures. See also under specific metal.**
 dimple shapes (F) 79
 stress states (F) 36-37
- Torsion loading, effect on fracture-surface features (F)** 43
- Tough pitch copper**
 dimples (T) 468
 inclusions (T) 468
 tension-overload fracture (T) 468
- Track-bar stud, segregation (M)** 34
- Tractor axle, torsional-fatigue fracture (L)** 389-390
- Tractor bull gears**
 failure analysis (L,T) 406
 fatigue fracture (L,T) 406
- Tractor chassis-frame bar, transverse fracture (L)** 131
- Tractor equalizer bar, fatigue fracture (L)** 418
- Transcrystalline fractures**
 features revealed by SEM (S) 64-70
 features revealed by TEM (T) 79-89
 Tiemann's description 5
- Transducer spring, fatigue fracture (L,T)** 318

Transgranular fractures

- features revealed by SEM (S) 64-70
 features revealed by TEM (T) 79-89
 in corrosive environments 91
 stress-corrosion-cracking fractures (S) 76-77
 stress-orientation determination 109
- Transmission-electron-microscope fractographs (A)** 297-376
 artifacts (T) 61, 63, 288, 289, 291, 294, 295, 296
 cleavage fractures (F,T) 82-84
 corrosion-fatigue fractures (T) 91-92
 dimples, compared with scanning-electron-microscope fractographs (S,T) 61
 discontinuities revealed (T) 94, 96, 99, 101-102
 fatigue fractures (F,T) 84, 85-89
 features revealed (A) 79-92
 hydrogen-embrittlement fractures (T) 90-91
 intergranular fractures (T) 89-90
 microvoid-coalescence fractures (T) 79-81
 quasicleavage fractures (F,T) 84-85
 stress-corrosion-cracking fractures (T) 90-91
 transgranular fractures (T) 79-89
- Transmission-electron-microscope fractography**
 fracture-surface analysis 26
 historical background 54
 replicas (F) 56-59, 281
 shadowing of replicas (F) 59-60, 281
 single-stage replicas (F) 59
 specimens 54
 contamination 56
 thinning specimens 26
 two-stage replicas (F) 58, 59
 use for failure analysis (A) 106-124
 uses other than failure analysis (A) 103-105
 viewing of fractographs 59
- Transmission electron microscopes (A,F)** 54-56
 accelerating voltage 54
 advantages for fractography 63-64, 68
 area of specimen covered 64
 depth of field 54
 design (F) 54-55
 features 54
 fidelity 63
 image contrast 55
 image intensity 55
 image quality 54-55
 lens system 54
 limitations for fractography 63
 magnification limits 54, 55, 63
 magnification methods (F) 54, 55
 resolution (F) 55-56, 63
 specimen stages 54
- Transmission-electron-microscope stereofractographs (A)** 63, 281-296
 compared with scanning-electron-microscope fractographs (S,T) 281-296
 replica preparation 281
 viewing stereo pairs 282
- Transmission gear**
 failure analyses (L,P) 198, 400
 fatigue fractures (L,P) 198, 400
- Transmission scanning-electron-microscope fractography** 52
- Transmitted-light fractographs (L)** 120, 123
- Transmitted-light fractography (L)** 24, 25
- Transparent-tape replicas (L)** 24
- Trigonal symmetry**
 antimony (L) 153
 bismuth-zinc alloy (L) 155
- Tripods** 23
- Truck axles**
 failure analysis (L) 390
 fatigue fracture (L) 390

Tungsten

- cleavage facets (L,T)158, 375
- cleavage steps (L,T)158, 475
- deoxidized, fracture (L)158, 159
- feathers (T)83, 375
- fracture originating at weld
 - discontinuity (S)95
- gas cavities (L)158
- impact fractures (L,T)158-159, 475
 - effect of deoxidation practice (L)158-159
- inclusions (L)158-159
- intergranular fracture
 - (L,S,T)70, 71, 158, 375
- separated-grain facets (T)475
- sintered, impact fracture (T)475
- tension fracture (S)71
- tension-overload fracture (L,T)375
- transgranular fracture (L)159
- vacuum-arc cast (L)158-159

Tungsten-fiber - silver composite

- cleavage fracture (S)279
- dimples (S)279
- tension-overload fracture (S)279

Tungsten powder-metal compacts

- crack propagation (L,T)376
- impact fractures (L,T)159, 475
- intergranular fractures (L,T)159, 376
- pores (T)104, 475
- recrystallized (T)475
- swaged, fracture (L)159
- thermal-shock fracture (L,T)376

Tungsten-rhenium alloy

- intergranular fracture (S)70, 71
- tension fracture (S)71

Tungsten single crystal, impact

- fracture (T)475

Tunmer, P.

- 3

Turbine blade

- fracture, effect of inclusion (L,S)97
- overload fracture, effect of
 - porosity (S)99, 100

Turbine planet gear, fatigue fracture (L,T)

- 319

Turbine rotor blades, corrosion-fatigue

- fracture (L,P,T)334

Turbine wheels

- crack origin (S)234
- failure analysis (L,S)234
- fatigue fracture (L,S)234

Turbocharger housing

- failure analysis (L,M,P)450
- impact fracture (L,M,P)450

Turbosupercharger impeller,

- fracture (L,M,P)137-138

Twin-lens reflex cameras

- 12

Twins

- effect on cleavage features (T)83
- in 301 stainless steel (S)223
- in alloy 718 (T)338
- in antimony (L)153
- in Armco iron (L)140, 142
- in bismuth (L)154
- in high-purity iron (S)162, 169
- in iron-nickel alloy (S)202
- in iron-silicon alloys (L)150
- in low-carbon iron (S)168
- in molybdenum (L)156
- in Waspaloy (T)342
- in zinc (L)160
- plane of65

Twist boundaries

- in columbium alloy B-66 (T)83
- in iron-nickel alloy (S)202
- in TZM alloy (T)367

Two-stage replicas

- for light-microscope fractography24
- for transmission-electron-microscope
 - fractography (F)58, 59

TZM alloy

- cleavage facets (S,T)272, 367
- cleavage steps (S)272
- feather marks (T)367
- fracture-toughness-test fracture (S)272
- notched, fracture (L,T)367
- secondary cracks (S)272
- tension-overload fracture (L,T)367
- tilt boundary (T)367
- transgranular fracture (T)367
- twist boundary (T)367

U**U-700 alloy**

- dimples (T)346
- elevated-temperature fracture (L,S)230
- fatigue-fracture progression (T)346-347
- fatigue fractures (L,S,T)230, 346-347
 - effect of frequency of stress
 - application (L,S)230
- fatigue striations (L,T)230, 346, 347
- fracture appearance, effect of
 - crystallographic orientation (T)346, 347
- intergranular rupture (T)346
- notched, fatigue fracture (L,T)346-347
- notched, tension-overload fracture
 - (L,T)346
- precipitate particles (S)230
- secondary cracks (T)347
- separated-grain facets (T)346
- slip (T)347
- stretching (T)346
- tension-overload fracture (L,T)346

Ultrasonic cleaning of fracture surfaces

- 10

Ultraviolet lighting (P)

- 17-18, 32

Unidirectional-bending loading, effect on

- fracture-surface features (F)43, 44

Unnotched specimens, tensile-fracture

- features (F,L)27-29

Upsetting-machine crankshaft

- failure analysis (L)420-421
- fatigue fracture (L)420-421

V**Vacuum, fractures in (T)**

- 91, 462

Vacuum-arc cast molybdenum,

- fracture (L)156-157

Vacuum-arc cast tungsten,

- fracture (L)158-159

Vacuum deposition of carbon replica

- 58

Vacuum deposition of shadowing metal

- 60

Valve blocks

- corrosion-fatigue fracture
 - (E,L,P,T)114-115, 116
- failure analysis (E,L,P,T)114-115, 116

Valves

- failure analyses (L,M,T)452, 470
- fatigue fracture (L)452
- fracture (L)454

Valve spindle

- cleavage fracture (M,P)471
- failure analysis (M,P)471

Valve springs

- failure analysis (L,P)408
- fatigue fracture (L,P)408, 409

Vehicle arm, impact fracture (S)

- 174

Vertical lighting (F)

- 13, 15
- of etched surfaces (M)17
- of fracture surfaces (L)14
- to show grain flow and inclusions (F)17

View cameras

- film11-12
- 12

Viewers for stereofractographs

- 282

Viewing fractographs

- 53, 282

Visual examination of fractures

- 11, 106

Voids (M,S)

- 100, 185, 192, 197, 200, 201, 219, 241, 247

von Borries, B.

- 54

W**Wallner lines (L,T)**

- 83, 84, 135

Waspaloy

- dimples (T)339, 340, 341
- elevated-temperature fracture (L,T)340-341
- fatigue-fracture progression (T)341-342
- fatigue striations (T)341, 342
- glide-plane decohesion (T)341
- grain-boundary separation (T)341
- intergranular fracture (S)231
- notched, fatigue fractures (T)341-342
- notched, tension-overload fracture
 - (L,T)340-341
- oxidation of fracture surface
 - (S,T)231, 340, 341
- ripples (T)340, 341
- secondary cracks (S)231
- serpentine glide (T)340, 341
- stress-rupture fracture (S)231
- stretching (T)339, 340, 341
- tension-overload fracture (L,T)339-341
- twin boundaries (T)342

Welds

- crack origins25
- cracks, revealed by fractography109
- discontinuities (L,P,S)33, 94, 95, 379, 384-385, 394-395, 401
- effect on fatigue fractures
 - (L,M,P)401, 413, 430
- effect on fractures (L,S)94, 95, 455
- fracture origins (E,L,M,P,T)109, 110, 383, 384, 385, 386, 394, 395

fracture profiles (M)

- 25

geometric patterns (T)

- 89

illumination for photography (M)

- 17

impact fracture (L)

- 144

interdendritic fractures (T)

- 89

porosity (L,S,T)

- 100-101

structure (M)

- 17

Wheels, aircraft

- corrosion-fatigue fracture (P,T)366
- failure analysis (E,L,F,T)123, 124
- fatigue-crack-growth rate (E,L,F,T)123, 124
- fatigue fracture (L,M,P)458-459

Wheels, crane

- failure analysis (L)407
- fatigue fracture (L)407

Wing-attachment fitting

- failure analysis (L)413
- fatigue fracture (L)413

Wing spar, stress-corrosion-cracking

- fracture (T)467

Wing-spar caps

- failure analyses (L,M,P)413, 461
- fatigue fracture (L,M,P)413, 461

Wing-spar forging

- failure analysis (L,S)254-255
- fatigue fracture (L,S)254-255

Wing-transport-joint fingers, failure

- analysis (E,F,L,T)122, 123-124

Wire cloth

- tension fracture (M,P)469
- wear (P)468-469

Woody fractures (F,L)

- 29, 30, 136
- crack origins (L)103
- de Réaumur's illustration (F)2, 3
- in 11L40 steel (L)396
- in steel castings (L)454
- in wrought iron (L)300

Worm-gear shaft

failure analysis (L,M)431
 fatigue fracture (L,M)431

Worm track marks, in fracture

surface of 4340 steel (T)312

Wrought iron

impact fracture (L,M,P,T)300, 378
 effect of stringer orientation (T) ...300
 effect of temperature (T)300
 microstructure (M)300
 effect of specimen orientation (M) ..300
 microvoid-coalescence fracture (T) ...300
 notch-impact fracture (L,T)300
 stringers (L,M,T)300

X, Y, Z

X-ray spectrometers 26

Yokes

failure analysis (L,P,S)240-241
 fatigue fractures (L,P,S)240-241

Zapffe, Carl A.6-7, 129, 139

Zinc

cleavage fracture (L)160
 impact fractures (L)160
 kink bands (L)160
 twin bands (L)160

Zinc-aluminum alloy

fracture, relation to microstructure
 (L,M) 8
 impact fracture (L) 8
 microstructure (M) 8

Zinc single crystal, cleavage fracture (L) 160

Zircaloy-2

dimples (S)280
 fatigue fractures (P,S)280
 fatigue striations (S)280
 tension-compression fracture (S)280

Zircaloy-4

fatigue fracture (S)280
 fatigue striations (S)280

[illegible]

IUPUI
UNIVERSITY LIBRARIES
COLUMBUS CENTER
COLUMBUS, IN 47201

no card

REFERENCE

TA
459
.A5
1961
v.9

American Society for Metals.
Metals handbook/ prepared under the
direction of the ASM Handbook
Committee. 8th ed. Metals Park, Ohio:
The Society, [1961-
v. : ill. ; 18-28 cm.

AUG 17 1978



3 0000 000 038 210

STEREO VIEWER

The pocket below contains a stereo viewer for use in

Toward light source

KEEP

parallel to the
stereo picture

